(19)

ASPECTS OF HYDRODYNAMICS AND HEAT TRANSFER IN CIRCULATING FLUIDIZED BEDS

by

Matthew R. Hyre

M.S. Mech Eng., Villanova University (1991)
B.S. Nuclear Eng., United States Military Academy, West Point (1987)

Submitted to the Department of
Mechanical Engineering in Partial
Fulfillment of the Requirements
for the Degree of

Doctor of Philosophy in Mechanical Engineering

at the

MASSACHUSETTS INSTITUTE OF TECHNOLOGY

May 1995
[June 1995]

Signature of Author _____
Department of Mechanical Engineering
8 May 1995

Certified by _____
Leon R. Glicksman
Professor, Department of Mechanical Engineering
Thesis Supervisor

Accepted by _____
Ain A. Sonin
Chairman, Departmental Committee on Graduate Studies
Department of Mechanical Engineering

Aspects of Hydrodynamics and Heat Transfer in Circulating Fluidized Beds

by

Matthew Hyre

Submitted to the Department of Mechanical Engineering on May 8, 1995
in Partial Fulfillment of the Requirements for the Degree of
Doctor of Philosophy in Mechanical Engineering

ABSTRACT

Simplifications to the set of scaling parameters for dynamic similarity of fluidized beds derived from dimensional analysis of the equations of motion for a particle-fluid suspension were explored. A new set of simplified scaling laws includes the Froude number based on column diameter, the solid to gas density ratio, the ratio of superficial to minimum fluidization velocity, bed geometric ratios, and particle sphericity and size distribution. When the gas to particle drag is represented by either the Ergun equation or a single particle drag equation, the new simplified laws hold exactly in both the viscous dominated and gas inertia dominated limits. For intermediate conditions, the gas to particle drag is well approximated in models based on the simplified scaling laws. The simplified scaling laws allow very small models to be constructed which properly simulate the hydrodynamics of a full size reactor or combustor.

Experimental confirmation of the new simplified scaling laws and the viscous limit scaling parameters, where equality of the density ratio is omitted, were carried out in circulating fluidized beds. Within the viscous limit, the solid to gas density ratio is an important modeling parameter when the slugging regime is approached. In general, the solid to gas density must be matched to achieve good similarity. Using the new simplified scaling laws, good agreement was observed even when the length scale of the air fluidized model was as small as 1/16 that of an atmospheric combustor.

The parameters which govern the convective heat transfer to the wall a CFB were determined from an analysis of the non-dimensional energy equation. Experiments were performed for an evaluation of similarity in convection heat transfer between hydrodynamically and thermally similar beds. Heat transfer measurements were taken at three different bed heights in a 1/4 and 1/16 scale model of the Studsvik 2.5 MWth atmospheric circulating fluidized bed combustor. Results showed good agreement between Nusselt numbers over a range of operating conditions and bed heights.

Heat transfer to the walls of circulating beds is primarily due to conduction from clusters of particles falling along the walls. The magnitude of the heat transfer coefficient decreases with increased contact time of particle clusters at the wall. Conditions which promote more rapid cluster breakup can augment heat transfer if the fraction of the surface covered by particles is not significantly reduced. An experimental investigation was conducted to determine if bed to wall heat transfer in a circulating fluidized bed could be significantly enhanced through the use of heat transfer surfaces constructed to minimize the time of cluster contact while not drastically reducing the fraction of the wall covered by clusters. Convective heat transfer measurements were taken at three separate axial locations in a 1/16 scale cold model of the Studsvik 2.5 MWth combustor. The bed wall geometry was altered

to include small horizontal ridges placed at systematic intervals along a heat transfer panel. The use of the altered heat transfer geometries was found to increase the bed to wall heat transfer by up to 30 percent over the flat wall case. Very small amplitude roughness elements ($\sim d_p$) were effective in disrupting wall flow.

The surface renewal model of heat transfer from a CFB was extended to include the transient aspects of the effective gas layer thickness between the wall and first layer of clusters, the contact time at the wall, and the fraction of the wall covered by clusters. The resulting model allows fro the prediction of heat transfer from a surface including uniformly spaced horizontal ridges which has been designed to augment the heat transfer by controlling the time a cluster remains at the wall.

A numerical model of the solids flow and distribution within a circulating fluidized bed is developed. The model is based on a Lagrangian simulation for determining particle dispersion. In this approach, dispersion effects are determined by tracking particles through a continuous succession of turbulent eddies superimposed upon the mean gas flow. Each eddy is characterized by a mean time and length scale, and the velocity fluctuations are randomly generated in a Gaussian manner as a particle enters an eddy. This approach results in a Monte-Carlo procedure where many particle trajectories (realizations) must be computed to obtain averaged properties. The simulation includes the effects of particle inertia, 'crossing-trajectories,' particle sphericity, bed voidage, and particle-particle interactions. Calculated dispersion coefficients are then used to predict the average dilute phase axial solid fraction profile in the core of a CFB. Overall mass and momentum equations for the core-annular structure of a CFB are solved to determine the annular layer thickness, voidage, and fall velocity. Model results are in good agreement with experimental data for CFB's, and FCC reactors.

Previous research has shown the diameter of a circulating fluidized bed has a significant effect on the heat transfer rates to peripheral walls. In order to understand the effect of bed diameter on heat transfer, two laboratory-sized scale models were built and run at room temperature. The two units were the same height and were run at the same operating conditions with the same particles; the only difference was that the diameter of the second unit was 50% larger than that of the first. The two scale models were designed to simulate the hydrodynamic behavior of pressurized CFB's 14.3 m tall with diameters of 0.33 m and 0.50 m respectively. To compare the effect of bed diameter on heat transfer, the fraction of the wall covered by clusters of particles was measured. The coverage of the wall by clusters was determined from visual data recorded with a digital high-speed video camera through the transparent wall, with subsequent measurements using image-analysis software. The results show that a 50% increase in bed diameter can nearly double the fraction of the wall covered by clusters. Using the surface renewal model of heat transfer from a CFB, an increase in the convective heat transfer (excluding radiation) of up to 60% can be predicted due to the increase coverage of the wall by clusters.

Thesis Committee:

Prof. Leon R. Glicksman (Chairman)
Prof. Peter Griffith
Prof. John H. Lienhard
Prof. Adel F. Sarofim

ACKNOWLEDGMENTS

I would like to thank Prof. Leon Glicksman for his support and guidance during the past four years. The confidence he expressed in allowing me to shape the direction of much of this thesis made for an enjoyable stay at MIT. Any criticisms as to the length or shape of this thesis should be directed entirely at the author.

Many students directly influenced the ideas and paths taken in this thesis. For those ideas which turned out to be really lousy and those paths which were dead ends, I'm sure their influence was entirely unintentional. With this disclaimer, thanks go to members of the MIT Fluidization Group during the course of this work: Peter Noymer, Mike Lints, and Tom Yule. I would especially like to thank Paul Farrell and Detlef Westphalen with whom I worked closely over the course of this thesis. The many discussions and debates we had were an invaluable addition to my education - even the few about fluidized beds.

Finally, I wish to express my deepest thanks for my soon-to-be-wife, Wendy. She kept all night vigils for me during the weeks before the qualifying exams, and put up with ranting tirades during the more frustrating times of this project. Additionally, Wendy endured the rough draft, in inebriated monologue form, of everything contained in this document at one time or another. Her love and understanding were truly inspiring.

This project was funded by several agencies. The support of the Electric Power Research Institute, DOE METC, and the National Science Foundation is greatly appreciated.

Intentionally Blank Page

TABLE OF CONTENTS

CHAPTER 1

GENERAL INTRODUCTION

TABLE OF CONTENTS

CHAPTER 2

HYDRODYNAMIC SCALING FOR CIRCULATING FLUIDIZED BEDS

TABLE OF CONTENTS

APPENDICES

CHAPTER 3

THERMAL SCALING FOR CIRCULATING FLUIDIZED BEDS

TABLE OF CONTENTS

CHAPTER 4

HEAT TRANSFER ENHANCEMENT IN CIRCULATING FLUIDIZED BEDS

TABLE OF CONTENTS

APPENDICES

CHAPTER 5

THE HYDRODYNAMIC MODELING OF CIRCULATING FLUIDIZED BEDS

TABLE OF CONTENTS

CHAPTER 6

THE INFLUENCE OF BED DIAMETER ON HYDRODYNAMICS AND HEAT TRANSFER IN CIRCULATING FLUIDIZED BEDS

TABLE OF CONTENTS

ORGANIZATION OF THESIS

This thesis is divided into five distinct chapters, each of which has numerous sections. The chapters were written to stand alone such that the reader can skip from one to another without a loss of continuity. The nomenclature is defined within the text of each chapter. The figures and equations are numbered consecutively within each section of each chapter. The following provides a brief description of each chapter and its importance relative to the rest of the thesis. Additionally, the more important Sections in the chapters are pointed out.

Chapter One: General Introduction

This chapter provides an overview of the circulating fluidized bed technology and compares it to other conventional combustion technologies. Those who already have a good understanding of the main components and operation of CFB's can skip this chapter.

Chapter Two: Hydrodynamic Scaling

This chapter describes the major effort of this thesis. Section 2 provides a rigorous development of the complete set of scaling parameters. For those not interested in the math, it is suggested that you skip to section 2.12. Section 3 presents how the "complete" set of scaling parameters were simplified for use in the scaling studies in this thesis. This is the most important theoretical section in this chapter. Section 4 describes the experimental equipment used. The final 4 sections present the verification of the parameters developed in section 3. The more important verifications were done on hot combustors (sections 7 and 8).

Chapter Three: Thermal Scaling

This chapter is essentially an extension of chapter 2. It is fairly short and easy to read. It extends the hydrodynamic scaling parameters to include thermal scaling parameters.

Chapter Four: Heat Transfer Enhancement

This chapter is based on a study which was a direct result of interesting phenomena discovered during the thermal scaling. It is the least important part of the thesis. The ultimate conclusion reached from this section is that one can increase the heat transfer

between the CFB bed and wall by placing horizontal ribs on the wall. Theory and experimental results are presented which support this conclusion. The most important section in this chapter is section 3, which describes the experimental results for the different wall geometries.

Chapter Five: CFB Hydrodynamic Modeling

This chapter represents an attempt to model the hydrodynamics in a CFB through a simplified numerical scheme. Regardless of all the simplifying assumptions made. It is still a rather difficult chapter to read. The most important sections in this chapter are sections 2 (which describes the dispersion model), 4 (which describes the global CFB model), and 10 (which represents the results). Additionally, a summary section (section 8) is included so that one can skip the complex derivations and proceed right to this sections.

Chapter Six: Effect of Bed Width on CFB Hydrodynamics

The preliminary results of a study aimed at determining the effects of bed width on hydrodynamic phenomena in CFB's are presented in this chapter. The study is specifically aimed at determining the relationship between bed width and bed-to-wall heat transfer.

CHAPTER 1

GENERAL INTRODUCTION

1.0 INTRODUCTION

A circulating fluidized bed is a device for generating steam by burning fossil fuels in a furnace operated under a special hydrodynamic condition: fine solids are transported through the furnace by gas flowing at a velocity exceeding the average terminal velocity of the particles, yet at a low enough velocity to allow a degree of refluxing of solids adequate to ensure uniformity of temperature in the furnace. CFB systems were first developed and applied commercially in the early 1940's for the fluid catalytic cracking processes and functioned as chemical reactors.

Figure 1.1 illustrates the basic components of a CFB system. The component of major interest in the CFB is the vertical riser, wherein the desired gas solid contacting is achieved. Solids introduced at the base of the riser are entrained by means of upflowing gas. The resulting gas-solid suspension within the riser forms the CFB. This gas-solid suspension then exits the top of the riser and enters a gas solid separation system, indicated as a cyclone. The captured solid particles are then returned back into the base of the riser by means of a return line and solid feed system to complete the closed-loop path of the solid particle flow. The gas makes only a single pass through the riser and exhausts through the top of the cyclone.

The creation of the special hydrodynamic conditions of particle refluxing, is the key to the CFB process. The combination of gas velocity, solids recirculation rate, solids characteristics, volume of solids, and the geometry of the system gives rise to this special hydrodynamic conditions under which solid particles are fluidized at a velocity greater than the terminal velocity of individual particles. Yet these particles are not entrained immediately as expected in pneumatic transport systems. Solids move up and down in the form of aggregates, causing a high degree of refluxing. These aggregates are continuously formed, dispersed, and formed again.

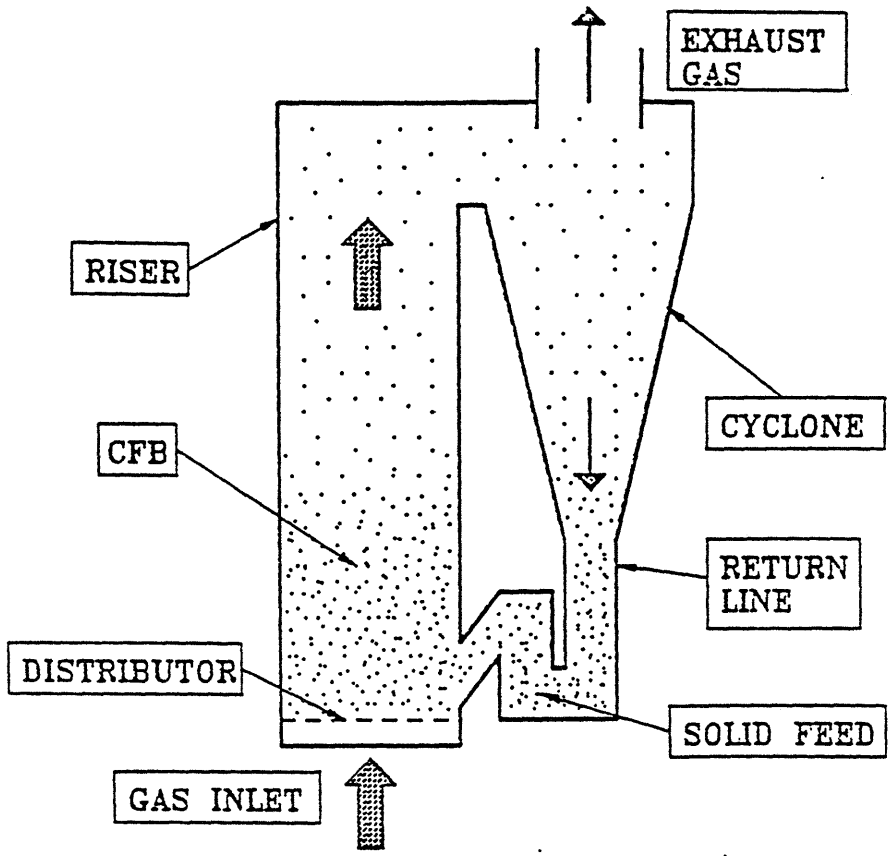

Figure 1.1: Basic Components of a CFB System

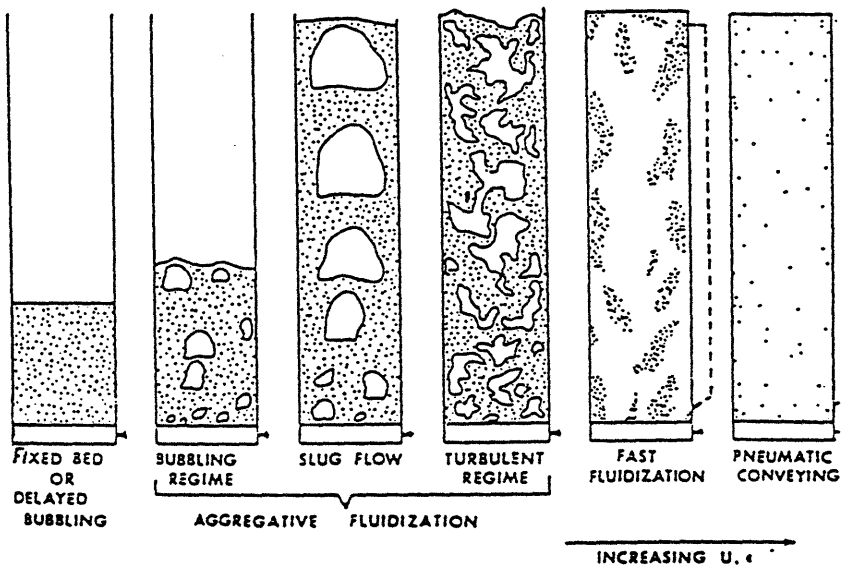

Figure 1.2: Vertical Gas-Solid Flow Regimes

CFB boilers have a number of features that make them more attractive than other solid fuel fired boilers. These features include:

1. Fuel flexibility due to excellent gas-solid and solid-solid mixing

2. High combustion efficiency due to good gas-solid mixing, high burn rates, and recycling of unburned fuel particles back to the furnace

3. Efficient sulfur removal due to high gas residence times, small sorbent sizes and good gas-solids mixing

4. Low NOx emissions due to the staging of combustion

5. Small furnace cross section because of the high heat release rates due to high superficial gas velocities and intense gas-solid mixing

6. Fewer fuel feed points required because of the good gas-solids mixing in the bottom of CFB's along with the extended combustion zone

7. Good turndown and load following capability by adjusting the solids recycle rate

Table 1.1 presents a comparison of CFB combustors with other types of boilers.

Table 1.1: Comparison of Combustor Technologies

Characteristic	Stoker	Bubbling	Circulating	Pulverized
Height of bed or fuel burning zone	0.2	1 - 2	15 - 40	27 - 45
Superficial velocity (m/s)	1.2	1.5 - 2.5	4 - 8	4 - 6
Excess air	20 - 30	20 - 25	10 - 20	15 - 30
Grate heat release rate (MW/m^2)	0.5 - 1.5	0.5 - 1.5	3 - 5	4 - 6
Turn down ratio	4:1	3:1	3-4:1	
Combustion efficiency	85 - 90	90 - 96	95 - 99	99
NO_x emission (ppm)	400 - 600	300 - 400	50 - 200	400 - 600
SO_2 capture in furnace (%)	None	80 - 90	80 - 90	Small

Atmospheric pressure CFB technology has matured to the point where manufacturers are offering units of up to 300 MW size which are designed to meet all current thermal and emissions requirements. Pressurization of CFB's, however, is a relatively new technology with only pilot scale plants in operation, and a few utility scale plants currently planned. Significant construction and design is underway or has been completed despite deficiencies in the understanding of heat transfer and hydrodynamic in CFB's. Instead of using theoretical models, manufacturers extrapolate to larger designs based on past experience.

A major issue facing developers of new technologies is the risks associated with scaling developmental and demonstration facilities to large commercial plants successfully. In order to qualify for performance guarantees, as well as financing in many cases, developers are often conservative in scaling to larger unit sizes, resulting in a longer development-to-commercial time. Issues associated with scaling to larger sized combustion systems includ heat release and heat transfer - which effect thermal efficiencies, combustor hydrodynamics - which can effect both combustion and environmental efficiency, boiler operability, and availability.

To reduce scaling risks and accelerate commercialization of new technology physical models can be developed to simulate larger designs for very low costs, and can provide basic information as to the hydrodynamics, erosion potential and heat transfer characteristics of new designs. This not only provides data for validating a specific plant design, but can also be used to improve operability and performance of existing and new plants.

In the last decade, the concept of properly scaled cold experimental models to simulate the hydrodynamics and heat transfer of a hot bed combustor has been put forward [Nicastro and Glicksman, (1984), Glicksman *et al.* (1993)]. Results have shown that a suitably designed cold fluidized bed can closely simulate the behavior of an atmospheric combustor. Proper scaling involves the use of particles and bed dimensions so that the controlling dimensionless parameters are equal for the hot and cold bed.

2.0 FLUIDIZATION REGIMES

The gas-solid two-phase flow regime that is desired within the CFB can be described through an analysis of the various regimes of fluidization (see Figure 1.2). Assume that an initial charge of particles is placed on top of the gas distributor plate within the riser and the superficial gas velocity is increased slowly from an initial value of zero. At low superficial gas velocities, the particles would remain fixed in the bed. At a slightly higher velocity, the minimum fluidization point would be reached, at which the hydrodynamic forces on the particles balance the weight of the particles. At slightly higher superficial gas velocities, gas bubbles would begin to form within the bed and the bubbling regime of fluidization is encountered. At still higher superficial gas velocities these bubbles would coalesce into large bubbles and possibly grow to approach the diameter of the riser causing the slugging regime to be encountered. As the gas velocity is raised through the slugging regime, there is a gradual transition to the turbulent regime of fluidization. This regime is characterized by the gradual breakdown of the two-phase structure that exists within bubbling and slugging fluidized beds, in which a dense phase emulsion forms the continuous phase with gas voids interspersed. In the turbulent state of fluidization gas voids or bubbles no longer exist. The turbulent bed consists of refluxing strands of particles and neither the dense phase nor the lean phase are continuous. The transition from slugging to turbulent fluidization is apparent by observing the sudden decrease in the pressure fluctuations within the bed. The measured slip velocities in the turbulent fluidized bed may become an order of magnitude

greater than the terminal velocity of an individual particle. Surprisingly, the high slip velocity condition exists with little entrainment from the bed. Therefore, the turbulent bed may be characterized as having stationary solid particles and an identifiable bed surface, although much more diffuse than exists for bubbling and slugging beds.

As the superficial gas velocity is increased through the turbulent fluidized bed regime, the CFB regime is entered. Like the transition from slugging to turbulent fluidization, the transition from the turbulent regime to the CFB regime is also gradual. This transition is marked by an increasing rate of particle entrainment with increasing gas velocity which eventually becomes so high that unless the entrained particles are returned to the bed, the inventory of particles is soon depleted. This gas velocity, above which the rate of particle entrainment through a vertical riser of sufficient height has increased sharply, marks the transition to the CFB regime and is known as the transport velocity. Beyond the transport velocity, solids pass through the riser in fully entrained flow and the volumetric concentration of solids in the riser depends not only on the gas velocity, but also on the rate at which solids are fed back into the base of the riser.

With further increases in superficial gas velocity and at relatively low solid mass fluxes, the dilute-phase flow regime is encountered. Solid particle concentrations in this regime are very low and the particles stream upwards in relatively straight paths. Measured slip velocities approximately equal particle terminal velocities. As the solid mass flux in the riser is increased while holding the gas velocity constant, the solid suspension in the riser becomes progressively denser. At a sufficiently high mass flux within the riser, the CFB regime is established. The CFB regime, in comparison to the dilute phase flow regime, is characterized by relatively high solid particle concentrations within the riser, aggregation of particles in clusters which may break apart and reform in rapid succession, and extensive backmixing. Table 2.1 presents a comparison of the principle continuous gas-solid contactors range of operation.

Table 2.1: Comparison of Fluidization Technologies

Property	Packed Bed	Bubbling Bed	Circulating Bed	Pneumatic Transport
Application in Boilers	Stoker Fired	Bubbling Fluidized Bed Combustors	Circulating Fluidized Bed Combustors	Pulverized Coal Power Plants
Mean particle diameter (mm)	< 300	0.03 - 3	0.05 - 5	0.02 - 0.08
Gas velocity through combustor zone (m/s)	1 - 3	0.5 - 3	3 - 12	15 - 30
Typical u_o/u_t	0.01	0.3	2	40
Gas motion	up	up	up	up
Solids motion	Static mixing	Up and down	Mostly up, some down	Up
Gas mixing	Near plug flow	Complex two phases	Dispersed plug flow	Near plug flow
Solids mixing	None	Good	Near perfect	Near plug flow
Overall voidage	0.4 - 0.5	0.5 - 0.8	0.85 - 0.99	0.98 - 0.998
Temperature Gradient	Large	Very small	Small	Large
Typical bed-to-surface heat transfer coefficient (W/m^2-K)	50 - 150	200 - 550	100 - 250	50 - 100
Attrition	Little	Some	Some	Considerable
Agglomeration	Considerable	Some	None	None

3.0 OVERVIEW OF CFB HYDRODYNAMIC MODELS

A variety of models for the hydrodynamics of CFB's have been published. These can be broadly classified into three groups

1. Simple Axial Solids Distribution Models - those models that predict the axial variation of solids volume fraction but do not predict explicitly the radial distribution of solids

2. Core-Annulus Models - those models that approximate the radial distribution of solids by division of the flow into two or more regions

3. CFD Models - those models that use computational fluid dynamic techniques to predict two phase gas/solid flow from fundamental equations.

3.1 Simple Axial Solids Distribution Models

The simple axial distribution models usually are aimed at approximating the voidage as a function of bed height. Knowledge of the average voidage as a function of height is important for estimating total CFB pressure drop, heat transfer, heat release by combustion, and bed inventory requirements. An approximation of the voidage profile is fairly easy to determine for an experimental facility by using differential pressure measurements. Typically, the voidage profile of a CFB is has an "S" shape, with low voidage near the bottom and higher voidage near the top. The Kwauk log profile model (Kwauk *et al.* 1986) is frequently cited because of its mathematical simplicity:

$$\frac{\varepsilon - \varepsilon_a}{\varepsilon_* - \varepsilon} = \exp\left(-\frac{(z - z_i)}{z_0}\right) \tag{1}$$

where ε is the cross-sectional average voidage at height z, ε_a and ε_* are the voidages which are approached asymptotically at the bottom and top of the bed. The parameter z_0 is a characteristic length over which the voidage increases for ε_a to ε_*, and z_i is the inflexion point, which is centered on the region of voidage increase. The model was based on a balance between the upward diffusion flux of clusters and their downward gravitational flux. The variables ε_a, ε_*, and z_0 must be determined through empirical correlation. Determination of z_i is based on a pressure balance between the riser and the downcomer. The underlying mechanisms of the model of Kwauk are based on a number of unstated assumptions, not least of which was a postualtion for the axial diffusion mechanism which is inconsistent with Newton's second law [Harris (1993)].

Rhodes and Geldart (1990) proposed a model which described the dilute region of a CFB as being analogous to the freeboard of a bubbling bed. The dense region of a CFB was

approximated as a bubbling bed. Entrainment from the surface of the dense region was modeled using well known approximations [see, for example, Wen and Chen (1982)]:

$$\frac{E - E_\infty}{E_0 - E_\infty} = \exp\left(-K(z - z_0)\right) \tag{2}$$

where E_0 is the entrainment at the bed surface, E_∞ is the saturated carrying capacity, z_0 is the height of the bed surface, and K is the decay coefficient. The net flux G_s for the column is the value of E at the top of the riser. Equation (2) describes the entrainment for that portion of the riser above the dense bed. Rhodes and Geldart suggested ignoring the downflowing solids and solving for the voidage by assuming that the slip velocity is equal to the single particle terminal velocity. The resulting equation for voidage can be shown to be:

$$u_t\varepsilon^2 - \varepsilon\left(u_o + u_t + \frac{E}{\rho_s}\right) + u_o = 0 \tag{3}$$

Bubbling bed models were used to describe the dense region of a bubbling bed. Correlations for the entrainment values at the bed surface and infinity were given by Wen and Chen (1982). Westphalen (1993), predicted the bed surface flux E_0 to be lower than the net solid flux G_s. In addition, the voidage calculated was much too close to 1 for any reasonable value of E. This is not surprising since the available correlations for E_0 are generally based on bubbling bed data for which the gas fluxes are much lower than that in a CFB. With all its problems and assumptions, the Rhodes/Geldart model is beginning to gain more acceptance with recent data indicating that large CFB's behave as if the dense region were a bubbling bed [Johnsson *et al.* (1992)].

Kunii and Levenspiel (1990) provided improvements to the Rhodes and Geldart model by showing that for typical CFB flows the volumetric solid fraction decreases exponentially with the same decay coefficient K which applies to the upward solid flux. The resultant equation is then

$$\frac{\phi - \phi_\infty}{\phi_0 - \phi_\infty} = \exp\left(-K(z - z_0)\right) \tag{4}$$

where ϕ_∞ is the solid fraction at large heights, and ϕ_0 is the solid fraction at the bed surface. This simplification allows one to correlate for the solid fraction rather than the entrainment

rate. For a given riser, the solid fraction profile can be calculated once ϕ_∞, ϕ_0, and K are known.

Kunii and Levenspiel also presented correlations to determine K, ϕ_∞ and ϕ_0. These correlations are somewhat more reliable than those of Rhodes and Geldart simply because they are based on CFB data rather than bubbling bed data. The database for determination of the fitting parameters in (4) has recently been extended by Adanez *et al.* (1994).

The main problem with the approaches of Rhodes/Geldart and Kunii/Levenspiel is that they assume a CFB can be broken into a distinct dense bottom region and a dilute upper region. For most CFB's, there is not distinct bed surface, rather there is a gradual transition from a region of high solids volume fraction to a much more dilute region. Additionally, these models do not explain the radial variation of flow in CFB's

3.2 Core/Annulus Models

Core annulus models for vertical flow of particulate suspensions predate the current interest in CFB's: Nakamura and Capes (1973) used a core/annulus model to account for their experimental observations in a pneumatic conveying system. Models of this type have found widespread acceptance in the literature.

Yang (1988) presented a model for CFB flow based on a core annulus description of the flow structure. According to this model, flow is upward in the core and downward in the annulus. A continuous exchange of particles occurs between the two regions. The net solid flow is equal to upward flow in the core minus downward flow in the annulus. The core flow was described as pneumatic transport flow at the choking condition in which slip velocity is equal to terminal velocity. The annulus flow was assumed to be at terminal velocity and the annulus voidage was assumed to be equal to minimum fluidization voidage. This model was incomplete in that it did not describe the exchange of particles between the two regions.

Ishii *et al.* (1989) proposed a model based on the assumption that particles move upward in the form of clusters in the core, and downward in clusters in the annulus. Slip velocities in both regions were based on cluster rather than particle diameter; the equation of Richardson and Zaki was used to determine the drag on the cluster. Additionally, the clusters were assumed to be homogeneously distributed throughout the core and annulus. Cluster

diameters and voidages were introduced in the model as dependent variables. Completeness of the model was achieved by assuming minimization of energy dissipation across the bed. This allowed differentiation of a pressure gradient expression with respect to some of the variables, producing additional equations.

Other core-annular models can be found in the literature [Berruti and Kalogerakis (1989), Werther *et al.* (1991), Senior and Brereton (1992), Harris and Davidson (1993)]. In general these models are incomplete, having too many variables. Closure is provided in some cases by an assumption of minimum pressure drop minimization. This approach, while convenient, is not justified physically [Hyre and Glicksman, (1995)]. In addition, most core-annulus models, although providing a detailed description across the riser do not address particle movement across the core annulus boundary rigorously.

3.3 CFD Techniques

Mixture theory equations describing the motion of two-component flows for use in fluidized beds have been developed by Anderson and Jackson (1967). The models typically involve the time/volume/and or ensemble averaging of mass, momentum, and energy balance relations, resulting in a separate set of equations for each of the flow components. These equations are connected by terms for interaction between the phases in the forms of drag, heat transfer, and mass transfer. Ensemble averaged equations are presented in detail in Chapter 2. Time averaging of the equations is usually a preliminary step. An alternate approach is to bypass the volume averaging, thus starting out with a time averaged set of equations. This was first accomplished by Ishii (1975).

Time, volume, and ensemble averaging result in a set of equations which are very complex. The time-averaged equations include many terms representing cross-correlations of various groups of variables. Closure of the system of equations requires that these terms be represented as function of the time-averaged variables. Determination of the closure scheme which accurately represents the physics of the problem is the most difficult problem in the solution of the equations.

Determination of the role of particles in gas turbulence modulation or enhancement, and the gas turbulence and collision induced fluctuations in the particle velocities must all be modeled. The interactions between the particles and gas provide a path for the dissipation of kinetic energy. Additionally particle collisions which occur due to the differences in

particle terminal velocities tend to redistribute turbulent energy from small particles to large particles, which respond much less readily to the gas turbulence. This provides an additional path for dissipation of turbulent kinetic energy. In situations involving only large particles which do not respond significantly to the gas turbulence, the solid fluctuating velocity can be almost entirely due to collisions. Discussions of gas and particle turbulent velocity characteristics are discussed in detail in Chapter 5.

Modeling of stresses in the dense region of a CFB will require consideration of granular shear stresses caused by inertial interaction between successive particle layers. These stresses have been used to describe such things as the motion of sand down a slope (Bagnold, 1954) and avalanches. Recent formulations of equations for gas/particle flows have included granular stress terms. These stresses may be important in understanding the flow of particle layers at the walls and the motion of particles in the dense lower regions of CFB's.

The solution of time-averaged two-component flow equations for a CFB has been investigated by Gidaspow *et al.* (1990) and Lyczkowski *et al.* (1990). These efforts require coefficients which must be determined experimentally and which probably change from condition to condition. The use of such models for design purposes is not yet accepted.

4.0 CONCLUSIONS ON CFB MODELS

While the attraction of CFD models is obvious (ability to deal with complex geometries, multiple air inlets, etc.) there is much controversy regarding the nature of the constituent equations, let alone the numerical complexity of the solution algorithms. Furthermore, the computational effort required for solution is substantial. The simple axial profile models contain many inconsistencies both in terms of the postulated mechanisms and/or the experimental evidence cited in support of the models [see Harris (1992) for a complete discussion of these models]. The core-annulus type models are currently the most promising avenue for providing a comprehensive model which describes the flow and distribution of solids within a CFB. This type of model will be pursued further in Chapter 5, in an attempt to develop a model which takes into account much of the physics of CFB riser hydrodynamics, without requiring the solution of the complete two-phase equations of motion.

5.0 STUDY GOALS

The main goals of this study are fivefold. The first was to develop a set of scaling parameters which allows one to build a small scale model of a large combustor (length ratios of the order 1/16), and then to demonstrate the use of these parameters as an alternative to analytical or numerical modeling for prediction of atmospheric and pressurized CFB behavior. The success of this approach depends on achieving dynamic similarity between a scale model and a full size prototype; all important forces must be modeled in such a way that ratios of force magnitudes are preserved.

The question of whether a set of scaling parameters which allows one to arbitrarily select the size of the scale model used to simulate the combustor can be developed depends on how many independent parameters are required in order to specify the flow. The work described below takes the following approach:

Step 1. A model for the flow with qualifying assumptions is developed

Step 2. A set of independent parameters describing the flow is determined

Step 3. The set of independent parameters developed in step 2 is analyzed to determine possible simplifications due to effects which are secondary or insignificant

Step 4. Experiments are conducted which indicate the validity of the simplified set of parameters

This work is described in Chapter 2.

The second goal of this study was to extend the hydrodynamic scaling parameters to include convective heat transfer. To do this an evaluation of the equations governing heat transfer to the walls of a CFB combustor were analyzed. The set of parameters necessary for insuring thermal similarity were determined, and combined with those necessary for hydrodynamic similarity. Experiments were then performed to indicate the validity of the thermal scaling parameter through a comparison of dimensionless heat transfer coefficients. This work is described in Chapter 3.

The third goal of this study was to develop a model which evaluated the effect of wall geometry on the bed to wall heat transfer in a CFB. Heat transfer to the walls of CFB's is primarily due to conduction from clusters of particles falling along the walls. The

magnitude of the heat transfer coefficient decreases with increased contact time of particle clusters at the wall. Conditions which promote more rapid cluster breakup can augment heat transfer if the fraction of the surface covered by clusters is not significantly reduced.

An experimental investigation was conducted to determine if bed to wall heat transfer in a circulating fluidized bed could be significantly enhanced through the use of heat transfer surfaces constructed to minimize the time of cluster contact while not drastically reducing the fraction of the wall covered by clusters. Convective heat transfer measurements were taken at three separate axial locations in a 1/16 scale cold model of the Studsvik 2.5 MWth combustor. The bed wall geometry was altered to include small horizontal ridges placed at systematic intervals along a heat transfer panel. The experimental data was then compared to a theoretical model which was an extension of the surface renewal model of heat transfer from a CFB. This work is described in Chapter 4.

The fourth goal of this study was to model the lateral solid mixing in CFB risers, and to use this model in the development of an overall hydrodynamic model capable of predicting the time averaged behavior of CFB's. A detailed numerical model was developed which calculated the dispersion of solids in the core of a CFB through a Lagrangian particle tracking technique. The model determined particle dispersion due to gas turbulence and particle-particle collisions. Numeric model results were compared to the solids dispersion data and CFB hydrodynamic data obtained by other investigators. This work is described in Chapter 5.

The final goal of this study was to determine the effect of bed width on overall bed performance. Two beds with the same height, but with different diameters were constructed, using the scaling parameters developed as a result of the first goal. The hydrodynamic effects of bed width on the vertical solids distribution were evaluated. Additionally, visual observations of the transparent wall sections were made with a high speed image analysis system to gain a qualitative estimate of wall coverage by clusters. The wall coverage fraction has a direct influence on the bed to wall heat transfer rate. Results of this work are given in Chapter 6.

6.0 REFERENCES

Anderson, T.B., and R. Jackson, "A Fluid Mechanical Descriptoin of Fluidized Bed," *I & EC Fundamentals*, **6**, p. 527, 1967.

Bagnold, R.A., "Experiments on a Gravity-Free Dispersion of Large Solid Spheres in a Newtonian Fluid Under Shear," *Proc. R. Soc. Lond.*, **A225**, p. 49, 1954.

Berruti, F., and N. Kalogerakis, "Modelling the Internal Flow Structure of Circulating Fluidized Beds," *Canadian Journal of Chem. Engineering*, **67**, p. 1010, 1989.

Gidaspow, D., Y.P. Tsuo, and J. Ding, "Hydrodynamics of Circulating and Bubbling Fluidized Beds," *EPRI Proc. Materials Issues in CFBC*, p. 4-1, 1990.

Glicksman, L.R., M.R. Hyre, and D. Westphalen, "Verification of Scaling Relationships for Circulating Fluidized Beds, *Proc. 12th Int. Conf. on Fluidized Bed Combustion*, p. 69, 1993.

Harris, B.J., and J.F. Davidson, "Modelling Options for Circulating Fluidized Beds: A Core/Annulus Deposition Model," *4th Int. Conf. on Circulating Fluidized Beds*, p. 35, Somerset, PA, August 1-5, 1993.

Harris, B.J., and J.F. Davidson, "Modelling Options for Circulating Fluidized Beds: A Core/Annulus Deposition Model," *4th Int. Conf. on Circulating Fluidized Beds*, p. 35, Somerset, PA, August 1-5, 1993.

Harris, B.J., Ph.D. Dissertation, University of Cambridge, 1992.

Ishii, H., T. Nakajima, and M. Horio, "The Clustering Annular Flow Model of Circulating Fluidized Beds," *Journal of Chemical Engineering of Japan*, **22**, p. 484, 1989.

Ishii, M., *Thermo-Fluid Dynamic Theory of Two-Phase Flow*, Eyrolles, Paris, 1975.

Johnsson, F., A. Svensson, and B. Leckner, "Fluidization REgimes i Circulaitng Fluidized Bed Boilers," *Seventh International Fluidization Conference*, Engineering Foundation, Broadbeach, Gold Coast, Australia, May, 1992.

Kunii, D., and O. Levenspiel, "Entrainment of Solids from Fluidized Beds: I. Hold-Up of Solids in the Freeboard; II. Operation of Fast Fluidized Beds," *Powder Technol.*, **61**, p. 193, 1990.

Kwauk, M., W. Ningde, L. Youchu, and C. Bingyu, "Fast Fluidization at ICM," *Circulating Fluidized Bed Technology*, P. Basu, ed., Pergamon Press, p. 33, 1986.

Lyczkowski, R.W., J.X. Bouillard, S.L. Chany, and G.F. Berry, "Modelling of Hydrodynamics and Erosion in Bubbling and Circulating Fluidized Beds," *EPRI Proc. Materials Issues in CFBC*, p. 5-1, 1990.

Nakamura, K., and C.E. Capes, "Vertical Pneumatic Conveying: A Theoretical Study of Uniform and Annular Particle Flow Models," *Can. J. Chem. Eng.*, **51**, p. 39, 1973.

Nicastro, M.T. and L.R. Glicksman, "Experimental Verification of Scaling Relationships for Fluidized Beds," *Chem. Engng. Sci.*, **39**, 1381-1391, 1984.

Rhodes, M.J., and D. Geldart, "The Upward Flow of Gas/Solid Suspensions Part 1: A Model of the Circulating Fluidized Bed Incorporating Dual Level Gas Entry in the Riser," *Chem. Eng. Res. Des.*, **67**, p. 20, 1989.

Richardson, J.F., and W.N. Zaki, "Sedimentation and Fluidization, Part 1," *Trans. Inst. Chem. Engr*, **32**, p. 35, 1954.

Senior, R.C., and Cl. Brereton, "Modellig of Circulating Fluidised-Bed Solids Flow and Distribution," *Chem. Eng. Sci.*, **47**, p. 281, 1992.

Wen, C.Y., and L.H. Chen, "Fluidized Bed Freeboard Phenomena: Entrainment and Elutriation," *AIChE Journal*, **28**, p. 117, 1982.

Werther, J., E.-U. Hartge, M. Kruse, and W.. Nowak, *Circulating Fluidized Bed Technology III*, eds. P. Basu, M. Horio and M. Hasatani, Pergamon Press, p. 593, 1991.

Westphalen, D., *Scaling and Lateral Solid Mixing in Circulating Fluidized Beds*, Ph.D. Dissertation, Massachusetts Institute of Technology, 1993.

Yang, W.C., "A Model for the Dynamics of a Circulating Fluidized Bed Loop," *Circulating Fluidized Bed Technology II*, P. Basu and J.F. Large, eds, Pergamon Press, p. 181, 1988.

CHAPTER 2

HYDRODYNAMIC SCALING FOR CIRCULATING FLUIDIZED BEDS

1.0 INTRODUCTION

Fluidized beds are employed in a wide variety of applications such as combustors of dirty fuels, chemical reactors, ore roasters and coating applicators, to name a few. In many commercial applications the fluidized bed has a large diameter and height and operates at elevated temperature and pressure. To properly design a fluidized bed the fluid dynamics must be well understood since it directly influences the bed performance. For example, in a bubbling fluidized bed, the size, frequency and distribution of bubbles are directly linked to particle mixing and gas to solid contacting. A bed of uniformly distributed fine bubbles will yield higher chemical conversion than a bed containing a few large bubbles concentrated at the center. The particle residence time in a circulating fluidized bed combustor has a strong influence on the combustion efficiency and the level of pollutant emission.

The dynamics of a fluidized bed has been found to change as the bed size is increased. Designers are particularly concerned about the relationship between the performance of large commercial beds and results obtained from much smaller pilot plants. There is a critical need to understand and predict the fluid dynamics of large fluidized beds. However, there is a dearth of relevant information available in the field concerning large beds, particularly beds operating at high temperature and pressure. Because of the complexity of the multiphase phenomena, a theoretical solution for the bed behavior based on first principles remains a distant unfulfilled goal. There is a large body of data and approximate analytical models based on results from small experimental beds. It is not obvious how this data can be applied to larger commercial designs.

Detailed fluid dynamic investigations can be carried out more conveniently on small beds at ambient conditions. However, there must be a technique to confidently assure that these experimental results accurately duplicate conditions of larger reactors. Similitude or dimensional analysis represents a powerful tool which will allow a small laboratory experiment at ambient conditions to simulate a much larger commercial bed.

Similitude has been used in many fields to allow small controlled experiments to closely simulate physical phenomena. Wind tunnels are commonly used to determine the aerodynamic properties of aircraft and automobiles. Towing tanks are used to judge the performance of proposed ship designs. Water tables are used to simulate the drainage

and flow patterns of large bodies of water. Small scale models are used to determine the performance of building structures in high winds or earthquakes.

Within the last decade investigators have begun applying similitude principles to the study of fluidized bed dynamics. Large commercial fluidized bed combustors have been simulated using smaller laboratory models to determine proper strategy for part load operation, identify possible causes of erosion of in-bed surfaces and to determine heat transfer performance. The simulations have helped to identify parameters controlling bed dynamics and to investigate fundamental flow phenomena. Of particular note is the initiation of studies to determine the influence of increased bed size on performance: the scale up issue.

Similitude is a powerful experimental tool which can aid the fluidized bed designer and researcher. However, the same maxim holds in this field as in computer programming, a less than careful application can yield useless output or worse, highly misleading design projections. Over its history the field of fluidization has its share of model studies carried out without careful consideration of the similitude relations. Simply building and operating a model with the same geometric shape as the full scale bed will not lead to valid results. In some cases the particles used in the small scale ambient temperature model were identical to those used in the large scale high temperature bed! The results of such studies were less than illuminating.

Similitude principles make it possible to build an experimental model which duplicates the performance of another bed. That bed may be a larger experimental model operated at the same pressure and temperature or it may be a large commercial bed or pilot plant operated at elevated temperature and/or pressure, possibly with a different fluid and particle material.

As boiler manufacturers build larger commercial size fluidized bed combustors, a critical problem they face is the influence of bed size on the bed performance. Without a base of experience in large beds it is difficult for them to anticipate the performance characteristics of large beds or to correct problems which arise in new systems. A key issue of the larger beds is the influence of the bed hydrodynamics on such properties as uniformity of mixing of the coal feed, bed temperature uniformity and the ratio of heat release by combustion to heat transfer to in-bed heat exchanger surfaces.

In addition, correction of problems on large combustors is hampered by the lack of good diagnostic tools which can be used in a hot environment. Tests which vary the operating or design parameters of a large hot bed are lengthy and can be prohibitively expensive.

In a previous paper (Glicksman [1984]), a set of scaling relations was developed which allowed a bed operating at ambient conditions to model a bed at elevated temperature and pressure. In the general case both beds must have equal values of the Reynolds numbers based on bed diameter and particle diameter, equal Froude numbers and solid to gas density ratios. In addition the beds must be geometrically similar and have identical dimensionless particle size distributions and sphericity. These conditions will be referred to the full set of scaling parameters.

Several experimental confirmations of the full set of scaling parameters have been carried out. Nicastro and Glicksman (1984), showed close agreement between the time resolved pressure differences in a bubbling bed combustor at atmospheric pressure and a cold model. With the full set of scaling parameters the scale model had linear dimensions of the bed and the particles which were one quarter of the combustor. Fitzgerald *et al.* (1983) showed qualitative agreement between two beds fluidized with different gases; the disagreements were probably due to static electric effects. Newby and Keairns (1986) carried out a validation of the full scaling laws using a bed of 200 micron glass spheres fluidized with air at standard conditions and a geometrically similar bed of 100 micron steel particles fluidized with pressurized air. They found close agreement between the dimensionless bubble size and frequency for both beds. Glicksman *et al.* (1989) presented results for the TVA atmospheric fluidized bed combustor; these results were in close agreement with results obtained in a cold scale model designed with the full set of scaling parameters. Chang and Louge (1992) were able to simulate combustors of different bed diameters with a single experimental model by varying the composition of the fluidizing gas. They also found that when the surface of the particle was treated to yield artificially low friction factors, the behavior of the bed was altered. They conclude that the friction coefficient should not be an additional scaling factor when ordinary particles, without the special treatment, are used in the full scale and model beds. Glicksman *et al.* (1991) carried out comparisons between a small circulating bed combustor and a cold model constructed using the full set of scaling laws. For circulating beds, a dimensionless solids flow rate must also be matched between the two beds. The two beds showed close agreement. The wall roughness was found to exert an important influence on the bed behavior; a dimensionless wall roughness must be included in the

geometric similarity relationships for the model. Westphalen (1993) compared average solid fraction profiles between a 2.5 MWt Studsvik combustor and a 1/4 scale model using the full set of scaling parameters. Agreement was good, especially near the top of the bed.

When constructing a model fluidized with ambient air, matching the full set of scaling parameters results in an unique set of values for the particle density and diameter and for the linear dimensions of the bed. To model an atmospheric combustor operating at about 800°C, the model has linear dimensions one quarter those of the combustor. By simplifying the set of scaling relationships, it is possible to relax the constraint on the dimensions of the model relative to the full scale bed. Glicksman (1984) identified a viscous region, for small particles and low velocities, where the gas inertial effects are negligible. Similarly, an inertial dominated region exists in beds of large particles at high velocities where the gas viscous effects should be minimal. Modified criteria for the applicability of these scaling relationships were later suggested by Horio (1990). In both of these regions, the simplified scaling laws permit some flexibility in model design. Horio *et al.* (1986) proposed a set of scaling relationships which differed from those mentioned above. Glicksman (1988) demonstrated that Horio's set was identical to the viscous limit for the full set of scaling laws. Roy and Davidson (1988) examined the limits of the viscous region as proposed by Glicksman in bubbling beds at different temperatures and pressures (see Table 1.1). They compared measurements of the major frequency, maximum amplitude and standard deviation of the amplitude to determine similarity. Most of their tests were carried out at a particle Reynolds numbers of 8 or below. For tests at low Reynolds number they found that it was not necessary to match the gas to solid density ratio and the particle to bed diameter ratio. Two tests carried out at Reynolds numbers of 64 and 105, respectively, did not agree with companion tests using the reduced set of parameters valid for the viscous limit. A single test carried out at a Reynolds number of 33 did agree with companion tests; in this test the solid to gas density ratio was also identical to the ratio for the companion tests.

Horio *et al.* (1989) derived a scaling law for circulating bed from consideration of the core and annulus regions in a circulating bed. The resulting scaling law matched superficial gas, particle velocity, and particle terminal velocity to the square root of the linear dimensions. The particle size was determined to satisfy the terminal velocity criteria. They built two scale models of a circulating bed combustor with linear dimensions which varied by a factor of four. The two models exhibited reasonably good agree-

ment with each other for vertical voidage distributions. The two models used the same particle density and fluidizing gas conditions. Although equality of gas to solid density ratio was mentioned as one possible scaling parameter, no attempt to match this parameter between the model and the combustor was made. The solid to gas density ratio for the models differ from that for the combustor by a factor of 5.5. Data was not presented for the combustor; thus proper scaling between the cold models and the combustor could not be verified. Ishii and Murakami (1991) compared two geometrically similar beds using the same particle material and fluidizing gas properties, the scaling was based on the parameters given by Horio *et al.* (1989). They found close agreement in measured peak frequency, flow transition, and measurements made with a light reflecting probe. Their peak particle Reynolds number was about 4.5.

Tsukada *et al.* (1991) compare the behavior of a circulating bed fluidized at pressures between 0.1 MPa and 0.35 MPa. They maintained the particle diameter, the solids flow rate and the gas velocity constant. They found similar results between 0.1 MPa and 0.18 MPa but found considerable differences at the highest pressure which they attribute to exceeding an upper limit in Reynolds number or to a change in gas bypassing, their highest value of Reynolds number was approximately 5.

The goal of the present study is the systematic identification and verification of a simplified subset of scaling parameters. This subset should allow the scale model to simulate much larger hot combustors. The development of a set of heat transfer scaling parameters will also be undertaken. The heat transfer scaling will allow the bed to wall convective heat transfer to be simulated and measured in a cold model.

Section 2 presents a rigorous development of the full set of scaling parameters. Section 3 deals with the simplification of these parameters. Section 4 describes the experimental setups used to validate the varous simplified relationships. Section 5 presents the results of attempts to scale CFB hydrodynamics using the viscous limit relationships. Section 6 presents the results of scaling using the simplified scaling laws with constant density ratio. The simplified scaling laws were used to construct a small cold models of an atmospheric and pressurized combustor, hydrodynamic comparisons are given in Sections 7 and 8.

Table 1.1: Runs Conducted by Roy and Davidson (1988)

RUNS AT LOW AND HIGH TEMPERATURES					
Condition/Run	**A**	**B**	**C**	**D**	**E**
Agreement with Run A	-	Yes	Yes	No	Yes
ρ_s (kg/m^3)	2650	7100	7100	7100	2650
d_p (x 10^6 m)	600	180	500	900	240
u_{mf} (m/s)	0.15	0.09	0.64	1.25	0.07
p (bara)	1	1	1	1	1
T (K)	1023	288	288	288	288
D (m)	0.135	0.045	0.045	0.045	0.045
u_o (m/s)	0.78	0.45	1.0	1.6	0.43
$u_{mf}/(gD)^{0.5}$	0.13	0.14	0.9	1.9	0.11
$Fr=(u_o-u_{mf})/(gD)^{0.5}$	0.55	0.56	0.55	0.54	0.55
d_p/D (x 10^3)	4.4	4	11	20	4.2
ρ_f/ρ_s (x 10^4)	1.5	1.7	1.7	1.7	4.9
$Re = \rho_f u_o d_p/\mu$	4.1	5.5	33	105	7.4

RUNS AT LOW AND HIGH PRESSURES						
Condition/Run	**F**	**G**	**H**	**I**	**J**	**K**
Agreement with Run F	-	Yes	Yes	Yes	No	Yes
ρ_s (kg/m^3)	384	2650	2650	2650	2650	2650
d_p (x 10^6 m)	240	120	120	240	550	550
u_{mf} (m/s)	0.02	0.01	0.02	0.07	0.09	0.14
p (bara)	1	6	1	1	6	1
T (K)	288	288	288	288	288	288
D (m)	0.28	0.1	0.1	0.28	0.1	0.1
u_o (m/s)	0.27	0.16	0.17	0.32	0.24	0.29
$u_{mf}/(gD)^{0.5}$	0.01	0.01	0.02	0.03	0.09	0.14
$Fr=(u_o-u_{mf})/(gD)^{0.5}$	0.15	0.15	0.15	0.15	0.15	0.15
d_p/D (x 10^3)	0.9	1.2	1.2	0.9	5.5	5.5
ρ_f/ρ_s (x 10^4)	3.3	2.9	4.9	4.9	2.9	4.9
$Re = \rho_f u_o d_p/\mu$	5	8	1.5	4	64	12

2.0 DERIVATION OF SCALING RELATIONSHIPS

2.1 Introduction

The full set of scaling parameters will be derived in this section. This will form the basis for an initial set of simplifications to the scaling laws. With the scaling laws in hand, a review of past work will be undertaken with particular emphasis on attempts to simplify the governing relationships. Those readers not interested in the rigorous derivation of the full set of scaling parameters should proceed directly to Section 2.12.

When the equations governing a particular phenomenon can be written, the most insightful way to derive the scaling relationships is to non-dimensionalize the governing equations (Kline, 1965). Thus, the equations reveal useful information even though they cannot be solved in general.

2.2 Mixture Theory Equations

Mixture theories are based on the idea of interpenetrating continua in which actual material points are no longer identifiable; the solid and fluid phases are both present at each and every material point. The ideas of mixture theory can be traced back to that branch of mechanics which calls itself rational; a complete account is given by Bowen (1971), with more recent developments given in papers by Nunziato *et al.*, (1986) and Passman *et al.* (1984). Related ideas based on ensemble averaging can be found in Drew (1986). Let ρ, $\mathbf{V}$, P and $\mathbf{T}^*$ be the true density, velocity, pressure and stress in the flowing composite. Let ϕ be the solids fraction and $\varepsilon = 1 - \phi$ the fluid fraction. In mixture theory, equations of balance are postulated for interpenetrating fields with variables γ_f, γ_s, $\mathbf{v}_f$, $\mathbf{v}_s$, $\mathbf{T}_f$, $\mathbf{T}_s$, p_f, p_s, where $\gamma_f = \rho_f\varepsilon$ and $\gamma_s = \rho_s\phi$ are partial densities. No algorithm is presented for computing interpenetrating fields in the classical approach, say in the approach of Bowen (1971) or Passman *et al.* (1984). Other authors, Anderson and Jackson (1964) and Drew (1983, 1986) notable among them, generate mixture theories from different kinds of averaging, but spatial averaging is the most popular.

The classical equations of mixture theory for incompressible constituents are [Anderson and Jackson (1967)]:

$$\frac{\partial \gamma_f}{\partial t} + \mathbf{v}_f \cdot \nabla \gamma_f + \gamma_f \operatorname{div} \mathbf{v}_f = 0 \tag{1}$$

$$\frac{\partial \gamma_s}{\partial t} + \mathbf{v}_s \cdot \nabla \gamma_s + \gamma_s \operatorname{div} \mathbf{v}_s = 0 \tag{2}$$

$$\gamma_f \left(\frac{\partial \mathbf{v}_f}{\partial t} + \mathbf{v}_f \cdot \nabla \mathbf{v}_f \right) = \mathbf{m}_f + \gamma_f \mathbf{b}_f + \operatorname{div} \mathbf{T}_f \tag{3}$$

$$\gamma_s \left(\frac{\partial \mathbf{v}_s}{\partial t} + \mathbf{v}_s \cdot \nabla \mathbf{v}_s \right) = \mathbf{m}_s + \gamma_s \mathbf{b}_s + \operatorname{div} \mathbf{T}_s \tag{4}$$

$$\mathbf{m}_f + \mathbf{m}_s = \operatorname{div} \mathbf{S} \tag{5}$$

where $\mathbf{b}_f$ and $\mathbf{b}_s$ are the body force per unit mass, $\mathbf{m}$ is the force of interaction between constituents and $\mathbf{S}$ is an interaction stress. The quantities $\mathbf{m}$ and $\mathbf{S}$ are unknown. They are basic quantities which need to be modeled in the theory.

Equations (1) and (2) can be written as

$$\frac{\partial \varepsilon}{\partial t} + \operatorname{div} \varepsilon \mathbf{v}_f = 0 \tag{6}$$

$$\frac{\partial \phi}{\partial t} + \operatorname{div} \phi \mathbf{v}_s = 0 \tag{7}$$

By adding equations (6) and (7)

$$\operatorname{div} \mathbf{v}_c = 0 \tag{8}$$

where

$$\mathbf{v}_c = \varepsilon \mathbf{v}_f + \phi \mathbf{v}_s \tag{9}$$

Equations (6) and (7) can be combined with (3) and (4) to give:

$$\rho_f \left(\frac{\partial\, \varepsilon \mathbf{v}_f}{\partial t} + \operatorname{div} \left(\varepsilon \mathbf{v}_f \mathbf{v}_f \right) \right) = \mathbf{m}_f + \varepsilon \rho_f \mathbf{b}_f + \operatorname{div} \mathbf{T}_f \tag{10}$$

$$\rho_s\left(\frac{\partial\, \varepsilon \mathbf{v}_s}{\partial t} + \text{div}\left(\phi \mathbf{v}_s \mathbf{v}_s\right)\right) = \mathbf{m}_s + \phi\rho_s \mathbf{b}_s + \text{div}\, \mathbf{T}_s \tag{11}$$

Equations (6), (7), (10), (11), and (5) are the basic system of equations for mixture theories.

2.3 Ensemble Averaging

Two-fluid equations for incompressible fluid-particle suspensions can be generated by ensemble averaging. The techniques for doing this were set down by Saffman (1971) in his study of flow through porous media and by Lundgren (1972) in his study of dense suspensions and porous media, and in a review article by Drew (1983).

Define an indicator function

$$H(\mathbf{x}) = \begin{Bmatrix} 0 & \text{if } \mathbf{x} \text{ is in the solid} \\ 1 & \text{if } \mathbf{x} \text{ is in the fluid} \end{Bmatrix} \tag{12}$$

and let $\langle\ \rangle$ designate the operating of taking the average. The average is over many identical trials. Consider an experiment which is started at a certain time. At a later time and at a certain place, we record the value of some flow variable. We repeat the experiment, wait the same time, look at the same place and record again. After many trials we average the values by summing and dividing by the number of trials, and we let $N \to \infty$. In this manner, we generate a function $\langle\ \rangle(\mathbf{x}, t)$.

Using the indicator function it can be shown that [Drew, (1983)]

$$\langle H \rangle = \varepsilon(\mathbf{x}, t) = 1 - \phi(\mathbf{x}, t) \tag{13}$$

and

$$\langle 1 - H \rangle = 1 - \langle H \rangle = \phi(\mathbf{x}, t) \tag{14}$$

Since $\mathbf{V}(\mathbf{x}, t)$ is the true velocity

$$\mathbf{V}_f(\mathbf{x}, t) = \frac{\langle H\mathbf{V} \rangle}{\langle H \rangle} = \frac{\langle H\mathbf{V} \rangle}{\varepsilon} \tag{15}$$

and an average solid velocity

$$\mathbf{V}_s(\mathbf{x}, t) = \frac{\langle (1-H)\mathbf{V} \rangle}{\langle (1-H) \rangle} = \frac{\langle (1-H)\mathbf{V} \rangle}{\phi} \tag{16}$$

We define composite average and mass averages of any quantity f by

$$f_c = \langle f \rangle = \varepsilon f_f + \phi f_s \tag{17}$$

and

$$f_m = \frac{\langle \rho f \rangle}{\langle \rho \rangle} = \frac{(\rho f)_c}{\varepsilon \rho_f + \phi \rho_s} \tag{18}$$

The mass averaged velocity is

$$\mathbf{V}_m = \frac{\langle \rho \mathbf{V} \rangle}{\langle \rho \rangle} = \frac{\rho_f V_f \varepsilon + \rho_s V_s \phi}{\varepsilon \rho_f + \phi \rho_s} \tag{19}$$

Next note that H(x,t) is a material variable for materials which do not change phase, always one following fluid particles, always zero following solids; i.e.

$$\frac{\partial H}{\partial t} + \mathbf{V} \cdot \nabla H = 0 \tag{20}$$

Using this and div $\mathbf{V} = 0$,

$$0 = \left\langle \frac{\partial H}{\partial t} + \mathbf{V} \cdot \nabla H \right\rangle = \left\langle \frac{\partial H}{\partial t} + \text{div } H\mathbf{V} \right\rangle \tag{21}$$

$$= \frac{\partial \langle H \rangle}{\partial t} + \text{div } \langle H\mathbf{V} \rangle \tag{22}$$

$$= \frac{\partial \varepsilon}{\partial t} + \text{div } \varepsilon \mathbf{V}_f \tag{23}$$

Similarly, one can show

$$\frac{\partial \phi}{\partial t} + \text{div}\, \phi \mathbf{V}_s = 0 \tag{24}$$

These are the equations of mass balance assumed by mixture theory. It follows that

$$\text{div}\, \mathbf{V}_c = 0 \tag{25}$$

It can also be shown (Drew, 1986) that

$$\frac{\partial \rho}{\partial t} + \text{div}\left(\rho_c \mathbf{V}_m\right) = 0 \tag{26}$$

Addressing the momentum equations, since

$$\frac{\partial H}{\partial t} + \left(\mathbf{V} \cdot \nabla\right) H = 0 \quad \text{and} \quad \text{div}\, \mathbf{V} = 0 \tag{27}$$

we have the identity

$$H\left(\frac{\partial \mathbf{V}}{\partial t} + \left[\mathbf{V} \cdot \nabla\right]\mathbf{V}\right) = \frac{\partial H\mathbf{V}}{\partial t} + \text{div}\, H\mathbf{V}\mathbf{V} \tag{28}$$

The momentum equation for the fluid and solid is

$$\rho\left(\frac{\partial \mathbf{V}}{\partial t} + \left[\mathbf{V} \cdot \nabla\right]\mathbf{V}\right) = \rho \mathbf{b}_s + \text{div}\, \mathbf{T}^* \tag{29}$$

Multiplying (29) by H and ensemble average, using (27)

$$\rho_f \frac{\partial}{\partial t}\langle H\mathbf{V}\rangle + \rho_f \text{div}\, \langle H\mathbf{V}\mathbf{V}\rangle = \langle H\, \text{div}\, \mathbf{T}^*\rangle + \rho_f \mathbf{b}_f \varepsilon \tag{30}$$

Differentiating by parts gives

$$\langle H\, \text{div}\, \mathbf{T}^*\rangle = \text{div}\, \langle H\, \mathbf{T}^*\rangle - \langle \nabla H \cdot \mathbf{T}^*\rangle \tag{31}$$

where

$$\nabla H = \delta_\Sigma(\mathbf{x})\mathbf{n}, \quad \nabla\langle H\rangle = \langle \nabla H\rangle = \langle \delta_\Sigma \mathbf{n}\rangle = \nabla\varepsilon(\mathbf{x}, t) \tag{32}$$

$\delta_\Sigma(\mathbf{x})$ is a one-dimensional Dirac delta-function across the solid-fluid interface and $\mathbf{n}$ is the outward normal to the solid. Note that $\mathbf{n}\cdot\mathbf{T}^* = \mathbf{t}$ is that traction vector at a point $\mathbf{x}_\Sigma$ on the interface. From the definitions of $\mathbf{T}_f^*$,

$$\langle H\mathbf{T}^*\rangle = \varepsilon\mathbf{T}_f^*(\mathbf{x}, t) \tag{33}$$

Using the above relations, equation (30) can be written as

$$\rho_f\left(\frac{\partial}{\partial t}\varepsilon\mathbf{V}_f + \text{div}\,\langle H\mathbf{V}\mathbf{V}\rangle\right) = \text{div}\,\varepsilon\mathbf{T}_f^* - \langle \delta_\Sigma(\mathbf{x})\mathbf{t}\rangle + \rho_f\mathbf{b}_f\varepsilon \tag{34}$$

Using the same method, the momentum equation for the solid is

$$\rho_s\left(\frac{\partial}{\partial t}\phi\mathbf{V}_s + \text{div}\,\langle H\mathbf{V}\mathbf{V}\rangle\right) = \text{div}\,\phi\mathbf{T}_s^* - \langle \delta_\Sigma(\mathbf{x})\mathbf{t}\rangle + \rho_s\mathbf{b}_s\phi \tag{35}$$

Assume that the fluid phase is Newtonian, then

$$\mathbf{T}^* = -P\mathbf{1} + 2\mu\mathbf{D}[\mathbf{V}] \tag{36}$$

in the fluid; and the solid phase is a rigid body, for which

$$\mathbf{D}[\mathbf{V}] = 0 \tag{37}$$

on solids; where

$$\mathbf{D}[\mathbf{V}] = \frac{1}{2}\left(\nabla\mathbf{V} + [\nabla\mathbf{V}]^T\right) \tag{38}$$

is the rate of strain.

The stress for the fluid phase in mixture theory is given by Nunziato *et al.* (1986):

$$\mathbf{T}_f = -\varepsilon p_f\mathbf{1} + 2\varepsilon\mu\mathbf{D}[\mathbf{v}_f] \tag{39}$$

This differs from the fluid stress arising from ensemble averaging:

$$\mathbf{T}_f = \varepsilon \mathbf{T}_f^* = \langle H\mathbf{T}^* \rangle = \left\langle H\left(-P\mathbf{1} + 2\mu \mathbf{D}[\mathbf{V}]\right)\right\rangle \tag{40}$$

$$= -\varepsilon P_f \mathbf{1} + 2\mu \left\langle (H-1)\mathbf{D}[\mathbf{V}]\right\rangle + 2\mu \langle \mathbf{D}[\mathbf{V}]\rangle \tag{41}$$

$$= -\varepsilon P_f \mathbf{1} + 2\mu \mathbf{D}\left[\langle \mathbf{V}\rangle\right] \tag{42}$$

$$= -\varepsilon p_f \mathbf{1} + 2\mu \mathbf{D}[\mathbf{v}_c] \tag{43}$$

where $P_f = p_f$, $\langle \mathbf{V}\rangle = \mathbf{V}_c$ and

$$\left\langle (H-1)\mathbf{D}[\mathbf{V}]\right\rangle = 0 \tag{44}$$

because H - 1 is zero in the fluid and $\mathbf{D}[\mathbf{V}] = 0$ in the solid. The relation $\langle \mathbf{D}[\mathbf{V}]\rangle = \mathbf{D}\left[\langle \mathbf{V}\rangle\right]$ used above is true because $\mathbf{V}$ is continuous, $\mathbf{D}[\mathbf{V}]$ is uniformly bounded.

The stresses given by (39) and (43) are different because

$$\mathbf{D}[\mathbf{v}_c] = \mathbf{D}[\varepsilon \mathbf{v}_f + \phi \mathbf{v}_s] \tag{45}$$

is different from $\varepsilon \mathbf{D}[\mathbf{v}_f]$.

In the modeling of multiphase flows of rigid particles, it is convenient to write

$$\mathbf{T}^* = -P\mathbf{1} + \boldsymbol{\tau} \tag{46}$$

where P is the mean normal stress. The ensemble average of this is

$$\mathbf{T}_s = \phi \mathbf{T}_s^* = -\phi p_s \mathbf{1} + \left\langle (\mathbf{1} - H)\boldsymbol{\tau}\right\rangle \tag{47}$$

where it is assumed that $P_s = p_s$ and

$$\phi P_s = \left\langle (1-H)P \right\rangle \tag{48}$$

For dilute suspensions, it is normally postulated that $\tau = 0$ (Nunziato *et al.* 1986; Passman *et al.* 1984; McTigue *et al.* 1986).

Using (43), (44), and (47), and rearranging the inertial terms, the following system of ensemble averaged equations results:

$$\frac{\partial \varepsilon}{\partial t} + \operatorname{div} \varepsilon \mathbf{v}_f = 0 \tag{49}$$

$$\frac{\partial \phi}{\partial t} + \operatorname{div} \phi \mathbf{v}_s = 0 \tag{50}$$

$$\rho_f \varepsilon \left(\frac{\partial}{\partial t} \mathbf{v}_f + \mathbf{v}_f \cdot \nabla \mathbf{v}_f \right) + \rho_f \operatorname{div} \left\langle H(\mathbf{V} - \mathbf{v}_f)(\mathbf{V} - \mathbf{v}_f) \right\rangle = -\nabla(\varepsilon p_f) + \mu \nabla^2 \mathbf{v}_c - \left\langle \delta_\Sigma(\mathbf{x})\mathbf{t} \right\rangle + \rho_f \mathbf{b}_f \varepsilon \tag{51}$$

$$\rho_s \phi \left(\frac{\partial}{\partial t} \mathbf{v}_s + \mathbf{v}_s \cdot \nabla \mathbf{v}_s \right) + \rho_s \operatorname{div} \left\langle H(\mathbf{V} - \mathbf{v}_s)(\mathbf{V} - \mathbf{v}_s) \right\rangle = -\nabla(\phi p_s) + \left\langle \delta_\Sigma(\mathbf{x})\mathbf{t} \right\rangle + \rho_s \mathbf{b}_s \phi + \operatorname{div} \left\langle (1-H)\tau \right\rangle \tag{52}$$

The boundary condition between the fluid and the particle takes form in the traction vector term in (51) and (52) and it is probably best not to combine the equations. Joseph and Lundgren (1990) have shown $-\rho_s \operatorname{div} \left\langle H(\mathbf{V} - \mathbf{v}_s)(\mathbf{V} - \mathbf{v}_s) \right\rangle + \left\langle \delta_\Sigma(\mathbf{x})\mathbf{t} \right\rangle = \mathbf{m}_s$ and $-\rho_f \operatorname{div} \left\langle H(\mathbf{V} - \mathbf{v}_f)(\mathbf{V} - \mathbf{v}_f) \right\rangle - \left\langle \delta_\Sigma(\mathbf{x})\mathbf{t} \right\rangle = \mathbf{m}_f$. $\mathbf{m}_s$ and $\mathbf{m}_f$ are related through equation (5).

The existence of two fluid equations even when one of the fluids is solid is perfectly justified by ensemble averaging. These equations, like other two-fluid models, are not closed and methods of closure, or constitutive models for the interaction terms are required.

2.4 Constitutive Relations

2.4.1 Particle Pressure

The simplest assumption one could make concerning the closure equation for the phase pressure difference is to assume equal pressures. In this case, the model equation for the two-phase flow system retain only one independent pressure field. Stuhmiller (1977) has shown that this assumption leads to instabilities for initial-value problems in flows where the phase velocities are not equal. The instabilities are a result of complex characteristic roots imparted to the fundamental equation set by assuming equal pressures.

For the case of a particulate phase of spherical particles suspended in a fluid, Stuhmiller (1977) and Prosperetti and Jones (1984) have investigated the local flow in the vicinity of an isolated sphere, where their interpretations of the interface pressure account for the local inertia of the flow. By considering the flow of an inviscid fluid around a sphere, Prosperetti and Jones (1984) have proposed the following form for the pressure difference:

$$p_s - p_f = -\frac{1}{4}\gamma_f\left(\mathbf{v}_f - \mathbf{v}_s\right)^2 \tag{53}$$

This expression indicates the solid-phase pressure is less than the bulk fluid pressure. This assumption will lead one to calculate particle concentration profiles which contradict experimental observations for 2-D, Poiseuille flow of a dilute suspension. Specifically, this expression leads to a particle flux in the direction of increasing particle concentration gradient (McTigue *et al.*, 1986).

Ho and Leal (1974) showed that the local inertial effects are responsible for lateral particle migrations in bounded shearing flows of dilute suspensions of spherical particles. If the suspension is dilute, no contribution to the solid-phase pressure arises from particle interaction forces. It is therefore reasonable to assume that the solid-phase pressure is due to the local disturbance field created by the relative motion between a particle and the fluid. This is the postulate made by Giveler (1987) to develop an expression for the relative particle/fluid pressure. A brief description of his derivation is given below.

Giveler used the expression given in a paper by Chester and Breach (1969) to describe the local fluid pressure on the surface of a spherical particle

$$p - p_f = -\int^{\theta} \left(\frac{\partial^3 \psi}{\partial r^3}\right)_{r=1} \frac{d\theta}{\sin(\theta)} \tag{54}$$

where ψ is the normalized stream function of the inner expansion and r is the normalized radial coordinate. The pressure difference in (54) has been normalized by the quantity $\frac{\mu_f(v_f - v_s)}{a}$ and vanishes far from the body. Through terms of order Re,

$$\psi = \psi_0 + \mathrm{Re}\,\psi_1 + \ldots, \tag{55}$$

$$\psi_0 = \frac{1}{4}\left(2r^2 - 3r + \frac{1}{r}\right)\sin^2(\theta) \tag{56}$$

$$\psi_1 = \frac{3}{32}\left(2r^2 - 3r + \frac{1}{r}\right)\sin^2(\theta) - \frac{3}{32}\left(2r^2 - 3r + 1 - \frac{1}{r} + \frac{1}{r^2}\right)\cos(\theta)\sin^2(\theta) \tag{57}$$

The origin of the spherical polar coordinate system (r, θ, ϕ) is fixed at the center of the particle and the polar angle, θ, is measured counterclockwise with respect to the uniform streaming fluid velocity. From (54)

$$p - p_f = \left[-\frac{3}{2}\left(1 + \frac{3}{8}\mathrm{Re}\right)\cos(\theta) + \frac{27}{32}\mathrm{Re}\cos^2(\theta)\right] + O\left(\mathrm{Re}^2 \log(\mathrm{Re})\right) \tag{58}$$

The first two terms on the r.h.s. of (58) are related to the pressure field calculated from the Stokes expansion, while the third term accounts for the influence of inertia which enters the inner expansion through the process of matching near and far field solutions in the overlap region.

Giveler then defines the solid-phase pressure in the continuum sense to be, in part, the average pressure experienced by a single particle and derived from the local disturbance pressure field. This inertial correction may be obtained by integrating (58) over the particle surface Ω,

$$p_s - p_f = \frac{1}{\Omega}\int (p - p_f)\, d\Omega = \frac{9}{32}\mathrm{Re} + O(\mathrm{Re}^2) \tag{59}$$

Note that it is only the third term on the r.h.s. of (58) which contributes to the interfacial

pressure through terms of order Re. This term is the first correction to the flow field close to the particle from inertia. In dimensional form,

$$p_s = p_f + \frac{9}{32}\gamma_f\left(\mathbf{v}_f - \mathbf{v}_s\right) \tag{60}$$

Obviously this expression is only valid for dilute regions of fluidized beds and where suspended particles are laege enough for Brownian motion to be unimportant. When the dispersed, solid-phase contribution exceeds the dilute limit, particle-particle interactions become important. To model these flows with multiphase mixture theories, researchers have either defined (Homsy *et al.* 1980), or implied (Anderson and Jackson, 1967) the concept of a collision pressure to account for the elastic interactions between the particles. The effects are significant if the bed is less than fully fluidized. In other related work (Stiehadieh *et al.*, 1984) similar expressions are used for the interface pressure in attempts to model particle contact forces in non dilute suspensions.

2.4.2 Steady-State Momentum Exchange Between Phases

In the solid-phase momentum equation, the vector-valued term $\mathbf{m}_s$ must be defined. Assume the interphase momentum exchange contains a steady state and time dependent term ($\mathbf{m}_s = \mathbf{m}_{s_\infty} + \mathbf{m}_s(t)$). Let

$$\mathbf{m}_{s_\infty} = \hat{\mathbf{m}}_s\left(\phi,\, \mathbf{v}_f - \mathbf{v}_s,\, \text{div}\, \mathbf{D}_f,\, \mathbf{D}_f\right) \tag{61}$$

where $\mathbf{m}_{s_\infty}$ is the steady state portion of the momentum transfer to the solid phase. It is known that each of the arguments of this function is objective. It is also usual to assume that $\mathbf{m}_{s_\infty}$ is frame-indifferent (Passman *et al.*, 1984; Bowen, 1971). It then follows that $\hat{\mathbf{m}}_s$ is an isotropic function, and subject to the representation given by Passman *et al.* (1984).

$$\begin{aligned}\mathbf{m}_{s_\infty} = {} & \alpha_{10}\left(\mathbf{v}_f - \mathbf{v}_s\right) + \alpha_{11}\text{tr}\,\mathbf{D}_f\left(\mathbf{v}_f - \mathbf{v}_s\right) + \alpha_{20}\mathbf{D}_f\left(\mathbf{v}_f - \mathbf{v}_s\right) \\ & + \beta_{10}\text{div}\,\mathbf{D}_f + \beta_{11}\text{tr}\,\mathbf{D}_f\text{div}\,\mathbf{D}_f + \beta_{20}\mathbf{D}_f\text{div}\,\mathbf{D}_f\end{aligned} \tag{62}$$

with each coefficient a function of ϕ. Assume that

$$\text{tr}\,\mathbf{D}_f = 0 \tag{63}$$

and that the coefficient functions are linear in ϕ. Then it follows from (62) that

$$\mathbf{m}_{s_\infty} = \alpha_1\phi(\mathbf{v}_f - \mathbf{v}_s) + \alpha_2\phi\mathbf{D}_f(\mathbf{v}_f - \mathbf{v}_s) + \beta_1\phi\,\mathrm{div}\,\mathbf{D}_f + \beta_2\phi\mathbf{D}_f\mathrm{div}\,\mathbf{D}_f \tag{64}$$

This is the equation McTigue *et al.* have assumed in their analysis of constitutive relations. It arises as an exact second-order approximation to the general constitutive equation (61). The first term is associated with the particle-fluid drag, the second with the Saffman lift force (Saffman, 1965), the third with the Faxen force (Faxen, 1922), and the fourth with the Ho and Leal lift force (1974). The forms of these terms are motivated by approximate solutions to the Navier-Stokes equations for a finite rigid body in a fluid.

Define the general form of $\mathbf{m}_{s_\infty}$

$$\mathbf{m}_s = \phi\mathbf{F}(\mathbf{v}_f - \mathbf{v}_s) + 2\phi\mathbf{G}\,\nabla\cdot\mathbf{D}_f + p_f\nabla\phi \tag{65}$$

where the coefficient tensors **F** and **G** are linear isotropic functions of $\mathbf{D}_f^*$, from (64),

$$\mathbf{F} = \alpha_1\mathbf{1} + 2\alpha_2\mathbf{D}_f \tag{66}$$

$$\mathbf{G} = \beta_1\mathbf{1} + 2\beta_2\mathbf{D}_f \tag{67}$$

The drag forces are characterized by the diagonals of **F** and **G**, diag **F** and diag **G**, while (**F** - diag **F**) and (**G** - diag **G**) represent the lift forces. The last term in (65) represents the buoyant force of the fluid on the particles. The coefficients α_1, α_2, β_1, and β_2, depend on ϕ and the invariants of $\mathbf{D}_f$, and approach the low-concentration limit. As mentioned above, α_1 can be identified with the drag force, α_2 with the lift force due to interaction of the slip velocity with the mean shearing analyzed by Saffman, β_1 with the Faxen force, and β_2 with the lift on a single particle in plane Poiseuille flow resulting from counteracting forces due to the interaction of the perturbation flow field near the particle with the mean flow velocity gradient and curvature. This gives:

$$\alpha_1 \to \frac{3}{8}\left(\frac{\rho_f C_D(\mathbf{v}_f - \mathbf{v}_s)}{a}\right) \tag{68}$$

$$\alpha_2 \to \frac{3(6.46)}{4\pi a}\left(\frac{\gamma_f^2\mu_f^2}{2\mathrm{tr}\,\mathbf{D}_f^2}\right)^{\frac{1}{4}} \tag{69}$$

$$\beta_1 \to \frac{7\mu_f}{4} \tag{70}$$

$$\beta_2 \to -\left[\frac{\left(\mathrm{tr}\,\mathbf{D}_f^2\right)^{\frac{1}{2}}}{|\nabla\cdot\mathbf{D}_f|}g_1 - g_2\right] \tag{71}$$

where g_1 and g_2 are functions which depend on the geometry of the flow. If the analysis of Ho and Leal (1974) is used and axial velocity gradients are neglected:

$$\alpha_2 \to \frac{3(6.46)}{4\pi a}\left(\frac{\gamma_f^{\frac{1}{2}}\mu_f^{\frac{1}{2}}}{\left|\frac{\partial \mathbf{v}_f}{\partial y}\right|^{1/2}}\right) \tag{72}$$

$$\beta_2 \to -\frac{3\gamma_f aD}{4\pi}\left[\frac{1}{D}\left|\frac{\frac{\partial \mathbf{v}_f}{\partial y}}{\frac{\partial^2 \mathbf{v}_f}{\partial y^2}}\right| G_1(y) - G_2(y)\right] \tag{73}$$

The forces on the solid are related to the forces on the fluid by

$$\mathbf{m}_{f_\infty} = -\mathbf{m}_{s_\infty} + \nabla\cdot\mathbf{S} \tag{74}$$

It is known from Einstein's analysis that the fluid-particle interaction results in additional viscous transport (Lin, 1970). So it can be assumed that

$$\mathbf{S} = 2\phi\eta\mathbf{D} \tag{75}$$

where η is an interaction viscosity, and $\mathbf{D}$ is the deformation rate of the mixture. When the particles move with a velocity close to that of the fluid, as in Einstein's analysis, the mixture shear stress is

$$\mathbf{T}^* = \mathbf{T} - \tfrac{1}{3}(\mathrm{tr}\,\mathbf{T})\mathbf{1} \tag{76}$$

where $\mathbf{T}_a^* = \mathbf{T}_a + \phi_a p_a \mathbf{1}$. (The above expression utilizes the result developed by Passman (1977) who evaluated Truesdell's (1969) physical concepts to obtain the expression $\mathbf{T} - \rho \mathbf{v} \otimes \mathbf{v} = \sum \left(\mathbf{T}_a - \rho_a \mathbf{v}_a \otimes \mathbf{v}_a \right)$ for the mixture stress; see Passman *et al.* [1984] for a complete discussion).

This expression results in the correct effective viscosity to within $O(\phi^2)$ provided

$$\eta = \frac{7\mu_f}{2} \tag{77}$$

2.4.3 Unsteady-State Momentum Exchange Between Phases

Additional forces on particles are due to unsteady flow effects. The first of these is the virtual mass term. This force is proportional to the acceleration of the particle and, for small particles, can be given as (Boussinesq, 1885; Basset, 1888):

$$\mathbf{m}_s(t)_{virt.\ mass} = \tfrac{1}{2}\rho_f \frac{d(\mathbf{v}_f - \mathbf{v}_p)}{dt} \tag{78}$$

Basset also developed an expression which takes into account the fact that the interaction force depends, not only on the instantaneous motion of the particle, but also on the instantaneous fluid velocity in which it moves, which in turn depends on the complete history of the particle's motion. This term is generally known as the "Basset", or more correctly "Boussinesq-Basset" history term, and is given as:

$$\mathbf{m}_s(t)_{history} = \frac{9}{d_p}\mu_f \int_{t_0}^{t} \left[\frac{d(\mathbf{v}_f - \mathbf{v}_p)}{d\tau} \right] \frac{d\tau}{\left(\pi \nu (t - \tau) \right)^{1/2}} \tag{79}$$

The final force to be included is the force resulting from stress gradients of the fluid flow in the absence of particles. The term defining the influence of fluid stress-gradients on the particle is expressed in terms of the change in fluid velocity along its own trajectory (see Maxey and Riley, 1983):

$$\mathbf{m}_s(t)_{fld.\,stress} = \rho_f \frac{D(\mathbf{v}_f)}{dt} \tag{80}$$

For typical velocities, particle sizes and fluid properties found in circulating fluidized beds, the requirement of $Re_{u_{rel},d_p} \rightarrow 0$ implicit in Basset's derivation of the virtual mass and history term does not hold. For example, a CFB operating at 800 °C with a mean particle diameter of 250 μm, the Reynolds number is about 2.5. This indicates the advective terms in the equation of motion cannot be ignored such that the problem reduces to one of unsteady Stokes flow. Based on the work of Odar and Hamilton (1964), Berlemont *et al.* (1990) modified the results of Basset to take into account non-small Reynolds numbers. Their results give:

$$\mathbf{m}_s(t)_{virt.\,mass} = C_A \rho_f \frac{d(\mathbf{v}_f - \mathbf{v}_p)}{dt} \tag{81}$$

$$\mathbf{m}_s(t)_{history} = \frac{3C_H}{2d_p}\mu_f \int_{t_0}^{t} \left[\frac{d(\mathbf{v}_f - \mathbf{v}_p)}{d\tau}\right] \frac{d\tau}{\left(\pi\nu(t-\tau)\right)^{1/2}} \tag{82}$$

The only difference between Basset's result and the Berlemont equation is the coefficients C_A and C_H which take into account non-small particle Reynolds numbers. These coefficients will be shown in Section 3 to depend on the bed Reynolds number and the bed geometry. An evaluation of the appropriateness of equations (81) and (82) will also be discussed in Section 3.

2.5 Non-Dimensionalization of the Two-Fluid Equations

For a turbulent flow there is no single set of scales but rather a continuous spectrum of velocity and length scales which must be considered in any application of the mixture equations of motion. In the core of a CFB or freeboard of a bubbling bed, the larger, more energetic motions are more characteristic. In this case the length scale is D and the velocity scale is u_τ (Hinze, 1975). The corresponding time scale is D/u_τ.

Non-dimensionalizing equations (49)-(52) using these scales results in:

$$\frac{\partial \varepsilon}{\partial \bar{t}} + \operatorname{div} \varepsilon \bar{v}_f = 0 \tag{83}$$

$$\frac{\partial \phi}{\partial \bar{t}} + \operatorname{div} \phi \bar{v}_s = 0 \tag{84}$$

$$\left(\frac{\partial}{\partial \bar{t}}\bar{v}_f + \bar{v}_f \cdot \bar{\nabla}\bar{v}_f\right) + \frac{D}{u_\tau^2 \rho_f}\mathbf{m}_f = -\bar{\nabla}\left(\varepsilon \frac{p_f}{u_\tau^2 \rho_f}\right) + \frac{\mu}{\rho_f u_\tau D}\bar{\nabla}^2 \bar{v}_c + \frac{Dg}{u_\tau^2}\varepsilon \tag{85}$$

$$\frac{\rho_s}{\rho_f}\phi\left(\frac{\partial}{\partial t}\bar{v}_s + \bar{v}_s \cdot \bar{\nabla}\bar{v}_s\right) + \mathbf{m}_s\left(\frac{D}{u_\tau^2 \rho_f}\right) = -\bar{\nabla}\left(\phi \frac{p_s}{u_\tau^2 \rho_f}\right) + \frac{\rho_s g D}{\rho_f u_\tau^2}\phi \tag{86}$$

The controlling dimensionless parameters which appear in (83)-(86) are:

$$\frac{\rho_s}{\rho_f};\ \frac{gD}{u_\tau^2};\ \frac{D}{\rho_f u_\tau^2}\mathbf{m}_s;\ \frac{D}{\rho_f u_\tau^2}\mathbf{m}_f;\ \frac{p_f}{\rho_f u_\tau^2};\ \frac{p_s}{\rho_f u_\tau^2} \tag{87}$$

The steady state terms in the momentum exchange term $\mathbf{m}_s$

$$\frac{D\,\mathbf{m}_{s_\infty}}{\rho_f u_\tau^2} = \frac{D}{\rho_f u_\tau^2}\left[\begin{array}{l}\alpha_1 \phi u_\tau\left(\bar{v}_f - \bar{v}_s\right) + \alpha_2 \phi D \bar{\mathbf{D}}_f\left(\bar{v}_f - \bar{v}_s\right) \\ + \beta_1 \frac{D}{u_\tau}\phi \operatorname{div} \bar{\mathbf{D}}_f + \beta_2 \phi \frac{D}{u_\tau^2}\bar{\mathbf{D}}_f \overline{\operatorname{div}}\, \bar{\mathbf{D}}_f\end{array}\right] \tag{88}$$

Utilizing the values of α_1, α_2, β_1, and β_2 defined above, the dimensionless groups resulting form equation (88) are:

$$\begin{aligned}\frac{D\,\mathbf{m}_{s_\infty}}{\rho_f u_\tau^2} = {} & \frac{3}{8}\phi \frac{D}{a} C_D\left(\bar{v}_f - \bar{v}_s\right) + \frac{3(6.46)\phi}{2\sqrt{2}\pi}\left[\frac{\mathrm{Re}_{u_\tau, D}}{\left(\mathrm{Re}_{u_\tau, d_p}\right)^2}\right]^{1/2} \bar{\mathbf{D}}_f^{\frac{1}{2}}\left(\bar{v}_f - \bar{v}_s\right) \\ & + \frac{7\phi}{2}\mathrm{Re}_{u_\tau, D}\bar{\nabla} \cdot \bar{\mathbf{D}}_f - \frac{3\phi}{\pi}\frac{a}{D}\bar{\mathbf{D}}_f \bar{\nabla} \cdot \bar{\mathbf{D}}_f \left[\frac{\dfrac{\partial \bar{v}_f}{\partial \bar{y}}}{\dfrac{\partial^2 \bar{v}_f}{\partial \bar{y}^2}} G_1(\bar{y}) - G_2(\bar{y})\right]\end{aligned} \tag{89}$$

From (74) and (75),

$$\bar{\mathbf{m}}_f = -\bar{\mathbf{m}}_s + \frac{7\phi}{\mathrm{Re}_{u_\tau, D}}\bar{\nabla} \cdot \bar{\mathbf{D}}_m \tag{90}$$

The dimensionless time dependent forces on the particle are:

$$\bar{m}_s(t) = -\frac{3}{2\sqrt{\pi}}\left(Re_{u_\tau,D}\right)^{1/2}\left(\frac{D}{d_p}\right)C_H\int_{t_0}^{t}\frac{d\left(\bar{v}_f-\bar{v}_p\right)}{d\bar{\tau}}\frac{d\bar{\tau}}{\left(\bar{t}-\bar{\tau}\right)}+ C_A\frac{d\left(\bar{v}_f-\bar{v}_p\right)}{d\bar{t}}+\frac{D\bar{v}_f}{d\bar{t}} \tag{91}$$

The remaining terms in (87) are the dimensionless fluid and particle pressures. The dimensionless fluid pressure can be dropped from the list since it is a dependent parameter. The dimensionless particle pressure can be shown from (60) to be:

$$\bar{p}_s = \bar{p}_f + \frac{9}{32}\left(\bar{v}_f-\bar{v}_s\right) \tag{92}$$

From (87), (89), (90), (91), and (92), the governing dimensionless groups are:

$$\frac{\rho_f}{\rho_s};\ Re_{u_\tau,d_p};\ Re_{u_\tau,D};\ Fr_{u_\tau,D};\ C_H;\ C_A;\ C_D \tag{93}$$

2.6 Evaluation of Coefficients for Finite Reynolds Numbers (C_H, C_A, C_D)

Expressions for C_H, C_A, C_D are needed to complete the list of parameters given in (93). The coefficients C_A and C_H are functions of an acceleration number defined as the ratio of convective to local acceleration.

$$C_A = 1.05 - \frac{0.066}{Ac^2+0.12} \tag{94}$$

$$C_A = 2.88 + \frac{3.12}{\left(Ac+1\right)^3} \tag{95}$$

This number was used by Iversen and Balent (1951) and Keim (1956) who derived it by dimensional reasoning alone. If the local length and velocity scales are on the order of the eddy length and the fluctuating velocity, and convective length and velocity scales are L and u_τ, the acceleration number scales as:

$$Ac = \frac{\rho_f u\left(\frac{\partial u}{\partial x}\right)}{\rho_f\left(\frac{\partial u}{\partial t}\right)} \sim \frac{l_e}{L}\frac{u_\tau^2}{u_{rms}^2} \sim 2.73 f \frac{D}{L} \qquad (96)$$

where the single phase pipe flow correlations of Hinze to estimate u_τ, the eddy length scale (l_e) and the fluid fluctuating velocity (u_{rms}) were used. For typical fluid bed operating conditions, f (the gas friction factor) is about 0.04. Hence, for moderate to large aspect ratios, the acceleration number will be small resulting in the coefficients C_A and C_H tending toward their constant limit of 1/2 and 6, respectively. For conditions where the acceleration number is not small, C_A and C_H will depend on the bed geometry and the bed Reynolds number.

Some words are appropriate at this point concerning the form of the Boussinesq-Basset history term described above. In general, corrections of the form introduced by Odar and Hamilton (1964) and Berlemont *et al.*, (1990) are not valid. This because the entire integration kernel associated with the Boussinesq-Basset history term changes due to the non-linearity of the system with velocity oscillations in the free stream and finite Reynolds numbers. The integration kernel decays at a greater rate than the classical behavior of $(t-\tau)^{\frac{1}{2}}$ for longer time scales (Mei and Adrian, 1992; Mei *et. al.*, 1991b; Lovalenti and Brady, 1993a,b,c).

Recent investigations into a more exact form of the hydrodynamic forces in unsteady motion have indicated that the hydrodynamic force will also depend on a Strouhal number. If the characteristic time scale is D/u_τ, the Strouhal number scales as d_p/D. If the characteristic time scale is $\frac{\nu}{u_\tau^2}$, the Strouhal number scales as Re_{u_τ, d_p}.

Neither time scale introduces additional dimensionless parameters. Therefore, while not strictly valid for long time scales, the use of (82) provides a good approximation of particle motion without the loss of any dimensionless groups.

The drag coefficient C_D for dilute flows is generally written in terms of a Reynolds number based on particle diameter and terminal velocity. For example Clift *et al.* (1978) give:

$$C_D = \frac{24}{Re_{u_t, d_p}}\left(1 + 0.15 Re_{u_t, d_p}^{0.687}\right) \qquad (97)$$

2.7 Governing Parameters in Core Region of a CFB

From (93)-(97), the governing parameters are

$$\frac{\rho_f}{\rho_s};\ \mathrm{Re}_{u_\tau, d_p};\ \mathrm{Re}_{u_\tau, D};\ \mathrm{Fr}_{u_\tau, D};\ \text{bed geometry} \tag{98}$$

If relationships of the form for single phase flow are valid, the shear velocity is of the functional form

$$\frac{u_\tau}{u_o} \cong fnc\left(\frac{1}{\mathrm{Re}_{u_\tau, D}}\right) \tag{99}$$

the list of governing parameters can be rewritten as

$$\frac{\rho_f}{\rho_s};\ \mathrm{Re}_{u_o, d_p};\ \mathrm{Re}_{u_o, D};\ \mathrm{Fr}_{u_o, D};\ \text{bed geometry} \tag{100}$$

The Reynolds number based on particle diameter and relative velocity does not need to be included in the list because it scales with the Reynolds number based on terminal velocity (u_t) and particle diameter if

$$u_{rel} \sim u_t \tag{101}$$

The terminal velocity based Reynolds number (Re_{u_t, d_p}) is a function of only the Archimedes number which can be written as a combination of dimensionless parameters included in (100)

$$\mathrm{Ar} = \left(\frac{\rho_s}{\rho_f}\right)\frac{\left(\mathrm{Re}_{u_o, d_p}\right)^3}{\left(\mathrm{Re}_{u_o, D}\,\mathrm{Fr}_{u_o, D}\right)} \tag{102}$$

Equation (100) shows that the governing dimensionless parameters of the two-phase equations of motion as derived using the dilute limit ensemble averaging method above are identical to those derived using the spatially averaged Anderson-Jackson equations [see Glicksman *et al.* (1994)].

For most fluidized beds, the ratio of the fluid to solid density is very small. This allows one

to ignore the added mass term and the term representing the influence of the fluid stress-gradients on the particle. Moreover, the Faxen forces give rise to a relative motion scale of $\frac{d_p^2 u_\tau}{D^2}$, which is very small in fluid bed applications. This permits one to neglect the Faxen forces. However, even with these simplifications it can be shown that the governing dimensionless groups do not change. In fact, even when all terms except the drag, temporal, and gravitational are ignored, the set of dimensionless groups does not change.

2.8 Governing Parameters Near the Wall of a CFB

Near the wall of a fluidized bed the fluid-particle drag becomes a function of the particle to wall distance. The presence of a wall will increase the drag coefficient of the particle as compared to that in the case of unbounded flow (Faxen, 1923). To account for this effect, modifications to the drag force of the form determined by Faxen (1923), Brenner (1961), and Maude (1961) can be used. Faxen's expression of the correction to the drag on a small sphere in the direction parallel to the wall, χ_x, is a function of d_p/Y. Y is the particle to wall distance. Brenner (1961) and Maude (1961) independently determined the modification to the drag force for a small particle moving normal to the wall χ_r, It was also found to a be a function of d_p/Y (see equations 104a and 104b).

Near the wall neither the bed diameter nor the boundary layer thickness is a suitable length scale. Since the flow there is determined solely by u_τ and ν, the proper length scale is ν/u_τ. The velocity and time scales are u_τ, and $\frac{\nu}{u_\tau^2}$, respectively (Hinze, 1975). The dimensionless governing parameters are now

$$\frac{\rho_s}{\rho_f};\ \frac{g\nu}{u_\tau^3};\ \frac{\nu}{\rho_f u_\tau^3}\mathbf{m}_s;\ \frac{\nu}{\rho_f u_\tau^3}\mathbf{m}_f;\ \frac{p_f}{\rho_f u_\tau^2};\ \frac{p_s}{\rho_f u_\tau^2} \tag{103}$$

The steady state terms in the momentum exchange term $\mathbf{m}_s$

$$\begin{aligned}\frac{\nu\,\mathbf{m}_{s_\infty}}{\rho_f u_\tau^3} &= \frac{3}{8}\phi\left(\mathrm{Re}_{u_\tau, d_p}\right)^{-1} C_D \bar{\chi}\left(\bar{\mathbf{v}}_f - \bar{\mathbf{v}}_s\right) + \frac{3(6.46)\phi}{2\sqrt{2}\pi}\left(\mathrm{Re}_{u_\tau, d_p}\right)^{-1} \bar{\mathbf{D}}_f^{\frac{1}{2}}\left(\bar{\mathbf{v}}_f - \bar{\mathbf{v}}_s\right) \\ &+ \frac{7\phi}{2}\bar{\nabla}\cdot\bar{\mathbf{D}}_f - \frac{3\phi}{\pi}\left(\mathrm{Re}_{u_\tau, d_p}\right)\left(\mathrm{Re}_{u_\tau, D}\right)\bar{\mathbf{D}}_f\bar{\nabla}\cdot\bar{\mathbf{D}}_f\left[\frac{1}{\left(\mathrm{Re}_{u_\tau, D}\right)}\frac{\frac{\partial \bar{v}_f}{\partial \bar{y}}}{\frac{\partial^2 \bar{v}_f}{\partial \bar{y}^2}}G_1(\bar{y}) - G_1(\bar{y})\right]\end{aligned} \tag{104}$$

$$\chi_x = \left[1 - \frac{9}{16}\left(\frac{d_p}{2Y}\right) + \frac{1}{8}\left(\frac{d_p}{2Y}\right)^3 - \frac{45}{256}\left(\frac{d_p}{2Y}\right)^4 - \frac{1}{16}\left(\frac{d_p}{2Y}\right)^5\right]^{-1} \tag{104a}$$

$$\chi_r = \left[1 + \frac{9}{8}\left(\frac{d_p}{2Y}\right) + \left(\frac{9}{16}\left(\frac{d_p}{2Y}\right)\right)^2\right] \tag{104b}$$

where

$$\bar{\chi} = fnc\left(\mathrm{Re}_{u_\tau, d_p}\right).$$

From (74) and (75),

$$\bar{m}_f = -\bar{m}_s + 7\phi\bar{\nabla}\cdot\bar{D}_m \tag{105}$$

The dimensionless time dependent forces on the particle are:

$$\bar{m}_s(t) = -\frac{3}{2\sqrt{\pi}}\left(\mathrm{Re}_{u_\tau, d_p}\right)^{-1} C_H \int_{i_0}^{i} \frac{d\left(\bar{v}_f - \bar{v}_p\right)}{d\bar{\tau}} \frac{d\bar{\tau}}{\left(\bar{t} - \bar{\tau}\right)} + C_A \frac{d\left(\bar{v}_f - \bar{v}_p\right)}{d\bar{t}} + \frac{D\bar{v}_f}{d\bar{t}} \tag{106}$$

The remaining terms in (103) are the dimensionless fluid and particle pressures. The dimensionless fluid pressure can be dropped from the list since it is a dependent parameter. The dimensionless particle pressure can be shown from (60) to be:

$$\bar{p}_s = \bar{p}_f + \frac{9}{32}\left(\bar{v}_f - \bar{v}_s\right) \tag{107}$$

From (103)-(107), the governing dimensionless groups are:

$$\frac{\rho_f}{\rho_s};\ \mathrm{Re}_{u_\tau, d_p};\ \mathrm{Re}_{u_\tau, D};\ \mathrm{Fr}_{u_\tau, D};\ C_H;\ C_A;\ C_D \tag{108}$$

Note that

$$\frac{g\mu}{\rho_f u_\tau^3} = \left(\frac{1}{Re_{u_\tau, d_p} Fr_{u_\tau, d_p}} \right) \tag{109}$$

As discussed earlier C_H, C_A are nearly constant for conditions found in fluidized beds. For conditions where they are not constant, they only depend on bed geometry and bed Reynolds number. C_D depends on the Reynolds number based on particle diameter and terminal velocity, which in turn depends on the Archimedes number. Hence, the set of dimensionless groups which govern particle hydrodynamics in the near-wall region is identical to those governing particle motion in the core, namely

$$\frac{\rho_f}{\rho_s};\ Re_{u_o, d_p};\ Re_{u_o, D};\ Fr_{u_o, D};\ \text{bed geometry} \tag{110}$$

If the Faxen terms, Boussinesq-Basset history term, added mass term, the term representing fluid stress gradients on the particle, and the Saffman and Ho and Leal lift terms are ignored, the governing independent parameters do not change.

It should be noted that in general the particle fluid drag will also be a function of particle sphericity and bed voidage [Wen and Yu, (1966); Ganser (1993); Barnea and Mizrahi, (1973)].

$$F_{drag} = f(\varepsilon) g(\phi_s) \frac{\pi}{8} d_p^2 \rho_f (v_f - v_s) | v_f - v_s | \tag{111}$$

The inclusion of $f(\varepsilon)$ and $g(\phi_s)$ in the drag term extends the analysis to include non-spherical particles. This results in the particle sphericity being added to the list of parameters in (100) and (110).

2.9 Boundary Conditions

At the bottom of the column, $p_f = p_o$ and

$$v_f(x,y,0,t) = \frac{u_o}{\varepsilon} i \tag{112}$$

Also at the bottom of the column

$$\mathbf{v}_s(x,y,0,t) = \frac{G_s}{\rho_s \phi}\mathbf{i} \tag{113}$$

At the side walls the gas velocity is zero and the solid velocity is parallel to the wall.

Non-dimensionalization of the boundary conditions yields a dimensionless pressure at the distributor $\frac{p_o}{\rho_f u_\tau^2}$ along with

$$\bar{\mathbf{v}}_f(\bar{x},\bar{y},0,\bar{t}) = \frac{1}{\varepsilon}\mathbf{i} \tag{114}$$

$$\bar{\mathbf{v}}_s(\bar{x},\bar{y},0,\bar{t}) = \frac{G_s}{\rho_s u_o \phi}\mathbf{i} \tag{115}$$

and

$$\bar{\mathbf{v}}_f(\bar{x},0;1,\bar{z},\bar{t}) = \mathbf{n} \cdot \bar{\mathbf{v}}_s(\bar{x},0;1,\bar{z},\bar{t}) = 0 \tag{116}$$

The dimensionless pressure $\frac{p_o}{\rho_f u_\tau^2}$ can be ignored when the fluid velocity is small compared to sonic velocity or the absolute pressure does not change enough to influence the thermodynamic properties of the fluid.

From (100), (110), (111), and (114)-(116) the controlling dimensionless parameters are

$$\frac{\rho_f}{\rho_s};\ \mathrm{Re}_{u_o,d_p};\ \mathrm{Re}_{u_o,D};\ \mathrm{Fr}_{u_o,D};\ \frac{G_s}{\rho_s u_o};\ \phi_s;\ \text{bed geometry} \tag{117}$$

This is the result obtained by Glicksman *et al.* (1994) using the spatially averaged equations of Anderson and Jackson.

2.10 Development of the Scaling Laws Using the Single Particle Equation of Motion

In dilute regions of CFB's and in the freeboard of bubbling beds, gas/solid hydrodynamics may be best represented as individual particles interacting with a turbulent fluid. If this is the case, the assumption of a continuum for the mass of particles in the bed implicit in the Anderson-Jackson equations of motion will not be valid. Additionally, ensemble averaging may not be appropriate in that it may lead to correct but irrelevant statements, like "the

average density of the bed is fairly dilute." To investigate the governing hydrodynamic parameters of a particle suspended in homogeneous or wall bounded turbulence, the equation of motion for an individual particle will be written in its entirety. The equation will be non-dimensionalized to determine the controlling dimensionless groups.

A particle suspended in a turbulent fluid responds to the random fluid velocity. Calculations presented in the literature relating the turbulence characteristics of particle motion to the turbulence characteristics of the fluid have been based on Tchen's (1947) equation of motion or on Maxey and Riley's (1983) equation. These relations include the effects of the Stokes drag, the body force, the Boussinesq-Basset history force and the forces due to added mass and local fluid acceleration. Faxen terms which account for local curvature of the velocity field are also included in Maxey and Riley's equation.

2.10.1 Core Region of a CFB or Freeboard Region of a Bubbling Bed

In the core region of a CFB or freeboard of a bubbling bed where particles are far from the wall, the turbulence can be approximated as unbounded and homogeneous. Maxey and Riley gave the following equation of motion for a sufficiently small spherical particle suspended in unbounded homogeneous turbulence:

$$\begin{aligned}
&\frac{1}{6}\pi d_p^3 \rho_s \frac{d\mathbf{v}_p}{dt} = \frac{1}{6}\pi d_p^3 (\rho_s - \rho_f)\mathbf{g} - 3\pi\mu d_p\left(\mathbf{v}_p - \mathbf{v}_{fp} - \frac{1}{24}d_p^2\nabla^2\mathbf{v}_{fp}\right) \\
&-\frac{3}{2}\pi\mu d_p^2 \int_{t_0}^{t} \frac{d}{d\tau}\left[\mathbf{v}_p - \mathbf{v}_{fp} - \frac{1}{24}d_p^2\nabla^2\mathbf{v}_{fp}\right]\frac{d\tau}{\left(\pi\nu(t-\tau)\right)^{1/2}} \\
&-\frac{1}{12}\pi d_p^3 \rho_f \frac{d}{dt}\left[\mathbf{v}_p - \mathbf{v}_f - \frac{1}{40}d_p^2\nabla^2\mathbf{v}_{fp}\right] + \frac{1}{6}\pi d_p^3 \rho_f \frac{D\mathbf{v}_{fp}}{dt}
\end{aligned} \tag{118}$$

The Eulerian fluid velocity at $\mathbf{x}$ is denoted by $\mathbf{v}_f(\mathbf{x},t)$ and the Lagrangian position and velocity of the particle are denoted by $\mathbf{r}(t)$ and $\mathbf{v}_p(t)$ respectively. The fluid velocity seen by the particle is $\mathbf{v}_{fp} = \mathbf{v}_f(\mathbf{r}(t),t)$. It assumed to have zero mean, or the coordinate system is assumed to be moving with a mean fluid velocity that is uniform in space.

Terms on the r.h.s. of (118) are the gravitational force (minus the buoyancy force), the Stokes drag, the Boussinesq-Basset history force, the force due to added mass and the force resulting

from the stress gradients of the fluid flow in the absence of a particle. The added mass term is expressed in terms of the time derivative seen by the particle as it moves through trajectory d/dt. The term defining the influence of fluid stress-gradients on the particle is expressed in terms of the change in fluid velocity along its own trajectory.

The validity of the Maxey-Riley equation of motion is subject to the following limitations:

$$\frac{d_p\left(v_p - v_{fp}\right)}{\nu} < 1 \tag{119}$$

$$\frac{d_p^2 u_o^2}{D\nu} < 1 \tag{120}$$

$$\frac{d_p^2}{D} < 1 \tag{121}$$

For typical velocities, particle sizes and fluid properties found in fluidized beds, the last two inequalities certainly hold. However, the first inequality may not be satisfied. For a CFB operating at 800 °C with a mean particle diameter of 250 μm, the left hand side of the inequality is about 2.5. In other words, the particle Reynolds number based on relative velocity is finite for the particle flows found in fluidized beds. This indicates that the advective terms in the equation of motion cannot be ignored such that the problem reduces to one of unsteady Stokes flow - as mentioned above. Based on the work of Odar and Hamilton (1964), the Berlemont *et al.* (1990) modifications to the Maxey-Riley equation to account for non-small Reynolds numbers discussed earlier gives

$$\begin{aligned}
&\frac{1}{6}\pi d_p^3 \rho_s \frac{dv_p}{dt} = \frac{1}{6}\pi d_p^3\left(\rho_s - \rho_f\right)g - \frac{\rho_f \pi C_D d_p^2}{8}\left(v_p - v_{fp} - \frac{1}{24}d_p^2 \nabla^2 v_{fp}\right)\left|v_p - v_{fp}\right| \\
&- \frac{\pi\mu d_p^2 C_H}{4}\int_{t_0}^{t} \frac{d}{d\tau}\left[v_p - v_{fp} - \frac{1}{24}d_p^2\nabla^2 v_{fp}\right]\frac{d\tau}{\left(\pi\nu\left(t-\tau\right)\right)^{1/2}} \\
&- \frac{1}{6}\pi d_p^3 \rho_f C_A \frac{d}{dt}\left[v_p - v_f - \frac{1}{40}d_p^2\nabla^2 v_{fp}\right] + \frac{1}{6}\pi d_p^3 \rho_f \frac{Dv_{fp}}{dt}
\end{aligned} \tag{122}$$

The only difference between the Maxey-Riley equation and the Berlemont equation is the coefficients C_D, C_A, and C_H, which take into account non-small particle Reynolds numbers and

particle acceleration. $C_A \to 1/2$, $C_H \to 6$, and $C_H \to \frac{24}{Re_{u_\tau, d_p}}$ for flows where the Reynolds number based on particle diameter and particle/gas relative velocity along with the particle convective acceleration approach zero. This limit results in the Maxey-Riley equation. The same reservations concerning the form of the Boussinesq-Basset history term discussed above apply here.

Many effects have been neglected in the modified Maxey-Riley equation. The sphere is assumed to be isolated and far from any boundary so that the particle-particle interactions and particle-boundary interactions can be excluded. This requires that the distance to the nearest particle or boundary is much larger than the particle radius. Effects of particle rotation and lateral forces due to the shear of the undisturbed flow are also not included. In addition electrostatic forces are ignored. These forces will be discussed below.

As discussed above, in the core of a CFB or freeboard of a bubbling bed, the length scale is D and the velocity scale is u_τ. The corresponding time scale is D/u_τ. The dimensionless form of the single particle equation of motion is then:

$$\frac{d\bar{v}_p}{dt} = \left(\frac{\rho_s - \rho_f}{\rho_s}\right)\frac{gD}{u_\tau^2} - \frac{3C_D}{4}\left(\frac{D}{d_p}\right)\left(\frac{\rho_f}{\rho_s}\right)\left(\bar{v}_p - \bar{v}_{fp} - \frac{1}{24}\frac{d_p^2}{D^2}\bar{\nabla}^2\bar{v}_{fp}\right)\left|\bar{v}_p - \bar{v}_{fp}\right|$$
$$- \frac{3C_H}{2\sqrt{\pi}}\left(Re_{u_\tau, d_p}\right)^{-1/2}\left(\frac{\rho_f}{\rho_s}\right)\left(\frac{D}{d_p}\right)\int_{i_0}^{i}\frac{d}{d\bar{\tau}}\left[\bar{v}_p - \bar{v}_{fp} - \frac{1}{24}\frac{d_p^2}{D^2}\bar{\nabla}^2\bar{v}_{fp}\right]\frac{d\bar{\tau}}{\left(\pi\nu\left(\bar{t}-\bar{\tau}\right)\right)^{1/2}} \qquad (123)$$
$$- \left(\frac{\rho_f}{\rho_s}\right)C_A\frac{d}{d\bar{t}}\left[\bar{v}_p - \bar{v}_{fp} - \frac{1}{40}\frac{d_p^2}{D^2}\bar{\nabla}^2\bar{v}_{fp}\right] + \left(\frac{\rho_f}{\rho_s}\right)\frac{D\bar{v}_{fp}}{d\bar{t}}$$

The controlling dimensionless parameters which appear are:

$$\left(\frac{\rho_s - \rho_f}{\rho_s}\right)\frac{gD}{u_\tau^2};\ C_D\left(\frac{D}{d_p}\right)\left(\frac{\rho_f}{\rho_s}\right);\ C_H\left(Re_{u_\tau, d_p}\right)^{-1/2}\left(\frac{\rho_f}{\rho_s}\right)\left(\frac{D}{d_p}\right);\ \left(\frac{\rho_f}{\rho_s}\right)C_A;\ \left(\frac{\rho_f}{\rho_s}\right);\ \left(\frac{D}{d_p}\right)^2 \qquad (124)$$

From the first term and last term, the density ratio and Froude number based on bed diameter and friction velocity must be constant for similarity. Since C_D is a complex function of Reynolds number based on particle diameter and relative velocity (assumed to be equal to the terminal velocity), $\left(Re_{u_\tau, d_p}\right)$ must also be constant. From the second or the fifth term, the ratio of bed to particle diameter must also be included as a governing dimensionless group. Finally, the third

term requires that the Reynolds number based on bed diameter and friction velocity must also be constant. Referring to the dependence of C_A and C_H on the bed geometry and bed Reynolds number discusses above, the set of dimensionless parameters can be written as:

$$\frac{\rho_f}{\rho_s};\ \mathrm{Re}_{u_\tau, d_p};\ \mathrm{Re}_{u_\tau, D};\ \mathrm{Fr}_{u_\tau, D};\ \text{bed geometry} \tag{125}$$

which can then be written as equation (100)

$$\frac{\rho_f}{\rho_s};\ \mathrm{Re}_{u_o, d_p};\ \mathrm{Re}_{u_o, D};\ \mathrm{Fr}_{u_o, D};\ \text{bed geometry} \tag{126}$$

Neglecting all terms except the gravitational and drag terms does not change the controlling dimensionless groups. This is in agreement with the ensemble averaged equations.

2.10.2 Single Particle Equation of Motion Near a Solid Boundary

Near the wall of a CFB, the lift forces associated with shear of the undisturbed flow may become important. In addition, the fluid-particle drag becomes a function of the particle to wall distance, as discussed above. It is important that these forces be scaled properly when evaluating phenomena very near the wall of the fluid bed. For example, bed-to-wall heat transfer may be a function of this force.

Near the wall of a fluid bed the flow is determined by u_τ and ν, the length scale is ν/u_τ. The velocity and time scales are u_τ and $\frac{\nu}{u_\tau^2}$, respectively. Using these scales the equation of motion yields:

$$\begin{aligned}
\frac{d\bar{v}_p}{dt} = {} & \left(\frac{\rho_s-\rho_f}{\rho_s}\right)\frac{g\nu}{u_\tau^3} - \frac{3C_D}{4}\bar{\chi}\left(\frac{\nu}{d_p u_\tau}\right)\left(\frac{\rho_f}{\rho_s}\right)\left(\bar{v}_p - \bar{v}_{fp} - \frac{1}{24}\frac{d_p^2 u_\tau^2}{\nu^2}\bar{\nabla}^2\bar{v}_{fp}\right)\left|\bar{v}_p - \bar{v}_{fp}\right| \\
& - \frac{3C_H}{2\sqrt{\pi}}\left(\mathrm{Re}_{u_\tau, d_p}\right)^{-1}\left(\frac{\rho_f}{\rho_s}\right)\int_{t_0}^{t}\frac{d}{d\bar{\tau}}\left[\bar{v}_p - \bar{v}_{fp} - \frac{1}{24}\frac{d_p^2 u_\tau^2}{\nu^2}\bar{\nabla}^2\bar{v}_{fp}\right]\frac{d\bar{\tau}}{\left(\pi\nu\left(\bar{t}-\bar{\tau}\right)\right)^{1/2}} \\
& - \left(\frac{\rho_f}{\rho_s}\right)C_A\frac{d}{d\bar{t}}\left[\bar{v}_p - \bar{v}_{fp} - \frac{1}{40}\frac{d_p^2 u_\tau^2}{\nu^2}\bar{\nabla}^2\bar{v}_{fp}\right] + \left(\frac{\rho_f}{\rho_s}\right)\frac{D\bar{v}_{fp}}{d\bar{t}} + \bar{m}_{\text{Saffman}} + \bar{m}_{\text{Ho \& Leal}}
\end{aligned} \tag{127}$$

where (see equations 104a and 104b)

$$\bar{\chi} = fnc\left(\mathrm{Re}_{d_p, u_\tau}\right) \tag{128}$$

The governing parameters for the near wall equation are:

$$\frac{g\mu}{\rho_f u_\tau^3};\ \frac{1}{C_D}\left(\mathrm{Re}_{u_\tau, d_p}\right)\left(\frac{\rho_s}{\rho_f}\right);\ \frac{1}{C_H}\left(\mathrm{Re}_{u_\tau, d_p}\right)\left(\frac{\rho_s}{\rho_f}\right);\ \left(\frac{\rho_f}{\rho_s}\right)C_A;\ \left(\frac{\rho_f}{\rho_s}\right);\ \mathrm{Re}_{u_\tau, d_p};\ \bar{m}_{\text{Saffman}};\ \bar{m}_{\text{Ho \& Leal}} \tag{129}$$

Saffman's lift force (1965) and a wall induced lift of the form of Ho and Leal (1971) yields two additional dimensionless terms:

$$\begin{aligned}\bar{m}_{\text{Sfmn}} + \bar{m}_{\text{H\&L}} &= \frac{3(6.46)}{2\sqrt{2}\pi}\left(\mathrm{Re}_{u_\tau, d_p}\right)^{-1}\bar{D}_f^{\frac{1}{2}}\left(\bar{v}_{fp} - \bar{v}_p\right) \\ &- \frac{3}{\pi}\left(\mathrm{Re}_{u_\tau, d_p}\right)\left(\mathrm{Re}_{u_\tau, D}\right)\bar{D}_f\bar{\nabla}\cdot\bar{D}_f\left[\frac{1}{\left(\mathrm{Re}_{u_\tau, D}\right)}\frac{\frac{\partial \bar{v}_f}{\partial \bar{y}}}{\frac{\partial^2 \bar{v}_f}{\partial \bar{y}^2}}G_1(\bar{y}) - G_2(\bar{y})\right]\end{aligned} \tag{130}$$

The independent dimensionless parameters are

$$\frac{\rho_f}{\rho_s};\ \mathrm{Re}_{u_\tau, d_p};\ \mathrm{Re}_{u_\tau, D};\ \mathrm{Fr}_{u_\tau, D};\ C_H;\ C_A;\ C_D \tag{131}$$

Note that

$$\frac{g\mu}{\rho_f u_\tau^3} = \left(\frac{1}{\mathrm{Re}_{u_\tau, d_p}\mathrm{Fr}_{u_\tau, d_p}}\right) \tag{132}$$

As discussed earlier C_H, C_A are nearly constant for conditions found in fluidized beds. For conditions where they are not constant, they only depend on bed geometry and bed Reynolds number. C_D depends on the Reynolds number based on particle diameter and terminal velocity, which in turn depends on the Archimedes number. Hence, the set of dimensionless groups which govern particle hydrodynamics in the near-wall region is identical to those governing particle motion in the core, namely

$$\frac{\rho_f}{\rho_s};\ \mathrm{Re}_{u_o, d_p};\ \mathrm{Re}_{u_o, D};\ \mathrm{Fr}_{u_o, D};\ \text{bed geometry} \tag{133}$$

If the Faxen terms, Boussinesq-Basset history term, added mass term, the term representing fluid stress gradients on the particle, the Saffman and Ho and Leal lift terms are ignored, the governing independent parameters do not change.

The inclusion of $f(\varepsilon)$ and $g(\phi_s)$ in the drag term [Wen and Yu, (1966); Ganser, (1993); Barnea and Mizrahi, (1973)] extends the analysis to include non-spherical particles. This results in the particle sphericity being added to the list of parameters.

2.10.3 Boundary Conditions

A particle with location y(t) in the flow field is required to satisfy the following boundary conditions:

$$\mathbf{v}_f = \mathbf{v}_p + \Omega \times \left[\mathbf{x} - \mathbf{y}(t)\right] \quad \text{on the particle} \tag{134}$$

$$\mathbf{v}_f(\mathbf{x},t) = \frac{\mathbf{u}_o \mathbf{i}}{\varepsilon} \quad \text{as} \quad \left| \frac{\mathbf{x} - \mathbf{y}(t)}{d_p} \to \infty \right| \tag{135}$$

$$\mathbf{v}_p = \frac{G_s(t)\mathbf{i}}{\rho_s \phi} \quad \text{as} \quad \mathbf{y}(t) \to 0 \tag{136}$$

$$\mathbf{v}_p(\mathbf{x},t) = \frac{\mathbf{u}_o \mathbf{i}}{\varepsilon} \quad \text{as} \quad \mathbf{y}(t) \to L \tag{137}$$

where Ω is the angular velocity of a particle.

The initial condition is set such that the particle velocity is zero as it enters the flow field, and the disturbance field is zero before t = 0.

$$\mathbf{v}_p(\mathbf{x},0) - \mathbf{v}_f(\mathbf{y}(0),0) - \frac{1}{6} d_p^2 \nabla^2 \mathbf{v}_f = 0 \tag{138}$$

Assuming that particle rotation is negligible, the non-dimensional form of the boundary equation is:

$$\bar{\mathbf{v}}_f = \bar{\mathbf{v}}_p \tag{139}$$

$$\bar{v}_f(\bar{x},t) = \frac{\bar{i}}{\varepsilon} \quad \text{as} \quad \left| \frac{\bar{x} - \bar{y}(t)}{d_p} \to \infty \right| \tag{140}$$

$$\bar{v}_p = \frac{G_s \bar{i}}{\rho_s u_o \phi} \quad \text{as} \quad \bar{y}(t) \to 0 \tag{141}$$

$$\bar{v}_p(\bar{x},t) = \frac{\bar{i}}{\varepsilon} \quad \text{as} \quad \bar{y}(t) \to L \tag{142}$$

For fluidized beds, the Faxen force contribution to the initial condition can be dropped resulting in

$$\bar{v}_p(\bar{x},0) - \bar{v}_f(\bar{y}(0),0) = 0 \tag{143}$$

The controlling set of dimensionless groups which result from the single particle equation of motion and boundary conditions is then

$$\frac{\rho_f}{\rho_s};\ Re_{u_o,d_p};\ Re_{u_o,D};\ Fr_{u_o,D};\ \frac{G_s}{\rho_s u_o};\ \phi_s;\ \text{bed geometry} \tag{144}$$

This set is identical to the set resulting from the ensemble averaged equations presented above and spatially averaged equations of Anderson-Jackson as scaled by Glicksman *et al.* (1994).

2.11 Other Forces

2.11.1 Brownian Movement

For very small particles, individual gas molecules may displace the particle by a significant amount. This type of motion is presented in detail in Fuchs (1964) and Green (1957). Particles will move an rms displacement $\bar{\xi}^2$ due to random molecular collisions after time t:

$$\bar{\xi}^2 = \frac{2kTt}{3\pi\mu d_p} \tag{145}$$

where T is the absolute temperature of the gas and k is Boltzmann's constant.

For a combustor operating at 1100 K with 200 micron particles, the rms displacement after

100 seconds is on the order of 1 x 10^{-11} m^2. Clear Brownian movement is insignificant in fluidized beds.

2.11.2 Magnus Effects

Particles subject to a gas undergoing shear tend to rotate. For a fluid with a velocity gradient $\frac{dv_f}{dy}$, the angular rotation of a particle considered to be a small fluid element in the fluid is (Kay, 1957)

$$\Omega_p = \frac{1}{2}\frac{dv_f}{dy} \tag{146}$$

This rotation gives rise to a Magnus force of the order (Owen, 1969)

$$F_L = \rho_f\left(v_f - v_s\right)d_p^3\frac{dv_f}{dy} \tag{147}$$

which is trivial for flows encountered in fluidized beds.

2.11.3 Van der Waals Forces

The van der Waals forces between molecules were first derived theoretically by London (1937). According to his theory, the interaction energy between two molecules is

$$V_{ss} = -\frac{C_{ss}}{\Gamma^6} \tag{148}$$

where C_{ss} is the London - van der Waals constant in Jm^6, which depends on the nature of the interacting molecules. Γ is the distance between molecules. Rietema (1993) has used the empirical expression for the interaction potential between molecules of Lennard-Jones (1937) and integrated it over all molecules in the particle according to Hamaker (1937) to derive an interaction potential between identical particles:

$$U_m = \frac{A\bar{d}_p}{12z}\left[-1 + \frac{1}{420}\left(\frac{r_{ss}}{z}\right)^6\right] \tag{149}$$

where A is the Hamaker constant, $\bar{d}_p$ is the equivalent diameter of contacting particles, r_{ss} is

the molecule parameter, and z is the smallest distance between particles. The net force between particles in dimensionless notation was found as (Rietema, 1993)

$$\Phi = \frac{12F_p r_{ss}}{A\bar{d}_p} = \frac{1}{\xi^2}\left[1 - \frac{1}{60}\xi^6\right] \tag{150}$$

where $\xi = z/r_{ss}$.

For most solids $A \cong 10^{-19}$ (Visser, 1972), and Φ is a maximum at $\xi = 0.6368$. Figure 2.1 shows the ratio of the cohesive force with the weight of the particles using glass beads (ρ_s = 2540 kg/m^3) of the same diameter. In this plot an average value of r_{ss} and z_m ($r_{ss} = 3.5 \times 10^{-10}$m, $z_m = 2.23 \times 10^{-10}$ m) recommended by Rietema *et al.* (1993) was used.

Figure 2.1
Dimensionless Interaction Force as a Function of the Dimensionless Particle-Particle Distance

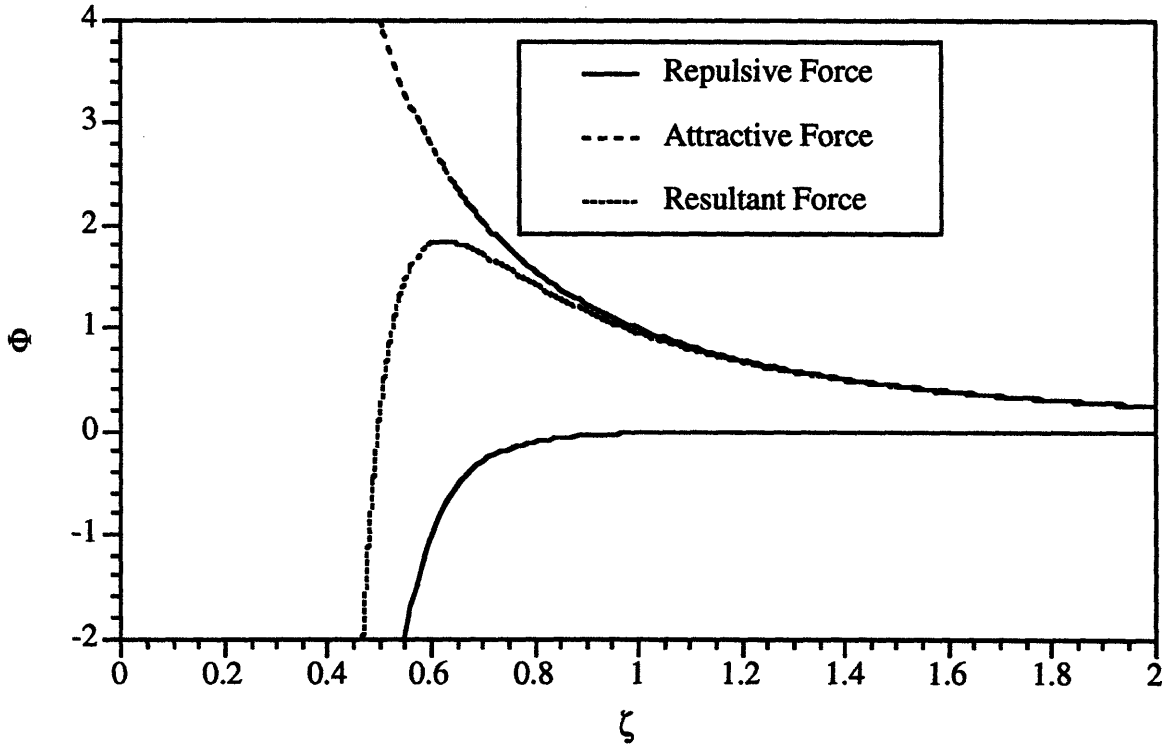

It is clear that cohesive forces may play a large role in determining bed hydrodynamics for small to moderate sized particles which are closely packed. Rietema *et al.* (1993) note that many particles are not smooth but have rough surfaces with many protuberances which

determine the contact area. The correct cohesion force is then the cohesion force per asperity and the diameter of the asperity should be used in determining F_p (most asperities have radii of curvatures less than 0.1 microns). This reduces the calculated cohesive force significantly. The cohesion force is therefore a strong function of the surface structure of the particles. Figure 2.2 shows the ratio of cohesion to gravity forces for glass particles as a function of particle diameter when the cohesive forces are based on the particle diameter and an asperity diameter of 0.1 microns.

Figure 2.2
Dimensionless Interaction Force as a Function of Particle Diameter

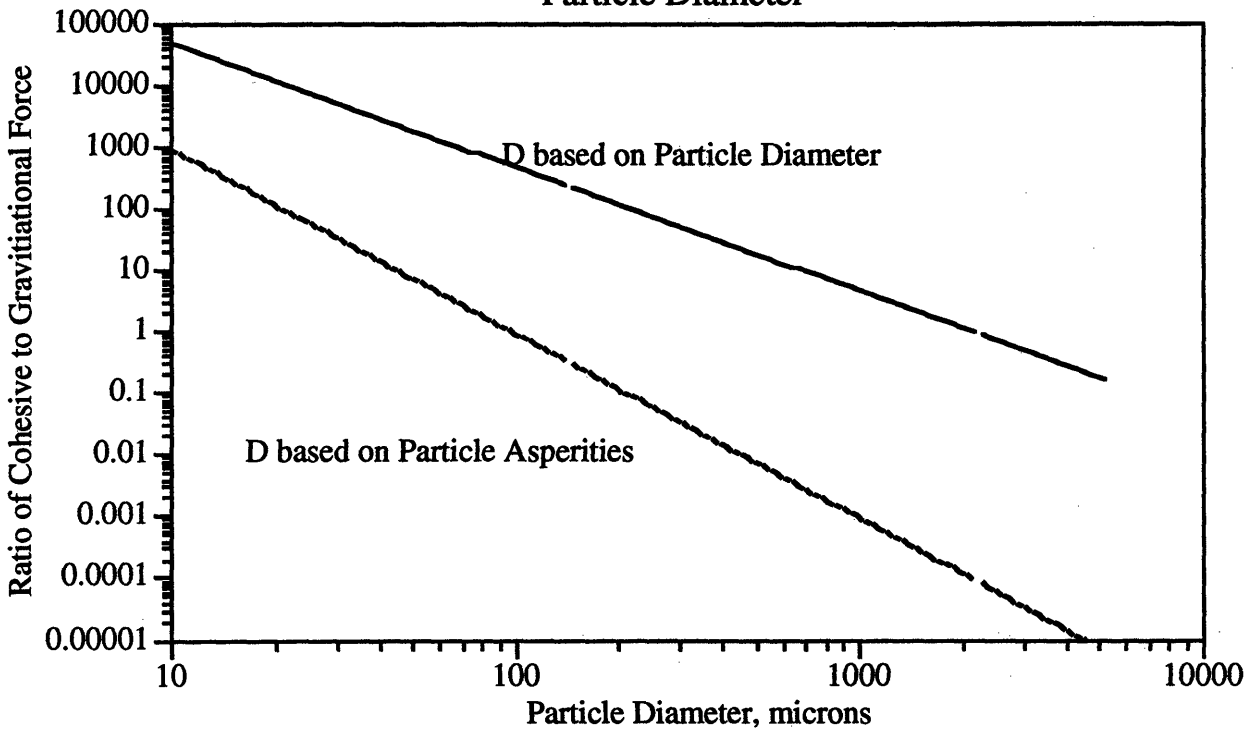

For closely packed particles it is necessary to match the particle size distribution, and the particle surface structure to ensure similarity of the cohesion forces. This is obviously not desirable from a scaling perspective because it is difficult to ensure similarity of surface structure between the target and scale beds. For beds which are not closely packed, cohesion forces become less important. Figure 2.3 depicts the ratio of cohesive to gravitational forces as a function of z.

Figure 2.3
Ratio of Cohesive to Gravitational Forces as a Function of Distance Between Particles

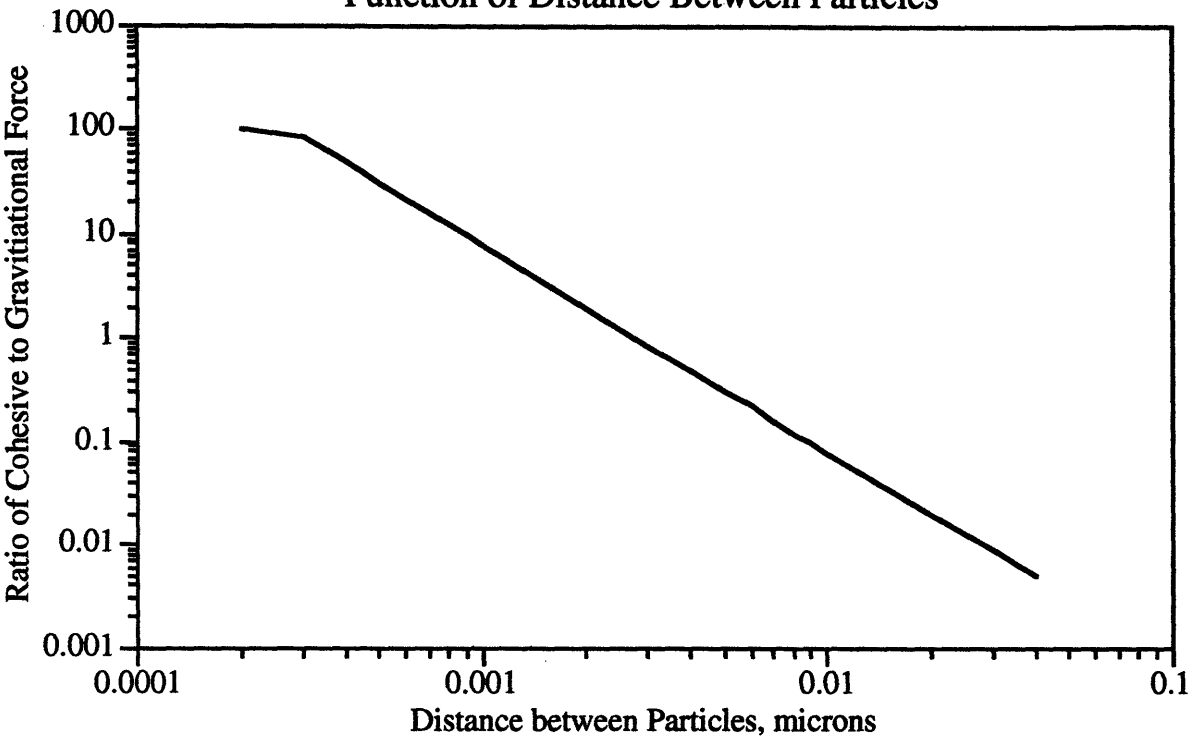

An increase in the smallest distance between particles drastically reduces the cohesion force. Because of the strong dependence of the cohesion force on z and the particle surface structure, it is not clear how sensitive a bubbling bed would be to differences in this force. It is not anticipated that circulating beds would be sensitive to cohesion forces due to the large voidages throughout the bed. Litka and Glicksman (1985) conducted a study to determine the effects of interparticle forces on large particle bubbling fluidized beds. They compared the behavior of beds fluidized with two kinds of particles with identical properties save one. In one test, the particles of the same density, size, sphericity but different coefficients of restitution were compared. In the second series of tests, smooth and frosted glass particles with two different coefficients of sliding friction were compared. In each series of tests, beds with two different particles were found to have the same bubble frequency and size at a given height and u_o - u_{mf}. The bed also exhibited identical vertical particle dispersion, measured by following heated particles within the cold bed. The only exception was the particle with the higher coefficient of friction which exhibited a modest increase ε_{mf} and u_{mf}. Since van der Waals forces involve short range interactions, changes in the roughness should produce different contact profiles and noticeable changes in bed behavior if such

forces are important. The lack of substantial observable effects suggest the contrary conclusion for modest or large particles.

Change and Louge (1992) carried out scaling tests in a circulating fluidized bed. They found that coated glass powders with an artificially low surface friction and possibly a different coefficient of restitution gave a substantially different vertical solid density distribution in the column than a bed of common glass powder. However, the authors conclude that for typical materials with friction coefficients larger than the specially treated powders variations of friction coefficients are expected to have only a minor influence on fluid mechanics.

Most available evidence suggests that particle mechanical properties related to van der Waals forces can be omitted. Because of uncertainty in determining r_{ss} and z, additional study is clearly needed to quantify the effects of van der Waals forces on both bubbling beds and in the bottom sections of circulating fluidized beds where cohesion forces are more likely to be important.

2.11.4 Particle-Wall Collisions

The frictional pressure drop due to the particles will depend on the nature of wall/particle impacts. Parameters which must be included to take into account these collisions are the coefficient of restitution of impact between the particles and wall, particle surface characteristics, and bed wall roughness. The Chang and Louge study cited above has indicated that this effect will be minimal for materials used in fluidized beds and scale models. This is consistent with the results of Glicksman *et al.* (1991).

2.11.5 Particle-Particle Collisions

In the stability analysis of Jackson (1963), a particle inertia was included along with a drag force of the form

$$\mathbf{D} = \beta(n_p)(\mathbf{v}_f - \mathbf{v}_p) \tag{151}$$

where $\beta(n_p)$ is a function of number density, $\mathbf{v}_f$ is the mean fluid velocity, and $\mathbf{v}_p$ is the mean velocity of the particle phase. Jackson's development resulted in the conclusion that the homogeneous state of a fluidized bed is unstable. The continuum theories of Didwania

and Homsy (1982) and Batchelor (1988) include particle interactions which are incorporated into a "particle pressure" and particle diffusivity to obtain criteria for the stability of homogeneously fluidized beds. The particle pressure, similar to the kinetic theory of gases, relates to the rms of the fluctuating velocities of the particles (Koch, 1990; Jenkins and Richman, 1985).

Kumeran and Koch (1993a, 1993b) have developed velocity distributions for bidisperse particle-gas suspensions in the limits where the collision time is small compared with the viscous relaxation time and where the viscous relaxation time is small compared with the collision time. Their evaluation assumed a suspension of particles settling in a gas in the low Reynolds number limit. In this limit, the drag force on the particles is a linear function of its velocity. It was also assumed that the drag force was independent of the volume fraction of particles. These simplifications allowed for the incorporation of the collisional interactions in a detailed fashion. While these limits do not strictly hold in fluidized beds, the analysis does provide an understanding of the effect of collisions on velocity fluctuations and provides insight into the dimensionless groups which govern the influence of collisions on fluid bed hydrodynamics.

The time between collisions is related to the radius, number density and fluctuating velocity of the particles by [Kumaran and Koch (1993a)]

$$t_{cij} = \frac{1}{n_{pj}\pi d_{pij}^2 v'_{rms}} \tag{152}$$

where t_{cij} is the time between successive collisions of particles of species i with particles of species j, v'_{rms} is the magnitude of the fluctuating velocity of the particles and d_{ij} is the sum of the radii of particles of species i and j. The rate of energy dissipation is inversely related to the viscous relaxation time t_{vi}, which is the time it takes for a particle to reach its terminal velocity:

$$t_{vi} = \frac{m_i}{6\pi d_{pi}\mu} \tag{153}$$

when $\frac{t_{cij}}{t_{vi}} v_m << u_{ti} - u_{tj}$, the ratio of the collision time scale to the viscous relaxation time is

$$\frac{t_{cij}}{t_{vi}} = \left(n_{pj}\pi d_{pij}^2 v_m t_{vi}\right)^{-2/3} \tag{154}$$

This ratio is proportional to $\left(St(1-\varepsilon)\right)^{-2/3}$, where St is the Stokes number defined as

$$St = \left(\frac{m_p u_t}{6\pi\mu d_{pij}^2}\right) \tag{155}$$

When the fluctuating velocity is of the same order as the difference in terminal velocities of the particles the collision time is

$$t_{cij} = \frac{1}{n_{pj}\pi d_{pij}^2 \left(u_{ti} - u_{tj}\right)} \tag{156}$$

so that the ratio of collisional to viscous relaxation time is proportional to St (1 - ε).

When the collisional time scale is much smaller than the viscous relaxation time scale, a particle does not experience significant viscous deceleration between successive collisions. By neglecting deceleration in the leading-order approximation, Kumaran and Koch (1993) showed that the distribution functions for the two species are the Maxwell-Boltzmann distribution with equal mean velocities. Balance equations for three moments of the fluctuating velocity were then derived using a slightly perturbed form of the distribution functions and these were solved to give the mean and mean-square velocities.

From the balance equations and the collisional rate of change of velocity moment expressions, the dimensionless groups which govern particle collision impacts on bed hydrodynamics are:

$$\frac{t_{cij}}{t_{vi}}, \frac{t_{vi}}{t_{v1}}, \frac{t_{c12}}{t_{cii}}, \frac{m_{pk}}{m_{pi}+m_{pk}}, \frac{u_{ti}}{u_{tj}} \tag{157}$$

or

$$\left(\frac{m_{pi}}{m_{p1}}\right)\left(\frac{d_{p1}}{d_{pi}}\right); \; St; \; \left(\frac{m_{pi}}{m_{pk}}\right); \left(\frac{n_2 d_{p12}^2}{n_i d_{pik}^2}\right); \left(\frac{n_2 d_{p12}^2}{n_i d_{pii}^2}\right) \tag{158}$$

Fore the same density particles within a bed, the independent dimensionless groups are

and particle/wall collisions is small requiring one to only match the particle size distribution and the Stokes number to adequately take into account particle collisions.

2.11.6 Electrostatics

In studies which discuss the problems of scaling two-phase gas/solid systems, static electricity is often cited as a potential source of error. Fluidization is characterized by the continual contact and separation as well as frictional contact between the particles in the system and between the particles and other parts of the fluidizing equipment. When two surfaces are brought into contact, a separation of opposite charges takes place so that, on separation of the surfaces, an equal and opposite static charge resides on the two surfaces. Therefore, the main requirement for static electrification is the making and breaking of surface contact. Unfortunately both the mechanism of electrification and the laws which govern it as they apply to fluidized beds have not been thoroughly investigated. In this Section, the fundamental dynamics of electrostatically charged particles will be presented and the impact of electrostatic charging on fluid bed hydrodynamics will be discussed.

The motion of charged particles in electrostatic fields has been studied by several investigators (Kraemer, 1955; Ranz, 1952; Soo, 1964a,b; Chen 1970). The force on a particle moving in a magnetic field simultaneously with an electrostatic field is given in many fundamental physics texts

$$\mathbf{F} = q\left(\mathbf{E} + \mathbf{v}_p \times \mathbf{B}\right) \times \nabla\left(\mathbf{p} \cdot \mathbf{E}\right) \tag{160}$$

where q is the charged carried by the particle which has an electrostatic dipole moment **p**.

2.11.6.1 Electrostatic Forces Between Particles

The case of a spherically symmetric cloud of charged particles has been studied by Soo (1964a,b) and Cheng (1970). Using a Lagrangian frame of reference, equation (160) reduces to

$$m_p \frac{dv_{pr}}{dt} = qE + \frac{\partial pE}{\partial r} \tag{161}$$

where v_{pr} is the particle velocity in the radial direction.

Equation (161) neglects any hydrodynamic interaction between the particles and the carrier gas. The first term in (161) is the normal coulomb force on the particle and second term arises from the dipole moment. E is given by Gauss' law

$$E = \frac{1}{4\pi\varepsilon r^2}\int_0^r 4\pi r'^2 n_p q dr' = \frac{\left(\frac{q}{m_p}\right)}{4\pi\varepsilon r^2} M_r \tag{162}$$

and

$$M_r = \int_0^r 4\pi\rho_s\left(1-\varepsilon\right)n_p r^2 dr \tag{163}$$

in a cloud of equally charged particles. The dipole moment is (Soo, 1964a)

$$P = \frac{M_r}{\rho_s}\frac{3\left(K-1\right)}{\left(K+2\right)}\varepsilon_o E \tag{164}$$

K in equation (164) is the dielectric constant. Substitution of equations (162), (163) and (164) into equation (161) gives

$$m_p\frac{dv_{pr}}{dt} = \frac{1}{\varepsilon_o}\left(\frac{q}{m_p}\right)^2\frac{M_r}{4\pi r^2} - \frac{12}{\rho_s\varepsilon_o}\left(\frac{\left(K-1\right)}{\left(K+2\right)}\right)\left(\frac{q}{m_p}\right)^2\frac{M_r}{\left(4\pi\right)^2 r^5} \tag{165}$$

where $M_r = M_r(R)$ at $t = 0$ where $v_{pr} = 0$.

In general the force due to the dipole moment can be neglected since the ratio of this force to the coulomb force is

$$\frac{F_d}{F_c} = 4\left(\frac{\left(K-1\right)}{\left(K+2\right)}\right)\left(1-\varepsilon\right) \tag{166}$$

which for low dielectric constants results in

$\left(\frac{d_{pi}}{d_{pk}}\right)$ and St which are equivalent if the dimensionless particles size distribution and the Stokes number are held constant between beds.

Additionally, if collisions are not perfectly elastic, the coefficient of restitution , e, must be included.

In the limit where the viscous relaxation time is much less than the time between collisions, particles relax close to their terminal velocities. Kumeran and Koch (1993b) evaluated this limit by performing a perturbation analysis in the parameter $\alpha = \left(\frac{t_{v1}}{t_{c12}}\right) << 1$ about a base state in which all the particles settle at their terminal velocities.

From the steady state balance equations, the momentum equations, and the energy equation, the governing dimensionless groups are:

$$\frac{t_{v1}}{t_{vi}}; \frac{t_{c12}}{t_{cij}}\frac{t_{vi}}{t_{v1}}; \frac{m_{pk}}{m_{pi}+m_{pk}}; \frac{u_{ti}}{u_{tj}}; e \qquad (159)$$

which are equivalent between beds when St, the particle size distribution, and e are the same.

The above analysis suggests that the dimensionless particle size distribution, Stokes number and coefficient of restitution should be included in the set of dimensionless parameters if particle collisions significantly affect bed hydrodynamics. This is true in the limits where the viscous relaxation time is large compared to the time between successive collision, and when the time between successive collisions is much larger than the viscous relaxation time. This result supports the suspicions of Scharff (1978) that the dimensionless particle size distribution and particle elasticity must be matched along with the hydrodynamic parameters to achieve similarity in the solid pressure term.

For a CFB operating at 12 atmospheres with particles of mean size 200 microns and density 2600 kg/m^3, the ratio of viscous relaxation time to the collisional time scale is of order one when the bed solid fraction is about 0.005. This indicates that one cannot ignore particle collisions out of hand. The Litka-Glicksman study (1985) and the Chang-Louge (1992) study mentioned above indicate that the overall effect of not matching the coefficient of restitution in the range of materials used in fluid bed and scale models will not significantly affect the bed hydrodynamics. It may be that the effect of e on collisions between particles

$$\frac{F_d}{F_c} = \frac{4}{3}(K-1)(1-\varepsilon) \tag{167}$$

and for high dielectric constants results in

$$\frac{F_d}{F_c} = 4(1-\varepsilon) \tag{168}$$

both of which are small in CFB's.

So the equation of motion for electrostatically charged particles can be written as

$$\frac{dv_{pr}}{dt} = \left(\frac{q}{m_p}\right)^2 \frac{\rho_s}{\varepsilon_o r^2} \int_0^r (1-\varepsilon) r^2 dr \tag{169}$$

Non-dimensionalization with d_p and u_o gives

$$\frac{d\bar{v}_{pr}}{d\bar{t}} = \frac{d_p^2}{u_o^2}\left(\frac{q}{m_p}\right)^2 \frac{\rho_s}{\varepsilon_o \bar{r}^2} \int_0^r (1-\varepsilon) \bar{r}^2 d\bar{r} \tag{170}$$

The governing dimensionless parameter for similarity in a cloud of electrostatically charged particles is then

$$Es = \frac{d_p^2}{u_o^2}\left(\frac{q}{m_p}\right)^2 \frac{\rho_s}{\varepsilon_o} \tag{171}$$

If electrostatic charging is significant, the bed must be controlled such that the charge carried by the particles can be adjusted to keep this parameter constant between beds.

2.11.6.2 Charged Particles Near the Wall of a Fluidized Bed

For small particles near the wall of a CFB, the electrostatic force due to mirror charging may become important. The particle acceleration due to mirror charging is given by Boothroyd (1971) and Johansen (1991).

$$\frac{V_E}{t_p} = \frac{q^2}{t_p 12\pi^2 \varepsilon_o \mu d_p y^2} \tag{172}$$

where V_E is the electrostatic drift velocity, q is the particle's electric charge, ε_o is the electric permittivity of a vacuum, y is the distance between the wall and the orgin of the particle, and t_p is the Stokes relaxation time. If the particle and the wall are made of poorly conducting materials, the electrical permittivity for the wall and the particle material must be introduced (Hesketh, 1977).

The dimensionless drift velocity can be written as

$$\bar{V}_E = \frac{Mi}{Re_{d_p, u_o}, Re^2_{D, u_o}} \tag{173}$$

where the dimensionless group Mi which represent mirror charging is

$$Mi = \frac{q^2 u_o^2}{12\pi^2 \varepsilon_o \mu \nu^3} \tag{174}$$

Therefore,

$$\bar{V}_E = Es\, Re_{d_p, u_o} \left(\frac{Re_{d_p, u_o}}{Re_{D, u_o}} \right)^2 \left(\frac{\rho_s}{\rho_f} \right) \tag{175}$$

Particle dynamics due to both interaction between electrically charged particles and mirror charging between walls and particles are governed by the parameter Es when the hydrodynamic parameters discussed above are held constant.

Achieving similarity of electrostatic charges is clearly a problem unless corona charging equipment is accessible. In addition, electrostatic charging effects will not be significant in a hot combustor due to the presence of ions in the reactor and the larger particles relative to the scale model. For a combustor with particles on the average of 200 microns, the maximum possible drift velocity due to electrostatic forces (assuming maximum field strength at which air breaks down and maximum electron charge on a single particle in dry air) will be on the order of 0.1 m/s. In reality the velocity will be much smaller (< 0.01 m/s) due to the presence of ions in the combustion gas and smaller charges on the particles. On the other hand, for a scale model using 30 μm particles, the ratio of electrostatic to viscous forces could be of the order 1. Figure 2.4 shows the ratio of electrostatic to gravity force assuming the amount of charge acquired by a particle is one tenth the maximum which is limited by the

electrical breakdown strength of air. This assumption is consistent with the observations of Billings and Wilder (1970). Also shown is the ratio of electrostatic to gravity forces if the charged acquired by each particle is best described by the data taken by Ban *et al.* (1994). Ban *et al.* measured the charge accumulation from particle-particle and particle-wall contacting on spherical silica particles in pneumatic transport using an argon laser based phase Doppler velocimeter technique.

Figure 2.4
Ratio of Electrostatic to Gravitational Forces versus Particle Diameter

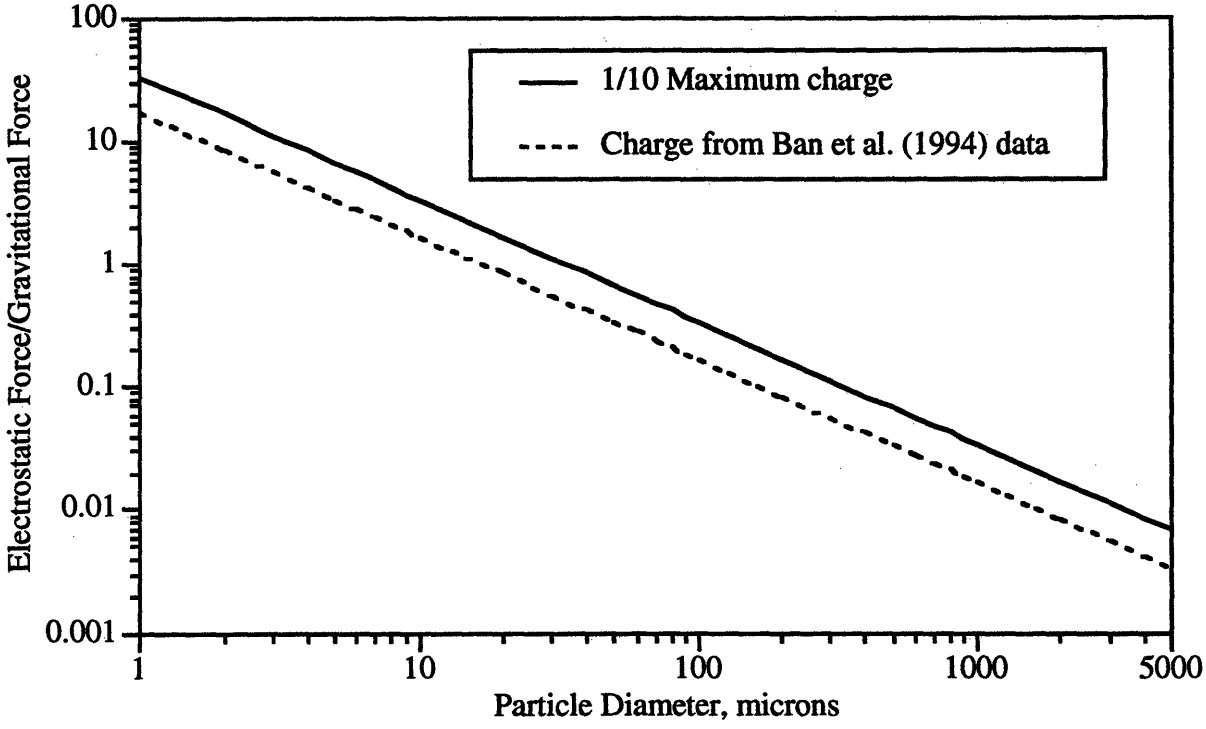

In order to ensure that electrostatic effects are not significant in scale models, treatment of the equipment and/or particles is often necessary. Ammonium ethosulfate salt powder additives have proven to be effective in eliminating much of the electrostatics in fluid bed models (Chang and Louge, 1992; Glicksman *et al.*, 1993). Other mitigation techniques include coating the bed and/or particles with conductive coatings and waxes, humidifying the inlet air, ionizing the inlet air, and grounding the bed wherever possible. When attempting to reduce static electricity effects, care should be taken not to significantly alter the fluidization properties of the particles or to change the air properties to such a degree that the hydrodynamic scaling parameters are not longer matched.

2.12 Full Set of Scaling Parameters

Based on the non-dimensionalization of the ensemble averaged equations of motion or the single particle equation of moation, if it is assumed that Brownian movement, Magnus effects, and electrostatic forces are insignificant, or have been mitigated, the parameters which govern the particle/gas hydrodynamics are:

$$\frac{\rho_f}{\rho_s};\ Re_{u_o,d_p};\ Re_{u_o,D};\ Fr_{u_o,D};\ \frac{G_s}{\rho_s u_o};\ \phi_s;\ \text{PSD};\ \text{bed geometry} \tag{176}$$

where PSD is the particle size distribution.

2.13 Calculation of Scale Model Operating Conditions Using the Full Set of Parameters

To construct a model which will give behavior similar to another bed, all of the parameters in (176) must have the same value. The requirements of similar bed geometry is met by use of geometrically similar beds; the ratio of all linear bed dimensions to a reference dimension such as the bed diameter must be the same for the model and combustor. The dimensions of the elements external to the bed such as the particle return loop do not have to be matched as long as the retrun loop is designed to provide the proper external solids flow rate, inlet conditions, and size distribution (Rhodes and Laussman, 1992; Chang and Louge, 1992).

Proper conditions must be chosen to design a scale model to match the dimensionless parameters of the target bed. To model a gas fluidized commercial bed, a scale model using air at standard conditions is most convenient, although several investigators have used other gases (Fitzgerald and Crane, 1980; Fitzgerald *et al.*, 1984; Chang and Louge, 1992) or pressurized scale models (Almstedt and Zakkay, 1990; DiFelice *et al.*, 1992a,b). The full set of scaling parameters can be combined to give dimensionless groups which include only one of the unknown dimensional parameters. This combination yields

$$\frac{Re_{u_o,D}}{Re_{u_o,d_p}\left(Fr_{u_o,D}\right)^{1/2}}\frac{\rho_f}{\rho_s} = \frac{D^{1.5}\sqrt{g}}{\nu} \tag{177}$$

$$\frac{Re_{u_o,D}}{Re_{u_o,d_p}}\frac{\rho_f}{\rho_s}Fr_{u_o,D} = \frac{u_o^3}{g\nu} \tag{178}$$

$$\left(\frac{G_s}{\rho_s u_o}\right)^3 \frac{u_o^3}{gv} = \frac{\left(\frac{G_s}{\rho_s}\right)^3}{gv} \tag{179}$$

If all experiments are done under the same gravitational conditions, length ratios scale with the 2/3 power of the gas kinematic viscosity and superficial velocity and solid volumetric flux scale with the 1/3 power of the kinematic viscosity. Scale model operating conditions are determined as follows (in what follows, "m" stands for model and "c" stands for combustor):

Assuming that the fixed hot bed parameters such as L_h, D_h, ρ_{sh}, d_{ph}, ρ_{fh}, and μ_h are all known, and ρ_{fm} and μ_m are evaluated at atmospheric conditions, the cold bed particle density is specified by equality of the solid-gas density ratios of the two beds

$$\rho_{sm} = \frac{\rho_{sc}}{\rho_{fc}}\rho_{fm} \tag{180}$$

For a combustor operating at 1 atmosphere and 1100 K, the gas density is about 0.3 kg/m^3. If the hot bed particle densities assumed to be 2600 kg/m^3, the required cold bed particle density is 10130 kg/m^3. For 10 atmosphere combustor, the cold bed particle density is about 1000 kg/m^3.

The length ratios are determine from equation (177)

$$\frac{D_m}{D_c} = \left(\frac{\mu_m \rho_{fc}}{\mu_c \rho_{fm}}\right)^{2/3} \tag{181}$$

The diameter ratios for a room temperature, atmospheric pressure scale model of an atmospheric pressure combustor is roughly 1/4. For a 10-atmosphere pressurized combustor, the diameter ratio is about 1/1. The diameter ratio applies to all bed dimensions. It also applies to the particle diameter when the full set of scaling parameters is used. The model and combustor particles should also have the same sphericity.

Model operating parameters are u_o and G_s. These are determined from:

$$\frac{u_{om}}{u_{oc}} = \left(\frac{D_m}{D_c}\right)^{1/2} \tag{182}$$

and

$$\frac{\left(\frac{G_{sm}}{\rho_{fm}}\right)}{\left(\frac{G_{sc}}{\rho_{fc}}\right)} = \left(\frac{D_m}{D_c}\right)^{1/2} \tag{183}$$

To satisfy the full set of dimensionless parameters, once the model fluid pressure and temperature are chosen there is one unique set of parameters for the model which gives similarity. The dimensionless dependent variables will be the same in the respective dimensionless time and spatial coordinates of the model as the hot or commercial bed. Prediction of the hot bed operating conditions can be determined from the dimensionless cold bed operating conditions by converting the similar hot bed dimensionless group to dimensional form:

$$\left(\frac{\Delta P}{\rho_s g \Delta L}\right)_c = \left(\frac{\Delta P}{\rho_s g \Delta L}\right)_m ; \text{ Pressure Drop} \tag{184}$$

$$\varepsilon_c = \varepsilon_m; \text{ Voidage} \tag{185}$$

$$(v)_c = (v)_m \left(\frac{D_c}{D_m}\right)^{1/2} ; \text{ Velocity} \tag{186}$$

$$(l)_c = (l)_m \left(\frac{D_c}{D_m}\right); \text{ Length} \tag{187}$$

$$(t)_c = (t)_m \left(\frac{D_c}{D_m}\right)^{1/2} ; \text{ Time} \tag{188}$$

$$(\omega)_c = (\omega)_m \left(\frac{D_c}{D_m}\right)^{-1/2} ; \text{ Frequency} \tag{189}$$

Table 2.1 gives the values of design and operating parameters of a scale model fluidized with air at ambient conditions which simulates the dynamics of a fluidized bed combustor operating at 1100 K. The linear dimensions of the model are about 1/4 those of the hot bed. The particle density in the model is much higher due to the low combustor gas density. For

a pressurized hot bed (Table 2.2) the linear dimensions are roughly equal to those of the hot bed while the particle density is lower than the particle density in the combustor.

Table 2.1: Atmospheric Combustor Modeled by a Bed Fluidized with Ambient Air

	Commercial Bed	Scale Model
Temperature, K	1100	300
Gas Viscosity (10^{-5} kg/m-s)	4.45	1.81
Density (kg/m^3)	0.314	1.20
Derived from Scaling Laws		
Solid Density	ρ_{sc}	$3.82\rho_{sc}$
Bed Diameter, geometry	D_c	$0.225D_c$
Particle Diameter	d_{pc}	$0.225d_{pc}$
Superficial Velocity	u_{oc}	$0.47u_{oc}$
Volumetric Solids Flux	$\left(\frac{G_s}{\rho_s}\right)_c$	$0.47\left(\frac{G_s}{\rho_s}\right)_c$
Time	t_c	$0.47t_c$
Frequency	f_c	$2.13f_c$

Table 2.2: Pressurized Combustor Modeled by a Bed Fluidized with Ambient Air

	Commercial Bed	Scale Model
Temperature, K	1100	300
Gas Viscosity (10^{-5} kg/m-s)	4.45	1.81
Density (kg/m^3)	3.14	1.20
Pressure (Pa)	10^6	10^5
Derived from Scaling Laws		
Solid Density	ρ_{sc}	$0.382\rho_{sc}$
Bed Diameter, geometry	D_c	$1.05D_c$
Particle Diameter	d_{pc}	$1.05d_{pc}$
Superficial Velocity	u_{oc}	$0.47u_{oc}$
Volumetric Solids Flux	$\left(\frac{G_s}{\rho_s}\right)_c$	$1.05\left(\frac{G_s}{\rho_s}\right)_c$
Time	t_c	$1.05t_c$
Frequency	f_c	$0.98f_c$

2.14 Experimental Verification of Full Set of Scaling Parameters

There have been many demonstrations of the full set of scaling parameters as applied to bubbling beds. Table 2.1 presents a summary of these experiments. The methods of validating the scaling laws generally focus on bed properties associated with bubble characteristics. The results generally showed good agreement when all the dimensionless parameters were held constant.

There has also been limited work in applying the full set of scaling parameters to circulating fluidized beds. Westphalen *et al.* (1992) have shown that the full set of scaling laws allow a cold model of a circulating bed to closely simulate the behavior of a hot combustor. Two combustors have been modeled, a small, 15 cm square, combustor, and a 2.5 MW_t combustor which was approximately 0.6 m square. CFB experimental work utilizing the full set of scaling parameters is given in Table 2.2.

Table 2.1: Experimental Verification of Full Set of Scaling Parameters in Bubbling Beds

Investigator	Bed Diam. (mm)	Gas Properties	d_p (μm)	Particle Denisty (kg/m^3)	Re_p	Scalaing Parameters	Measurements Compared	Agreement
Fitzgeral et al., 1983	127 x 483 64 x 241	Helium, Cold 27 psia Air, Cold	930 490	2500 9000	28 38	Full Set	Pressure Fluctuations	Agreeement, but not within 95%
Nicastro and Glicksman, 1984	610 x 610 150 x 150	Hot Cold	677 170 677	2630 7380 2630	5.2 5.3 42	Full Set	Pressure Fluctuations	Good Agreement
Newby and Keairns, 1986	150 x 360 75 x 180	Cold Cold, 2.9 bar	200 200 100	2467 2931 7625	1-2 1-2 1-2	Full Set	Bubble Frequency; Pressure Fluctuations	Good Agreement
Glicksman et al. (1987)	3700 x 7300 1200 x 1200	Hot Cold	615 200	2480 8097	8.7 6.7	Full Set	Bed Expansion	Good Agreement
Almstedt and Zakkay, 1990	780 394	Hot, 790 kPa Cold, 240 kPa	962 486 486 962	2200 3000 2200 2200	68 70 70 139	Full Set	Capacitance Probe Measurements of Bubble Properties	Good Agreement
Ackeskog, Almstedt, and Zakkay, 1993	780 394	Hot, 790 kPa Cold, 240 kPa	962 486 486	2200 3000 2200	68 70 70	Full Set	Heat Transfer Measurements	Translation Procedure needed to Predict Hot Bed Heat Transfer
Di Felice et al., 1992	192 106 49.5 49.5 192	92 kPa 200 kPa 660 kPa 620 kPa 92 kPa	597 348 158 163 348	1216 2640 8770 7300 2640	19 18 19 17 11	Full Set	Pressure Fluctuations; Bed Expansion	Agreement in Bubbling Regime, Poor in Slugging Regime

Table 2.2: Experimental Verification of the Full Set of Scaling Parameters in Circulating Fluidized Beds

Investigator	Bed Diam. (mm)	Length (m)	T (C)	Press. (kPa)	Particle d_p (μm)	Particle Denisty (kg/m^3)	Re	Scalaing Parameters	Measurements Compared
Glicksman et. al. (1990); Westphalen (1990)	152 x 152 34 x 34	7.3 1.62	850 25	100 100	185 52	2700 7250	1.3 1.6	Full Set	Voidage Profile; Pressure Fluctuations
Change and Louge (1992)	200 Mixtures of Helium and CO_2 as gas	7.0	25	100	234 109 67	1440 2350 7400	2 2 2	Modified Full Set	Voidage Profile; Pressure Fluctuations
Westphalen (1993)	700 x 600	8	870	100	240 58	2600 7250	2.5 2.3	Full Set	Voidage Profile

3.0 SIMPLIFICATIONS TO THE FULL SET OF SCALING PARAMETERS

3.1 Introduction

When constructing a model fluidized with ambient air, matching the full set of scaling parameters results in a unique set of values for the particle density and diameter and for the linear dimensions of the bed. By simplifying the set of scaling relationships, it is possible to relax the constraint on the dimensions of the model relative to the full scale bed.

The full set of scaling relationships were obtained by non-dimensionalizing the ensemble-averaged equations of motion for the particles and the fluid in a fluidized bed along with their boundary conditions. Identical results were obtained by non-dimensionalizing the single particle equation of motion. To begin the simplification process, the dimensionless governing equations [equations (83)-(86) in Section 2] and the dimensionless constitutive equations, [equations (89)-(92) in Section 2] can be analyzed in order to eliminate terms which will be negligible when compared to others in the same equation.

3.2 General Simplifications

In most situations, the viscous forces associated with the macroscopic gas and particle velocity gradients are negligible compared to the interphase drag. This can be seen in the gas phase momentum equation where the terms representing the fluid viscous stresses are multiplied by the inverse of the Reynolds number based on shear velocity and bed diameter. It should be noted, that for dense suspensions where the solid phase stress tensor can be modeled in a form analogous to a Newtonian fluid, the solid viscous stresses would be dropped from the particle phase momentum equation [Glicksman *et al.*, (1994)].

If the equation for the steady state dimensionless interphase momentum transfer for the solid is evaluated, it becomes obvious that the term representing the interphase drag dominates the Faxen forces. The drag term is multiplied by a factor of D/a while the Faxen term is multiplied by the inverse of the bed Reynolds number. Additionally, the macroscopic gas velocity gradients will be relatively small in the core of a fluidized bed such that the Saffman unbounded shear lift force can be ignored. Finally, the Ho-Leal lift force is only significant very near the wall of the fluid bed [$y/d_p \sim O(1)$] so that it may be ignored for all but phenomena which occur very near the wall of the fluid bed (heat transfer, erosion). These simplifications result in the steady-state momentum transfer for the solid to be controlled only by the interphase drag; a result which is not surprising.

The dimensionless time dependent force equation [(91) in Section 2] contains three terms: the Boussinesq-Basset history term, the virtual mass term, and the term resulting from the stress gradients of the fluid flow in the absence of particles. The Boussinesq-Basset force is included because the interaction force depends, not only on the instantaneous motion of the particle, but also on the instantaneous fluid velocity field in which it moves, which in turn depends on the complete history of the particle's motion. However, in a fluid bed the presence of large assemblies of particles dispersed throughout the fluid is likely to erase any historical effects of the motion of a given particle on the fluid flow in its own neighborhood. In Part 5 of this thesis it will be shown that this is, in fact, the case. For the remainder of this Section, the Boussinesq-Basset history term will be ignored.

The simplifications described above result in the following dimensionless groups appearing in the particle and gas phase momentum equations:

$$\frac{\rho_s}{\rho_f};\ \frac{gD}{u_\tau^2};\ \frac{D}{\rho_f u_\tau^2}\mathbf{m}_s;\ \frac{D}{\rho_f u_\tau^2}\mathbf{m}_f;\ \frac{p_s}{\rho_f u_\tau^2} \tag{1}$$

where the steady state dimensionless interphase momentum transfer for the solid is governed only by a dimensionless interphase drag (virtual mass and fluid flow stress gradient terms in the unsteady part of the momentum transfer for the solid do not introduce any dimensionless parameters):

$$\frac{D\,\mathbf{m}_{s_\infty}}{\rho_f u_\tau^2} = \frac{3}{8}\phi\frac{D}{a}C_D\left(\bar{v}_f - \bar{v}_s\right) \tag{2}$$

$$\bar{m}_s(t) = C_A\frac{d\left(\bar{v}_f - \bar{v}_p\right)}{dt} + \frac{D\bar{v}_f}{dt} \tag{3}$$

and

$$\mathbf{m}_s = \mathbf{m}_{s_\infty} + \mathbf{m}_s(t) \tag{4}$$

From equation (90) of Section 2, it is also clear that for bed Reynolds number of the order 100 or larger

$$\bar{m}_s \cong -\bar{m}_f \tag{5}$$

which states that the dimensionless interaction stress is small

$$\frac{\bar{\nabla}\cdot\bar{\bar{S}}}{Re_{u_\tau,D}} \to 0 \tag{6}$$

The particle phase pressure does not introduce any independent dimensionless groups for relatively disperse flows (see equation (92), Section 2). Additionally, for flows typical of fluidized beds, the Acceleration number defined in Section 2, will tend toward its non-accelerating limit of 1/2. These assumptions along with equations (2)-(6) allow equation (1) to be written as:

$$\frac{\rho_s}{\rho_f};\ \frac{gD}{u_\tau^2};\ \frac{\beta D}{\rho_f u_\tau};\ \text{bed geometry} \tag{7}$$

where the dimensionless interphase momentum transfer is represented by the dimensionless interphase drag. This is done for two reasons. The first is that the only term in the interphase momentum transfer equation which introduces any dimensionless groups is the drag term. Second, and perhaps more importantly, no assumptions have been introduced at this point which apply only to dilute particulate flows, except for the form of the particle pressure and solids stress tensor. Therefore, assuming the particle pressure is still governed by a form similar to equation (109) of Section 2, the parameters in (7) apply not only to the dilute flows found in circulating fluidized beds, but also to the more dense flows of bubbling beds.

Note that for dilute flows, the drag force is

$$\mathbf{F}_D = f(\varepsilon)g(\phi_s)\frac{\pi d_p^2}{4}\frac{\rho_f(\mathbf{v}_f-\mathbf{v}_p)^2}{2}C_D \tag{8}$$

where $f(\varepsilon)$ is a function of voidage and $g(\phi_s)$ is a function of sphericity. The term $\beta(\mathbf{v}_f-\mathbf{v}_s)$ is drag force per unit volume. The number of particles per unit volume N is

$$N = \frac{6(1-\varepsilon)}{\pi d_p^3} \tag{9}$$

such that the dimensionless interphase drag for dilute flows can be written as

$$\frac{\beta D}{\rho_f u_\tau} = \frac{3}{4}f(\varepsilon)g(\phi_s)(\mathbf{v}_f-\mathbf{v}_s)\frac{D}{d_p}C_D \tag{10}$$

Introducing the dimensionless boundary equations as developed in Section 2 results in the following governing parameters

$$\frac{\rho_s}{\rho_f};\ \frac{gD}{u_\tau^2};\ \frac{\beta D}{\rho_f u_\tau};\ \frac{p_o}{\rho_f u_\tau^2};\ \frac{G_s}{\rho_s u_\tau};\ \text{bed geometry} \tag{11}$$

The dimensionless pressure boundary condition can be ignored when the fluid velocity is small compared to sonic velocity or the absolute pressure does not change enough to influence the thermodynamic properties of the fluid, as stated earlier. Additionally, the friction velocity can be shown to be a weak function of bed Reynolds number (Hinze, 1975) allowing the list of controlling dimensionless groups to be written as:

$$\frac{\rho_s}{\rho_f};\ \frac{gD}{u_o^2};\ \frac{\beta D}{\rho_f u_o};\ \frac{G_s}{\rho_s u_o};\ \text{bed geometry} \tag{12}$$

This result agrees with previous derivations by Glicksman *et al.*, (1994) using the spatially averaged equations of Anderson and Jackson.

3.3 Viscous Limit Scaling

For viscous dominated flows, it can be assumed that the gas inertial and the gas gravitational forces are negligible. In most situations, the viscous forces in the gas which are associated with the macroscopic gas velocity gradients are negligible compared with the interphase drag; the term representing these forces can be removed from the gas momentum equation. The dimensionless gas momentum equation becomes

$$\frac{D\beta}{u_o\rho_f} = -\overline{\nabla}\left(\varepsilon\frac{p_f}{u_\tau^2\rho_f}\right) \tag{13}$$

For low voidages typical of bubbling beds, the Ergun relationship or similar form can be used. In that case β can be expressed as

$$\frac{\beta D}{u_o\rho_f} = 150\frac{\varepsilon(1-\varepsilon)^2}{\varepsilon^3}\frac{\mu D}{\rho_s u_o(\phi_s d_p)^2} + 1.75\frac{\varepsilon^2(1-\varepsilon)}{\varepsilon^3}\frac{|v_f - v_s|\rho_f}{\phi_s d_p u_o}\frac{D}{\rho_s} \tag{14}$$

From the Ergun equation, the dimensionless drag coefficient in the viscous limit is

$$\frac{\beta D}{u_o \rho_f} = 150 \frac{\varepsilon(1-\varepsilon)^2}{\varepsilon^3} \frac{\mu D}{\rho_s u_o (\phi_s d_p)^2} \tag{15}$$

The remaining set of dimensionless equations does not include a density ratio. The ratio between the bed and particle diameters and the Reynolds number based on bed diameter, superficial velocity and solid density appear only in the modified drag expression, in which they are combined. These parameters form a single parameter, as has been discussed by Glicksman (1988) and other investigators. The set of independent parameters controlling viscous dominated flow are then (including collisional effects):

$$\frac{\rho_s u_o d_p^2}{\mu D};\ \frac{gD}{u_o^2};\ \frac{G_s}{\rho_s u_o};\ \phi_s;\ \text{PSD};\ \text{bed geometry} \tag{16}$$

The first term in the list multiplied by the second term has been shown by Glicksman (1988) to be equivalent to the ratio of superficial and minimum fluidization velocities. The controlling parameters can therefore be written as

$$\frac{u_{mf}}{u_o};\ \frac{gD}{u_o^2};\ \frac{G_s}{\rho_s u_o};\ \phi_s;\ \text{PSD};\ \text{bed geometry} \tag{17}$$

For very small particles or small particle-gas relative velocities in dilute flows, the drag coefficient C_D is

$$C_D = \frac{24}{Re_{u_{rel}, d_p}} \tag{18}$$

and the dimensionless interphase drag is

$$\frac{\beta D}{u_o \rho_f} = \frac{18 \mu D}{\rho_s u_o (d_p)^2} (\bar{v}_f - \bar{v}_s) g(\phi_s) \tag{19}$$

Resulting in the same set of parameters as when the Ergun equation is used.

If the terms in the Maxey-Riley equation of motion with a coefficient of $\frac{\rho_f}{\rho_s}$ in addition to the Faxen forces are neglected, and it is assumed that the friction velocity is a weak function of bed Reynolds number, the controlling dimensionless parameters are identical to those determined from the continuum and ensemble averaged field analysis. The viscous limit requirement is based on the assumption that the dimensionless interphase drag can be

modeled as a linear function of the particle Reynolds number (as in equation 18). Because of the clustering of particles, this may not be a valid assumption, and the requirements for neglecting gas inertial effects may be much more stringent. As will be discussed in the experimental verification of simplified scaling laws, a viscous limit for interphase drag may not exist in CFB's.

It must be borne in mind that this set is valid only when fluid inertial effects are negligible, i.e., they are a subset of the general relationships. Glicksman (1984) used the criteria for the viscous limit in a bubbling bed that the ratio of viscous forces to fluid inertial forces in the Ergun equation is ten or larger. For a bed of glass or sand fluidized with air at standard conditions with $\frac{u_o}{u_{mf}}$ of 3, the viscous limit occurs when the particles are less than about 200 μm. In regions where particles behave individually, the viscous limit occurs for particles less than 60 μm (assuming the particle/gas relative velocity is equal to the particle terminal velocity and the single particle viscous limit criterion is $Re_{u_{rel}, d_p} < 1$).

3.4 Inertial Limit Scaling

In the inertial limit, the bulk gas friction is clearly negligible, and this term can be dropped from the gas momentum equation. From the dimensionless equations of motion, it can be shown that the controlling dimensionless parameters are

$$\frac{\rho_s}{\rho_f};\ \frac{gD}{u_o^2};\ \frac{\beta D}{\rho_f u_o};\ \frac{G_s}{\rho_s u_o};\ \text{bed geometry} \tag{20}$$

In the high Reynolds number limit, the Ergun equation simplifies to

$$\frac{\beta D}{u_o \rho_f} = 1.75 \frac{\varepsilon^2 (1-\varepsilon) \left| \bar{v}_f - \bar{v}_s \right| \rho_f}{\varepsilon^3 \quad \phi_s d_p u_o \quad \rho_s} D \tag{21}$$

The dimensionless interphase drag is only a function of $\frac{D}{d_p}\frac{\rho_f}{\rho_s}$, ε and φ; the gas viscosity is not important. The governing parameters are then (including collisional effects):

$$\frac{\rho_s}{\rho_f};\ \frac{gD}{u_o^2};\ \frac{D}{d_p};\ \frac{G_s}{\rho_s u_o};\ \phi_s;\ \text{PSD};\ \text{bed geometry}$$

At high Reynolds numbers, the viscous drag forces between a single particle and gas are negligible compared to the inertial force. The interphase drag expression can be simplified

by setting the drag coefficient equal to 0.44. This coefficient applies for Reynolds numbers based on the relative velocity in the range from 1000 to 100,000. The dimensionless interphase drag for a single particle is then

$$\frac{\beta D}{u_o \rho_f} = \frac{0.3D}{d_p}\frac{\rho_f}{\rho_s}\left(\bar{v}_f - \bar{v}_s\right) g\left(\phi_s\right) \tag{22}$$

The controlling dimensionless parameters which result from the non-dimensionalization of the equations of motion for the dilute limit are the same as those resulting from the dense limit. If the dimensionless drag of equation (22) is used in the Maxey-Riley equation of motion for a single particle, the same dimensionless groups appear.

The minimum size of the particle diameter at the inertial limit in a bubbling bed was approximated by Glicksman (1984) in a manner similar to that for the viscous limit. It was found that at one atmosphere d_{pmin} is approximately 2.6 and 7.3 mm for bed temperatures of 15 and 800 °C respectively (assuming a particle density of 2.5 g/cm^3). For particles which behave individually, the respective diameters are 1.6 and 4.5 mm (assuming the particle/gas relative velocity is equal to the particle terminal velocity and the inertial limit criterion is $Re_{u_{rel}, d_p} > 1000$).

It is interesting to note that the density ratio enters as a separate parameters in the list developed from the single particle equation of motion only if the particle motion is accelerating or highly time dependent (virtual mass and Boussinesq-Basset history terms become significant). This is a direct result of how the general equation of motion was developed. One of the assumptions used to develop particle equations of motion of the type of Maxey and Riley is that the advective terms in the gas momentum equation can be neglected. This results in the density ratio only entering the list of parameters as a product with the ratio of bed to particle diameters. Similar results are obtained in the inertial limit using the continuum analysis if gas-phase inertial contributions are negligible (Zhang and Yang, 1987). If this assumption is not made, the solid to fluid density ratio appears in the list of governing dimensionless groups.

3.5 Generalized Simplified Scaling Parameters

The full set scaling relationships are obtained by non-dimensionalizing the equations of motion for the particles and the fluid in a fluidized bed along with their boundary conditions. Using the bed dimension, D, as a typical length dimension, non-dimensionalization of the equations yields [see equation (12)]:

$$\frac{\rho_s}{\rho_f};\ \frac{gD}{u_o^2};\ \frac{\beta D}{\rho_f u_o};\ \frac{G_s}{\rho_s u_o};\ \text{bed geometry} \tag{23}$$

Factors omitted include surface forces on particles due to static charge or Van der Waals forces. Also the influence of the particle coefficient of restitution or friction coefficient on inter-particle forces is omitted. Litka and Glicksman (1985) showed that the friction coefficient and coefficient of restitution have a negligible influence on bubbling beds.

In Equation 1, ß is the coefficient of the fluid-to-particle drag force per unit volume expressed as $ß(v_f-v_s)$ where v_f and v_s are the fluid and particle velocities, respectively. In the general case, $ßD/\rho_s u_o$ is related to the viscous and inertial forces of the fluid through the Ergun equation or through the expression for drag on a single sphere. These relationships indicate that $ßD/\rho_s u_o$ is dependent on the Reynolds number based on the particle diameter, d_p/D and the dimensionless particle size distribution. Substituting these parameters into equation (23) yields the full set of scaling parameters given in Section 2,

$$\frac{\rho_f}{\rho_s};\ Re_{u_o,d_p};\ Re_{u_o,D};\ Fr_{u_o,D};\ \frac{G_s}{\rho_s u_o};\ \phi_s;\ \text{PSD};\ \text{bed geometry} \tag{24}$$

When the particles are closely spaced in a bubbling bed or possibly in the lower, dense portion, of a circulating bed, the Ergun equation is appropriate for the drag forces,

$$\frac{\beta D}{u_o \rho_f} = 150\frac{\varepsilon(1-\varepsilon)^2}{\varepsilon^3}\frac{\mu D}{\rho_s u_o(\phi_s d_p)^2} + 1.75\frac{\varepsilon^2(1-\varepsilon)}{\varepsilon^3}\frac{|\bar{v}_f - \bar{v}_s|\rho_f}{\phi_s d_p u_o}\frac{\rho_f}{\rho_s}D \tag{25}$$

For the most general case if ϕ, d_p/D, ρ_f/ρ_s, the dimensionless particle size distribution, and $\rho_f u_o d_p/\mu$ are matched between the full sized fluidized bed and the model, the dimensionless drag coefficient given by equation (25) will remain the same over all conditions. Substituting these dimensionless parameters for $ßD/\rho_s u_o$ in the group given in equation (23) leads to the full set of scaling relationships. Note that with the bed geometry, particle properties, gas properties, gas superficial velocity, and solids recycle rate fixed, steady state conditions in the fast bed or riser are fixed. This should be independent of the specific geometry and inventory of the recycle system provided that the recycle system can deliver the desired solids recycle rate. A study by Rhodes and Laussmann (1992) has shown that the solids holdup is, in fact, independent of changes in the inventory of the solids in the recycle system.

To obtain more flexibility in the modeling process, simplifications to the full set of scaling laws must be identified, such as the viscous and inertial limit cases discussed above. This can be accomplished by first exploring the simplifications which hold for several drag limiting cases. These limiting cases will span the range of operation from incipiently fluidized beds to dilute circulating beds or pneumatic transport. With such a broad range, the limits of the simplification can be explored over a wide range of fluidization conditions.

3.5.1 Low Reynolds Number

At low particle Reynolds numbers the Ergun expression can be simplified using only the first term in Equation (25).

Thus,

$$\frac{\beta D}{u_o \rho_f} = 150 \frac{\varepsilon(1-\varepsilon)^2}{\varepsilon^3} \frac{\mu D}{\rho_s u_o (\phi_s d_p)^2} \tag{26}$$

At the same limit, the minimum fluidization velocity can be written as,

$$\frac{\Delta p}{D} = (\rho_s - \rho_f) g (1-\varepsilon_{mf}) = 150 \frac{(1-\varepsilon_{mf})^2}{\varepsilon_{mf}^3} \frac{\mu u_{mf}}{(\phi_s d_p)^2} \tag{27}$$

For gas fluidized beds where $\rho_S - \rho_f$ can be replaced by ρ_S,

$$u_{mf} = \frac{\rho_s g (1-\varepsilon_{mf})}{\left[150 \frac{(1-\varepsilon_{mf})^2}{\varepsilon_{mf}^3} \frac{\mu}{(\phi_s d_p)^2}\right]} \tag{28}$$

Substituting equation (28) into equation (26),

$$\frac{\beta D}{\rho_s u_o} = \frac{g(1-\varepsilon)^2}{(1-\varepsilon_{mf})\varepsilon^2 u_{mf}} \frac{\varepsilon_{mf}^3 D}{\rho_s u_o} \tag{29}$$

and

$$\frac{\beta D}{\rho_s u_o} Fr = \frac{u_o}{u_{mf}} \frac{(1-\varepsilon)^2 \varepsilon_{mf}^3}{(1-\varepsilon_{mf})\varepsilon^2} \tag{30}$$

Thus, in the low particle Reynolds number limit, maintaining u_O/u_{mf}, ε_{mf}, and Fr identical between two fluidized bed guarantees that $\beta L/\rho_S u_O$ is also identical. Although ϕ and d_p are eliminated between Equations (26) and (28), in general particle sphericity and dimensionless size distribution should be held constant in the scaling. The use of ϕ and a mean diameter in the Ergun expression only approximates the effects of these parameters. Note if the two models display identical dynamic characteristics then ε is a dependent variable whose distribution throughout the bed should be identical for both fluidized beds. In this limit, the governing parameters given in equation (23) can be expressed as,

$$\frac{u_o^2}{gD}, \frac{\rho_s}{\rho_f}, \frac{u_o}{u_{mf}}, \frac{G_s}{\rho_s u_o}, \phi_s, \text{PSD, bed geometry} \tag{31}$$

where ε_{mf} will be a function of particle sphericity and size distribution.

In the viscous limit, derived earlier (Glicksman, 1988), the independent governing parameters were

$$\frac{u_{mf}}{u_o}; \frac{gD}{u_o^2}; \frac{G_s}{\rho_s u_o}; \phi_s; \text{ PSD; bed geometry} \tag{32}$$

The new simplified scaling parameters, equation (31), contain all of the viscous limit parameters along with the particle to gas density ratio. The new simplified scaling relationships should cover a wider range than the viscous limit previously defined by the author, since the inertial term in the fluid momentum equation is retained. Only the drag term is simplified.

3.5.2 High Reynolds Numbers

Consider the limit of high particle Reynolds numbers where the inertial term in the Ergun equation dominates.

In this limit,

$$\frac{\beta D}{u_o \rho_f} = 1.75 \frac{\varepsilon^2 (1-\varepsilon) |v_f - v_s| \rho_f}{\varepsilon^3 \quad \phi_s d_p u_o \quad \rho_s} D \tag{33}$$

The minimum fluidization velocity can be expressed as,

$$\frac{\Delta p}{D} = (\rho_s - \rho_f) g(1-\varepsilon_{mf}) = 1.75 \frac{(1-\varepsilon_{mf})}{\varepsilon_{mf}^3} \rho_f \frac{u_{mf}^2}{\phi_s d_p} \tag{34}$$

rearranging and using ρ_S in place of $\rho_S - \rho_f$,

$$\frac{g(1-\varepsilon_{mf})}{u_{mf}^2} = 1.75 \frac{(1-\varepsilon_{mf})}{\varepsilon_{mf}^3} \frac{\rho_f}{\phi_s d_p \rho_s} \tag{35}$$

Substituting this into equation (33) and multiplying by Fr,

$$Fr \frac{\beta D}{\rho_s u_o} = \frac{u_o^2}{gD} \frac{\varepsilon_{mf}^3 D |\bar{v}_f - \bar{v}_s| g(1-\varepsilon)}{\varepsilon u_{mf}^2} = \frac{u_o^2}{u_{mf}^2} \frac{\varepsilon_{mf}^3 (1-\varepsilon) |\bar{v}_f - \bar{v}_s|}{\varepsilon} \tag{36}$$

At large particle Reynolds numbers, just as at low Reynolds numbers, the dimensionless drag, $\beta L/\rho_s u_o$, is identical when u_o/u_{mf}, ε_{mf} and Fr are identical. ε, $\bar{v}_f$ and $\bar{v}_s$ are dependent dimensionless variables which are identical for two similar fluidized beds. In this limit the same set of governing dimensionless parameters applies as in the low Reynolds number limit, given by equation (31).

3.5.3 Low Slip Velocity

Finally, consider the case when the magnitude of the slip velocity between the particles and the gas is close to u_{mf}/ε everywhere in the fluidized bed. With the vertical pressure drop equal to the particle weight the following holds for any value of the particle Reynolds number,

$$\frac{\Delta p}{D} = \beta |v_f - v_s| \approx \beta \frac{u_{mf}}{\varepsilon} = \rho_s g(1-\varepsilon) \tag{37}$$

$$\beta = \rho_s g(1-\varepsilon) \frac{\varepsilon}{u_{mf}} \tag{38}$$

and

$$\frac{\beta D}{\rho_s u_o} Fr = u_o (1-\varepsilon) \frac{\varepsilon}{u_{mf}} \quad \text{for } |\bar{v}_f - \bar{v}_s| \to \frac{1}{\varepsilon} \frac{u_{mf}}{u_o} \tag{39}$$

Again, when u_o/u_{mf} and Fr are identical for two beds and the slip velocity is close to u_{mf}/ε the dimensionless drag coefficient is also identical for two beds.

For all three limiting cases identified above, similitude can be obtained by maintaining constant values for the dimensionless parameters,

$$\frac{u_o^2}{gD}, \frac{\rho_s}{\rho_f}, \frac{u_o}{u_{mf}}, \frac{G_s}{\rho_s u_o}, \phi_s, \text{PSD, bed geometry} \tag{40}$$

provided that the forces between the particles and gas can be represented by the Ergun equation or an equivalent expression.

The advantage of the simplified set of scaling parameters over the full set is the increased flexibility in the design of a model to simulate a combustor or chemical reactor. With the full set, after the gas properties in the model have been chosen, e.g. by use of air at ambient conditions, there is only one unique set of particle size and density, bed size, gas velocity and solids circulation rate which can be used in the model.

Using the simplified set of scaling parameters, the choice of the fluidizing gas in the model fixes the solid density. However, the model size can be altered, as long as the Froude number is maintained constant by altering u_o. The particle size is then set to maintain u_o/u_{mf} constant. This flexibility allows a model to simulate much larger combustors or reactors than is possible with the full set of scaling relationships.

3.5.4 General Case

Since the same simplified set of dimensionless parameters holds exactly at both high and low Reynolds numbers, it is reasonable to expect that they hold, at least approximately, over the entire range of conditions for which the drag coefficient can be determined by the Ergun equation or an equation of similar form. The validity of the simplified parameters can be checked numerically for the intermediate range of values.

From the Ergun equation,

$$\frac{\beta D}{\rho_s u_o} = 150 \frac{(1-\varepsilon)^2}{\varepsilon^2} \frac{\mu D}{\rho_s u_o (\phi_s d_p)^2} + 1.75 \frac{(1-\varepsilon)}{\varepsilon} \frac{|\bar{v}_f - \bar{v}_s|}{\phi_s d_p} \frac{\rho_f}{\rho_s} D \tag{41}$$

where $\left|\bar{v}_f - \bar{v}_s\right|$ can also be represented as u_{rel}/u_o. Using the Ergun equation to determine u_{mf},

$$\frac{\Delta p}{D} = \rho_s g\left(1-\varepsilon_{mf}\right) = 150\,\frac{\left(1-\varepsilon_{mf}\right)^2}{\varepsilon_{mf}^{\,3}}\,\frac{\mu u_{mf}}{\left(\phi_s d_p\right)^2} + 1.75\,\frac{\left(1-\varepsilon_{mf}\right)}{\varepsilon_{mf}^{3}}\,\frac{u_{mf}^2\rho_f}{\phi_s d_p} \tag{42}$$

Dividing equation (41) by (42), and rearranging,

$$\left(\frac{\beta L}{\rho_s u_o}\right)\frac{Fr\left(1-\varepsilon_{mf}\right)\varepsilon^2}{\left(\frac{u_o}{u_{mf}}\right)\left(1-\varepsilon\right)^2\varepsilon_{mf}^3} = \left[\frac{1+\frac{1.75}{150}\,\frac{\phi_s Re}{\left(1-\varepsilon\right)}\varepsilon\left|\bar{v}_f-\bar{v}_s\right|}{1+\frac{1.75}{150}\,\frac{\phi_s Re}{\left(1-\varepsilon_{mf}\right)}\,\frac{u_{mf}}{u_o}}\right] \tag{43}$$

where $Re = \rho_f u_o d_p/\mu$.

It is easy to verify by use of Equation (43) the three limits defined previously.

For the more general case, Figure 1 shows the value of ß given by Equation 43 relative to ß at low Re over a range of conditions when u_o/u_{mf} is 10 and 3, respectively and Fr and ϕ_s remain constant. When u_o/u_{mf} and the slip velocity is high there is a larger variation of dimensionless drag coefficient with Reynolds number. Note that ß does not vary with particle Reynolds number when the Reynolds number remains above about 10^3 or below about 10. Figure 2 illustrates the results when u_o/u_{mf} is 1000, a condition approached with very fine particle bubbling beds or circulating beds. In the latter instance the use of the Ergun relationship is questionable except for the dense lower part of the bed. In this figure the slip velocity is 1/50 u_o or less, which corresponds to 20 u_{mf}. This limit on the slip velocity is roughly twice the terminal velocity of large particles. Note, if Figure 2 had been extended to higher Reynolds numbers, ß would approach a constant value, as it did in Figure 1.

Figure 1
Drag Coefficient Using Ergun Equation

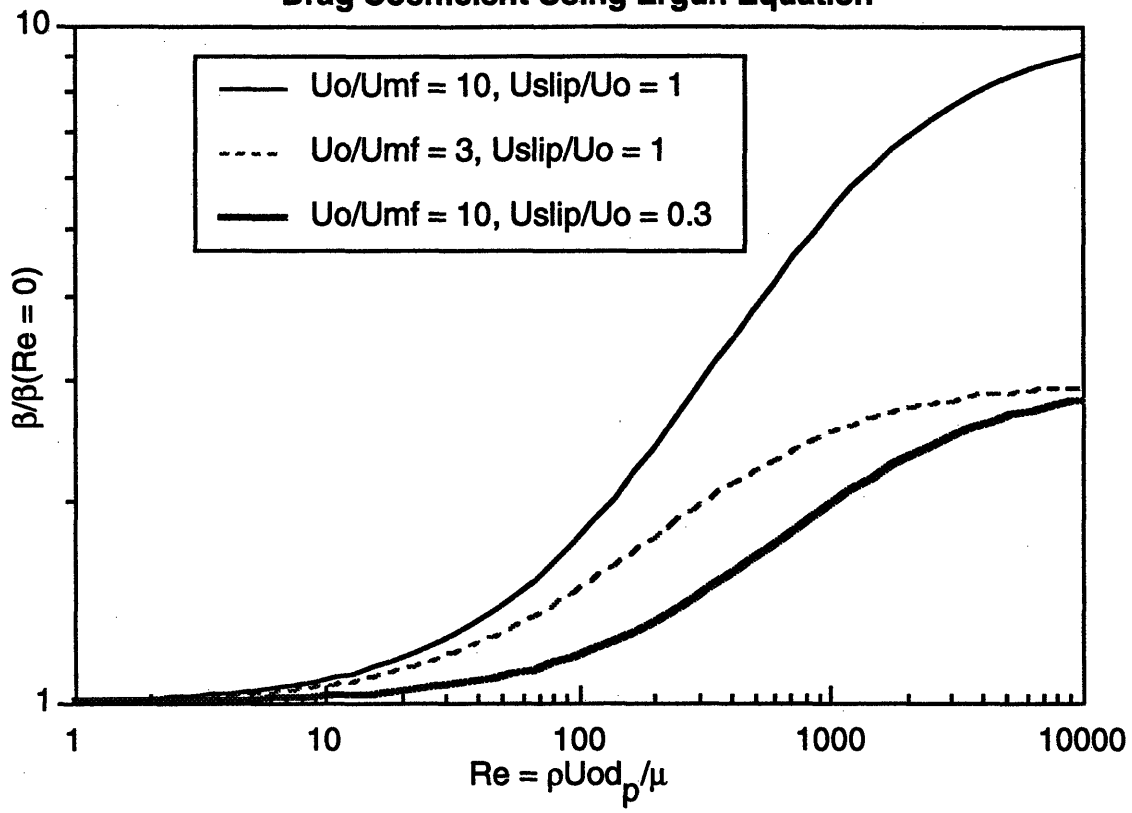

Figure 2
Drag Coefficient Using Ergun Equation, Uo/Umf = 1000

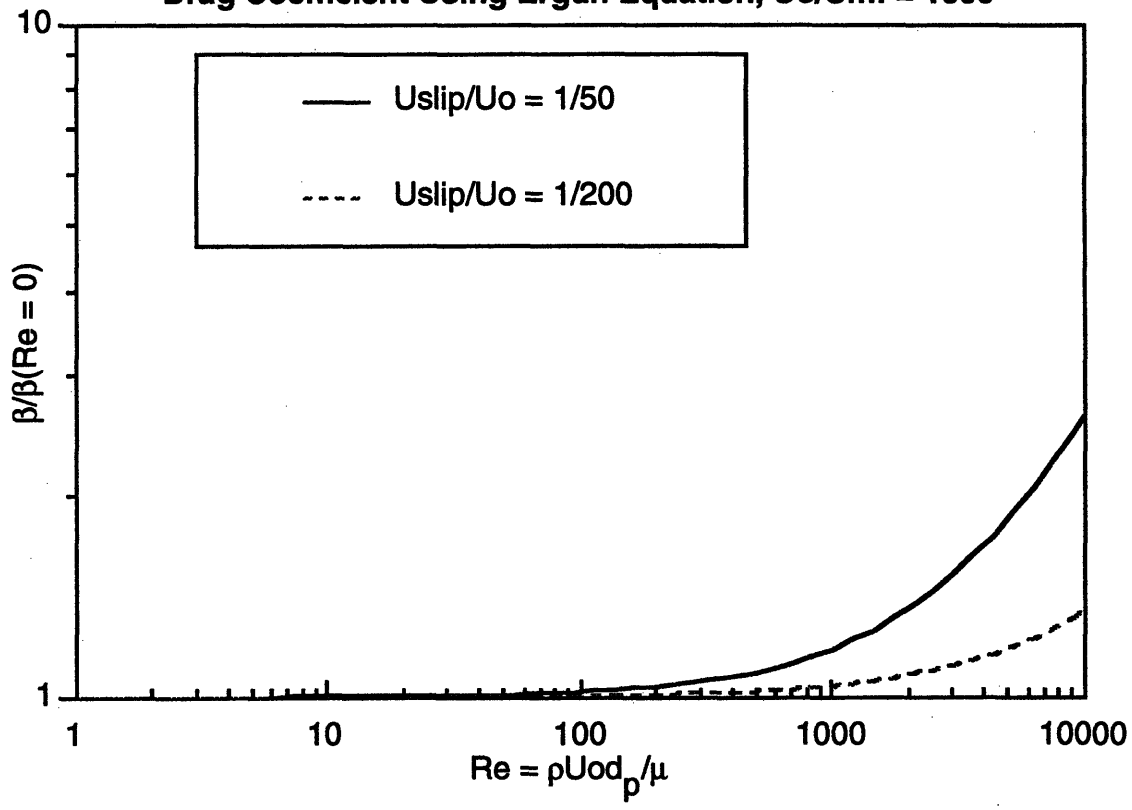

Of particular concern is the error in the dimensionless drag coefficient when a scale model is designed using the simplified set of scaling rules, equation (40). The simplified scaling parameters allows small models to simulate a given sized combustor. As the length scale is reduced the superficial velocity must also be reduced to maintain a constant Froude number. The particle diameter must also be reduced to keep u_o/u_{mf} constant.

To determine the validity of the simplified scaling laws over a wide range of conditions the simplified scaling laws, Equation 40, were used to design hypothetical models whose linear dimensions are 1/4 and 1/16, respectively, of the linear dimensions of a model designed using the full set of scaling laws. To determine the validity of the smaller, simplified models, the dimensionless drag coefficient $\beta L/\rho_s u_o$ is compared between the simplified models and the model using the full set of scaling laws. Figure 3 shows a comparison of the exact model and the simplified models for a pressurized (12 bar) fluidized combustor. Using the full set of scaling laws the exact model, fluidized by ambient air, is approximately the same size as the combustor. The simplified models are reduced in size by their respective assumed length scale. The other parameters of the simplified model are then calculated to match the simplified parameters. For example, when the length scale is reduced to 1/4 that of the exact model, the velocity is reduced by 1/2 to keep the Froude number constant. The particle diameter is then reduced appropriately to keep the ratio of u_o/u_{mf} constant. These calculations were carried out over a range of particle Reynolds numbers, Re_{pE}, based on the full scaling law, or exact, model. It was found that the particle Reynolds number for the 1/4 scale simplified model remained roughly equal to 0.34 Re_{pE} over a wide range of values for Re_{pE}. Whereas the particle Reynolds number for the 1/16 scale model was roughly 0.12 Re_{pE}. Tables 2 and 3 give the values for the exact and simplified scale models of pressurized and atmospheric combustors, respectively.

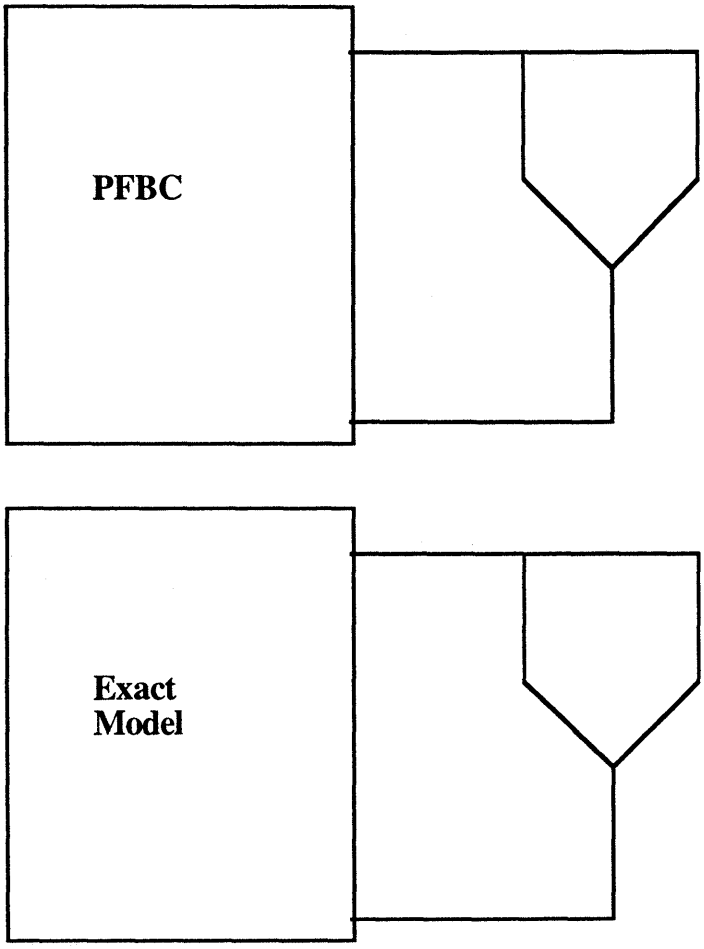

Figure 3: Exact and Simplified Models of a Pressurized Combustor

1/4 Scale Simplified Model

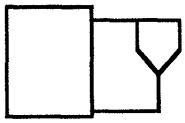

1/16 Scale Simplfied Model

	P	T(C)	L	Uo
PFBC	**10 atm**	**800**	**Lo**	**Uo**
Exact Model	**1 atm**	**20**	**Lo**	**Uo**
1/4 Scale Simplified Model	**1 atm**	**20**	**Lo/4**	**Uo/2**
1/16 Scale Simplified Model	**1 atm**	**20**	**Lo/16**	**Uo/4**

Using these Reynolds number scale factors, the errors in the dimensionless drag coefficient $\beta D/\rho_s u_o$ using the simplified scaling models, can be found from Figures 1 and 2. These errors are shown on Figures 4 and 5 for u_o/u_{mf} of 10 and 1000, respectively, plotted as a

function of Re_{pE} based on parameters for the exact scaled bed. For a particle Reynolds number of 1000 or less, which corresponds to pressurized beds with particles of 1mm or less operating at 1100 K, the error in the drag coefficient with the simplified scaling laws is twenty percent or less for a one quarter length scale model. The error is forty percent or less for a one sixteenth length scale model. At u_o/u_{mf} of 1000 and u_{sl}/u_{mf} of 1/50 the errors for the 1/16 scale model are twenty percent or less for Re_{pE} less than 10^3. For particles of 0.2mm or less, corresponding to a Reynolds number of 100 or less, the errors in drag coefficient are minimal. When the Ergun equation applies for the drag coefficient, a one quarter scale model based on the simplified scaling laws should be valid for any condition. A 1/16 scale model should be valid for diameters of about 0.2 mm or less for a pressurized bubbling bed with u_o/u_{mf} of 10 and u_{sl}/u_o of 0.3. At u_o/u_{mf} of 1000 and u_{sl}/u_o of 1/50, the 1/16 scale model should be valid for pressurized beds with particles up to 1 mm in diameter. These conclusions apply when the particle to fluid drag time is given by the Ergun equation or similar relationships and the scaled particles are not so small that inter particle surface forces come into play.

The particle to gas density ratio does not appear explicitly in the expression for ß, Equation (43). However, u_{mf} is a function of the density ratio. If the wrong solid to gas density ratio is used in the simplified model, the particle diameter in the simplified model required to match u_o/u_{mf} changes. For example, if the simplified model of a combustor pressurized at 1 MPa uses a particle density of 2500 kg/m^3 instead of the required 900 kg/m^3, the Reynolds number, $\rho_s u_{mf} d_p/\mu$, is reduced by 40 percent. This increases the error in ß between the simplified and the exact model when ß is derived from the Ergun equation.

For scaling beds with intermediate or large Reynolds numbers the solid to gas density ratio is an important parameter in the fluid momentum equation. It must appear in the set of scaling parameters irrespective of its influence on the drag coefficient.

3.5.5 Clusters

In the freeboard of a bubbling bed or in the upper portion of a circulating bed where particles generally are considered to act in clusters or groups, a similar examination of scaling of the gas to solid drag can be made. Consider all of the particles grouped into clusters with an effective diameter d_c and the clusters occupying a volume fraction ε_c of the bed volume. The cluster to gas drag will be represented by the drag coefficient for a solid sphere of diameter d_c,

$$\beta\left|\bar{v}_f-\bar{v}_s\right|\frac{\pi d_c^3}{6\left(1-\varepsilon_c\right)}=\frac{1}{2}\rho_f\frac{\pi d_c^2}{4}\left|\bar{v}_f-\bar{v}_s\right|^2 C_D \tag{44}$$

This can be rewritten as,

$$\frac{\beta D}{\rho_s u_o}=\frac{3}{4}\left(\frac{\rho_f}{\rho_s}\right)\left|\bar{v}_f-\bar{v}_s\right| C_D\frac{D}{d_c}\left(1-\varepsilon_c\right) \tag{45}$$

If the diameter of individual particles does not influence the drag of a cluster of particles, then when the solid to gas density ratio is held constant between the combustor and the model, the dimensionless drag, $\beta D/\rho_s u_o$, in equation (45) is a function of C_D. We will use the drag coefficient of solid spheres as a first approximation for the relative change of C_D with Reynolds number based on cluster diameter. The drag coefficient of a solid sphere can be closely represented by the empirical expression given by White (1974),

$$C_D=\frac{24}{Re_{d_c}}+\frac{6}{1+\sqrt{Re_{d_c}}}+0.4 \tag{46}$$

In the limit of large cluster Reynolds number, C_D approaches a constant and $\beta D/\rho_s u_o$ is properly scaled when the fluid to gas density ratio is held constant between the model and the combustor. The ratio D/d_c, and ε_{cl} should be the same between the properly scaled model and the combustor. In this limit, u_o/u_{mf} does not appear explicitly as one of the simplified scaling parameters. However, if the cluster was formed by bubble eruptions at the surface of a bubbling bed u_o/u_{mf} will certainly be important for the bed. Similarly, in a fast bed, u_o/u_{mf} will be important in the lower, dense portion of the bed.

In the limit of small cluster Reynolds number, the dimensionless drag $\beta D/\rho_s u_o$ will not be the same for the exact model and the simplified scale model unless the cluster size scales with the particle diameter rather than the bed dimensions.[1] However, as we will see below, under any realistic conditions the cluster Reynolds number will be near the upper limit.

If the reduced scale model faithfully reproduces the dynamics of the exact case, then the cluster dimensions should scale directly with the linear dimensions of the bed. Thus a one quarter linear scale model which has a velocity one half that of the exact case will have a

[1] In the lower limit of Reynolds number, for clusters and particles, C_D is equal to $24/Re_{dc}$ and u_{mf} is proportional to $\rho_s d_p^2/\mu$, Equation 7. It can be shown that $\beta L/\rho_s u_o$ in Equation 24 is proportional to $\frac{1}{Fr}\frac{u_o}{u_{mf}}\frac{d_p^2}{d_c^2}$. Complete similitude is not obtained unless d_c is also proportional to the bed length, resulting in the full set of scaling laws.

cluster Reynolds number one eighth that of the exact bed. From the relationship of C_D with Re we can determine the change of C_D with model scale at a given Reynolds number of the exact bed. Figure 6 shows the shift in C_D for length scale of 1/4, 1/8, and 1/16, respectively, of the exact bed length as a function of the cluster Reynolds number of the exact bed. Also shown on the figure is the typical Reynolds number of an atmospheric combustor with a 0.3 m cluster diameter, approximately 1.5×10^4. In a bubbling bed, the cluster diameter in the freeboard should be at least equal in size to the diameter of bubbles erupting at the bed surface. For beds with horizontal tubes, the bubble diameter will be equal to or larger than the horizontal tube spacing. In a bubbling bed without tubes, the bubbles and clusters can be much larger. In an open circulating bed the cluster diameter is more difficult to determine. It is reasonable to assume its diameter is proportional to the bed diameter, equal in magnitude to the bed diameter or one order of magnitude smaller. From these considerations, the Reynolds number based on the cluster diameter should be 10^4 or larger in an atmospheric combustor with a cluster diameter of 0.2m. The cluster Reynolds number should be 10^5 or larger in a pressurized combustor. From Figure 6 it can be seen that a one quarter scale or an eight scale model should have drag coefficients similar to the exact bed. For pressurized beds, the drag coefficients should be very close in magnitude.

Figure 4
Error in Drag Coefficient, Uo/Umf = 10, Uslip/Uo = 0.3

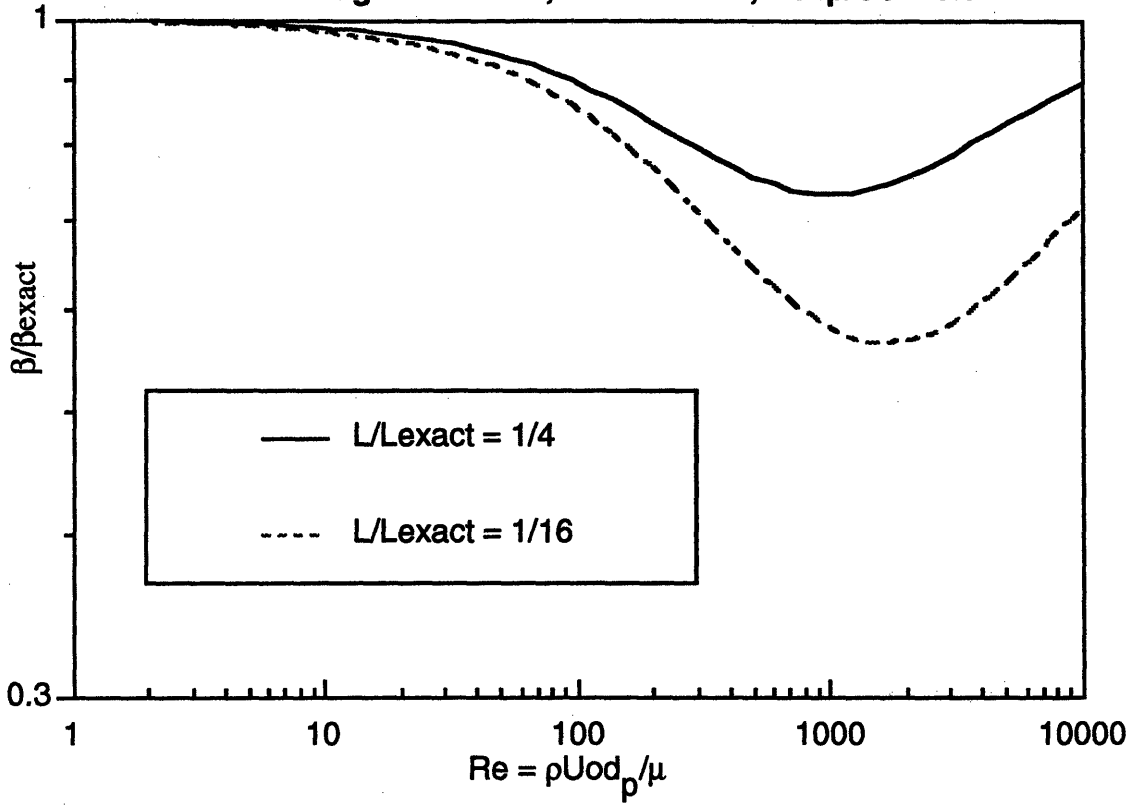

Figure 5
Error in Drag Coefficient, Uo/Umf = 1000, Uslip/Uo = 1/50

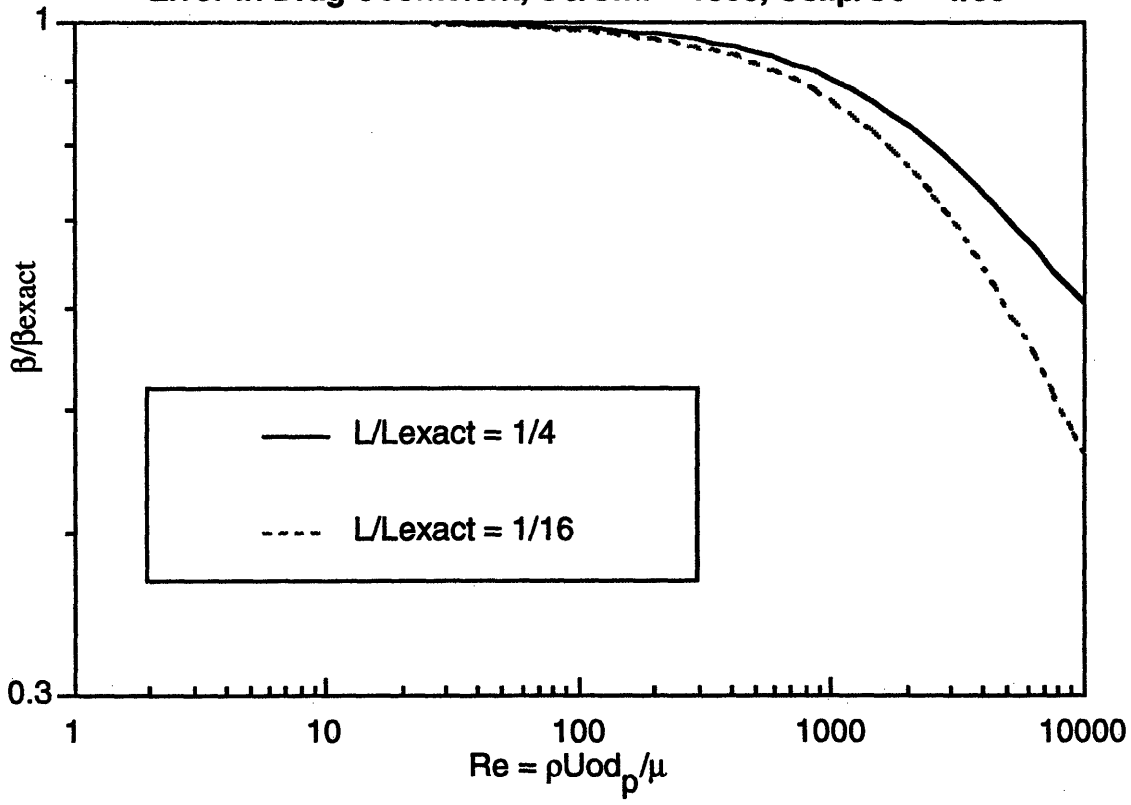

Figure 6
Error in Cd for Fixed Uo/Umf (Cd for Solid Sphere)

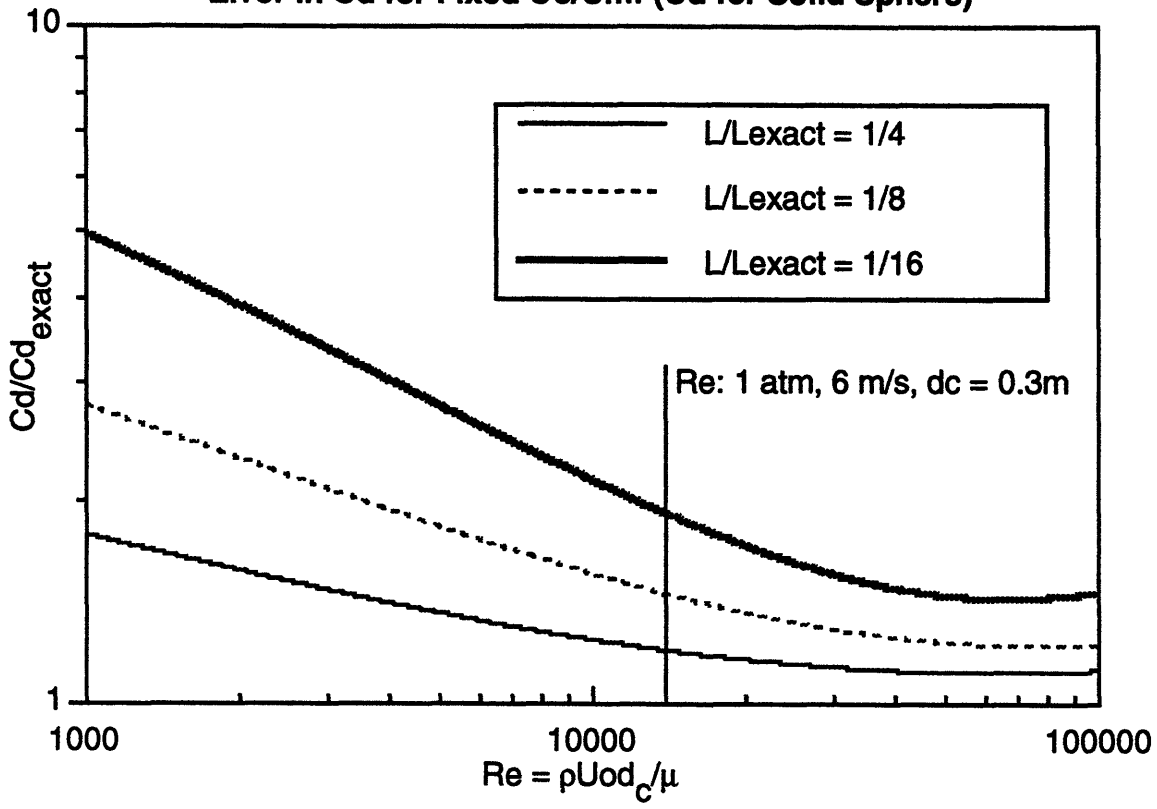

3.5.6 Terminal Velocity of Particles

If the drag coefficient, ß, is influenced by the characteristics of individual particles, the detailed particle dynamics of the simplified scale models must be examined.

In this case,

$$\frac{\beta D}{\rho_s u_o} = \frac{3}{4}\left(\frac{\rho_f}{\rho_s}\right)\left|\bar{v}_f - \bar{v}_s\right| C_D \frac{D}{d_p}(1-\varepsilon) \tag{47}$$

where C_D is the drag coefficient of a single particle. This can be rewritten in terms of the single particle terminal velocity which can be found from,

$$\frac{\rho_s \pi d_p^3 g}{6} = \frac{1}{2}\frac{\rho_f \pi d_p^2}{4} C_D u_t^2 \tag{48}$$

Substituting equation (48) into equation (49) to eliminate C_D, one obtains,

$$\frac{\beta D}{\rho_s u_o} Fr = \frac{u_o^2}{u_t^2} \left| \bar{v}_f - \bar{v}_s \right| \left(1 - \varepsilon\right) \tag{49}$$

Since u_o/u_{mf} and Fr is held constant in the simplified scaling process, we will examine the ratio u_t/u_{mf} to determine if the drag coefficient, $\beta D/\rho_s u_o$, remains constant.

The Ergun equation can be solved to find u_{mf},

$$\rho_f \frac{u_{mf} d_p}{\mu} = \frac{\dfrac{-(150)(1-\varepsilon_{mf})^2}{\varepsilon_{mf}^3} + \sqrt{\left[\dfrac{-(150)(1-\varepsilon_{mf})^2}{\varepsilon_{mf}^3}\right]^2 + \dfrac{7(1-\varepsilon_{mf})^2}{\varepsilon_{mf}^3}\phi_s^3 Ar}}{\dfrac{3.5(1-\varepsilon_{mf})\phi_s}{\varepsilon_{mf}^3}} \tag{50}$$

where $Ar = \dfrac{\rho_s \rho_f d_p^3 g}{\mu^2}$ is the Archimedes number.

In the limit of low Ar, equation (50) becomes

$$\frac{\rho_f u_{mf} d_p}{\mu} = \frac{\varepsilon_{mf}^3}{150(1-\varepsilon_{mf})} Ar \quad Ar \to 0 \tag{51}$$

while for large Ar,

$$\frac{\rho_f u_{mf} d_p}{\mu} = \frac{1}{3.5}\sqrt{7\varepsilon_{mf}^3 \phi_s Ar} \quad Ar >> 1 \tag{52}$$

The terminal velocity for a particle can be obtained as,

$$\rho_s \frac{\pi d_p^3 g}{6} = \frac{1}{2}\rho_f \frac{\pi d_p^2}{4} u_t^2 C_D \tag{53}$$

Rearranging, and using Equation (46) for C_D,

$$Re_t^2 = \frac{\frac{4}{3}Ar}{\frac{24}{Re_t} + \frac{6}{1+\sqrt{Re_t}} + 0.4} \tag{54}$$

where $Re_t = \frac{\rho_f u_t d_p}{\mu}$.

For small values of Ar, equation (54) becomes

$$Re_t = \frac{4}{72} Ar \quad Ar \to 0 \tag{55}$$

while for large Ar

$$Re_t = \frac{4}{72} Ar \quad Ar \to 0 \tag{36}$$

At small and large values of Ar, the ratio of u_t/u_{mf} approaches a constant value. In these two limits, the simplified scaling laws will yield exact agreement of u_t/u_{mf} between the combustor and the simplified models. In general, u_{mf} and u_t should be a function of the Archimedes number for a given value of ϕ_s and ε_{mf}. Figure 7 illustrates the dependence of u_t/u_{mf} on Ar. Also shown are the values of the Archimedes number for a pressurized combustor at two particle diameters. Associated with the Archimedes number for the exact model are the corresponding Archimedes number for two models scaled using the simplified relationships at linear dimensions one quarter and one sixteenth the exact dimensions.

The errors in u_t/u_{mf} are shown on Figures 8 and 9 for simplified scale models at two different linear dimensions. Scaling a combustor with comparatively small particles, 0.2 mm or less, gives good agreement for u_t/u_{mf} even at one sixteenth linear scale, while for large particles a linear scale of one fourth gives fair agreement for u_t/u_{mf}. Since u_o/u_{mf} is held constant in the simplified scaling laws, close agreement of u_t/u_{mf} also results in close agreement of u_t/u_o.

Figure 7

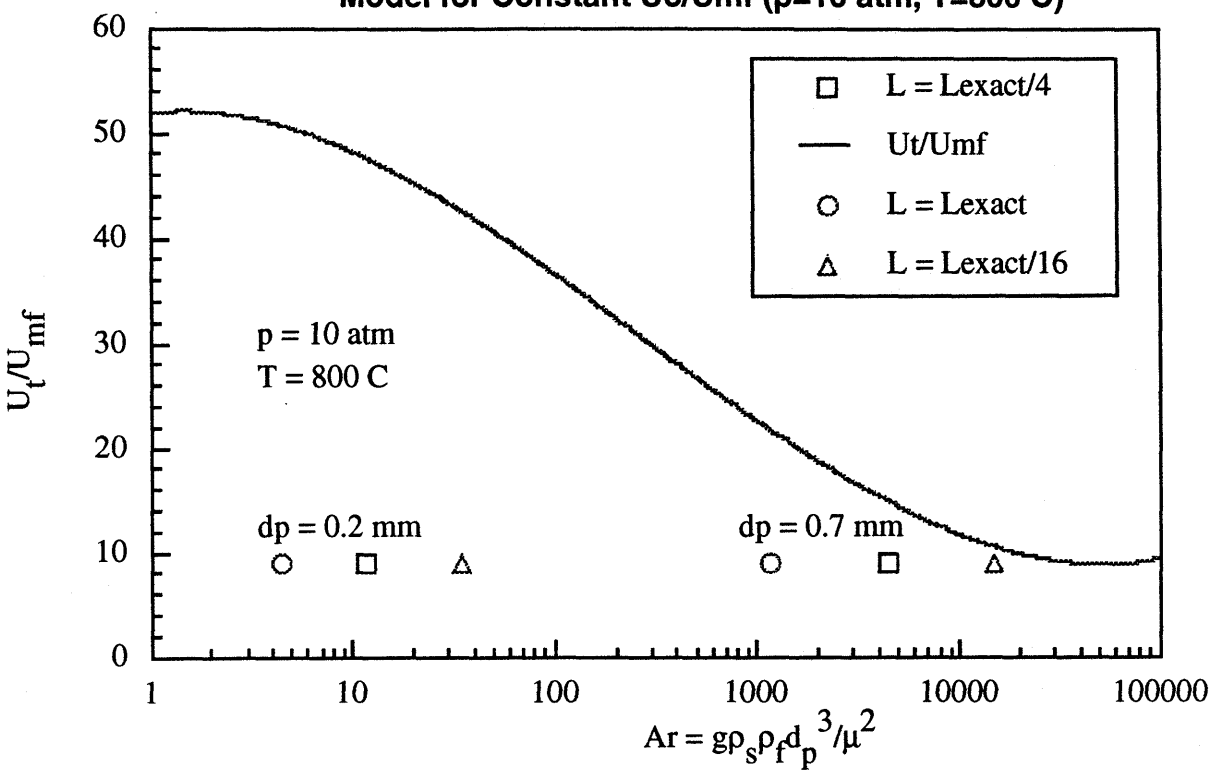

Figure 8

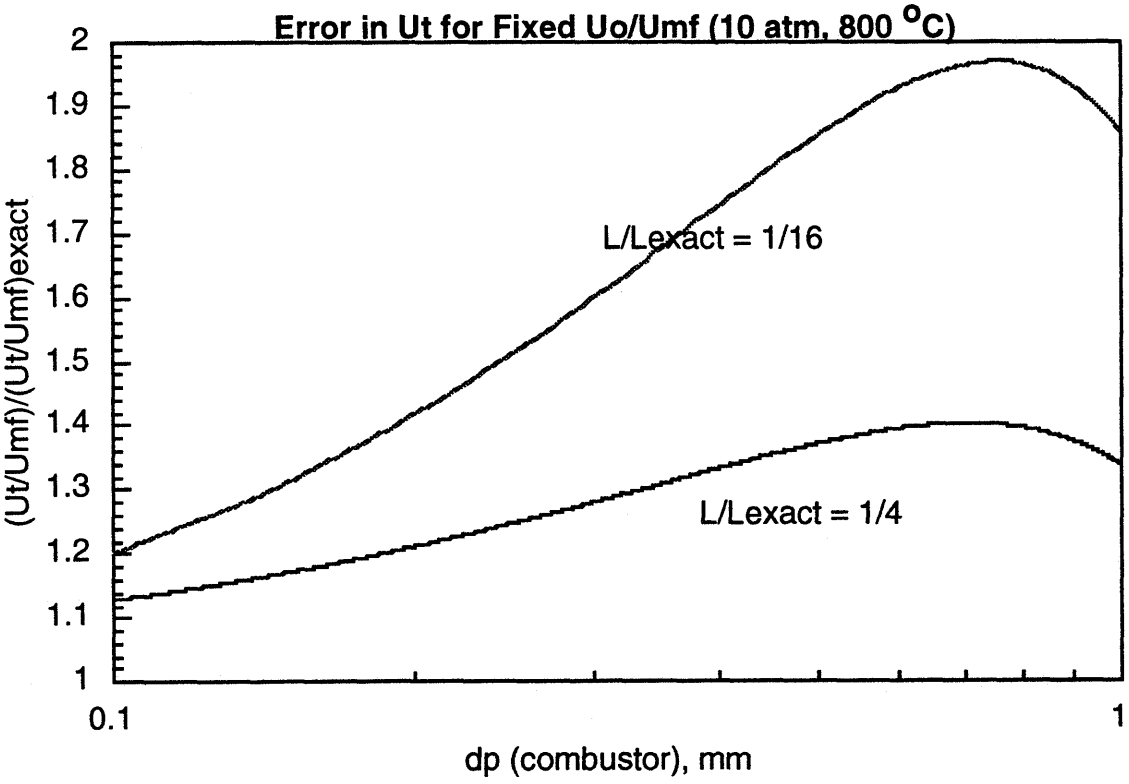

Figure 9

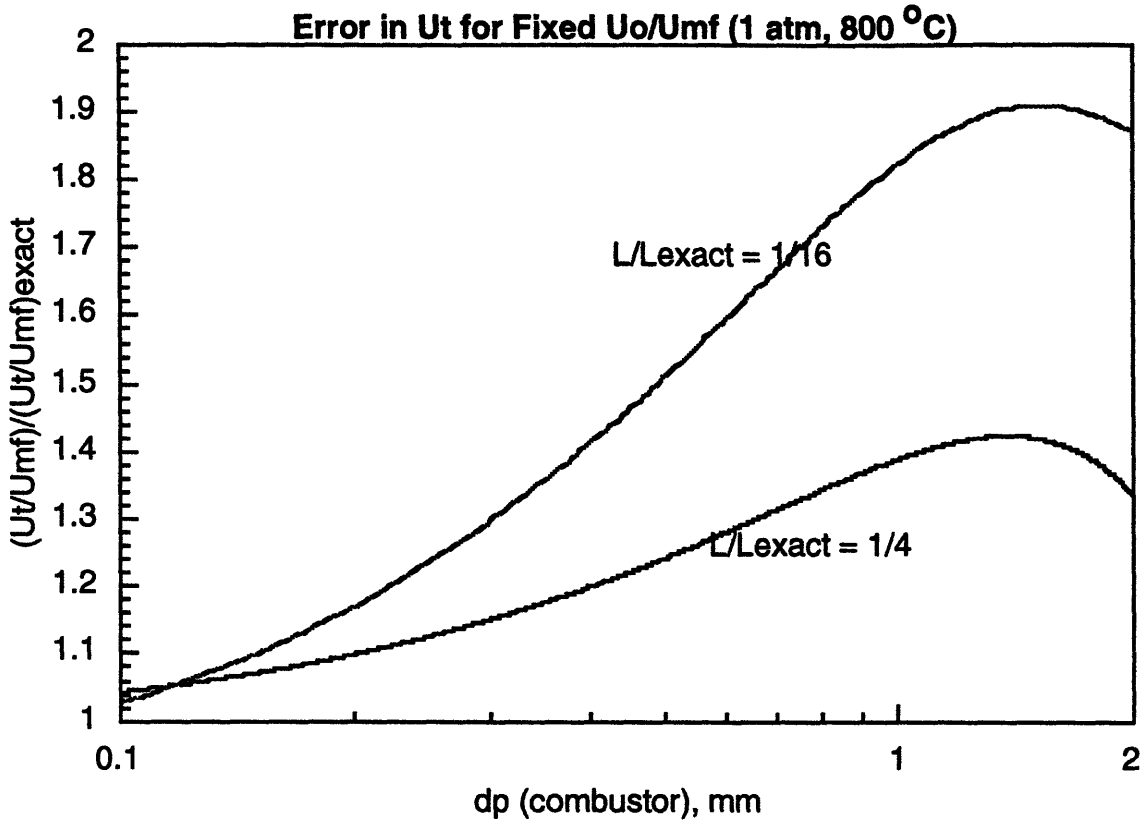

3.6 Conclusions

The full set of dimensionless parameters for scaling can be reduced to the simplified set, $\frac{u_o^2}{gD}$, $\frac{\rho_s}{\rho_f}$, $\frac{u_o}{u_{mf}}$, $\frac{G_s}{\rho_s u_o}$, ϕ_s, PSD, bed geometry in the limits of small and large particle Reynolds number as well as when the slip velocity approaches u_{mf}.

In the more general range of conditions, the simplified form of the scaling relationships gives acceptable agreement for the drag coefficient and the ratio of terminal velocity to minimum fluidization velocity when the simplified model has reduced linear dimensions between one quarter and unity. For combustors with particle diameter of 0.2 mm or less, a simplified scale model with reduced linear dimensions up to one sixteenth the exact model should give acceptable agreement.

If the particle size of the simplified model becomes very small, care must be taken to insure that interparticle forces do not become important. A dimensionless form of Geldart's particle classification will aid in determining the approximate range for the onset of the inter particle forces.

4.0 EXPERIMENTAL ARRANGEMENTS FOR VERIFYING SIMPLIFIED SCALING PARAMETERS

4.1 Introduction

The cold bed sizes and operation conditions were selected so that the assumed group of governing dimensionless parameters for the two beds would be equal. The viscous limit set of dimensionless parameters which were used in the first series of tests is:

$$\frac{u_{mf}}{u_o};\ \frac{gD}{u_o^2};\ \frac{G_s}{\rho_s u_o};\ \phi_s;\ \text{PSD};\ \text{bed geometry} \tag{1}$$

The simplified set of dimensionless parameters which were used in the second series of tests is:

$$\frac{u_o^2}{gD},\ \frac{\rho_s}{\rho_f},\ \frac{u_o}{u_{mf}},\ \frac{G_s}{\rho_s u_o},\ \phi_s,\ \text{PSD, bed geometry} \tag{2}$$

The viscous limit parameters reduce the number of dimensionless groups from the full set by combining the particle diameter to bed length ratio with the particle Reynolds number and eliminating the density ratio. The new proposed simplified set reduces the number of parameters by only one since the requirement of constant density ratio is still included. In both cases, reducing the number of dimensionless parameters allows for the construction of models which are much smaller than the 1 to 4 length scale required by the full set of scaling parameters.

To test the viscous limit scaling parameters, one bed was used in which particles of different densities were fluidized under the same conditions. Initial tests to verify the simplified scaling parameters with constant density ratio used two different beds with a length scale of 4. Further tests were then conducted to verify these parameters when scaling from hot combustors with dimensions 16 times that of the model.

In what follows, three topics will be discussed in the following order:

1. Bed geometries
2. Particle characteristics
3. Measurement equipment and associated uncertainty

4.2 Dimensions and Construction of Cold Beds

Four cold circulating beds models were used during the course of the project:

1. 1/4 scale model of the UBC pilot scale combustor
2. 1/4 scale model of the 2.5 MWt Studsvik circulating fluidized bed combustor
3. 1/16 scale model of the 2.5 MWt Studsvik circulating fluidized bed combustor
4. 1/2 sclae model of the Foster Wheeler Development Corp. pilot scale second generation pressurized circulating fluidized bed combustor

4.2.1 1/4 Scale Model of the UBC Pilot Scale Combustor

The first bed utilized was a 1/4 scale model of the pilot scale circulating fluidized bed combustor facility located at the University of British Columbia without the in bed tube bundle. A schematic of the UBC hot bed is given as Figure 4.1 This bed was constructed as part of a previous study which verified the complete set of scaling relationships for circulating fluidized beds (Westphalen, 1990) and was used in the evaluation of the viscous limit scaling laws when scaling with steel and glass. The bed consists of three main parts:

1. Main bed test section
2. Return leg
3. Cyclone

A drawing of the 1/4 scale cold bed is presented in Figure 4.2. The bed was mounted with angle irons at a distance of about 25 cm from a vertical support board. Five supports were used to distribute the bed load evenly.

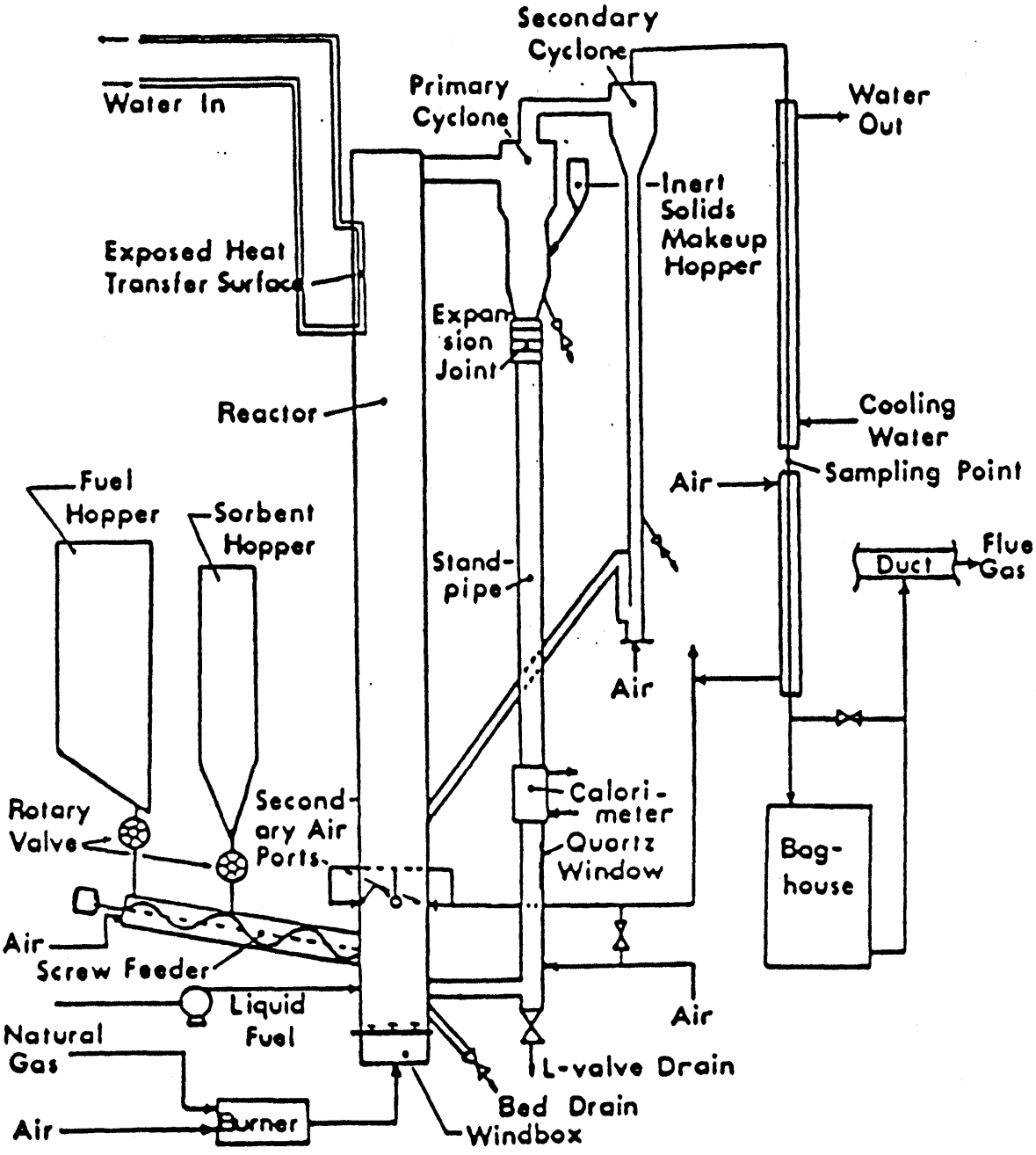

Figure 4.1: UBC CFBC Pilot Scale Test Facility (Hot Bed)

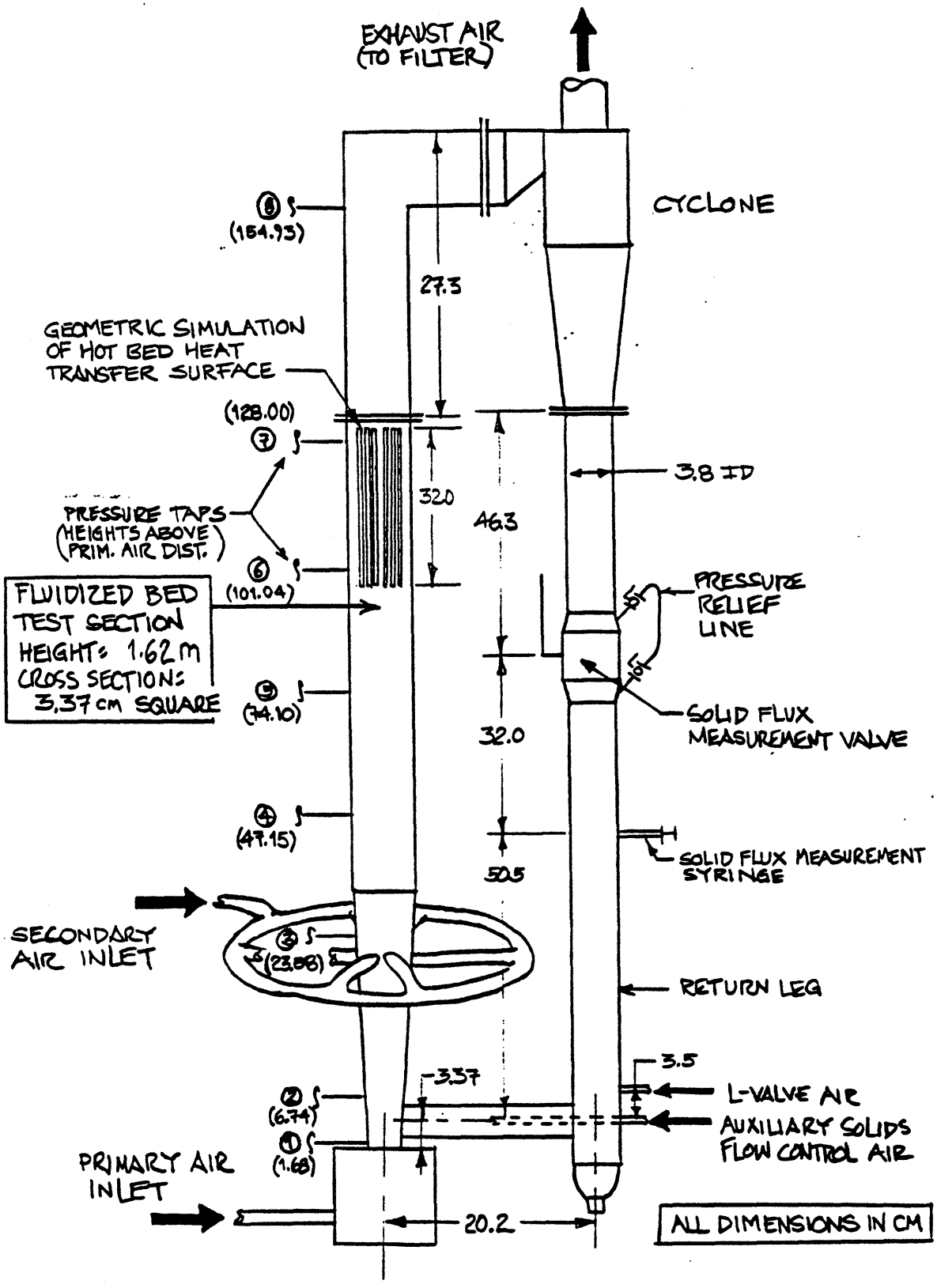

Figure 4.2: 1/4 Scale UBC Bed

4.2.1.1 Main Bed Test Section

The main test section was constructed with a geometry similar to the UBC test bed. It was constructed of 1/2-inch (1.27 cm) acrylic sheet with a scratch-resistant surface finish. The cross sectional area of the bed is 3.37 cm^2, and the bed's length is 1.62 m. The bottom of the bed is tapered. The elbow at the top of the bed is separable from the bed.

Air is divided into primary and secondary streams before being introduced into the bed (see Figure 4.3). Primary air is introduced at the bottom of the bed through a half-cylindrical distributor (Figure 4.4).

Secondary air is introduced at a height of 20 cm through four of six flexible tubes. The six tubes allow introduction of secondary air from opposite sides of the bed, or from all four sides of the bed in an off-center arrangement designed to create a swirl in the flow. Clamps are used to stop flow through the unused tubes. Orifices inserted into the tubes provide enough pressure drop so that the tube header pressure drop is insignificant, thus insuring equal flow through each tube. A drawing of the secondary air supply tubing is shown in Figure 4.5.

Eight pressure taps used to measure axial pressure drop are located on the side of the bed opposite the solid return leg (see Figure 4.2).

The solids return port at the bottom of the bed is just above the primary air feed and is 7/8" (2.22 cm) in diameter. A 7/8" x 1/16" (2.22 x 0.16 cm) acrylic tube and a 1" x 1/8" (2.54 x 0.32 cm) flexible transparent tube connect the main bed to the solids return leg.

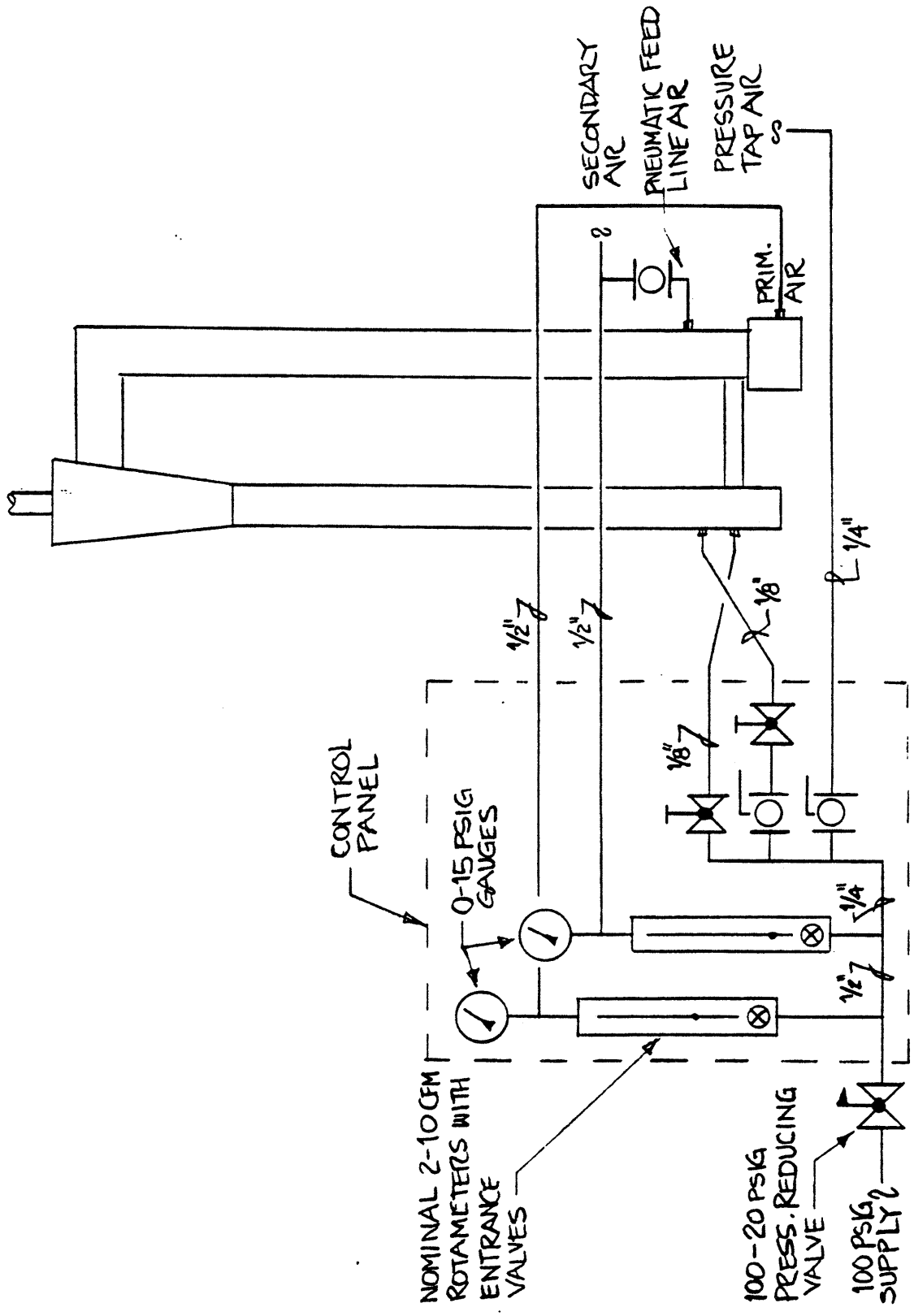

igure 4.3: Schematic of 1/4 Scale UBC Air Flows

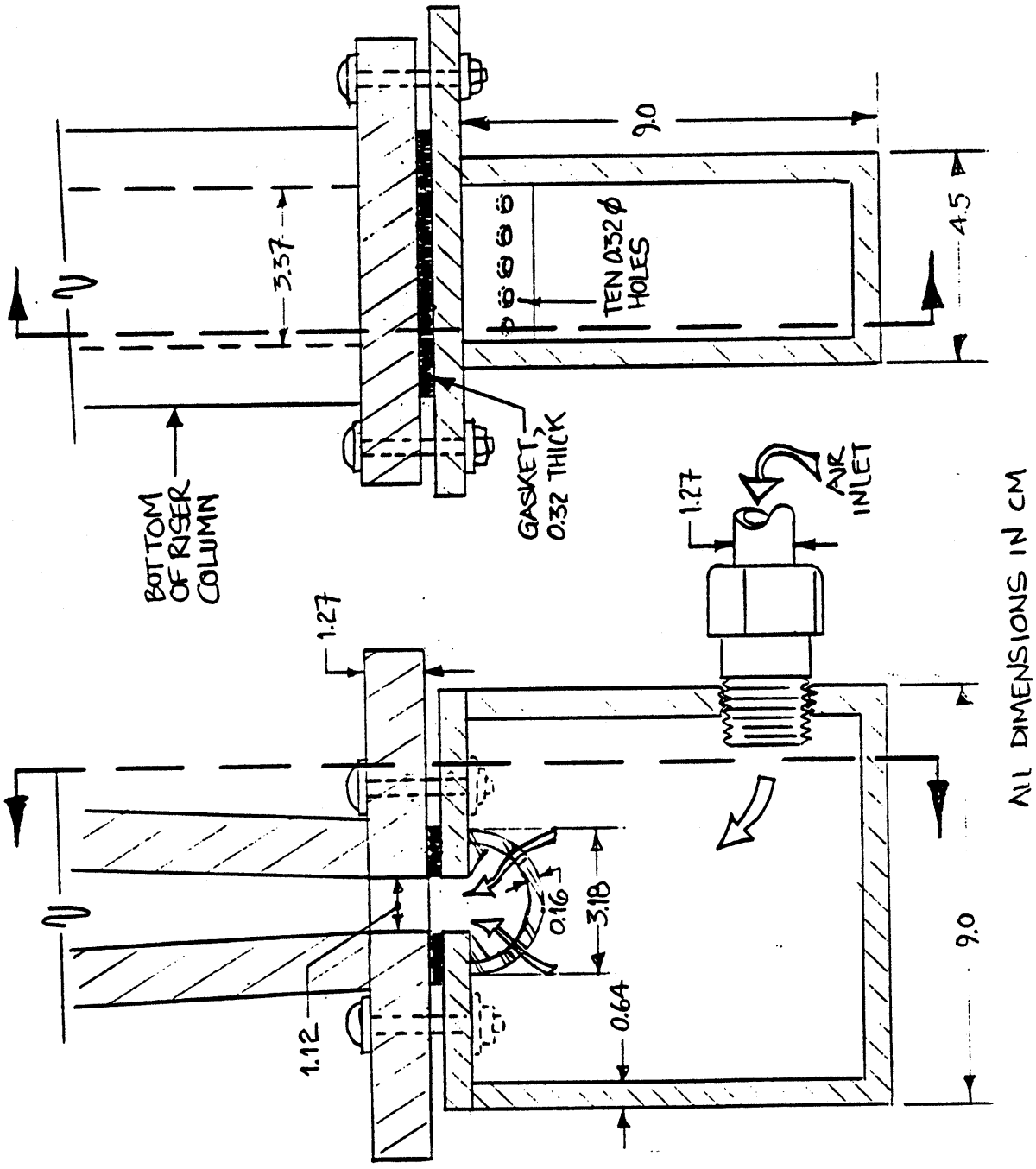

Figure 4.4: Schematic of 1/4 Scale UBC Air Distributor

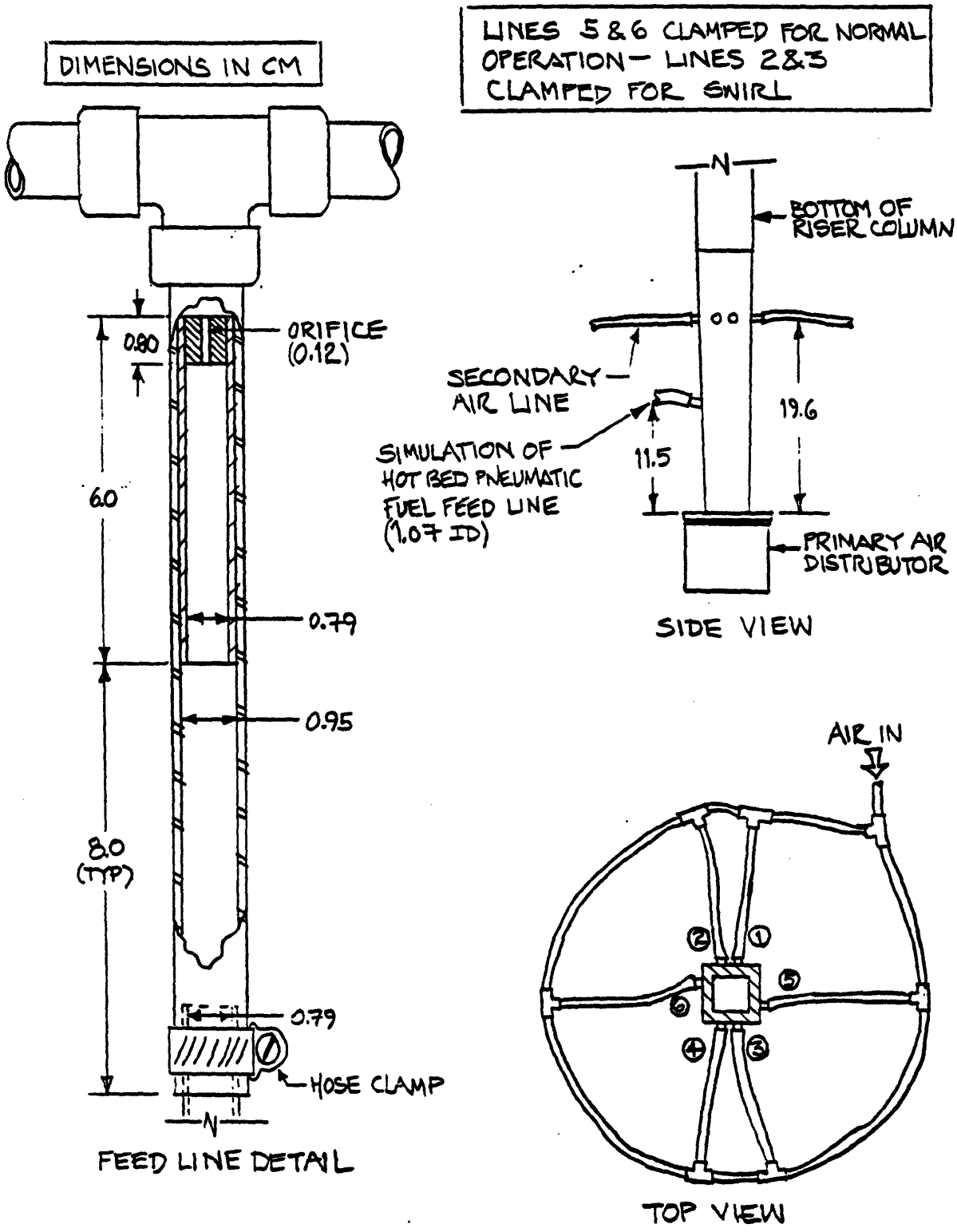

gure 4.5: Schematic of 1/4 Scale UBC Secondary Air Tubing

4.2.1.2 Cyclone and Filter

The cyclone was constructed geometrically similar to the UBC bed cyclone. It was constructed primarily of 1/4-inch acrylic. The cyclone connects to the main bed section, the solid return leg, and the air exhaust line with flanges. Hose-and-clamp connections were later added for final connections to the solid return leg and air exhaust line in order to relieve stresses. See Figure 4.6 for diagrams of the cyclone and filter.

The cyclone was operated with a filter utilizing two automobile air filters to allow easy retrieval of filtered solid and provide adequate filtration.

4.2.1.3 Solid Return Leg

The solid return leg is primarily constructed of 1.5" x 1/8" (3.81 x 0.32 cm) acrylic tube. The return leg consists of two sections, one above and one below the solid flow measurement valve. Connections between return leg parts were made with flexible hose and clamps to reduce stresses.

The bottom of the return leg was constructed of a 1-1/2" (3.81 cm) copper tube and a 1-1/2" x 1-1/2" x 1" (3.81 x 3.81 x 2.54 cm) tee. A 1" x 1/8" (2.54 x 0.32 cm) flexible transparent tube connects the bottom of the return leg to the main bed section. The bottom of the return leg reduces to a 1/2" NPT plug for drainage of solid. Air lines for solid flow control connect to the side of the copper tee. These include the standard L-Valve air and additional air for improvement of solid flow. The latter air is fed to the horizontal feed tube through a 1/4" (0.64 cm) sparge tube. An additional sparge tube for distribution of L-Valve air to the center of the return leg had been installed, but was removed because of its detrimental effects on solid flow.

The valve and syringe used for the measurement of solid circulation rate, built into the solid return leg, are discussed in Section 4.4.2. The valve, located at the middle of the return leg, is a nominal 1-1/2" (3.81 cm) full-bore three-piece ball valve. The syringe is a modified 1-cc syringe, installed with friction fit into a 1/4" (0.64 cm) hole in the side of the return leg.

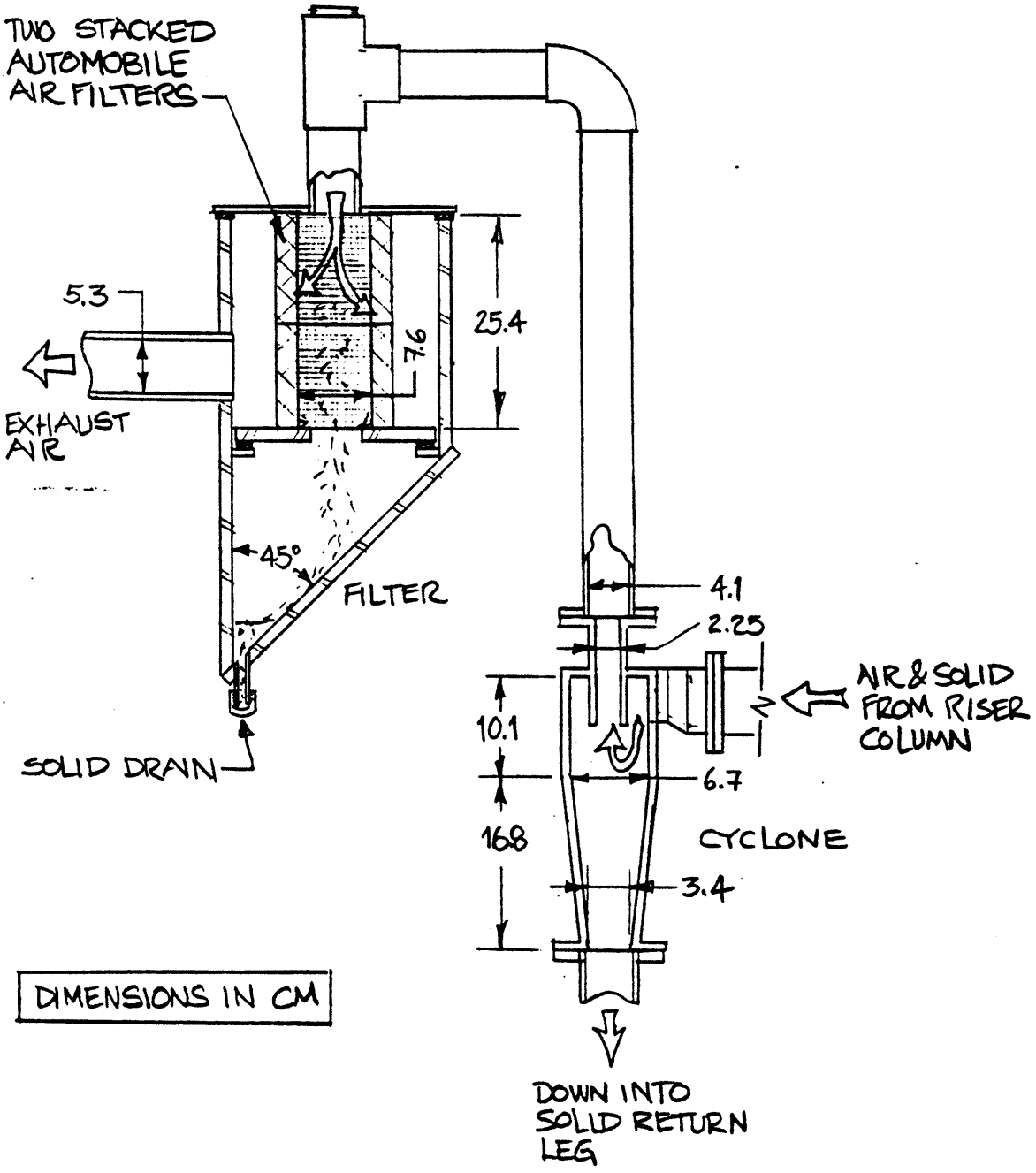

Figure 4.6: Schematic of 1/4 Scale UBC Cyclone and Air Filter

4.2.2 1/4 Scale Model of the 2.5 MWt Studsvik Circulating Fluidized Bed Combustor

The second bed utilized was a 1/4 scale model of the Studsvik circulating bed operated by Studsvik Energiteknik AB. This bed was constructed as part of an ongoing study to verify the complete set of scaling relationships for commercial sized circulating fluidized beds (Westphalen, 1993). The 1/4 scale Studsvik bed was slightly modified for use as the larger of two beds (the smaller being the 1/16 scale model of the Studsvik combustor) in the verification of the simplified scaling laws and convective heat transfer scaling relationships. It also provided a means of comparison between scaling the Studsvik hot bed with the full set of scaling laws and the simplified set of scaling laws. The bed consists of four main parts:

1. Main bed test section
2. Primary separator and downcomer
3. Secondary separator and return leg
4. Distributor box and boot

A drawing of the bed is presented in Figure 4.7.

4.2.2.1 Main Bed Test Section

The main test section was constructed with a geometry similar to the Studsvik hot bed. Three of the bed sides (front and sides) were constructed of 1/2-inch (1.27 cm) Lexan sheet and lined with 1/16 inch (0.16 cm) scratch-resistant acrylic. The back of the bed was constructed from 1/4-inch (0.635 cm) aluminum plate which extends 147.6 cm down from the top of the bed. A groove was machined around the perimeter of the aluminum back and a Viton gasket inserted to seal the aluminum back to the bed. This arrangement allows for easy removal of the aluminum panel and quick access to the inside of the bed. The cross sectional area of the bed is 252 cm^2, and the bed length is 1.83 m.

Figure 4.7: 1/4 Scale Studsvik Bed

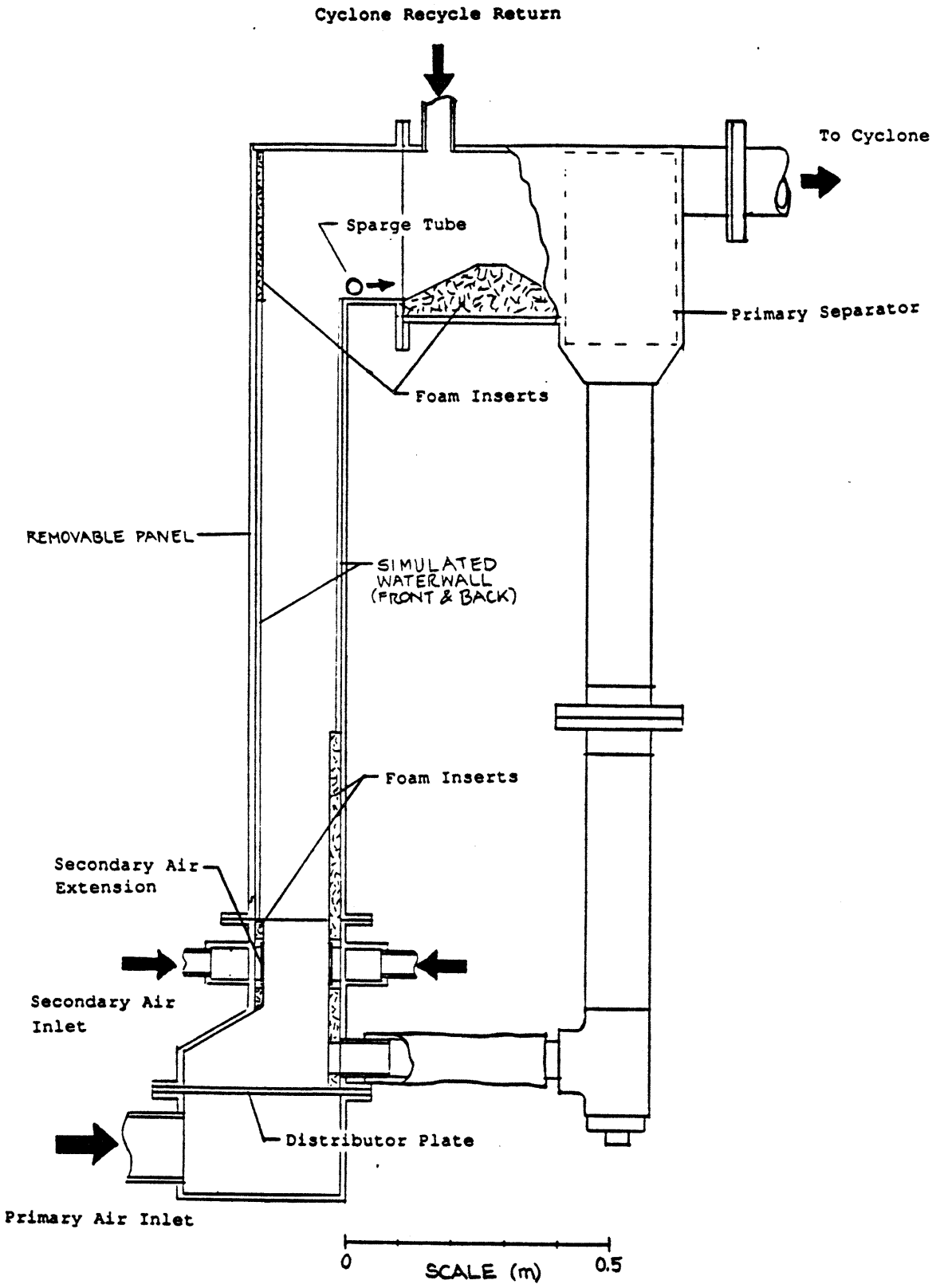

The foam inserts depicted in Figure 4.7 around the secondary air ports and on the aluminum back at the top of the bed were included to simulate refractory lining found in the Studsvik hot bed. Simulated waterwall (1/2-inch [1.27 cm] 1/2 round dowel) was also included to model the waterwalls found in the hot bed. In tests which were not aimed at modeling the hot bed (i.e., tests with glass and plastic particles), the simulated refractory and waterwalls were removed from the 1/4 scale cold bed.

In order to prevent solid backflow from the top of the bed due to excessive solid buildup in the horizontal section in front of the primary separator, a 1" (2.54 cm) diameter sparge tube and foam insert were included to blow the solids into the primary separator (see Figure 4.8).

Air is divided into primary and secondary streams before being introduced into the bed. Primary air is introduced at the bottom of the bed through a screen distributor mounted on a 0.2 m high distributor box (Figure 4.9). Secondary air is introduced at a height of 21 cm through slotted distributors in the front and back of the bed. Both the primary and secondary air flows are measured utilizing square edged orifice plates with flanged taps and manometers. A drawing of the air supply tubing is shown in Figure 4.10. The secondary air system in the 1/4 scale Studsvik bed was not used in the verification of the simplified scaling parameters.

Nine pressure taps used to measure axial pressure drop are located on one of the side walls of the bed. These taps are angled down in order to prevent solids from accumulating in the lines. One tap is located immediately above the distributor plate, and the others are located at distances of 10.4, 17.3, 29.0, 46.7, 76.2, 106.7, 137.2, 167.6 cm from the bottom of the bed.

4.2.2.2 Primary Separator and Downcomer

Primary solids separation is achieved by means of a U-tube separator. Six rows of 5/8" x 1/2" x 12.5" (1.6 x 1.3 x 31.8 cm) aluminum U-tubes were arranged in an offsetting pattern of seven and six across (see Figure 4.11). The solids drop into a 4" (10.2 cm) diameter graduated downcomer for return to the bed. A grounded 1/2" (1.3 cm) aluminum rod was hung in the downcomer to aid in the discharge of static electricity.

Figure 4.8: Sparge Tube

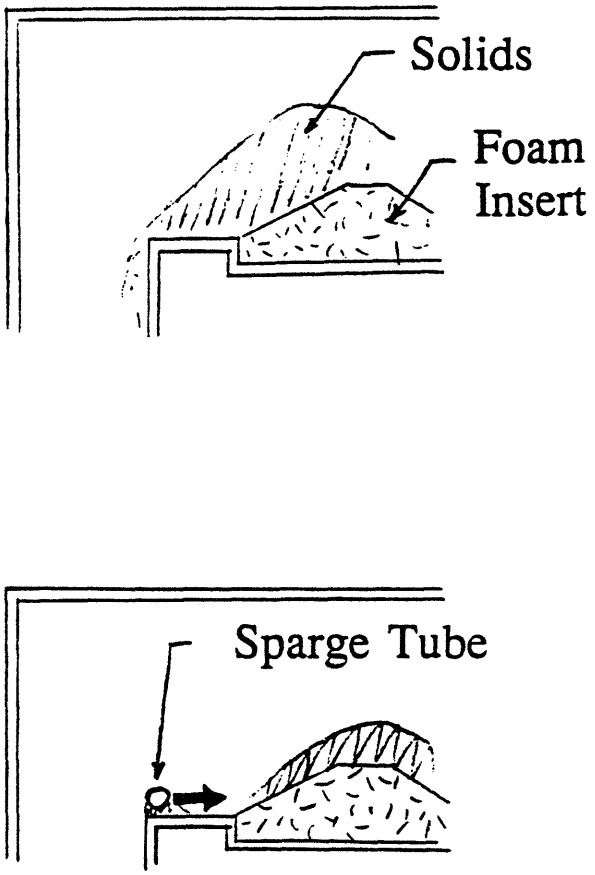

TOP ELBOW SHOWING SOLIDS ACCUMULATION WITH AND WITHOUT SPARGE TUBE

1/4 Scale Studsvik Bed Distributor Box and Disbribution Plate

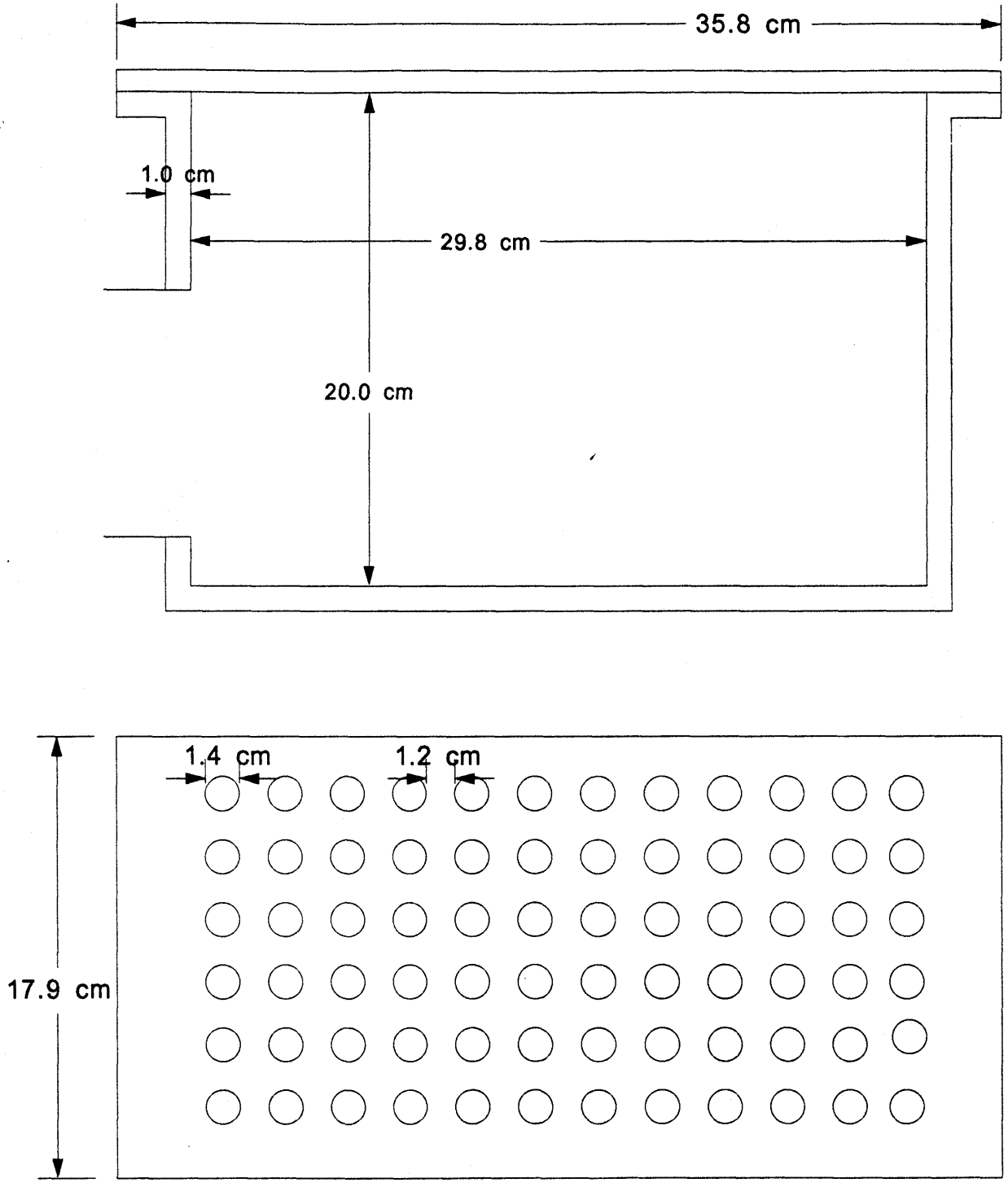

Figure 4.9: 1/4 Scale Studsvik Bed Distributor and Distributor Box

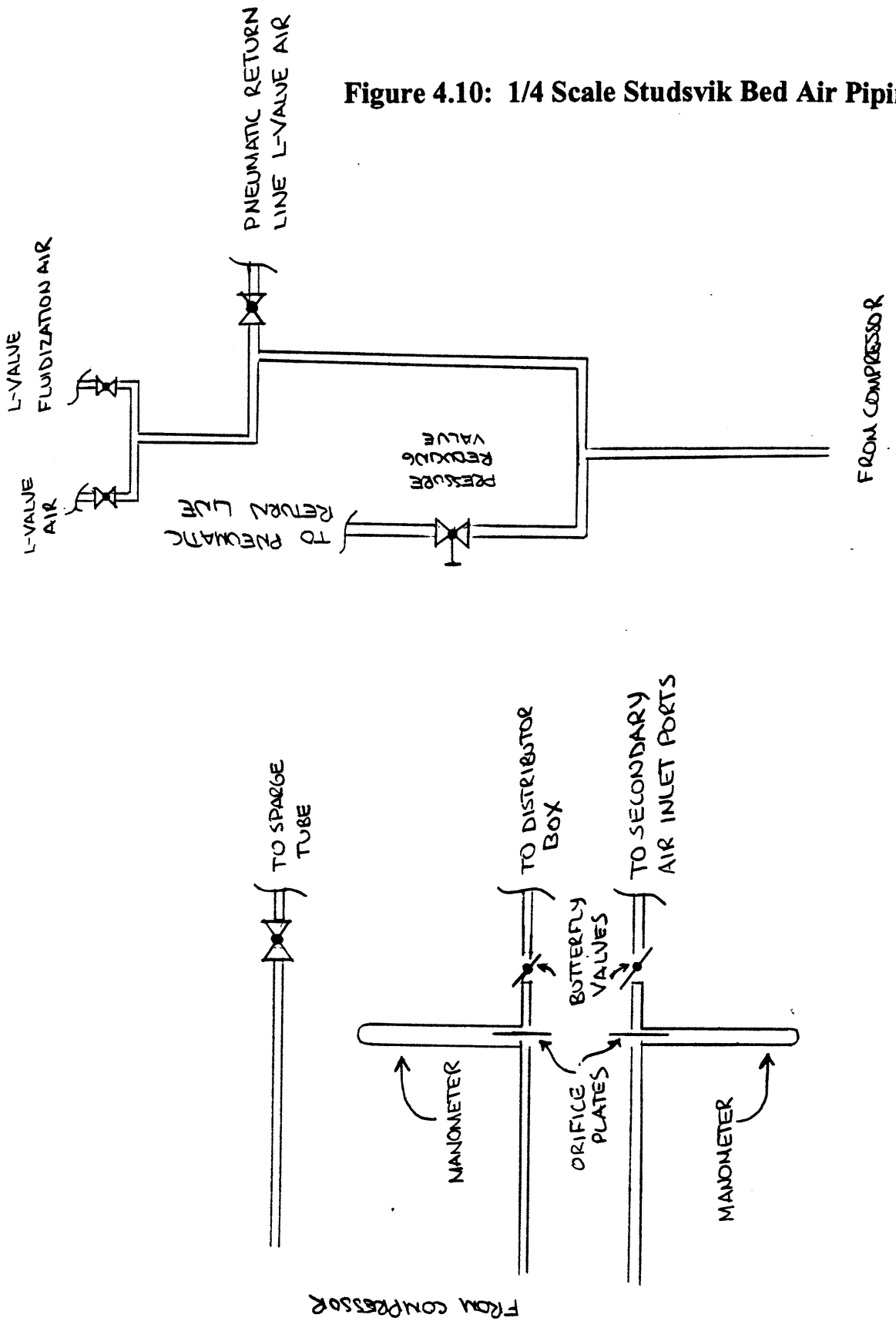

Figure 4.10: 1/4 Scale Studsvik Bed Air Piping Diagram

Figure 4.11: 1/4 Scale Studsvik Bed U-Tube Separator

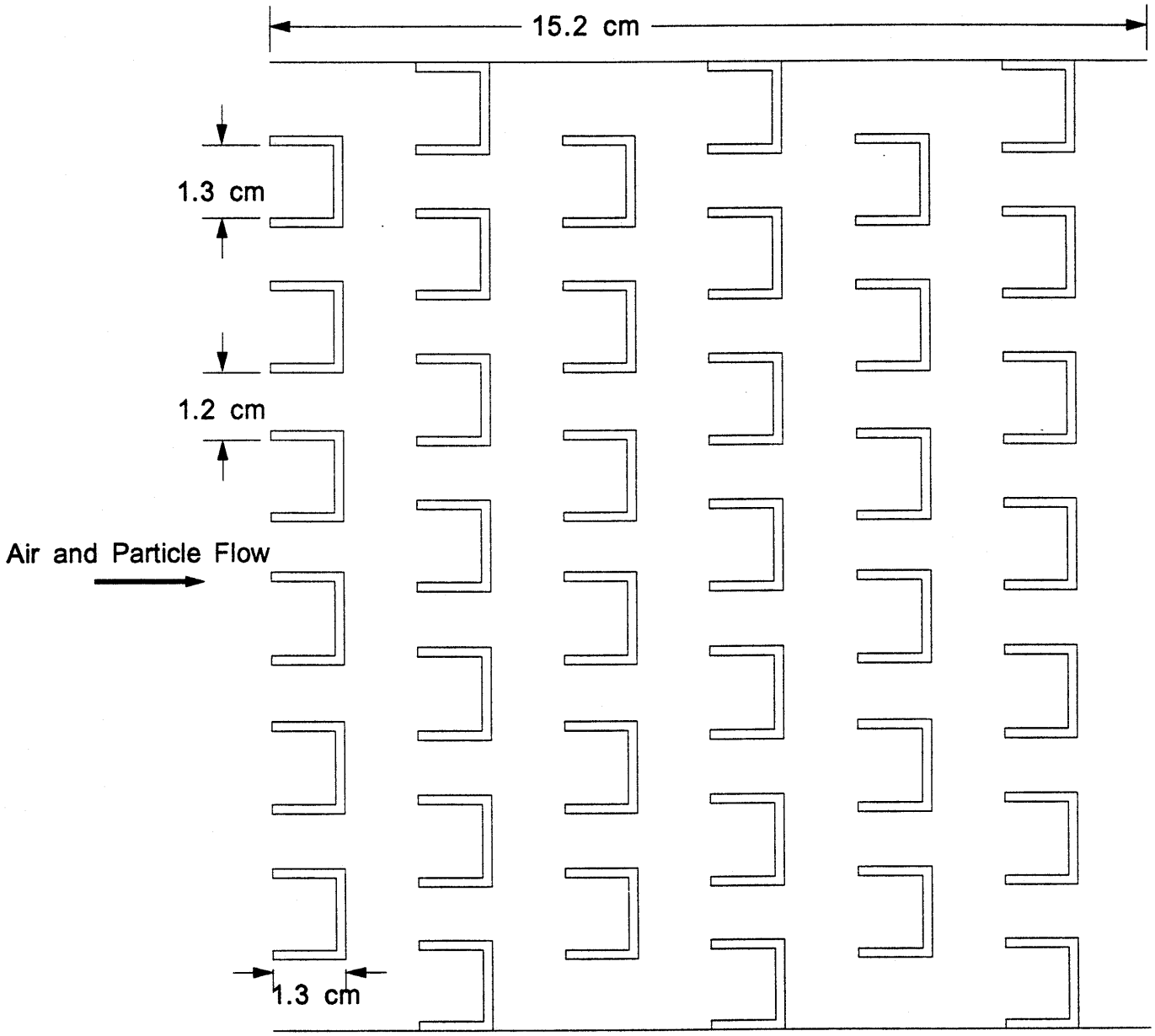

U-Tube Height = 31.75 cm

The solids return port at the bottom of the bed is just above the primary air feed and is 2.25" (5.7 cm) in diameter. The solids are returned to the main bed through a 2-1/4" (5.7 cm) flexible hose which connects the main bed to the solids return leg. A threaded plug at the bottom of the downcomer is used for the discharge of solids when emptying the bed.

4.2.2.3 Secondary Separator and Return Leg

The secondary separator consists of a Plexiglas cyclone. The cyclone, constructed primarily of 1/4-inch (0.635 cm) Plexiglas, has a total length of 3 feet (0.91 m) with the top 18 inches (45.7 cm) having an inside diameter of 9-7/16" (24.0 cm). The bottom 18 inches (45.7 cm) tapers down to a flanged 2.0" (5.1 cm) solids exit. Air exits to a filter box through a 4.0" (10.2 cm) outlet in the top of the cyclone.

Solids were recycled to the bed in one of two ways. The first method was to collect the solids in a 4.0" (10.2 cm) diameter tube and feed them through an L-Valve to a 1.0" (2.54 cm) ID pneumatic line which returned the solids to the top of the bed in front of the primary separator. This method was used when running glass in the bed. Due to laboratory renovations which occurred during the project, it became possible to raise the cyclone up an additional 4 feet (1.22 m). After this modification, the solids were fed directly into the downcomer (1 foot [30.5 cm] below the primary separator) through a 1-1/2" (3.8 cm) ID flexible tube. This method was used when running plastic in the bed. See Figure 4.12 for diagrams of the secondary separator and return leg.

The air exiting from the cyclone is fed into a large filter box containing a 24" x 12" x 2" (61.0 x 30.5 x 5.1 cm) high density microfine glass fiber prefilter and a 24" x 12" x 12" (61.0 x 30.5 x 30.5 cm) hepa filter.

Figure 4.12: 1/4 Scale Studsvik Bed Secondary Return System

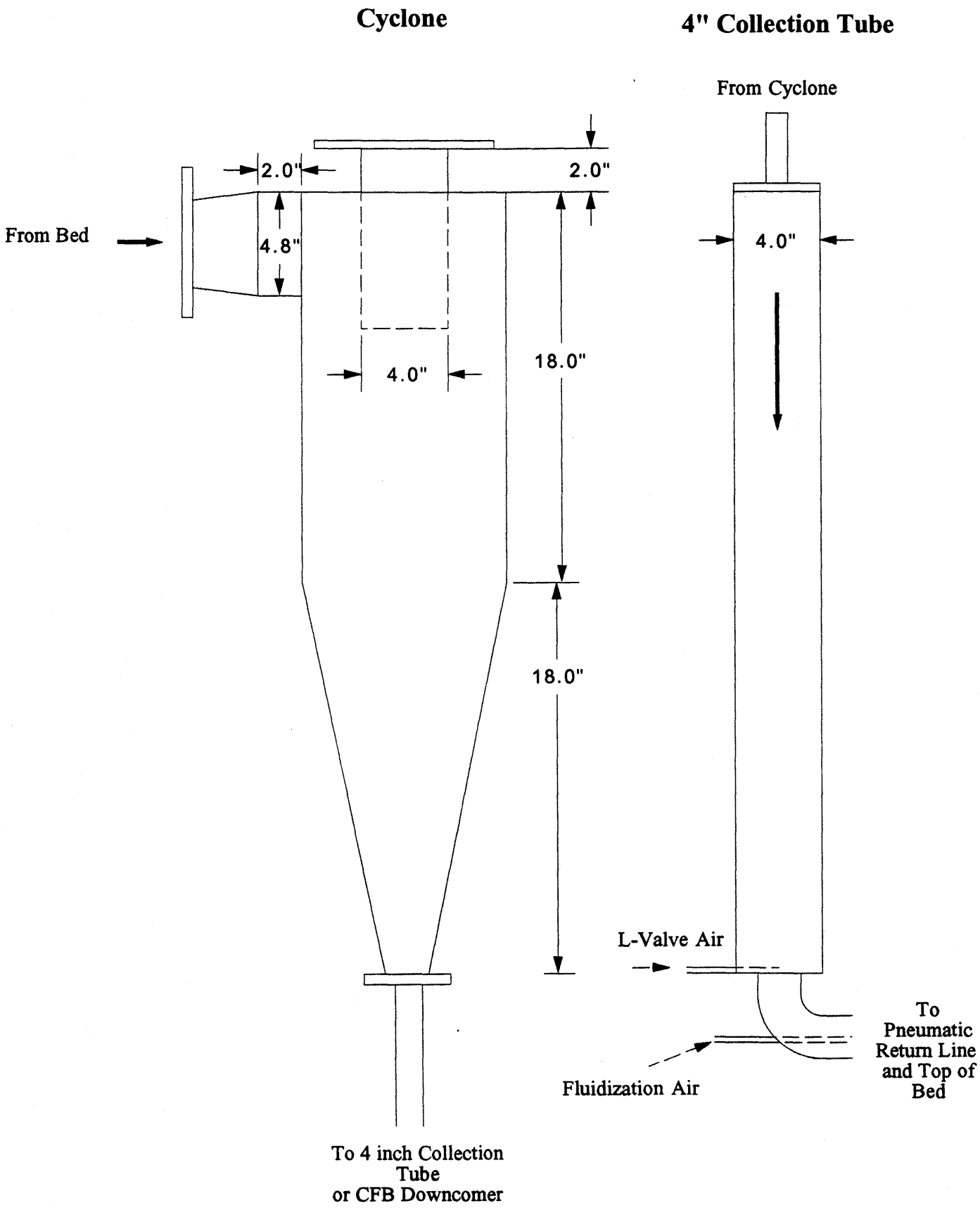

4.2.2.4 Distributor Box and Boot

Primary air enters the bed through a 11.7" x 6.25" x 7.9" (29.8 x 15.9 x 20 cm) distributor box. The air then flows through the screen distributor plate into the bottom of the bed. The bottom of the Studsvik circulating bed is unique in that it narrows from cross-sectional dimensions of 11.7" x 6.25" (29.8 x 15.9 cm) at a distance of 2-1/2" (6.7 cm) above the distributor plate to a square cross section of 6.25" x 6.25" (15.9 x 15.9 cm) at a distance of 5.9" (15 cm) above the distributor plate (see Figure 4.7). During verification of the simplified scaling parameters with constant density ratio, the boot section of the bed was blocked off such that the bed cross-section remained constant at all bed heights.

It should be noted that in a previous study a bubble cap distributor was built for the 1/4 scale Studsvik bed to verify the full set of scaling parameters. However, it was shown that the effect of using this bubble cap distributor versus a screen distributor plate was negligible as depicted in Figure 4.13 (see Westphalen, 1993).

4.2.3 1/16 Scale Model of the 2.5 MWt Studsvik Circulating Fluidized Bed Combustor

The third bed utilized was a 1/16 scale model of the Studsvik circulating bed operated by Studsvik Energiteknik AB. This bed was constructed in two phases. During the first phase, the bed was built without the boot, secondary air ports, simulated refractory, or simulated waterwall. This was done in order to reduce the construction time and amount of uncertainty when attempting to validate a simplified set of scaling laws. This version of the 1/16 scale Studsvik bed was used as the smaller of two beds (the larger being the 1/4 scale model of the Studsvik combustor similarly modified) in the verification of the simplified scaling laws and convective heat transfer scaling relationships.

Figure 4.13

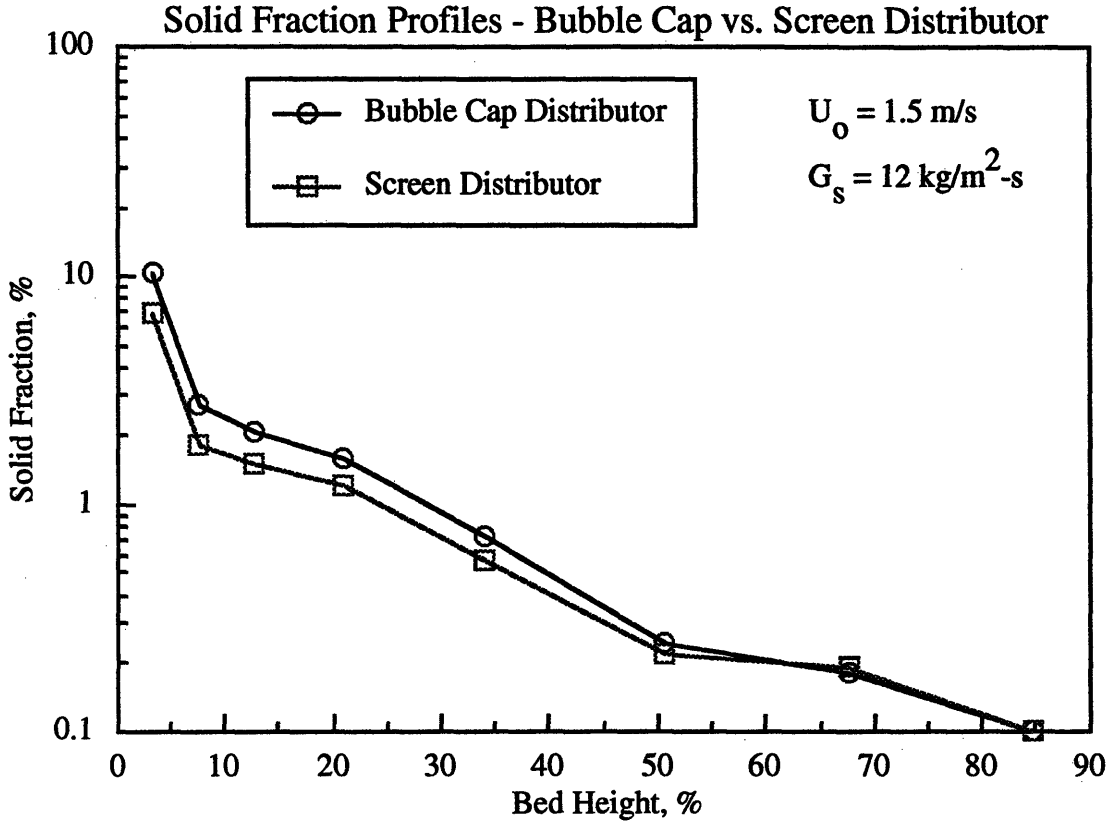

The second phase of construction added the boot, secondary air ports, and simulated refractory in order that the bed be able to model the Studsvik hot bed using the simplified set of scaling laws. The simulated waterwall was not added since it had been shown that this modification had negligible impact on the macro hydrodynamics of the bed (Westphalen, 1993). The bed consists of three main parts:

1. Main bed test section
2. Primary separator and downcomer
3. Solid return leg

A drawing of the bed is presented in Figure 4.14.

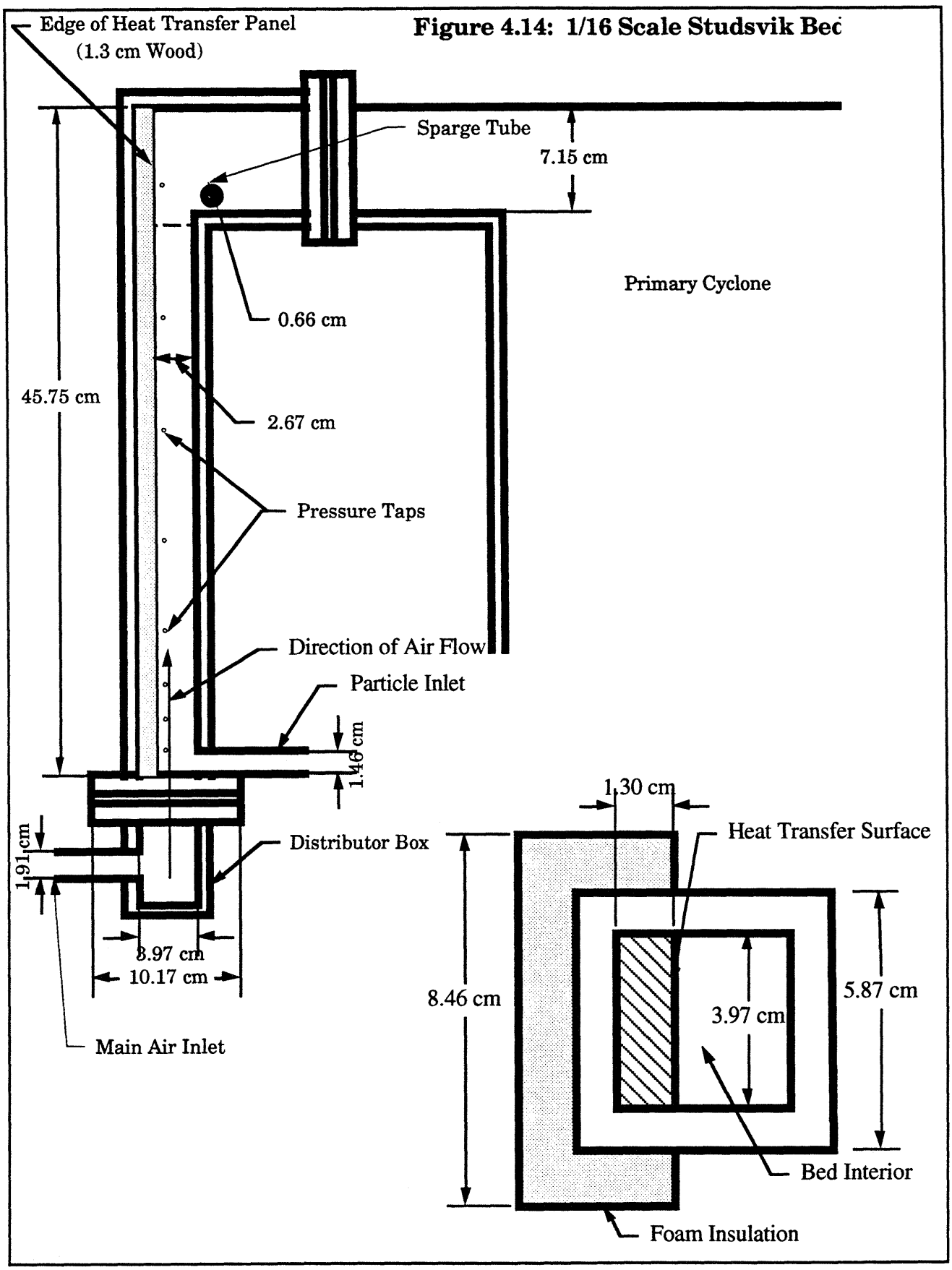

Figure 4.14: 1/16 Scale Studsvik Bed

4.2.3.1 Main Bed Test Section

The main test section was constructed with a geometry 1/4 the size of the 1/4 scale Studsvik model (1/16 the size of the Studsvik hot bed). All four sides of the bed side were constructed of 3/8-inch (0.95 cm) acrylic sheet. The back of the bed was held on by RTV 108 silicone rubber sealant, which allowed for its removal. The cross sectional area of the bed is 15.75 cm^2, and the bed's length is 0.46 m.

As in the larger Studsvik model, a 1/4" (0.64 cm) diameter sparge tube was included in the horizontal section in front of the primary separator to prevent solid backflow from the top of the bed due to excessive solid buildup.

During the first phase of tests, no secondary air was introduced into the bed. Primary air was introduced at the bottom of the bed through a screen distributor mounted on a 2.5-inch (6.35 cm) high distributor box. A drawing of the air supply system for the first phase of tests is depicted in Figure 4.15.

During the second phase of tests, secondary air ports, simulated refractory, a bed boot, and a new distributor box were added in order to model the Studsvik hot bed. Air was divided into primary and secondary streams before being introduced into the bed. Primary air was introduced at the bottom of the bed through a screen distributor mounted on a 2.0-inch (5.1 cm) high distributor box. Secondary air was introduced at a height of 6.1 cm through slotted distributors in the front and back of the bed in a similar fashion to the 1/4 scale model. A drawing of the air supply system for the second phase of tests is shown in Figure 4.16.

Nine pressure taps located on one of the side walls were used to measure axial pressure drop in each of the beds used. These taps were angled down in order to prevent solids from accumulating in the lines. The first tap was located immediately above the distributor plate, and the others were located at distances of 1.4, 3.5, 5.9, 9.6, 15.6, 23.2, 31.0, 38.8 cm from the distributor plate.

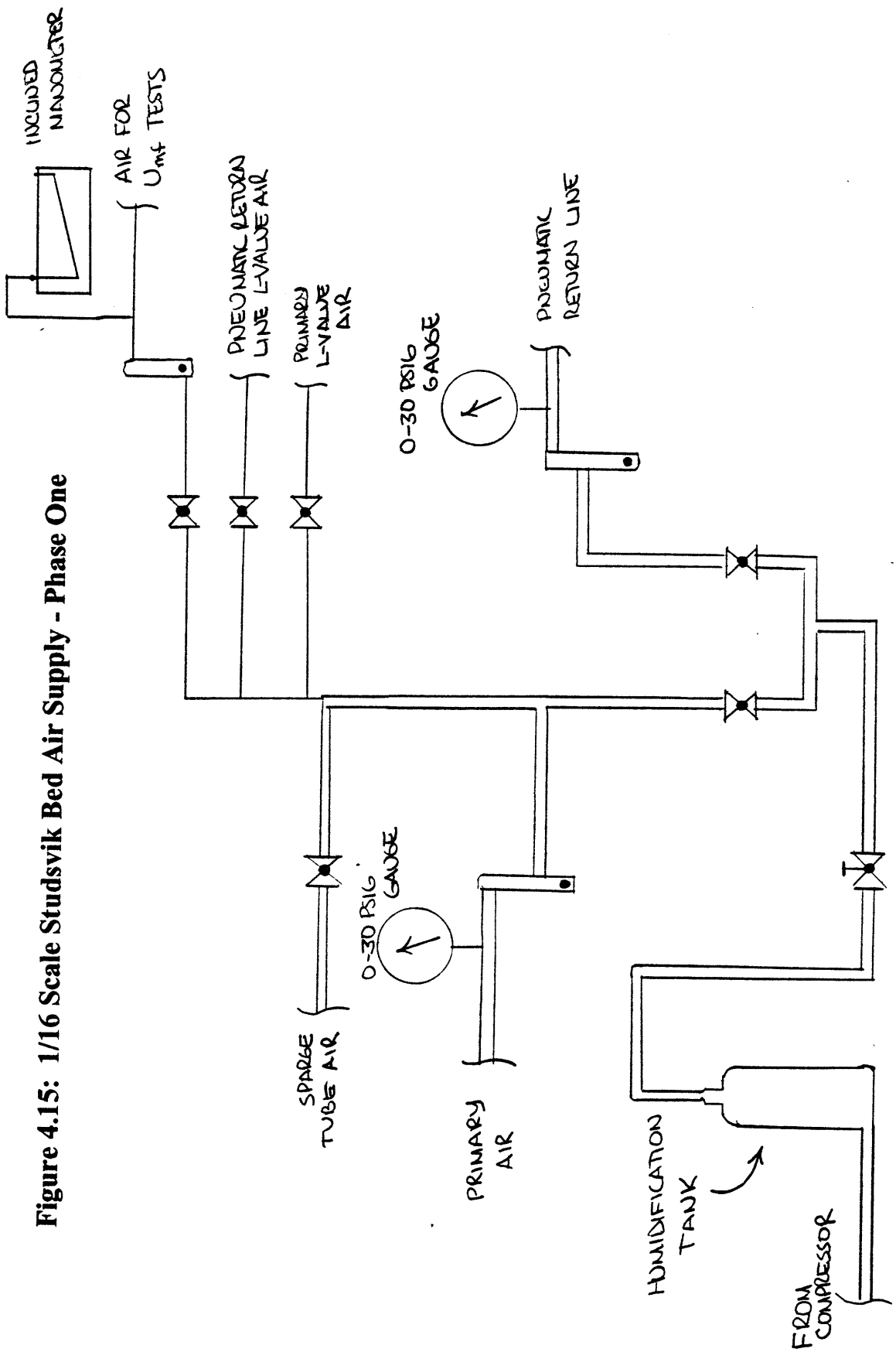

Figure 4.15: 1/16 Scale Studsvik Bed Air Supply - Phase One

Figure 4.16: 1/16 Scale Studsvik Bed Air Supply - Phase Two

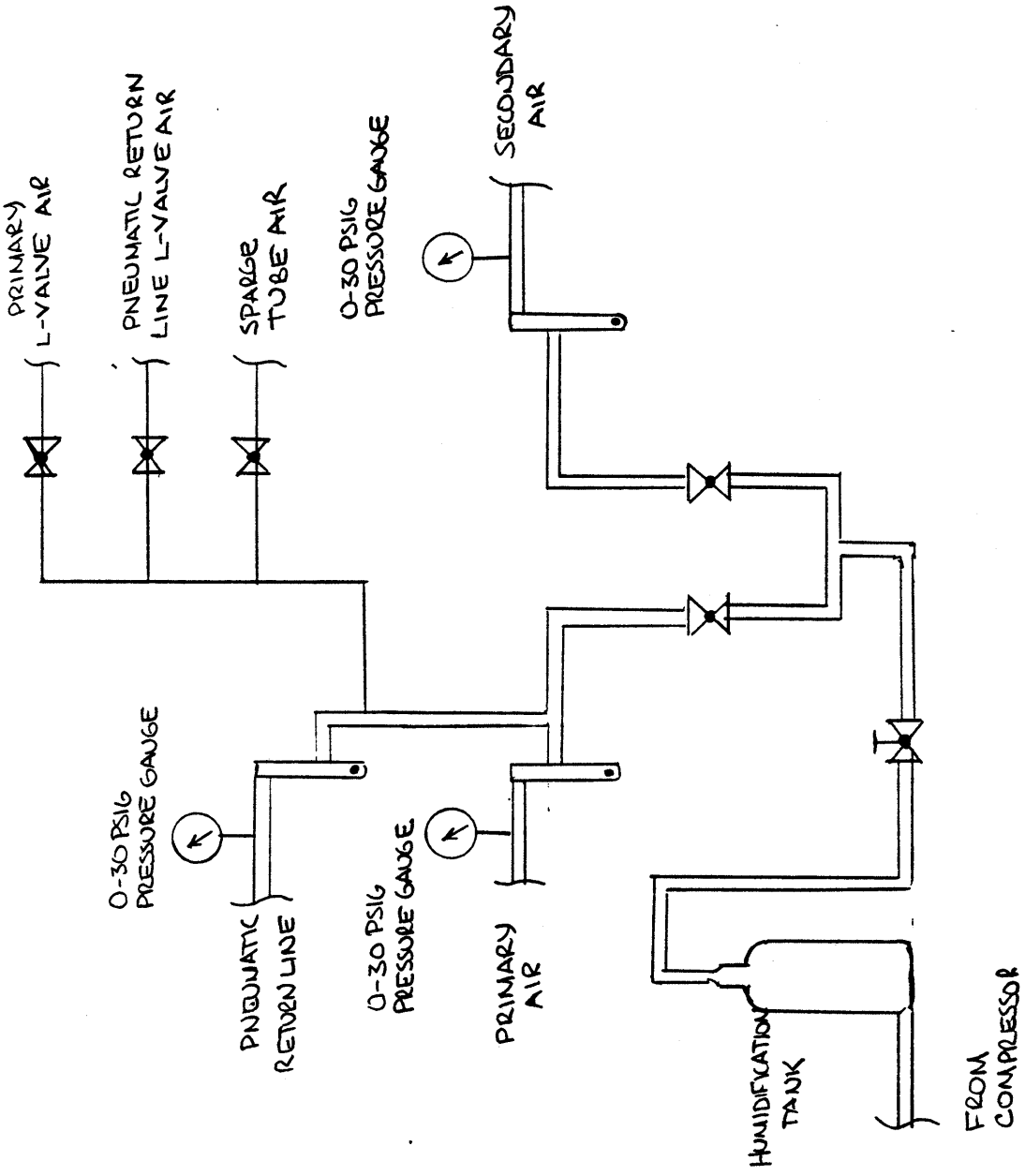

4.2.3.2 Primary Separator

Primary air/solid separation was achieved by means of a cyclone. The primary cyclone was constructed primarily of 1/4-inch (0.635 cm) acrylic. The primary cyclone connects to the main bed section, the solid return leg, and the air exhaust line with flanges. Hose-and-clamp connections were later added for final connections to the solid return leg and air exhaust line in order to relieve stresses. See Figure 4.17 for diagrams of the primary cyclone and filter.

The air exhaust leaving the primary cyclone was directed through the same filter used with the 1/4 scale model of the UBC circulating bed described above.

4.2.3.3 Solid Downcomer and Return Leg

The primary solid downcomer was largely constructed of 1.5" x 1/8" (3.81 x 0.32 cm) acrylic tube. The primary downcomer consists of two sections, one above and one below the solid flow measurement valve. Connections between return leg parts were made with flexible hose and clamps to reduce stresses.

The bottom of the primary downcomer was constructed of a 1-1/2" (3.81 cm) copper tube and a 1-1/2" x 1-1/2" x 1" (3.81 x 3.81 x 2.54 cm) tee. A 1" x 1/8" (2.54 x 0.32 cm) flexible transparent tube connects the bottom of the primary downcomer to a pneumatic return line. The bottom of the primary downcomer reduces to a 1/2" NPT plug for drainage of solid. Air lines for solid flow control connect to the side of the copper tee. These include the standard L-Valve air and additional air for improvement of solid flow. The latter air was fed to the horizontal feed tube through a 1/4" (0.64 cm) sparge tube.

The pneumatic return line recycled the solid up to a secondary cyclone several feet above the top of the bed. The solids then dropped to a secondary downcomer for return to the test bed. Air from the pneumatic return line exhausted to the filter.

Figure 4.17: 1/16 Scale Studksvik Bed - Overall Schematic

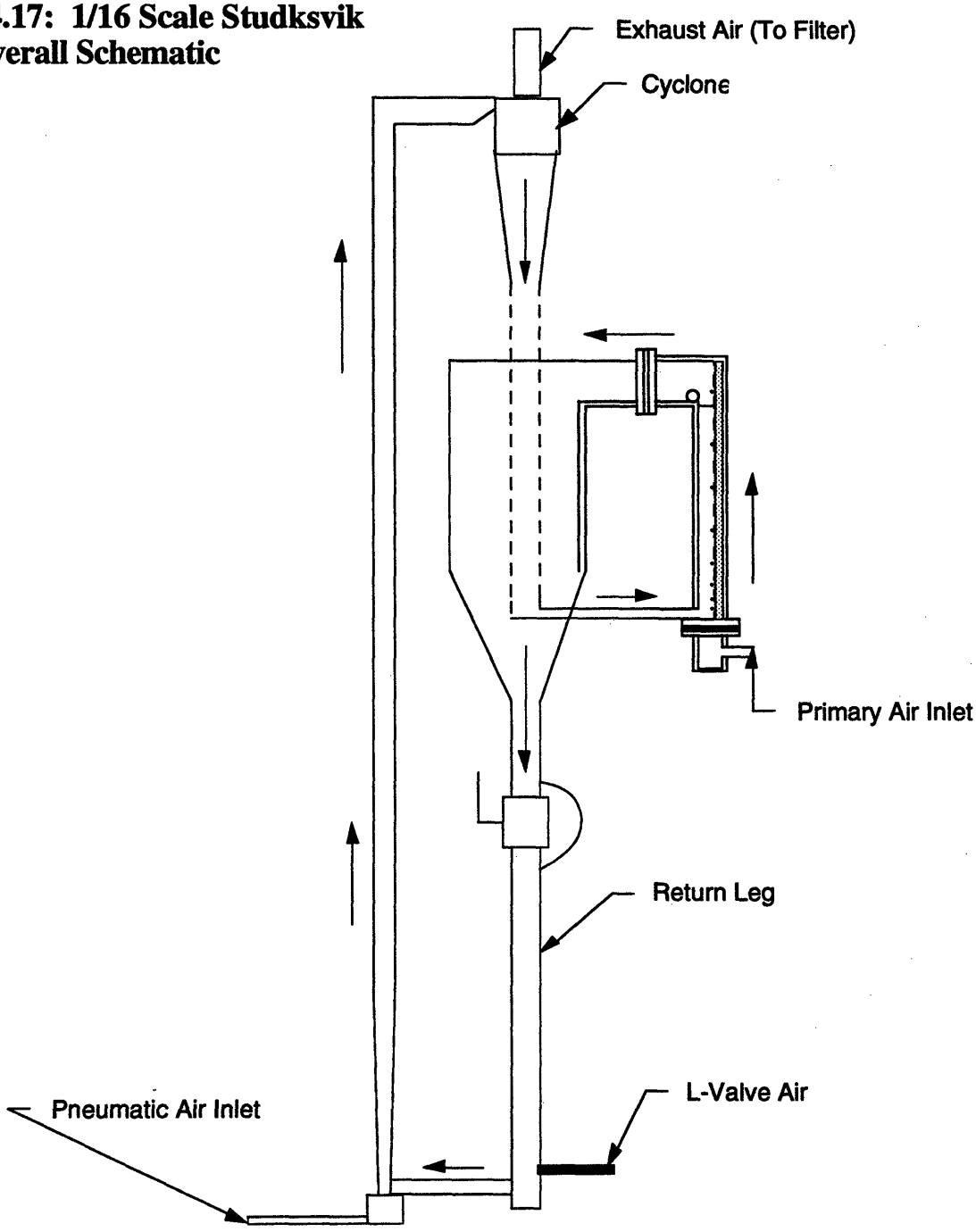

Arrows Denote Direction of Solids Flow

The valve used for the measurement of the solid circulation rate, built into the primary solid downcomer, is discussed in Section 4.4.2. The valve, located 10-inches (25.4 cm) below the primary cyclone, is a nominal 1-1/2" (3.8 cm) full-bore three-piece ball valve.

4.2.4 1/2 Scale Model of the Foster Wheeler Pilot Second Generation Pressurized CFB

The fourth bed utilized was a 1/2 scale model of the Foster Wheeler second generation pressurized circulating bed operated by Foster Wheeler Development Corp. in Livingston NJ. At the request of Foster Wheeler Development Corporation, a detailed description of the Foster Wheeler bed and the cold scale model will not be given. Rather the general layout and a description of the instrumentation will be given.

4.2.4.1 Foster Wheeler Hot Bed

The Foster Wheeler pilot plant is described in a series of DOE METC progress reports (Robertson *et al.*, 1989). The bed is round and consists of a 20.3 cm (8 in.) ID x 1.4 m (56.5 in.) tall primary zone and a 20.3 (8 in.) ID x 6.9 m (270.75 in) tall secondary zone. The primary zone bed height is 93 cm (36.6 in.). Four nozzles, two 0.40 m (15.875 in.) above and two 2.2 m (85.375 in.) above the top of the bed, permit the injection of varying amounts of secondary air into the riser. Coal/char and sorbent are pneumatically injected into the unit through a 2.5 cm (1.0 in.), central, vertical pipe at the bottom; an outer-concentric pipe injects primary air radially into the bed. The PCFBC contains no cooling tubes; its temperature is controlled by the continual circulation of cooled sorbent and fly ash between an external FBHE (fluid bed heat exchanger) and the PCFBC. A nitrogen-aerated packed-bed cooler at the bottom of the unit cools the spent bed material to 150 °C (300 °F); it is intermittently withdrawn in batches via a lock hopper. Exhaust gas exits through a 7.6 cm (3 in.) ID nozzle at the top of the unit. This gas passes through a 33 cm (13 in.) diameter primary cyclone that captures entrained particulate material and drains it to the FBHE via a nitrogen-aerated non-mechanical J-valve. The FBHE is a 1 meter (42 in.) O.D. x 10.5 meter (34 ft., 6 in.) tall vessel, refractory lined to a 40.63 cm (16 in.) square cross section, with eight 2.5 cm (1 in.) O.D. x 0.32 cm (1/8 in.) wall and four 1.9 cm (3/4 in.) O.D. x .165 cm (0.065 in.) wall water-cooled Incoloy 800HT tubes. The tubes are separated by four air sparger pipes, each containing five aeration nozzles. The PCFBC secondary air fluidizes the FBHE before proceeding to the PCFBC; it enters via the aerator nozzles, passes through and fluidizes the collected material, exits through a 3.8 cm (1.5 in.) Sch. 80 water-jacketed nozzle, and is piped to the PCFBC secondary air nozzles.

The four tubes below the aeration nozzles operate in a moving, packed bed; they cool the portion of the FBHE bed material that is being drained for disposal via a lock hopper. A screw feeder controls the drain rate to the lock hopper; it also sets the FBHE bed level, thereby controlling the inventory of solids (sorbent) in the system. FBHE bed material is trnasferred back to the PCFBC via a 15.2 cm (6 in.) Sch. 40 nitrogen-aerated nonmechanical L-valve at the bottom. The L-valve controls the solids transfer rate, and the bed drain screw controls the bed/solids return temperatures by varying the bed height/amount of cooling tube surface immersed in the bed.

The PCFBC has been designed for a 4 m/s (12 ft/s) operating velocity at 1.42 MPa (14 atm) and 1150 K (1600 °F). Combustor excess-air levels rnage from 30 to 210 percent, and depending on the performance experienced, the fluidizing velocity may be reduced to as low as 2.4 m/s (8 ft/s). As a result the combustor heat relase that must be transferred to the FBHE will range from zero to approximately 450 W. The heat to be absorbed in the PCFBC, together with the solids circulation rate, determines the FBHE bed operating temperature and hence immersed tube bundle/bed height.

Figures 4.18 provides a schematic of the integrated PCFBC/FBHE test unit. Figures 4.19 through 4.21 provides the instrumentation schematics of the PCFBC/FBHE arrangement.

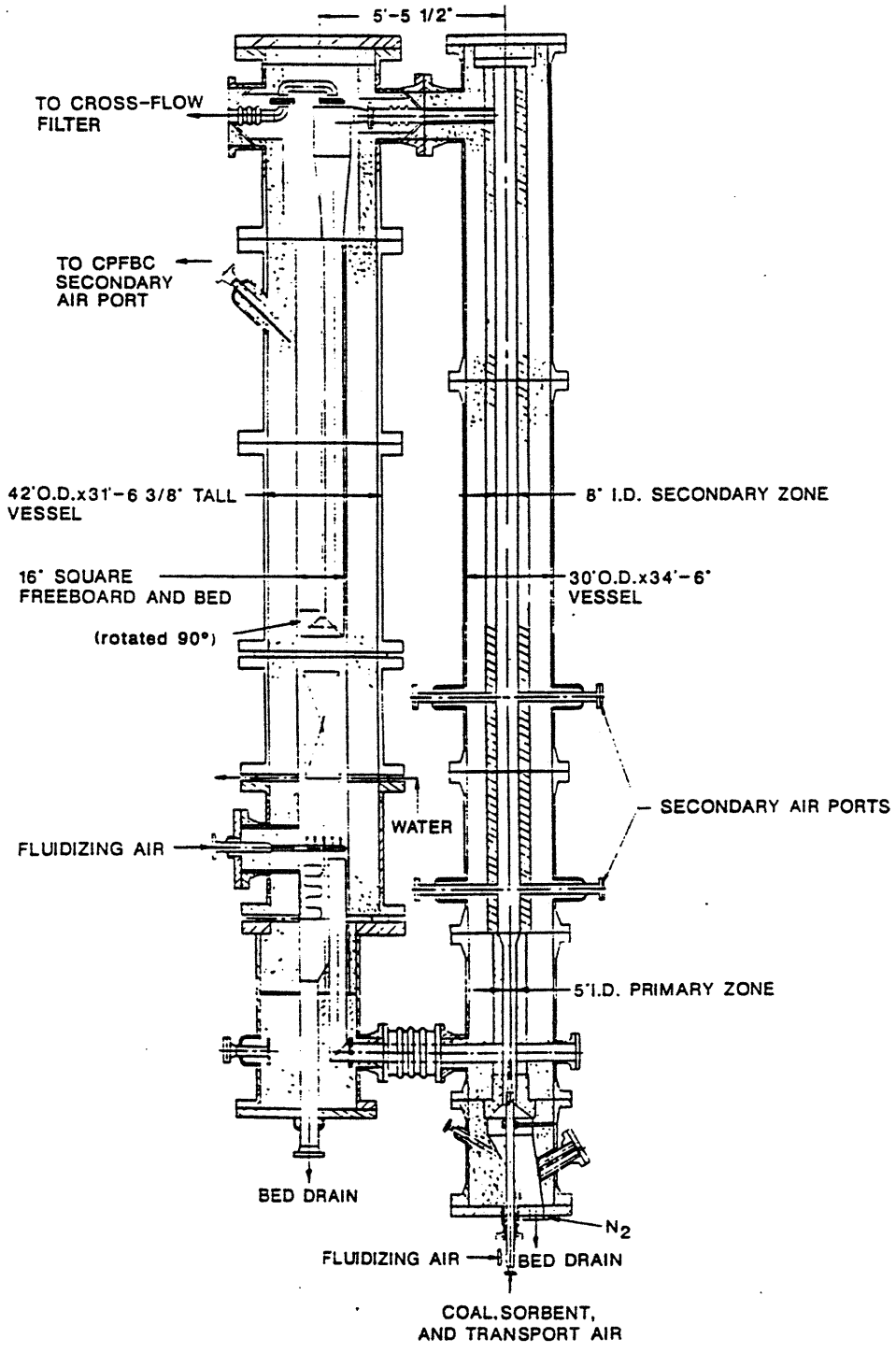

Figure 4.18 Integrated CPFBC/FBHE Test Unit

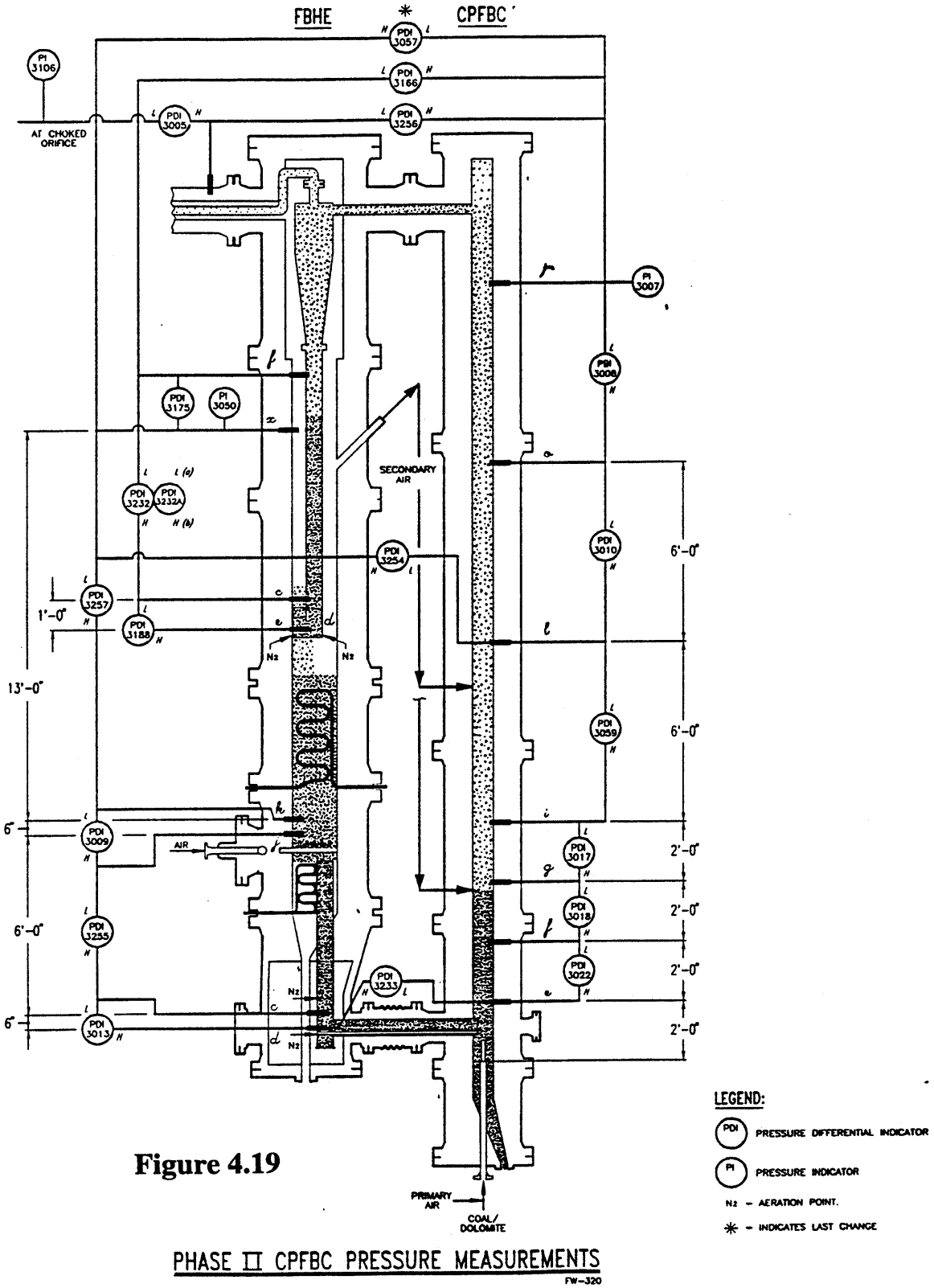

Figure 4.19

PHASE II CPFBC PRESSURE MEASUREMENTS

FW-320

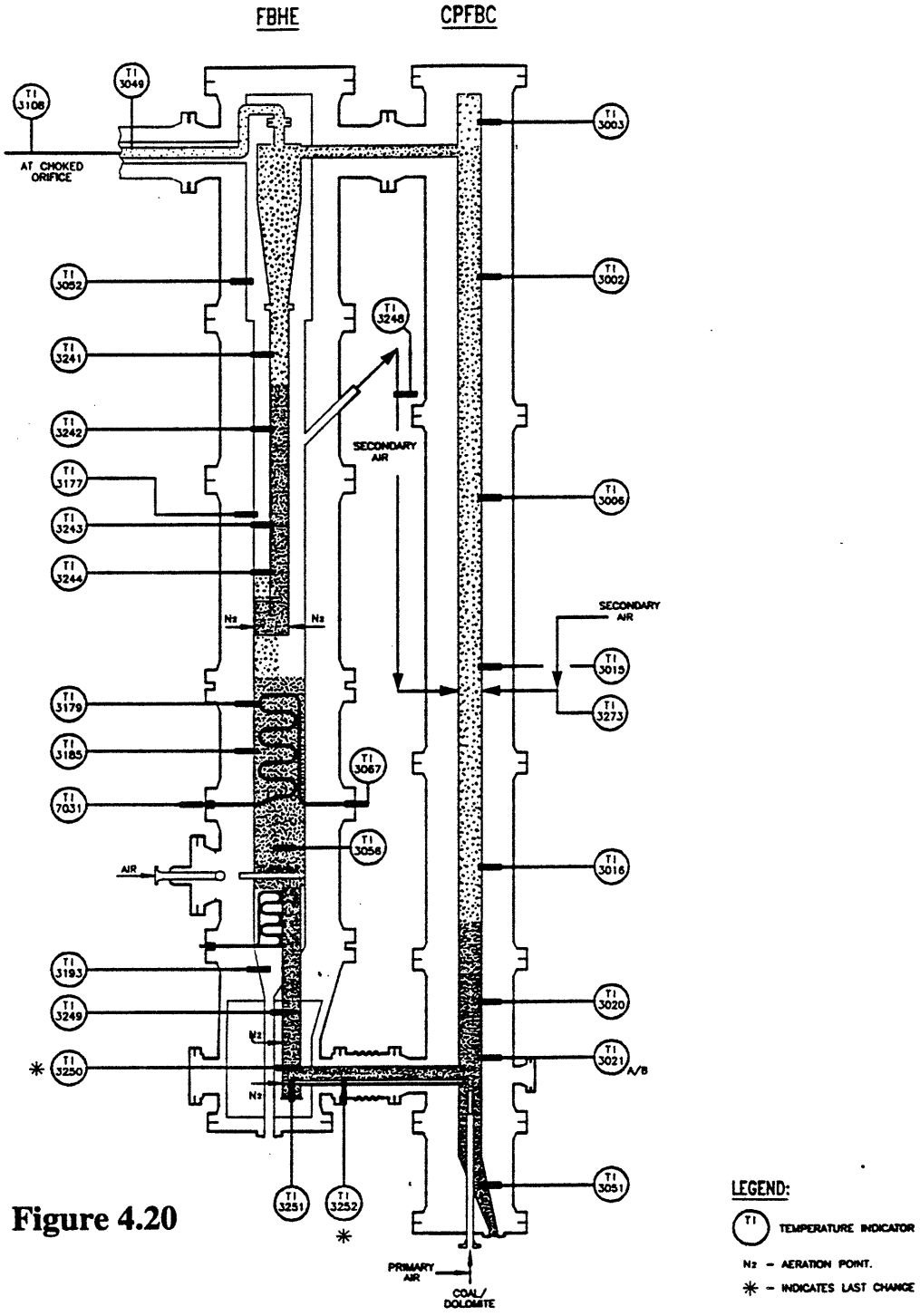

Figure 4.20

PHASE II CPFBC TEMPERATURE MEASUREMENTS

FW-322

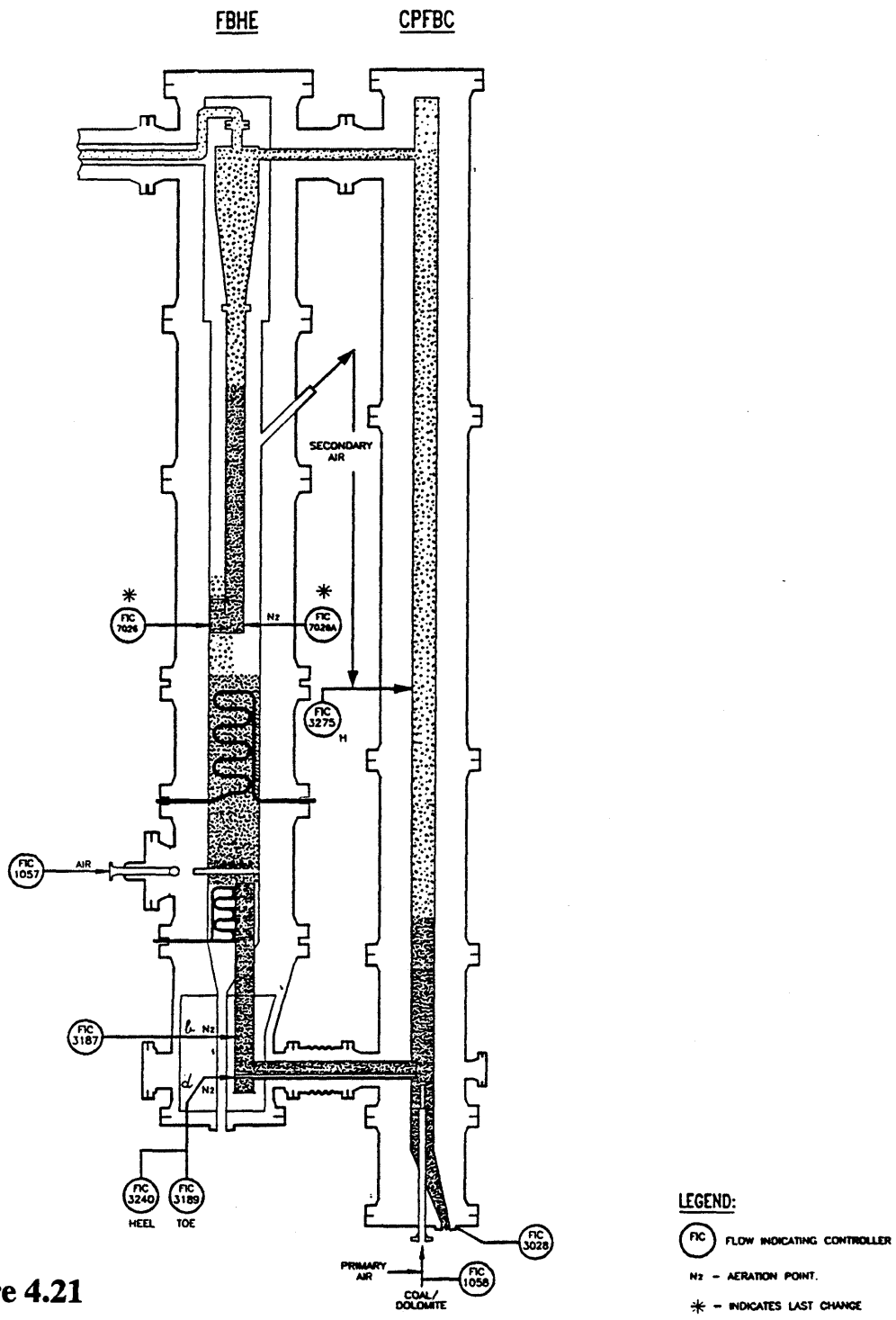

Figure 4.21

PHASE II CPFBC FLOW MEASUREMENTS

FW-325

4.2.4.2 1/2 Scale Model of the Foster Wheeler Hot Bed

The main test section was constructed with a geometry similar to the Foster Wheeler hot bed described above. The bed is made from 10.2 cm (4 in.) Sch. 40 clear PVC plastic pipe. The bed was construted in five sections (in exactly the same manner as the Foster Wheeler bed):

1. Distributor section
2. L-valve section
3. Lower secondary air port section
4. Upper secondary air port section
5. Exhaust section

Flange and penetration (secondary air, pressure taps, etc.) were located in geometrically similar fashion to the hot bed. The PCFBC, L-valve, exhaust, and piping to the cyclone were all exactly scaled.

The primary separator consists of a Plexiglas cyclone. The cyclone, constructed primarily of 1/4-inch (0.635 cm) Plexiglas, has a total length of 3 feet (0.91 m) with the top 18 inches (45.7 cm) having an inside diameter of 9-7/16" (24.0 cm). The bottom 18 inches (45.7 cm) tapers down to a flanged 2.0" (5.1 cm) solids exit. Air exits to a secondary cyclone through a 4.0" (10.2 cm) outlet in the top of the cyclone. Below the primary cyclone, a flexible hose was connected to help relieve stresses. Below this hose, a 4-in butterfly valve was installed for the measurement of solids circulation. To determine the solids circulation rate, the butterfly valve was shut and the rate of pileup of solids recorded. A 1" (2.5 cm) PVC pipe circumvents the valve in order to equalize pressure around the valve when shut. The butterfly valve exits to a 3" (7.6 cm) clear PVC downcomer pipe.

Secondary air/solid separation was achieved by means of a cyclone. The secondary cyclone was constructed primarily of 1/4-inch (0.635 cm) acrylic. The secondary cyclone connects to the primary cyclone exhaust, a solid storage leg, and the air exhaust line with flanges. The solid storage line located below the secondary cyclone is used to collect fines which are not separated by the primary cyclone. The bottom of the line is equipped with a removable cap to allow easy removal of accumulated particles.

Final filtration was achieved by means of a filter box which was constructed and installed on the above the scale model. A 4-in exhaust line connected the secondary cyclone to the filter box.

The filter box contains a 24" x 12" x 2" (61.0 x 30.5 x 5.1 cm) high density microfine glass fiber prefilter and a 24" x 12" x 12" (61.0 x 30.5 x 30.5 cm) hepa filter to collect any fines which were not separated by either the primary or secondary cyclone. Pressure taps on the filter box allow for the measurement of pressure drops across the filters to determine when they need to be changed.

The downcomer is not entirely similar to the downcomer of the Foster Wheeler bed. It is not anticipated that this will affect similarity in the riser section of the bed. Previous studies have shown that the riser sections of CFB's are independent of the downcomer configuration if the L-valve operates in a similar manner . In order to ensure that the L-valves do operate similarly, the section of the downcomer below the external heat exchanger in the Foster Wheeler hot bed was scaled exactly. Additionally, differential pressure measurements were made around the L-valve in both the cold and hot bed in order to provide evidence of similarity in operation.

Air is divided into primary and secondary streams before being introduced into the bed. Primary air is introduced radially at the bottom of the bed through a 3/4" (1.9 cm) Sch. 80 pipe distributor. There are two sets of secondary air ports. The lower ports are located at a distance of 55 1/2-in above the bottom of the bed, and the upper ports are located at a distance of 96-in above the bottom of the bed. Each set of ports is equipped with its own valving to allow for varying combinations of secondary air flows. Both the primary and secondary air flows are measured utilizing square edged orifice plates with flanged taps and manometers.

Seven pressure taps used to measure axial pressure drop are located on one of the side walls of the bed. These taps are angled down in order to prevent solids from accumulating in the lines. Pressure tap locations are located at similar fractional bed heights as that of the hot bed. Hot bed pressure transducer locations which were included on the cold model are given in Table 4.1 (see Figure 4.19).

Table 4.1

Cold Bed Pressure Transducers (see Figure 4.19)

Transducer	Location
PDI-3022	Riser
PDI-3233	L-Valve
PDI-3017	Riser
PDI-3166	Across Primary Cyclone
PDI-3010	Riser
PDI-3008	Riser
PDI-3280	Riser
PDI-3013	Downcomer
PDI-3255	Downcomer
PDI-3018	Riser
PI-3007	Absolute Riser Pressure
PDI-3254	Between Downcomer and Riser

In addition to the pressure measurments indicated in Table 4.1, pressure measurements were taken across the primary and scondary air orifice plates for air flow determination, and across the barrier and hepa filters.

The air exiting from the cyclone is fed into a large filter box containing the 24" x 12" x 2" (61.0 x 30.5 x 5.1 cm) high density microfine glass fiber prefilter and a 24" x 12" x 12" (61.0 x 30.5 x 30.5 cm) hepa filter.

4.3 Bed Solid Materials

In order to evaluate the applicability of the viscous limit scaling laws in the fast fluidization regime, and to simulate circulating beds operating at different pressures, three bed solid materials were selected:

1. Steel
2. Glass
3. Plastic

4.3.1 Basis of Selection for Steel

Assuming that the Studsvik bed operated at about 1600 ^{o}F with sand (measured density of 2650 kg/m^3), the solid density needs to be 10,095 kg/m^3 to keep the solid to gas density ratio constant when constructing a cold scale model. A summary of solids with densities close to this value is given in Table 4.2.

Table 4.2

Solids with Densities Near Target Density

Solid	Density (g/cc)
Cadmium	8.65
Cobalt	8.9
Copper	8.96
Iron	7.87
Lead	11.35
Molybdenum	10.22
Nickel	8.9
Niobium	8.57
Rhodium	12.41
Silver	10.5
Thorium	11.7
Braggite (PtS)	10.0
Dyscrasite (Ag_3Sb)	9.67 - 9.81
Litharge (PbO)	9.14
Minium (Pb_3O_4)	8.9 - 9.2
Montroydite (HgO)	11.23
Platinum	14 - 19
Sperrylite ($PtAs_2$)	10.58
Terlinguaite (Hg_2OCl)	8.73
Thorianite (ThO_2)	9.7
Uraninite (UO_2)	8 - 11

Due to cost, health considerations, form of availability, and feasibility of establishing a desired size distribution, the material chosen for the cold models of the Studsvik circulating bed was steel. Steel was available in a variety of particle sizes at modest costs. An extensive

investigation to find an alternative material with a better specific gravity match was not carried out. It is unlikely that any of the other materials in the desired density range would satisfy feasibility requirements.

4.3.2 Steel Density Measurements

Steel densities were measured using a helium displacement pycnometer. The steel density was measured to be 7250 kg/m^3. This is nearly 30 percent lower than the desired density of 10,095 kg/m^3. Since the actual density was different than the desired density, it was not possible to match both solid volumetric and mass flux. Because the similarity evaluations involved matching the volumetric flux and comparing solid fraction profiles, the solid flux parameter $\frac{G_s}{\rho_s u_o}$ based on the actual solid density was matched between runs. Previous evaluation of the difference in matching solid volumetric flux versus matching the solid mass flux indicated that the volume-based measurements give slightly better agreement between cold bed and hot bed (Westphalen, 1990). However, the differences were slight so that a case could still be made for either method of nondimensionalizing the solid circulation rate.

4.3.3 Preparation of Steel Powders

In order to achieve the correct mean particle size and particle size distribution as compared to the Studsvik hot bed for the 1/4 and 1/16 scale models, several size distributions of steel powder were combined to match the reported particle size distribution. Measurement of size distributions and separation of the cold model solids were done with 8-inch U.S. Standard laboratory sieves with sieve numbers of 400 ($38 < dp < 45$ μm), 325 ($45 < dp < 53$ μm), 270 ($53 < dp < 63$ μm), and 230 ($63 < dp < 75$ μm), and 200 ($75 < dp < 90$ μm). The particle size distribution for the 1/4 scale Studsvik bed steel along with the sand used in the Studsvik hot bed are depicted in Figure 4.22.

Figure 4.22

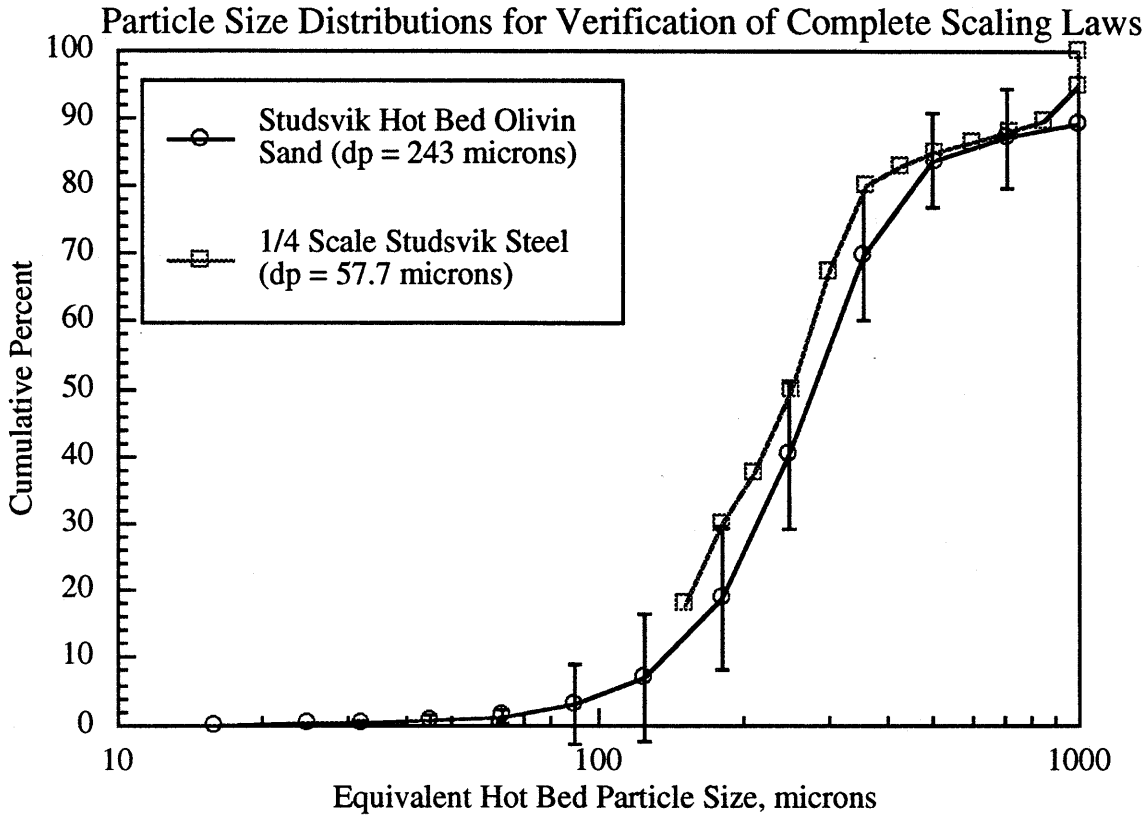

The required mean particle diameter for the 1/16 scale model was calculated to be approximately 35 microns. Since the smallest sieve mean diameter was 38 microns, it was not possible to accurately predict the size distribution of the particles required for use in the 1/16 scale model. In order to circumvent this problem, no attempt was made to accurately measure the mean diameter of the particles for use in the 1/16 scale model, rather the particle distribution was selected based on the minimum fluidization velocity. This is possible since, unlike the 1/4 scale model, the 1/16 scale model utilized the simplified scaling laws in which the particle diameter enters only indirectly (it is a factor in determining the minimum fluidization velocity), and the actual particle diameter is not required.

In order to estimate what the mean particle diameter of the steel powder used in the 1/16 scale model was, a series of tests was conducted in which the minimum fluidization velocity was determined for steel powders of known diameter. These data are give in Table 4.3. The minimum fluidization velocities were then plotted and compared to those calculated from the Ergun equation for the known particle diameters. All minimum fluidization velocities were measured in the 1/16 scale Studsvik bed operating in a bubbling bed mode at room temperature and atmospheric pressure. The sphericity of the steel particles required by the Ergun equation was determined in an earlier study using image analysis (Westphalen, 1990). A plot of the

measured and predicted particle diameter vs. minimum fluidization velocity is given in Figure 4.23. This curve predicts a mean particle diameter of 27 microns for a minimum fluidization velocity of 0.75 cm/s. Results of the minimum fluidization tests can be found in Appendix A.

A separate steel particle size distribution was used to evaluate the viscous limit scaling laws when scaling between steel and glass. All properties were determined in the same manner as the properties for the 1/4 scale bed. The steel/glass viscous limit tests were conducted in the 1/4 scale UBC bed.

In addition to particle density, the loose-pack bulk densities of the steel powders were measured. A summary of the steel particle properties is given in Table 4.3.

Table 4.3

Minimum Fluidization Data for Steel Powder

Particle Diameter (μm)	U_{mf} (cm/s)	ε_{mf}
41.5	1.25	0.65
49.0	1.50	0.65
58.0	1.65	0.65
69.0	1.75	0.65

Figure 4.23

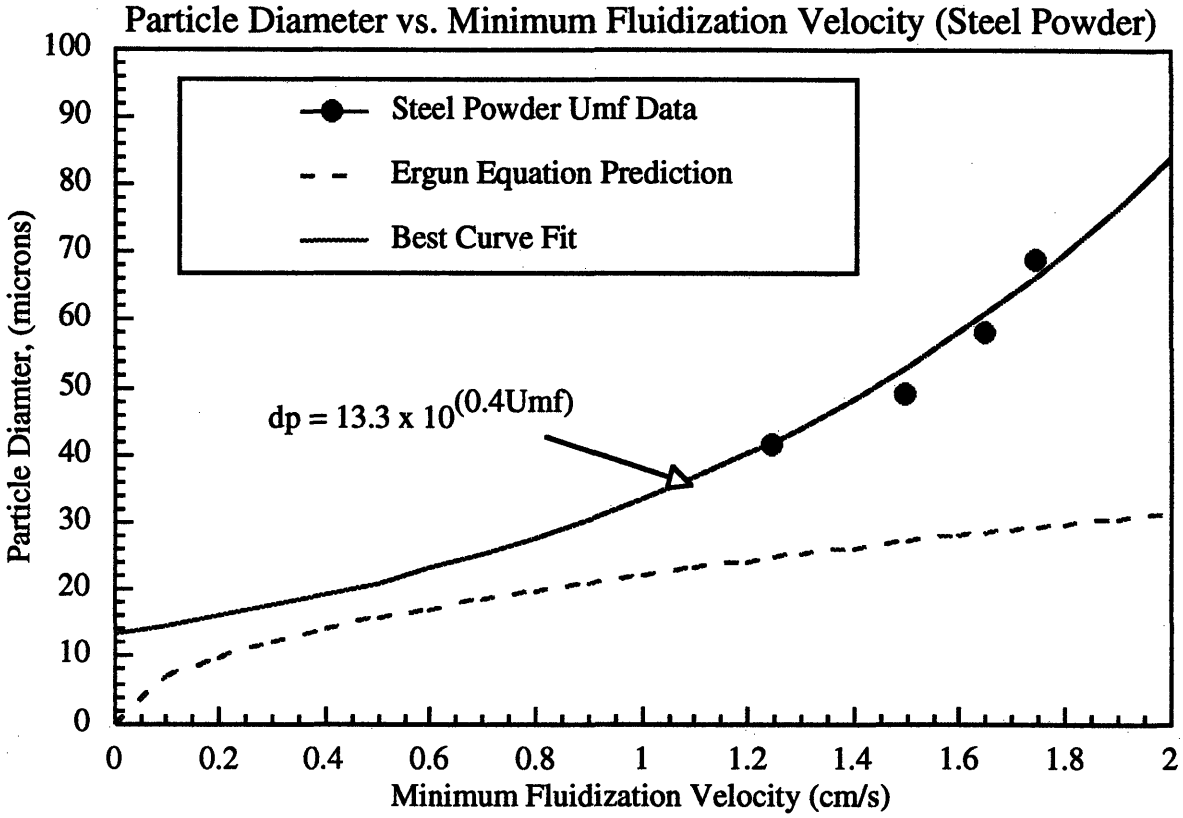

Table 4.4

Steel Powder Properties

	Viscous Limit Steel	Constant ρ_s/ρ_f Steel
Density	7.25 g/cc	7.25 g/cc
Mean Diameter	49.5 microns	~27 microns
Loose Pack Voidage	65%	65%
Sphericity	0.6 - 0.8	0.6 - 0.8
U_{mf}	1.40 cm/s	0.75 cm/s

4.3.4 Selection of Glass Powders

Four glass size distributions were utilized in this study. The first two glass distributions were used in the evaluation of the viscous limit scaling laws between glass and steel. As with the 1/4 scale Studsvik steel, mean particle diameters were determined using laboratory sieves. Minimum fluidization velocities for these glass distributions were determined in a small 4-inch (10.2 cm) bubbling bed operating at room temperature and atmospheric pressure. Mean particle sizes and distributions were selected based on the viscous limit scaling laws and the steel powder selected for these tests as discussed above. A summary of glass particle properties for use in comparison against steel utilizing the viscous limit scaling laws are given in Table 4.4. Particle size distributions for the two glasses, along with the steel used in the viscous limit tests, are given in Figure 4.24.

Table 4.5
Viscous Limit Glass Properties

	Viscous Limit Glass I	Viscous Limit Glass II
Density	2.54 g/cc	2.54 g/cc
Mean Diameter	88.3 microns	81.6 microns
Loose Pack Voidage	42%	42%
Sphericity	1.0	1.0
u_{mf}	1.40 cm/s	1.70 cm/s

Figure 4.24

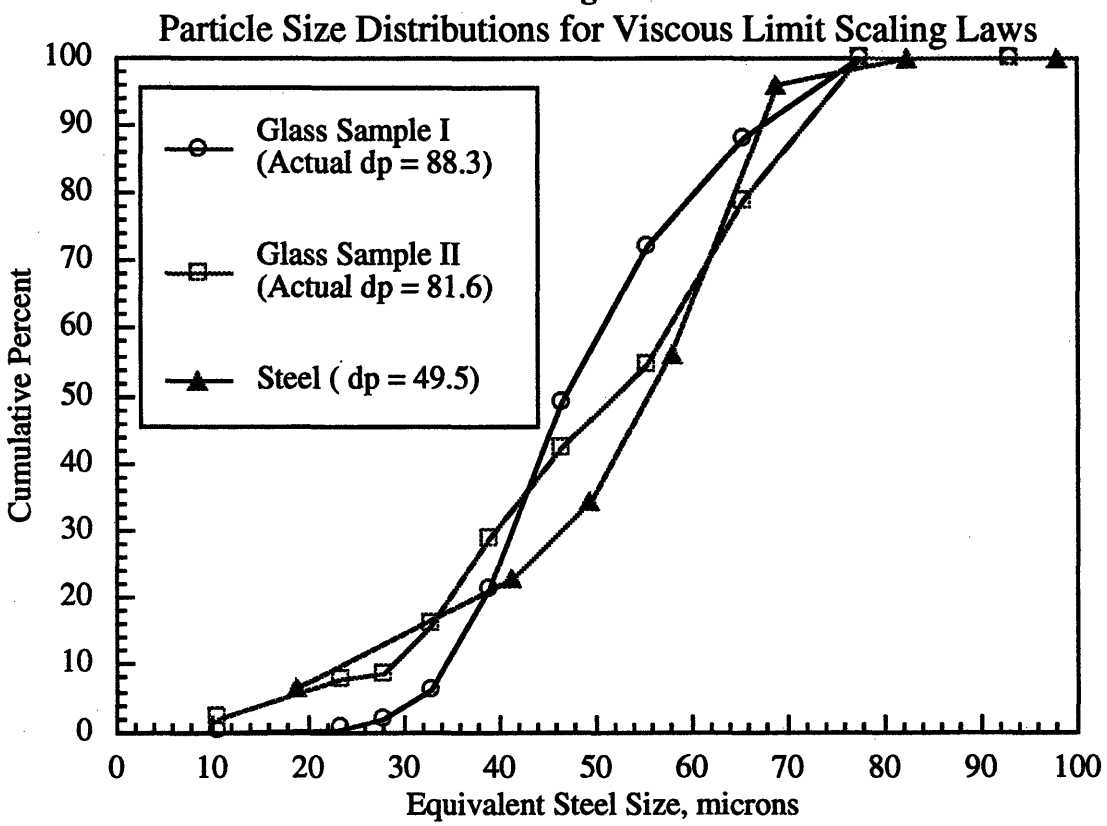

For the evaluation of the simplified set of scaling laws between beds of different sizes, two different glass distributions were selected which allowed matching of the ratio of superficial to minimum fluidization velocities.

A summary of glass particle properties for this series of tests is given in Table 4.5. Particle size distributions for the two glasses are depicted in Figure 4.25. The 1/16 scale glass diameters are multiplied by 0.707 when shown in Figure 4.25 to compare with the 1/4 scale glass size distribution. Results of the minimum fluidization tests can be found in Appendix A.

For the evaluation of the viscous limit scaling laws when glass and plastic are used as the bed solid, the glass used in the 1/16 scale Studsvik bed was used to compare against the smaller plastic distribution discussed below.

Table 4.5

Glass Properties for Scaling with Constant ρ_s/ρ_f

	1/4 Scale Studsvik	1/16 Scale Studsvik
Density	2.54 g/cc	2.54 g/cc
Mean Diameter	112.3 microns	78.7 microns
Loose Pack Voidage	42%	42%
Sphericity	1.0	1.0
U_{mf}	2.8 cm/s	1.4 cm/s

Figure 4.25

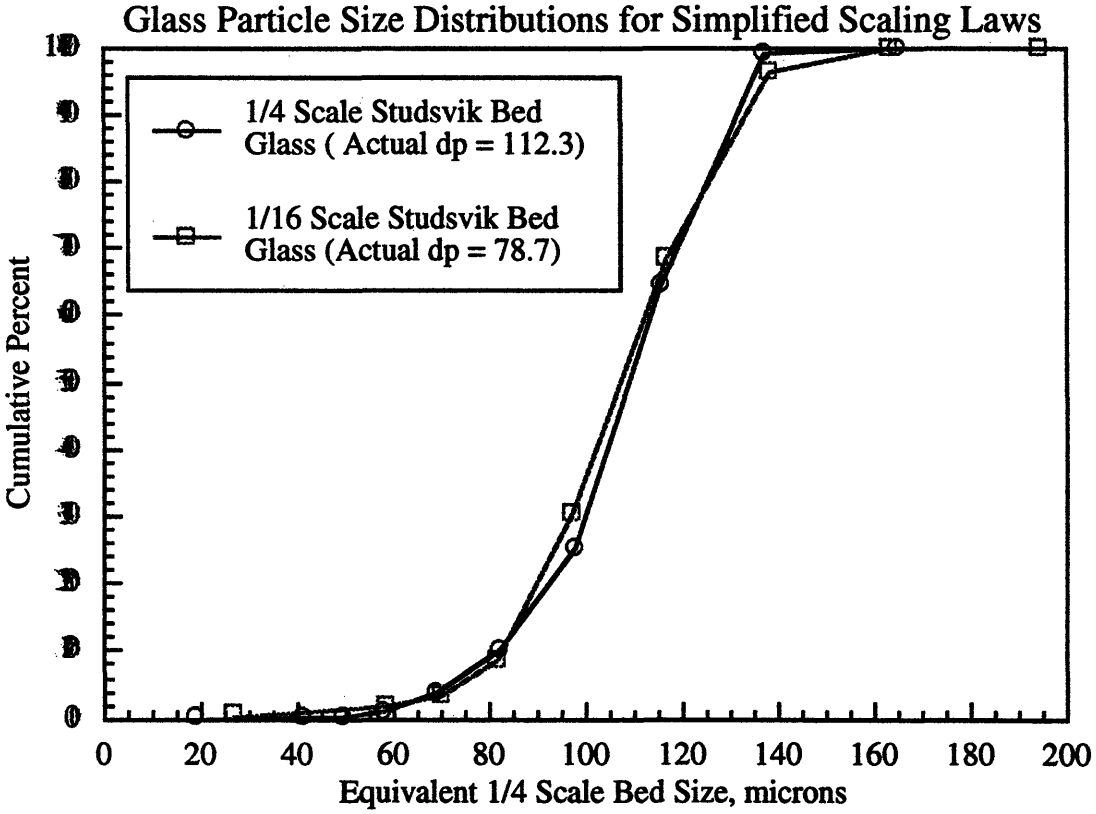

4.3.5 Selection of Plastic Powders

4.3.5.1 Plastic Powders for Viscous Limit and Cold Bed Scaling

The non-dimensional parameter governing convective heat transfer when scaling between glass and plastic is (this is discussed in detail in Chapter 3).

$$\frac{h_e d_p}{k_f} \sim \frac{u_o \rho_s c_{p_s} d_p^2}{D k_f} \tag{3}$$

Since $\frac{u_o \rho_s d_p^2}{\mu_f D}$ is already matched when scaling hydrodynamics with either the viscous limit or simplified scaling laws, the heat transfer parameter can be maintained constant between two different models if $\frac{c_{p_s} \mu_f}{k_f}$ is the same for both materials. An evaluation of the heat transfer scaling can be made by comparing the Nusselt number on a bed side between the plastic and glass particles if the plastic particles have the same specific heat as the glass particles. An investigation into the thermal properties, availability within the boundaries of an acceptable size distribution, and price of plastic powders was conducted with results of the most promising plastics summarized in Table 4.6. In order to match the heat transfer parameter between glass and plastic, a plastic with a specific heat of 0.2 cal/g-K was required. On the basis of this investigation, it was determined that PVC powder would be used.

Two plastic size distributions were utilized in this study for evaluation of the viscous limit scaling parameters and the simplified set of scaling parameters. As with the 1/4 scale Studsvik steel, mean particle diameters were determined using laboratory sieves. This has been shown to be an accurate method of determing particle size distributions for PVC powders (Davidson, 1992). Particle densities were measured utilizing a water displacement technique. Minimum fluidization velocities for the plastic distributions were determined in the 1/16 scale Studsvik bed operating in bubbling bed mode at room temperature and atmospheric pressure.

Table 4.6

Plastics with Specific Heats Near 0.2 cal/g-K

Plastic	Specific Heat (cal/g-K)
PVC	0.26
Nylon-6	0.41
Delrin (Polyacetal)	0.35
Polystyrene	0.33
Polyethylene	0.46
Polypropylene	0.46
Teflon	0.24
Acrylic	0.35
Phenols	0.30
Lexan	0.29
Ryton	0.25
Polysulfone	0.25
Torlon	0.25
Halon/Aclar	0.21
Poly(Vinyl Fluoride)	0.34

Mean particle sizes and distributions were selected based on the viscous limit scaling laws, the 78.7 micron glass distribution described above, and the simplified set of scaling laws based upon scaling between bed whose linear dimensions differ by a factor of four. The plastic selected for use in the 1/16 scale Studsvik bed when scaling between glass and plastic using the viscous limit scaling laws was also used when evaluating the simplified set of scaling laws. A summary of the plastic particle properties used in this study is given in Table 4.7. Particle size distributions for the two plastic powders, are given in Figure 4.26. Results of the minimum fluidization tests can be found in Appendix A.

Table 4.7

Plastic Properties for Scaling with Constant ρ_s/ρ_f

	1/4 Scale Studsvik	1/16 Scale Studsvik
Density	1.40 g/cc	1.40 g/cc
Mean Diameter	144.5 microns	99.5 microns
Loose Pack Voidage	57%	55%
Sphericity	0.5 - 0.7	0.5 - 0.9
u_{mf}	1.5 cm/s	0.85 cm/s

Figure 4.26

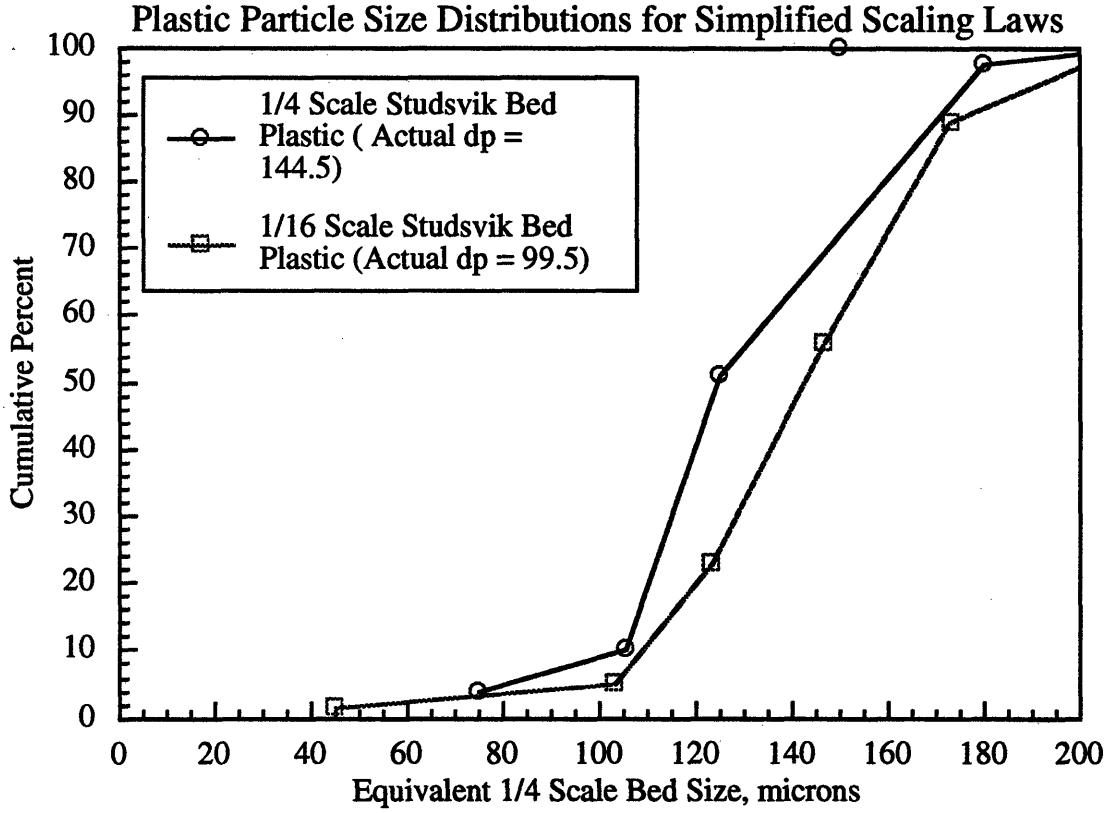

4.3.5.2 Plastic Powders for Scaling the Foster Wheeler Pressurized Combustor

The solid used in the hot column for the Foster Wheeler pressurized fluidized bed tests described herein was dolomite with a measured surface mean d_p equal to 165 microns, a measured density of 2650 kg/m^3, and an estimated minimum fluidization velocity of 2.5 cm/s (0.083 ft/s) at 12.1 bar (12 atm) and 900 ^oC (1650 ^oF). The solid material used in the cold column is polyethylene plastic. This material was readily available and provided the best match for density as required by the simplified scaling laws. The powder was prepared so that the scaled size distribution along with the ratio of superficial to minimum fluidization velocity would match that of the hot bed solid operating at high pressure and temperature. Figure 27 shows a comparison of the dimensionless particle size distribution between the hot and cold bed material. Powder testing included size analysis by sieving, sphericity determination using two-dimensional image analysis, measurement of u_{mf}, density measurement, and bulk density measurements. A summary of hot and cold bed particle properties is given in Table 8.

Table 8

Summary of Hot and Cold Bed Solids

	Hot Bed Solid	Cold Bed Solid
Material	Dolomite	Polyethylene Plastic
Surface Mean d_p (microns)	165	180
Density (kg/m^3)	2650	905
Sphericity	0.84	0.85
ε_{mf}	0.52	0.49
u_{mf} (cm/s)	2.39 (est. at 12 bar, 900 ^oC)	1.77

Figure 27

Comparison of Dimensionless Particle Size Distributions for Foster Wheeler Pressurized Combustor and Cold Model

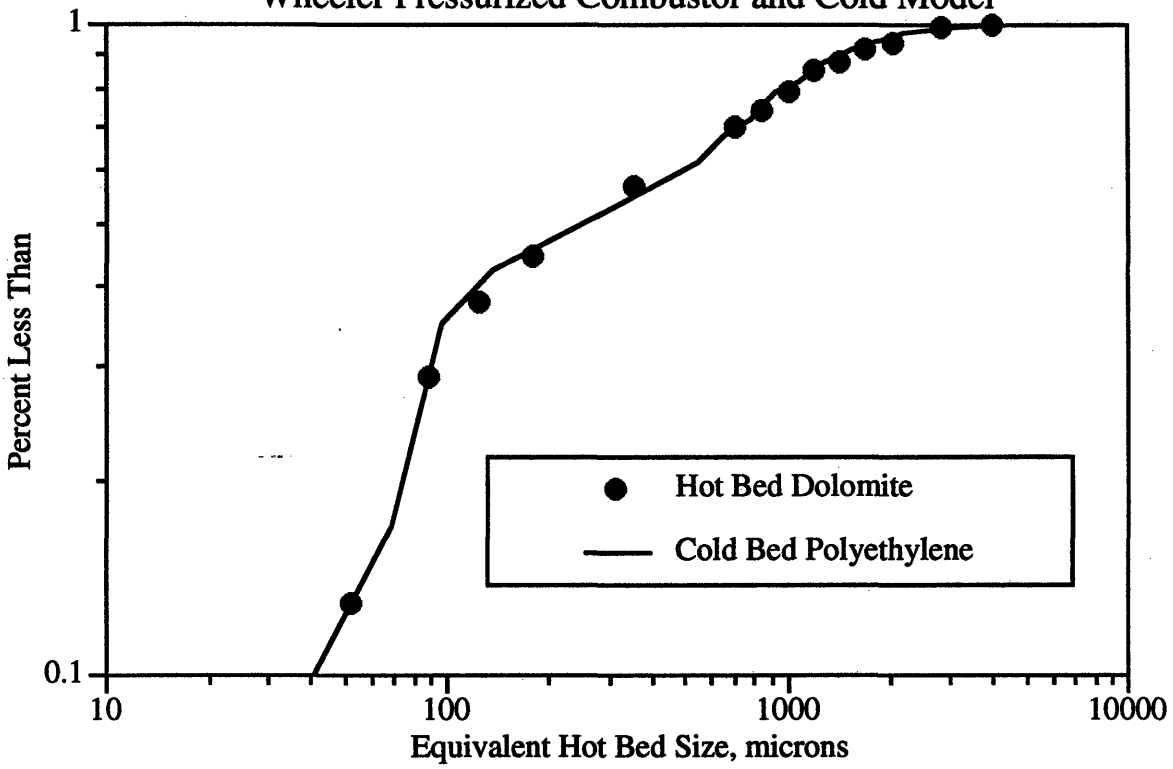

4.3.6 Preparation of Glass and Plastic Particles

In addition to the separation and recombination process in order to achieve satisfactory size distributions, the glass and plastic particles were also treated with anti-static compounds in an attempt to reduce the level of static electricity generated in the bed. The first compound was Larostat 519, a fine powder which was mixed in with the glass and plastic powders. Since the mass fraction of Larostat in the mixtures was very small, it was not anticipated that this would have any significant effect on the hydrodynamics of the beds other than through the reduction of static electricity.

While the Larostat worked quite well in the reduction of static, as more was added during operation, it began to severely inhibit the flow characteristics of the glass and plastic mixtures in the L-Valves and other constricted areas, limiting the amount of Larostat allowable in the beds. In order to further reduce bed static electricity levels, the glass and plastic, along with the inside of the beds, were spray coated with Anstac 2-M, an alcohol based anti-static solution for acrylic and other plastics. After drying, this treatment virtually eliminated any remaining static effects.

It was anticipated that static electricity would especially be a problem in the scale model of the Foster Wheeler pressurized combustor since the bed and the particles were made of low density plastics. In order to further reduce bed static levels, the plastic particles in the Foster Wheeler cold scale model along with the entire cold scale model was coated with electrically conductive floor wax.[1] Re-sieving the particles indicated that the wax coating did not significantly affect the mean diameter or size distribution of the plastic powder. The conductive floor wax was found to be superior in eliminating static electricity effects in the Foster Wheeler scale model.

4.3.7 Elimination of Static Electricity Effects

In addition to the use of Larostat and Anstac as described above, several other precautions were taken to reduce problems caused by static electricity. The first measure taken was to wrap copper gauze around areas of the beds which accumulated large amounts of static electricity (this included the cyclones, pneumatic return lines, and sections of the downcomers). Copper ribbon was then used to ground the gauze as well as the supporting structure and other metallic components (pressure transducer housings, valves, aluminum walls, etc.). In the 1/4 scale Studsvik bed, a 3 foot (0.9 m) long 1/2-inch (1.3 cm) diameter hollow copper rod was hung in the downcomer by threading copper ribbon up the center of the rod and out to ground through a small hole at the exit of the primary separator.

In the 1/16 scale Studsvik bed, three 6 x 1-1/2 inch (15.2 x 3.8 cm) pieces of copper sheet were connected in a helix fashion and inserted in the bottom section of the pneumatic return line. Copper wire was run along the perimeter of the copper sheet and out through a flexible connecting piece to ground. In addition to the static discharge device, a humidification system was constructed in which all the air being introduced into the bed was bubbled through a steel tank which was half full of water. This increased the humidity of the entering air (during the winter typical increases in relative humidity would range from 20-25 percent) and aided in the reduction of static electricity. The air humidity was continually monitored during bed runs utilizing an encased wall mounted hygrometer (relative humidity accuracy of +/-2.5 %).

Even with all the precautions taken above, static electricity remained a concern during the winter months of the project, and was directly linked to the death of several electronic components.

[1] Statguard electrically conducting floor wax - available from Charleswater Products.

4.4 Variable Measurement

Cold bed and hot measurement techniques are described in the following sections. Accuracy of the cold bed measurements is discussed in Section 4.5. The Studsvik hot bed measurements are discussed in Section 4.5.5.

4.4.1 Air Flow

4.4.1.1 1/4 Scale UBC Bed

The air flow measurement equipment for the 1/4 Scale UBC Bed was obtained and calibrated as part of an earlier study to verify the full set of scaling laws for circulating fluidized beds (Westphalen, 1990). A summary of the equipment and calibration techniques is included here for convenience.

Air entered the 1/4 Scale UBC bed in two locations. The two air streams were designated the primary and secondary air. The two air flows were measured separately with rotameters fitted with exit pressure gauges. The rotameters measured in the range from 2 to 10 cfm, and the pressure gauges were 15 psig full scale. Calibration of the rotameters and gauge combinations was done with a square-edged orifice plate fitted with flange taps. The tests covered flow ranges at expected pressure ranges. The data was analyzed to determine the calibration constants A and B for the following equation.

$$Q_a = (AR+B)\sqrt{\left(1+\frac{P_g}{P_a}\right)}$$

where Q_a is the flow at atmospheric pressure P_a, P_g is the gauge pressure at the rotameter exit, and R is the rotameter reading.

4.4.1.2 1/16 Scale Studsvik Bed

For the phase one 1/16 scale Studsvik bed (no boot, secondary air or simulated refractory), air entered the bed through the distributor box and at the bottom of the pneumatic return line. The two air flows were measured separately with rotameters fitted with exit pressure gauges. The rotameters measured in the range from 2 to 10 cfm, and the pressure gauges were 15 psig full scale. Calibration of the rotameters and gauge combinations was done in the same manner as the

1/4 scale UBC bed setup (i.e., with a square-edged orifice plate fitted with flange taps). The tests covered flow ranges at expected pressure ranges with the data again being fit to the equation:

$$Q_a = (AR+B)\sqrt{\left(1+\frac{P_g}{P_a}\right)}$$

For the phase two 1/16 scale Studsvik bed (boot, secondary air ports, and simulated refractory added), air entered the bed through the secondary air ports, the distributor box, and at the bottom of the pneumatic return line. All three air flows were measured separately with an additional rotameter fitted with exit pressure gauge being added to measure the secondary air flow. Calibration of the rotameter and gauge combinations was conducted using the same technique as that used with the phase one setup.

4.4.1.3 1/4 Scale Studsvik Bed

For the tests in which steel was run in the 1/4 Scale Studsvik bed to model the Studsvik hot bed, air entered the bed through the distributor box and secondary air ports (air was also used for the pneumatic return line, sparge tube, and various valves but was not measured). The two air flows were measured separately utilizing a square edged orifice plate with flanged taps and manometers. The orifice plate was calibrated using hot wire velocity profiles.

For the tests with glass and plastic run in the 1/4 scale Studsvik bed, the secondary air ports were blocked off so that air entered only through the distributor box. The air flow was again measured utilizing a square edged orifice plate with flanged taps and a manometer.

4.4.1.4 1/2Scale Foster Wheeler Bed

For the tests in which plastic was run in the 1/2 scale Foster Wheeler bed to model the Foster Wheeler hot bed, air entered the bed through the distributor pipe and secondary air ports (air was also used for L-valve, but was not measured). The two air flows were measured separately utilizing a square edged orifice plate with flanged taps and manometers. The orifice plate was calibrated using hot wire velocity profiles and rotameters.

4.4.2 Solid Circulation

Solid flow measurement techniques for the various beds utilized in this study are described below. Figures 4.28 illustrates the equipment and methods used for these beds.

4.4.2.1 1/4 Scale UBC Bed

Measurement of solid circulation in the 1/4 scale UBC bed was done primarily with a valve in the solid return leg. A 1-1/2" (3.8 cm) full-bore three-piece ball valve was used for this purpose. Shims were installed between the sections of the valve in order to reduce handle torque. The valve measurement technique involved observation of solid pileup when the flow of solids was interrupted by closing the valve. A pressure relief line was installed around the valve to reduce the effects on pressures in the bed during valve closure.

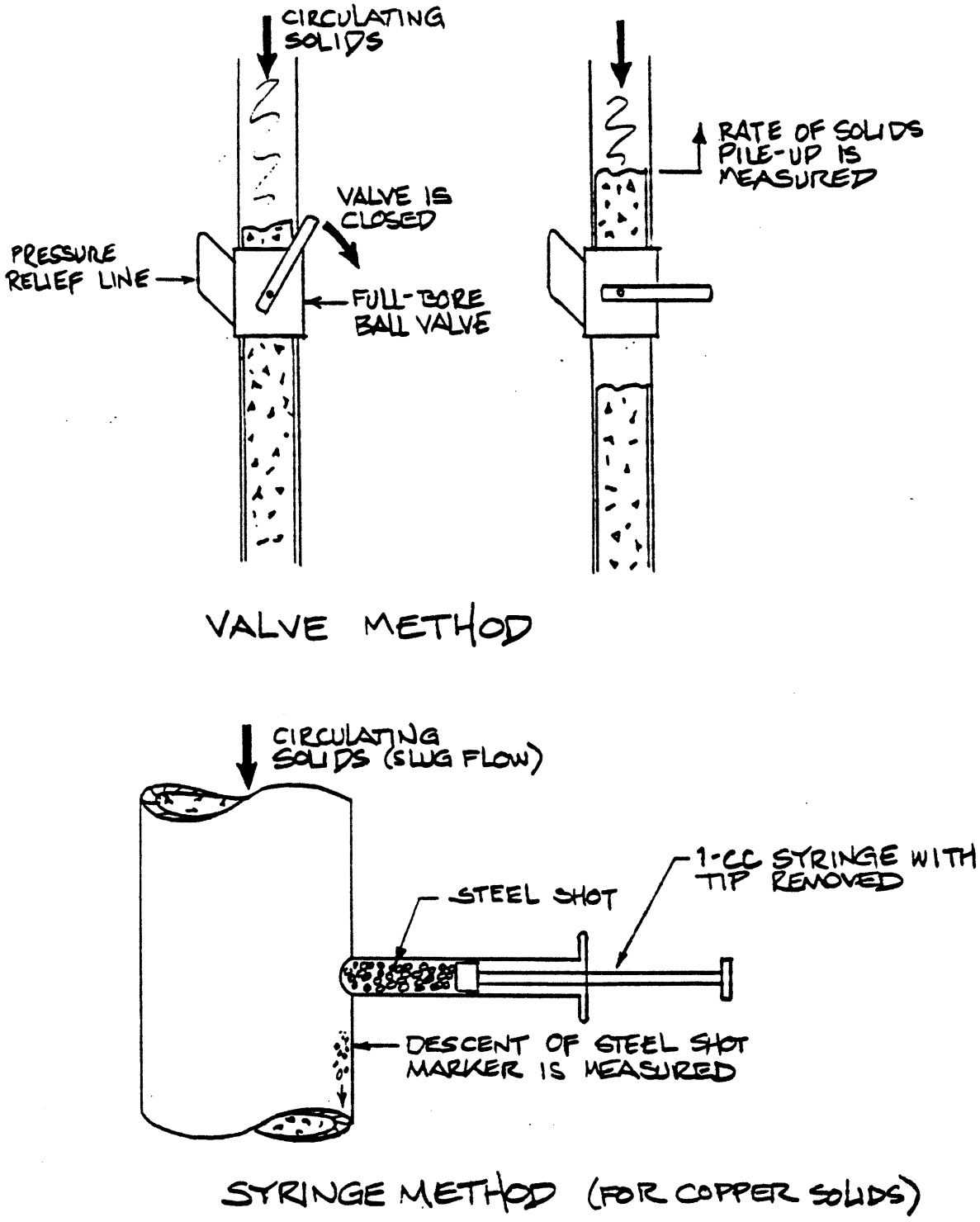

Figure 4.28: Solid Flow Measurement Techniques

It has been shown that the valve closure technique may be accompanied by a corresponding reduction in bed solid fraction (Westphalen, 1990). However, further calibration of this technique was obtained by injecting a material which provided enough visual contrast to the bed material in the downcomer. Measurement of the rate of descent in the downcomer has indicated that the valve closure technique is reasonably accurate (within 20 percent of visual descent measurement) in spite of its alteration of normal bed behavior.

4.4.2.2 1/16 Scale Studsvik Bed

In both the phase one and phase two setups of the 1/16 scale Studsvik bed, the solid circulation was measured in the same way as was the 1/4 Scale UBC bed. A 1-1/2" (3.8 cm) full-bore three-piece ball valve with shims installed between sections of the valve in order to reduce handle torque was used to observe the solid pileup. A pressure relief line was installed around the valve to reduce the effects on pressures in the bed during valve closure.

4.4.2.3 1/4 Scale Studsvik Bed

When using steel to model the full scale hot Studsvik bed, the valve closure technique was used to measure the solid circulation rate. A 4-inch (10.2 cm) diameter butterfly valve was designed and inserted into the downcomer 2.3 feet (0.7 m) below the primary separator. The solid pileup rate when the flow of solids was interrupted by closing the valve was then measured to determine the solid circulation rate.

Measurement of solid circulation in the 1/4 scale Studsvik bed when charged with plastic and glass was achieved by viewing the descent of solid in the solid downcomer. This was possible because of visual contrast associated with the plastic and glass particles run.

4.4.2.4 1/2 Scale Foster Wheeler Bed

The valve closure technique was used to measure the solid circulation rate in the 1/2 scale model of the Foster Wheeler PCFBC. A 4-inch (10.2 cm) diameter butterfly valve was inserted into the downcomer below the primary cyclone. The solid pileup rate when the flow of solids was interrupted by closing the valve was then measured to determine the solid circulation rate. Measuements of the solid circulation by viewing the descent of solid in the solid downcomer yielded similar results.

4.4.3 Pressure Measurement

Pressure measurement techniques for the various beds utilized in this study are described below. In all of the beds except the Foster Wheeler scale model, measurement and recording of the pressure transducer voltage output was done with a Metrabyte DAS-8PGA data acquisition board in an IBM AT compatible computer. The software used to control the data acquisition was UNKELSCOPE.

In the Foster Wheeler scale model, a Gateway 486 PC computer, along with a Metrabyte 16 channel data acquisition board and EasyLX, a high speed data acquisition program was used for data acquisition. The pressure transducer calibration curves were entered into the data acquisition program allowing for direct conversion of voltages to pressures.

4.4.3.1 1/4 Scale UBC Bed

The pressure measurement system for the 1/4 scale UBC bed has been described in detail elsewhere (Westphalen, 1990). A summary of that description is given below for convenience.

There were eight pressure taps in the main bed section which were used to measure axial pressure differences. The pressure taps are 1/8" (0.32 cm) in diameter. Measurement of pressures was done with a set of manometers and with pressure transducers.

The manometers used to measure average pressure differences between adjacent pressure taps were mounted on a board next to the bed. An eighth manometer measured the gauge pressure at Pressure Tap No. 1. The manometers were three meters tall and filled with colored water. Damping of pressure signals was provided by orifices in the pressure lines leaving the pressure taps and air volumes connected to the tops of the manometers. Pressure fluctuations faster than about 0.5 Hz were successfully damped.

Pressure transducers were located near their associated pressure taps. The pressure transducers used were Micro Switch 170PC series. The transducers measured differential pressures between adjacent pressure taps. They had millivolt output, and had a 10 volt power supply. Although the rated pressure range for the transducers was 0 to 14 in. wc (0-3.5 kPa), they were also successful in measuring down to -14 in wc (-3.5 kPa). The pressure transducer used to measure overall bed pressure was a 1 psi (6.9 kPa) differential pressure transducer which had 1 to 6 volt output, and used the same 10-volt input as the 7 other pressure transducers.

In order to keep the pressure lines clear of particles, air was injected into the pressure tap lines to continuously clear them and keep particles out. Pressure drop through the pressure tap lines due to this cleaning air flow was assumed to remain essentially constant, since the flow is driven by a pressure drop from the header to the bed which is significantly larger than bed pressure gradients or fluctuations. Actual pressure measurements were modified by measurements of the apparent pressures when the bed is empty. A previous investigation into the effect of this cleaning air on bed pressure measurements indicates the error caused by the use of this system was not significant (Westphalen, 1990).

4.4.3.2 1/16 Scale Studsvik Bed

There were nine pressure taps in the main bed section of the 1/16 scale Studsvik bed which were used to measure axial pressure differences. The pressure taps and lines were 1/8" (0.32 cm) in diameter. All pressure lines were less than 0.5 m in length. Pressure measurements were done using a set of pressure transducers.

The pressure transducers were located near their associated pressure taps. The transducers measured differential pressures between adjacent pressure taps. The four transducers nearest the bottom of the bed had millivolt output, and had a 12 volt power supply. The rated pressure range for the transducers were -14 to 14 in. wc (-3.5-3.5 kPa). Calibration of the transducers was done with an inclined manometer covering all expected pressure ranges. Results of the transducer calibrations are given in Appendix B. The top four transducers were series 600 transducers supplied and calibrated by Auto Tran, Inc. They had output on the order of 1-4 volts, and utilized the same 12 volt DC power supply as the bottom four transducers. The rated pressure range for the top four transducers was -1 to 1 in. wc (-0.25-0.25 kPa) with a sensitivity accuracy of +/- 1 percent of full scale output.

Rather than injecting air into the pressure tap lines to continuously clear them and keep particles out, the pressure taps were angled down 40^{o} into the bed. Since the particle motion is downward at the wall, this proved successful in preventing particles from entering the lines. A more detailed evaluation of the differences in these techniques is given in the discussion of the 1/4 scale Studsvik pressure measurements.

4.4.3.3 1/4 Scale Studsvik Bed

There were nine pressure taps in the main bed section of the 1/4 scale Studsvik bed used to measure axial pressure differences. The pressure taps were 1/8" (0.32 cm) in diameter. Measurement of pressures was done with a set of manometers and with pressure transducers.

In order to provide an approximation of the differential pressure between pressure taps, manometers were installed and mounted on a board behind the bed. The manometers were three meters tall and filled with water. Damping of pressure signals was provided by orifices in the pressure lines leaving the pressure taps and air volumes connected to the tops of the manometers. Pressure fluctuations faster than about 0.5 Hz were successfully damped.

Pressure transducers were located near their associated pressure taps. The transducers measured differential pressures between adjacent pressure taps. They had output on the order of volts, and had a 10 volt power supply. The rated pressure range for the transducers was 0 to 14 in. wc (0-3.5 kPa), although they were also successful in measuring down to -14 in wc (-3.5 kPa). Calibration of the transducers was done with an inclined manometer covering all expected pressure ranges. Results of the transducer calibrations are given in Appendix B.

As was the case with the 1/16 scale Studsvik bed, the pressure taps were angled down 40^{o} into the bed to prevent particle inflow into the pressure tap lines as opposed to using horizontal taps with purge air. A plot depicting typical deviations between the two methods is given as Figure 4.29.

4.4.3.4 1/2 Scale Foster Wheeler Bed

There were seven pressure taps in the main bed section of the 1/2 scale Foster Wheeler bed which were used to measure axial pressure differences. The pressure taps and lines were 1/8" (0.32 cm) in diameter. All pressure lines were less than 0.5 m in length. Pressure measurements were done using a set of pressure transducers.

The pressure transducers were located near their associated pressure taps. The transducers measured differential pressures between adjacent pressure taps. The riser transducers were series 600 transducers supplied and calibrated by Auto Tran, Inc. They had output on the order of 1-5 volts, and utilized a 12 volt DC power supply. The rated pressure range for the bottom four transducers was -2 to 15 in. wc (-0.5-3.75 kPa). The rated pressure range for the top two riser transducers was -1 to 7 in wc (-0.25-1.75 kPa). Sensitivity accuracy of the transducers is +/- 1

percent of full scale output. Calibration of the transducers was done with an inclined manometer covering all expected pressure ranges. Results of the transducer calibrations are given in Appendix B.

The riser pressure taps were angled down 40° into the bed. Since the particle motion is downward at the wall, this proved successful in preventing particles from entering the lines. A more detailed evaluation of the differences in these techniques is given in the discussion of the 1/4 scale Studsvik pressure measurements.

Figure 4.29

Typical Deviation in Solid Fraction Profile Between Horizontal and Angled Taps

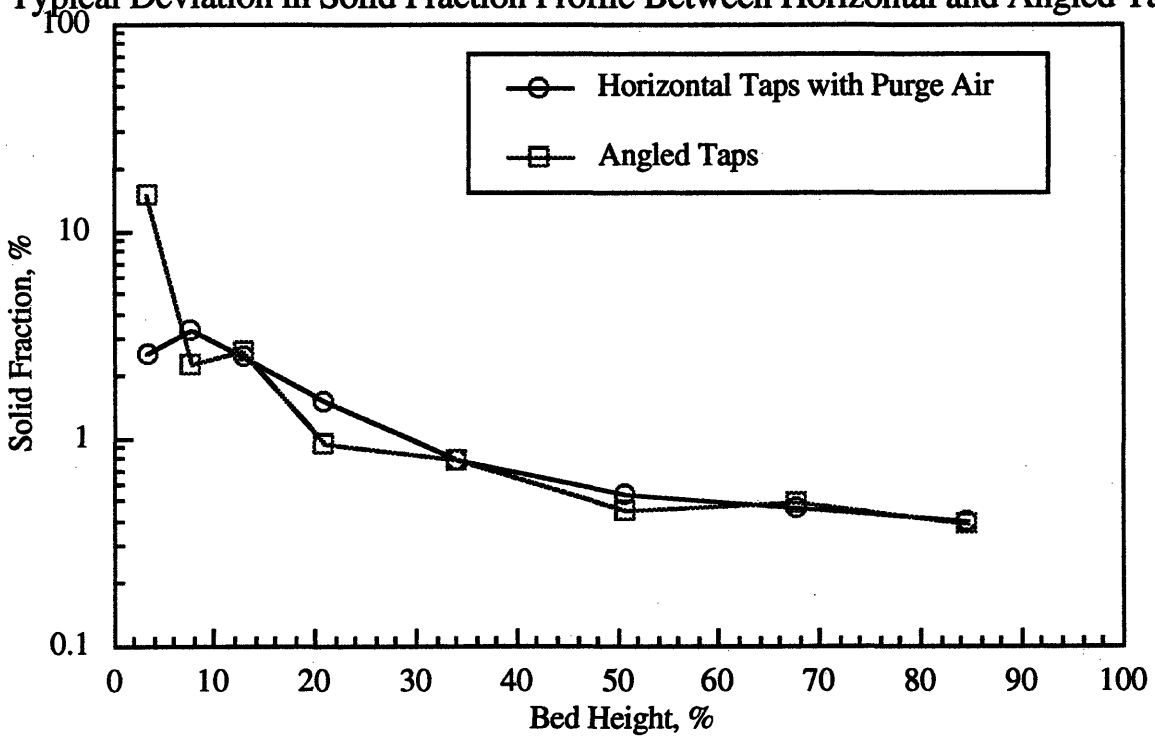

4.5 Uncertainty Analysis

4.5.1 Air Flow

For the 1/4 scale UBC bed and the 1/16 scale Studsvik bed, the air flows were measured with 2-10 cfm rotameters fitted with exit pressure gauges. Calibration of the rotameters involved about 70 data points for each rotameter. The standard deviation from the linear calibration curves was about 0.05 cfm for each rotameter. The low end of the measurement range used in the experiments was about 3 scfm. The standard deviation represents about 2 percent of this lowest measurement.

The 1/4 scale Studsvik bed and the 1/2 scale Foster Wheeler bed utilized two square edged orifice plates with flanged taps and manometers to measure the primary and secondary air flows. The orifice plates were calibrated using hot wire velocity profiles and rotameters.

The minimum fluidization test bed air flows for the glass and steel used in the viscous limit scaling tests were measured with 20-scfh and 100-scfh nominal rotameters. Fifteen test points were used in calibrating the 20-scfh rotameter. The standard deviation from the linear calibration curve for this rotameter was 0.093 scfh, or about 0.5 percent of full scale. Thirty-nine points were used in calibrating the 100-scfh rotameter. Standard deviation from the calculated linear calibration curve was 0.59, or about 0.6 percent of full scale.

Minimum fluidization tests for all other bed materials were measured in the 1/16 scale Studsvik bed operating in a bubbling mode. The air flows for these tests were measured with 2.5 and 10.0 lpm rotameters. Ten test points were used in calibrating the 2.5-lpm rotameter. The standard deviation from the linear calibration curve for this rotameter was 0.013 lpm, or about 0.5 percent of full scale. Fifteen points were used in calibrating the 10-lpm rotameter. Standard deviation from the calculated linear calibration curve was 0.042 lpm, or about 0.4 percent of full scale.

4.5.2 Solid Circulation Rate

Confidence in the accuracy of the solid circulation rate measurements was based on the repeatability of solid loose-packed density measurements and the repeatability of solid fraction profile results when measurements indicate that flow conditions are the same. In addition, previous study has indicated that the various methods used provide similar agreement (Westphalen, 1990). The study performed by Westphalen also addresses the expected errors as a result of different rates of solid entrainment at the top of the bed, uncertainty about the solid bulk density as solid accumulates during measurement, and the variation in accumulation rates for successive measurements. It was determined that the both the visual tracking and valve methods provide an adequate degree of accuracy for the solid circulation rate.

In an attempt to estimate the standard deviation of successive measurements in solid circulation using the valve and visual descent techniques, ten measurements were made at three different solids fluxes for both the valve and visual techniques. Table 4.9 presents the results of these tests. The standard deviation for the valve measurement techniques ranged from 2 to 5 percent of the average value. For the visual descent method, the standard deviation ranged from 3 to 5 percent of the average value.

Figures 4.30 through 4.33 show solid fraction profiles for three tests of the same operating conditions in the beds used. The tests in the 1/4 scale UBC bed, 1/16 scale Studsvik bed, and 1/2 scale Foster Wheeler bed used the valve measurement techniques, whereas the tests in the 1/4 scale Studsvik bed used the visual descent technique. The similarity of the profiles indicate that either method produces a repeatable measurement, and that variation in successive measurements is not a problem.

Table 4.9

Valve and Visual Techniques for Solids Flux Measurement

	Valve Technique (Time to Fill 2 inches)			Visual Technique (Time to Descend 2 inches)		
Run	1	2	3	1	2	3
1	3.24	4.12	5.07	3.03	4.07	5.01
2	3.16	4.37	5.21	3.22	4.17	4.77
3	3.55	4.27	5.17	3.15	4.20	4.92
4	3.11	4.11	5.03	2.95	4.11	4.88
5	3.22	3.95	4.99	2.87	4.10	5.10
6	3.45	3.87	5.18	3.11	4.01	4.89
7	3.14	4.05	5.12	3.15	4.31	4.81
8	3.13	4.14	5.02	2.85	4.27	5.12
9	3.07	4.05	4.95	3.30	3.94	5.08
10	3.32	4.01	5.19	3.05	3.87	5.13
Avg.	3.24	4.09	5.09	3.07	4.11	4.97
Std. Dev.	0.157	0.146	0.0932	0.147	0.140	0.134

Table 4.9a

Bulk Voidage Measurements for Various Bed Materials

Bed Material	Bulk Voidage	Std. Dev.
1/4 Scale UBC Viscous Limit Glass I	0.42	0.0185
1/4 Scale UBC Viscous Limit Glass II	0.42	0.037
1/4 Scale UBC Viscous Limit Steel	0.59	0.030
1/16 Scale Studsvik Const. ρ_s/ρ_f Glass	0.42	0.020
1/16 Scale Studsvik Const. ρ_s/ρ_f Plastic	0.55	0.022
1/4 Scale Studsvik Const. ρ_s/ρ_f Glass	0.42	0.021
1/4 Scale Studsvik Const. ρ_s/ρ_f Plastic	0.57	0.027
1/16 Scale Studsvik Steel for Hot Bed Scaling	0.65	0.021
1/4 Scale Studsvik Steel for Hot Bed Scaling	0.59	0.036
1/2 Scale Foster Wheeler Plastic	0.49	0.020

Figure 4.30
Repeatability of Solid Fraction Profiles

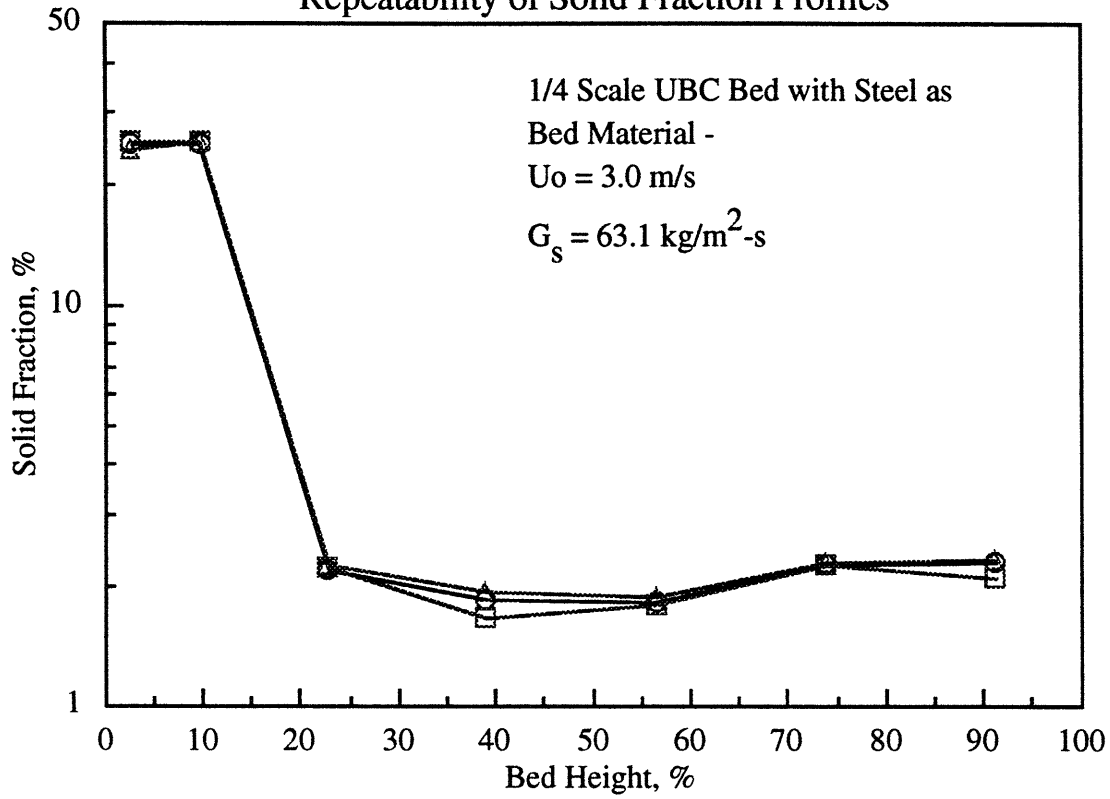

Figure 4.31
Repeatability of Solid Fraction Profiles

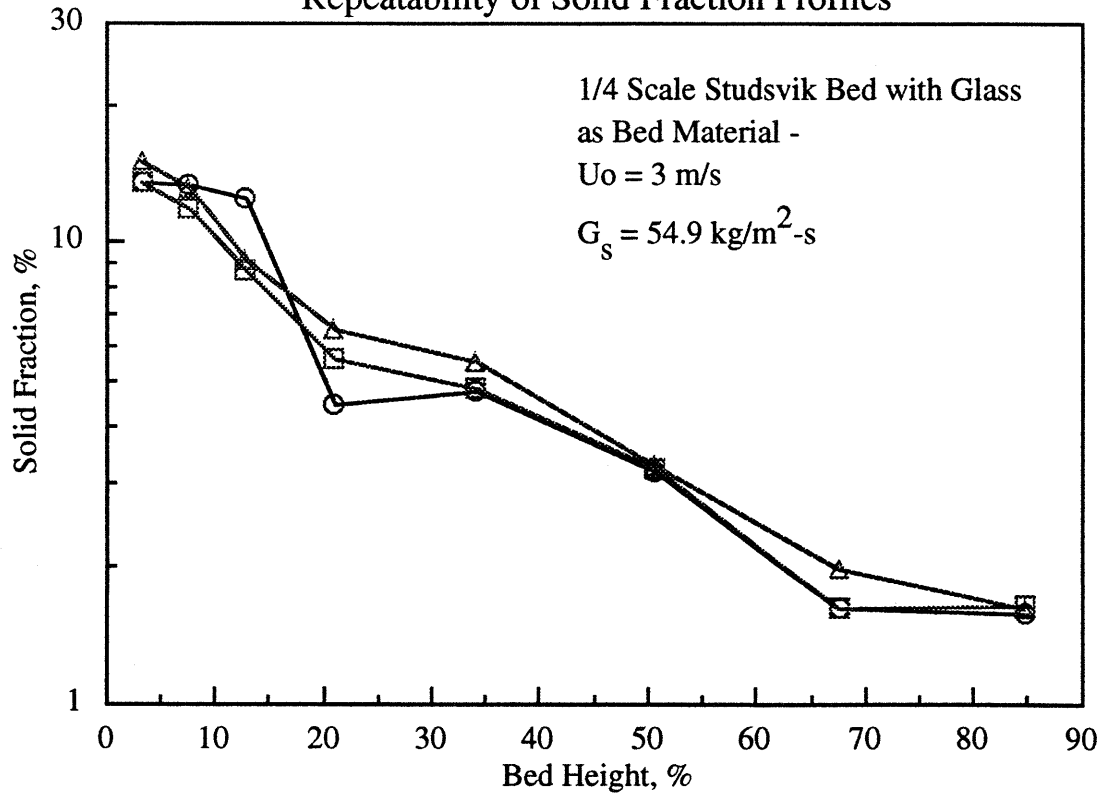

Figure 4.32
Repeatability of Solid Fraction Profiles

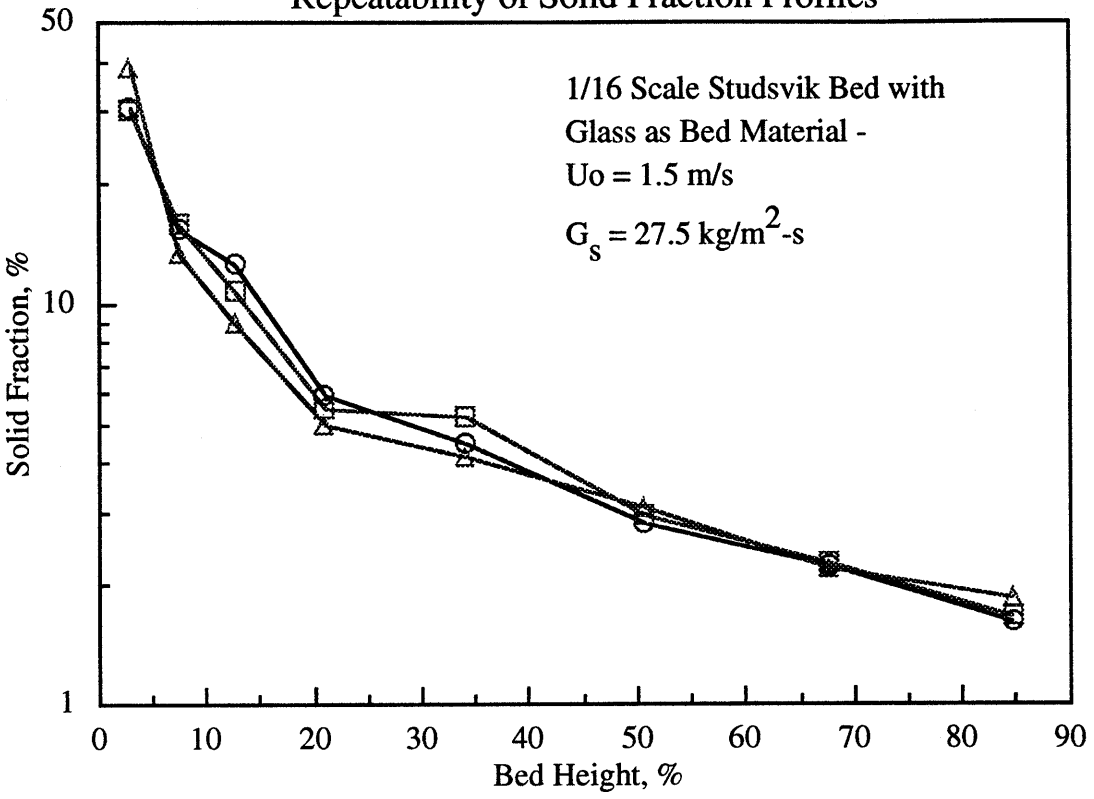

Figure 4.33
Repeatability of Solid Fraction Profiles

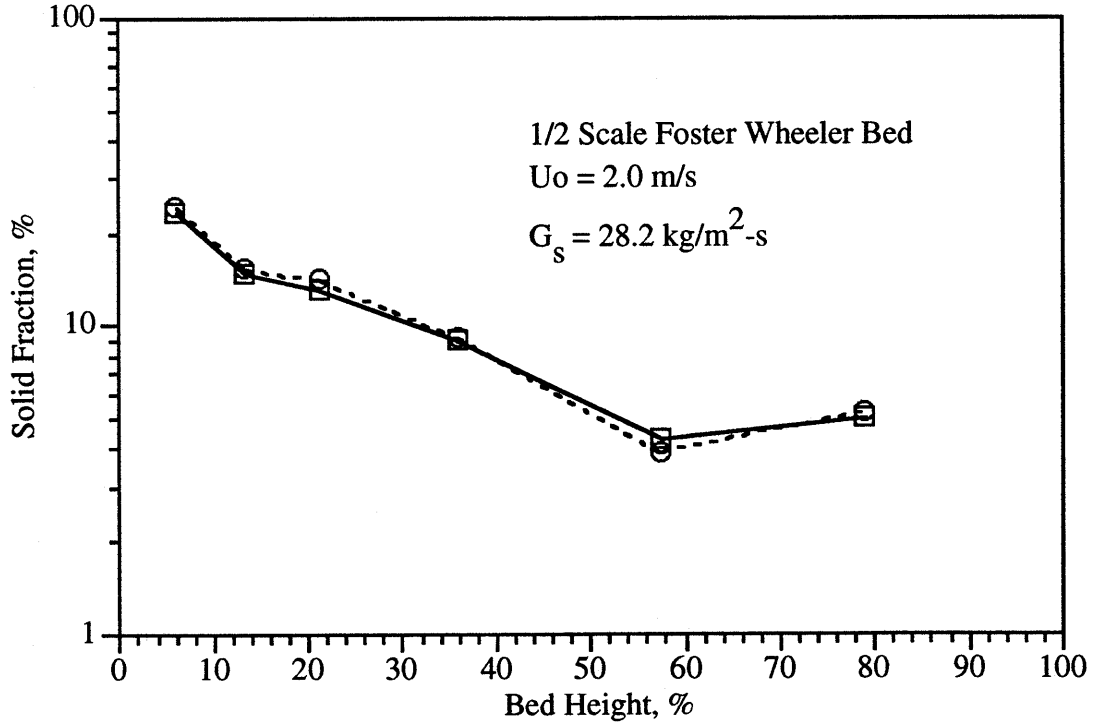

4.5.3 Pressure Measurements

All bed pressures were measured using pressure transducers whose output voltages were measured by a computer-based data acquisition system. Calibration of the transducers was accomplished by comparison with an oil filled inclined manometer. The pressure transducers were calibrated before each series of tests (e.g., whenever there was a change in bed materials). Linear calibration curves were used for reduction of data to convert the transducer output voltages to differential pressures. Table 4.10 presents typical values for the standard deviation of pressure transducers in the various beds.

Table 4.10
Standard Deviation of Transducers Used in Study

	Ratio of Standard Deviation to Average Voltage Output	
Bed	Worst Case	Typical
1/4 Scale UBC Bed	25%	2.5%
1/16 Scale Studsvik Bed (Bottom Four Transducers)	20%	5%
1/16 Scale Studsvik Bed (Top Four Transducers)	< 1%	<1%
1/4 Scale Studsvik Bed	6%	2%
1/2 Scale Foster Wheeler Bed	< 1%	< 1%

The data acquisition board is rated for 12 bit resolution; this represents 0.024 percent of full scale. Typical full scale range used for the pressure transducers with the 1/4 scale UBC bed and 1/16 scale Studsvik bed was +/- 50 mv (although +/- 10 mv was used in the more lean regions when running with plastic), allowing 24.4 μv resolution. The worst case voltage resolution represented about 4 percent of the smallest measured mean pressure difference of about 0.13 cm wc when running the plastic at very lean conditions in the 1/16 scale Studsvik bed.

The typical full scale range used with the 1/4 scale Studsvik bed and 1/2 scale Foster Wheeler bed was +/- 5 v. The voltage resolution in this bed was then 2.44 mv. This represents 0.024 % of the full scale range, and about 0.4 percent of the smallest average voltage which occurred when running plastic at very lean conditions. Comparison of the data acquisition system measurement of voltages and frequencies with known signals indicated that there was no significant A/D conversion error.

A larger source of error in pressure measurements may have occurred when measuring bed pressures in the 1/4 scale UBC bed because of the air flow arrangement used to keep the pressure taps clear of solid particles described earlier. Accurate measurement required that the flow to each pressure tap would not change significantly as pressure in the bed varied.

The error in pressure measurement associated with readjustment of the pressure tap air flow due to changing bed pressure was examined as part of a previous study (Westphalen, 1990). The results indicated that the pressure measured with the pressure taps with clearance air was about two percent less than the actual pressure for a tested pressure range up to 100 cm wc (9.8 kPa).

In order to determine the possibility that pressure signals may be attenuated in the pressure tap lines between the pressure tap opening and pressure transducer, a rough dynamic line analysis was conducted which indicated that the break (maximum transmission) frequency based on the cold bed setups would be about 3500 Hz. The maximum frequency of the data acquisition board A/D conversion may be as low as 500 Hz when all eight pressure taps are being sampled which suggests that this is not a limiting condition for the cold models. In addition, it has been shown that the fluctuations of interest in the cold beds would have frequencies less than 100 Hz (Westphalen, 1990).

For the Foster Wheeler hot bed the break frequency is about 50 Hz. Although this is fairly low, the power spectral densities indicate that the energy contained in frequencies above 20 Hz is very low. This suggests that attenuation does not occur for frequencies of interest.

Pressures time traces were taken for 10 seconds at a frequency of 100 Hz. For each trace, the average and standard deviation was calculated. These standard deviations, along with the standard deviation in solids flux measurement, were used in constructing error bars for the cold bed data solid fraction profiles. Error bars represent one standard deviation (i.e., 67 percent of the data fell into the interval based on a normal distribution).

4.5.4 Sensitivity of Solid Fraction Profiles

In order to determine the sensitivity of the solid fraction profiles to changes in superficial velocity and solid circulation rates, tests were conducted with steel particles in the 1/4 scale UBC bed in which these two variables were individually altered. Figure 4.34 shows the sensitivity of the solid fraction profile to changes in superficial velocity when the mass flux is kept constant. Figure 4.35 shows the sensitivity of the solid fraction profile to changes in mass flux when the superficial velocity is kept constant. The results indicate that the sensitivity to both variables is well within operational tolerance limits.

Figure 4.34

Effect of Superficial Velocity on Solid Fraction Profile

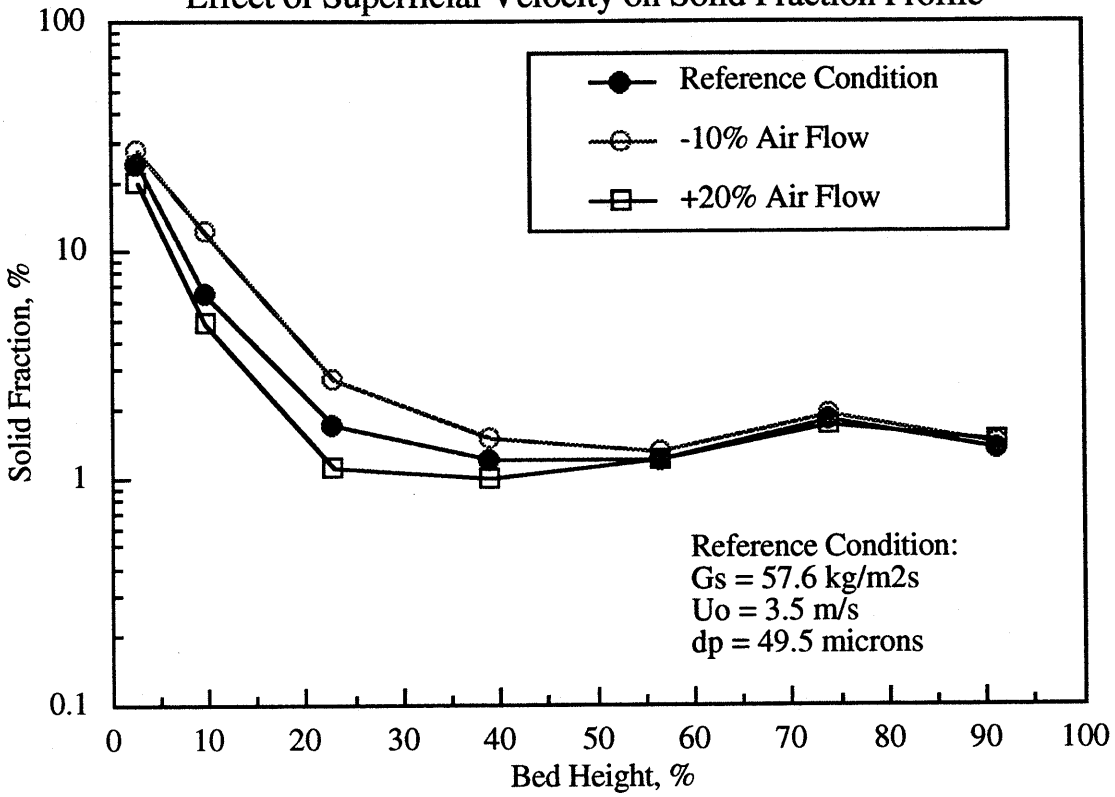

Figure 4.35

Effect of Solid Flux on Solid Fraction Profile

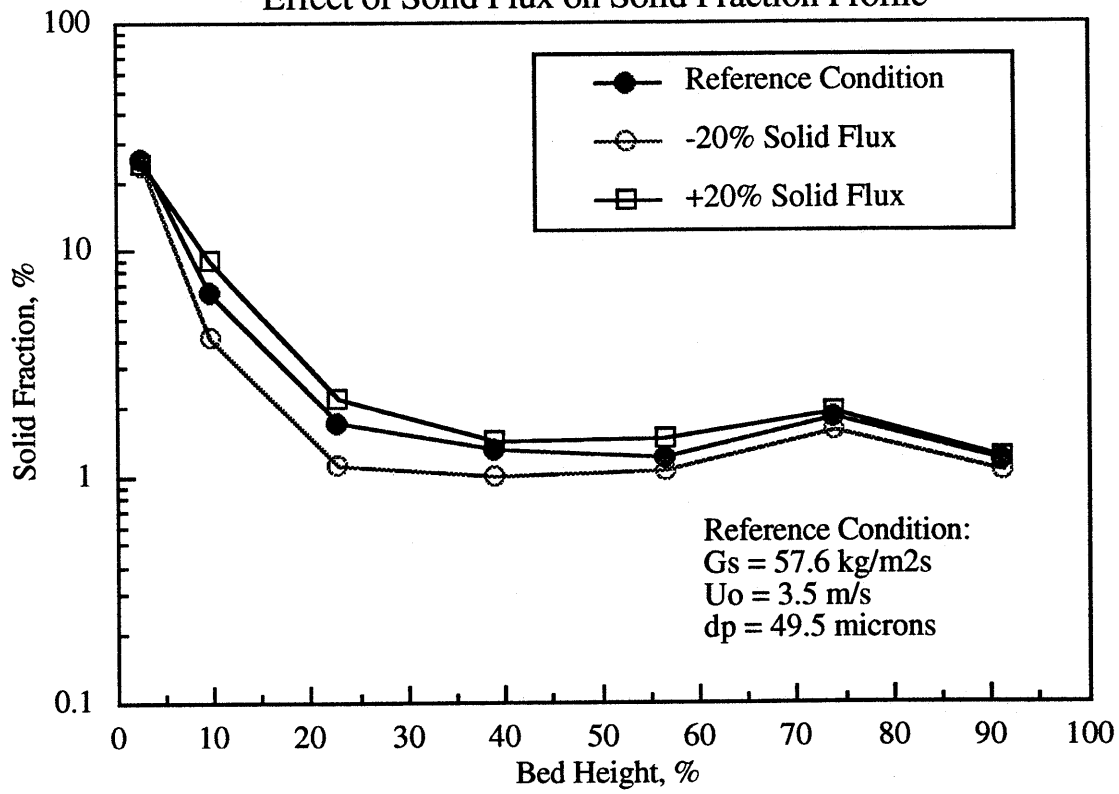

4.5.5 Hot Bed Measurements

In the Studsvik hot bed, all hot bed measuring instruments with electric output signals were sampled using a data logger. Data sampling was carried out three times a minute. The average of these three values was then stored on tape cartridge. These average values were used for further evaluation.

In the Foster Wheeler hot bed, time-mean pressure drops, temperature profiles, and flow measurments along the riser were determined by a series of pressure transducers and thermocouples, and are recorded with a computer data acquisition system. High speed pressure data was obtained using the same pressure transducers connected to a separate data acquisition system.

4.5.5.1 Solid Circulation Measurements

The Studsvik 2.5 MW CFB prototype is described in detail in other reports (Kobro, 1985). All hot bed measurements were taken by Studsvik Energiteknik AB personnel. The L-valve solids flow rate, which utilized isotope pills, is described in detail in Studsvik report EP-86/70. The isotope pill was used to determine an averaged value of solids velocity in the L-valve standpipe. Assuming plug flow, a corresponding value of mass flow was then calculated. The velocity measurements within the standpipe showed considerable variation. However, it was determined that sufficient velocity readings were taken (normally eight per run) to give a representative measurement of the true average solids velocity. In addition, solids flow rate measurements were made at the beginning, middle, and end of a four hour steady state condition for one of the operating points in an attempt to investigate the effects of velocity cycling, fluidization in the L-valve standpipe, variation in solid velocity within the L-valve standpipe and other effects which would cause the solids velocity to change within the standpipe. In light of the small variation in solids flow rate between measurements (at the beginning, middle, and end of the steady state conditions) it was felt that the solids flow rates measured were genuine, and that the difference in solids flow rates were not due to aberrant conditions in the L-valve standpipe.

A brief analysis of the data supplied by Studsvik Energiteknik AB was conducted in order to determine the variation and repeatability of the solids velocity measurements. While it was stated that the variation in solids flow of the steady state conditions was felt to be small, the value determined for the flow rate in the middle of the steady state test was nearly 10 percent

lower than that at the beginning, and the flow rate at the end of the test was over 30 percent lower that at the beginning.

Figures 4.36 and 4.37 illustrate the variations and standard deviations for the isotope velocity measurements. In some cases, measured velocities were over four times the average value. In all the higher mass flux cases (high isotope velocity) the variation in data is significant, calling into question the validity of using the average value to represent the true solids flow rate in the bed. The differences in isotope velocity measurements could be caused by any one of several bed independent phenomena such as:

1. Solids flow is not plug
2. Standpipe fluidization
3. L-valve standpipe surface characteristics
4. Variation in solids velocity within the standpipe

It is evident that the solids flow rate may be a large source of error in the hot bed measurements. Sensitivity studies on solid fraction profiles when varying bed solids flux conducted in the cold bed have indicated that the percent change in average cross-sectional solid fraction changes on the order of the same percentage as the change in solids flux. So for a case in which the solids flow rate is twice as high as the average value (a reasonable assertion in light of the variation in isotope velocity measurements), the solid fraction profile would also appear about twice as high as what would occur if the bed were actually operating at a solids flow rate equal to the average.

Determination of the solids recycle rate in the Foster Wheeler hot column was accomplished using two separate methods. The first was a calorimetric technique involving a heat balance on the FBHE. The second utilized differential pressure measurements in the upper portion of the riser to estimate the solids circulation rate (Patience *et al*, 1992). Agreement between the two methods in estimating recycle rates was very good.

4.5.5.2 Air Flows

The total air flow to the Studsvik hot bed was measured with a Venturi operating at 68 °F (20 °C) and 1 atmosphere. The secondary air flow is measured using a pressure drop sensor after the primary/secondary air split. Table 4.11 presents the total, primary, and secondary air flows along with the variance in measurements of the total and secondary air flows for the six hot bed conditions.

Figure 4.36
Variation in Studsvik Hot Bed Isotope Velocity Measurements

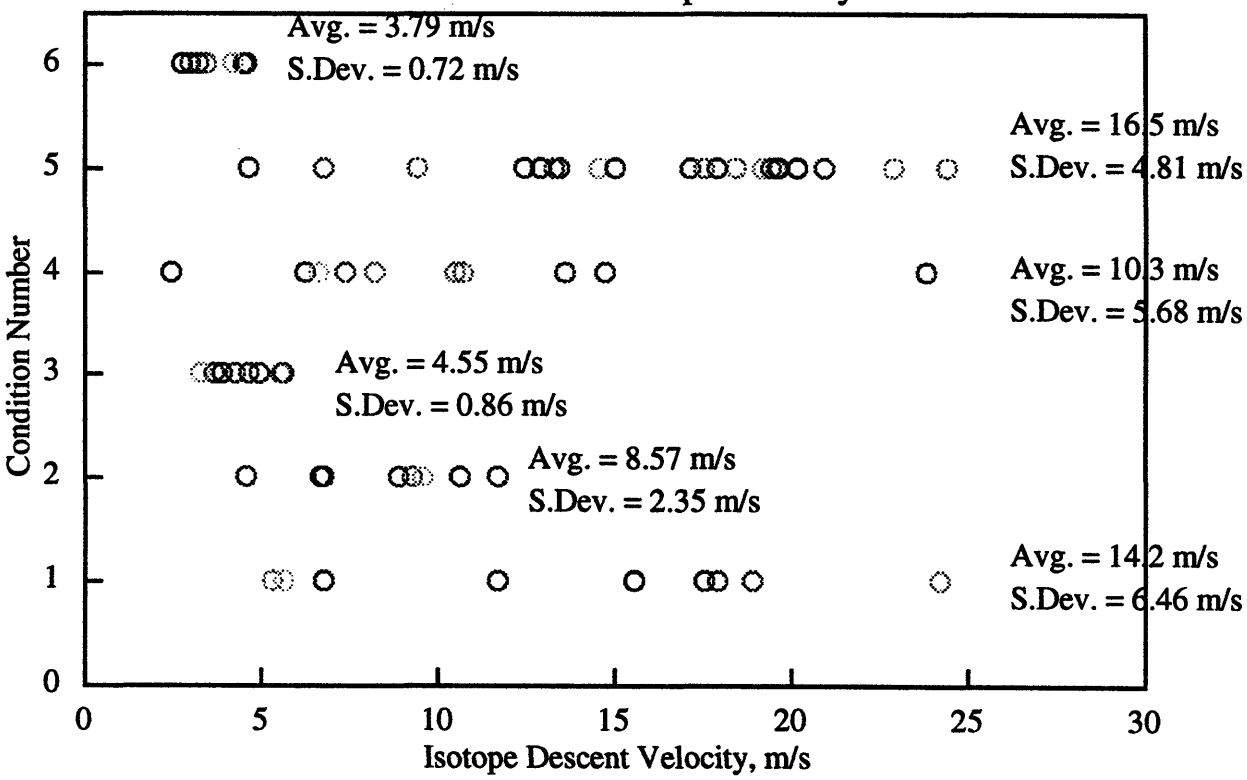

Figure 4.37

Variation in Studsvik Hot Bed Isotope Velocity Measurements

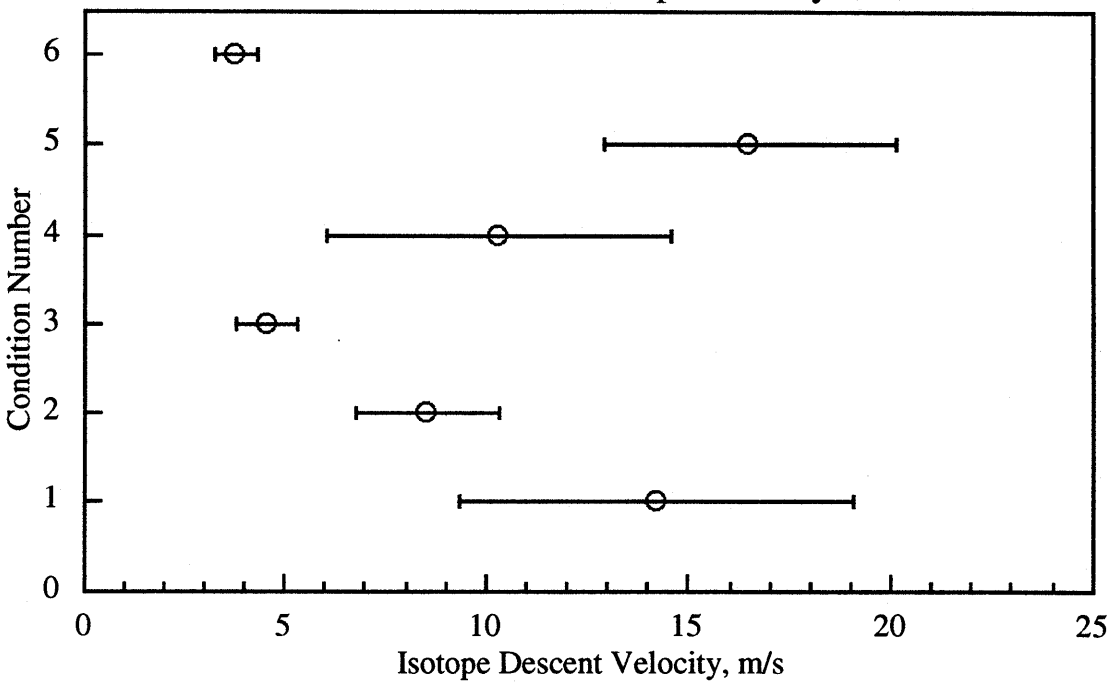

Table 4.11

Air Flows and Standard Deviations for Studsvik Hot Bed

Condition	Total Air Flow (m^3/'hr)	Std. Dev. (m^3/'hr)	Secondary Air Flow (m^3/'hr)	Std. Dev. (m^3/'hr)
1	2305.2	15.05	1172.9	24.65
2	3009.2	33.93	928.4	20.4
3	2903.7	40.0	1398.3	32.0
4	2296.5	48.7	662.5	18.8
5	2379.0	31.0	732.4	9.9
6	3033.4	25.0	923.4	18.5

Measurements of the total air flow are quite accurate with 90 percent of the measurements falling within 2.0 percent of the mean in the worst case run (Condition 4). Measurements of the secondary air flow were nearly as accurate with only 10 percent of the measurements falling outside of 2.5 percent of the mean. It is not anticipated that the air flow measurements were the cause of any significant error.

Air flow measurments in the Foster Wheeler hot bed were made with orifice plates and pressure transducers. Foster Wheeler Development Corp. has indicated that the error resulting from inaccuracies in the measurment of air flow is insignificant.[2]

4.5.5.3 Pressure Measurement

Pressures were measured in the Studsvik and Foster Wheeler hot beds utilizing differential pressure transducers. The absolute furnace pressure was measured at the top of the furnace (7.60 m above the water cooled distributor plate in the Studsvik bed and 8 m above the air inlet in the Foster Wheeler bed). In the Studsvik bed, this pressure was the reference for the differential pressure transducers located between tube number four and five in the side wall of the furnace. The elevation of the pressure taps and and overall schematic of the Studsvik hot bed are given in Figure 4.38. Schematics of the Foster Wheeler bed are given in Figures 4.18-4.21.

The average bulk density profile of the hot circulating fluidized bed is obtained in the same manner as the cold beds (i.e., assuming the pressure drop between two pressure taps is equal to the average bulk density between the two pressure measurement points). The average pressure (or solid fraction) and standard deviations for the six conditions evaluated for the Studsvik bed, and the four conditions evaluated for the Foster Wheeler bed are given in Tables 4.12 and 4.13.

Most of the Studsvik pressure measurement series have significant standard deviations when compared to the mean values, especially at the top of the bed. While this data represents the worst case measurements, it illustrates that significant error may be introduced through the hot bed differential pressure measurements. In order to help quantify this data when comparing data for similarity, the hot and cold bed solid fraction profiles will be plotted with error bars representing one standard deviation (assuming a normal distribution).

Since time varying pressure measurements were not taken in the Studsvik combustor, no comparison of solid fraction probability density functions or power spectral densities for pressure fluctuations between the atmospheric hot and cold bed were made. Of course, these comparisons will be made between the Foster Wheeler pressurized CFB and the cold model.

[2]Personal communication with Mark Torpey, FWDC.

Table 4.12

Pressure Measurements and Standard Deviations for Studsvik Hot Bed

	Condition 1		Condition 2		Condition 3	
Tap	ΔP (kPa)	Std. Dev.	ΔP (kPa)	Std. Dev.	ΔP (kPa)	Std. Dev.
1	9.42	0.15	9.32	0.211	11.06	0.032
2	3.45	0.33	3.73	0.505	5.03	0.721
3	1.03	0.05	2.31	0.115	2.55	0.356
4	0.65	0.05	?	?	1.66	0.132
5	0.41	0.03	1.28	0.0761	1.28	0.0862
6	0.16	0.015	0.726	0.0626	0.752	0.0820
7	0.0389	0.0175	0.330	0.0670	0.315	0.124
8	0.0288	0.0014	0.234	0.040	0.234	0.009
9	0.0029	0.0252	0.131	0.0979	0.0509	0.0793
10	-0.0141	0.0020	0.0099	0.0163	0.0058	0.0103
	Condition 4		Condition 5		Condition 6	
Tap	ΔP (kPa)	Std. Dev.	ΔP (kPa)	Std. Dev.	ΔP (kPa)	Std. Dev.
1	8.50	0.438	8.63	0.0811	8.43	0.855
2	2.66	0.670	3.08	0.436	3.97	0.708
3	1.31	0.0975	1.35	0.0918	2.63	0.400
4	1.74	0.349	0.875	0.0368	3.08	0.509
5	0.600	0.0511	0.734	0.0630	1.52	0.311
6	0.252	0.0214	0.334	0.0628	?	?
7	0.0739	0.0196	-0.0261	0.0782	0.238	0.137
8	0.1718	0.0086	0.0955	0.0284	?	?
9	0.0478	0.0437	-0.0178	0.0088	0.128	0.169
10	-0.0066	0.0083	0.0045	0.0121	0.0173	0.0265

Table 4.13

Solid Fraction Measurements and Standard Deviations for Foster Wheeler Hot Bed

	Condition 1		Condition 2	
Tap	SF, %	Std. Dev.	SF, %	Std. Dev.
PDI-3022	15.68	2.21	16.31	2.62
PDI-3018	12.41	2.17	12.55	2.28
PDI-3017	12.09	2.17	13.68	2.18
PDI-3280 - (PDI-3017 +PDI-3018 +PDI-3022)	7.01	1.0	8.12	1.0
PDI-3010	3.55	0.34	4.28	0.44
PDI-3008	4.55	0.64	5.02	0.48
	Condition 3		Condition 4	
Tap	SF, %	Std. Dev.	SF, %	Std. Dev.
PDI-3022	17.15	2.94	37.73	10.8
PDI-3018	13.84	2.9	31.86	12.7
PDI-3017	14.28	3.12	29.39	16.1
PDI-3280 - (PDI-3017 +PDI-3018 +PDI-3022)	9.01	1.1	8.23	7.23
PDI-3010	5.43	0.73	1.68	0.70
PDI-3008	5.85	0.76	1.02	0.02

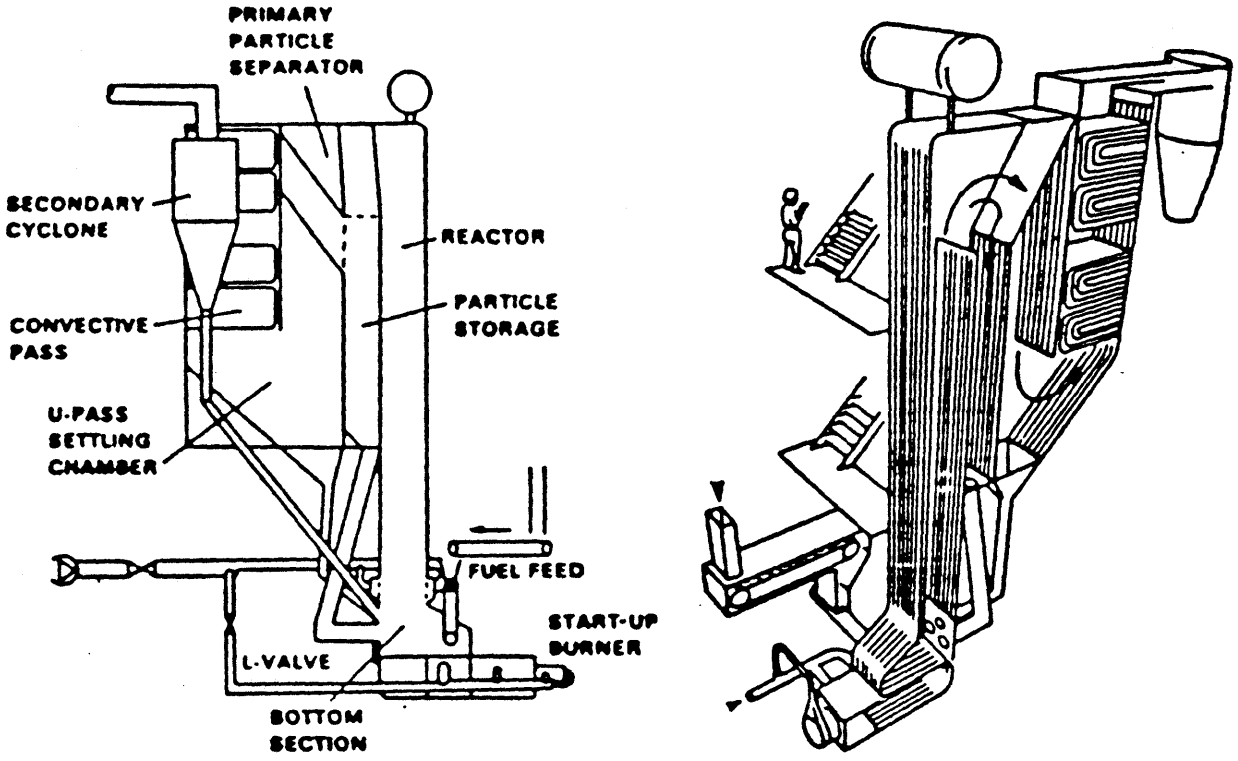

STUDSVICK 2.5 MW CFB COMBUSTOR

Figure 4.38: Studsvik 2.5 MW Combustor

4.6 Data Reduction

The following Section discusses the manner in which the data was reduced to develop average solid fraction profiles, histograms, and power spectral densities.

4.6.1 Average Solid Fraction Profiles

Solid fraction profiles discussed in the following Sections are based on pressure drop measurements. In converting pressure drop to solid fraction, it has been assumed that pressure differentials are due entirely to solid hold up

$$SF = \frac{\Delta P}{\rho_s g \Delta L}$$

This relation neglects acceleration effects and wall shear stresses, which may comprise a portion of the total pressure drop. Therefore, measured solid fractions are more correctly defined as dimensionless pressure differences, which are equal to the true solid fraction in the limit of negligible acceleration and wall shear.

Solid fractions are plotted versus the average of the heights of the associated pressure taps.

4.6.2 Pressure Fluctuation Data

Pressure fluctuations of the cold beds and in the Foster Wheeler hot bed were measured with pressure transducers and computer based data acquisition systems as discussed above. Pressure data for the cold beds consisted of sets of 1024 data taken at 100 Hz sampling rate. Pressure data for the Foster Wheeler hot bed conssited of sets of 2048 data taken at 100 Hz sampling rate.

4.6.2.1 Probability Density Functions

Histograms of the solid fraction data of both cold beds were created to assess whether pressure fluctuation amplitudes of scaled runs were similar. Construction of the histograms was conducted as follows. For each set of data a separate set of 20 bins was created. The bins were centered on the average for the data set with the bin widths equal to 2/5ths times the standard deviation of the data set. The number of data points of the data set which fell into each bin was recorded. For the plots of the histograms, the centers of the bins were plotted on the horizontal axis and the data points per bin on the vertical axis. The bin centers were normalized by the

average of the data set for plotting. The bin counts were normalized so that the sum of the twenty bin counts was one. Histograms between corresponding pressure taps could then be compared to determine the similarity of probability density functions.

4.6.2.2 Power Spectral Densities

Fast fourier transforms (FFT's) of the pressure fluctuation data were conducted with the cold bed data to determine the similarity of pressure fluctuation frequencies between properly scaled runs. The sampling frequency used for the comparisons was 100 Hz. A previous study has indicated that this sampling rate is adequate for measurement of the cold bed fluctuations of interest, and does not result in the hiding of higher frequencies due to an inadequate sampling rate (Westphalen, 1990).

In order to smooth the FFT's and to get a better representation of the average behavior of the pressure fluctuations, sets of 256 data points were transformed and the transformations themselves were averaged. Before transformation, the averages of the data were subtracted from the data sets so that the signal strength for the zero frequency would be negligible. No conditioning windows were used prior to the transformations. The analysis resulted in averages of four FFT's. The FFT averages were normalized so that the mean of the signal strengths would be one. FFT's were then compared for similarity between properly scaled runs.

5.0 RESULTS OF VISCOUS LIMIT SCALING

This Section presents the results of tests conducted to evaluate the viscous limit scaling laws which were developed in Section 3. The governing parameters for hydrodynamic similarity in the viscous limit are:

$$\frac{\rho_s u_o d_p^2}{\mu D};\ \frac{gD}{u_o^2};\ \frac{G_s}{\rho_s u_o};\ \phi_s;\ \text{PSD};\ \text{bed geometry} \qquad (1)$$

The first parameter is proportional to the inverse of the Froude number times the ratio of superficial to minimum fluidization velocity based on the Ergun equation. An equivalent set of scaling parameters is the Froude number, the ratio of superficial to minimum fluidization velocities, nondimensional solids flux, and geometric similarity This simplified set of scaling parameters is based on the assumption that for small particles, the inertial effects of the gas can be ignored and viscous resistance effects will dominate. When this is the case, the solid to fluid density ratio can be eliminated from the full set of scaling laws. In addition, in the viscous dominated region where gas inertial effects are negligible, the ratio of particle diameter to bed length does not appear explicitly in the parameter list, only the ratio of bed geometries appear.

In order to evaluate the validity of applying these scaling parameters in the fast-fluidization regime, two series of tests were conducted. In the first series of tests, hydrodynamic scaling was attempted between steel and a glass particle sample with the same minimum fluidization, along with a glass sample with a slightly different minimum fluidization velocity but a more similar particle size distribution. The 1/4 scale UBC bed was used during these tests. In the second series of tests, hydrodynamic scaling was attempted between glass and plastic particles with the same minimum fluidization velocity in the same bed. The phase one 1/16 scale Studsvik bed was used during these tests. Tables 5.1 and 5.2 present test matrices for evaluation of the viscous limit scaling parameters.

Table 5.1

Test Matrix - Steel/Glass Viscous Limit Scaling

Parameter	Steel Particles	Glass 1 Particles	Glass 2 Particles
Particle Density (gm/cm^3)	7.25	2.54	2.54
Particle Diameter (microns)	49.5	88.3	81.6
u_{mf}	u_{mf}	Same	$1.2u_{mf}$
Bed Diameter	D	Same	Same
u_o/u_{mf}	100-500	Same	Same
u_o^2/gL	Fr	Same	Same
$Re = \frac{\rho_f u_o d_p}{\mu_f}$	$\frac{\rho_f u_o d_p}{\mu_f}$	$\frac{1.8\rho_f u_o d_p}{\mu_f}$	$\frac{1.6\rho_f u_o d_p}{\mu_f}$
$\frac{\rho_s}{\rho_f}$	6042	2117	2117
$M = \frac{G_s}{u_o \rho_s}$	0.0029	Same	Same
Specific Heat (cal/gm)	0.10	0.20	0.20

Table 5.2

Test Matrix - Glass/Plastic Viscous Limit Scaling

Parameter	Glass Particles	Plastic Particles
Particle Density (gm/cm^3)	2.54	1.40
Particle Diameter (microns)	78.7	99.5
u_{mf}	u_{mf}	Same
Bed Diameter	D	Same
u_o/u_{mf}	100-200	Same
u_o^2/gL	Fr	Same
$Re = \frac{\rho_f u_o d_p}{\mu_f}$	$\frac{\rho_f u_o d_p}{\mu_f}$	$\frac{1.3\rho_f u_o d_p}{\mu_f}$
$\frac{\rho_s}{\rho_f}$	2117	1167
$M = \frac{G_s}{u_o \rho_s}$	0.0043 - 0.0072	Same
Specific Heat (cal/gm)	0.20	0.25

5.1 Viscous Limit Scaling Between Steel and Glass

Tables 5.3 through 5.5 provide the operational data, along with information concerning the particles and bed utilized in the steel/glass viscous limit evaluations in a CFB fluidized with ambient air. In these Tables, Ga represents the Galileo number defined as $\frac{\rho_s^2 d_p^3 g}{\mu_f^2}$. Tests were conducted at three different superficial velocities, and at the same nondimensional solid flux. No heat transfer data was taken during these tests.

5.1.1 Solid Fraction Profiles

The solid fraction profiles discussed in this Section and all remaining sections are based on average pressure drop measurements. The average solid fraction profiles for the steel/glass viscous limit evaluation are given in Figures 5.1 through 5.3. The tabulated data is given in Appendix E. The calculated solid fractions are plotted versus the average of the heights of the associated pressure taps. Error bars are based on calculated standard deviations in solid flow measurements and pressure time traces.

5.1.2 Histograms

Histograms of the solid fraction data of the viscous limit scaling for steel and glass are depicted in Figures 5.4 through 5.7. Histograms are shown for solid fractions between pressure taps 1 and 2, 3 and 4, 5 and 6, 7 and 8 (see Section 4.0 for locations). In these plots, probability is plotted versus the solid fraction (recall that the pressure taps are numbered from the bottom of the bed to the top).

Table 5.3

Glass/Steel Viscous Limit Scaling - Condition 1

	Glass 1	Glass 2	Steel
u_o (m/s)	3.0	3.0	3.0
u_{mf} (cm/s) Ergun Eqn.	1.79	1.53	1.60
u_{mf} (cm/s) measured	1.40	1.70	1.70
d_p (microns)	88.3	81.6	49.5
L (m)	1.62	1.62	1.62
A_{cs} (m^2)	1.13E-3	1.13E-3	1.13E-3
G_s (kg/m^2-s)	22.1	22.1	63.1
$Re_{dp,uo}$	17.4	16.2	9.8
$Re_{L,uo}$	3.22E5	3.22E5	3.22E5
Fr	0.57	0.57	0.57
$\left(\frac{u_o}{u_{mf}}\right)_{Ergun\ eqn.}$	167.6	196.1	187.5
$\left(\frac{u_o}{u_{mf}}\right)_{measured}$	214.3	176.5	214.3
$\left(\frac{G_s}{\rho_s u_o}\right)$	2.9E-3	2.9E-3	2.9E-3
$\left(\frac{\rho_s}{\rho_f}\right)$	2117	2117	6042
Ga	1.33E5	1.05E5	1.90E5

Table 5.4

Glass/Steel Viscous Limit Scaling - Condition 2

	Glass 1	Glass 2	Steel
u_o (m/s)	5.5	5.5	5.5
u_{mf} (cm/s) Ergun Eqn.	1.79	1.53	1.60
u_{mf} (cm/s) measured	1.40	1.70	1.70
d_p (microns)	88.3	81.6	49.5
L (m)	1.62	1.62	1.62
A_{cs} (m^2)	1.13E-3	1.13E-3	1.13E-3
G_s (kg/m^2-s)	40.5	40.5	115.6
$Re_{dp,uo}$	32.1	29.7	18.0
$Re_{L,uo}$	5.89E5	5.89E5	5.89E5
Fr	1.90	1.90	1.90
$\left(\frac{u_o}{u_{mf}}\right)_{Ergun\ eqn.}$	307.3	359.5	343.8
$\left(\frac{u_o}{u_{mf}}\right)_{measured}$	392.9	323.5	392.9
$\left(\frac{G_s}{\rho_s u_o}\right)$	2.9E-3	2.9E-3	2.9E-3
$\left(\frac{\rho_s}{\rho_f}\right)$	2117	2117	6042
Ga	1.33E5	1.05E5	1.90E5

Table 5.5

Glass/Steel Viscous Limit Scaling - Condition 3

	Glass 1	Glass 2	Steel
u_o (m/s)	7.0	7.0	7.0
u_{mf} (cm/s) Ergun Eqn.	1.79	1.53	1.60
u_{mf} (cm/s) measured	1.40	1.70	1.70
d_p (microns)	88.3	81.6	49.5
L (m)	1.62	1.62	1.62
A_{cs} (m^2)	1.13E-3	1.13E-3	1.13E-3
G_s (kg/m^2-s)	51.6	51.6	147.2
$Re_{dp,uo}$	40.9	37.8	22.9
$Re_{L,uo}$	7.51E5	7.51E5	7.51E5
Fr	3.08	3.08	3.08
$\left(\frac{u_o}{u_{mf}}\right)_{Ergun\ eqn.}$	391.1	457.5	437.5
$\left(\frac{u_o}{u_{mf}}\right)_{measured}$	500.0	411.8	500.0
$\left(\frac{G_s}{\rho_s u_o}\right)$	2.9E-3	2.9E-3	2.9E-3
$\left(\frac{\rho_s}{\rho_f}\right)$	2117	2117	6042
Ga	1.33E5	1.05E5	1.90E5

Figure 5.1

Solid Fraction Profiles - Glass/Steel Viscous Limit Scaling

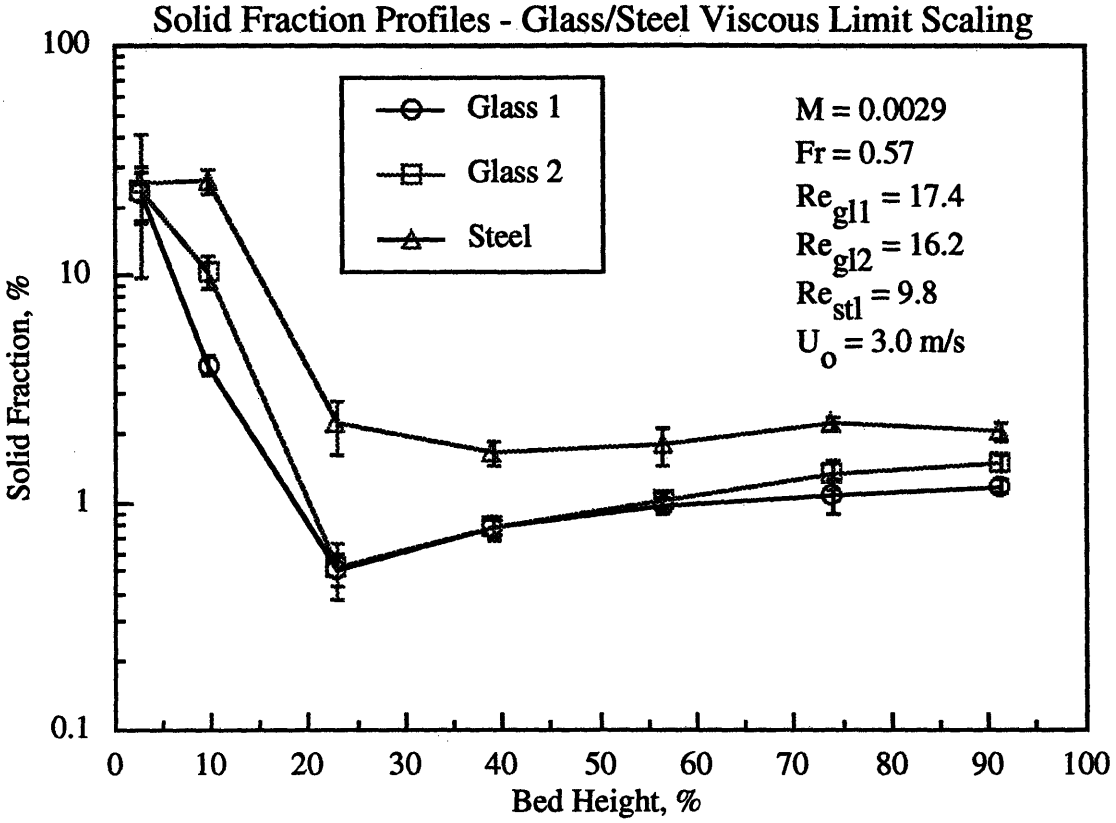

Figure 5.2

Solid Fraction Profiles - Glass/Steel Viscous Limit Scaling

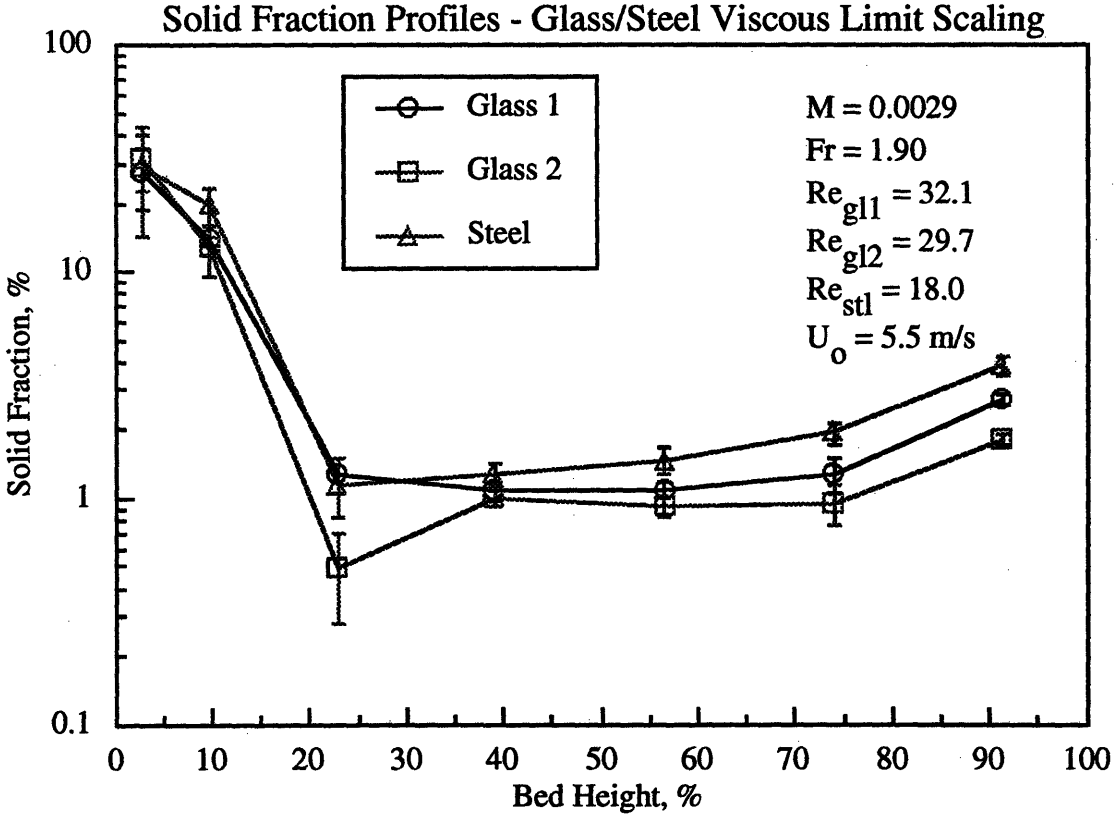

Figure 5.3

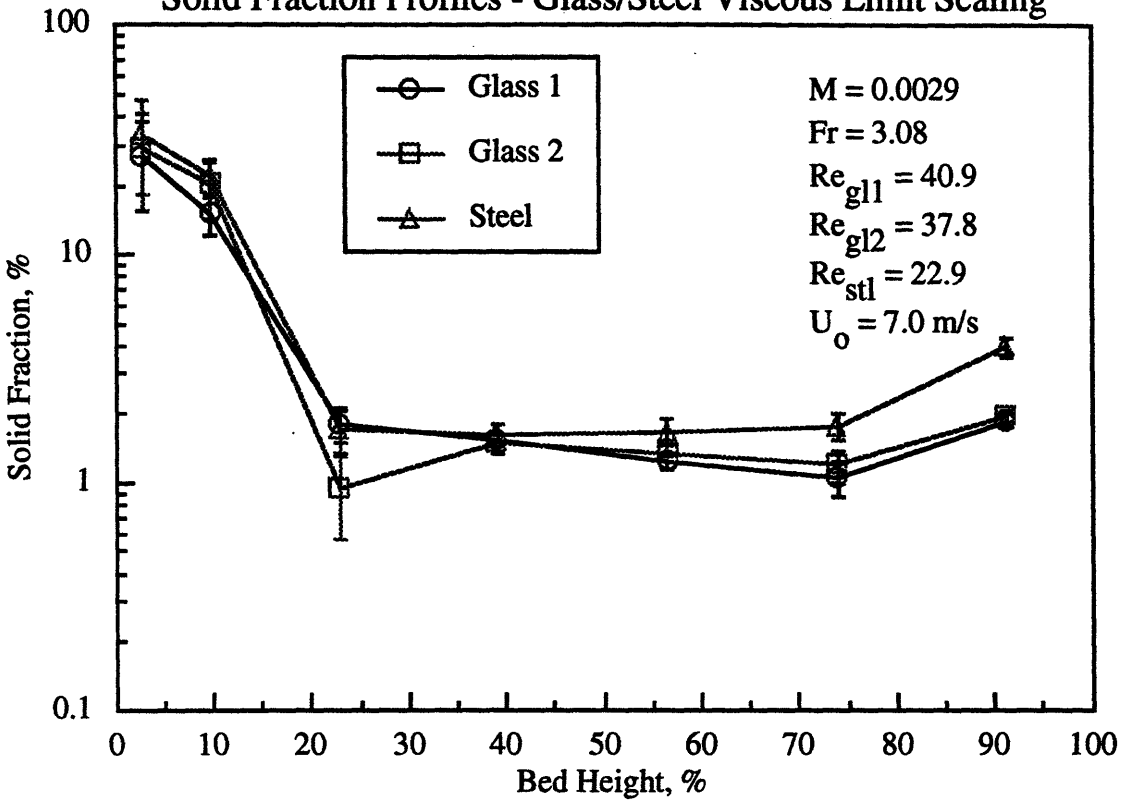

Figure 5.4

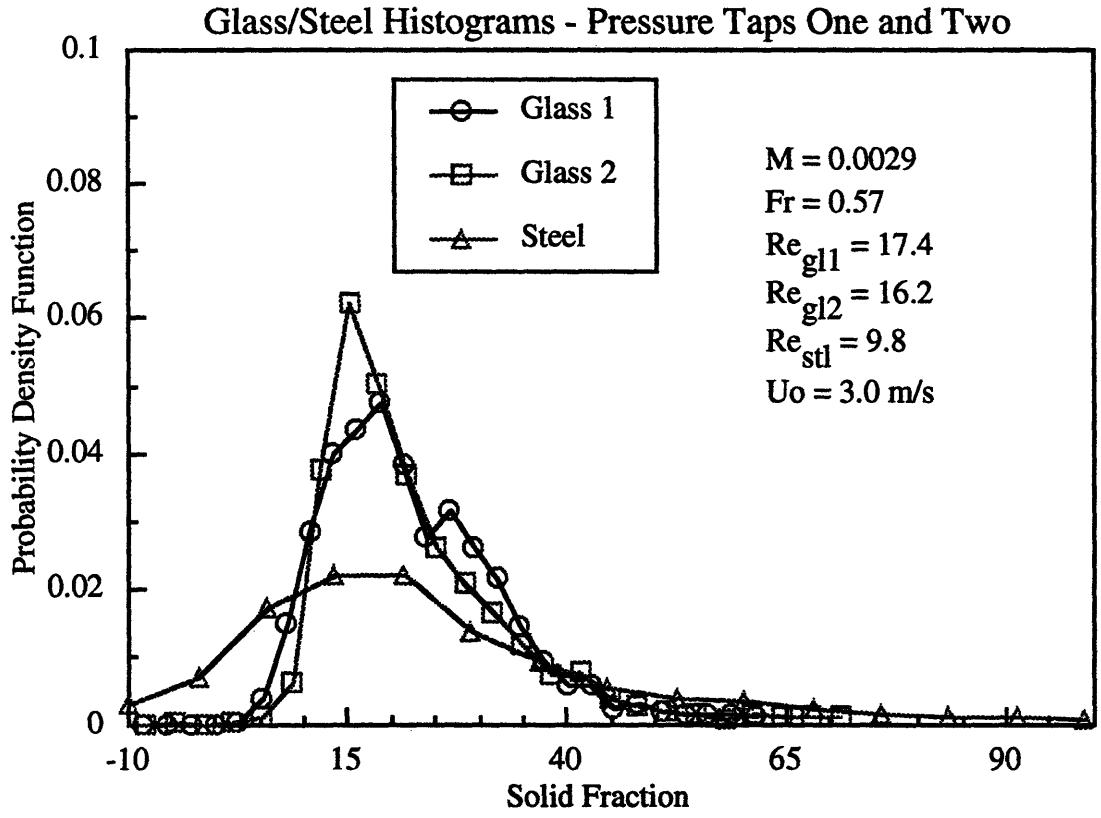

Figure 5.5

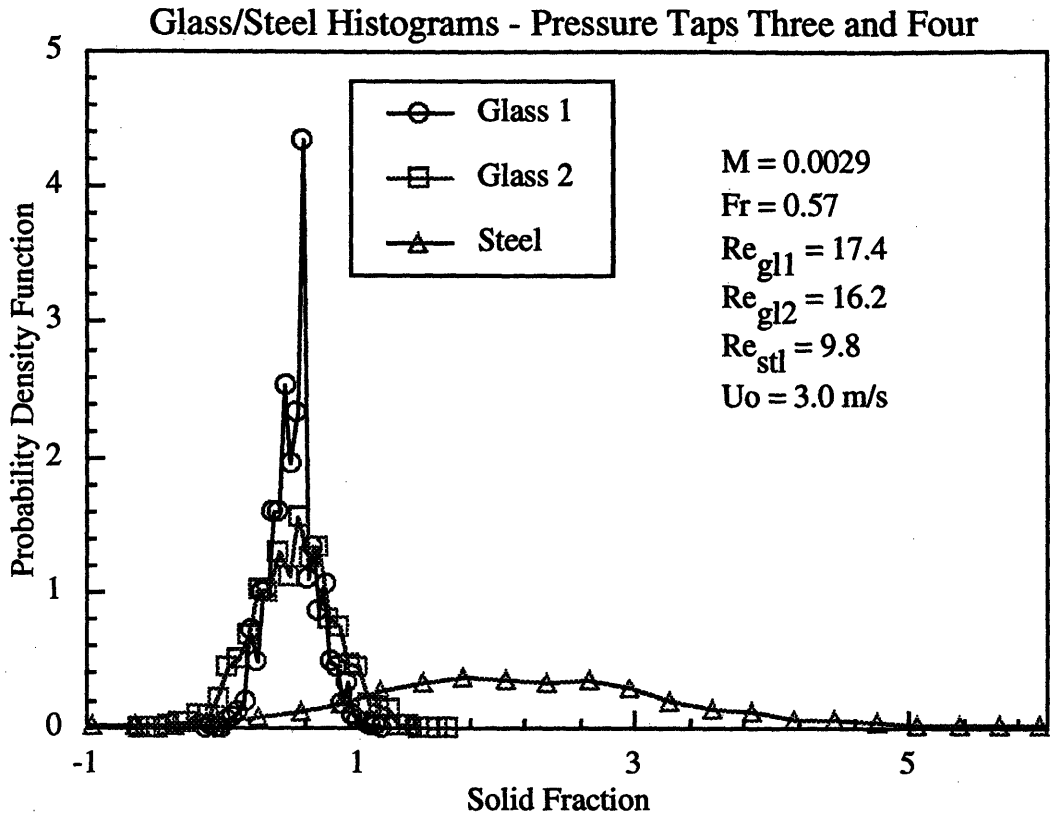
Glass/Steel Histograms - Pressure Taps Three and Four
Glass 1
Glass 2
Steel
M = 0.0029
Fr = 0.57
Re gl1 = 17.4
Re gl2 = 16.2
Re stl = 9.8
Uo = 3.0 m/s
Probability Density Function
Solid Fraction
0
1
2
3
4
5
-1
1
3
5

Figure 5.6

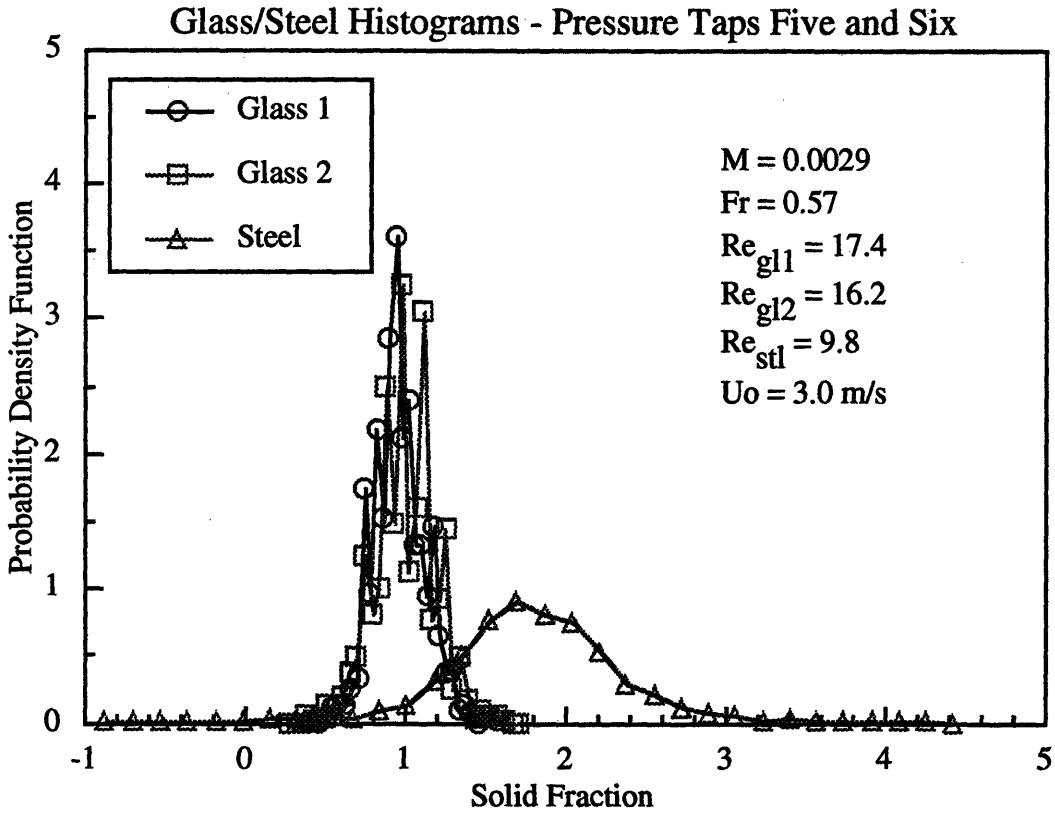
Glass/Steel Histograms - Pressure Taps Five and Six
Glass 1
Glass 2
Steel
M = 0.0029
Fr = 0.57
Re gl1 = 17.4
Re gl2 = 16.2
Re stl = 9.8
Uo = 3.0 m/s
Probability Density Function
Solid Fraction
0
1
2
3
4
5
-1
0
1
2
3
4
5

Figure 5.7

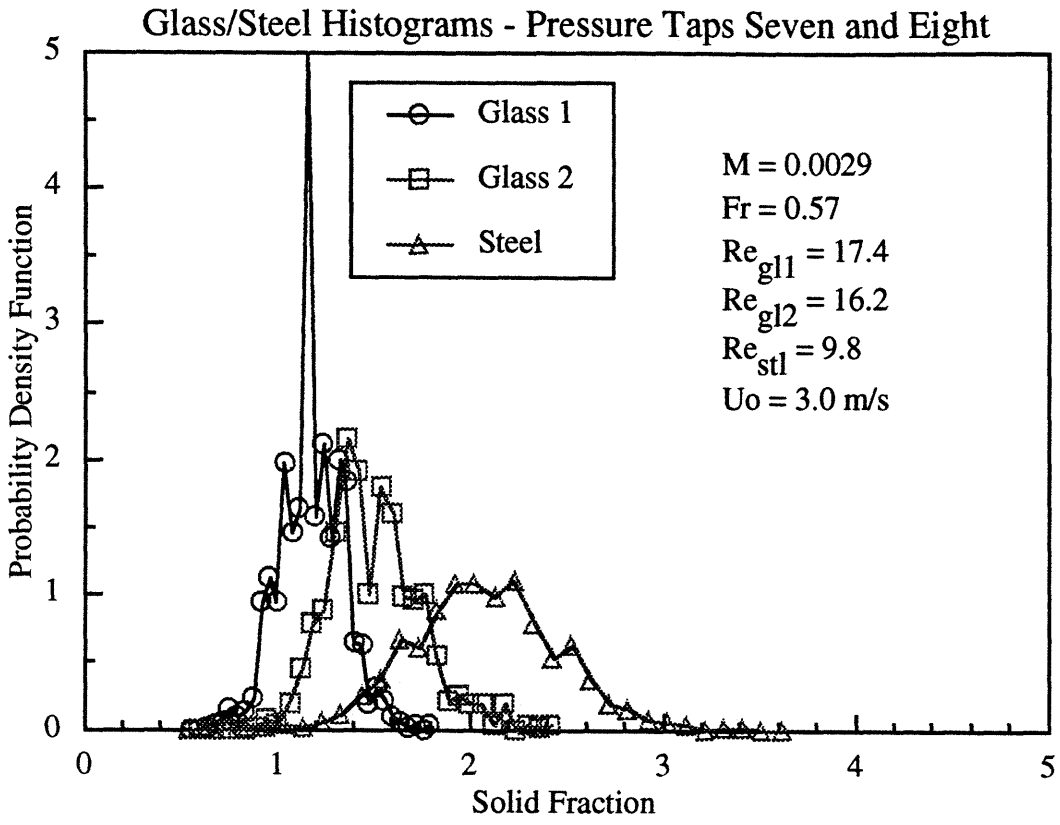

Figure 5.8

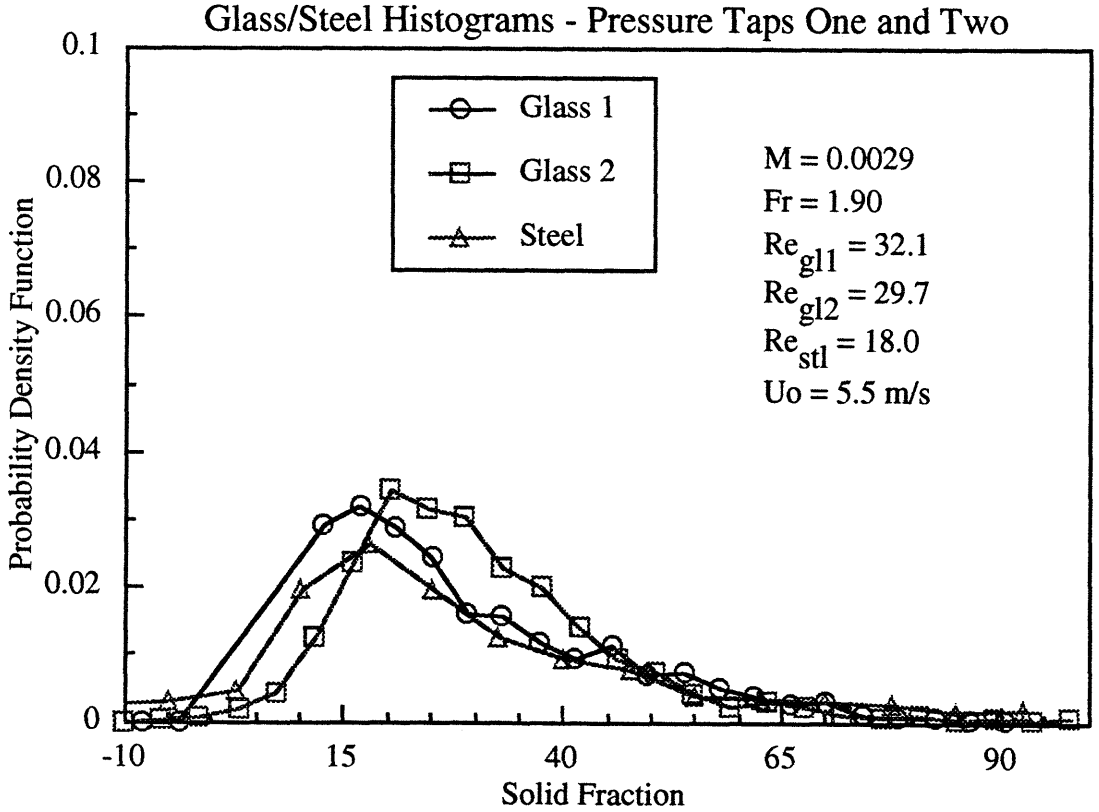

Figure 5.9

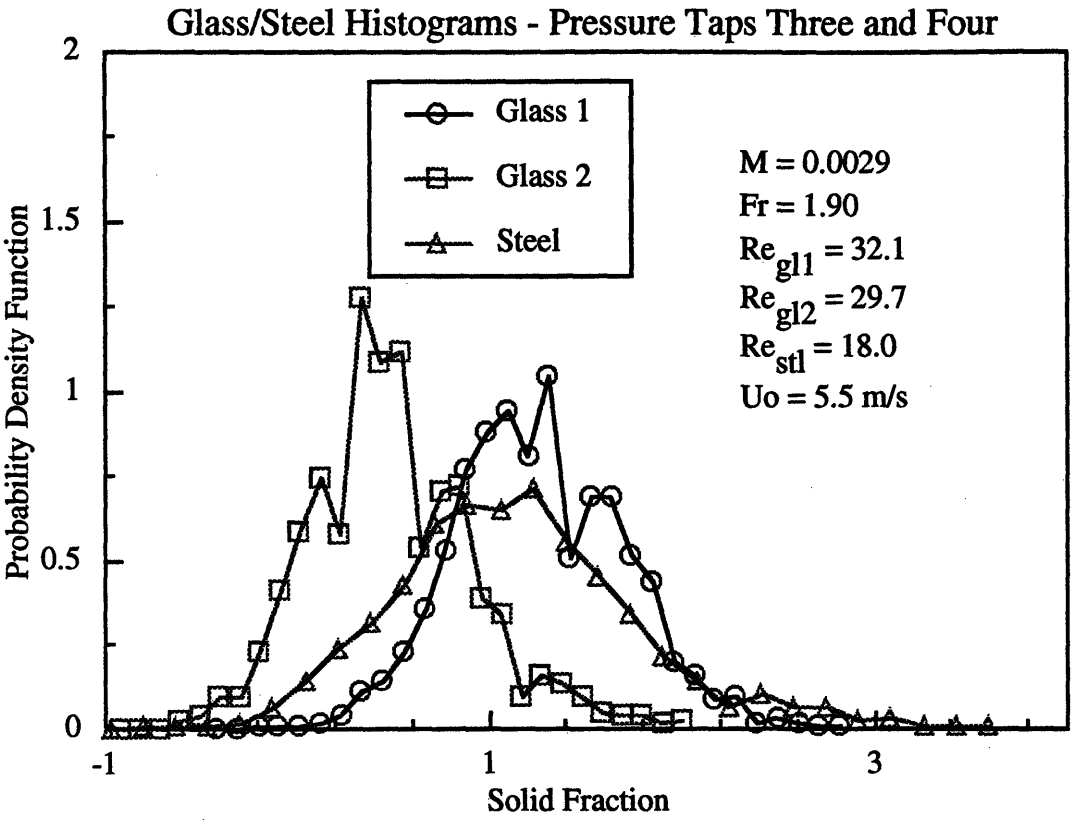

Figure 5.10

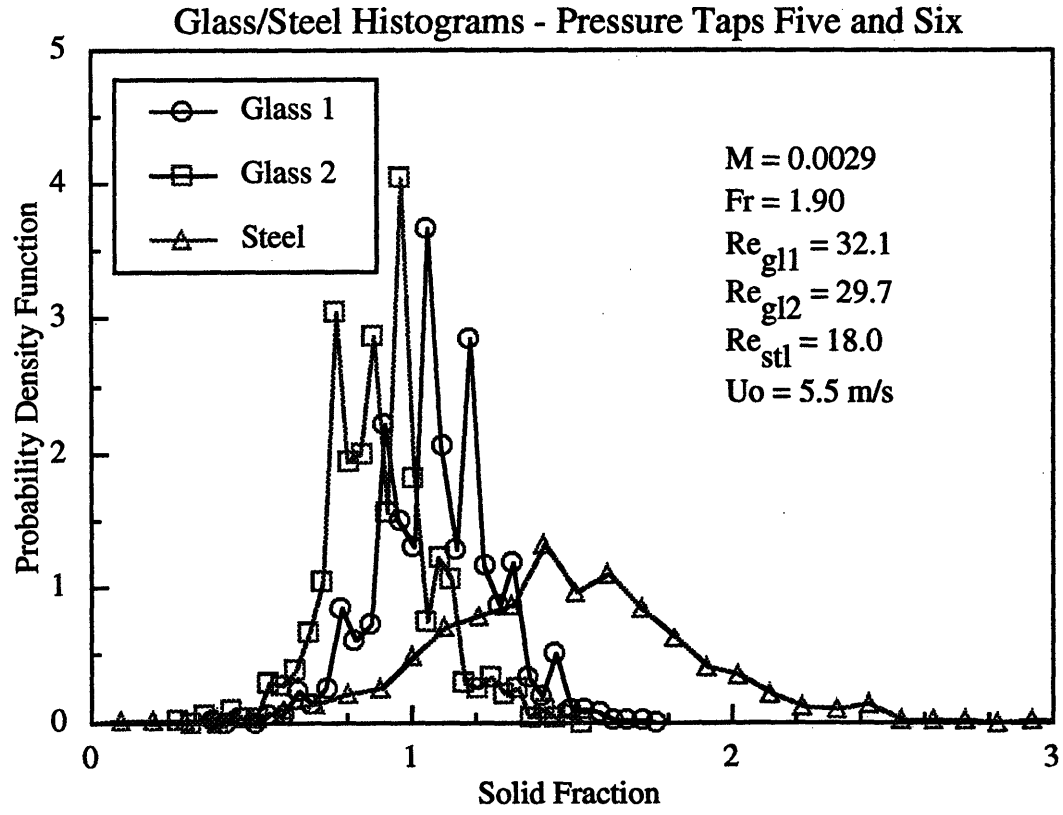

Figure 5.11

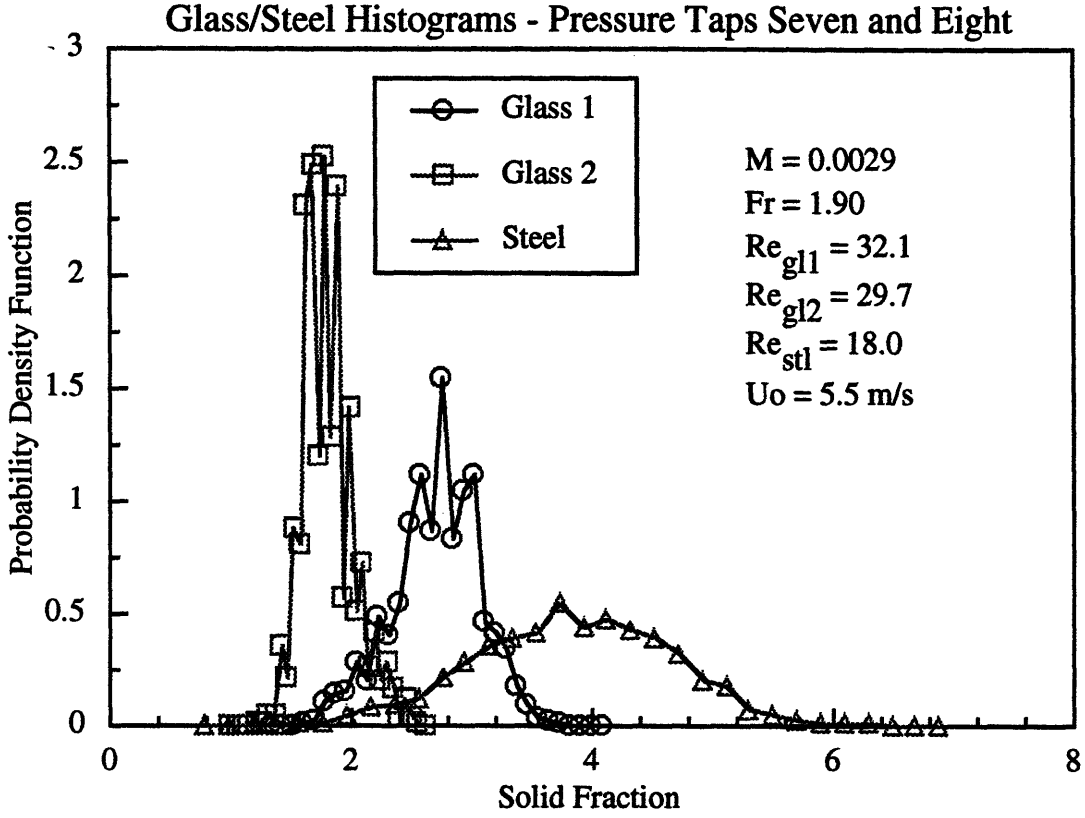

Figure 5.12

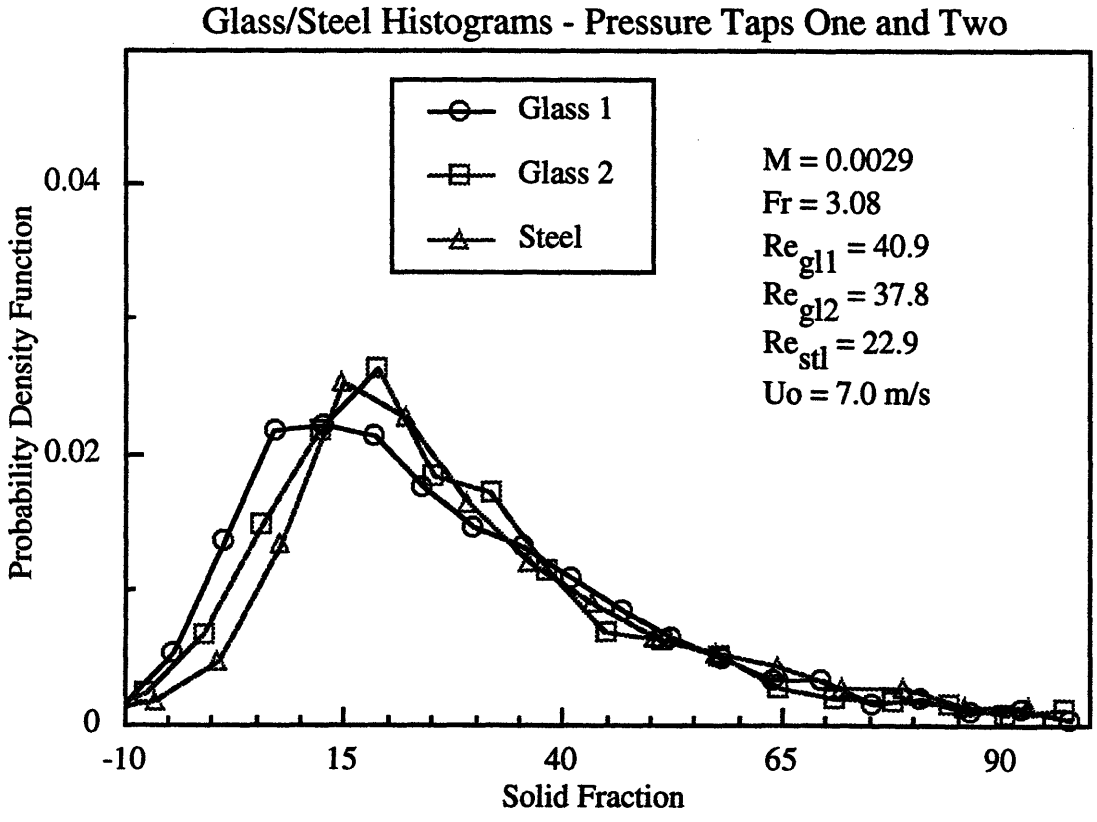

Figure 5.13

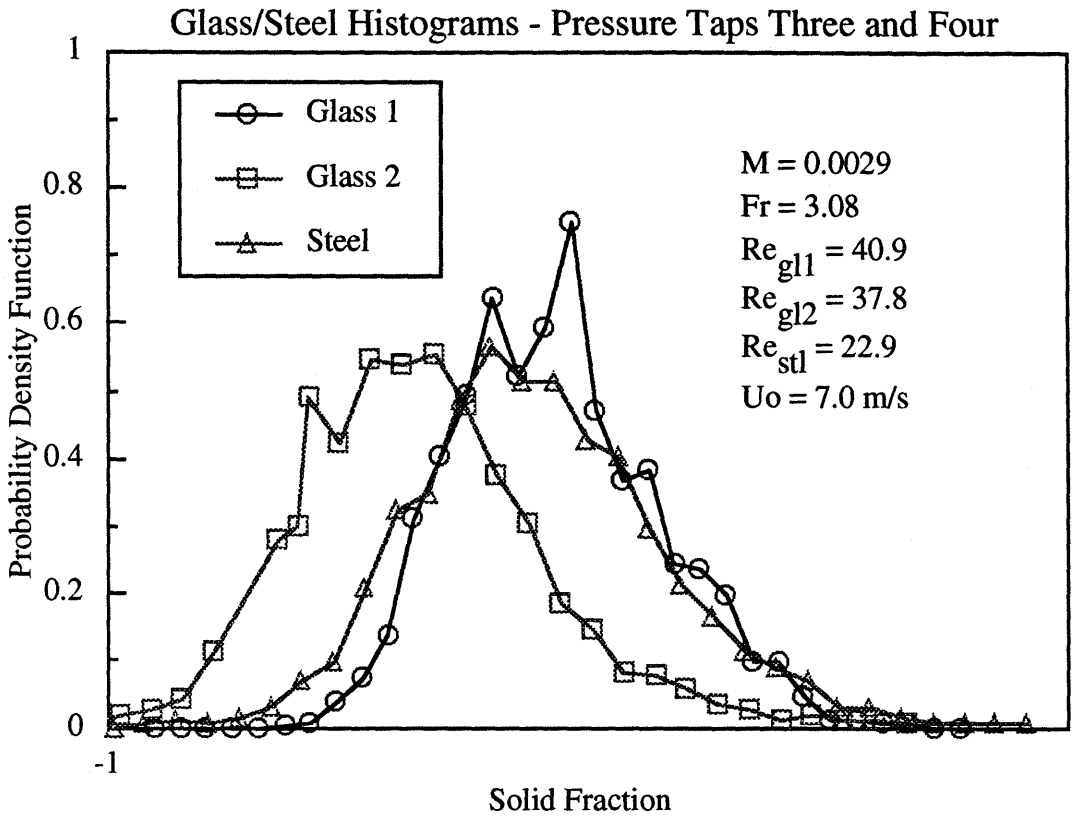

Figure 5.14

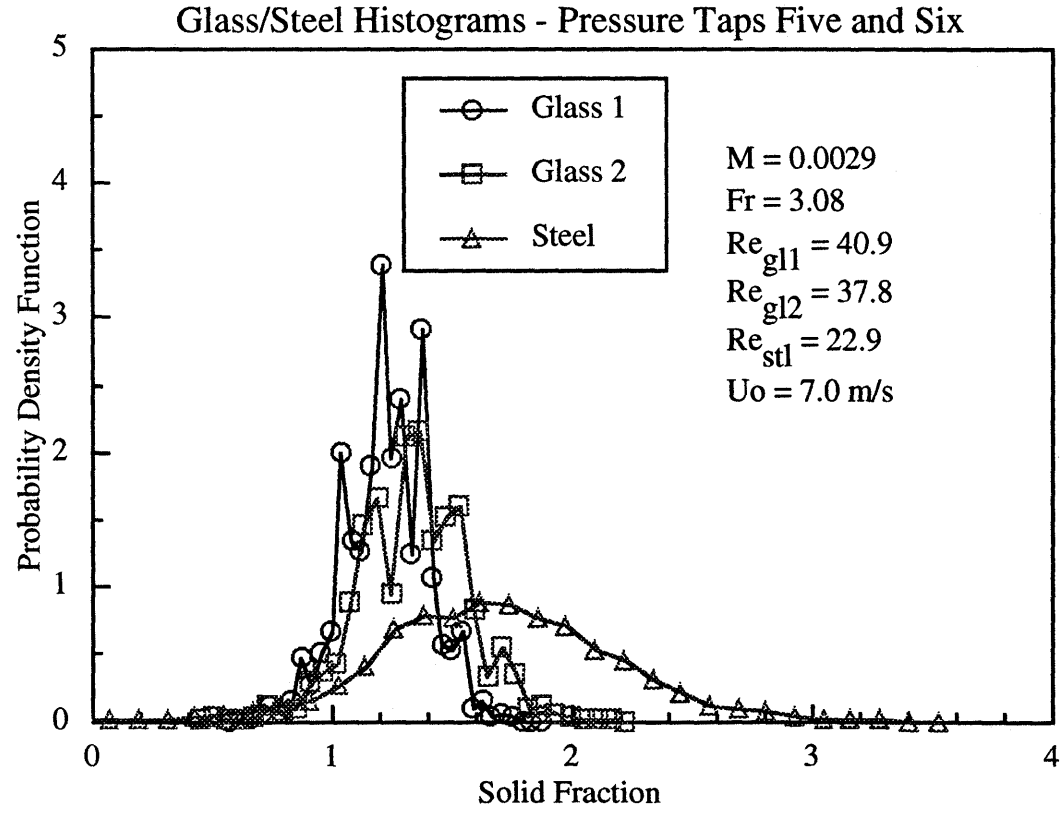

Figure 5.15

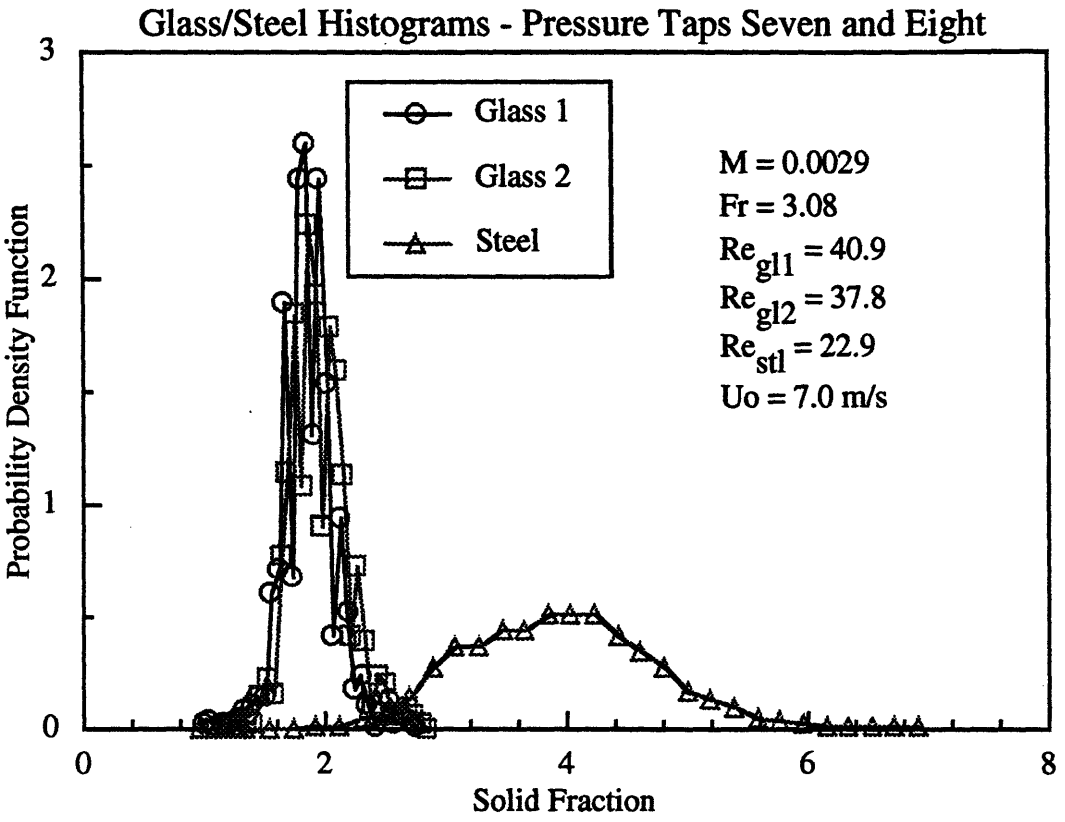

5.1.3 Power Spectral Densities

FFT's of the pressure fluctuation data for the steel/glass viscous limit tests are given in Figures 5.16 through 5.27. FFT's are shown for the same pressure taps as the probability density functions. In these plots, the fourier transform in plotted versus the frequency in Hz.

Figure 5.16

Glass/Steel FFT's - Pressure Taps One and Two

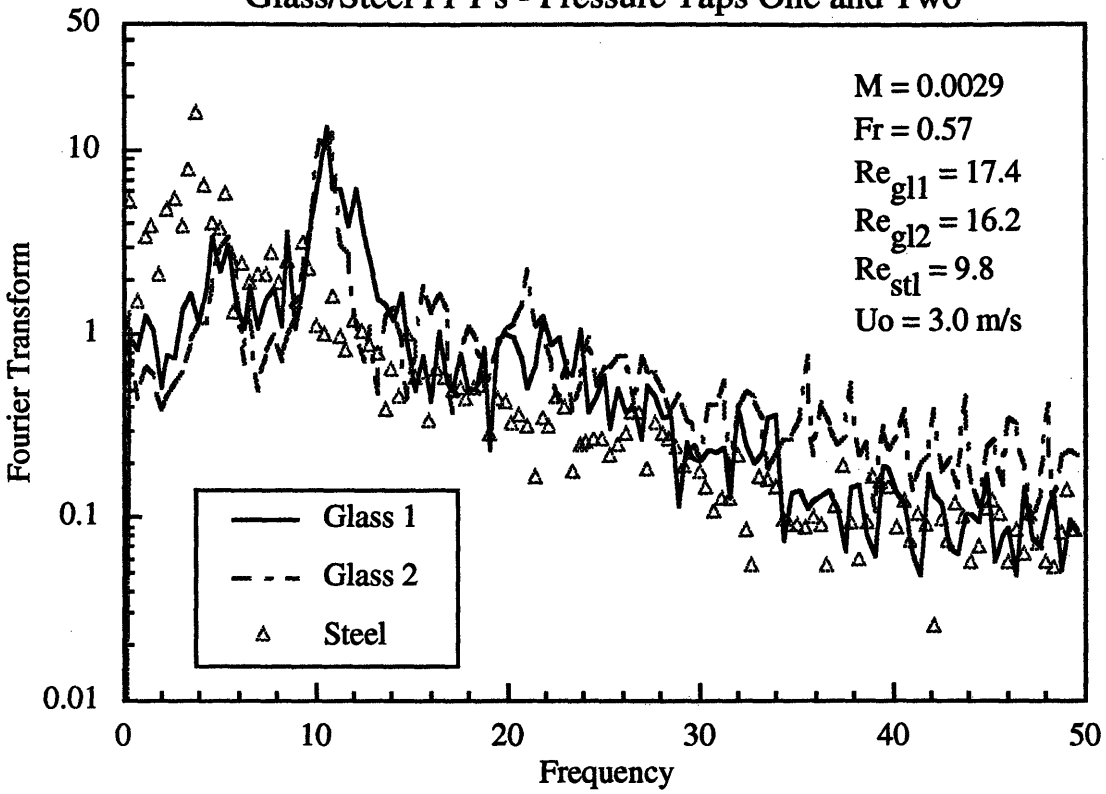

Figure 5.17

Glass/Steel FFT's - Pressure Taps Three and Four

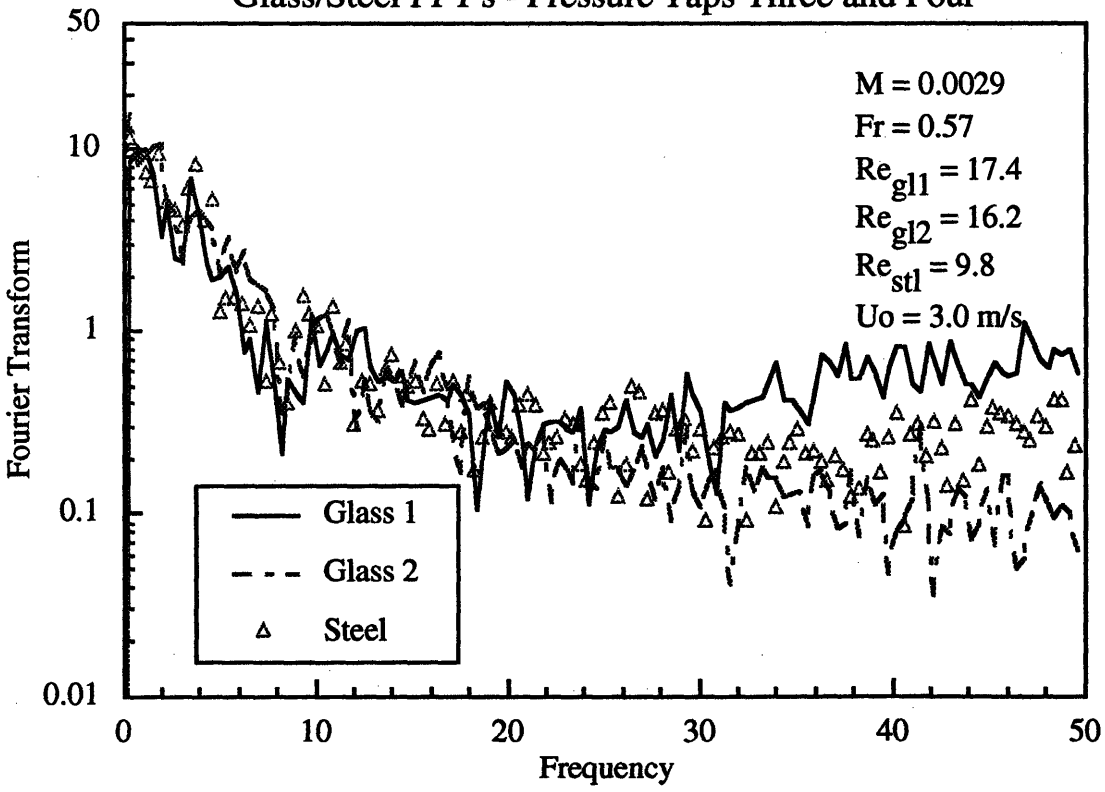

Figure 5.18

Glass/Steel FFT's - Pressure Taps Five and Six

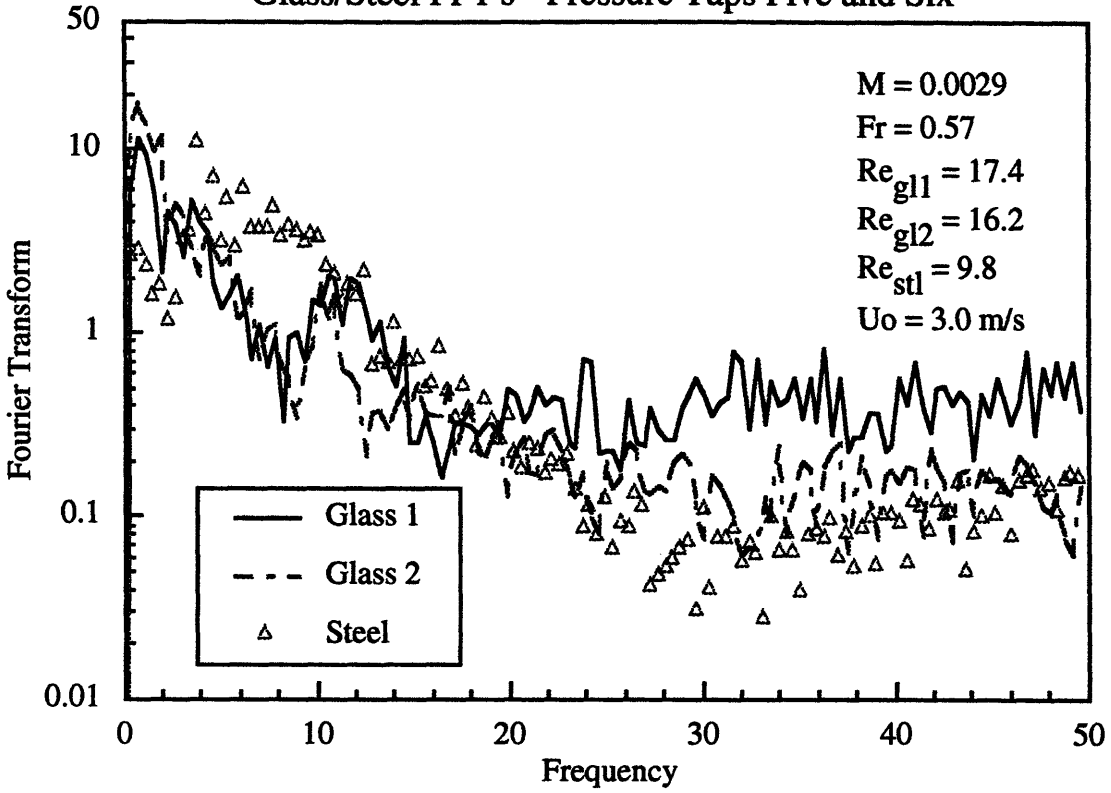

Figure 5.19

Glass/Steel FFT's - Pressure Taps Seven and Eight

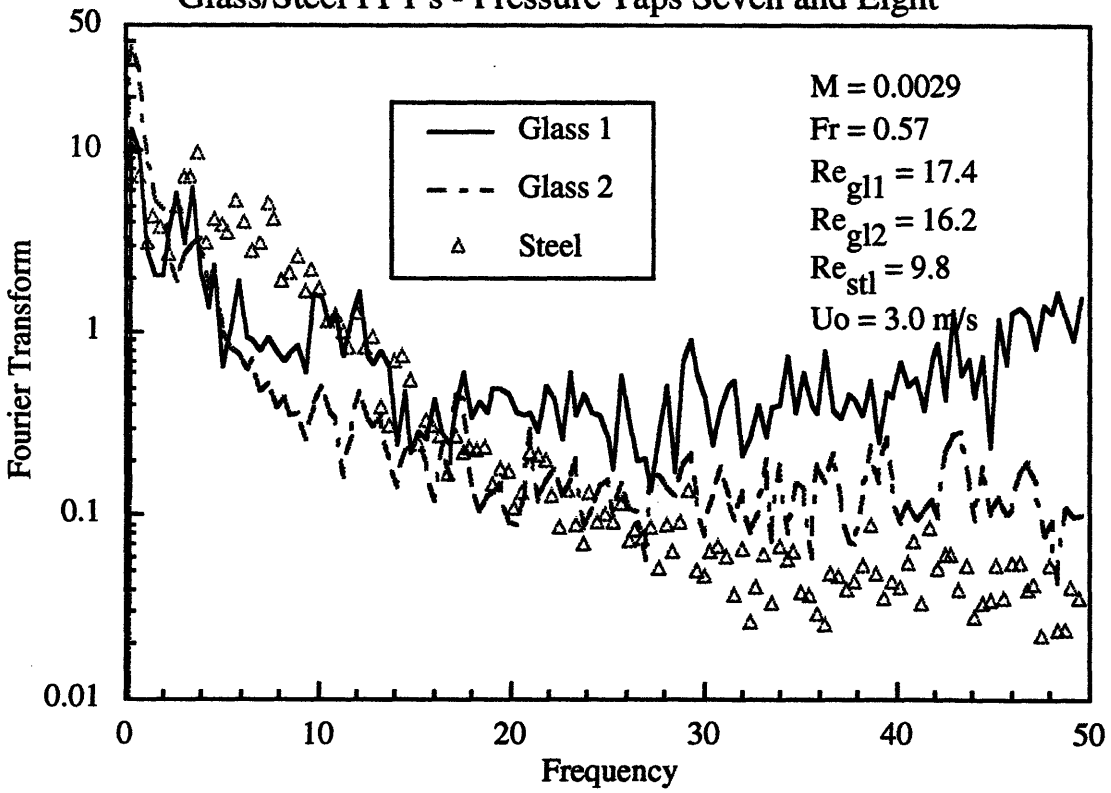

Figure 5.20

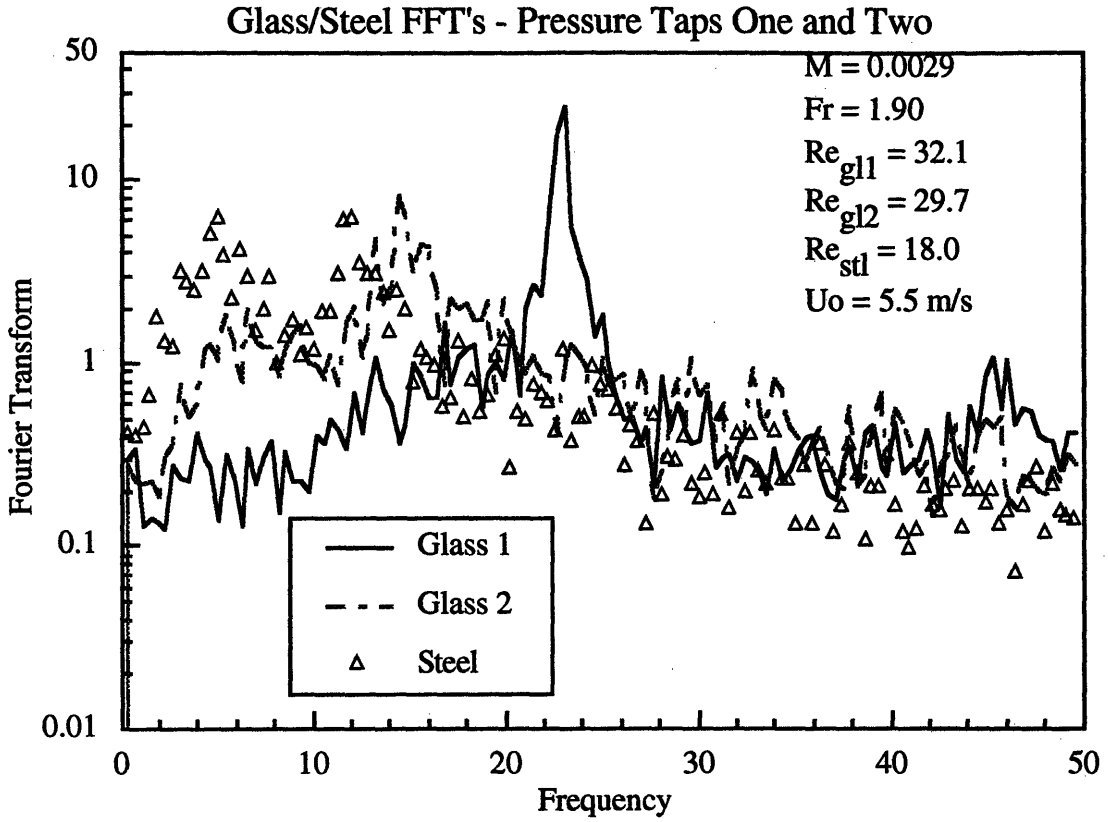

Figure 5.21

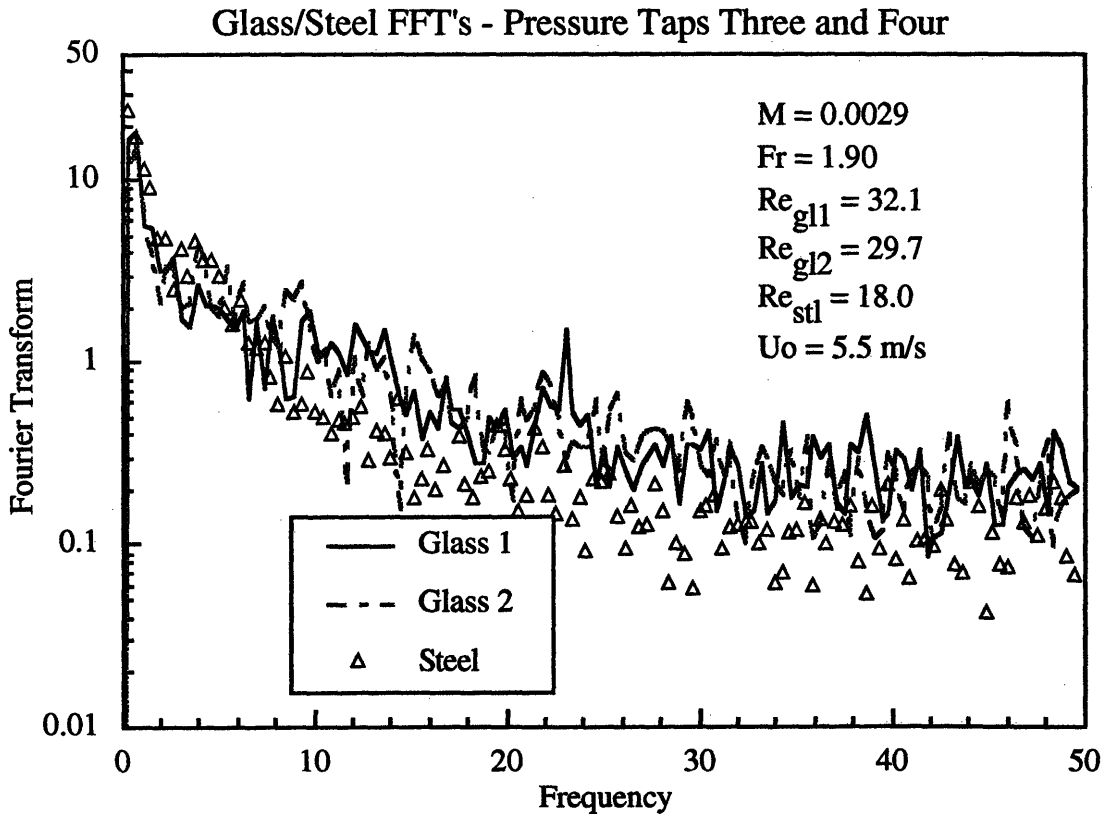

Figure 5.22

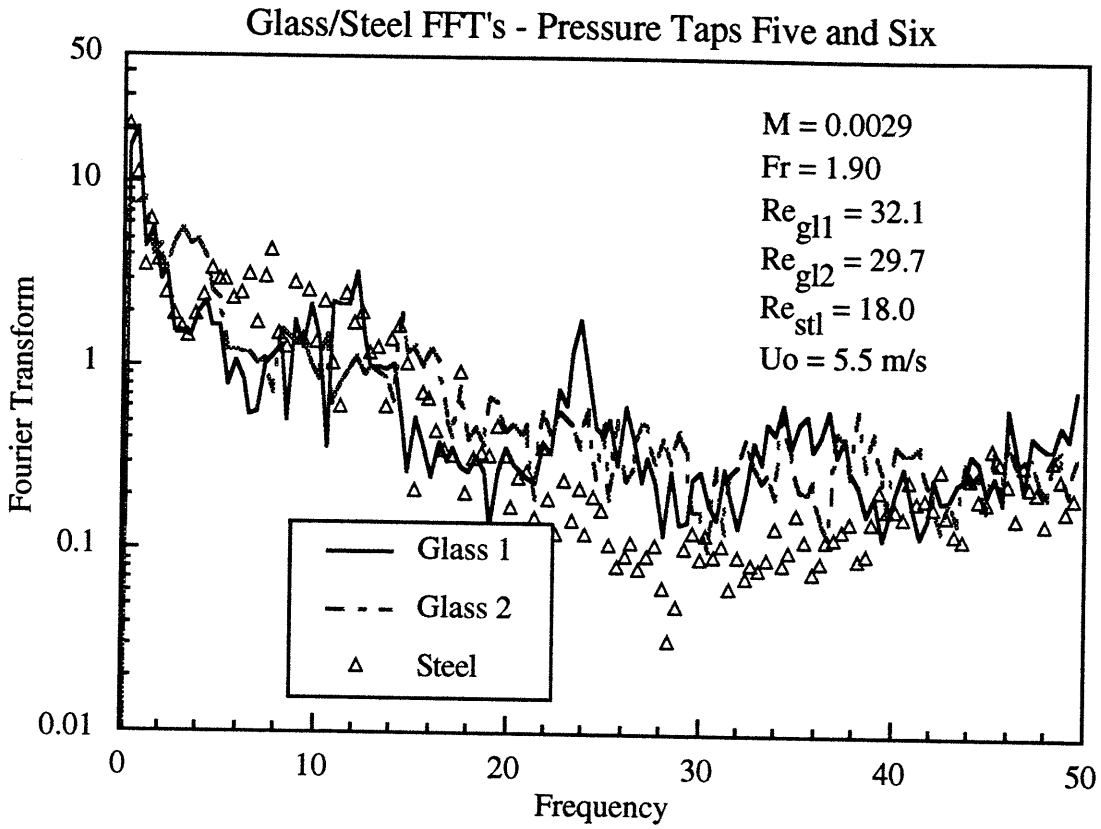

Figure 5.23

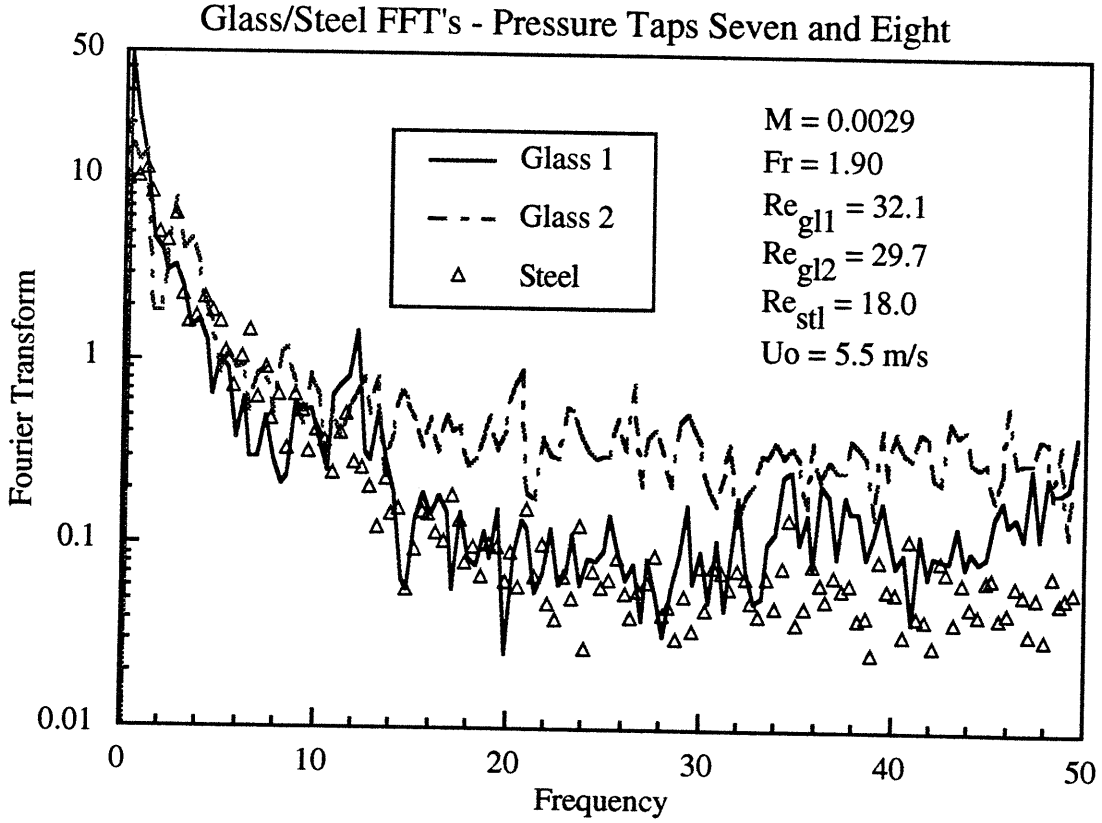

Figure 5.24

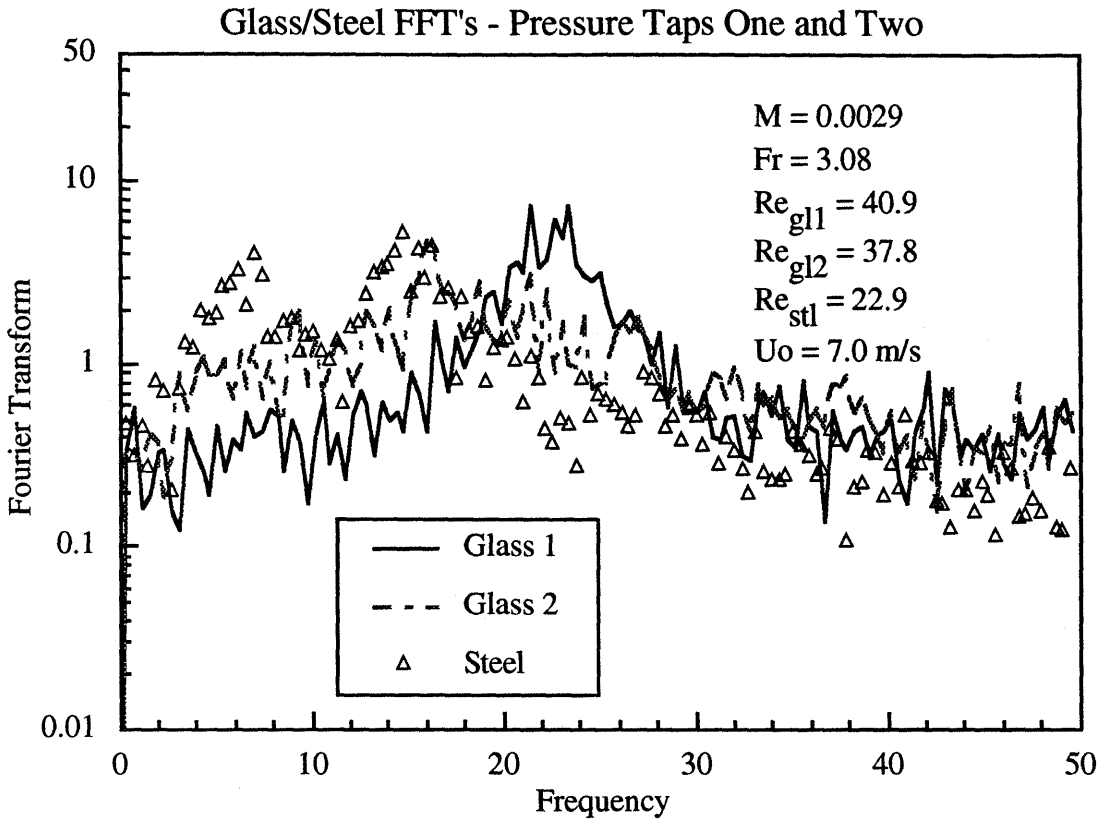

Figure 5.25

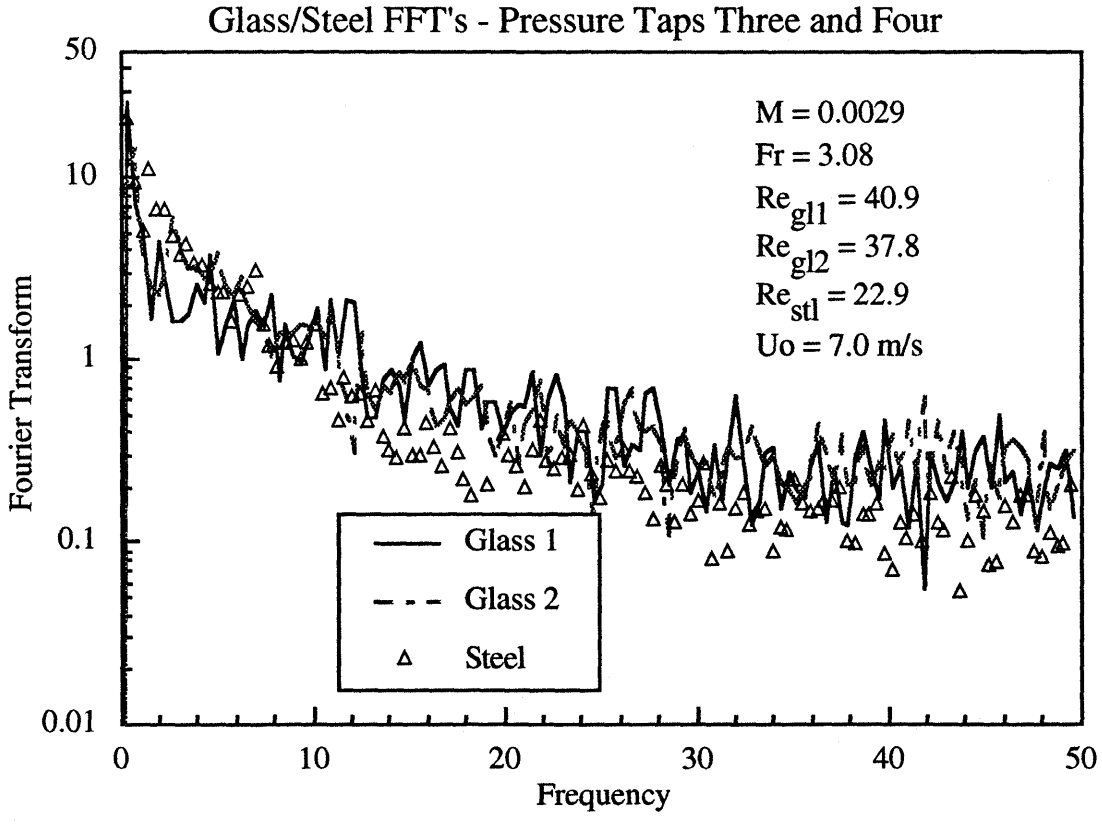

Figure 5.26

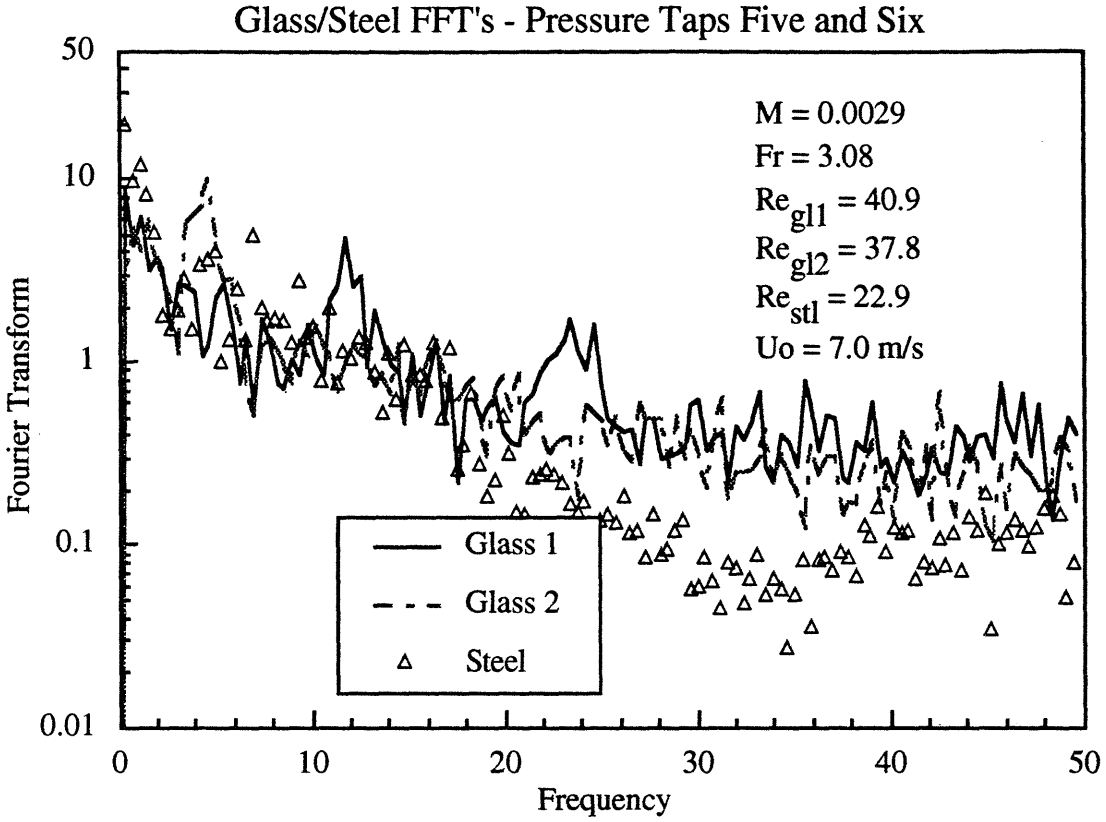

Figure 5.27

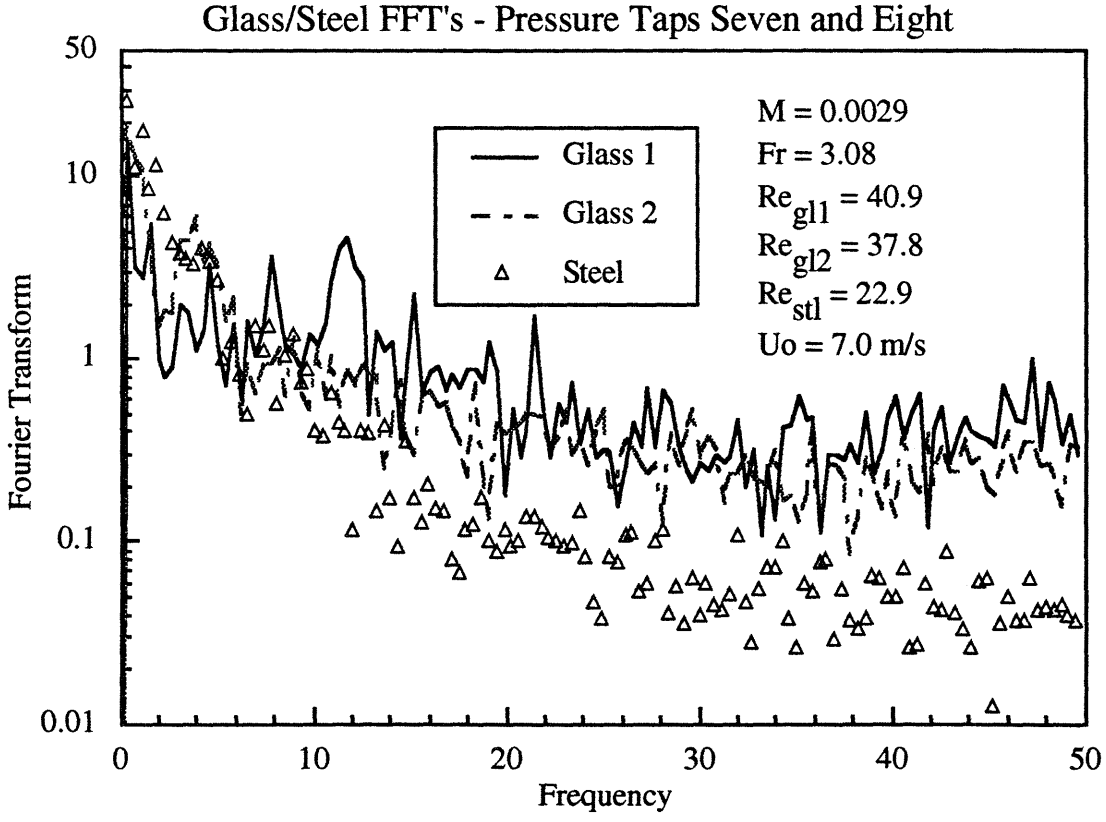

5.1.4 Discussion of Results

The average solid fraction profiles when utilizing the viscous limit scaling laws to scale between glass and steel are not in good agreement over the range of Reynolds numbers based on particle diameter, where the viscous limit parameters should hold. Even more puzzling is the improvement as the superficial velocity, and hence particle Reynolds number, is increased. This is counterintuitive to the argument used to derive the viscous limit scaling laws which predicts that at lower Renolods numbers inertial effects should be less important. Under all operating conditions and in all areas of the bed, the solid fraction profile for the steel was much greater than that for the glass.

The probability density functions for the glass/steel runs were also in poor agreement at low superficial velocities with the steel histograms, covering a much broader band than the glass. As the superficial velocity increased, the probability density functions began to agree somewhat better, although the agreement is still far from satisfactory in the bottom of the bed at 5.5 m/s. At the highest velocity, 7.0 m/s, the agreement is actually better in the bottom of the bed than the top. This is opposite the trend of the lower two velocities. One explanation for these trends is due to bed choking which has been observed in lower sections of beds simulating combustors of larger diameter.

Choking in CFB depends on particle properties, gas properties, and bed geometry. In more dilute systems such as pneumatic transport, choking occurs when the superficial velocity is decreased to the point where the particle weight overcomes the gas shear forces and the suspension begins to collapse. Yang has proposed an empirical relation for the onset of choking based on a study of dense pneumatic systems (Yang, 1983),

$$\frac{2gD\left(\varepsilon_c^{-4.7} - 1\right)}{\left(u_c - u_t\right)^2} = 6.81 \times 10^5 \left(\frac{\rho_g}{\rho_s}\right)^{2.2} \tag{5.2}$$

where the right hand side of the equation is based on frictional losses attributed to the particle phase. Yang went on to suggest that for a uniform suspension with average particle slip velocity u_t

$$G_c = \left[\left(u_f\right)_c - u_t\right]\rho_s\left(1 - \varepsilon_c\right) \tag{5.3}$$

These equations allow for the calculation of solid mass flux and average bed solid fraction at the onset of choking. Chang and Louge (1992) compared Yang's correlation with data they

obtained for choking in a cold circulating fluidized bed for plastic and steel powders and found it to be in excellent agreement.

For the steel and glass particles used in the present experiments, Yang's correlation gave the predictions shown in Figure 5.28. It can be seen that for the nondimensional solids flow rate used in the tests, the predicted superficial velocity at the onset of choking for steel is about 3.0 m/s and for glass is 1.25 m/s. For tests conducted at 3.0 m/s, choking would be predicted in the steel runs. Because the Yang correlation indicates that choking is a strong function of the solid to gas density ratio, it may be that the viscous limit scaling laws are unable to model choked bed hydrodynamics or the transition to choking. For the test condition with the highest superficial velocity where both the steel and glass are well above choking, the viscous limit gives the best agreement between the glass and steel particles. A more detailed discussion of choking and its impact on hydrodynamic scaling is included in Section 6.3.

Figure 5.28
1/4 Scale UBC Bed Velocities of Incipient Choking - Yang Correlation

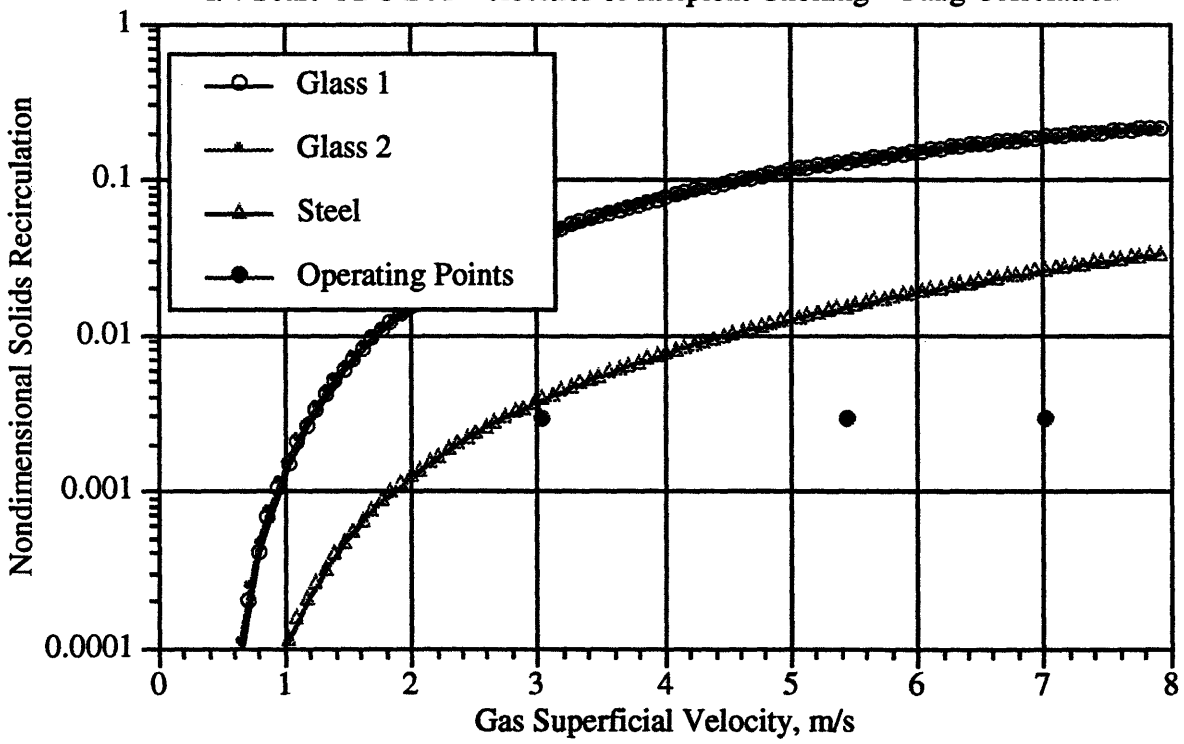

The power spectral densities for the glass/steel runs showed better agreement at the lower sections of the bed than closer to the top. This is especially true of the tests conducted at the highest superficial velocity (7.0 m/s). This contradicts the histograms which generally showed better agreement near the top of the bed.

Attempts to reduce to the superficial velocity further (superficial velocities around 2.5 m/s) to lower the particle Reynolds number were not successful because of violent slugging when running with steel which posed a threat to the bed's integrity.

The difference in the particle size distributions between glass sample one and two should illuminate deviations caused by not matching distributions as opposed to the elimination of the solid to gas density ratio. However, no clear consistent trend can be deduced from the data except, perhaps, that a change in particle size and distribution of this magnitude is of relatively little significance when compared to the steel curve.

An investigation was conducted to determine if scaling similarity could be achieved with the viscous limit scaling laws if one or several of the remaining nondimensional parameters were modified. From the average solid fraction profiles and histograms, it is obvious that the glass runs require a larger pressure drop and fluctuations over a broader range of frequencies if the runs were to be similar to the steel. It was determined that the particle size and solid mass flux should be reanalyzed to determine their effects on similarity.

The effect of particle diameter is shown in Figure 5.29. Glass particles with a mean diameter of 117.8 microns are compared to glass particles with a mean diameter of 88.3 microns at a superficial velocity of 3.0 m/s. The result was a small increase in solid fraction over most of the bed length, but still much too small to account for the disagreement with the steel. It is possible that further increses in particle size may have the desired effect, but it is difficult to postulate a model that would justify doing so. The data suggests that the bed behavior is not sensitive to mean particle diameter.

Figure 5.29

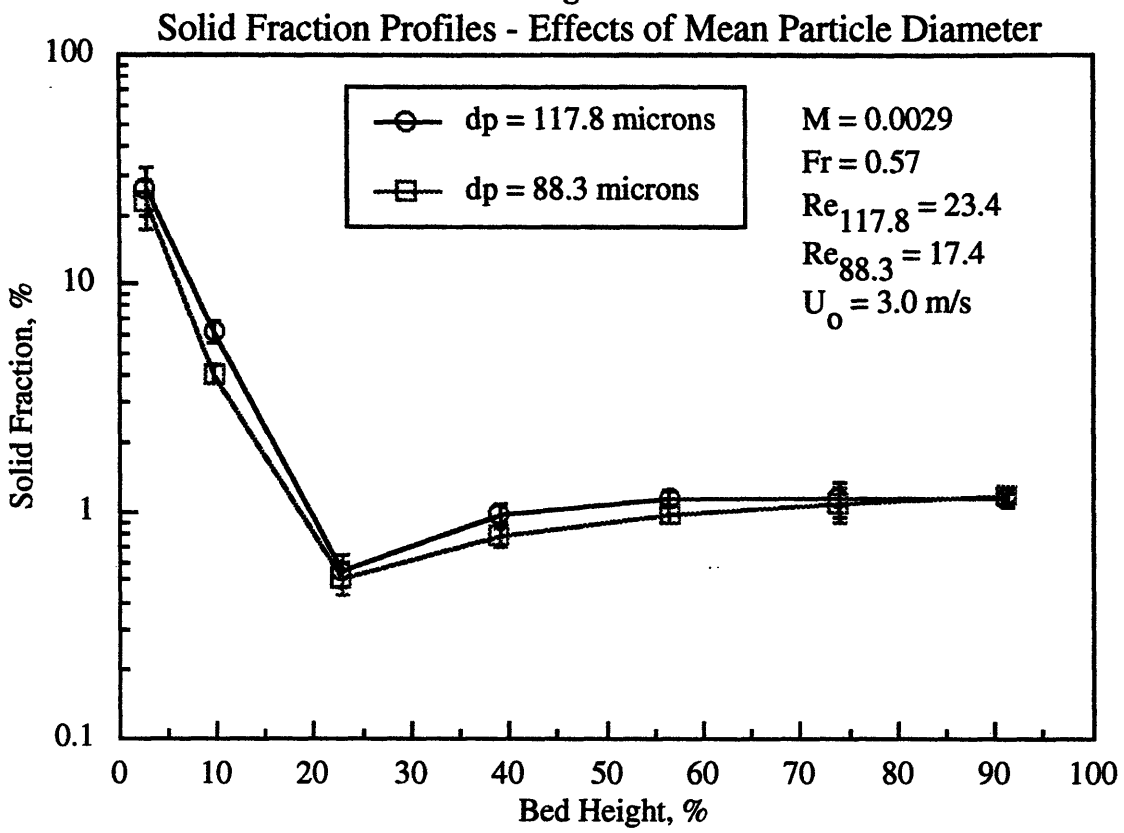

The effect of increasing the mass flux by a factor equal to the diameter ratio between the glass and steel (a factor of 1.65) on the solid fraction profile is depicted in Figures 5.30 and 5.31. There is a significant improvement in both the magnitude of the solid fraction and in the histograms of solid fractions. It may be that the scaling parameter $\frac{\dot{m}}{\mu d_p}$ can be justified as a reduction of $\frac{\dot{m}u_o}{F_{Drag}}$, where F_{Drag} is the drag force on a single particle, in the following manner:

$$F_{Drag} \sim \frac{1}{2} A_{cs} C_D \rho_f u_o^2 \tag{5.4}$$

and

$$C_D \sim \frac{\mu}{u_o d_p \rho_f} \text{ in the viscous regime where } u_o \sim u_{sl}. \tag{5.5}$$

Then

$$F_{Drag} \sim u_o \mu d_p \tag{5.6}$$

and

$$\frac{\dot{m}u_o}{F_{Drag}} \sim \frac{\dot{m}}{\mu d_p} \tag{5.7}$$

Figure 5.30
Solid Fraction Profiles - Effect of Increasing Solids Loading

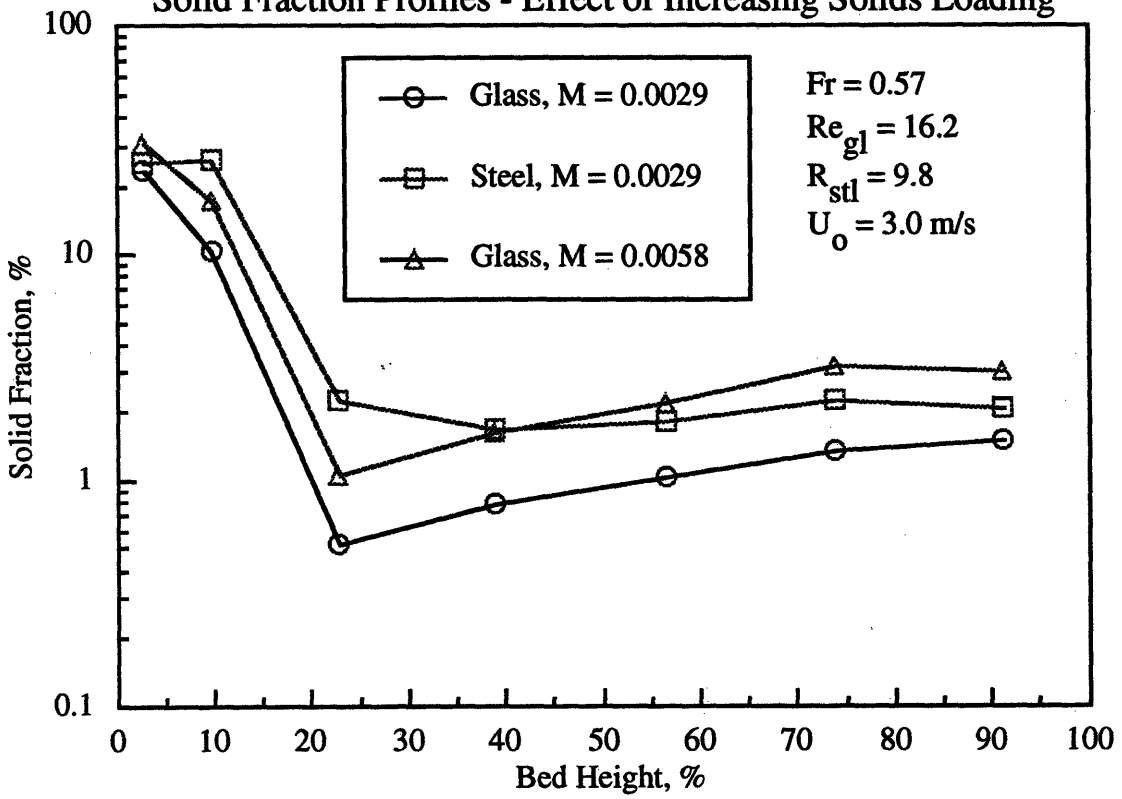

Figure 5.31

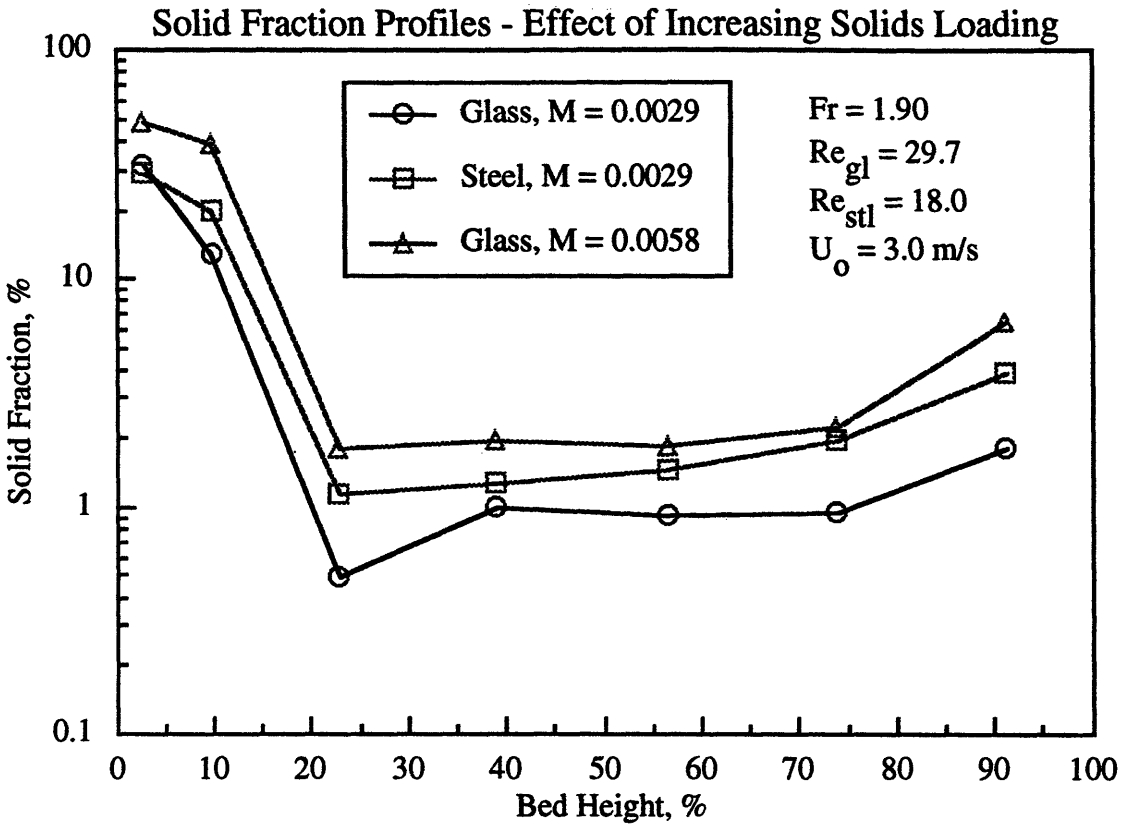

But it is not likely that this scaling will hold under different test conditions. This ad hoc scaling parameter cannot be justified based on the formal scaling laws; it is not much more than an empirical fit to the data. Figure 5.32 depicts the effect of varying the solids loading through a wide range.

Figure 5.32

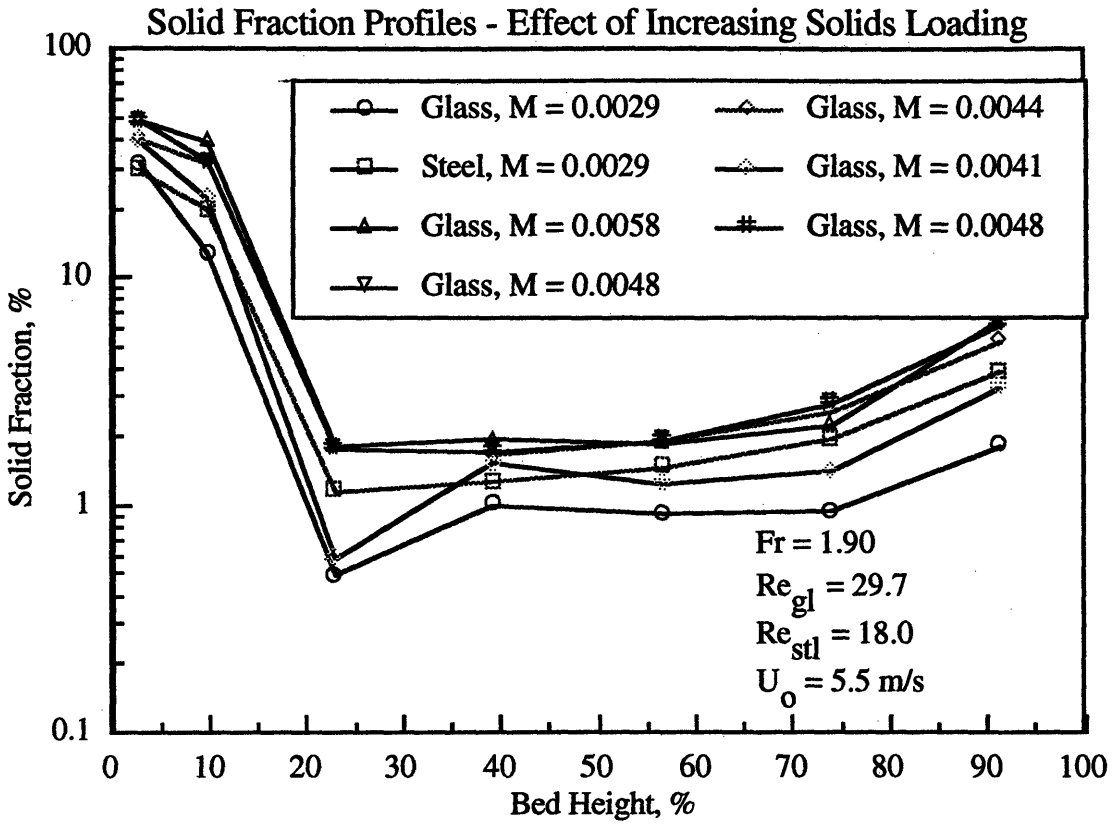

5.2 Viscous Limit Scaling Between Glass and Plastic

Tables 5.6 through 5.8 provide the operational data, along with information concerning the particles and bed utilized in the glass/plastic viscous limit evaluations. In these Tables, Ga represents the Galileo number defined as $\frac{\rho_s^2 d_{pg}^3 g}{\mu_f^2}$. Tests were conducted at three different superficial velocities, and at the same nondimensional solid flux utilizing the phase one 1/16 scale Studsvik bed.

Table 5.6

Glass/Plastic Viscous Limit Scaling - Condition 1

	Glass 1	Steel
u_o (m/s)	1.5	1.5
u_{mf} (cm/s) Ergun Eqn.	1.42	1.25
u_{mf} (cm/s) measured	1.40	0.85
d_p (microns)	78.7	99.5
L (m)	0.46	0.46
A_{cs} (m^2)	1.05E-3	1.05E-3
G_s (kg/m^2-s)	27.5	15.1
$Re_{dp,uo}$	7.81	9.88
$Re_{L,uo}$	4.54E4	4.54E4
Fr	0.50	0.50
$\left(\frac{u_o}{u_{mf}}\right)_{Ergun\ eqn.}$	105.7	120.0
$\left(\frac{u_o}{u_{mf}}\right)_{measured}$	107.1	176.5
$\left(\frac{G_s}{\rho_s u_o}\right)$	7.2E-3	7.2E-3
$\left(\frac{\rho_s}{\rho_f}\right)$	2117	1167
Ga	9.39E5	5.76E4

Table 5.7

Glass/Plastic Viscous Limit Scaling - Condition 2

	Glass 1	Steel
u_o (m/s)	2.0	2.0
u_{mf} (cm/s) Ergun Eqn.	1.42	1.25
u_{mf} (cm/s) measured	1.40	0.85
d_p (microns)	78.7	99.5
L (m)	0.46	0.46
A_{cs} (m^2)	1.05E-3	1.05E-3
G_s (kg/m^2-s)	27.5	15.1
$Re_{dp,uo}$	10.4	13.2
$Re_{L,uo}$	6.06E4	6.06E4
Fr	0.89	0.89
$\left(\frac{u_o}{u_{mf}}\right)_{Ergun\ eqn.}$	140.9	160.0
$\left(\frac{u_o}{u_{mf}}\right)_{measured}$	142.9	235.3
$\left(\frac{G_s}{\rho_s u_o}\right)$	5.4E-3	5.4E-3
$\left(\frac{\rho_s}{\rho_f}\right)$	2117	1167
Ga	9.39E5	5.76E4

Table 5.8

Glass/Plastic Viscous Limit Scaling - Condition 3

	Glass 1	Steel
u_o (m/s)	2.5	2.5
u_{mf} (cm/s) Ergun Eqn.	1.42	1.25
u_{mf} (cm/s) measured	1.40	0.85
d_p (microns)	78.7	99.5
L (m)	0.46	0.46
A_{cs} (m^2)	1.05E-3	1.05E-3
G_s (kg/m^2-s)	27.5	15.1
$Re_{dp,uo}$	13.0	16.5
$Re_{L,uo}$	7.57E4	7.57E4
Fr	1.39	1.39
$\left(\frac{u_o}{u_{mf}}\right)_{Ergun\ eqn.}$	176.1	200.0
$\left(\frac{u_o}{u_{mf}}\right)_{measured}$	178.6	294.1
$\left(\frac{G_s}{\rho_s u_o}\right)$	4.3E-3	4.3E-3
$\left(\frac{\rho_s}{\rho_f}\right)$	2117	1167
Ga	9.39E5	5.76E4

5.2.1 Solid Fraction Profiles

The average solid fraction profiles for the glass/plastic viscous limit evaluation are given in Figures 5.33 through 5.35. The tabulated data is given in Appendix E. The calculated solid fractions are plotted versus the average of the heights of the associated pressure taps. Error bars are based on calculated standard deviations in solid flow measurements and pressure time traces.

5.2.2 Histograms

Histograms of the solid fraction data of the viscous limit scaling for glass and plastic are depicted in Figures 5.36 through 5.47. Histograms are shown for solid fractions between pressure taps 1 and 2, 3 and 4, 5 and 6, 7 and 8. In these plots, probability is plotted versus

the solid fraction (recall that the pressure taps are numbered from the bottom of the bed to the top).

5.2.3 Power Spectral Densities

FFT's of the pressure fluctuation data for the glass/plastic viscous limit tests are given in Figures 5.48 through 5.59. FFT's are shown for the same pressure taps as the probability density functions. In these plots, the fourier transform in plotted versus the frequency in Hz.

Figure 5.33

Solid Fraction Profiles - Glass/Plastic Viscous Limit Scaling

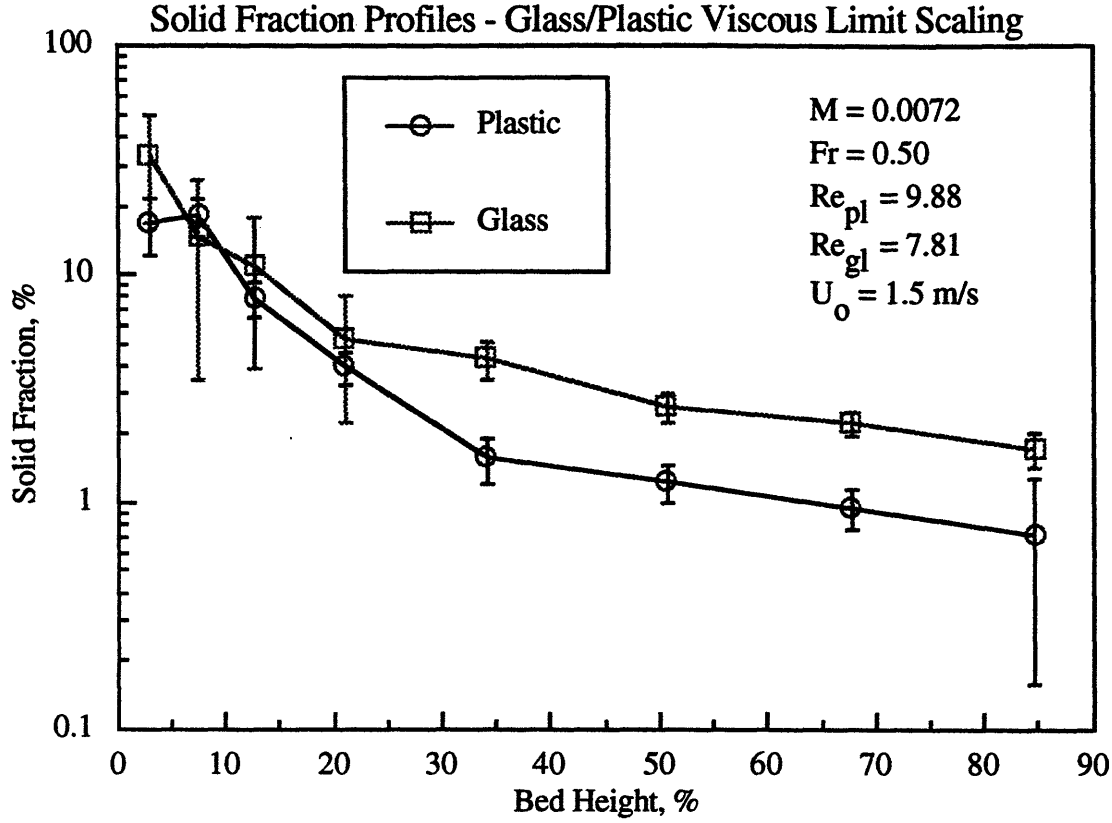

Figure 5.34

Solid Fraction Profiles - Glass/Plastic Viscous Limit Scaling

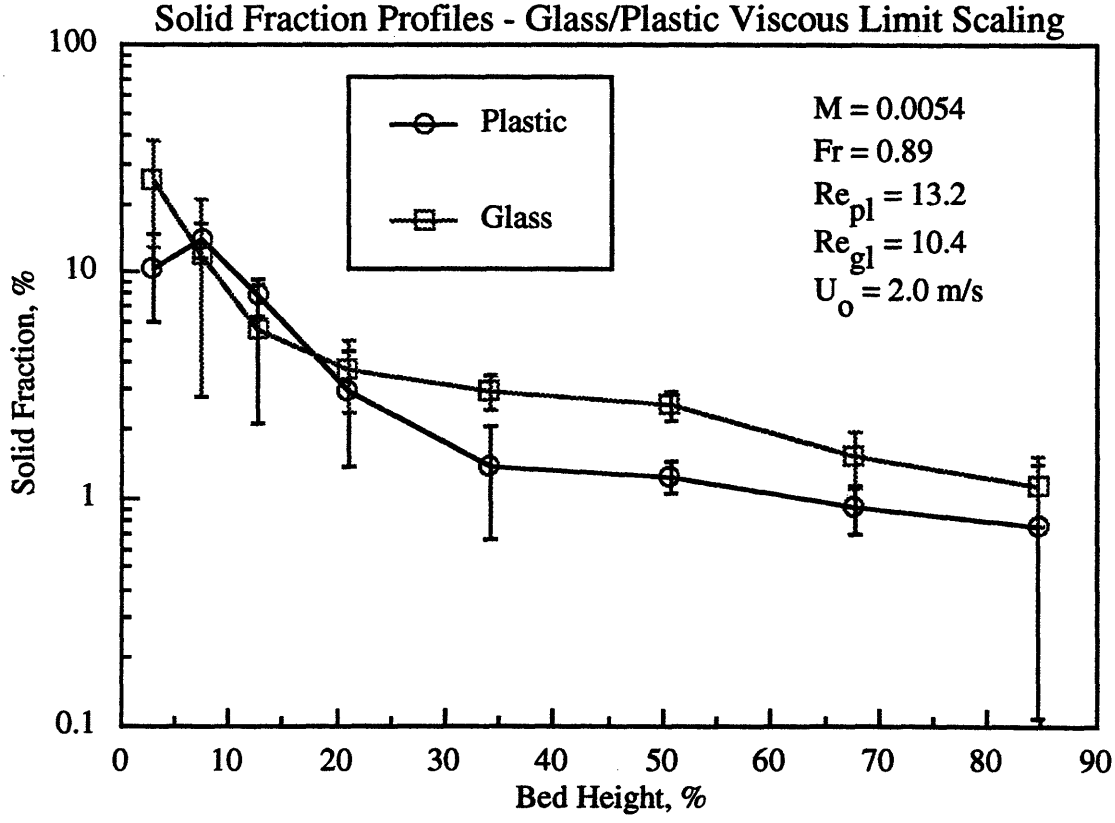

Figure 5.35

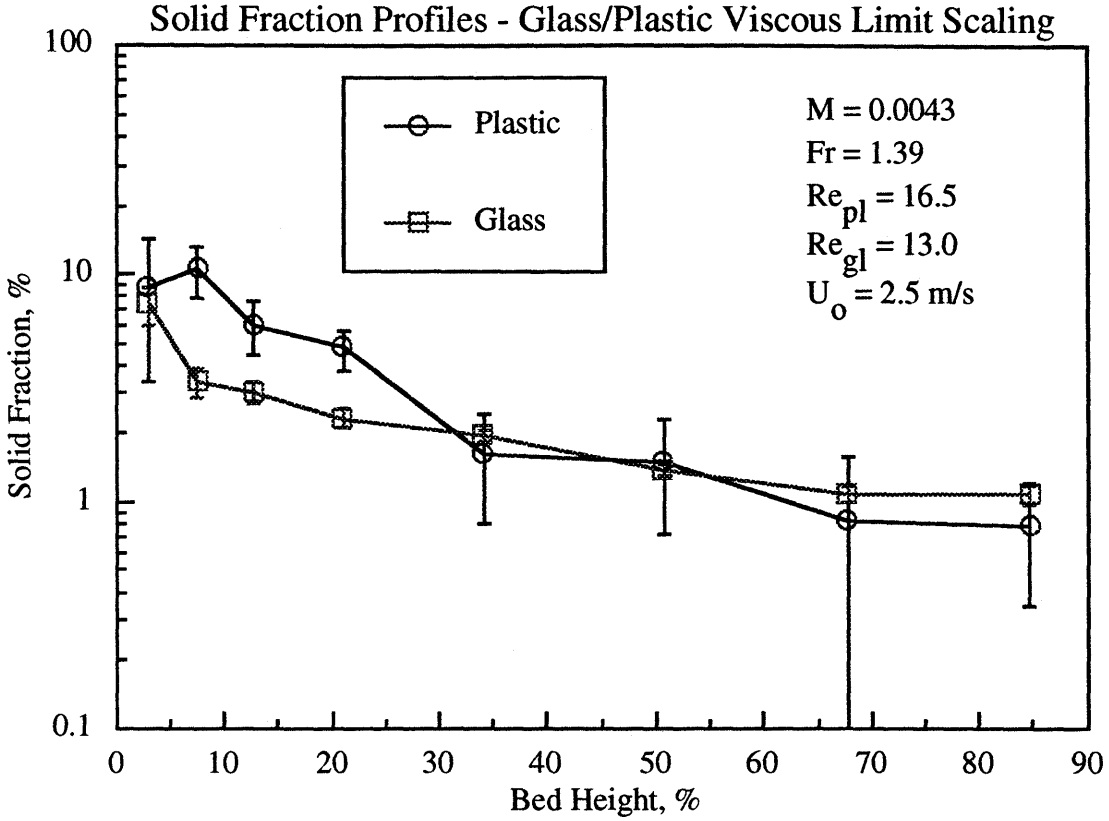

Figure 5.36

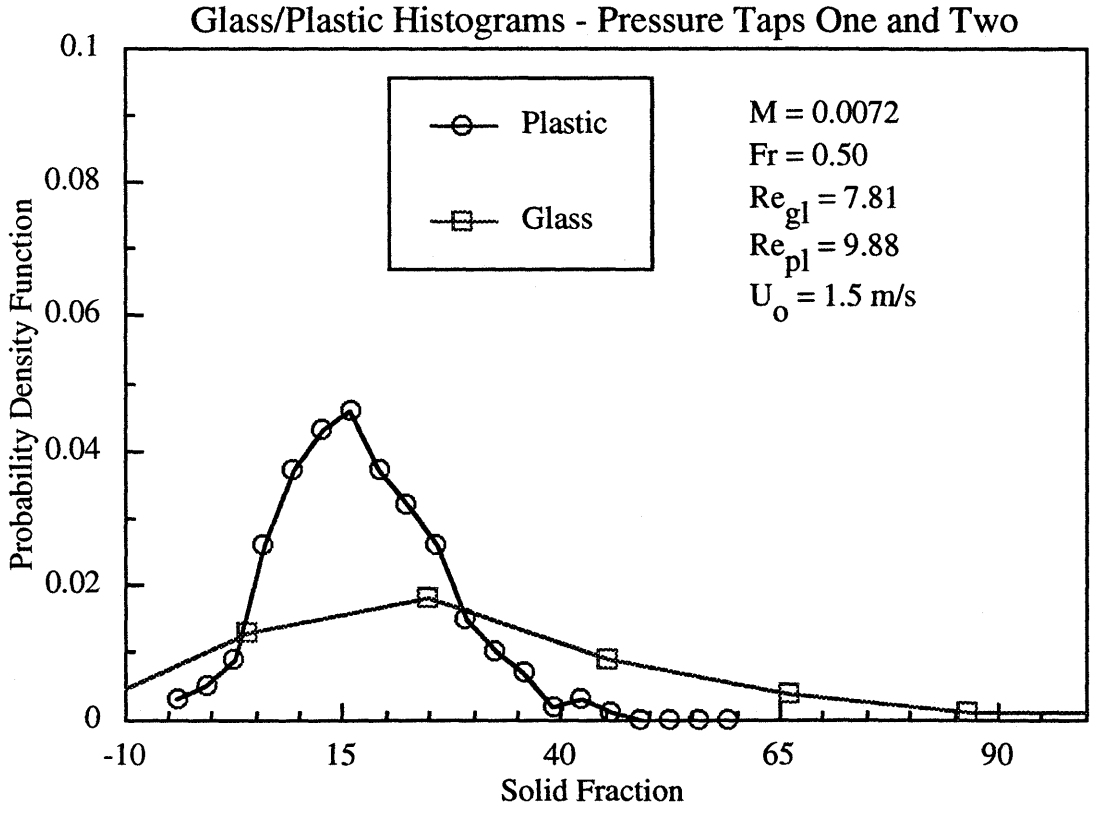

Figure 5.37

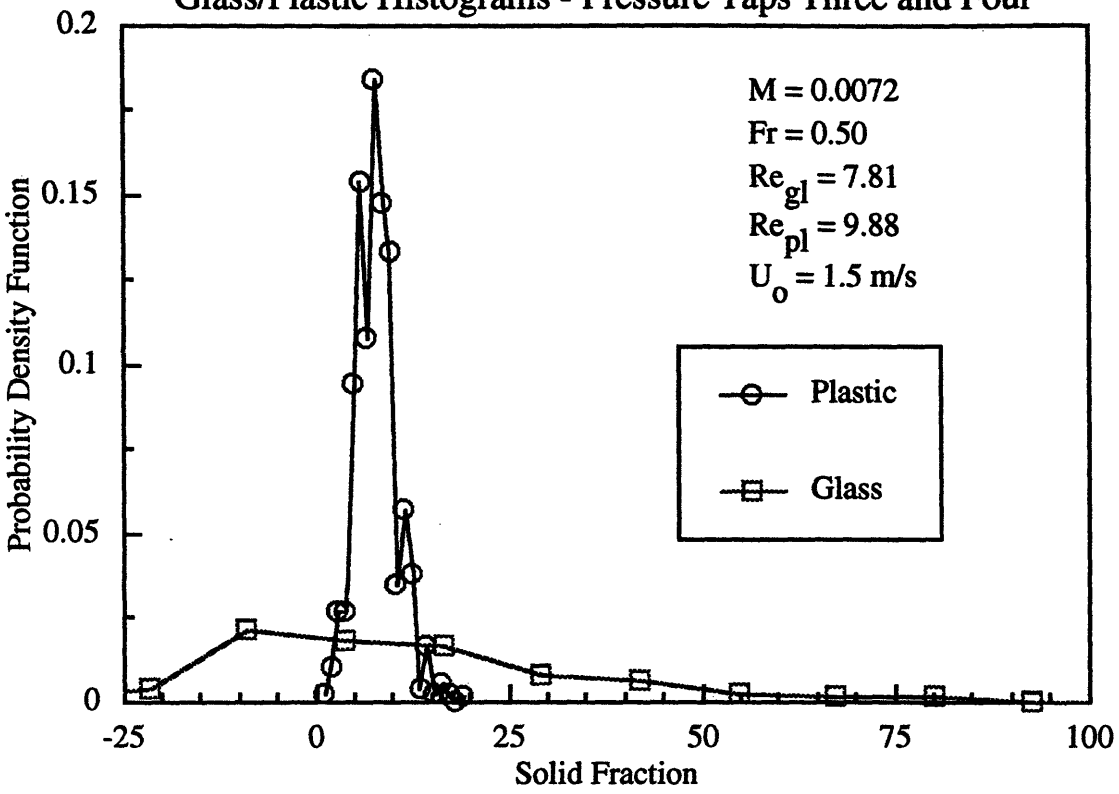

Figure 5.38

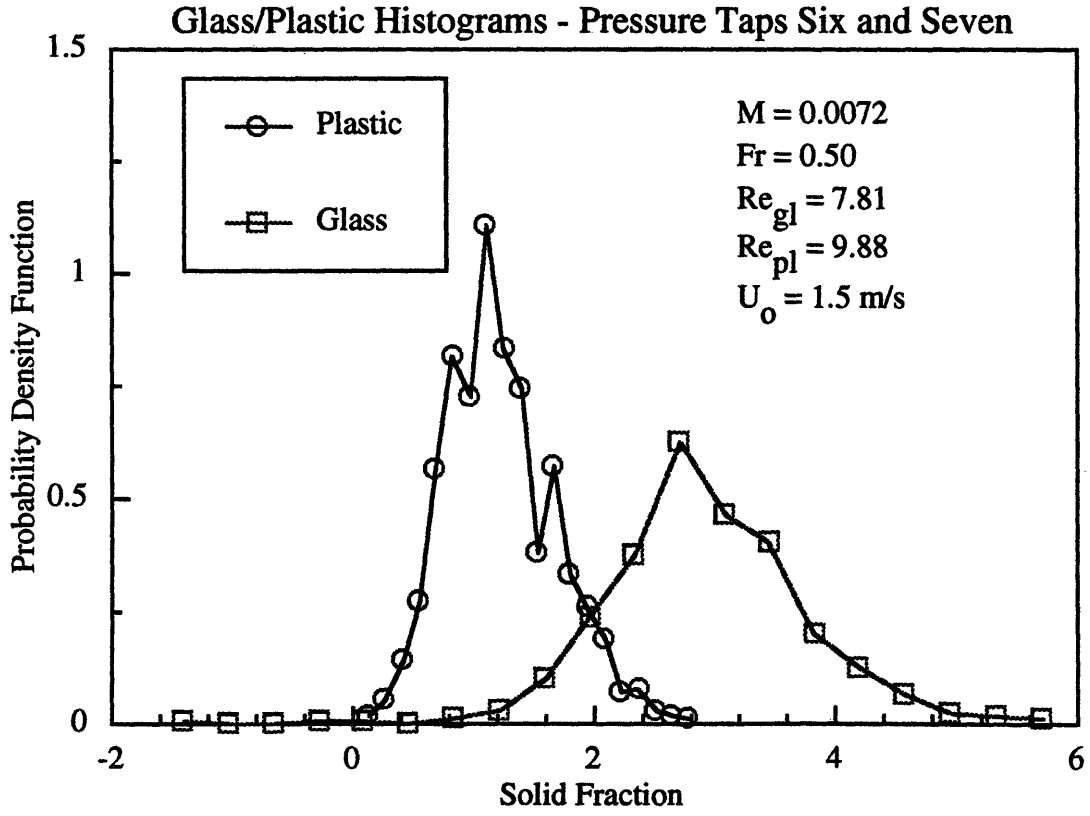

Figure 5.39

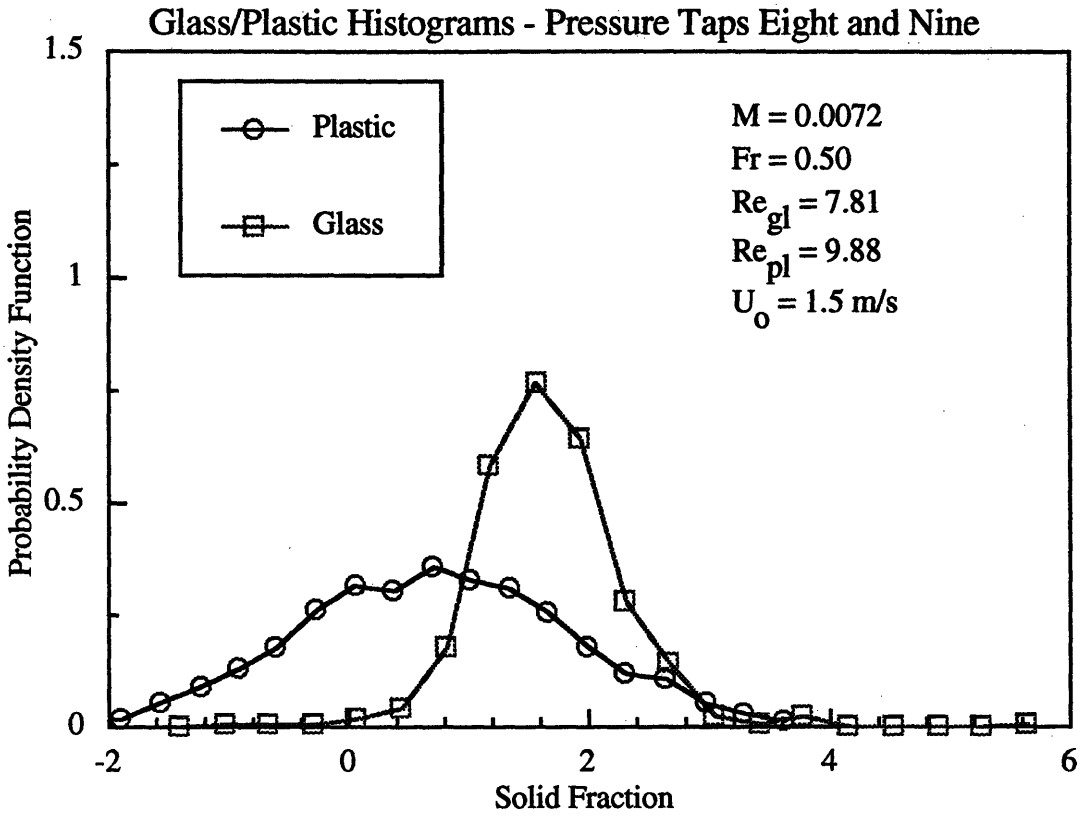

Figure 5.40

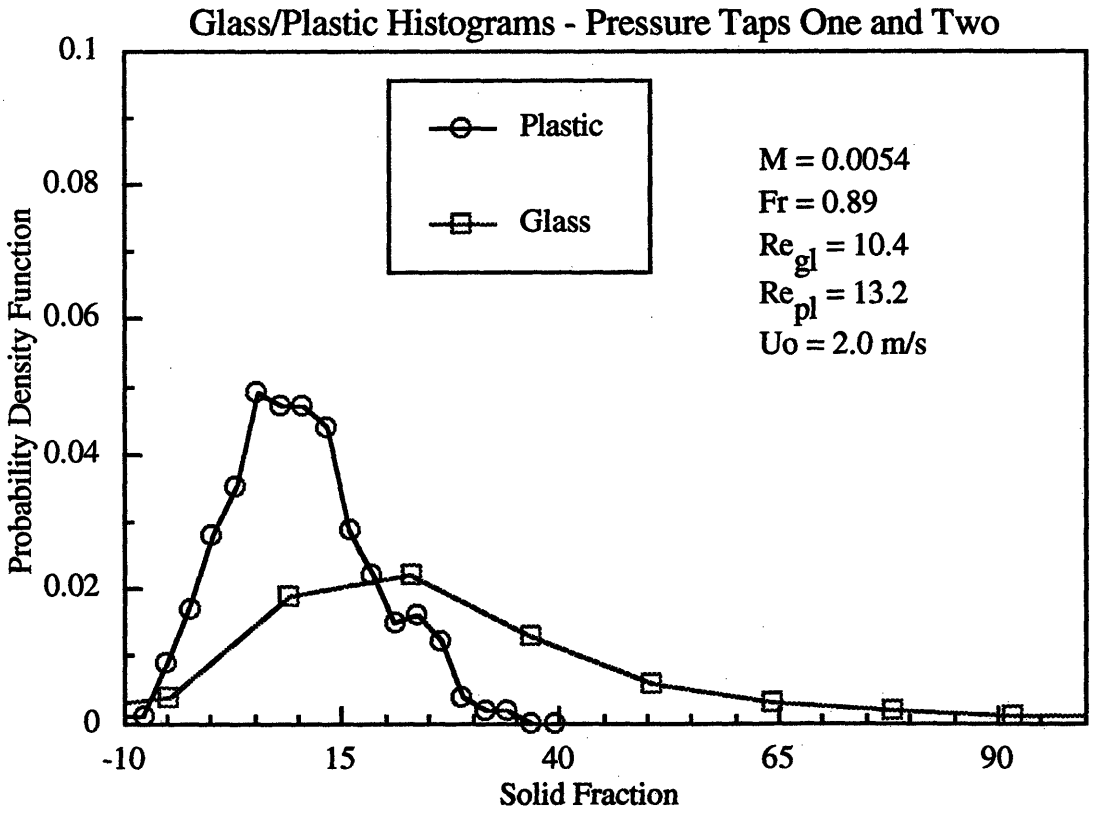

Figure 5.41

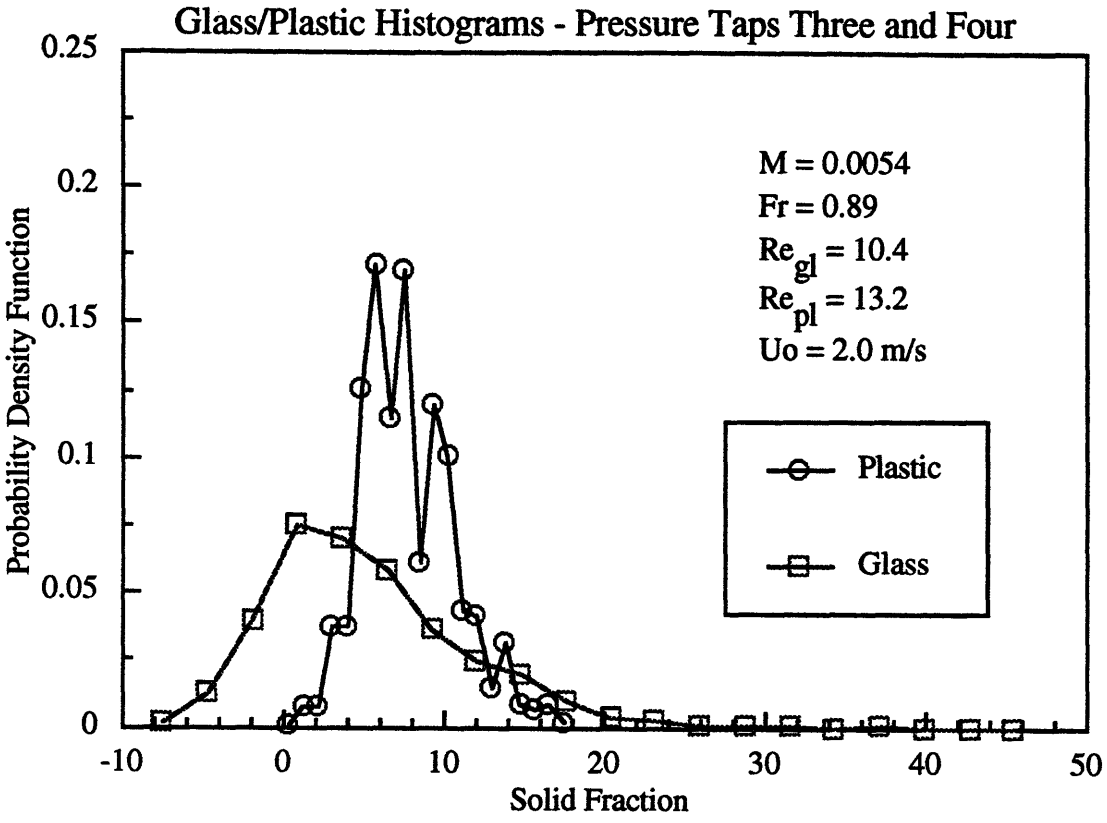

Figure 5.42

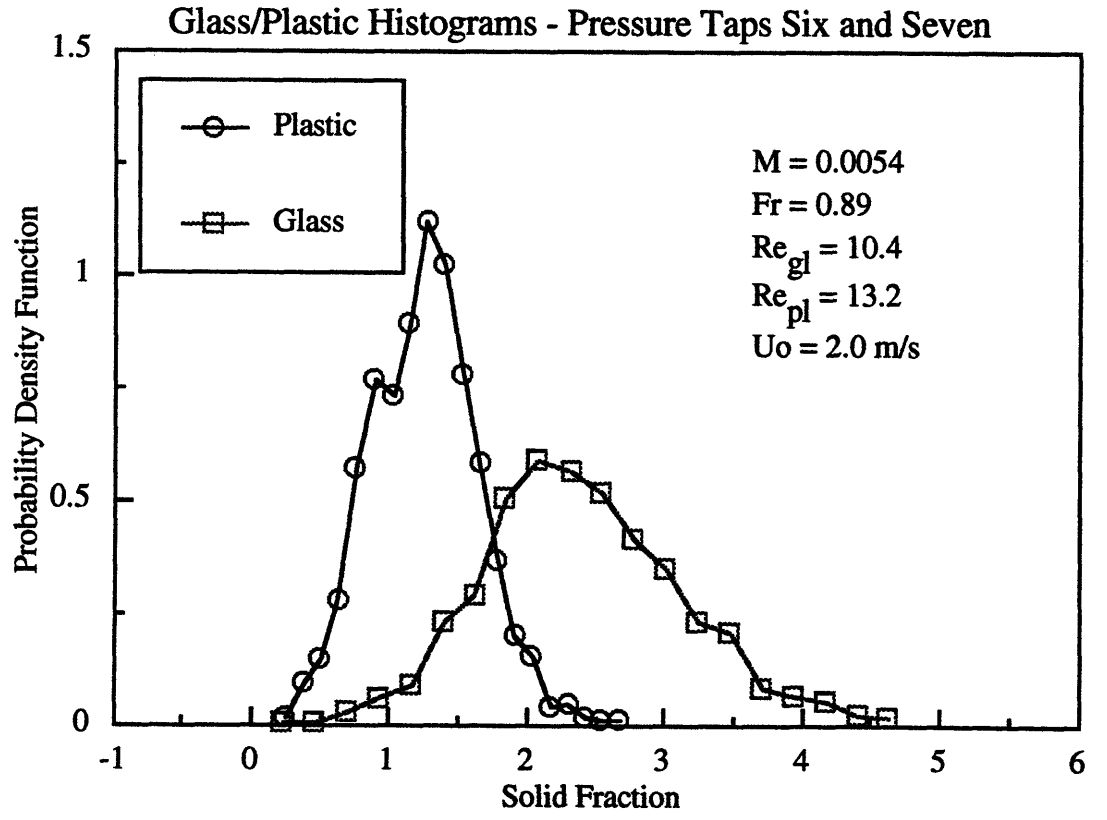

Figure 5.43

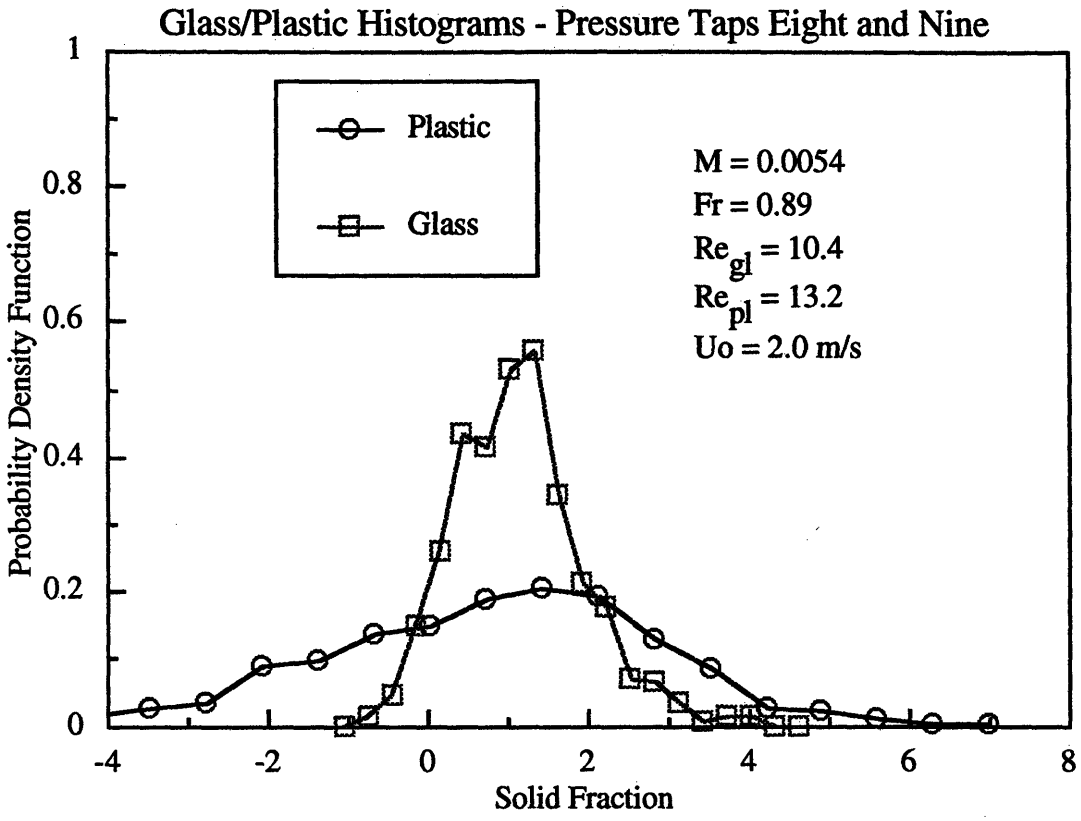

Figure 5.44

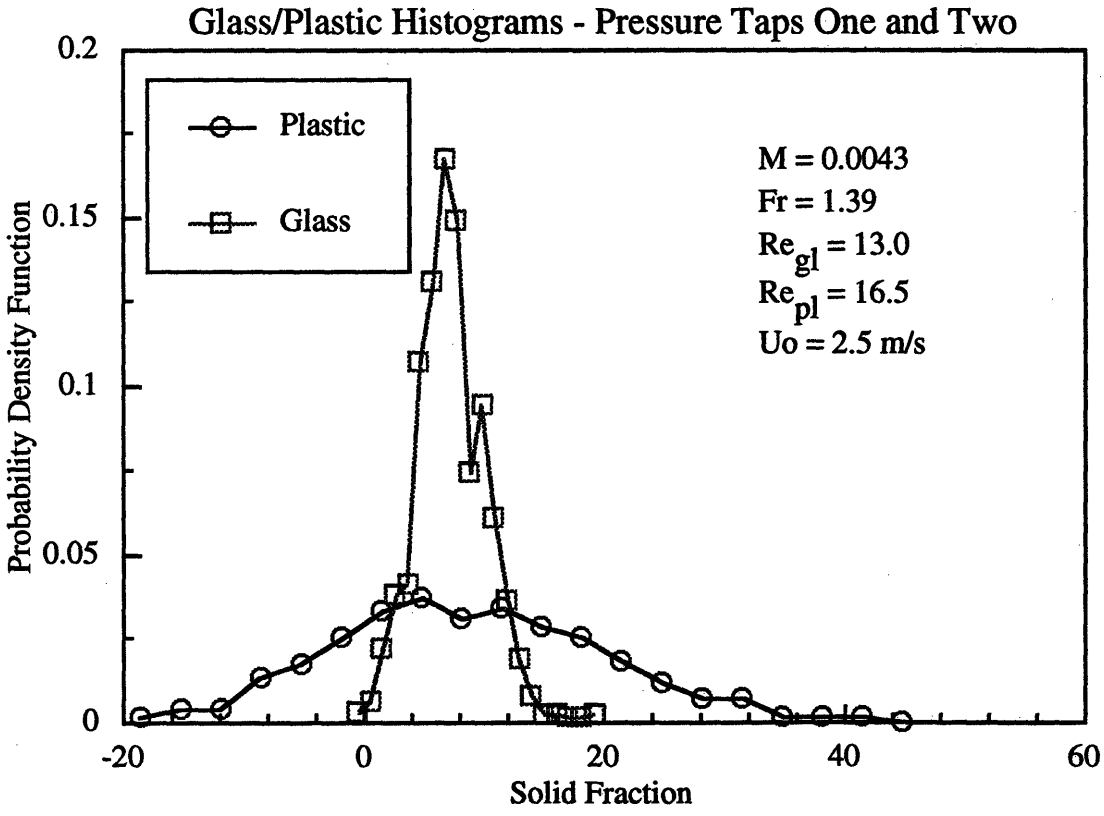

Figure 5.45

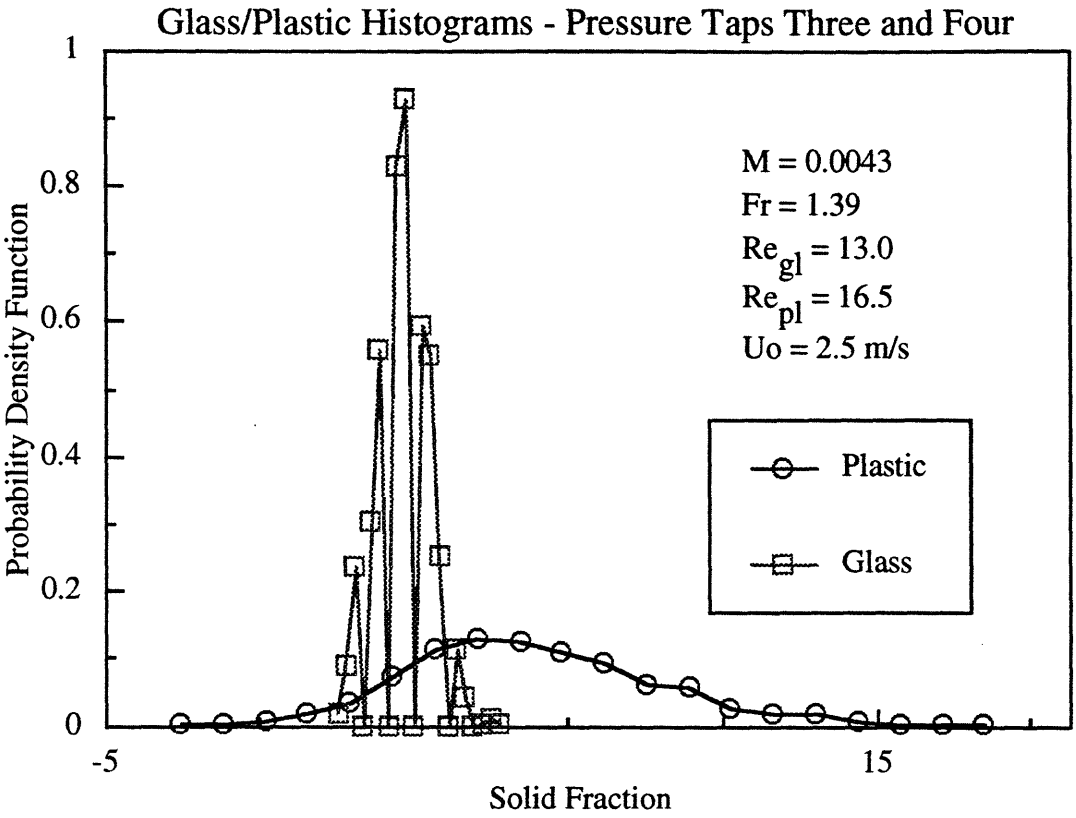

Figure 5.46

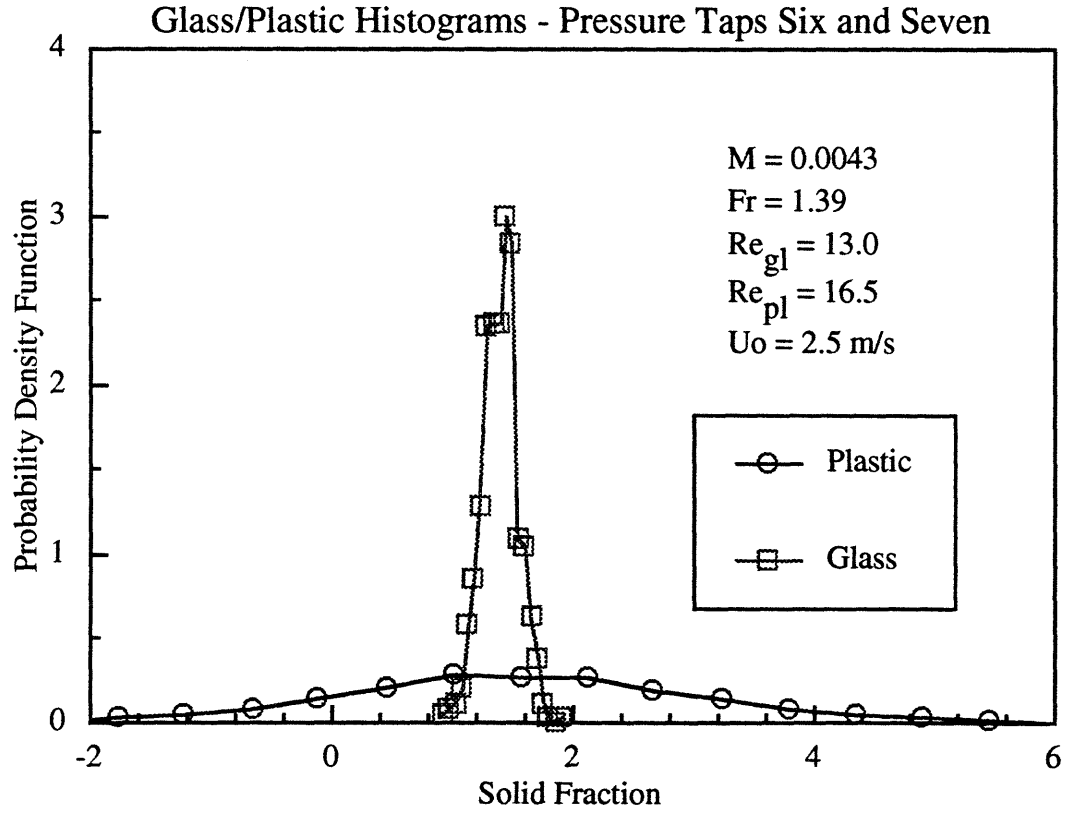

Figure 5.47

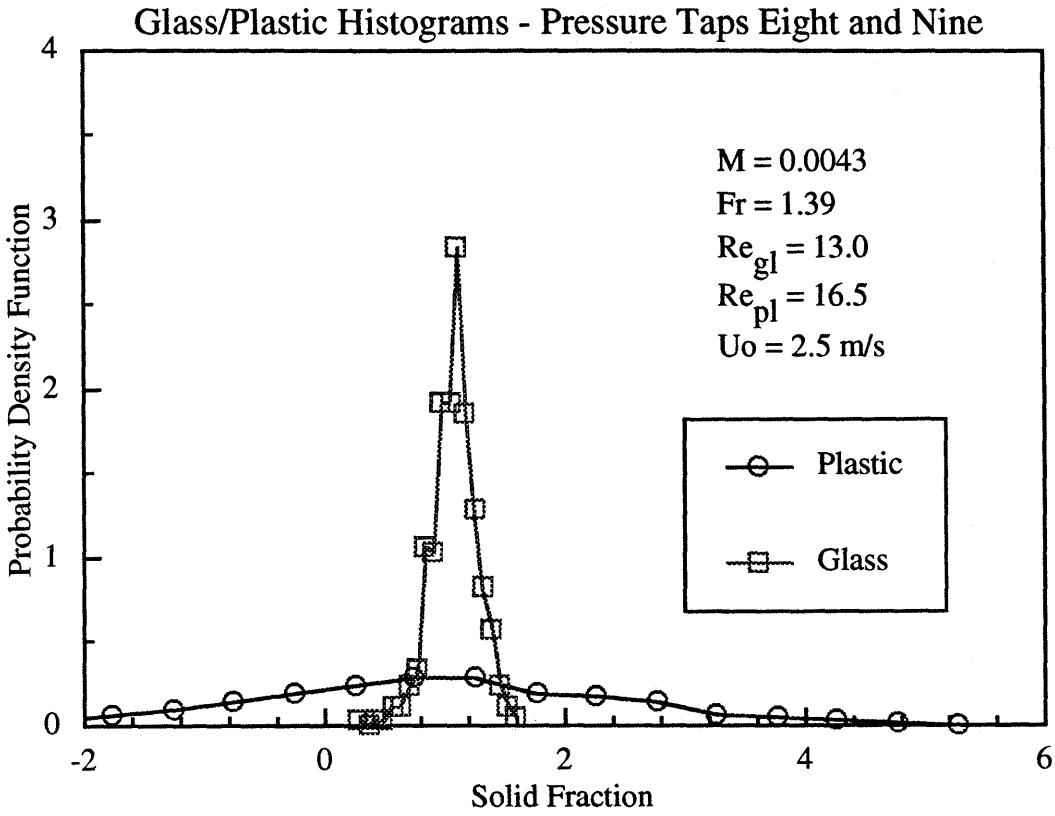
Glass/Plastic Histograms - Pressure Taps Eight and Nine
Probability Density Function
Solid Fraction
M = 0.0043
Fr = 1.39
Re_gl = 13.0
Re_pl = 16.5
Uo = 2.5 m/s
Plastic
Glass
0
1
2
3
4
-2
0
2
4
6

Figure 5.48

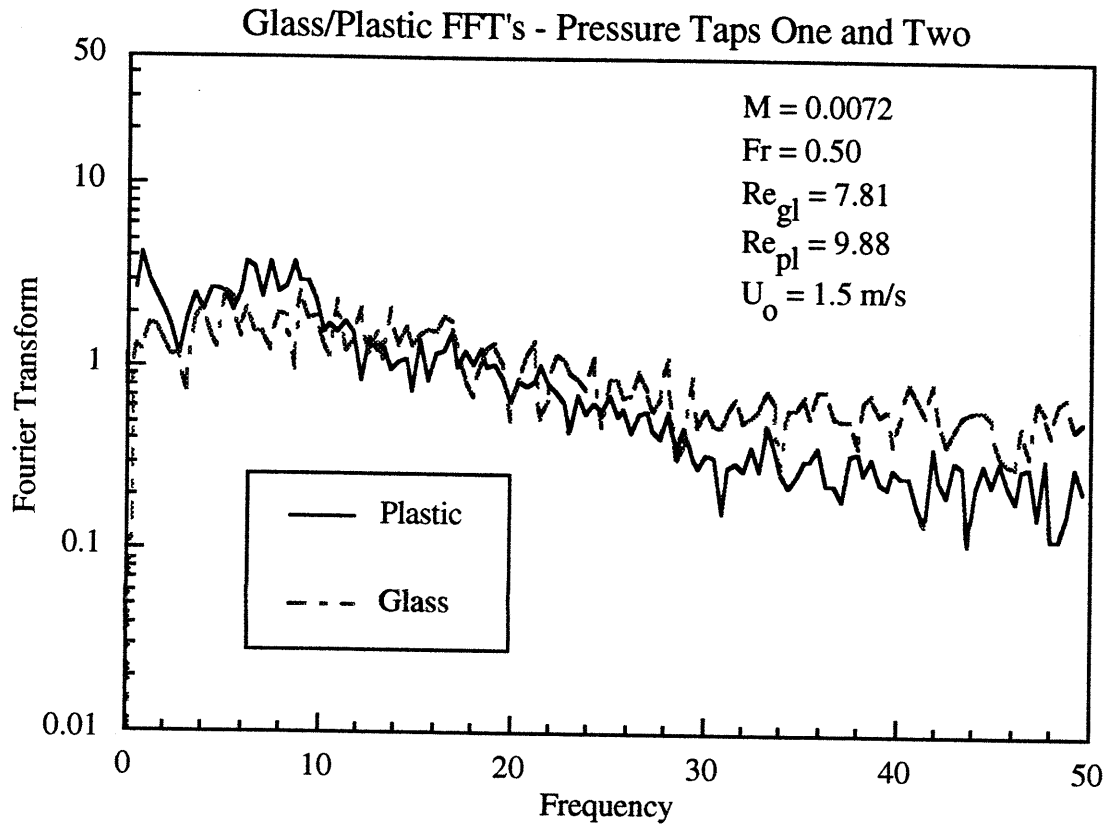

Figure 5.49

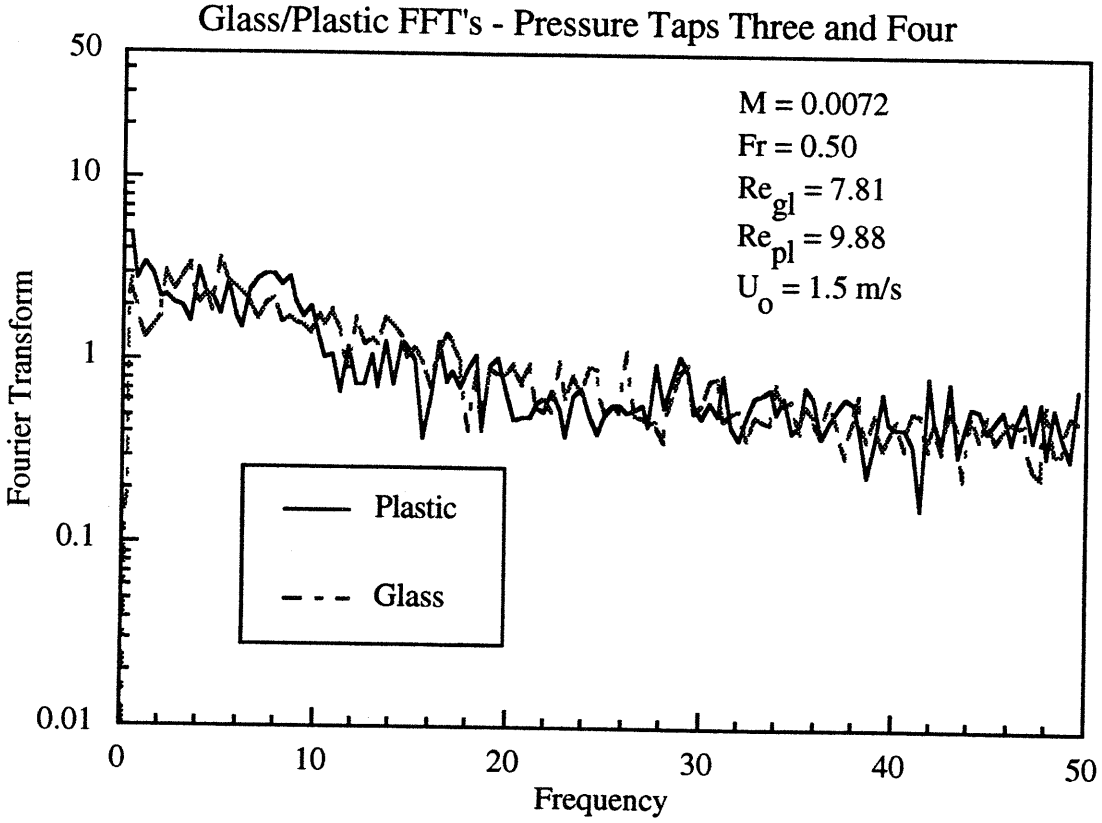

Figure 5.50

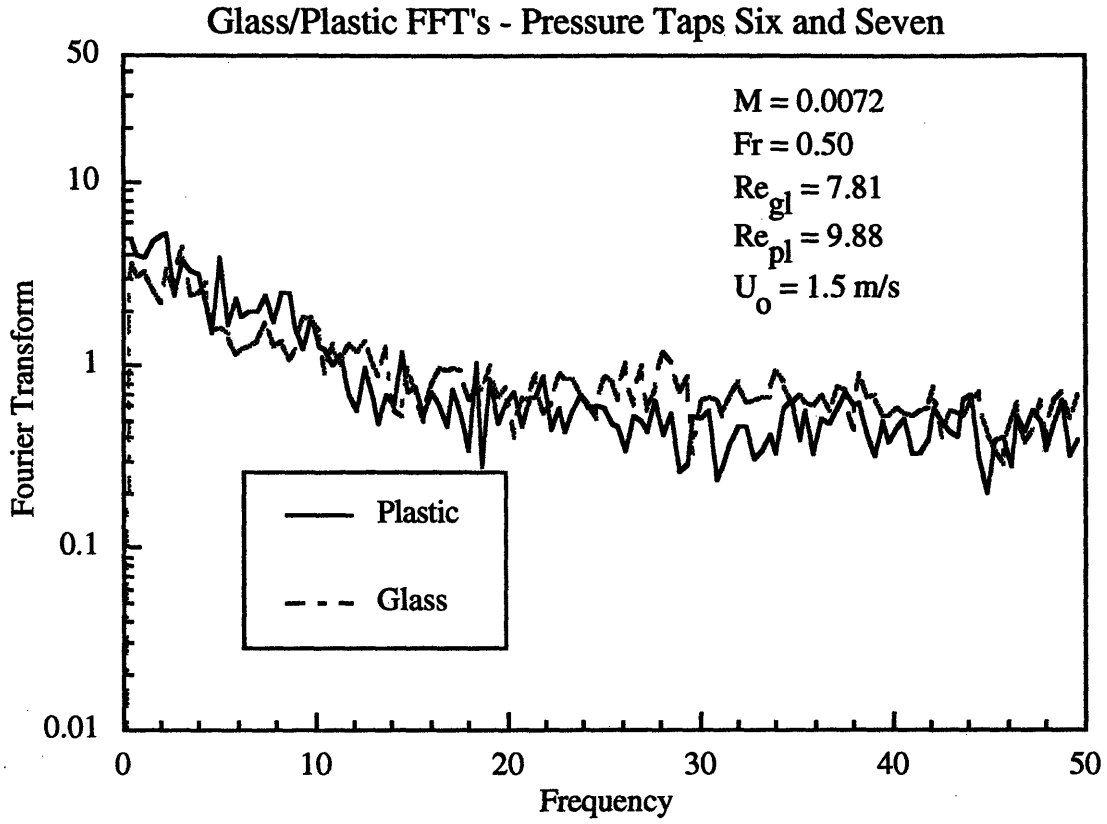

Figure 5.51

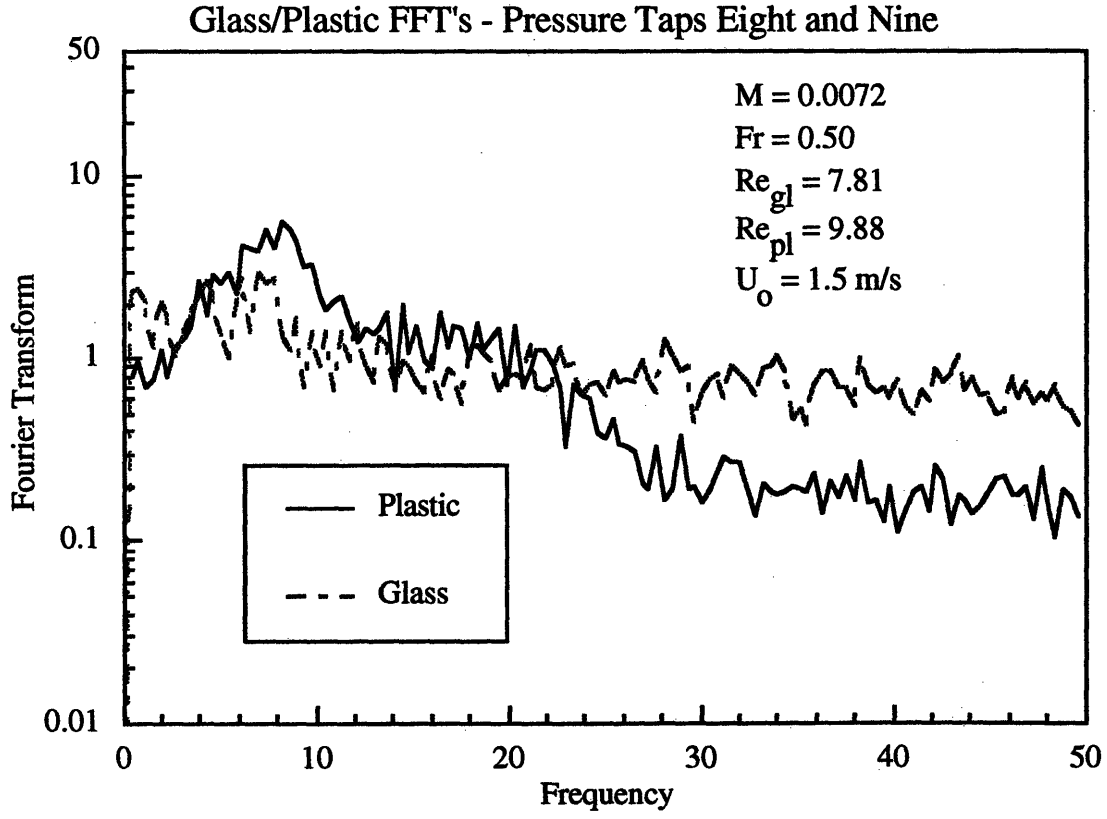

Figure 5.52

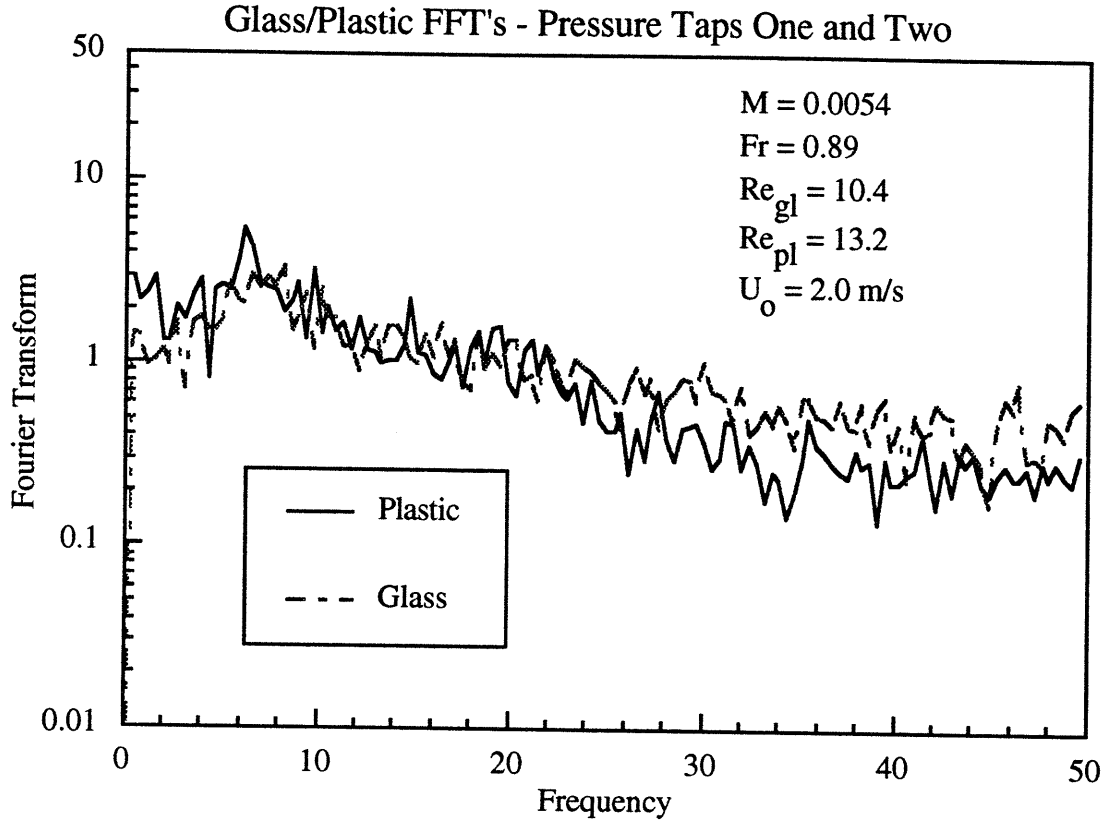

Figure 5.53

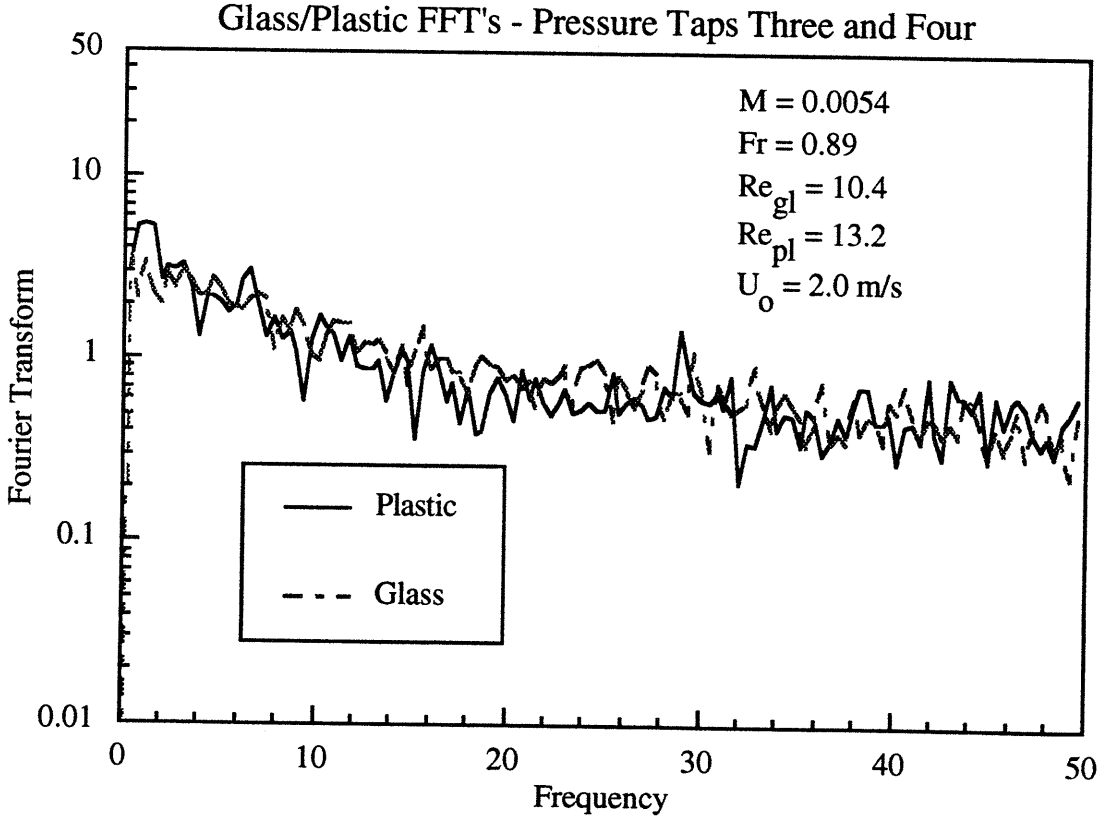

Figure 5.54

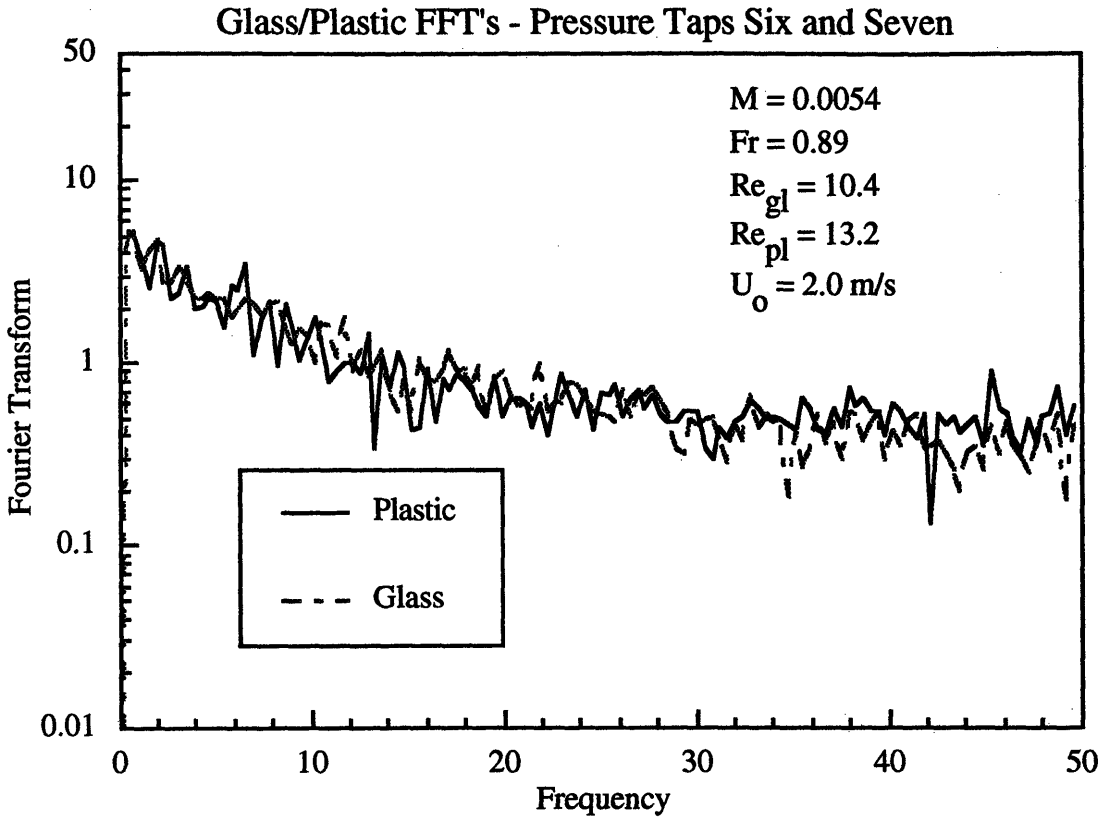

Figure 5.55

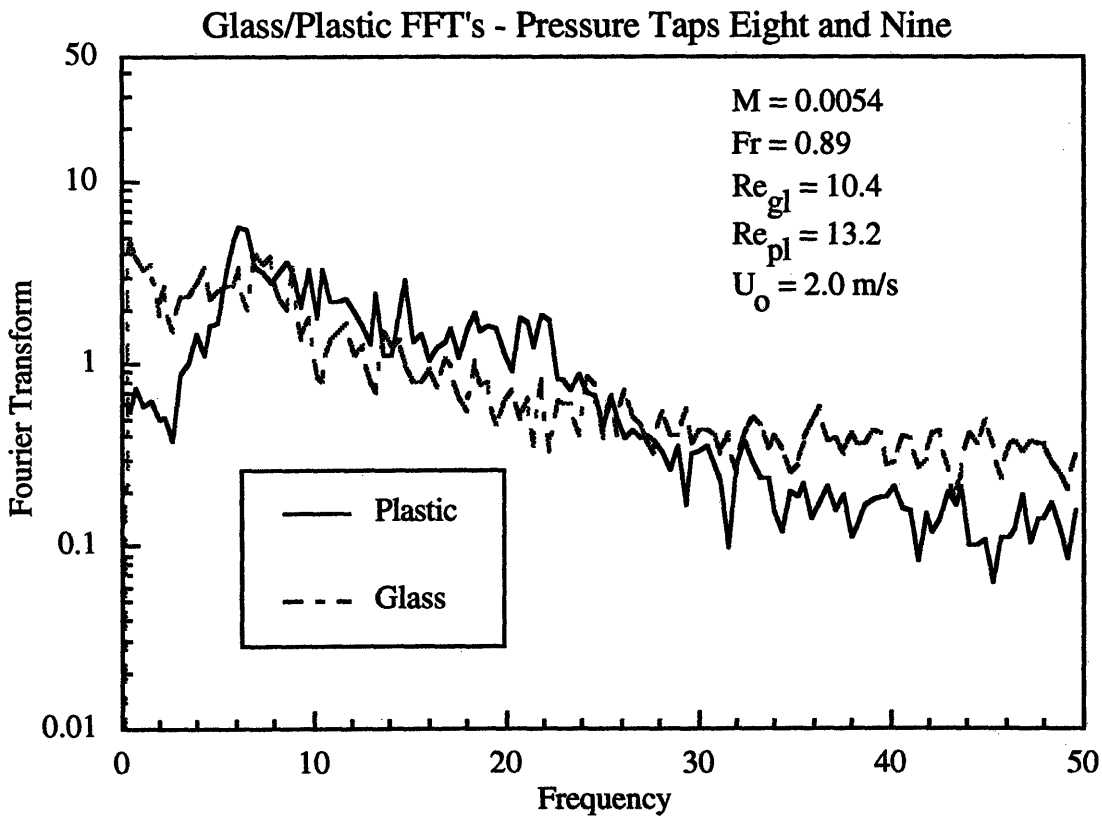

Figure 5.56

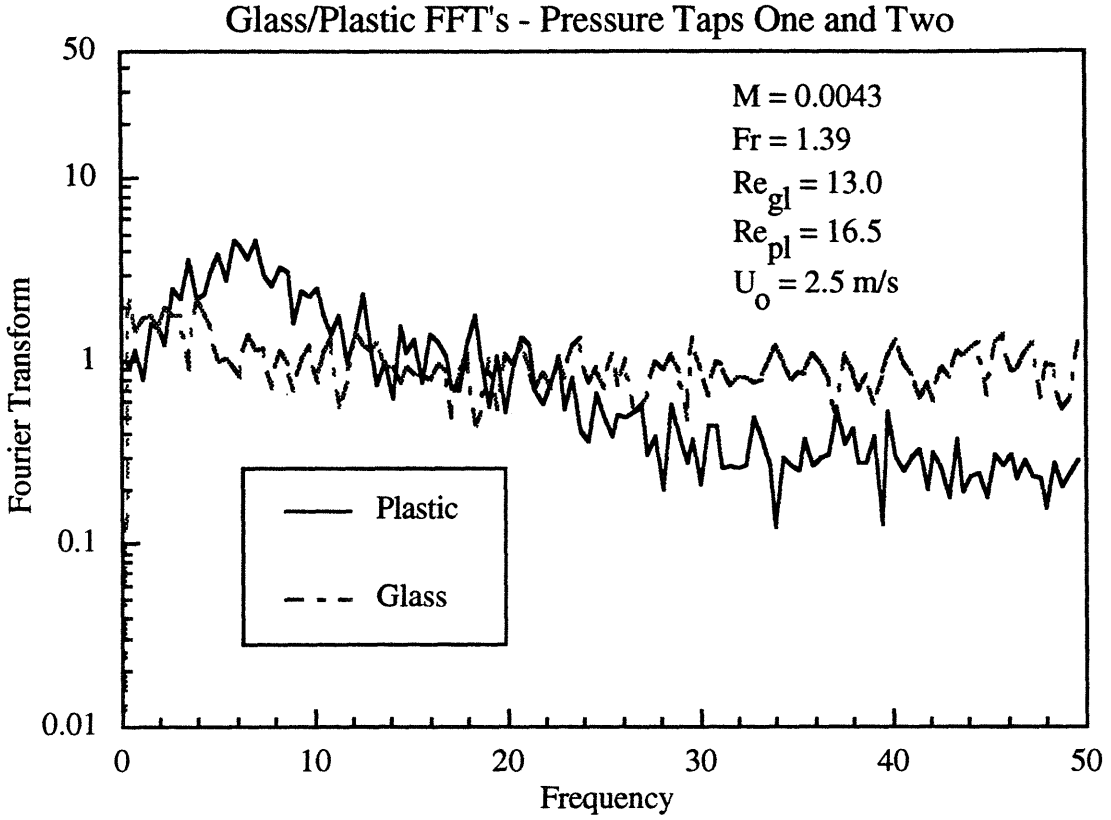

Figure 5.57

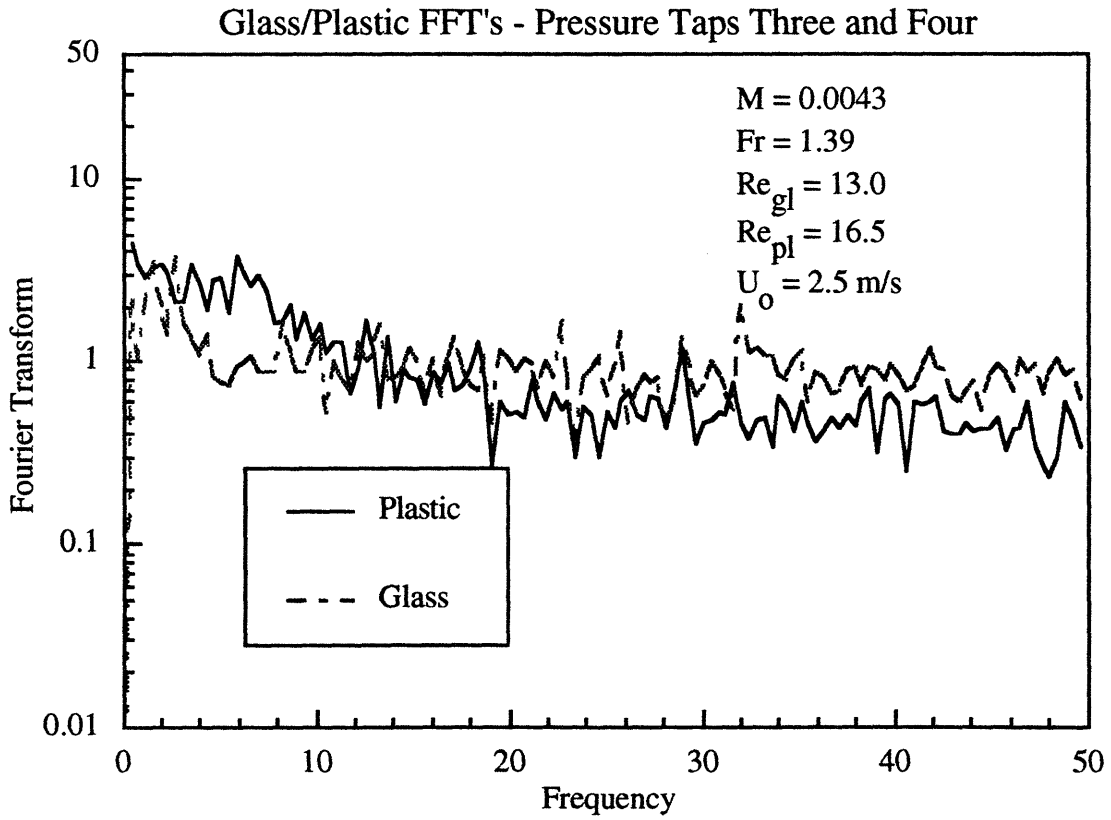

Figure 5.58

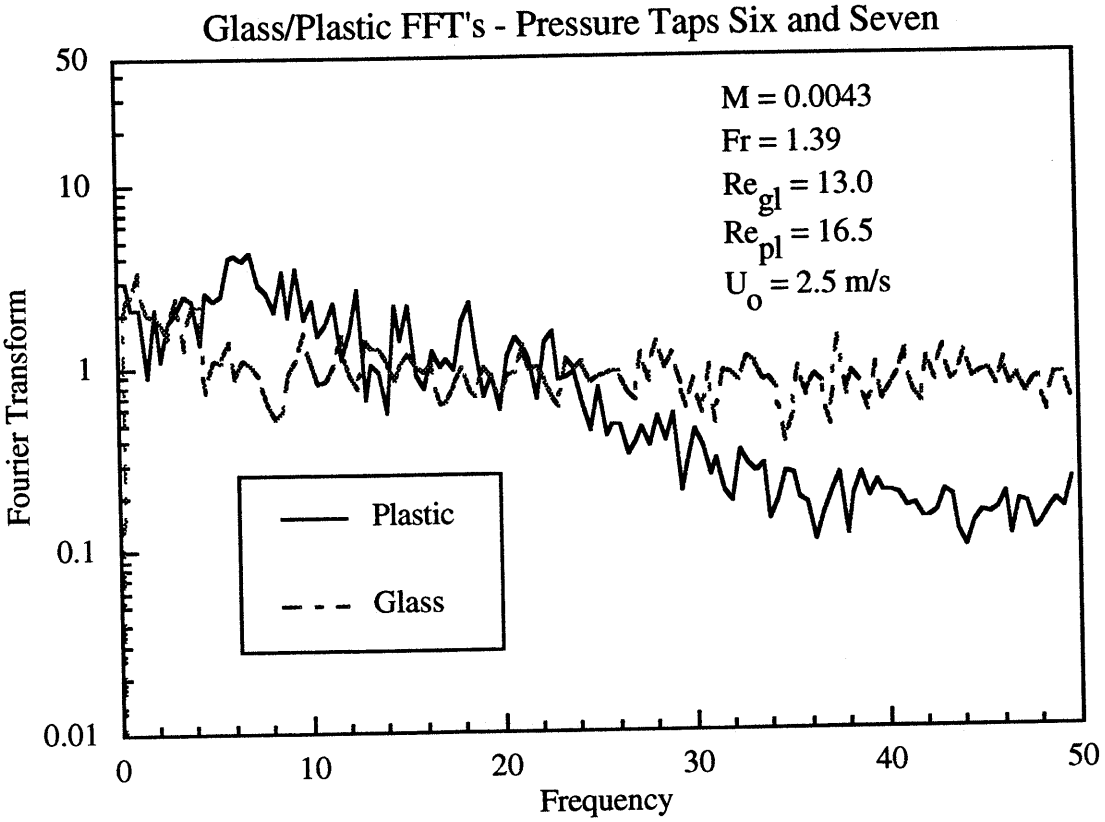

Figure 5.59

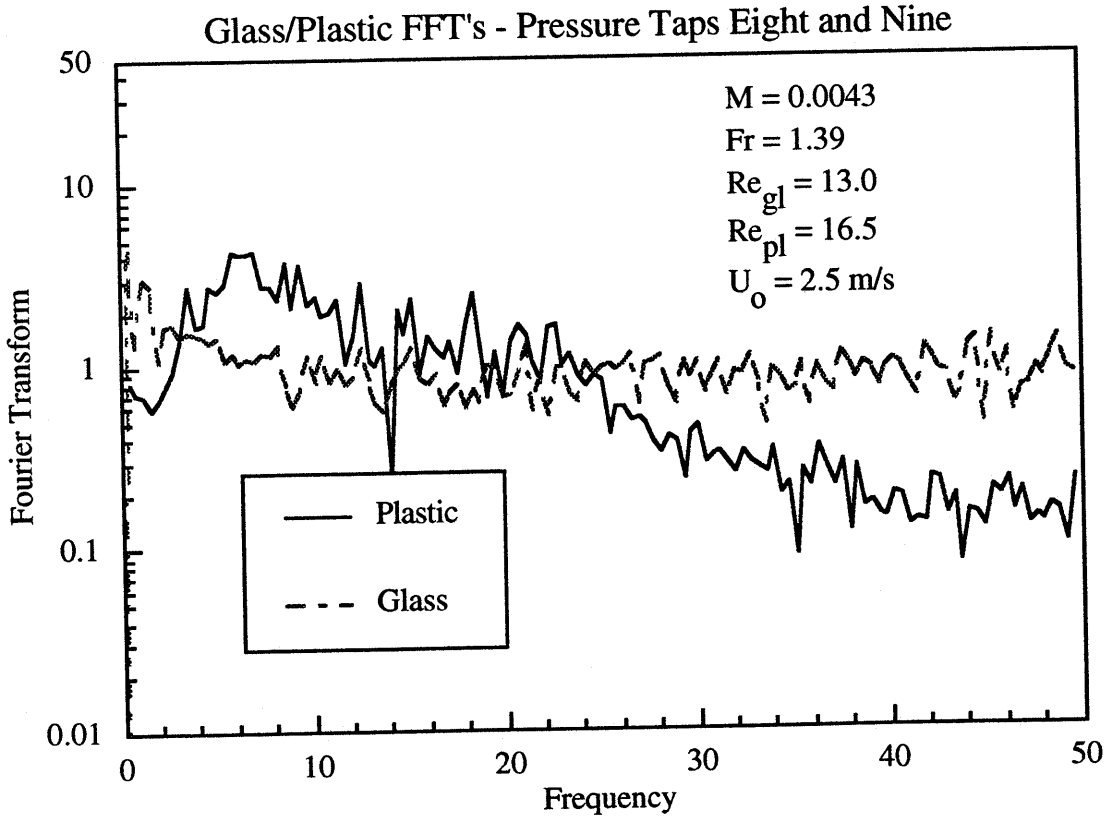

5.2.4 Discussion of Results

Consistent with the results obtained when utilizing the viscous limit scaling laws to scale between glass and steel, the solid fraction profiles measured when scaling between glass and plastic are not in good agreement even below particle diameter based Reynolds number where the viscous limit parameters should hold. The trend of better agreement at higher superficial velocities which was seen when scaling between steel and glass, was also seen in these runs. The solid fraction profile for the glass was much greater than that for the plastic, suggesting that the more dense solids will consistently give higher solid fractions when scaling in the fast-fluidization regime using the viscous limit scaling laws.

The probability density functions for the glass/plastic runs were also in poor agreement at low superficial velocities with the glass histograms covering a much broader band than the glass. As the superficial velocity increased, the probability density functions began to agree somewhat better, although the agreement is still far from satisfactory in any of the runs. The trend of better agreement in histograms at the higher sections of the bed for low superficial velocities, and better agreement at the lower sections of the bed for higher superficial velocities, which was seen when scaling between steel and glass, was also seen in the glass/plastic runs. Again, the phenomenon of choking seen in lower sections of beds may be the cause of the disagreement at the lower velocities.

Yang's correletion predictions for the glass and plastic particles used in the runs are given in Figure 5.60. It can be seen that for the nondimensional solids flow rate used in the runs, all glass runs were at 1.5 and 2.0 m/s were close to choking, while none of the plastic runs were choked. A more thorough discussion of the possible impact of this condition is included in Section 6.3.

Figure 5.60
Modified 1/16 Studsvik Bed Velocities of Incipient Choking - Yang Correlation

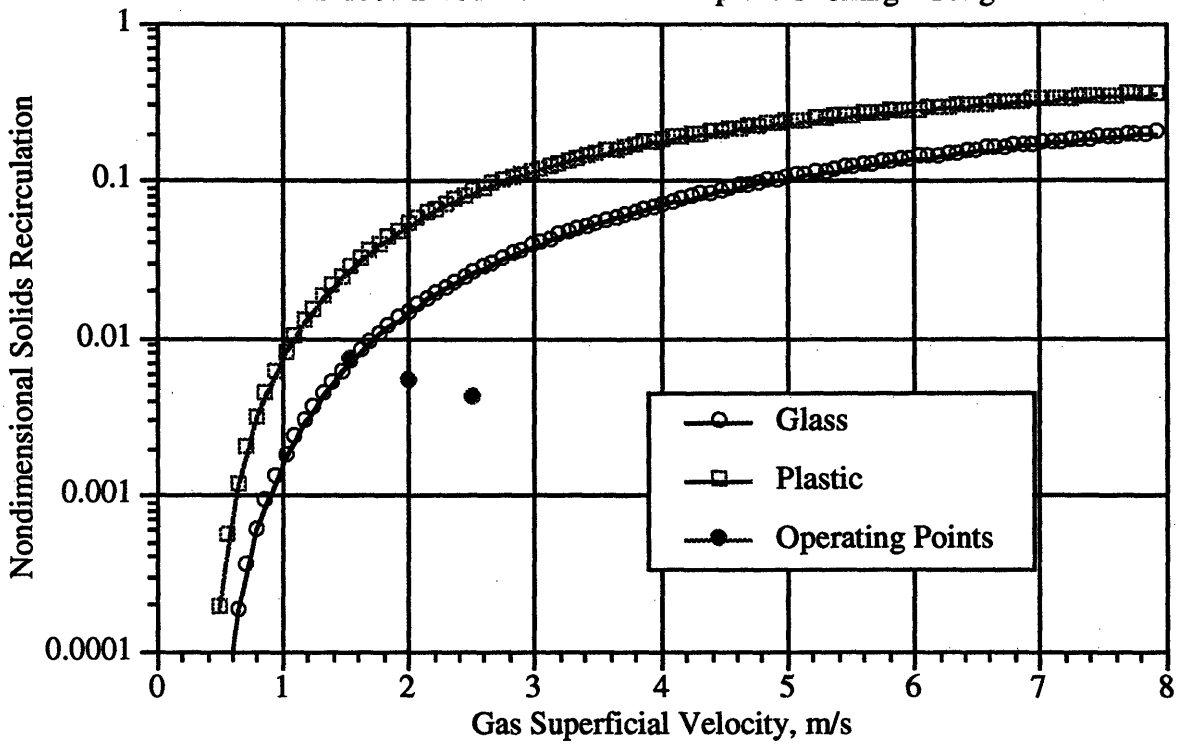

The power spectral densities for the glass/plastic runs showed better agreement at the lower sections of the bed than closer to the top. This contradicts the histograms which generally showed better agreement near the top of the bed.

6.0 RESULTS OF SIMPLIFIED SCALING LAWS

This Section presents the results of tests conducted to evaluate the simplified scaling laws which were discussed in Section 3. The governing parameters for hydrodynamic similarity utilizing the simplified set of scaling laws are:

$$\frac{u_o^2}{gD}, \frac{\rho_s}{\rho_f}, \frac{u_o}{u_{mf}}, \frac{G_s}{\rho_s u_o}, \phi_s, \text{PSD, bed geometry} \qquad (6.1)$$

Derivation of the simplified set of scaling parameters showed that the dimensionless drag term is governed by the superficial to minimum fluidization velocity, voidage at minimum fluidization, the bed length based Froude number and, in some instances, the solid to fluid density ratio. As opposed to the viscous limit scaling laws which ignore the inertial term in the fluid momentum equation, the fluid inertial effects are retained in the simplified set as is evident by the ratio of solid to gas density. Only the drag term is simplified in the derivation. As was mentioned in Section 3, these parameters should apply not only for low Reynolds number flows, but also for high Reynolds number flows, and flows in which the magnitude of the slip velocity between the particles and gas is close to u_{mf}/ε.

In order to evaluate the validity of applying these scaling parameters in the fast-fluidization regime, two series of tests were conducted. In the first series of tests, hydrodynamic scaling was attempted with glass samples properly scaled using the simplified laws, between two different sized but geometrically similar beds. The phase one 1/16 scale Studsvik bed and the modified 1/4 scale Studsvik bed were used during these tests. In the second series of tests the same type of tests were run, but the bed material was changed to plastic. The phase one 1/16 scale Studsvik bed and the modified 1/4 scale Studsvik bed were used during these tests also. Table 6.1 presents a test matrix for evaluation of the simplified set of scaling parameters.

Table 6.1

Test Matrix - Simplified Scaling Laws

Parameter	Large Bed	Small Bed
Bed Diameter	D	0.25D
Superficial Velocity	u_o	$0.5u_o$
Minimum Fluidization Velocity	u_{mf}	$0.5u_{mf}$
Particle Diameter	d_p	$0.707d_p$*
Particle Density	ρ_s	Same
$Re_{d_p} = \frac{\rho_f u_o d_p}{\mu_f}$	$\frac{\rho_f u_o d_p}{\mu_f}$	$\frac{0.35\rho_f u_o d_p}{\mu_f}$
$Re_D = \frac{\rho_f u_o D}{\mu_f}$	$\frac{\rho_f u_o D}{\mu_f}$	$\frac{\rho_f u_o D}{8\mu_f}$
$\frac{\rho_s}{\rho_f}$ $\frac{\rho_s}{\rho_f}$	Same	
$M = \frac{\dot{m}_s}{u_o A_{cs} \rho_s}$	0.0023 - 0.0072	Same

* Valid for low to moderate particle Reynolds numbers

6.1 Scaling With Glass Particles

Tables 6.2 through 6.4 provide the operational data, along with information concerning the particles and beds utilized in the simplified scaling analysis utilizing glass particles. In these Tables, Ga represents the Galileo number defined as $\frac{\rho_s^2 d_p^3 g}{\mu_f^2}$. Tests were conducted at three different superficial velocities, and at the same solids flux. The heat transfer data taken is presented in Chapter 3.

Table 6.2

Simplified Scaling Using Glass - Condition 1

	Large Bed	Small Bed
u_o (m/s)	3.0	1.5
u_{mf} (cm/s) Ergun Eqn.	2.88	1.42
u_{mf} (cm/s) measured	2.80	1.40
d_p (microns)	112.3	78.7
L (m)	1.83	0.46
A_{cs} (m^2)	1.68E-2	1.05E-3
G_s (kg/m^2-s)	54.9	27.5
$Re_{dp,uo}$	22.2	7.81
$Re_{L,uo}$	3.63E5	4.54E4
Fr	0.50	0.50
$\left(\frac{u_o}{u_{mf}}\right)_{Ergun\ eqn.}$	103.9	105.7
$\left(\frac{u_o}{u_{mf}}\right)_{measured}$	107.1	107.1
$\left(\frac{G_s}{\rho_s u_o}\right)$	7.2E-3	7.2E-3
$\left(\frac{\rho_s}{\rho_f}\right)$	2117	2117
Ga	2.73E5	9.39E3

Table 6.3

Simplified Scaling Using Glass - Condition 2

	Large Bed	Small Bed
u_o (m/s)	4.0	2.0
u_{mf} (cm/s) Ergun Eqn.	2.88	1.42
u_{mf} (cm/s) measured	2.80	1.40
d_p (microns)	112.3	78.7
L (m)	1.83	0.46
A_{cs} (m^2)	1.68E-2	1.05E-3
G_s (kg/m^2-s)	54.9	27.5
$Re_{dp,uo}$	29.7	10.4
$Re_{L,uo}$	5.33E5	6.05E4
Fr	0.89	0.89
$\left(\frac{u_o}{u_{mf}}\right)_{Ergun\ eqn.}$	138.5	140.8
$\left(\frac{u_o}{u_{mf}}\right)_{measured}$	142.9	142.9
$\left(\frac{G_s}{\rho_s u_o}\right)$	5.4E-3	5.4E-3
$\left(\frac{\rho_s}{\rho_f}\right)$	2117	2117
Ga	2.73E5	9.39E3

Table 6.4

Simplified Scaling Using Glass - Condition 3

	Large Bed	Small Bed
u_o (m/s)	5.0	2.5
u_{mf} (cm/s) Ergun Eqn.	2.88	1.42
u_{mf} (cm/s) measured	2.80	1.40
d_p (microns)	112.3	78.7
L (m)	1.83	0.46
A_{cs} (m^2)	1.68E-2	1.05E-3
G_s (kg/m^2-s)	54.9	27.5
$Re_{dp,uo}$	37.2	13.0
$Re_{L,uo}$	6.66E5	7.57E4
Fr	1.39	1.39
$\left(\frac{u_o}{u_{mf}}\right)_{Ergun\ eqn.}$	173.1	176.1
$\left(\frac{u_o}{u_{mf}}\right)_{measured}$	178.6	178.6
$\left(\frac{G_s}{\rho_s u_o}\right)$	4.3E-3	4.3E-3
$\left(\frac{\rho_s}{\rho_f}\right)$	2117	2117
Ga	2.73E5	9.39E3

6.1.1 Solid Fraction Profiles

The average solid fraction profiles in the two different sized beds for the glass scaling tests using the simplified scaling parameters are given in Figures 6.1 through 6.3. The calculated solid fractions are plotted versus the average of the heights of the associated pressure taps in each bed. As discussed in Section 4, error bars are based on calculated standard deviations in solid flow measurements and pressure time traces.

6.1.2 Histograms

Histograms of the solid fraction data of the simplified scaling for glass are depicted in Figures 6.4 through 6.15. Histograms are shown for solid fractions between pressure taps 1 and 2, 3 and 4, 5 and 6, 7 and 8 in each bed. In these plots, probability is plotted versus the solid fraction.

6.1.3 Power Spectral Densities

FFT's of the pressure fluctuation data for the glass simplified scaling tests are given in Figures 6.16 through 6.27. FFT's are shown for pressure taps corresponding to the same percentage height up the bed as the probability density functions. In these plots, the fourier transform is plotted versus the equivalent 1/4 scale Studsvik frequency in Hz. The 1/16 scale frequency is shifted by $\left[\frac{D_{1/16}}{D_{1/4}}\frac{u_{o}{}^{1/4}}{u_{o}{}^{1/16}}\right]$.

Figure 6.1

Glass Solid Fraction Profiles - Simplified Scaling Laws

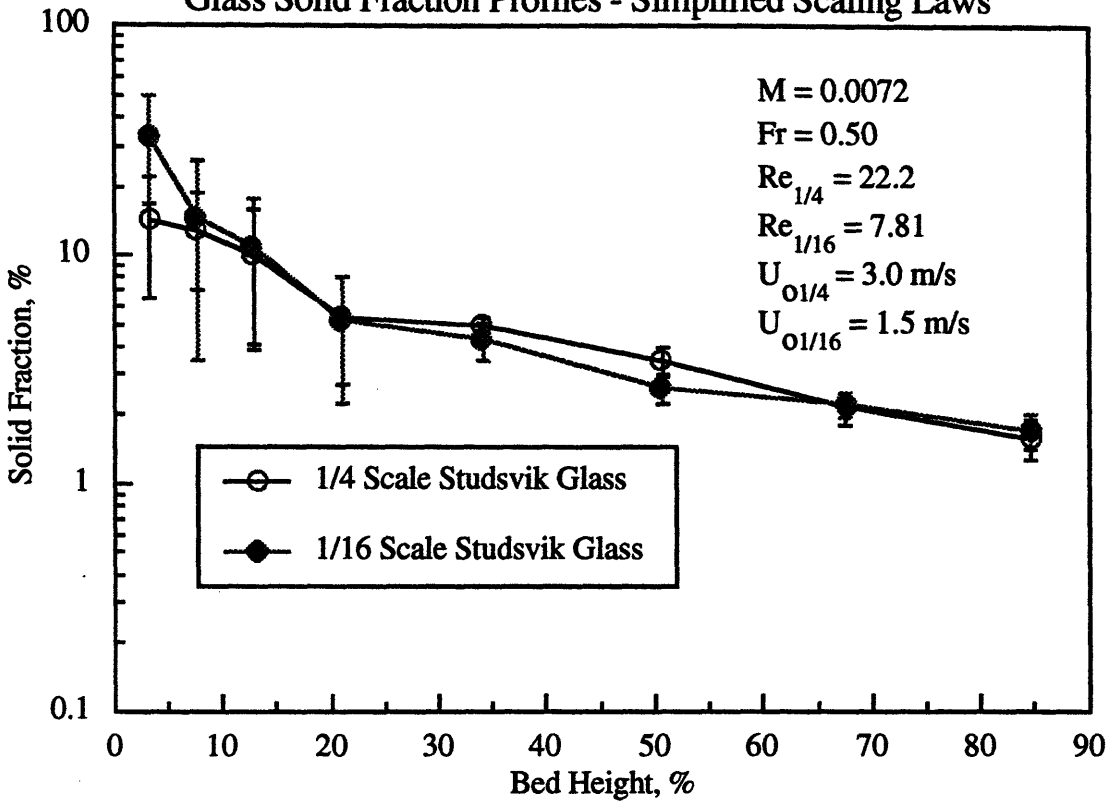

Figure 6.2

Glass Solid Fraction Profiles - Simplified Scaling Laws

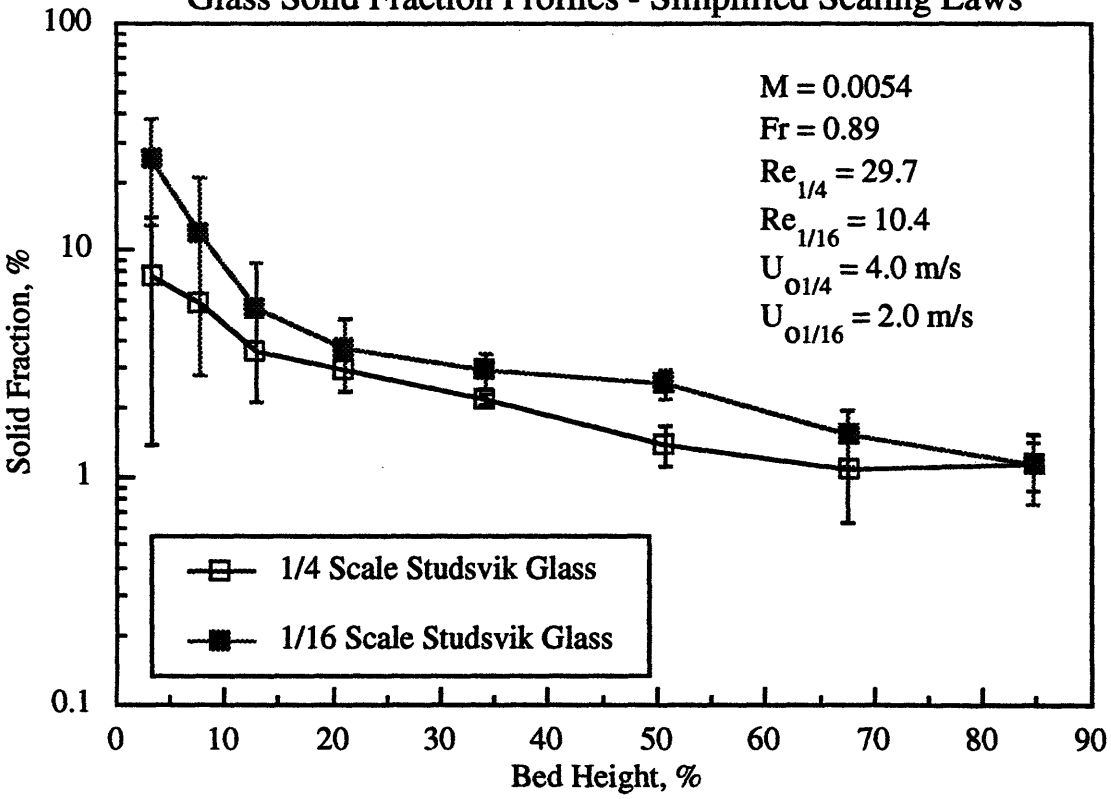

Figure 6.3
Glass Solid Fraction Profiles - Simplified Scaling Laws

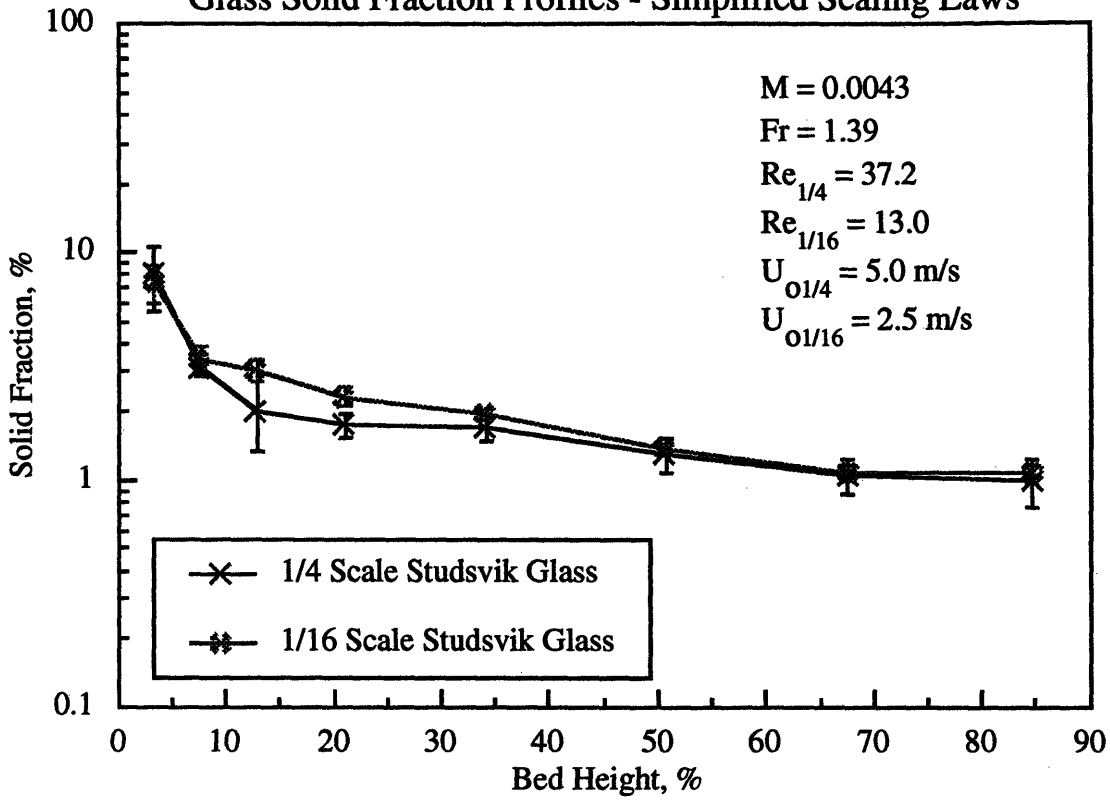

Figure 6.4
Glass Histograms - Pressure Taps One and Two

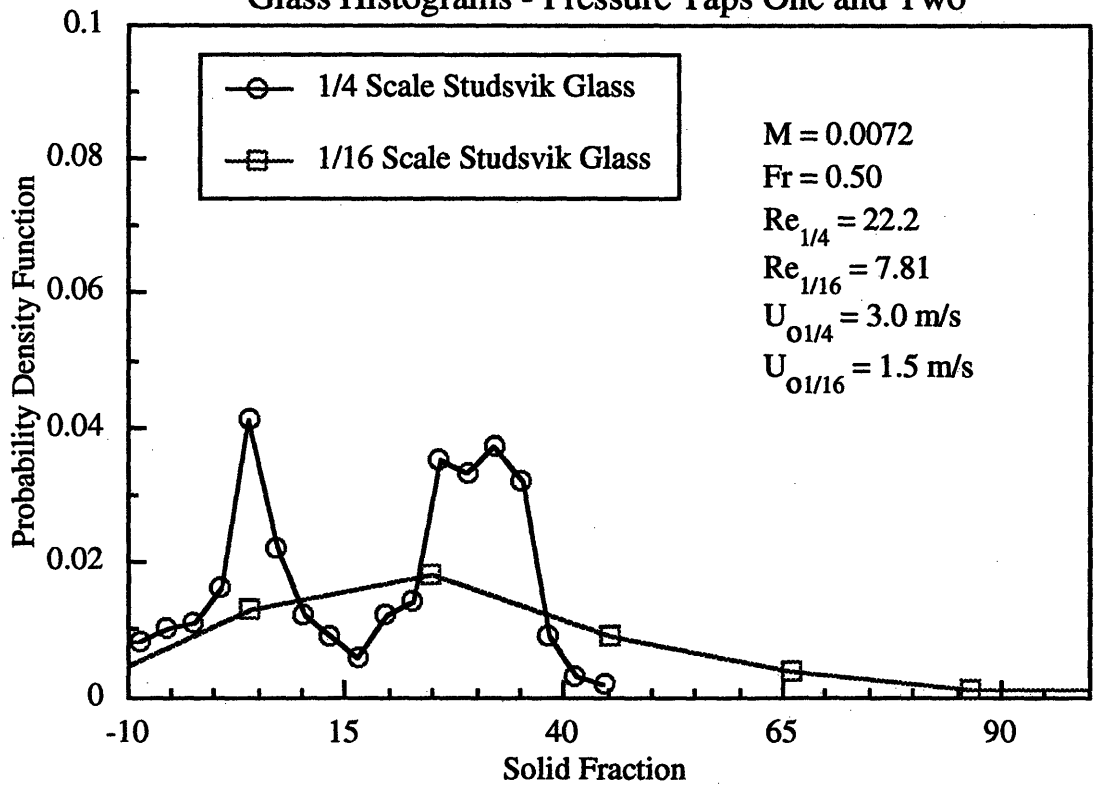

Figure 6.5

Glass Histograms - Pressure Taps Two and Three

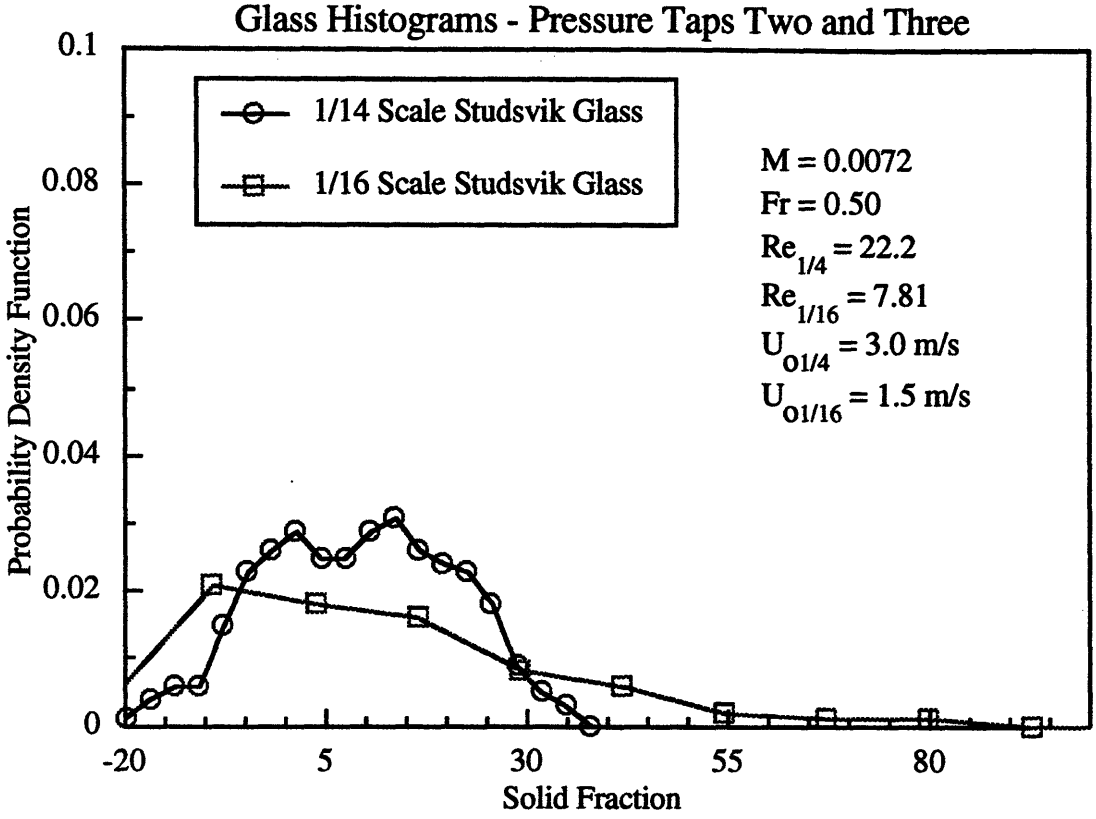

Figure 6.6

Glass Histograms - Pressure Taps Six and Seven

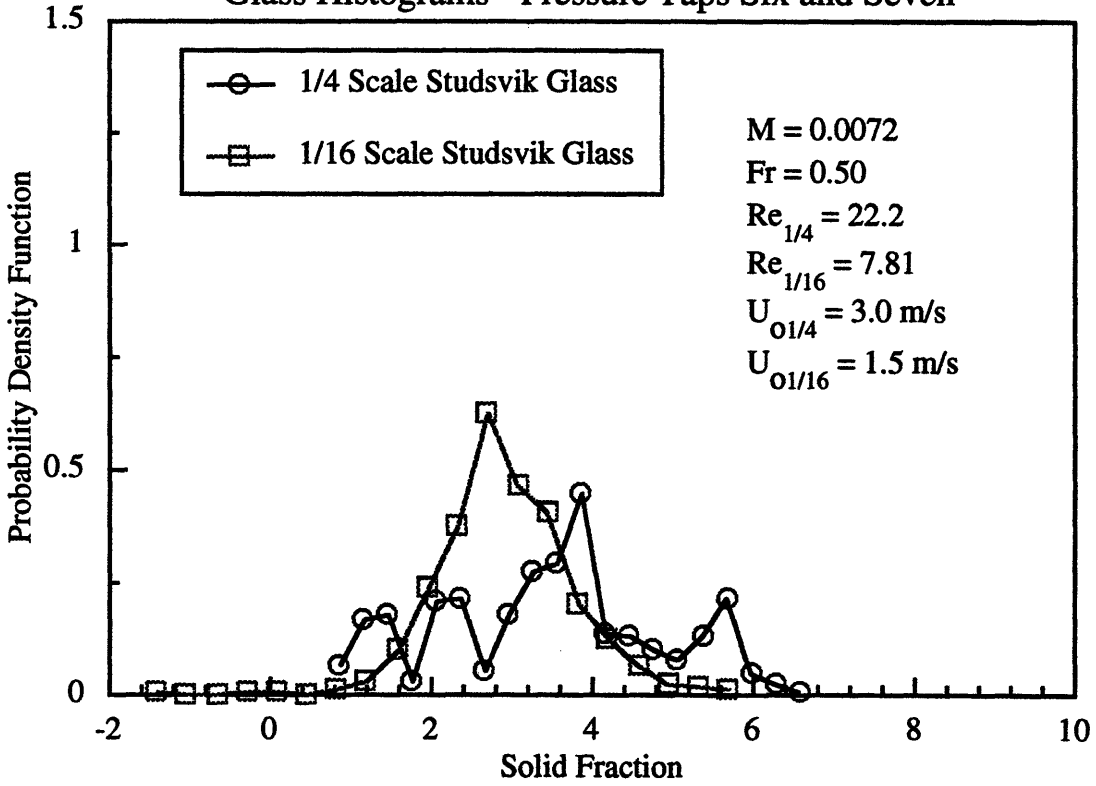

Figure 6.7

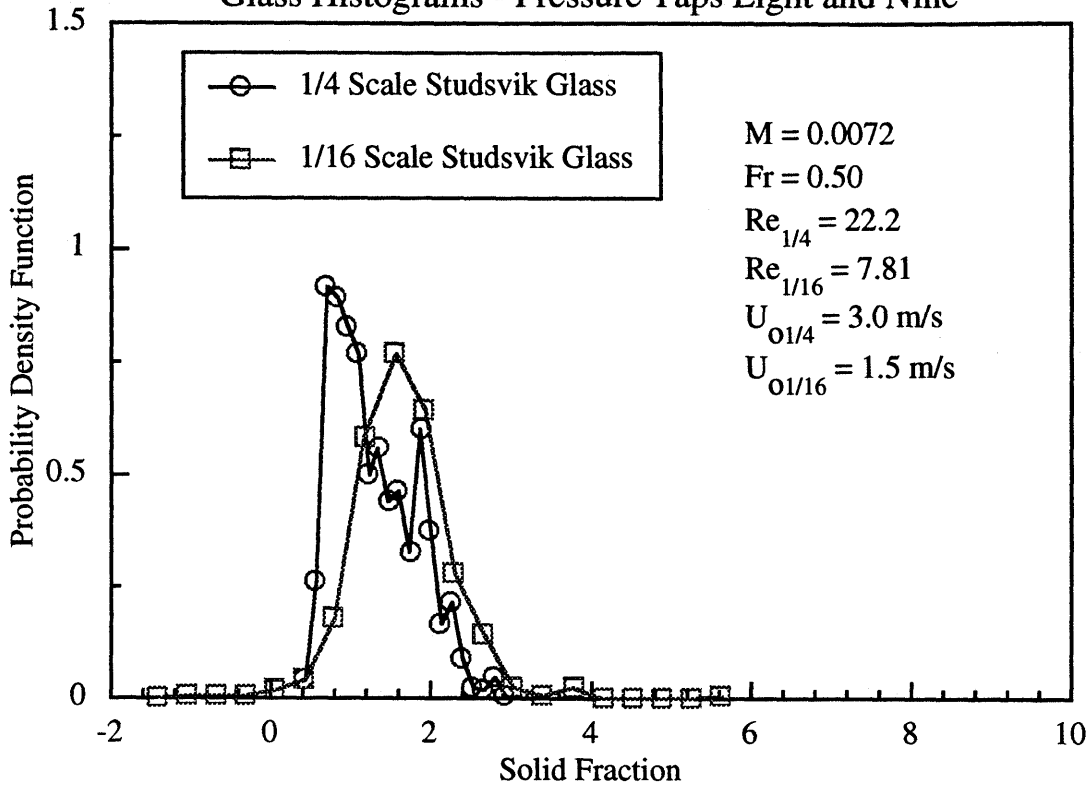

Figure 6.8

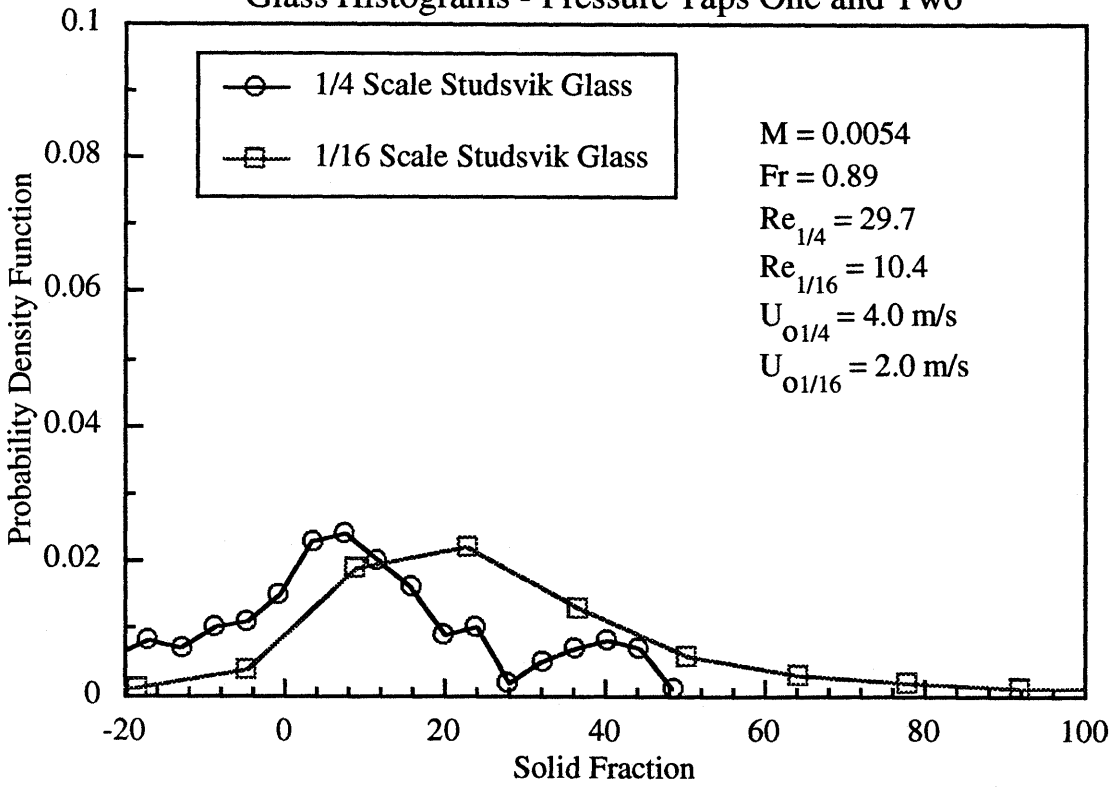

Figure 6.9

Glass Histograms - Pressure Taps Three and Four

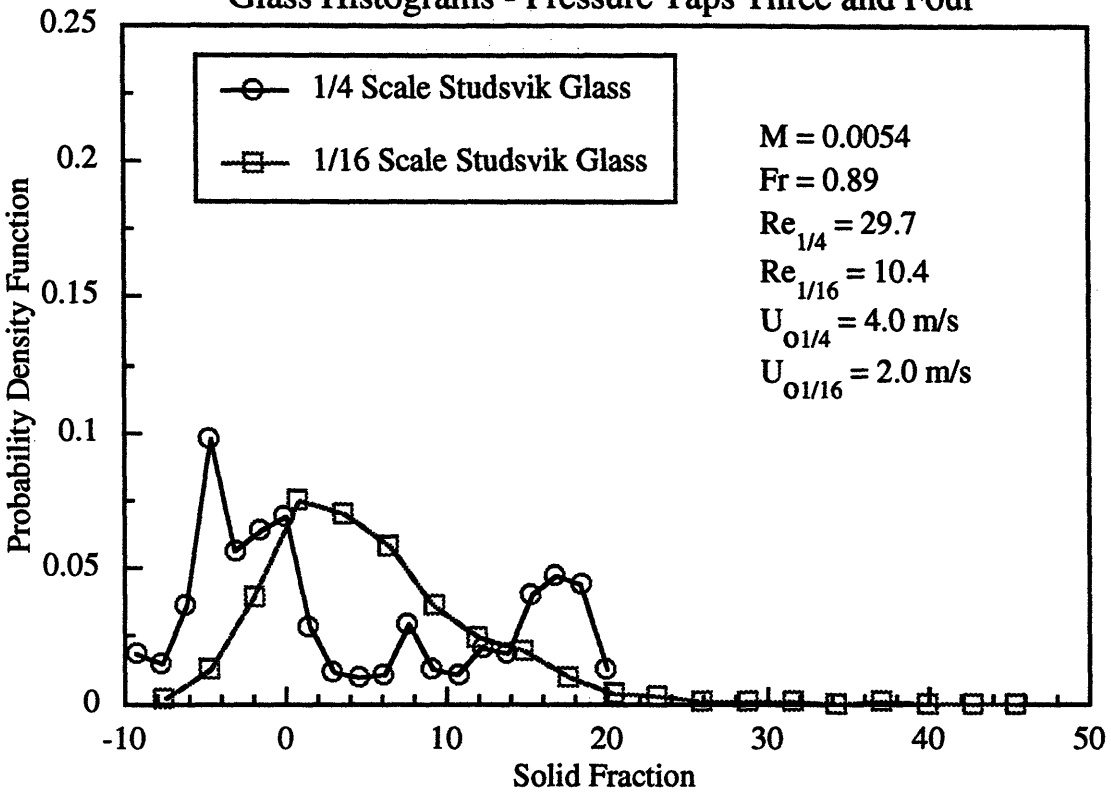

Figure 6.10

Glass Histograms - Pressure Taps Six and Seven

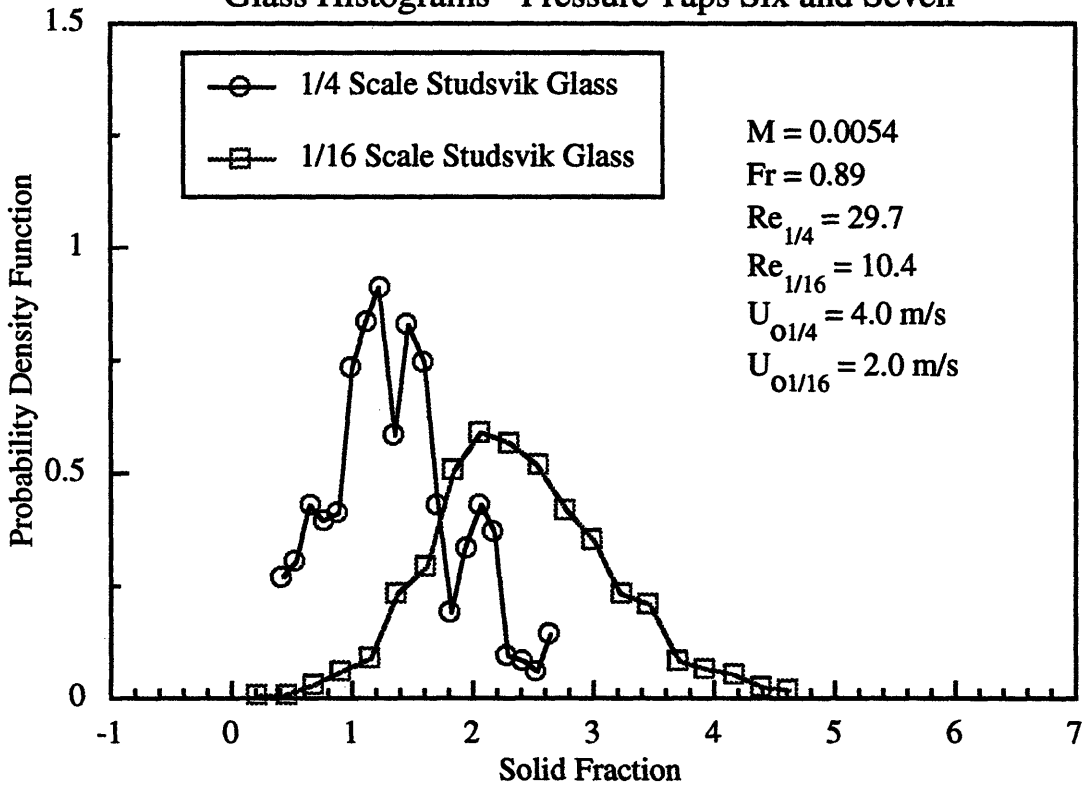

Figure 6.11

Glass Histograms - Pressure Taps Eight and Nine

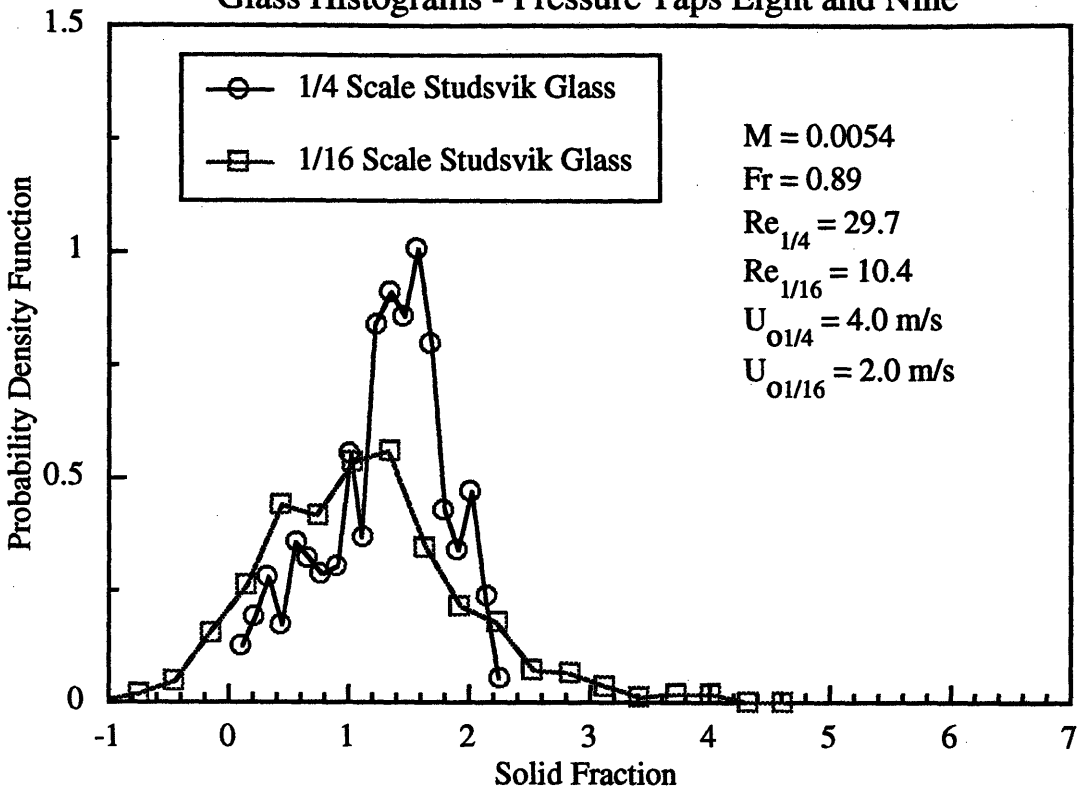

Figure 6.12

Glass Histograms - Pressure Taps One and Two

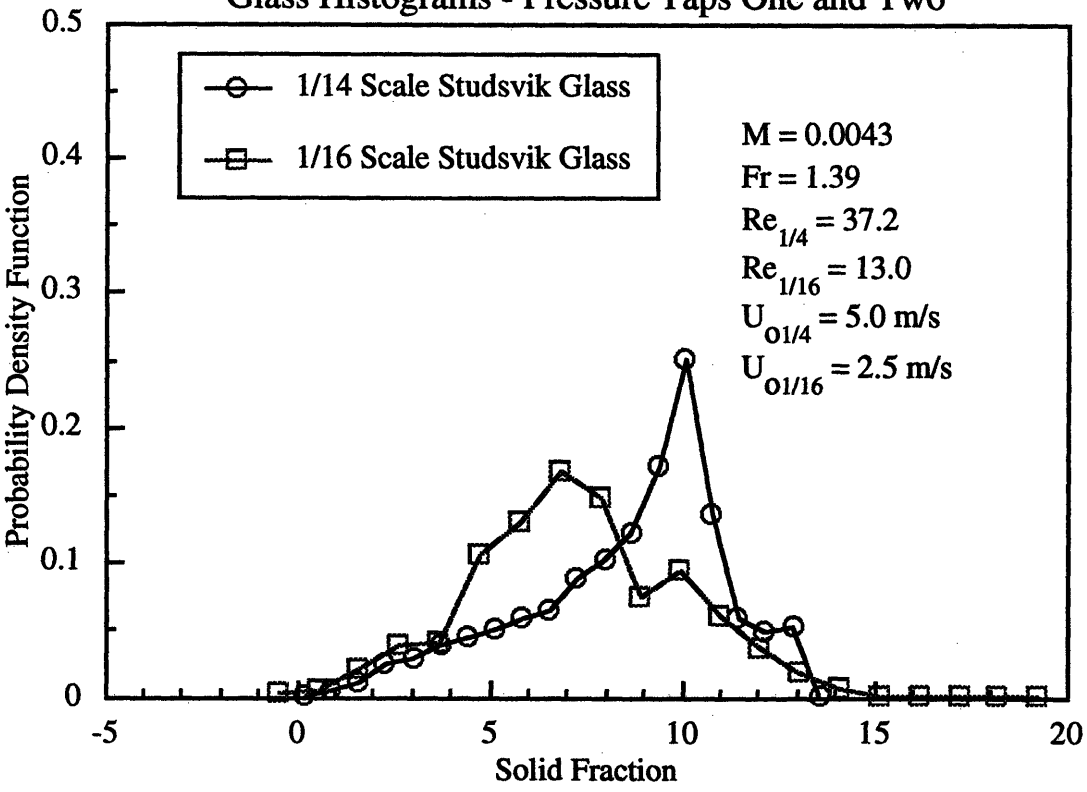

Figure 6.13

Glass Histograms - Pressure Taps Three and Four

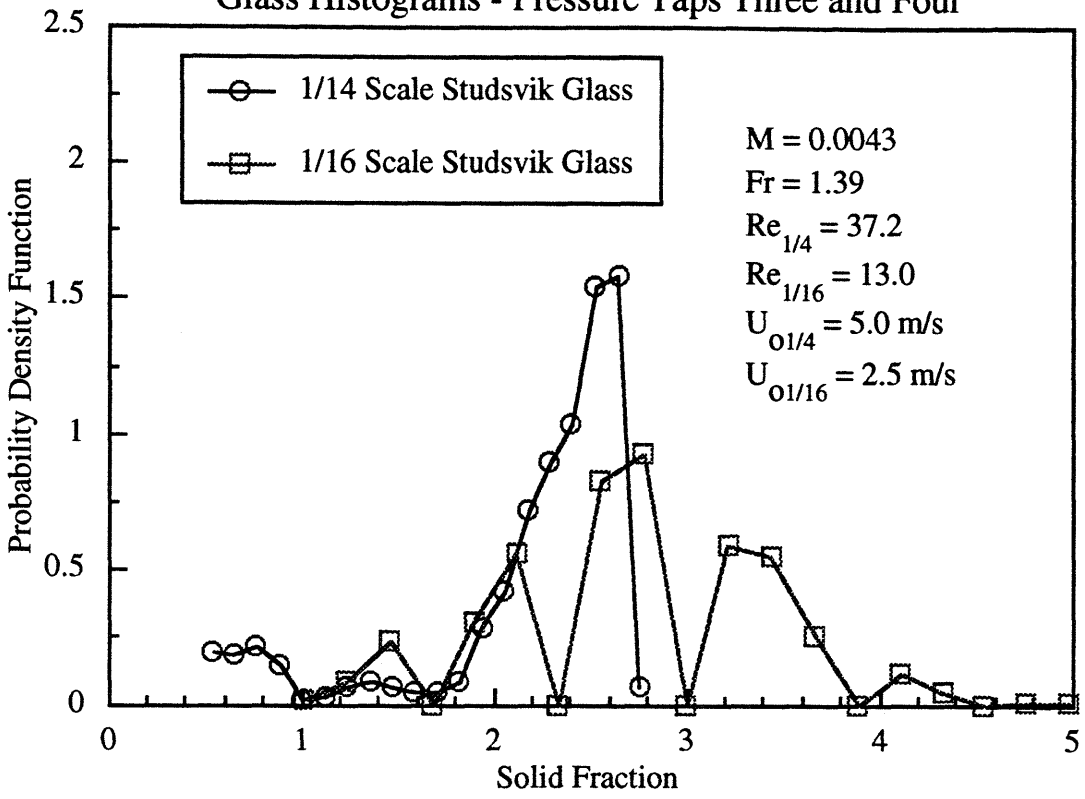

Figure 6.14

Glass Histograms - Pressure Taps Six and Seven

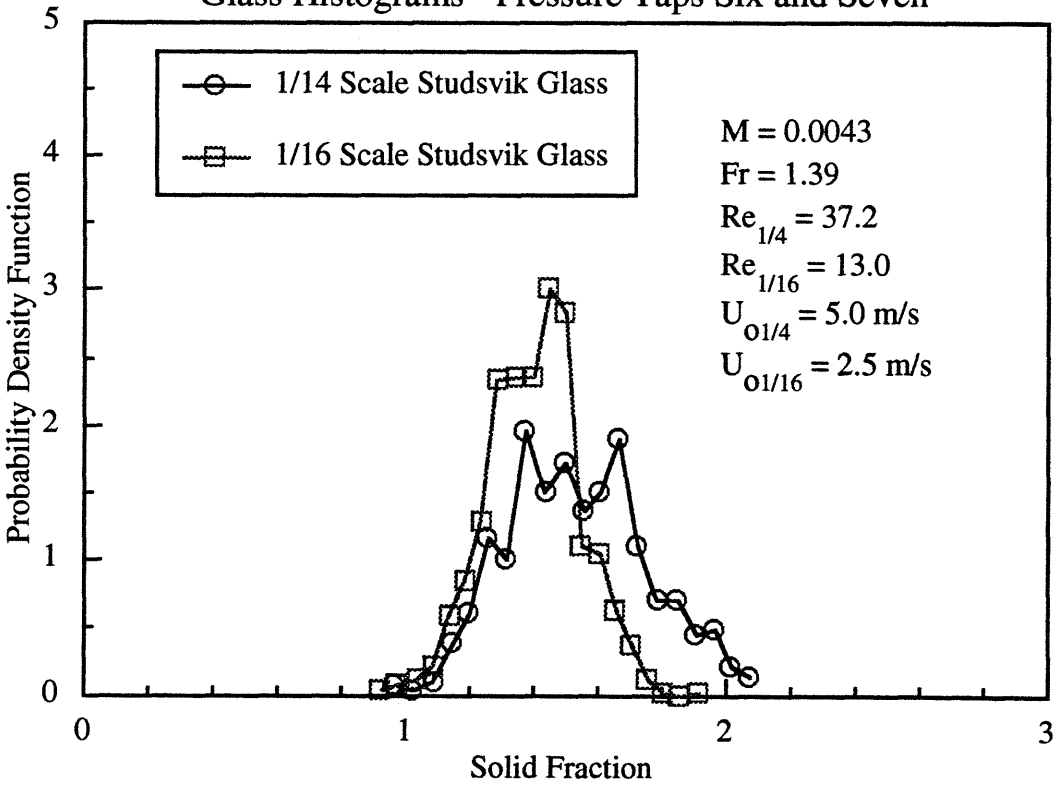

Figure 6.15

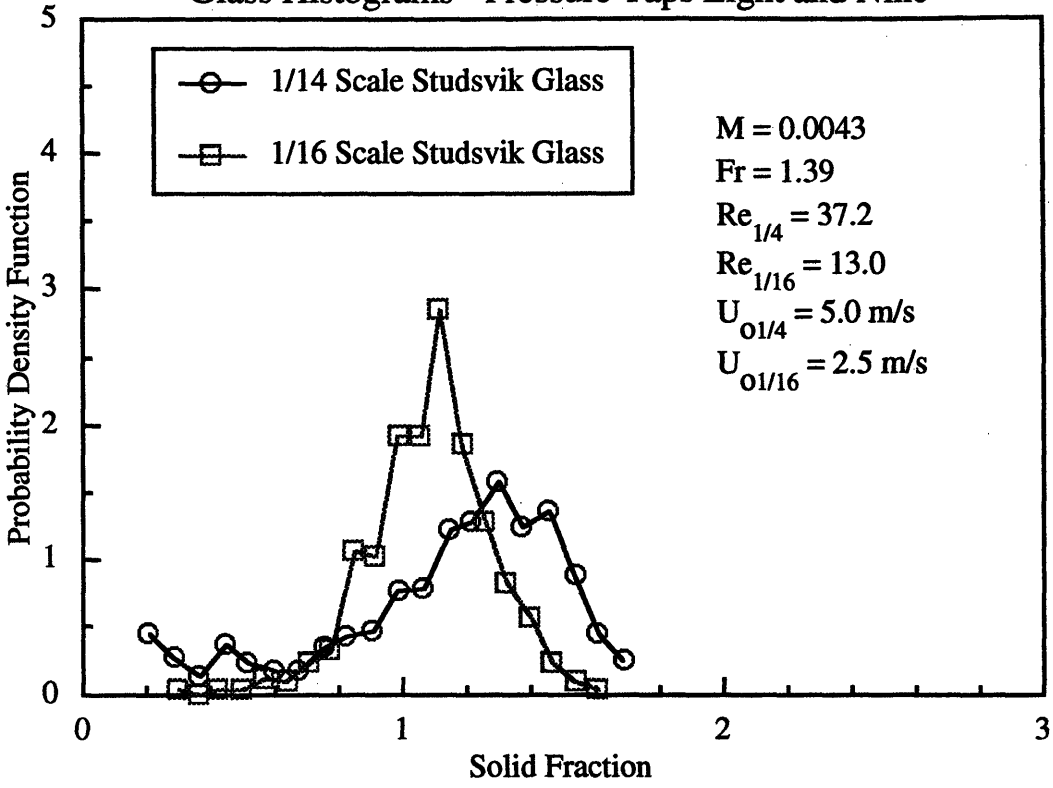

Figure 6.16

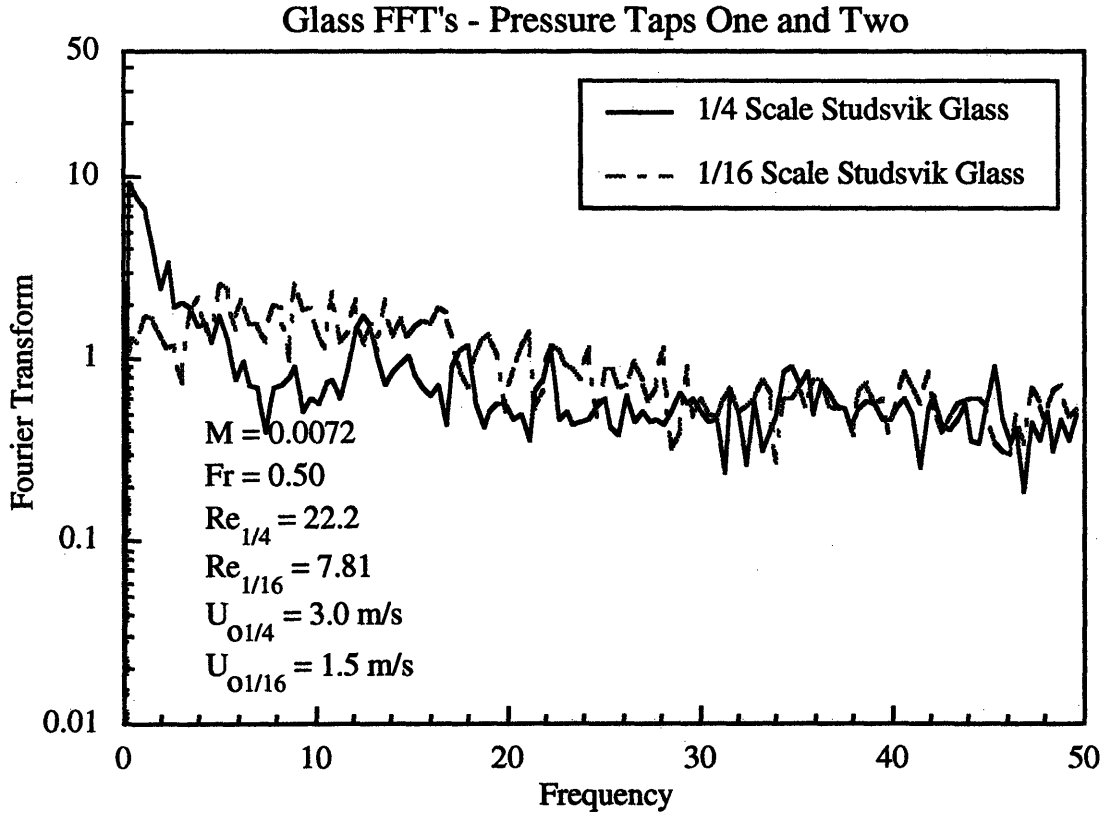

Figure 6.17

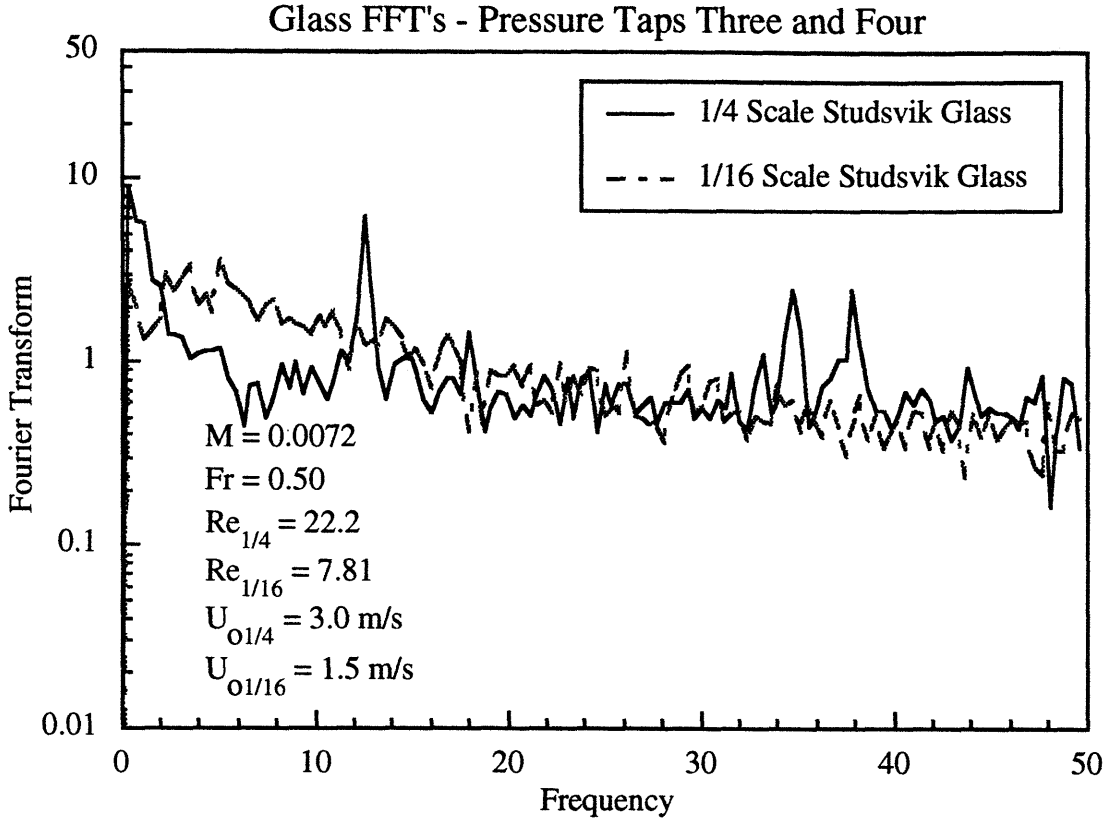

Figure 6.18

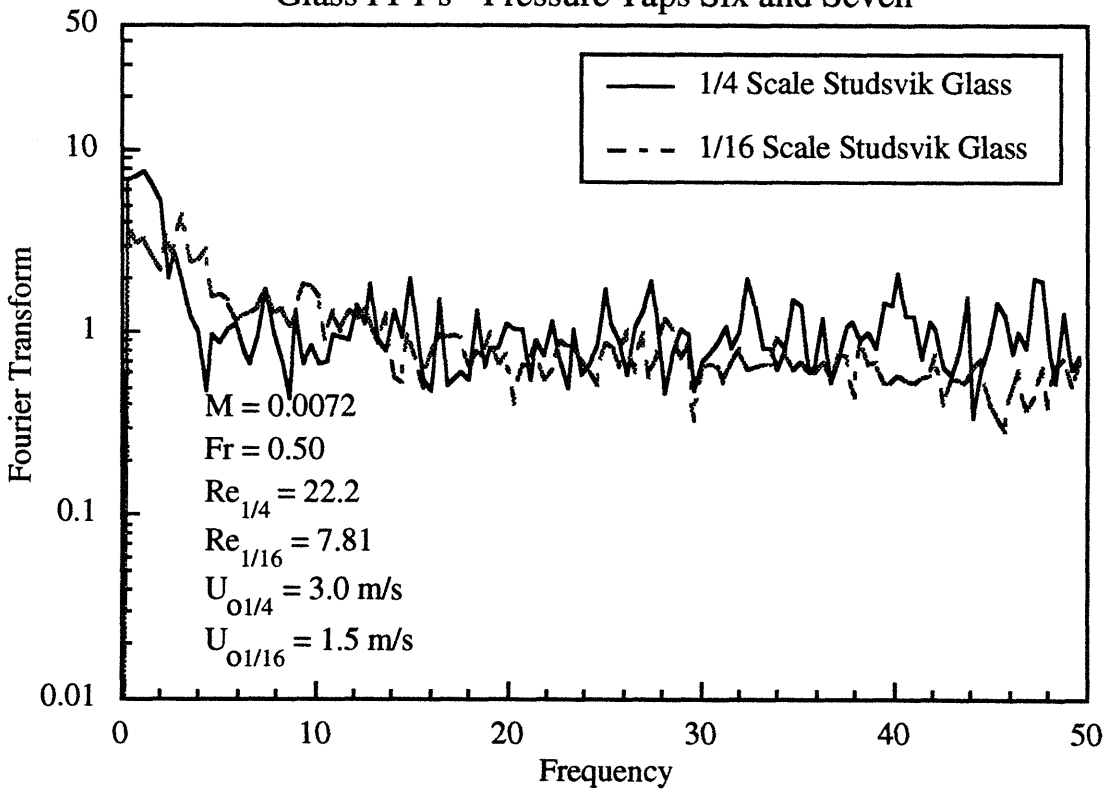

Figure 6.19

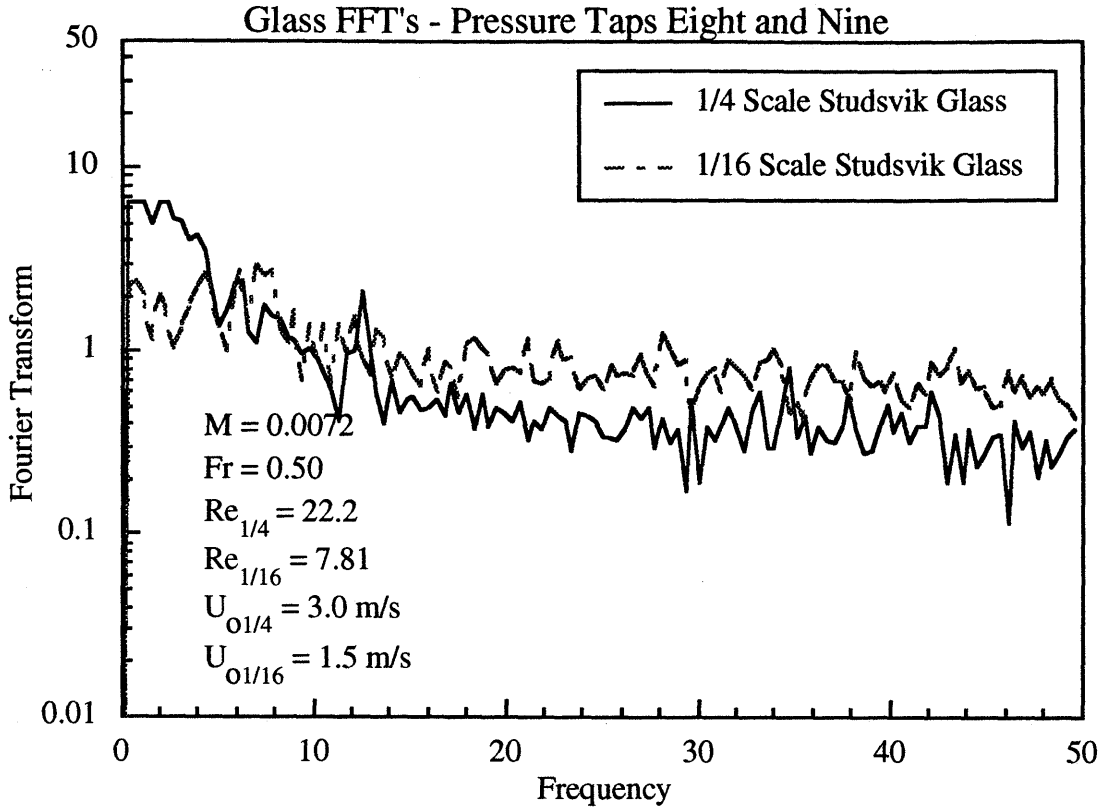

Figure 6.20

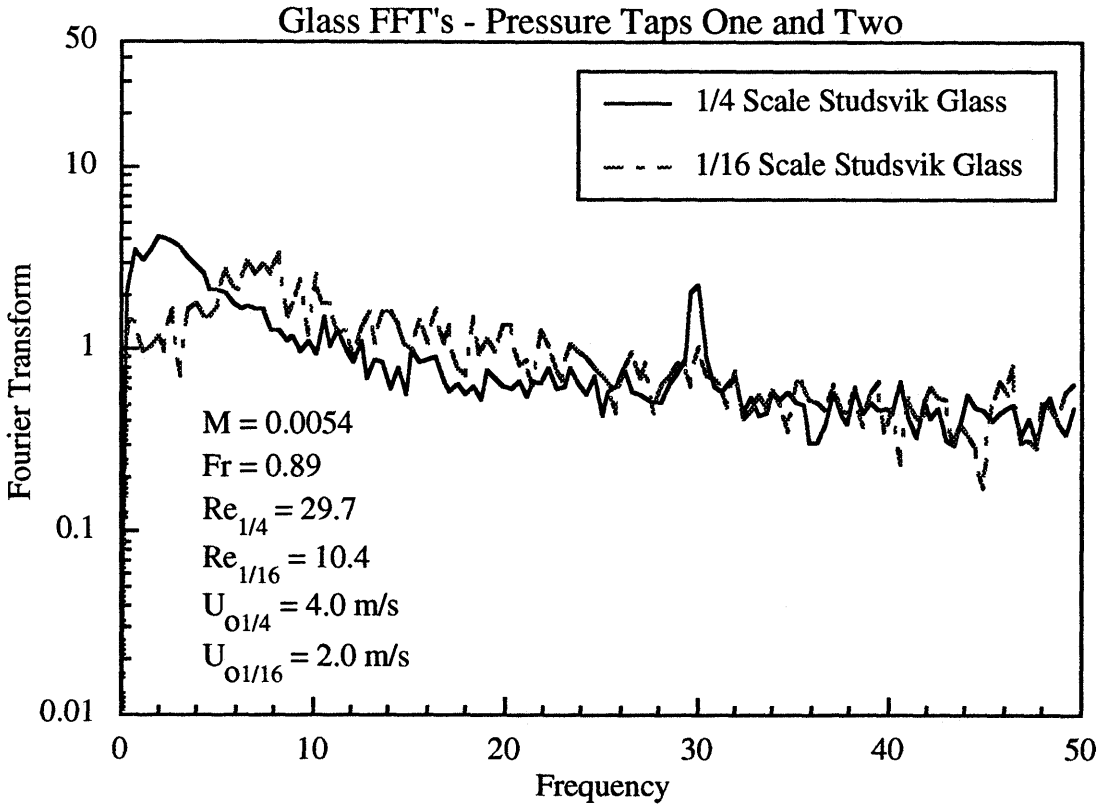

Figure 6.21

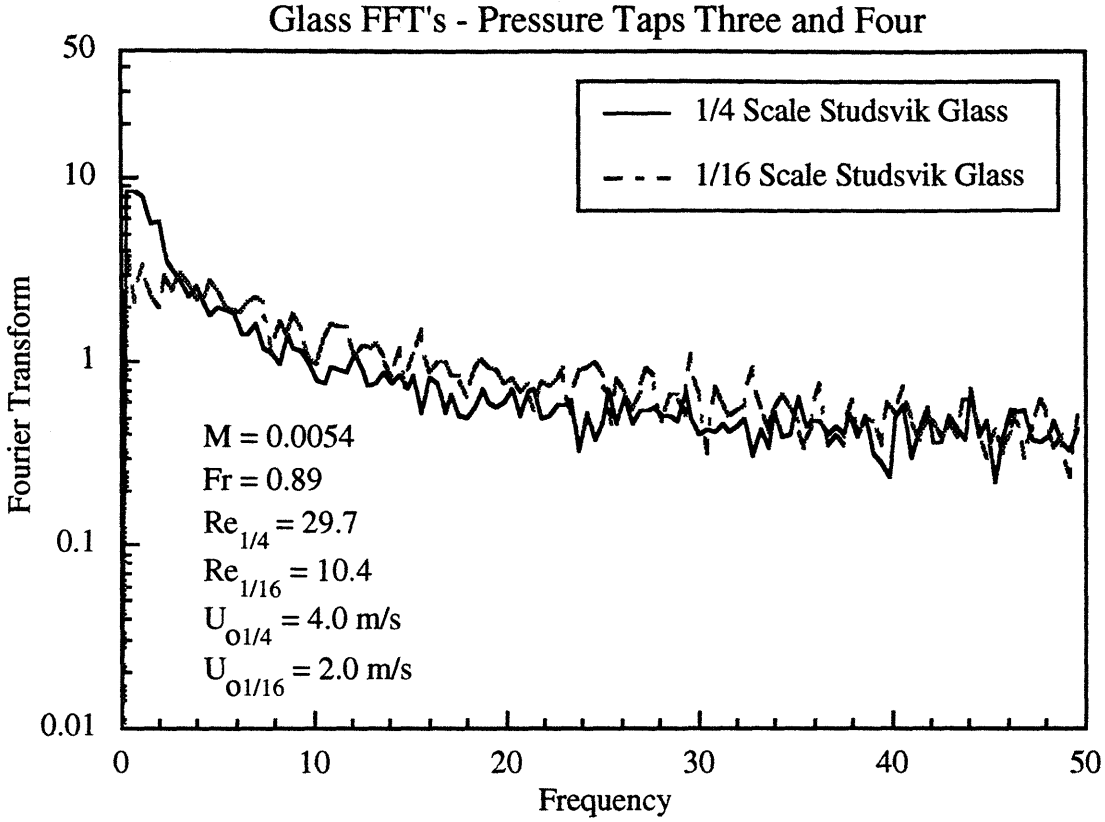

Figure 6.22

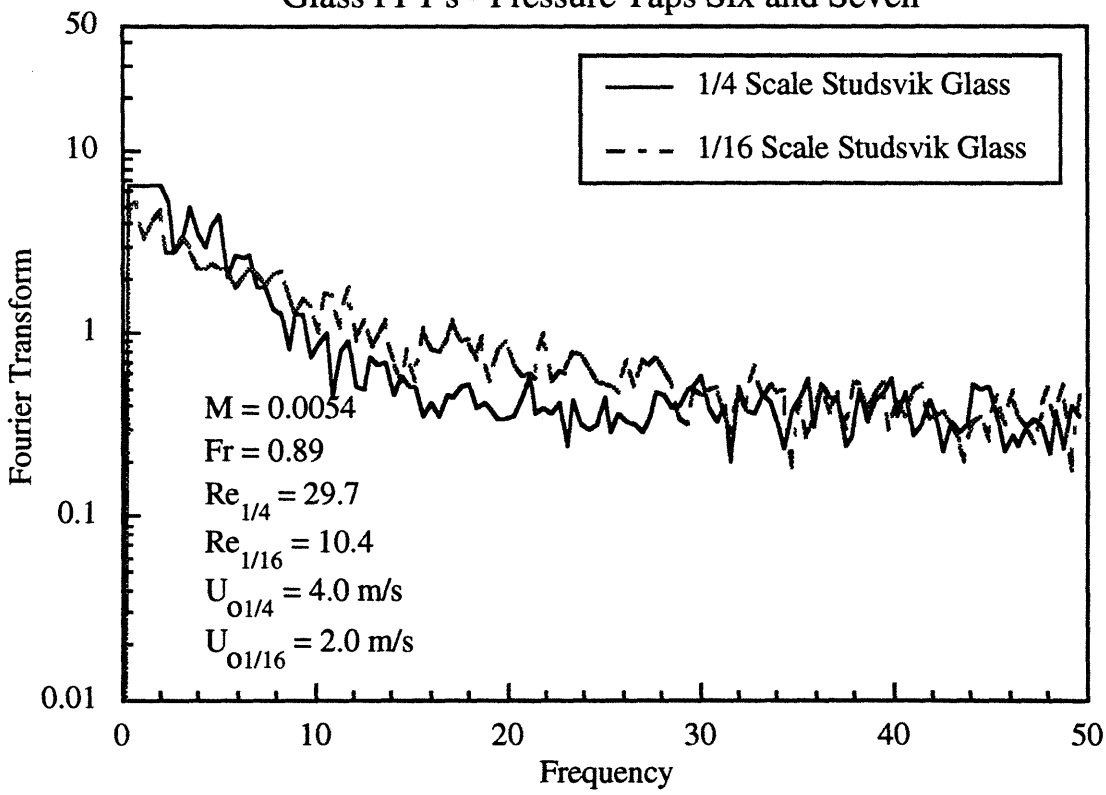

Figure 6.23

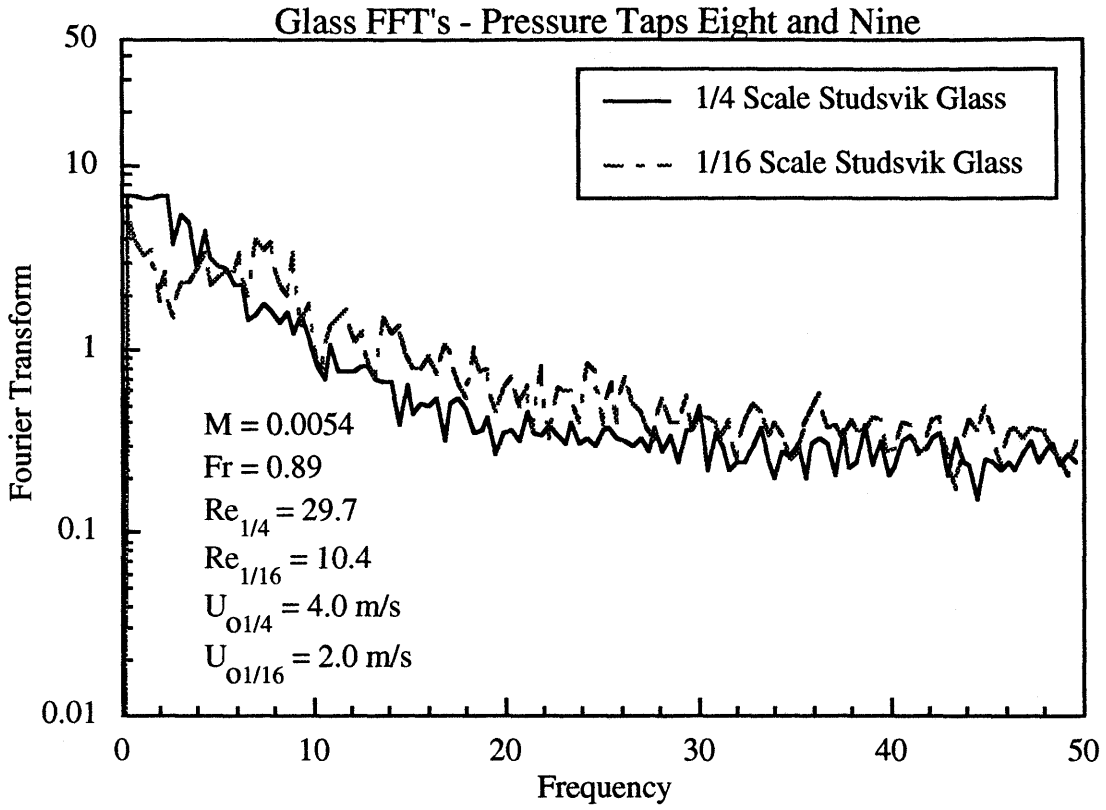

Figure 6.24

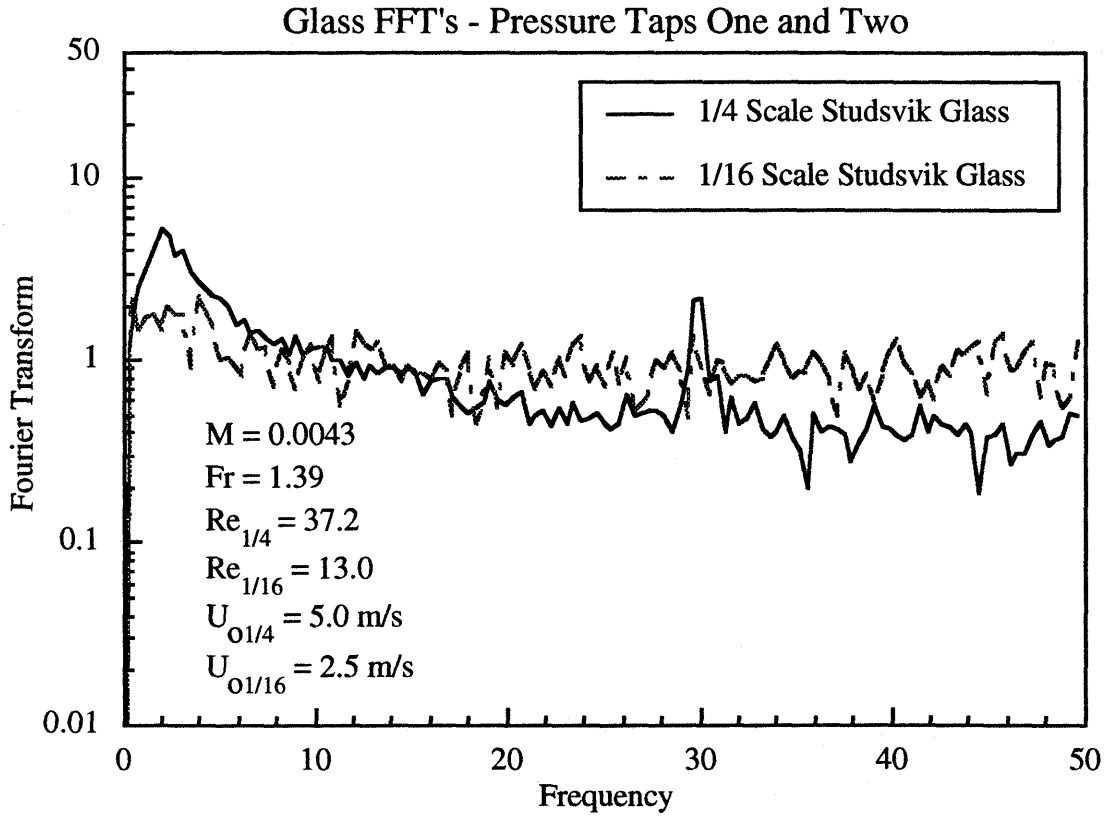

Figure 6.25

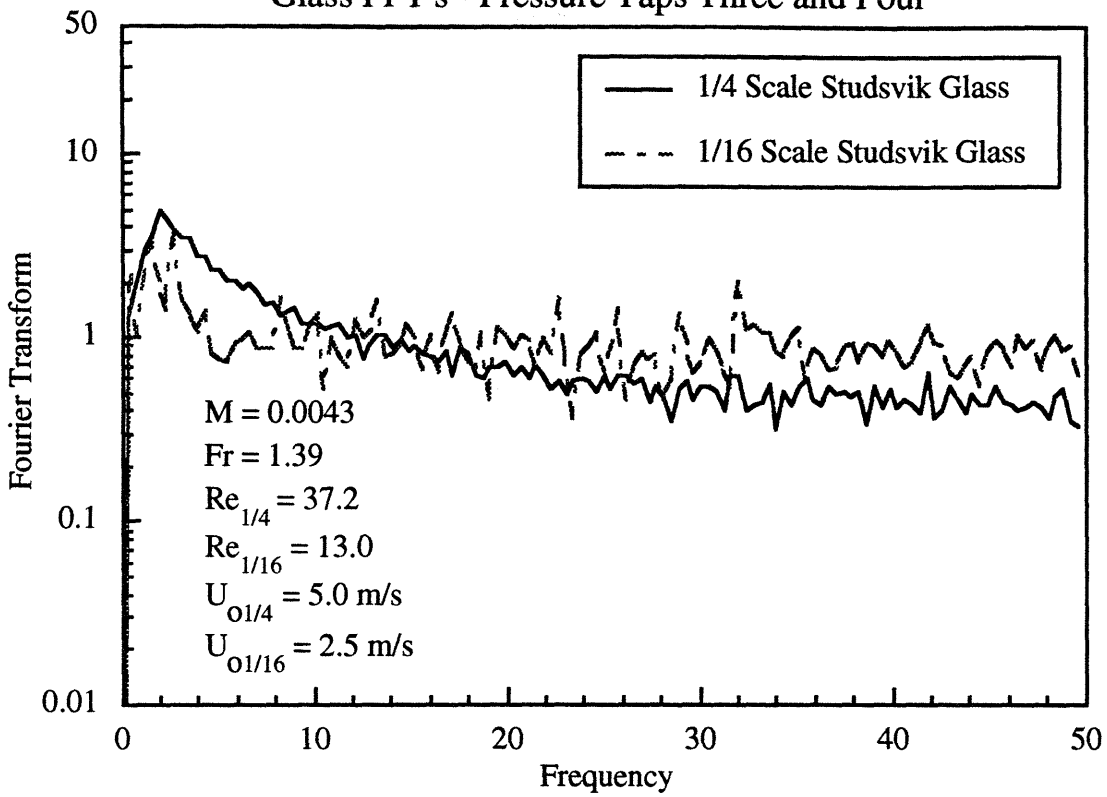

Figure 6.26

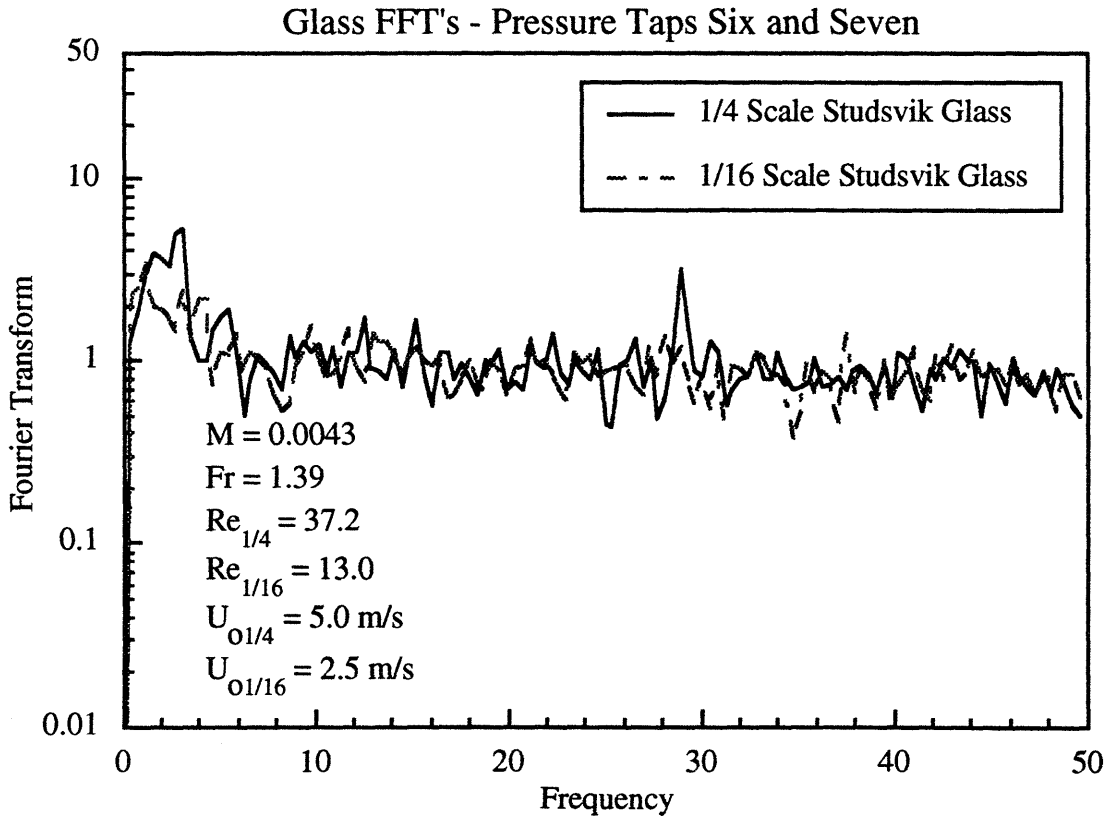

Figure 6.27

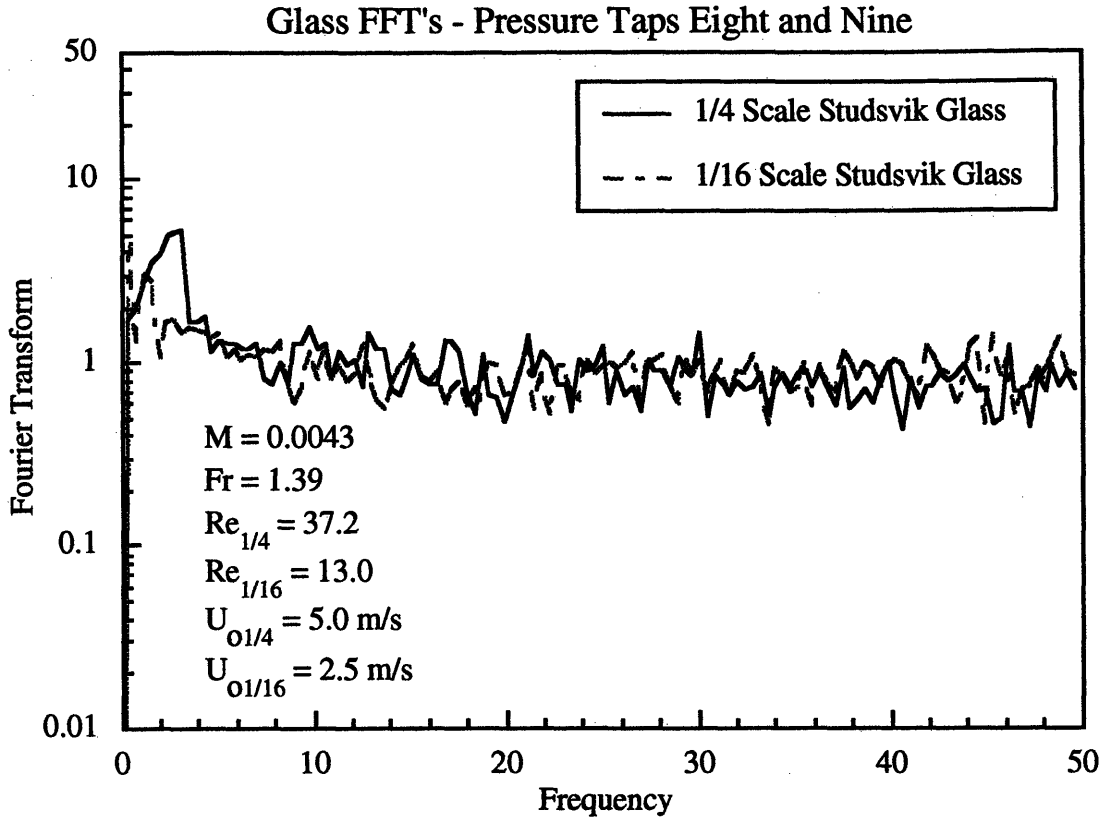

6.1.4 Discussion of Results

The average solid fraction profiles when utilizing the simplified scaling laws to scale between properly scaled glass samples in two different sized geometrically similar beds are in good agreement for all superficial velocities tested; the particle diameter based Reynolds numbers varied significantly between runs. Nearly all portions of the all the curves lie within confidence interval limits. It can be seen that as the velocity increased, the solid fraction profile decreased at the given solids mass flux. This is consistent with trends observed by other investigators.

The probability density functions for the glass runs demonstrated acceptable agreement. There does not seem to be a strong correlation between the superficial velocity and the agreement in the probability density functions, although the histograms appear to be more erratic at lower velocities in the 1/4 scale Studsvik bed. In most cases, the agreement in histograms is better in the top of the bed. This is consistent with agreement of the solid fraction profiles.

The power spectral densities for the glass runs do not show the dominant frequencies which might be seen in a bubbling bed. However, the results for the two beds appear to be in

reasonable agreement.

6.2 Scaling With Plastic Particles

Tables 6.5 through 6.7 provide the operational data, along with information concerning the particles and bed utilized in the simplified scaling tests using plastic in geometrically similar beds of different size. In these Tables, Ga represents the Galileo number defined as $\frac{\rho_s^2 d_p^3 g}{\mu_f^2}$. Tests were conducted at three different superficial velocities utilizing the phase one 1/16 scale Studsvik bed and the modified 1/4 scale Studsvik bed. Heat transfer data taken during these tests is presented in Chapter 4.

6.2.1 Solid Fraction Profiles

The average solid fraction profiles for the simplified scaling tests using plastic are given in Figures 6.28 through 6.30. The calculated solid fractions are plotted versus the average of the heights of the associated pressure taps. Error bars are based on calculated standard deviations in solid flow measurements and pressure time traces.

Table 6.5

Simplified Scaling Using Glass - Condition 1

	Large Bed	Small Bed
u_o (m/s)	3.0	1.5
u_{mf} (cm/s) Ergun Eqn.	2.64	1.25
u_{mf} (cm/s) measured	1.50	0.85
d_p (microns)	144.5	99.5
L (m)	1.83	0.46
A_{cs} (m^2)	1.68E-2	1.05E-3
G_s (kg/m^2-s)	12.6	6.25
$Re_{dp,uo}$	26.7	9.88
$Re_{L,uo}$	3.63E5	4.54E4
Fr	0.50	0.50
$\left(\frac{u_o}{u_{mf}}\right)_{Ergun\ eqn.}$	113.6	120.0
$\left(\frac{u_o}{u_{mf}}\right)_{measured}$	200.0	176.5
$\left(\frac{G_s}{\rho_s u_o}\right)$	3.0E-3	3.0E-3
$\left(\frac{\rho_s}{\rho_f}\right)$	1167	1167
Ga	1.76E5	5.76E4

Table 6.6

Simplified Scaling Using Glass - Condition 1

	Large Bed	Small Bed
u_o (m/s)	4.0	2.0
u_{mf} (cm/s) Ergun Eqn.	2.64	1.25
u_{mf} (cm/s) measured	1.50	0.85
d_p (microns)	144.5	99.5
L (m)	1.83	0.46
A_{cs} (m^2)	1.68E-2	1.05E-3
G_s (kg/m^2-s)	14.0	7.0
$Re_{dp,uo}$	38.3	13.2
$Re_{L,uo}$	5.33E5	6.05E4
Fr	0.89	0.89
$\left(\frac{u_o}{u_{mf}}\right)_{\text{Ergun eqn.}}$	151.5	160.0
$\left(\frac{u_o}{u_{mf}}\right)_{\text{measured}}$	266.7	235.3
$\left(\frac{G_s}{\rho_s u_o}\right)$	2.5E-3	2.5E-3
$\left(\frac{\rho_s}{\rho_f}\right)$	1167	1167
Ga	1.76E5	5.76E4

Table 6.7

Simplified Scaling Using Glass - Condition 1

	Large Bed	Small Bed
u_o (m/s)	5.0	2.5
u_{mf} (cm/s) Ergun Eqn.	2.64	1.25
u_{mf} (cm/s) measured	1.50	0.85
d_p (microns)	144.5	99.5
L (m)	1.83	0.46
A_{cs} (m^2)	1.68E-2	1.05E-3
G_s (kg/m^2-s)	16.1	8.0
$Re_{dp,uo}$	47.8	16.5
$Re_{L,uo}$	6.66E5	7.57E4
Fr	1.39	1.39
$\left(\frac{u_o}{u_{mf}}\right)_{Ergun\ eqn.}$	189.4	200.0
$\left(\frac{u_o}{u_{mf}}\right)_{measured}$	333.3	294.1
$\left(\frac{G_s}{\rho_s u_o}\right)$	2.3E-3	2.3E-3
$\left(\frac{\rho_s}{\rho_f}\right)$	1167	1167
Ga	1.76E5	5.76E4

6.2.2 Histograms

Histograms of the solid fraction data of the simplified scaling for plastic are depicted in Figures 6.31 through 6.42. Histograms are shown for solid fractions between pressure taps 1 and 2, 3 and 4, 5 and 6, 7 and 8 (recall that the pressure taps are numbered from the bottom to the top of the bed). In these plots, probability is plotted versus the solid fraction.

6.2.3 Power Spectral Densities

FFT's of the pressure fluctuation data for the plastic simplified scaling tests are given in Figures 6.43 through 6.54. FFT's are shown for the same pressure taps as the probability density functions. In these plots, the fourier transform in plotted versus the frequency in Hz.

Figure 6.28

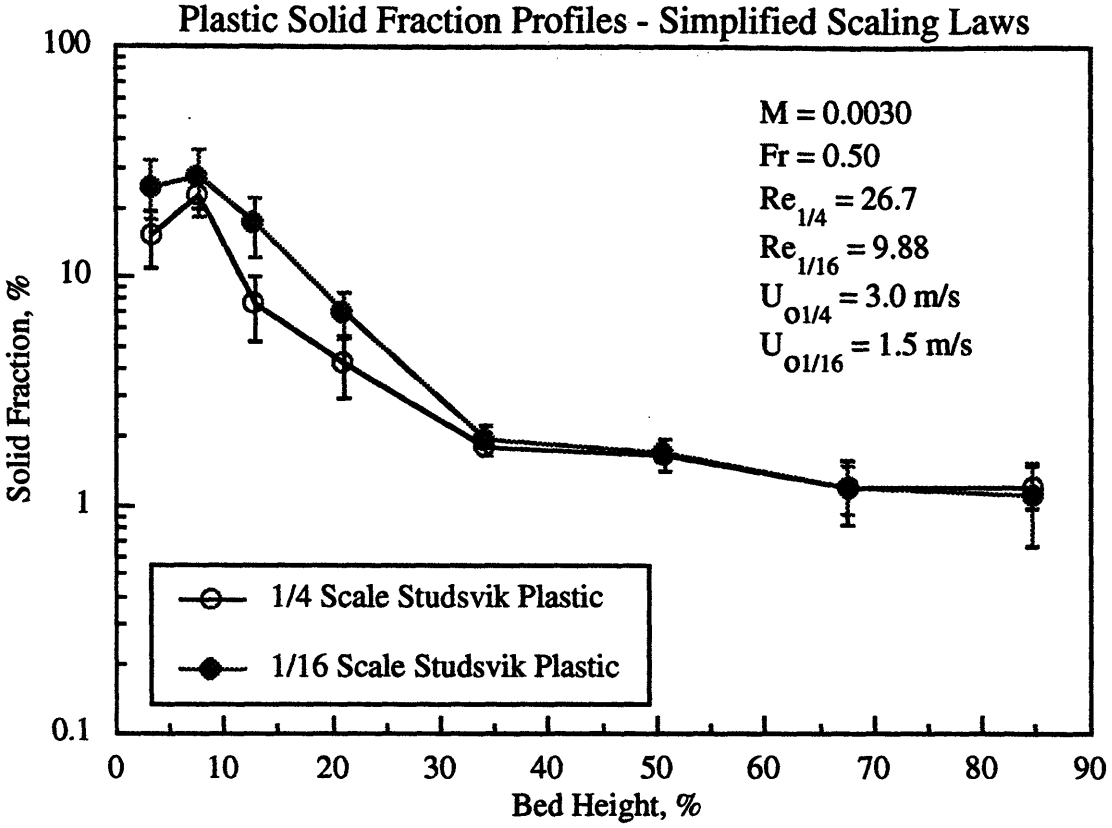

Figure 6.29

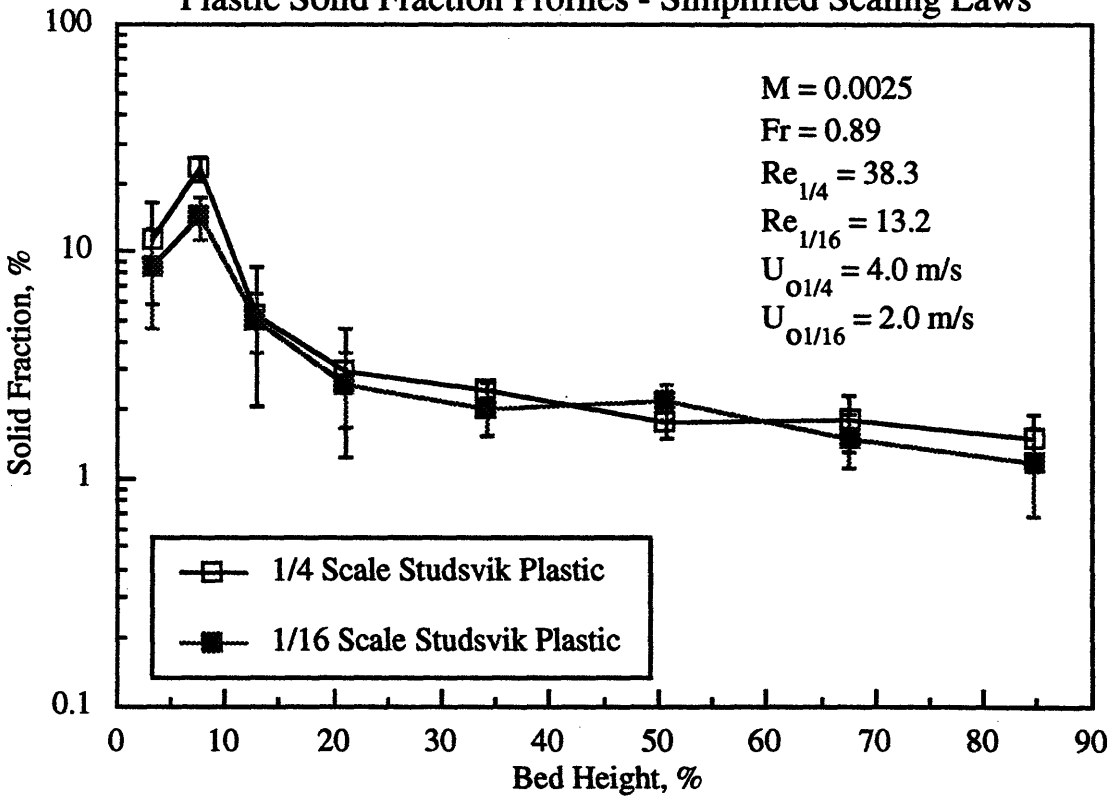

Figure 6.30

Plastic Solid Fraction Profiles - Simplified Scaling Laws

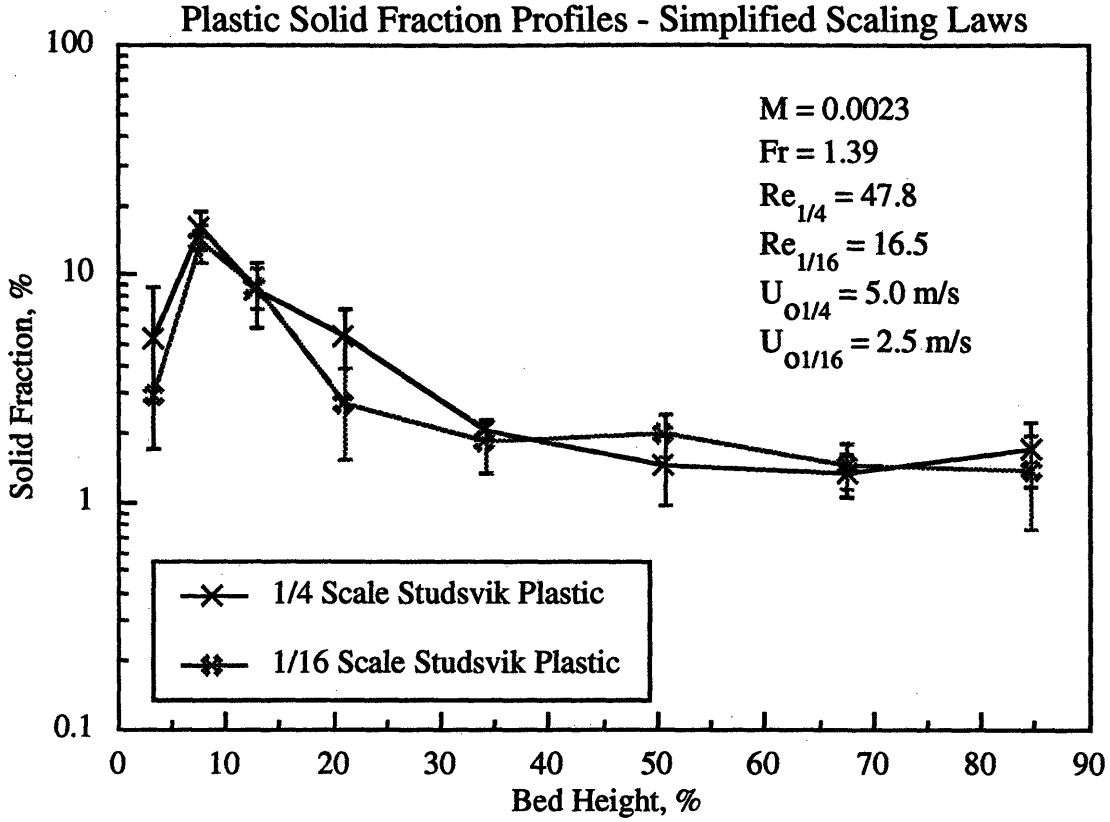

Figure 6.31

Plastic Histograms - Pressure Taps One and Two

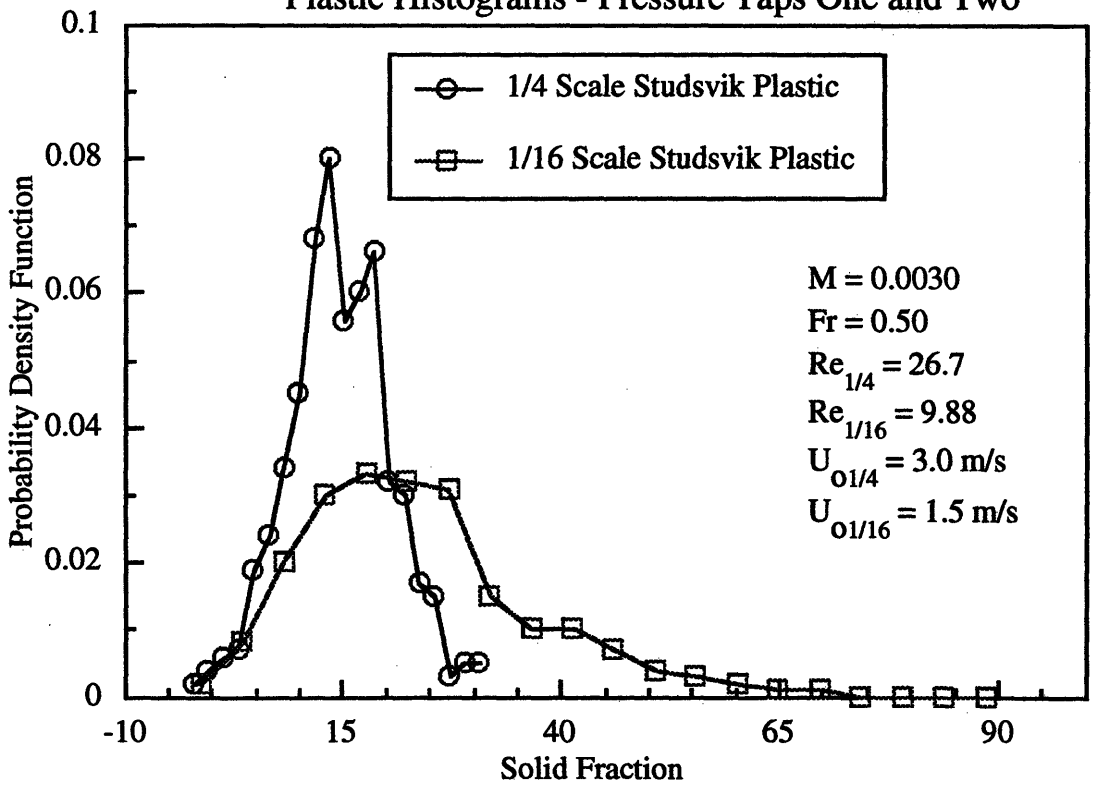

Figure 6.32

Plastic Histograms - Pressure Taps Three and Four

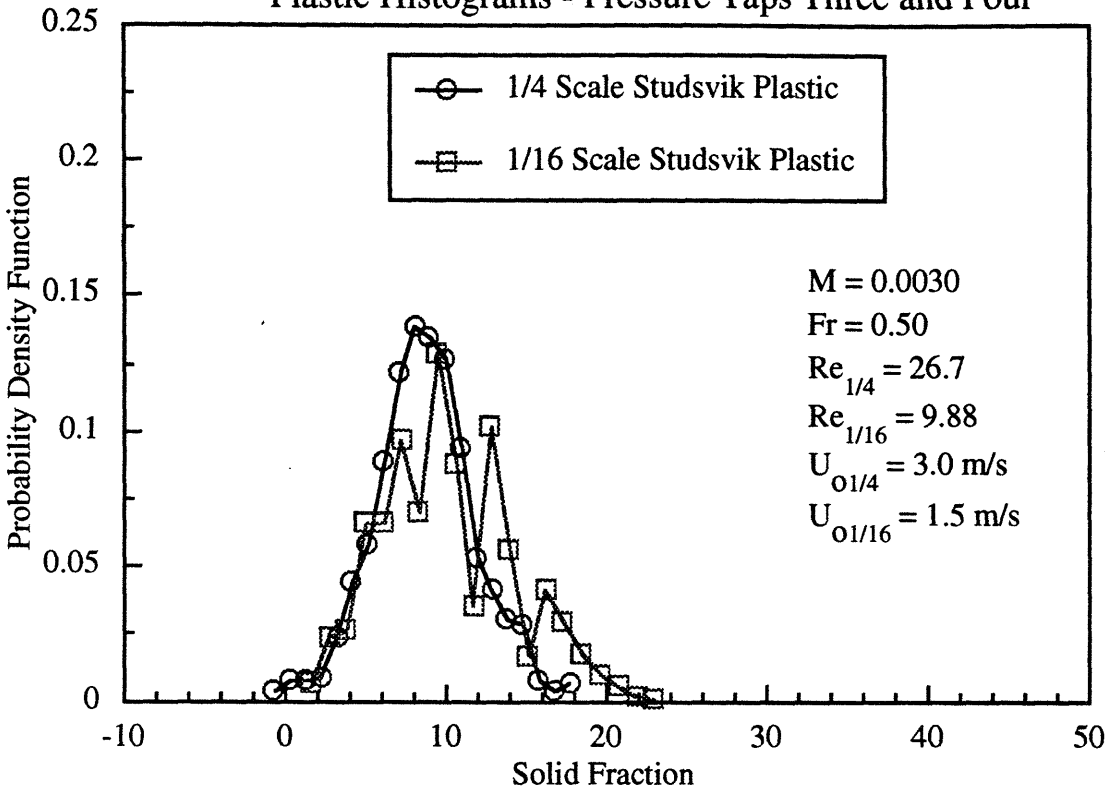

Figure 6.33

Plastic Histograms - Pressure Taps Six and Seven

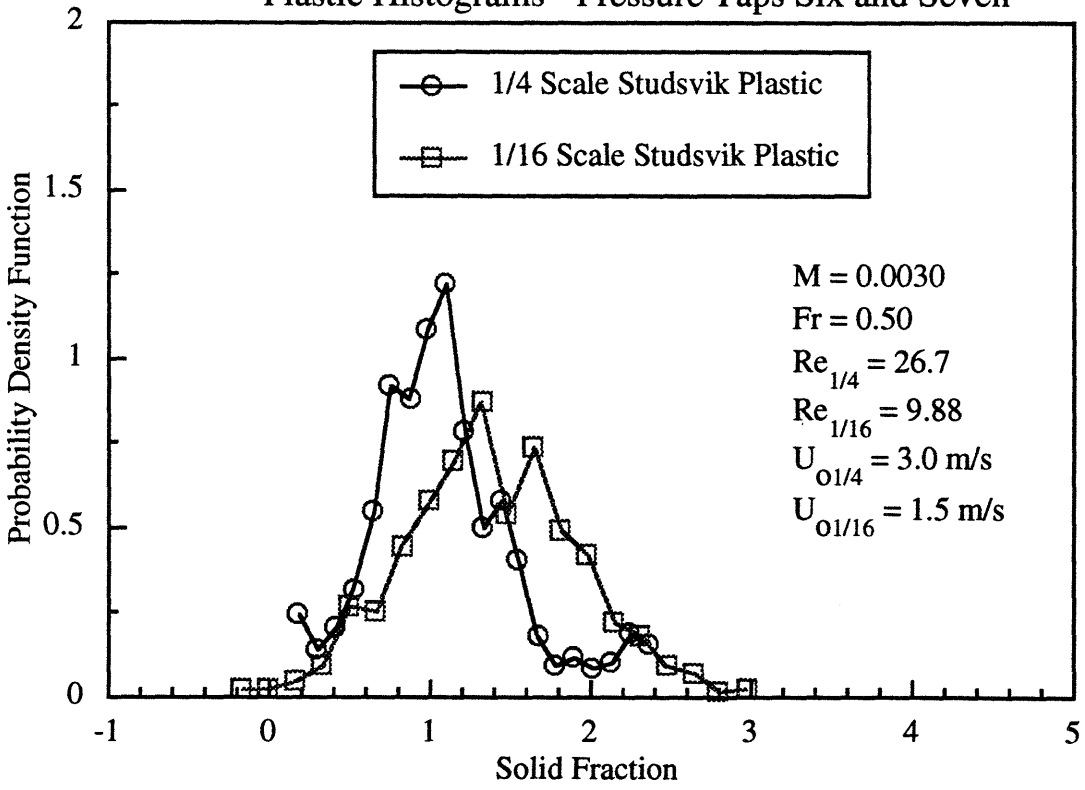

Figure 6.34

Plastic Histograms - Pressure Taps Eight and Nine

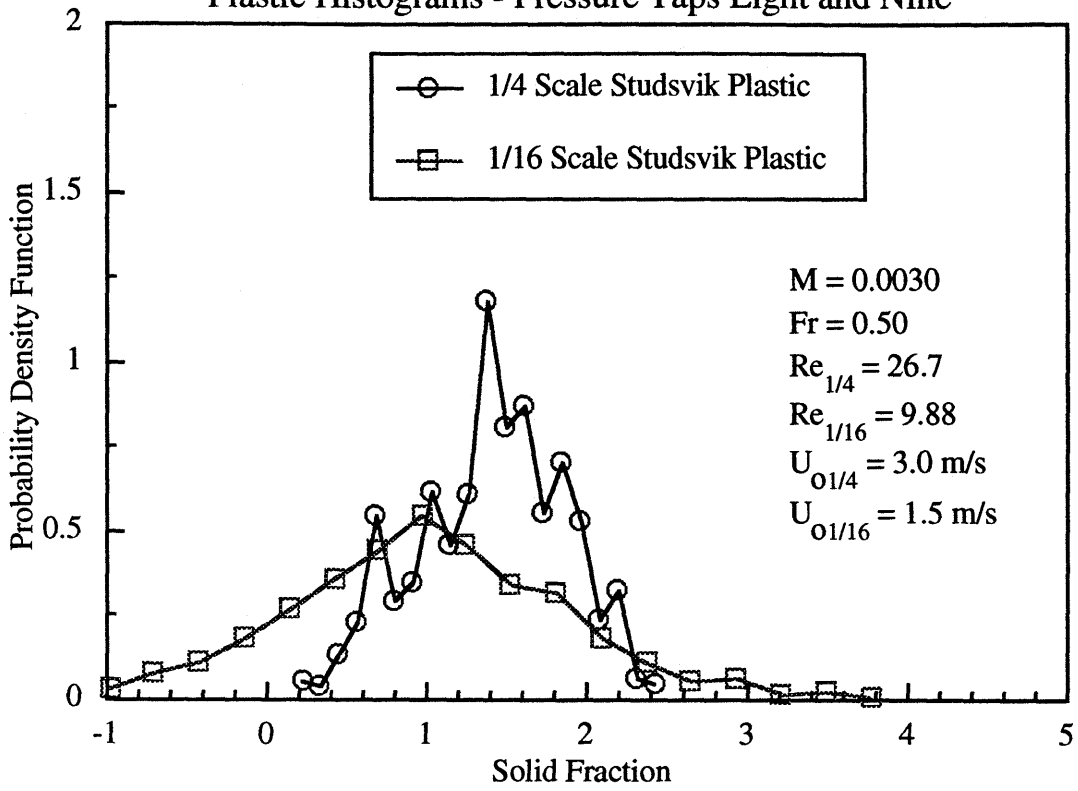

Figure 6.35

Plastic Histograms - Pressure Taps One and Two

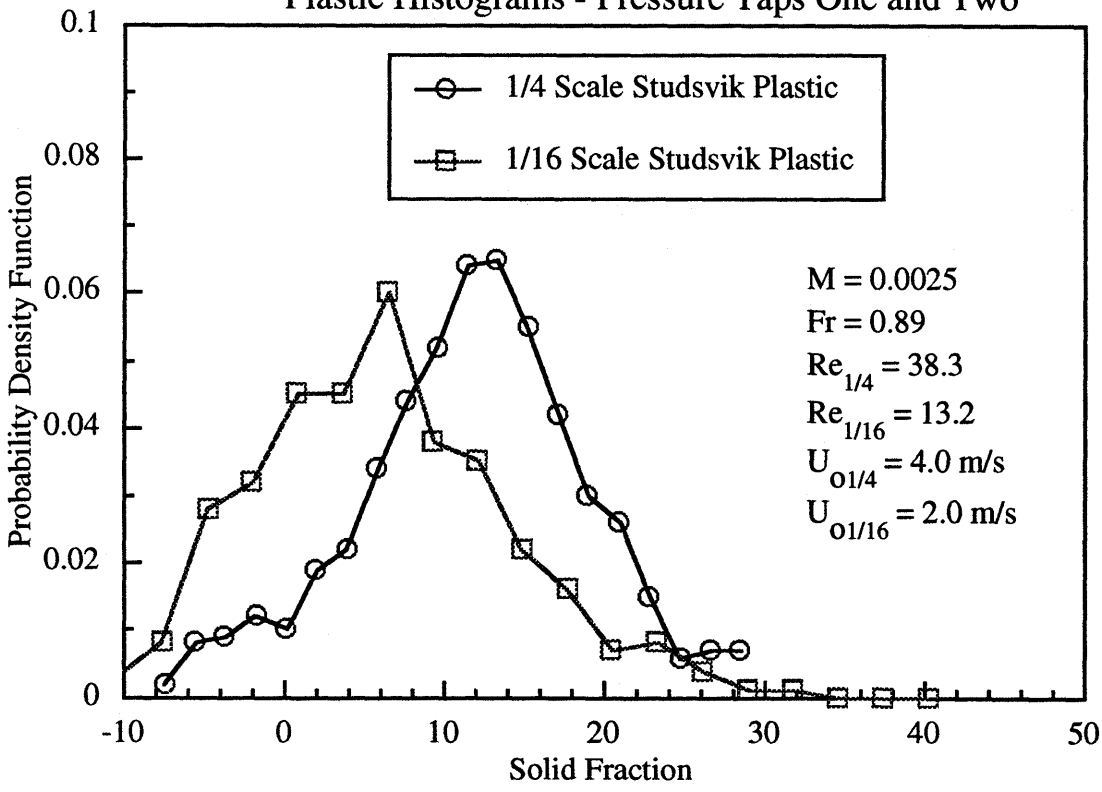

Figure 6.36

Plastic Histograms - Pressure Taps Three and Four

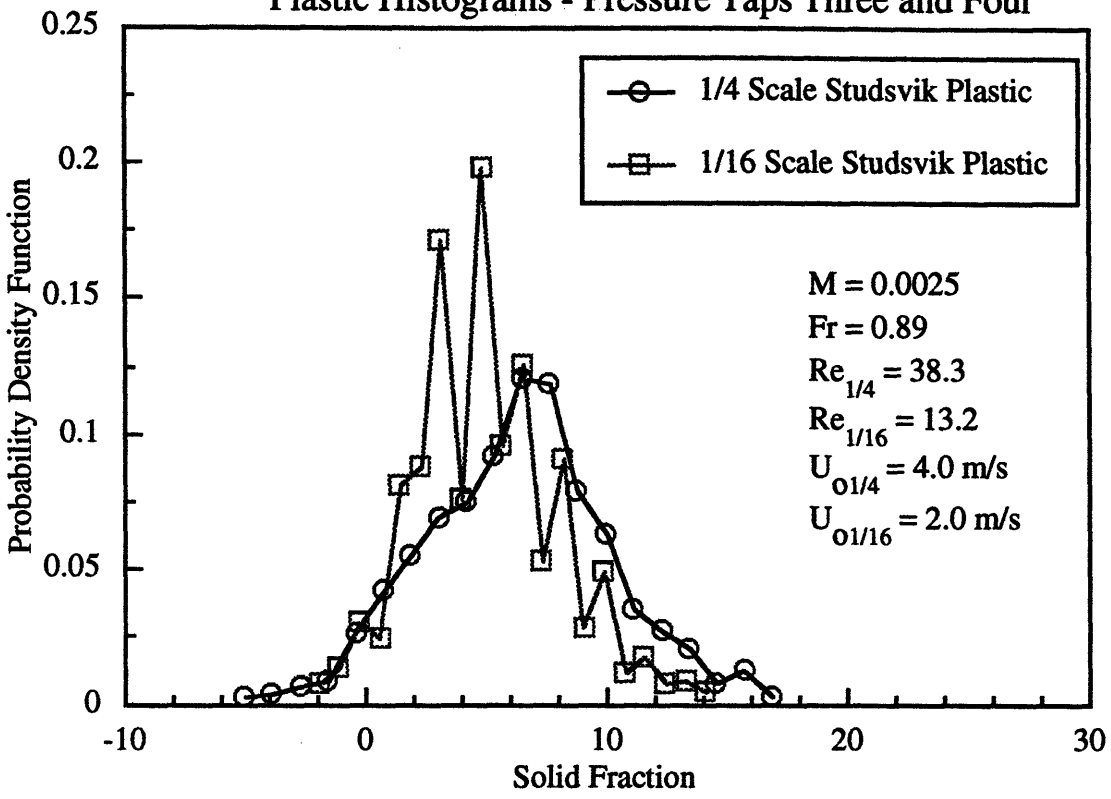

Figure 6.37

Plastic Histograms - Pressure Taps Six and Seven

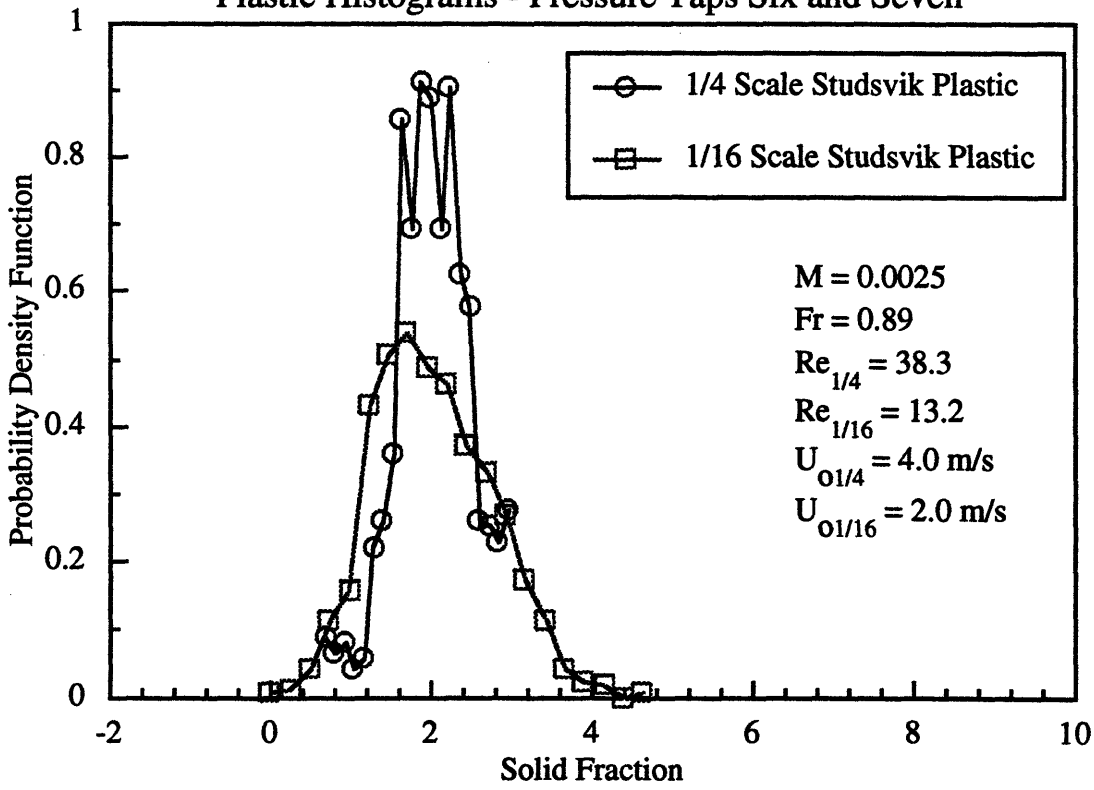

Figure 6.38

Plastic Histograms - Pressure Taps Eight and Nine

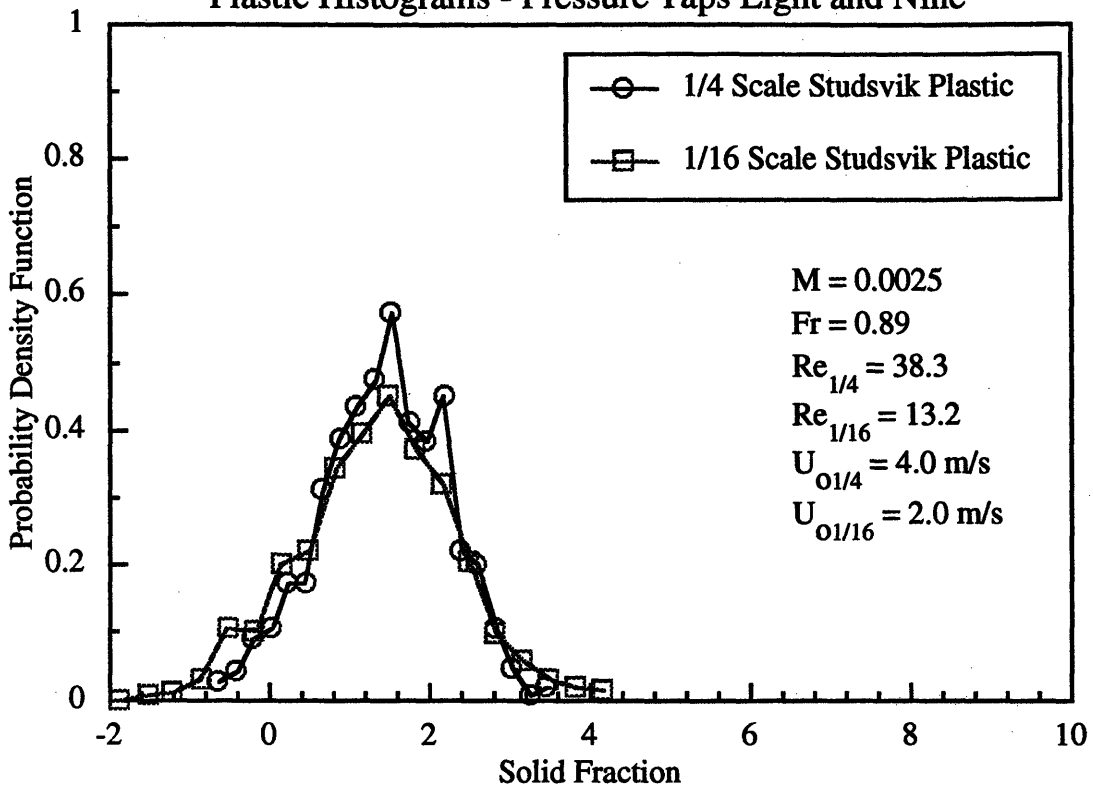

Figure 6.39

Plastic Histograms - Pressure Taps One and Two

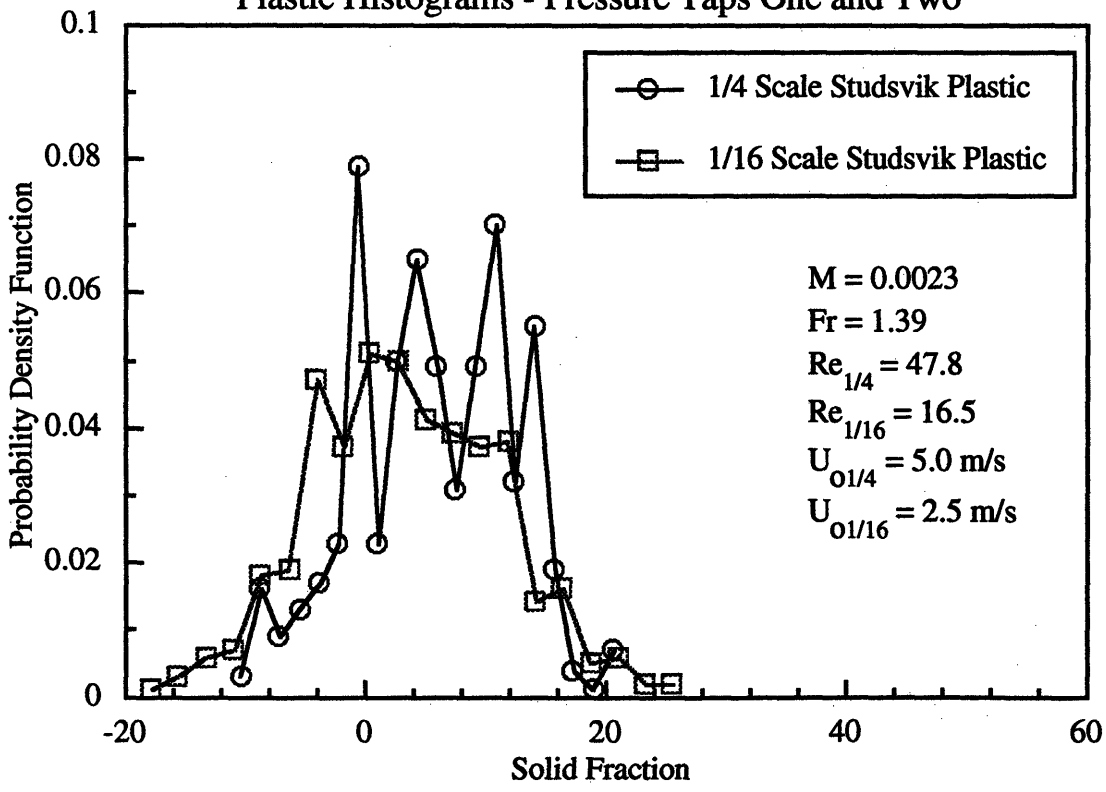

Figure 6.40

Plastic Histograms - Pressure Taps Three and Four

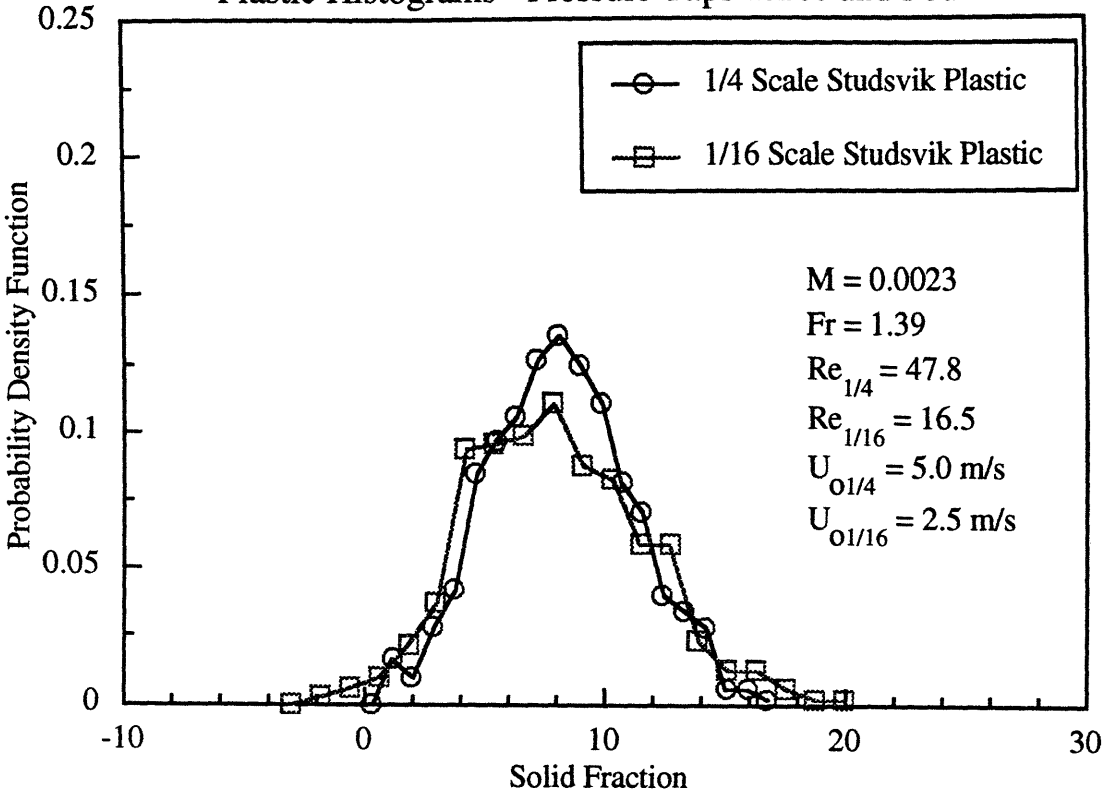

Figure 6.41

Plastic Histograms - Pressure Taps Six and Seven

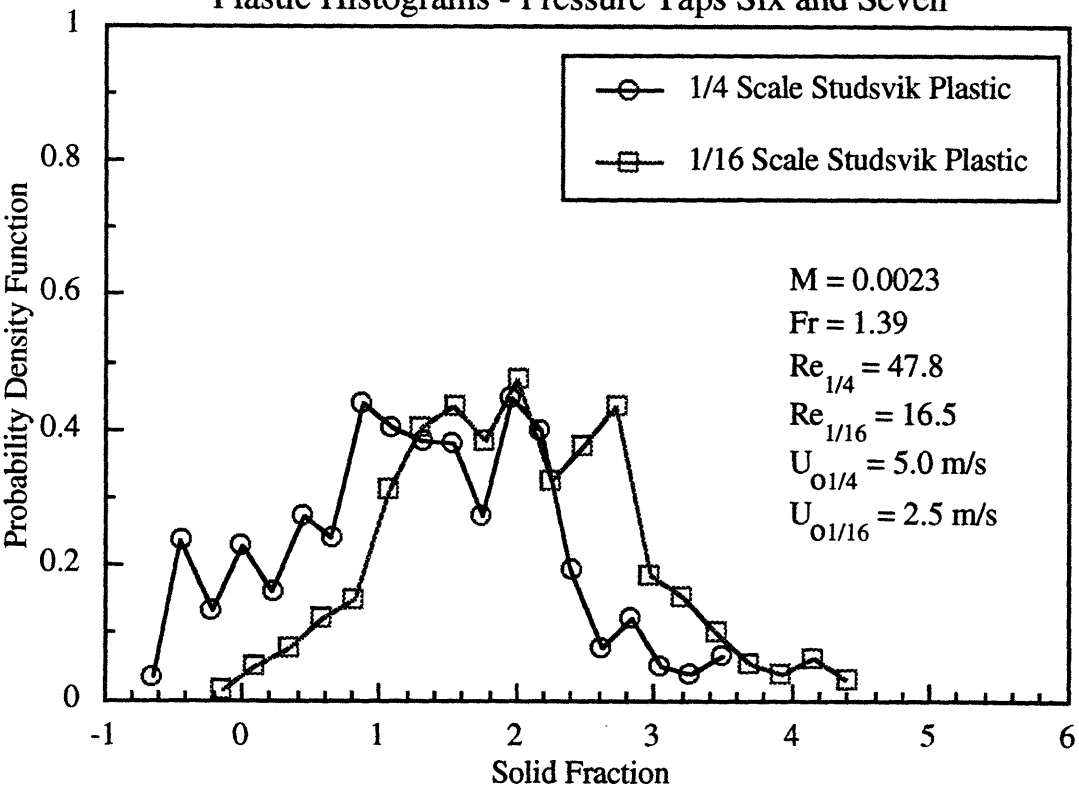

Figure 6.42

Plastic Histograms - Pressure Taps Eight and Nine

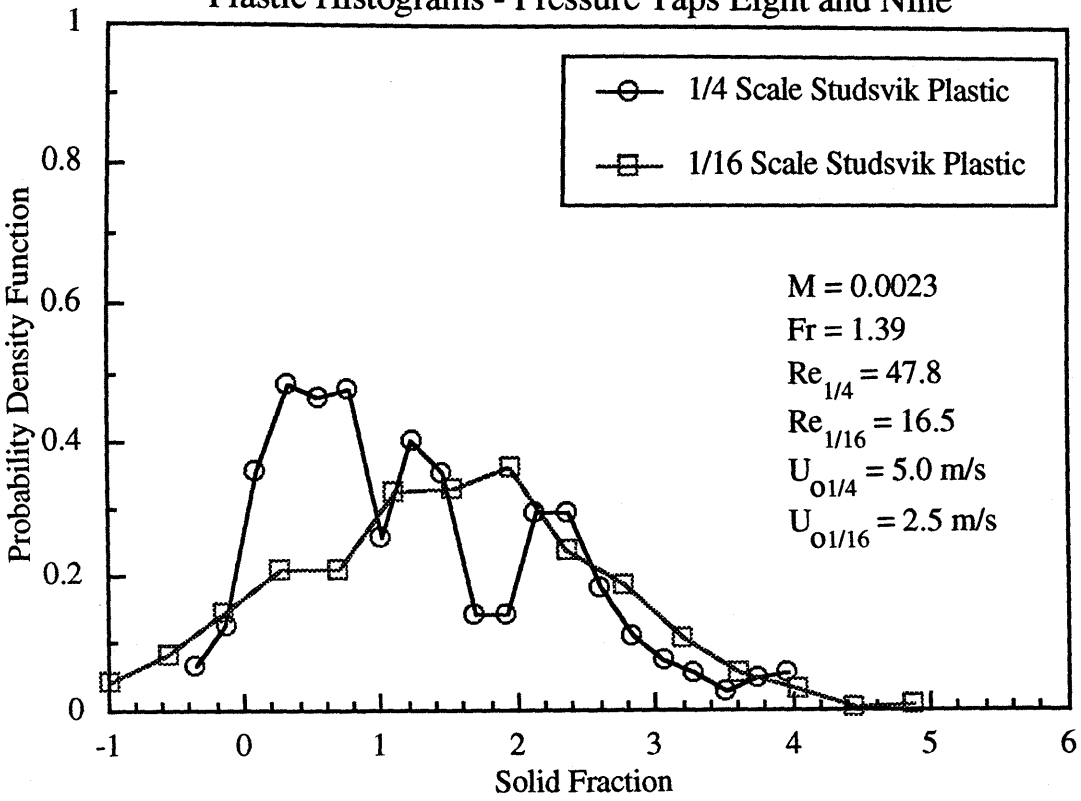

Figure 6.43

Plastic FFT's - Pressure Taps One and Two

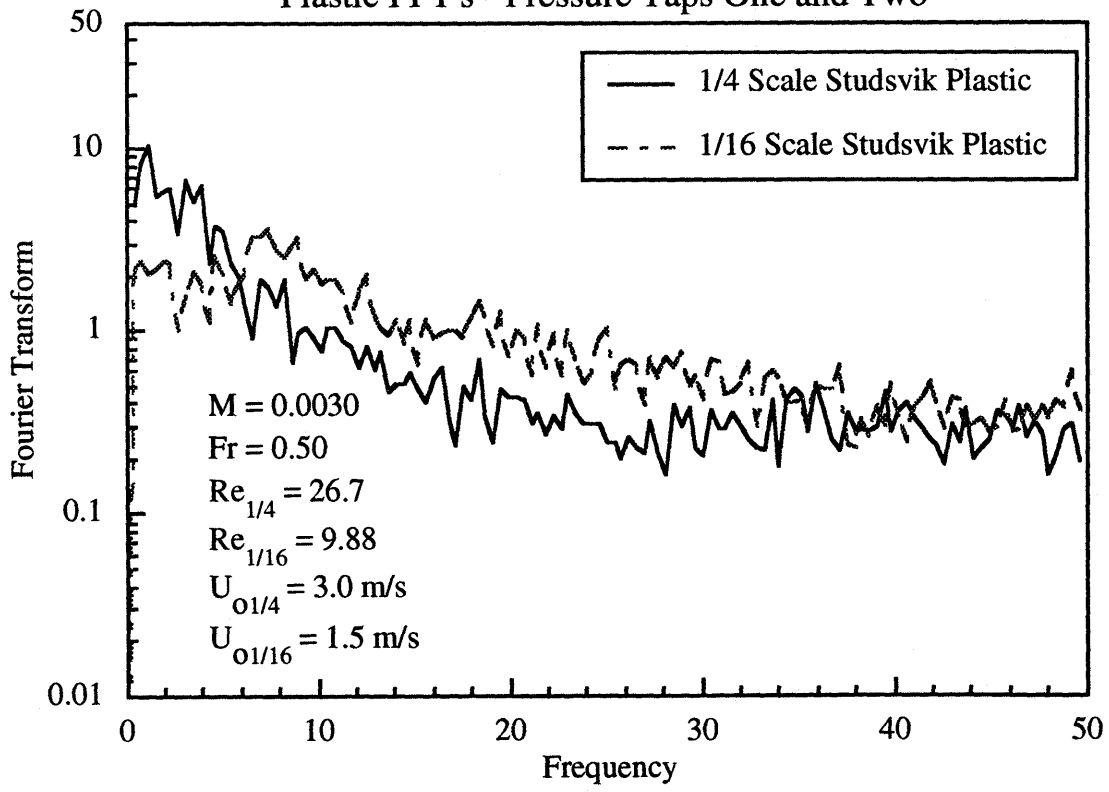

Figure 6.44

Plastic FFT's - Pressure Taps Three and Four

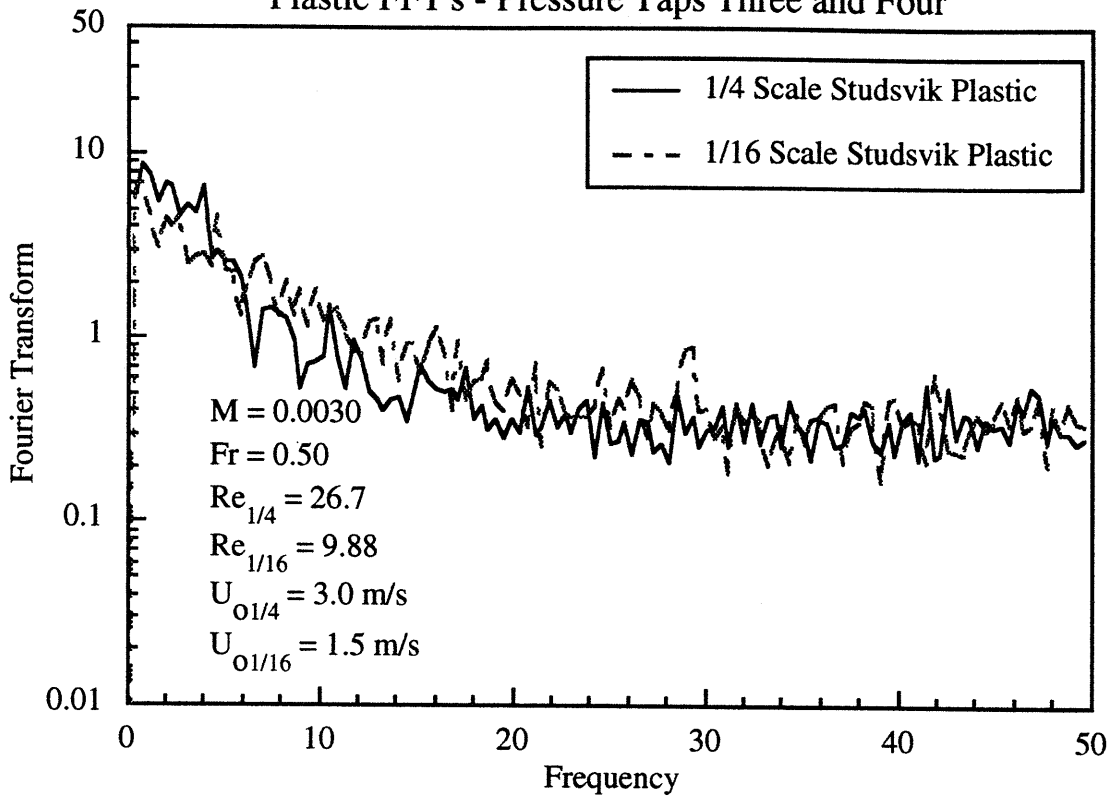

Figure 6.45

Plastic FFT's - Pressure Taps Six and Seven

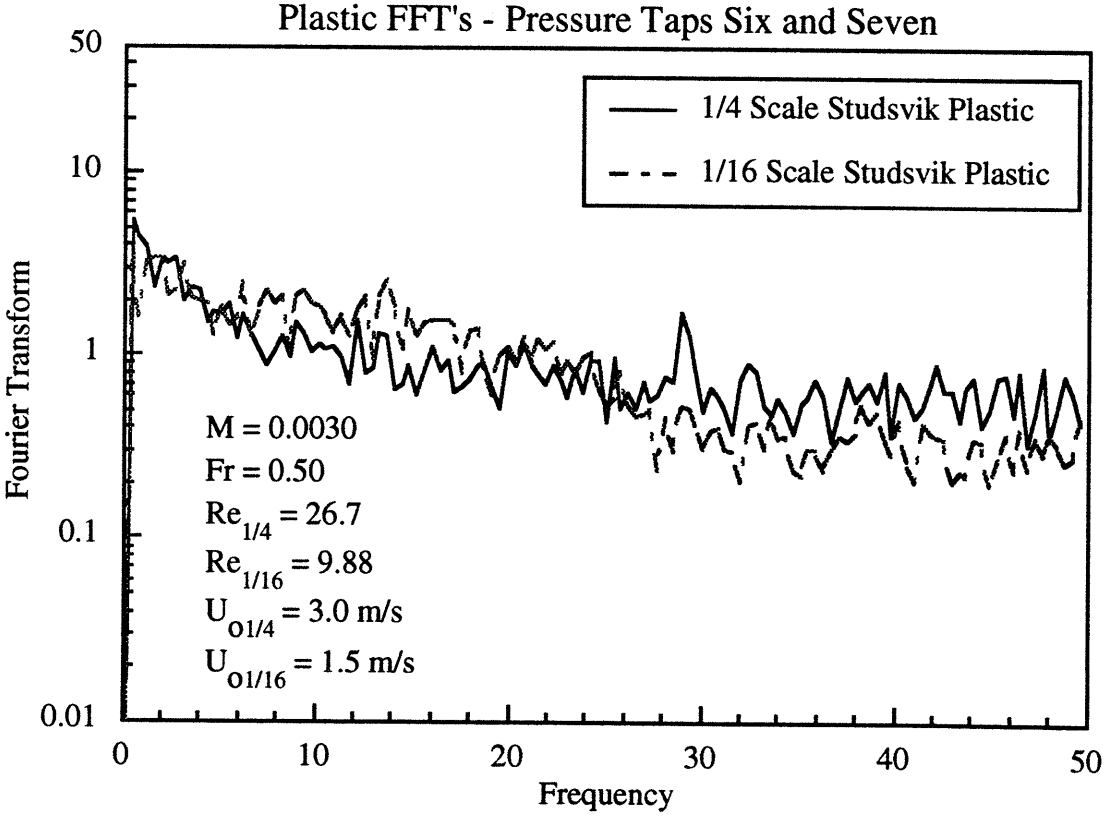

Figure 6.46

Plastic FFT's - Pressure Taps Eight and Nine

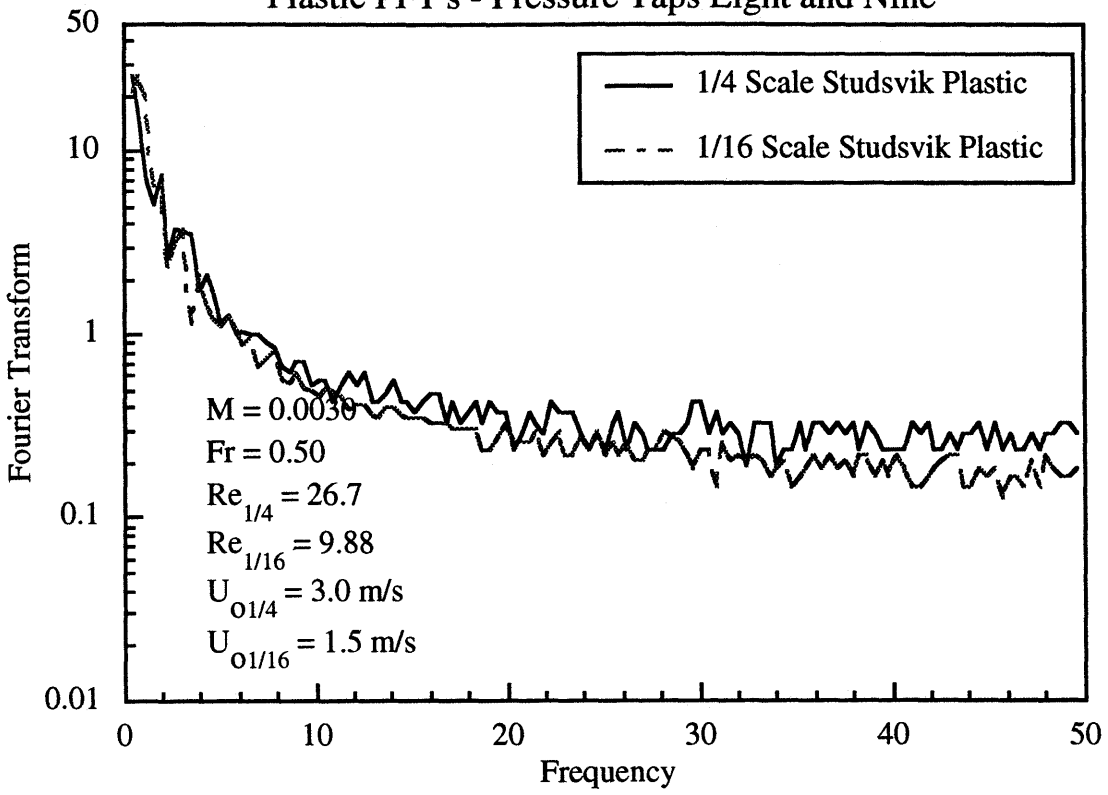

Figure 6.47

Plastic FFT's - Pressure Taps One and Two

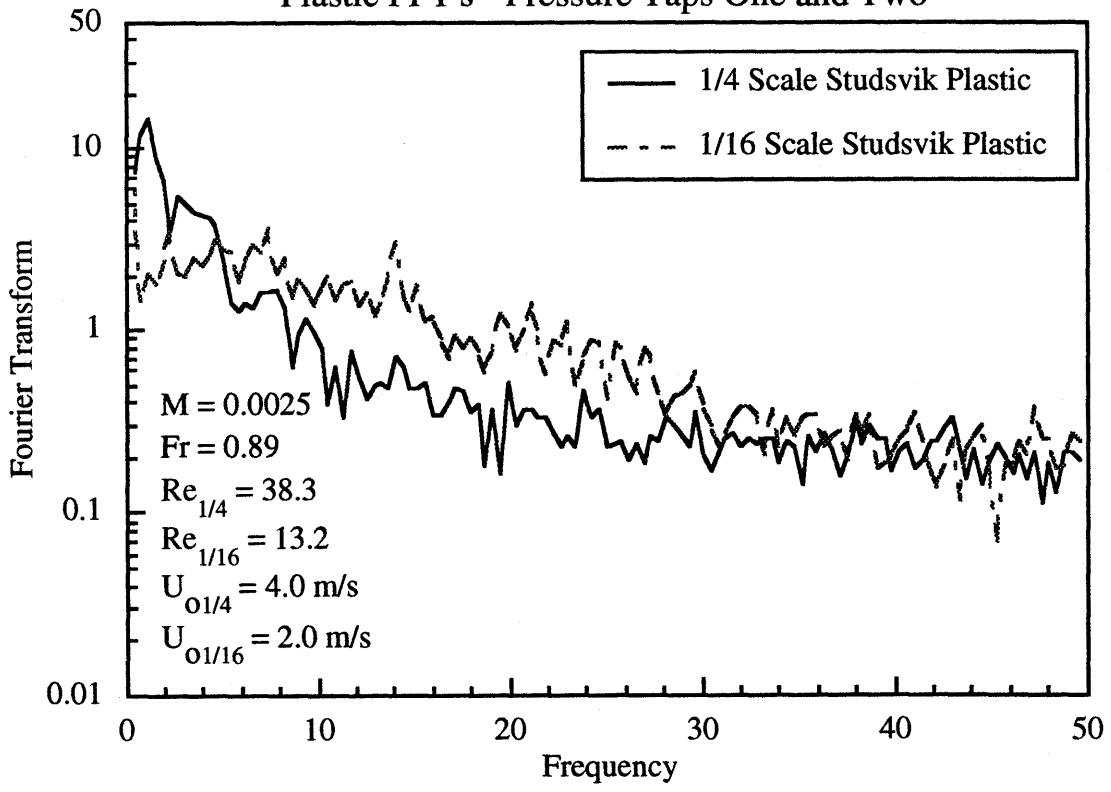

Figure 6.48

Plastic FFT's - Pressure Taps Three and Four

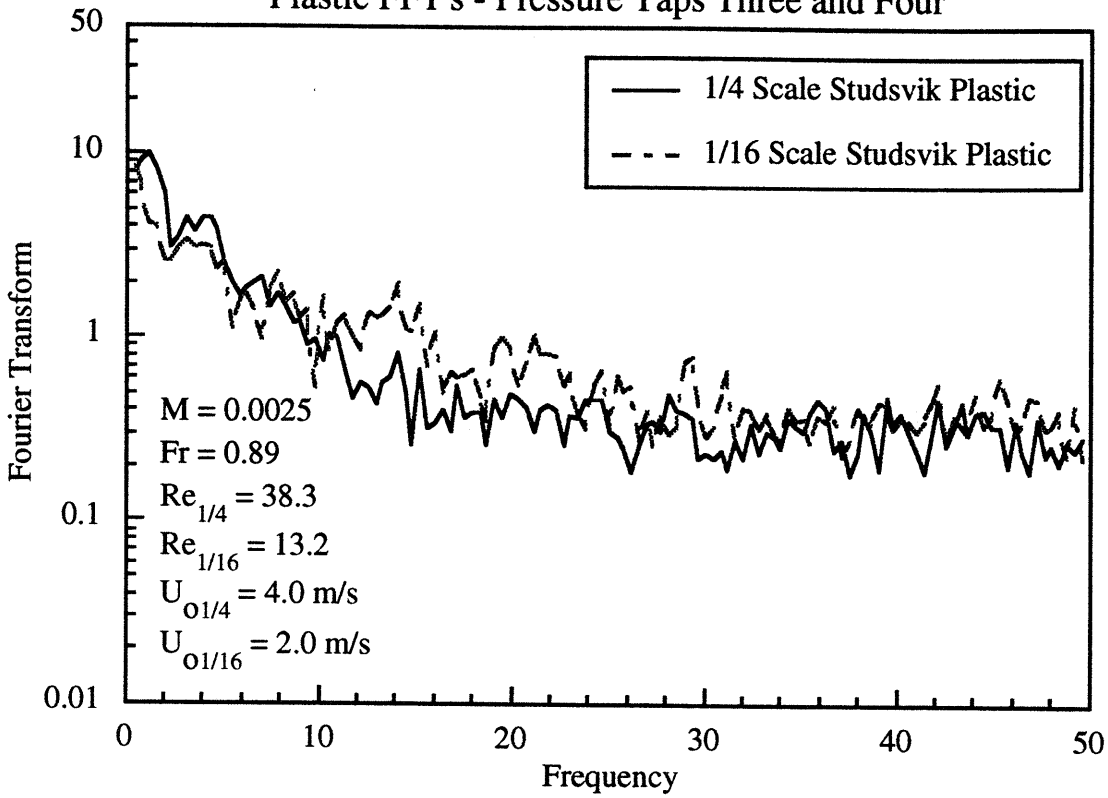

Figure 6.49

Plastic FFT's - Pressure Taps Six and Seven

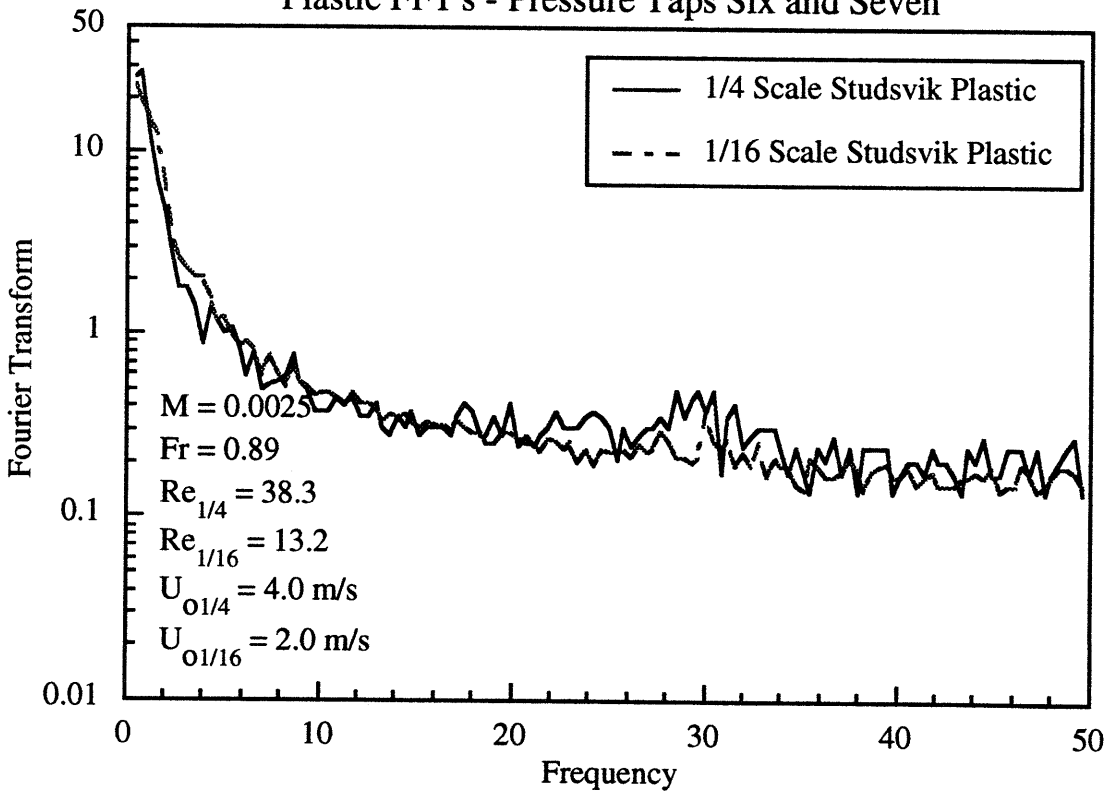

Figure 6.50

Plastic FFT's - Pressure Taps Eight and Nine

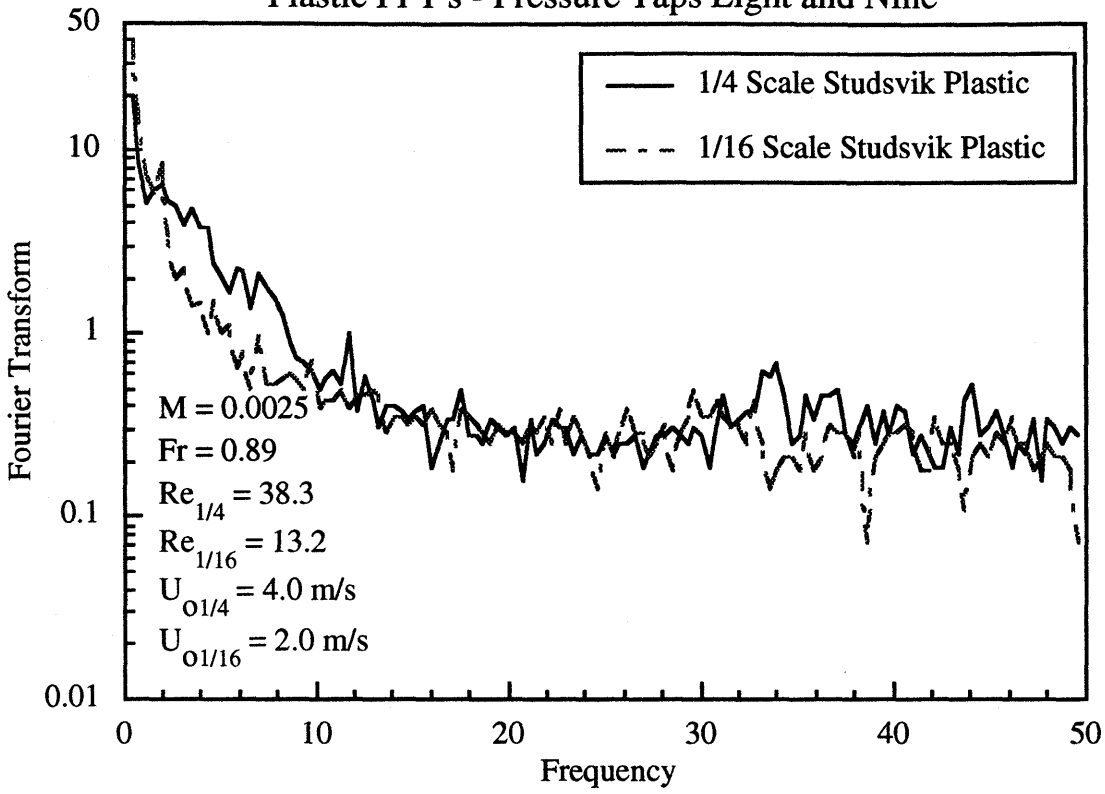

Figure 6.51

Plastic FFT's - Pressure Taps One and Two

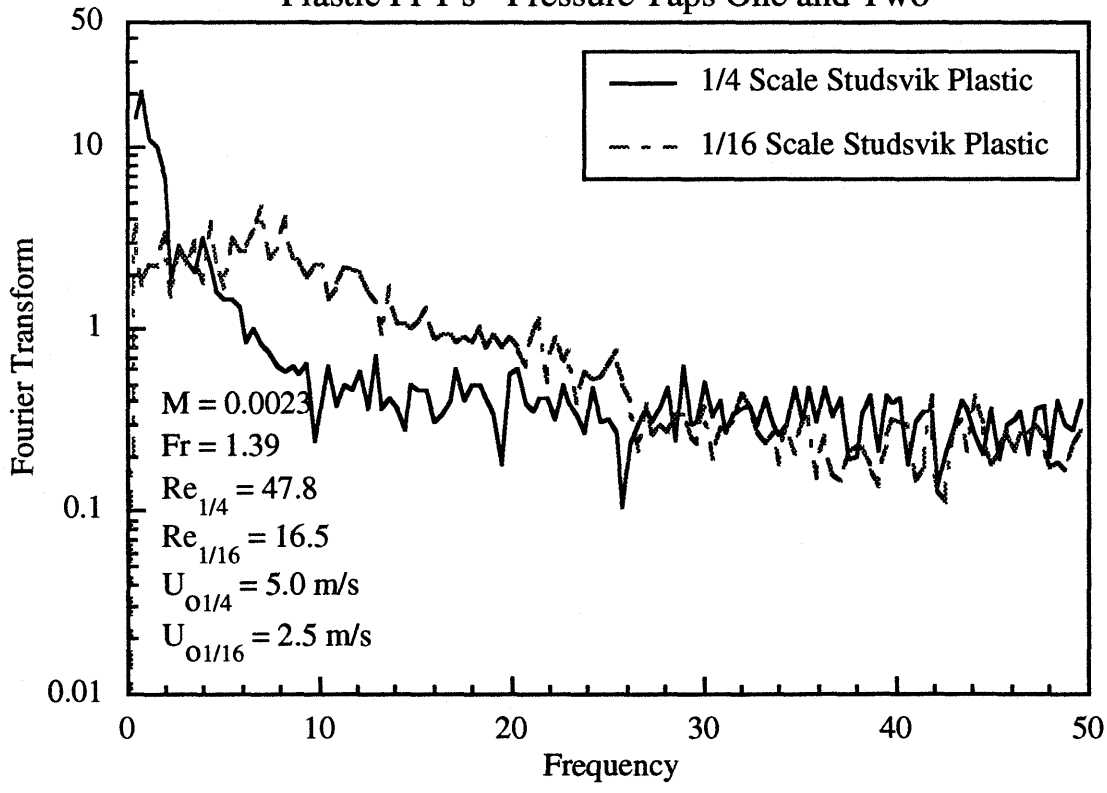

Figure 6.52

Plastic FFT's - Pressure Taps Three and Four

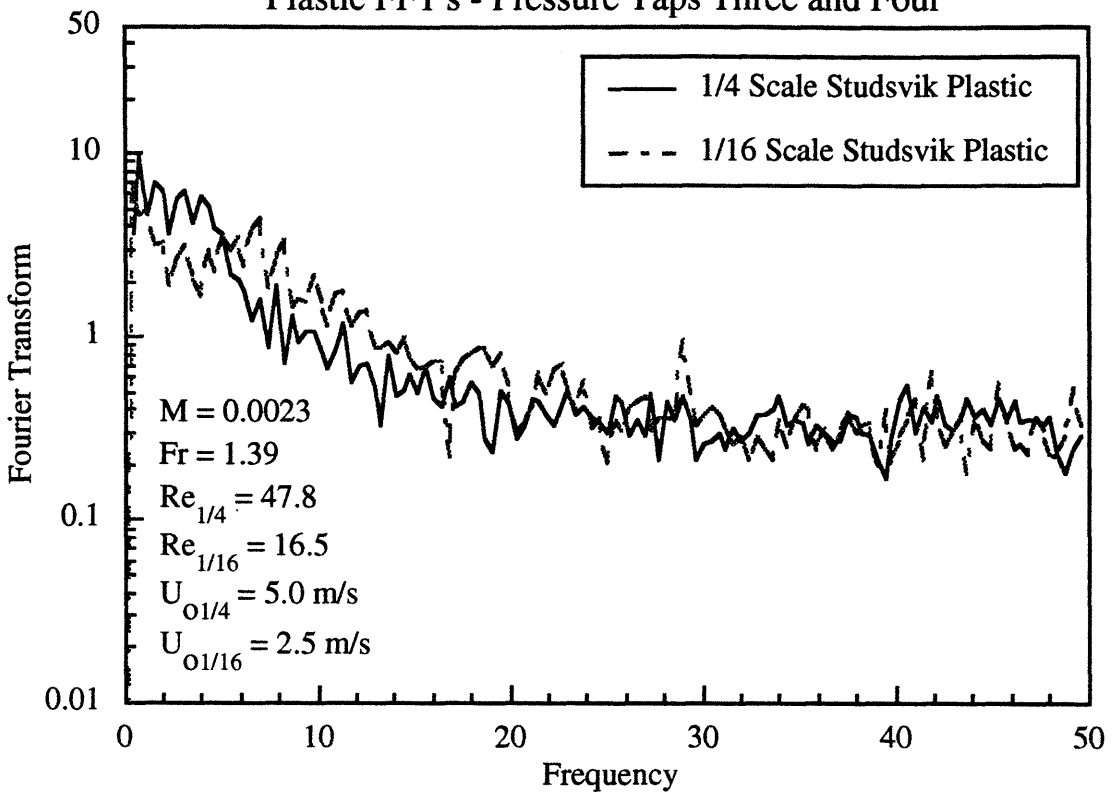

Figure 6.53

Plastic FFT's - Pressure Taps Six and Seven

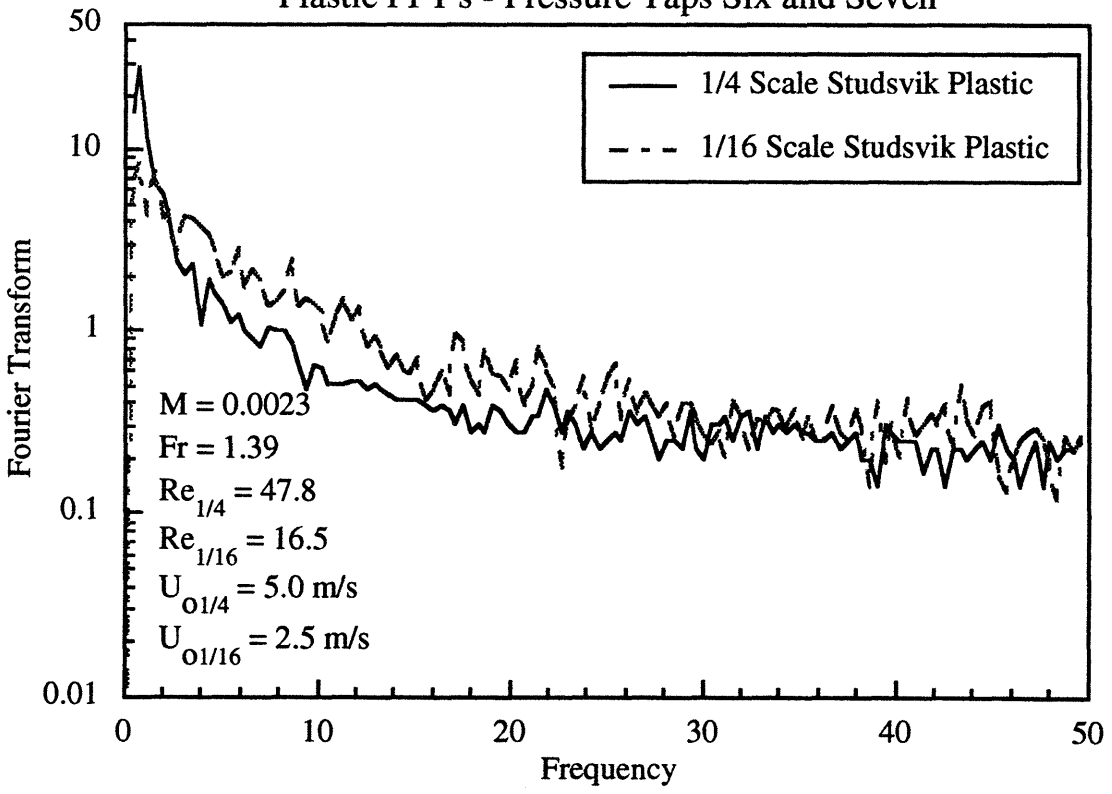

Figure 6.54

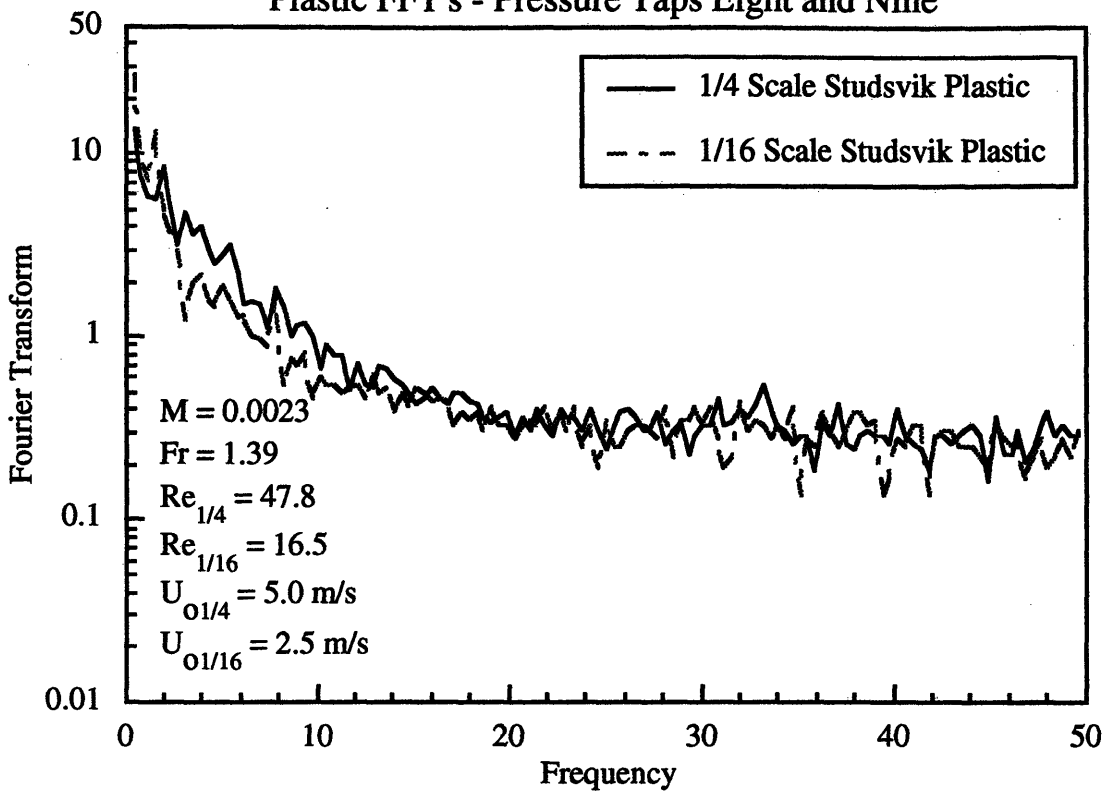

6.2.4 Discussion of Results

Much of the discussion which addressed the simplified scaling laws when glass was used as the bed material applies also with plastic. The average solid fraction profiles when utilizing the simplified scaling laws to scale between properly sized plastic samples in two different sized geometrically similar beds are in good agreement for all superficial velocities tested, even though particle diameter based Reynolds numbers varied significantly between runs. Nearly all portions of the all the curves lie within confidence interval limits. One notable feature of the solid fraction profiles is the measured dip in solid fraction directly above the distributor plate. This phenomena was visually verified in the 1/4 scale Studsvik bed where a small very dilute region was observed directly over the distributor plate. It appeared that gas formed a series of voids directly above the distributor preventing the solid from reaching the distributor plate, much in the same manner as film boiling prevents liquid from reaching a surface.

The probability density functions for the glass runs demonstrated acceptable agreement. As was the case with the glass runs, there does not seem to be a strong correlation between the superficial velocity and the agreement in the probability density functions. In most cases, the agreement in histograms is better in the top of the bed, with the exception in some runs

of the area near the bed exit. The slight disagreement at the top of the beds may be due to the difference in geometries in the horizontal section of the beds. The larger bed has a foam insert directly behind the sparge tube which is followed by the primary U-tube separator. The horizontal section in the smaller bed only has the sparge tube. In addition, some of the disagreement may be an artifact of the width of the frequency interval used to compile the data. Discrepancies near the exit of the bed are described in more detail in Section 7.

Consistent with previous data, the power spectral densities for the plastic runs do not show dominant frequencies. However, the results for the two beds appear to be in reasonable agreement.

6.3 Hydrodynamic Scaling in Choked Beds

The choking correlations of Yang (1975 and 1983) and Youfsi and Gau (1974) indicate that in many of the runs conducted in conjunction with the simplified scaling laws using glass and plastic, significant portions of the bed were choked (Figures 6.55 and 6.56). Visual observations supported this prediction. However, it was noted in Section 5 that the viscous limit scaling laws do not predict or model the choking behavior in circulating fluidized beds. In order to determine the validity of the simplified scaling laws as they apply to choked beds, a brief dimensional analysis was conducted on the correlations which are best able to predict the choking phenomenon which bounds the fast fluidization regime.

Figure 6.55
Superficial Velocities at Incipient Choking for Glass - Yang Correlation

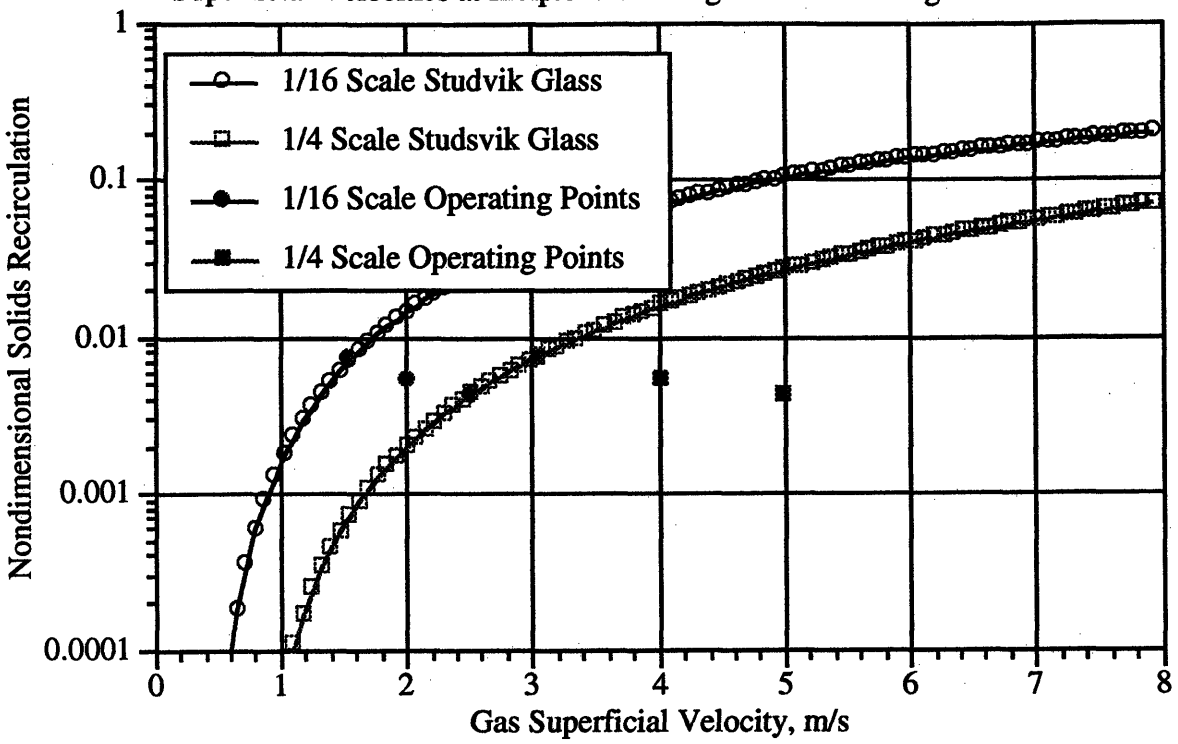

Figure 6.56
Superficial Velocities at Incipient Choking for Plastic - Yang Correlation

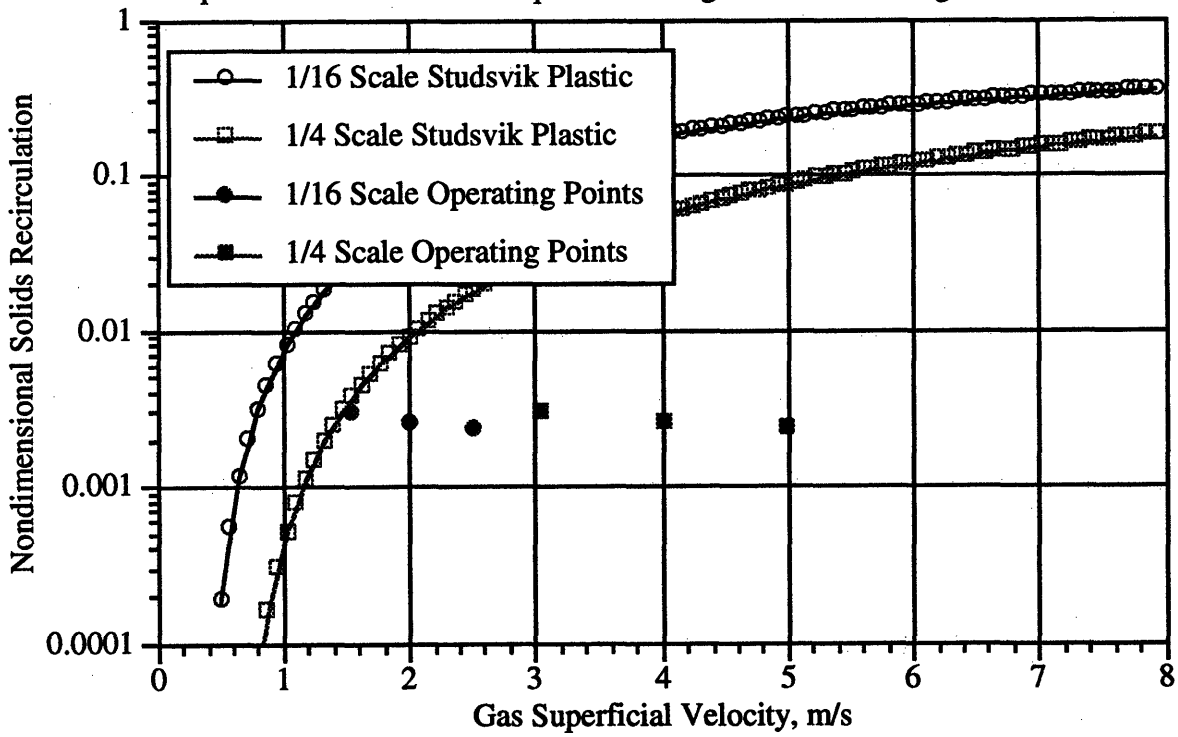

In order to describe the hydrodynamics of choked fast fluidized beds, it is necessary to state what is considered the definition of the fast fluidization regime. An extensive development of a practical definition for the fast fluidization regime was presented by Karri and

Knowlton (1990) based on the flow regime diagram developed by Takeuchi *et al.* (1986). This definition describes the regime as being bounded by two gas velocities which are termed U_{FF} and U_{DT}. U_{FF} was defined as the gas velocity below which the solids circulation flux cannot be maintained constant while decreasing the riser gas velocity. U_{DT} was characterized as the gas velocity at which the pressure gradients measured at different heights in the riser approach a constant for a given solids mass flux as the velocity is decreased. In light of this definition, the choking velocity, U_{FF}, represents the demarcation between the fast fluidized bed regime and the dense phase (turbulent/bubbling) regime. The velocity at minimum pressure drop on the phase diagram is the boundary between fast fluidization and dilute phase pneumatic conveying.

Several correlations have been developed in attempts to accurately predict the choking velocity for various particle types at a given mass flux (Leung *et al.*, 1971, Yousfi and Gau, 1974, Yang, 1983, Punwani *et al*, 1976, and Matsen, 1982). Chong and Leung (1986) have compared choking gas velocity correlations in order to determine which correlations are best suited for each class of gas-solid system using Geldart's (1973) classification. The data used for comparison consisted of particles with various sizes and densities. Table 6.8 presents their results. The root mean square relative error of the Yang correlation is the lowest when all particle groups are included. However, for the particles most often associated with circulating fluidized beds (i.e., system groups A and B), the correlation proposed by Yousfi and Gau (1974) resulted in the lowest error. A brief dimensional analysis of both of these correlations is presented below.

Table 6.8
Comparison of Root-Mean-Square Relative Error for Different Choking Equations Compared to Data (Chong, 1986)

	Particle Types					
	A,B, & D	**A**	**B**	**D**	**A & B**	**B & D**
Choking Eqn.	*Root-Mean-Square Relative Error, %*					
Leung (1971)	31	63	25	20	37	22
Yousfi and Gau (1974)	42	9	10	61	10	45
Yang (1983)	18	31	16	16	20	16
Punwani (1976)	33	53	36	21	40	29
Matsen (1982)	125	53	150	110	130	130

6.3.1 Yang Correlation (1975, 1983)

Yang's choking correlations are based on the assumption that the slip velocity is equal to the free-fall velocity at choking. The dynamic relationship between the solids and gases for a vertical pneumatic conveying line was developed through a force balance to give

$$v_p = v_f - \sqrt{\left(1 + \frac{f_p u_p^2}{2gD}\right) \cdot \frac{4}{3} \frac{(\rho_s - \rho_f) d_p g}{C_D \rho_f} \cdot \varepsilon^{4.7}} \tag{6.2}$$

If the terminal velocity is defined as $u_p = u_f - u_t$, a modified terminal velocity equation can be defined as

$$v_{tt} = \sqrt{\left(1 + \frac{f_p v_p^2}{2gD}\right) \cdot \frac{4}{3} \frac{(\rho_s - v_f) d_p g}{C_D \rho_f} \cdot e^{4.7}} \tag{6.3}$$

The term $\frac{f_p u_p^2}{2gD}$ corrects for particle friction losses in an assemblage of particles and $\varepsilon^{4.7}$ corrects for the drag coefficient. At choking Equation (6.2) can be written as

$$\frac{2gD\left(\varepsilon_c^{-4.7} - 1\right)}{\left(u_c - u_t\right)^2} = 6.81 \times 10^5 \left(\frac{\rho_f}{\rho_s}\right)^{2.2} \tag{6.4}$$

The right hand side of the equation represents the solids friction factor at choking. The appearance of a density ratio to model the solids friction factor suggests that Yang's model does not account for all the physics since it is not clear why this would improve the estimate of solids friction. However, if this ratio was not included and a constant friction factor was utilized (Yang, 1973), choking velocity predictions for particles with widely differing densities do not agree well with published data.

A dimensional analysis, conducted in order to determine the dimensionless groups which govern this correlation, is given below.

If gravitational and drag forces are balanced neglecting wall friction, the terminal velocity can be defined as

$$u_t = \sqrt{\frac{2mg(\rho_s - \rho_f)}{A_{cs} C_D \rho_s \rho_f}} \tag{6.5}$$

Many drag coefficient expressions are available; using White's (1974)

$$C_D = \frac{24}{Re_t} + \frac{6}{1+\sqrt{Re_t}} + 0.4 \tag{6.6}$$

where $Re_t = \frac{u_t d_p \rho_f}{\mu}$

Substituting 6.6 into 6.5 and simplifying gives

$$Re_t^2 = \frac{\frac{4}{3} Ar}{\frac{24}{Re_t} + \frac{6}{1+\sqrt{Re_t}} + 0.4} \tag{6.7}$$

where

$$Ar = \frac{\rho_s \rho_f d_p^3 g}{\mu} \tag{6.8}$$

It was shown in Section 3 that

$$\rho_f \frac{u_{mf} d_p}{\mu} = \frac{\frac{-(150)(1-\varepsilon_{mf})^2}{\varepsilon_{mf}^3} + \sqrt{\left[\frac{-(150)(1-\varepsilon_{mf})^2}{\varepsilon_{mf}^3}\right]^2 + \frac{7(1-\varepsilon_{mf})^2}{\varepsilon_{mf}^3}\phi_s^3 Ar}}{\frac{3.5(1-\varepsilon_{mf})\phi_s}{\varepsilon_{mf}^3}} \tag{6.9}$$

So both u_t and u_{mf} are functions of $Ar^{1/2}$ and Equation 6.4 can be rewritten as

$$\left(\varepsilon_c^{-4.7} - 1\right) \sim \frac{\left(\frac{u_o}{\varepsilon_c} - u_{mf}\right)^2}{gD}\left(\frac{\rho_f}{\rho_s}\right)^{2.2} \quad \text{where } u_{mf} = u_{mf}(Ar) \tag{6.10}$$

Expanding and simplifying results gives

$$\left(\varepsilon_c^{-4.7} - 1\right) \sim \left[\frac{u_o^2}{gD}\left(\frac{1}{\varepsilon_c^2} - \frac{2u_{mf}}{\varepsilon_c u_o} + \frac{u_{mf}^2}{u_o^2}\right)\right]\left(\frac{\rho_f}{\rho_s}\right)^{2.2} \tag{6.11}$$

So the nondimensional parameters governing the void fraction at choking are

$$\left[\frac{u_o^2}{gD}, \left(\frac{\rho_f}{\rho_s}\right), \frac{u_o}{u_{mf}}, Ar, \varepsilon_{mf}\right] \tag{6.12}$$

Figure 3.7 in Section 3 illustrates the dependence of u_t/u_{mf} on Ar. Also shown are the values of the Archimedes number for a pressurized combustor at two particle diameters. Associated with the exact model are the corresponding Archimedes number for two models scaled using the simplified relationships at linear dimensions one quarter and one sixteenth the exact dimensions. The errors in u_t/u_{mf} are shown on Figures 3.8 and 3.9 for scaling at two different linear dimensions. Scaling a combustor with comparatively small particles, 0.2 mm or less, gives good agreement for u_t/u_{mf} even at one sixteenth linear scale, while for large particles a linear scale of one fourth gives fair agreement of u_t/u_{mf}. Therefore the parameters governing the void fraction at choking can be written as:

$$\left[\frac{u_o^2}{gD}, \left(\frac{\rho_f}{\rho_s}\right), \frac{u_o}{u_{mf}}, \varepsilon_{mf}\right] \tag{6.13}$$

These parameters are included in the simplified scaling laws.

6.3.2 Discussion of the Parameters Governing the Yang Correlation

The nondimensional parameters which govern the Yang correlation include a density ratio. This indicates that the viscous limit scaling will not accurately predict the choking behavior of circulating fluidized beds. This may explain the poor agreement in solid fraction profiles and probability density functions when scaling with glass/steel and glass/plastic at low velocities. However, when the density ratio is included, as it is with the simplified scaling laws, all the dimensionless parameters which govern the Yang correlation are included in the scaling laws. Louge (1992) has compared choking data taken in a cold scale circulating fluidized bed using both plastic and steel with values predicted by the Yang correlation and found it to be in excellent agreement when scaling with the full set of scaling laws.

6.3.3 Correlation of Yousfi and Gau (1974)

Yousfi and Gau proposed a model based on a hypothesis that the stability of a vertical uniform suspension flow is dependent on the Froude number

$$Fr_t = \frac{u_t}{\sqrt{(gd_p)}} \tag{6.14}$$

The Froude number for choking was then correlated as a function of the particle Reynolds

number

$$Re = \frac{\rho_f u_t d_p}{\mu} \tag{6.15}$$

and the solid to gas mass flow ratio

$$R = \frac{W_s}{W_f} \tag{6.16}$$

The correlation they developed is:

$$Fr_c = \frac{u_c}{\sqrt{(gd_p)}} = 32Re_p^{-0.06}R^{0.28} \tag{6.17}$$

It should be noted that this correlation does not include the tube diameter as one of its parameters. This was pointed out as an obvious deficiency by Chong and Leung (1986). Most correlations include the bed diameter in order to predict the criteria for slug formation at choking using a maximum bubble size theory such as the one proposed by Davidson and Harrison (1963). A brief analysis was conducted to determine the dimensionless parameters governing the Yousfi and Gau correlation in terms of the parameters used in fluidized bed scaling.

Equation 6.17 can be rewritten as

$$u_c \sim \sqrt{gd_p} \cdot \left(\frac{\rho_f u_t d_p}{\mu}\right)^{-0.06}\left(\frac{W_s}{W_f}\right)^{0.28} \tag{6.18}$$

If the terminal velocity is found from a balance of gravitational and drag forces

$$u_t \sim \sqrt{\frac{4gd_p(\rho_s - \rho_f)}{3C_D\rho_f}} \tag{6.19}$$

Equation 6.19 can be written as

$$u_c \sim \sqrt{gd_p} \cdot \left[\left(\frac{4g\rho_f\rho_s d_p^3}{3C_D\mu^2}\right)^{\frac{1}{2}}\right]^{-0.06}\left(\frac{W_s}{W_f}\right)^{0.28} \tag{6.20}$$

If the White expression for drag is substituted for C_D, and a choking Reynolds number is

defined as

$$Re_c = \frac{\rho_f u_c d_p}{\mu} \tag{6.21}$$

Equation 6.20 can be expanded to

$$Re_c \sim \sqrt{\frac{g\rho_f^2 d_p^3}{\mu^2}} \cdot \left[\left(\frac{Ar}{\frac{24}{Re_c} + \frac{6}{1+\sqrt{Re_c}} + 0.4}\right)^{\frac{1}{2}}\right]^{-0.06} \left(\frac{W_s}{W_f}\right)^{0.28} \tag{6.22}$$

If the solid and gas mass flow rates are defined as

$$W_s = (v_f - u_t)\rho_s(1-\varepsilon)A_{cs};\ W_f = v_f \varepsilon \rho_f A_{cs} \tag{6.23}$$

and we recognize from Section 3 that $u_t \sim u_{mf}$, Equation 6.22 can be rewritten as

$$Re_c \sim \left[Ar\left(\frac{\rho_f}{\rho_s}\right)\right]^{\frac{1}{2}} \cdot \left[\left(\frac{Ar}{\frac{24}{Re_c} + \frac{6}{1+\sqrt{Re_c}} + 0.4}\right)^{\frac{1}{2}}\right]^{-0.06} \left[\left(1 - \frac{u_{mf}}{u_o}\right)\left(\frac{\rho_s}{\rho_f}\right)\left(\frac{1-\varepsilon_c}{\varepsilon_c}\right)\right]^{0.28} \tag{6.24}$$

So the Yousfi and Gau correlation is governed by

$$\left[\frac{u_o}{u_{mf}}, \frac{\rho_s}{\rho_f}, Ar\right] \tag{6.25}$$

We have shown that $u_t \sim f(Ar)$ and $u_{mf} \sim g(Ar)$ so that $u_t/u_{mf} \sim h(Ar)$, which allows the parameters to be written as

$$\left[\frac{u_o}{u_{mf}}, \frac{\rho_s}{\rho_f}, \frac{u_t}{u_{mf}}\right] \tag{6.26}$$

6.3.4 Discussion of the Parameters Governing the Yousfi and Gau Correlation

Consistent with the Yang correlation, a density ratio and the superficial to minimum fluidization velocity appears in the list of nondimensional parameters governing the Yousfi and Gau correlation. Due to the inclusion of the density ratio, there is no reason to believe that the viscous limit scaling laws will accurately predict the choking behavior of circulating fluidized beds. However, the terminal to minimum fluidization velocity ratio also appears in

place of the Froude number seen in the Yang correlation. While this nondimensional parameters does not appear in either the viscous limit scaling laws or the simplified scaling laws, Figures 3.7-3.9 show that for the particle sizes of interest in circulating fluidized beds, the error in this ratio will be very small when the simplified scaling laws are used - even when scaling to bed diameters of 1/16 the size of the full scale bed.

6.3.5 Discussion of Analysis

Because Yang's correlation predicts that some of the tests described above were conducted under conditions in which the bed was choked, the above analysis indicates that while the viscous limit scaling laws will not allow for modelling bed hydrodynamics in regions of choking, the simplified set of scaling parameters do. It also suggests that there are competing interests in the selection of a superficial velocity which allows for verification of the viscous limit scaling laws for circulating fluidized beds. On the one hand, the superficial velocity must be kept low enough to remain in the viscous limit. On the other hand, the superficial velocity must be high enough to prevent significant choking in the bed.

Horio (1989) attempted to predict the choking points in two scaled cold beds utilizing the scaling parameters he developed through his clustering annular flow model. These parameters are equivalent to the viscous limit scaling parameters described in Section 3. While Horio argued that the solid to fluid density ratio was not critical in scaling CFB's, this parameter was matched in the two scale models. This had the effect of making his nondimensional parameter list the same as the simplified set proposed in this study. Utilizing his scaling parameters along with the additional parameter of density ratio, he was able to match choking points between the two beds quite well. This suggests that the simplified set may, in fact, be able to model the transition to choking in CFB's.

7.0 SCALING THE STUDSVIK HOT BED COMBUSTOR USING THE SIMPLIFIED SCALING PARAMETERS

This Section presents the results of tests conducted to evaluate the simplified scaling laws when scaling between a utility sized hot atmospheric CFB and a 1/16 scale cold model. The governing parameters for hydrodynamic similarity utilized were the simplified set of scaling laws derived earlier which were successful in matching hydrodynamics between two scaled cold beds with a length ratio of 1/4.

In order to evaluate the validity of applying these scaling parameters to large scale hot beds using length ratios on the order of 1/16, solid fraction profiles between the Studsvik hot bed and a 1/16 scale cold model were compared for six different operating conditions. The phase two 1/16 scale Studsvik bed and the Studsvik hot bed (both described in Section 4) were used during these tests. In addition, data from an earlier study which scaled the Studsvik hot bed using a cold model designed with the full set of scaling parameters is included in the evaluation. This model was used to simulate the first five conditions. Condition six could not be simulated with the model built using the full set of scaling parameters because of limits on its range of operability. Table 7.1 presents a test matrix for evaluation of the simplified set of scaling parameters. Tables 7.2 through 7.7 provide the operational data, along with information concerning the particles and beds utilized in the simplified scaling analysis. In these Tables, Ga represents the Galileo number defined as $\frac{\rho_s^2 d_p^3 g}{\mu_f^2}$. Since time varying pressure traces were not taken for the Studsvik hot bed, histograms and FFT comparisons will be made only between the 1/4 and 1/16 scale cold beds. No heat transfer data were taken during these runs.

Table 7.1

Test Matrix - Hot Bed Scaling Using the Simplified Scaling Laws

Parameter	Full Scale Hot Bed	1/4 Scale Cold Bed	1/16 Scale Cold Bed
Particle Diameter (microns)	d_p	$0.25d_p$	$0.18d_p$
u_{mf}	u_{mf}	$0.5u_{mf}$	$0.25u_{mf}$
Bed Diameter	D	0.25D	0.0625D
u_o/u_{mf}	100-500	Same	Same
u_o^2/gL	Fr	Same	Same
$Re = \frac{\rho_f u_o d_p}{\mu_f}$	$\frac{\rho_f u_o d_p}{\mu_f}$	$\frac{\rho_f u_o d_p}{\mu_f}$	$\frac{0.35\rho_f u_o d_p}{\mu_f}$
$\frac{\rho_s}{\rho_f}$	$\frac{\rho_s}{\rho_f}$	$\cong \frac{\rho_s}{\rho_f}$	$\cong \frac{\rho_s}{\rho_f}$
$M = \frac{G_s}{u_o \rho_s}$	M	Same	Same

Table 7.2

Hot Bed Scaling Using Simplified Scaling Laws - Condition 1

	Studsvik Hot Bed	1/4 Scale Cold Bed	1/16 Scale Cold Bed
u_o (m/s)	6.07	2.91	1.44
u_{mf} (cm/s) Ergun Eqn.	5.75	2.18	0.46
u_{mf} (cm/s) measured		1.40	0.75
d_p (microns)	243	57.7	~ 26
L (m)	7.32	1.83	0.46
A_{cs} (m^2)	0.434	0.0252	1.575E-3
G_s (kg/m^2-s)	10.2	12.8	6.5
% Primary Air	49	50	50
$Re_{dp,uo}$	10.3	11.1	2.53
$Re_{L,uo}$	3.14E5	3.52E5	4.36E4
Fr	0.51	0.47	0.46
$\left(\frac{u_o}{u_{mf}}\right)_{Ergun\ eqn.}$	105.6	133.7	313.6
$\left(\frac{u_o}{u_{mf}}\right)_{measured}$		207.9	192.0
$\left(\frac{G_s}{\rho_s u_o}\right)$	6.22E-4	6.07E-4	6.23E-4
$\left(\frac{\rho_s}{\rho_f}\right)$	8413	6042	6042
Ga	4.99E5	3.01E5	2.92E4

Table 7.3

Hot Bed Scaling Using Simplified Scaling Laws - Condition 2

	Studsvik Hot Bed	1/4 Scale Cold Bed	1/16 Scale Cold Bed
u_o (m/s)	7.92	3.69	1.88
u_{mf} (cm/s) Ergun Eqn.	5.75	2.18	0.46
u_{mf} (cm/s) measured		1.40	0.75
d_p (microns)	243	57.7	~ 26
L (m)	7.32	1.83	0.46
A_{cs} (m^2)	0.434	0.0252	1.575E-3
G_s (kg/m^2-s)	16.6	22.0	10.7
% Primary Air	69	69	69
$Re_{dp,uo}$	13.6	14.2	3.30
$Re_{L,uo}$	4.10E5	4.46E5	5.69E4
Fr	0.87	0.76	0.79
$\left(\frac{u_o}{u_{mf}}\right)_{Ergun\ eqn.}$	137.7	169.0	409.6
$\left(\frac{u_o}{u_{mf}}\right)_{measured}$		263.5	251.7
$\left(\frac{G_s}{\rho_s u_o}\right)$	7.91E-4	8.22E-4	7.84E-4
$\left(\frac{\rho_s}{\rho_f}\right)$	8413	6042	6042
Ga	4.99E5	3.01E5	2.92E4

Table 7.4

Hot Bed Scaling Using Simplified Scaling Laws - Condition 3

	Studsvik Hot Bed	1/4 Scale Cold Bed	1/16 Scale Cold Bed
u_o (m/s)	7.65	3.64	1.81
u_{mf} (cm/s) Ergun Eqn.	5.75	2.18	0.46
u_{mf} (cm/s) measured		1.40	0.75
d_p (microns)	243	57.7	~ 26
L (m)	7.32	1.83	0.46
A_{cs} (m^2)	0.434	0.0252	1.575E-3
G_s (kg/m^2-s)	30.7	38.3	19.6
% Primary Air	52	52	52
$Re_{dp,uo}$	13.2	13.9	3.17
$Re_{L,uo}$	3.96E5	4.40E5	5.48E4
Fr	0.82	0.74	0.73
$\left(\frac{u_o}{u_{mf}}\right)_{Ergun\ eqn.}$	133.0	167.0	394.3
$\left(\frac{u_o}{u_{mf}}\right)_{measured}$		260.0	241.3
$\left(\frac{G_s}{\rho_s u_o}\right)$	1.51E-3	1.45E-3	1.49E-3
$\left(\frac{\rho_s}{\rho_f}\right)$	8413	6042	6042
Ga	4.99E5	3.01E5	2.92E4

Table 7.5

Hot Bed Scaling Using Simplified Scaling Laws - Condition 4

	Studsvik Hot Bed	1/4 Scale Cold Bed	1/16 Scale Cold Bed
u_o (m/s)	6.05	3.01	1.44
u_{mf} (cm/s) Ergun Eqn.	5.75	2.18	0.46
u_{mf} (cm/s) measured		1.40	0.75
d_p (microns)	243	57.7	~ 26
L (m)	7.32	1.83	0.46
A_{cs} (m^2)	0.434	0.0252	1.575E-3
G_s (kg/m^2-s)	13.8	18.2	8.88
% Primary Air	71	69	71
$Re_{dp,uo}$	10.4	11.5	2.53
$Re_{L,uo}$	3.14E5	3.65E5	4.36E4
Fr	0.51	0.51	0.46
$\left(\frac{u_o}{u_{mf}}\right)_{Ergun\ eqn.}$	105.2	138.1	313.7
$\left(\frac{u_o}{u_{mf}}\right)_{measured}$		215.0	192.0
$\left(\frac{G_s}{\rho_s u_o}\right)$	8.61E-4	8.34E-4	8.51E-4
$\left(\frac{\rho_s}{\rho_f}\right)$	8413	6042	6042
Ga	4.99E5	3.01E5	2.92E4

Table 7.6

Hot Bed Scaling Using Simplified Scaling Laws - Condition 5

	Studsvik Hot Bed	1/4 Scale Cold Bed	1/16 Scale Cold Bed
u_o (m/s)	6.16	3.09	1.49
u_{mf} (cm/s) Ergun Eqn.	5.75	2.18	0.46
u_{mf} (cm/s) measured		1.40	0.75
d_p (microns)	243	57.7	~ 26
L (m)	7.32	1.83	0.46
A_{cs} (m^2)	0.434	0.0252	1.575E-3
G_s (kg/m^2-s)	9.0	11.3	5.75
% Primary Air	69	69	69
$Re_{dp,uo}$	10.6	11.8	2.61
$Re_{L,uo}$	3.19E5	3.74E5	4.51E4
Fr	0.53	0.53	0.50
$\left(\frac{u_o}{u_{mf}}\right)_{Ergun\ eqn.}$	107.1	143.1	324.6
$\left(\frac{u_o}{u_{mf}}\right)_{measured}$		220.7	198.7
$\left(\frac{G_s}{\rho_s u_o}\right)$	5.51E-4	5.04E-4	5.32E-4
$\left(\frac{\rho_s}{\rho_f}\right)$	8413	6042	6042
Ga	4.99E5	3.01E5	2.92E4

Table 7.7

Hot Bed Scaling Using Simplified Scaling Laws - Condition 6

	Studsvik Hot Bed	1/4 Scale Cold Bed	1/16 Scale Cold Bed
u_o (m/s)	6.16		1.89
u_{mf} (cm/s) Ergun Eqn.	5.75		0.46
u_{mf} (cm/s) measured			0.75
d_p (microns)	243		~ 26
L (m)	7.32		0.46
A_{cs} (m^2)	0.434		1.575E-3
G_s (kg/m^2-s)	9.0		23.5
% Primary Air	70		70
$Re_{dp,uo}$	13.7		3.32
$Re_{L,uo}$	4.12E5		5.72E4
Fr	0.88		0.80
$\left(\frac{u_o}{u_{mf}}\right)_{Ergun\ eqn.}$	138.1		411.8
$\left(\frac{u_o}{u_{mf}}\right)_{measured}$			252.0
$\left(\frac{G_s}{\rho_s u_o}\right)$	1.79E-3		1.78E-3
$\left(\frac{\rho_s}{\rho_f}\right)$	8413		6042
Ga	4.99E5		2.92E4

7.1 Solid Fraction Profiles

The average solid fraction profiles in the three different size beds using the full set of scaling parameters for the 1/4 scale model and the simplified scaling parameters for the 1/16 scale model are given in Figures 7.1 through 7.6. The tabulated data is given in Appendix G. The calculated solid fractions are plotted versus the average of the heights of the associated pressure taps in each bed. As discussed in Section 4, error bars are based on calculated standard deviations in solid flow measurements and pressure time traces.

7.2 Histograms

Probability density functions for the solid fractions in the 1/4 and 1/16 scale beds are given in figures 7.7 through 7.26. Histograms are shown for solid fractions between pressure taps 1 and 2, 3 and 4, 5 and 6, 7 and 8 in each bed. In these plots, probability is plotted versus the solid fraction.

7.3 Power Spectral Densities

FFT's of the pressure fluctuation data for the 1/4 and 1/16 scale cold beds are given in Figures 7.27 through 7.46. FFT's are shown for pressure taps corresponding to the same percentage height up the bed as the probability density functions. In these plots, the fourier transform is plotted versus the equivalent 1/4 scale Studsvik bed frequency in Hz.

Figure 7.1

Solid Fraction Profiles - Hot Bed Scaling With Simplified Scaling Laws

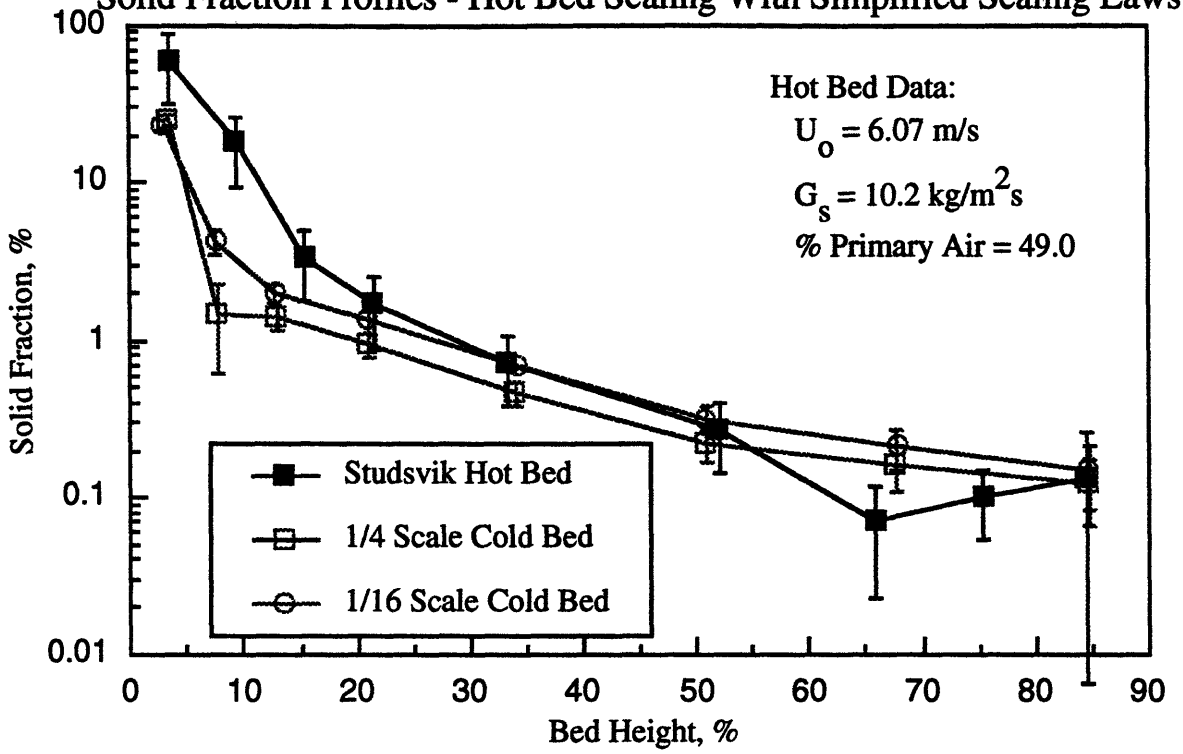

Figure 7.2

Solid Fraction Profiles - Hot Bed Scaling With Simplified Scaling Laws

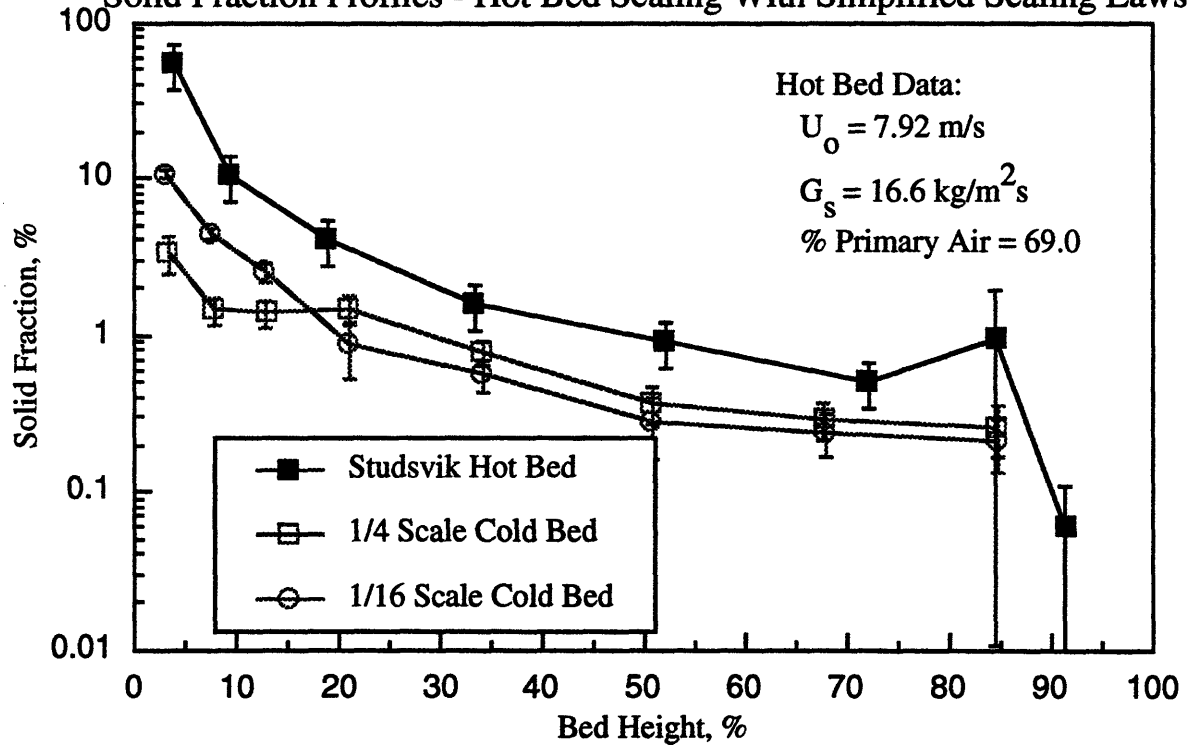

Figure 7.3

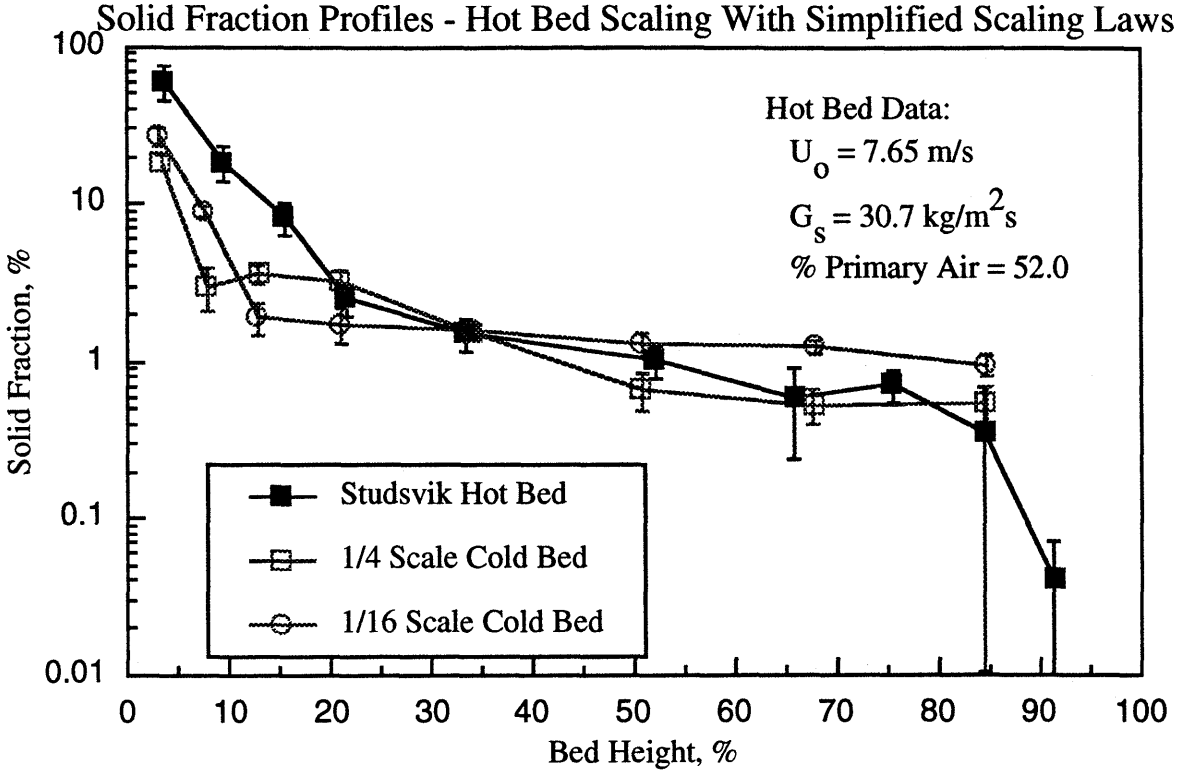

Figure 7.4

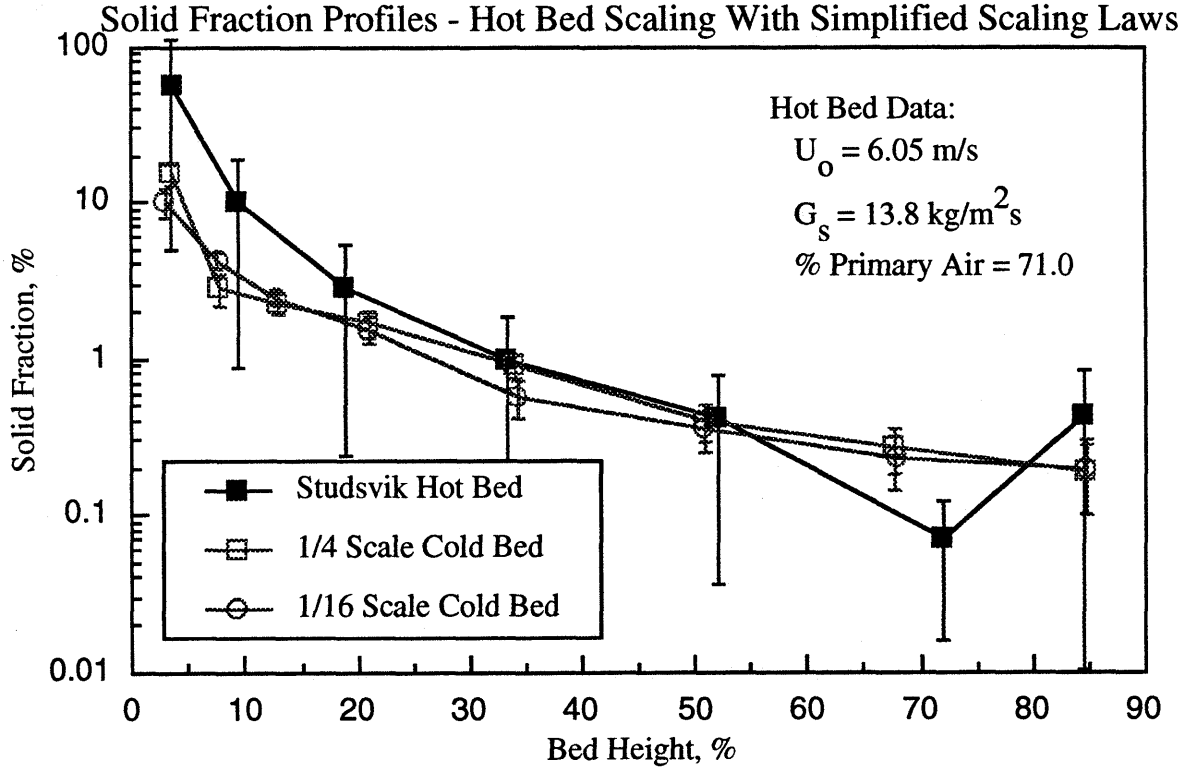

Figure 7.5

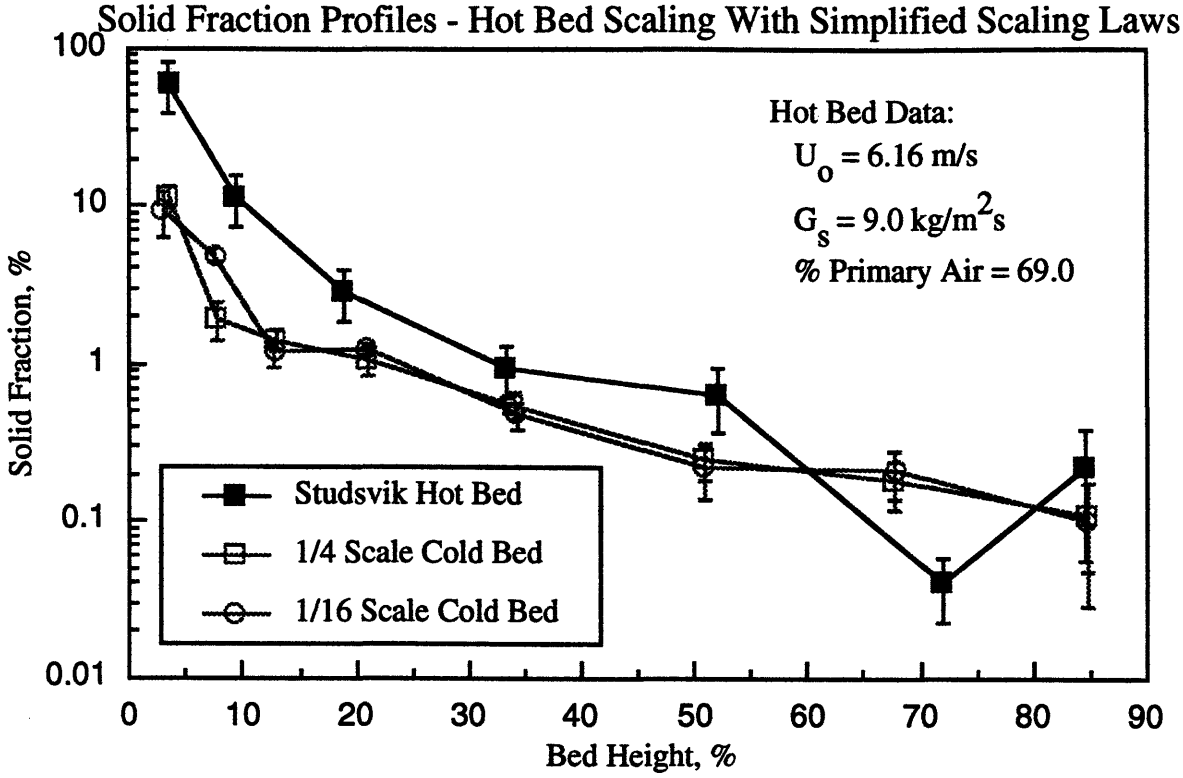
Solid Fraction Profiles - Hot Bed Scaling With Simplified Scaling Laws
Hot Bed Data:
U_o = 6.16 m/s
G_s = 9.0 kg/m^{2}s
% Primary Air = 69.0
Studsvik Hot Bed
1/4 Scale Cold Bed
1/16 Scale Cold Bed
Solid Fraction, %
Bed Height, %
100
10
1
0.1
0.01
0
10
20
30
40
50
60
70
80
90

Figure 7.6

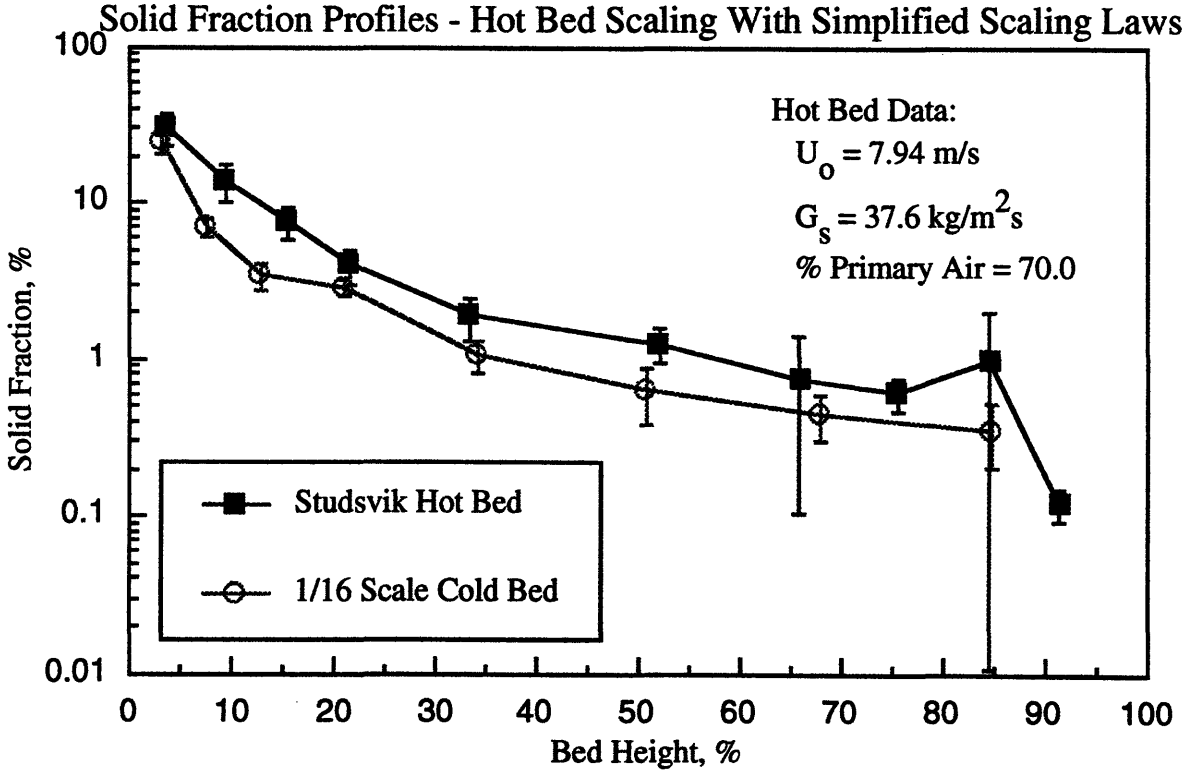
Solid Fraction Profiles - Hot Bed Scaling With Simplified Scaling Laws
Hot Bed Data:
U_o = 7.94 m/s
G_s = 37.6 kg/m^{2}s
% Primary Air = 70.0
Studsvik Hot Bed
1/16 Scale Cold Bed
Solid Fraction, %
Bed Height, %
100
10
1
0.1
0.01
0
10
20
30
40
50
60
70
80
90
100

Figure 7.7: Condition 1

Steel Histograms - Pressure Taps One and Two

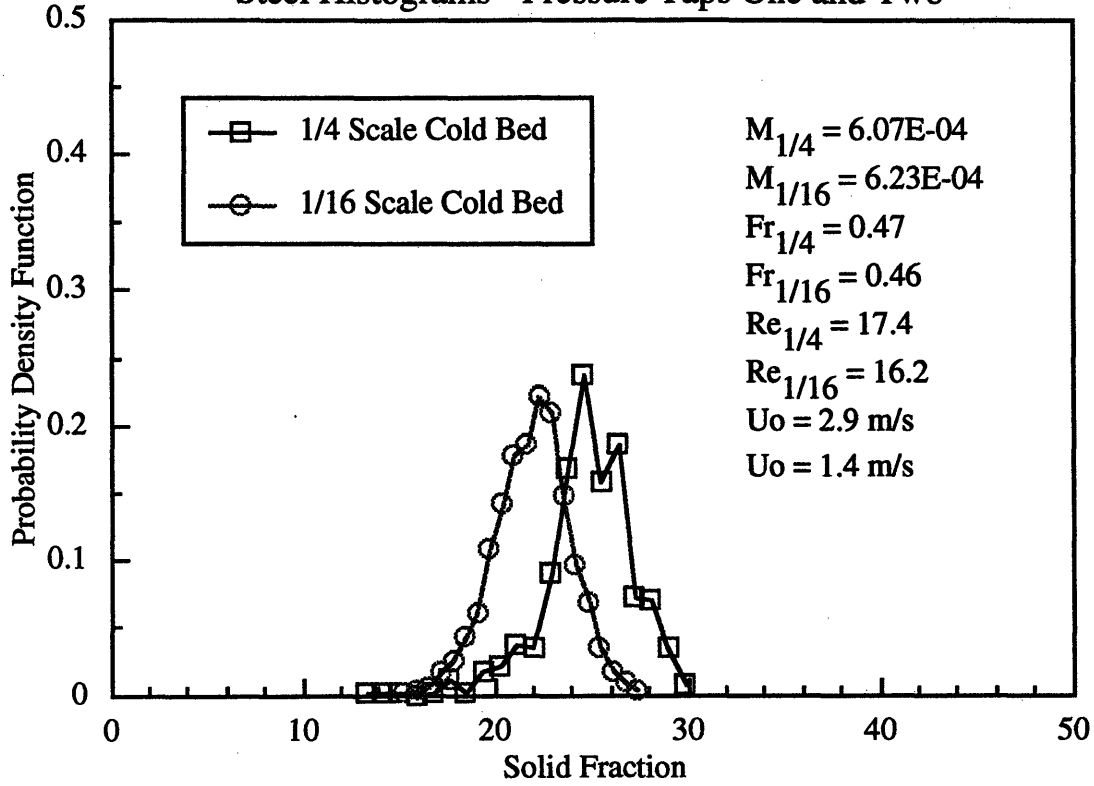

Figure 7.8: Condition 1

Steel Histograms - Pressure Taps Three and Four

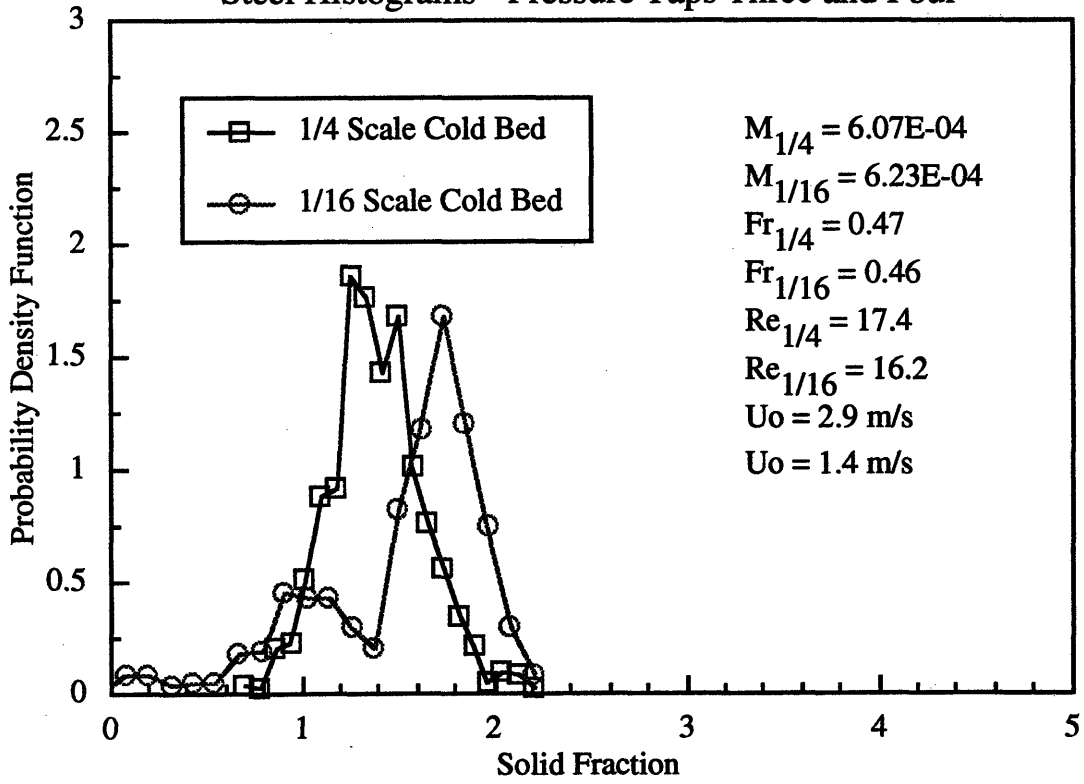

Figure 7.9: Condition 1

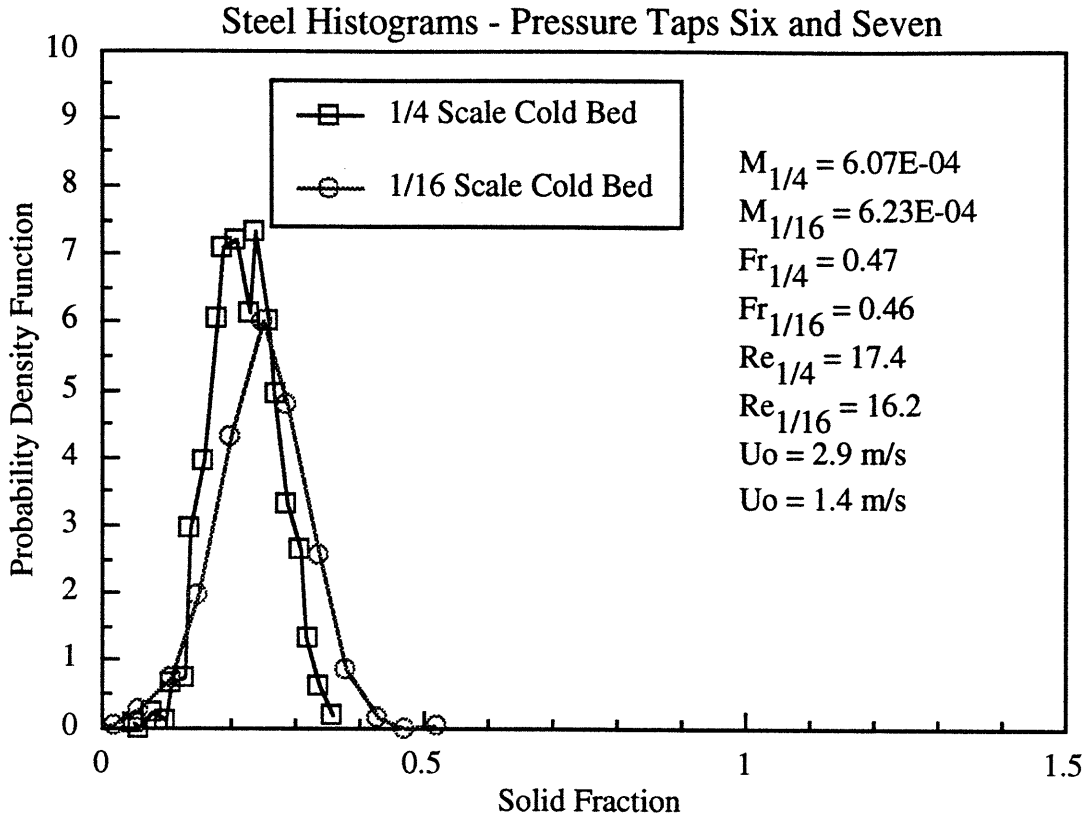

Figure 7.10: Condition 1

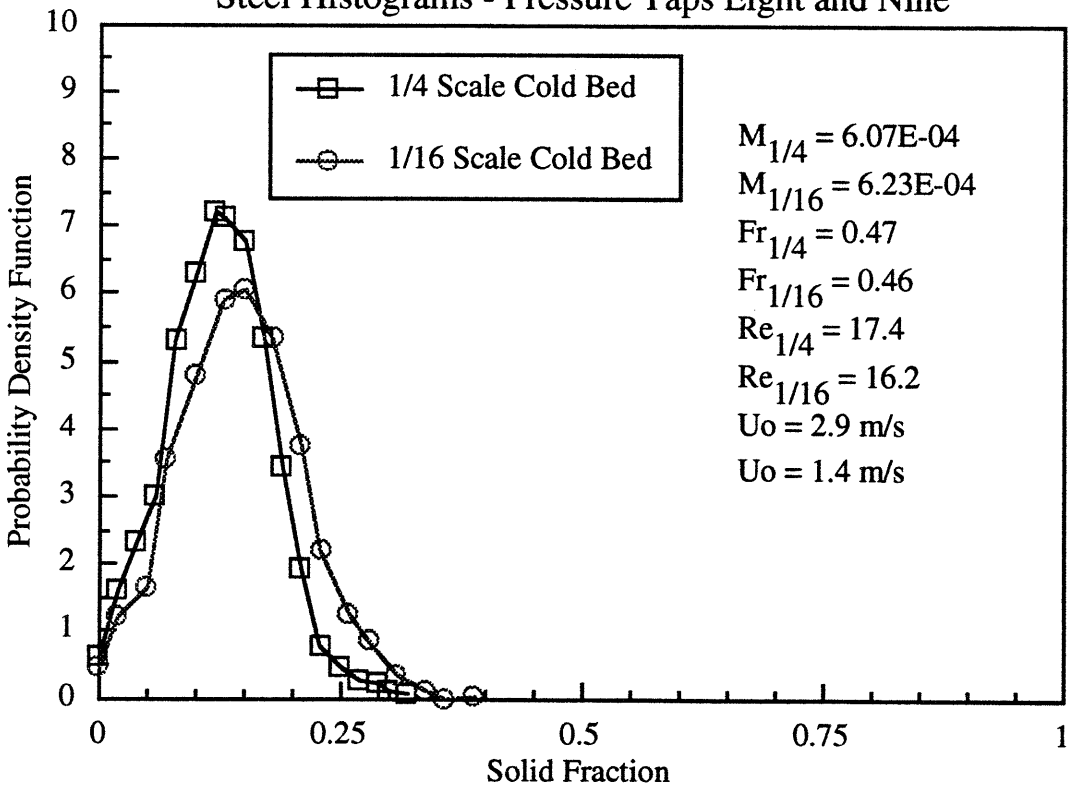

Figure 7.11: Condition 2

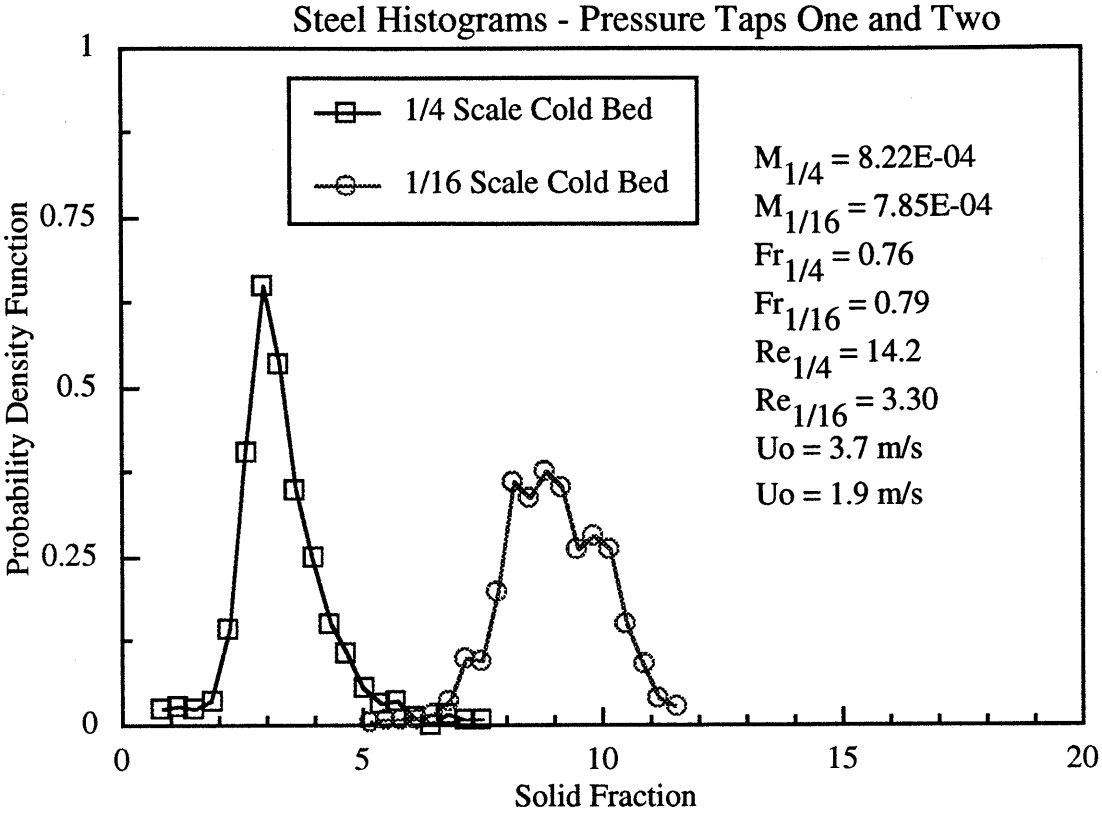

Figure 7.12: Condition 2

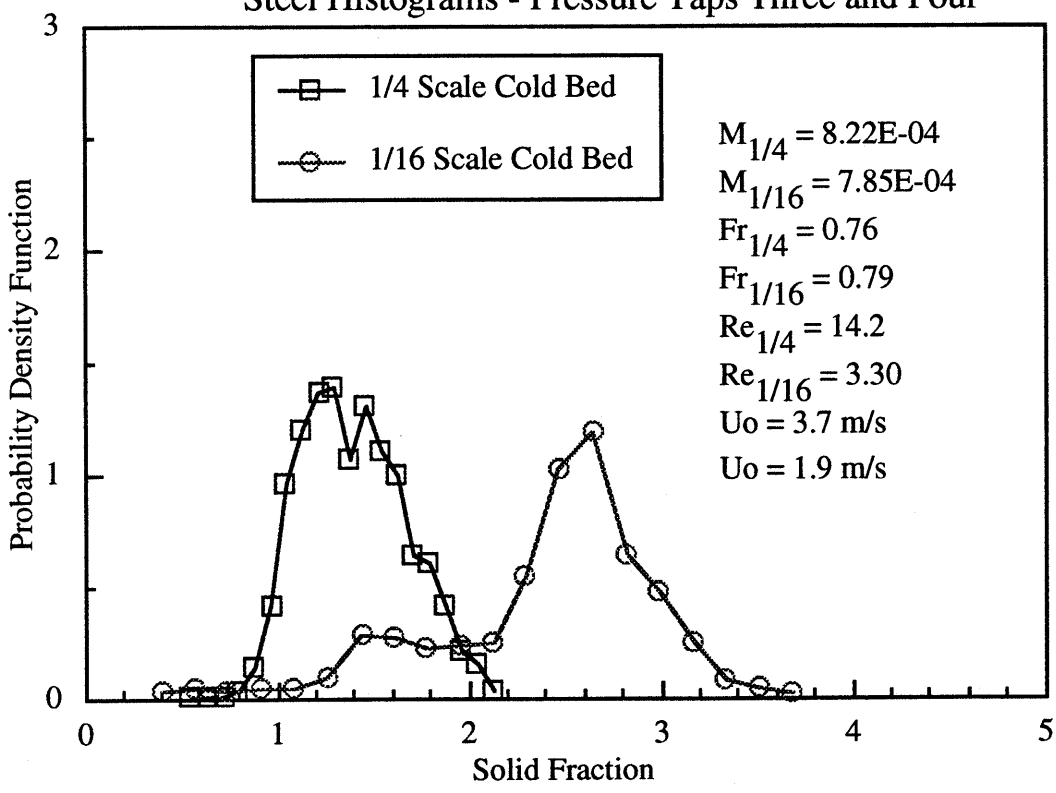

Figure 7.13: Condition 2

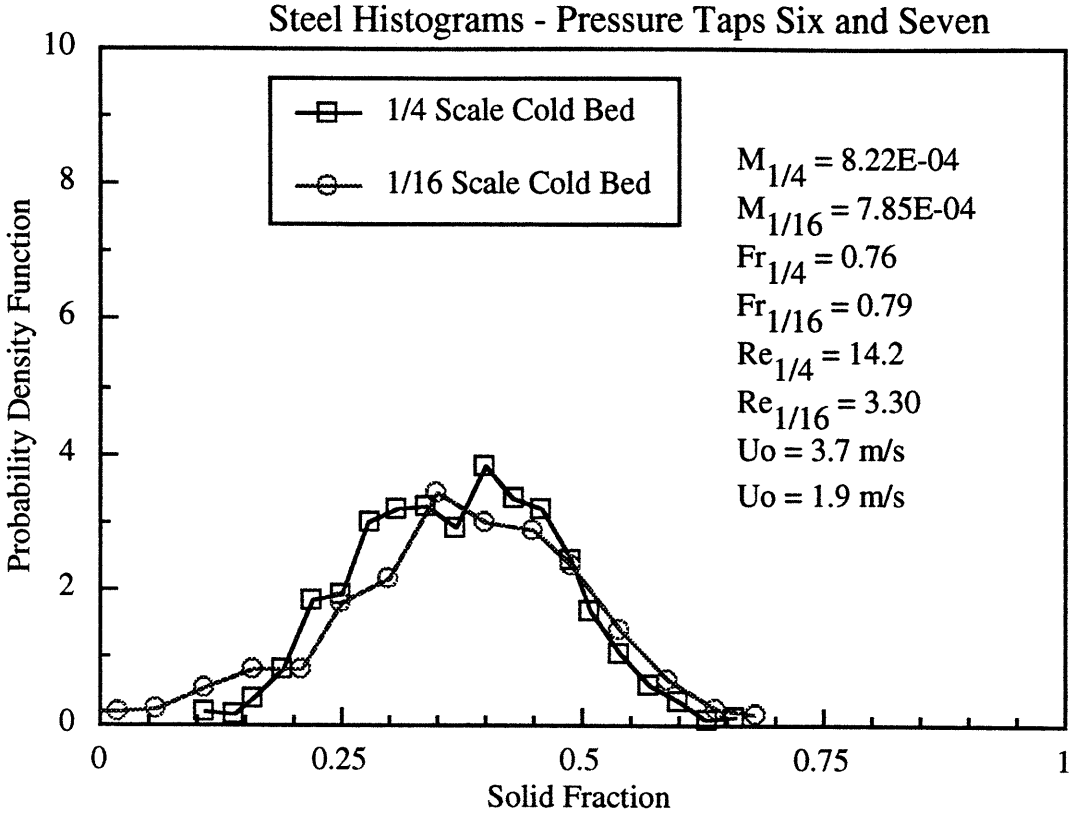

Figure 7.14: Condition 2

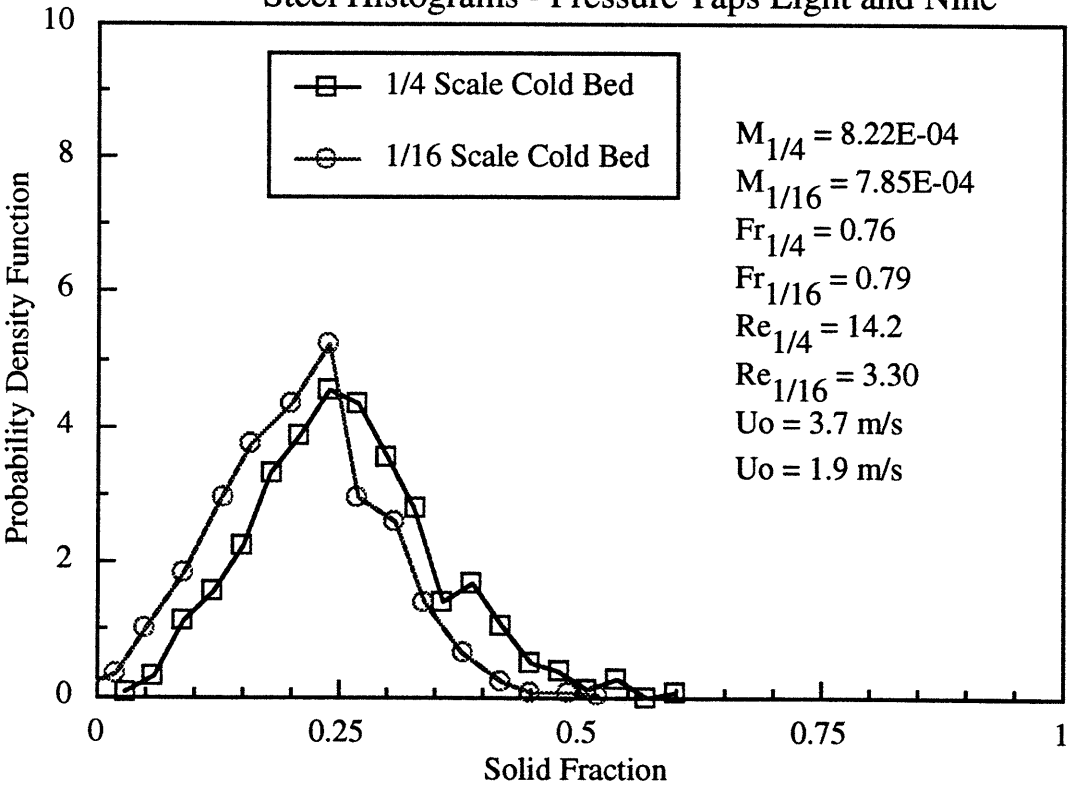

Figure 7.15: Condition 3

Steel Histograms - Pressure Taps One and Two

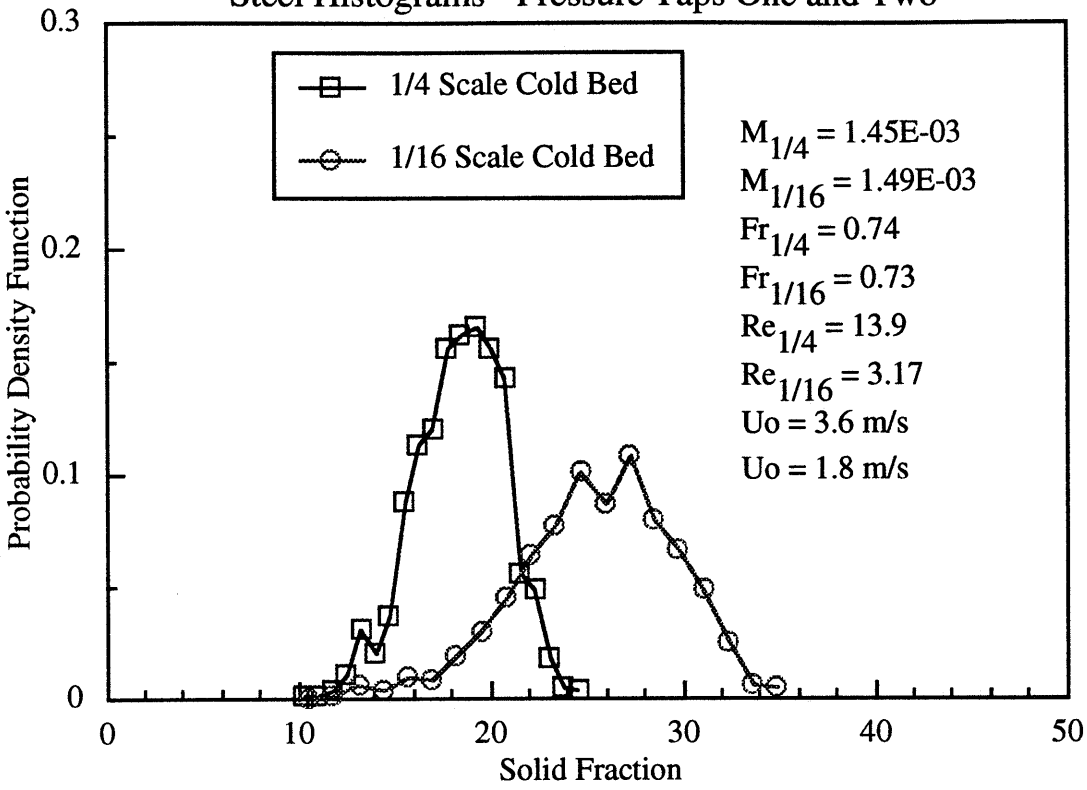

Figure 7.16: Condition 3

Steel Histograms - Pressure Taps Three and Four

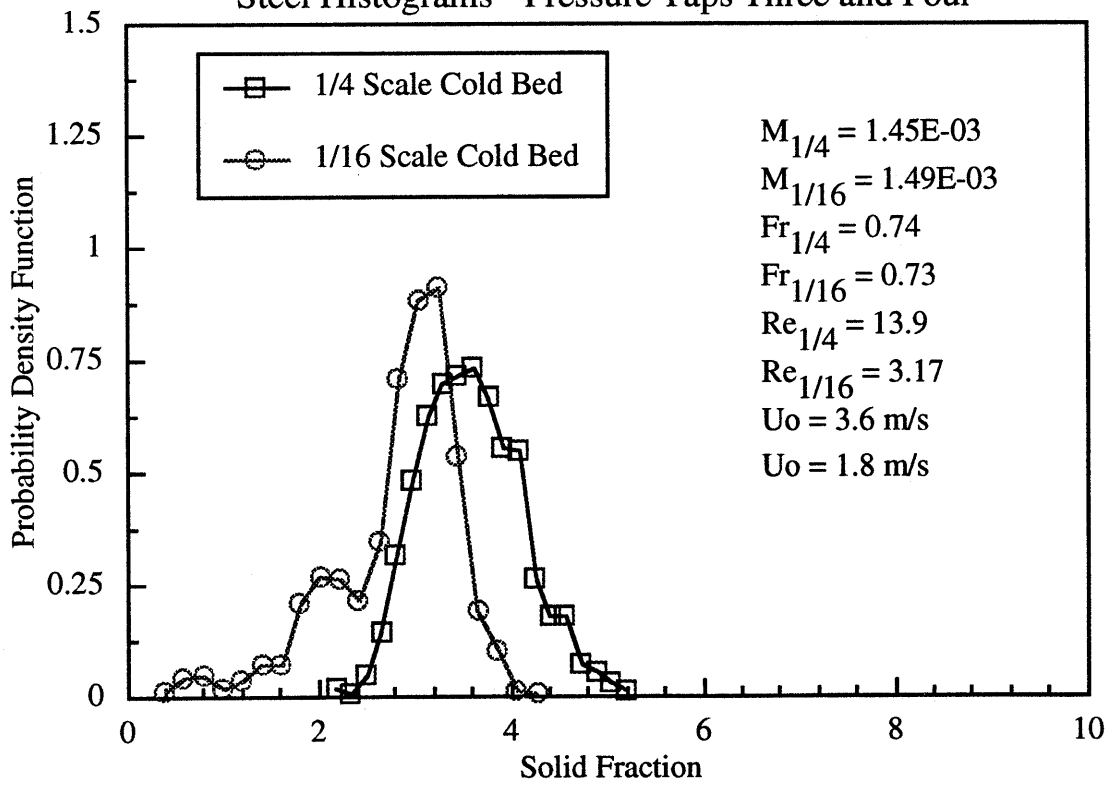

Figure 7.17: Condition 3

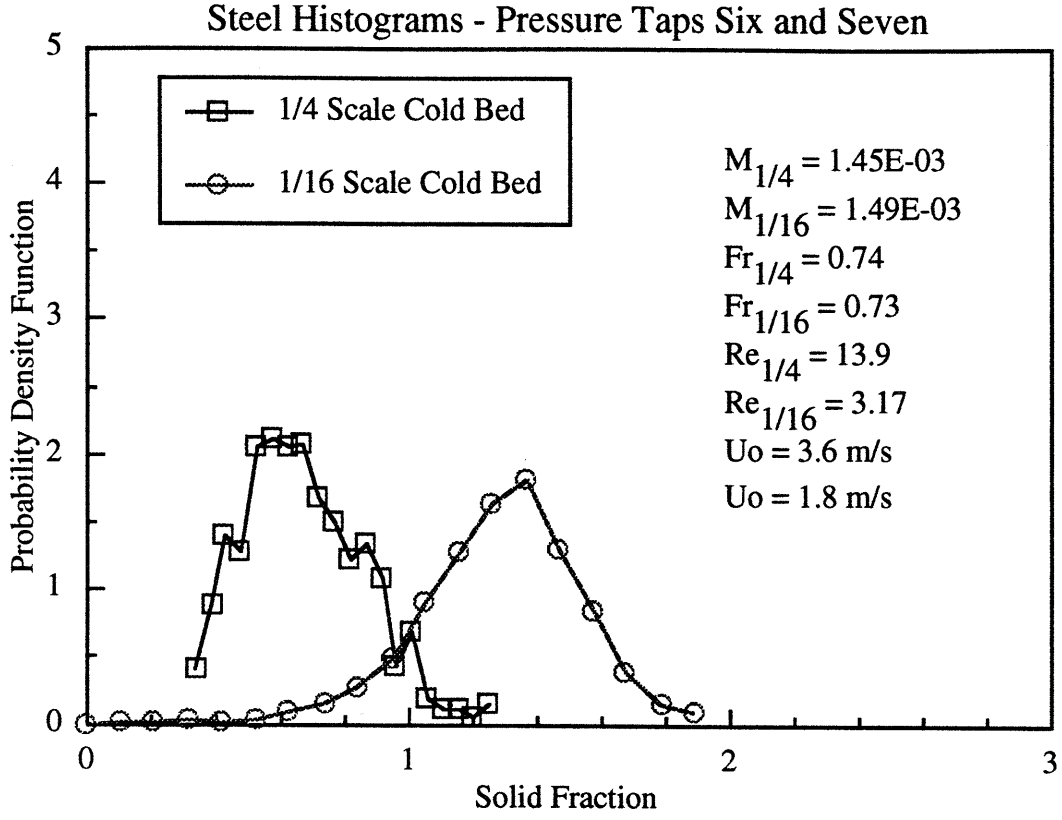

Figure 7.18: Condition 3

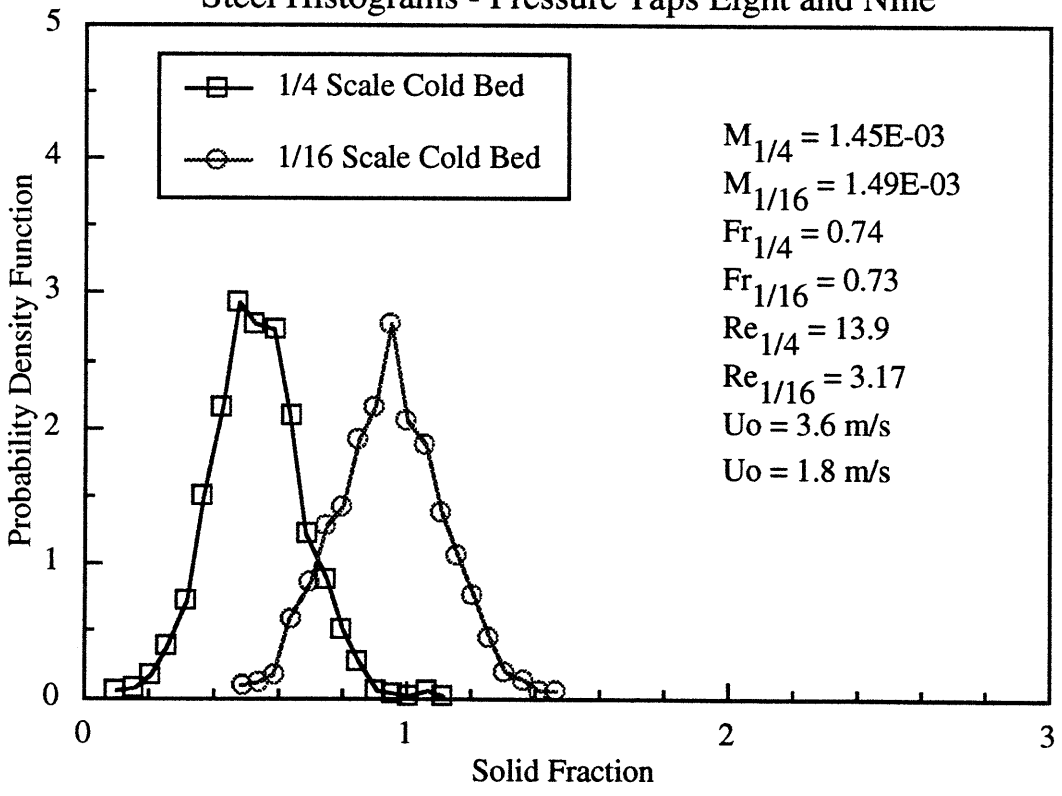

Figure 7.19: Condition 4

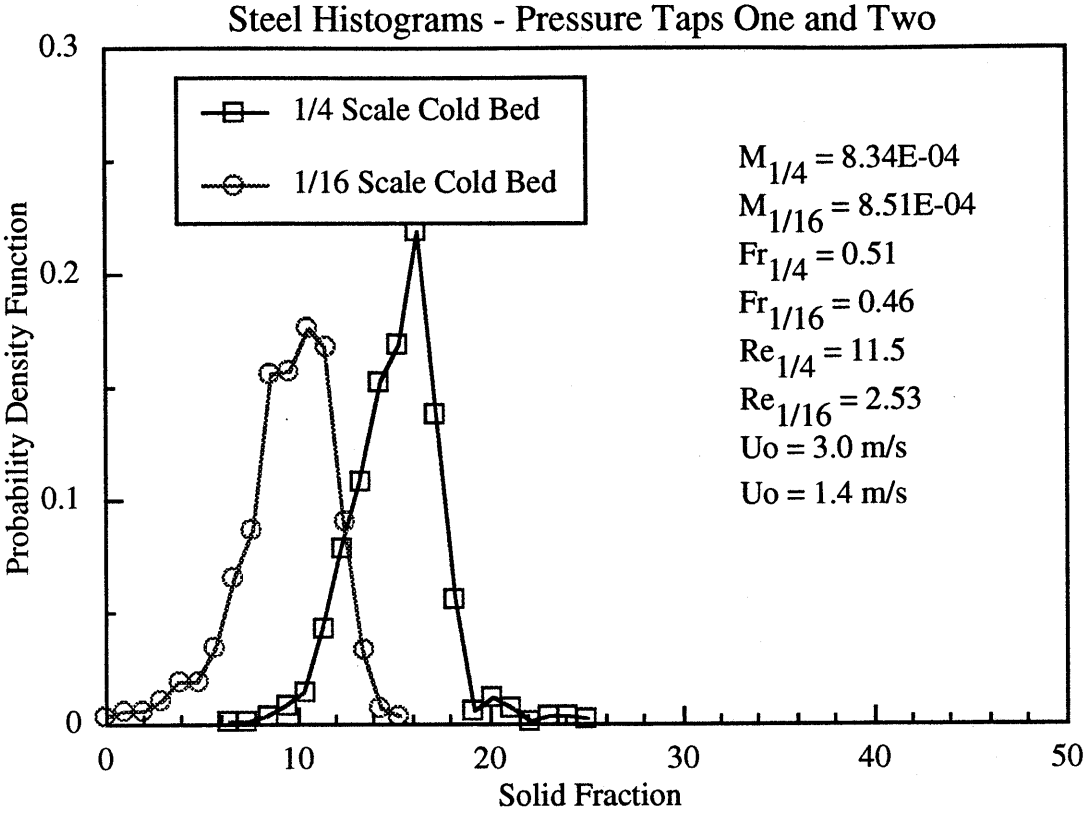

Figure 7.20: Condition 4

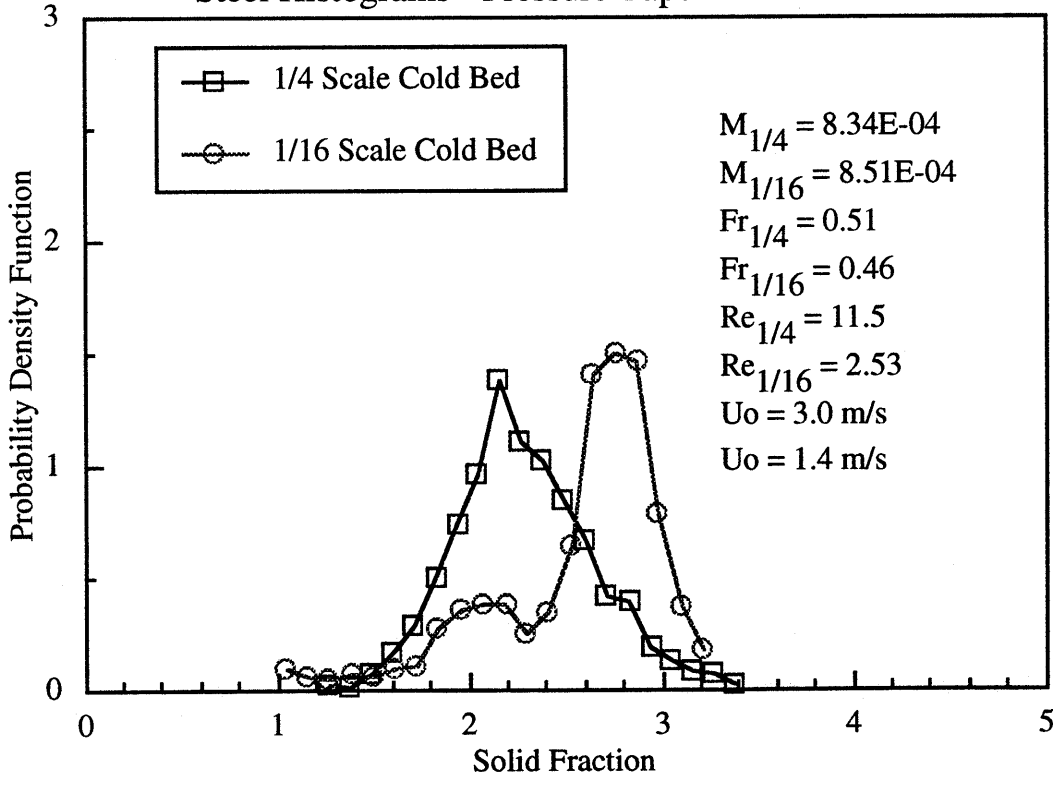

Figure 7.21: Condition 4

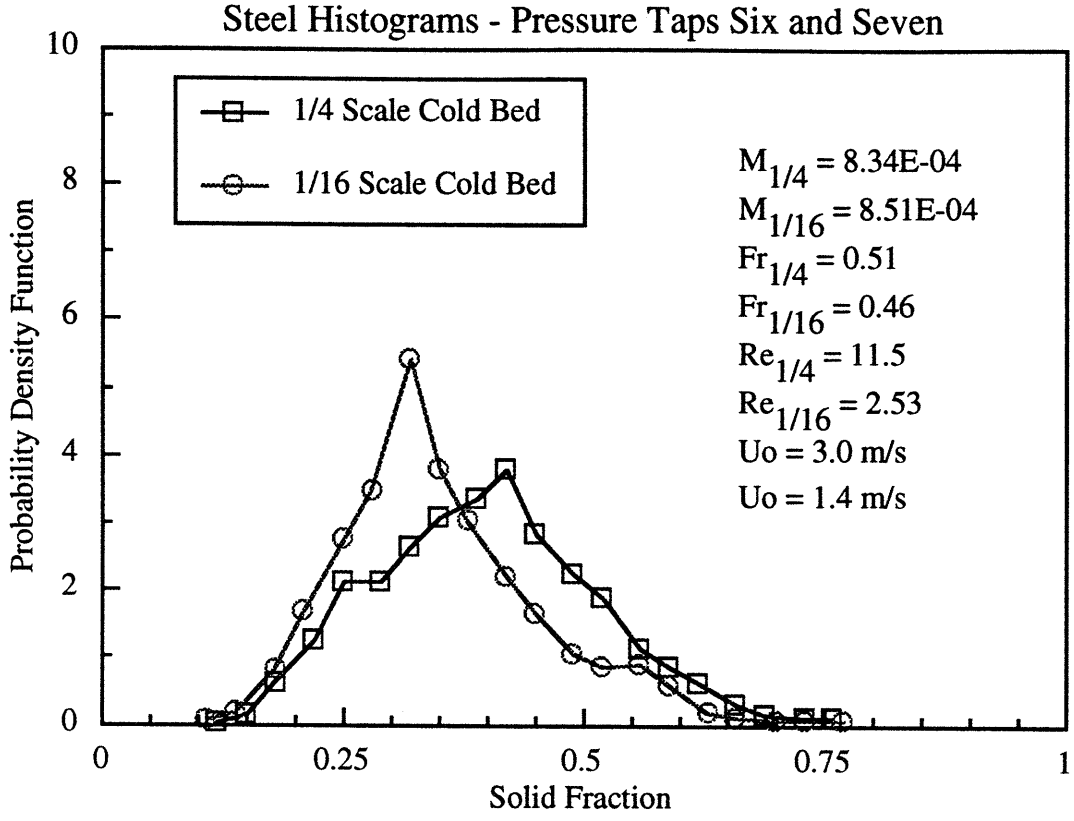

Figure 7.22: Condition 4

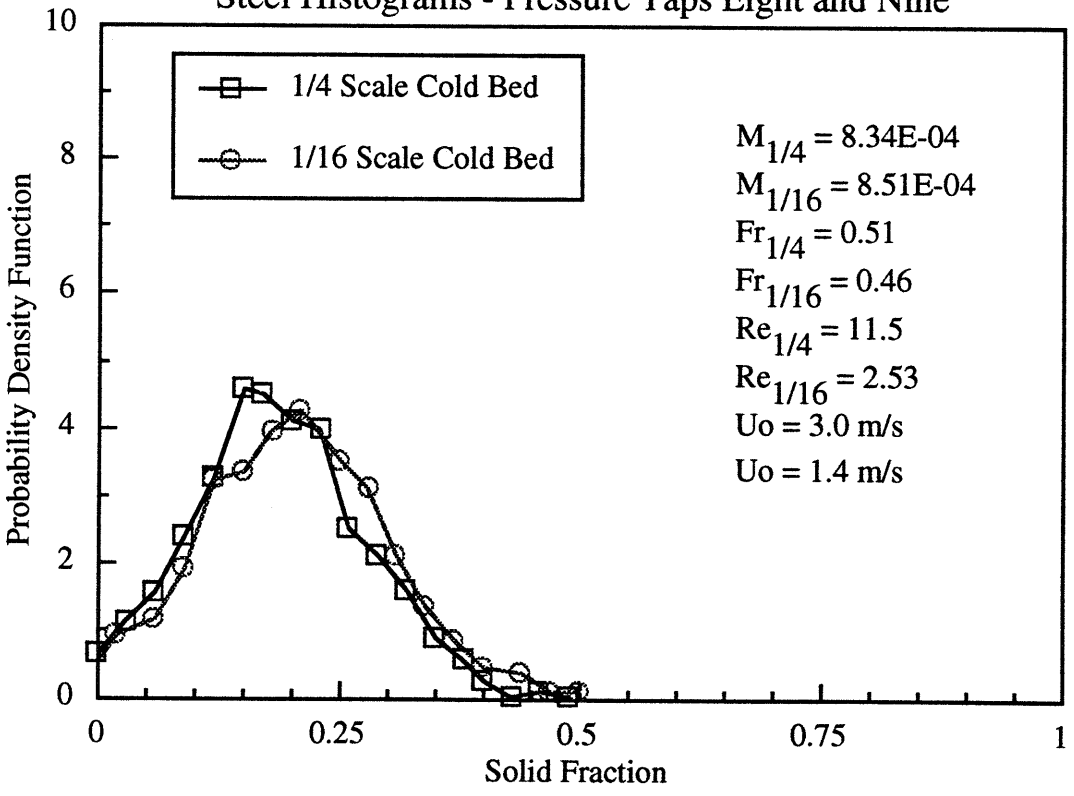

Figure 7.23: Condition 5

Steel Histograms - Pressure Taps One and Two

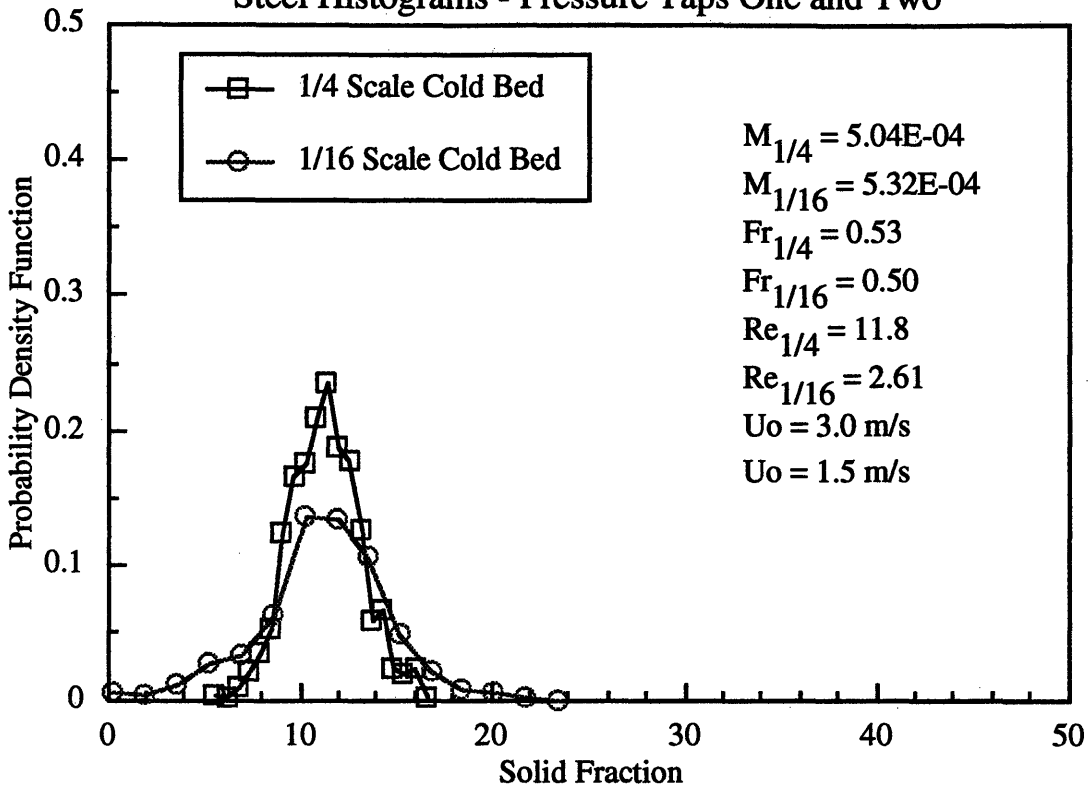

Figure 7.24: Condition 5

Steel Histograms - Pressure Taps Three and Four

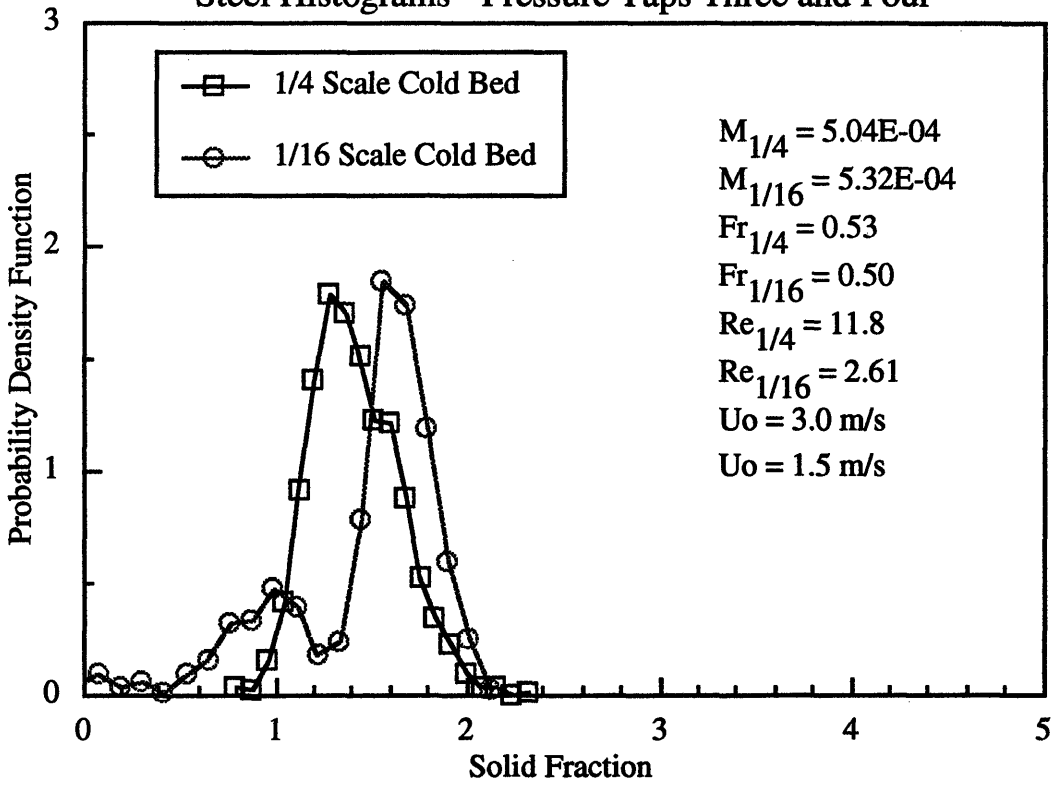

Figure 7.25: Condition 5

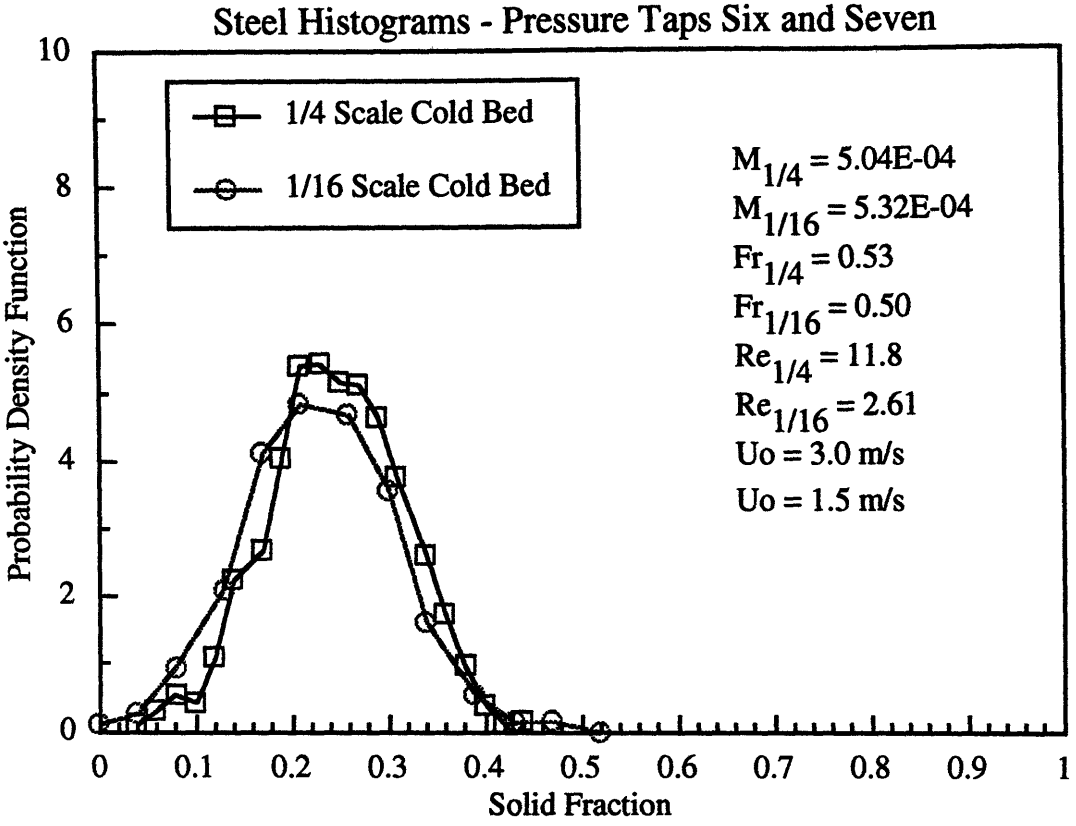

Figure 7.26: Condition 5

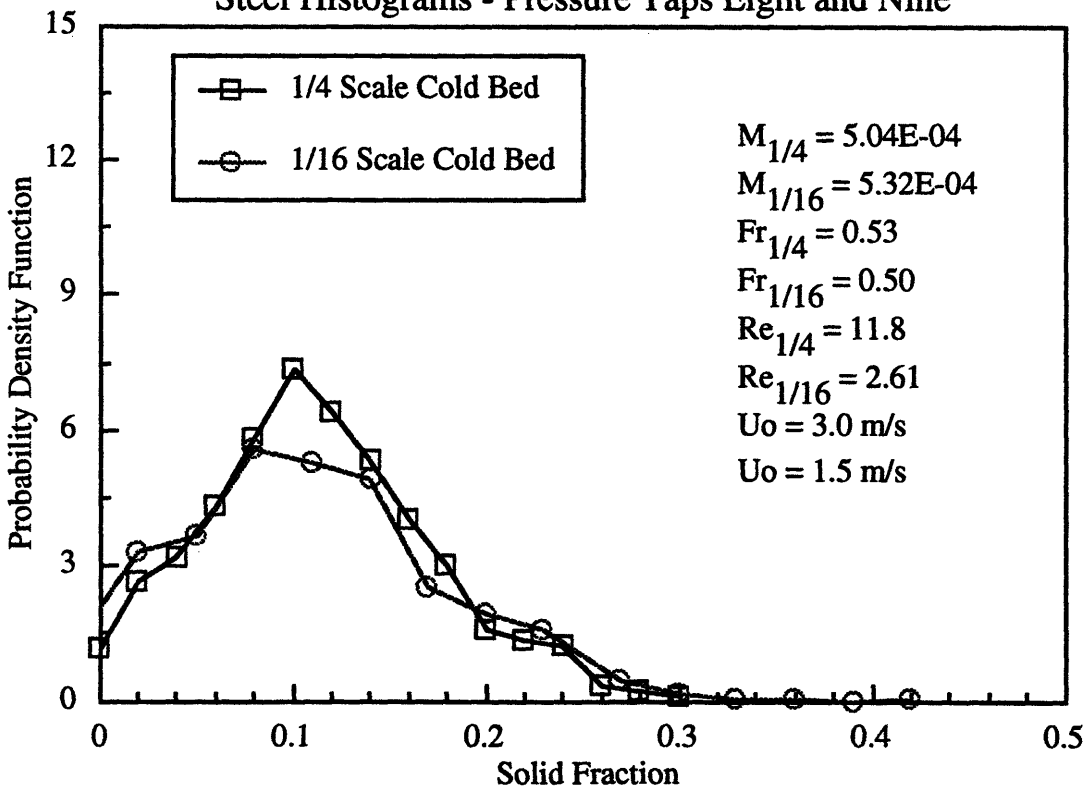

Figure 7.27: Condition 1

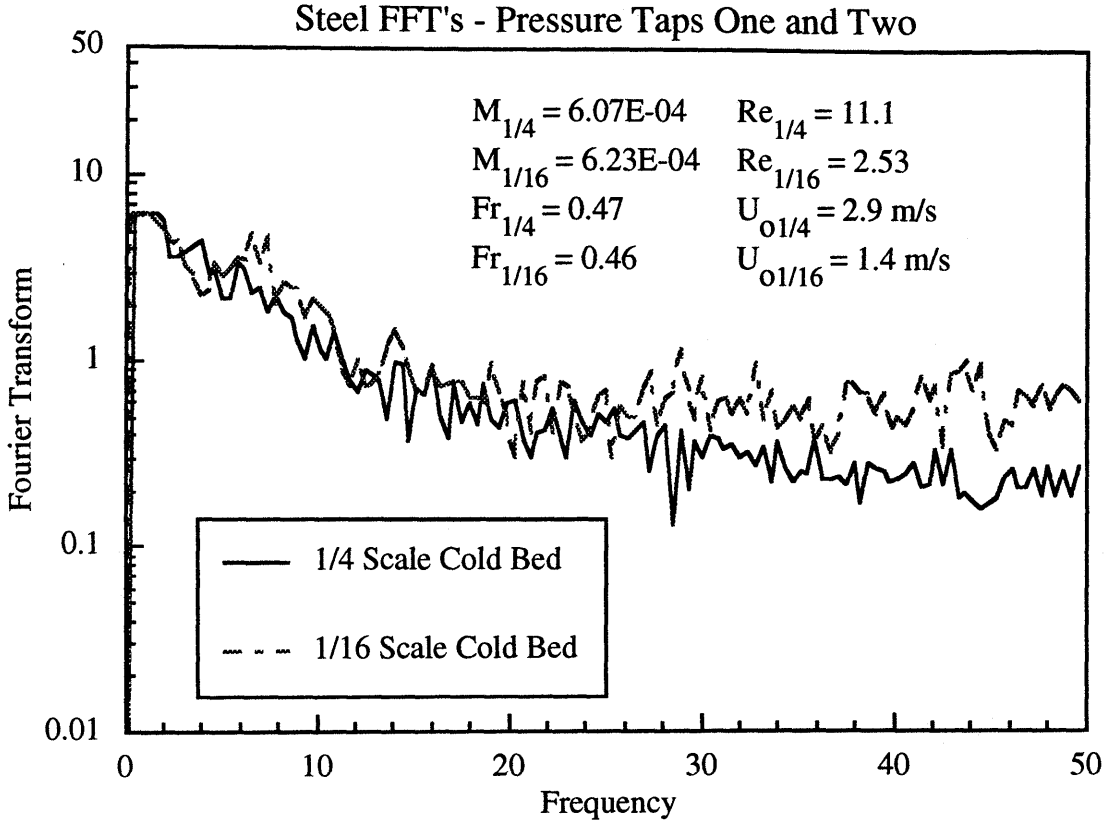

Figure 7.28: Condition 1

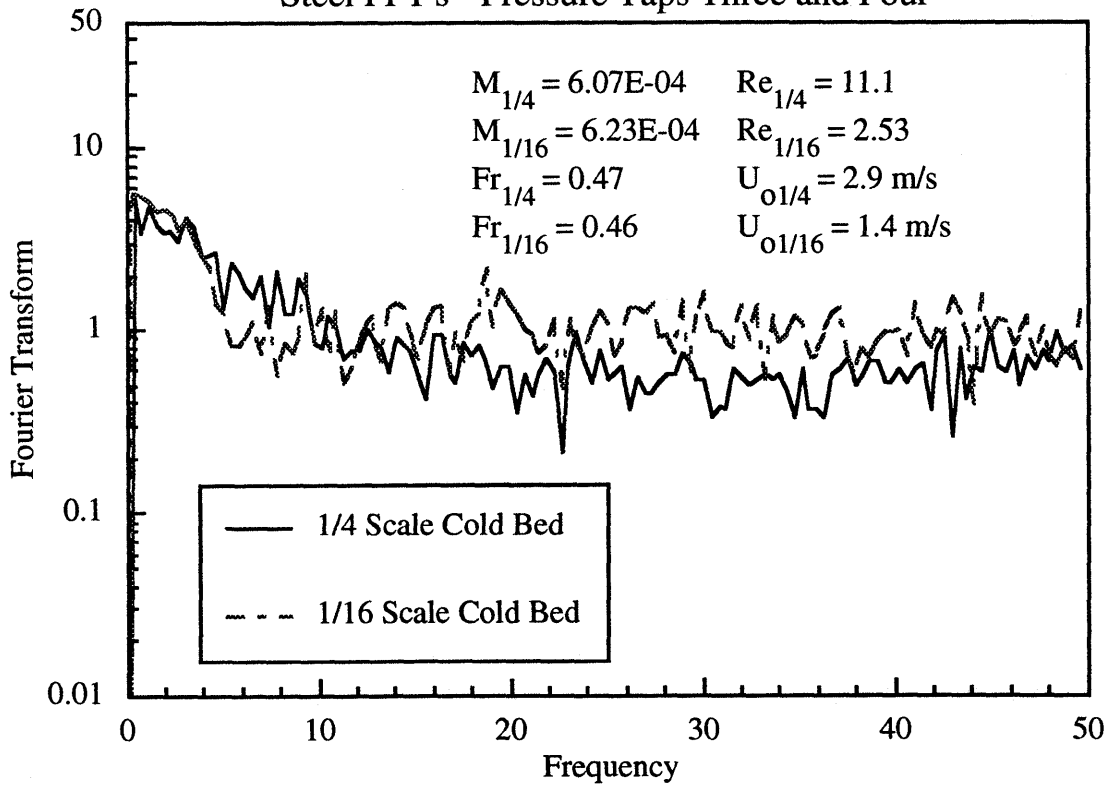

Figure 7.29: Condition 1

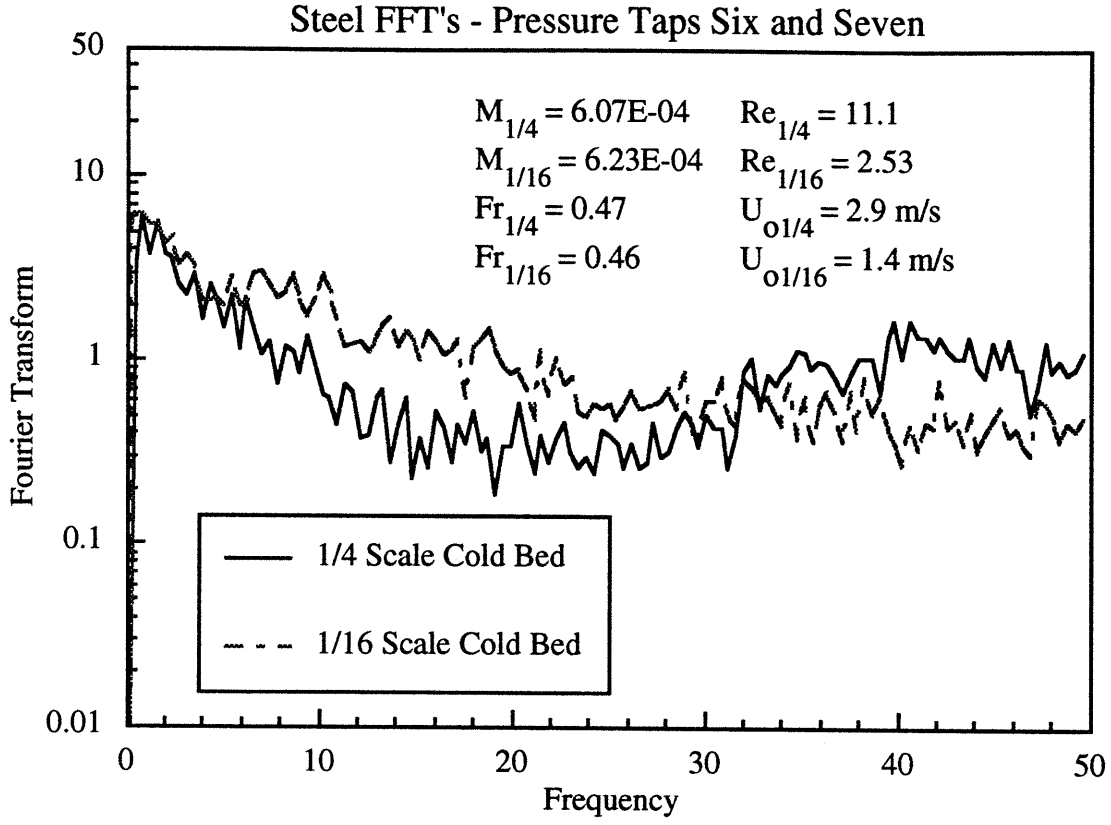

Figure 7.30: Condition 1

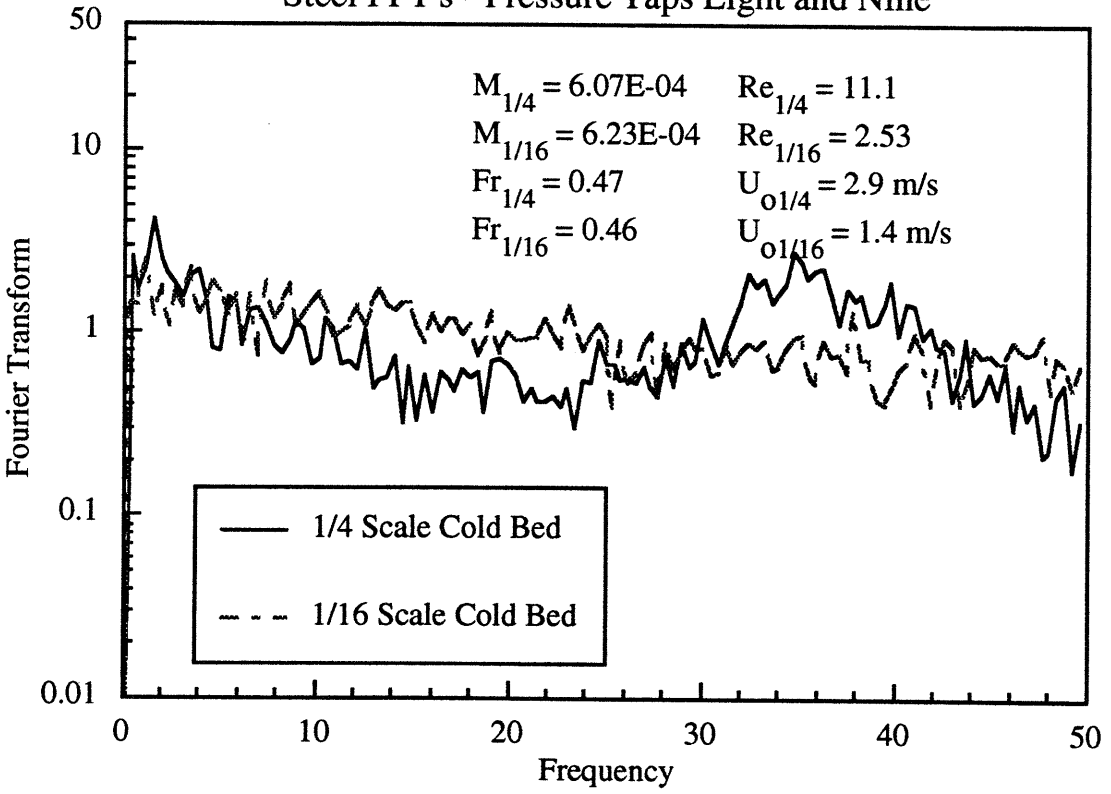

Figure 7.31: Condition 2

Steel FFT's - Pressure Taps One and Two

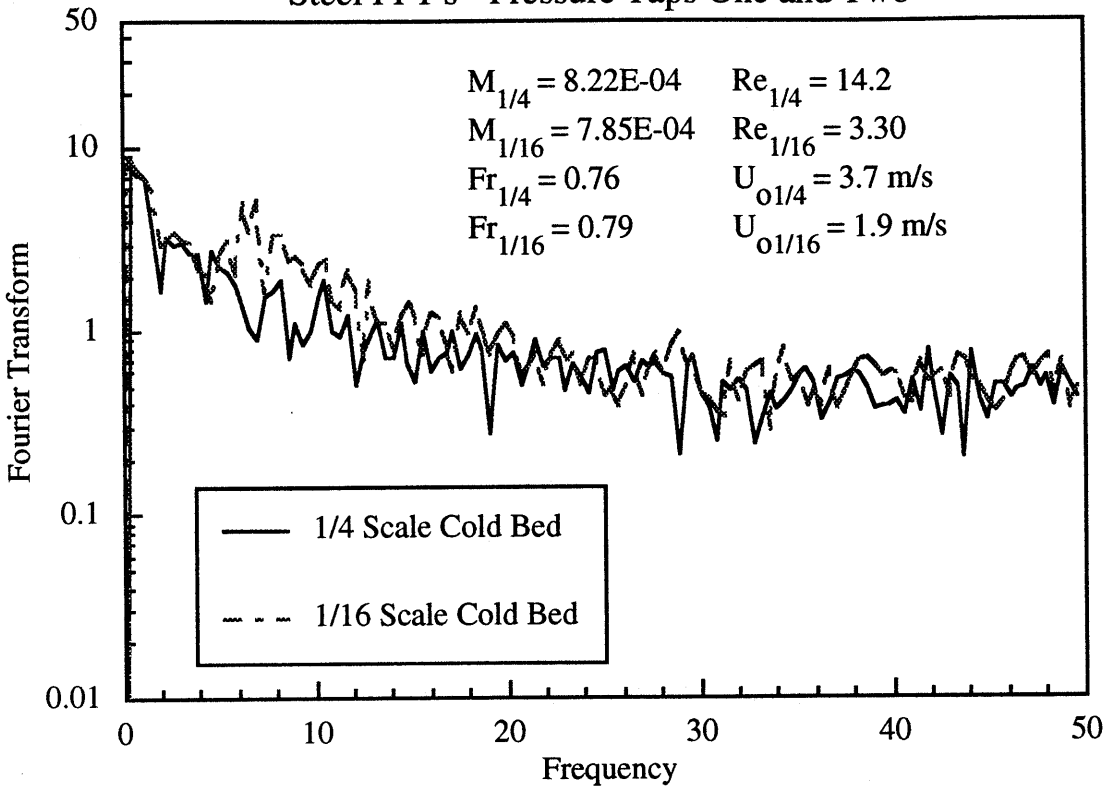

Figure 7.32: Condition 2

Steel FFT's - Pressure Taps Three and Four

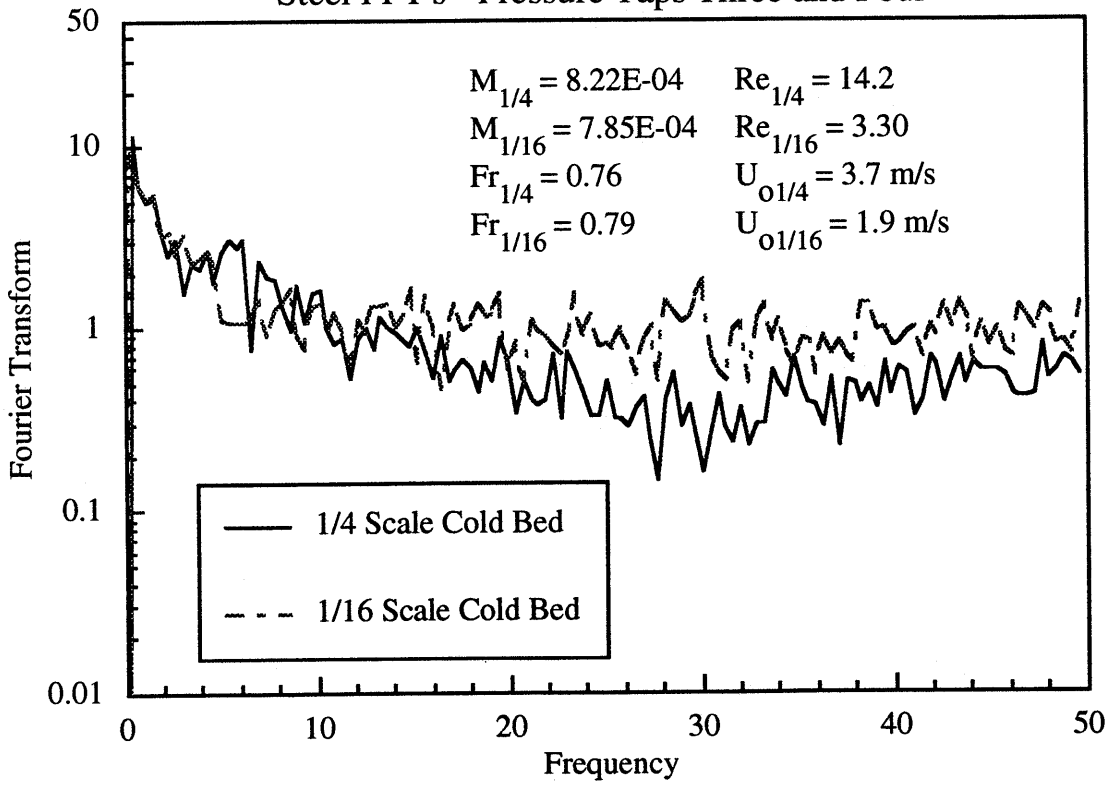

Figure 7.33: Condition 2

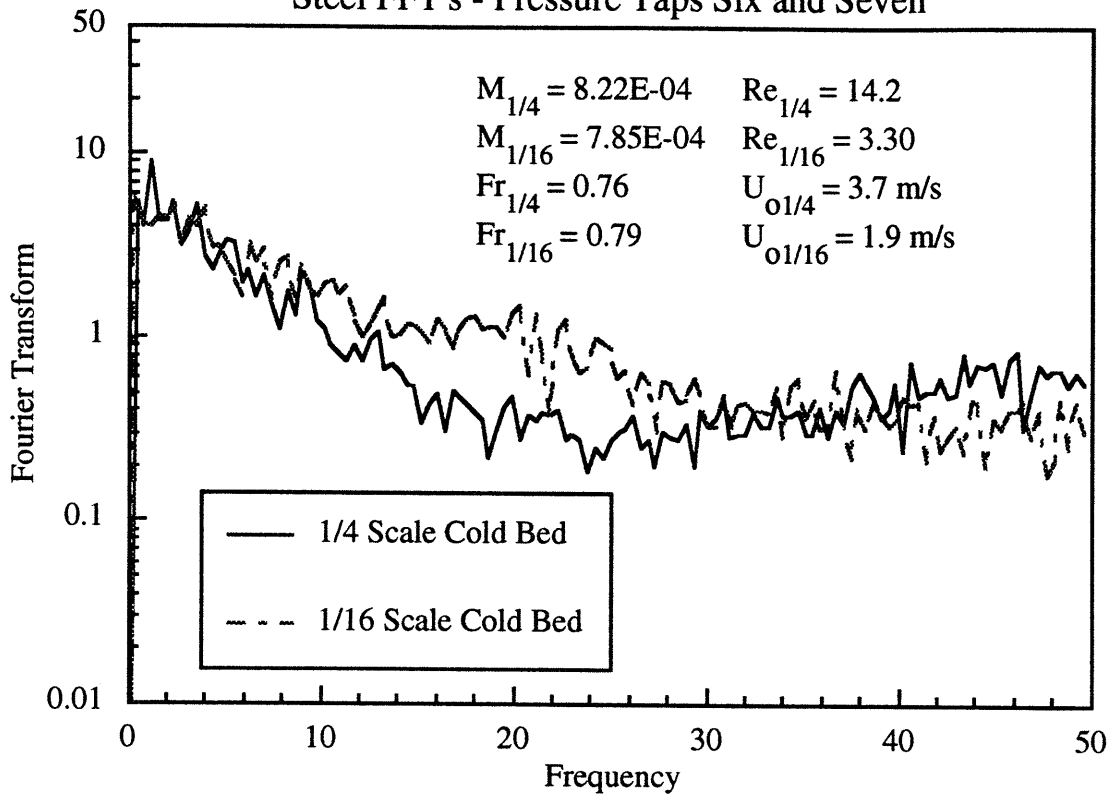

Figure 7.34: Condition 2

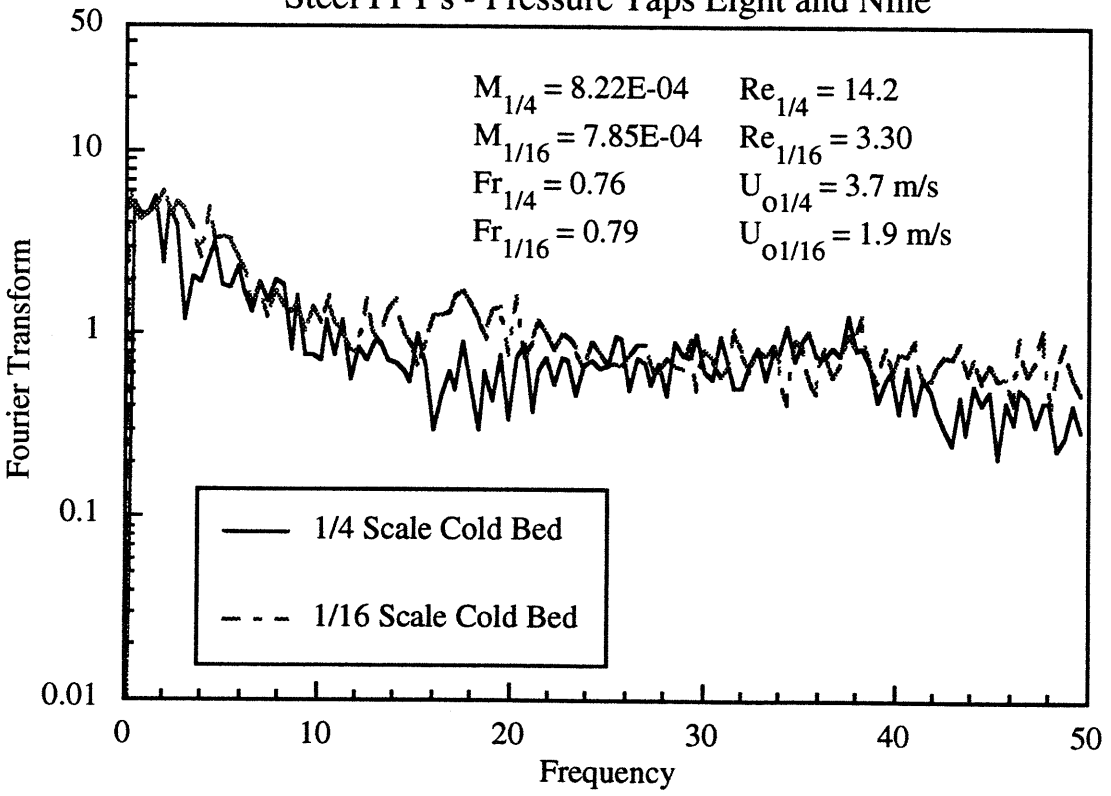

Figure 7.35: Condition 3

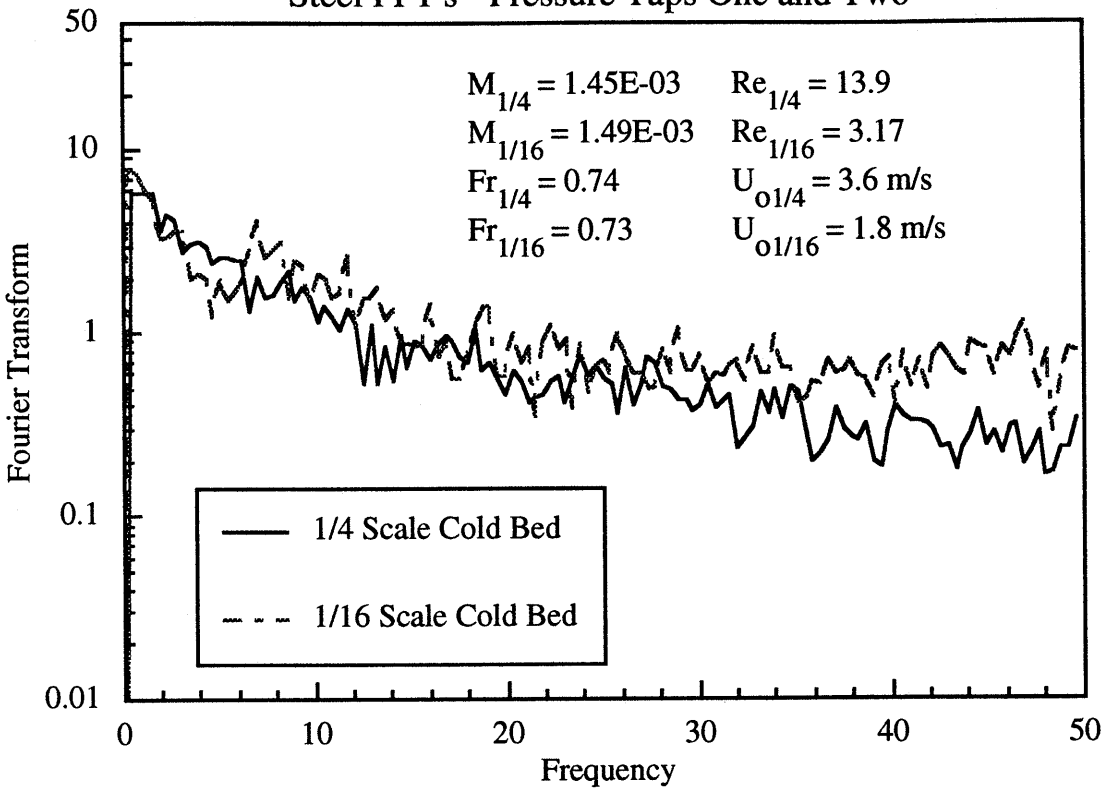

Figure 7.36: Condition 3

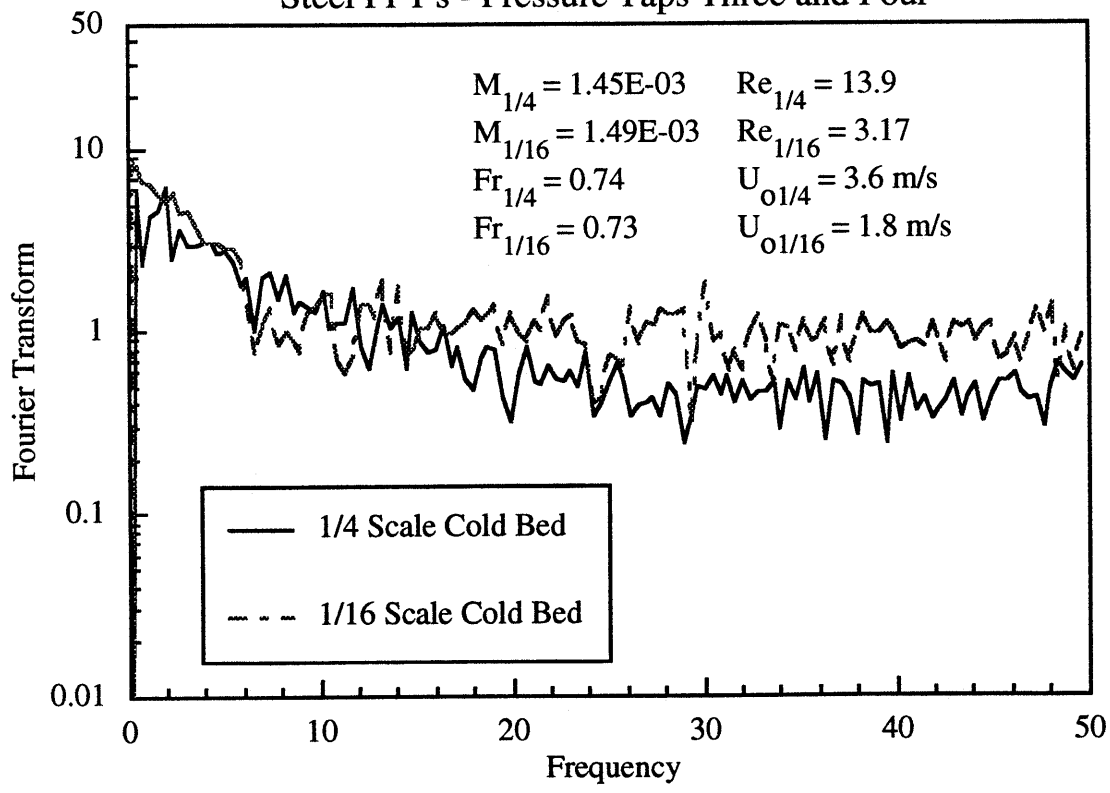

Figure 7.37: Condition 3

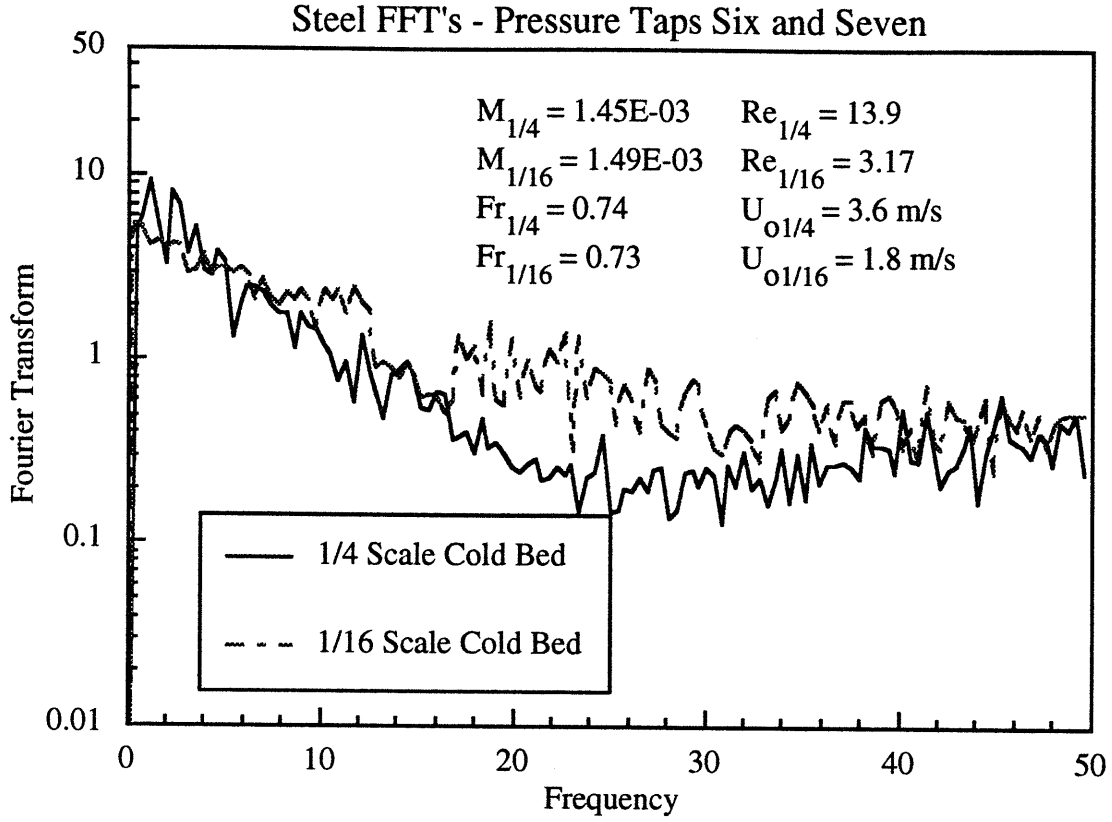

Figure 7.38: Condition 3

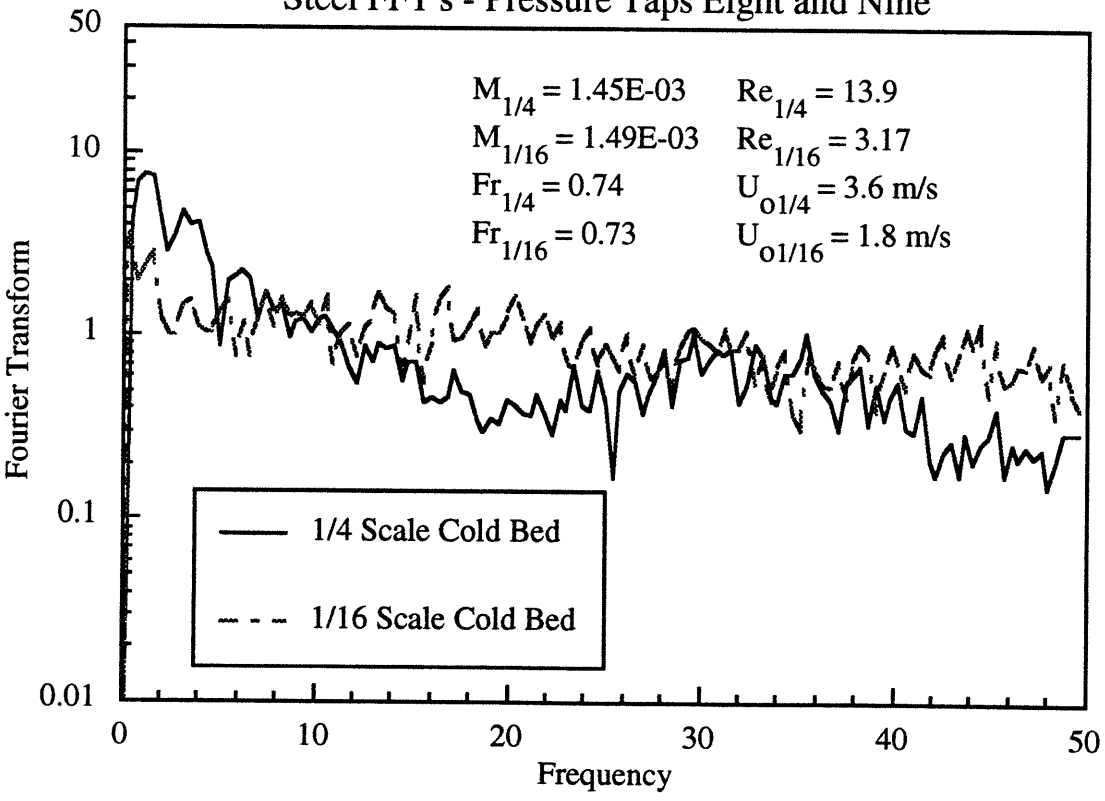

Figure 7.39: Condition 4

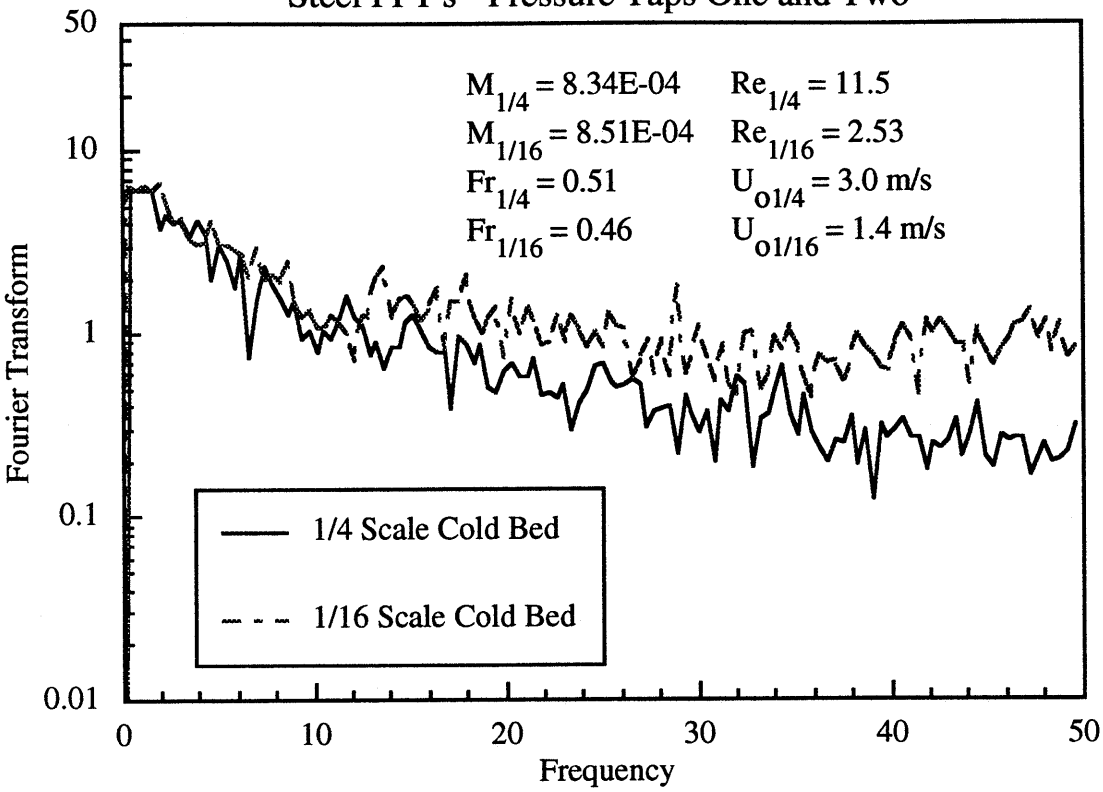

Figure 7.40: Condition 4

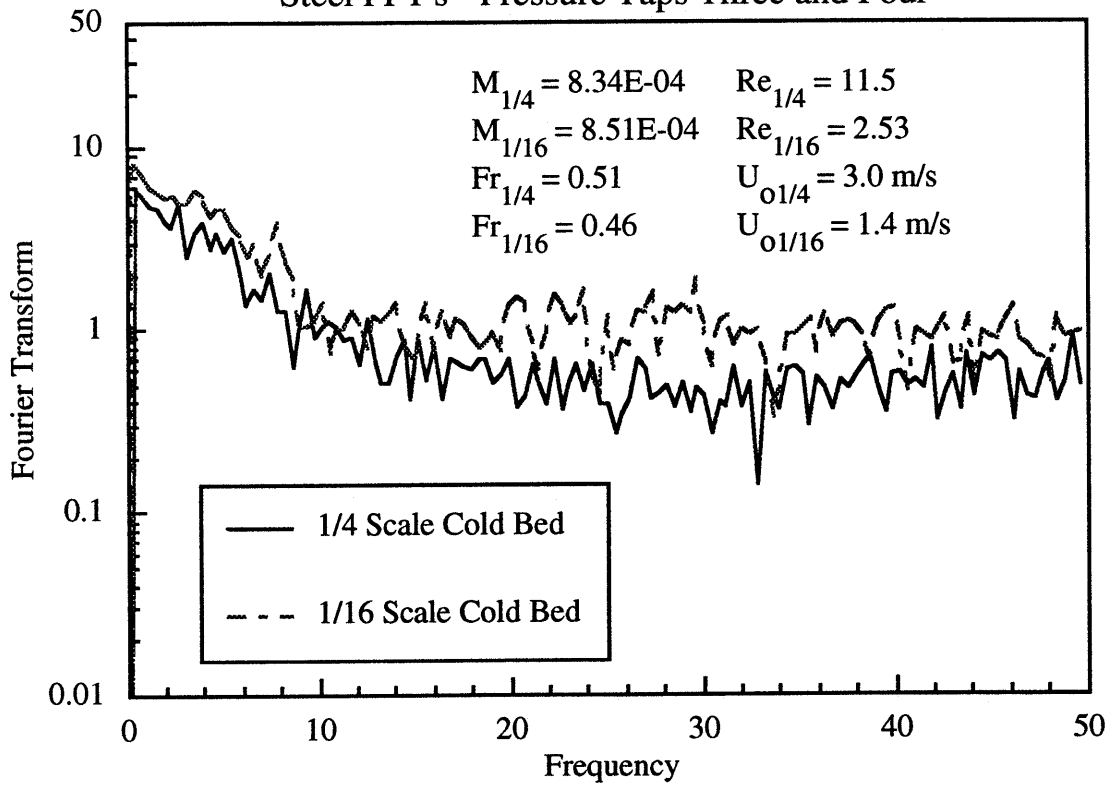

Figure 7.41: Condition 4

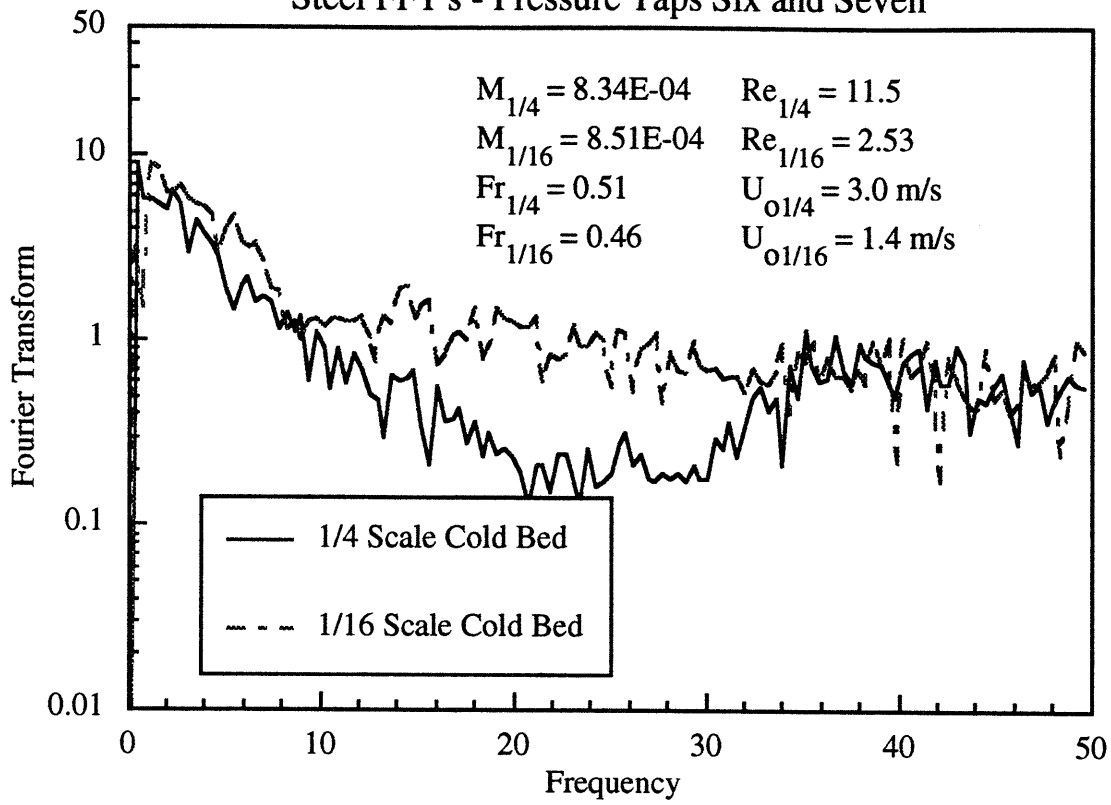

Figure 7.42: Condition 4

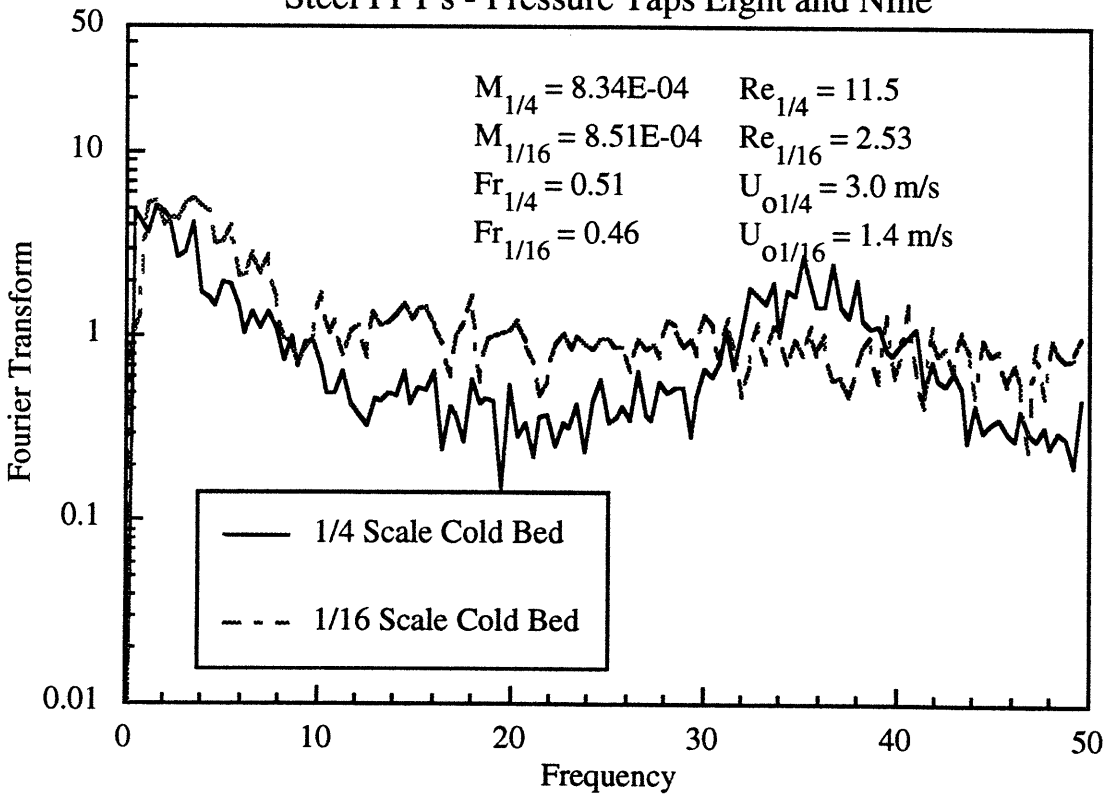

Figure 7.43: Condition 5

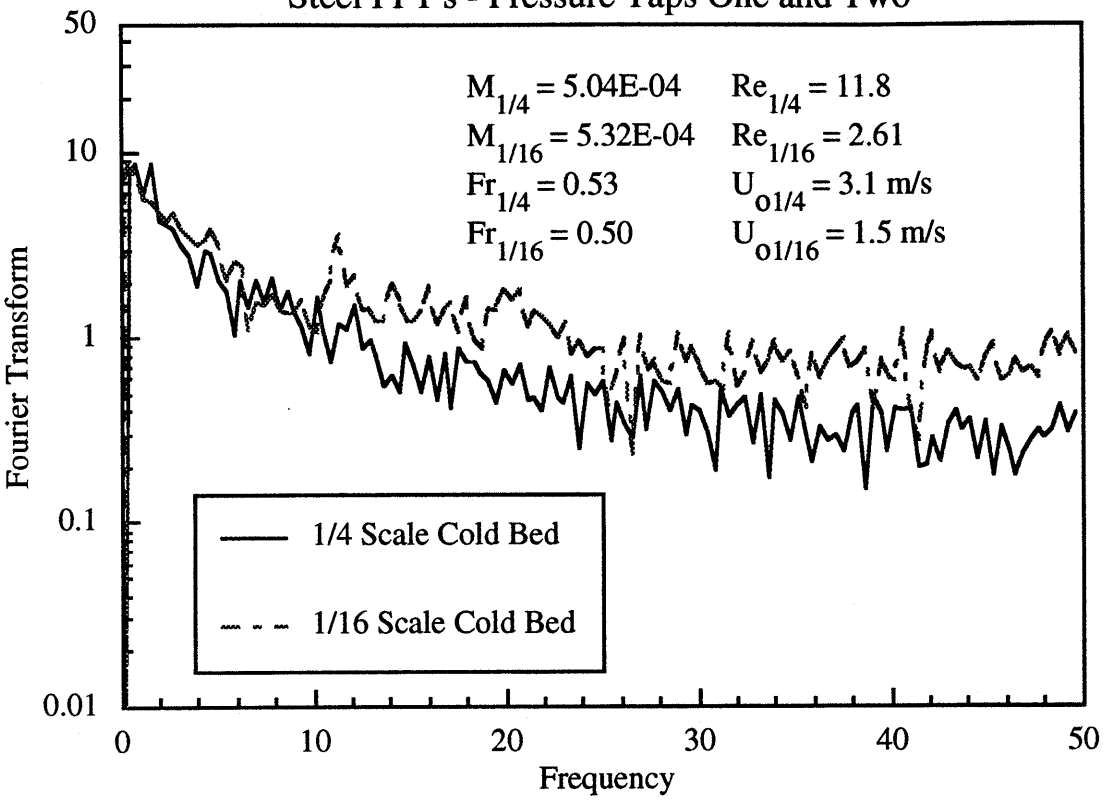

Figure 7.44: Condition 5

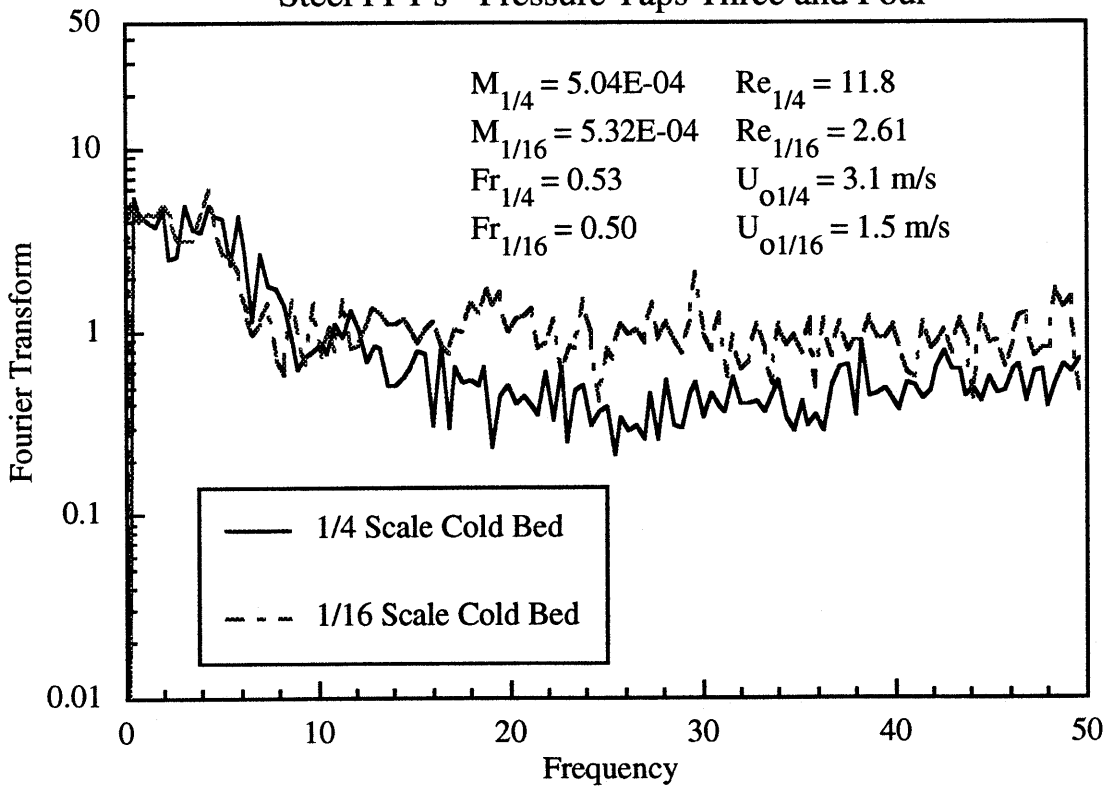

Figure 7.45: Condition 5

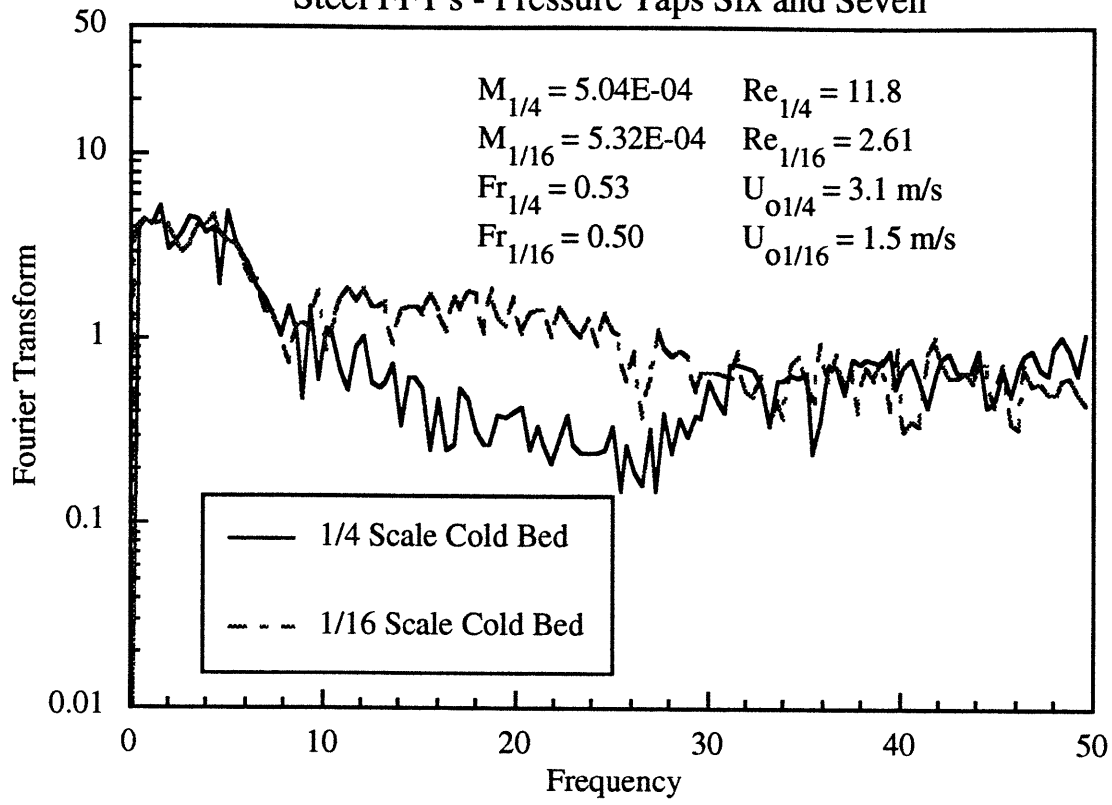

Figure 7.46: Condition 5

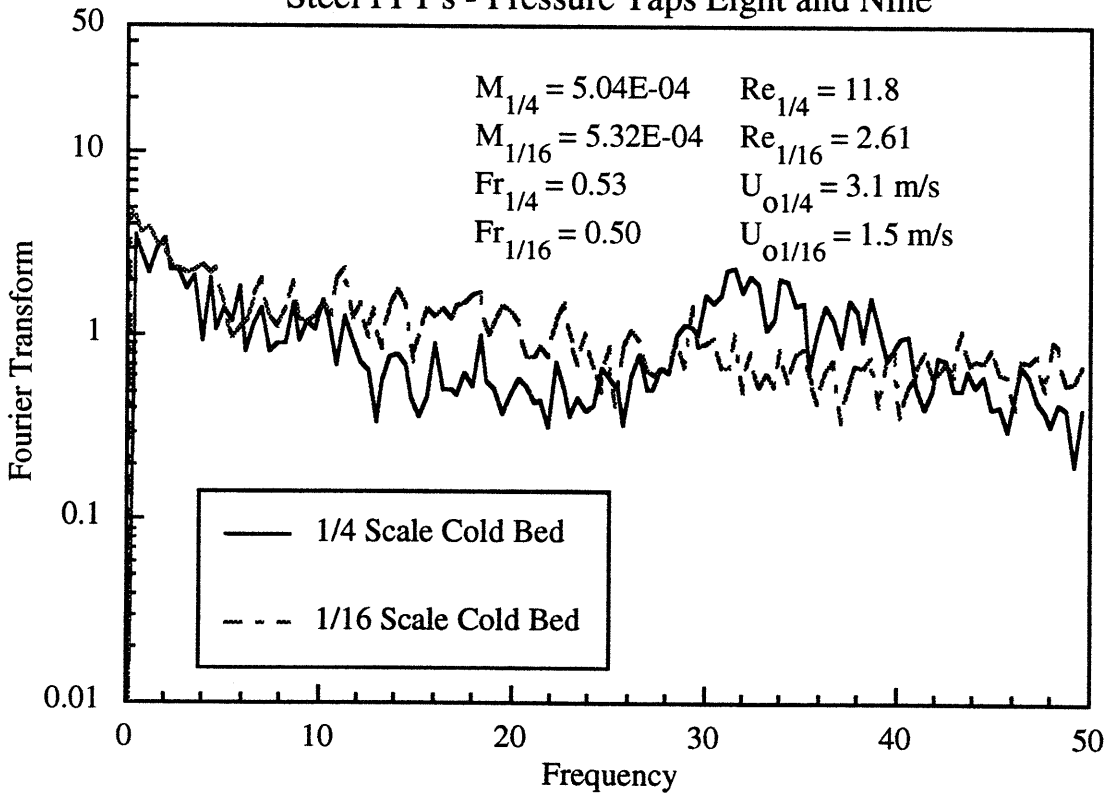

7.4 Discussion of Results

The average solid fraction profiles when utilizing the simplified scaling laws to scale between a utility sized hot CFB and 1/16 scale cold model using the simplified scaling laws are in good agreement for most of the conditions tested. Agreement between the 1/4 scale cold model which utilized the full set of scaling parameters, and the 1/16 scale model which utilized the simplified set of parameters is in excellent agreement for all conditions tested. Agreement between the hot bed and cold models is generally better near the top of the bed. This may be explained in light of the choking phenomenon described in Section 6.3. Since there was a significant amount of error in the solid to fluid density ratio when scaling between the hot and cold beds, one would expect that there would be significant error in the predicted choking voidages resulting in different degrees and heights of choking in the bed. Figure 7.47 depicts the lines of incipient choking for all three beds, along with the points of actual operation.

Comparison between the probability density functions for the 1/4 and 1/16 scale cold models demonstrated excellent agreement. In most cases, the agreement in histograms is better in the top of the bed. This is consistent with agreement of the solid fraction profiles. The power spectral densities for the 1/4 and 1/16 scale Studsvik beds appear to be in reasonable agreement. However, near the top of the 1/4 scale bed an anomaly appears which is not easily explained. Frequencies between 30 and 40 Hz seem to be amplified. It is not likely that this is due to the hydrodynamics in the bed itself. Several of the factors which may have caused the strange behavior in pressure fluctuations near the top of the 1/4 scale bed are:

1. Vortex shedding near the sparge tube
2. Dominant high frequency response of downstream equipment

However, no conclusive evidence exists that either phenomenon is occurring.

Figure 7.47
Choking Limits for Particles Used in Hot Bed Scaling Tests

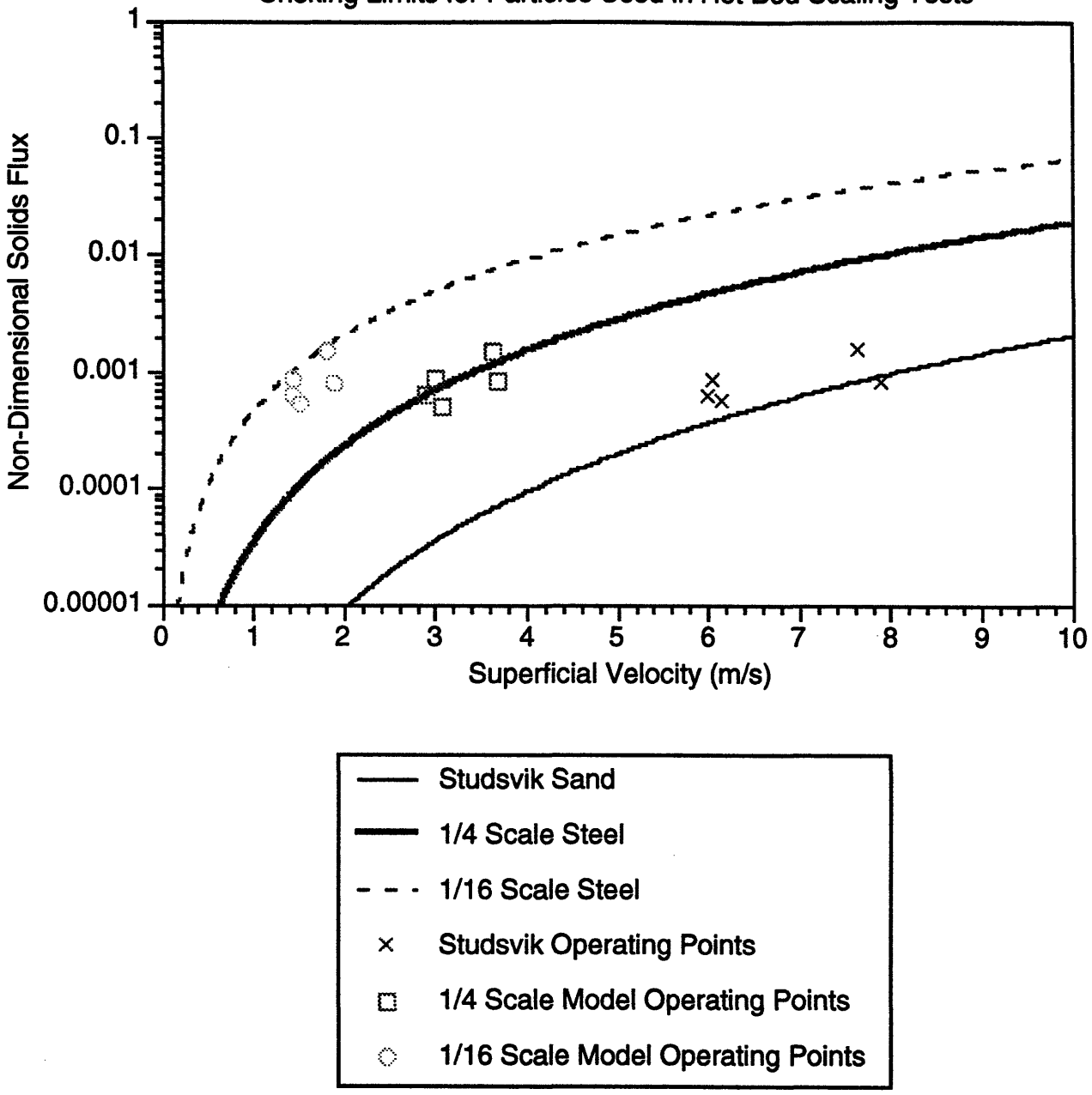

Results of these hydrodynamic scaling experiments show good agreement when using the simplified set of scaling laws and strongly suggest that this new set of parameters is acceptable over the range of conditions tested in the fast fluidization regime. Based on the results of the viscous limit scaling, it appears that the ratio of particle to gas density is a parameter which cannot be ignored in the fast fluidization regime when significant choking occurs. However, the simplified set of parameters which includes this ratio has shown to give acceptable results over a wide range of particle densities and bed sizes, even when the length ratio is as small as 1/16. This has significant implications on the ability to model large scale hot combustors with relatively small cold laboratory models.

7.5 Discussion of Discrepancies with the CFB Scaling Parameters Developed by Horio *et al.*

An extensive discussion of the differences between the viscous limit scaling parameters and the proposed simplified set of scaling parameters has already been given. The scaling between particles of different densities has indicated that the viscous limit parameters are not capable of predicting bed hydrodynamics when significant choking occurs. Since the superficial velocity of the gas must be low to ensure the gas inertial effects are negligible, the constraints on superficial velocity may be quite severe if scaling is attempted using these parameters.

7.5.1 Description of the Model

This Section describes the only other set of scaling laws for CFB's that the author is aware of. While several different formulations of the scaling laws for bubbling beds exist, the only significantly different derivation of the scaling laws for circulating fluidized beds from that presented in Section 2 was conducted by Horio. Horio has proposed a set of scaling laws for circulating fluidized beds based on the clustering annular flow model developed by Ishii *et al.* (1989). This model is a combination of the core-annulus model of Nakamura and Capes (1973) and the cluster flow model of Yerushalmi *et al.* (1978). The flow is described as clusters moving upward in the core and a downward annulus near the walls. Slip velocities in both regions are based on cluster diameter rather than particle diameter, and it is assumed that cluster distribution is homogenous (the particulate fluidization equation of Richardson and Zaki (1973) is used). Cluster diameters and voidages within clusters for the core and for the annulus are introduced in the model as dependent variables. The analysis is similar to that of Nakamura and Capes. This model is also incomplete. Ishii *et al.* suggested that completeness could be achieved by assuming that pressure drop is minimized. This is the same assumption made by Nakamura and Capes, although no theoretical or physical explanation was given by either Ishii *et al.* or Nakamura and Capes as to the validity of this assumption. Ishii *et al.* present an expression for the core-annulus diameter ratio based on this assumption, which compares reasonably well with their data.

7.5.2 Results of Experiments Conducted by Horio *et al.*

Surprisingly, regardless of the drastic difference in the method of derivation, Horio's CFB scaling laws end up being nearly equivalent with the viscous limit scaling laws described in Section 2 of this Chapter. Horio's scaling laws require:

$$\frac{u_t}{(u_t)_o} = \sqrt{\frac{L}{L_o}}$$

$$\frac{G_s}{(G_s)_o} = \sqrt{\frac{L}{L_o}}$$

$$\left(\frac{\rho_s}{\rho_f}\right) = \left(\frac{\rho_s}{\rho_f}\right)_o$$

Horio argues that if particles of the same density are used for tests of hot-to-cold or high pressure-to-ambient scaling, similarity would not necessarily be ensured. He goes on to postulate that "this does not mean necessarily that the macroscopic flow field cannot be made similar, since it is probable that the macroscopic flow field remains similar sacrificing the similarity of cluster size" (Horio, 1989).

Horio has achieved good agreement between solid fraction profiles, probability density distribution of light reflection intensity from an optical fiber probe, and prediction of incipient choking using these laws to scale between cold beds which differ in size but utilize the same bed material (Horio, 1989, and Ishii, 1990). In both studies, the beds also satisfied the simplified set of scaling parameters proposed in this report even though the solid-to-fluid density ratio was not considered to be an important parameter.

A later study (Tsukada, 1991) compared the solid fraction profiles and optical fiber probe signals in a bed in which the gas pressure was changed to evaluate the effect of the density ratio. While it was anticipated and claimed that the similarity in solid fraction profiles was reasonable, when the density ratio was changed significantly (pressure was doubled), the figures show a significant shift in the solid fraction profile, indicating that the density ratio may, in fact, be important. It is worth noting that the trend shown in the solid fraction profiles is consistent with the trends found between particles of different density which was discussed in Section 4 (i.e., solid fraction profiles for larger values of ρ_S/ρ_f where higher than those for lower values of ρ_S/ρ_f).

7.5.3 Discussion of the Assumption of Minimum Energy Dissipation in CFB's

In a markedly similar statement to Ishii and Nakamura and Capes' assumption of minimum pressure drop across the bed, Li *et al.* (1988) have stated that "particles in vertical flow are considered to tend toward certain dynamic array of minimum potential energy, so as to permit the fluid to flow across the system with minimal resistance". This statement was based, in part,

on a postulate made by Reh (1971) on the aggregative behavior of fluidized particles. The statement made by Reh that the aggregative behavior of particles in a fluidized bed was due to the principle of minimum energy dissipation did not evolve from a theoretical development, but rather from an intuitive argument based on observations. Due to the lack of experimental evidence it is not clear why Li's argument that "the fluid dynamics of gas/solid flow in a circulating fluidized bed is governed by the principle of energy minimization," (Li *et al.*, 1991) and that "for a heterogeneous two-phase flow system, the energy consumption in the suspension/transport subsystem always tends toward a minimum" (Li *et al.*, 1988) should be necessarily valid.

7.5.3.1 History of the Assumption of Minimum Energy Dissipation

Helmholtz (1868) and later Korteweg (1883) showed that for the steady flow of a fluid under constant extraneous forces, the currents in the fluid are distributed so that the loss of energy due to viscosity is a minimum, *provided the inertial terms in the governing equations can be neglected* and the velocities along the boundaries of the fluid are given. Rayleigh (1913) pointed out that the theorems of minimum energy dissipation proposed by Helmholtz and Korteweg could be extended so as to apply to any system for which

$$\nabla^2 u = \frac{\partial H}{\partial x}, \quad \nabla^2 v = \frac{\partial H}{\partial y}, \quad \nabla^2 w = \frac{\partial H}{\partial z}$$

where H is a single-valued function of x, y, and z. These equations include the motion of a fluid between parallel planes or coaxial cylinders.

Some time later, it was hypothesized that for small spheres moving at sufficiently slow motions in a particle/fluid system "tend to adopt that motion which, of all motions possible, corresponds to the least dissipation of energy" (Jeffery, 1922). If correct, Jeffery's hypothesis should be deducible from the Navier-Stokes equations. To apply his principle to the problem of particle/fluid systems operating in the viscous regime, Jeffery utilized the result of Einstein (1906) for the excess dissipation of energy produced by the introduction of a sphere into a uniform shear flow. Einstein has shown that the excess dissipation is proportional to the square of the vorticity of the incident flow at the particle. Since the velocity distribution Jeffery was concerned with was Poiseuille flow, the vorticity is proportional to the distance from the axis and the excess energy dissipation to the square of the distance from the axis. Thus, Jeffery concluded that if his assumption concerning the minimization of energy dissipation is correct, neutrally buoyant particles would move along the axis (a phenomena which has been observed with blood corpuscles flowing in the capillaries of the body).

7.5.3.2 Energy Dissipation in Suspensions of Neutrally Buoyant Bodies

Jeffery's hypothesis was further developed and tested by Müller (1936) using suspensions of small rubber discs, Vejlens (1938) working with single rigid spheres, and Starkey (1955, 1956) in which he used solutions of eosin and carbon black stabilized with gum. These investigators attributed the observed inward migration of particles near the wall of tube flow to the principle of least action (Starkey theorized that the "form" resisting component of a stream of suspended particles in a non-uniform velocity field tends to decrease progressively towards a minimum value at a rate which increases with particle size and rate of shear) or that of minimum energy dissipation in the flow. However, other early experiments conducted by

Taylor (1923), Binder (1939), Trevelyand and Mason (1951), and Mason and Manley (1956) using neutrally buoyant spheroids and/or cylindrical rods in viscous fluids produced contradictory results. Taylor's and Trevelyand and Mason's experiments tended to support Jeffery's hypothesis while the others did not. In fact, in some of the experiments, the suspended particles oriented themselves in orbits of *maximum* energy dissipation. In perhaps the most exhaustive study on the tendency of spheres, rods, and discs made from various materials in various fluids to migrate towards positions of minimum pressure drop, Goldsmith and Mason (1961) could find no conclusive proof of a preferred orientation of the particles, except for deformable fluid drops flowing in air. They concluded that spherical particles would migrate towards regions of minimum energy dissipation only if the particles are deformable.

Subsequent work performed by Segre' and Silberberg (1961,1962) aimed at determining the validity of Jeffery's hypothesis through extremely accurate measurements of the lateral migration of neutrally buoyant particles indicated conclusively that the spheres in a particle/fluid suspension operating in a viscous regime did indeed align themselves in an annulus at a specific distance from the tube centerline regardless of their initial entry distribution. However, the particles tended to aggregate at a distance r/R = 0.6, which is not the position for minimum energy dissipation. Attempts were made to explain this result through the effects of fluid inertia since the particle/fluid equations of motion resulting from a viscous limit analysis do not predict transverse forces (Saffman, 1956; Brenner and Happel, 1958; Bretherton, 1962). Unfortunately, the difficulty of solving the complete Navier-Stokes equations of motion prevents a thorough analysis of the effects of the inertial terms. Early work by Saffman (1956) and Tollert (1954) managed to develop equations for the transverse force on particles in a viscous shear flow through the inclusion of quadratic terms made possible by postulating a transverse force which arises from the combination of a rotary and a translatory motion relative to the undisturbed flow of the fluid. Saffman's formulation was able to predict, within an order of magnitude, the centripetal removal of particles from the wall, but was unable to explain the centrifugal force acting at the tube center. While they were unable to fully explain the "tubular pinch effect," Segre' and Silberberg did point out that the criteria of minimum energy dissipation according to which one would expect the particles to congregate at the center of the tube was contravened. The results of Segre' and Silberberg's experiments were later confirmed by Oliver (1962), and in square ducts by Repetti and Leonard (1964).[1] Karnis *et al.* (1963, 1966) repeated the exhaustive experiments conducted

[1] Experiments by Segre' and Silberberg were conducted at particle Reynolds numbers $\left(Re_p = \frac{|u_f - u_p| d_p \rho_f}{\mu}\right)$ less than 0.01. The range of particle Reynolds numbers for the experiments of Oliver (1962) and Repetti and Leonard (1964) were 1-13 and 10-27 respectively. For an atmospheric circulating fluidized bed combustor operating at 850 °C with 200 micron limestone, the particle Reynolds number is about 2. For a 10 bar pressurized CFB, it is about 10. All experiments were conducted at tube Reynolds numbers below

by Goldsmith and Mason in 1961 to investigate the discrepancies between the Goldsmith experiments and the results found by Segre' and Silberberg. They found that at higher particle Reynolds numbers in the viscous regime ($Re_p \sim 10^{-2}$; original experiments were conducted at $Re_p \sim 10^{-6}$) the rigid spheres, discs, and rods did, in fact migrate to r/R of 0.6. This confirms that inertial forces are necessary for radial particle migration. In none of the cases (in the original experiments or the later experiments) did the rigid particles tend toward a position of minimum energy dissipation.

7.5.3.3 Energy Dissipation in Suspensions of Non-Neutrally Buoyant Bodies

The results of the experiments of Segre' and Silberberg initiated a number of studies related to determining the equilibrium radial positions of particles in particle/fluid suspensions. In addition to the experiments which observed the radial migration of neutrally buoyant particles across streamlines to a stable position at about 0.6 tube radius from the axis, studies were conducted to determine how non-neutrally buoyant particles behaved. For non-neutrally buoyant bodies, the rate of energy dissipation stems from three sources:

1. Translation of the particles relative to the fluid
2. Rotation of the particles relative to the fluid
3. Inability of the solid particles to undergo deformation and thereby accommodate itself to the dilational components of the original fluid motion

In the case of small spherical particles, the rotational contribution to energy dissipation will normally vanish. In many macroscopic systems, where the densities of the particles and fluid are not matched, the dilational contribution , which constitutes an effective suspension "viscosity," will also be small with respect to that due to frictional drag. For the limiting case where the radius of the tube is much larger than the radius of the particles, the average pressure drop is equal to the sum of the drag on the particles. Therefore, to minimize energy dissipation, non-neutrally buoyant bodies would tend to move to positions which minimize fluid/particle drag.

For the case of a non-neutrally buoyant spherical particle immersed in a Poiseuille flow with a low particle-wall areal ratio, the pressure drop is:

$$\Delta P = \frac{6\mu d_p u_t}{R^2}\left(1 - \frac{r^2}{R^2}\right)$$

where u_t is the particle terminal velocity, r refers to the radial distance at which the center of the sphere (diameter = d_p) is located from the cylinder axis, and R is the tube radius. To minimize pressure drop, non-neutrally buoyant particles should move to a position of r= R; to the tube

---

1000 to eliminate effects arising from fluid turbulence.

wall. It is important to observe that the pressure drop will be different from that required to support the particle itself, essentially equivalent to multiplication of Stokes' law drag by a factor of $2\left(1-\frac{r^2}{R^2}\right)$. For the limiting case $\frac{R}{d_p} \rightarrow \infty$, where a parabolic flow pattern is not maintained because of the occurrence of high particle-wall areal ratio, the pressure drop force is essentially equal to the sum of the Stokes' law drags on the particles.

As was the case with the neutrally buoyant spheres, lateral forces were observed in suspensions of non-neutrally buoyant spheres. However, the particles no longer attained a fractionally eccentric equilibrium position. Instead, they migrated to either the wall or the tube axis depending upon whether the terminal velocity was of the same sign or of opposite sign to that of the fluid velocity. If the sphere was more dense than the fluid and flow was downward, there was an increase in r/R, whereas when a less dense sphere was in a downward flowing fluid, or a denser sphere was in an upward flowing fluid (the case most analogous to a CFB), the equilibrium position was displaced toward the tube axis (Denson, *et al.*, 1966 [$6 < Re_p < 120$]; Eichorn and Small [$80 < Re_p < 247$], 1964; Jeffery and Pearson [$0.01 < Re_p < 2$], 1965, Theodore [$0.1 < Re_p < 8$], 1964; and Repetti and Leonard [$10 < Re_p < 30$], 1964). The same results were obtained in couette systems by Halow and Wills (1970a,b,). Particles tended to migrate across streamlines toward positions which increased the particle/fluid slip velocity. Stated more generally, the particles will attain a stable equilibrium position at the axis if the scalar $(\rho_p - \rho_f)\mathbf{V_m} \cdot \mathbf{g}$ is negative, and, conversely, attained a stable equilibrium position at the wall if this scalar was positive. In an upflow of particles more dense than the fluid (the situation in a CFB), particles always migrated to the tube axis. This does not minimize the pressure drop in either particle-wall areal ratio limit. In the case of low particle-wall areal ratio, the particles should move to the wall. For large particle-wall areal ratios, when particles cross streamlines toward positions of higher particle/fluid slip velocity they increase the particle fluid drag resulting in higher energy dissipation than if they did not migrate radially. It is interesting to note that this result is consistent with experimental results of bubbly two-phase liquid/gas flow. In upward bubbly flow (liquid up, bubbles up) the bubbles tend to migrate toward the wall, whereas in downward bubbly flow (liquid down, bubbles up) the bubbles tend to migrate toward the tube axis (see for example Wang *et al.*, 1987; Oshinowo and Charles, 1974; Kensuke and Kazuo, 1989 and Avdeev, 1984).

In addition to the analyses performed by Saffman (1956, 1965) and Tollert (1954), several attempts have been made to provide a sound theoretical basis for the prediction of lateral forces in Poiseuille flow through first-order approximations of inertial forces (Rubinow and Keller, 1961; Cox and Brenner, 1967; Slezkin, 1952; Slezkin and Shustov, 1954; and Ho and Leal, 1974). Theoretical investigations have continued to the present (see for example McLaughlin, 1993 and Hogg, 1994). While it is generally agreed that the lateral migration of the particles is

due to inertial effects (and possibly non-Newtonian effects), only qualitative verifications of their expressions for the lift force and transverse velocities are possible. None of the analyses attributed the migration of particles to a principle of minimum energy dissipation since the experimental evidence does not support such an assertion. Moreover, theoretical analysis of energy dissipation resulting from particles in shear flows have indicated that even in the restricted class of flows considered by Jeffery, the minimum energy dissipation hypothesis does not hold (Harper and Chang, 1968).

7.5.3.4 Extremum Principles for Particle/Fluid Systems

The use of extremum principles (maximum and minimum principles of entropy production and energy dissipation) in Stokes flow and similar problems have been discussed by Helmholtz (1868), Korteweg (1883), and Rayleigh (1913). In addition, there have been several studies concerned with applying variational techniques to obtain bounds on the mass and momentum transport coefficients in slow viscous suspensions (Hill and Power, 1956, Keller *et al.*, 1967, Weinberger, 1972, Prager, 1963, and Nir *et al.*, 1975).

In a study of extremum principles for slow viscous suspension flows, Keller *et al.* show that the Stokes flows yield a smaller drag on a body in translation and a smaller resistive torque on a body in rotation in an incompressible fluid than do the corresponding Navier-Stokes flows. This is consistent with the facts that the Oseen correction to the Stokes formula for the drag on a rigid sphere is positive and the Brenner and Cox (1963) result that the correction to the Stokes drag on an arbitrary object is positive. Thus, extremum principles predict that for a given distribution of particles, the flow which minimizes energy dissipation corresponds to Stokes flow at very low Reynolds number - a condition not normally associated with circulating fluidized beds.

Based on an analogy between the field equations for an elastic solid in equilibrium and a viscous newtonian fluid in steady creeping flow, Hill and Power (1956) derived a pair of extremum principles. These theorems bracket the energy dissipation in a given boundary value problem between upper and lower bounds corresponding to arbitrarily chosen admissible functions. The one function which provides an upper limit is given by Helmholtz's theorem. For the lower bound, stresses must be assumed which will result in a finite force and/or couple on the body. Based on their analysis Hill and Power conclude that the drag on a body tends to be increased by the presence of other bodies which are either in fixed position or free to move without restraint. However, Smoulchowski (1912) showed that if the bodies move in an unbounded medium, that the opposite is true.

It is interesting to note that variational principles exist when inertial terms are important and

viscous terms are not and when viscous terms are important but inertial terms are not. Attempts to derive variational principles when both inertial and viscous terms are included have so far failed. In fact Finlayson (1972) has shown that a variational principle for the incompressible, steady-state Navier-Stokes equations does not exist unless $u \cdot \nabla u = 0$ or $u \times (\nabla \times u) = 0$. Recent experiments (Glicksman *et al.*, 1993) have indicated that fluid inertial effects cannot be neglected in circulating fluidized beds, even at low particle Reynolds numbers. This brings into question the possibility of using any variational principle to approximate CFB energy dissipation.

7.5.3.5 Thermodynamic Aspects

In addition to the lack experimental evidence in the fluid mechanics literature, it is not obvious that this principle should be valid thermodynamically. The argument of Li *et al.* is based on what they term the "principle of minimum total potential energy." It is true that among the many states of a system that have given values of entropy, constituents, and external forces (S, **n**, β), the energy of the unique stable equilibrium state is smaller than that of all the other states with the given values of S, **n**, and β (Gyftopoulos, 1991). However, a circulating fluidized bed (even without chemical reactions) is not in an equilibrium state. Gyftopoulos defines an equilibrium state as one "that does not change as a function of time while the system is isolated - a state that does not change spontaneously." The fluid/particle flow in a CFB is not isolated, and if it were, it would certainly change with time until all the particles were lying at the bottom of the bed. The flow in a CFB is better defined as in a bulk flow state from which, as opposed to a stable equilibrium state, energy can be extracted. The authors of this report are not aware of any law which indicates that bulk flow systems necessarily tend toward a state of minimum energy dissipation. In fact, if such a law did exist, the well known phenomenon of the transition of a fluid from laminar to turbulent flow should not occur since the energy dissipation in turbulent flow is far higher than in laminar flow.

In the field of non-equilibrium thermodynamics, it has been shown that under certain conditions stationary non-equilibrium states are characterized by minimum entropy production (de Groot and Mazur, 1984). This property is only valid if the phenomenological coefficients are constants and the phenomenological equations are linear (e.g. Fourier's law of heat conduction, Fick's laws of diffusion, Ohm's law of electric conduction). Recent studies have indicated that the convective terms in the governing fluid/particle system equations cannot be ignored (Glicksman *et al.*, 1993). This suggests that the phenomenological equations which govern fluid bed behavior cannot be approximated as linear. It is also unlikely that the temporal terms in the gas/particle equations can be ignored. Since the governing equations may neither be linear nor stationary, it is unlikely that a CFB can be characterized by minimum entropy production based on the arguments of non-equilibrium thermodynamics.

7.5.3.6 Conclusions

Experiments for viscous flows where fluid inertial effects are small have not substantiated early hypotheses of energy minimization for fluid-solid flows. For gas-solid flows where both fluid inertial and viscous forces are important, no experimental or theoretical evidence exists to suggest that the flow condition is one which minimizes energy dissipation.

In light of past experimental evidence, there seems to be little reason to make the assumption that heterogeneous two-phase flows tend toward a state of minimum energy dissipation or minimum pressure drop. Such a hypothesis needs to be substantiated by detailed experimental proof before it can be considered for fluidized beds.

8.0 SCALING PRESSURIZED FLUIDIZED BEDS USING THE SIMPLIFIED SCALING PARAMETERS

This Section presents the results of tests conducted to evaluate the simplified scaling laws when scaling between a pilot scale hot *pressurized* CFB and a 1/2 scale cold model. The governing parameters for hydrodynamic similarity utilized were the simplified set of scaling laws derived earlier which were successful in matching hydrodynamics between two scaled cold beds with a length ratio of 1/4 and a large hot atmospheric CFB and a 1/16 scale model.

8.1 Introduction

A new set of simplified scaling laws has been successfully demonstrated for scaling atmospheric combustors. The new set of simplified scaling laws includes

(1) Froude number based on bed height
(2) Solid to gas density ratio
(3) Ratio of superficial to minimum fluidization velocity
(4) Bed geometric similarity
(5) Particle sphericity and size distribution
(6) Dimensionless solids flux (circulating beds)

When the gas to particle drag can be represented by the Ergun equation or similar expression, the new simplified scaling laws hold exactly in both the viscous dominated and gas inertial dominated limits. When the gas to particle drag is represented by the drag on an isolated particle, the simplified scaling laws also give the correct limiting conditions for both the viscous and inertial limits. For intermediate conditions the gas to particle drag is also well approximated in models using the simplified scaling laws.

The advantage of the simplified set of scaling parameters over the full set is the increased flexibility in the design of a model to simulate a combustor or chemical reactor. With the full set, after the gas properties in the model have been chosen, e.g. by use of air at ambient conditions, there is only one unique set of particle size and density, bed size, gas velocity and solids circulation rate which can be used in the model. Using the simplified set of scaling parameters, the choice of the fluidizing gas in the model fixes the solid density. However, the model size can be altered, as long as the Froude number is maintained constant by altering u_o. The particle size is then set to maintain u_o/u_{mf} constant. This flexibility allows a model to simulate much larger combustors or reactors than is possible with the full set of scaling relationships.

Table 8.1 presents the values of several important physical and hydrodynamic parameters when the simplified

scaling relationships are used to scale the Foster Wheeler[1] pilot pressurized circulating fluidized bed combustor. The last column in the Table also depicts the values of these parameters when the full or exact set of scaling parameters are used. In the Table, $\bar{\beta}$ represents the dimensionless interphase drag as determined from the Ergun equation and C_{Dcl} represents the drag on a cluster determined from drag over a solid sphere.

Table 8.1 indicates that if the interphase drag is best represented by the Ergun equation, the dimensionless drag coefficient will be 0.915 times that in the hot bed. If the drag is better represented by the drag on a single particle, the ratio of terminal to minimum fluidization velocity (or superficial velocity) is within 16 percent of the hot bed for a 1/2 scale model and within 33 percent for a 1/4 scale model. If particles in the upper portion of the bed act in clusters or groups, the cluster drag coefficient will be 4 percent lower in a 1/2 scale model and 19 percent larger in a 1/4 scale model (assuming that the cluster diameter scales as the bed diameter).

The small deviations in drag coefficients and terminal velocities when using the simplified scaling laws for a 1/2 scale model suggests that a 1/2 scale model should give acceptable similarity. In addition, the deviations in the hydrodynamic parameters for a 1/4 scale model do not appear to be terribly large. This indicates that a 1/4 scale model may also result in acceptable hydrodynamic similarity.

Table 8.1: Scaled Physical and Hydrodynamic Parameters

	Foster Wheeler Hot Bed	1/2 Scale Model	1/4 Scale Model	Scale Model Using Exact Scaling Laws
Bed Diameter, m	0.203	0.102	0.0508	0.274
Bed Height, m	10.5	5.26	2.63	14.2
d_p, microns	216.5	227.0	190.8	291.4
u_o, m/s	3.05	2.16	1.52	3.49
Bed Pressure, atm	14	1	1	1
u_{mf}, cm/s	1.47	1.04	0.74	1.71
Solid Density, kg/m^3	2564	709	709	709
$\frac{\bar{\beta}}{\bar{\beta}_{\text{hot bed}}}$ (Ergun Equation)	1	0.94	0.915	1
$(u_t/u_{mf})/(u_t/u_{mf})_{\text{hot bed}}$	1	1.19	1.32	1
$C_{Dcl}/C_{Dcl\ \text{hot bed}}$	1	0.96	1.19	1

[1]The numbers in this Table are based on data reported in - Robertson, A., et al., "Second Generation Pressurized Fluidized Bed Combustion Plant," work performed under DOE Contract DE-AC02-82CE40543, September, 1989.

In order to evaluate the validity of applying these scaling parameters to pressurized hot beds, solid fraction profiles, pressure probability density functions, and pressure power spectral densities were compared between the Foster Wheeler second generation pressurized circulating fluidized bed and a 1/2 scale cold model at four different operating conditions. Table 8.2 presents a test matrix for evaluation of the simplified set of scaling parameters. Tables 8.3 provides the operational data, along with information concerning the particles and beds utilized in the simplified scaling analysis.

Solid fraction discussed in this paper is based on differential pressure measurements as discussed in Section 4.0. Since solid fraction estimations only include gravity effects, this interpretation neglects particle acceleration and shear stress at the column walls. The differential pressure measurement yields an apparent solid fraction. However, it should be noted that the dimensionless pressure gradient in the combustor and cold bed should be similar if properly scaled regardless of whether the measurements represent a true measure of the average cross-sectional solid fraction.

Histograms of the solid fraction data were created for both the hot and cold bed data to assess whether pressure fluctuation amplitudes of the scaled beds were similar. In addition, fast fourier transforms (FFT's) of the pressure fluctuation data were computed to determine the similarity of pressure fluctuation frequencies in the scaled beds. The power spectral densities (PSD) were determined using the algorithm outlined by Press *et al.* (1992). PSD's were based on eight Welch-windowed 256-point overlapping data segments.

Table 8.2

Test Matrix - Pressurized Hot Bed Scaling Using the Simplified Scaling Laws

Parameter	Full Scale Hot Bed	1/2 Scale Cold Bed
Particle Diameter (microns)	d_p	$1.05d_p$
u_{mf}	u_{mf}	$0.71u_{mf}$
Bed Diameter	D	0.5D
u_o/u_{mf}	100-500	Same
u_o^2/gL	Fr	Same
$Re = \frac{\rho_f u_o d_p}{\mu_f}$	$\frac{\rho_f u_o d_p}{\mu_f}$	$\frac{0.47\rho_f u_o d_p}{\mu_f}$
$\frac{\rho_s}{\rho_f}$	$\frac{\rho_s}{\rho_f}$	Same
$M = \frac{G_s}{u_o \rho_s}$	M	Same

Table 8.3: Foster Wheeler PCFBC and Cold Bed Operating Conditions

Operating Conditions								
Test	Condition 1		Condition 2		Condtion 3		Condition 4	
Bed	Hot	Cold	Hot	Cold	Hot	Cold	Hot	Cold
u_o - primary zone (m/s)	1.49	1.05	1.71	1.21	1.31	0.926	1.19	0.84
u_o - secondary zone (m/s)	2.74	1.93	2.96	2.09	2.83	2.00	2.77	1.96
System Pressure (bar)	11.7	1.00	13.0	1.00	12.4	1.00	13.0	1.00
G_s (kg/m^2s)	115	27.8	124	30.1	111	26.9	25.8	6.27
% Primary Air	54.0	54.0	58.0	58.0	46.2	46.2	42.0	42.0
ρ_s/ρ_f	758	758	681	758	718	758	688	758
u_o/u_{mf}	113	107	124	118	118	113	116	111
Fr_D	3.66	3.62	4.40	4.38	4.02	4.01	3.85	3.85
$G_s/\rho_s u_o$	0.016	0.016	0.016	0.016	0.015	0.015	0.0035	0.0035
Re_{dp}	35.3	22.2	43.2	24.4	39.2	23.4	40.0	22.9

8.2 Solid Fraction Profiles

The average solid fraction profile comparisons between the 1/2 scale cold model and the Foster Wheeler combustor are given in Figures 8.1 through 8.4. The tabulated data is given in Appendix H. The calculated solid fractions are plotted versus the average of the heights of the associated pressure taps in each bed. As discussed in Section 4, error bars are based on calculated standard deviations in solid flow measurements and pressure time traces.

8.3 Histograms

Probability density functions for the solid fractions in the hot and cold beds are given in figures 8.5 through 8.28. In these plots, probability is plotted versus the solid fraction.

8.4 Power Spectral Densities

FFT's of the pressure fluctuation data for the hot and cold beds are given in Figures 8.29 through 8.52. In these plots, the fourier transform is plotted versus the equivalent Foster Wheeler hot bed frequency in Hz.

Figure 8.1

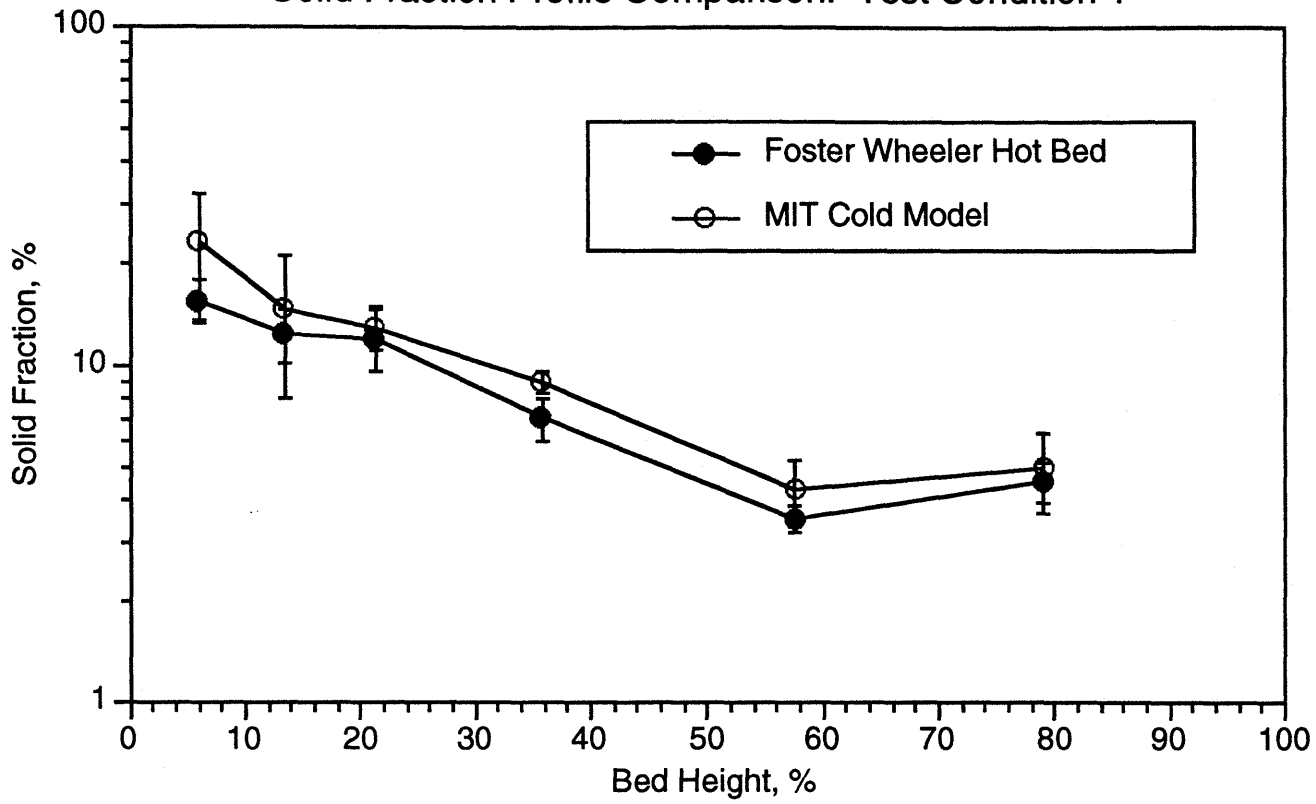

Figure 8.2

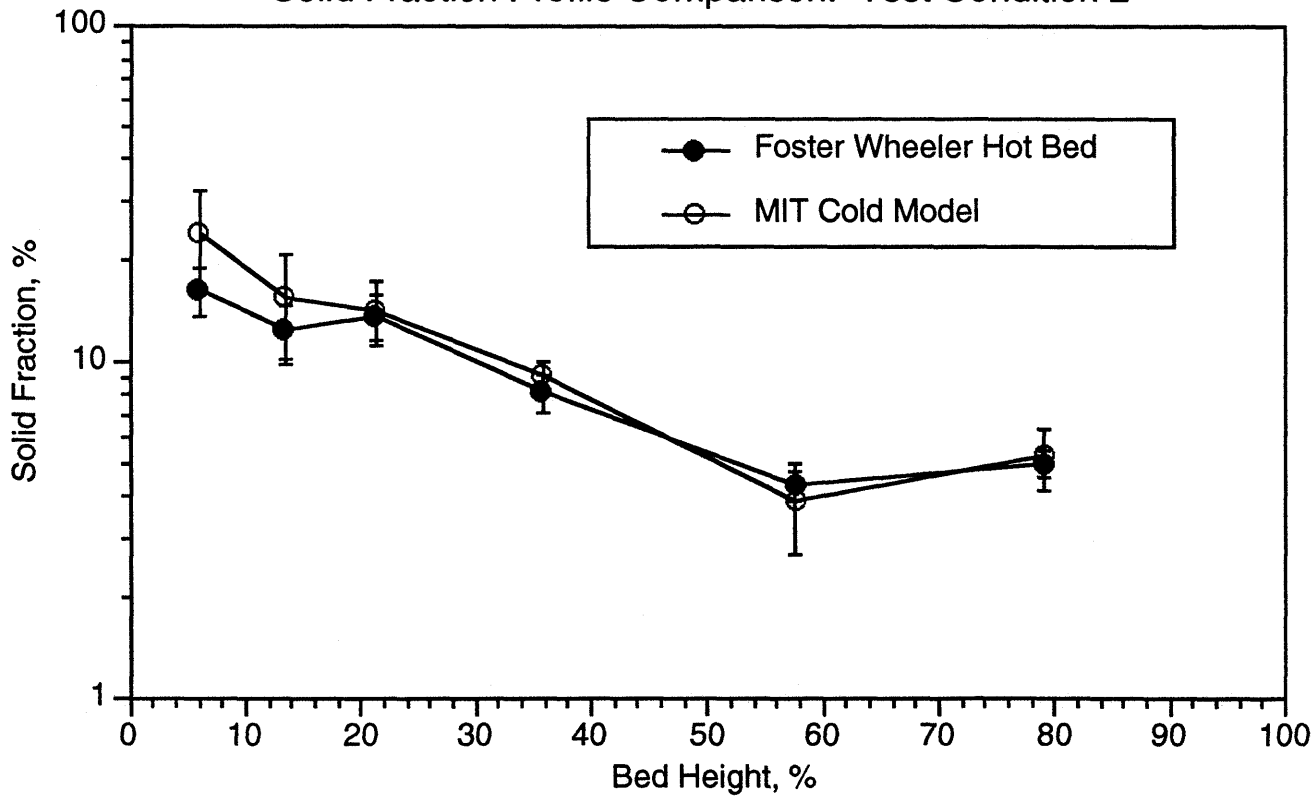

Figure 8.3

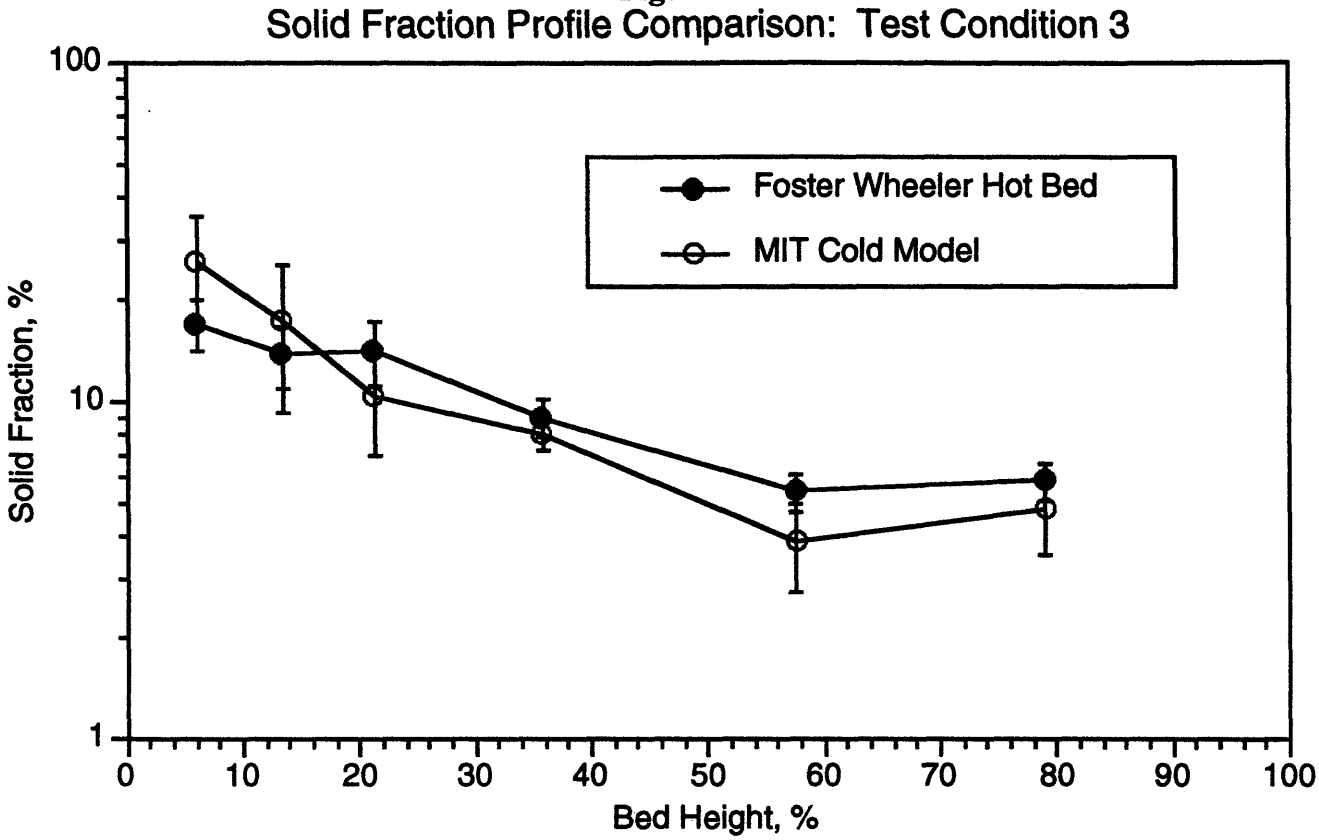

Figure 8.4

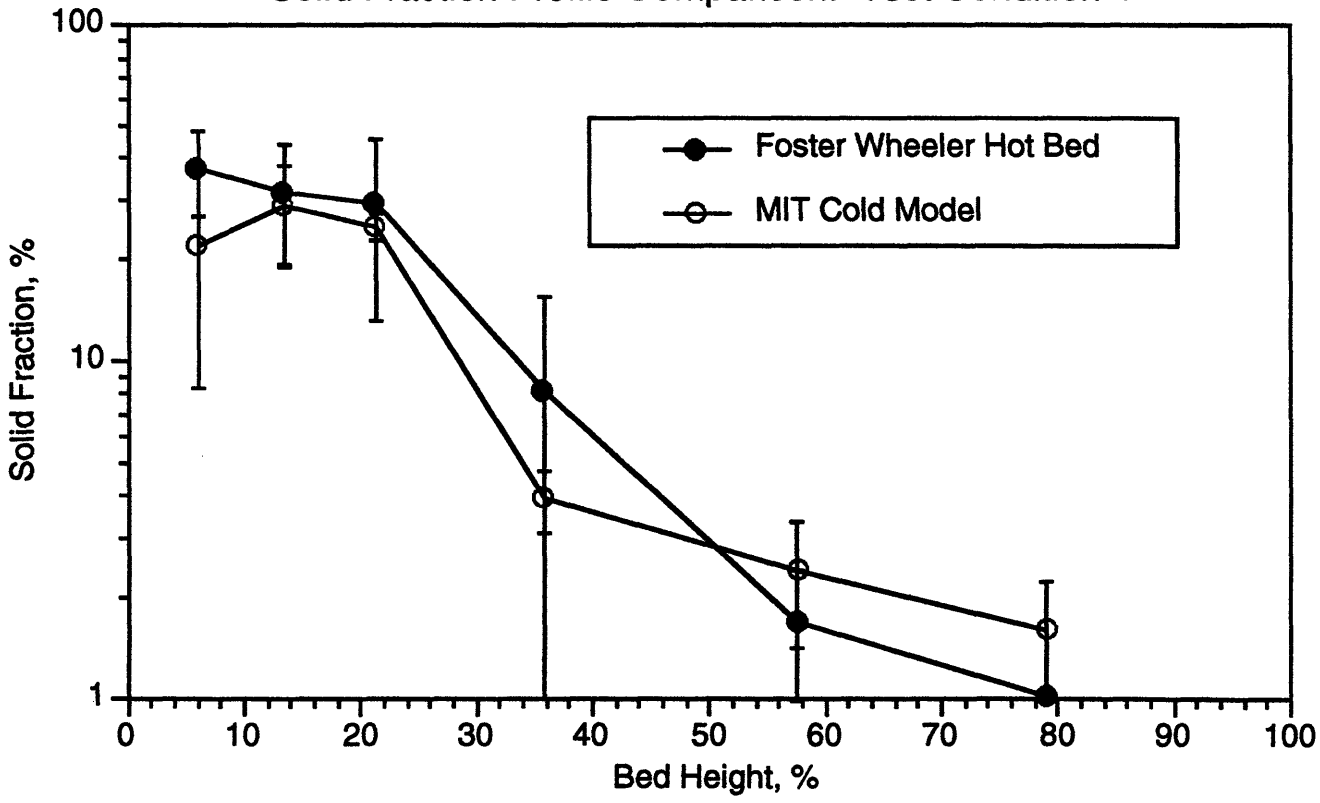

Figure 8.5

Histograms: Test Condition 1, Dimensionless Distance up Bed (x/H) = 0.06

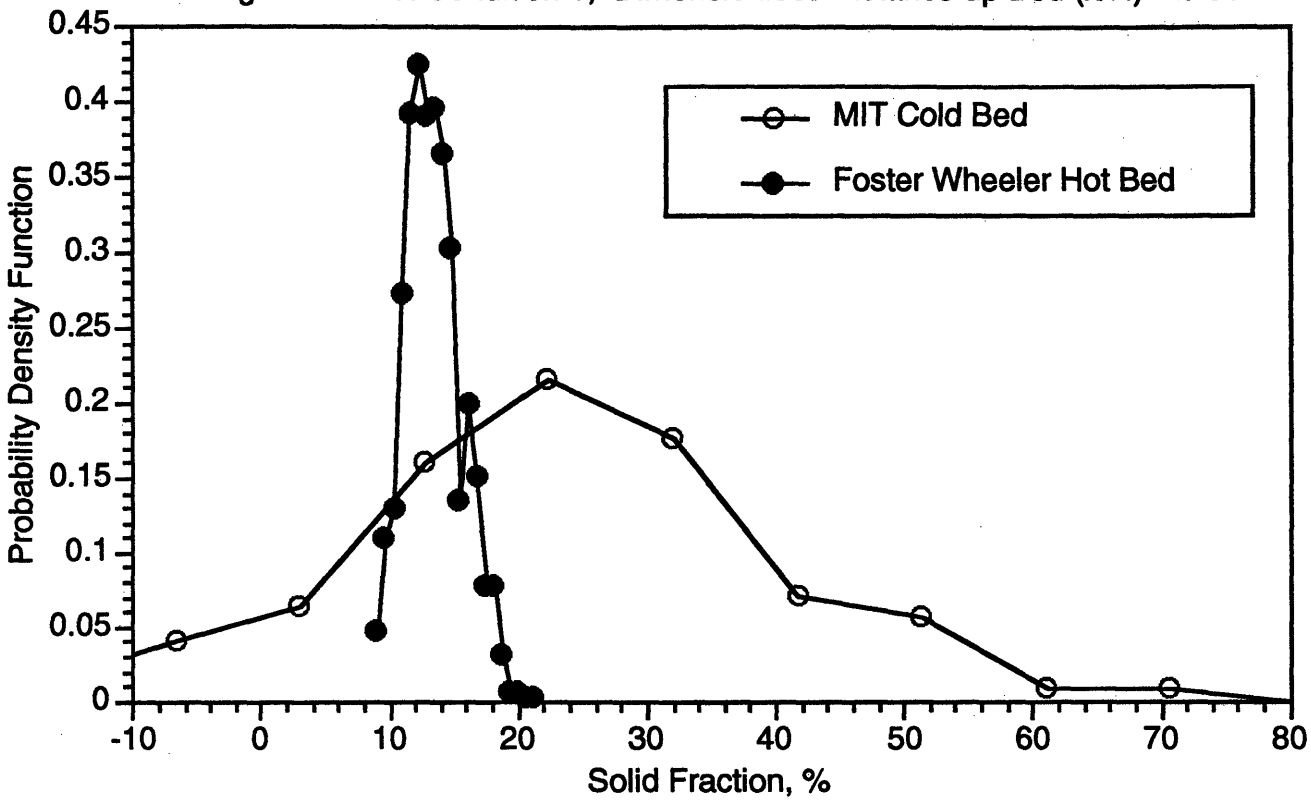

Figure 8.6

Histograms: Test Condition 1, Dimensionless Distance up Bed (x/H) = 0.13

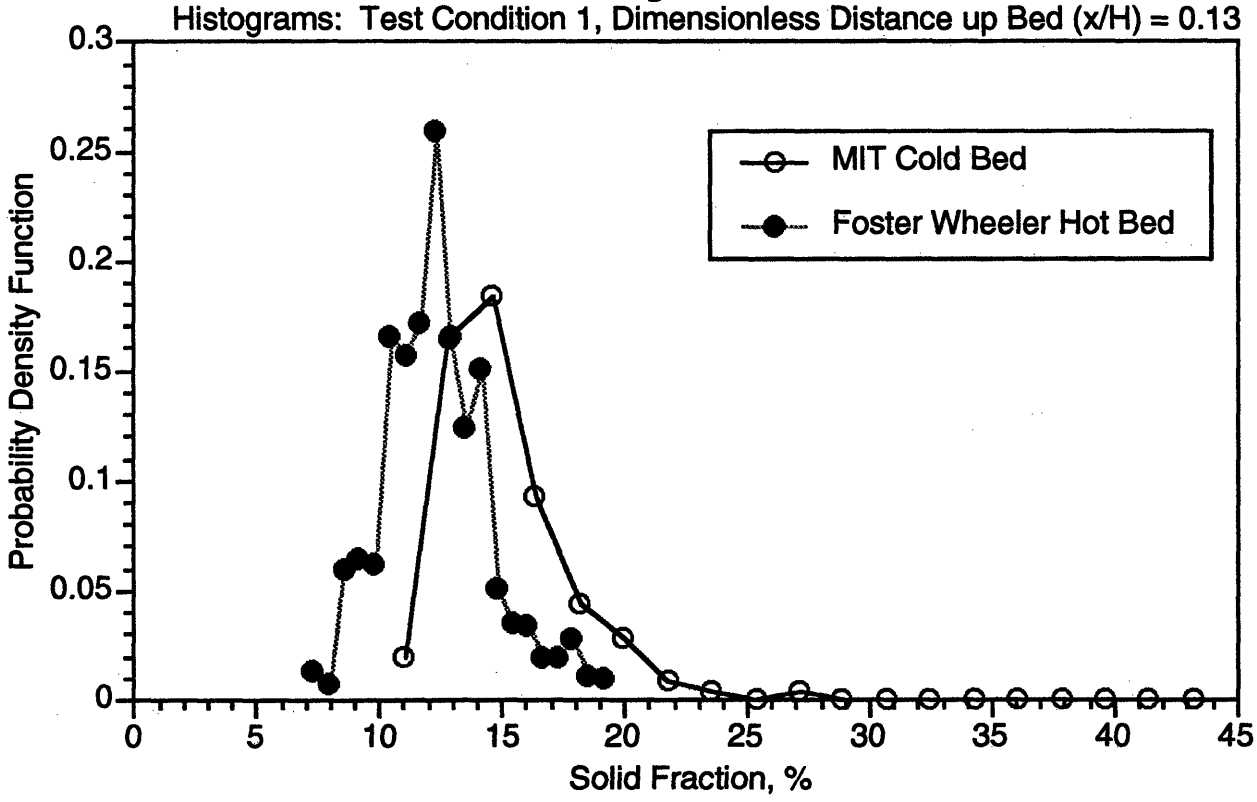

Figure 8.7

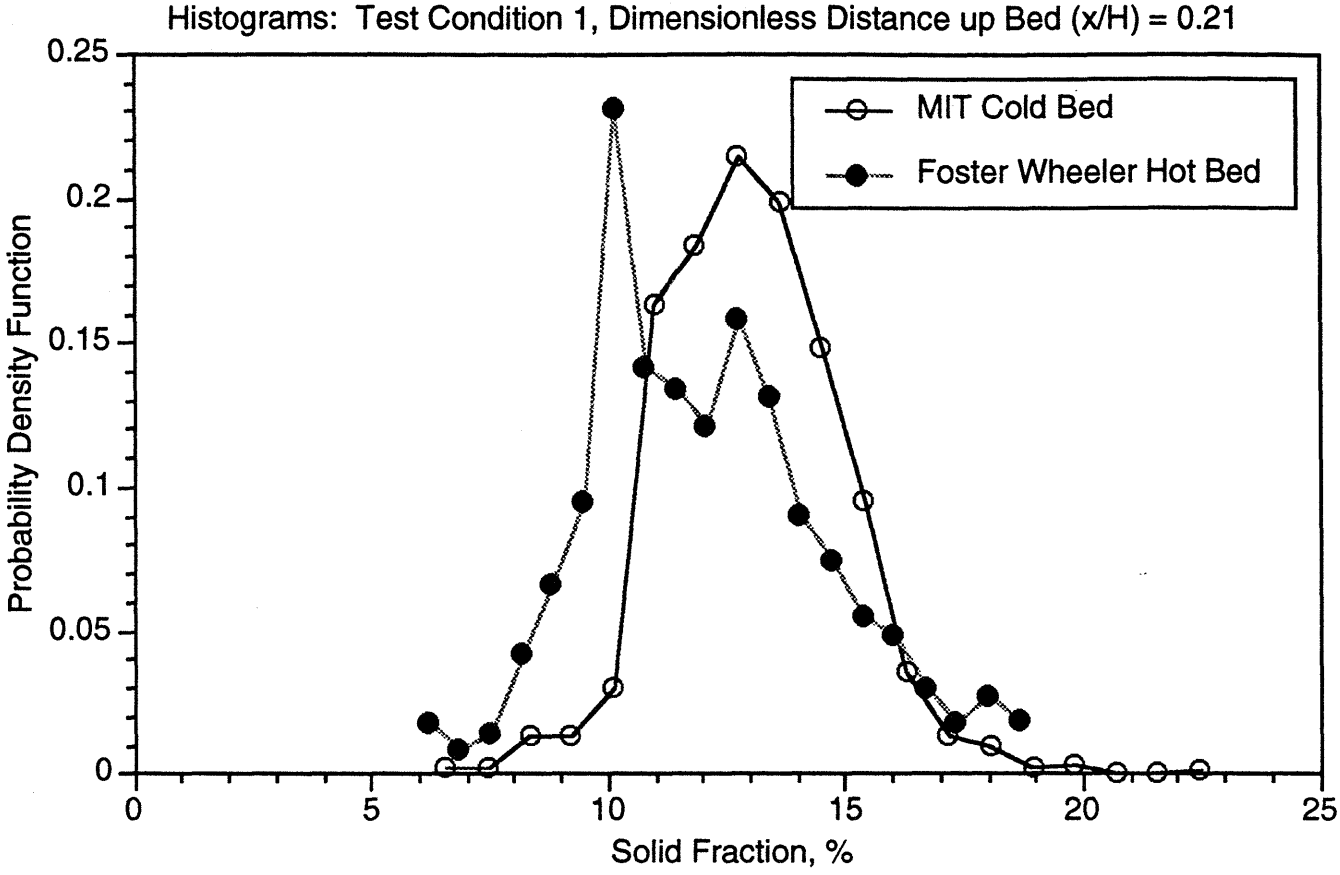
Histograms: Test Condition 1, Dimensionless Distance up Bed (x/H) = 0.21
MIT Cold Bed
Foster Wheeler Hot Bed
Probability Density Function
Solid Fraction, %
0.25
0.2
0.15
0.1
0.05
0
0
5
10
15
20
25

Figure 8.8

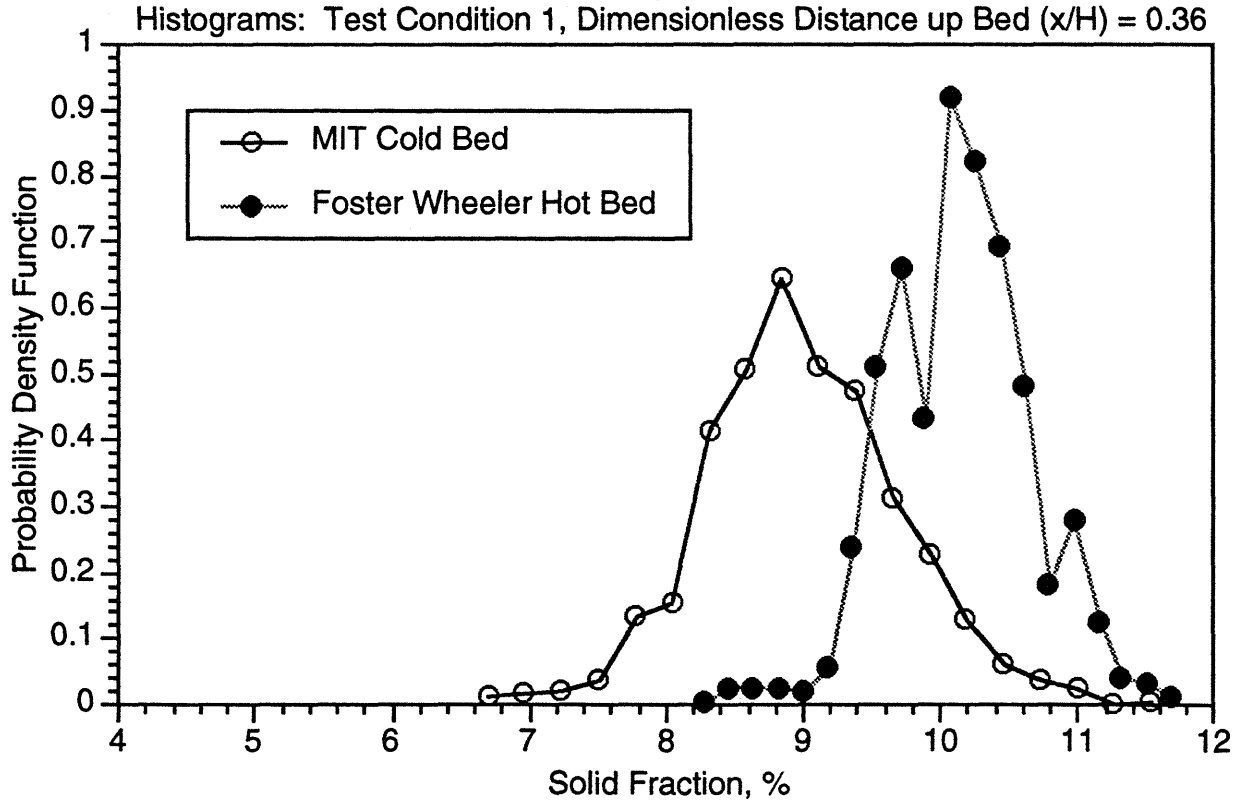
Histograms: Test Condition 1, Dimensionless Distance up Bed (x/H) = 0.36
MIT Cold Bed
Foster Wheeler Hot Bed
Probability Density Function
Solid Fraction, %
1
0.9
0.8
0.7
0.6
0.5
0.4
0.3
0.2
0.1
0
4
5
6
7
8
9
10
11
12

Figure 8.9

Histograms: Test Condition 1, Dimensionless Distance up Bed (x/H) = 0.57

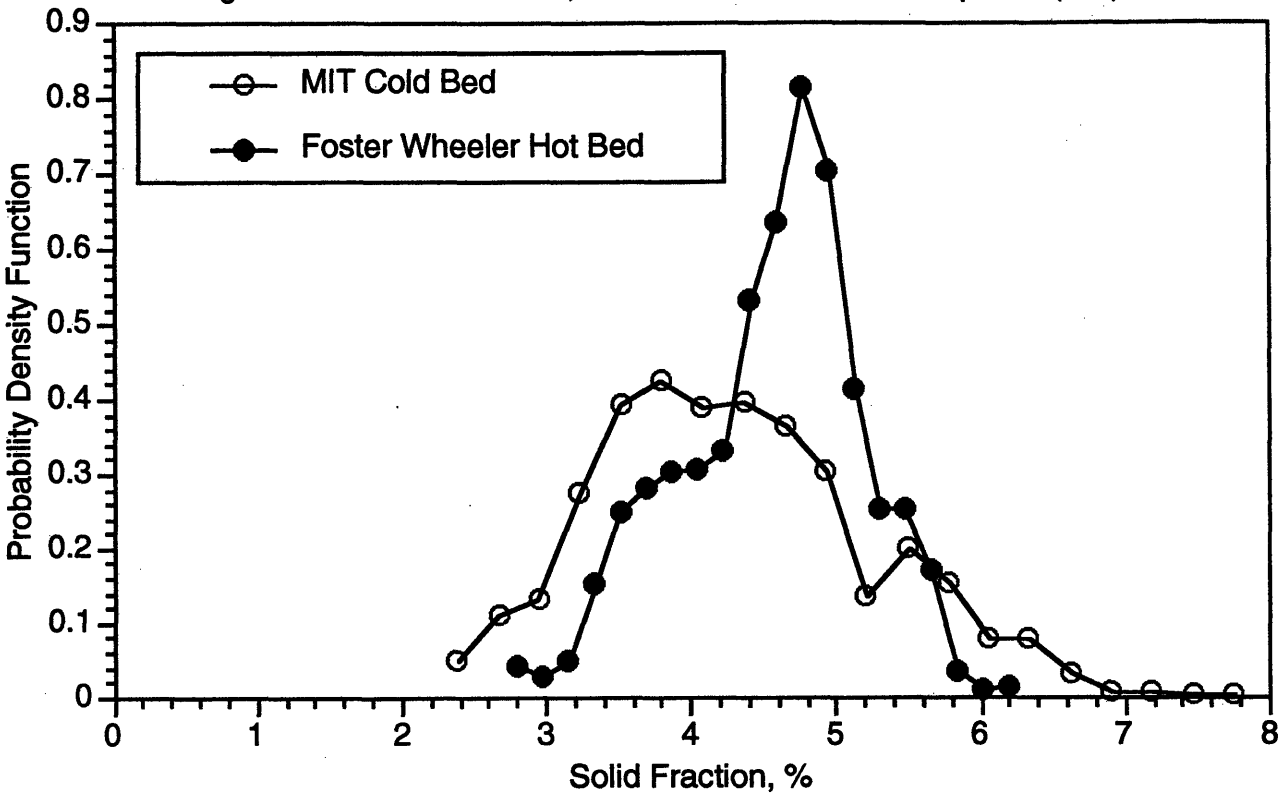

Figure 8.10

Histograms: Test Condition 1, Dimensionless Distance up Bed (x/H) = 0.80

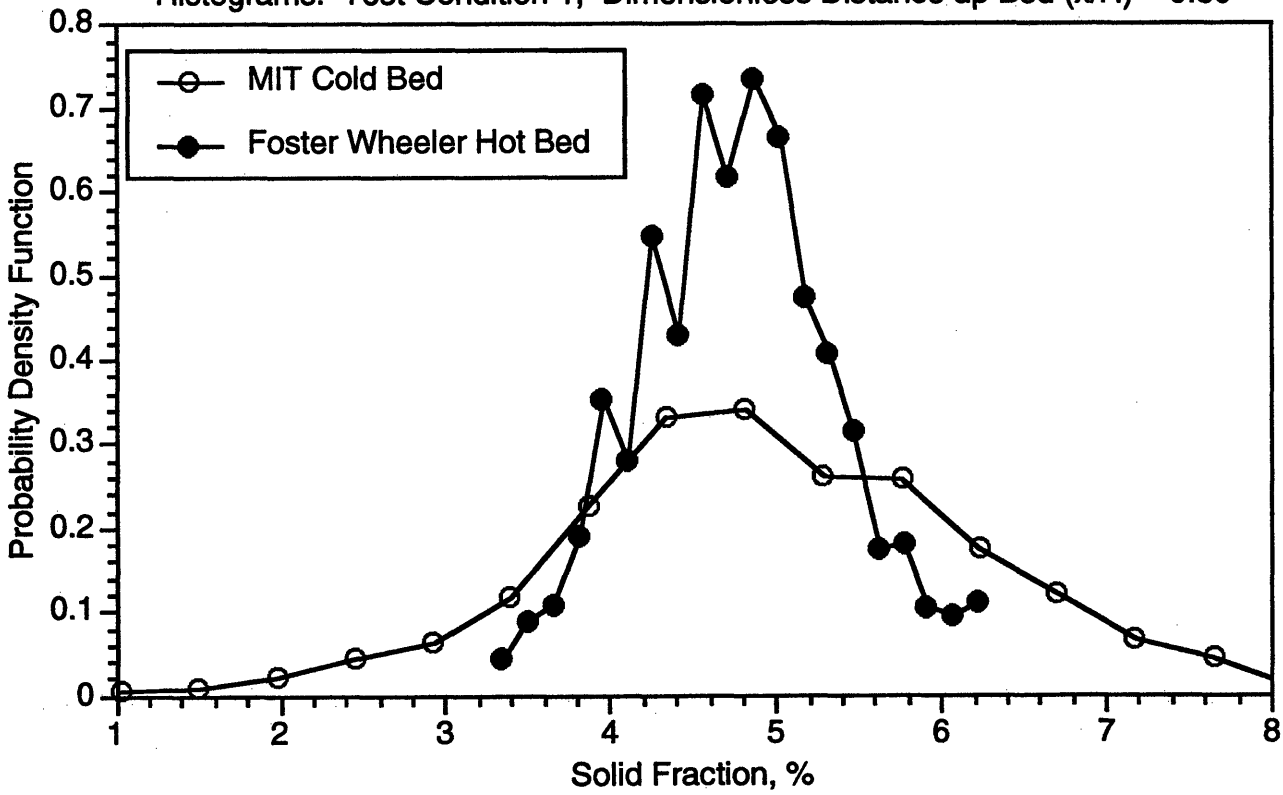

Figure 8.11

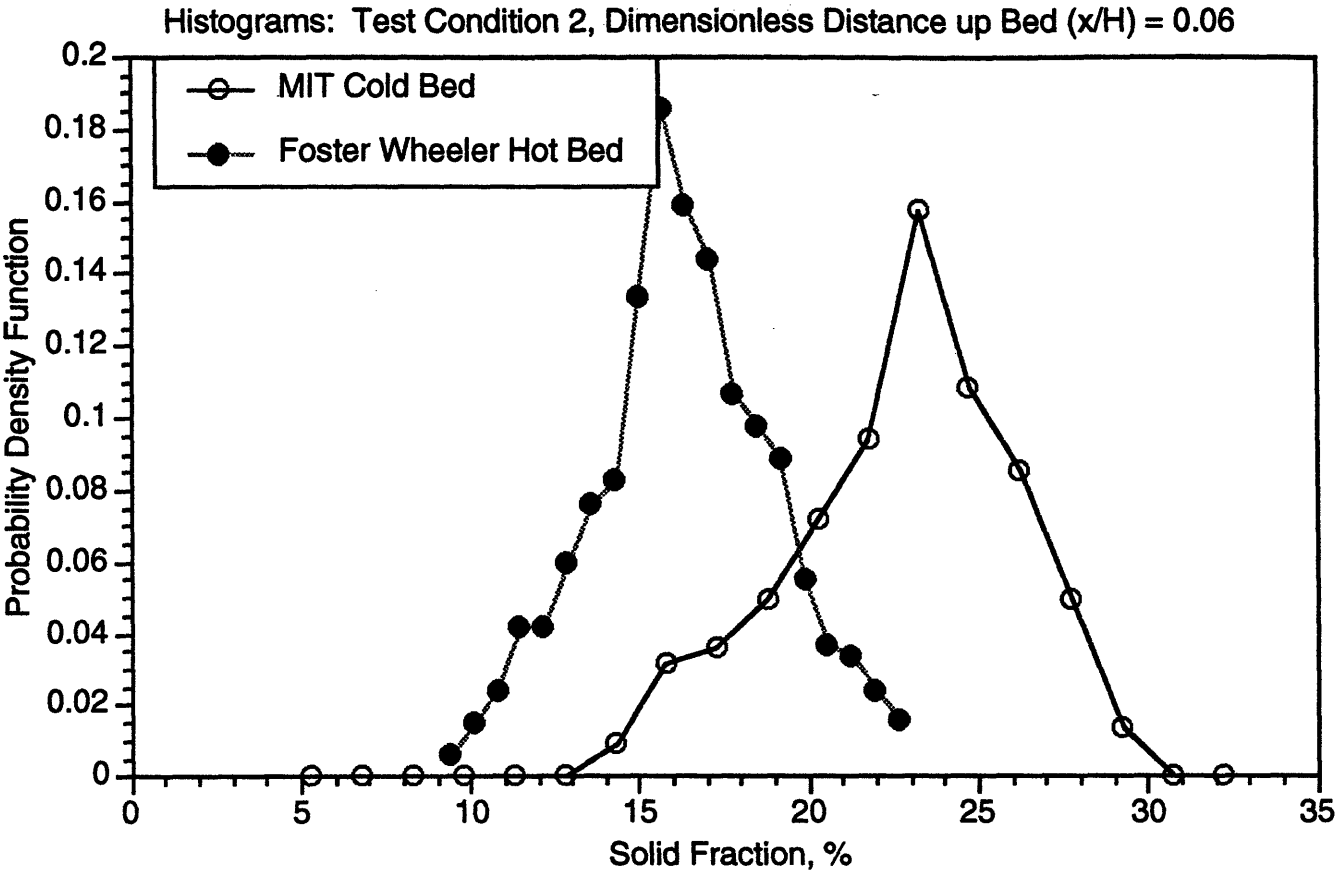

Figure 8.12

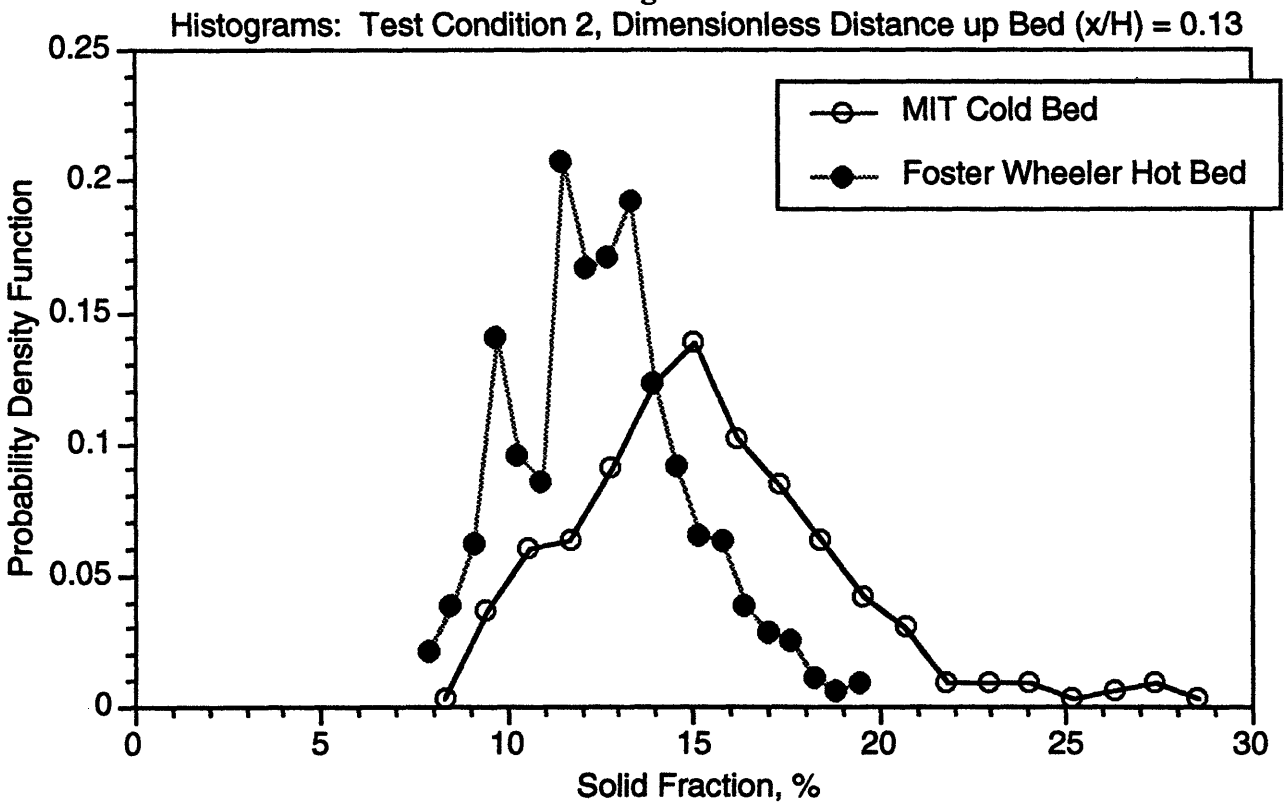

Figure 8.13

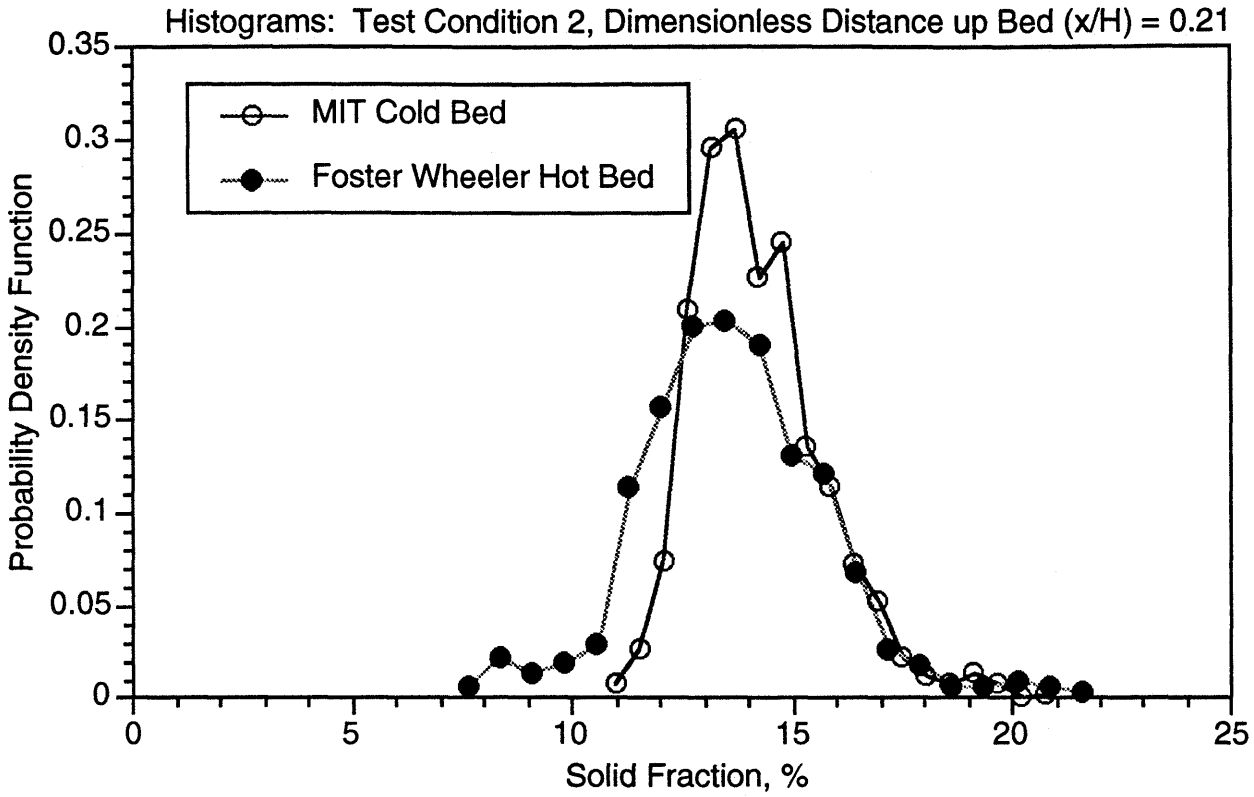

Figure 8.14

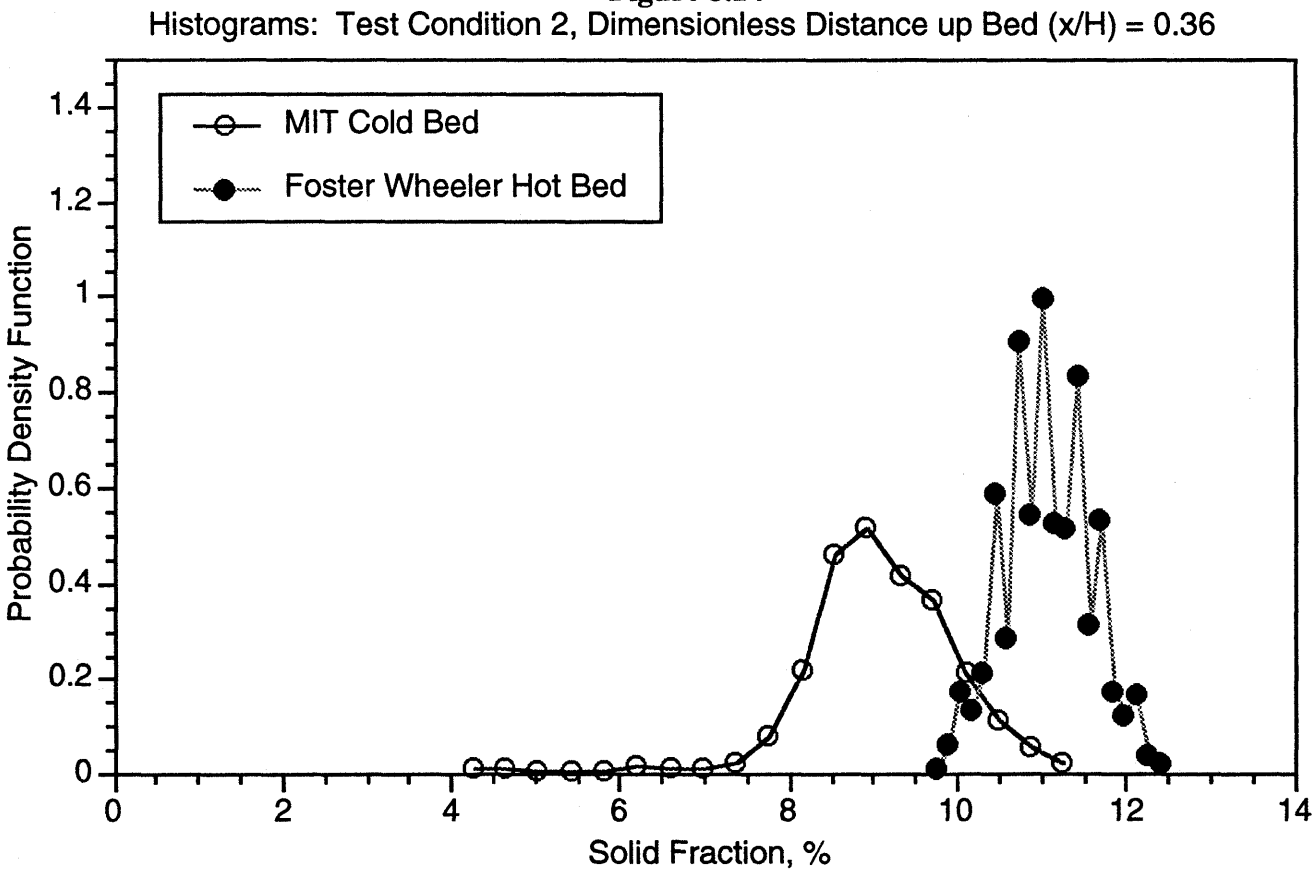

Figure 8.15

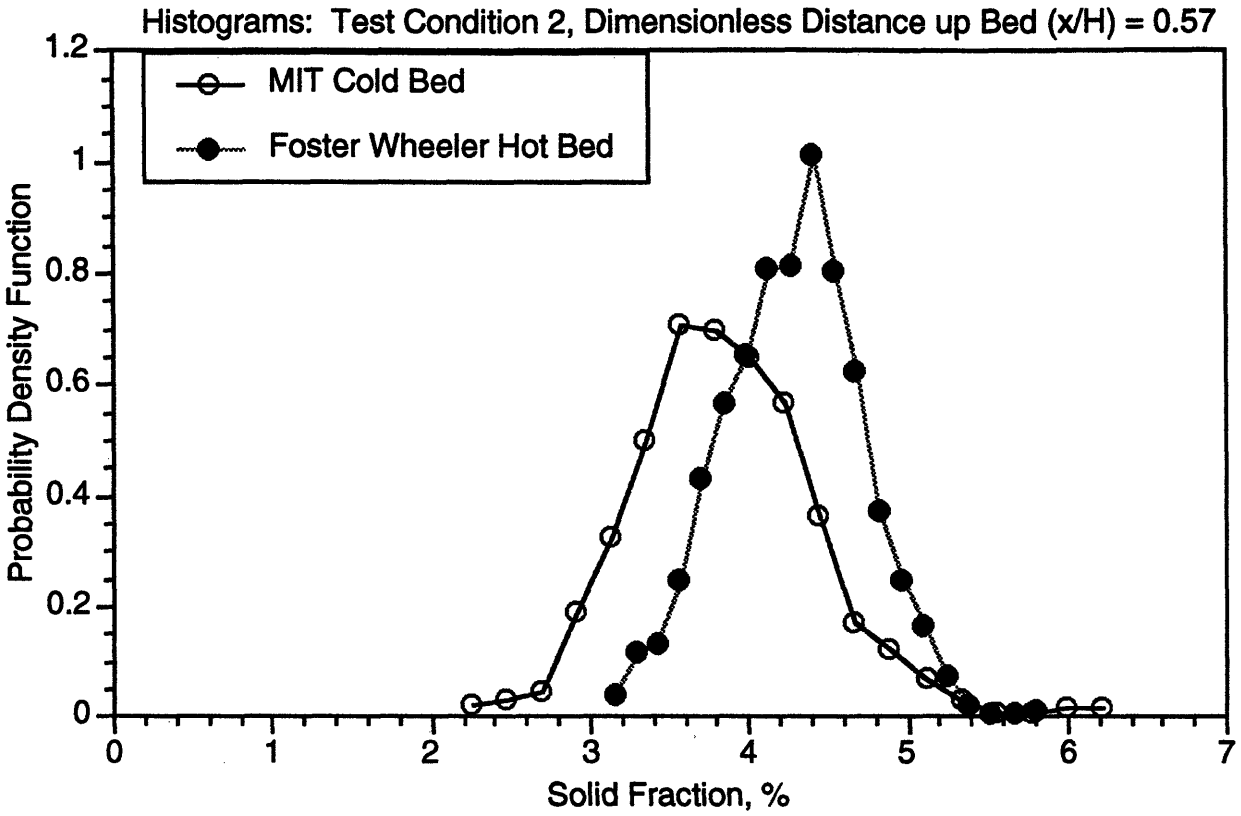
Histograms: Test Condition 2, Dimensionless Distance up Bed (x/H) = 0.57
MIT Cold Bed
Foster Wheeler Hot Bed
Probability Density Function
Solid Fraction, %
0
0.2
0.4
0.6
0.8
1
1.2
0
1
2
3
4
5
6
7

Figure 8.16

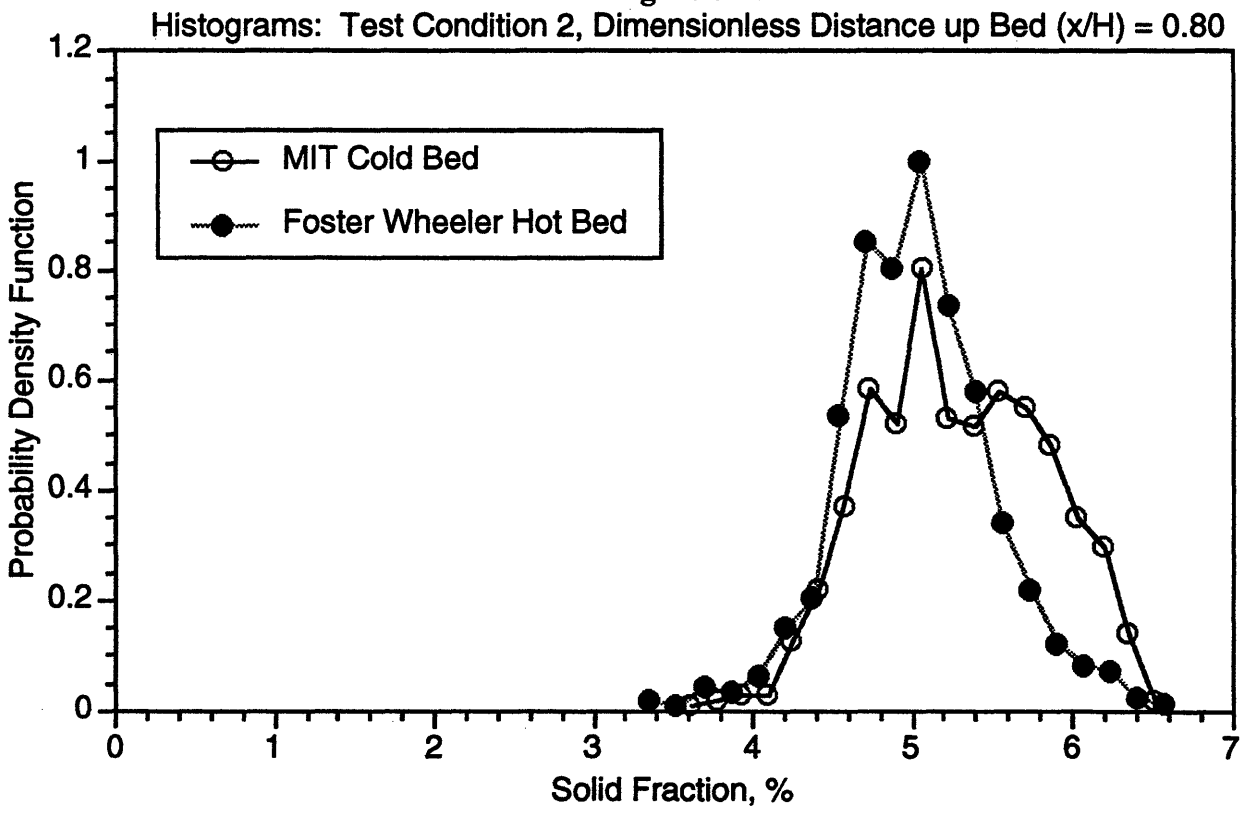
Histograms: Test Condition 2, Dimensionless Distance up Bed (x/H) = 0.80
MIT Cold Bed
Foster Wheeler Hot Bed
Probability Density Function
Solid Fraction, %
0
0.2
0.4
0.6
0.8
1
1.2
0
1
2
3
4
5
6
7

Figure 8.17

Histograms: Test Condition 3, Dimensionless Distance up Bed (x/H) = 0.06

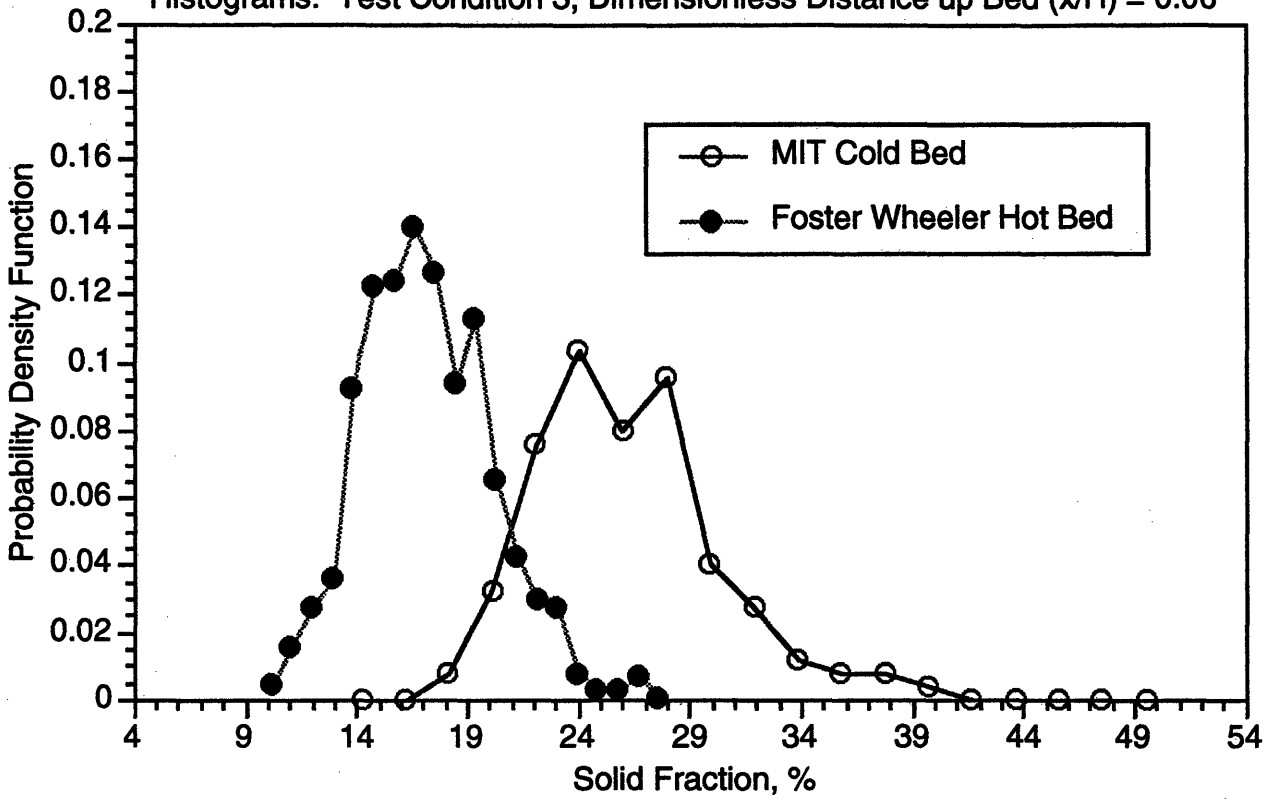

Figure 8.18

Histograms: Test Condition 3, Dimensionless Distance up Bed (x/H) = 0.13

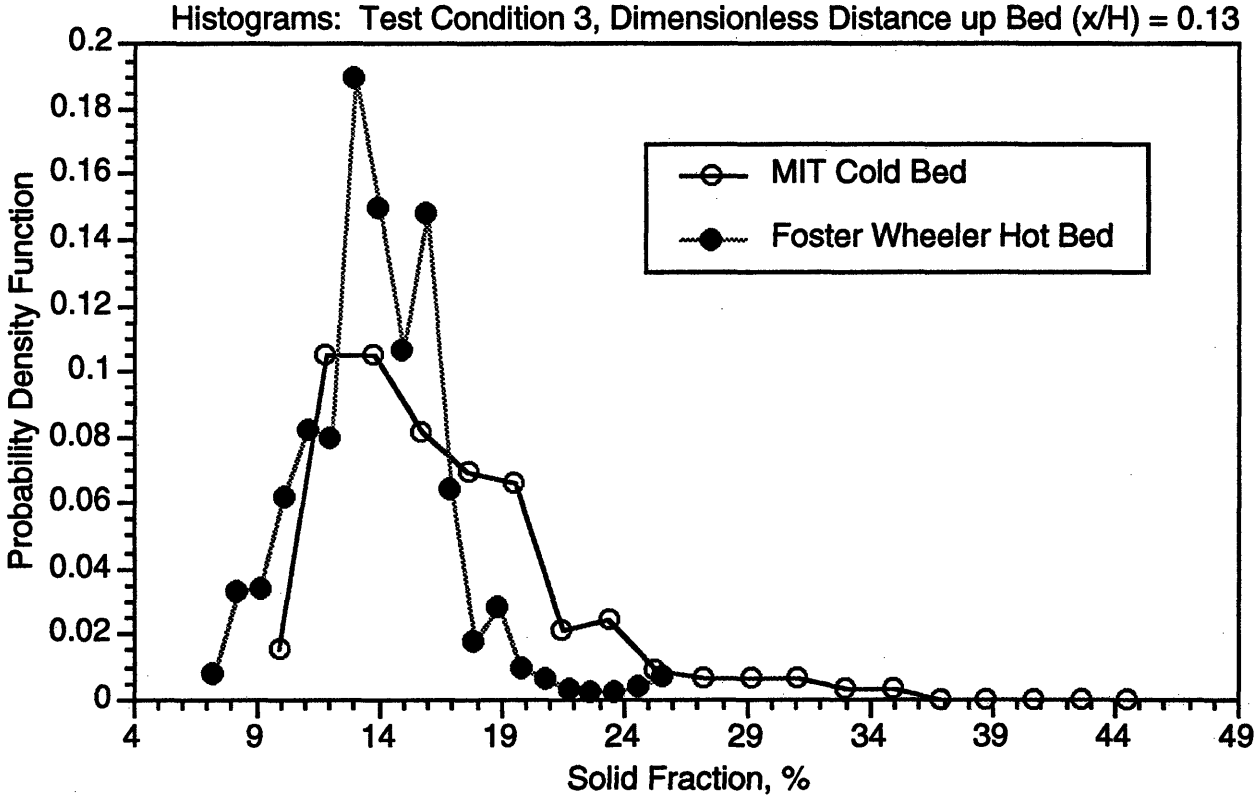

Figure 8.19

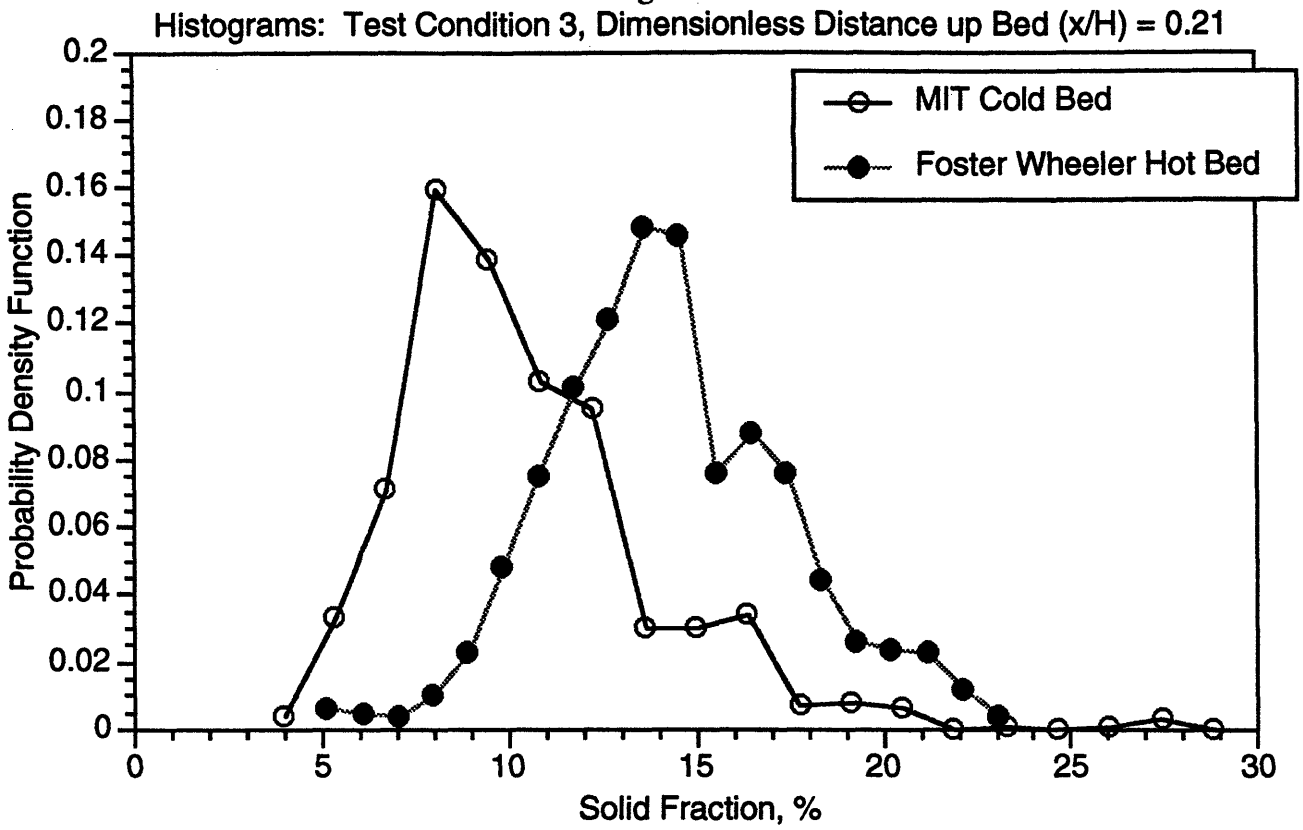

Figure 8.20

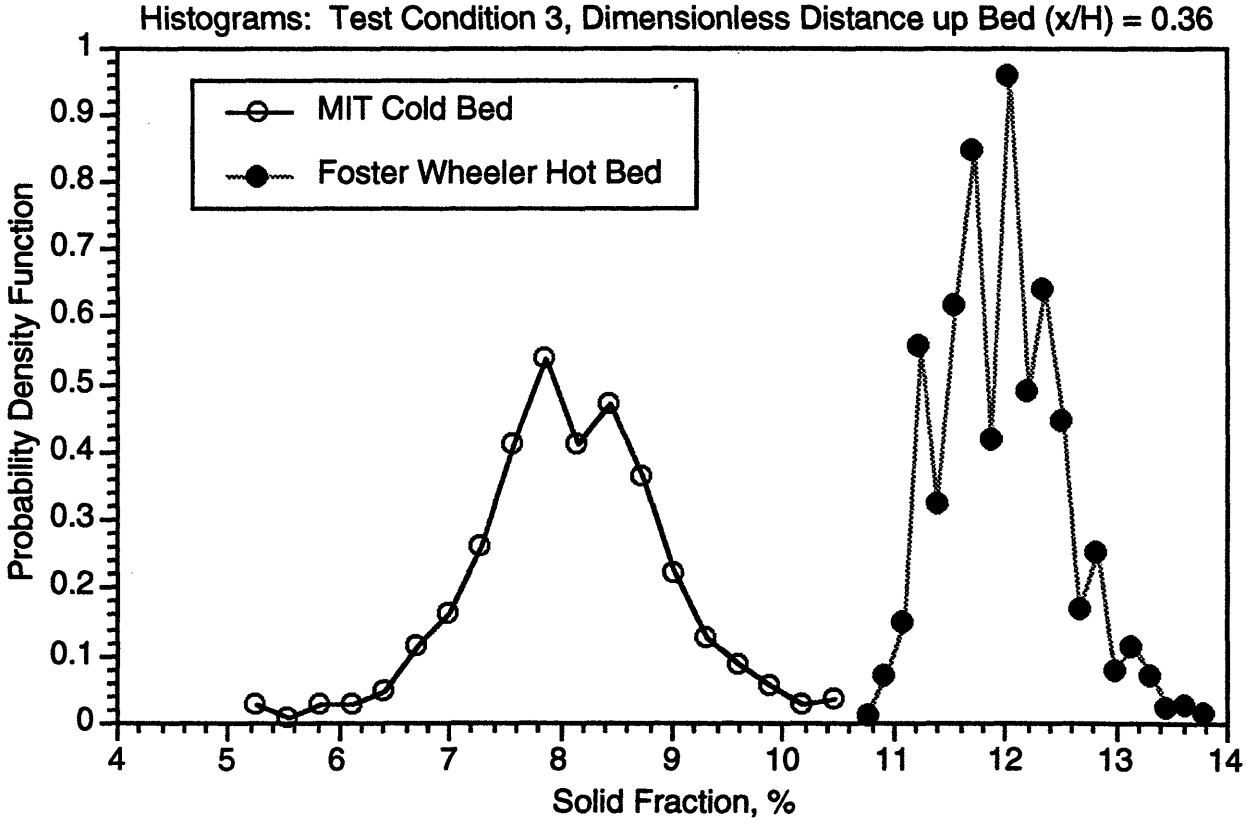

Figure 8.21

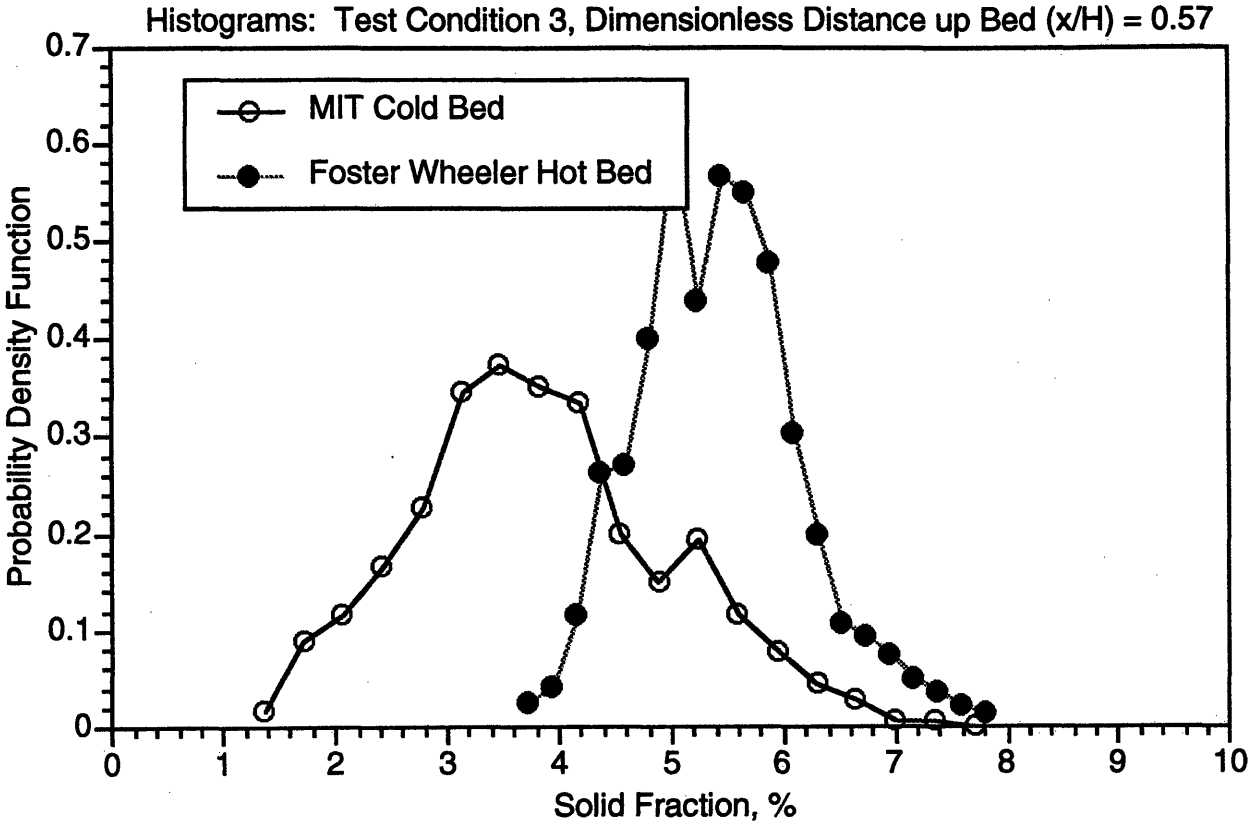

Figure 8.22

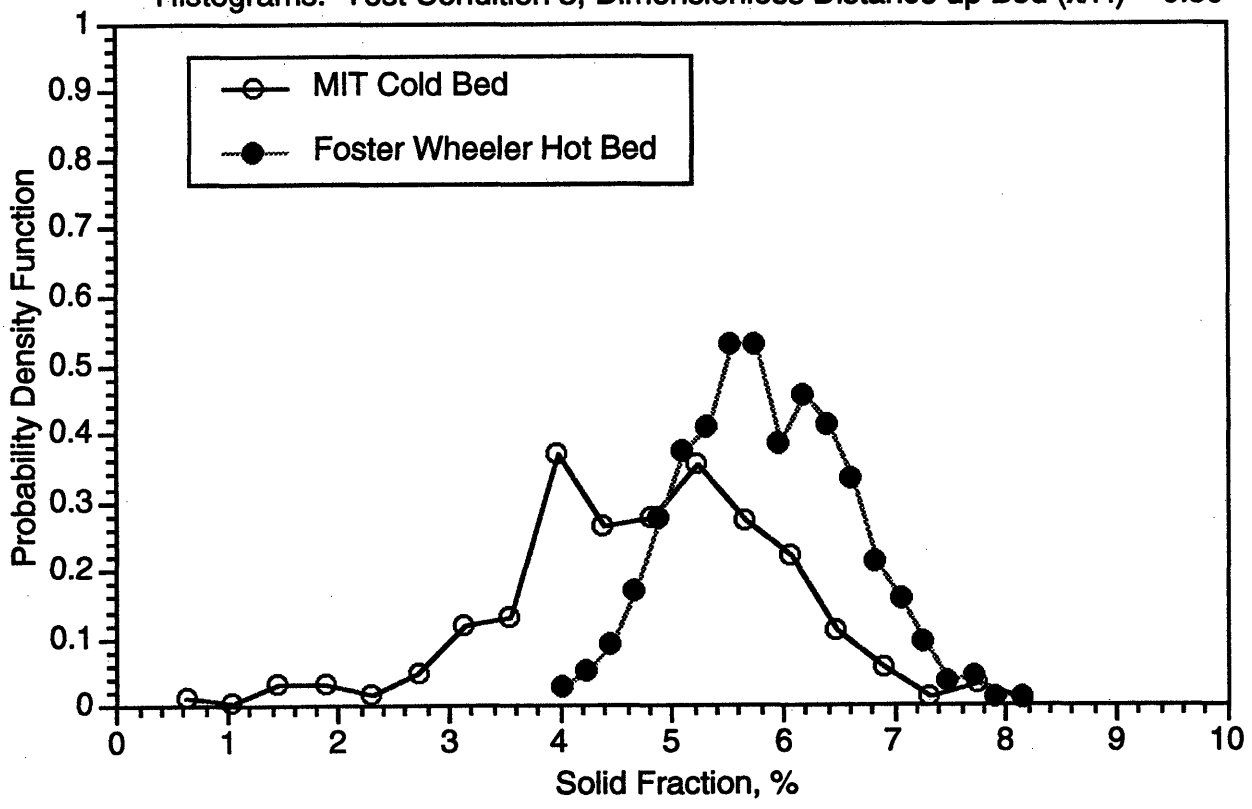

Figure 8.23

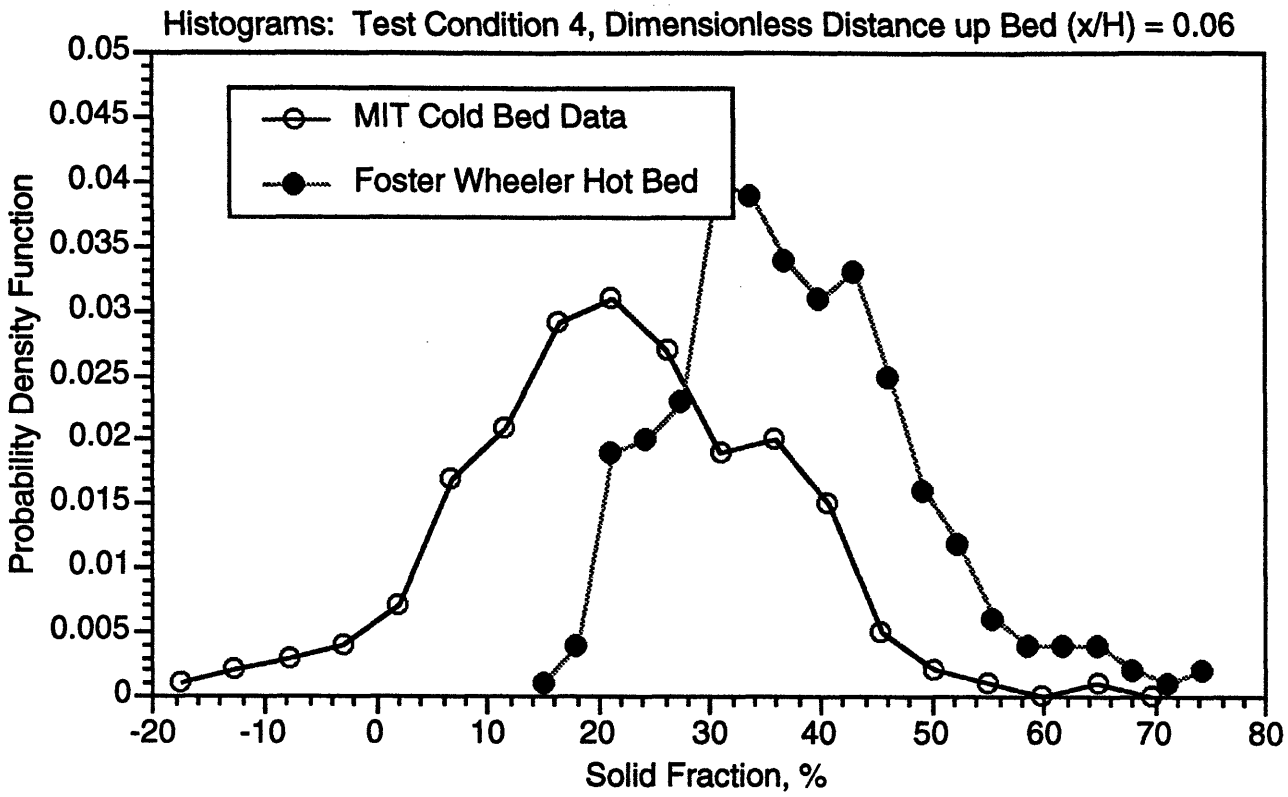

Figure 8.24

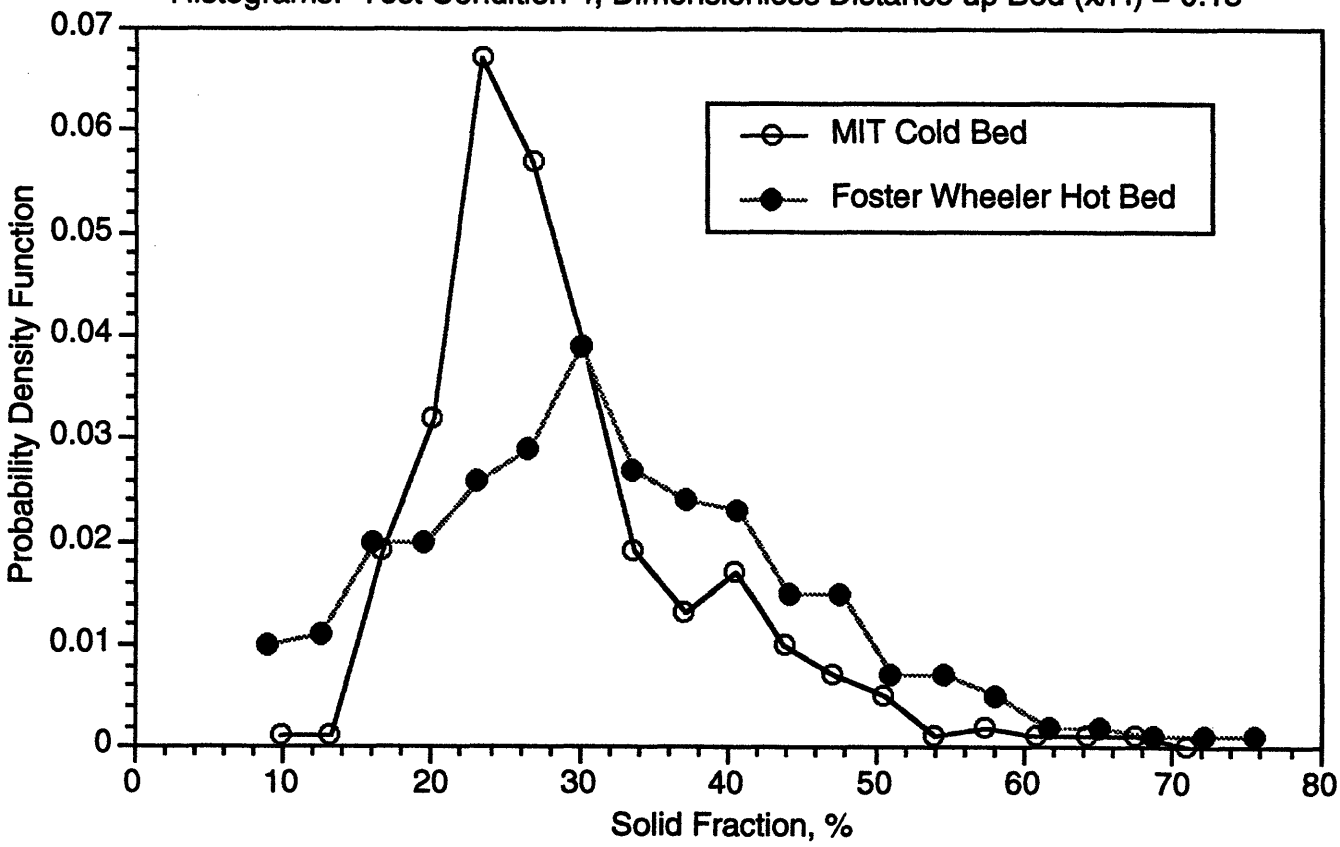

Figure 8.25

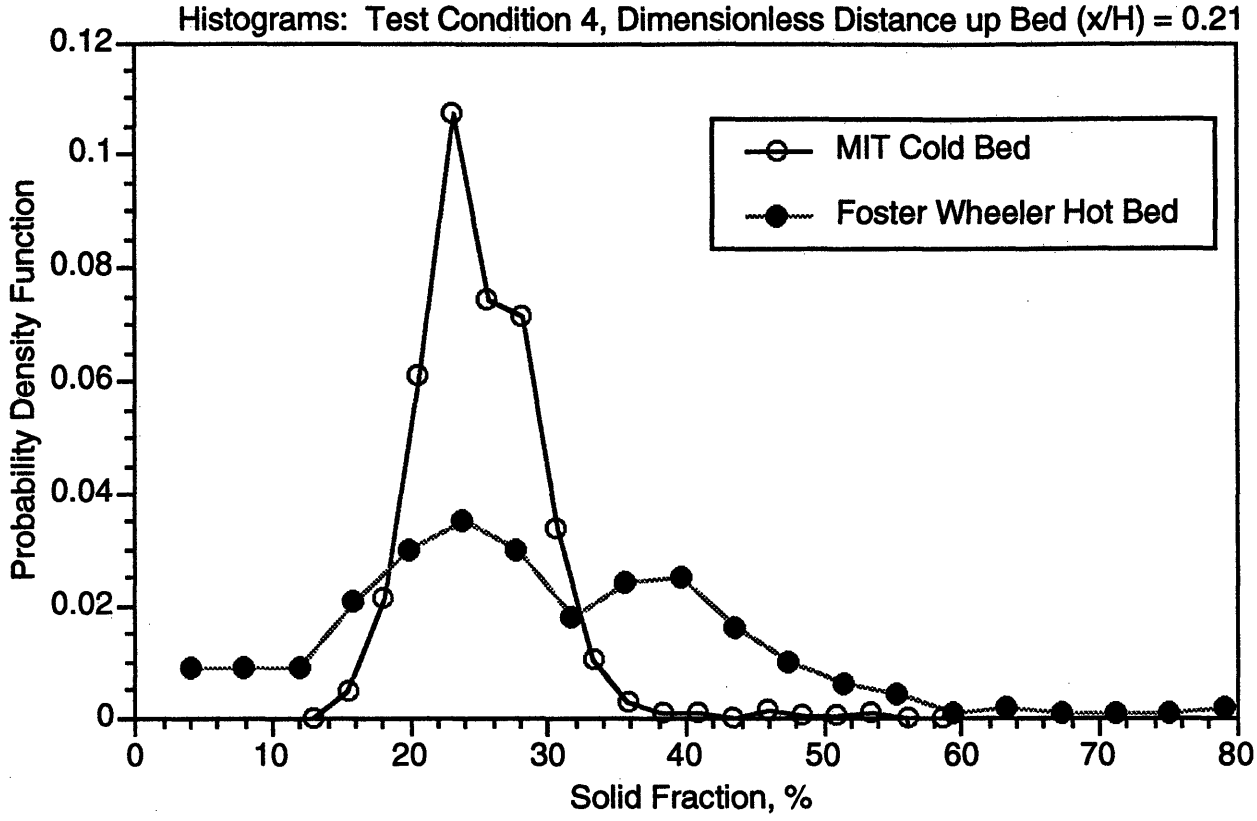
Histograms: Test Condition 4, Dimensionless Distance up Bed (x/H) = 0.21
Probability Density Function
Solid Fraction, %
MIT Cold Bed
Foster Wheeler Hot Bed
0.12
0.1
0.08
0.06
0.04
0.02
0
0
10
20
30
40
50
60
70
80

Figure 8.26

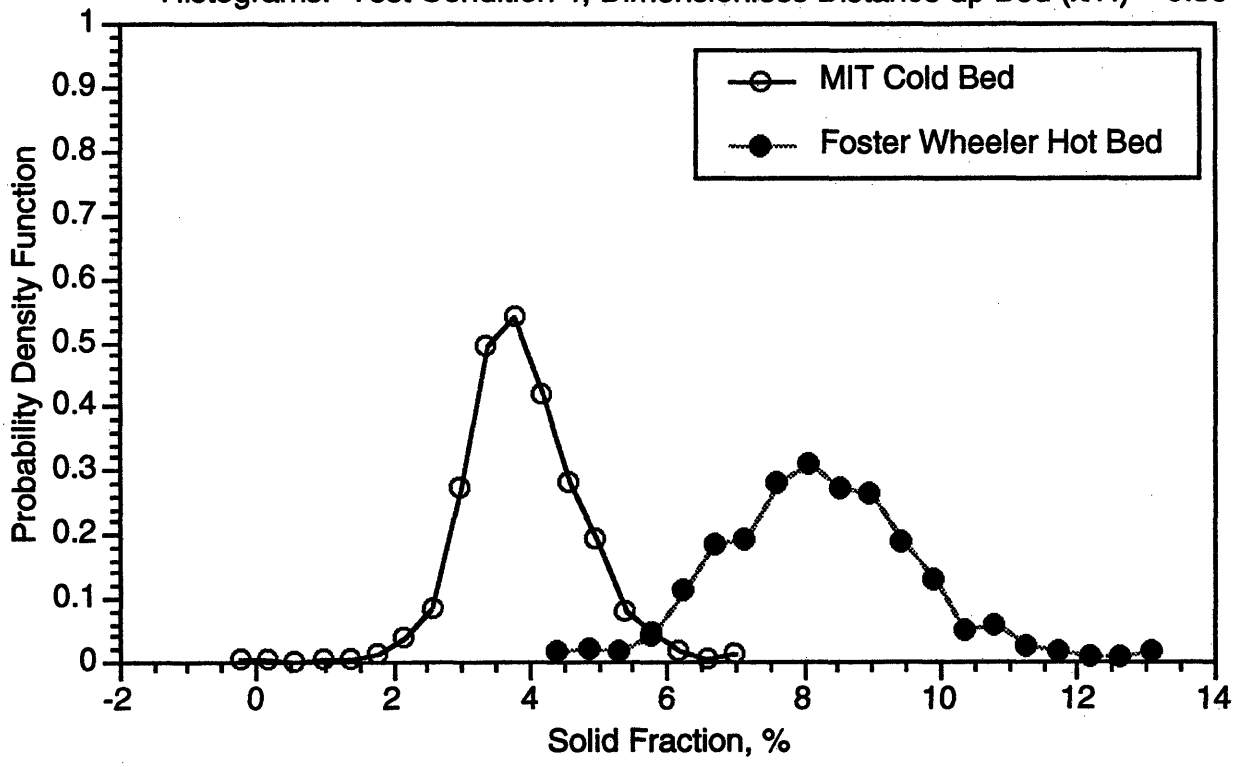
Histograms: Test Condition 4, Dimensionless Distance up Bed (x/H) = 0.36
Probability Density Function
Solid Fraction, %
MIT Cold Bed
Foster Wheeler Hot Bed
1
0.9
0.8
0.7
0.6
0.5
0.4
0.3
0.2
0.1
0
-2
0
2
4
6
8
10
12
14

Figure 8.27

Histograms: Test Condition 4, Dimensionless Distance up Bed (x/H) = 0.57

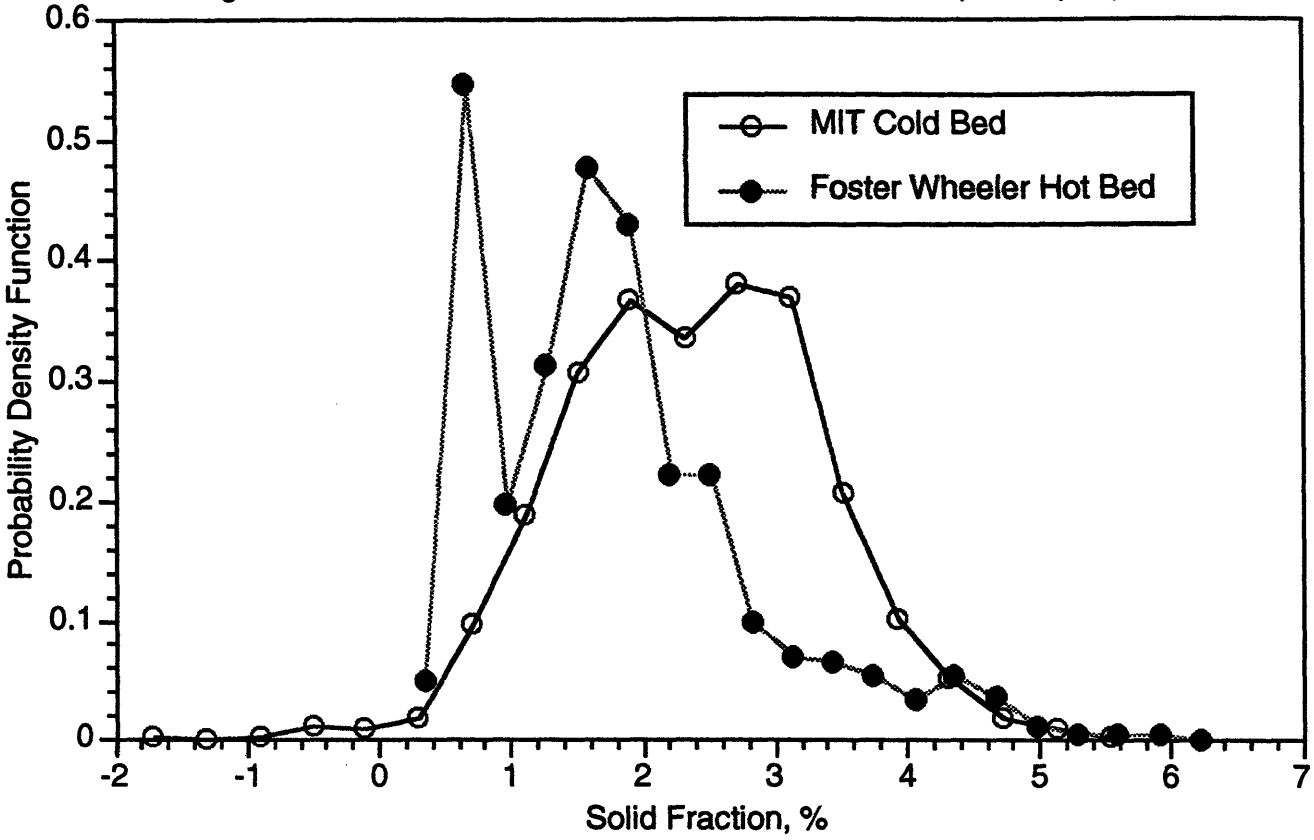

Figure 8.28

Histograms: Test Condition 4, Dimensionless Distance up Bed (x/H) = 0.80

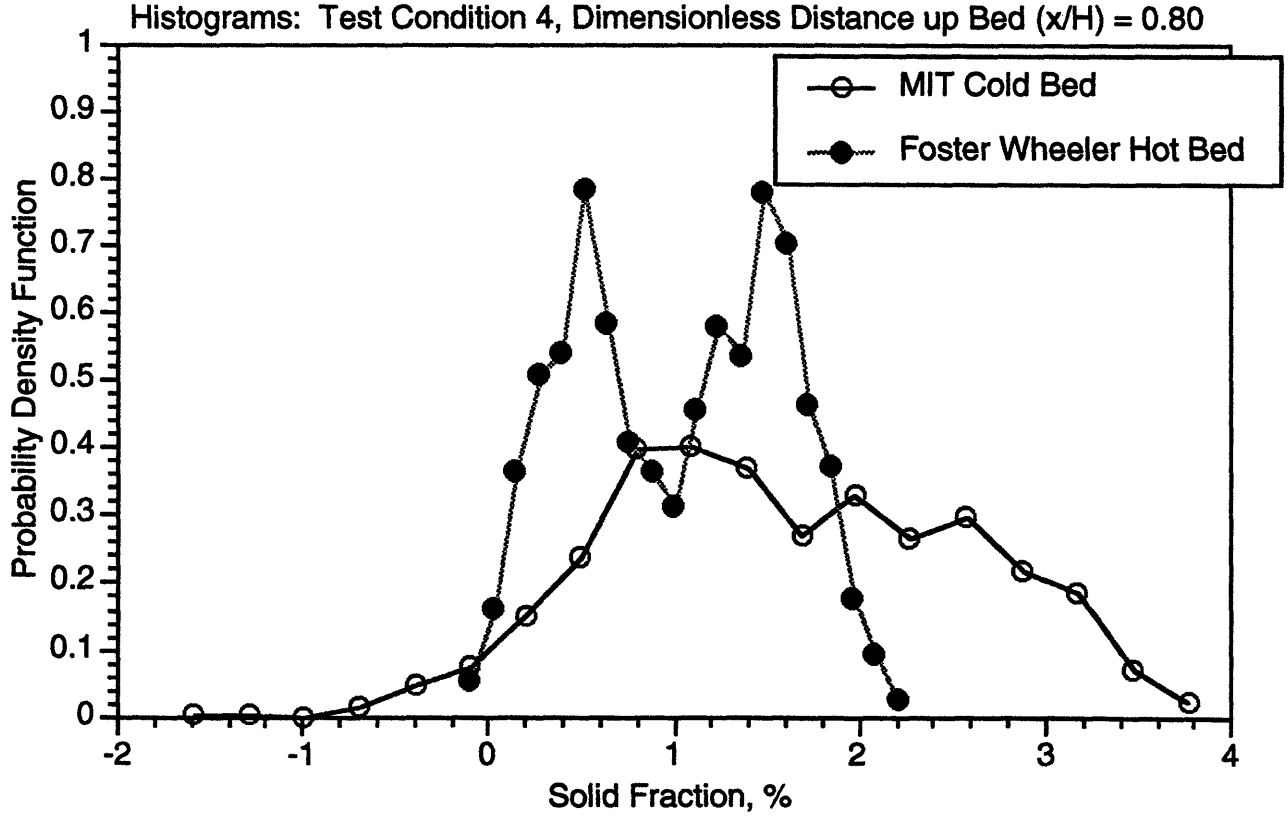

Figure 8.29
FFT's: Test Condition 1, Dimensionless Distance up Bed (x/H) = 0.06

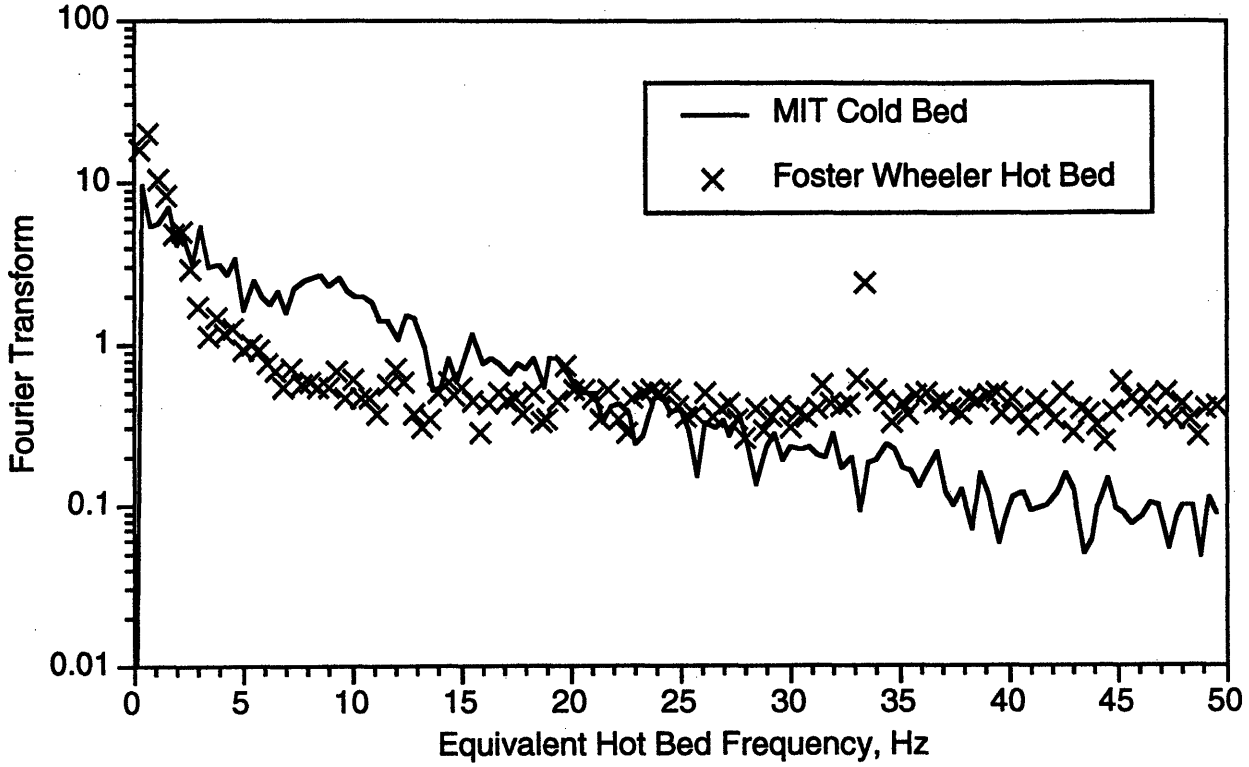

Figure 8.30
FFT's: Test Condition 1, Dimensionless Distance up Bed (x/H) = 0.13

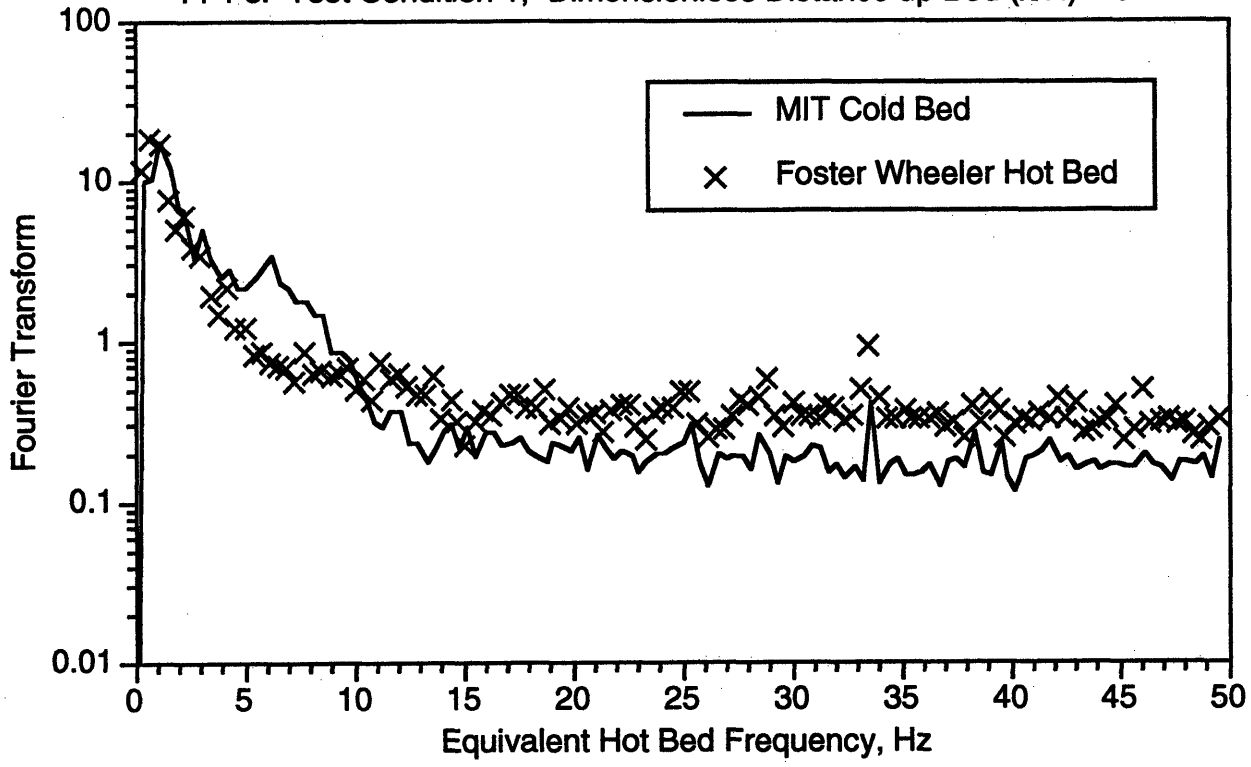

Figure 8.31

FFT's: Test Condition 1, Dimensionless Distance up Bed (x/H) = 0.21

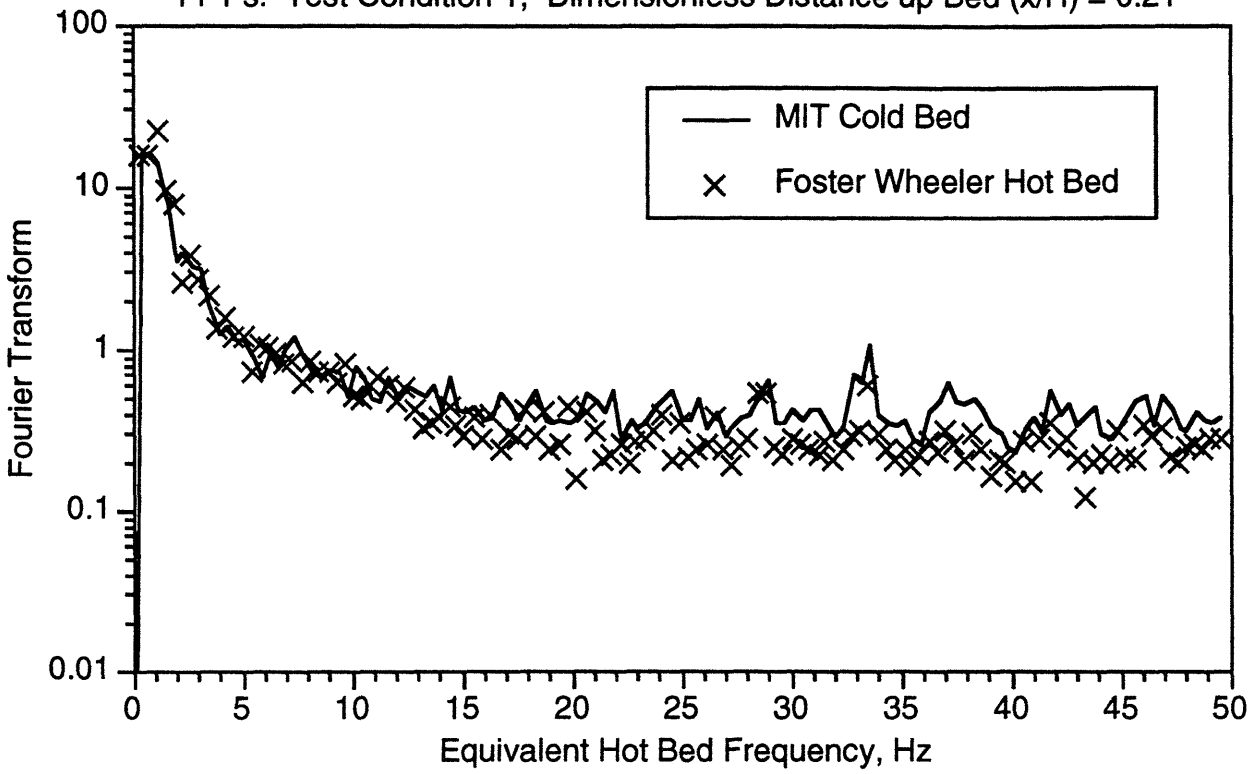

Figure 8.32

FFT's: Test Condition 1, Dimensionless Distance up Bed (x/H) = 0.36

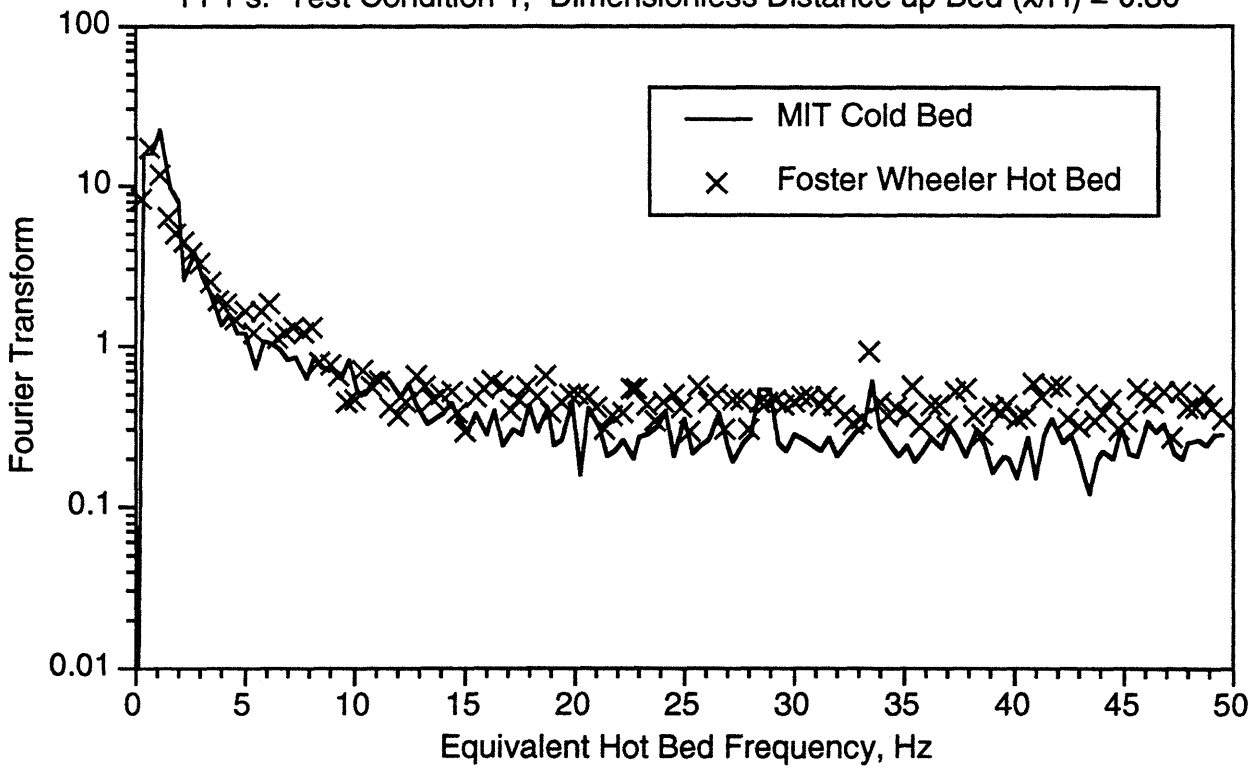

Figure 8.33
FFT's: Test Condition 1, Dimensionless Distance up Bed (x/H) = 0.57

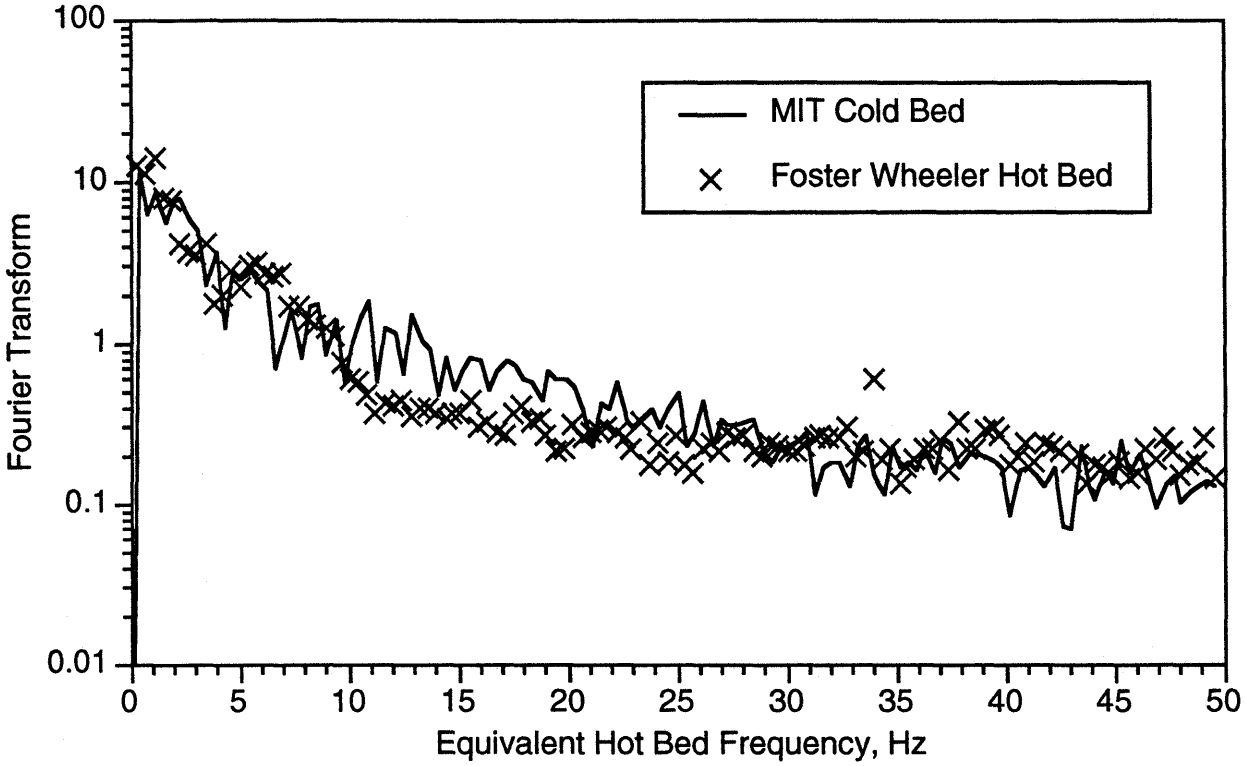

Figure 8.34
FFT's: Test Condition 1, Dimensionless Distance up Bed (x/H) = 0.80

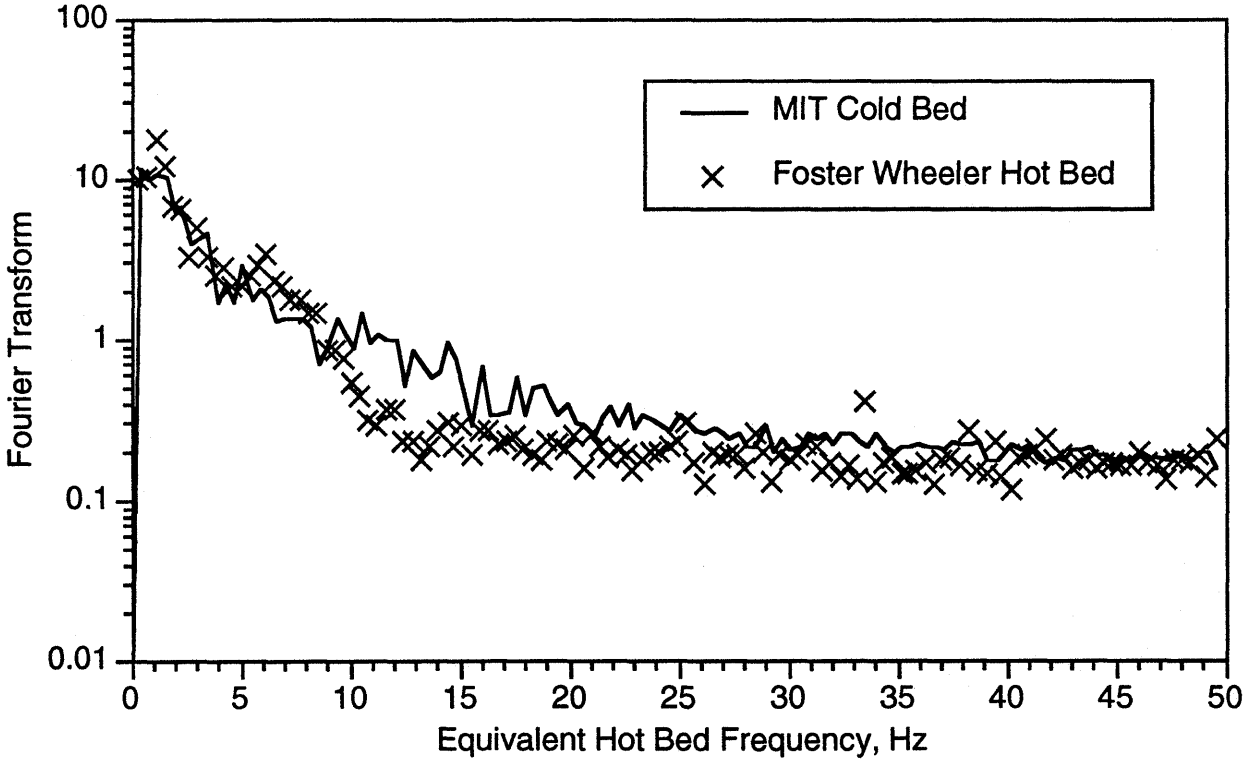

Figure 8.35

FFT's: Test Condition 2, Dimensionless Distance up Bed (x/H) = 0.06

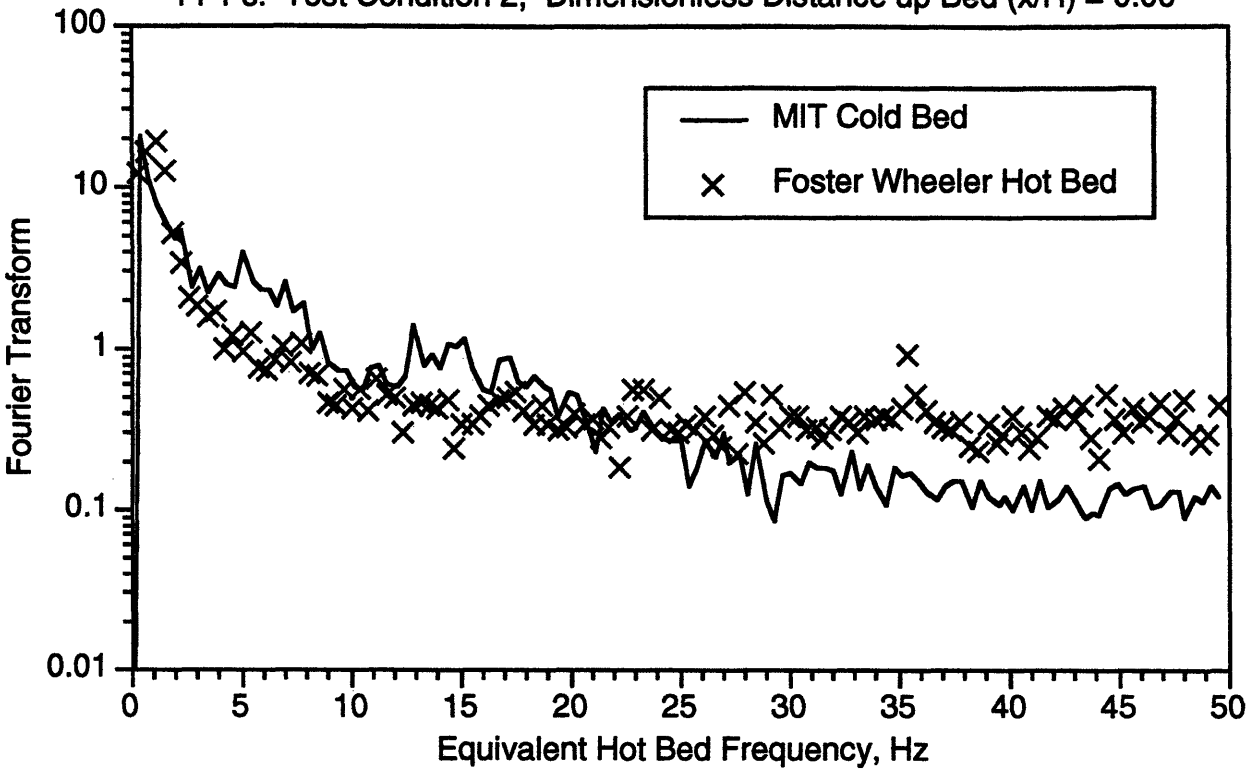

Figure 8.36

FFT's: Test Condition 2, Dimensionless Distance up Bed (x/H) = 0.13

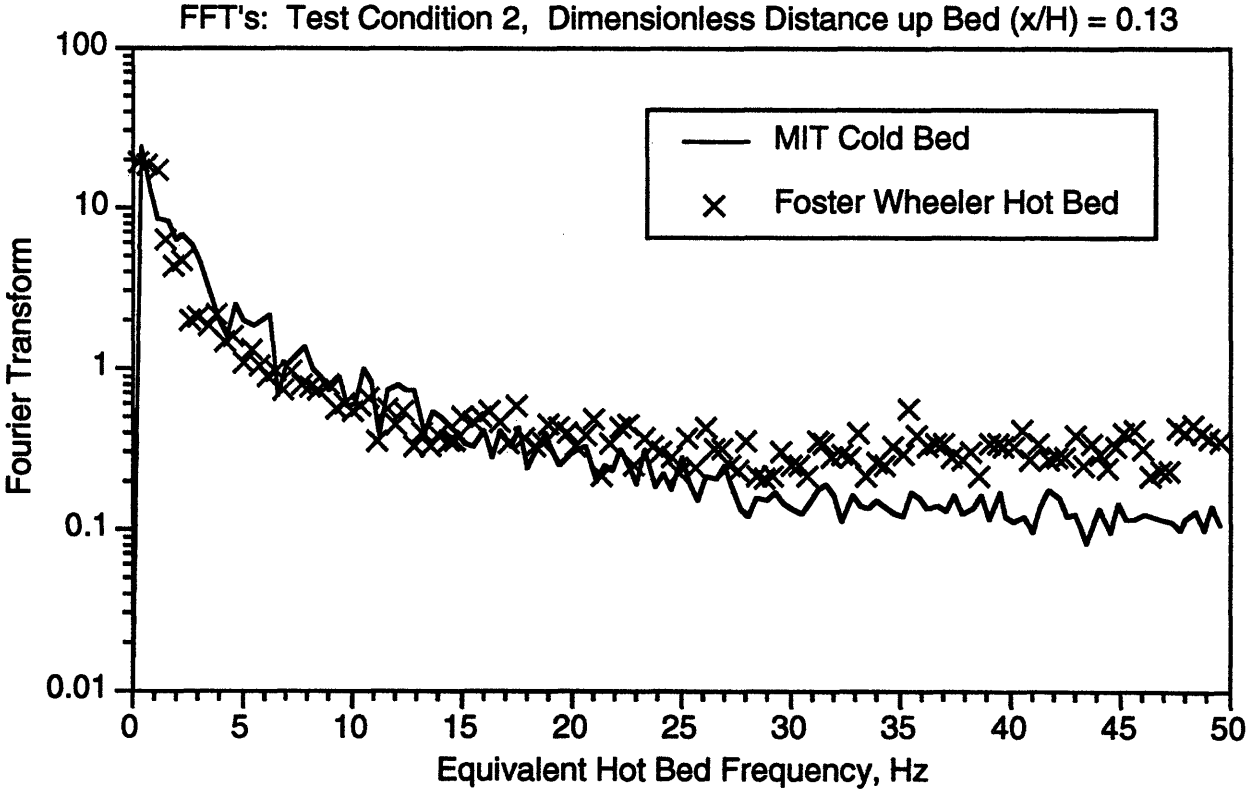

Figure 8.37

FFT's: Test Condition 2, Dimensionless Distance up Bed (x/H) = 0.21

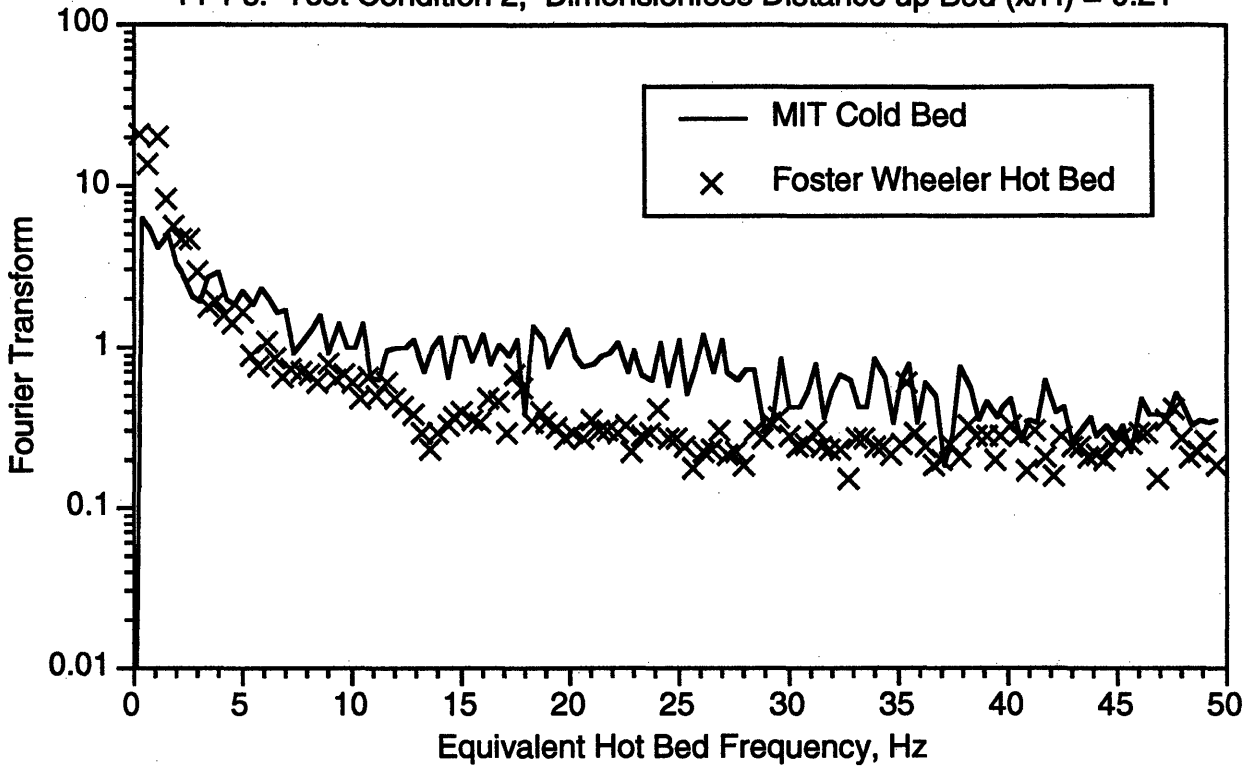

Figure 8.38

FFT's: Test Condition 2, Dimensionless Distance up Bed (x/H) = 0.36

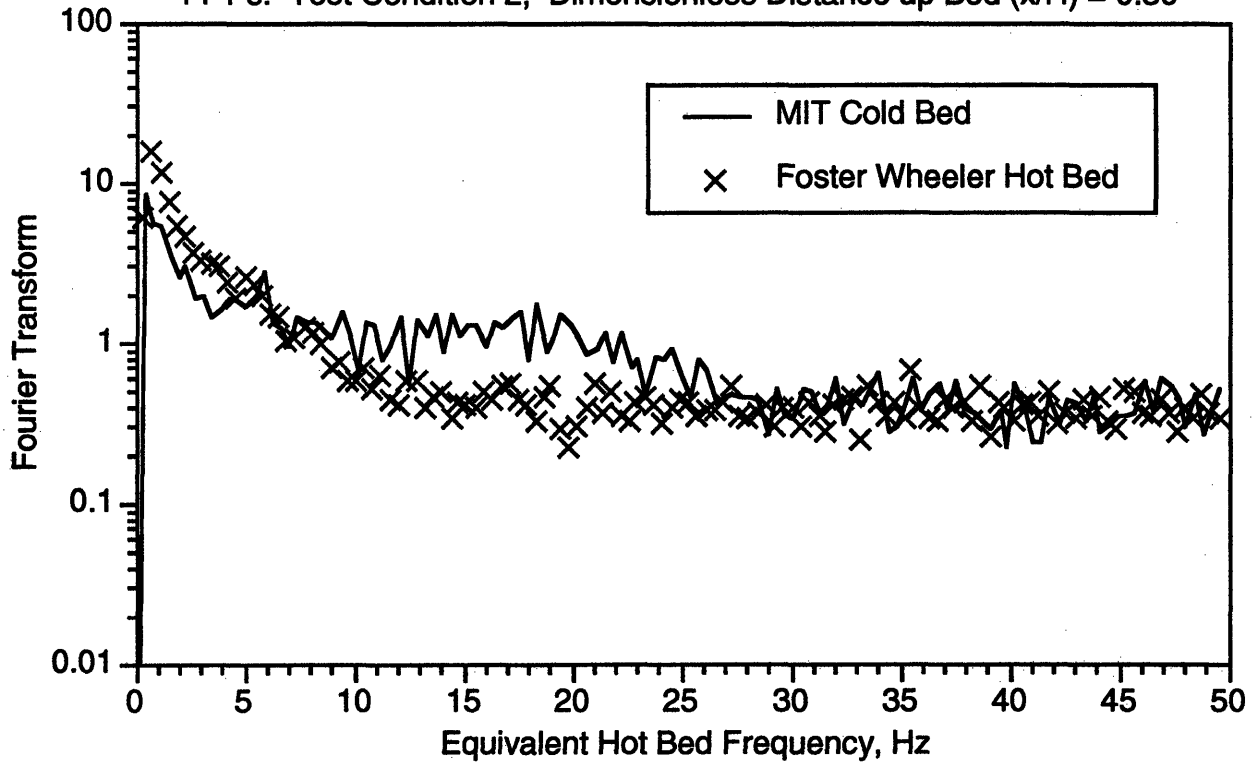

Figure 8.39

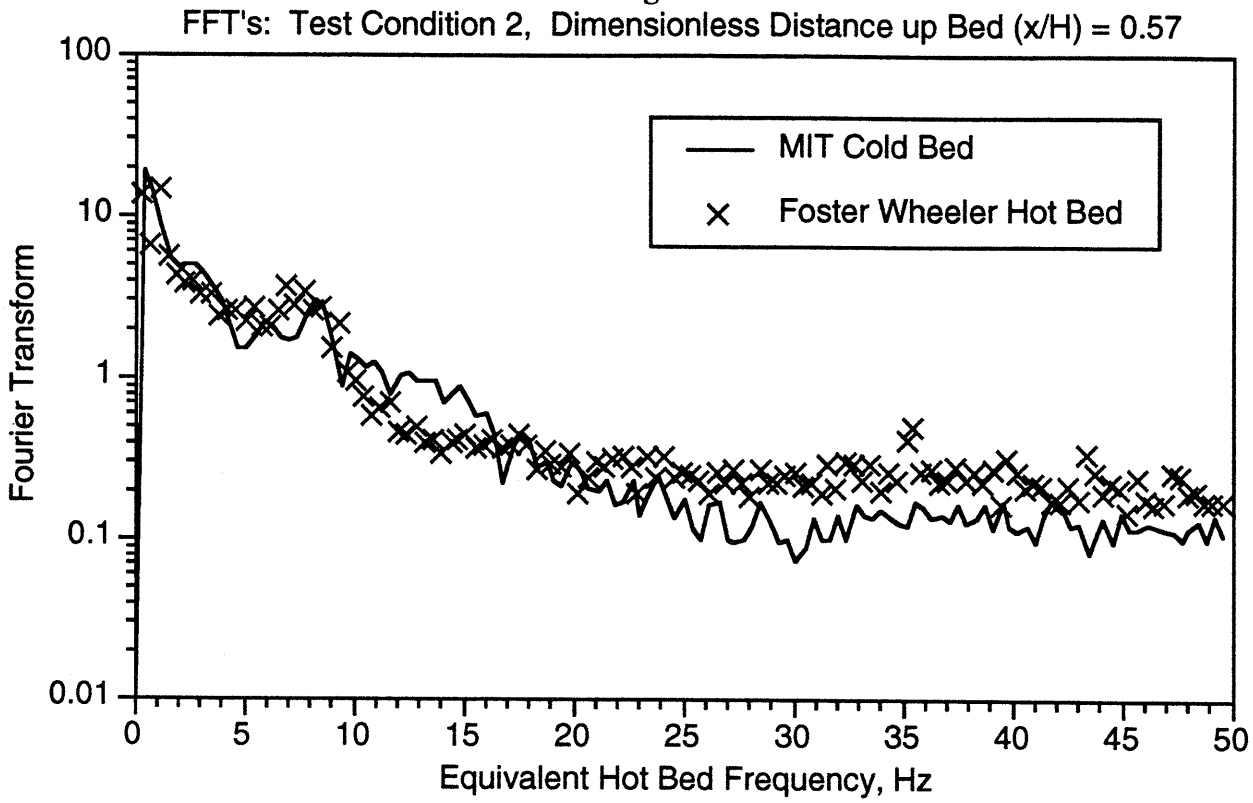

Figure 8.40

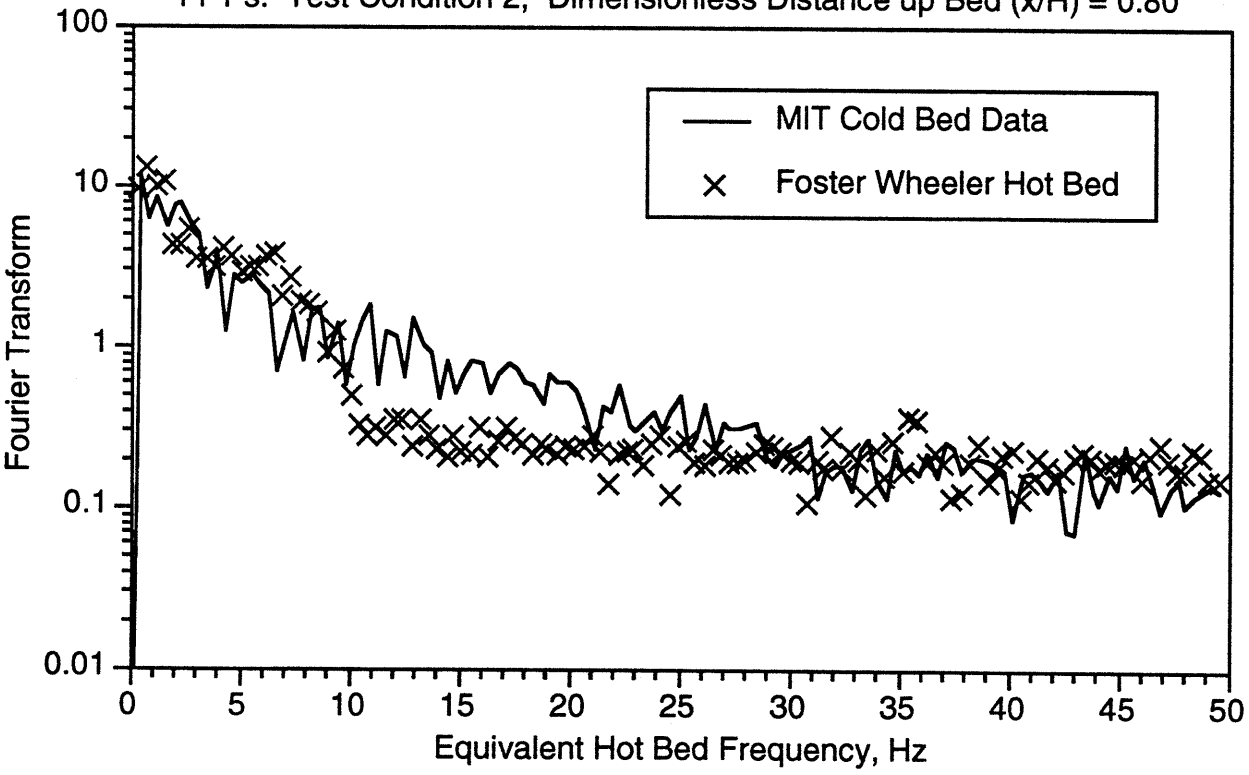

Figure 8.41

FFT's: Test Condition 3, Dimensionless Distance up Bed (x/H) = 0.06

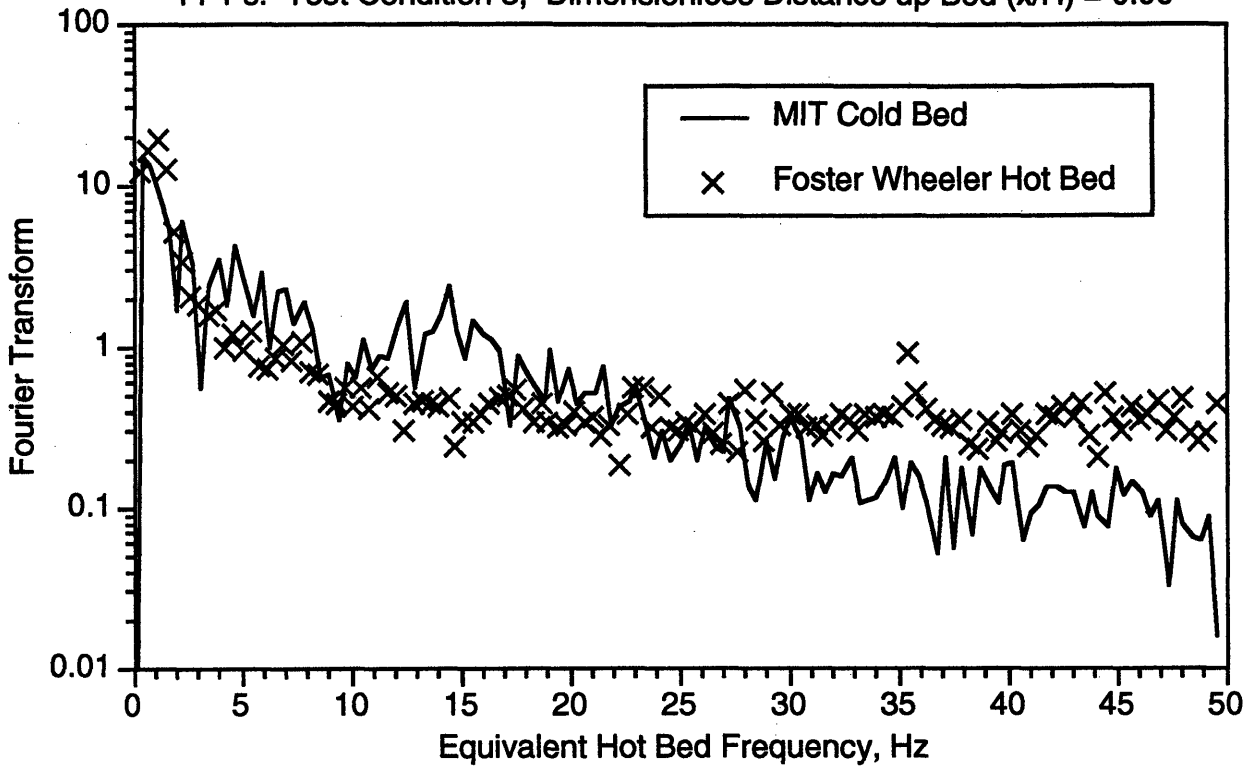

Figure 8.42

FFT's: Test Condition 3, Dimensionless Distance up Bed (x/H) = 0.13

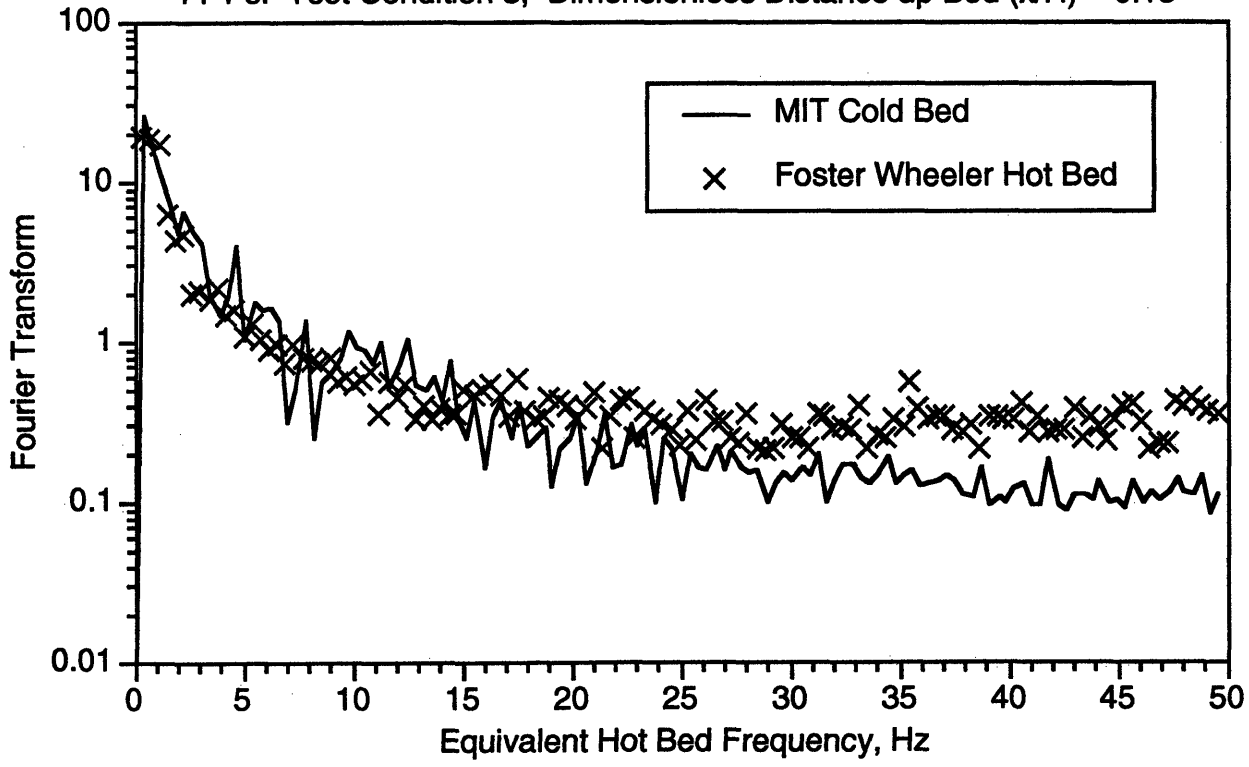

Figure 8.43

FFT's: Test Condition 3, Dimensionless Distance up Bed (x/H) = 0.21

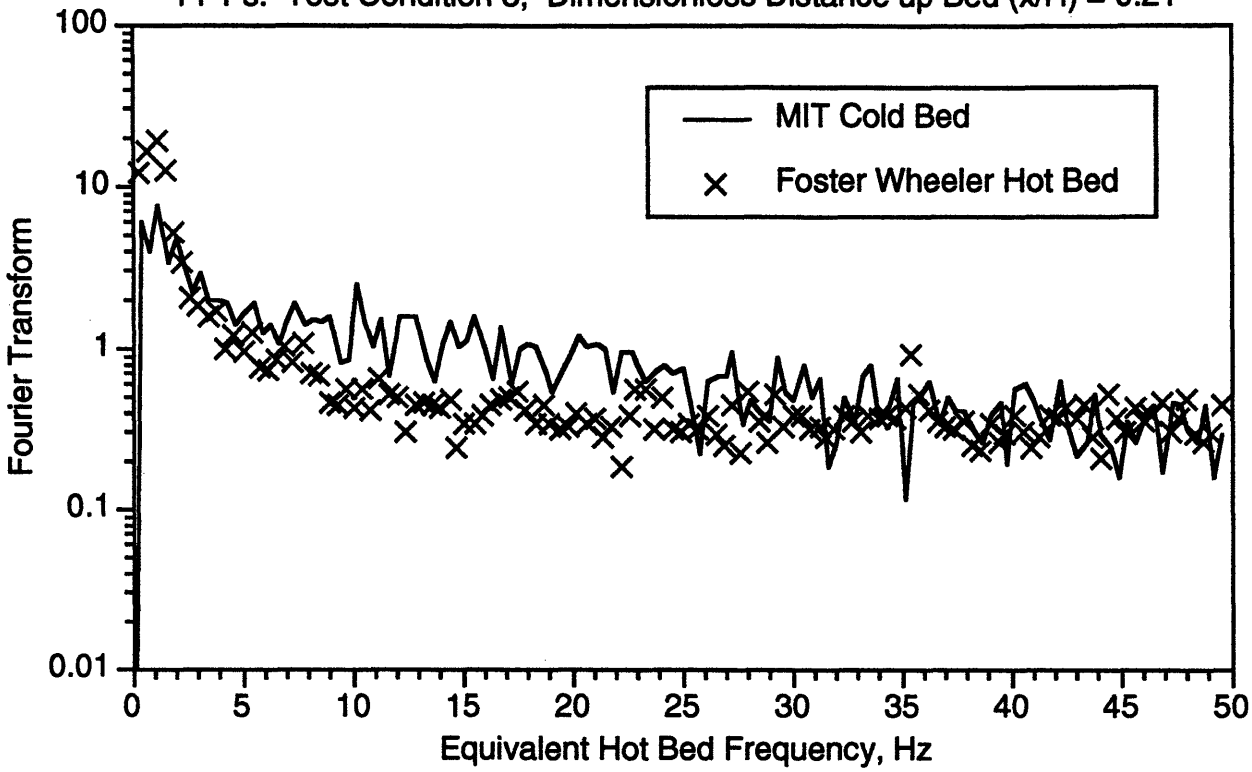

Figure 8.44

FFT's: Test Condition 3, Dimensionless Distance up Bed (x/H) = 0.36

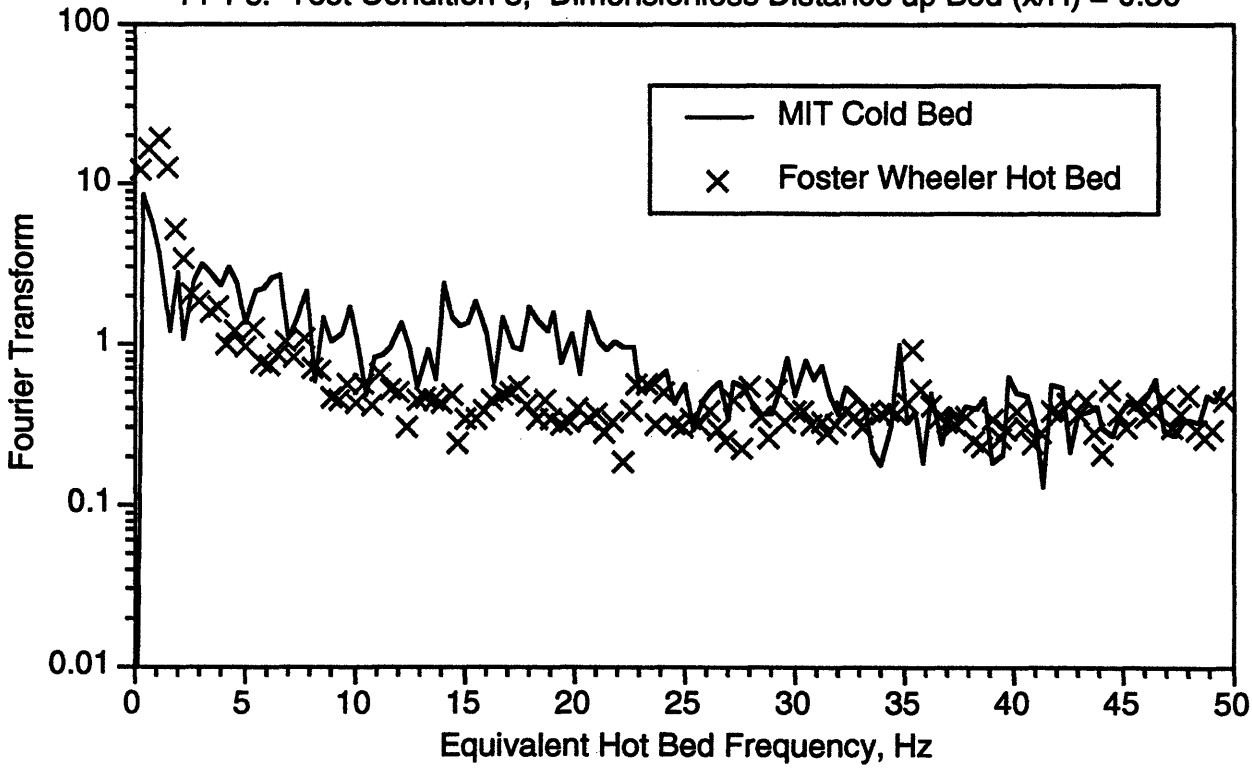

Figure 8.45

FFT's: Test Condition 3, Dimensionless Distance up Bed (x/H) = 0.57

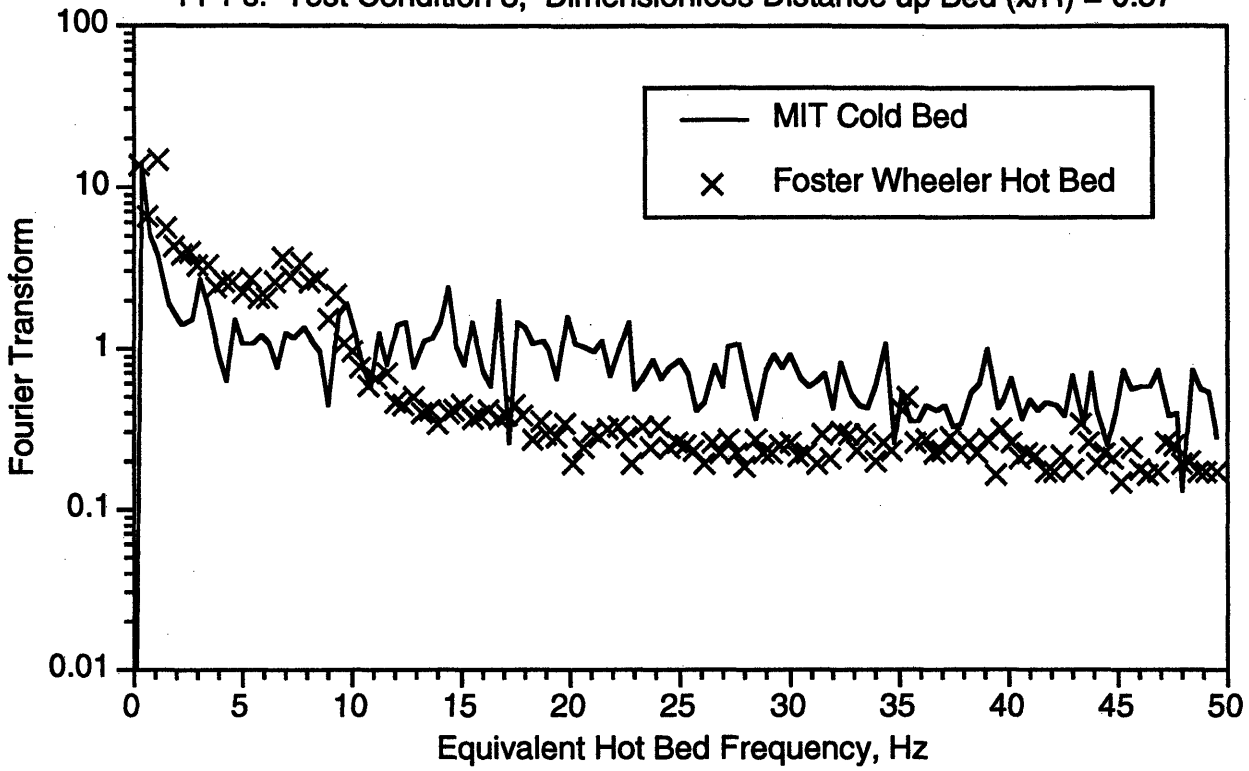

Figure 8.46

FFT's: Test Condition 3, Dimensionless Distance up Bed (x/H) = 0.80

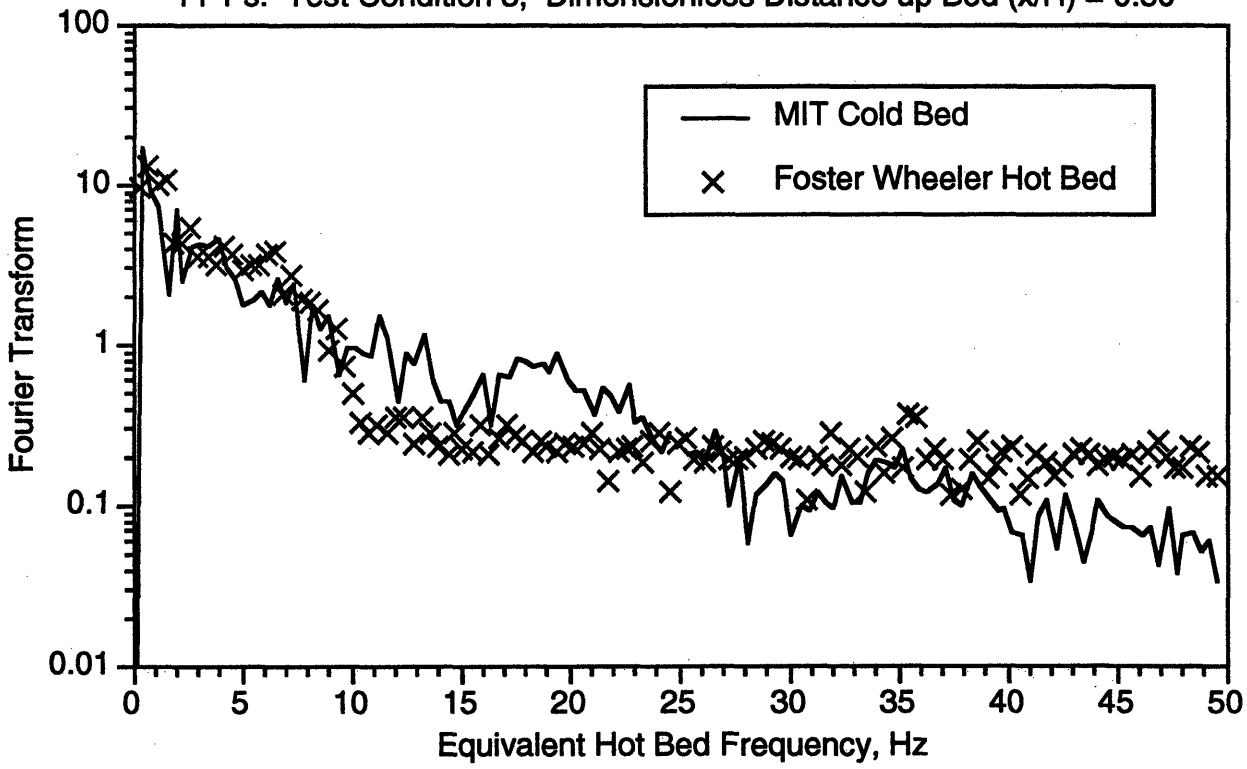

Figure 8.47

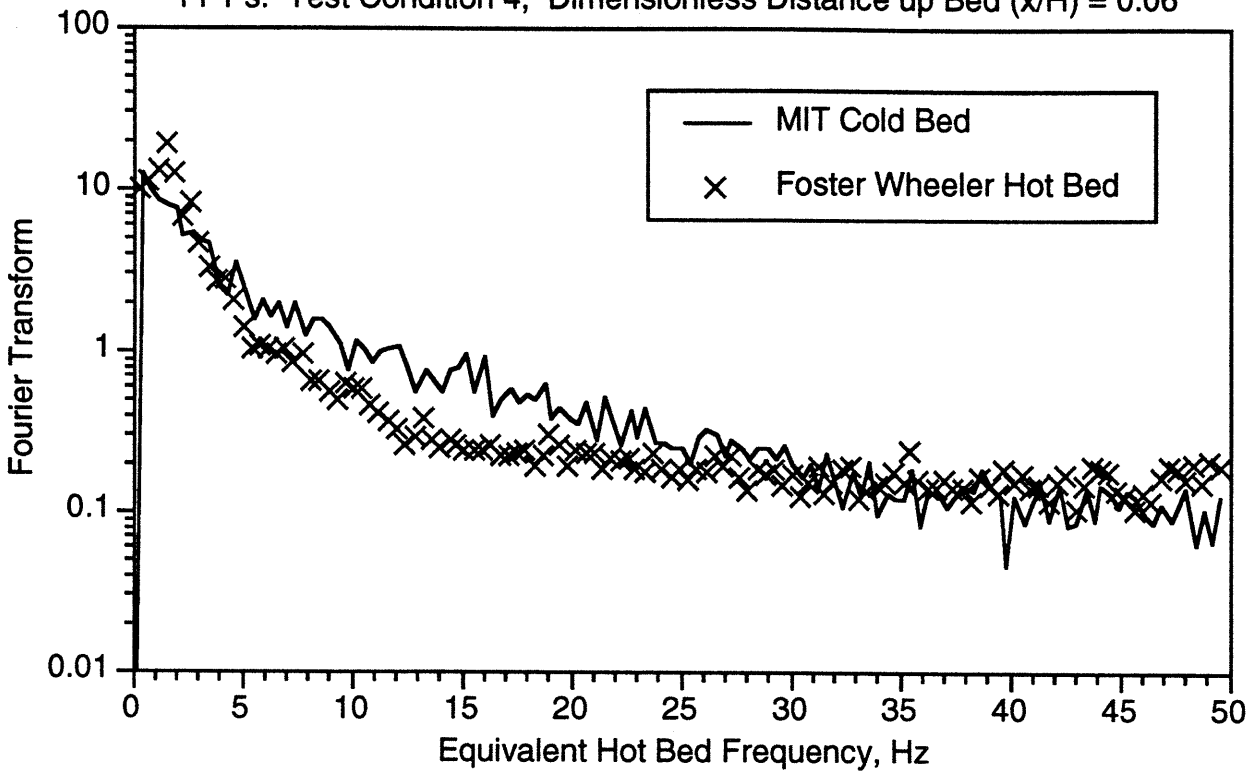

Figure 8.48

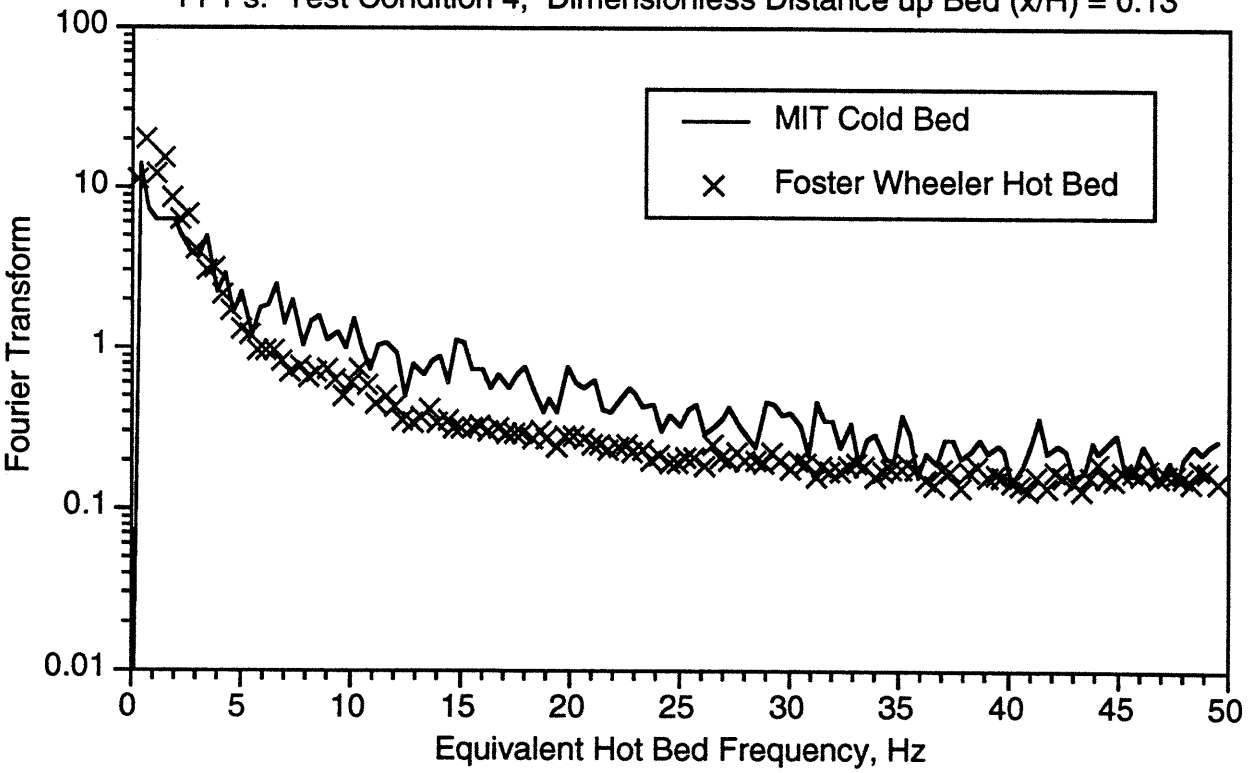

Figure 8.49

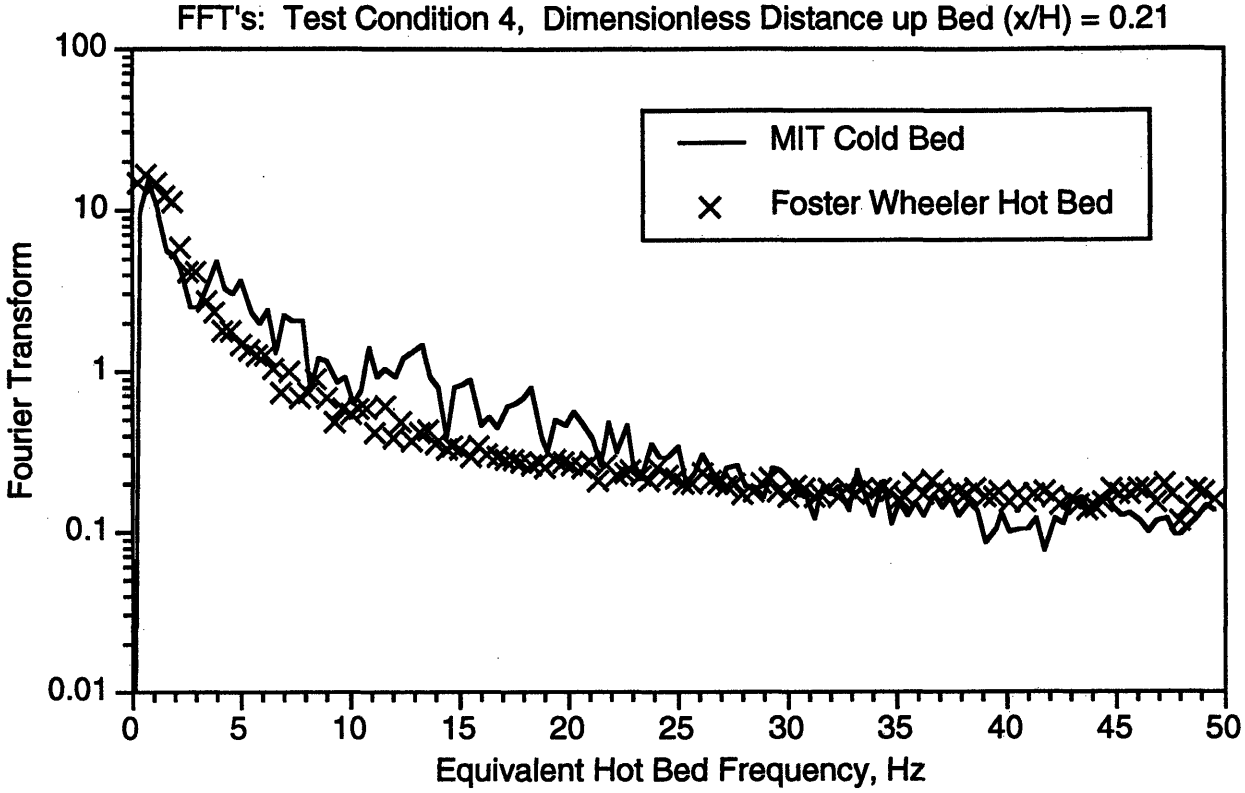

Figure 8.50

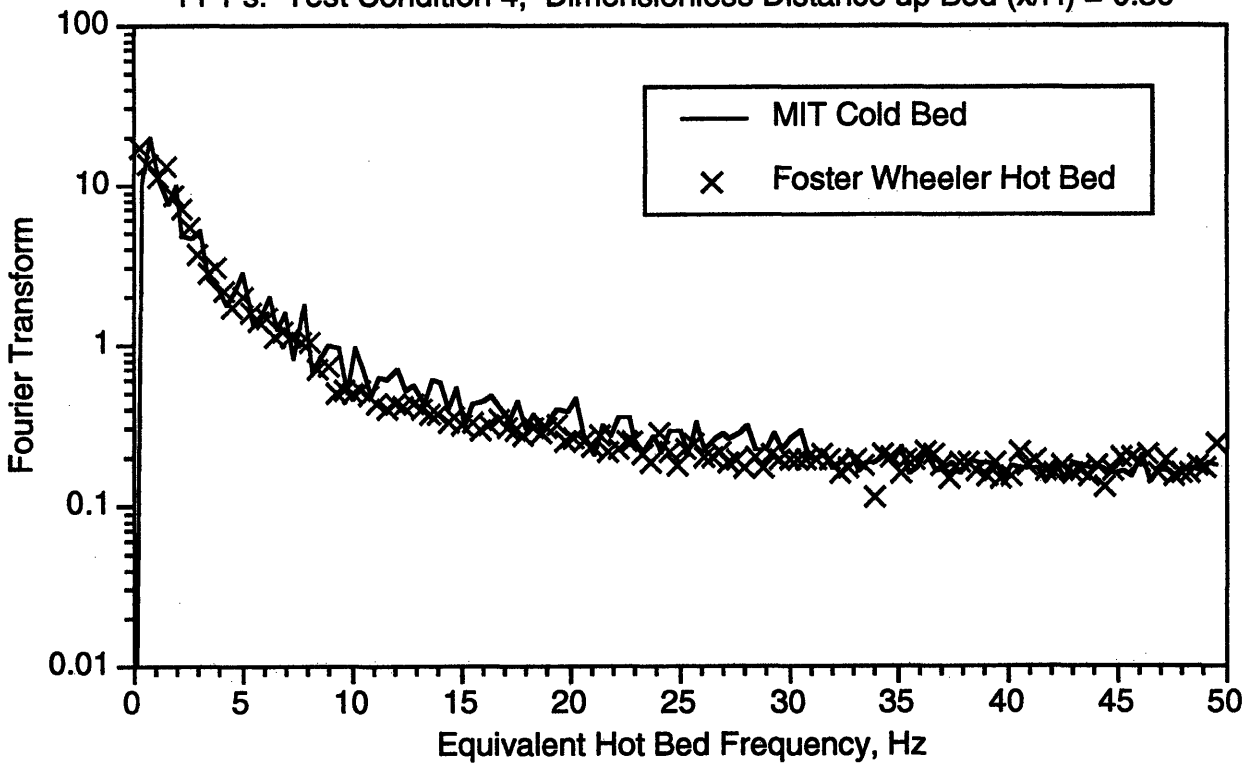

Figure 8.51

FFT's: Test Condition 4, Dimensionless Distance up Bed (x/H) = 0.57

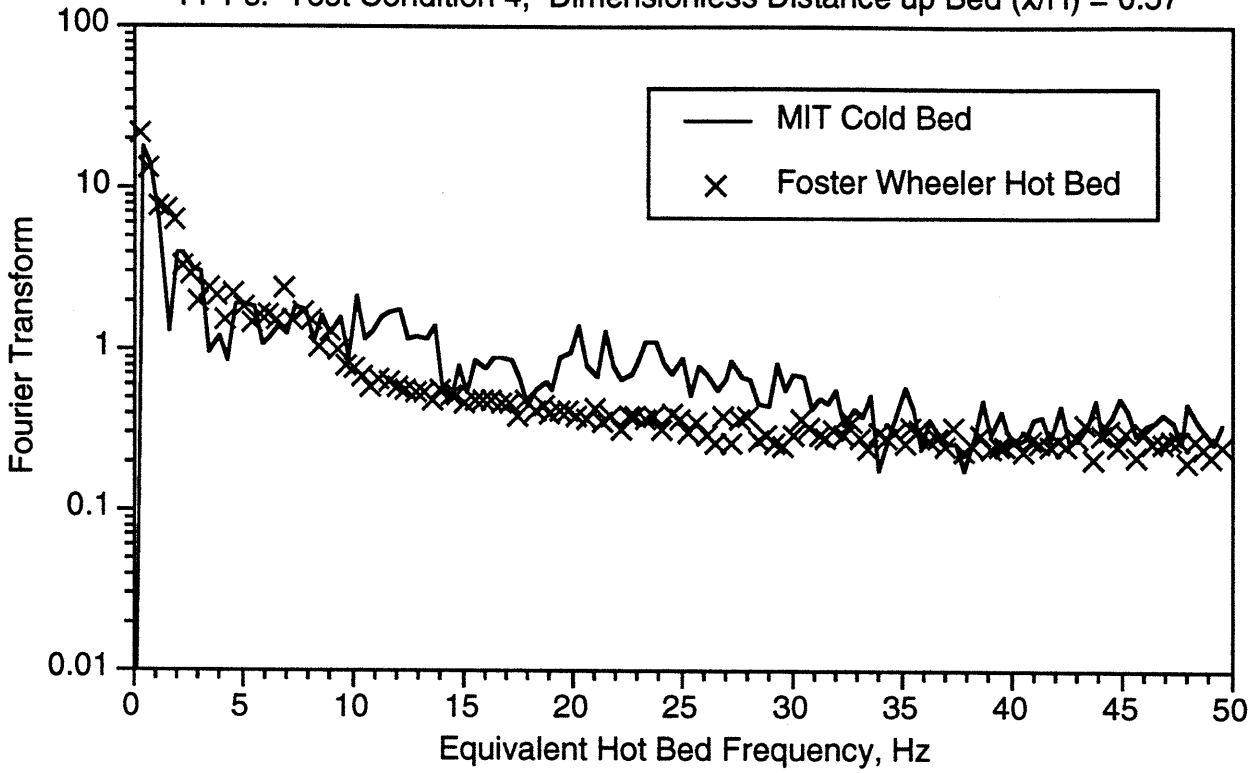

Figure 8.52

FFT's: Test Condition 4, Dimensionless Distance up Bed (x/H) = 0.80

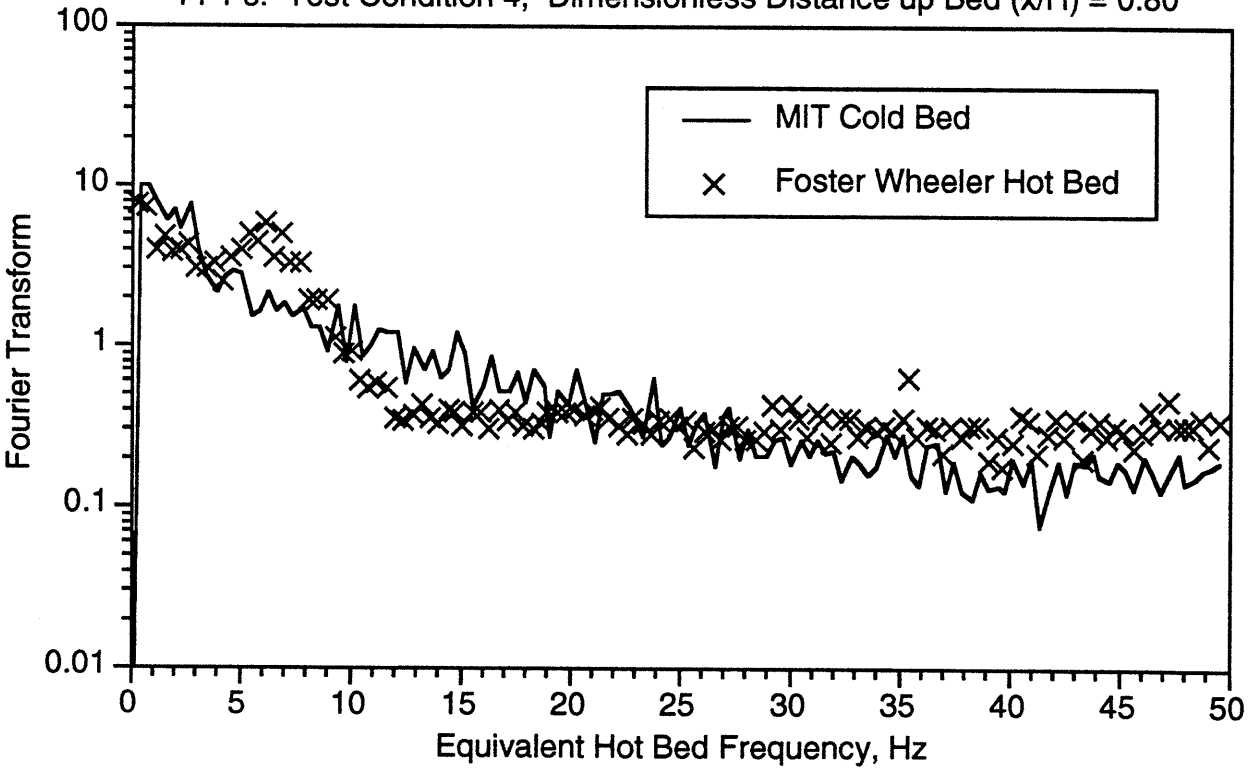

8.5 Discussion and Conclusions

Agreement is good for all test conditions, especially in the upper regions of the bed. In the lower regions of the bed, the cold model solid fraction profiles were consistently higher except for test condition four which had a very low solids recycle rate and a low primary zone superficial velocity; a state not typical of a normal operating condition. The run at condition four was close to the bubbling regime. Comparison of case four with the previous three cases emphasizes the ability of the cold model to match the hydrodynamics of the hot bed over a wide range of conditions (see Figure 8.53). Agreement in the probability density functions is good in all regions of the bed, but deviated somewhat at x/H of 0.36. The differential pressure measurement at this height included the entry of secondary air. The disagreement is probably caused by the difference in secondary air sources. In the Foster Wheeler hot bed, the secondary air is taken from the region above the freeboard of the FBHE. In the cold bed, the secondary air is supplied from a separate compressor line. It may be that the hydrodynamics of the FBHE, for example pressure fluctuations above the freeboard due to bubble eruptions, are affecting the hydrodynamics of the PCFBC in the region near the secondary air ports. The power spectral densities exhibit a similar trend showing good agreement in all regions of the bed. Note that no substantial deviations are indicated at an x/H of 0.36.

Results of these hydrodynamic scaling experiments show good agreement when using the simplified set of scaling laws and strongly suggest that this new set of parameters is acceptable over the range of conditions tested in the fast fluidization regime. Scale modeling experiments using the simplified set of scaling parameters can be used for prediction of the behavior of pressurized CFB combustors. Excellent predictions of the solid fraction profiles for the Foster Wheeler pilot PCFB has been made by using a half-scale room-temperature model constructed and operated using these parameters. Cold bed prediction of the time averaged solid fraction, and the pressure fluctuation amplitudes and fourier transforms showed excellent agreement indicating that larger scale factors may be possible.

Future efforts will focus on constructing a 1/6.5 scale model of the Foster Wheeler Phase III PCFBC. This should provide evidence as to the range of applicability of the simplified scaling laws to pressurized circulating fluidized beds.

Figure 8.53

Comparison of Average Solid Fraction Profiles for Various Cases

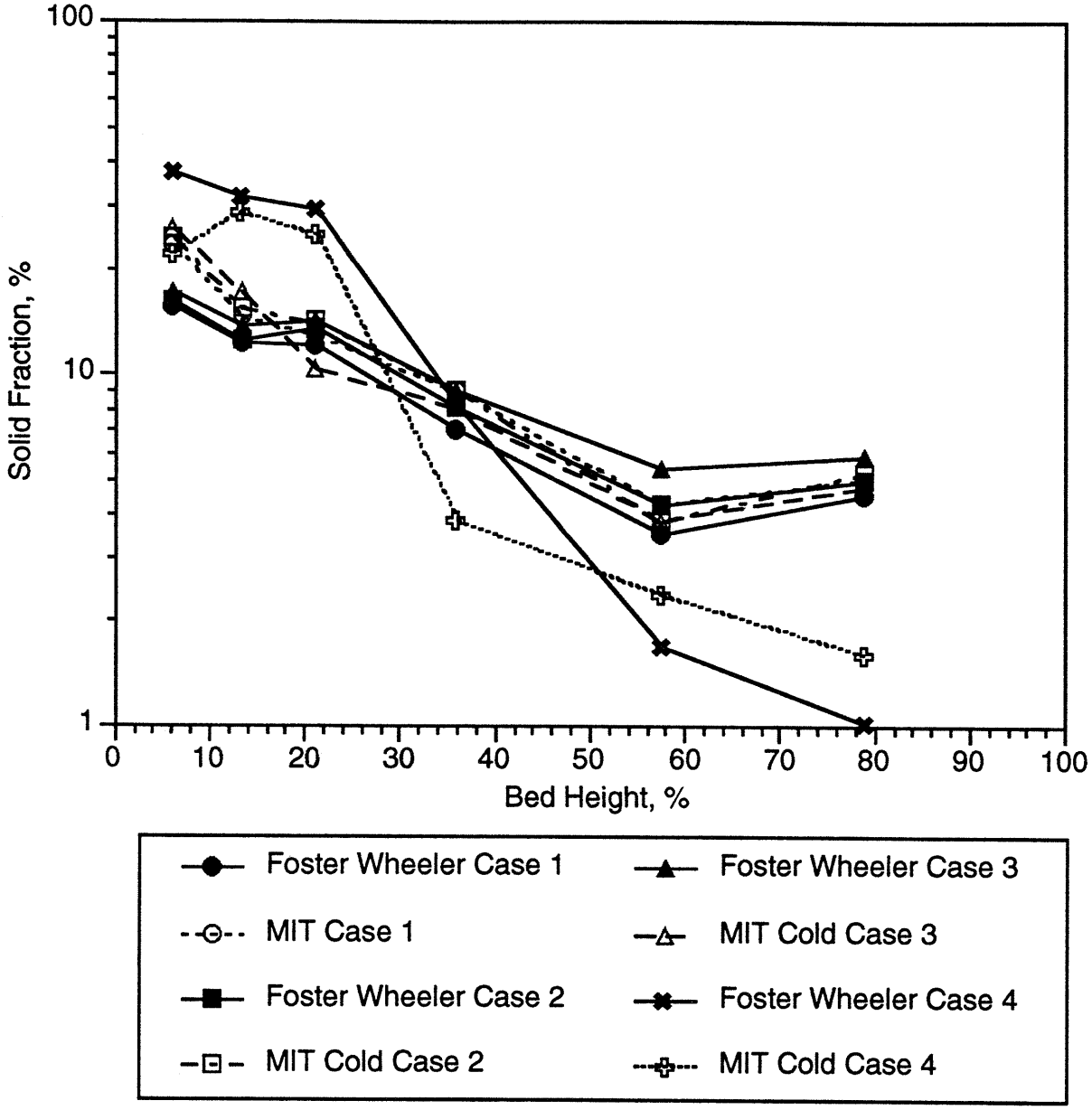

9.0 REFERENCES

Ackeskog, H.B.R., A.E. Almstedt, and V. Zakkay, "An Investigation of Fluidized Bed Scaling: Heat Transfer Measurements in a Pressurized Fluidized Bed Combustor and a Cold Model Bed," *Chem. Eng. Sci.*, **48**, p. 1459, 1993.

Almstedt, A.E., and V. Zakkay, "An Investigation of Fluidized-Bed Scaling - Capacitance Probe Measurements in a Pressurized Fluidized-Bed Combustor and a Cold Model Bed," *Chem. Engng. Sci.*, **45**, pp. 1071-1078, 1990.

Anderson, T.B., and R. Jackson, "A Fluid Mechanical Description of Fluidized Beds," *Ind. Engng. Chem. Fundam.*, **6**, pp. 52-58, 1964.

Avdeev, A. A., "Turbulent Flow Hydrodynamics of a Bubbly Two-Phase Mixture," *Teplofizika Vysokikh Temperatur*, **21**, pp. 707-715, 1983.

Barnea, E. and J. Mizrahi, "A Generalized Approach to the Fluid Dynamics of Particulate Systems," *Chem. Eng. J.*, **5**, pp. 171-189, 1973.

Basset, A.B., *A Treatise on Hydrodynamics*, Deighton Bell: London, 1888.

Batchelor, G.K., "A New Theory for the Instability of a Fluidized Bed," *J. Fluid Mech.*, **31**, pp. 657-668, 1988.

Berlemont, A., P. Desjonqueres and G. Gouesbet, "Particle Lagrangian Simulation in Turblent Flows," *Int. J. Multiphase Flow*, **16**, pp. 19-34, 1990.

Binder, A., "The Motion of Cylindrical Particles in Viscous Flow," *J. Appl. Phys*, **10**, pp. 711-713, 1939.

Biswas, J. and L. S. Leung, "Applicability of Choking Correlations for Fast-Fluid Bed Operations," *Powder Technol.*, **51**, pp. 179-180, 1987.

Boothroyd, R.G., *Flowing Gas-Solids Suspensions*, Chapman and Hall Ltd.: London, 1971.

Boussinesq, *Applications a l'Etude des Potentieles* (Originally printed in 1885). Re-edition by Blanchard: Paris, 1969.

Boussinesq, "Sur la Resistance qu'Oppose un Liquide Indefini en Repos," *C.R. Acad. Sci. Paris*, **100**, pp. 935-937, 1885.

Bowen, R.M., *Continuum Physics, Vol. II* (Edited by Eringen, A.C.), Academic Press: New York, 1971.

Brenner, H. and J. Happel, "Flow Viscous Flow Past a Sphere in a Cylindrical Tube," *J. Fluid Mech.*, **4**, pp. 195-213, 1958.

Brenner, H. and R. G. Cox, "The Resistance to a Particle of Arbritrary Shape in Translational Motion at Small Reynolds Numbers," *J. Fluid Mech.*, **17**, pp. 561-595, 1963.

Brenner, H., "The Slow Motion of a Sphere Through a Viscous Fluid Towards a Plane Surface," *Chem. Engng. Sci.*, **16**, pp. 242-251, 1961.

Bretherton, F. P., "The Motion of Rigid Particles in a Shear Flow at Low Reynolds Number," *J. Fluid Mech.*, **14**, pp. 284-304, 1962.

Change, H., and M. Louge, "Fluid Dynamic Similarity of Circulating Fluidized Beds," *Powder Technol.*, **70**, pp. 259-270, 1992.

Chen, L. and S.L. Soo, "Charging of Dust Particles by Impact," *J. Appl. Phys.*, **41**, pp. 585-591, 1970.

Chester, W., and D.R. Breach, "On the Flow Past a Sphere at Low Reynolds Numbers," *J. Fluid Mech.*, **37**, pp. 751-760, 1969.

Chong, Y. O., and L. S. Leung, "Comparison of Choking Velocity Correlations in Vertical Pneumatic Conveying," *Powder Technol.*, **47**, pp. 43-50, 1986.

Clift, R., J.R. Grace, and M.E. Weber, *Bubbles, Drops, and Particles*, Academic Press: New York, 1978.

Cox, R. G., and H. Brenner, "The Lateral Migration of Solid Particles in Poiseuille Flow -I Theory," *Chem. Eng. Sci.*, **23**, pp. 147-173, 1968.

Davidson, J. A., et al., "A Comparison of Image Analysis With Other Methods of Particle Size Measurements for General Purpose PVC Resins," *Part. Part Syst. Charact.* **9**, pp 94-104, 1992.

Davidson, J. F., and D. Harrison, *Fluidized Particles*, Cambridge University Press: Cambridge, 1963.

de Groot, S.R., and P. Mazur, *Non-Equilibrium Thermodynamics*, Dover: New York.

Denson, C. D., E. B. Christiansen, and D. L. Salt, "Particle Migration in Shear Fields," 1966, *A.I.Ch.E. Journal,* **12**, pp. 589-595, 1984.

Di Felice, R., S. Rapagna, and P.U. Foscolo, "Dynamic Similarity Rules: Validity Check for Bubbling and Slugging Fluidized Beds," *Powder Technol.*, **71**, pp. 281-287, 1992a.

Di Felice, R., S. Rapagna, P.U. Foscolo, and L.G. Gibilaro, "Cold Modelling Studies of Fluidised Bed Reactors," *Chem. Engng. Sci.*, **47**, pp. 2233-2238, 1992b.

Didwania, A.K., and G.M. Homsy, "Resonant Sideband Instabilities in Wave Propagation of Fluidized Beds," *J. Fluid Mech.*, **122**, pp. 433-438, 1982.

Drew, D., "A Flow in the Poiseuille Flow of a Particle-Fluid Mixture," in *Advances in Multiphase Flow and Related Problems* (Edited by G. Papanicolau), SIAM, Philadelphia, PA, 1986.

Drew, D., "Mathematical Modeling of Two-Phase Flow," *A. Rev. Fluid Mech.*, **15**, pp. 261-291, 1983.

Eichhorn, R. and S. Small, "Experiments on the Lift and Drag of Spheres Suspended in Poiseuille Flow," *J. Fluid Mech.*, **20**, pp. 513-527 1964.

Einstein, A, "A New Determination of Molecular Dimensions," PhD. Dissertation, University of Zurich, published in, *Ann. Phys.* [Leipzig], **19**, p. 289, 1906.

Faxen, H., Die Bewegun einer Starren Kugel Langs der Achse eines mit zaher Flussigkeit gefullten Rohres, *Arkiv. Mat. Astron. Fys.*, **17**, pp. 1-28, 1923.

Finlayson, B., "Existence of Variational Principles for the Navier-Stokes Equation," *Phys. of Fluids*, **15**, pp. 963-967, 1972,.

Fitzgerald, T., D. Bushnell, S. Crane, and Y. Shieh, "Testing for Cold Scaled Bed Modeling for Fluidized-Bed Combustors," *Powder Technol.*, **38**, pp. 107-120, 1984.

Fitzgerald, T., D. Bushnell, S. Crane, and Y. Shieh, "Testing for Cold Scaled Bed Modeling for Fluidized-Bed Combustion," *Proceedings 7th Int. Conf. on Fluidized Bed Comb.*, Philadelphia, p. 766, 1983.

Fitzgerald, T.J., and S.D. Crane, "Cold Fluidized Bed Modeling," *Proc. 6th Int. Conf. Fluidized Bed Combustion,* pp. 815-820, 1980.

Fuchs, N.A., *Mechanics of Aerosols*, Trans. Ed., C.N. Davies, Pergamon: Oxford, 1964.

Ganser, G. H., "A Rational Approach to Drag Prediction of Spherical and Nonspherical Particles," *Powder Technol.*, **77**, pp. 143-152, 1993.

Geldart, D., "Types of Gas Fluidization," *Powder Technol.*, **7**, pp. 285-292, 1973.

Givler, R.C., "An Interpretation for the Solid-Phase Pressure in Slow, Fluid-Particle Flows," *Int. J. Multiphase Flow*, **13**, pp. 717-722, 1987.

Glicksman, L.R., D. Westphalen, K. Woloshum, T. Ebert, K. Roth, M. Lints, C. Brereton and J. Grace, "Experimental Scale Models of circulating Fluidized Bed Combustors", *Proc. 11th Int. Conf. on Fluidized Bed Combustion*, Montreal, 1991.

Glicksman, L.R., Hyre, M.R., and K. Woloshun, "Simplified Scaling Relationships for Fluidized Beds," *Powder Technol.*, **77**, pp. 177-199, 1993.

Glicksman, L.R., M.R. Hyre, and P.A. Farrell, "Dynamic Similarity in Fluidization," *Int. J. Multiphase Flow*, **20 Suppl.**, pp. 331-386, 1994.

Glicksman, L.R., "Scaling Relationships for Fluidized Beds," *Chem. Engng. Sci.*, **39**, pp. 1373-1379, 1984.

Glicksman, L.R., "Scaling Relationships for Fluidized Beds", *Chemical Engineering Science*, **43**, 6. pp. 1419-1424, 1988.

Glicksman, L.R., T. Yule, R. Carson and R. Vincent, "Comparison of Results from TVA 20MW Fluidized Bed Combustor with MIT Cold Scale Model", *Proceedings: 1988 Seminar on Fluidized Bed Combustion Technology for Utility Applications*, p. 1-20-1, Feb. 1989.

Glicksman, L.R., T. Yule, A. Dryness, R. Carson, "Scaling the Hydrodynamics of Fluidized Bed Combustors with Cold Models: Experimental Confirmation," *Ninth International Fluidized Bed Combustion Conf.*, ASME, 1987.

Glicksman, L.R., Westphalen, D., Brereton, C., and J. Grace, "Verification of the Scaling Laws for Circulating Fluidized Beds," In *Circulating Fluidized Bed Technology III* (Edited by Basu, P., Horio, M., and M. Hasatani), Pergamon Press: Oxford, 1991.

Goldsmith, H. L., and S. G. Mason, "The Flow of Suspensions Through Tubes," *J. Colloid Science*, **17**, pp. 448-476, 1962.

Green, H.L., and W.R. Lane, *Particulate Clouds: Dusts, Smokes, and Mists*, Spon: London, 1957.

Gyftopoulos, E. P. and G. P. Beretta, *Thermodynamics: Foundations and Applications*, Macmillan : New York, 1991.

Halow, J. S. and G. B. Wills, "Experimental Observations of Sphere Migration in Couette Systems," *Ind. Eng. Chem Fund.*, **9**, pp. 603-607, 1970b.

Halow, J. S. and G. B. Wills, "Radial Migration of Spherical Partilces in Couette Systems," *A.I.Ch.E. Journal*, **16**, pp. 281-286, 1970a.

Hamaker, H.C., "The London - van der Waals Attraction Between Spherical Particles," *Physica*, **4**, pp. 1058-1072, 1937.

Happel, J, and N. Epstein, "Cubical Assemblages of Uniform Spheres," *Ind. Eng. Chem.*, 46, pp. 1187-1194, 1954.

Happel, J. and H. Brenner, " Viscous Flow in Multiparticle Systems: Motion of Spheres and a Fluid in a Cylindrical Tube," *AIChE Journal*, **3**, pp. 506-513, 1957.

Happel, J., and B. J. Byrne, "Motion of a Sphere and Fluid in a Cylindrical Tube," *Ind. Eng. Chem.*, **46**, pp.1181-1186, 1954.

Harper, E.Y., and I-D. Chang, "Maximum Dissipation Resulting from Lift in a Slow Viscous Shear Flow," *J. Fluid Mech.*, **33**, pp. 209-225, 1968.

Hassonjee, Q, R. Pfeffer, and P. Ganatos, "Behavior of Multiple Spheres in Shear and Poiseuille Flow Fields at Low Reynolds Number," *Int. J. Multiphase Flow*, **18**, pp. 353-370, 1992.

Helmholtz, "Zur Theorie der stationären Ströme in reibenden Flüssigkeiten," *Verh. des naturhist-med. Vereins zu Heidelberg*, Bd. v. S. 1-7; Collected Works, i. p. 223, 1868.

Hesketh, H.E., *Fine Particles in Gaseous Media*, Ann Arbor Science Pub. Inc.: Ann Arbor, MI, 1977.

Hill, R., and G. Power, "Extremum Principles for Slow Viscous Flow and the Approximate Calculation of Drag," *Quart. J. of Mech. Appl. Math.*, **9**, pp. 314-319, 1956.

Hinze, J.O., *Turbulence*, McGraw-Hill: New York, 1975.

Ho, B.P. and L.G. Leal, "Inertial Migration of Rigid Spheres in Two-Dimensional Unidirectional Flows," *J. Fluid Mech.*, **65**, pp. 365-400, 1974.

Hogg, A.J., "The Inertial Migration of Non-Neutrally Buoyant Spherical Particles in Two-Dimensional Shear Flows," *J. Fluid Mech.*, **272**, pp. 285-318, 1994.

Homsy, G.M., M.M. El-Kaissy, and A. Didwania, "Instability Waves and the Origin of Bubbles in Fluidized Beds - II," *Int J. Multiphase Flow*, **6**, pp. 305-318, 1980.

Horio, M., A. Nonaka, T. Sawa and I. Muchi, "A New Similarity Rule for Fluidized Bed Scale-up", *AIChE J.*, **32**, 1466, 1986.

Horio, M., Ishii, M, Kobukai, Y., and N. Yamanashi, "A Scaling Law for Circulating Fluidized Beds," *J. of Chem. Eng. of Japan*, **22**, pp. 587-592, 1989.

Horio, M., "Scaling Laws of Circulating Fludized Beds, *Proceedings of the Workshop on Materials Issues in Circulating Fluidized-Bed Combustors*, EPRI Report GS-6747, Feb. 1990.

Ishii, H. and I. Murakami, "Evaluation of the Scaling Law of Circulating Fluidized Beds in regard to Cluster Behavior", in *Circulating Fluidized Bed Technology III*, P.Basu, M. Horio, and M. Hasatani (eds.), Pergamon Press, 1991.

Ishii, H., T. Nakajima, and M. Horio, "The Clustering Annular Flow Model of Circulating Fluidized Beds," *J. Chem. Eng. Japan*, **22**, pp. 484-490, 1989.

Iverson, H.W., and R. Balent, "A Correlating Modulus for Fluid Resistance in Accelerated Motion," *J. Appl. Phys.*, **22**, pp. 324-328, 1951.

Jackson, R., "The Mechanics of Fluidized Beds, Parts 1 and 2", *Trans. Instn. Chem. Engrs.*, **41**, pp. 12-28, 1963.

Jeffery, G. B., The Motion of Ellipsoidal Particles Immersed in a Viscous Fluid," *Proc. Roy. Soc. A*, **102**, pp. 161-179, 1922.

Jeffrey, R. C., and J. R. A. Pearson, "Particle Motion in Laminar Vertical Tube Flow," *J. Fluid Mech.*, **22**, pp. 721-735, 1964.

Jenkins, J.T., and M.W. Richman, "Kinetic Theory for Plan Flows of a Dense Gas of Identical Rough, Inelastic Circular Disks," *Phys. Fluids A.*, **28**, pp. 3485-3494, 1985.

Johansen, S.T., "The Deposition of Particles on Vertical Walls," *Int J. Multiphase Flow*, **17**, pp. 355-376, 1991.

Joseph, D.D., T.S. Lundgren, R. Jackson, and D.A.Saville, "Ensemble Averaged and Mixture Theory Equations for Incompressible Fluid-Particle Suspensions," *Int. J. Multiphase Flow*, **16**, pp. 35-42, 1990.

Karnis, A., H. L. Goldsmith, and S. G. Mason, "Axial Migration of Particles in Poiseuille Flow," *Nature*, **200**, pp. 159-160, 1963.

Karnis, A., H.L. Goldsmith, and S.G. Mason, "The Kinetics of Flowing Dispersions: I. Concentrated Suspensions of Rigid Particles," *J. of Colloid and Interface Sci.*, **22**, pp. 531-553, 1966.

Karri, S. B. Reddy and T. M. Knowlton, "A Practical Definition of the Fast Fluidization Regime," *Proc. 3rd Int. Conf. on Circulating Fluidized Beds*, Nagoya, Japan, 1990.

Kay, J.M., *An Introduction to Fluid Mechanics and Heat Transfer*, Cambridge University Press: Cabridge, 1957.

Keller, J.B., Rubenfeld, L.A., and J.E. Molyneux, "Extremum Principles for Slow Viscous Flows with Applications to Suspensions," *J. Fluid Mech.*, **30**, pp. 97-125, 1967.

Kensuke, Usui and Sato Kazuo, "Vertically Downward Two-Phase Flow," *J. of Nucl. Sci. and Tech.*, **26**, pp. 670-680, 1989.

Kiem, S.R., "Fluid Resistance to Cylinders in Accelerated Motion," *Proc. ASCE, J. Hydraul. Div.*, **82**, 1956.

Kline, S.J., *Similitude and Approximation Theory*, McGraw-Hill: New York, 1965.

Kobro, Henrik, *Description of Studvik's Fast Fluidized Bed Prototype*, Studsvik Report No. EM-85/2, 1985.

Koch, D.L, "Kinetic Theory for a Monodisperse Gas-Solid Suspension, *Phys. Fluids A.*, **2**, pp. 1711-1723, 1990.

Korteweg, D. J., "On a General Theorem of the Stability of the Motion of a Viscous Fluid," *Phil. Mag. and Journal of Science*, **XVI**, pp. 112-118, 1883.

Kraemer, H.F., and H.F. Johnson, "Collection of Aerosol Particles in Presence of Electrostatic Fields," *Ind. Eng. Chem.*, **47**, pp. 2426-2434, 1955. Corrigendum, *Ind. Eng. Chem.*, **48**, p. 812, 1956.

Kumaran, V. and D.L. Koch, "Properties of a Bidisperse Particle-Gas Suspension. Part 1: Collision Time Small Compared with Viscous Relaxation Time," *J. Fluid Mech.*, **247**, pp. 623-641, 1993a.

Kumaran, V. and D.L. Koch, "Properties of a Bidisperse Particle-Gas Suspension. Part 2: Viscous Relaxation Time Small Compared with Collision Time," *J. Fluid Mech.*, **247**, pp. 643-660, 1993b.

Lennard-Jones, J.E., "The Equation of State of Gases and Critical Phenomena," *Physica*, **4**, pp. 941-956, 1937.

Leung, L. S., et al., *Ind. Eng. Chem. Process Des. Develop*, **10**, p. 183, 1971.

Li, J. L. Reh, and M. Kwauk, "Application of the Principle of Energy Minimization to the Fluid-Dynamics of Circulating Fluidized Beds," *Proc. 3rd Int. Conf. on Circulating Fluidized Beds*, Nagoya, Japan, 1990.

Li, J., Y. Tung, and M. Kwauk, "Energy Transport and Regime Transition in Particle-Fluid Two-Phase Flow," in *Circulating Fluidized Bed Technology II*, edited by P. Basu and J. F. Large, p. 75, Pergamon Press, Oxford, 1988.

Lin, C.-J., J.H. Peery, and W.R. Schowalter, *J. Fluid Mech.*, **44**, p. 1, 1970.

Litka, A., and L.R. Glicksman, "The Influence of Particle Mechanical Properties on Bubble Characteristics and Solid Mixing in Fluidized Beds," *Powder Technol.*, **42**, pp. 231-239, 1985.

London, F., "The General Theory of Molecular Forces," *Trans. Faraday Soc.*, **33**, pp. 8-26, 1937.

Lovalenti, P.M., and J.F. Brady, "The Force on a Bubble, Drop or Particle in Arbitrary Time-Dependent Motion at Small Reynolds Number," *Phys. Fluids A*, **5**, pp. 2104-2116, 1993c.

Lovalenti, P.M., and J.F. Brady, "The Force on a Sphere in a Uniform Flow with Small Amplitude Oscillations at Finite Reynolds Number," *J. Fluid Mech.*, **256**, pp. 607-614, 1993b.

Lovalenti, P.M., and J.F. Brady, "The Hydrodynamic Force on a Rigid Particle Undergoing Arbitrary Time-Dependent Motion at Small Reynolds Number, *J. Fluid Mech.*, **256**, pp. 561-605, 1993a.

Lundgren, T. "Slow Flow Through Stationary Random Beds and Suspensions of Spheres," *J. Fluid Mech.*, **51**, pp. 273-299, 1972.

Mason, S. G., and R. St. J. Manley, "Particle Motions in Sheared Suspensions: Orientations and Interactions of Rigid Rods," *Proc. Roy. Soc. (London)*, **A238**, pp. 117-131, 1956.

Matsen, John M., "Mechanisms of Choking and Entrainment," *Powder Technol.*, **32**, pp. 21-33, 1982.

Maude, A. D., and J. A. Yearn, "Particle Migrations in Suspension Flows," *J. Fluid Mech.*, **30**, pp. 601-621, 1967.

Maude, A.D., "The End Effects in a Falling-Sphere Viscometer," *Br. J. Appl. Phys.*, **12**, pp. 242-251, 1961.

Maxey, M.R. and J.J. Rieley, Equation of Motion of a Small Rigid Sphere in a Non-Uniform Flow," *Phys. Fluids A*, **26**, pp. 883-889, 1983.

McLaughlin, J.B., "The Lift on a Small Sphere in Wall-Bounded Linear Shear Flows," *J. Fluid Mech.*, **246**, pp. 249-265, 1993.

McTigue, D.F., R.C. Givler, and J.W. Nunziato, "Rheological Effects of Nonuniform Particle Distributions in Dilute Suspensions," *J. Rheology*, **30**, pp. 1053-1076, 1986.

Mei, R. R.J. Adrian and T.J. Hanratty, "Particle Dispersion in Isotropic Turbulence Under Stokes Drag and Basset Force with Gravitational Settling," *J. Fluid Mech.*, **225**, pp. 481-495, 1991a.

Mei, R., and R.J. Adrian, "Flow Past a Sphere with an Oscillation in the Free-Stream Velocity and Unsteady Drag at Finite Reynolds Number," *J. Fluid Mech.*, **237**, pp. 323-341, 1992.

Mei, R., C.J. Lawrence and R.J. Adrian, "Unsteady Drag on a Sphere at Finite Reynolds Number With Small Fluctuations in the Free-Stream Velocity," *J. Fluid Mech.*, **233**, pp. 613-633, 1991b.

Morris, Michael, *Particle Separtor Collection Efficiency Tests Using Isotope Pills for L-valve Solids Velocity Measurement*, Studsvik Report EP-86/70, 1986.

Muller, A., *Abhandlungen zur Mechanik der Flussigkeiten I*, Univ. of Freiburg Press, Breiburg, Switzerland, 1936.

Nakamura, K. and C. E. Capes, "Vertical Pneumatic Conveying: A Theoretical Study of Uniform and Annular Particle Flow Models," *Can. J. of Chem. Eng.*, **51**, pp. 39-46, 1973,

Newby, R.A. and D.L.Keairns, "Test of the Scaling Relationships for Fluid-Bed Dynamics", *Proc. Fluidization V Conference,* pp. 31-38, Elsinore Denmark, 1986.

Nicastro, M.T. and L.R. Glicksman, "Experimental Verification of Scaling Relationships for Fluidized Beds," *Chem. Engng. Sci.*, **39**, 1381-1391, 1984.

Nir, A., H. F. Weinberger, and A. Acrivos, "Variational Inequalities for a Body in a Viscous Shearing Flow," *J. Fluid Mech.*, **68**, pp. 739-755, 1975.

Nunziato, J., S. Passman, C. Givler, D. McTigue, and J. Brady, Continuum Theories for Suspensions. In *Advancements in Aerodynamic, Fluid Mechanics and Hydraulics* (Proc. ASCE Special Conf., Minneapolis, MN) (Edited by Arndt, R., A. Stefan, C. Farrell, and S.N. Peterson), pp. 465-472, 1986.

Odar, F., and W.S. Hamilton, "Forces on a Sphere Acclerating in a Viscous Fluid," *J. Fluid Mech.*, **18**, pp. 302-314, 1964.

Odar, F., "Verification of the Proposed Equation for Calculation of the Forces on a Sphere Accelerating in a Viscous Fluid," *J. Fluid Mech.*, **25**, pp. 591-592, 1966.

Oliver, D. R., "Influence of Particle Rotation on Radial Migration in the Poiseuille Flow of Suspensions," *Nature*, **194**, pp. 1269-1271, 1962.

Oshinowo, Toks, and M. E. Charles, "Vertical Two-Phase Flow - Part I. Flow Pattern Correlations," *Canadian J. of Chem Eng.*, **52**, pp. 25-35, 1974.

Owen, P.R., "Pneumatic Transport," *J. Fluid Mech.*, **39**, pp. 407-432, 1969.

Passman, S.L., J.W. Nunziato, and E.K. Walsh, "A Theory for Multiphase Mixtures" in *Rational Thermodynamics* (Edited by C. Truesdell), pp. 286-325, Springer: New York, 1984.

Passman, S.L., "Mixtures of Granular Materials," *Int. J. Eng. Sci.*, **15**, pp. 117-129, 1977.

Patience, G.S., J. Chaouki, F. Berruti, and R. Wong, "Scaling Considerations for Circulating Fluidized Bed Risers," *Powder Technol.*, **72**, pp. 31-37, 1992.

Prager, S., "Diffusion and Viscous Flow in Concentrated Suspensions," *Physica*, **29**, pp. 129-139, 1963.

Press, W. H., S. A. Teukolsky, W. T. Vetterling, and B.P. Flannery, *Numerical Recipes in C*, Cambridge University Press: Cambridge, 1992.

Prosperetti, A. and A.V. Jones, "Pressure Forces in Disperse Two-Phase Flow," *Int. J. Multiphase Flow*, **10**, pp. 425-440, 1984.

Punwani, D. V., M. V. Modi, and P. B. Tarman, *Proc. Int. Powder and Bulk Solids Handling and Processing Conference*, Powder Advisory Center, Chicago, IL, 1976.

Ranz, W.E., and J.B. Wong, "Impaction of Dust and Smoke Particles," *Ind. Eng. Chem.*, **44**, pp. 1371-1381, 1952.

Rayleigh, Lord, "On the Motion of a Viscous Fluid," *Philosophical Magazine and Journal of Science*, **26**, pp. 776-786, 1913.

Reh, L, "Fluidized Bed Processing," *Chemical Eng. Progress*, **67**, pp. 58-63, 1971.

Repetti, R. V., and E. F. Leonard, "Segre'-Silberberg Annulus Formation: A Possible Explanation,", *Nature*, **203**, pp. 1346-1350, 1964.

Rhodes, M.J., and P. Laussman, "A Study of the Pressure Balance Around the Loop of a Circulating Fluidized Bed," *Can. J. Chem. Engng.*, **70**, pp. 625-630, 1992.

Richardson, J. F., and W. N. Zaki, "Sedimentation and Fluidisation: Part I," *Trans. Instn. Chem. Engrs.*, **32**, pp. 35-53, 1973.

Rietema, K, and H.W. Piepers, "The Effect of Interparticle Forces on the Stability of Gas-Fluidized Beds - I. Experimental Evidence," *Chem. Engng. Sci.*, **45**, pp. 1627-1639, 1990.

Rietema, K., E.J.E. Cottar, and H.W. Piepers, "The Effect of Interparticle Forces on the Stability of Gas-Fluidized Beds - II. Theoretical Derivation of Bed Elasticity on the Basis of van der Waals Forces Between Powder Particles," *Chem. Engng. Sci.*, **48**, pp. 1687-1697, 1993.

Robertson, A. et al., *Second-Generation Pressurized Fluidized Bed Combustion Plant - Conceptual Design and Optimization of the Second-Generation PFB Combustion Plant*, Foster Wheeler Develoment Corporation, FWC/FWDC/TR-89/11 (Phase 1 - Task 1 Report), prepared for U.S. Department of Energy, 1989.

Roy, R. and J.F. Davidson, "Similarity between Gas Fluidized Beds Elevated Temperature Pressure", *Fluidization VI*, pp.293-300, 1988.

Rubinow, S. I., and J. B. Keller, "The Transverse Force on a Spinning Sphere Moving in a Viscous Fluid," *J. Fluid Mech.*, **11**, pp. 447-459, 1961.

Saffman, P. G., "On the Motion of Small Spheroidal Particles in a Viscous Liquid," *J. Fluid Mech.*, **1**, pp. 540-553, 1956.

Saffman, P., "On the Boundary Condition at the Surface of a Porous Medium," *Stud. Appl. Math.*, **93**, 1971.

Saffman, P.G., "The Lift on a Small Sphere in a Slow Shear Flow," *J. Fluid Mech.*, **22**, pp. 385-400, 1965. Corrigendum: *J. Fluid Mech.*, **31**, p. 624.

Scharff, M.F., S.R. Goldman, T.M. Flanagan, T.K. Gregory, and L.D. Smoot, *Project to Provide an Experimental Plan for the MERC 6' x 6' Fluidized Bed Cold Test Model*, Final Report J77-2042-FR, U.S. Dept. of Energy, Contract EY-77-C-21-8156, 1978.

Segre', G., and A. Silberberg, "Behavior of Macroscopic Rigid Spheres in Poiseuille Flow," *J. Fluid Mech.*, **14**, pp. 115-157, 1962.

Segre', G., and A. Silberberg, "Radial Particle Displacements in Poiseuille Flow of Suspensions," *Nature*, **189**, pp. 209-210, 1961.

Slezkin, N. A., and S. M. Shustov, "On Stability of Motion of Suspended Particles in Laminar Flow," *Dokladi Akad. Nauk. SSSR*, **96**, pp. 933-936, 1954.

Slezkin, N. A., "Differential Equations of Motion of Suspensions," *Dokladi Akad. Nauk. SSSR*, **96**, pp. 235-237, 1952.

Smoluchowski, M., "On the Practical Applicability of Stokes' Law of Resistance, and the Modifications of it Required by Certain Cases," Proc. 5th Intern. Cong. Math., Cambridge, pp. 192-201, 1912.

Soo, S.L, G.J. Trezek, R.C. Dimick, and G.F. Hohnstreiter, "Concentration and Mass Flow Distributions in a Gas-Solid Suspension," *I & EC Fund.*, **3**, pp. 98-106, 1964b.

Soo, S.L., "Effect of Electrification on the Dynamics of a Particulate System," *I & EC Fund.*, **3**, pp. 75-80, 1964a.

Starkey, T. V., "The Laminar Flow of Streams of Suspended Particles," *British J. of App. Phys.*, **7**, pp. 52-37, 1956.

Starkey, T. V., "The Laminar Flow of Suspensions in Tubes," *British J. of App. Phys.*, **6**, pp. 34-37, 1955.

Stiehadieh, B., D. Gidaspow, and R.W. Lyczkowski, "Hydrodynamics of Fluidization in a Semicircular Bed with a Jet," *AIChE Jl.*, **30**, pp. 529-536, 1984.

Stuhmiller, J.G., "The Influence of Interfacial Pressure Forces on the Character of Two-Phase Flow Model Equations," *Int. J. Multiphase Flow*, **3**, pp. 551-560, 1977.

Takeuchi, H., et al., "A Quantitative Definition and Flow Regime Diagram for Fast Fluidization," *Powder Technol.*, **47**, pp. 195-199, 1986.

Taylor, G. I., "The Motion of Ellipsoidal Particles in a Viscous Fluid," *Proc. Roy. Soc. A*, **103**, pp. 58-61, 1923.

Tchen, C.M., *Mean Value and Correlation Problems Connected with the Motion of Small Particles Suspended in a Turbulent Fluid*, Ph.D. thesis, Delft, Nijhoff, The Hague, Netherlands, 1947.

Theodore, L., "Sidewise Force Exerted on a Spherical particle in Poiseullian Flow Field," Eng. Sc.D. Dissertation, New York University, New York, 1964.

Tollert, H., "Die Wirkung der Magnus-Kraft in Laminaren Stromungen," *Chemi-Ing.-Techn.*, **26**, pp. 141-150, 1954.

Trevelyan, B. J. and S. G. Mason, "Particle Motions in Sheared Suspensions," *J. Coll. Sci.*, **6**, pp. 354-367, 1951.

Truesdell, C., *Rational Thermodynamics*, McGraw-Hill: New York, 1969.

Tsukada, M, D. Nakanishi, Y. Takii, H. Ishii, and M. Horio, "Hydrodynamic Similarity of Circulating Fluidized Bed under Different Pressure Conditions", *Proc. Int. Conf. Fluid. Bed Combustion,* v.2, pp. 829-834, ASME, N.Y. 1991.

Vejlens, G., *Acta Path. Microbiol. Scand. Suppl.*, **33**, 1938.

Visser, J., "On Hamaker Constants. A Comparison Between Hamaker Constants and Lifshitz - van der Waals Constants," *Adv. Colloid Interface Sci.*, **3**, pp. 331-363, 1972.

Wang, S. K., S.J. Lee, O.C. Jones Jr. and R.T. Lahey Jr., "3-D Turbulence Structure and Phase Distribution Measurements in Bubbly Two-Phase Flows," *Int. Journal Multiphase Flow*, **13**, p. 327-343, 1987.

Weinberger, H. F., "Variational Properties of Steady Fall in Stokes Flow," *J. Fluid Mech.*, **52**, pp. 321-344, 1972.

Wen, C.Y., and Y.H. Yu, "Mechanics of Fluidization," *Chem. Engng. Prog. Symp. Ser.*, **62**, pp. 100-111, 1966.

Westphalen, D., and L.R. Glicksman, "Experimental Verification of Scaling for a Commercial-Size CFB Combustor, *Proc. 4th Int. Conf. on CFB*, Hidden Valley, PA, 1993.

Westphalen, D., *Scaling and Lateral Solid Mixing in Circulating Fluidized Beds*, Ph.D. Thesis, Mass. Inst. of Tech., 1993.

Westphalen, Detlef, *Experimental Verification of Scaling Relationships for Circulating Fluidized Beds*, M.S. Thesis, Massachusetts Instititute of Technology, 1990.

White, F.M., *Viscous Fluid Flow*, McGraw-Hill: New York, 1974.

Yang, W. "Criteria for Choking in Vertical Pneumatic Conveying Lines," *Powder Technol.*, **35**, pp. 143-150, 1983.

Yang, W., "A Mathematical Definition of Choking Phenomenon and a Mathematical Model for Predicting Choking Velocity and Choking Voidage," *AIChE Journal*, **21**, 5, pp. 1013-1015, 1975.

Yang, W., "Correlations for Solid Friction Factors in Vertical and Horizontal Pneumatic Conveyings," *AIChE Journal*, **20**, 3, pp. 605-607, 1974.

Yang, W., "Estimating the Solid Particle Velocity in Vertical Pneumatic Conveying Lines," *Ind. Eng. Chem. Fundam.*, **12**, 3, pp. 349-352, 1973.

Yerushalmi, J., et al, "Flow Regimes in Gas-Solid Contact Systems," *AIChE Symp. Ser.*, **74**, pp. 1-13, 1978

Yousfi, Y. and G. Gau, "Aerodynamique de Lecoulement Vertical de Suspensions Concentrees Gas - Solides - I. Regimes d'Ecoulement et Stabilite Aerodynamique," *Chem. Eng. Science*, **29**, pp. 1939-1946, 1974.

APPENDIX A: MINIMUM FLUIDIZATION TESTS

Minimum fluidization tests for the glass and steel particles used in the viscous limit tests were carried out in a 4-inch diameter test bed. Freeboard height for this bed was typically about 2 inches. A nominal 0-20 cfh rotameter was used for these tests. Pressures at the rotameter exit were determined by manometer readings. Bed pressures were determined by subtracting calculated distributor pressure drops. The calculation of distributor pressure drop was based on separate tests involving measurements of pressure drop through just the distributor plate when the bed had no particles in it.

Minimum fluidization tests for all other particles were carried out in the phase one 1/16 scale Studsvik bed. Freeboard height was typically about 3 inches. Air flows were measured with nominal 2.5 lpm and 10.0 lpm rotameters. Pressures at the rotameter exit were determined by manometer readings. The distributor pressure drop was determined in the same manner as described above.

Figure A.1

Minimum Fluidization Test: Viscous Limit Scaling Steel

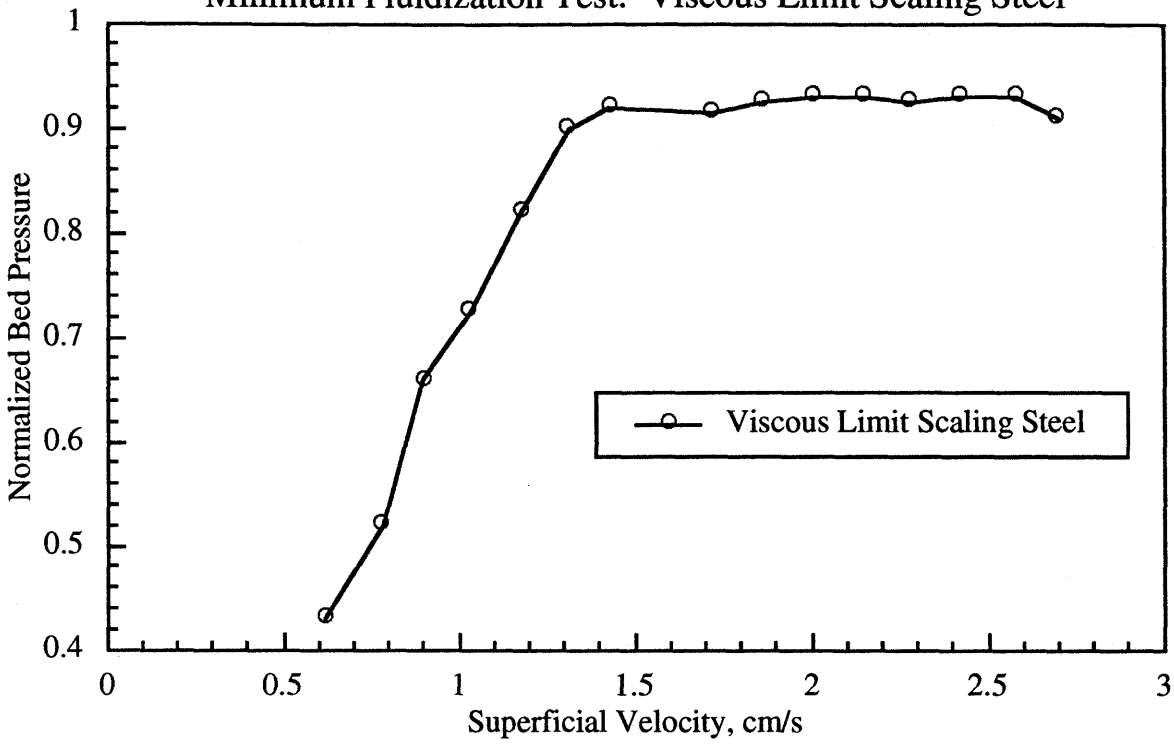

Figure A.2

Minimum Fluidization Test: Viscous Limit Scaling Glass I

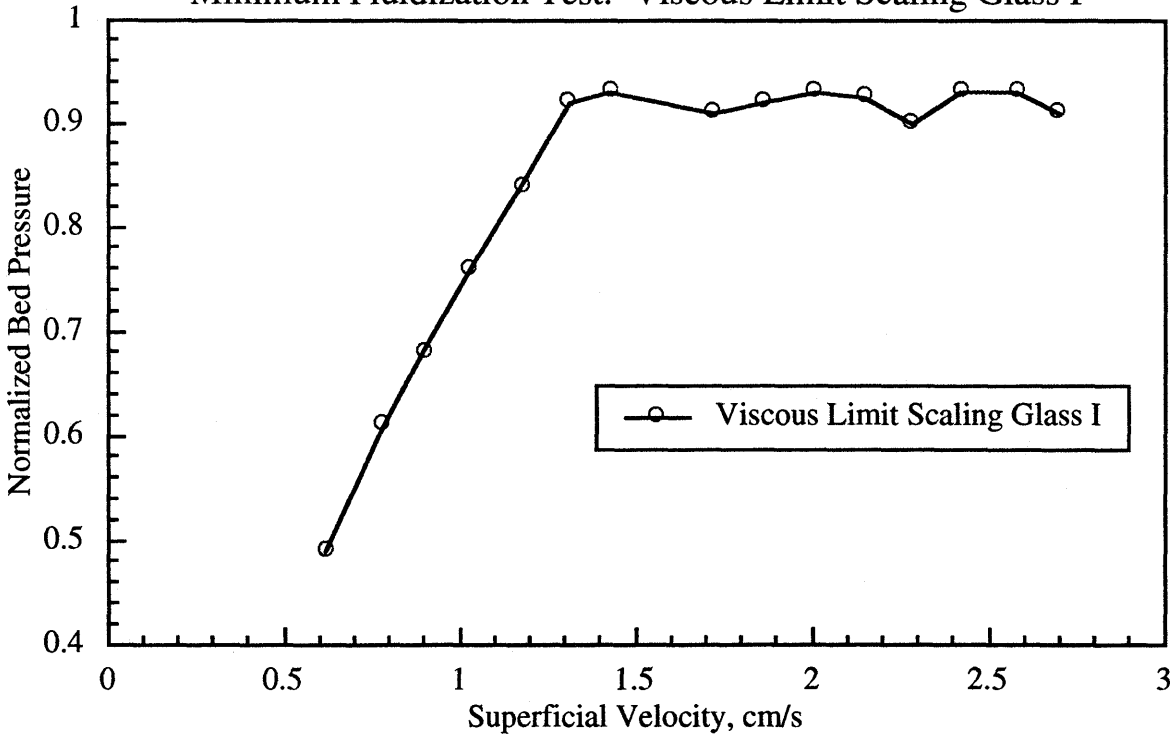

Figure A.3

Minimum Fluidization Test: Viscous Limit Scaling Glass II

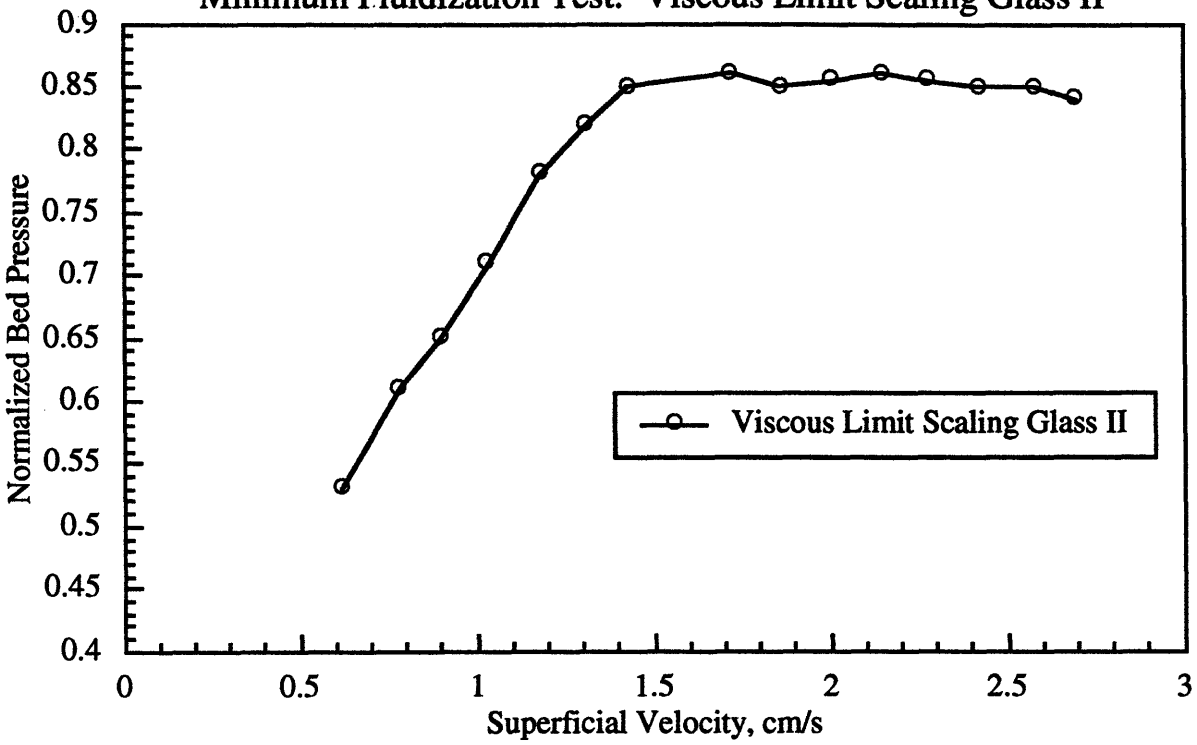

Figure A.4

Minimum Fluidization Test: Simplified Scaling Laws

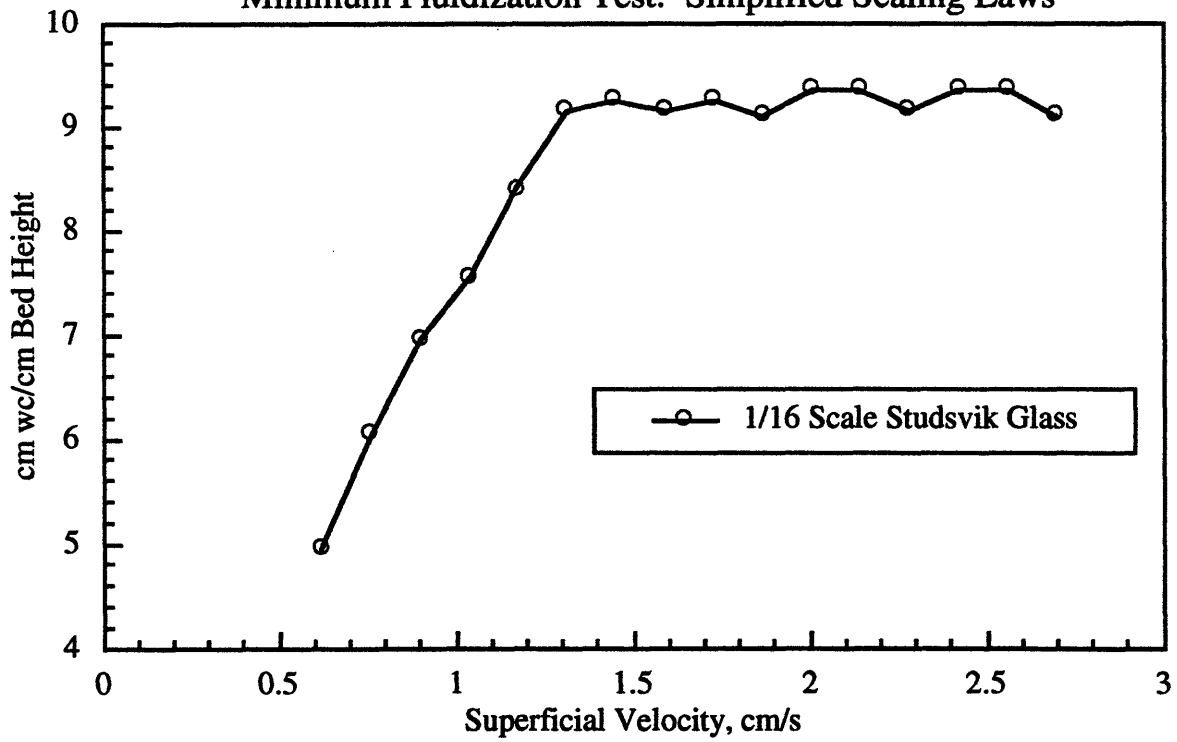

Figure A.5

Minimum Fluidization Test: Simplified Scaling Laws

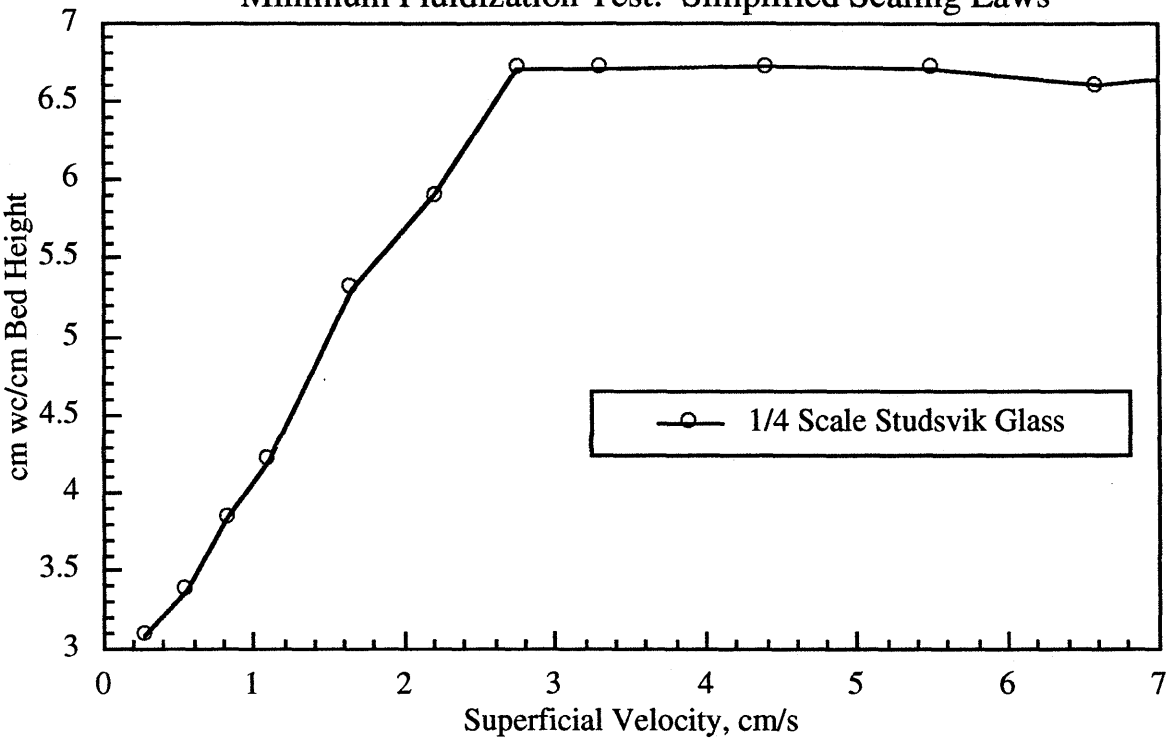

Figure A.6

Minimum Fluidization Test: Simplified Scaling Laws

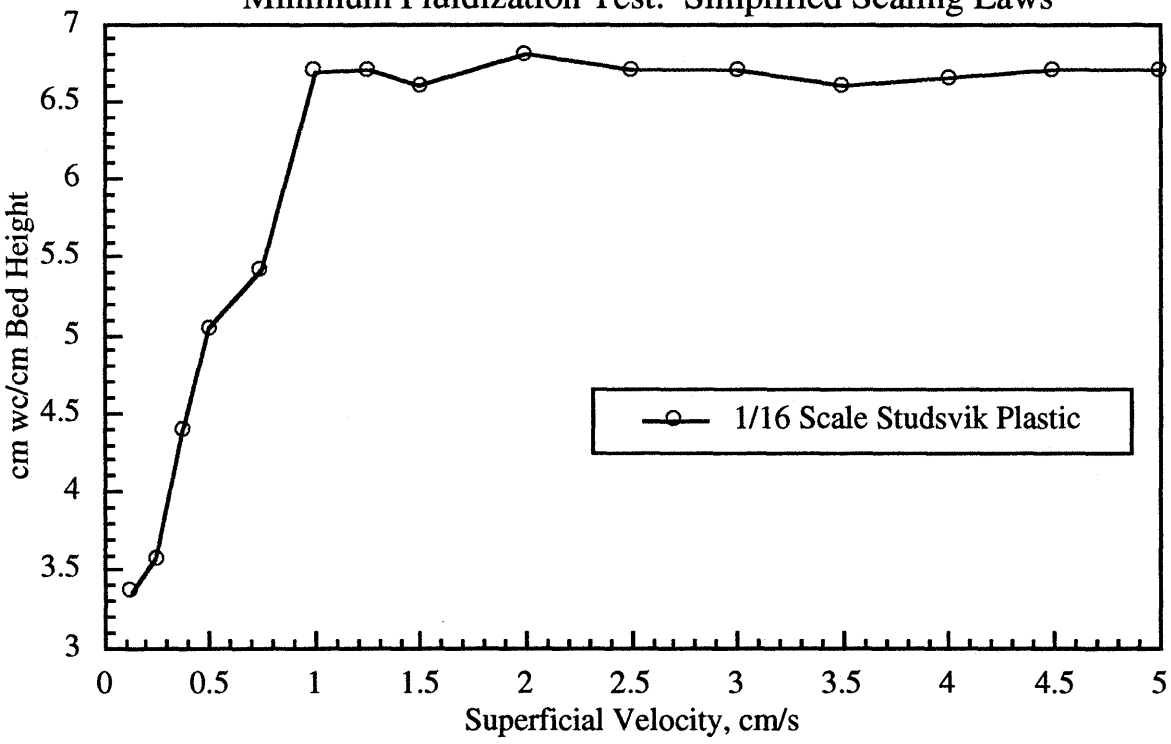

Figure A.7

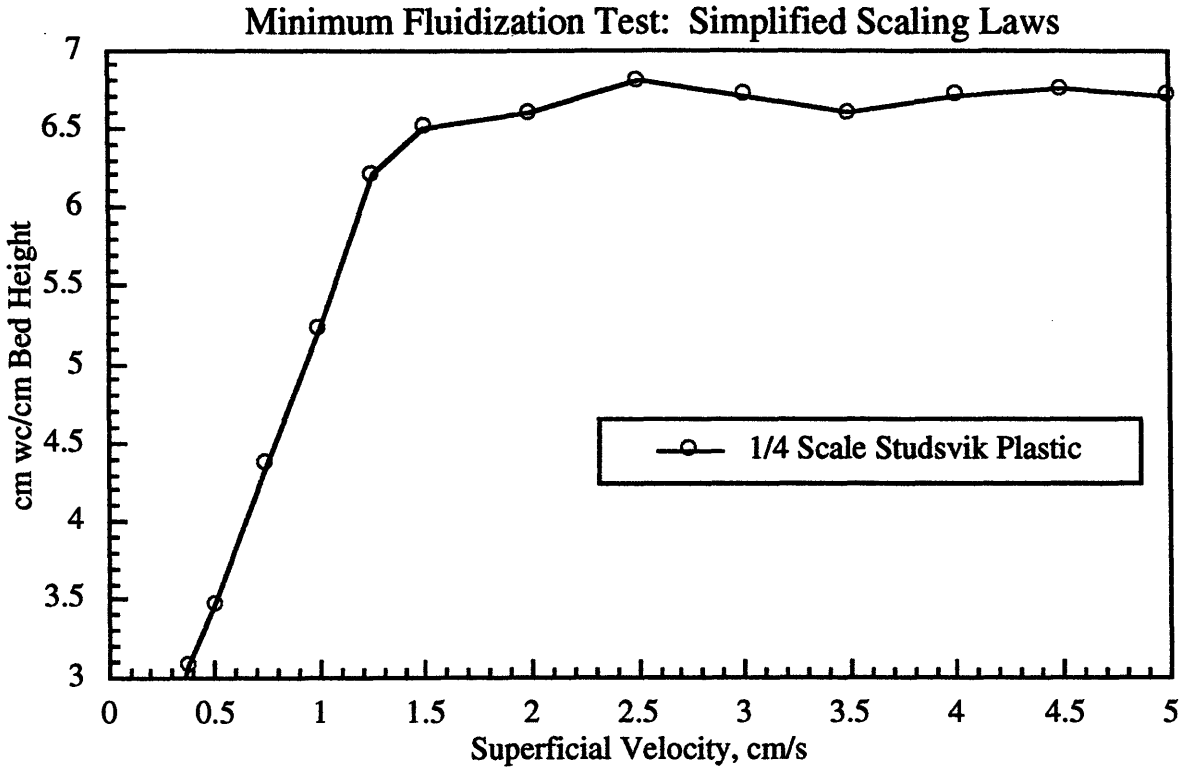

The required mean particle diameter for the 1/16 scale model when scaling the Studsvik hot bed was calculated to be approximately 35 microns. Since the smallest sieve mean diameter was 38 microns, it was not possible to accurately predict the size distribution of the particles required for use in the 1/16 scale model. In order to circumvent this problem, no attempt was made to accurately measure the mean diameter of the particles for use in the 1/16 scale model, rather the particle distribution was selected based on the minimum fluidization velocity. This is possible since, unlike the 1/4 scale model, the 1/16 scale model utilized the simplified scaling laws in which the particle diameter enters only indirectly (it is a factor in determining the minimum fluidization velocity), and the actual particle diameter is not required.

In order to estimate what the mean particle diameter of the steel powder used in the 1/16 scale model was, a series of tests was conducted in which the minimum fluidization velocity was determined for steel powders of known diameter. These plots are give below (Figures A.8-A.12). The minimum fluidization velocities were then plotted and compared to those calculated from the Ergun equation for the known particle diameters. All minimum fluidization velocities were measured in the 1/16 scale Studsvik bed operating in a bubbling bed mode at room temperature and atmospheric pressure. The sphericity of the steel particles required by the Ergun equation was determined in an earlier study using image analysis (Westphalen, 1990) and was determined

to be ~0.7. A plot of the measured and predicted particle diameter vs. minimum fluidization velocity is given in Figure A.13. This curve predicts a mean particle diameter of 27 microns for a minimum fluidization velocity of 0.75 cm/s. Figure A.14 shows the minimum fluidization test for the steel used in the 1/4 scale Studsvik bed when scaling the Studsvik hot bed with the complete set of scaling parameters.

Figure A.8

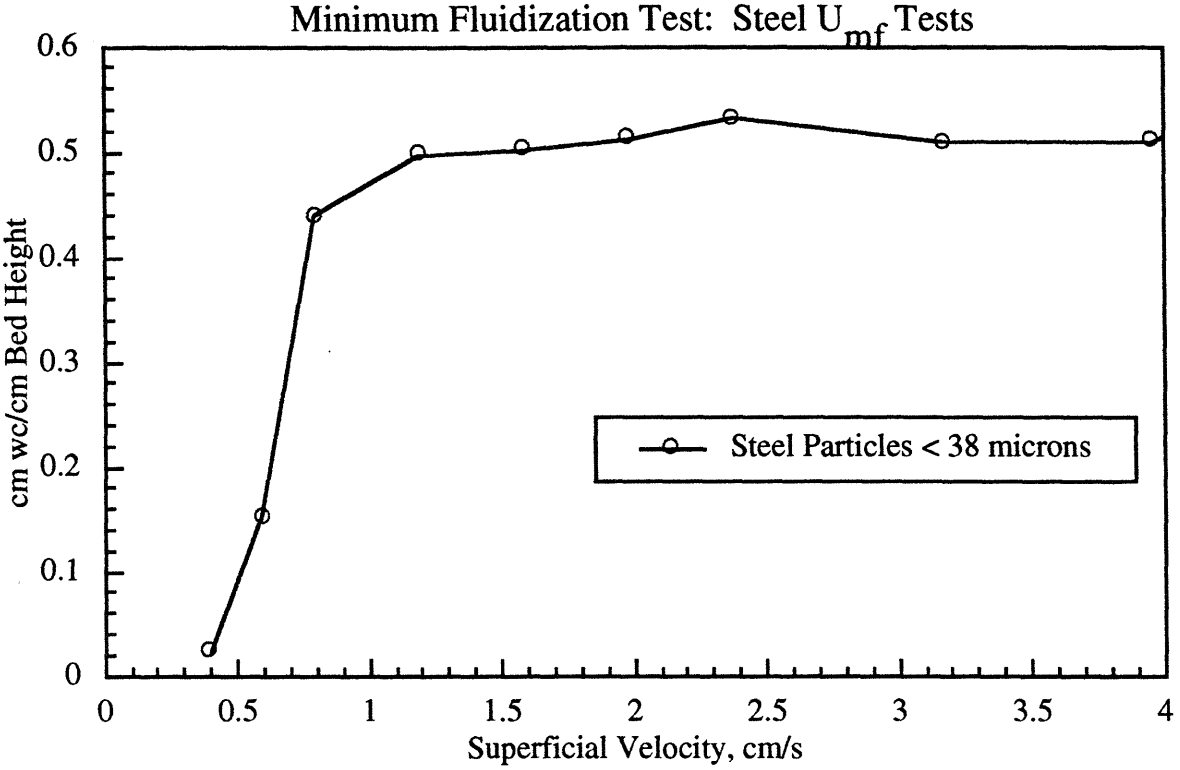

Figure A.9

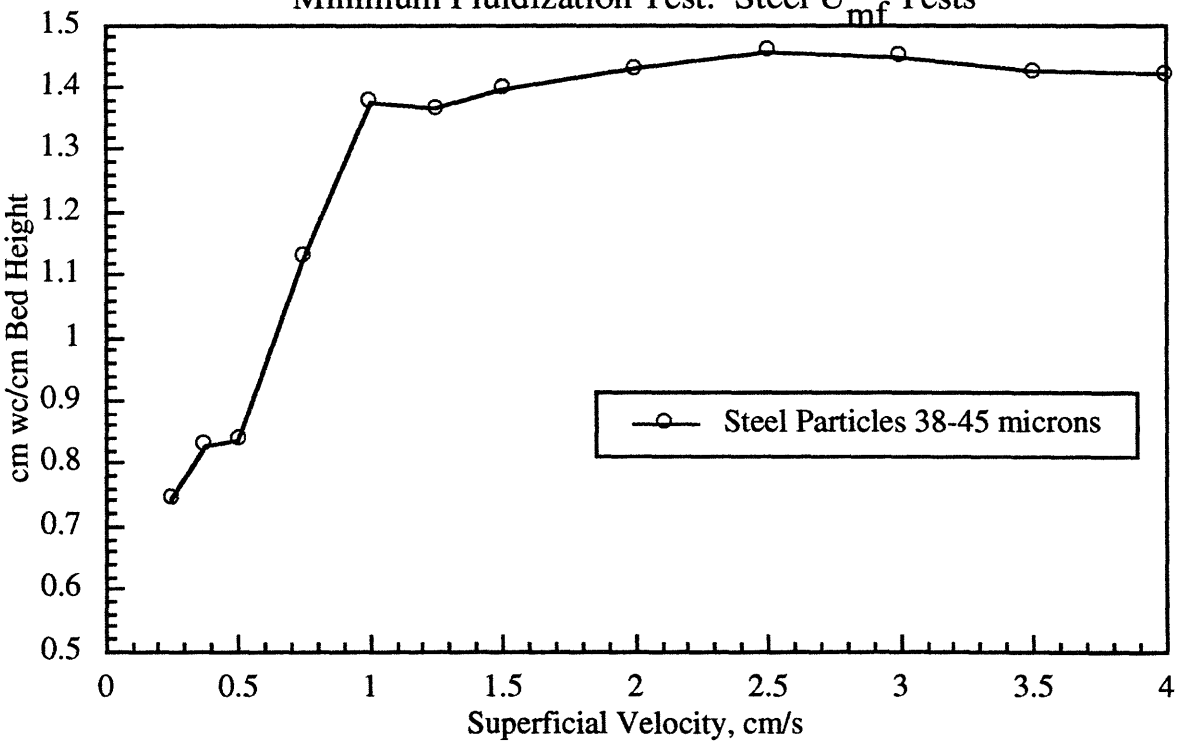

Figure A.10

Minimum Fluidization Test: Steel U_{mf} Tests

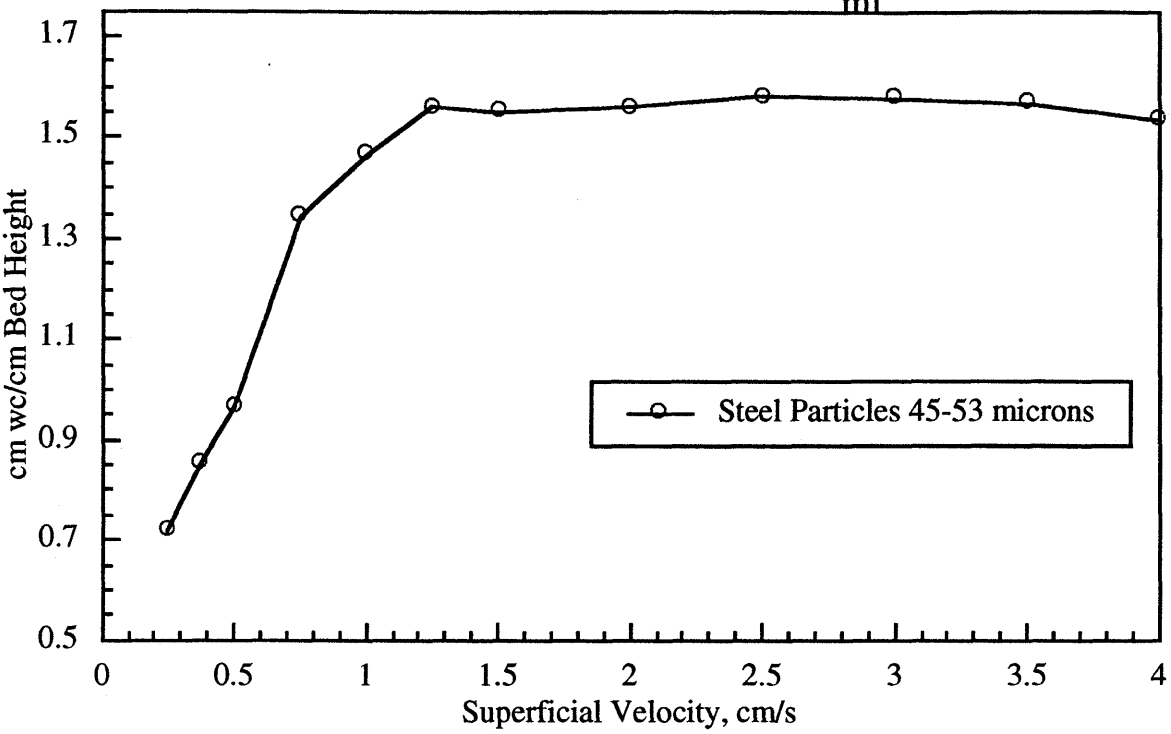

Figure A.11

Minimum Fluidization Test: Steel U_{mf} Tests

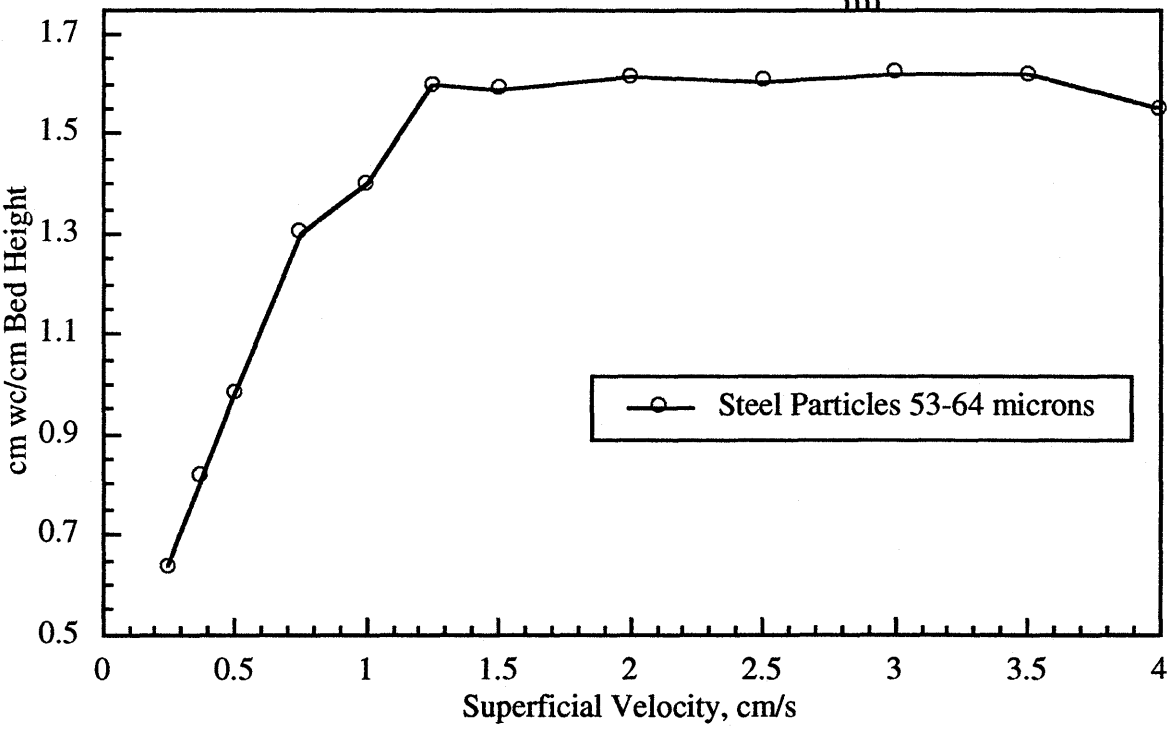

Figure A.12

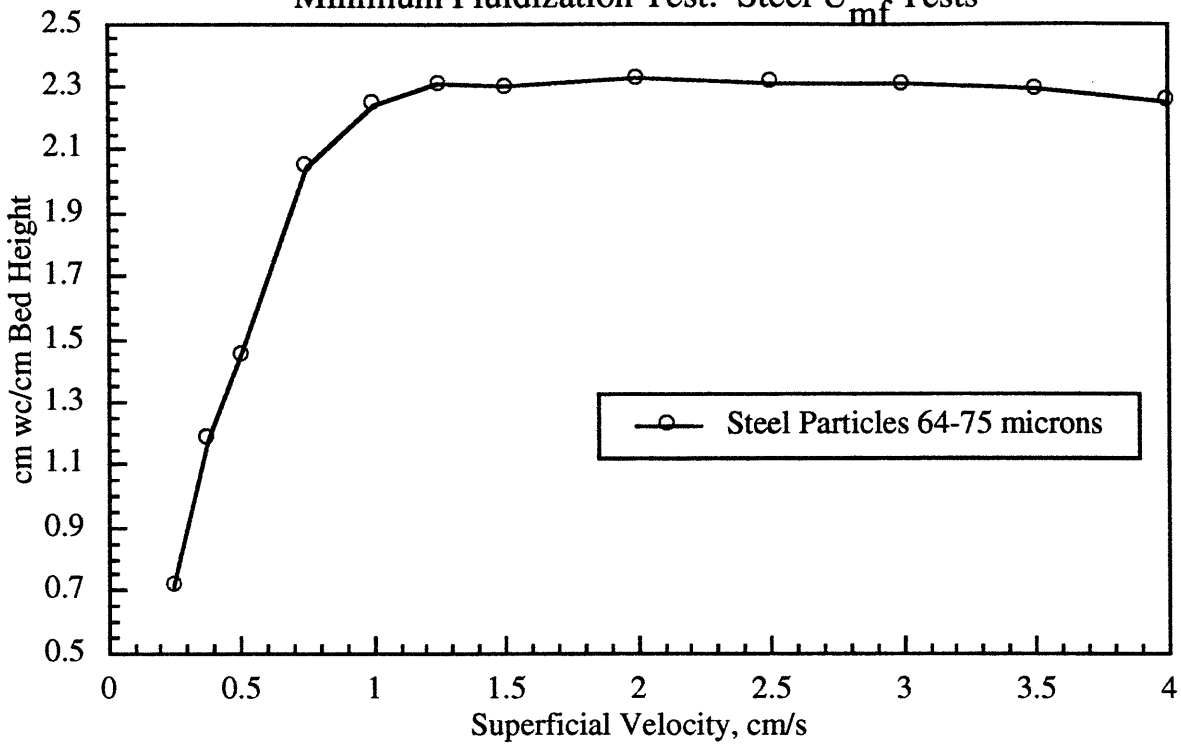

Figure A.13

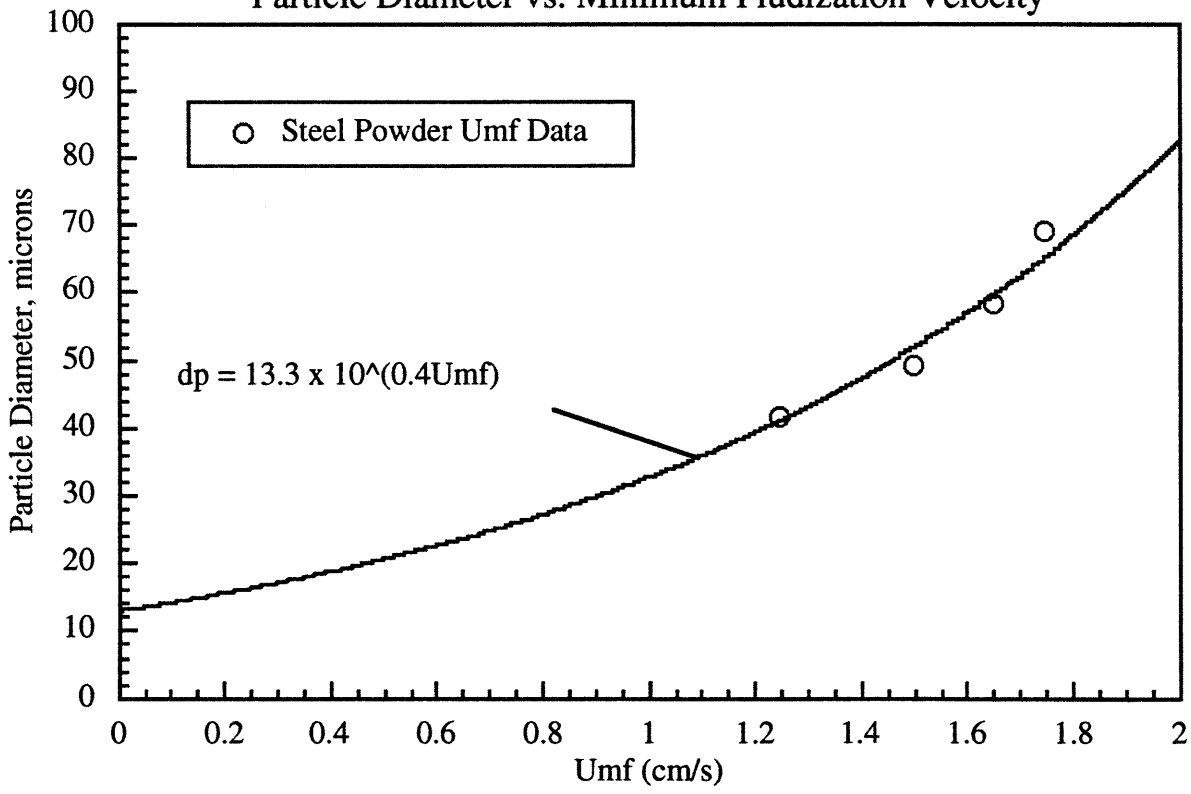

Figure A.14

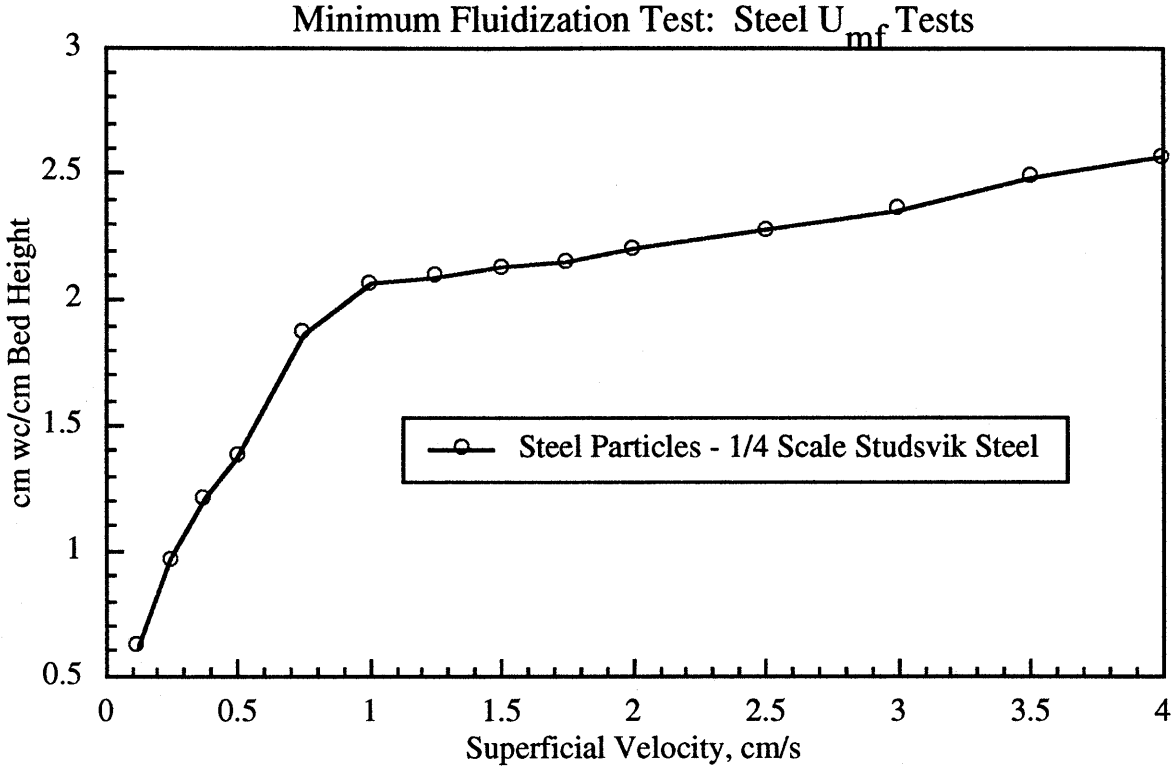

A summary of the minimum fluidization data is given in Table A.1.

Table A.1

Bed Material	Tests Used	Bed Used	Particle Diameter (microns)	U_{mf} (cm/s)
Steel	Viscous Limit Scaling	1/4 Scale UBC Bed	49.5	1.40
Glass I	Viscous Limit Scaling	1/4 Scale UBC Bed	88.3	1.40
Glass II	Viscous Limit Scaling	1/4 Scale UBC Bed	81.6	1.70
Glass	Viscous Limit and Simplified Scaling Laws	1/4 Scale UBC Bed and 1/16 Scale Studsvik Bed	78.7	1.40
Plastic	Viscous Limit and Simplified Scaling Laws	1/16 Scale Studsvik Bed	99.5	0.85
Glass	Simplified Scaling Laws	1/4 Scale Studsvik Bed	112.3	2.80
Plastic	Simplified Scaling Laws	1/4 Scale Studsvik Bed	144.5	1.50
Steel	Studsvik Hot Bed Scaling	1/16 Scale Studsvik Bed	~26	0.75
Steel	Studsvik Hot Bed Scaling	1/4 Scale Studsvik Bed	57.7	1.40

REFERENCES

Westphalen, Detlef, "Experimental Verification of Scaling Relationships for Circulating Fluidized Beds," M.S. Thesis, Massachusetts Institute of Technology, 1990.

APPENDIX B: PRESSURE TRANSDUCER CALIBRATIONS

B.1 1/4 SCALE UBC BED

Pressure transducers A through G, used to measure bed differential pressures, were all calibrated for pressures spanning their expected range of +/- 14 in. wc (+/- 3.5 kPa). Pressure transducer H, used to measure the overall bed differential pressure, was calibrated for its range of 0-1 psi (0-6.9 kPa). During calibration and subsequent use of the pressure transducers, power supply voltage was 10.4 volts. Transducers A through G were calibrated with a manometer inclined at 17.5 degrees from the horizontal. Transducer H was calibrated with the same manometer in a vertical direction orientation. Calibration data and linear curve fit constants are tabulated below. The constants are defined based on the following equation for measure pressure:

$$\text{Pressure} = G^*(\text{Voltage}) + P_r$$

Table B.1: Pressure Transducer Calibrations for 1/4 Scale UBC Bed

Transducer	G (cm wc/V)	P_r (cm wc)	σ (cm wc)
A	949.0	0.2247	0.63
B	941.1	0.2494	0.51
C	936.3	0.4489	1.05
D	970.0	0.4589	0.20
E	915.8	0.5354	0.85
F	942.2	0.3027	0.48
G	962.4	0.1021	0.21
H	10.80	-13.475	0.16

B.2 1/16 SCALE STUDSVIK BED

Pressure transducers A through D used to measure bed differential pressures near the bottom of the bed, were all calibrated for pressures spanning their expected range of +/- 14 in. wc (+/- 3.5 kPa). Pressure transducers E through H, also used to measure the differential pressures, were calibrated for its range of 0-1 psi (0-6.9 kPa). These transducers were used to measure differential pressures near the top of the bed. During calibration and subsequent use of the pressure transducers, power supply voltage was 12.2 volts. All transducers were calibrated with a manometer inclined at 17.5 degrees from the horizontal. Calibration data and linear curve fit constants are tabulated below. The constants are defined based on the following equation for measure pressure:

Pressure = G*(Voltage) + P_r

Table B.2: Pressure Transducer Calibrations for 1/16 Scale Studsvik Bed

Transducer	G (cm wc/V)	P_r (cm wc)	σ (cm wc)
A	949	-0.137	0.65
B	941	0.209	0.49
C	936	-0.308	0.93
D	971	-0.143	0.27
E	0.642	-1.802	0.00941
F	0.628	-1.764	0.00695
G	0.635	-1.533	0.00546
H	0.632	-1.793	0.00745

B.3 1/4 SCALE STUDSVIK BED

All pressure transducers (A through H) in the 1/4 scale Studsvik bed used to measure bed differential pressures were all calibrated for pressures spanning their expected range of +/- 14 in. wc (+/- 3.5 kPa). During calibration and subsequent use of the pressure transducers, power supply voltage was 10.1 volts. All transducers were calibrated with a manometer inclined at 17.5 degrees from the horizontal. Calibration data and linear curve fit constants are tabulated below. The constants are defined based on the following equation for measure pressure:

$$\text{Pressure} = G^*(\text{Voltage}) + P_r$$

Table B.3: Pressure Transducer Calibrations for 1/4 Scale Studsvik Bed

Transducer	G (cm wc/V)	P_r (cm wc)	σ (cm wc)
A	2.467	0.578	0.131
B	2.234	0.253	0.144
C	2.487	0.387	0.161
D	2.455	0.306	0.129
E	0.634	0.465	0.088
F	0.622	0.532	0.068
G	0.577	0.385	0.026
H	0.576	0.344	0.025

B.4 1/2 SCALE FOSTER WHEELER BED

All pressure transducers (1 through 6) in the 1/2 scale Foster Wheeler bed used to measure bed differential pressures were calibrated for pressures spanning their expected range. During calibration and subsequent use of the pressure transducers, power supply voltage was 12.0 volts. All transducers were calibrated with a manometer inclined at 17.5 degrees from the horizontal. Calibration data and linear curve fit constants are tabulated below. The constants are defined based on the following equation for measure pressure:

$$\text{Pressure} = G^*(\text{Voltage}) + P_r$$

Table B.4: Pressure Transducer Calibrations for 1/4 Scale Studsvik Bed

Transducer	G (cm wc/V)	P_r (cm wc)	σ (cm wc)
1	6.173	-6.296	0.173
2	6.173	-6.481	0.161
3	6.173	-6.358	0.127
4	0.840	-0.366	0.055
5	3.125	-3.281	0.037
6	3.145	-3.365	0.031

APPENDIX C: ROTAMETER CALIBRATION

C.1 1/4 SCALE UBC BED AIR FLOW SETUP

The air flow measurement equipment for the 1/4 Scale UBC Bed was obtained and calibrated as part of an earlier study to verify the full set of scaling laws for circulating fluidized beds. Air was designed to enter the 1/4 Scale UBC bed in two locations. The two air streams are designated the primary and secondary air. The secondary air ports were not utilized in this study. The primary air flow is fitted with an exit pressure gauge. The primary air rotameter measures in the range from 2 to 10 cfm, and the pressure gauge is 15 psig full scale. Calibration of the rotameter and gauge combination was done with a square-edged orifice plate fitted with flange taps. The tests covered flow ranges at expected pressure ranges (0-10 psig). The data was analyzed to determine the calibration constants A and B for the following equation.

$$Q_a = (AR+B)\sqrt{\left(1+\frac{P_g}{P_a}\right)}$$

where Q_a is the flow at atmospheric pressure P_a, P_g is the gauge pressure at the rotameter exit, and R is the rotameter reading.

C.2 1/16 SCALE STUDSVIK BED AIR FLOW SETUP

For the phase one 1/16 scale Studsvik bed (no boot, secondary air or simulated refractory), air enters the bed through the distributor box and at the bottom of the pneumatic return line. The two air flows are measured separately with rotameters fitted with exit pressure gauges. The rotameters measure in the range from 2 to 10 cfm, and the pressure gauges are 15 psig full scale. Calibration of the rotameters and gauge combinations was done in the same manner as the 1/4 scale UBC bed setup (i.e., with a square-edged orifice plate fitted with flange taps). The tests covered flow ranges at expected pressure ranges with the data again being fit to the equation:

$$Q_a = (AR+B)\sqrt{\left(1+\frac{P_g}{P_a}\right)}$$

For the phase two 1/16 scale Studsvik bed (boot, secondary air ports, and simulated refractory added), air enters the bed through the secondary air ports, the distributor box, and at the bottom of the pneumatic return line. All three air flows are measured separately with an additional rotameter fitted with exit pressure gauge being added to measure the secondary air flow. Calibration of the rotameter and gauge combinations was conducted using the same technique as that used with the phase one setup.

C.3 CALIBRATION OF PRIMARY AND SECONDARY AIR ROTAMETERS

Calibration data for the rotameters used to measure primary and secondary air flows are presented below. The rotameters used to measure the primary and secondary flows had nominal ranges from 2 to 10 cfm. Exit pressure gauges had a 1-15 psig ranges. The rotameters were calibrated with a square edge orifice plate fitted with flange taps. The orifice plate pipe size was two-inches, and the diameter ratio β was 0.15. Calibration covered rotameter indications ranging from 1.6 to 8 cfm at exit pressure ranging from about 1 to 10 psig. A valve at the exit of the rotameters allowed variation of exit pressure as well as flow rate. Orifice plate pressure drop was measured in a water-filled manometer.

The calibration data was fit to modified linear curve fits of the form

$$Q_a = (AR+B)\sqrt{\left(1+\frac{P_g}{P_a}\right)}$$

Were Q_a is the volumetric flow rate at atmospheric pressure, R is the rotameter reading, P_g is the rotameter exit gauge pressure, P_a is atmospheric pressure, and A and B are the calibration constants. Least squares solutions for A and B were determined.

Air flow with the orifice plate was calculated based on the ASME standard for square edge orifice plates (Bean, 1971). The calculation procedure was automated in a FORTRAN program.

The calculated calibration constants for the rotameters are as tabulated below. Standard deviation for the calibration data, also provided below, represents deviation of actual flow divided by the pressure correction function from the linear curve fit AR + B.

Table C.1: Rotameter Calibration Constants

Rotameter	Which Bed Used	A	B	σ
Primary Air (2-10 cfm)	1/4 Scale UBC	1.0343	0.0244	0.0507
Primary Air (2-10 cfm)	1/16 Scale Studsvik	1.0347	0.0239	0.0422
Secondary Air (2-10 cfm)	1/16 Scale Studsvik	1.0141	0.0003	0.0449

C.4 ROTAMETER CALIBRATION FOR MINIMUM FLUIDIZATION TESTS

The minimum fluidization test bed air flows for the glass and steel used in the viscous limit scaling tests were measured with 20-scfh and 100-scfh nominal rotameters. Calibration of the rotameters was done by timing entry of air into an inverted calibrated cylinder which was partially submerged in water. Air was delivered to the cylinder just above waterline, and the top of the cylinder had a removable cork. Pressure in the cylinder during measurement was kept equal to atmospheric pressure by raising the cylinder so that water levels inside and outside the cylinder were always equal. This arrangement allowed reading of the rotameter and measurement of the flow without disturbing the flow conditions. Pressure at the rotameter exits were measured with manometers Fifteen test points were used in calibrating the 20-scfh rotameter. The standard deviation from the linear calibration curve for this rotameter was 0.093 scfh, or about 0.5 percent of full scale. Thirty-nine points were used in calibrating the 100-scfh rotameter. Standard deviation from the calculated linear calibration curve was 0.59, or about 0.6 percent of full scale.

Minimum fluidization tests for all other bed materials were measured in the 1/16 scale Studsvik bed operating in a bubbling mode. The air flows for these tests were measured with 2.5 and 10.0 lpm rotameters. The rotameters were calibrated using a square edged orifice plate fitted with flange taps and a manometer inclined at 17.5 degrees from the horizontal. The orifice plate pipe size was two-inches, and the diameter ratio β was 0.15. Ten test points were used in calibrating the 2.5-lpm rotameter. The standard deviation from the linear calibration curve for this rotameter

was 0.013 lpm, or about 0.5 percent of full scale. Fifteen points were used in calibrating the 10-lpm rotameter. Standard deviation from the calculated linear calibration curve was 0.042 lpm, or about 0.4 percent of full scale.

Table C.2: U_{mf} Rotameter Calibration Constants

Rotameter	A	B	σ
Nom. 20-cfh	1.011	-0.54	0.093
Nom. 100-cfh	1.0133	-1.38	0.59
Nom. 10 lpm	1.018	0.26	0.042
Nom. 2.5 lpm	1.055	-0.15	0.013

C.5 REFERENCES

Bean, H. S., ed., "Fluid Meters - Their Theory and Application, ed., 6", ASME, 1971.

Westphalen, Detlef, "Experimental Verification of Scaling Relationships for Circulating Fluidized Beds," M.S. Thesis, Massachusetts Instititute of Technology, 1990.

APPENDIX D: PARTICLE CHARACTERIZATION

The size distributions of all solids were determined using sieve analysis. The sieves used were standard U.S. series sieves. Not all standard sieves in the measured size ranges were available for the sieve analyses. Where there were missing sieves, it was assumed that material falling in a smaller sieve would have been evenly distributed between it and the missing adjacent larger sieves.

The reported mean diameters were calculated based on surface area averaging. For these calculations, it was assumed that the mean diameter for a sieve size range is the arithmetic mean of the range size extremes. For the smallest and largest size ranges of a sieve test, the mean diameter was assumed to be the mesh size of the next smaller or larger sieve which was not used. Given these assumptions for size range diameters d and the measured range masses m, the overall surface mean diameter was calculated as follows.

$$d_{pm} = \frac{\sum_j m_j}{\sum_j \frac{m_j}{d_{pj}}}$$

Cumulative size distribution plots for the particles are given below.

Figure D.1

Particle Size Distributions for Verification of Complete Scaling Laws

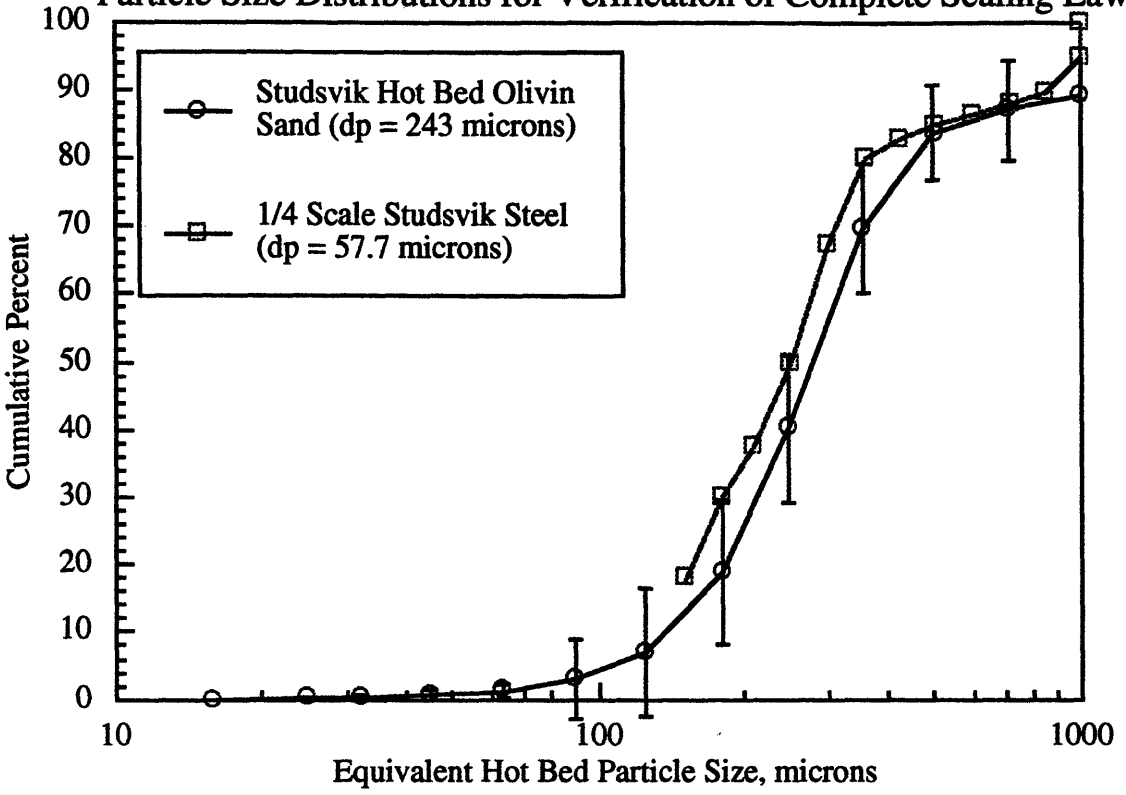

Figure D.2

Particle Size Distributions for Viscous Limit Scaling Laws

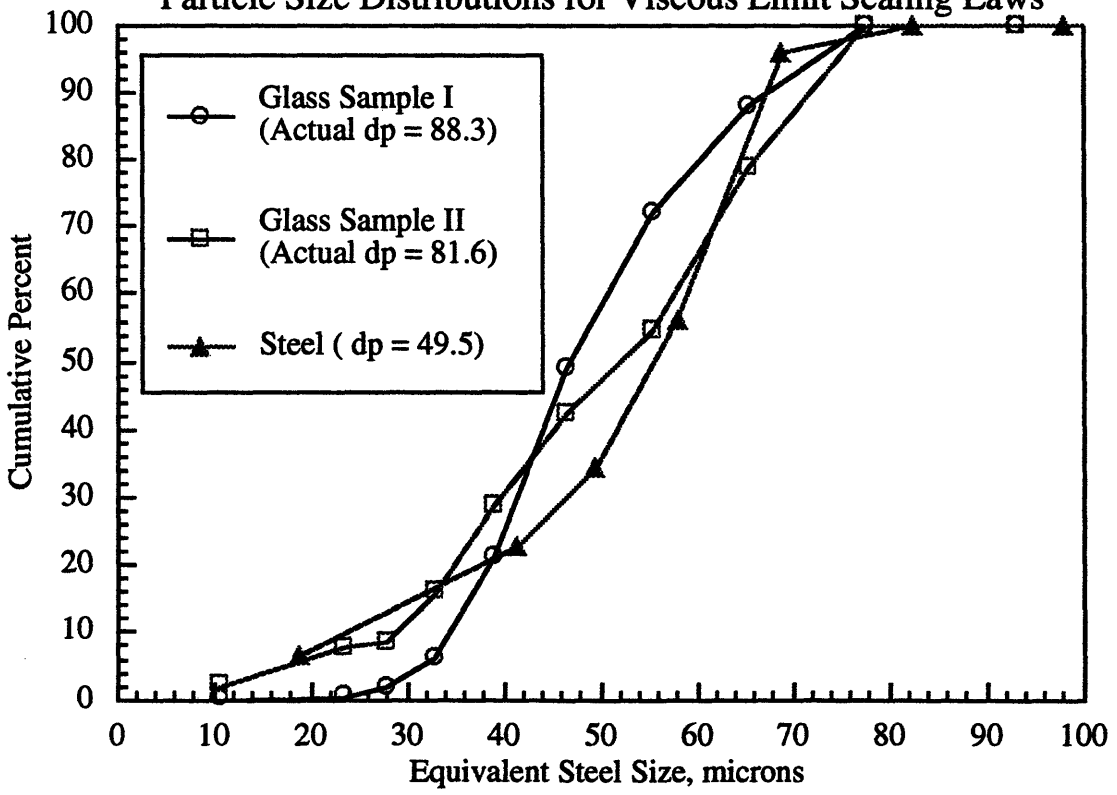

Figure D.3

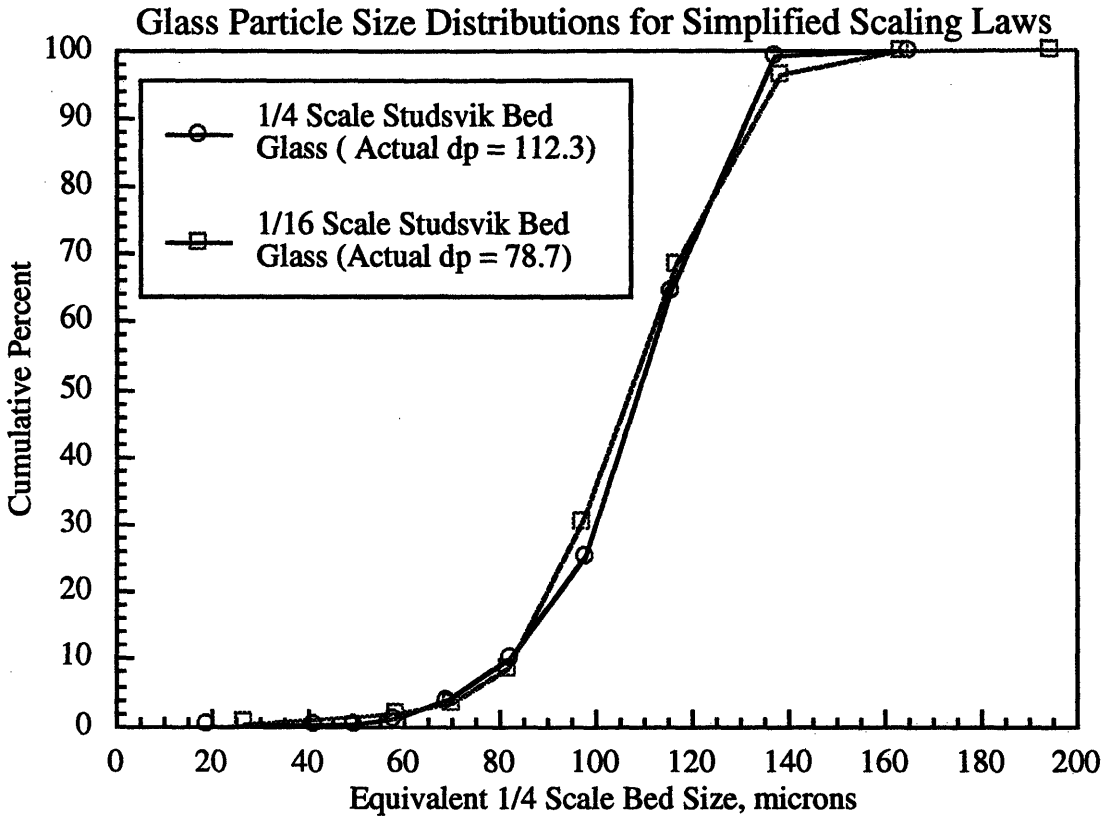

Figure D.4

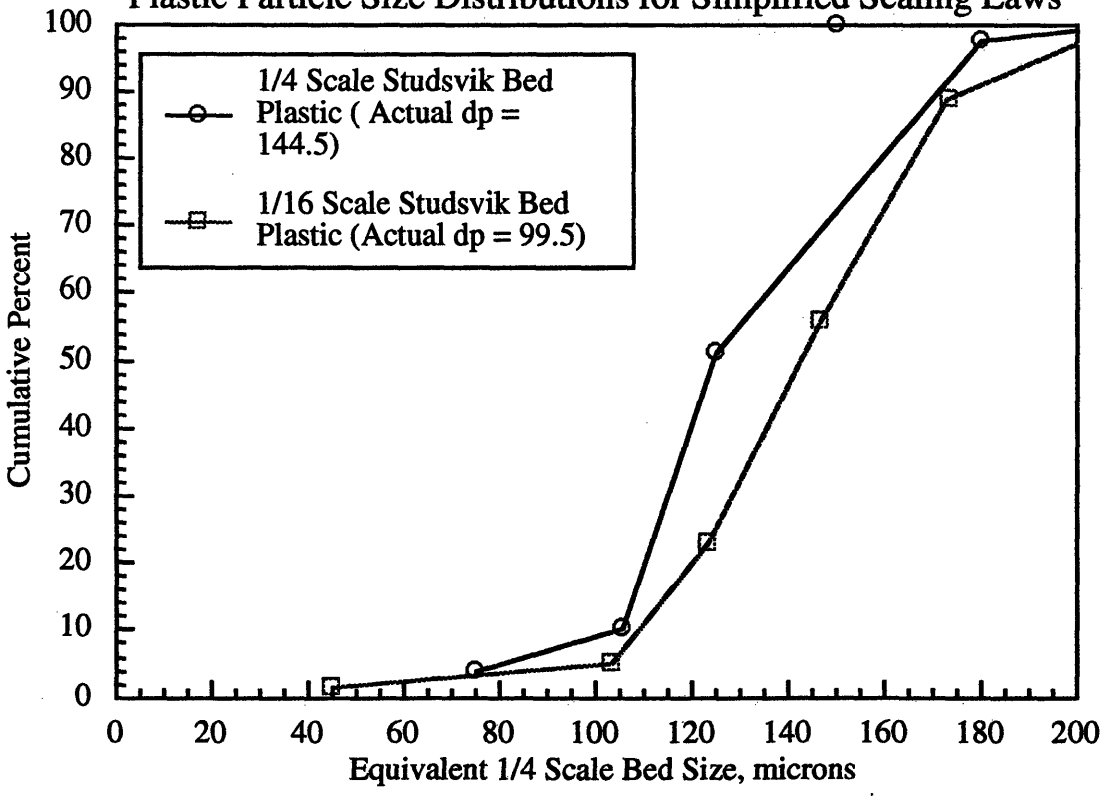

Figure D.5

Comparison of Dimensionless Particle Size Distributions - Pressurized Bed Scaling

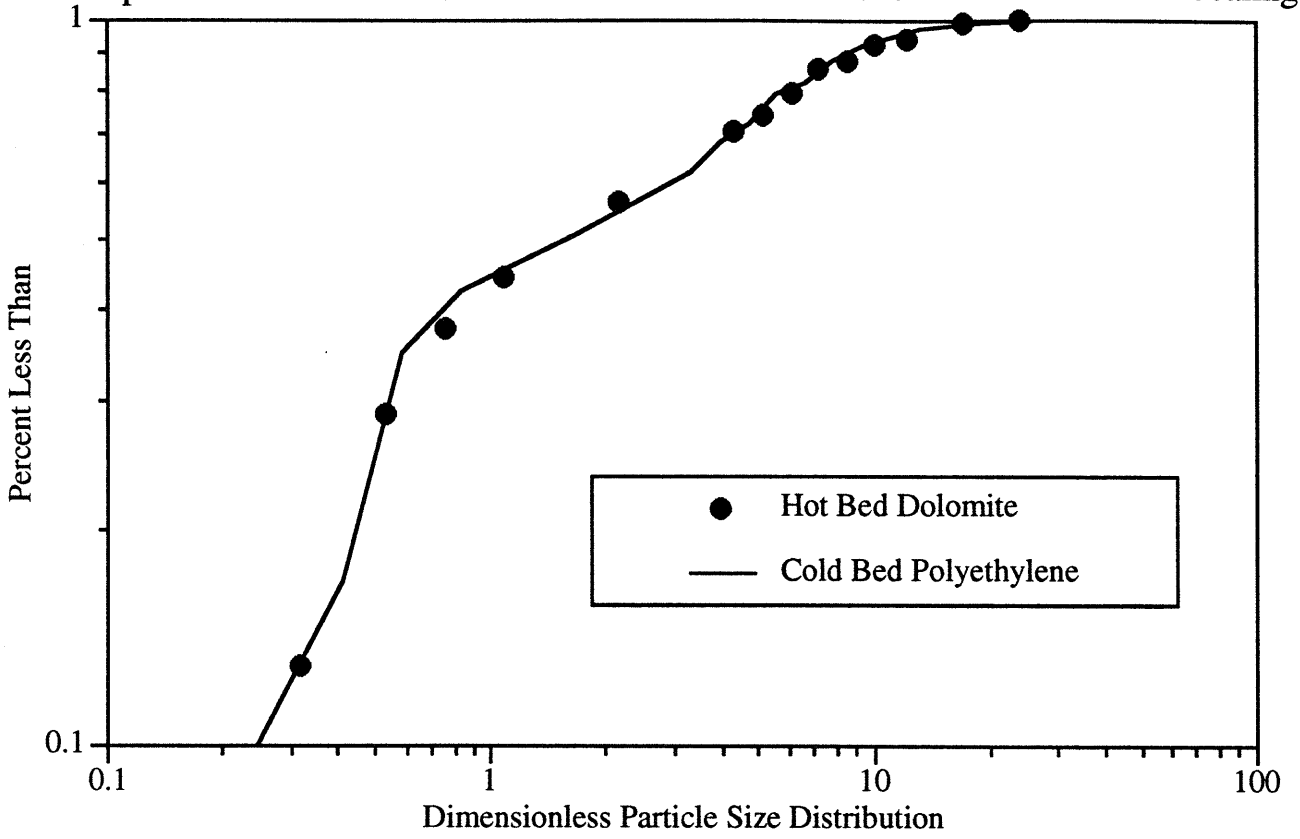

Table D.1
Viscous Limit Glass Properties

	Viscous Limit Glass I	Viscous Limit Glass II
Density	2.54 g/cc	2.54 g/cc
Mean Diameter	88.3 microns	81.6 microns
Loose Pack Voidage	42%	42%
Sphericity	1.0	1.0
u_{mf}	1.40 cm/s	1.70 cm/s

Table D.2
Viscous Limit Steel Powder Properties

	Viscous Limit Steel
Density	7.25 g/cc
Mean Diameter	49.5 microns
Loose Pack Voidage	65%
Sphericity	0.6 - 0.8
u_{mf}	1.40 cm/s

Table D.3
Plastic Properties for Scaling with Constant ρ_s/ρ_f

	1/4 Scale Studsvik	1/16 Scale Studsvik
Density	1.40 g/cc	1.40 g/cc
Mean Diameter	144.5 microns	99.5 microns
Loose Pack Voidage	57%	55%
Sphericity	0.5 - 0.7	0.5 - 0.9
u_{mf}	1.5 cm/s	0.85 cm/s

Table D.4
Glass Properties for Scaling with Constant ρ_s/ρ_f

	1/4 Scale Studsvik	1/16 Scale Studsvik
Density	2.54 g/cc	2.54 g/cc
Mean Diameter	112.3 microns	78.7 microns
Loose Pack Voidage	42%	42%
Sphericity	1.0	1.0
u_{mf}	2.8 cm/s	1.4 cm/s

Table D.5
Particles for Hot Bed Scaling with Constant ρ_s/ρ_f

	Studsvik Hot Bed	1/4 Scale Model	1/16 Scale Model
Density (g/cc)	2.70	7.25	7.25
Mean Diameter (microns)	243	57.7	~26
Loose Pack Voidage		0.65	0.65
Sphericity		~0.7	~0.7
u_{mf} (cm/s)		1.40	0.75

Table D.6
Particles for Pressurized Hot Bed Scaling with Constant ρ_s/ρ_f

	Hot Bed Solid	Cold Bed Solid
Material	Dolomite	Polyethylene Plastic
Surface Mean d_p (microns)	165	180
Density (kg/m^3)	2650	905
Sphericity	0.84	0.85
ε_{mf}	0.52	0.49
u_{mf} (cm/s)	2.39 (est. at 12 bar, 900 °C)	1.77

APPENDIX E: VISCOUS LIMIT EXPERIMENTAL DATA

Solid fraction profile test results for the glass/steel and plastic/glass viscous limit runs are presented in the following pages.

Figure E.1 - Glass 1, Uo = 3.0 m/s, M = 0.0029

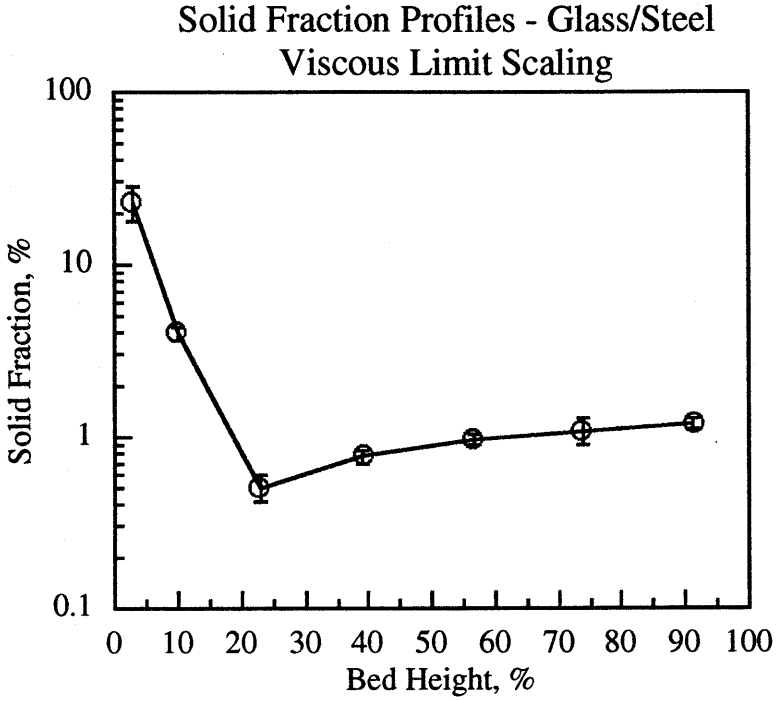

Bed Material: Glass I

% Bed Ht.	SF, %	Std. Dev.
2.72	22.72	10.7059
9.78	4.03	0.7754
22.83	0.51	0.1665
39.13	0.77	0.1406
56.52	0.97	0.1584
73.91	1.07	0.3768
91.3	1.18	0.1601

Figure E.2 - Glass 1, Uo = 5.5 m/s, M = 0.0029

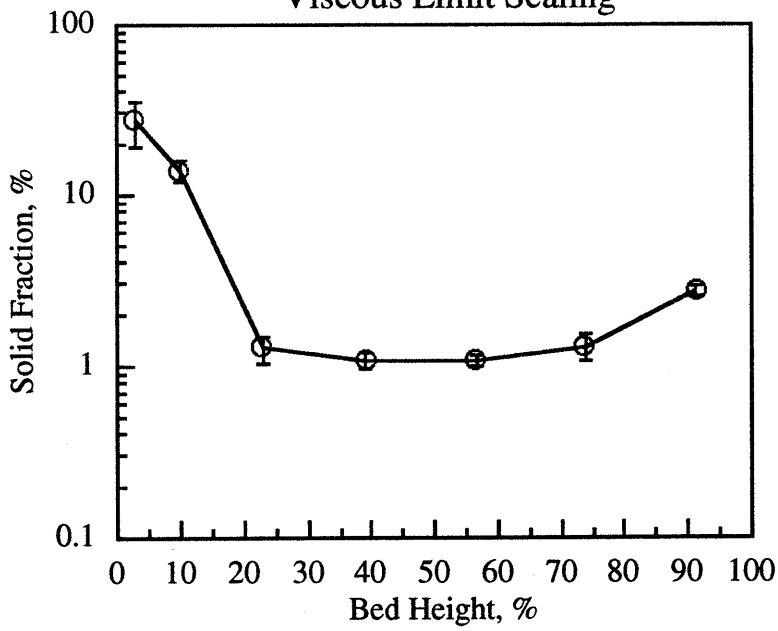

Bed Material: Glass I

% Bed Ht.	SF, %	Std. Dev.
2.72	27.08	16.415083
9.78	13.76	4.0388352
22.83	1.26	0.431424
39.13	1.08	0.2130408
56.52	1.08	0.1788588
73.91	1.28	0.4521472
91.3	2.72	0.355368

Figure E.3 - Glass 1, Uo = 7.0 m/s, M = 0.0029

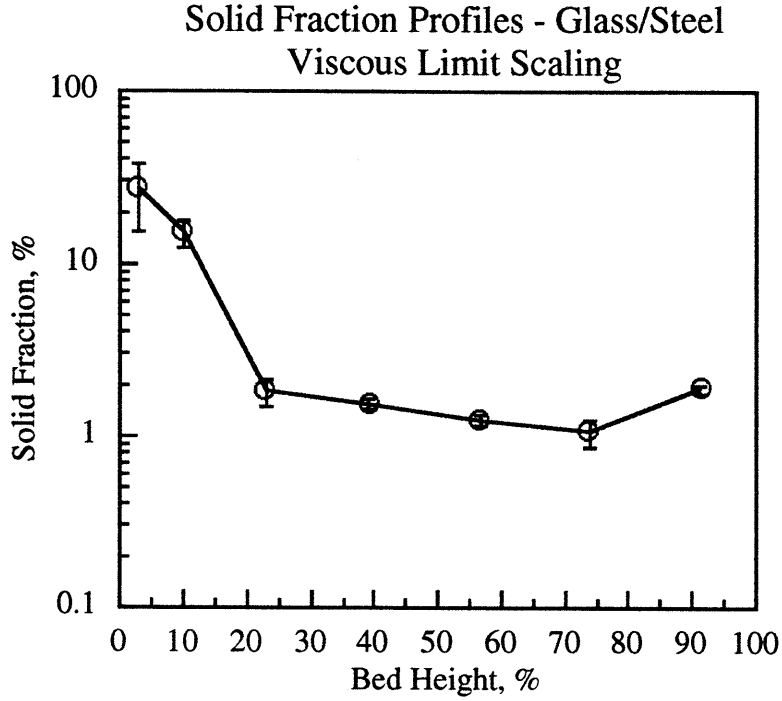

Bed Material: Glass I

% Bed Ht.	SF, %	Std. Dev.
2.72	26.91	22.735989
9.78	15.07	5.7467938
22.83	1.82	0.6491212
39.13	1.54	0.207823
56.52	1.23	0.1678089
73.91	1.06	0.3654668
91.3	1.88	0.2279124

Figure E.4 - Glass 2, Uo = 3.0 m/s, M = 0.0029

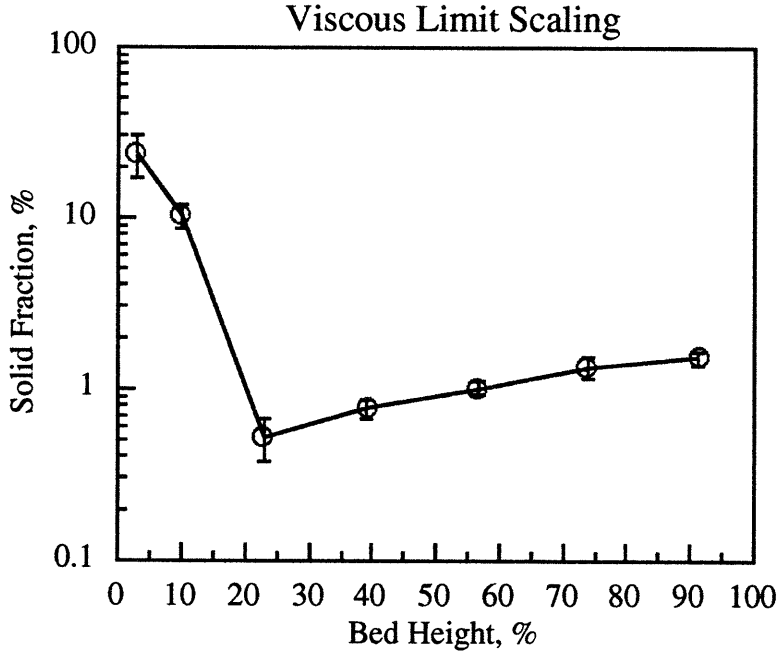

Bed Material: Glass 2

% Bed Ht.	SF, %	Std. Dev.
2.72	23.48	13.1699
9.78	10.36	3.3011
22.83	0.52	0.2927
39.13	0.77	0.1856
56.52	1.01	0.1848
73.91	1.35	0.3946
91.3	1.51	0.2352

Figure E.5 - Glass 2, Uo = 5.5 m/s, M = 0.0029

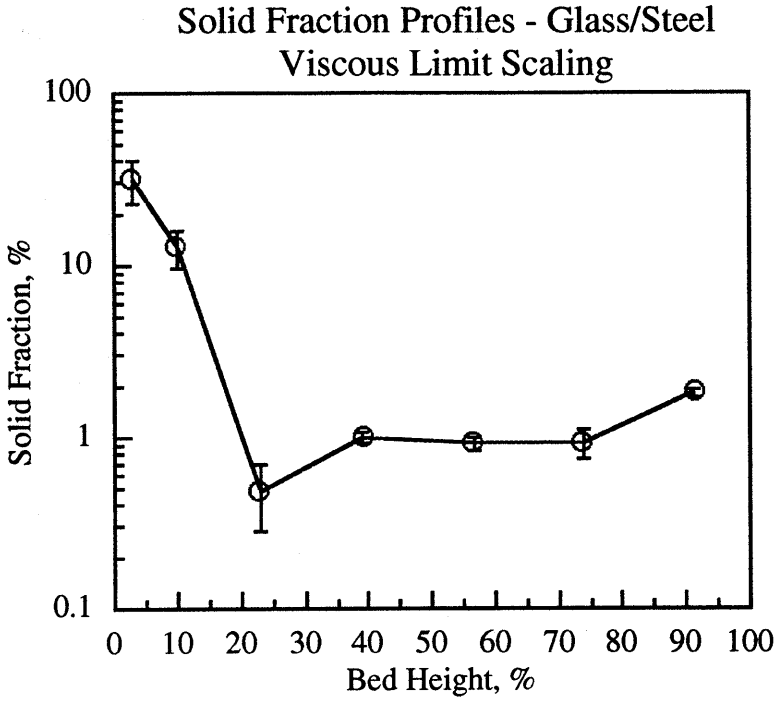

Bed Material: Glass 2

% Bed Ht.	SF, %	Std. Dev.
2.72	31.08	17.2478
9.78	12.78	6.3416
22.83	0.49	0.4174
39.13	1	0.1620
56.52	0.91	0.1620
73.91	0.94	0.3771
91.3	1.81	0.2081

Figure E.6 - Glass 2, Uo = 7.0 m/s, M = 0.0029

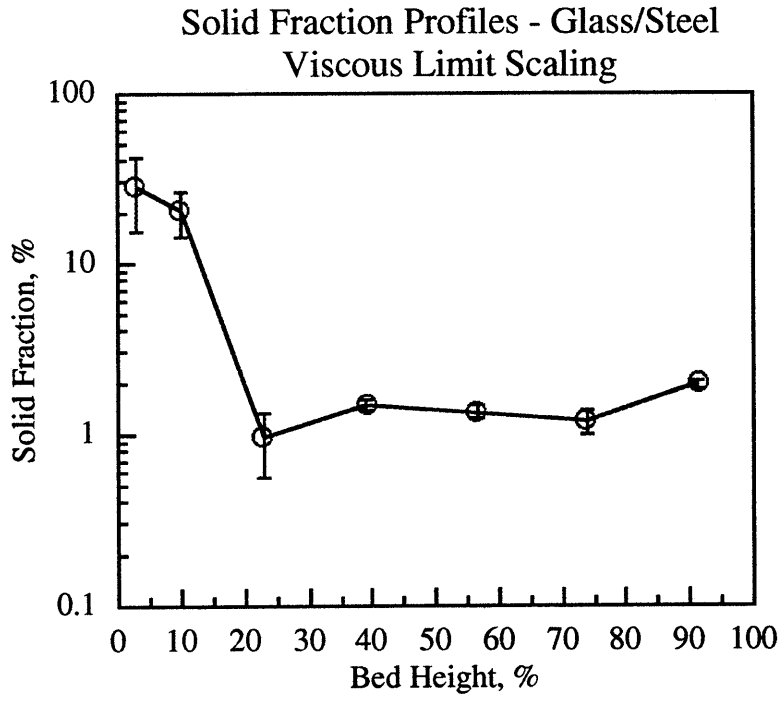

Bed Material: Glass 2

% Bed Ht.	SF, %	Std. Dev.
2.72	28.55	26.1629
9.78	20.19	11.4879
22.83	0.95	0.7868
39.13	1.48	0.2446
56.52	1.34	0.2284
73.91	1.19	0.3894
91.3	1.96	0.2308

Figure E.7 - Steel, Uo = 3.0 m/s, M = 0.0029

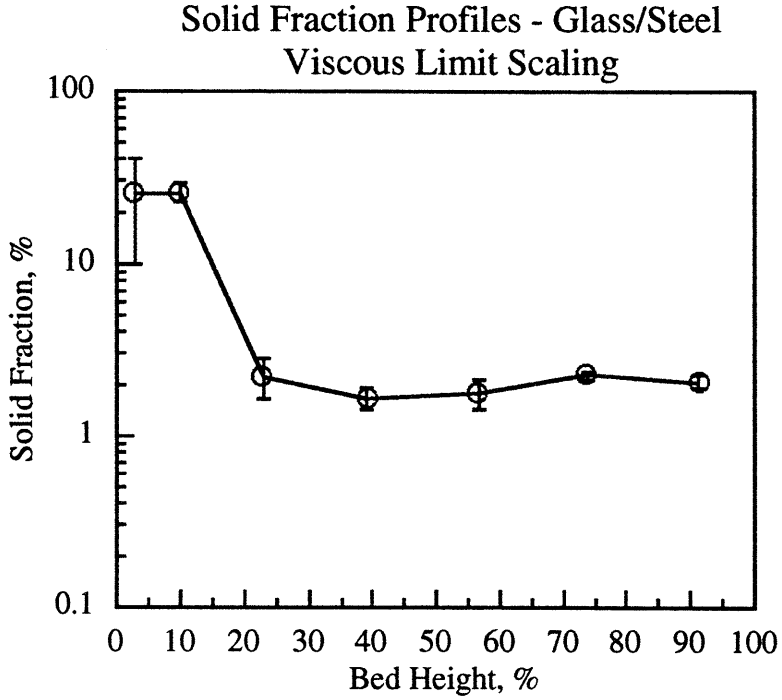

Bed Material: Steel

% Bed Ht.	SF, %	Std. Dev.
2.72	25.35	31.0968
9.78	25.71	6.5535
22.83	2.22	1.2003
39.13	1.66	0.4376
56.52	1.79	0.6837
73.91	2.24	0.3076
91.3	2.08	0.3964

Figure E.8 - Steel, Uo = 5.5 m/s, M = 0.0029

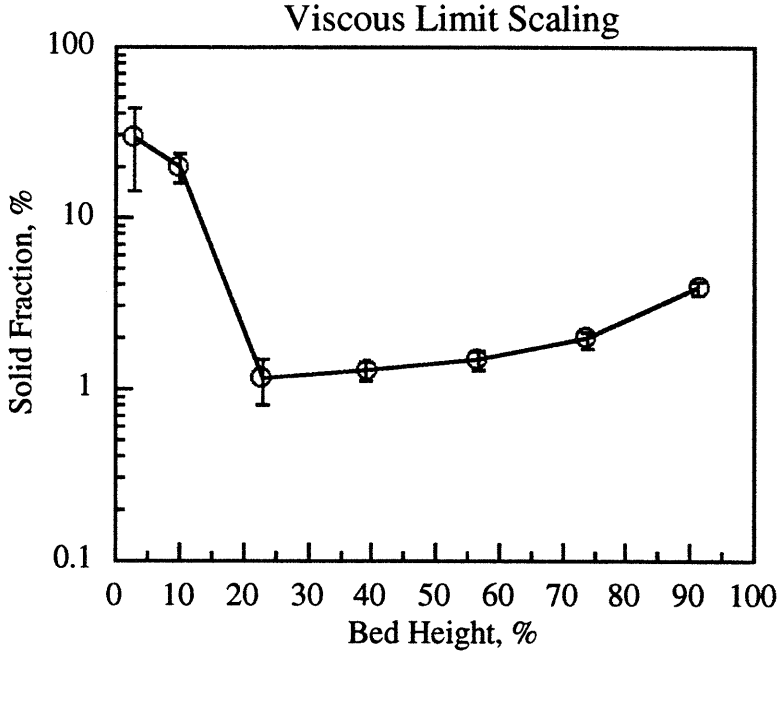

Bed Material: Steel

% Bed Ht.	SF, %	Std. Dev.
2.72	29.02	29.9022
9.78	19.67	7.5519
22.83	1.15	0.6754
39.13	1.27	0.2903
56.52	1.47	0.4059
73.91	1.94	0.4194
91.3	3.85	0.7860

Figure E.9 - Steel, Uo = 7.0 m/s, M = 0.0029

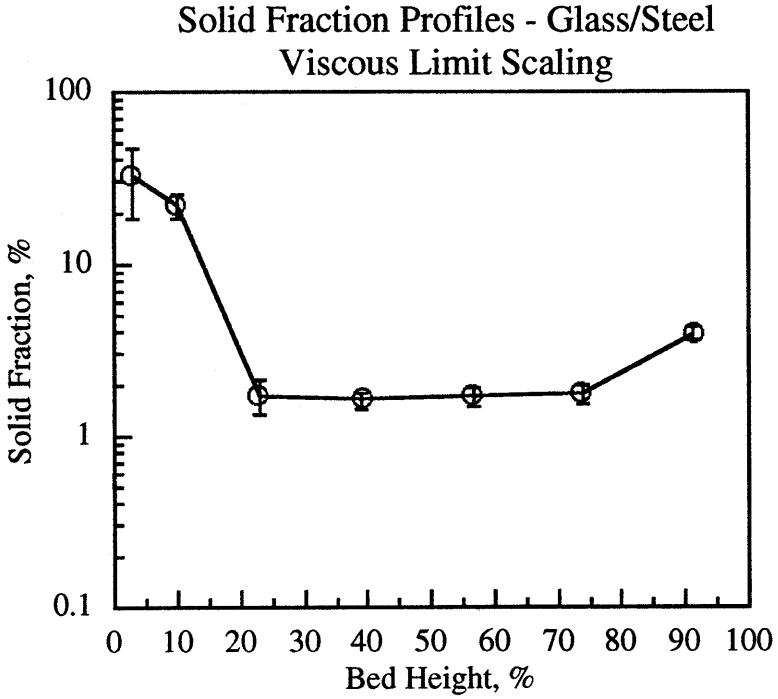

Bed Material: Steel

% Bed Ht.	SF, %	Std. Dev.
2.72	32.68	28.4620
9.78	21.81	7.2924
22.83	1.7	0.7879
39.13	1.62	0.3482
56.52	1.69	0.4757
73.91	1.77	0.4396
91.3	3.96	0.7684

Figure E.10 - Glass, Uo = 1.5 m/s, M = 0.0072

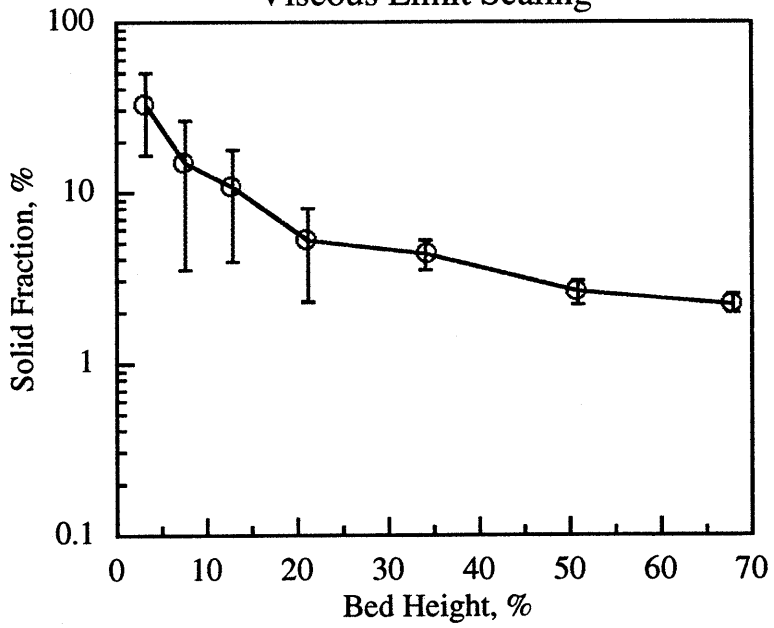

Bed Material: Glass

% Bed Ht.	SF, %	Std. Dev.
3	33.15	32.8758
7.6	14.83	22.6573
12.8	10.81	13.9384
21	5.16	5.7792
34.2	4.31	1.6650
50.8	2.63	0.7978
67.8	2.22	0.5621

Figure E.11 - Glass, Uo = 2.0 m/s, M = 0.0054

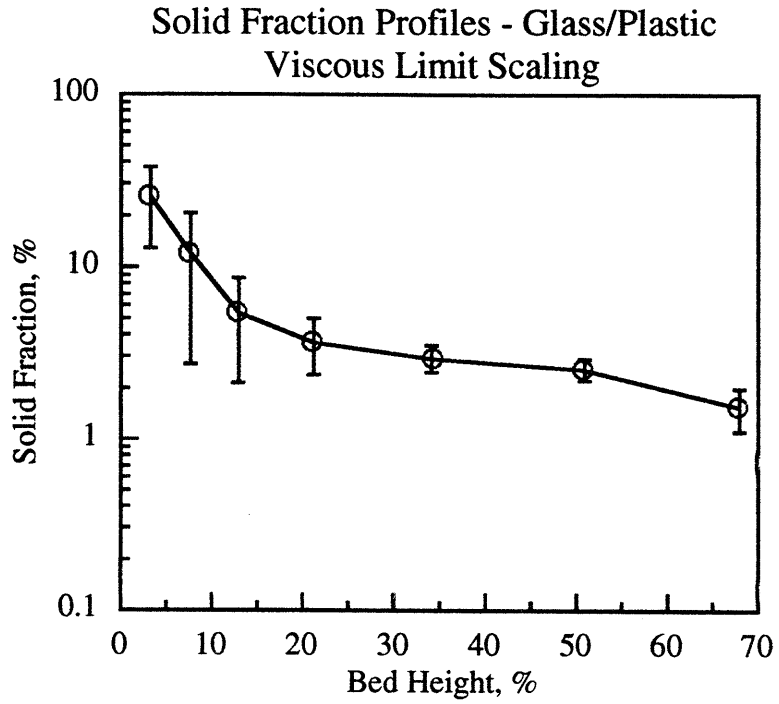

Bed Material: Glass

% Bed Ht.	SF, %	Std. Dev.
3	25.32	25.3276
7.6	11.76	17.9846
12.8	5.45	6.6125
21	3.68	2.5771
34.2	2.96	1.0461
50.8	2.57	0.7196
67.8	1.54	0.8524

Figure E.12 - Glass, Uo = 2.5 m/s, M = 0.0043

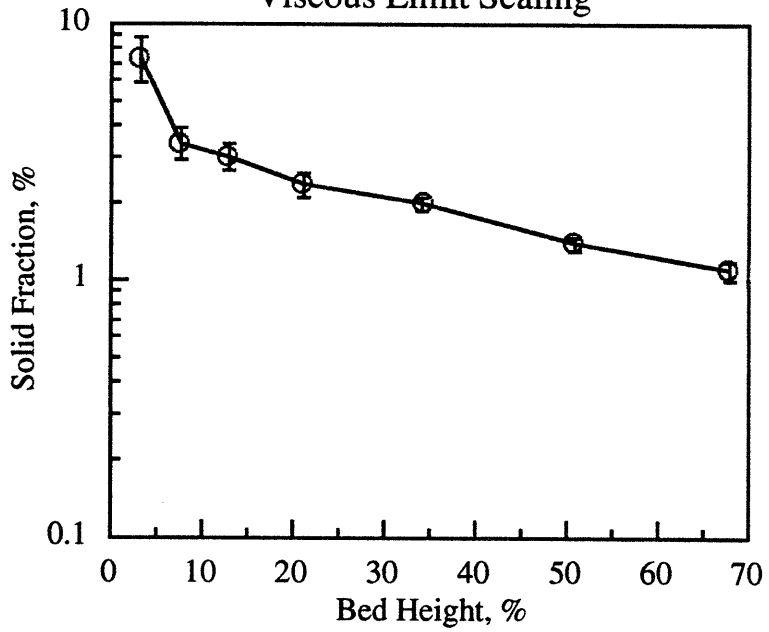

Bed Material: Glass

% Bed Ht.	SF, %	Std. Dev.
3	7.36	2.8442
7.6	3.41	1.0084
12.8	3.03	0.6789
21	2.34	0.4746
34.2	1.98	0.2307
50.8	1.38	0.1439
67.8	1.09	0.1738

Figure E.13 - Plastic, Uo = 1.5 m/s, M = 0.0072

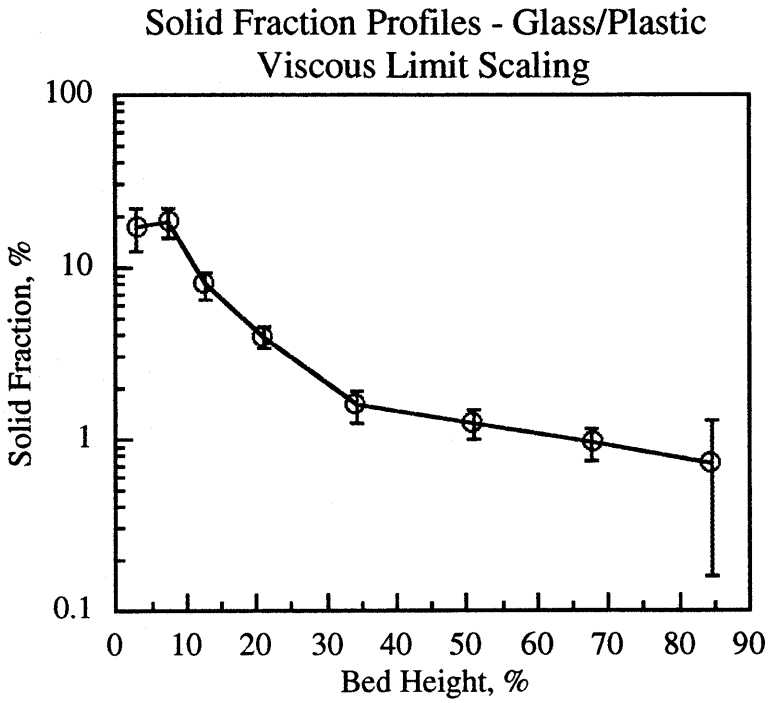

Bed Material: Plastic

% Bed Ht.	SF, %	Std. Dev.
3	16.92	9.3185
7.6	18.11	6.9479
12.8	7.88	2.6308
21	3.93	1.1951
34.2	1.57	0.7075
50.8	1.23	0.4460
67.8	0.95	0.3978
84.7	0.72	1.1253

Figure E.14 - Plastic, Uo = 2.0 m/s, M = 0.0054

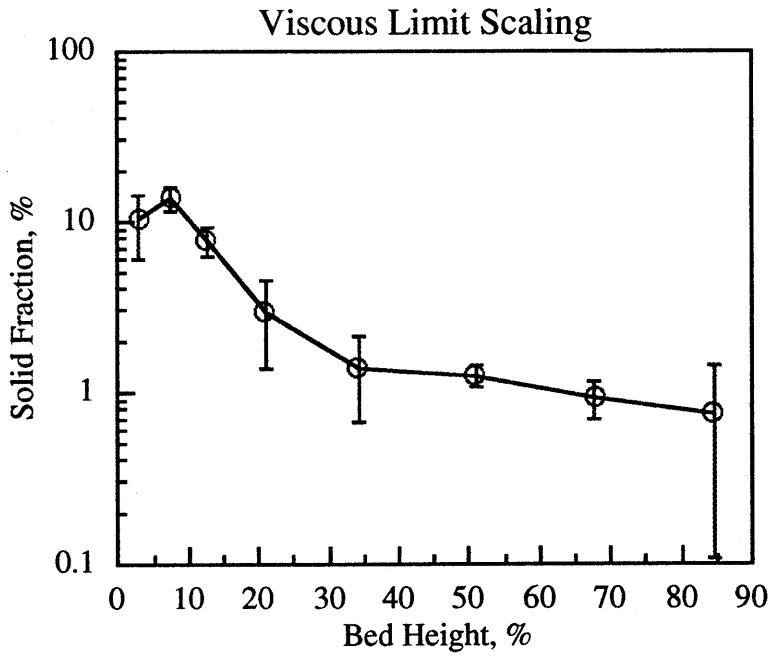

Bed Material: Plastic

% Bed Ht.	SF, %	Std. Dev.
3	10.23	8.4886
7.6	13.73	4.7651
12.8	7.74	2.9114
21	2.94	3.0885
34.2	1.38	1.4286
50.8	1.25	0.3816
67.8	0.92	0.4403
84.7	0.76	1.3042

Figure E.15 - Plastic, Uo = 2.5 m/s, M = 0.0043

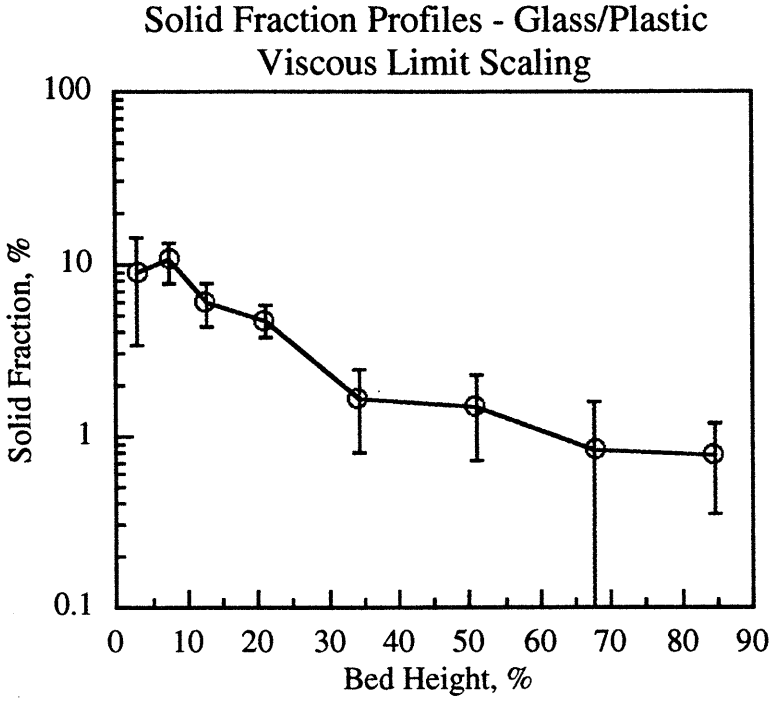

Bed Material: Plastic

% Bed Ht.	SF, %	Std. Dev.
3	8.79	10.8407
7.6	10.5	5.3235
12.8	6.05	3.2900
21	4.75	1.9470
34.2	1.62	1.6281
50.8	1.5	1.5587
67.8	0.83	1.4613
84.7	0.78	0.8642

APPENDIX F: SIMPLIFIED SCALING HYDRODYNAMIC AND HEAT TRANSFER DATA

Solid fraction profile test results and heat transfer measurements made for the glass/glass and plastic/plastic simplified scaling runs are presented in the following pages.

Figure F.1 - 1/16 Scale Glass, Uo = 1.5 m/s, M = 0.0072

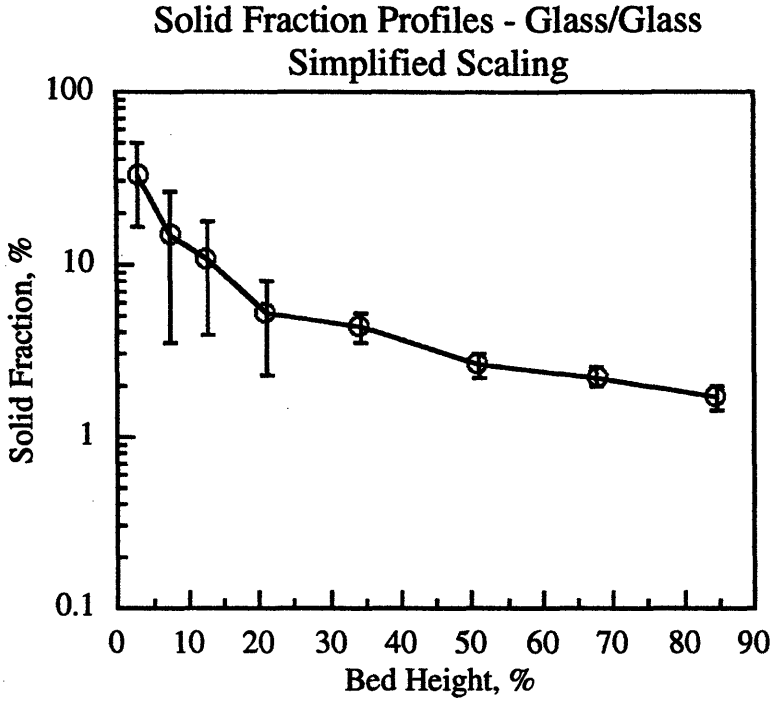

Bed Material: Glass

% Bed Ht.	SF, %	Std. Dev.
3	33.15	32.8758
7.6	14.83	22.6573
12.8	10.81	13.9384
21	5.16	5.7792
34.2	4.31	1.6650
50.8	2.63	0.7978
67.8	2.22	0.5621
84.7	1.7	0.5809

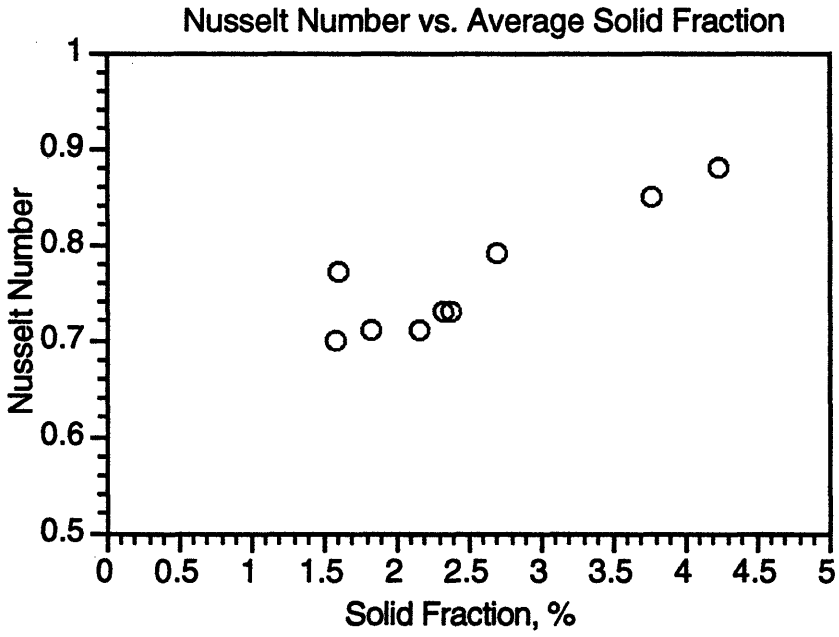

Solid Fraction	Nusselt Number	% Bed Height
3.78	0.85	41.4
2.34	0.73	64.4
1.61	0.77	87.5
4.25	0.88	41.4
2.39	0.73	64.4
1.6	0.7	87.5
2.71	0.79	41.4
2.17	0.71	64.4
1.84	0.71	87.5

Figure F.2 - 1/16 Scale Glass, Uo = 2.0 m/s, M = 0.0054

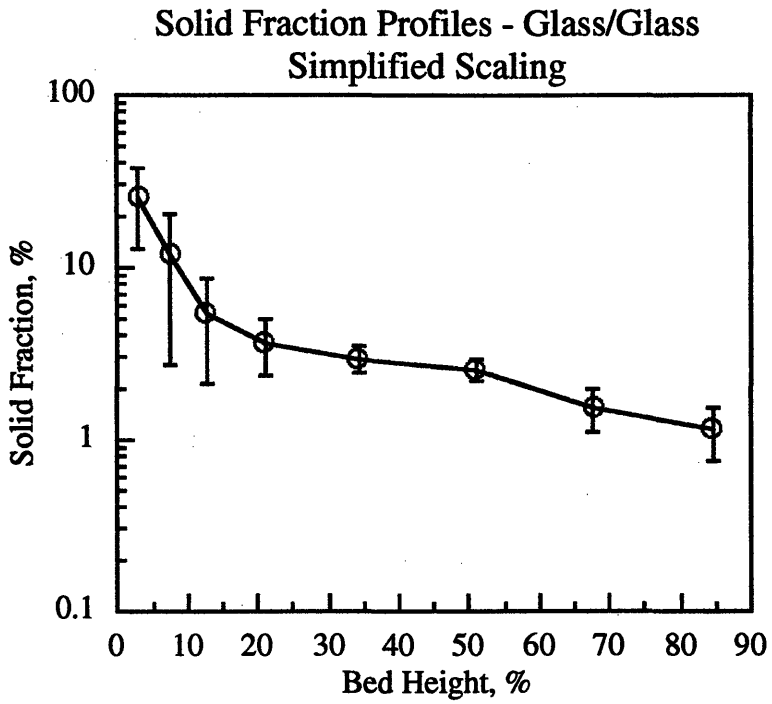

Bed Material: Glass

% Bed Ht.	SF, %	Std. Dev.
3	25.32	25.3276
7.6	11.76	17.9846
12.8	5.45	6.6125
21	3.68	2.5771
34.2	2.96	1.0461
50.8	2.57	0.7196
67.8	1.54	0.8524
84.7	1.15	0.7978

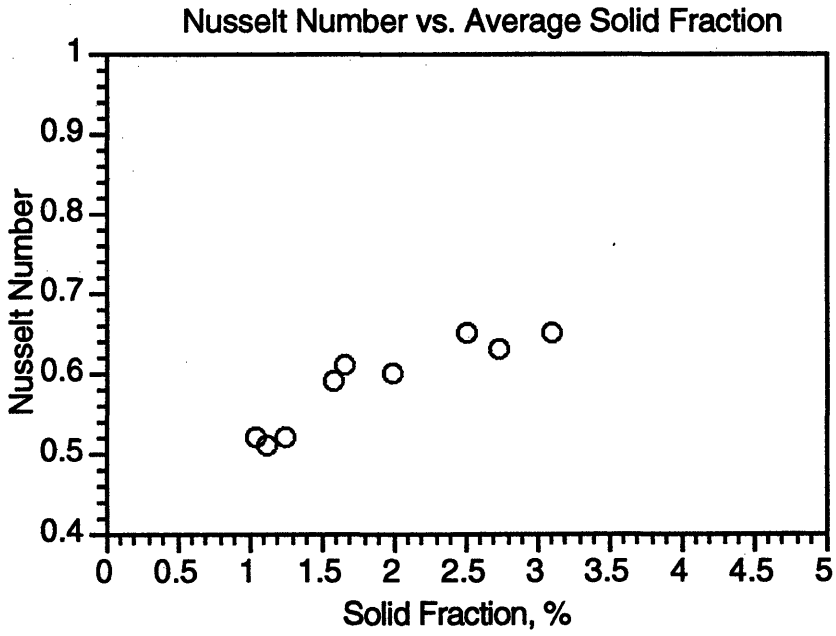

Solid Fraction	Nusselt Number	% Bed Height
3.11	0.65	41.4
1.66	0.61	64.4
1.05	0.52	87.5
2.75	0.63	41.4
2	0.6	64.4
1.26	0.52	87.5
2.52	0.65	41.4
1.59	0.59	64.4
1.13	0.51	87.5

Figure F.3 - 1/16 Scale Glass, Uo = 2.5 m/s, M = 0.0043

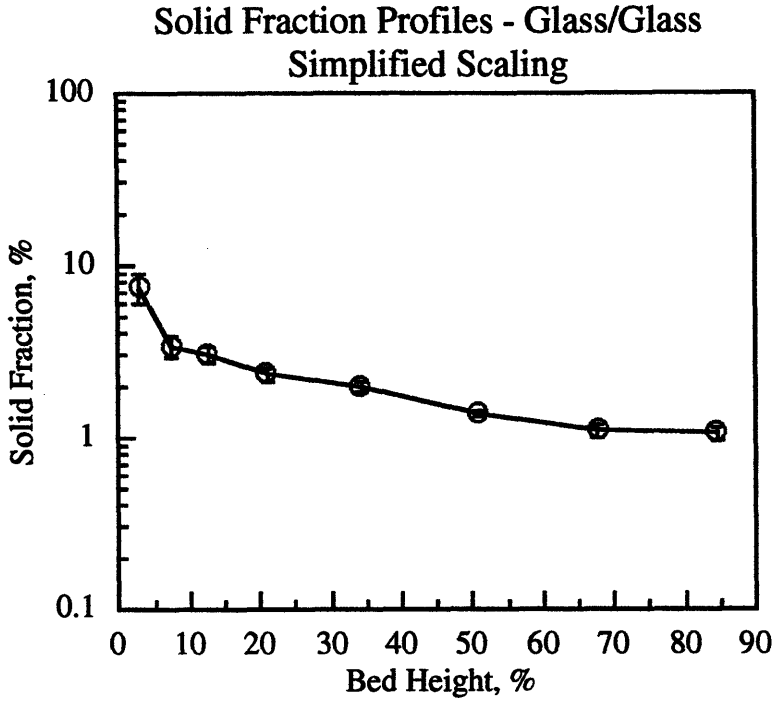

Bed Material: Glass

% Bed Ht.	SF, %	Std. Dev.
3	7.36	2.8442
7.6	3.41	1.0084
12.8	3.03	0.6789
21	2.34	0.4746
34.2	1.98	0.2307
50.8	1.38	0.1439
67.8	1.09	0.1738
84.7	1.07	0.1848

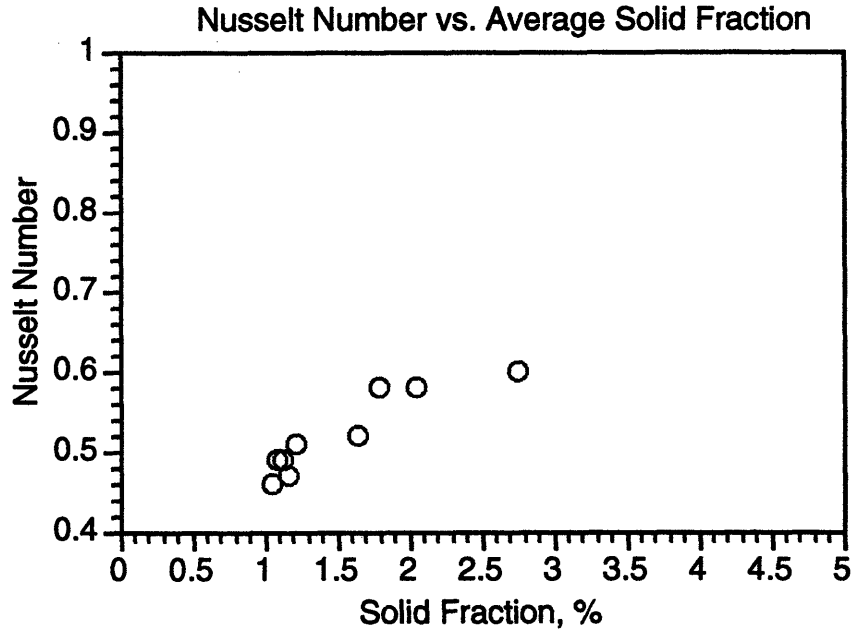

Solid Fraction	Nusselt Number	% Bed Height
1.65	0.52	41.4
1.13	0.49	64.4
1.09	0.49	87.5
1.79	0.58	41.4
1.17	0.47	64.4
1.06	0.46	87.5
2.76	0.6	41.4
2.05	0.58	64.4
1.22	0.51	87.5

Figure F.4 - 1/4 Scale Glass, Uo = 3.0 m/s, M = 0.0072

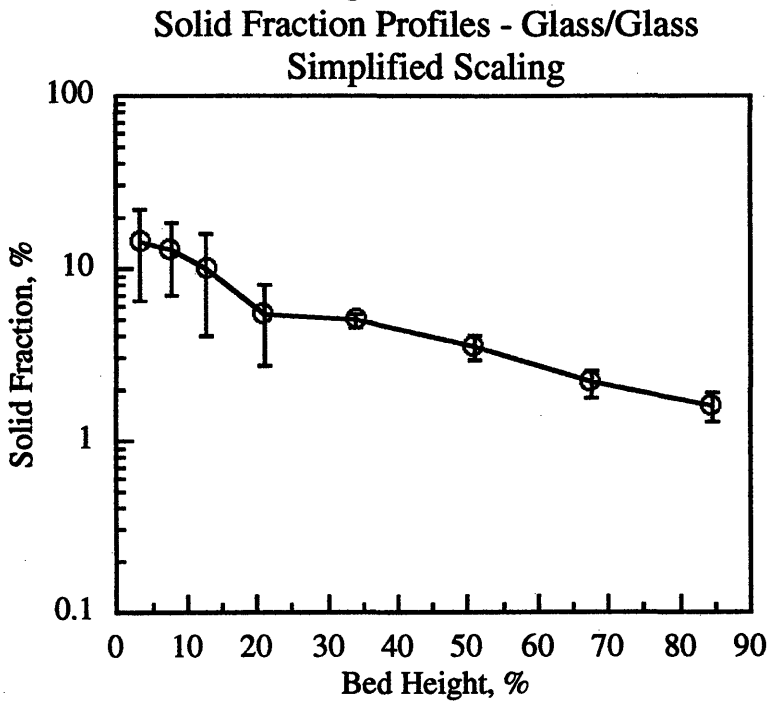

Bed Material: Glass

% Bed Ht.	SF, %	Std. Dev.
3.4	14.25	15.3587
7.7	12.77	11.6220
12.9	10.02	11.8617
21	5.4	5.3915
34.1	4.97	0.8900
50.8	3.47	1.0586
67.7	2.16	0.7234
84.7	1.6	0.6516

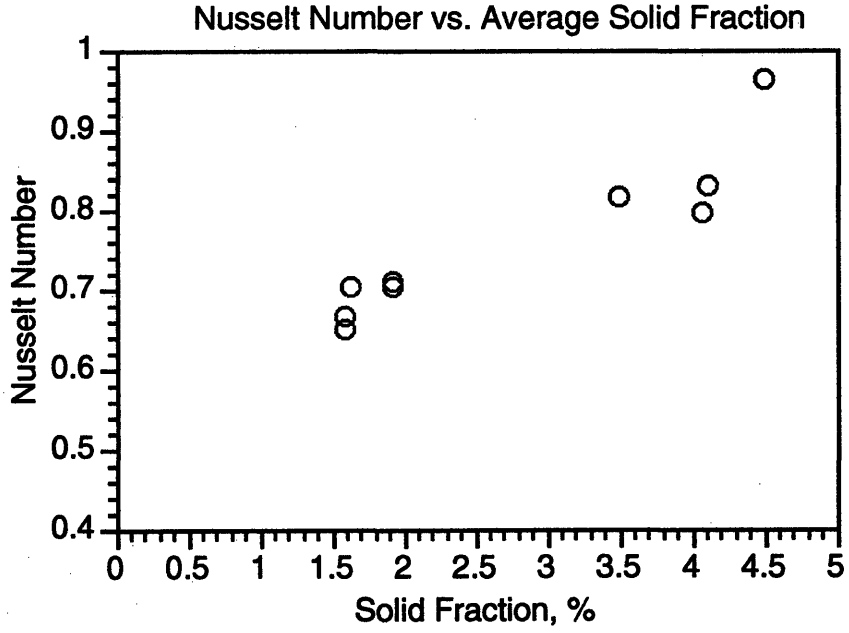

Solid Fraction	Nusselt Number	% Bed Height
4.07	0.7955	41.4
1.93	0.703	64.4
1.6	0.666	87.5
4.12	0.829	41.4
1.93	0.71	64.4
1.6	0.6475	87.5
4.5	0.962	41.4
3.5	0.814	64.4
1.63	0.703	87.5
3.7	0.9335	41.4
2.2	0.7485	64.4
1.58	0.673	87.5

Figure F.5 - 1/4 Scale Glass, Uo = 4.0 m/s, M = 0.0054

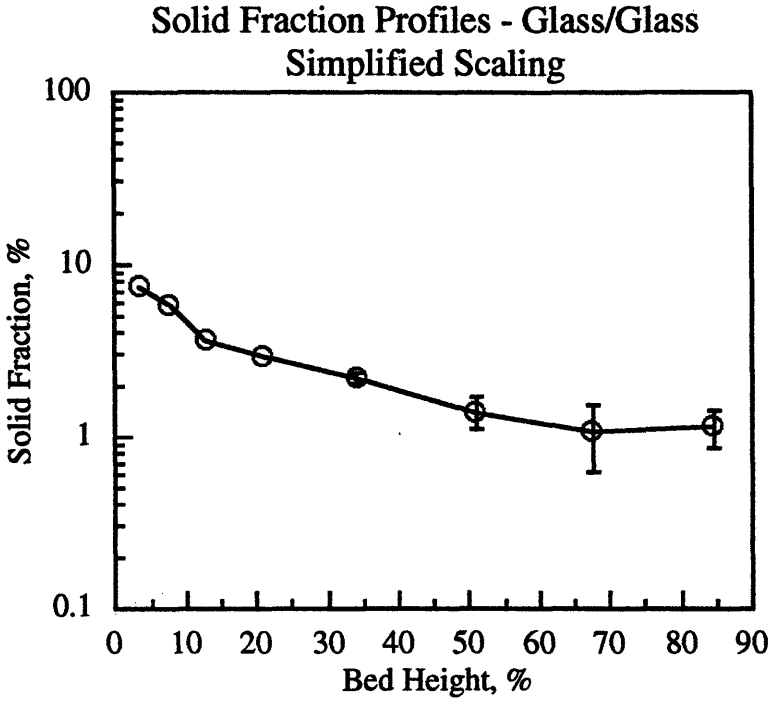

Bed Material: Glass

% Bed Ht.	SF, %	Std. Dev.
3.4	7.56	26.3980
7.7	5.88	15.1910
12.9	3.59	9.2162
21	2.91	7.3134
34.1	2.2	0.2572
50.8	1.39	0.5879
67.7	1.07	0.8796
84.7	1.14	0.5564

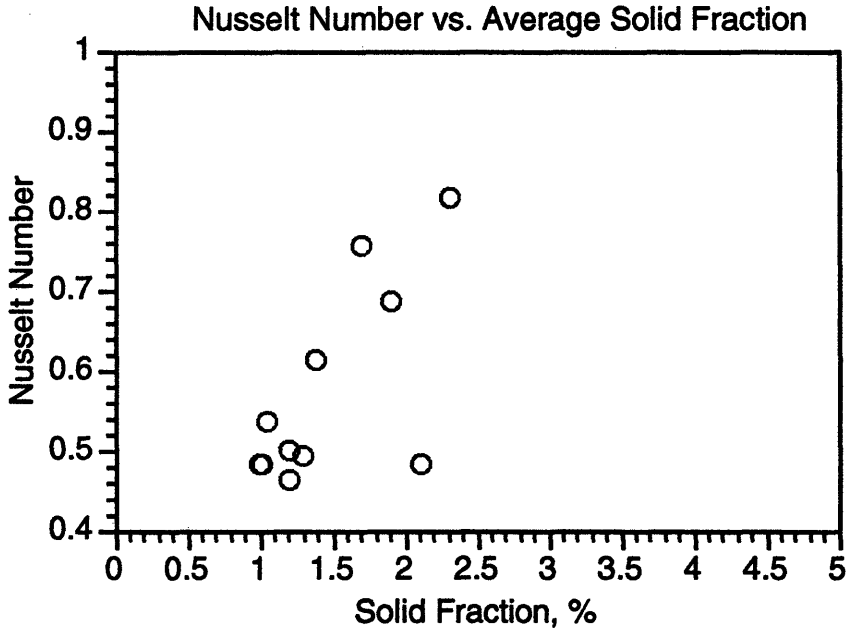

Solid Fraction	Nusselt Number	% Bed Height
2.32	0.815	41.4
2.11	0.481	64.4
1.2	0.4625	87.5
1.7	0.755	41.4
1.2	0.4995	64.4
1.3	0.4921	87.5
1.91	0.6845	41.4
1	0.481	64.4
1.02	0.481	87.5
1.4	0.6105	41.4
1	0.4821	64.4
1.06	0.5365	87.5

Figure F.6 - 1/4 Scale Glass, Uo = 5.0 m/s, M = 0.0043

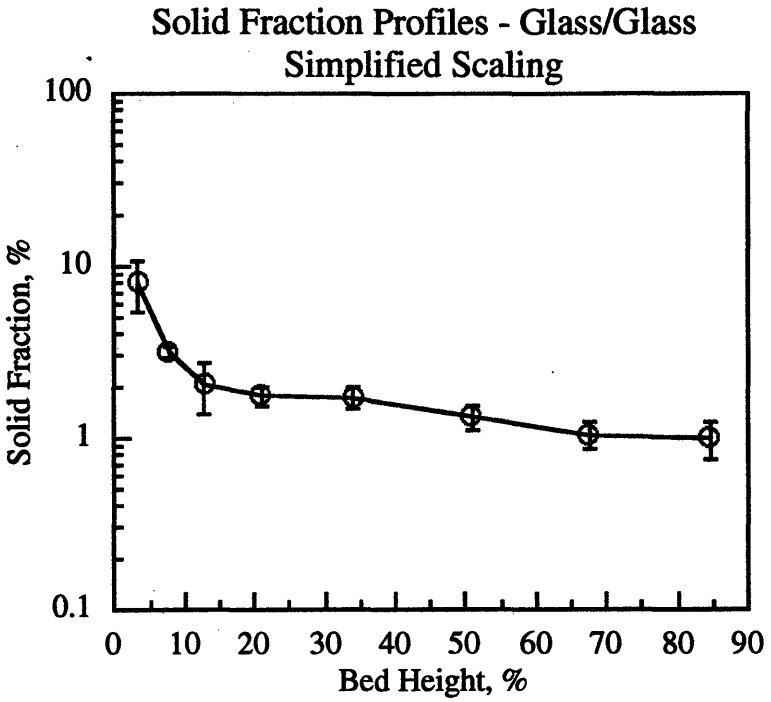

Bed Material: Glass

% Bed Ht.	SF, %	Std. Dev.
3.4	8	5.0473
7.7	3.14	0.4520
12.9	2.02	1.3288
21	1.74	0.4340
34.1	1.73	0.5046
50.8	1.31	0.4355
67.7	1.05	0.3483
84.7	1	0.4964

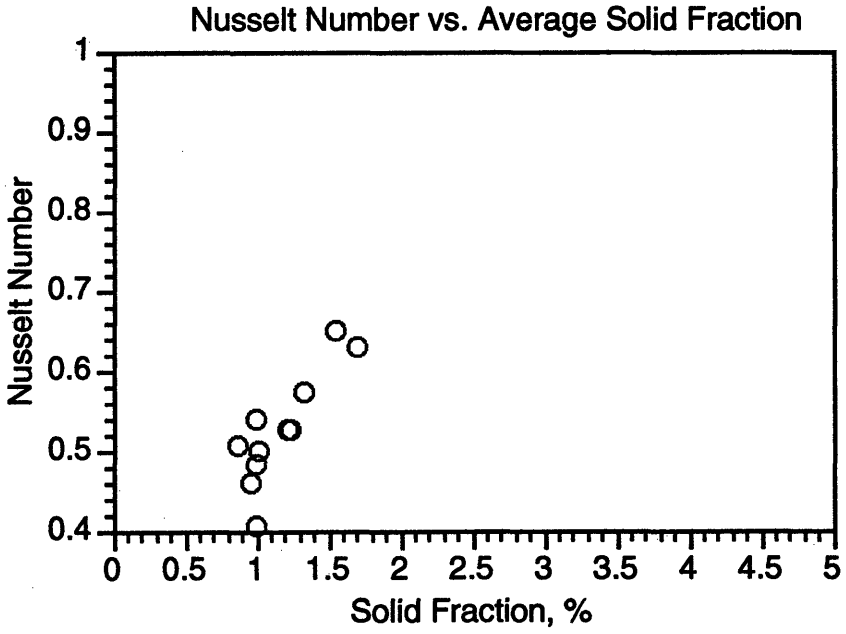

Solid Fraction	Nusselt Number	% Bed Height
1.71	0.6297	41.4
1.22	0.5243	64.4
1.01	0.483	87.5
1.55	0.648	41.4
1.25	0.524	64.4
1.02	0.499	87.5
1.34	0.5735	41.4
0.87	0.507	64.4
1	0.407	87.5
1.01	0.54	41.4
0.96	0.459	64.4
0.97	0.459	87.5

Figure F.7 - 1/16 Scale Plastic, Uo = 1.5 m/s, M = 0.0030

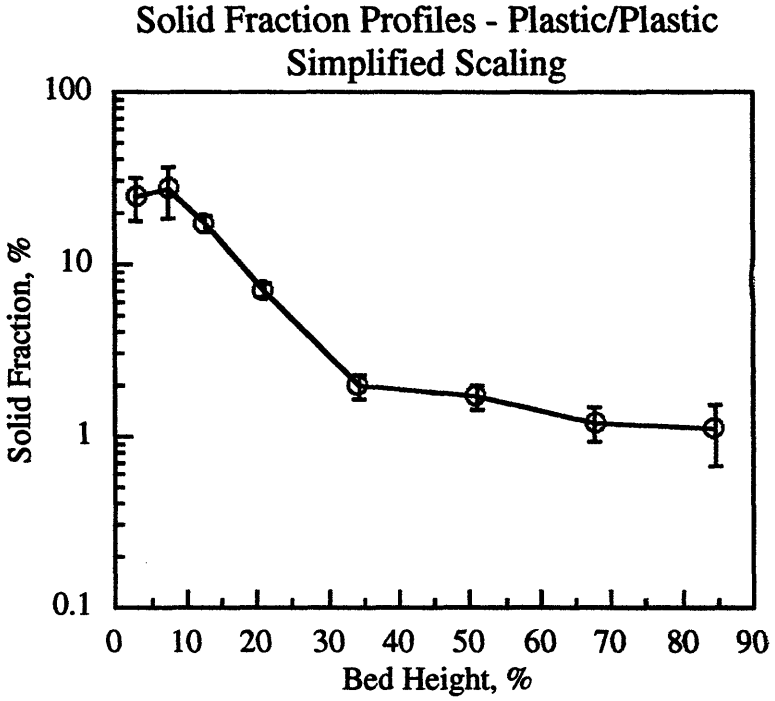

Bed Material: Plastic

% Bed Ht.	SF, %	Std. Dev.
3	24.82	14.1839
7.6	27.22	18.2401
12.8	17.25	4.0229
21	7	1.2154
34.2	1.96	0.5953
50.8	1.7	0.5335
67.8	1.2	0.5526
84.7	1.1	0.8609

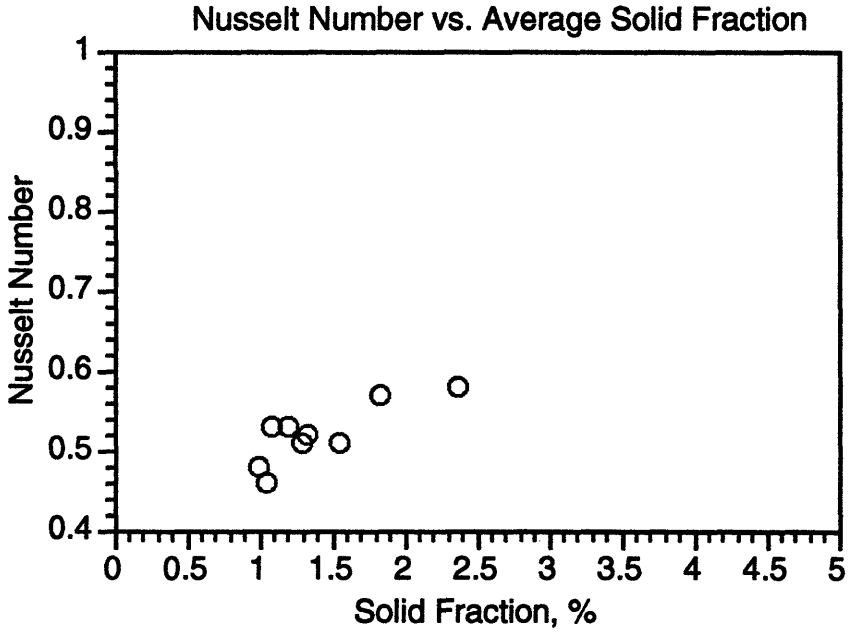

Solid Fraction	Nusselt Number	% Bed Height
2.37	0.58	41.4
1.55	0.51	64.4
1.21	0.53	87.5
1.83	0.57	41.4
1.29	0.51	64.4
1.1	0.53	87.5
1.34	0.52	41.4
1.05	0.46	64.4
1	0.48	87.5

Figure F.8 - 1/16 Scale Plastic, Uo = 2.0 m/s, M = 0.0025

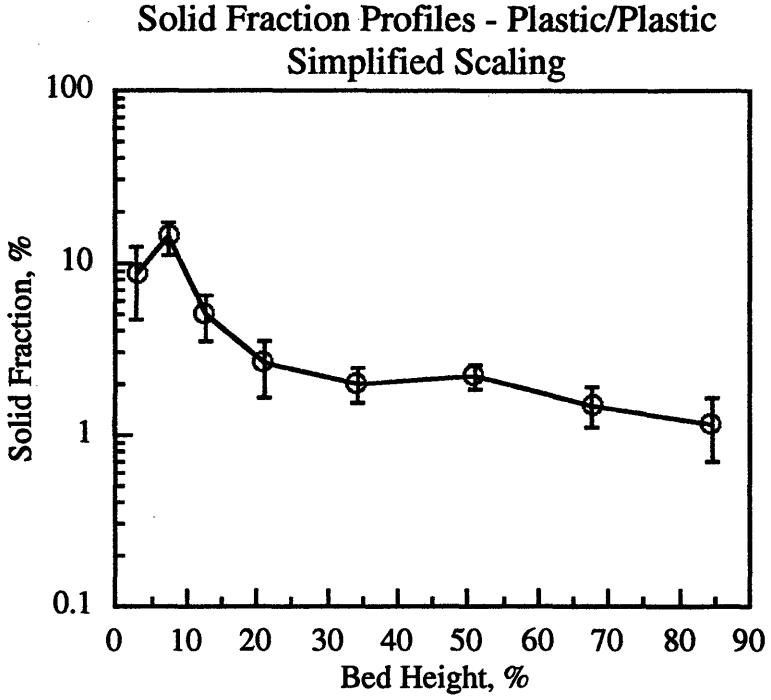

Bed Material: Plastic

% Bed Ht.	SF, %	Std. Dev.
3	8.55	7.9091
7.6	14.28	6.0546
12.8	4.99	2.9384
21	2.59	1.8834
34.2	1.99	0.8794
50.8	2.18	0.7388
67.8	1.5	0.8064
84.7	1.17	0.9743

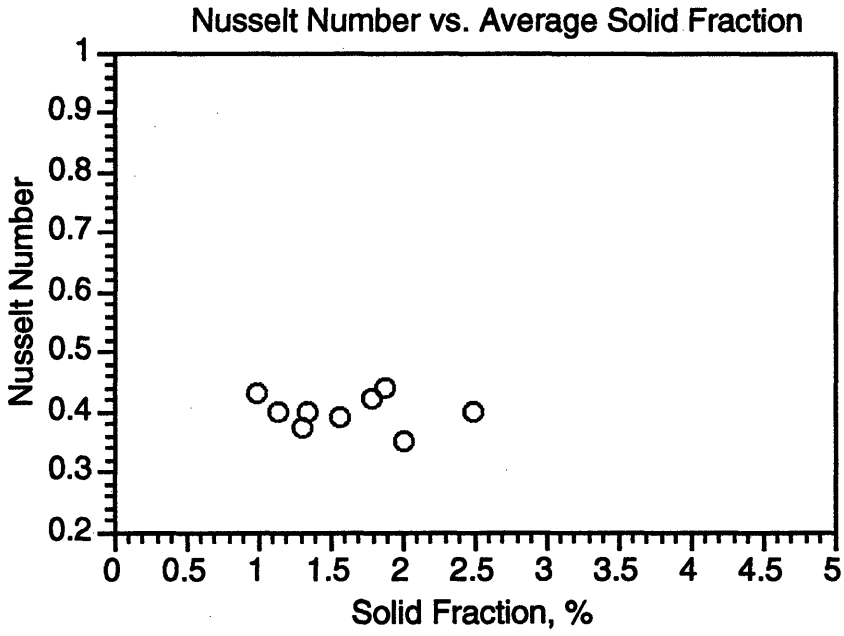

Solid Fraction	Nusselt Number	% Bed Height
2.51	0.4	41.4
2.02	0.35	64.4
1	0.43	87.5
1.9	0.44	41.4
1.31	0.37	64.4
1.15	0.4	87.5
1.8	0.42	41.4
1.58	0.39	64.4
1.35	0.4	87.5

Figure F.9 - 1/16 Scale Plastic, Uo = 2.5 m/s, M = 0.0023

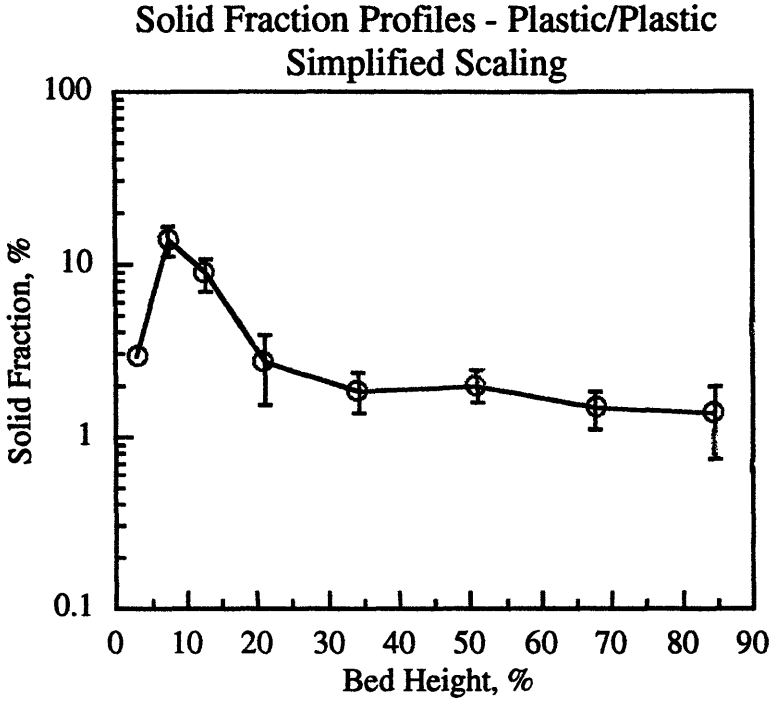

Bed Material: Plastic

% Bed Ht.	SF, %	Std. Dev.
3	2.93	7.8307
7.6	13.73	5.0160
12.8	8.82	3.6530
21	2.71	2.3446
34.2	1.84	0.9615
50.8	2	0.8769
67.8	1.47	0.6897
84.7	1.37	1.2272

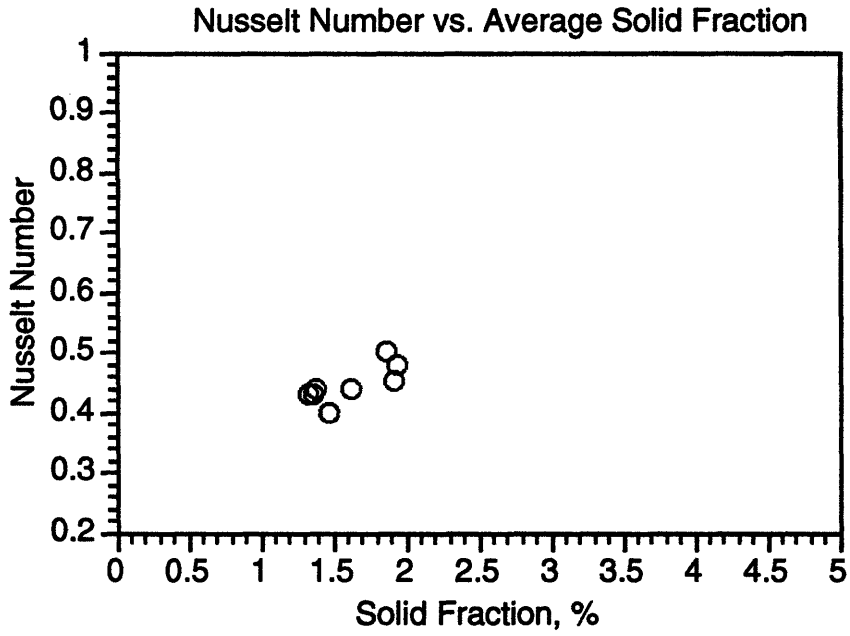

Solid Fraction	Nusselt Number	% Bed Height
1.92	0.45	41.4
1.48	0.4	64.4
1.38	0.43	87.5
1.94	0.48	41.4
1.63	0.44	64.4
1.4	0.44	87.5
1.88	0.5	41.4
1.63	0.44	64.4
1.33	0.43	87.5

Figure F.10 - 1/4 Scale Plastic, Uo = 3.0 m/s, M = 0.0030

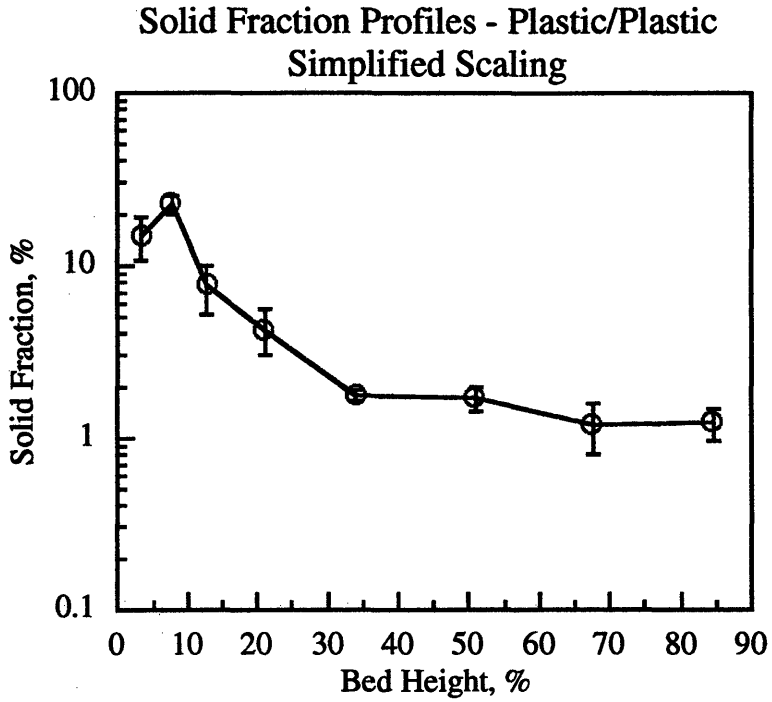

Bed Material: Plastic

% Bed Ht.	SF, %	Std. Dev.
3.4	14.94	8.3603
7.7	22.64	5.9032
12.9	7.63	4.9592
21	4.25	2.5335
34.1	1.79	0.2763
50.8	1.68	0.5174
67.7	1.19	0.7514
84.7	1.22	0.5219

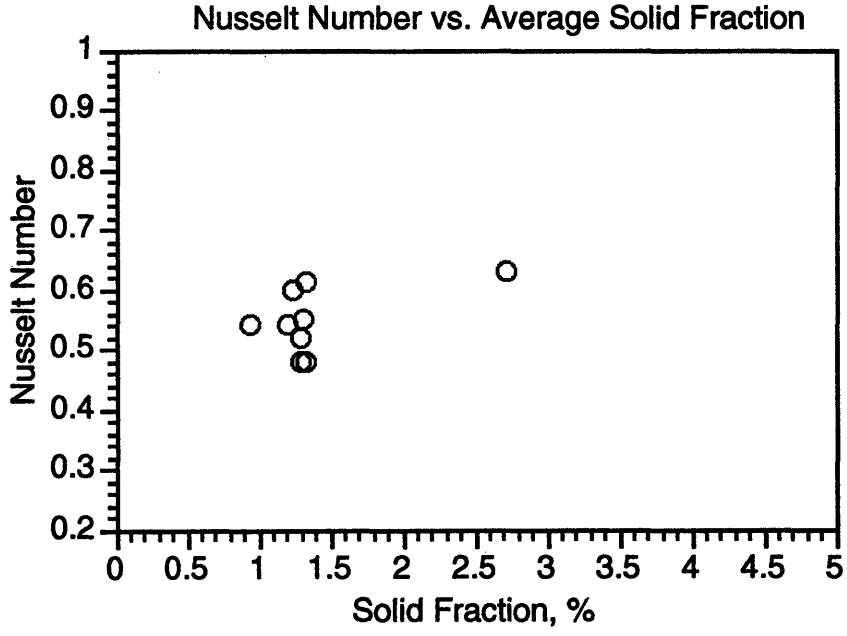

Solid Fraction	Nusselt Number	% Bed Height
2.73	0.63	41.4
1.25	0.6	64.4
0.95	0.54	87.5
1.21	0.54	41.4
1.31	0.55	64.4
1.34	0.61	87.5
1.3	0.52	41.4
1.3	0.48	64.4
1.34	0.48	87.5

Figure F.11 - 1/4 Scale Plastic, Uo = 4.0 m/s, M = 0.0025

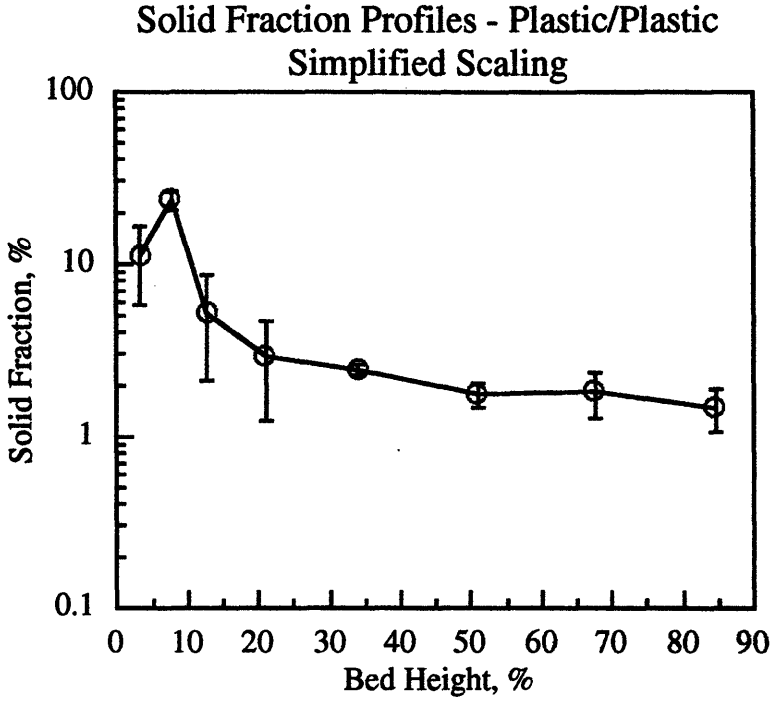

Bed Material: Plastic

% Bed Ht.	SF, %	Std. Dev.
3.4	11.02	10.4160
7.7	23.27	5.5078
12.9	5.28	6.3745
21	2.93	3.3686
34.1	2.45	0.3983
50.8	1.77	0.5426
67.7	1.81	1.0260
84.7	1.48	0.8265

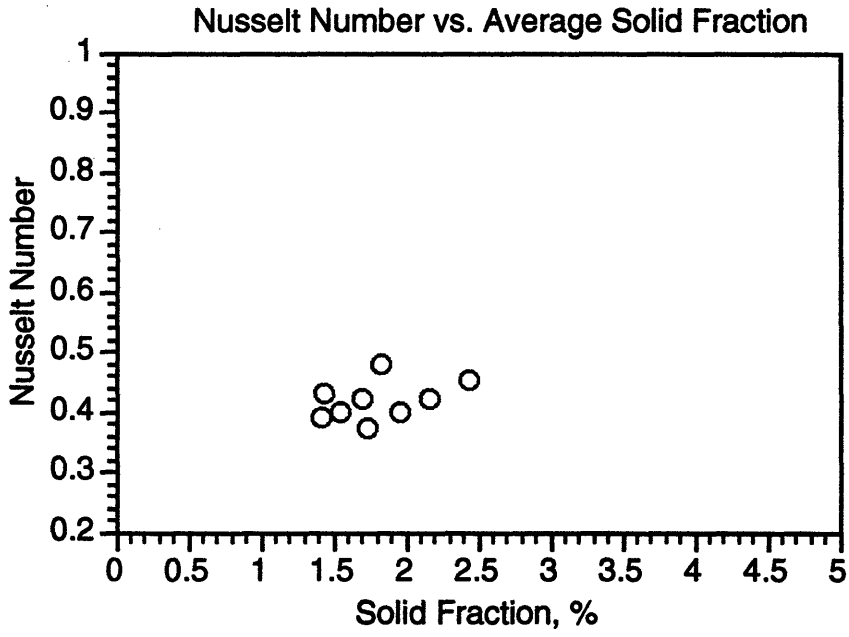

Solid Fraction	Nusselt Number	% Bed Height
1.84	0.48	41.4
1.71	0.42	64.4
1.45	0.43	87.5
2.44	0.45	41.4
1.96	0.4	64.4
1.56	0.4	87.5
2.17	0.42	41.4
1.75	0.37	64.4
1.43	0.39	87.5

Figure F.12 - 1/4 Scale Plastic, Uo = 5.0 m/s, M = 0.0023

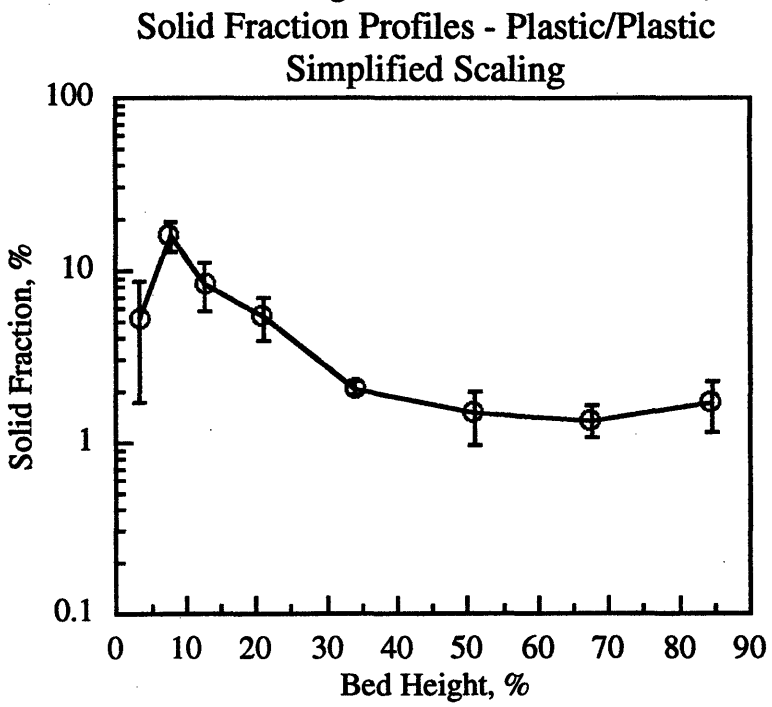

Bed Material: Plastic

% Bed Ht.	SF, %	Std. Dev.
3.4	5.23	7.0291
7.7	15.87	6.1123
12.9	8.42	5.2330
21	5.41	3.1384
34.1	2.08	0.3379
50.8	1.46	1.0038
67.7	1.35	0.5796
84.7	1.72	1.1094

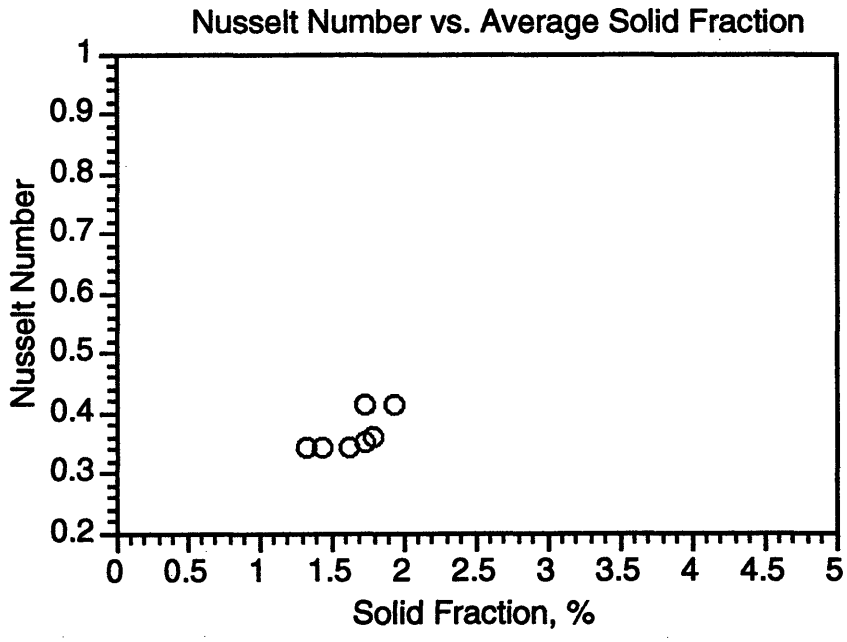

Solid Fraction	Nusselt Number	% Bed Height
1.75	0.41	41.4
1.34	0.34	64.4
1.79	0.36	87.5
1.74	0.41	41.4
1.33	0.34	64.4
1.74	0.35	87.5
1.94	0.41	41.4
1.44	0.34	64.4
1.63	0.34	87.5

APPENDIX G: HYDRODYNAMIC DATA FOR HOT BED SCALING

Solid fraction profile test results for the Studsvik hot bed and the scaling runs of the Studsvik hot bed utilizing both the simplified and complete set of scaling laws are presented in the following pages. The operating data and bed dimensions are given on the data sheets at the end of this Appendix.

Figure G.1 - 1/16 Scale Model, Condition 1

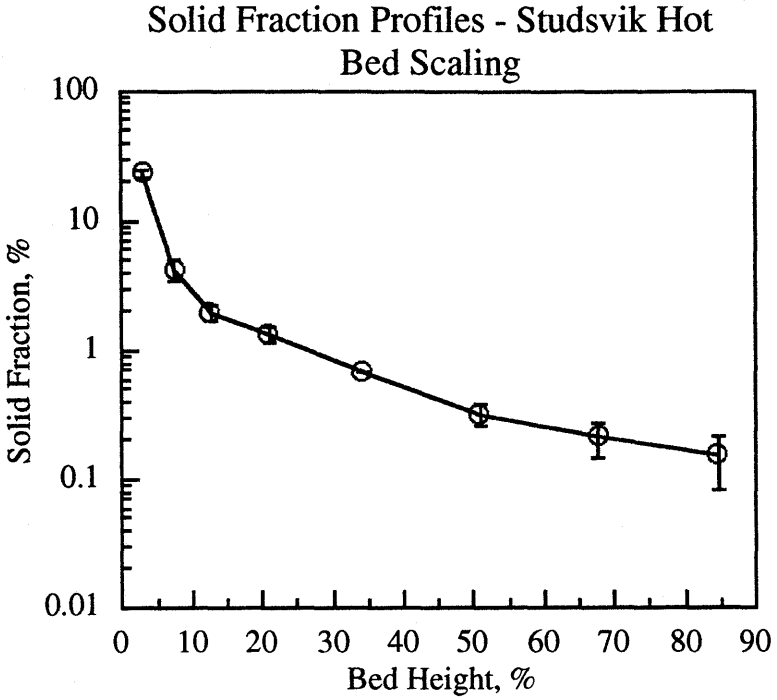

Bed Material: Steel

% Bed Ht.	SF, %	Std. Dev.
3	23.33	3.6395
7.6	4.24	1.6002
12.8	1.98	0.5318
21	1.33	0.4001
34.2	0.68	0.0181
50.8	0.32	0.1248
67.8	0.21	0.1266
84.7	0.15	0.1320

Figure G.2 - 1/16 Scale Model, Condition 2

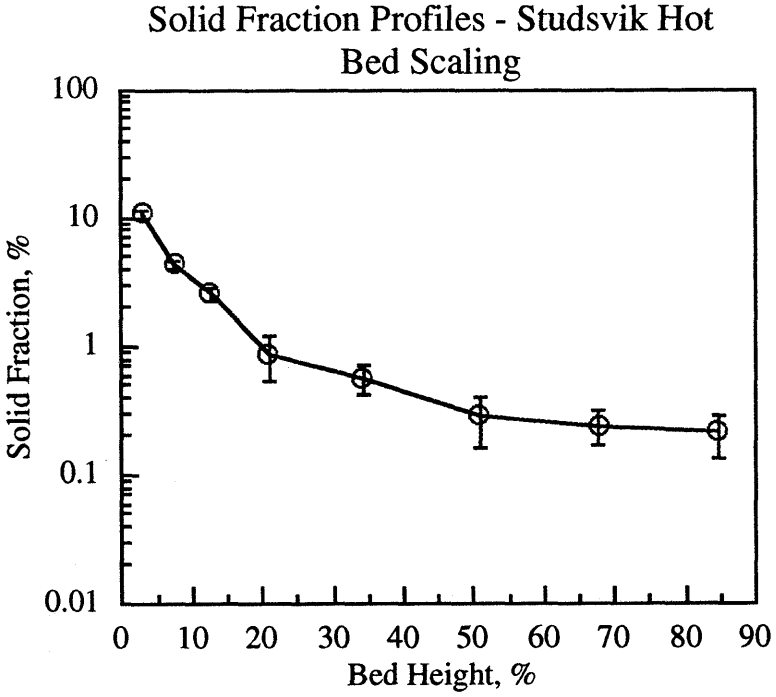

Bed Material: Steel

% Bed Ht.	SF, %	Std. Dev.
3	10.66	1.4945
7.6	4.36	0.6339
12.8	2.54	0.6721
21	0.87	0.6979
34.2	0.56	0.2680
50.8	0.28	0.2340
67.8	0.24	0.1464
84.7	0.21	0.1530

Figure G.3 - 1/16 Scale Model, Condition 3

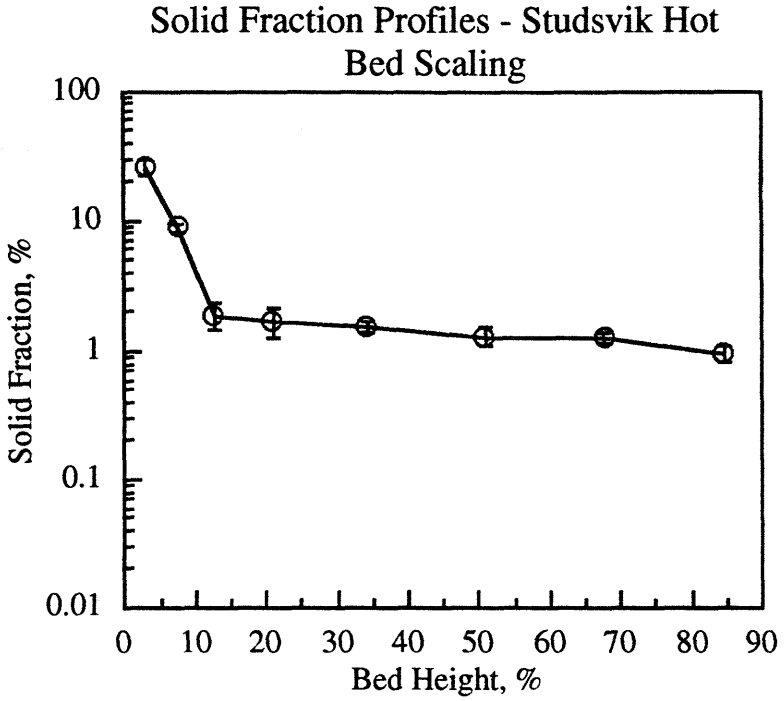

Bed Material: Steel

% Bed Ht.	SF, %	Std. Dev.
3	26.37	7.3783
7.6	8.89	1.3175
12.8	1.89	0.8781
21	1.72	0.8679
34.2	1.56	0.2780
50.8	1.29	0.4399
67.8	1.25	0.2500
84.7	0.95	0.2880

Figure G.4 - 1/16 Scale Model, Condition 4

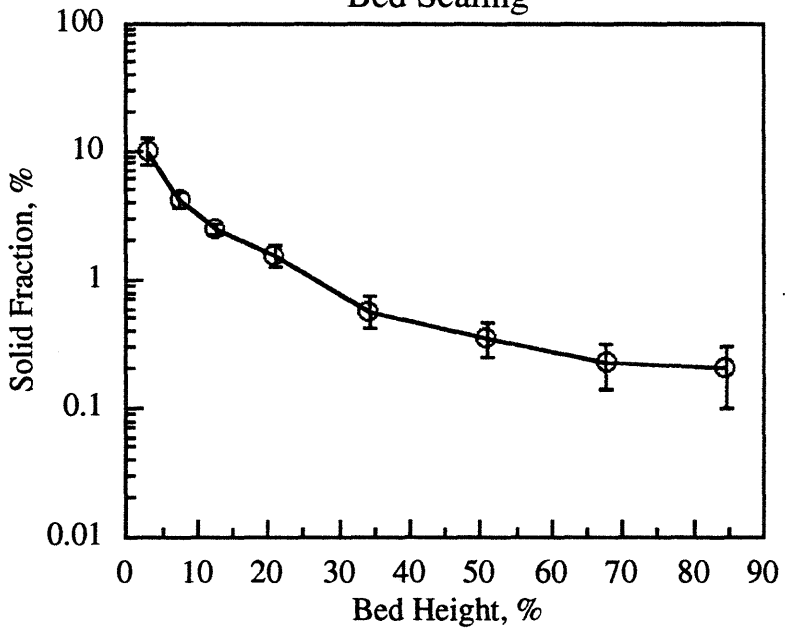

Bed Material: Steel

% Bed Ht.	SF, %	Std. Dev.
3	10.12	4.5196
7.6	4.23	1.0440
12.8	2.48	0.5322
21	1.53	0.5679
34.2	0.57	0.3179
50.8	0.35	0.2100
67.8	0.23	0.1782
84.7	0.2	0.2020

Figure G.5 - 1/16 Scale Model, Condition 5

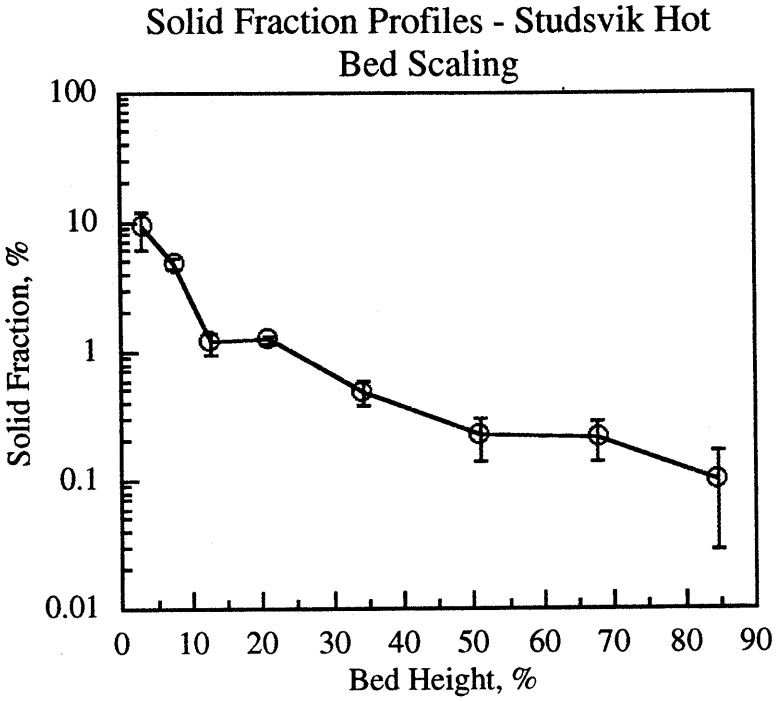

Bed Material: Steel

% Bed Ht.	SF, %	Std. Dev.
3	9.23	5.8998
7.6	4.82	1.0083
12.8	1.19	0.4620
21	1.26	0.1830
34.2	0.48	0.1949
50.8	0.22	0.1654
67.8	0.21	0.1430
84.7	0.1	0.1432

Figure G.6 - 1/16 Scale Model, Condition 6

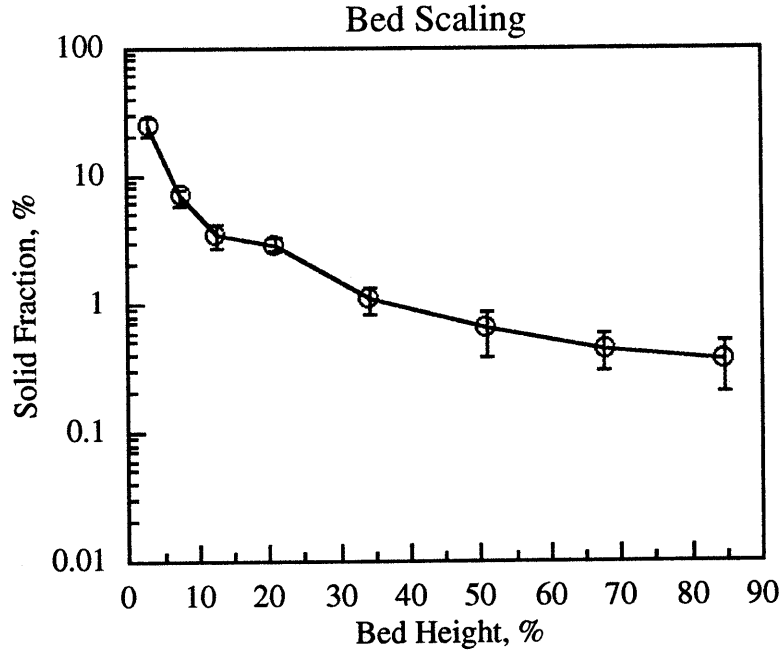

Bed Material: Steel

% Bed Ht.	SF, %	Std. Dev.
3	24.49	8.8605
7.6	6.94	1.9432
12.8	3.44	1.3237
21	2.88	0.6877
34.2	1.07	0.4901
50.8	0.63	0.4860
67.8	0.44	0.2840
84.7	0.36	0.3140

Figure G.7 - 1/4 Scale Model, Condition 1

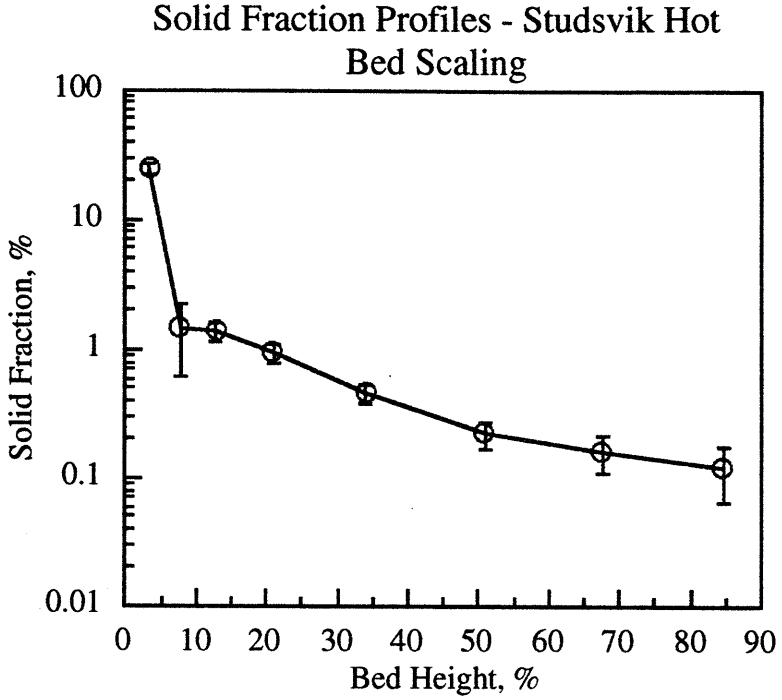

Bed Material: Steel

% Bed Ht.	SF, %	Std. Dev.
3.4	24.83	4.5526
7.7	1.44	1.6664
12.9	1.39	0.4827
21	0.93	0.3258
34.1	0.46	0.1509
50.8	0.22	0.1018
67.7	0.16	0.0996
84.7	0.12	0.1095

Figure G.8 - 1/4 Scale Model, Condition 2

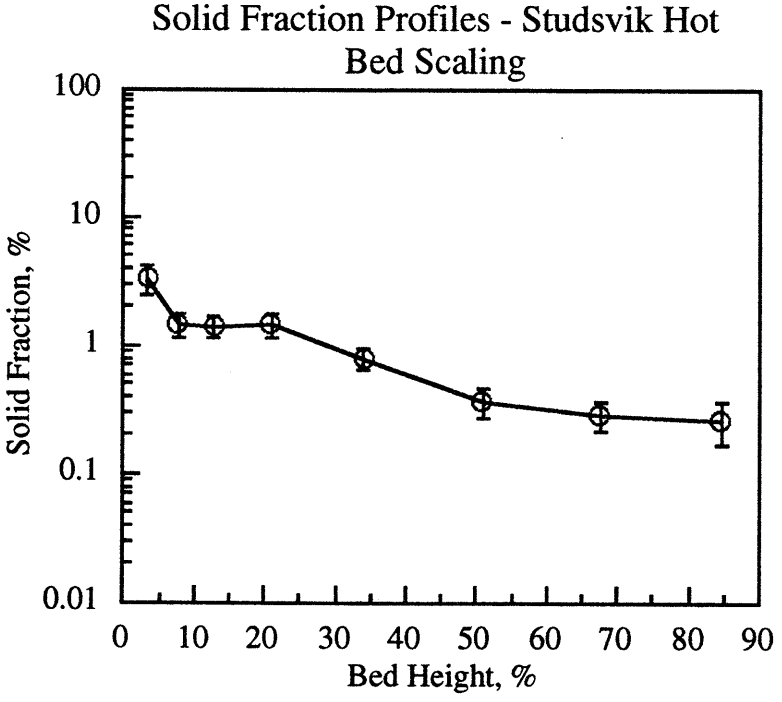

Bed Material: Steel

% Bed Ht.	SF, %	Std. Dev.
3.4	3.34	1.8083
7.7	1.45	0.5745
12.9	1.4	0.5436
21	1.48	0.6148
34.1	0.78	0.2889
50.8	0.37	0.2040
67.7	0.29	0.1579
84.7	0.26	0.1895

Figure G.9 - 1/4 Scale Model, Condition 3

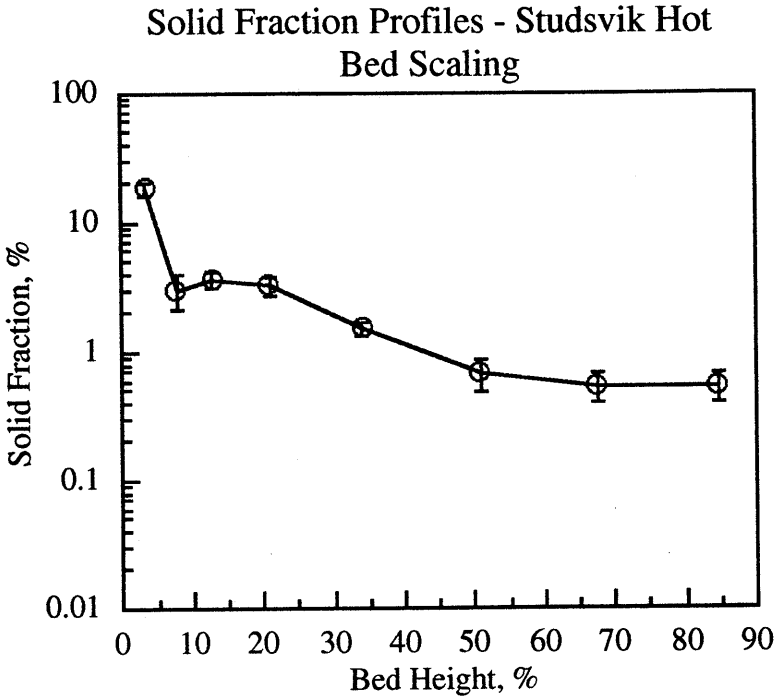

Bed Material: Steel

% Bed Ht.	SF, %	Std. Dev.
3.4	18.43	4.6256
7.7	3.02	1.8394
12.9	3.59	1.0254
21	3.23	1.1001
34.1	1.5	0.3224
50.8	0.67	0.3715
67.7	0.53	0.2760
84.7	0.54	0.2831

Figure G.10 - 1/4 Scale Model, Condition 4

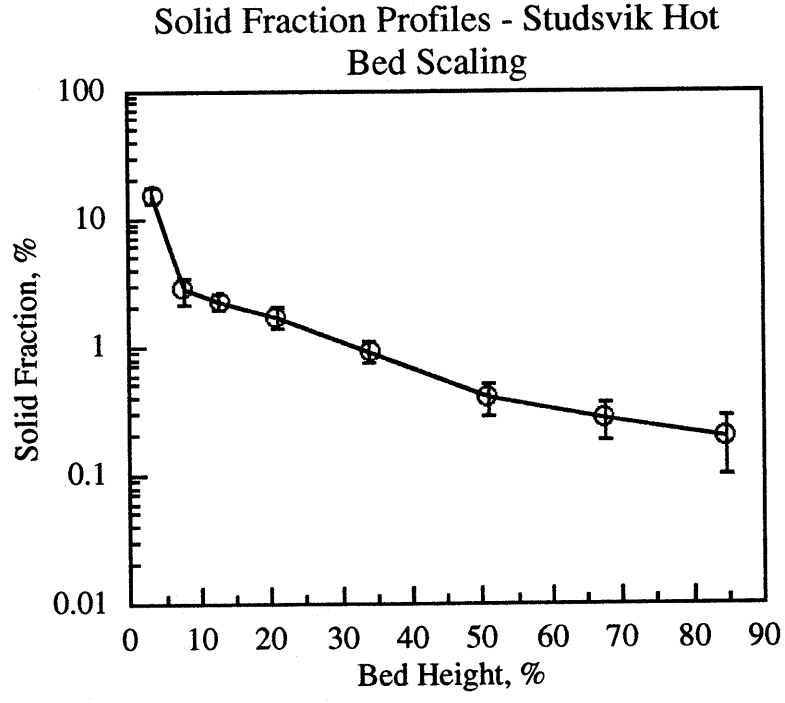

Bed Material: Steel

% Bed Ht.	SF, %	Std. Dev.
3.4	15.21	4.4751
7.7	2.83	1.3682
12.9	2.29	0.6977
21	1.69	0.6283
34.1	0.91	0.3341
50.8	0.4	0.2290
67.7	0.27	0.1762
84.7	0.19	0.1809

Figure G.11 - 1/4 Scale Model, Condition 5

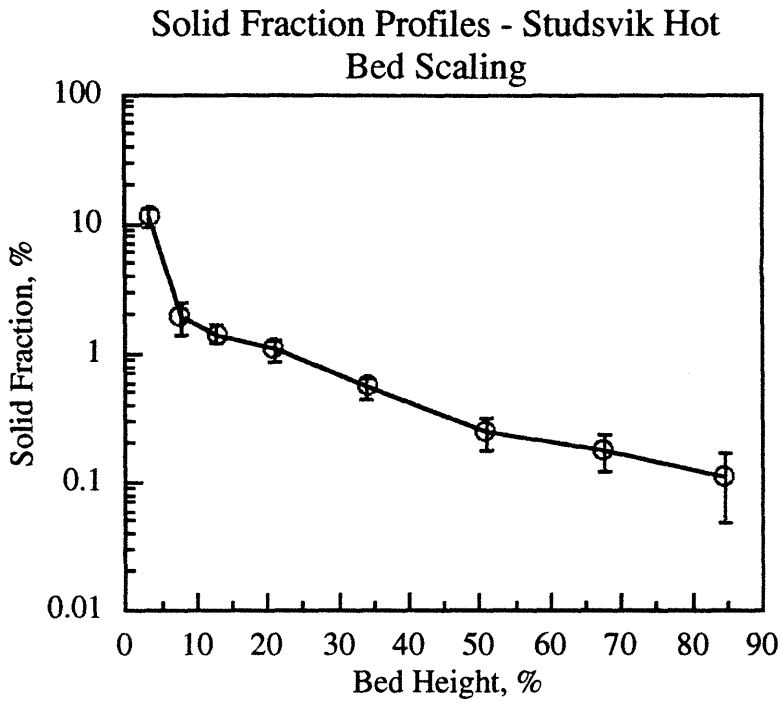

Bed Material: Steel

% Bed Ht.	SF, %	Std. Dev.
3.4	11.32	3.6435
7.7	1.93	1.0483
12.9	1.42	0.4605
21	1.07	0.4404
34.1	0.55	0.2085
50.8	0.25	0.1398
67.7	0.18	0.1203
84.7	0.11	0.1245

Figure G.12 - Studsvik Hot Bed, Condition 1

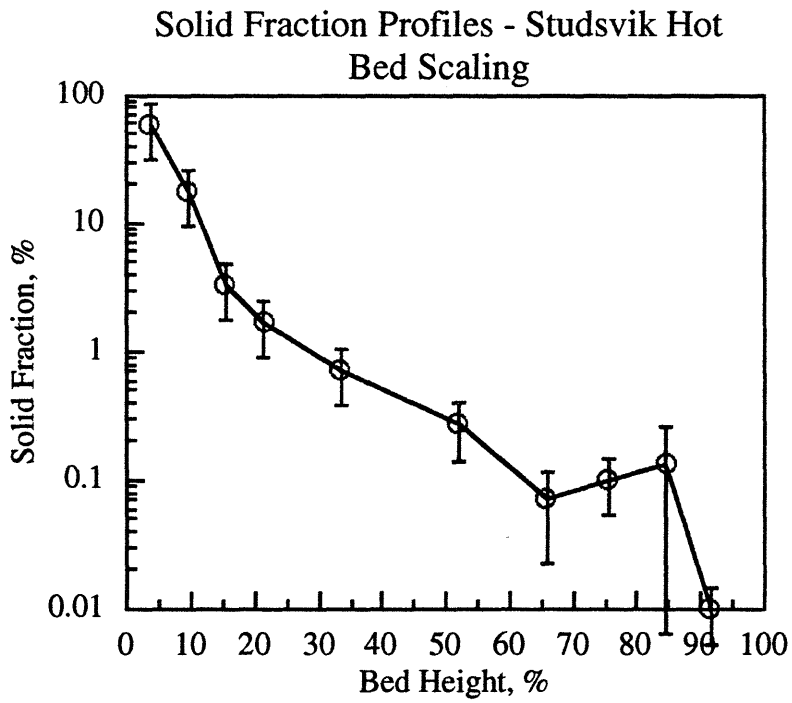

Bed Material: Olivin Sand

% Bed Ht.	SF, %	Std. Dev.
3.55	58.9	55.6605
9.4	17.87	16.8872
15.4	3.35	3.1658
21.5	1.69	1.5971
33.3	0.72	0.6804
52.1	0.27	0.2552
65.9	0.07	0.0945
75.4	0.1	0.0945
84.6	0.13	0.2470
91.4	0.01	0.0095

Figure G.13 - Studsvik Hot Bed, Condition 2

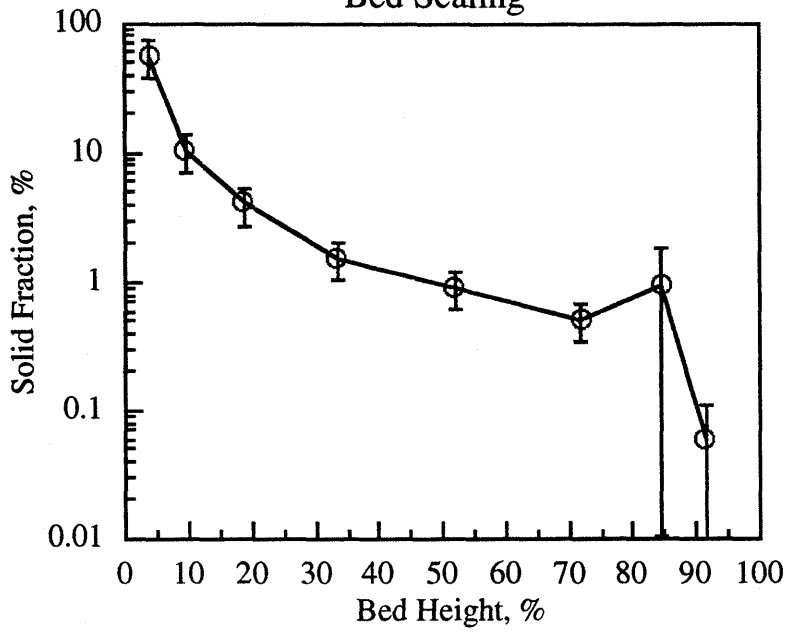

Bed Material: Olivin Sand

% Bed Ht.	SF, %	Std. Dev.
3.8	55.05	35.5073
9.4	10.48	6.7596
18.8	4.1	2.6445
33.3	1.55	0.9998
52.1	0.92	0.5934
72	0.5	0.3225
84.6	0.95	1.8791
91.4	0.06	0.0999

Figure G.14 - Studsvik Hot Bed, Condition 3

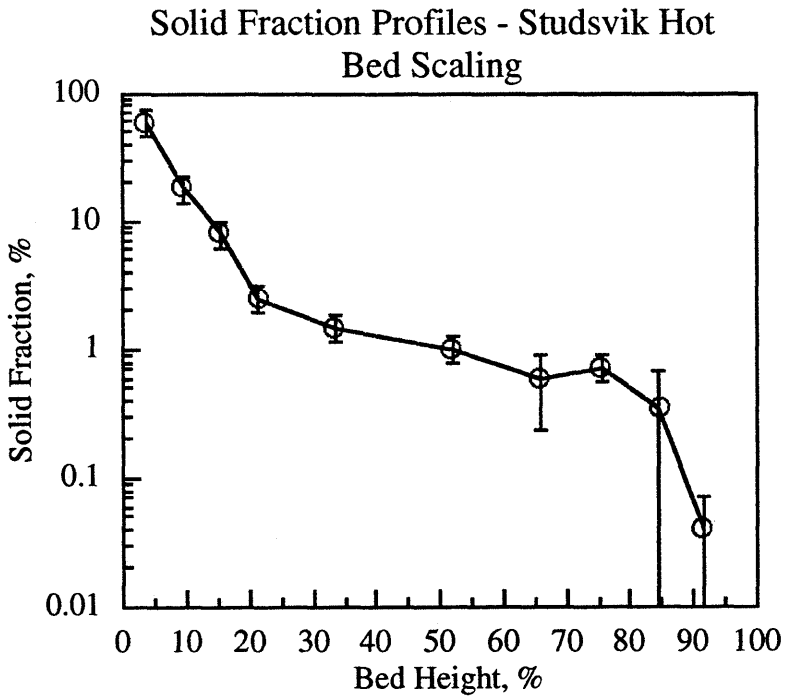

Bed Material: Olivin Sand

% Bed Ht.	SF, %	Std. Dev.
3.55	59.37	28.3195
9.4	18.32	8.7386
15.4	8.11	3.8685
21.5	2.5	1.1925
33.3	1.49	0.7107
52.1	1.01	0.4818
65.9	0.58	0.6856
75.4	0.72	0.3434
84.6	0.35	0.6797
91.4	0.04	0.0600

Figure G.15 - Studsvik Hot Bed, Condition 4

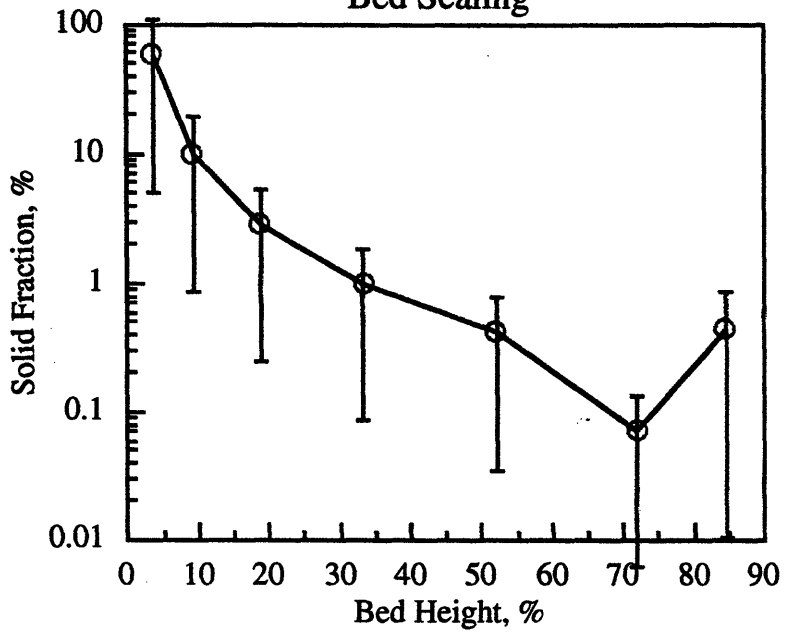

Bed Material: Olivin Sand

% Bed Ht.	SF, %	Std. Dev.
3.55	57.53	105.1073
9.4	10.01	18.2883
18.8	2.8	5.1156
33.3	0.98	1.7905
52.1	0.41	0.7491
72	0.07	0.1279
84.6	0.43	0.8396

Figure G.16 - Studsvik Hot Bed, Condition 5

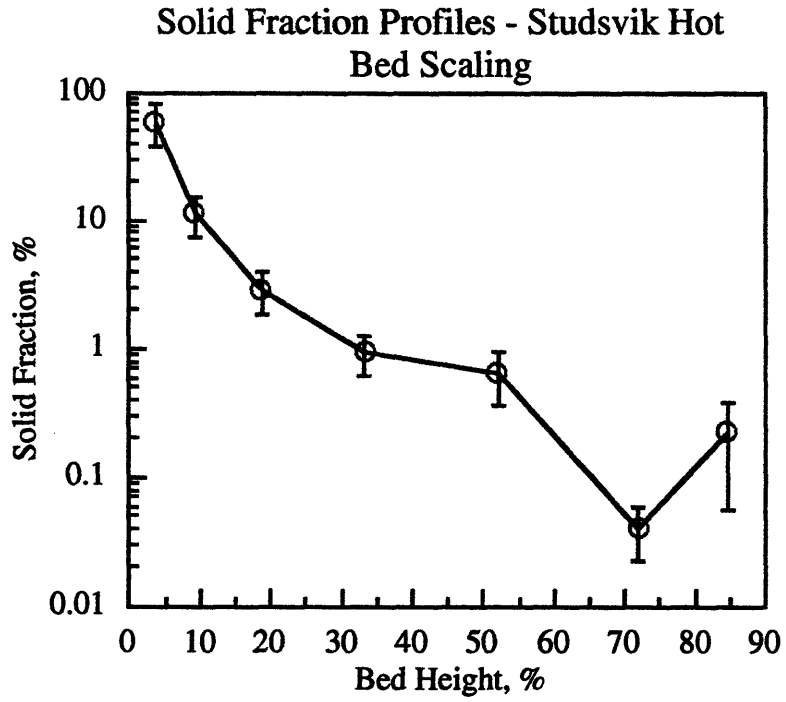

Bed Material: Olivin Sand

% Bed Ht.	SF, %	Std. Dev.
3.55	59.56	42.3472
9.4	11.42	8.1196
18.8	2.89	2.0548
33.3	0.94	0.6683
52.1	0.65	0.5668
72	0.04	0.0357
84.6	0.22	0.3265

Figure G.17 - Studsvik Hot Bed, Condition 6

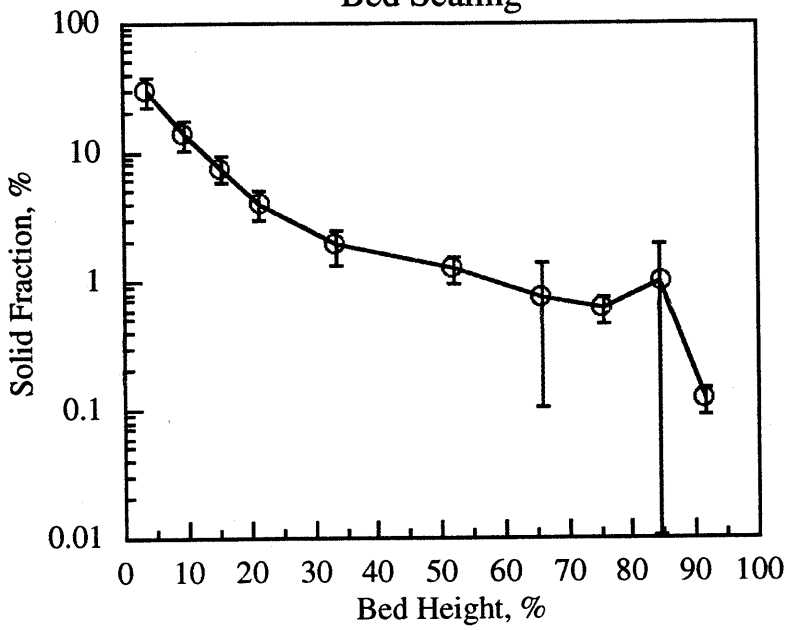

Bed Material: Olivin Sand

% Bed Ht.	SF, %	Std. Dev.
3.55	30	14.4000
9.4	13.89	7.4173
15.4	7.6	3.6480
21.5	3.99	1.9790
33.3	1.9	1.1666
52.1	1.25	0.6000
65.9	0.75	1.2915
75.4	0.61	0.2928
84.6	1	1.9790
91.4	0.12	0.0552

Table G.1

Hot Bed Scaling Using Simplified Scaling Laws - Condition 1

	Studsvik Hot Bed	1/4 Scale Cold Bed	1/16 Scale Cold Bed
u_o (m/s)	6.07	2.91	1.44
u_{mf} (cm/s) Ergun Eqn.	5.75	2.18	0.46
u_{mf} (cm/s) measured		1.40	0.75
d_p (microns)	243	57.7	~ 26
L (m)	7.32	1.83	0.46
A_{cs} (m^2)	0.434	0.0252	1.575E-3
G_s (kg/m^2-s)	10.2	12.8	6.5
% Primary Air	49	50	50
$Re_{dp,uo}$	10.3	11.1	2.53
$Re_{L,uo}$	3.14E5	3.52E5	4.36E4
Fr	0.51	0.47	0.46
$\left(\frac{u_o}{u_{mf}}\right)_{Ergun\ eqn.}$	105.6	133.7	313.6
$\left(\frac{u_o}{u_{mf}}\right)_{measured}$		207.9	192.0
$\left(\frac{G_s}{\rho_s u_o}\right)$	6.22E-4	6.07E-4	6.23E-4
$\left(\frac{\rho_s}{\rho_f}\right)$	8413	6042	6042
Ga	4.99E5	3.01E5	2.92E4

Table G.2

Hot Bed Scaling Using Simplified Scaling Laws - Condition 2

	Studsvik Hot Bed	1/4 Scale Cold Bed	1/16 Scale Cold Bed
u_o (m/s)	7.92	3.69	1.88
u_{mf} (cm/s) Ergun Eqn.	5.75	2.18	0.46
u_{mf} (cm/s) measured		1.40	0.75
d_p (microns)	243	57.7	~ 26
L (m)	7.32	1.83	0.46
A_{cs} (m^2)	0.434	0.0252	1.575E-3
G_s (kg/m^2-s)	16.6	22.0	10.7
% Primary Air	69	69	69
$Re_{dp,uo}$	13.6	14.2	3.30
$Re_{L,uo}$	4.10E5	4.46E5	5.69E4
Fr	0.87	0.76	0.79
$\left(\frac{u_o}{u_{mf}}\right)_{Ergun\ eqn.}$	137.7	169.0	409.6
$\left(\frac{u_o}{u_{mf}}\right)_{measured}$		263.5	251.7
$\left(\frac{G_s}{\rho_s u_o}\right)$	7.91E-4	8.22E-4	7.84E-4
$\left(\frac{\rho_s}{\rho_f}\right)$	8413	6042	6042
Ga	4.99E5	3.01E5	2.92E4

Table G.3

Hot Bed Scaling Using Simplified Scaling Laws - Condition 3

	Studsvik Hot Bed	1/4 Scale Cold Bed	1/16 Scale Cold Bed
u_o (m/s)	7.65	3.64	1.81
u_{mf} (cm/s) Ergun Eqn.	5.75	2.18	0.46
u_{mf} (cm/s) measured		1.40	0.75
d_p (microns)	243	57.7	~ 26
L (m)	7.32	1.83	0.46
A_{cs} (m^2)	0.434	0.0252	1.575E-3
G_s (kg/m^2-s)	30.7	38.3	19.6
% Primary Air	52	52	52
$Re_{dp,uo}$	13.2	13.9	3.17
$Re_{L,uo}$	3.96E5	4.40E5	5.48E4
Fr	0.82	0.74	0.73
$\left(\frac{u_o}{u_{mf}}\right)_{Ergun\ eqn.}$	133.0	167.0	394.3
$\left(\frac{u_o}{u_{mf}}\right)_{measured}$		260.0	241.3
$\left(\frac{G_s}{\rho_s u_o}\right)$	1.51E-3	1.45E-3	1.49E-3
$\left(\frac{\rho_s}{\rho_f}\right)$	8413	6042	6042
Ga	4.99E5	3.01E5	2.92E4

Table G.4

Hot Bed Scaling Using Simplified Scaling Laws - Condition 4

	Studsvik Hot Bed	1/4 Scale Cold Bed	1/16 Scale Cold Bed
u_o (m/s)	6.05	3.01	1.44
u_{mf} (cm/s) Ergun Eqn.	5.75	2.18	0.46
u_{mf} (cm/s) measured		1.40	0.75
d_p (microns)	243	57.7	~ 26
L (m)	7.32	1.83	0.46
A_{cs} (m^2)	0.434	0.0252	1.575E-3
G_s (kg/m^2-s)	13.8	18.2	8.88
% Primary Air	71	69	71
$Re_{dp,uo}$	10.4	11.5	2.53
$Re_{L,uo}$	3.14E5	3.65E5	4.36E4
Fr	0.51	0.51	0.46
$\left(\frac{u_o}{u_{mf}}\right)_{Ergun\ eqn.}$	105.2	138.1	313.7
$\left(\frac{u_o}{u_{mf}}\right)_{measured}$		215.0	192.0
$\left(\frac{G_s}{\rho_s u_o}\right)$	8.61E-4	8.34E-4	8.51E-4
$\left(\frac{\rho_s}{\rho_f}\right)$	8413	6042	6042
Ga	4.99E5	3.01E5	2.92E4

Table G.5

Hot Bed Scaling Using Simplified Scaling Laws - Condition 5

	Studsvik Hot Bed	1/4 Scale Cold Bed	1/16 Scale Cold Bed
u_o (m/s)	6.16	3.09	1.49
u_{mf} (cm/s) Ergun Eqn.	5.75	2.18	0.46
u_{mf} (cm/s) measured		1.40	0.75
d_p (microns)	243	57.7	~ 26
L (m)	7.32	1.83	0.46
A_{cs} (m^2)	0.434	0.0252	1.575E-3
G_s (kg/m^2-s)	9.0	11.3	5.75
% Primary Air	69	69	69
$Re_{dp,uo}$	10.6	11.8	2.61
$Re_{L,uo}$	3.19E5	3.74E5	4.51E4
Fr	0.53	0.53	0.50
$\left(\frac{u_o}{u_{mf}}\right)_{Ergun\ eqn.}$	107.1	143.1	324.6
$\left(\frac{u_o}{u_{mf}}\right)_{measured}$		220.7	198.7
$\left(\frac{G_s}{\rho_s u_o}\right)$	5.51E-4	5.04E-4	5.32E-4
$\left(\frac{\rho_s}{\rho_f}\right)$	8413	6042	6042
Ga	4.99E5	3.01E5	2.92E4

Table G.6

Hot Bed Scaling Using Simplified Scaling Laws - Condition 6

	Studsvik Hot Bed	1/4 Scale Cold Bed	1/16 Scale Cold Bed
u_o (m/s)	6.16		1.89
u_{mf} (cm/s) Ergun Eqn.	5.75		0.46
u_{mf} (cm/s) measured			0.75
d_p (microns)	243		~ 26
L (m)	7.32		0.46
A_{cs} (m^2)	0.434		1.575E-3
G_s (kg/m^2-s)	9.0		23.5
% Primary Air	70		70
$Re_{dp,uo}$	13.7		3.32
$Re_{L,uo}$	4.12E5		5.72E4
Fr	0.88		0.80
$\left(\frac{u_o}{u_{mf}}\right)_{Ergun\ eqn.}$	138.1		411.8
$\left(\frac{u_o}{u_{mf}}\right)_{measured}$			252.0
$\left(\frac{G_s}{\rho_s u_o}\right)$	1.79E-3		1.78E-3
$\left(\frac{\rho_s}{\rho_f}\right)$	8413		6042
Ga	4.99E5		2.92E4

APPENDIX H HYDRODYNAMIC DATA FOR FOSTER WHEELER PRESSURIZED HOT BED SCALING

Solid fraction profile test results for the Studsvik hot bed and the scaling runs of the Foster Wheeler hot bed utilizing the simplified set of scaling laws are presented in the following pages.

Figure H.1 - Foster Wheeler Combustor Condition 1

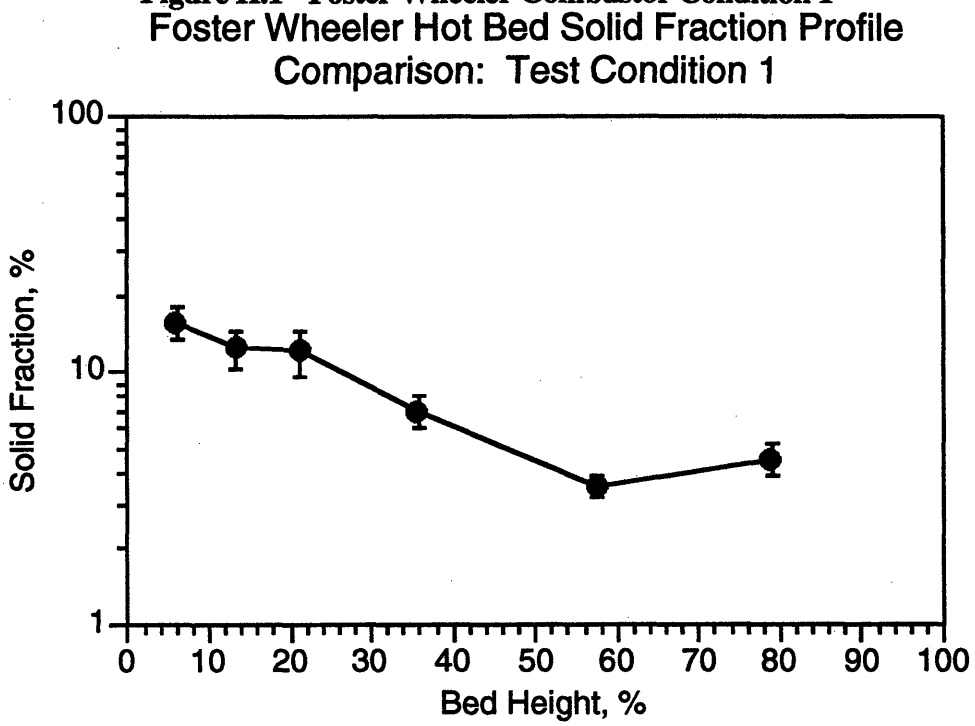

% Bed Ht.	SF, %	Std. Dev.
6.1	15.68	2.21
13.4	12.41	2.17
21.2	12.09	2.52
35.9	7.01	1
57.6	3.55	0.34
79.1	4.55	0.64

Figure H.1 - Foster Wheeler Combustor Condition 2

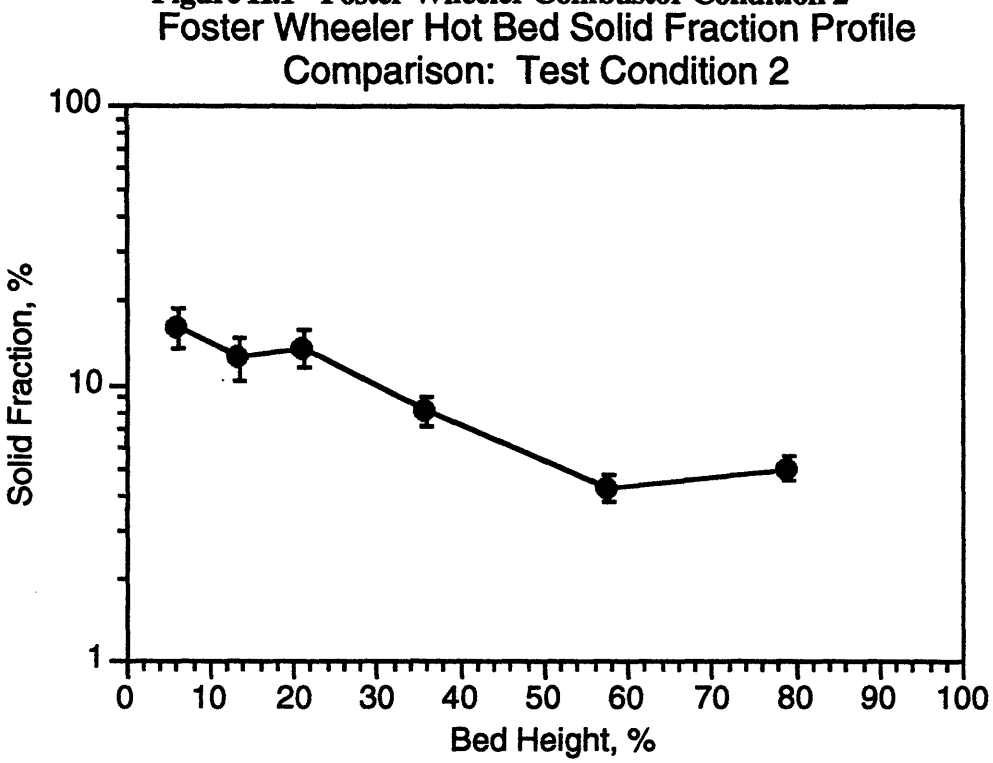

% Bed Ht.	SF, %	Std. Dev.
6.1	16.31	2.62
13.4	12.55	2.28
21.2	13.68	2.18
35.9	8.12	1
57.6	4.28	0.44
79.1	5.02	0.48

Figure H.3 - Foster Wheeler Combustor Condition 3

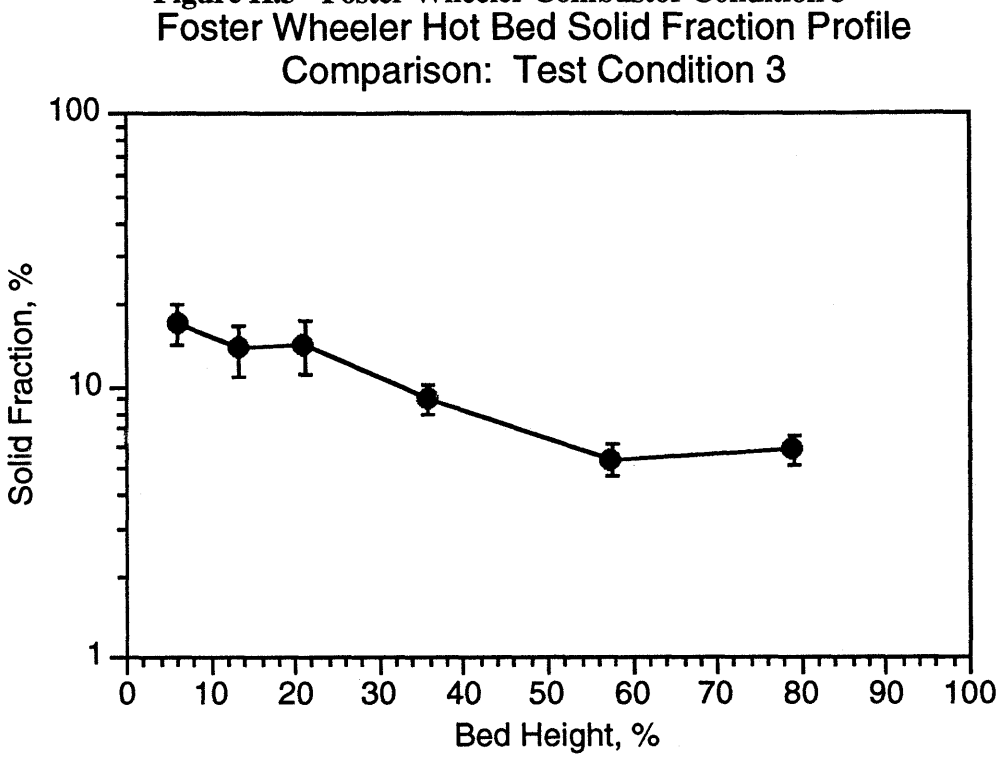

% Bed Ht.	SF, %	Std. Dev.
6.1	17.15	2.94
13.4	13.84	2.9
21.2	14.28	3.12
35.9	9.01	1.1
57.6	5.43	0.73
79.1	5.85	0.76

Figure H.4 - Foster Wheeler Combustor Condition 4

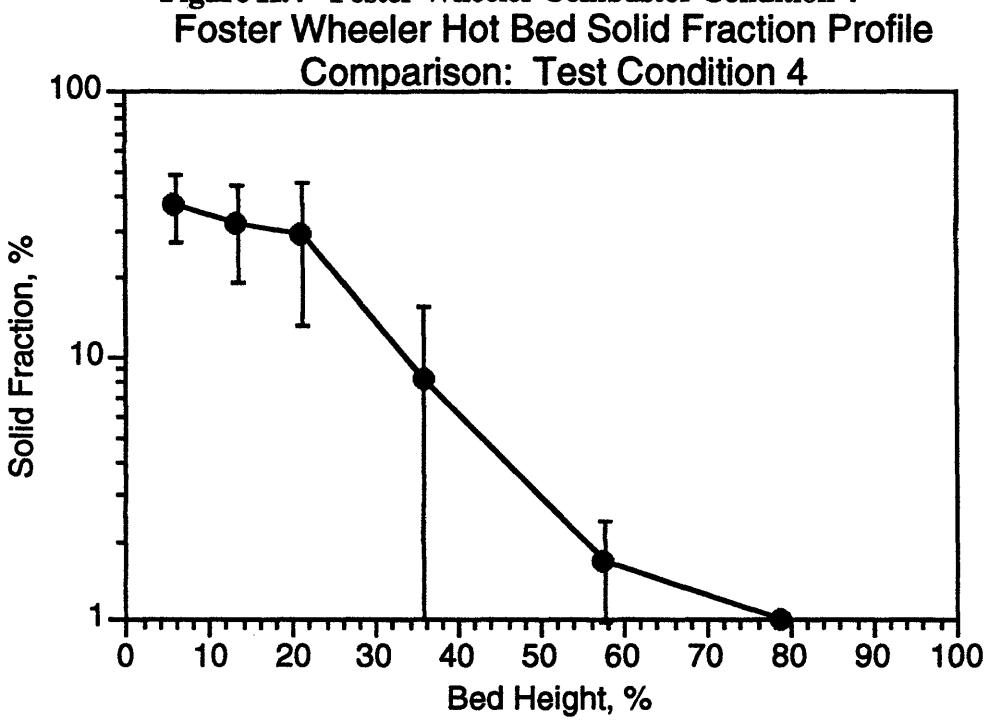

% Bed Ht.	SF, %	Std. Dev.
6.1	37.73	10.8
13.4	31.86	12.7
21.2	29.39	16.1
35.9	8.23	7.23
57.6	1.68	0.7
79.1	1.02	0.02

Figure H.5 - 1/2 Scale Model of Foster Wheeler Combustor Condition 1

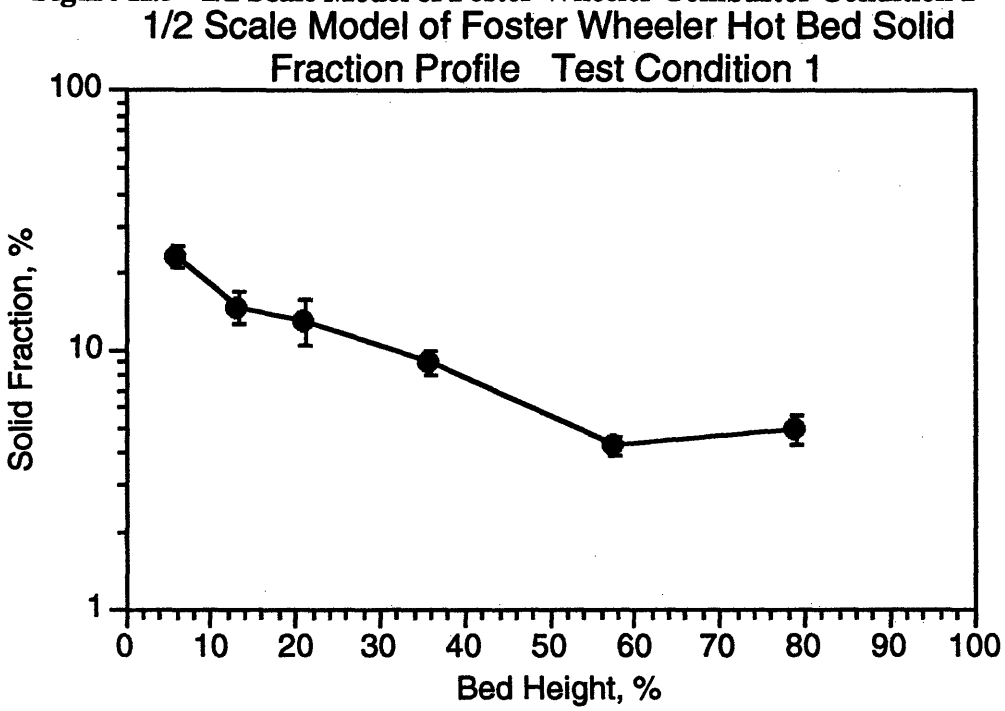

% Bed Ht.	SF, %	Std. Dev.
6.1	23.15	9.42
13.4	14.74	6.67
21.2	13.03	1.9
35.9	8.99	0.71
57.6	4.31	0.96
79.1	4.98	1.32

Figure H.6 - 1/2 Scale Model of Foster Wheeler Combustor Condition 2

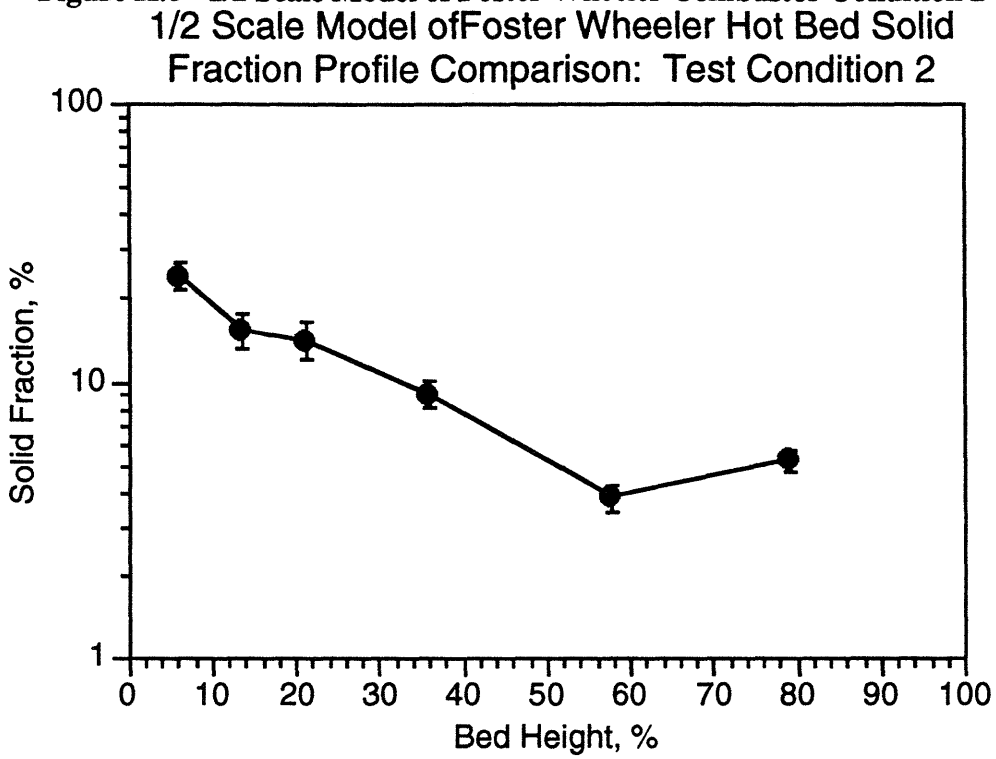

% Bed Ht.	SF, %	Std. Dev.
6.1	24.28	8.26
13.4	15.41	5.54
21.2	14.24	3.1
35.9	9.06	0.98
57.6	3.85	1.16
79.1	5.26	1.11

Figure H.7 - 1/2 Scale Model of Foster Wheeler Combustor Condition 3

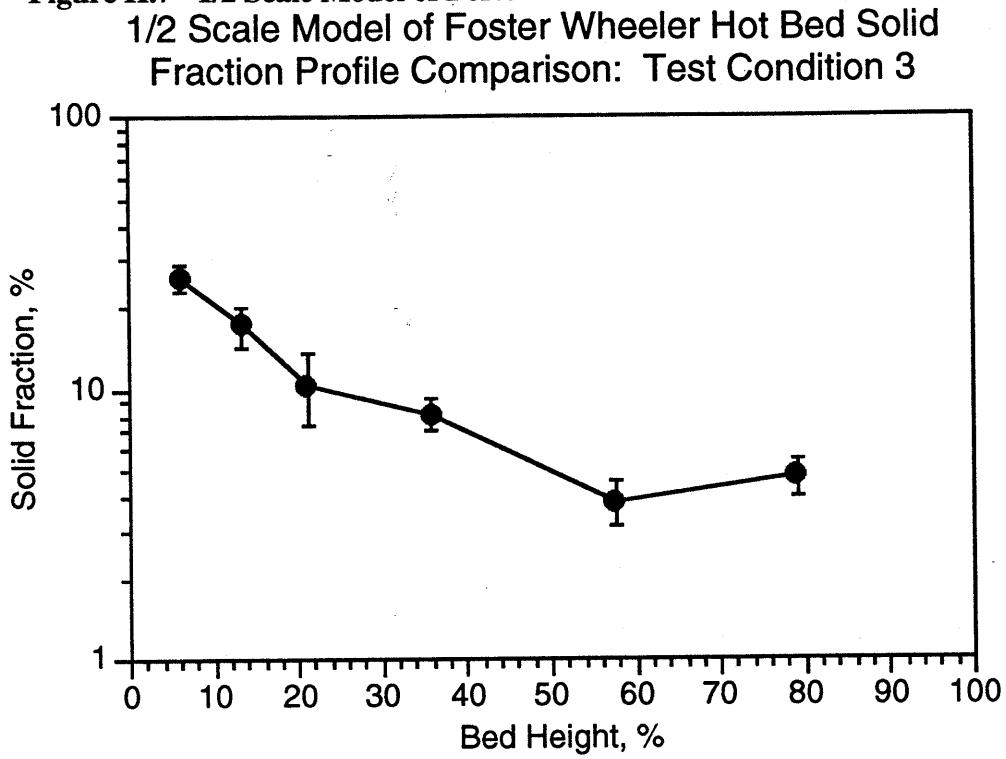

% Bed Ht.	SF, %	Std. Dev.
6.1	25.99	9.7
13.4	17.34	8
21.2	10.46	3.5
35.9	8.11	0.92
57.6	3.85	1.13
79.1	4.8	1.3

Figure H.8 - 1/2 Scale Model of Foster Wheeler Combustor Condition 4

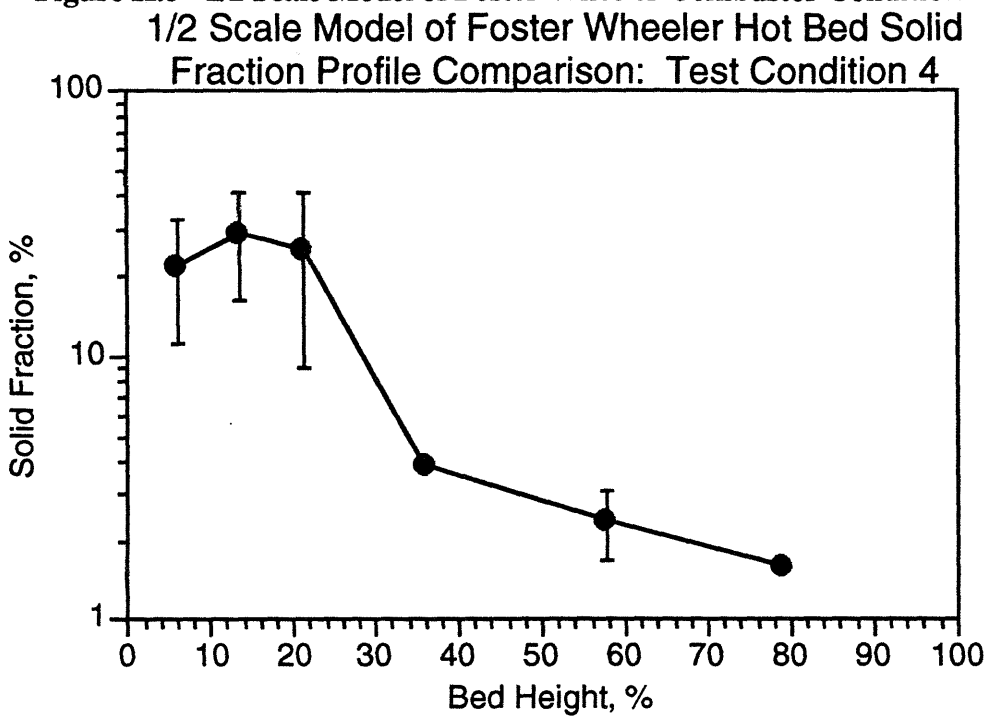

% Bed Ht.	SF, %	Std. Dev.
6.1	22.1	13.8
13.4	28.9	9.36
21.2	25.2	2.38
35.9	3.91	0.82
57.6	2.39	0.97
79.1	1.61	0.61

CHAPTER 3

THERMAL SCALING FOR CIRCULATING FLUIDIZED BEDS

1.0 INTRODUCTION

An important characteristic of a fluidized bed which is influenced by the hydrodynamics is the heat transfer to surfaces in the bed or to the bed walls. The heat transfer is not only controlled by the hydrodynamic variables, thermal properties must also be included. The two thermophysical properties which have an important bearing on convective heat transfer are the conductivity of the gas within the bed, especially the conduction of the gas film between the particles and the heat transfer surface, and the specific heat of the particles. The former property influences the contact resistance between the particles and the surface and the latter influences the emulsion or renewal resistance as proposed by Mickley (1955). It can be shown that the exact value of the solid thermal conductivity plays a minor role as long as the solid conductivity is several orders of magnitude greater than the gas conductivity.

The proper scaling of convective heat transfer has never been investigated in a cold fluidized bed model. With the full set of dimensionless parameters, there are no free design or independent operating parameters which can be used to assure correct scaling of the heat transfer. However, when the hydrodynamic scaling parameters are relaxed, there are free design parameters that can be used to provide proper scaling of the convection heat transfer. There is very little data or fundamental understanding of the convective heat transfer in circulating beds or at the bounding walls of bubbling beds, either in the dense bed or in the splash zone. The use of properly scaled models will provide data for a variety of flow conditions and geometry. Moreover, the heat transfer results, obtained in a properly scaled cold bed in which the hydrodynamics can be carefully observed, should provide the foundation for a mechanistic predictive model of the convective heat transfer in a combustor.

The following discussion applies only to the convective portion of the heat transfer. Radiation heat transfer adds additional parameters and cannot be directly simulated in a cold bed since it is dependent on the temperature level. For fluidized beds, simulation of the convective component is most important to understanding the overall heat transfer. Radiative heat transfer can be estimated analytically with more confidence than can convective heat transfer. In addition, the amount of heat transfer due to radiation is usually smaller in magnitude than that due to convection, especially in the more dense regions of the bed. This Chapter presents theoretical and experimental results of tests conducted to evaluate the scaling of convective heat transfer in circulating fluidized beds. The theoretical

issue will be approached by first setting out the full set of governing parameters and then examining circumstances where this set can be relaxed.

2.0 GOVERNING EQUATIONS FOR HEAT TRANSFER

A phenomenological view of the different heat transfer mechanisms will be taken and a set of governing dimensionless parameters will be developed by non-dimensionalizing the governing energy equations. Corresponding equations of motion which also bear on the problem will not be repeated since they have been developed in Chapter 2. Viewing the system as a continuum or as a collection of individual particles will yield similar forms for the parameters analogous to the results for hydrodynamics. Our attention will focus on heat transfer between a fluidized bed and an immersed heat transfer surface or a bounding wall. Typically, the heat transfer has been characterized as that due to particle convection, gas convection and thermal radiation. Particle convection is heat transfer due to the exchange of particles near the surface and the bed interior with their corresponding heat capacity. Gas convection is the heat transfer from the surface due to gas motion and its corresponding heat capacity. Operationally, gas convection is the balance of the convective heat transfer not ascribable to particle convection. For some cases the distinction between the two mechanisms is not precise. Radiation is a separate physical mechanism of heat transfer but it may interact with the other forms of heat transfer, particularly particle convection.

The overall phenomenological model of heat transfer for either bubbling, slugging or circulating beds is generally agreed to consist of the intermittent contact of a rather dense group of particles in the form of an emulsion, packet or cluster, interspersed with periods of contact with a high voidage fluid phase, e.g. a bubble. The time averaged heat transfer coefficient can be represented as,

$$h = f h_{pc} + (1 - f) h_{gc} \tag{1}$$

where h is the overall average heat transfer coefficient, h_{pc} represents the average heat transfer coefficient when the dense phase is in contact with the surface, h_{gc} is the heat transfer under the dilute phase and f is the temporal or spatial average fraction of the surface area occupied by the dense phase. For high temperatures, radiation effects must be include in both the dense and dilute phases.

The dense phase heat transfer is generally represented by a thermal resistance described by a renewal model for the emulsion (Mickley & Fairbanks, 1955) which for short times is considered in series with a thermal resistance at the fluid interface between the dense phase and the wall (Baskakov, 1964).

$$h_{pc}^{-1} = h_w^{-1} + h_e^{-1} \tag{2}$$

where h_w and h_e are the wall and dense phase coefficients, respectively.

With the boundary conditions on temperature $T = T_w$ at the bed wall and $T = T_b$ far from the wall. In dimensionless form[1]

$$\left(\frac{h_{pc}d_p}{k_f}\right)^{-1} = \left(\frac{h_w d_p}{k_f}\right)^{-1} + \left(\frac{h_e d_p}{k_f}\right)^{-1} \tag{3}$$

where k_f is the fluid thermal conductivity.

For a uniform emulsion or cluster with mean properties,

$$\frac{h_e d_p}{k_f} \sim \frac{d_p}{k_f}\frac{k_e}{\sqrt{\alpha_e t}} \sim \sqrt{\left(\frac{d_p k_e}{k_f}\right)^2 \left(\frac{(1-\varepsilon)\rho_s c_{p_s}}{k_e}\right)\frac{u}{Lt}} \tag{4}$$

where α_e, the effective thermal diffusivity of the cluster or emulsion, is expressed in terms of the emulsion properties, the effective emulsion conductivity, k_e and solid specific heat c_{ps}. The time of contact is non-dimensionalized as ut/L or t'. Rewriting (4),

$$\frac{h_e d_p}{k_f} \sim \frac{1}{\sqrt{t'}}\sqrt{\left(\frac{k_e}{k_f}\right)\left(\frac{u(1-\varepsilon_e)\rho_s c_{p_s} d_p^2}{Lk_f}\right)} \sim \frac{1}{\sqrt{t'}}\sqrt{(1-\varepsilon_e)\left(\frac{c_{p_s}}{c_{p_f}}\right)Pr_f\frac{u_{mf}}{u}Fr\left(1-\frac{\rho_s}{\rho_f}\right)\left(\frac{k_e}{k_f}+\frac{8}{9}\frac{d_p\sigma T^3}{k_f}\right)} \tag{5}$$

where ε_e and t' are set by the hydrodynamics.

[1] To non-dimensionlalize this a mean value of d_p is used, it is not clear if this should be averaged in the same way as the mean value used for the hydrodynamics. This point is moot if the same dimensionless size distribution is used for the model and the full size bed.

$\left(\frac{u\rho_s c_{p_s} d_p^2}{Lk_f}\right)$ is a dimensionless parameter which is the ratio of the thermal time constant of a particle to the time of contact set by the hydrodynamics. Note u is a characteristic velocity of particle clusters or bubbles in contact with the heat transfer surface. For bubbling beds the characteristic velocity is dependent on u_o, for circulating beds it should be the cluster falling velocity at the wall. The ratio $\left(\frac{k_e}{k_f}\right)$ for a uniform mixture of particles and fluid is found to be a function of the true particle conductivity, k_s, the fluid conductivity and the void fraction, see for example, Gelperin & Einstein (1971)

$$\left(\frac{k_e}{k_f}\right) = f\left(\frac{k_s}{k_f}, \varepsilon_e\right) \tag{6}$$

where it is shown that $\frac{k_e}{k_f}$ is a weak function of $\frac{k_s}{k_f}$.

If the bed is at high temperature and the fluid is a gas there will be radiant transfer between particles making up the media. For particles large compared to the wavelength of infrared radiation the radiant transfer within the media can be approximated by an effective conductivity, k_r (Chen & Churchill 1963; Glicksman & Decker 1982) as

$$k_r \cong \frac{8 d_p \sigma T^3}{9} \tag{7}$$

which should be added to k_e in (5). This leads to an additional dimensionless parameter $\frac{d_p \sigma T^3}{k_f}$ where σ is the Stefan Boltzmann constant and T is the absolute temperature. If the particle diameter approaches the wavelength of the radiation additional parameters enter, primarily the complex index of refraction of the particles and the fluid and the particle shape. These will be omitted in this treatment.

From the foregoing (5), (6) and (7) we can establish the functional relationship,

$$\frac{h_e d_p}{k_f} = f\left(\left(\frac{u\rho_s c_{p_s} d_p^2}{Lk_f}\right);\ t';\ \varepsilon_e;\ \frac{k_s}{k_f};\ \frac{d_p \sigma T^3}{k_f}\right) \tag{8}$$

The additional resistance at the wall, at low temperature and moderate particle size, can be approximated by a conduction resistance through a gas layer which is some fraction of a particle diameter. Such a gas layer may represent the actual situation at the wall of a circulating bed (Lints and Glicksman 1993a) whereas in a bubbling bed it is a simple approximation for contact resistance (Gloski *et al.* 1984). For larger particles and high slip velocities near the wall, the gas conduction term may be augmented by a convection term, given as a function of particle Reynolds number (see Glicksman and Decker, 1982) for bubbling beds or a function of Archimedes number (Baskakov and Suprun, 1972) which can be related to the Reynolds number at u_{mf}. The overall equation for the wall coefficient of heat transfer with radiation included becomes

$$\frac{h_w d_p}{k_f} = \delta^{-1} + Co\, Re_{d_p} Pr_f + \frac{d_p}{k_f} \frac{\sigma T_w^3 \left(1 + \frac{T_w}{T_e}\right)}{\left(\frac{1}{\varepsilon_w} + \frac{1}{\varepsilon_B} - 1\right)} \left(1 + \left(\frac{T_w}{T_e}\right)^2\right) \tag{9}$$

where Pr_f is the fluid Prandtl number and ε_w and ε_B are the emissivity of the wall and the effective emissivity of the medium, respectively. The latter is determined by the surface properties of the particles and the geometry of the dense medium. δ, the dimensionless particle to wall spacing, and Co are constants which should be hydrodynamic functions. Radiation enters through the dimensionless radiation conduction term, which also appeared in (8), along with the ratio of absolute temperatures. If the wall and bed are close in absolute temperatures this factor can be omitted and the radiation conduction term can be expressed using the mean temperature between the bed and the heat transfer surface. Note that T_e is an intermediate temperature between T_w and T_b which can be found once h_w and h_e are determined. Thus $\left(\frac{T_w}{T_e}\right)$ should be a function of the factors controlling h_w and h_e along with $\left(\frac{T_w}{T_B}\right)$.

Thus we can write

$$\frac{h_w d_p}{k_f} = f\left[Re_{d_p} Pr_f;\ \frac{d_p \sigma T_w^3}{k_f};\ \left(\frac{T_w}{T_B}\right);\ \varepsilon_w;\ \varepsilon_B;\ \varepsilon_e\right] \tag{10}$$

Combining these developments, the overall particle convection heat transfer coefficient can be expressed as,

$$\frac{h_w d_p}{k_f} = f\left[\left(\frac{u\rho_s c_{p_s} d_p^2}{L k_f}\right);\ \frac{k_s}{k_f};\ Re_{d_p} Pr_f;\ \frac{d_p \sigma T_w^3}{k_f};\ \left(\frac{T_w}{T_B}\right);\ \varepsilon_w;\ \varepsilon_B;\ \varepsilon_e;\ \text{bed hydrodynamics}\right] \quad (11)$$

For low temperatures, where radiation is unimportant the last four dimensionless terms can be omitted. For moderate particle Reynolds numbers in bubbling beds, below approximately 10-30, the product of Reynolds number and Prandtl number is unimportant for bubbling beds. The ratio of particle to gas conductivity has a modest influence on the ratio of effective emulsion to gas conductivity. For a gas fluidized bed with non-metallic particles, the emulsion to gas conductivity ratio at a fixed emulsion void fraction can be taken as approximately constant. For very large particles and short contact times at the heat transfer surface, e.g. 1 mm particles with a contact time of a second or less, the first term in (11) is unimportant since the particles remain close to T_B during their contact time. For smaller particles or longer contact time, this term is a key parameter influencing h_{pc}. For all cases it is necessary to properly simulate the bed hydrodynamics.

3.0 GAS CONVECTION COMPONENT

For dense bubbling or circulating beds, particle convection with radiation included dominates the heat overall transfer. Van Heerden *et al.* (1953) and Baskakov & Suprun (1972) carried out parallel mass and heat transfer experiments for gas fluidized bubbling beds, Ebert *et al.* (1990) did a similar experiment for air fluidized circulating beds to establish that particle convective effects dominate over gas convection. Here gas convection includes both gas convective effects at the surface in the vicinity of clusters as well as gas convection for surfaces covered by a dilute mixture of particles and fluid. For liquid fluidized beds and for circulating beds or freeboard regions of a bubbling bed where the particle concentration is very low, fluid convective heat transfer becomes important.

Lints & Glicksman (1933b) analyzed extensive data for a circulating bed which indicated that the gas convection can be approximated by the single phase heat transfer. This would suggest that

$$\frac{h_{gc}D}{k_f} = f\left[\left(\frac{u\rho_f D}{\mu_f}\right);\ Pr_f;\ \text{void geometry}\right] \tag{1}$$

where D is a typical system dimension, e.g. the bed diameter or heat transfer surface length. For bubbling beds, the bubble length along the heat transfer surface might be a more logical dimension, but the bubble length as well as any other void geometry should be related to D through the hydrodynamic parameters. Another possible factor is the gas turbulence level near the surface. If there are particles mixed within the void then an effective specific heat and gas conductivity should be used in the Prandtl number based on the mass fraction of solids and fluid.

4.0 HEAT TRANSFER SURFACE GEOMETRY

For particular heat transfer surface designs the surface geometry may influence the heat transfer and possibly the bed hydrodynamics. For tube bundles within a bubbling fluidized bed the inter-tube spacing may be important as well as the bundle orientation and location relative to the distributor, the bed wall or the free surface. Thus, the geometric ratios of tube spacing to tube diameter and tube vertical location to bed height must be scaled.

For finned surfaces the usual fin efficiency parameter, $\frac{h_{w_{perimeter}}}{k_{fin}A_{cross\ section}}$, holds as well as the ratio of fin spacing to particle diameter for tightly spaced fins (Glicksman & Modlin 1986). For non-circular horizontal tubes, the tube profile can influence heat transfer. Recent results suggest that the shape of a circulating bed wall (Wu *et al.* 1989) and its roughness (Hyre and Glicksman, 1995) can influence the bed to wall heat transfer. This would require a dimensionless wall roughness in the scaled model which matched the target bed.

5.0 HEAT TRANSFER SCALING PROCEDURES

Ideally, heat transfer measurements should be carried out in a scaled bed which simultaneously matches all of the hydrodynamic scaling parameters as well as all of the heat transfer parameters with the target bed. With proper hydrodynamic scaling the wall coverage fraction, average distance between the cluster or emulsion and the wall, the emulsion void fraction and the average time of emulsion contact with the heat transfer surface will be properly simulated. All of the above factors enter into the heat transfer mechanism. However, the heat transfer is also dependent on the thermal parameters to establish full similarity. In most instances, it is usually not possible to simultaneously match all of the hydrodynamic and thermal parameters. For example, the ratio of thermal to hydrodynamic time constants involves both hydrodynamic and thermal parameters. The hydrodynamic parameters ρ_s, u, L, and d_p are used to satisfy flow similarity while k_f is set by the choice of fluid. Thus, c_p of the solid is the only free parameter and it is limited by the choice of solids which satisfy hydrodynamic similarity.

To facilitate thermal scaling, the order of magnitudes in which each of the parameters can be neglected is given in Table 5.1. These considerations are based on the mechanistic model for heat transfer presented earlier.

Table 5.1: Range where Dimesionless Thermal Parameters can be Neglected

Parameter	Modest Influence in These Ranges
$\frac{\tau_T}{\tau_H} = \left(\frac{u\rho_s c_{p_s} d_p^2}{Lk_f}\right)$	$>>1$
$\frac{k_f}{k_s}$	~1, weak effect in other ranges
$Re_{d_p} Pr_f$	$Re_{d_p} Pr_f < 10$ for bubbling beds
$\frac{d_p \sigma T_w^3}{k_f}$	$<<1$
$\frac{T_w}{T_B}$	~ 1 and $\frac{d_p \sigma T_w^3}{k_f} << 1$
$\varepsilon_w, \varepsilon_p$	$\frac{d_p \sigma T_w^3}{k_f} << 1$

When $\frac{\tau_T}{\tau_H}$ is large the thermal time constant of particles is larger than the contact time at the heat transfer surface. The particle temperature remains approximately at the bulk bed

temperature during the contact period and exact match of $\frac{\tau_T}{\tau_H}$ is unnecessary, although it is important that the model also has $\frac{\tau_T}{\tau_H}$ large. Particular limiting values for this parameter depend on the specific flow regime. For horizontal tubes in bubbling beds the hydrodynamic time constant should be the average period between bubble passage at a given location. For heat transfer to the wall of a circulating bed τ_H is the particle or cluster contact time at the wall which can be approximated by taking the particle velocity at the wall as 1-2 m/s and the length of vertical travel generally believed to be between 10 and 100 cm.

As mentioned above the effective conductivity of the emulsion is a weak function of $\frac{k_f}{k_s}$ when this ratio is near unity; the effective conductivity is approximately equal to the fluid conductivity. $Re_{d_p}Pr_f$ enters in the gas convection which augments particle to wall heat transfer. It is only important at elevated pressure and large particle size.

At low temperatures or for high conductivity fluids where the radiation conduction ratio is small, radiation is unimportant eliminating the need to match any of the radiation parameters.

Note, when one or more parameters can be neglected in the target bed to be scaled it is important to construct the experimental model so that the corresponding dimensionless parameters are in the range where they can also be neglected.

6.0 INCOMPLETE THERMAL SCALING

Unfortunately, even when some of the thermal parameters can be neglected, it may be unlikely that proper scaling of all of the remaining parameters can be achieved. In that case, the experimental scaling results must be combined with modeling to achieve results which apply to the commercial bed.

At one extreme, only the hydrodynamic parameters are matched between model and full sized bed, while none of the thermal parameters are matched. Ackeskog *et al.* (1993) compared heat transfer measurements in a hot pressurized combustor and those in a cold pressurized model scaled using the full set of hydrodynamic scaling parameters. They made thermal measurements for a tube bundle and for heat transfer probes inserted in the bed. No attempt was made to match dimensionless heat transfer parameters. Rather, the authors used a model in the literature for the particle convective component and they assumed the hot bed and cold model had the same bed voidage. This allowed a prediction of the particle convection based on the cold bed results. The heat transfer model combined with the heat transfer results from the scaled bed were used to derive the hydrodynamic factors used in the model. These factors were used in applying the model to the hot bed. This technique depends on the validity of the heat transfer model. The comparison of the hot to cold results also requires an estimate of the radiative transfer. The authors obtained reasonable agreements between the hot and cold results with a maximum deviation of 19%. However some of the spatial variations of heat transfer differed between hot data and prediction based on the cold bed results.

7.0 COMPARISON BETWEEN COLD BEDS

Heat transfer experiments on two geometrically similar beds whose linear dimensions differed by a factor of four were carried out to verify the scaling of convective heat transfer. Three separate heat transfer sections were installed on one wall of the bed. The beds were both cold and were hydrodynamically scaled to match all of the simplified scaling parameters. By using the same particle material and gas at the same temperature in both beds the ratio of thermal to hydrodynamic time constants were also held constant. For small particles, u_{mf} can be approximated using only the viscous term of the Ergun equation, thus the ratio of the thermal, τ_T to hydrodynamic times, τ_H, can be given as,

$$\frac{\tau_T}{\tau_H} = \left(\frac{u\rho_s c_{p_s} d_p^2}{Lk_f}\right) = \left(\frac{c_{p_s}}{k_f}\right)\left(\frac{u\rho_s d_p^2}{L}\right) = \left(\frac{c_{p_s}}{k_f}\right)\frac{Fr\, g\rho_s d_p^2}{u} \sim \left(\frac{c_{p_s}}{k_f}\right)\frac{(Fr)\mu\rho_s u_{mf}}{u} \qquad (1)$$

In the simplified hydrodynamic scaling, $\frac{u_{mf}}{u}$, Fr and $\frac{\rho_s}{\rho_f}$ are held constant. Thus, by using the same solid between the two beds, $\frac{\tau_T}{\tau_H}$ and $\frac{k_p}{k_f}$ were held constant between the two beds. Both beds were at room temperature so that radiation is negligible. The convection augmentation $Re_{d_p}Pr_f$ is also small.

In general cases where the simplified scaling relationships are used and $\frac{u_{mf}}{u}$, $\frac{\rho_s}{\rho_f}$ and Fr are held constant then for small particles,

$$\frac{\tau_T}{\tau_H} = \left(\frac{c_{p_s}}{c_{p_f}}\right)\left(\frac{c_{p_s}\mu_f}{k_f}\right)Fr\frac{u_{mf}}{u} = \left(\frac{c_{p_s}}{c_{p_f}}\right)Pr_f Fr\frac{u_{mf}}{u} \qquad (2)$$

and constancy of $\frac{\tau_T}{\tau_H}$ requires the use of fluids and solids with identical values of the product $\left(\frac{c_{p_s}}{c_{p_f}}\right)Pr_f$. The Prandtl number remains constant at a value near 0.7 for most gases over a wide range of temperatures. To maintain $\frac{\tau_T}{\tau_H}$ constant between the model and target bed, the ratio of particle to fluid specific heat must be equal when the particles are small enough for u_{mf} to be governed by the viscous term in the Ergun equation. Note, at the other limit of large particles $\frac{\tau_T}{\tau_H}$ will become larger than unity and will not remain an important factor in the heat transfer.

When using a low temperature model to obtain heat transfer data to be applied to a bed fluidized with hot gas, it is unlikely that the radiation conduction parameter can be matched. If hydrodynamic similarity holds, the dimensionless wall coverage, wall to particle spacing and emulsion void fraction should be matched. At this point it is necessary to introduce a heat transfer model. Using a renewal model as described in the previous section one must determine the most important thermal parameters. For large heat transfer surfaces and small particle diameters typical of the walls of circulating beds, the emulsion resistance should predominate over the wall resistance. This becomes, with radiation included in the effective conductivity,

$$\frac{h_e d_p}{k_f} \sim \frac{1}{\sqrt{t'}}\sqrt{\left(\frac{k_e}{k_f}\right)\left(\frac{u(1-\varepsilon_e)\rho_s c_{p_s} d_p^2}{L k_f}\right)} \sim \frac{1}{\sqrt{t'}}\sqrt{(1-\varepsilon_e)\left(\frac{c_{p_s}}{c_{p_f}}\right)Pr_f \frac{u_{mf}}{u} Fr\left(1-\frac{\rho_s}{\rho_f}\right)\left(\frac{k_e}{k_f}+\frac{8}{9}\frac{d_p \sigma T^3}{k_f}\right)} \tag{3}$$

Thus in the case of the simplified scaling laws, which result in equal values of t', heat transfer similarity requires an equality between the terms,

$$\left[\left(\frac{c_{p_s}}{c_{p_f}}\right)Pr_f\left(\frac{k_e}{k_f}+\frac{8}{9}\frac{d_p \sigma T^3}{k_f}\right)\right]_{hot\ target} = \left[\left(\frac{c_{p_s}}{c_{p_f}}\right)Pr_f\left(\frac{k_e}{k_f}\right)\right]_{cold\ model} \tag{4}$$

Note, in this case it is unnecessary to also hold an additional term $\left(\frac{k_p}{k_f}\right)$ constant. If the cold bed parameter given by the right-hand side of (4) is not equal to the hot bed parameter, then the measured Nusselt number in the cold bed must be adjusted by the square root of the ratio of the left-hand side term to the right-hand side term in (4).

At the other extreme, for large particles with short residence time, e.g. a large particle bubbling bed with rapid particle exchange at the heat transfer surface, the surface resistance should predominate. Results for Nusselt number in a low temperature model should be adjusted by the ratio of $\frac{h_w d_p}{k_f}$ between the hot and cold bed to obtain a prediction of the hot bed Nusselt number.

In both the case of the large particle and small particle limits a measurement or estimate of the percent of surface covered by dilute phase must be made. For the cold bed the dilute phase heat transfer will be small unless f becomes very small. For the hot bed the heat transfer coefficient under the dilute phase is given by radiation between the heat transfer surface and the bulk bed. This correction is approximate only if f is not well known.

8.0 METHOD OF EXPERIMENTAL VERIFICATION OF HEAT TRANSFER SIMILARITY

The tests used in verifying the proposed simplified hydrodynamics scaling parameters were used for an initial evaluation of the convection heat transfer similarity rule which was derived above. The independent dimensionless parameter controlling the convective heat transfer scaling is

$$Hx = \left(\frac{u_o \rho_s c_p d_p^2}{L k_g} \right) \tag{1}$$

For hydrodynamic similarity using the simplified scaling laws, one of the controlling parameters (u_o/u_{mf}) is proportional to

$$\frac{u_o}{u_{mf}} \sim \frac{\rho_s d_p^2 u_o}{\mu L} \quad \text{at low Reynolds numbers.} \tag{2}$$

Thus, the heat transfer scaling parameter can be maintained constant between two different models if

$$\frac{c_{p_s} \mu}{k_f} \tag{3}$$

is maintained constant.

Two series of tests were conducted to evaluate the similarity of the dimensionless heat transfer coefficient between the 1/16 and 1/4 scale Studsvik beds. The heat transfer tests were conducted during the cold model runs discussed in Chapter 2 which verified the simplified hydrodynamic scaling parameters. The first series of tests were conducted during the runs with glass as the bed material and the second series of tests were conducted during the runs with plastic as the bed material.

9.0 EXPERIMENTAL ARRANGEMENT

9.1 Heat Transfer Panel Dimensions and Installation

In order to determine wall-to-bed heat transfer coefficients, two heat transfer panels were constructed. One for the 1/16 scalebed and one for the 1/4 scale bed described in Chapter 2. Each panel consisted of three heat transfer sections with separate heaters and power supplies. The purpose of the three separate heater sections was to evaluate the effects of average bed density and the downward movement of particles at the wall at various heights on heat transfer. Heater sections were separated to ensure negligible heat transfer between sections. The following Sections discuss the panels for both beds and the bed configuration when the heat transfer panels were installed.

9.1.1 Heat Transfer Panel for the 1/16 Scale Bed

The heat transfer panel for the 1/16 scale bed was used with the phase one configuration (i.e., without bed boot, secondary air, and simulated refractory). It consisted of a 18" x 1-1/2" x 1/2" (45.75 x 3.8 x 1.3 cm) piece of wood with three 3-3/4" x 1" (9.3 x 2.5 cm) squares routed out for heater and aluminum cover placement. The heaters were 3" x 1" x 1/32" (7.6 x 2.5 x .08 cm), 150 watt, 120 volt, aluminum strip heaters. Each heater was covered by a 3-3/4" x 1" x 1/8" (9.3 x 2.5 x 0.3 cm) aluminum plate which was flush to the wood surface. The tops of the aluminum plate covers were located at distances of 17.7, 13.5, and 9.3 inches (45.0, 34.3, and 23.7 cm) from the bottom of the wood panel and, therefore, the distributor plate. The wood panel was sealed to a 18" x 2-3/8" x 3/8" (45.75 x 6.0 x 0.95 cm) acrylic backing. A Chromel-Alumel (type K) thermocouple was embedded into the top and bottom of each aluminum plate. The thermocouple and heater leads were drawn back through the wood panel and acrylic backing.

In order to assure as smooth a surface as possible, the heat transfer surface (wood/aluminum surface) was coated with a layer of Omegatherm thermally conductive silicone paste, and a very thin plastic film was carefully attached to the surface with care taken to eliminate any air pockets between the plastic film and aluminum covers. The entire assembly was then attached to the back of the bed with the portion of the panel made of wood actually fitting inside the bed reducing the effective bed width by 1/2-inch (1.3 cm). The acrylic back was then screwed to the bed side walls and sealed with caulk. See Figure 9.1 for a view of the heat transfer panel for the 1/16 scale bed.

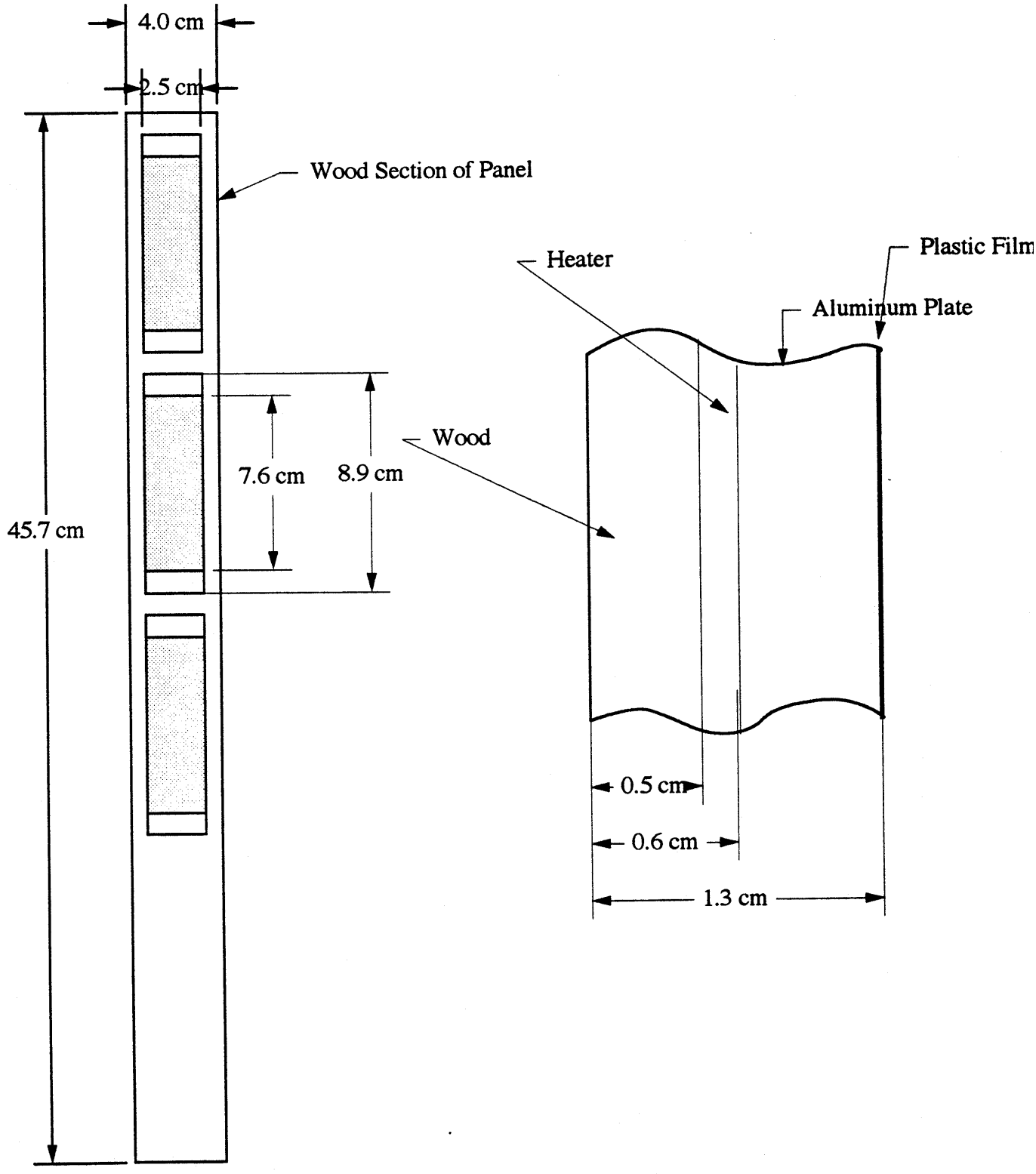

Figure 9.1: 1/16 Scale Studsvik Heat Transfer Panel

9.1.2 Heat Transfer Panel for the 1/4 Scale Bed

The heat transfer panel for the 1/4 scale bed was made in a similar way to the panel for the 1/16 scale bed. A 57" x 6-1/4" x 1/2" (182.9 x 15.9 x 1.3 cm) piece of wood was routed out in three locations which produced a geometrically similar pattern to the 1/16 scale panel; three 14" x 4" (35.5 x 10.2 cm) squares located with their tops at distances of 1.2", 18.0", and 34.7" (3.0, 45.7, 88.1 cm) from the top of the panel. The heaters were 12" x 4" x 1/16" (30.5 x 10.2 x 0.16 cm), 250 watt, 120 volt, flexible strip heaters. Each heater was covered by a 14" x 4" x 1/4" (35.6 x 10.2 x 0.64 cm) aluminum plate which was flush to the wood surface. A Chromel-Alumel (type K) thermocouple was embedded into the top and bottom of each aluminum plate. The thermocouple and heater leads were drawn back through the wood panel.

As was done with the smaller heat transfer panel, the heat transfer surface (wood/aluminum surface) was coated with a layer of Omegatherm thermally conductive silicone paste, and a very thin plastic film was carefully attached to the surface with care taken to eliminate any air pockets between the plastic film and aluminum covers.

A smaller piece of wood, 15" x 6-1/4" x 1/2" (38.1 x 15.9 x 1.3 cm) was used to block off the boot area in the bottom of the bed. In addition, small rubber stoppers were used to block off those distributor plate holes which were behind the area being used after the heat transfer panel was installed. The smaller piece of wood which isolated the boot area of the bed was sealed by filling 1/8" x 1/8" (0.32 x 0.32 cm) grooves cut around the outside perimeter of the wood with caulk before insertion into the bottom of the bed. The main section of the heat transfer panel was then placed on top of the smaller section and sealed using the same method. The installation of the heat transfer panel had the effect of eliminating the boot area of the bed and also reduced the effective bed width by 2-inches (5.1 cm).

A 1/8" (0.32 cm) hole was drilled and tapped into one of the sides of the bed behind the heat transfer panel. The thermocouple and heater leads were then pulled through a steel nipple which was screwed into the hole in the side wall. The thermocouple and heater lead access was then sealed using RTV silicone sealant.

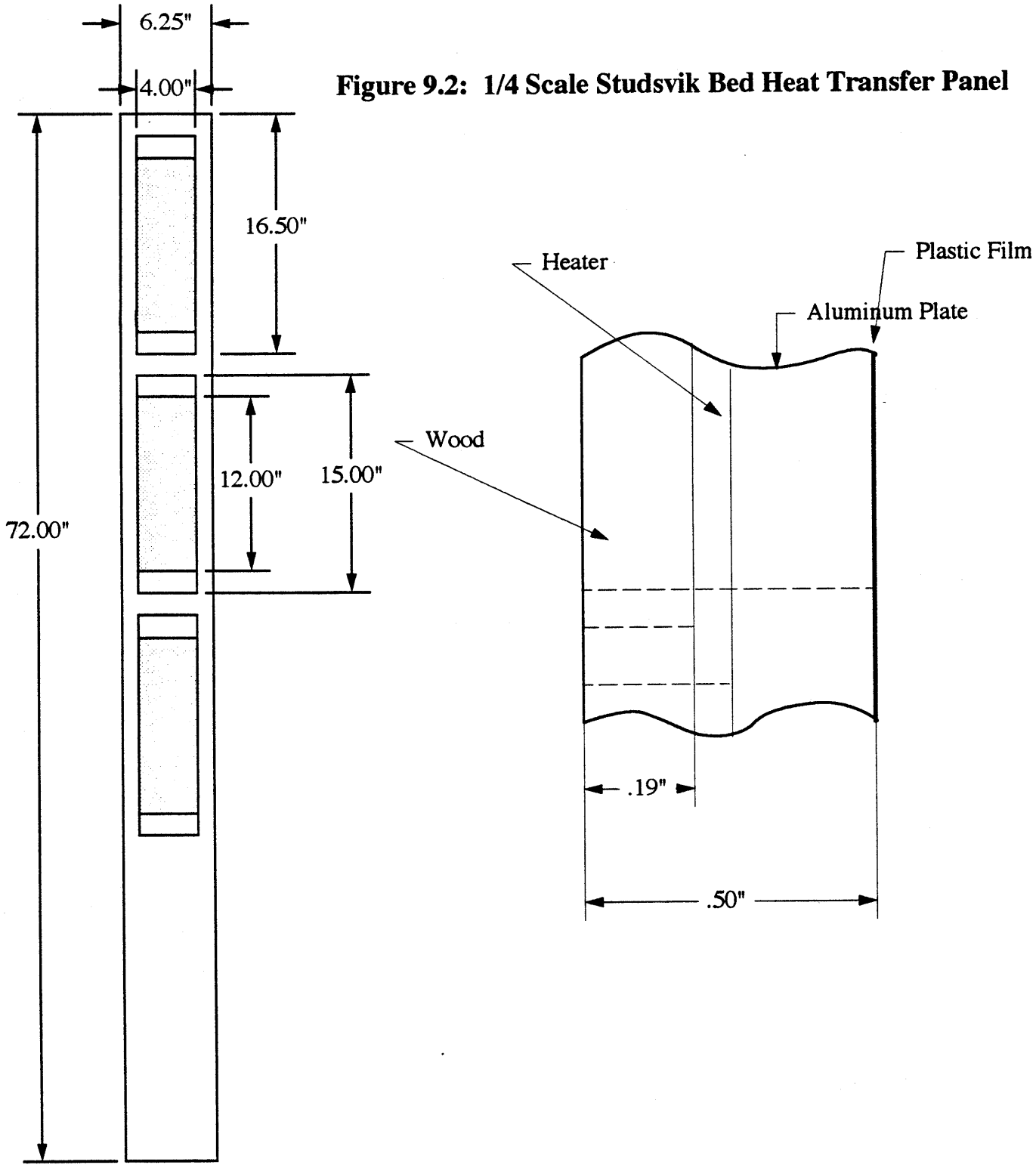

Figure 9.2: 1/4 Scale Studsvik Bed Heat Transfer Panel

A 72" x 6-1/4" x 1-3/4" (182.9 x 15.9 x 4.4 cm) piece of foam insulation was placed directly behind the heat transfer panel effectively eliminating all remaining space in the area behind the panel. The aluminum bed back was then installed in the usual manner. See Figure 9.2 for a view of the heat transfer panel for the 1/4 scale bed.

9.2 Heat Transfer Measurements

Heat transfer measurement techniques for the various beds utilized in this study are described below. Figure 9.3 illustrates the equipment and methods used for these beds.

9.2.1 1/16 Scale Studsvik Bed

The heat transfer measurement apparatus for the 1/16 scale Studsvik bed consisted of the heat transfer panel described above along with the associated thermocouple thermometer, power supplies, and other ancillary equipment. The thermocouple leads from the back of the bed were attached to a 14 position dial which was, in turn, connected to an Omega DP462 six channel digital thermometer capable of reading various types of thermocouples. An additional thermocouple which measured the bed temperature, located at the top of the bed, was also attached to the thermocouple dial. Each set of heater leads, which also emerged from the back of the bed, were attached to a variable autotransformer. Additional parallel leads allowed for the reading of voltage inputs and heater resistances during bed operation.

Enough voltage was supplied to each heater so that the temperature difference between the bed and the heat transfer surface was sufficiently large, about 30 ^{o}F (17 ^{o}C), and in a manner such that the wall temperature was fairly constant (within 3 or 4 ^{o}F). This voltage was usually somewhere between 30 to 40 volts depending on the bed density and material. The bed was allowed to run until the bed temperature no longer changed significantly (usually about an hour) before the temperatures, voltages and heater resistances were recorded. At the same time the heat transfer data was recorded, pressure measurements were taken through the pressure transducers to allow a consistent comparison of heat transfer and solid fraction data.

The heat transfer panel was calibrated by measuring the heat transfer coefficient with only air flowing over it while keeping the heat flux of the heated section of the panel constant. The Nusselt number for laminar flow over a constant heat flux flat plate with an unheated

starting length presented by Holman (1981) was used to calculate expected values of the Nusselt number:

$$Nu_x = \frac{0.453 Pr^{1/3} Re_x^{1/2}}{\left(1-\left(\frac{x_0}{x}\right)^{3/4}\right)^{1/3}}$$

Results of the heat transfer panel calibration are given in Figure 9.4.

9.2.2 1/4 Scale Studsvik Bed

The heat transfer data for the 1/4 scale Studsvik bed was taken in the same manner as that for the 1/16 scale Studsvik bed, with the obvious exception of the voltage needed to achieve acceptable bed/wall temperature differences. In the 1/4 scale bed, this voltage was usually between 80 and 90 volts.

Calibration of the 1/4 scale Studsvik bed heat transfer panel was performed in the same manner as the 1/16 scale calibration. Results of the calibration are given in Figure 9.5.

Figure 9.3

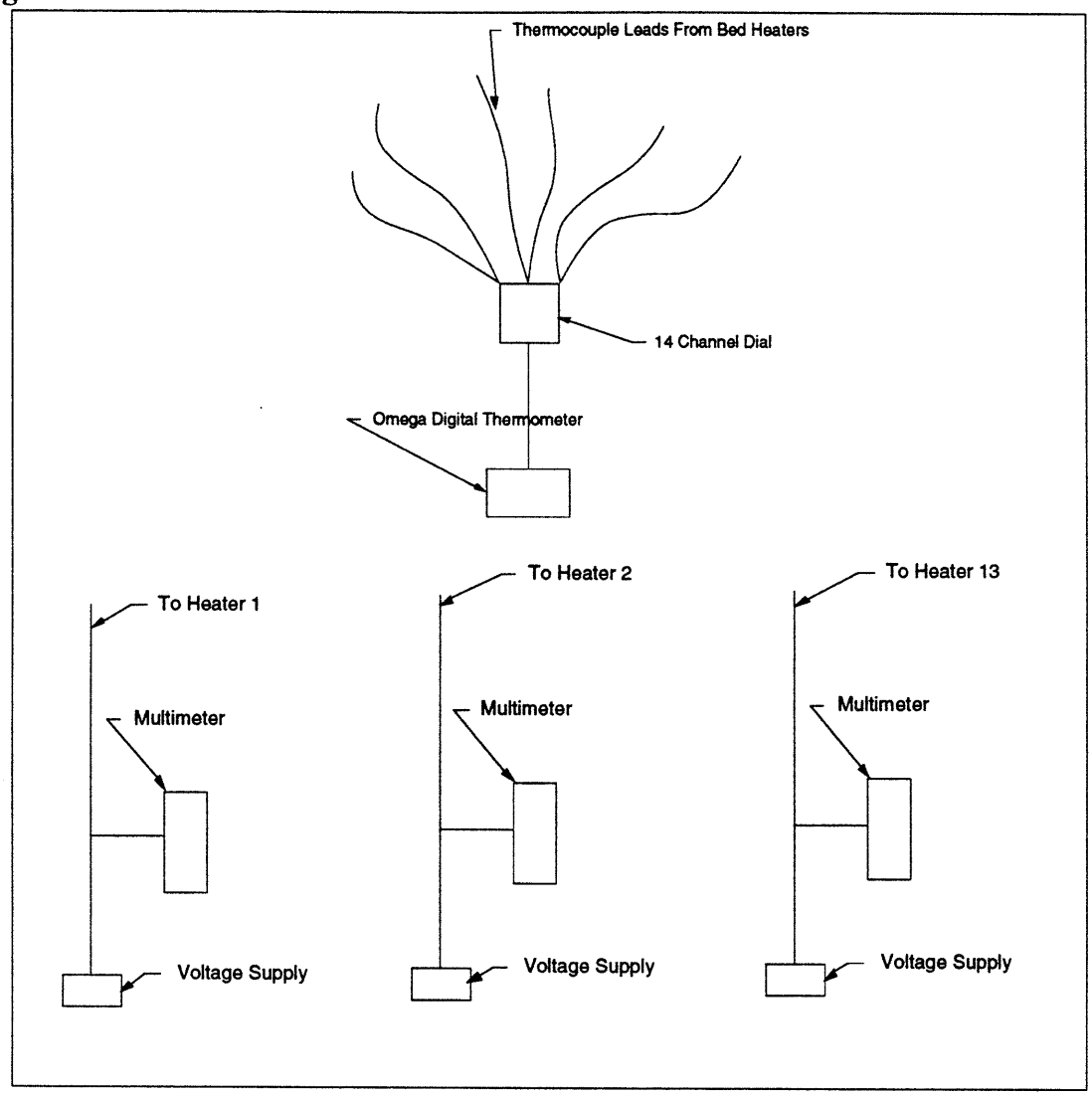
Thermocouple Leads From Bed Heaters
14 Channel Dial
Omega Digital Thermometer
To Heater 1
Multimeter
Voltage Supply
To Heater 2
Multimeter
Voltage Supply
To Heater 13
Multimeter
Voltage Supply

Figure 9.4

1/16 Scale Studsvik Bed Heat Transfer Panel Calibration

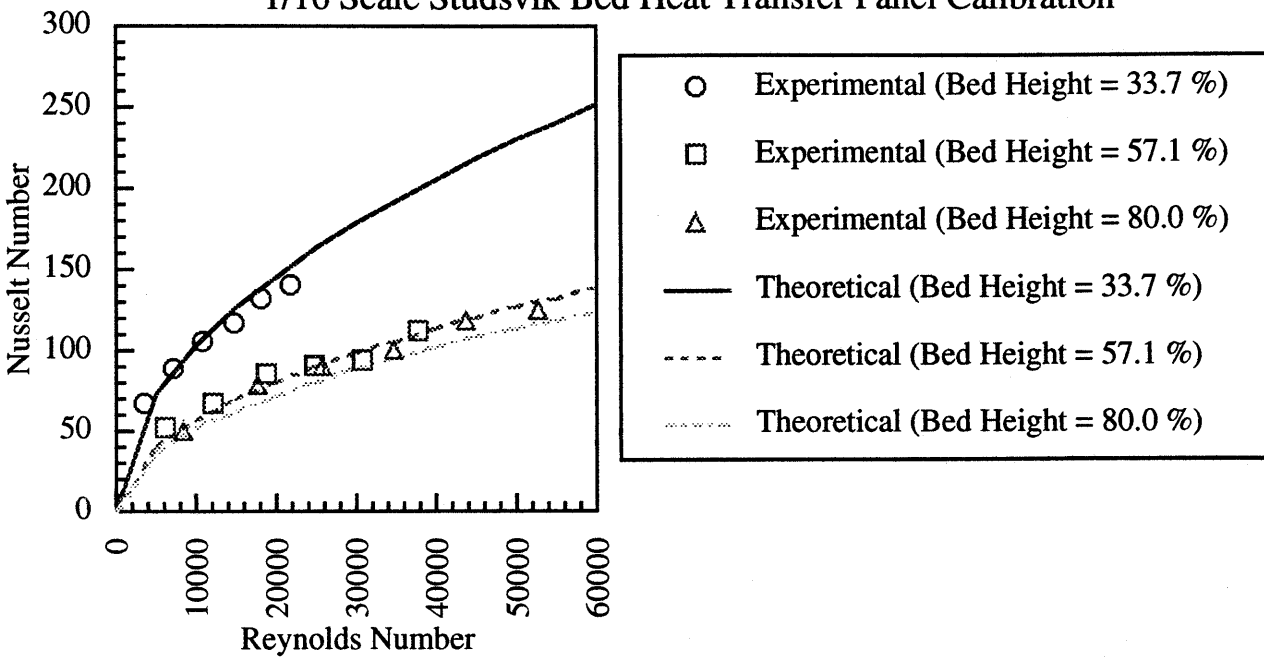

Figure 9.5

1/4 Scale Studsvik Bed Heat Transfer Panel Calibration

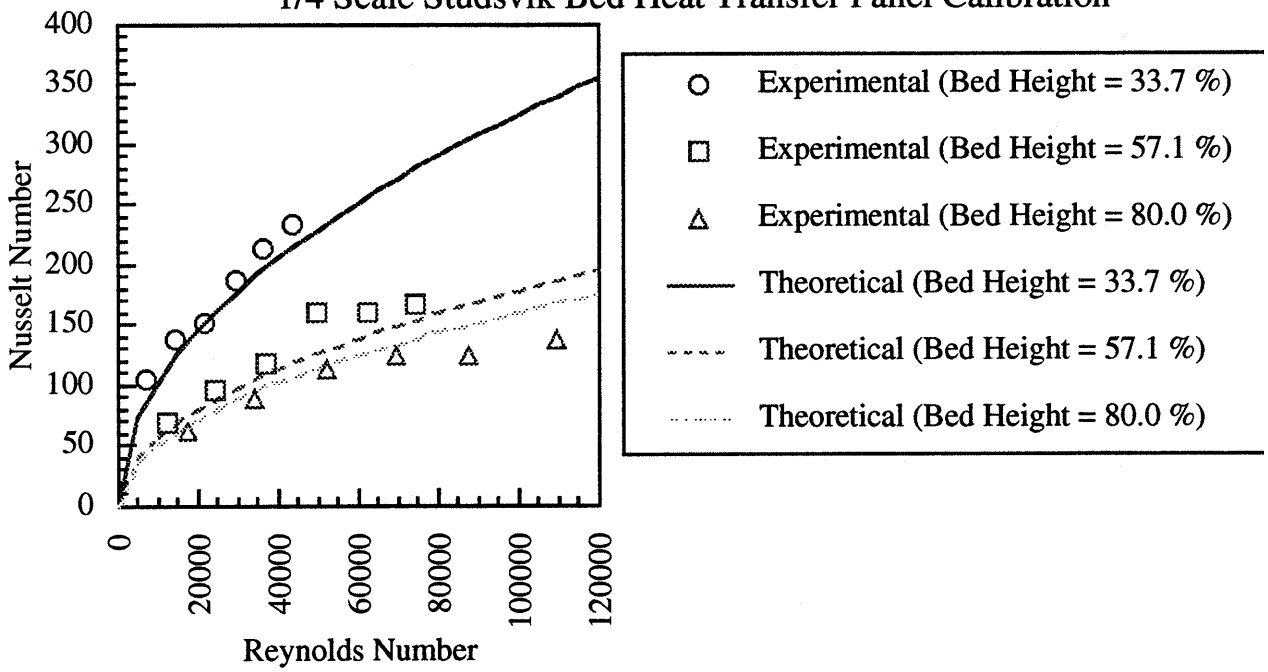

9.3 Uncertainty in Temperature Measurements

All temperatures were measure with an Omega DP462 digital thermometer with multi-channel input. This thermometer has 0.1 ^{o}F resolution up to 1000 ^{o}F, an accuracy of 0.9 ^{o}F (0.5 ^{o}C), and a reading rate of 1 per second. Since all temperature measurements were taken at steady state, it is not anticipated that the thermometer added any significant error.

The thermocouples which measured the wall temperature were imbedded in the aluminum plate covers. A thin layer of thermally conductive silicone paste was used to hold a thin plastic film over the panel to ensure a smooth heat transfer surface. This paste has a thermal conductivity of 16 Btu-in/hr-ft^2-F (0.0055 cal-cm/s-cm^2-C) and a temperature range of use from -40 - 392 ^{o}F (-40 - 200 ^{o}C). Rough calculations indicated the maximum temperature drop from the thermocouple to the wall surface did not exceed 1 ^{o}C.

One possible source of error in the measurement of heat transfer coefficients is the loss of heat through the back of the beds. In order to minimize this effect, the back and half the sides of the 1/16 scale Studsvik bed were covered with 1/2-inch (1.3 cm) foam insulation. In the 1/4 scale Studsvik bed, a 3/4-inch (1.9 cm) sheet of foam insulation was placed between the wood heat transfer panel and aluminum bed back. It should be noted that an additional 1/4-inch (0.64 cm) of insulation was provided by the wood since the area routed out for heater and aluminum cover placement only extended halfway through the 1/2-inch (1.3 cm) piece of wood.

Lateral heat transfer losses from the heat transfer panels in the 1/16 scale Studsvik bed were minimized by a 1/4-inch (0.64 cm) of wood, the bed walls (3/8-inch acrylic), and another 1/2-inch (1.3 cm) of foam insulation. In the 1/4 scale Studsvik bed, lateral heat transfer losses were reduced through 1-1/8 inches (2.86 cm) of wood on either side of the heaters, in addition to the bed walls.

Vertical heat transfer between heaters was reduced by keeping the heaters as close in temperature to each other as possible. In addition, the heaters were separated by 0.33 -inches (0.84 cm) of wood in the 1/16 scale Studsvik bed, and 1.33-inches (3.38 cm) of wood in the 1/4 scale Studsvik bed. Estimates of heat transfer losses from the panel are shown in Table 9.1.

Figure 9.1
Maximum Heat Losses from Heat Transfer Panels

Area of Loss	1/4 Scale Studsvik Bed	1/16 Scale Studsvik Bed
Through Back	1.7%	3.4%
Through Sides	0.08%	0.9%
Between Heaters	6.2E-4%	0.1%

As was discussed earlier, the heat transfer panels were calibrated by measuring the heat transfer coefficient with only air flowing over it while keeping the temperature of the heated section of the panel constant.

Because the heaters did not heat completely evenly, thermocouple readings were taken at the top and bottom of each aluminum cover. The temperatures were then averaged for use in the calculation of the heat transfer coefficient at the midpoint of the heater. The temperatures at the ends of the heaters never differed by more than 4.5 ^{o}F (2.5 ^{o}C) in either the 1/16 or 1/4 scale model. Typical differences were normally 1-1.5 ^{o}C.

9.4 Data Reduction for Heat Transfer Coefficients

Steady state heat transfer coefficients were calculated in the usual fashion by measuring the bed temperature and the wall temperature at steady state. Total power inputs were then computed by measuring the voltage input to the heaters, and the heater resistances. A corrected power input to the bed to account for heat losses through the back and sides of the bed was calculated by using the calibration curve described earlier. For each run in which heat transfer data was taken, temperatures at the top and bottom of each heater (total of six temperatures) along with the bed temperature were recorded three times at steady state during the period of about five minutes. The average of these temperature differences was then used in the heat transfer coefficient calculations.

While recording the temperature data, differential pressure data was taken utilizing a computer based data acquisition system to allow correlation between Nusselt numbers and average bed solid fraction. Immediately after bed and wall temperatures were recorded, total voltage inputs and heater resistances were recorded to allow determination of total power input.

10.0 EXPERIMENTAL RESULTS OF CONVECTIVE HEAT TRANSFER SCALING WITH GLASS

The test matrix for the heat transfer tests conducted with glass as the bed material is given as Table 10.1.

Table 10.1

Test Matrix for Heat Transfer Similarity - Series One

Bed Material: Glass

Parameter	**Large Bed**	**Small Bed**
Bed Diameter	D	0.25D
Superficial Velocity	u_o	$0.5u_o$
Minimum Fluidization Velocity, cm/s	$u_{mf} = 2.8$	$0.5u_{mf}$
Particle Diameter, μm	$d_p = 112.3$	$0.707d_p$
Particle Density, kg/m^3	2540	Same
$Re_{d_p} = \frac{\rho_f u_o d_p}{\mu_f}$	$\frac{\rho_f u_o d_p}{\mu_f}$	$\frac{0.35\rho_f u_o d_p}{\mu_f}$
$Re_D = \frac{\rho_f u_o D}{\mu_f}$	$\frac{\rho_f u_o D}{\mu_f}$	$\frac{\rho_f u_o D}{8\mu_f}$
$\frac{\rho_s}{\rho_f}$	2310	Same
$M = \frac{\dot{m}_s}{u_o A_{cs} \rho_s}$	0.0029	Same
$\frac{c_{p_s}\mu}{k_f}$	0.58	Same
$Hx = \left(\frac{u_o \rho_s c_p d_p^2}{L k_g}\right)$	Hx	Same

Heat transfer measurements were taken at three different locations in the bed. At each location a temperature reading was taken at the top and bottom of the heated wall section. The two temperatures were then averaged to determine the average heat transfer coefficient. The nondimensional heat transfer parameters were then plotted against the bed solid fraction which was determined by linear interpolation between the closest two differential pressure measurements. At each height, the nondimensional heat transfer parameter should be similar between the properly scaled 1/4 scale and 1/16 scale Studsvik models. Figures 10.1 through 10.9 show the results of these tests. In each of the these plots, similar geometric symbols (i.e., open circles and filled circles, open squares and closed squares, and open triangles and closed triangles) represent conditions which should result in similar values of Nusselt numbers. The error bars for the solid fraction represent the standard deviation determined from time varying pressure trace. The error bars for the Nusselt numbers represent the combined error from:

1. Error in bed and wall temperature measurements
2. Error due to the change in resistivity of the heaters with temperature
3. Error in voltage measurements
4. Error due to heat losses from the heat transfer panel

Figure 10.1: Glass Particles

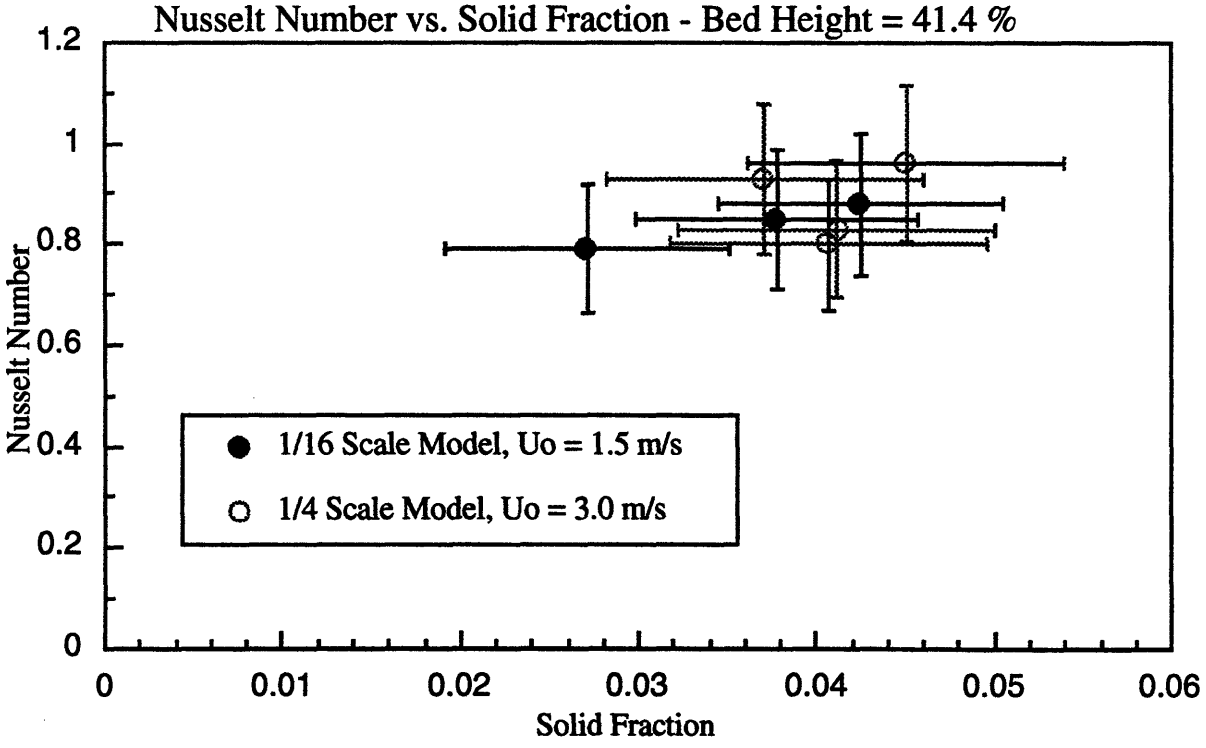

Figure 10.2: Glass Particles

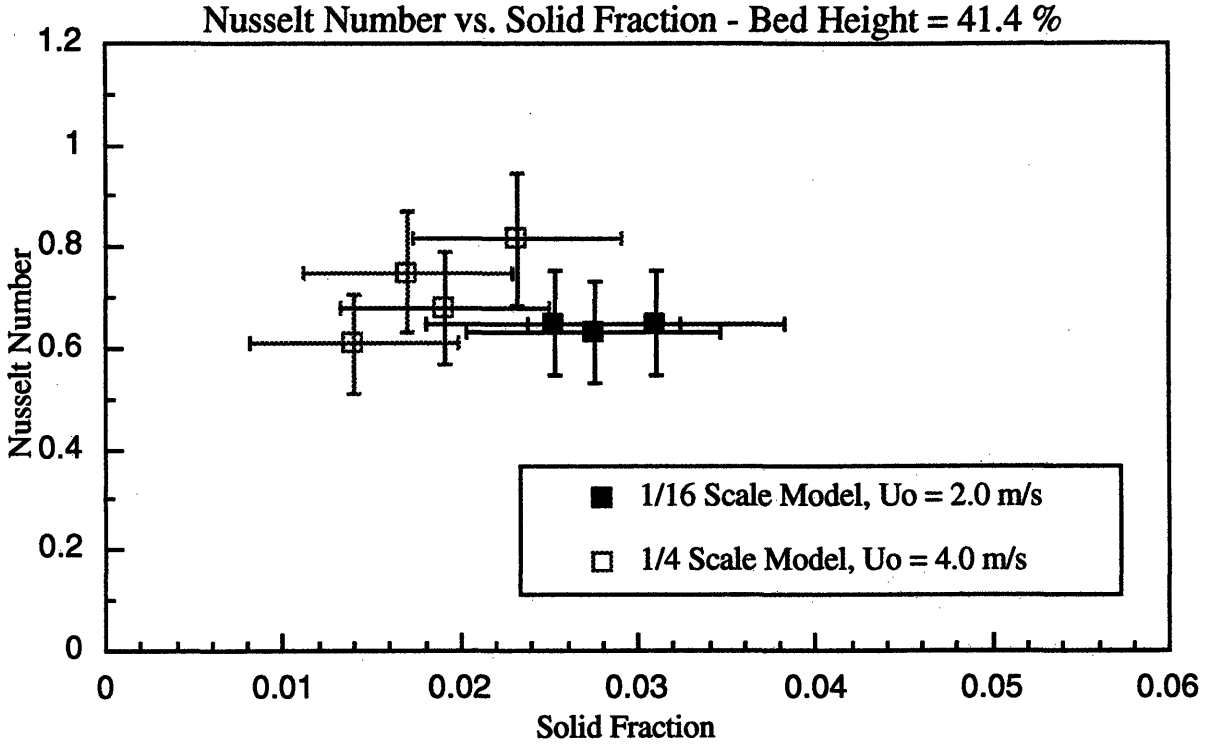

Figure 10.3: Glass Particles

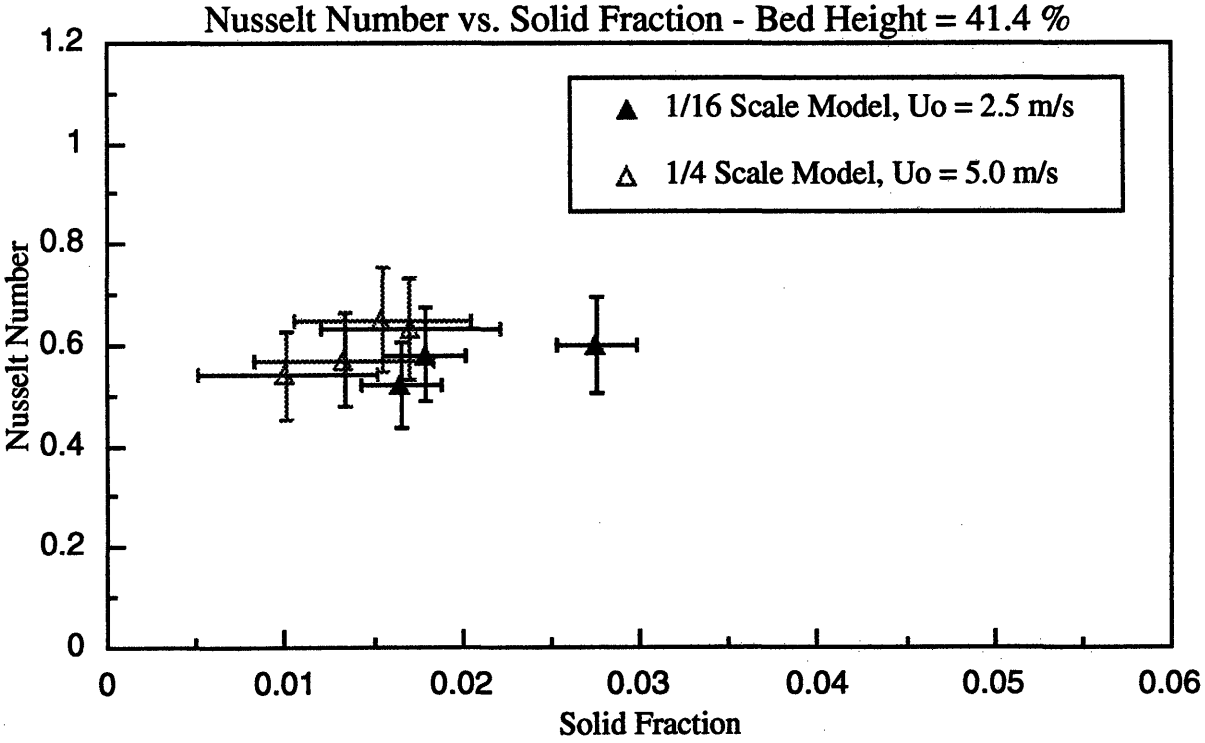

Figure 10.4: Glass Particles

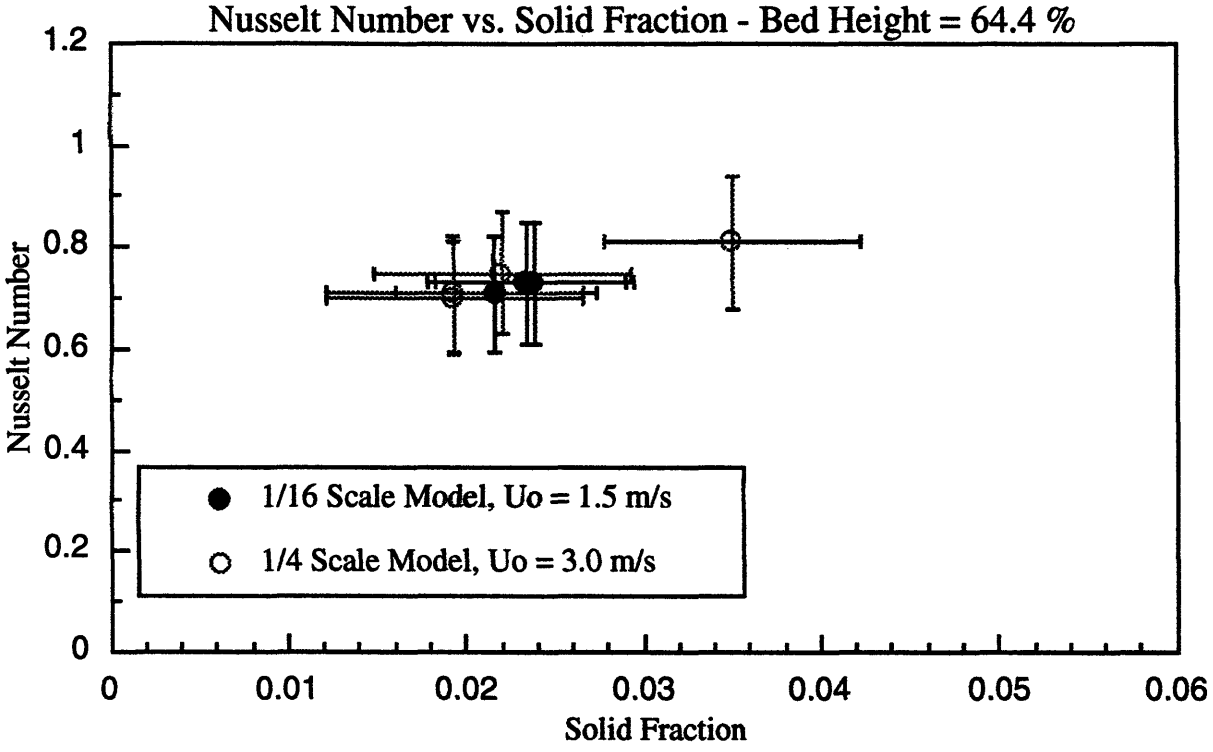

Figure 10.5: Glass Particles

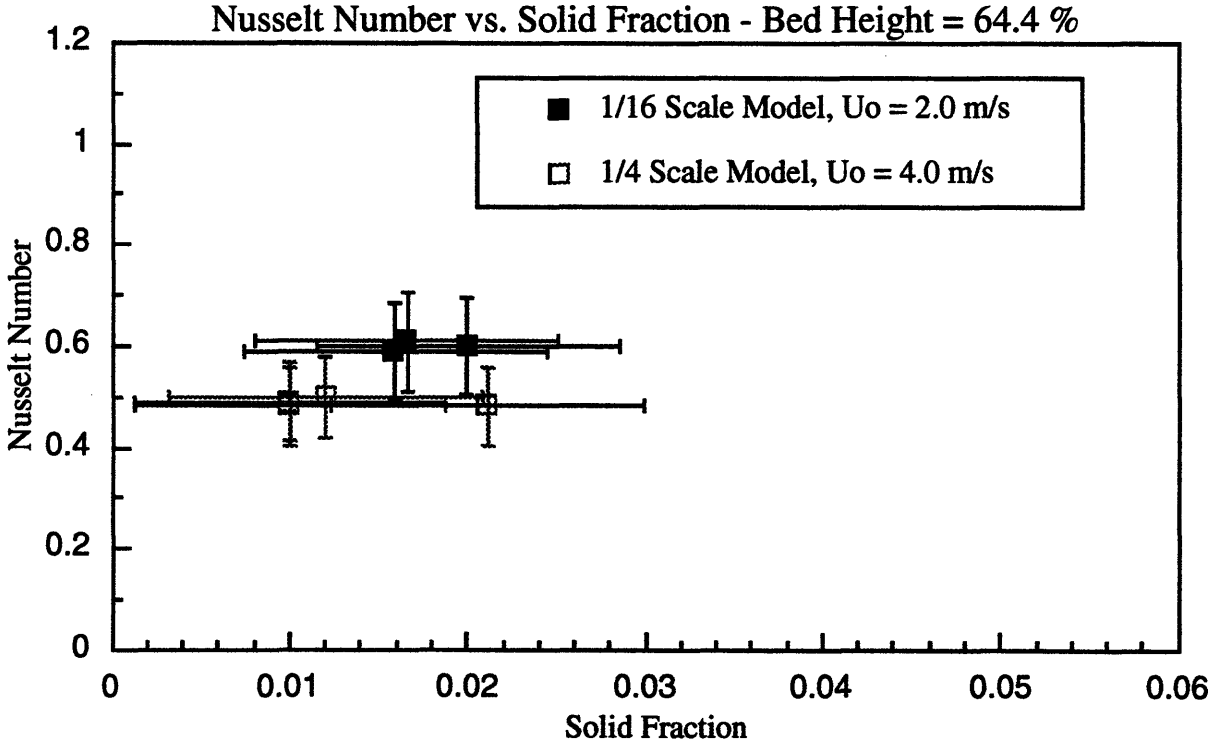

Figure 10.6: Glass Particles

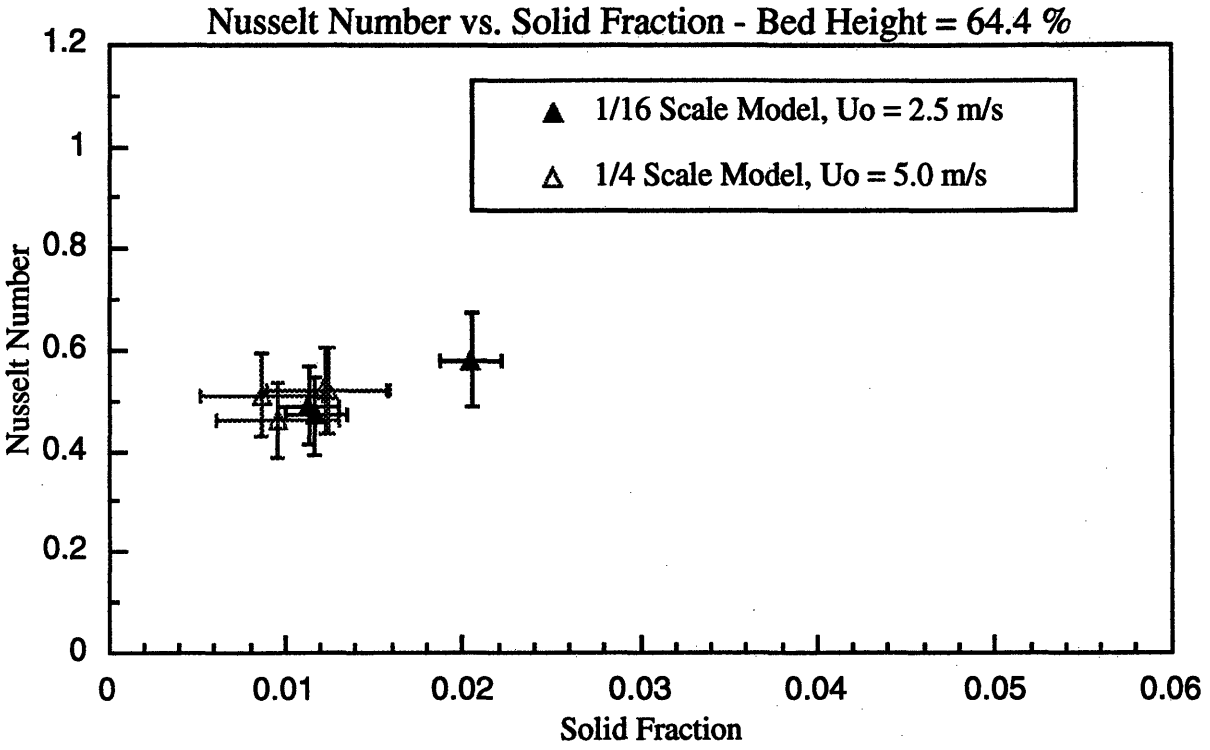

Figure 10.7: Glass Particles

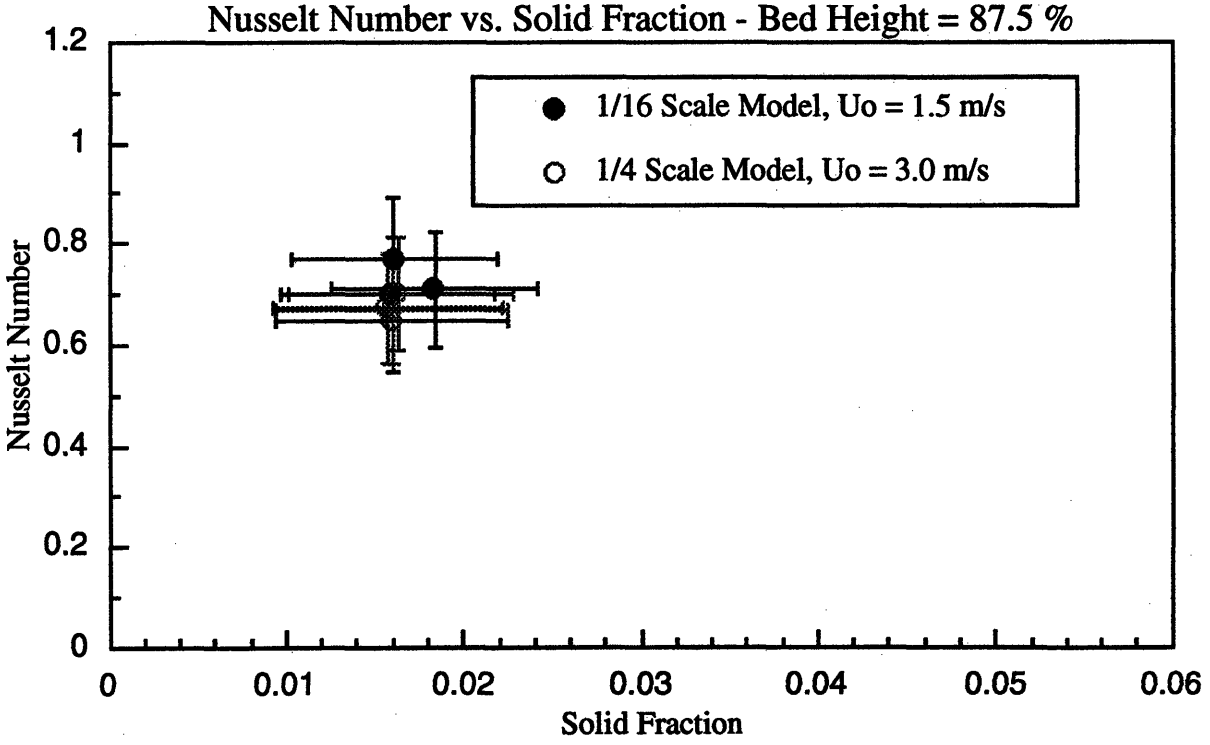

Figure 10.8: Glass Particles

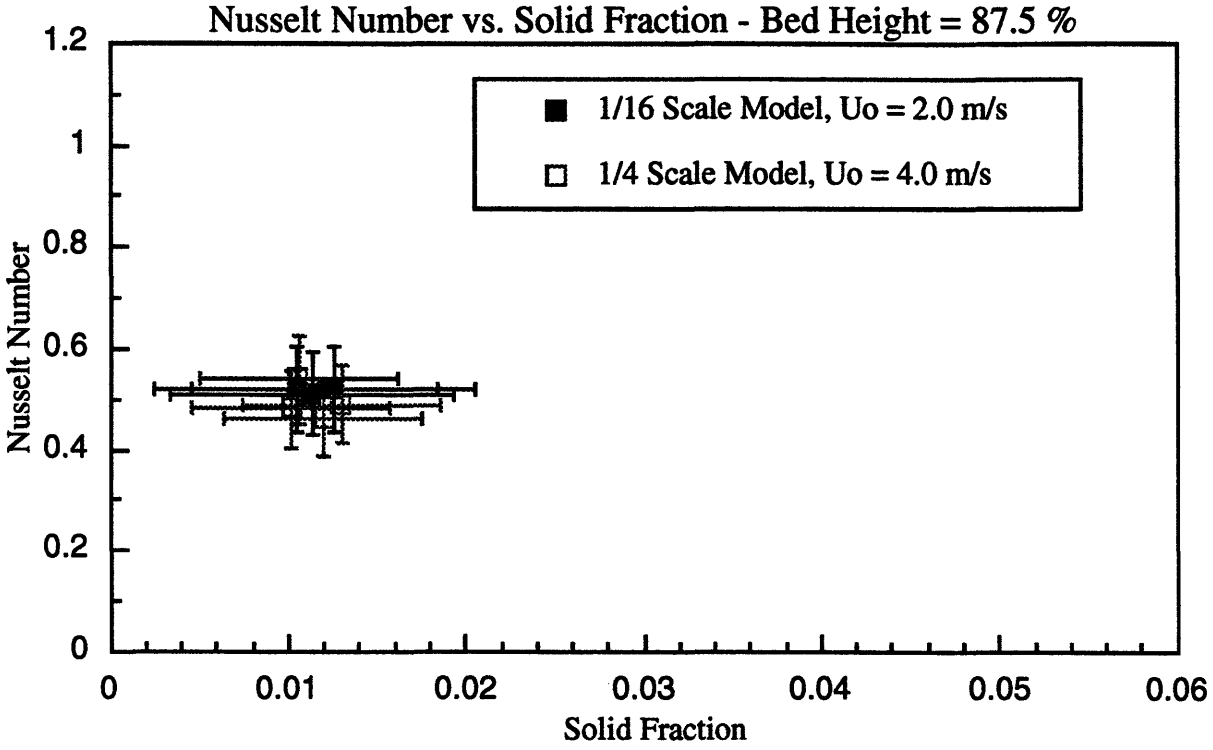

Figure 10.9: Glass Particles

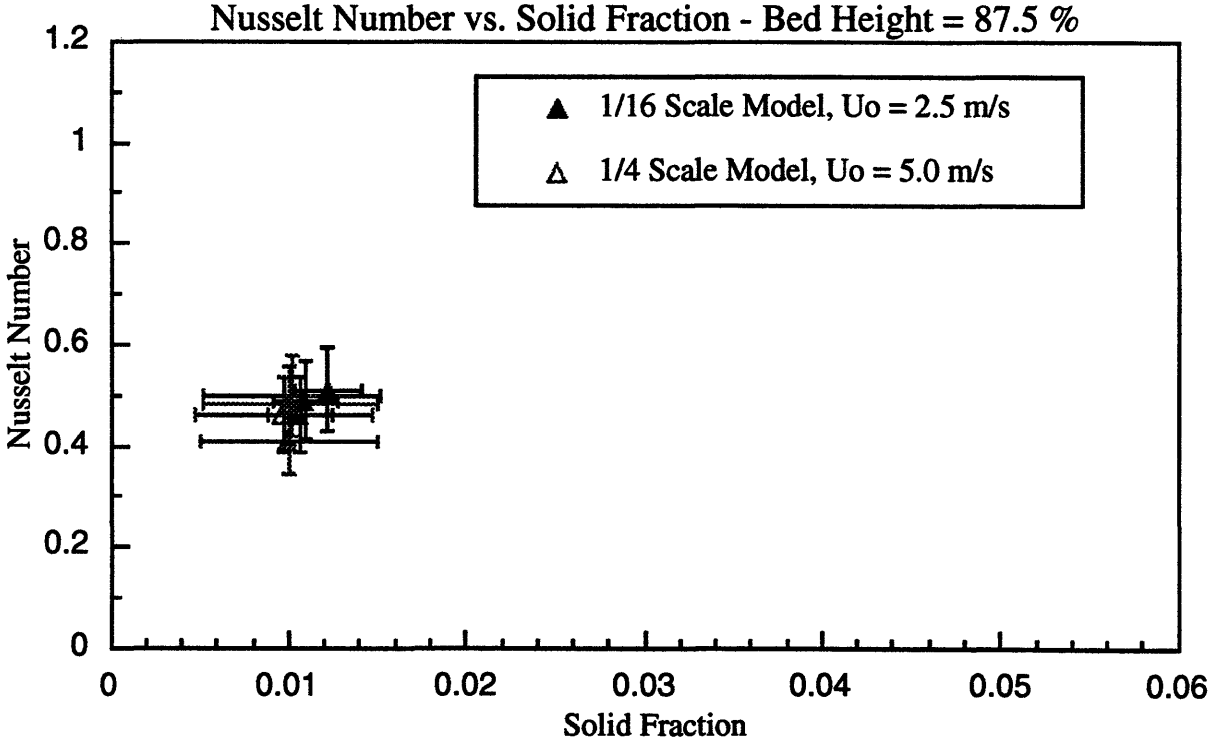

11.0 DISCUSSION OF RESULTS FOR HEAT TRANSFER SCALING WITH GLASS

At all bed heights and superficial velocities, the Nusselt numbers between the 1/4 scale Studsvik model and the 1/16 scale Studsvik model show good agreement. The Nusselt numbers appear to be a function of the average cross-sectional bed density, although this dependence will be shown to be secondary in a sense that the fractional wall coverage, which directly governs the heat transfer, has been shown to increase with increasing average bed density in the fast-fluidization regime (Lints, 1992). Figures 11.1 through 11.3 show mean values of solid fraction and Nusselt numbers calculated from the experimental results. The error bars in these plots were determined from standard deviations in the experimental data for runs with the same hydrodynamic conditions. Most of the plots show acceptable agreement. It should be noted that the error bars in these plots have very little statistical significance because of the low number of data points used in calculating the standard deviation. Figure 11.4 depicts the mean solid fractions and Nusselt numbers for the glass runs at all heights and superficial velocities.

Figure 11.1

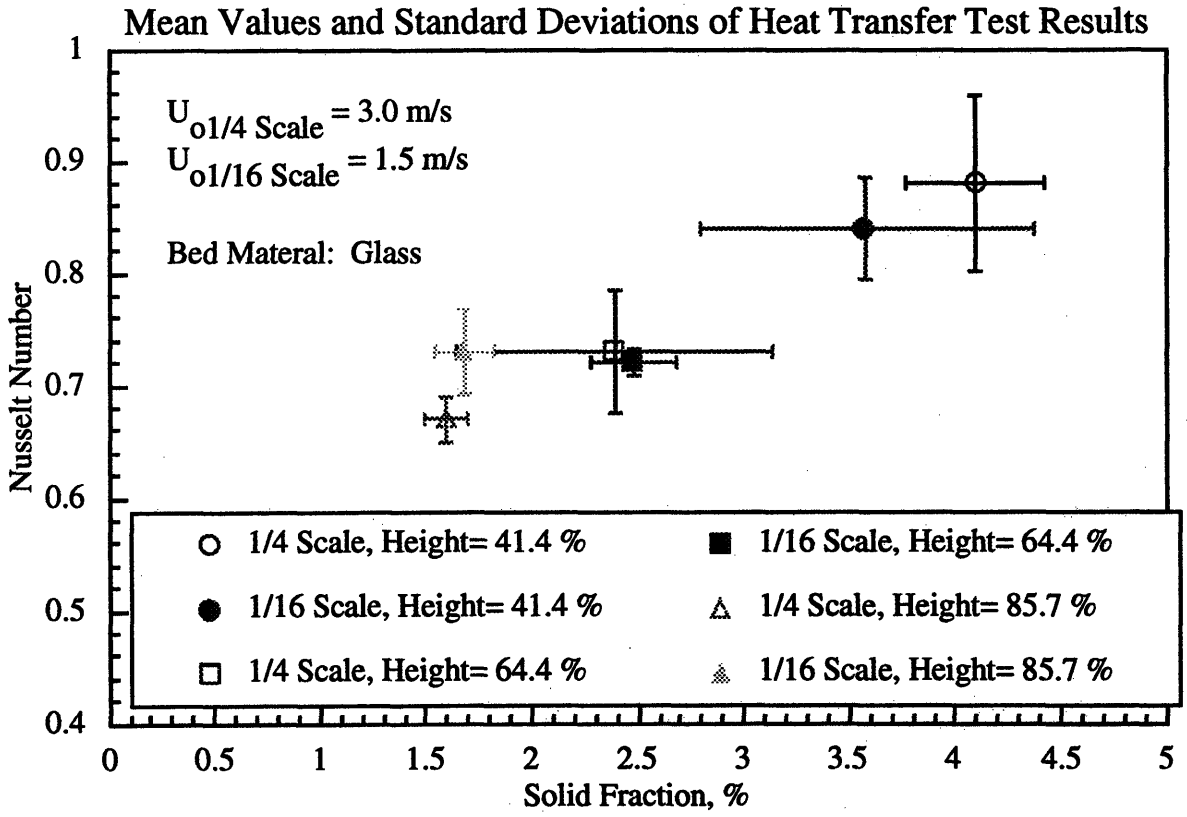

Figure 11.2

Mean Values and Standard Deviations of Heat Transfer Test Results

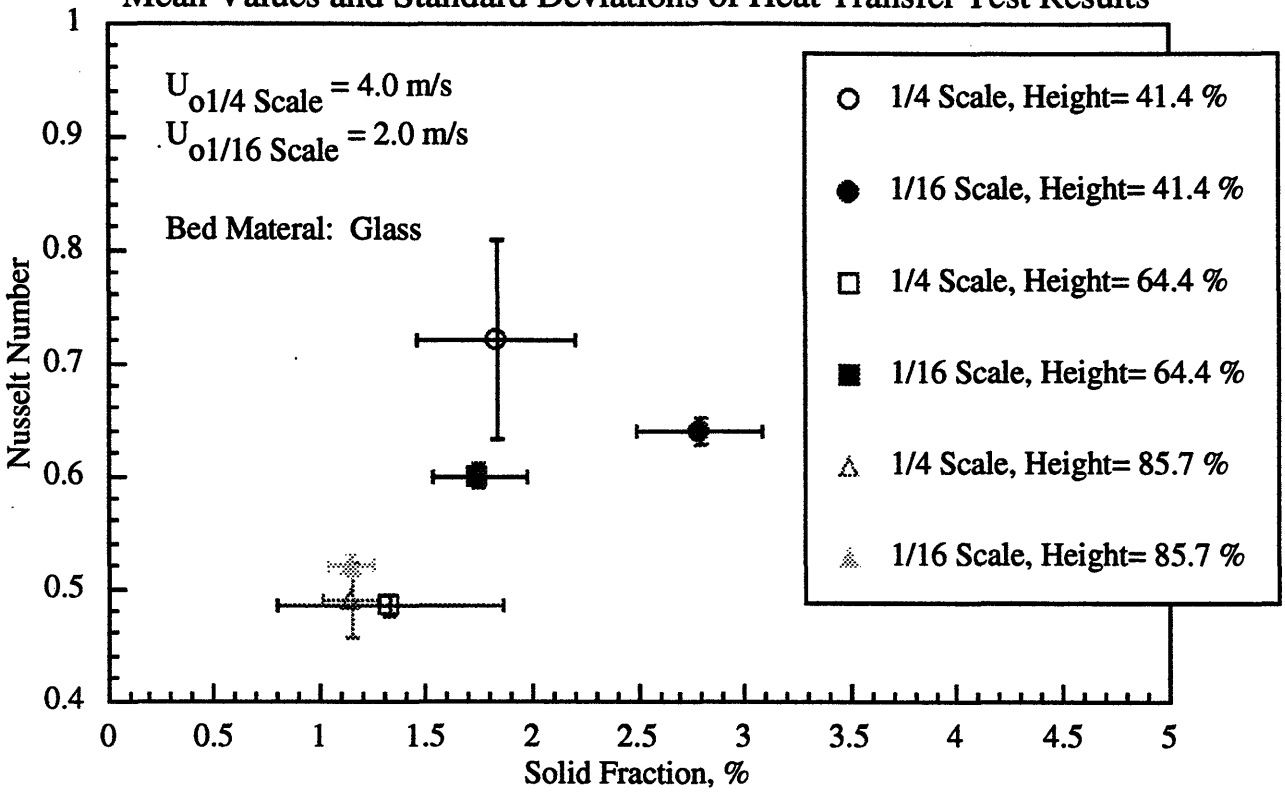

Figure 11.3

Mean Values and Standard Deviations of Heat Transfer Test Results

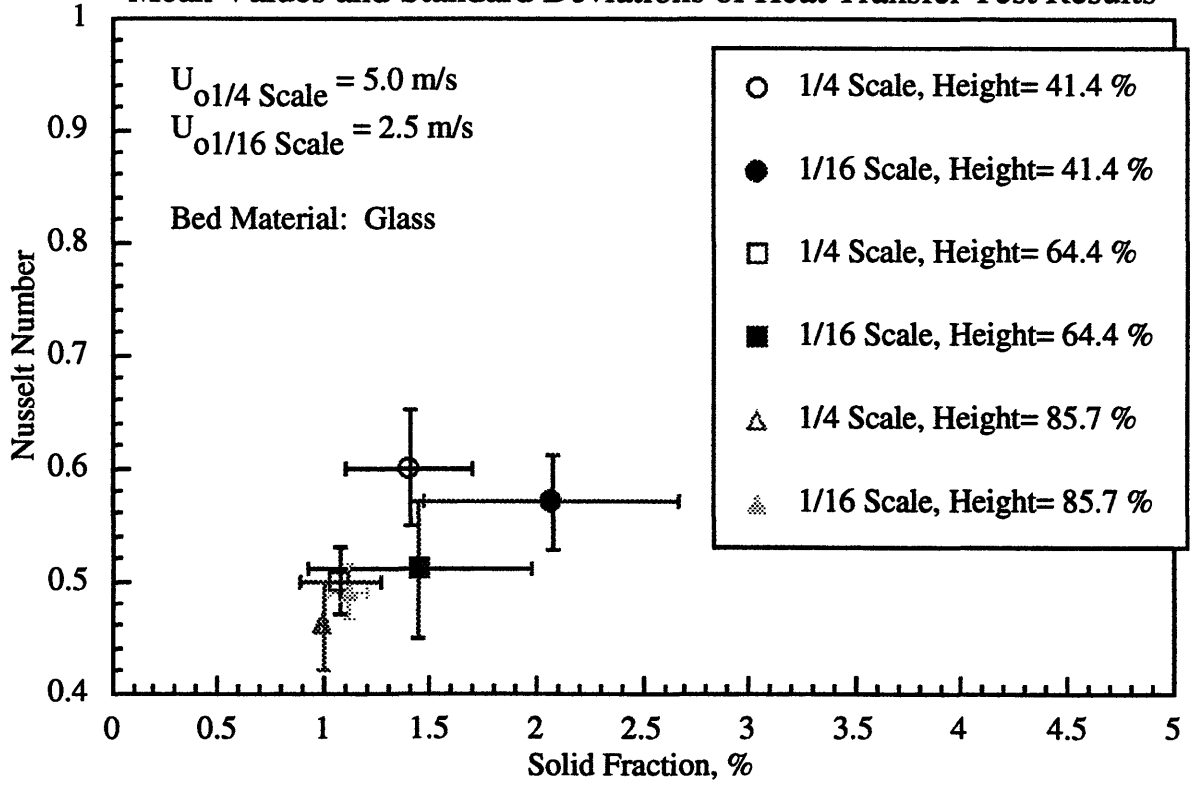

Figure 11.4

Mean Values of Heat Transfer Test Results - Glass Tests

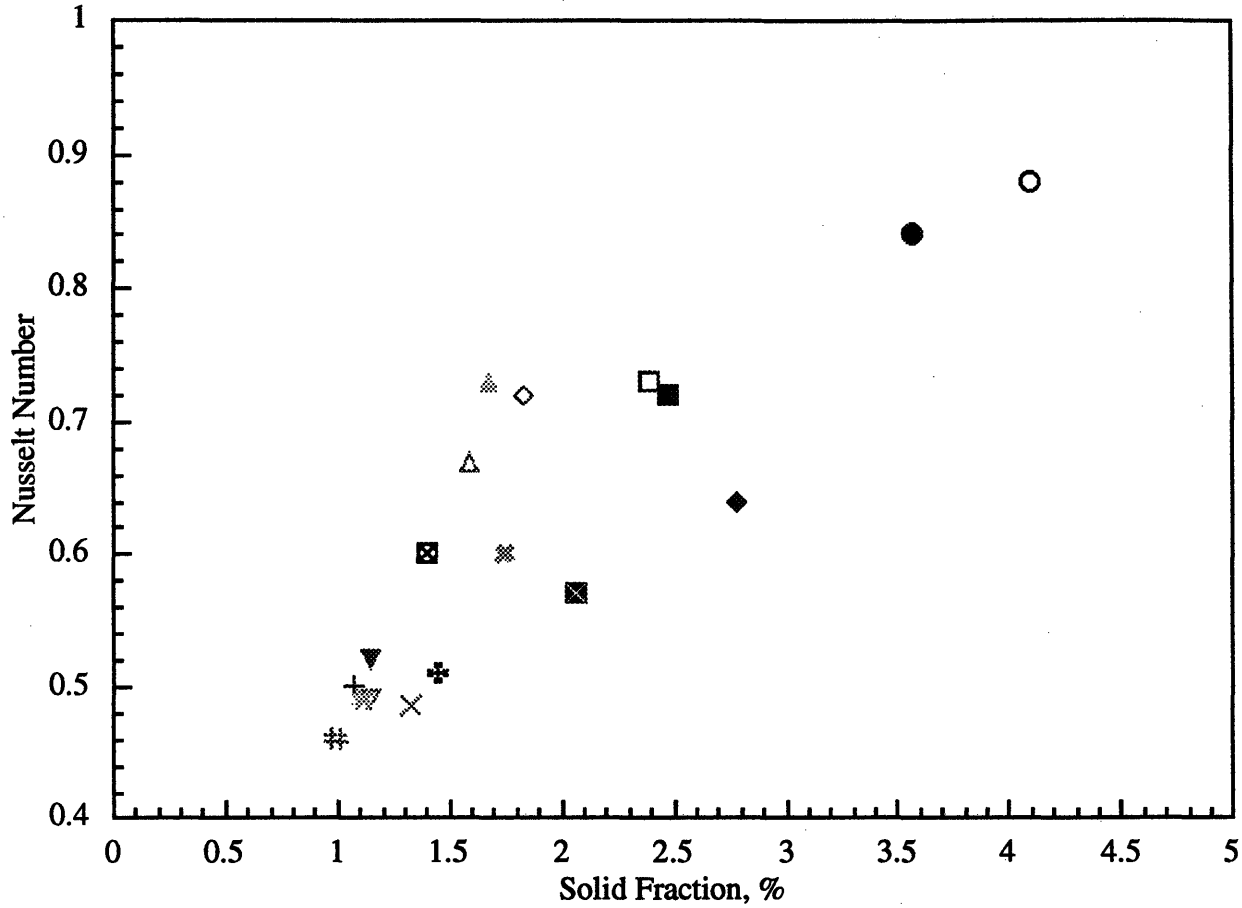

○ 1/4 Scale, Height= 41.4 %, Uo = 3.0 m/s	▒ 1/16 Scale, Height= 64.4 %, Uo = 2.0 m/s
● 1/16 Scale, Height= 41.4 %, Uo = 1.5 m/s	▽ 1/4 Scale, Height= 85.7 %, Uo = 4.0 m/s
□ 1/4 Scale, Height= 64.4 %, Uo = 3.0 m/s	▼ 1/16 Scale, Height= 85.7 %, Uo = 2.0 m/s
■ 1/16 Scale, Height= 64.4 %, Uo = 1.5 m/s	⊠ 1/4 Scale, Height= 41.4 %, Uo = 5.0 m/s
△ 1/4 Scale, Height= 85.7 %, Uo = 3.0 m/s	▩ 1/16 Scale, Height= 41.4 %, Uo = 2.5 m/s
▲ 1/16 Scale, Height= 85.7 %, Uo = 1.5 m/s	+ 1/4 Scale, Height= 64.4 %, Uo = 5.0 m/s
◇ 1/4 Scale, Height= 41.4 %, Uo = 4.0 m/s	✤ 1/16 Scale, Height= 64.4 %, Uo = 2.5 m/s
◆ 1/16 Scale, Height= 41.4 %, Uo = 2.0 m/s	# 1/4 Scale, Height= 85.7 %, Uo = 5.0 m/s
× 1/4 Scale, Height= 64.4 %, Uo = 4.0 m/s	▒ 1/16 Scale, Height= 85.7 %, Uo = 2.5 m/s

Figures 11.5 through 11.7 show the dependence of the Nusselt number on bed superficial velocity. The dependence of Nusselt number on superficial velocity for a given suspension density is not very strong. In general, the Nusselt number decreases for increasing bed velocity. This may be due to a decrease in the amount of particles at the wall of the bed, or an increase in the distance from the wall to the first layer of particles flowing down the wall (see Lints, 1992).

Figure 11.5

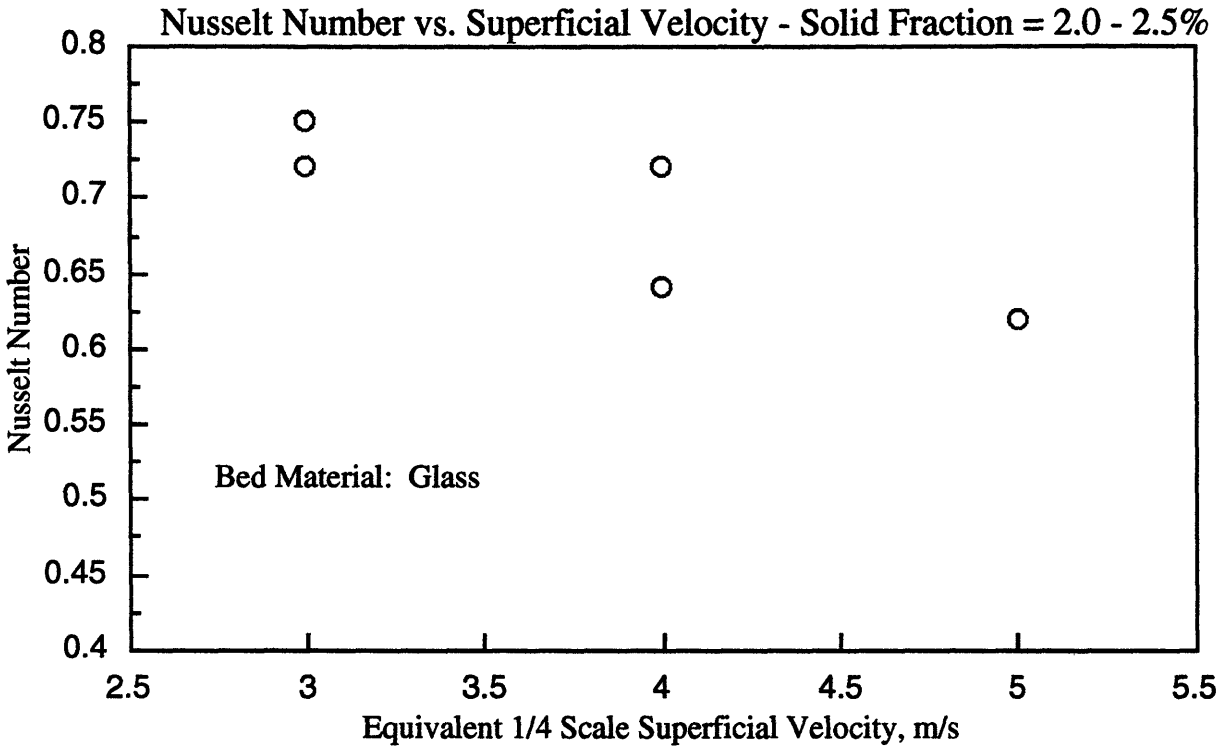

Figure 11.6

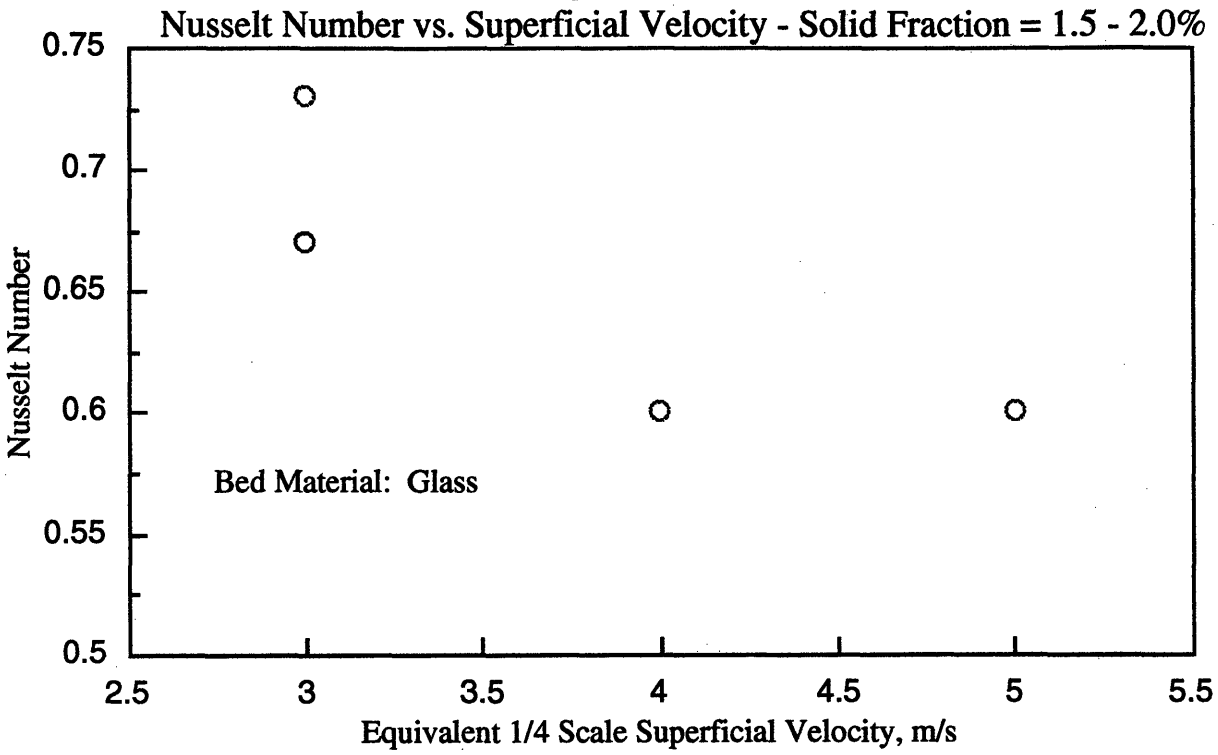

Figure 11.7

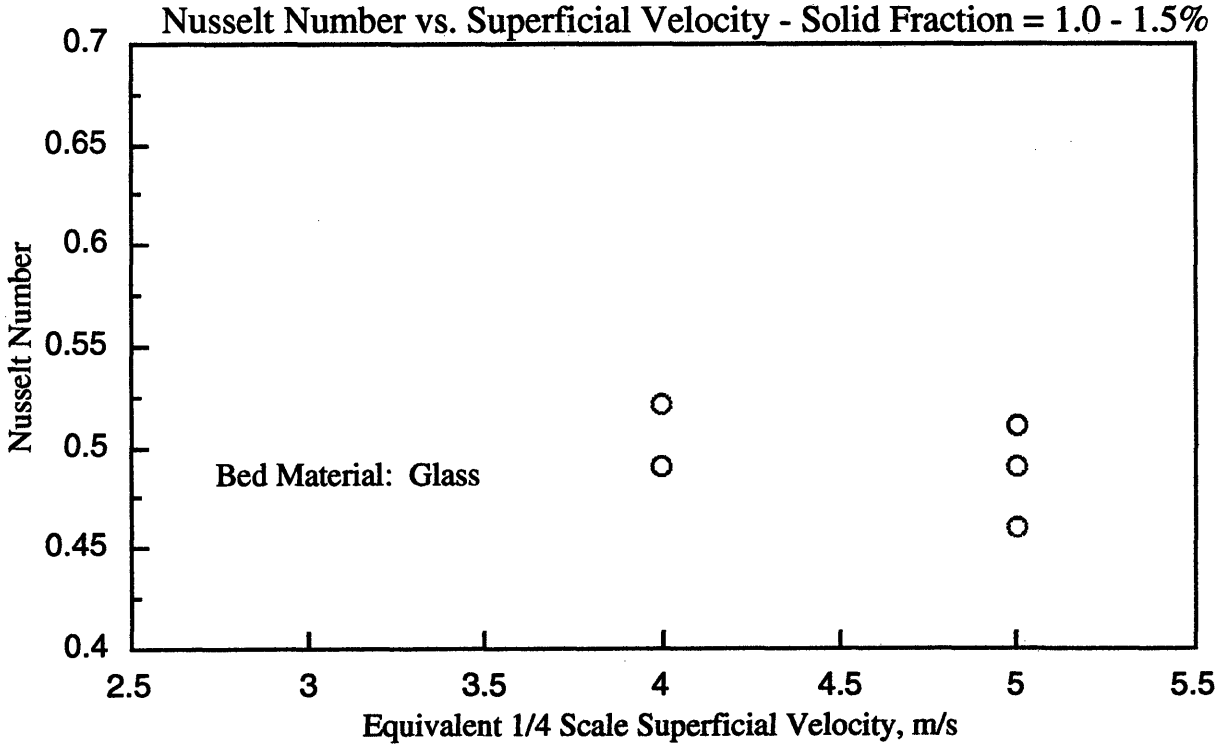

12.0 EXPERIMENTAL RESULTS OF CONVECTIVE HEAT TRANSFER SCALING WITH PLASTIC

The test matrix for the heat transfer tests conducted with plastic as the bed material is given as Table 12.1.

Heat transfer measurements were taken in the same manner as described in the previous Section. Figures 12.1 through 12.9 show the results of these tests. In each of the these plots, similar geometric symbols (i.e., open circles and filled circles, open squares and closed squares, and open triangles and closed triangles) represent conditions which should result in similar values of Nusselt numbers.

Table 12.1

Test Matrix for Heat Transfer Similarity - Series Two

Bed Material: Plastic

Parameter	**Large Bed**	**Small Bed**
Bed Diameter	D	0.25D
Superficial Velocity	u_o	$0.5u_o$
Minimum Fluidization Velocity, cm/s	$u_{mf} = 1.5$	$0.5u_{mf}$
Particle Diameter, μm	$d_p = 144.5$	$0.707d_p$
Particle Density, kg/m^3	1400	Same
$Re_{d_p} = \frac{\rho_f u_o d_p}{\mu_f}$	$\frac{\rho_f u_o d_p}{\mu_f}$	$\frac{0.35\rho_f u_o d_p}{\mu_f}$
$Re_D = \frac{\rho_f u_o D}{\mu_f}$	$\frac{\rho_f u_o D}{\mu_f}$	$\frac{\rho_f u_o D}{8\mu_f}$
$\frac{\rho_s}{\rho_f}$	1167	Same
$M = \frac{\dot{m}_s}{u_o A_{cs} \rho_s}$	0.0029	Same
$\frac{c_{p_s}\mu}{k_f}$	0.73	Same
$Hx = \left(\frac{u_o \rho_s c_p d_p^2}{L k_g}\right)$	Hx	Same

Figure 12.1: Plastic Particles

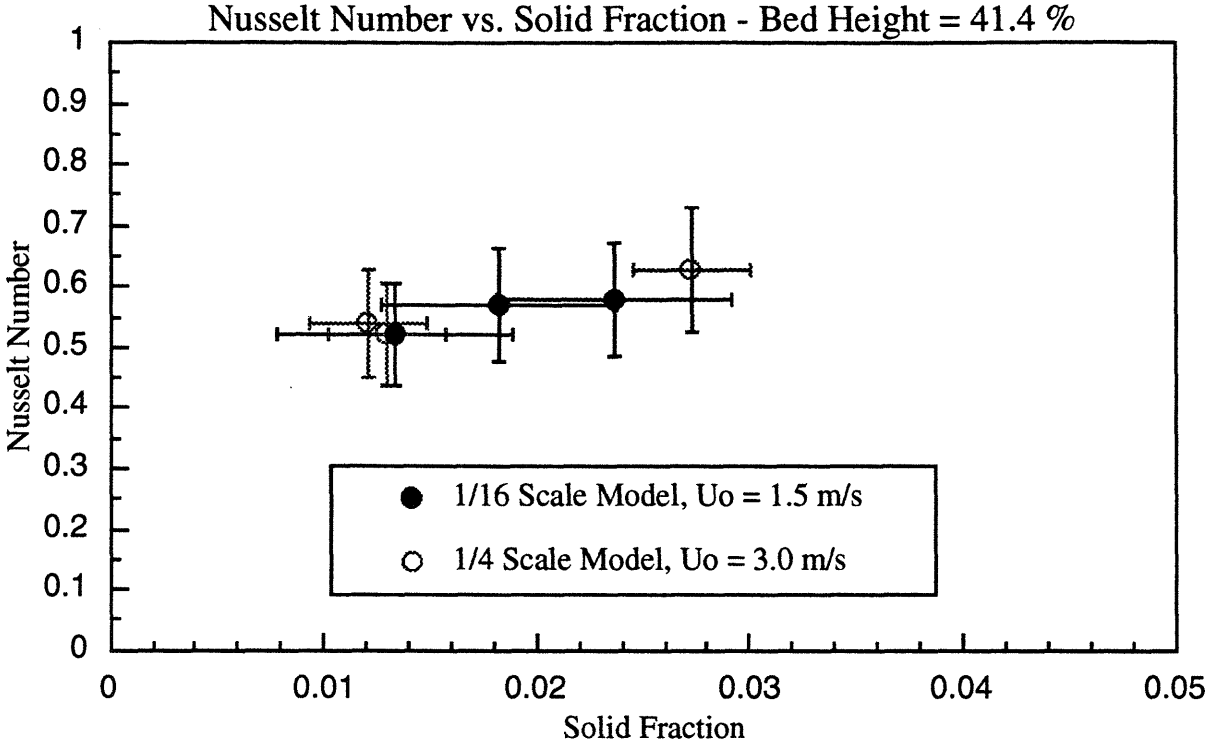

Figure 12.2: Plastic Particles

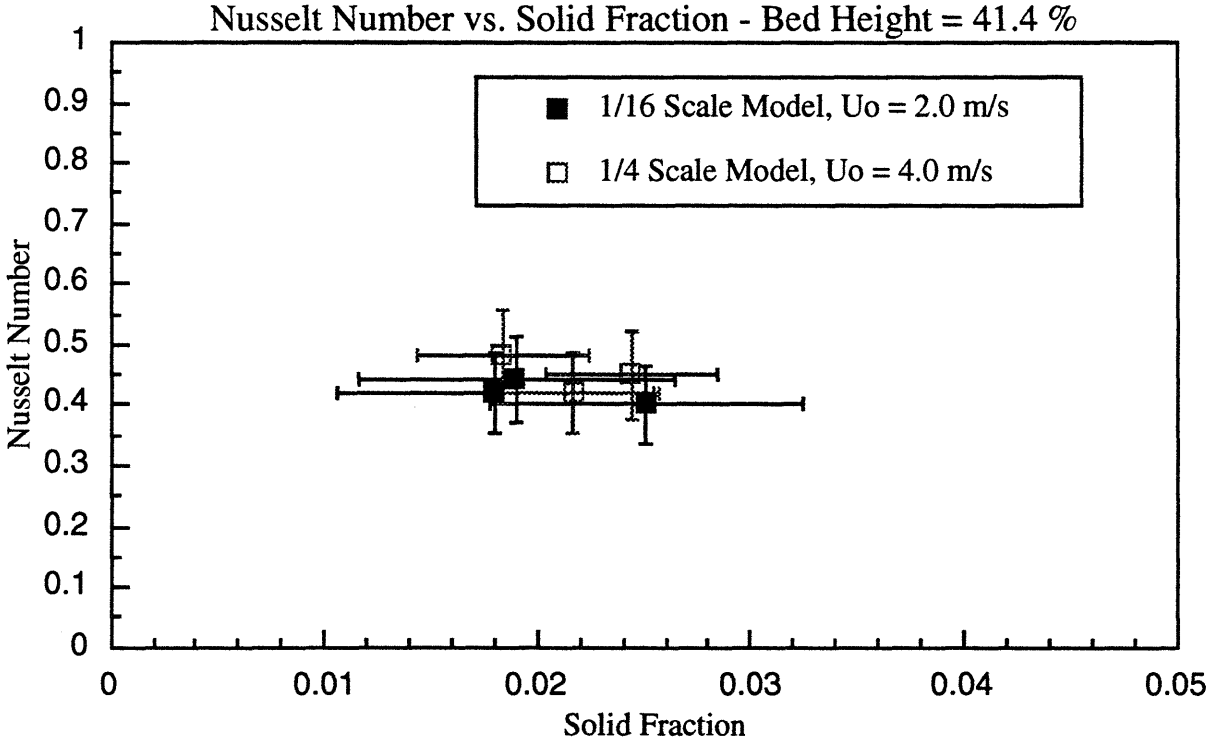

Figure 12.3: Plastic Particles

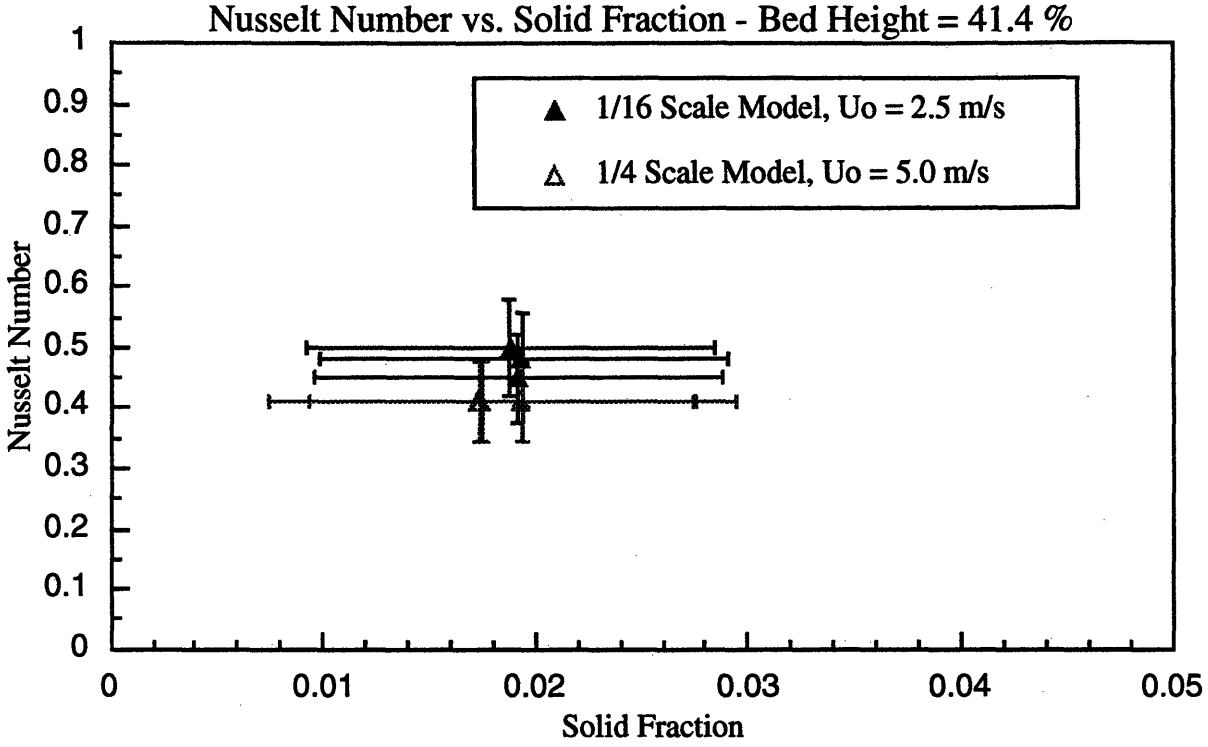

Figure 12.4: Plastic Particles

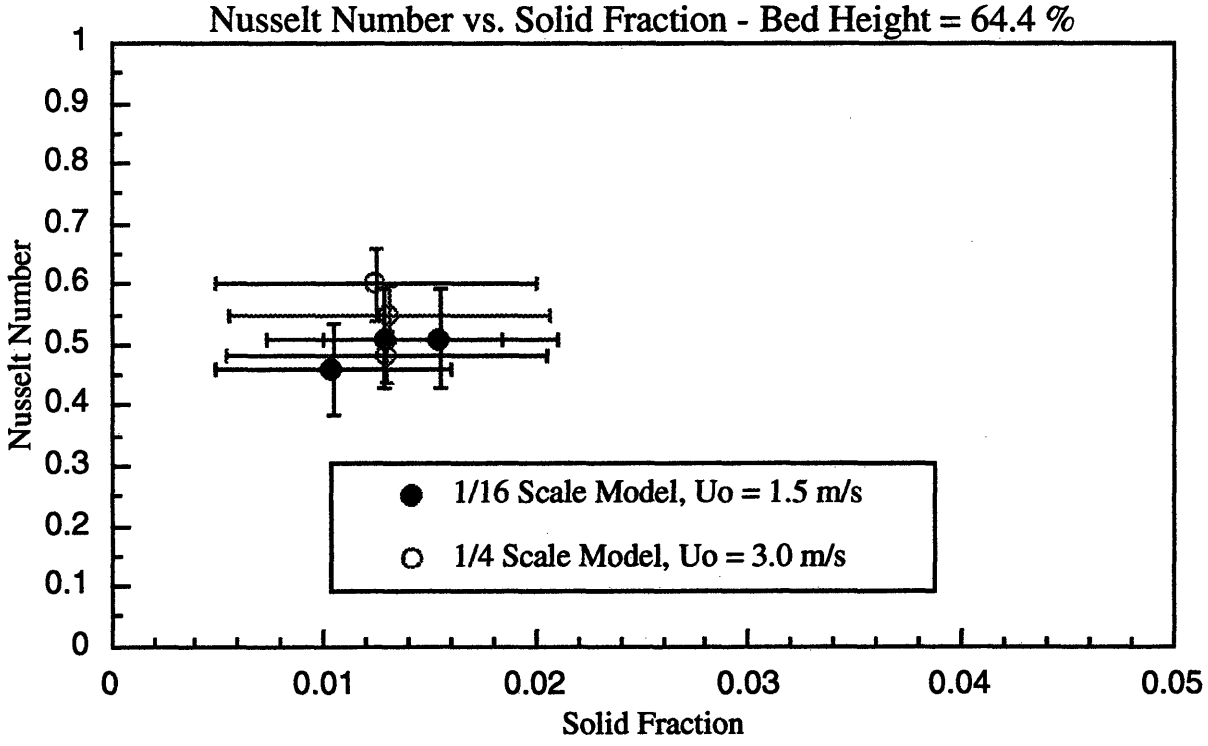

Figure 12.5: Plastic Particles

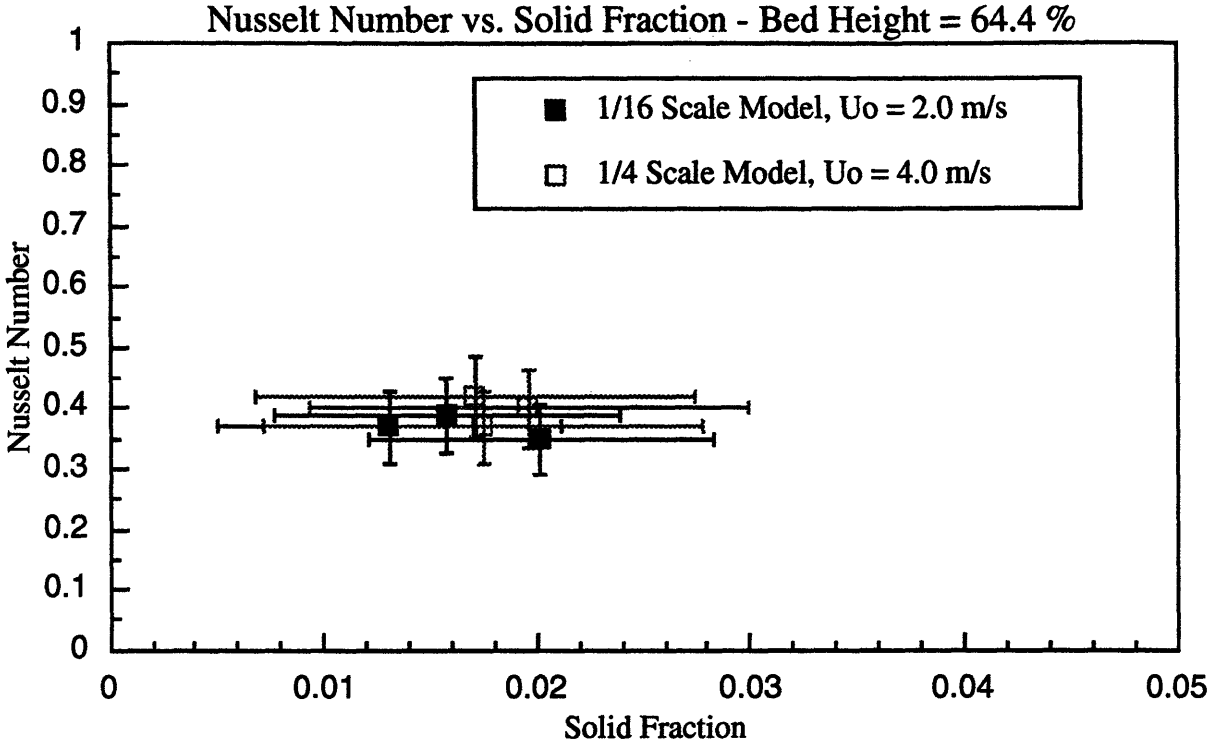

Figure 12.6: Glass Particles

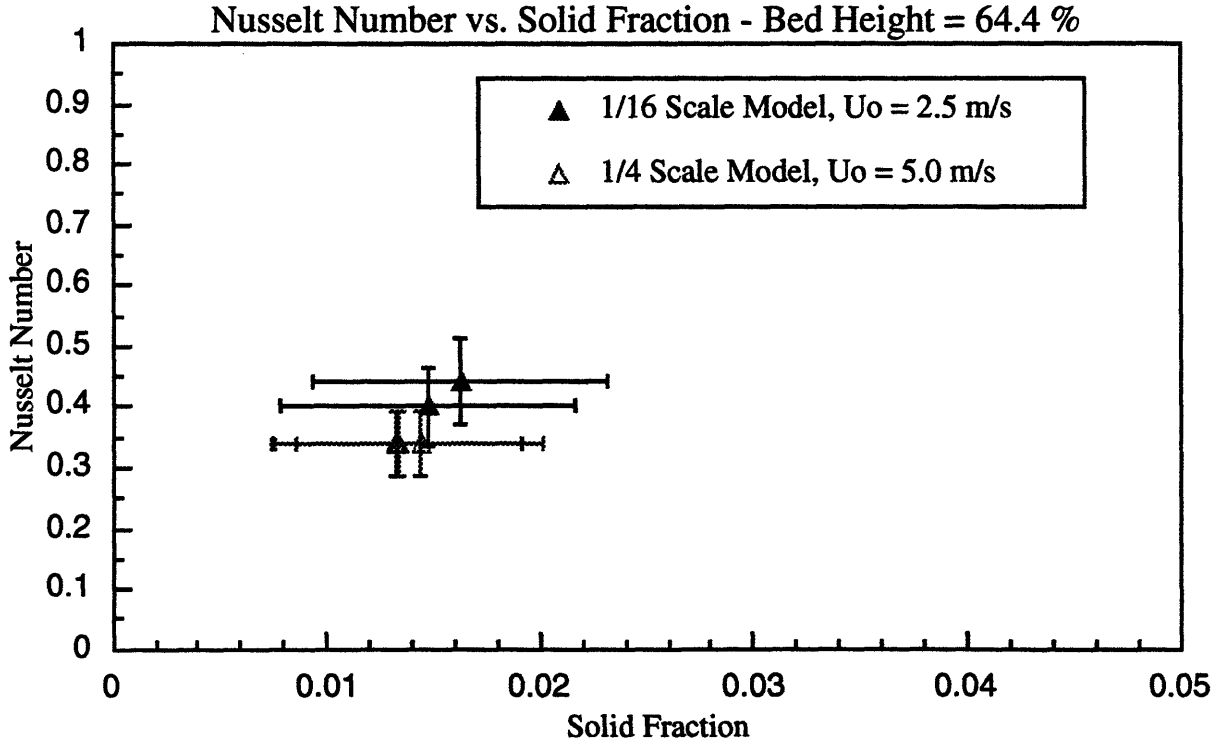

Figure 12.7: Plastic Particles

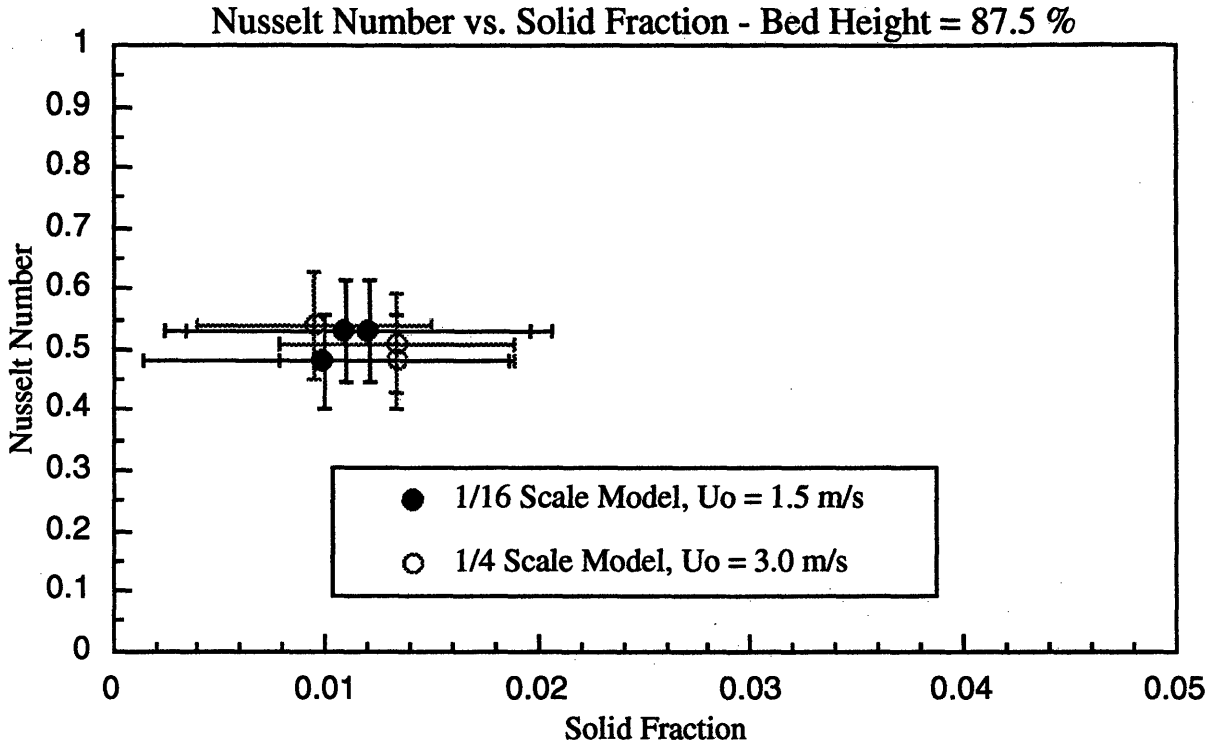

Figure 12.8: Plastic Particles

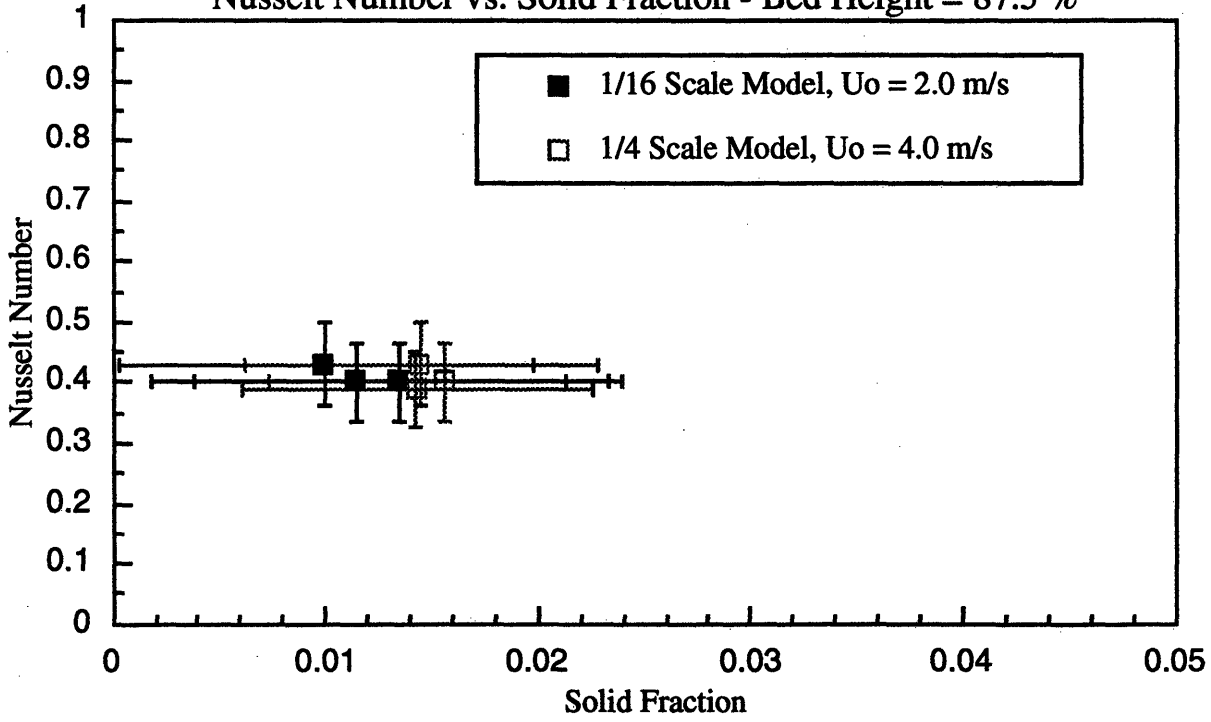

Figure 12.9: Plastic Particles

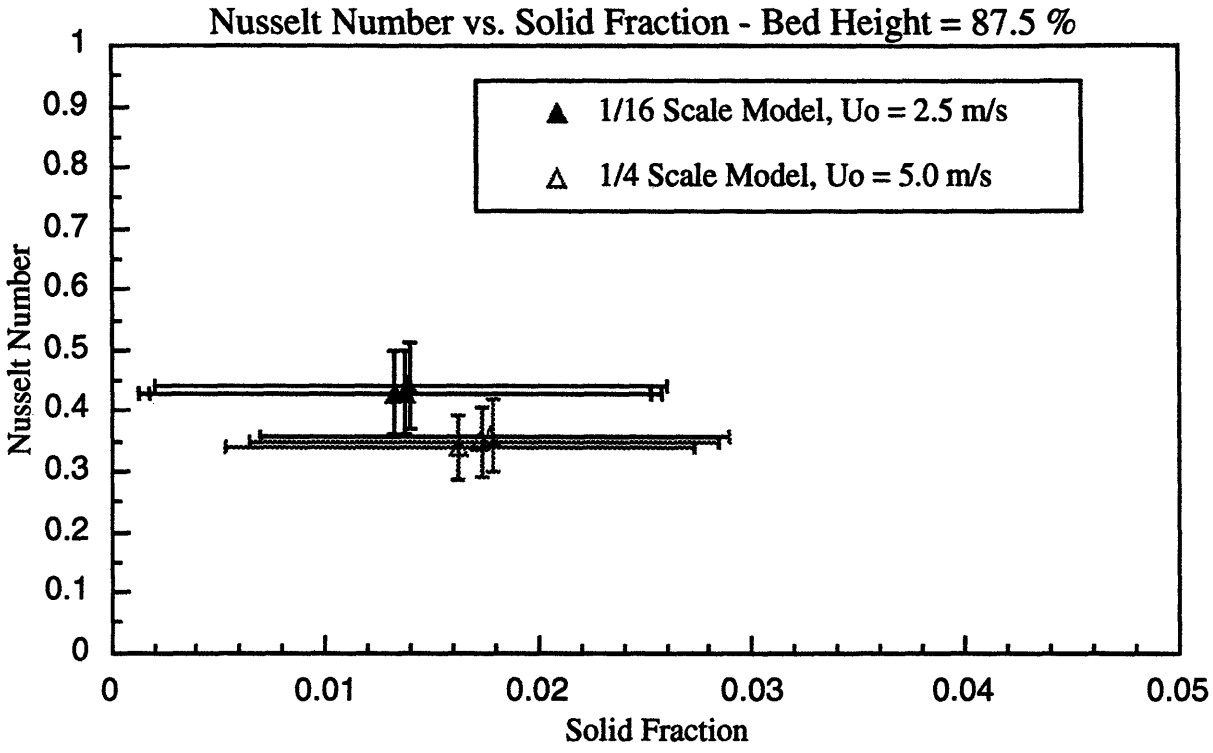

13.0 DISCUSSION OF RESULTS FOR HEAT TRANSFER SCALING WITH PLASTIC

At all bed heights and superficial velocities, the Nusselt numbers between the 1/4 scale Studsvik model and the 1/16 scale Studsvik model show good agreement. As was noted in the discussion of the Nusselt numbers measured with glass as the bed material, the Nusselt numbers appear to be proportional to the average cross-sectional bed density. A discussion of the limitations of this functional relationship is given in the next Section. Figures 13.1 through 13.3 show mean values of solid fraction and Nusselt numbers calculated from the experimental results. The error bars in these plots were determined from standard deviations in the experimental data for runs with the same hydrodynamic conditions. Most of the plots show acceptable agreement. It should be noted that the error bars in these plots have very little statistical significance because of the low number of data points used in calculating the standard deviation. Figure 13.4 depicts the mean solid fractions and Nusselt numbers for the plastic runs at all heights and superficial velocities.

Figure 13.1

Mean Values and Standard Deviations of Heat Transfer Test Results

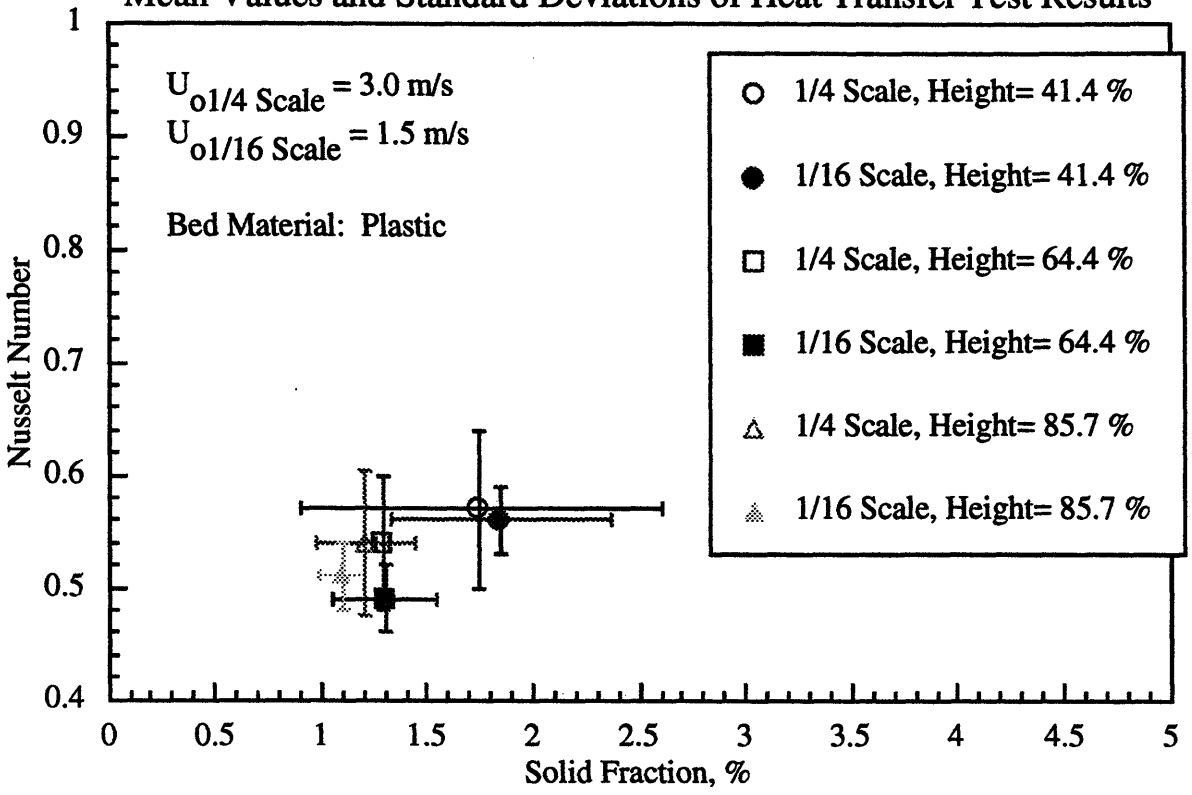

Figure 13.2

Mean Values and Standard Deviations of Heat Transfer Test Results

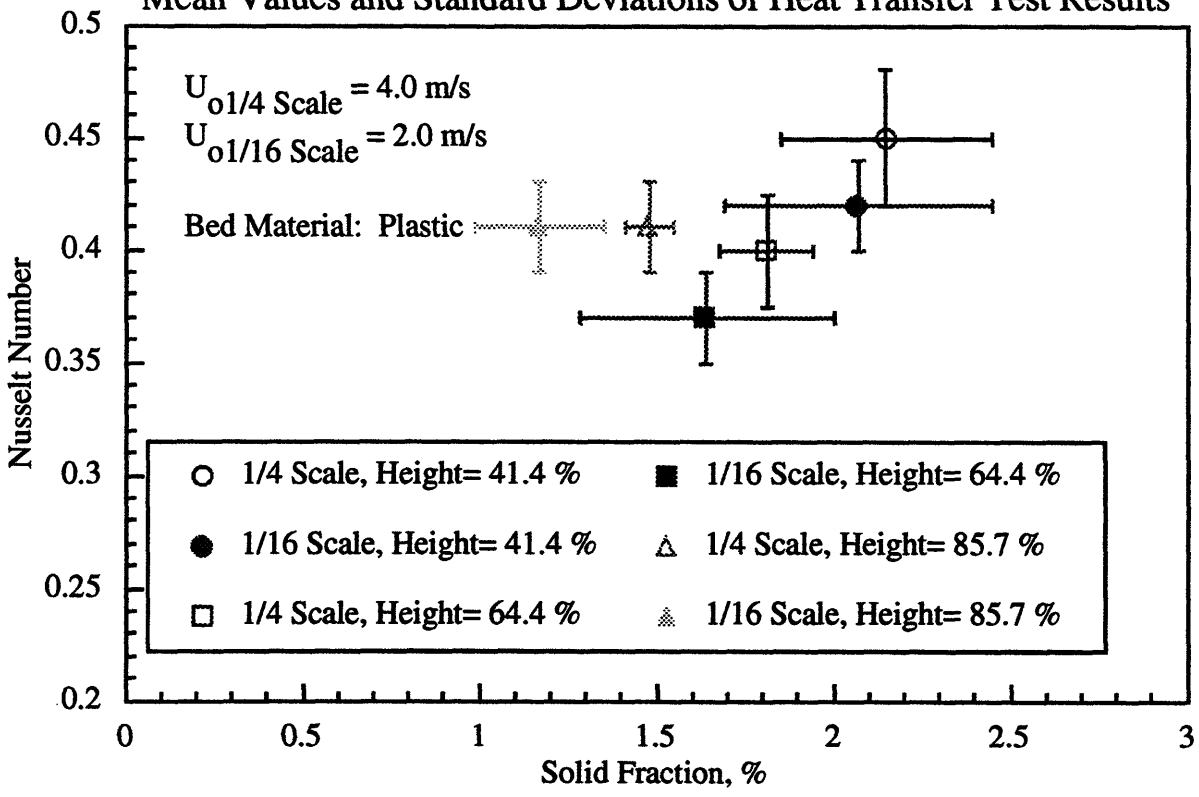

Figure 13.3

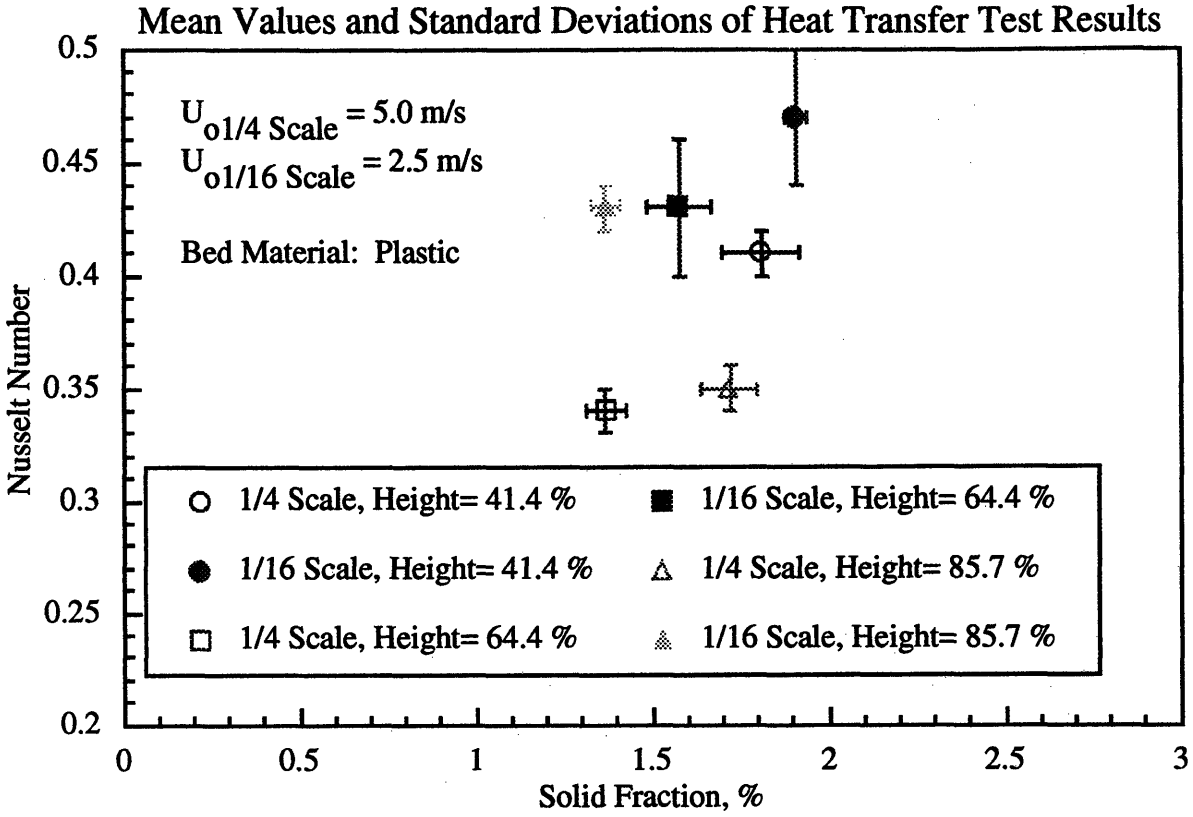

Figures 13.5 through 13.7 show the dependence of the Nusselt number on bed superficial velocity. Consistent with trends in the glass data, the dependence of Nusselt number on superficial velocity for a given suspension density is not very strong. In general, the Nusselt number decreases for increasing bed velocity. Further study is needed to determine the effect of superficial velocity on the fundamental hydrodynamics of particles near the wall of a CFB (i.e. the fraction of the wall covered by particles, the mean particle-to-wall contact time, and the thickness of the gas gap between the wall and the first layer of particles).

Figure 13.4
Mean Values of Heat Transfer Test Results - Plastic Tests

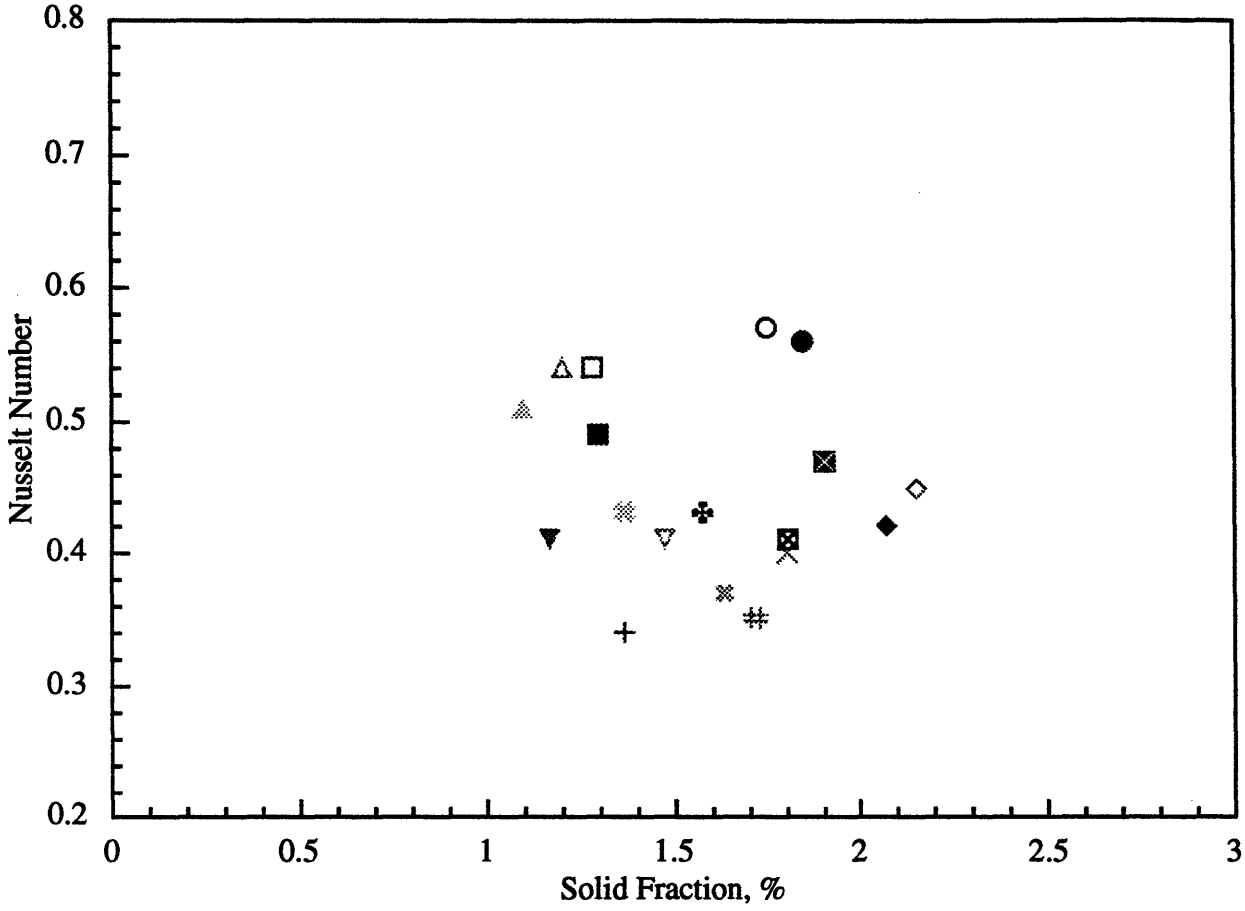

○ 1/4 Scale, Height= 41.4 %, Uo = 3.0 m/s	▒ 1/16 Scale, Height= 64.4 %, Uo = 2.0 m/s
● 1/16 Scale, Height= 41.4 %, Uo = 1.5 m/s	▽ 1/4 Scale, Height= 85.7 %, Uo = 4.0 m/s
□ 1/4 Scale, Height= 64.4 %, Uo = 3.0 m/s	▼ 1/16 Scale, Height= 85.7 %, Uo = 2.0 m/s
■ 1/16 Scale, Height= 64.4 %, Uo = 1.5 m/s	⊠ 1/4 Scale, Height= 41.4 %, Uo = 5.0 m/s
△ 1/4 Scale, Height= 85.7 %, Uo = 3.0 m/s	▩ 1/16 Scale, Height= 41.4 %, Uo = 2.5 m/s
▲ 1/16 Scale, Height= 85.7 %, Uo = 1.5 m/s	+ 1/4 Scale, Height= 64.4 %, Uo = 5.0 m/s
◇ 1/4 Scale, Height= 41.4 %, Uo = 4.0 m/s	✤ 1/16 Scale, Height= 64.4 %, Uo = 2.5 m/s
◆ 1/16 Scale, Height= 41.4 %, Uo = 2.0 m/s	# 1/4 Scale, Height= 85.7 %, Uo = 5.0 m/s
× 1/4 Scale, Height= 64.4 %, Uo = 4.0 m/s	▒ 1/16 Scale, Height= 85.7 %, Uo = 2.5 m/s

Figure 13.5

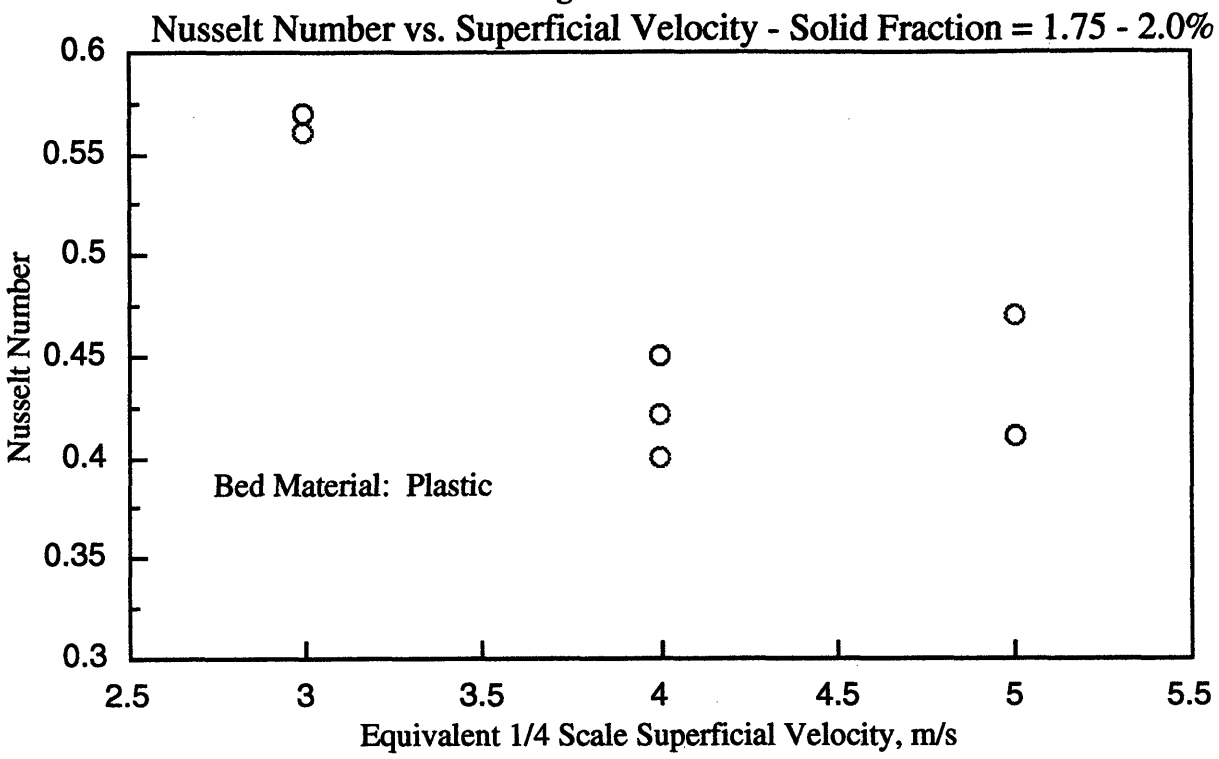

Figure 13.6

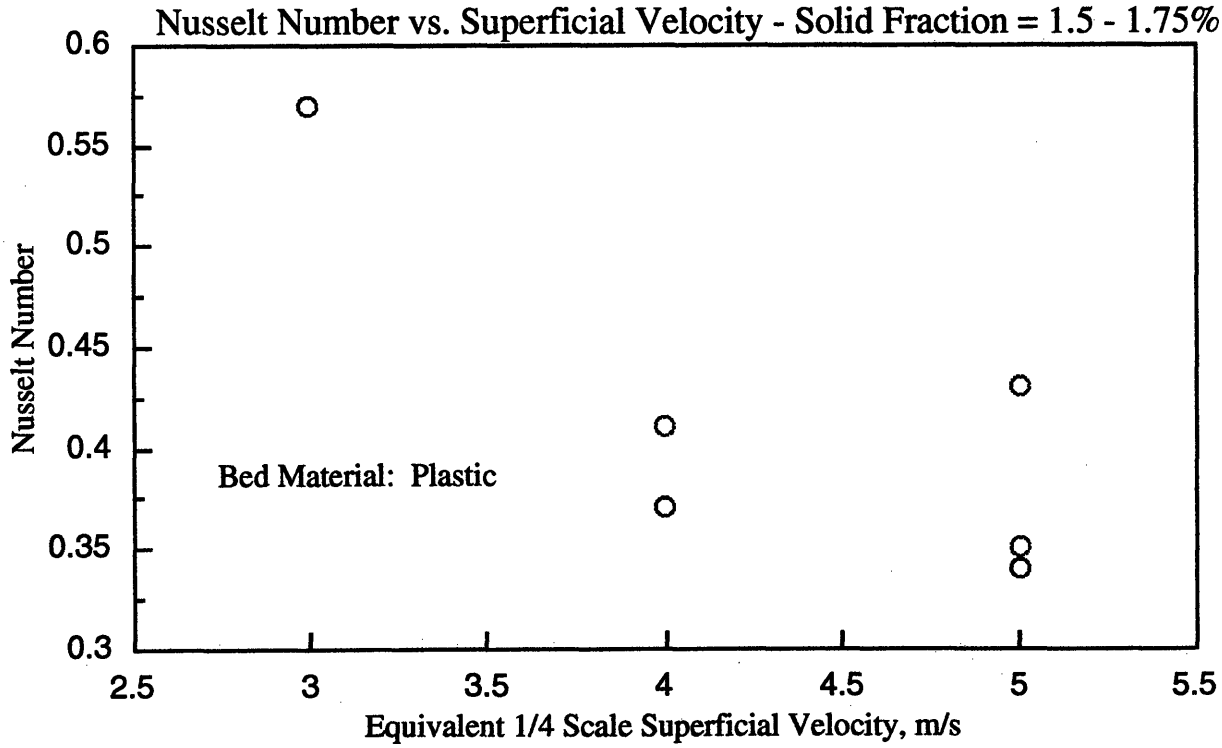

Figure 13.7

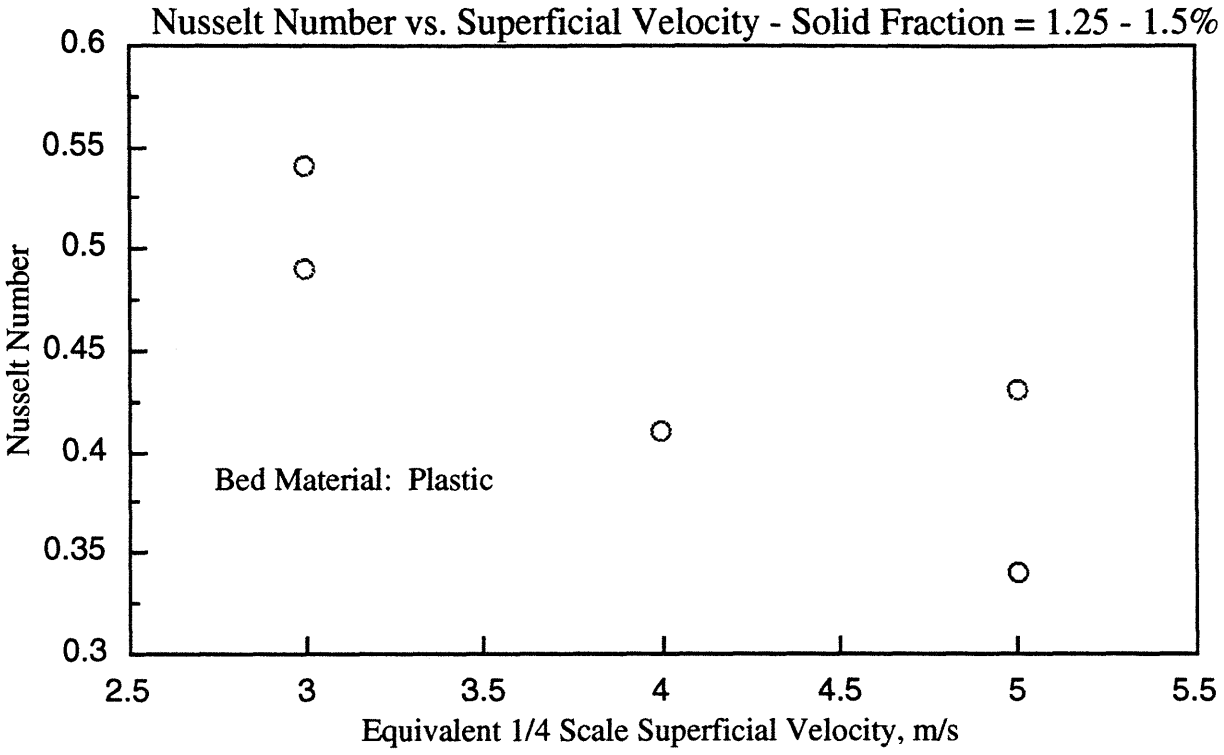
Nusselt Number vs. Superficial Velocity - Solid Fraction = 1.25 - 1.5%
Nusselt Number
0.6
0.55
0.5
0.45
0.4
0.35
0.3
Bed Material: Plastic
2.5
3
3.5
4
4.5
5
5.5
Equivalent 1/4 Scale Superficial Velocity, m/s

14.0 LIMITATIONS OF THE AVERAGE BED DENSITY/NUSSELT NUMBER FUNCTIONAL RELATIONSHIP

This Section discusses the limitations of correlating heat transfer data against the average bed density or solid fraction.

14.1 Scaling Heat Transfer Data to Large Commercial Units

Most authors plot heat transfer coefficient data against the average bed solid fraction. While the average bed density has proved to be a satisfactory indication of the level of heat transfer in small scale cold beds, it does not appear that the data can be extrapolated to predict heat transfer coefficients in commercial CFB's. Reported values of bed suspension densities and wall heat fluxes indicate much higher heat transfer coefficients than would be predicted from similar suspension densities in small cold scale models (Divilio and Boyd, 1993). This may be a result of the fact that as the bed diameter increases, the volume increases as D^3 whereas the surface area only increases as D^2. This could result in a much larger reflux of particles at the wall of larger beds than in smaller scale models. As a result, in order to make an accurate prediction of the heat transfer characteristics in a larger commercial unit, a scale model of the unit needs to be constructed to simulate the correct hydrodynamics. Moreover, much of the heat transfer data taken to date may not be applicable to larger commercial units.

14.2 Heat Transfer Data at the Transition to Dilute Pneumatic Conveying

In order to determine the effects of increasing the velocity to an operating regime where the downward flow of particles at the wall begins to disappear (i.e., from fast-fluidization to pneumatic transport), several runs were conducted in the phase one 1/16 scale Studsvik model at superficial velocities of 3, 4, 5, and 6 m/s.

The downward flow of particles at the wall was easily visible during the 3 m/s runs, but began to disappear during the 4 m/s runs. The wall layer was nearly eliminated during the 5 and 6 m/s runs. The bed solid fraction profiles for these runs is given in Figure 14.1.

Figure 14.1

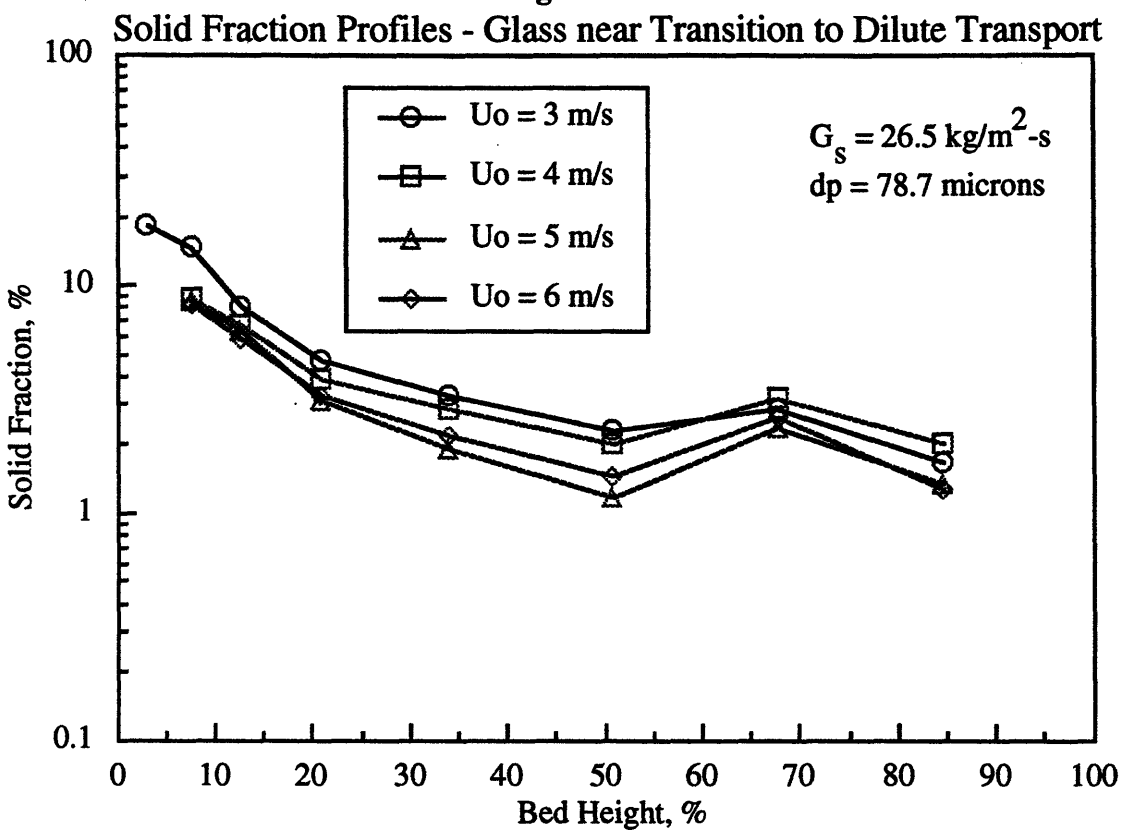

Figure 14.1 shows that the average solid fraction profiles are fairly similar with the expected trend of decreasing solid fraction profile with an increase in velocity (solid flux being constant). Figure 14.2 shows the Nusselt number versus local solid fraction data taken during these runs. The solid fractions were averaged over distances of about 16 percent of the bed height

Figure 14.2

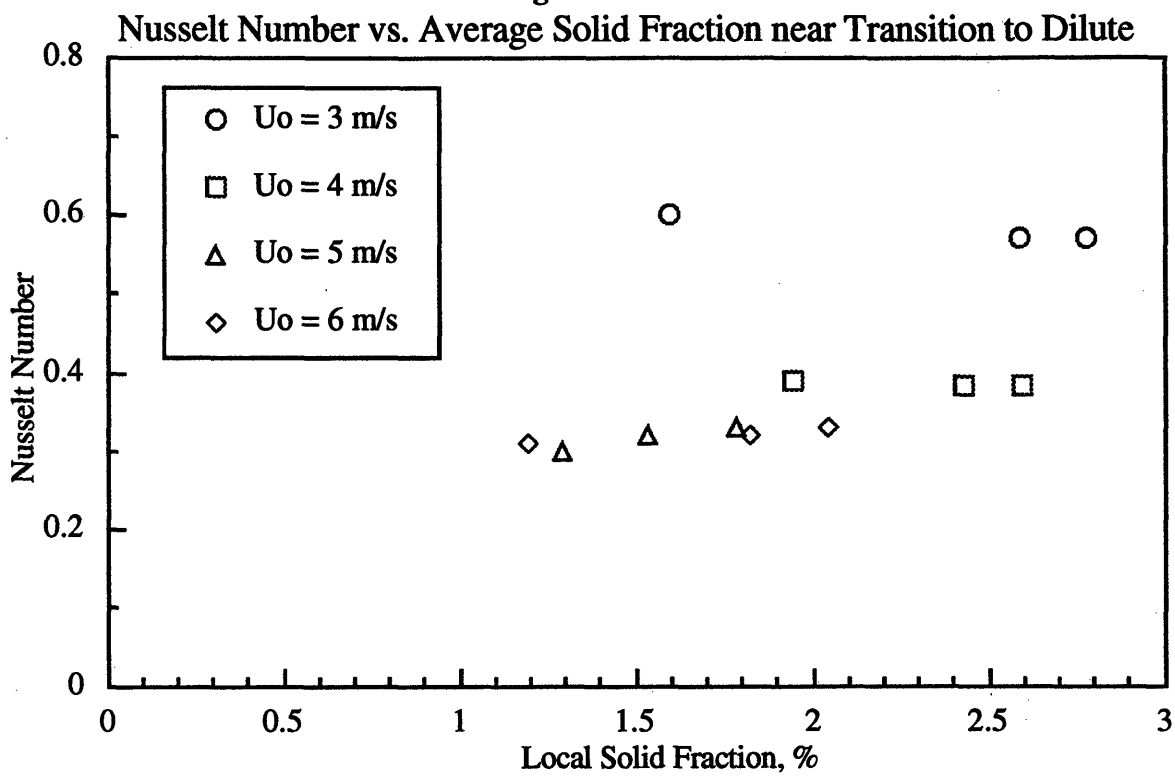

Figure 14.2 shows that the Nusselt numbers for velocities above 3 m/s tend to increase with increasing solid fractions, but only slightly. However, when the velocity is reduced to 3 m/s, the Nusselt numbers jump drastically to values which are up to twice as high as that for similar solid fractions at higher velocities. Figure 14.2 does not depict any consistent trend in Nusselt number as a function of average bed density.

In order to obtain a qualitative trend in the amount of solids at the wall of the bed during these runs, a 0.32 cm diameter suction probe was attached to the wall of the bed. The probe was attached to a side wall 31.5 cm from the bottom of the bed. Enough suction was applied in order to draw the particles immediately at the wall into a small cyclone which deposited the solids into a graduated cylinder for weighing. Figure 14.3 shows the wall solid collection rate as a function of the average bed solid fraction.

Figure 14.3

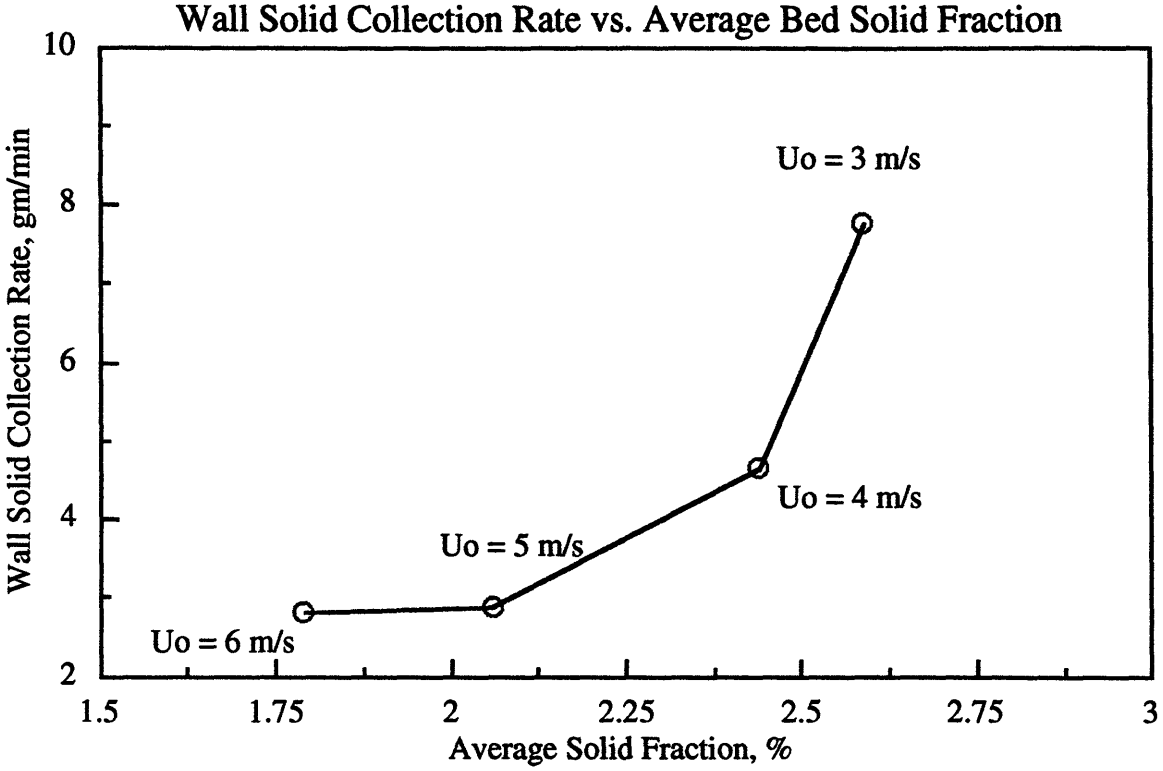

Figure 14.3 shows that as the superficial velocity is dropped from 5 m/s to 3 m/s, the amount of solids at the wall increases dramatically. This is the most probable cause for the large increase in Nusselt number when moving from 5 m/s down to 3 m/s. Figure 8.36 shows the Nusselt number versus the wall solid collection rate.

Figure 14.4 shows a much more reasonable trend than any that could be postulated from Figure 14.2. This indicates that while the average solid fraction profiles in the beds are not changing significantly between 3 and 6 m/s, the amount of solids at the wall is what accounts for the dramatic increase in Nusselt number between 5 and 3 m/s.

Figure 14.4

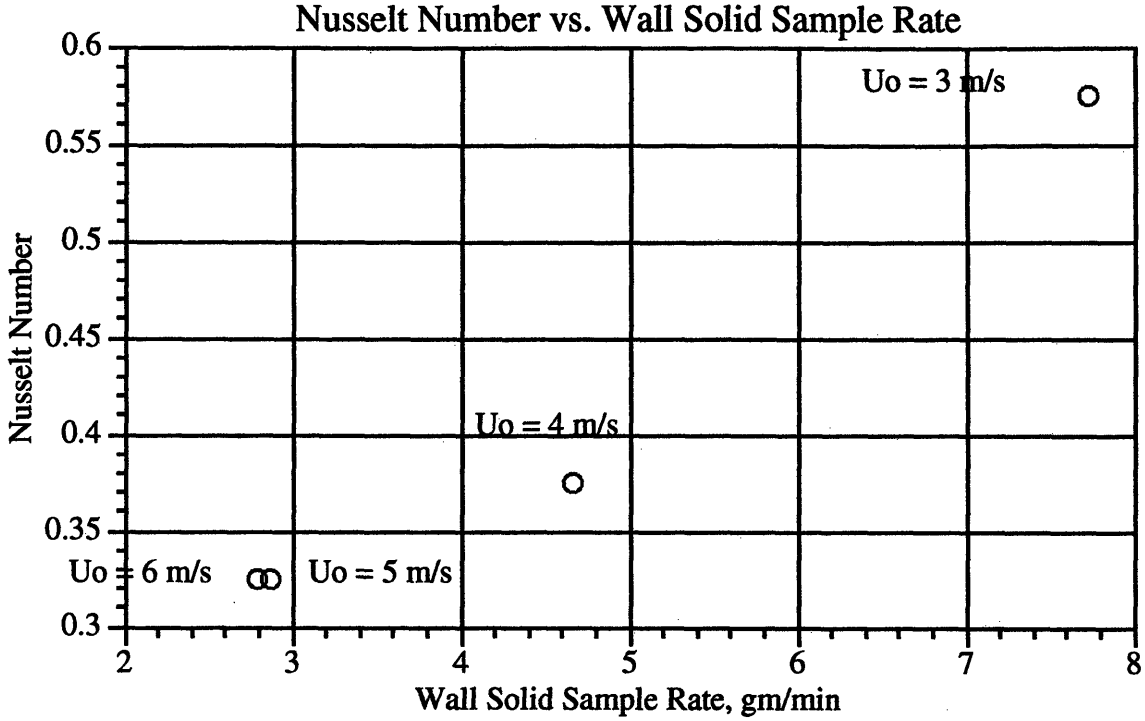

Figures 14.2 through 14.4 indicate that the flow structure of the bed changed when the superficial velocity was raised from 3 to 5 m/s. Visual observations support this evidence since the downward flowing layer was clearly visible at 3 m/s, began to disappear at 4 m/s, and was nearly gone at 5 and 6 m/s. In order to provide more quantitative evidence that the bed underwent a regime change between 3 and 5 m/s, the voidage gradient $\left|\frac{\partial \varepsilon}{\partial z}\right|_{inf}$ at the inflection point (see Figure 14.5) of the average solid fraction profile was plotted versus superficial velocity (see Figure 14.6). According to Karri and Knowlton (1990) and Takeuchi *et al.* (1986) the onset of dilute transport occurs at a gas velocity at which the pressure gradients measured in the riser approach a constant value for a given solids mass flux. This type of analysis was used by Horio *et al.* to determine the boundary between turbulent and fast fluidized beds (Horio *et al.*, 1992).

Figure 14.5

Example of Voidage Gradient Estimation at Inflection Point

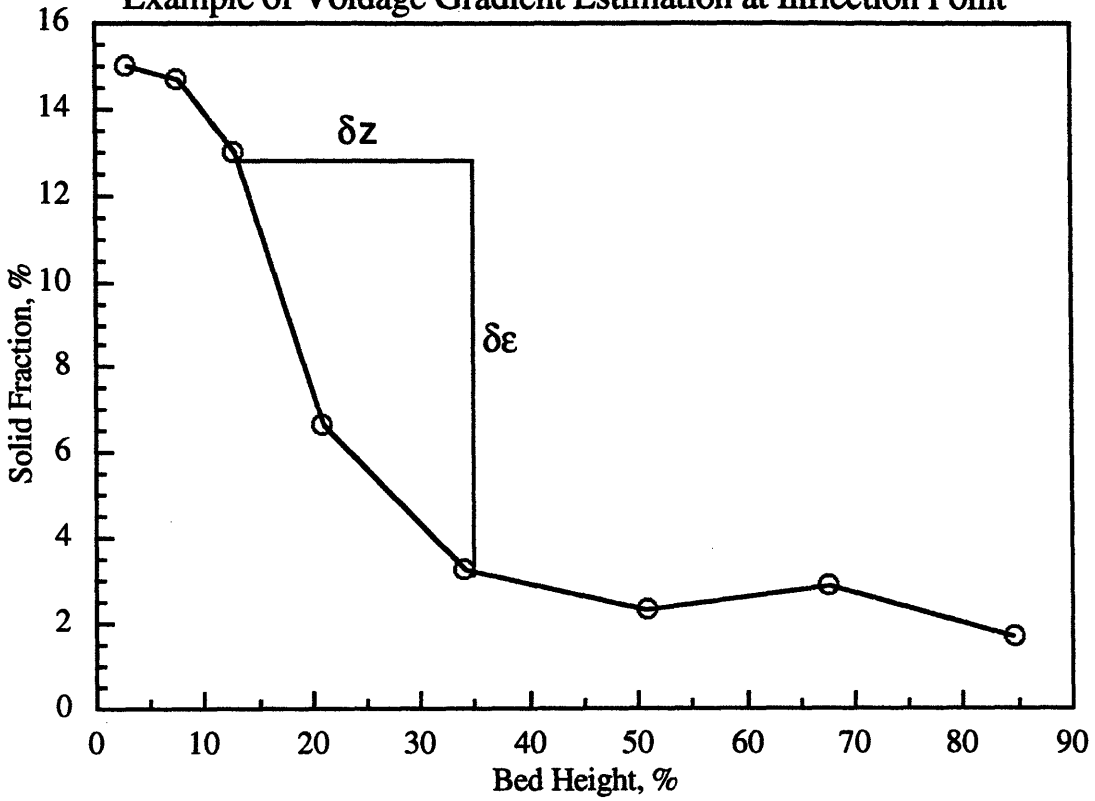

Figure 14.6

Voidage Gradient at Inflection Height vs. Superficial Velocity

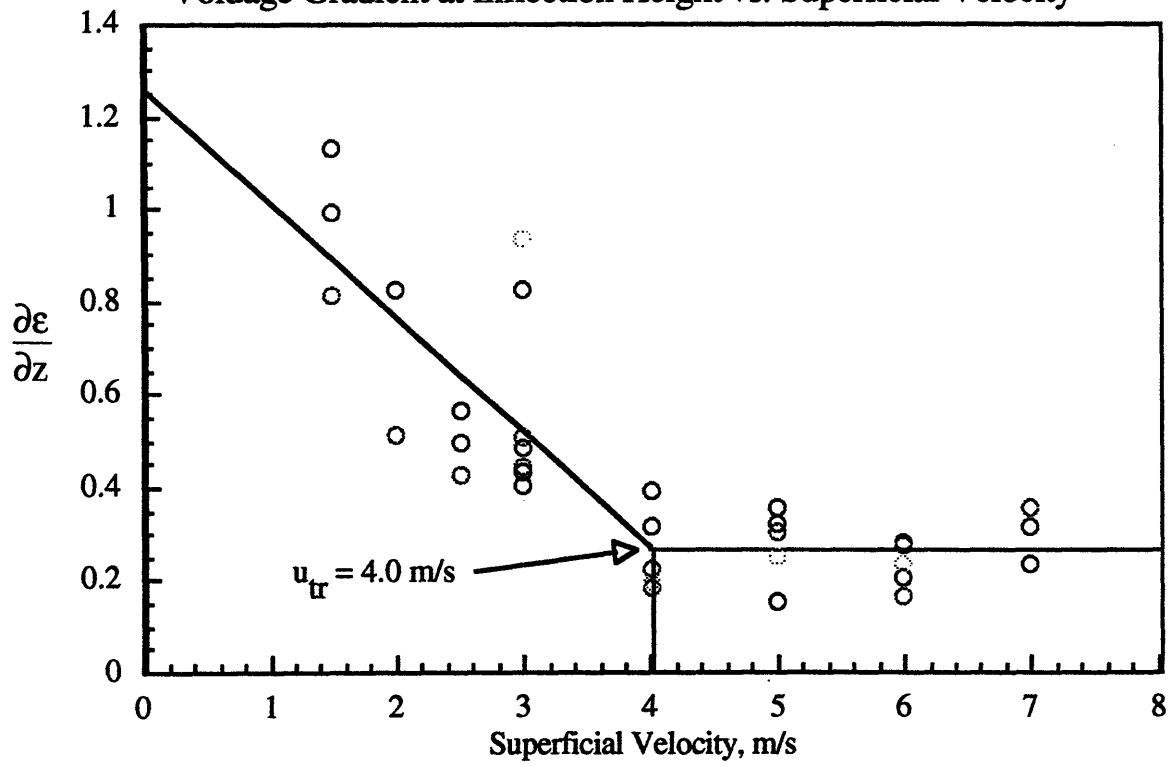

The voidage gradient at the inflection point decreased with increasing superficial velocity and then became almost constant with increasing u_O. Horio has shown that the voidage gradient at the inflection point is roughly a function of gas velocity alone because increases in solids flux only cause a shift in the average solid fraction profile but little change in its shape around the inflection point. The transition velocity predicted from Figure 14.6 is also shown in Figure 14.7. According to the plot, the regime transition occurs at about 4 m/s. This prediction is in good agreement with the conclusions reached from the heat transfer data where the wall solid collection rate and Nusselt number undergo a drastic reduction when the superficial velocity is increased from 3 to 5 m/s.

Another method which has been used to deliminate hydrodynamic regimes in fluidized beds is by comparing pressure variances at various superficial velocities (Horio *et al.*, 1992). Figure 14.7 shows the normalized pressure variances plotted against superficial velocity for several bed heights. At the lower heights, a clear change in pressure variance occurs at about 3 m/s. Higher up in the bed a change can bed seen between 3 m/s and 5 m/s. These data also support the theory of a regime change between 3 and 5 m/s.

Figure 14.7

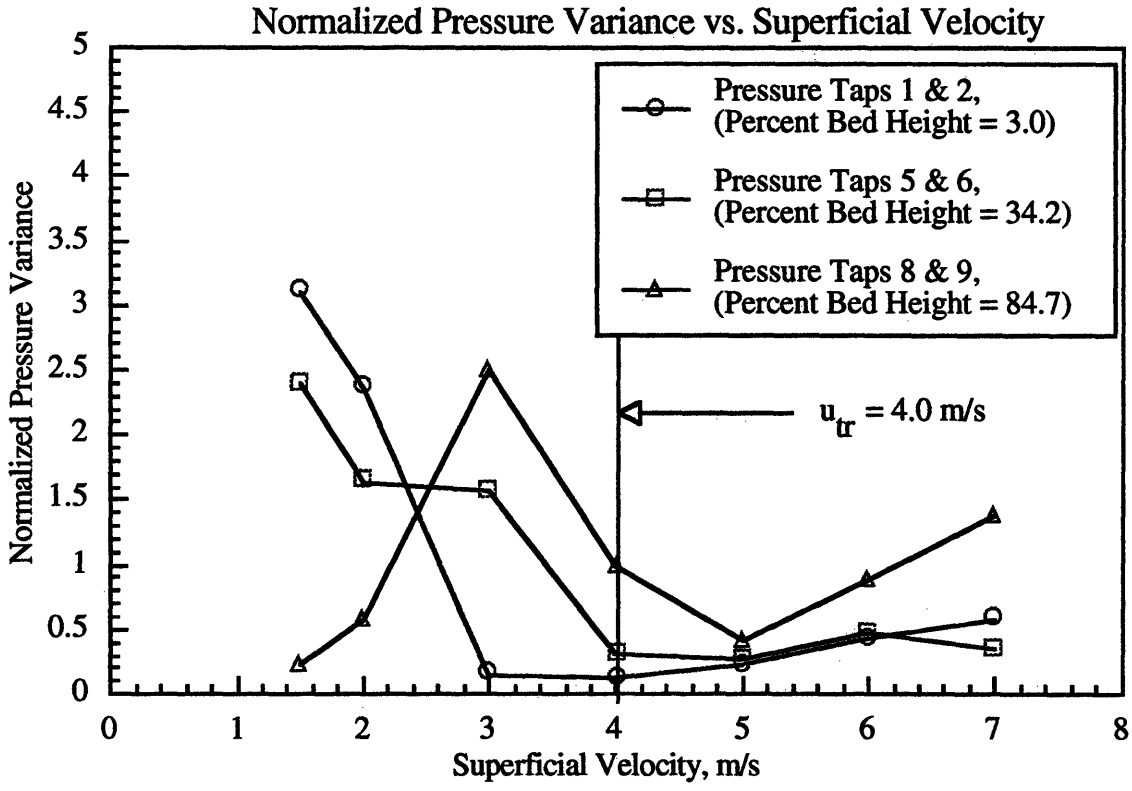

In summary, it appears that while the average bed solid fraction may be a satisfactory correlative variable for plotting heat transfer coefficients for small scale beds in some regimes, in other regimes and in large commercial units the dependence of heat transfer on average bed density is not as clear. Results presented above suggest that the wall coverage gives a much better indication of heat transfer rates at the wall of CFB. It should be noted that the fraction of wall covered by clusters is a variable which appears in most mechanistic models of the heat transfer at the wall of a CFB whereas the average cross-sectional solid fraction does not.

15.0 POSSIBILITY OF HEAT TRANSFER ENHANCEMENT BY WALL GEOMETRY MODIFICATIONS

During preliminary heat transfer runs in the phase one 1/16 scale Studsvik bed the heat transfer panel was installed with a rippled inside surface. The height of the ripples was about 2 mm and the distance between peaks was about 5 mm. The hydrodynamic and heat transfer data were then compared between these runs and runs with a smooth inside wall. The solid fraction profiles for both sets of runs are given in Figures 15.1 through 15.4. The Nusselt number versus average solid fraction curves are given in Figure 15.5.

Figure 15.1

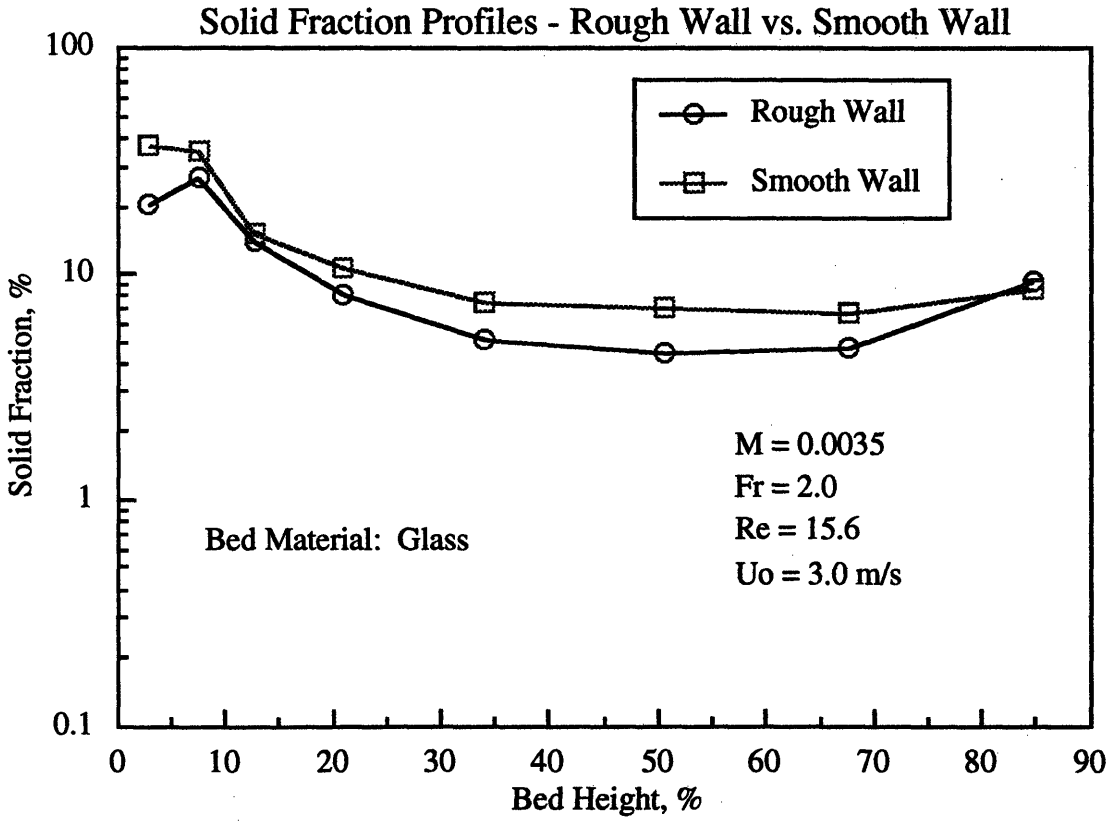

Figure 15.2

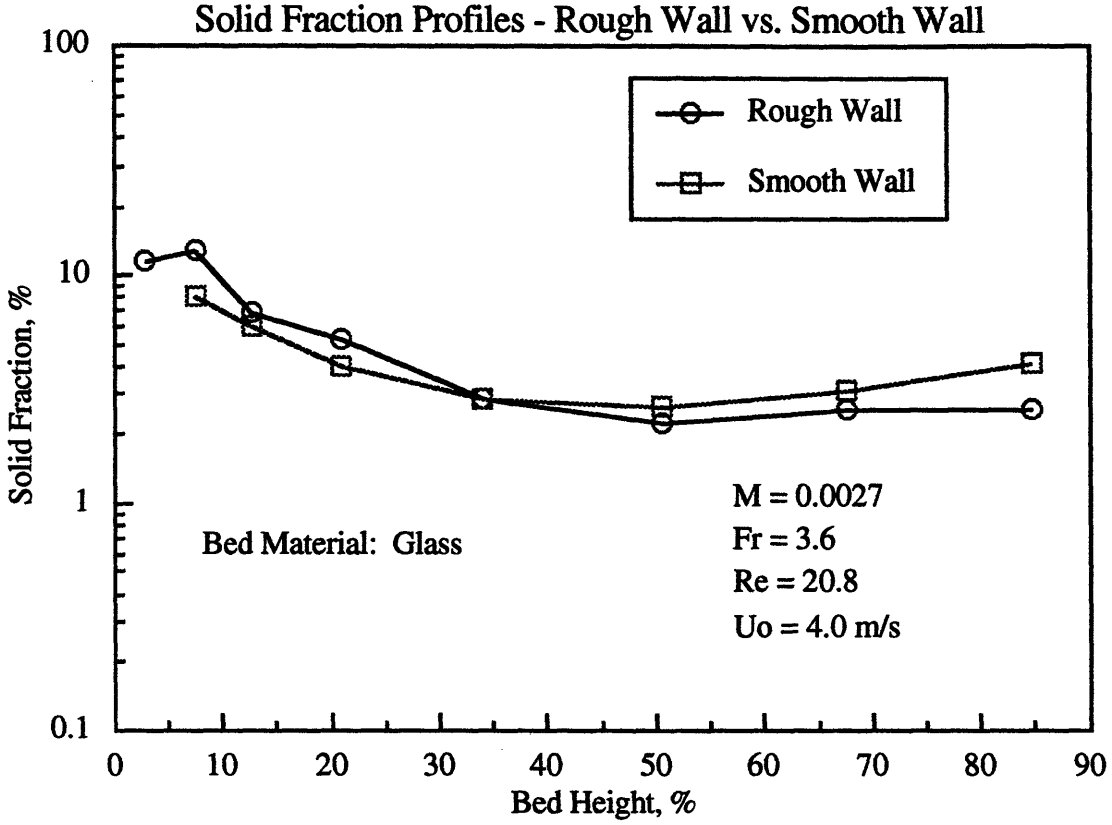

Figure 15.3

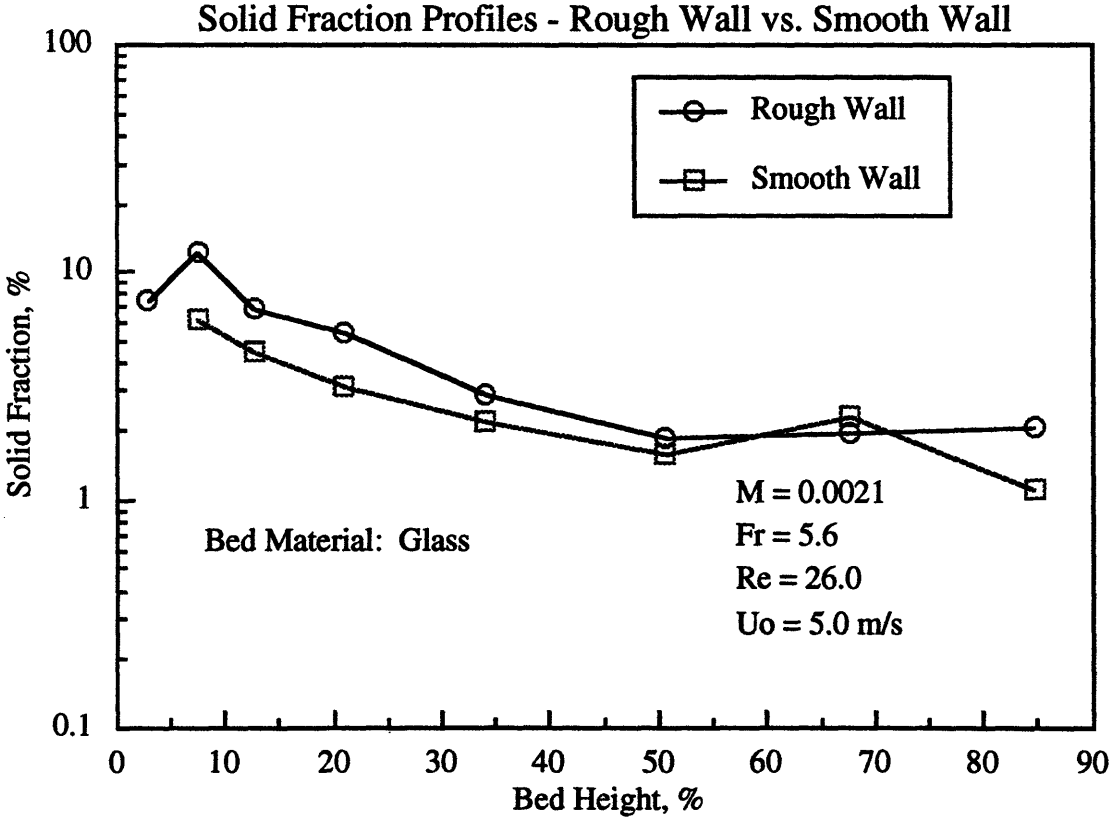

Figure 15.4

Solid Fraction Profiles - Rough Wall vs. Smooth Wall

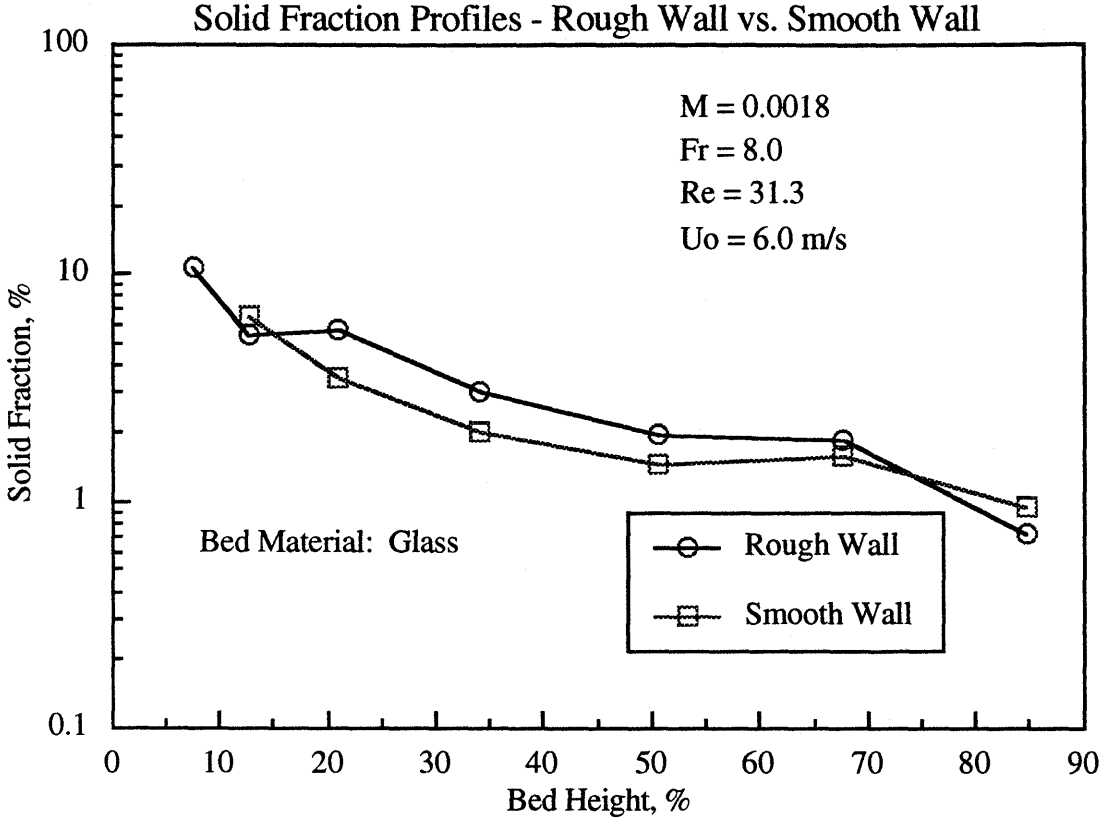

Figure 15.5

Nusselt Number vs. Average Bed Solid Fraction

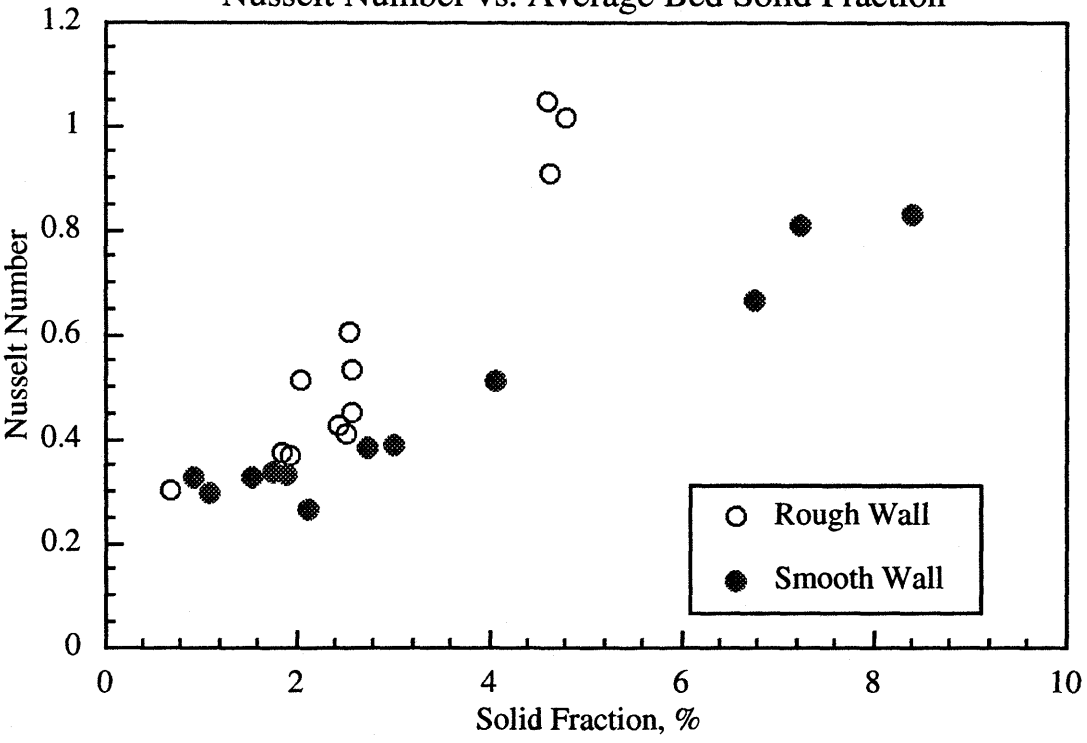

Figures 15.1 though 15.4 show that the hydrodynamics of the two test series were reasonably similar. However, Figure 15.5 shows that the rough wall tests resulted in higher Nusselt numbers for similar average solid fractions. This may be because the rippled surface disrupted the boundary layer at the wall and caused clusters flowing down the wall to become reentrained more readily than in the smooth wall tests. This reduces the average contact time at the wall, increasing the emulsion heat transfer coefficient. While these tests were only preliminary with no consideration given to impacts on wall erosion, they do suggest that wall geometries may be modified in such a was as to enhance heat transfer. A complete analysis of heat transfer enhancement in circulating fluidized beds using roughened surfaces is given in Chapter 4.

16.0 CORRELATION OF ALL HEAT TRANSFER DATA AGAINST AVERAGE BED CROSS-SECTIONAL VOIDAGE

Figure 16.1 shows all heat transfer data plotted as a function of the average cross-section solid fraction. Also shown is the best square root curve fit to the data. The result of the curve regression gave the best curve fit as:

$$Nu = 0.4(\phi)^{0.5} \tag{1}$$

where ϕ is the solid fraction. The variance is 0.48 and

$$\chi^2 = 1.97. \tag{2}$$

Figure 16.1 does not indicate which tests were run at hydrodynamically similar conditions, and while the curve fit is not terribly poor, the large spread in data at the same average solid fractions does indicate that in order to accurately predict heat transfer coefficients, it is important to simulate the correct bed hydrodynamics. Figure 16.1 does show that in the regime tested, the Nusselt number appears to follow a square root trend with the average bed solid fraction. This is consistent with previous studies of CFB heat transfer which have suggested that the fraction of the wall covered by clusters is proportional to the square root of the cross-section averaged bed density.

Figure 16.1

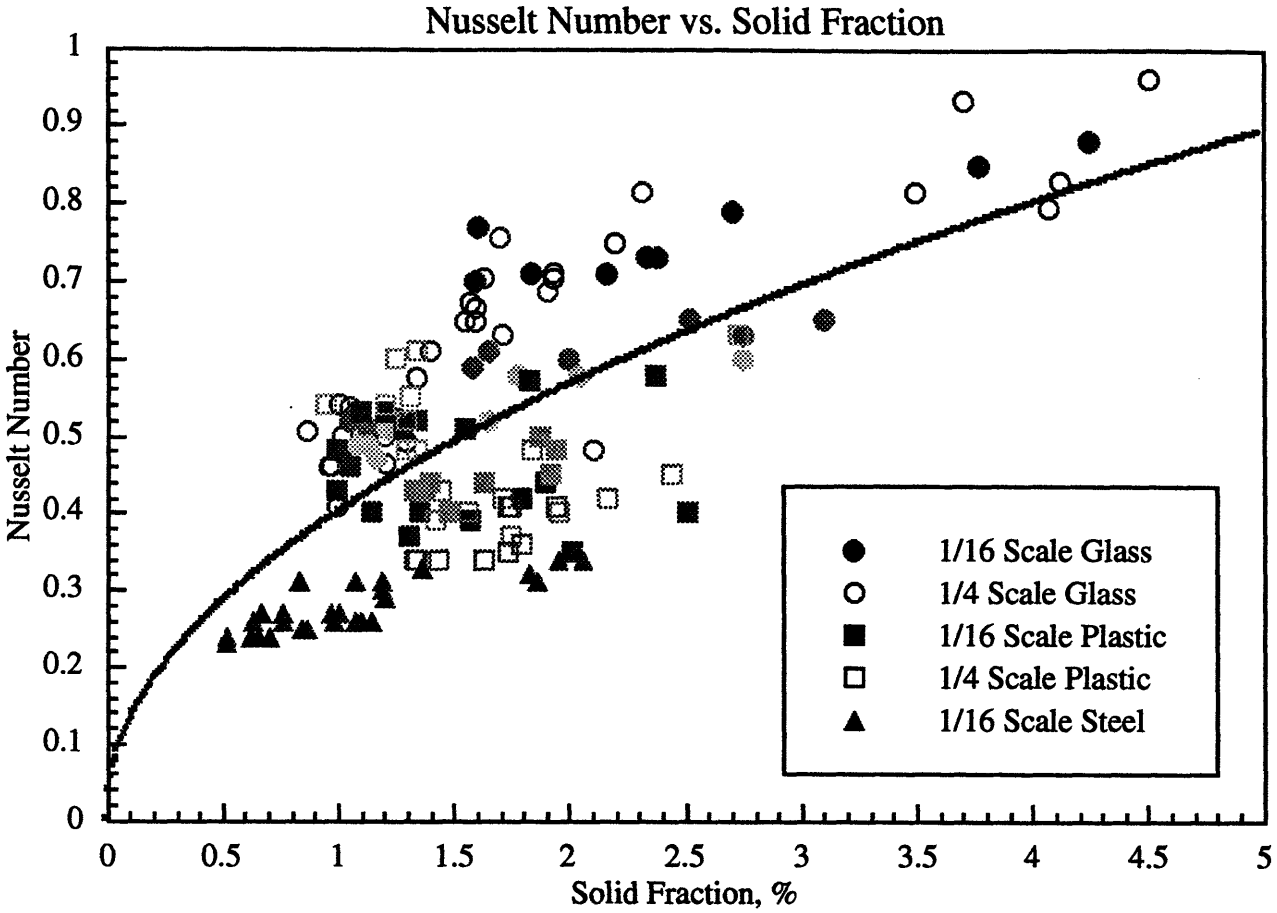

Figure 16.2 shows all heat transfer data plotted as a function of the nondimensional heat transfer parameter times the solid fraction

$$\left(\frac{100(1-\varepsilon)u_o\rho_s c_p d_p^2}{Lk_g}\right). \tag{3}$$

Also shown is the best square root curve fit to the data. The result of the curve regression gave the best curve fit as:

$$Nu = 0.27(Hx)^{0.5} \tag{4}$$

with a variance of 0.32 and

$$\chi^2 = 2.82 \tag{5}$$

It should be stressed that although most heat transfer data is plotted against the volume fraction of solids averaged over the bed cross-section, conclusive evidence does not exist to suggest that the solids fraction at the wall is a unique function of the solids averaged over the bed cross-section. The ratio of surface fraction to cross sectional averaged solids fraction may be a function of the bed diameter as well as other bed hydrodynamic parameters. Therefore, experimental heat transfer results obtained in small diameter beds should be used with caution by designers of large size units if the small beds were not constructed in order to be hydrodynamically similar to the larger hot bed. The tests do indicate that the use of correctly scaled heat transfer and hydrodynamic parameters at the same bed location gives close agreement for the convective heat transfer results.

Figure 16.2

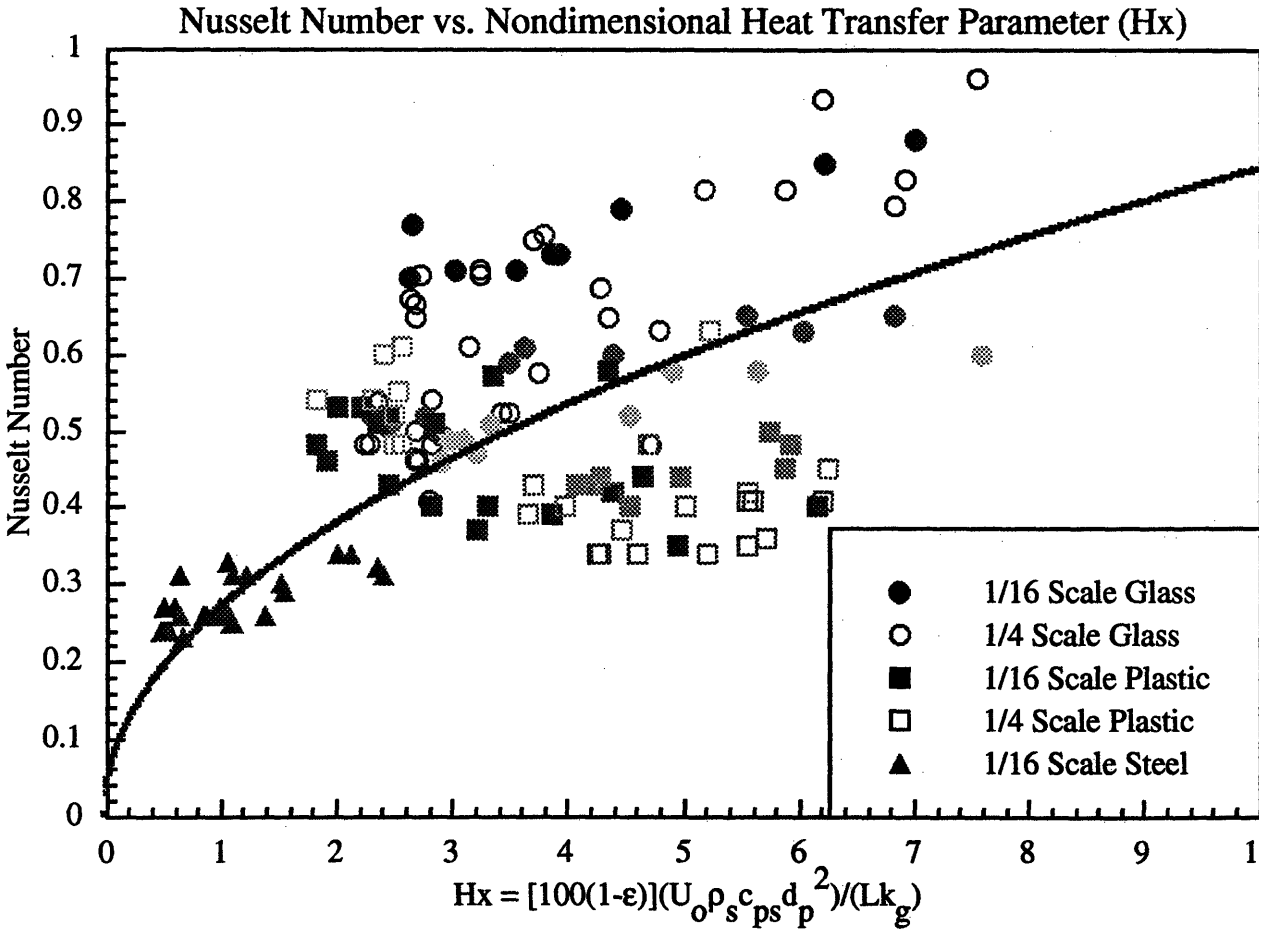

17.0 REFERENCES

Ackeskog, H.B.R., A.E. Almstedt, and V. Zakkay, "An Investigation of Fluidized-Bed Scaling: Heat Transfer Measurements in a Pressurized Fluidized-Bed Combustor and a Cold Model Bed," *Chem. Engng Sci.*, **48**, p. 1459, 1993.

Baskakov, A.P. and V.M. Suprun,"Determination of the Convective Component of the Heat Transfer Coefficient to a Gas in a Fluidized Bed," *Int. Chem. Engng.*, **12**, p. 324, 1972.

Baskakov, A.P., "The Mechanism of Heat Transfer between a Fluidized Bed and a Surface," *Int. Chem. Eng.*, **4**, p. 320, 1964.

Chen, J.C., and S.W. Churchill, "Radiant Heat Transfer in Packed Beds," *AIChE Jl.*, **9**, p. 35, 1963.

Divilio, R.J., and T.J. Boyd, "Practical Implications of the Effect of Solids Suspension Density on Heat Transfer in Large-Scale CFB Boilers," *4th International Conference on Circulating Fluid Beds*, Somerset, PA, p. 402, August 1-5, 1993.

Ebert, T.A., L.R. Glicksman, and M. Lints, "Determination of Particle and Gas Convective Heat Transfer Components in a Circulating Fluidized Bed," *Chem. Eng. Sci.*, **48**, p. 2179, 1993.

Ebert, T.A., L.R. Glicksman, and M. Lints, "Heat Transfer in Circulating Fluidized Beds: Determination of Particle Convective adn Gas Convective Components," *Proc. AIChE A. Mtng*, Chicago, II, 11-16, Nov., 1990.

Gelperin, N.I., and V.G. Einstein, "Heat Transfer in Fluidized Beds," *Fluidization*, J.F. Davidson and D. Harrison, eds., Academic Press, 1971.

Glicksman, L.R., and J. Modlin, "Heat Transfer with Low Density Particles in a Fluidized Bed," *Proc. of the Eighth Int. Heat Transfer Conf.*, San Francisco, p. 2605, 1986.

Glicksman, L.R., and N.A. Decker, "Heat Transfer From an Immersed Surface to Adjacent Particles in Fluidized Beds," *Proc. 7th Int. Conf. on Fluidized Beds*, Philadelphia, p. 45, 1982.

Glicksman, L.R., M.R. Hyre, and K. Woloshun, *Scale Models of Circulatig Fluidized Bed Combustors: Simplification of the Scaling Laws and the Scaling of Convective Heat Transfer*, Report #DOE/MC/25049-3372, USDOE, Washington, DC, 1993c.

Gloski, D., L. Glicksman, and N. Decker, "Thermal Resistance at a Surface in Contact with Fluidized Bed Particles," *Int. J. Heat Mass Transfer*, **27**, p. 599, 1984.

Holman, J.P., *Heat Transfer*, McGraw-Hill, New York, 1981.

Horio, M., H. Ishii, and M. Nishimuro, "On the Nature of Turbulent and Fast Fluidized Beds," *Powder Technology*, **70**, pp. 229-236, 1992.

Hyre, M.R. and L.R. Glicksman, "Experimental Investigation of Heat Transfer Enhancement in Cirulating Fluidized Beds," *4th ASME/JSME Thermal Engineering Conf.*, Maui, Hawaii, March, 1993.

Hyre, M.R. and L.R. Glicksman, "Heat Transfer Enhancment in Circulating Fluidized Beds," *Fluidization VIII*, Tours, France, May, 1995.

Karri, S. B. Reddy, and Ted M. Knowlton, "A Practical Definition of the Fast Fluidization Regime," *Proc. 3rd Int. Conf. on Circulating Fluidized Beds*, Nagoya, Japan, 1990.

Lints, M.C., and L.R. Glicksman, "Parameters Governing Particle to Wall Heat Transfer in a Circulating Fluidized Bed," *Proc. 4th Int. Conf. on Circulating Fluidized Bed Combustors*, Somerset, PA, 1993b.

Lints, M.C., and L.R. Glicksman, "The Structure of Particle Clusters Near the Wall of a Circulating Fluidized Bed," *AIChE Sump. Series*, **89**, p. 35, 1993a.

Lints, M.C., *Particle-to-Wall Heat Transfer in Circulating Fluidized Beds*, Ph.D. Thesis, Massachusetts Institute of Technology, 1992.

Mickley, H. S., and C. A. Trilling, "Heat Transfer Characteristics of Fluidized Beds," *Ind. Eng. Chem.*, **41**, 6, p. 1135, 1949.

Mickley, H. S., and D. F. Fairbanks, "Mechanisms of Heat Transfer to Fluidized Beds," *AIChE Journal*, p. 373, 1955.

Takeuchi, H. et al., "A Quantitative Definition and Flow Regime Diagram for Fast Fluidization," *Powder Technology*, **47**, pp. 195-199, 1986.

van Heerden, C., A.P.P. Nobel, and D.W. van Kreuelen, "Mechanism of Heat Transfer in Fluidized Beds," *Ind. Engng Chem.*, **48**, p. 1237, 1953.

Wu, R.L., J.R. Grace, C.J. Lim and C.M.H. Brereton, "Suspension-to-Surface Heat Transfer in a Circulaint-Fluidized-Bed Combustor," *AIChE Journal*, **35**, p. 1685, 1989b.

CHAPTER 4

HEAT TRANSFER ENHANCEMENT IN CIRCULATING FLUIDIZED BEDS

1.0 INTRODUCTION

As utility reserve margins as a whole dwindle, the need for new power plants is becoming increasingly serious. As a result, power producers must soon begin to build new power plants and will require that these plants be efficient, cost effective, and environmentally clean. Pressurized circulating fluidized bed combustion (PCFBC) plants which are currently being developed are expected to play a major role in this evolving marketplace.

Circulating beds are usually designed with heat exchange surfaces along the bed periphery. This means that while the heat generation rate in the bed is proportional to the cross-sectional area, the heat transfer rate is proportional to the bed periphery. This may cause problems when attempting to determine the effects of bed scale-up on heat transfer. Additionally, in pressurized beds the bed power density will be much larger than for atmospheric beds requiring additional heat transfer per unit volume from the bed. Many circulating beds use external heat exchangers to provide additional heat transfer surface and to aid in operational and part load control. New methods for increasing the rate of heat transfer from the walls of circulating beds may prove valuable in providing adequate heat transfer without resorting to external or in bed heat exchangers. Recent experimental studies (Glicksman, *et al.*, 1993) have shown that the smooth wall heat transfer can be augmented up to 20 percent by the use of uniformly space horizontal ridges along the wall surface (see Chapter 3). These ridges do not have to be large. Heights on the order of one particle diameter were found to have significant effects; possibly minimizing erosion. The ridges can simultaneously influence several important wall parameters: the time of cluster contact, percent wall coverage, and the wall-to-cluster spacing.

A preliminary study was undertaken in an attempt to quantify the effects of several heat transfer surface configurations on the rate of heat transfer from a cold scale model of a circulating fluidized bed. In the first half of this study, heat transfer and hydrodynamic measurements were made for various heat transfer surfaces. In the second half of the study, the surface renewal heat transfer model [Subbarao and Basu (1986), Glicksman (1988), Lints (1992)] was extended to include time varying characteristics. The model was then applied to the data obtained from the modified heat transfer surfaces. A relationship between the developing gas viscous sublayer between successive ridges and the cluster to wall separation is also advanced. These models are combined into an overall prediction of the wall heat transfer coefficient as a function of the spacing of the ridges. The extended

model was also applied to heat transfer data obtained by other investigators in both hot and cold circulating beds in order to determine its applicability under a variety of conditions.

This Chapter is organized into six Sections. In Section Two the experimental equipment and techniques used to obtain the heat transfer data will be discussed in detail. In Section Three the experimental data is presented and analyzed. Section Four contains a review of the surface renewal model and the derivation of the time dependent surface renewal model. Recommended values of each of the heat transfer parameters which are required by the model and the sensitivity of the model to these parameters is also given in this Section. Section Five compares the experimental data obtained as a part of this study and the experimental data of others with the model predictions. Finally, Section Six presents conclusions and recommendations for further work.

2.0 EXPERIMENTAL ARRANGEMENT

The bed used in obtaining the heat transfer data was the 1/16 scale model of the Studsvik 2.5 MWth combustor which was constructed in conjunction with the scaling studies described in Chapter 2.

In what follows, three topics will be discussed in the following order:

1. Bed geometry
2. Particle characteristics
3. Measurement equipment and associated uncertainty

2.1 Dimensions and Construction of the Cold CFB

The bed utilized was a 1/16 scale model of the Studsvik circulating bed operated by Studsvik Energiteknik AB. The boot, secondary air ports, and simulated refractory which were originally included when the bed was being used to evaluate CFB scaling laws were removed to reduce the complexity of the wall geometry and to eliminate bed specific designs. The bed consists of three main parts:

1. Main bed test section
2. Primary separator and downcomer
3. Solid return leg

A drawing of the bed is presented in Figure 2.1.

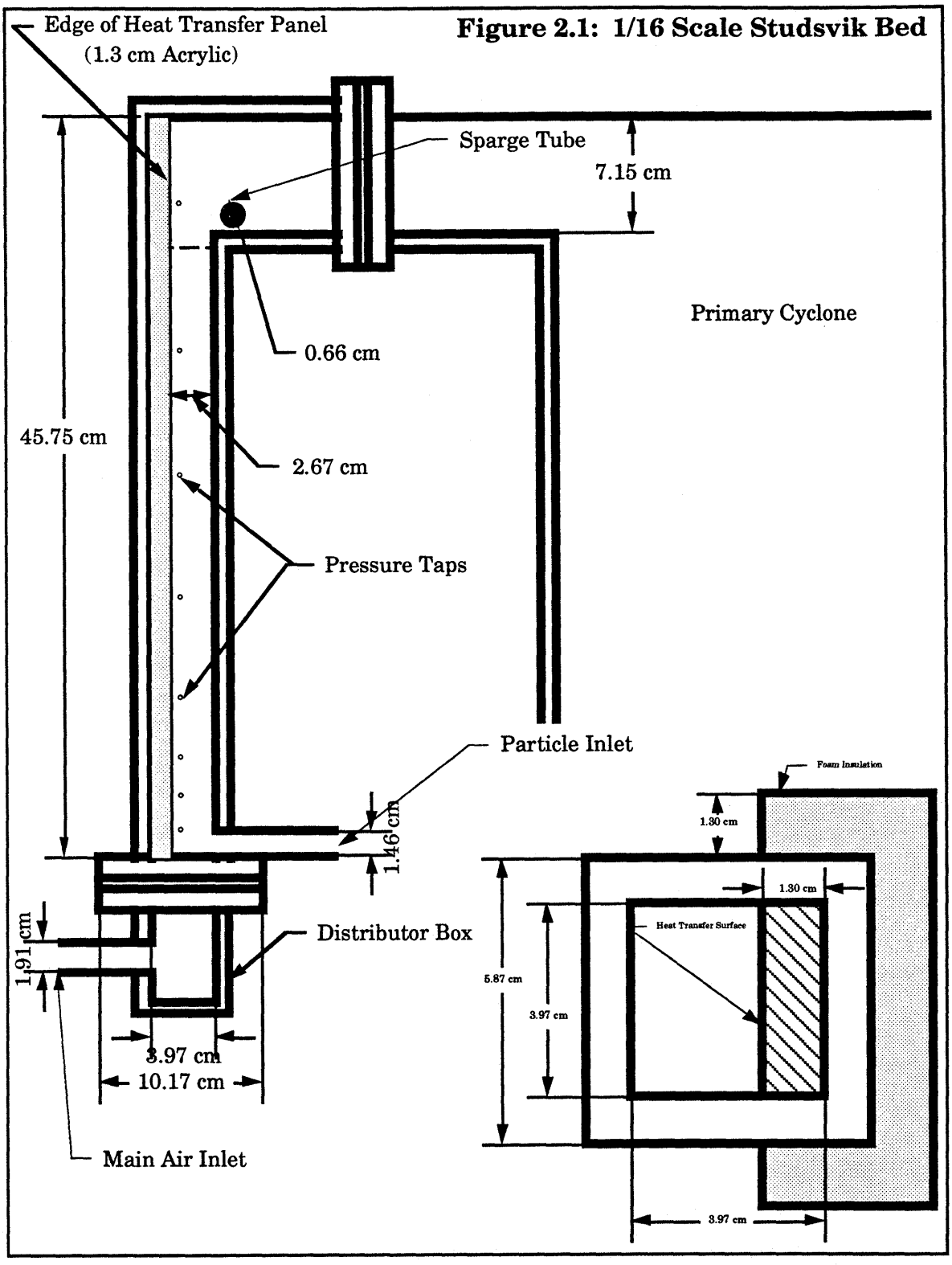
Edge of Heat Transfer Panel
(1.3 cm Acrylic)
Figure 2.1: 1/16 Scale Studsvik Bed
Sparge Tube
7.15 cm
Primary Cyclone
0.66 cm
45.75 cm
2.67 cm
Pressure Taps
Particle Inlet
1.46 cm
1.91 cm
Distributor Box
3.97 cm
10.17 cm
Main Air Inlet
Foam Insulation
1.30 cm
1.30 cm
Heat Transfer Surface
5.87 cm
3.97 cm
3.97 cm

2.1.1 Main Bed Test Section

The main test section was constructed with a geometry 1/16 the size of the of the Studsvik 2.5 MWth combustor used in conjunction with the scaling studies described in Chapter 2. All four sides of the bed side were constructed of 3/8-inch (0.95 cm) acrylic sheet. A groove was machined around the perimeter of the acrylic back and a Viton gasket inserted to seal the acrylic back to the bed. This arrangement allows for easy removal of the back panel and quick access to the inside of the bed. The cross sectional area of the bed without the heat transfer panel was 15.75 cm^2, and the bed length was 0.46 m.

In order to prevent solid backflow from the top of the bed due to excessive solid buildup in the horizontal section in front of the primary separator, a 1/4" (0.64 cm) diameter sparge tube was included in the horizontal section in front of the primary separator.

No secondary air was introduced into the bed. Primary air was introduced at the bottom of the bed through a screen distributor mounted on a 2.5-inch (6.35 cm) high distributor box. A drawing of the air supply system is depicted in Figure 2.2.

Nine pressure taps located on one of the side walls were used to measure axial pressure drop. These taps were angled down in order to prevent solids from accumulating in the lines. The first tap was located immediately above the distributor plate, and the others were located at distances of 1.4, 3.5, 5.9, 9.6, 15.6, 23.2, 31.0, 38.8 cm from the distributor plate.

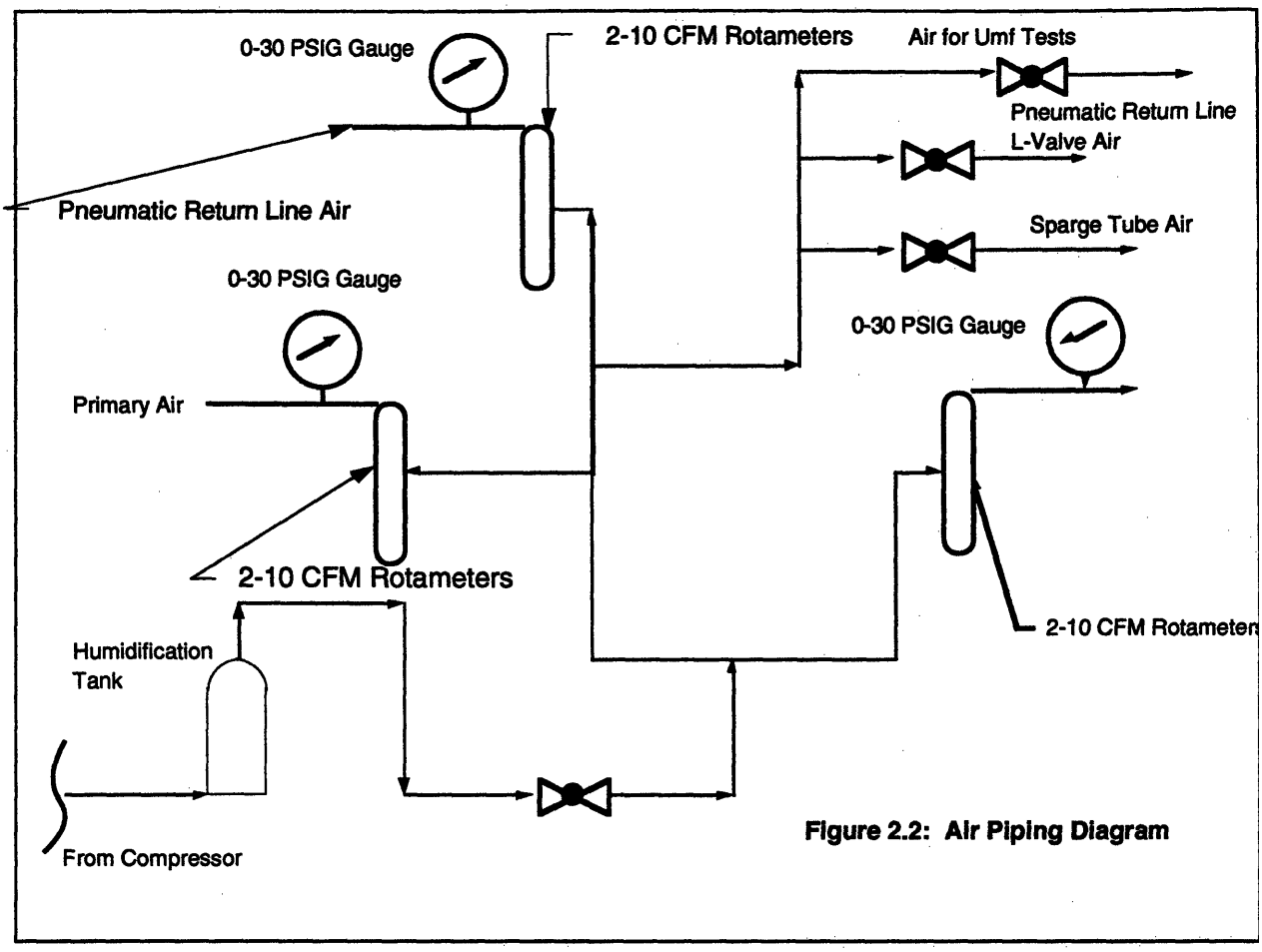

Figure 2.2: Air Piping Diagram

2.1.2 Primary Separator

Primary air/solid separation was achieved by means of a cyclone. The primary cyclone was constructed primarily of 1/4-inch (0.635 cm) acrylic. The primary cyclone connects to the main bed section, the solid return leg, and the air exhaust line with flanges. Hose-and-clamp connections were later added for final connections to the solid return leg and air exhaust line in order to relieve stresses. See Figure 2.3 for diagrams of the primary cyclone and filter.

The air exhaust leaving the primary cyclone was directed through a filter utilizing two automobile air filters to allow easy retrieval of filtered solid and provide adequate filtration.

Figure 2.3

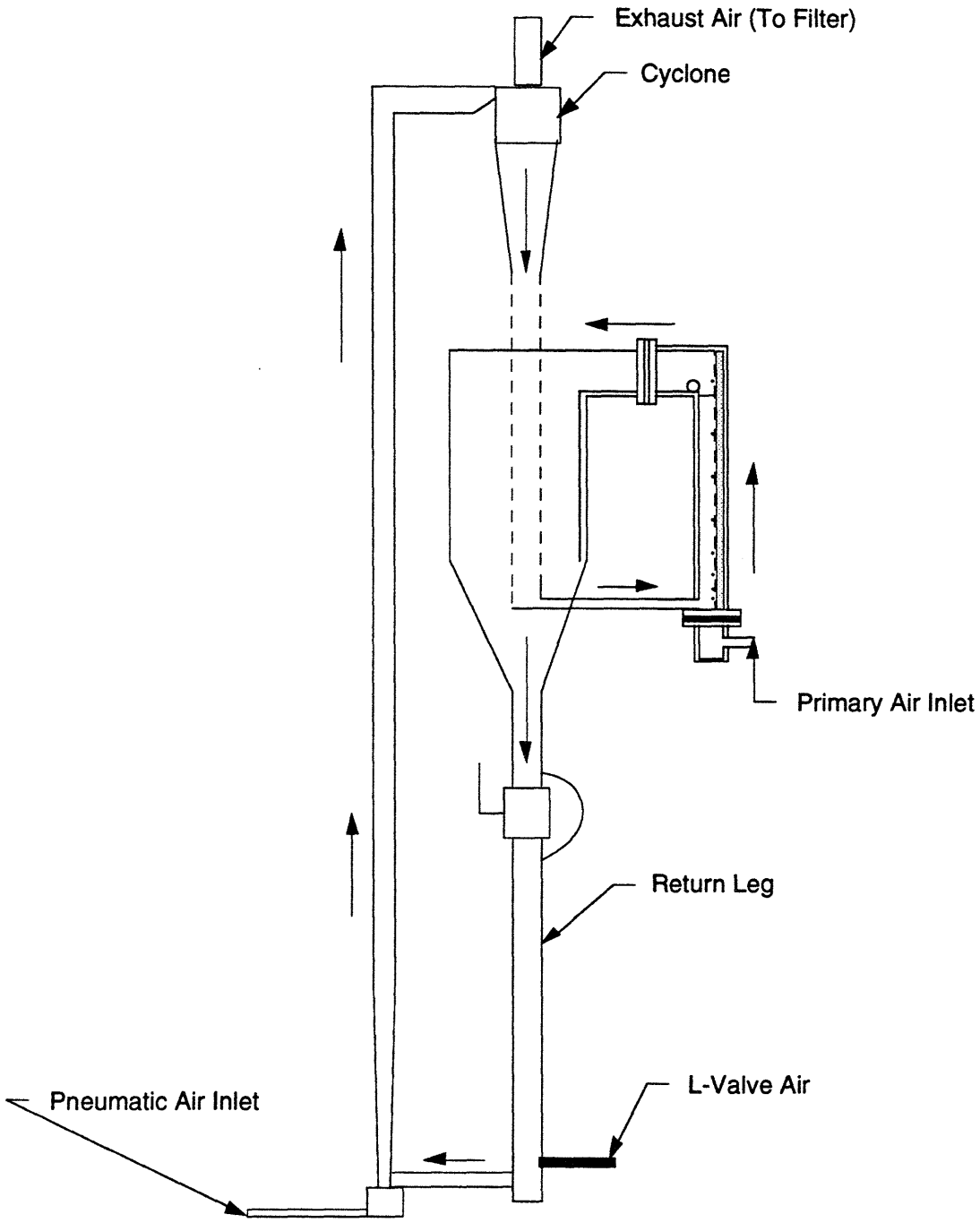

Arrows Denote Direction of Solids Flow

2.1.3 Solid Downcomer and Return Leg

The primary solid downcomer was largely constructed of 1.5" x 1/8" (3.81 x 0.32 cm) acrylic tube. The primary downcomer consists of two sections, one above and one below the solid flow measurement valve. Connections between return leg parts were made with flexible hose and clamps to reduce stresses.

The bottom of the primary downcomer was constructed of a 1-1/2" (3.81 cm) copper tube and a 1-1/2" x 1-1/2" x 1" (3.81 x 3.81 x 2.54 cm) tee. A 1" x 1/8" (2.54 x 0.32 cm) flexible transparent tube connects the bottom of the primary downcomer to a pneumatic return line. The bottom of the primary downcomer reduces to a 1/2" NPT plug for drainage of solid. Air lines for solid flow control connect to the side of the copper tee. These include the standard L-valve air and additional air for improvement of solid flow. The latter air was fed to the horizontal feed tube through a 1/4" (0.64 cm) sparge tube.

The pneumatic return line recycled the solid up to a secondary cyclone several feet above the top of the bed. The solids then dropped to a secondary downcomer for return to the test bed. Air from the pneumatic return line exhausted to the filter.

The valve used for the measurement of the solid circulation rate, built into the primary solid downcomer, is discussed in Chapter 2. The valve, located 10-inches (25.4 cm) below the primary cyclone, is a nominal 1-1/2" (3.8 cm) full-bore three-piece ball valve.

2.2 Heat Transfer Panel Dimensions and Installation

In order to determine wall-to-bed heat transfer coefficients, a heat transfer panel was constructed. The panel consisted of three heat transfer sections at different axial locations with separate heaters and power supplies. The purpose of the three separate heater sections was to evaluate the effects of average bed density and the downward movement of particles at the wall at various heights on heat transfer. Heater sections were separated to ensure negligible heat transfer between sections. Heat transfer coefficients were evaluated using the power input to the heaters and the temperature difference between the heater section and the bulk bed temperature. The following Section discusses the panel and the bed configuration when the heat transfer panel was installed.

2.2.1 Smooth Wall Heat Transfer Surface

The smooth heat transfer panel consisted of an 18" x 1-1/2" x 1/2" (45.75 x 3.8 x 1.3 cm) piece of acrylic with three 3-3/4" x 1" (9.3 x 2.5 cm) squares routed out for heater and copper cover placement. The heaters were 3" x 1" x 1/32" (7.6 x 2.5 x .08 cm), 150 watt, 120 volt, aluminum strip heaters. Each heater was covered by a 3-3/4" x 1" x 1/8" (9.3 x 2.5 x 0.3 cm) copper plate which was flush to the acrylic surface. The tops of the removable copper plate covers were located at distances of 17.7, 13.5, and 9.3 inches (45.0, 34.3, and 23.7 cm) from the bottom of the wood panel and, therefore, the distributor plate. The entire surface of the heat transfer surface was then covered by a thin plastic film [0.001" (0.0025cm) thick] which was held in place by a high conductivity paste [thermal conductivity of 16 Btu-in/hr-ft^2-F (2.3 W/m-K), which is stable in a temperature range from -40 to 392 ^{o}F (-40 to 200 ^{o}C)]. This was done in order to ensure a smooth heat transfer surface. Rough calculations indicate the maximum temperature drop from the thermocouple to the wall surface did not exceed 1 ^{o}C. Typical temperature differences between the heat transfer surface and bed were 30 ^{o}C. The acrylic panel was sealed to the 18" x 2-3/8" x 3/8" (45.75 x 6.0 x 0.95 cm) acrylic bed back. A Chromel-Alumel (type K) thermocouple was embedded into the top and bottom of each copper plate. The thermocouple and heater leads were drawn back through the acrylic panel and backing. The entire assembly was screwed to the back of the bed with the acrylic heater portion of the panel actually fitting inside the bed reducing the effective bed width by 1/2-inch (1.3 cm). The assembly was sealed to the bed side walls with caulk. See Figure 2.4 for a view of the heat transfer panel.

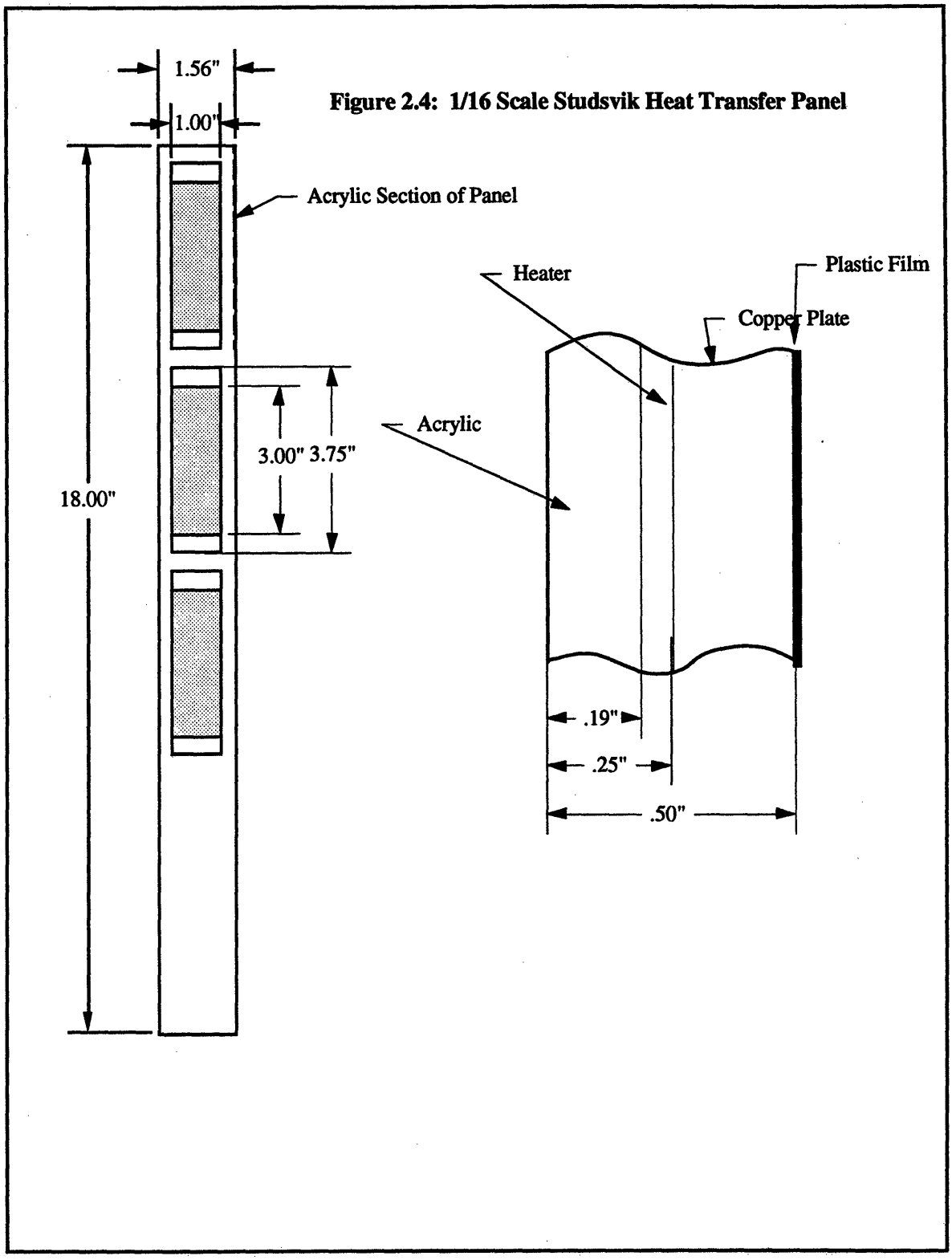

Figure 2.4: 1/16 Scale Studsvik Heat Transfer Panel

2.2.2 Ridged Heat Transfer Surfaces

The heat transfer enhancement surfaces evaluated in this study consisted of small horizontal ridges placed at specific intervals along the heat transfer panel. The ridges were made of 6/1000" (152 microns) steel wire strips which were attached to the removable copper cover plates using OMEGABOND 200 highly conductive thermal epoxy [k = 9.6 Btu-in/hr-ft^2-F (1.3 W/m-K)]. The ridge heights were chosen to be approximately equal to the mean particle diameter since previous results indicated that this height was sufficient to disrupt the particles [Lints, (1993)]. At the same time, it was felt that modest ridge heights would be less likely to cause erosion (this effect was not measured in this study). The copper covers were cured in an oven for two hours at 200 ^{o}C to set the epoxy and then attached to the heat transfer panel. New copper covers were made for each ridge interval. Three ridge intervals were evaluated in this study: 20 mm, 10 mm, and 5 mm. The epoxy increased the steel wire height on the wall to an average of 8/1000" (200 microns). No plastic film was used in the construction of the ridged surfaces. It was not anticipated that the difference in surface roughness between the copper covers and the plastic film would significantly effect the results because the standoff distance to the first layer of particles is much larger than the roughness of either the copper or plastic surfaces (for copper $\varepsilon \sim 5$ μm and the standoff distance is ~ 100 μm; the plastic is essentially smooth surface). Moreover, any change in the dilute phase heat transfer coefficient (h_d) has only minor effects on the overall heat transfer coefficient since h_d is normally less than 20 percent of the overall h. Figure 2.5 presents a typical ridged heat transfer surface.

2.3 Bed Solid Materials

Glass particles were utilized in this study. The mean particle diameter was determined using laboratory sieves. Minimum fluidization velocity for the glass was determined in a small 4-inch (10.2 cm) bubbling bed operating at room temperature and atmospheric pressure. A summary of glass particle properties is given in Table 2.1. The particle size distribution is given in Figure 2.6.

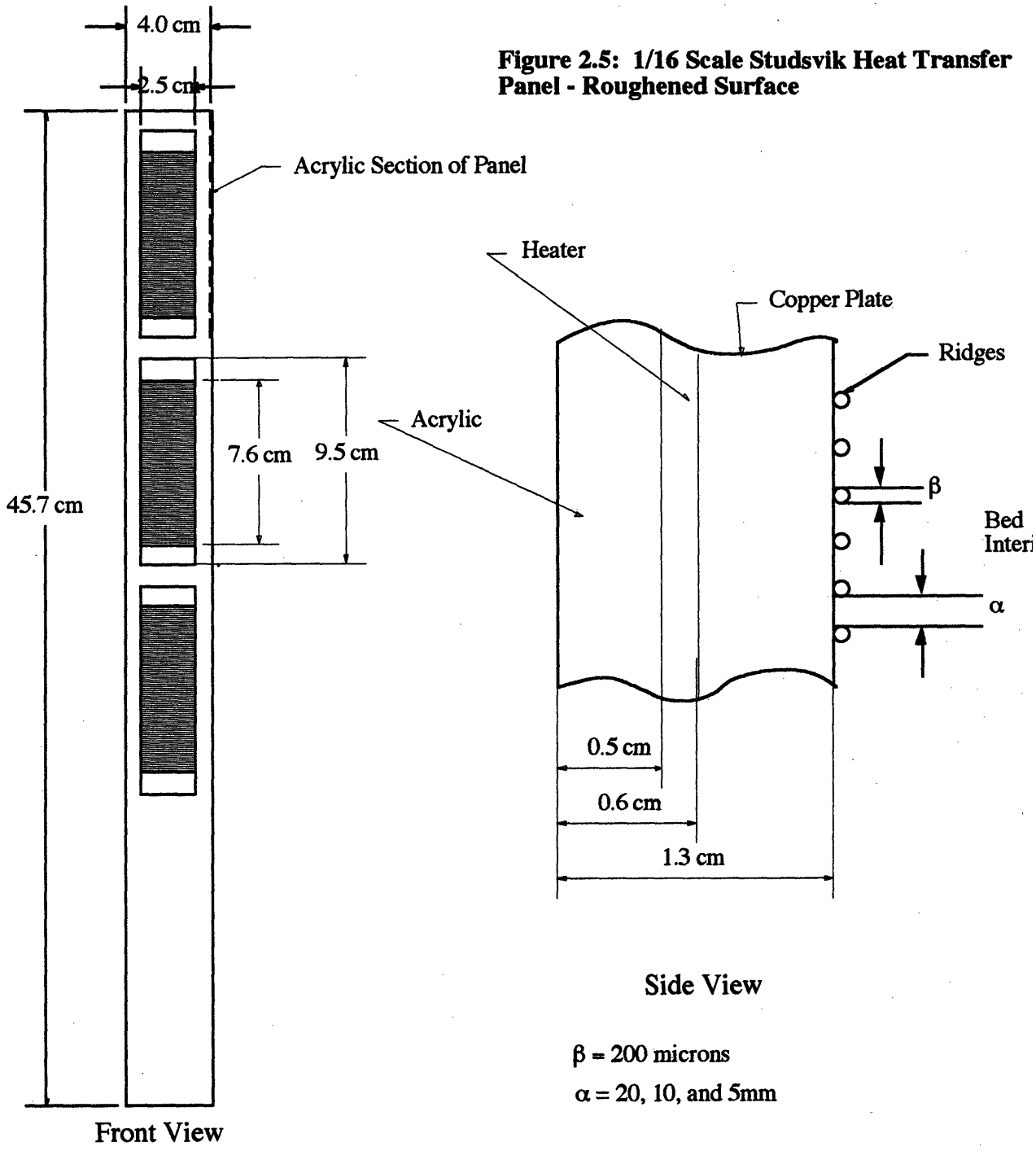

Figure 2.5: 1/16 Scale Studsvik Heat Transfer Panel - Roughened Surface

Table 2.1 Glass Properties

	Glass Properties
Density	2.54 g/cc
Mean Diameter	117 microns
Loose Pack Voidage	42%
Sphericity	1.0
U_{mf}	2.8 cm/s

Figure 2.6

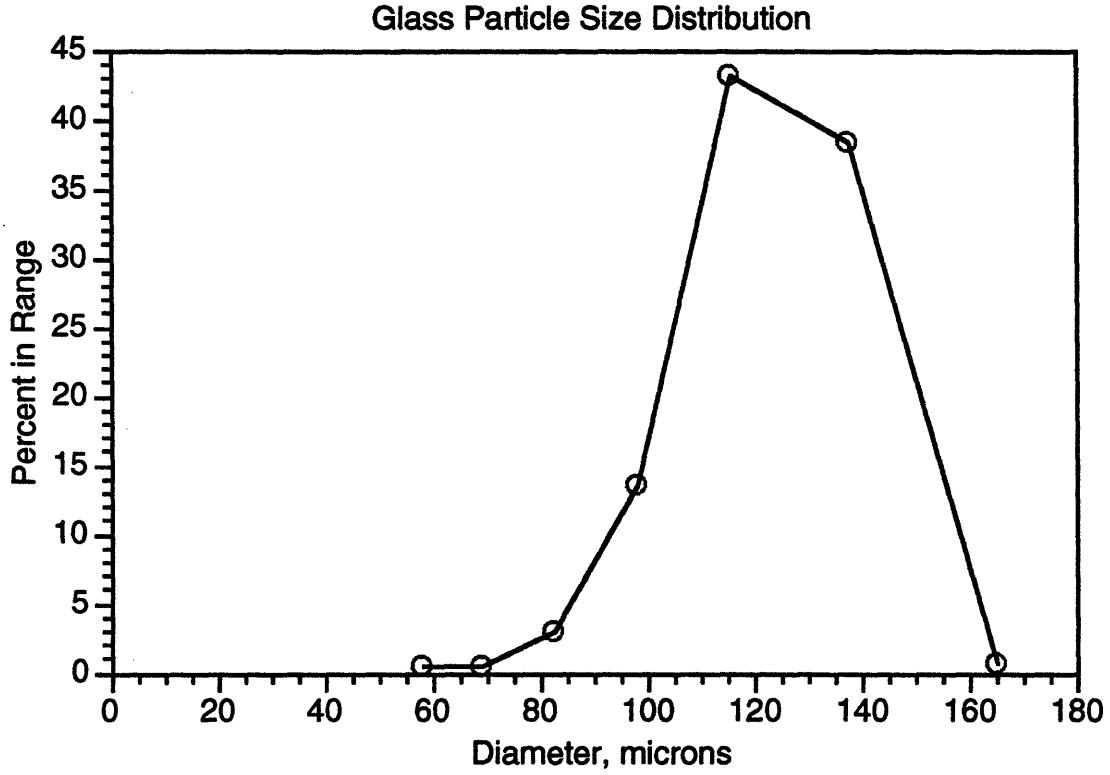

2.3.1 Preparation of Glass Particles

In addition to the separation and recombination process in order to achieve satisfactory size distributions, the glass particles were treated with anti-static compounds in an attempt to reduce the level of static electricity generated in the bed. The first compound was Larostat 519, a fine powder which was mixed in with the glass powder. Since the mass fraction of Larostat in the mixtures was very small, it was not anticipated that this would have any significant effect on the hydrodynamics of the beds other than through the reduction of static electricity.

While the Larostat worked quite well in the reduction of static, as more was added during operation, it began to severely inhibit the flow characteristics of the glass in the L-Valves and other constricted areas, limiting the amount of Larostat allowable in the bed. In order to further reduce bed static electricity levels, the glass particles, along with the inside of the bed, were spray coated with Anstac 2-M, an alcohol based anti-static solution for acrylic and other plastics. After drying, this treatment virtually eliminated any remaining static effects.

2.3.2 Elimination of Static Electricity Effects

In addition to the use of Larostat and Anstac as described above, several other precautions were taken to reduce problems caused by static electricity. The first measure taken was to wrap copper gauze around areas of the beds which accumulated large amounts of static electricity (this included the cyclones, pneumatic return lines, and sections of the downcomers). Copper ribbon was then used to ground the gauze as well as the supporting structure and other metallic components (pressure transducer housings, valves, aluminum walls, etc.). Three 6 x 1-1/2 inch (15.2 x 3.8 cm) pieces of copper sheet were connected in a helix fashion and inserted in the bottom section of the pneumatic return line. Copper wire was run along the perimeter of the copper sheet and out through a flexible connecting piece to ground. In addition to the static discharge device, a humidification system was constructed in which all the air being introduced into the bed was bubbled through a steel tank which was half full of water. This increased the humidity of the entering air (during the winter typical increases in relative humidity would range from 20-25 percent) and aided in the reduction of static electricity. The air humidity was continually monitored during bed runs utilizing an encased wall mounted hygrometer (relative humidity accuracy of +/-2.5 %).

2.4 Variable Measurement

Bed measurement techniques are described in the following sections. Accuracy of the cold bed measurements is discussed in Section 2.5.

2.4.1 Air Flow

Air entered the bed through the distributor box and at the bottom of the pneumatic return line. The two air flows were measured separately with rotameters fitted with exit pressure

gauges. The rotameters measured in the range from 2 to 10 cfm, and the pressure gauges were 15 psig full scale. Calibration of the rotameters and gauge combinations was done with a square-edged orifice plate fitted with flange taps. The tests covered flow ranges at expected pressure ranges with the data being fit to the equation:

$$Q_a = (AR+B)\sqrt{\left(1+\frac{P_g}{P_a}\right)}$$

Appendix C gives the results of the rotameter calibrations.

2.4.2 Solid Circulation

Measurement of solid circulation in the bed was done primarily with a valve in the solid return leg. A 1-1/2" (3.8 cm) full-bore three-piece ball valve was used for this purpose. Shims were installed between the sections of the valve in order to reduce handle torque. The valve measurement technique involved observation of solid pileup when the flow of solids was interrupted by closing the valve. A pressure relief line was installed around the valve to reduce the effects on pressures in the bed during valve closure.

It has been shown that the valve closure technique may be accompanied by a corresponding reduction in bed solid fraction (Westphalen, 1990). However, further calibration of this technique was obtained by injecting a material which provided enough visual contrast to the bed material in the downcomer. Measurement of the rate of descent in the downcomer has indicated that the valve closure technique is reasonably accurate (within 20 percent of visual descent measurement) in spite of its alteration of normal bed behavior.

2.4.3 Pressure Measurement

The pressure measurement technique for the bed utilized in this study is described below. Measurement and recording of the pressure transducer voltage output was done with a Metrabyte DAS-8PGA data acquisition board in an IBM AT compatible computer. The software used to control the data acquisition was UNKELSCOPE.

There were nine pressure taps in the main bed section of the 1/16 scale Studsvik bed which were used to measure axial pressure differences. The pressure taps and lines were 1/8" (0.32 cm) in diameter. All pressure lines were less than 0.5 m in length. Pressure measurements were obtained using a set of pressure transducers.

The pressure transducers were located near their associated pressure taps. The transducers measured differential pressures between adjacent pressure taps. The four transducers nearest the bottom of the bed had millivolt output, and had a 12 volt power supply. The rated pressure range for the transducers were -14 to 14 in. wc (-3.5-3.5 kPa). Calibration of the transducers was accomplised with an inclined manometer covering all expected pressure ranges. Results of the transducer calibrations are given in Appendix B. The top four transducers were series 600 transducers supplied and calibrated by Auto Tran, Inc. They had output on the order of 1-4 volts, and utilized the same 12 volt DC power supply as the bottom four transducers. The rated pressure range for the top four transducers was -1 to 1 in. wc (-0.25-0.25 kPa) with a sensitivity accuracy of +/- 1 percent of full scale output.

The pressure taps were angled down 40^{o} into the bed. Since the particle motion is downward at the wall, this proved successful in preventing particles from entering the lines.

2.4.4 Heat Transfer Measurements

The heat transfer measurement technique utilized in this study is described below. Figure 2.7 illustrates the equipment used.

Figure 2.7: Heat Transfer Equipment

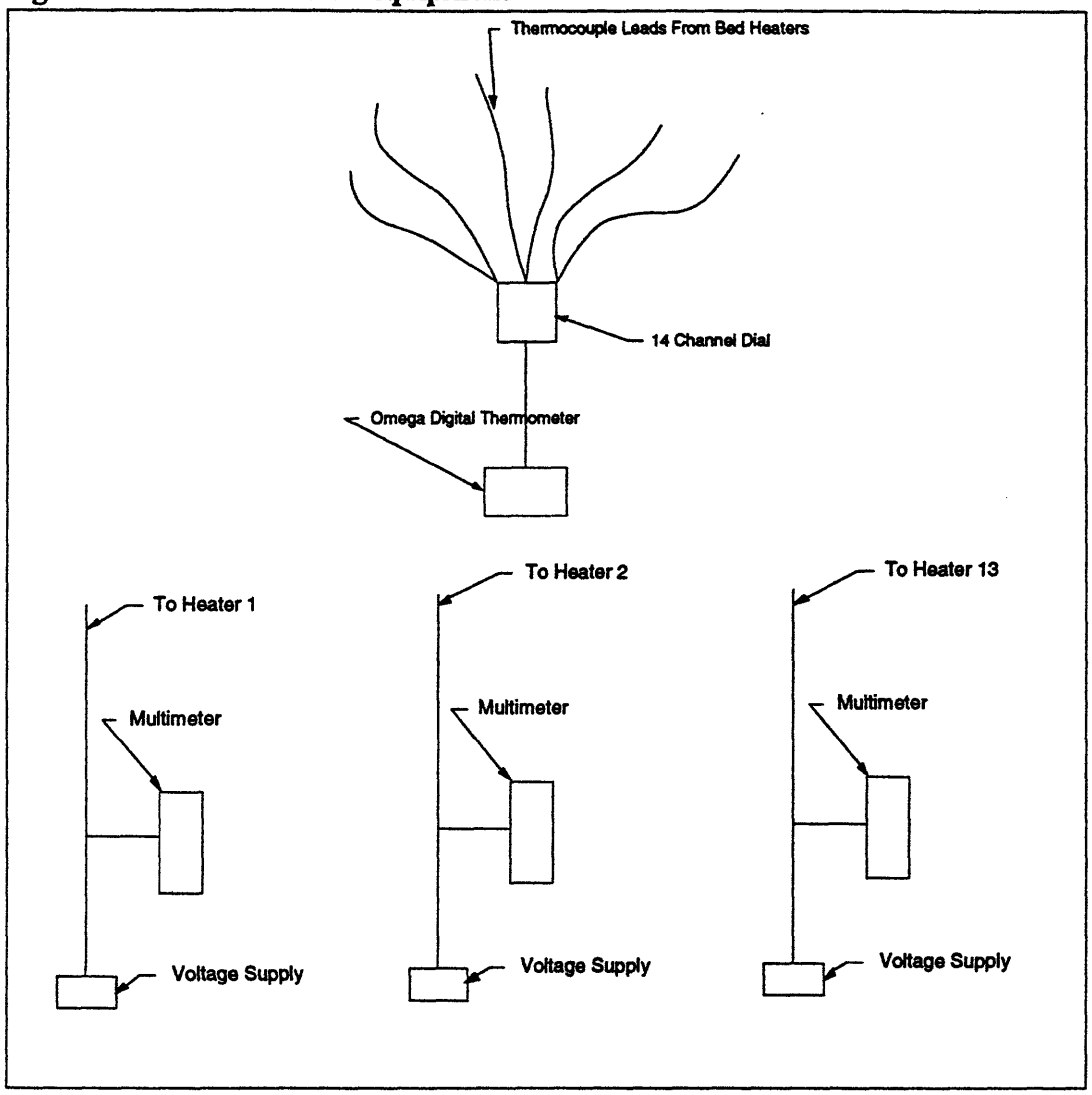

The heat transfer measurement apparatus consisted of the heat transfer panel described in Section 2.2.1 along with the associated thermocouple thermometer, power supplies, and other ancillary equipment. The thermocouple leads from the back of the bed were attached to a 14 position dial which was, in turn, connected to an Omega DP462 six channel digital thermometer capable of reading various types of thermocouples. An additional thermocouple which measured the bed temperature, located at the top of the bed, was also attached to the thermocouple dial. Each set of heater leads, which also emerged from the back of the bed, was attached to a variable autotransformer. Additional parallel leads allowed for the reading of voltage inputs and heater resistances during bed operation.

Enough voltage was supplied to each heater so that the temperature difference between the bed and the heat transfer surface was sufficiently large, about 30 ^{o}F (17 ^{o}C), and in a manner such that the wall temperature was fairly constant (within 3 or 4 ^{o}F). This voltage was usually somewhere between 30 to 40 volts depending on the bed density and surface configuration. The bed was allowed to run until the bed temperature no longer changed significantly (usually about an hour) before the temperatures, voltages and heater resistances were recorded. At the same time the heat transfer data was recorded, pressure measurements were taken through the pressure transducers to allow a consistent comparison of heat transfer and solid fraction data. The average cross-sectional solid fraction was determined by assuming the pressure differential between taps was due only to the holdup of particles.

The heat transfer panel was calibrated by measuring the heat transfer coefficient with only air flowing over it while keeping the heat flux of the heated section of the panel constant. The Nusselt number for laminar flow over a constant heat flux flat plate with an unheated starting length presented by Holman (1981) was used to calculate expected values of the Nusselt number:

$$Nu_x = \frac{0.453 Pr^{1/3} Re_x^{1/2}}{\left(1-\left(\frac{x_0}{x}\right)^{3/4}\right)^{1/3}}$$

Results of the heat transfer panel calibration are given in Figure 2.8.

Figure 2.8

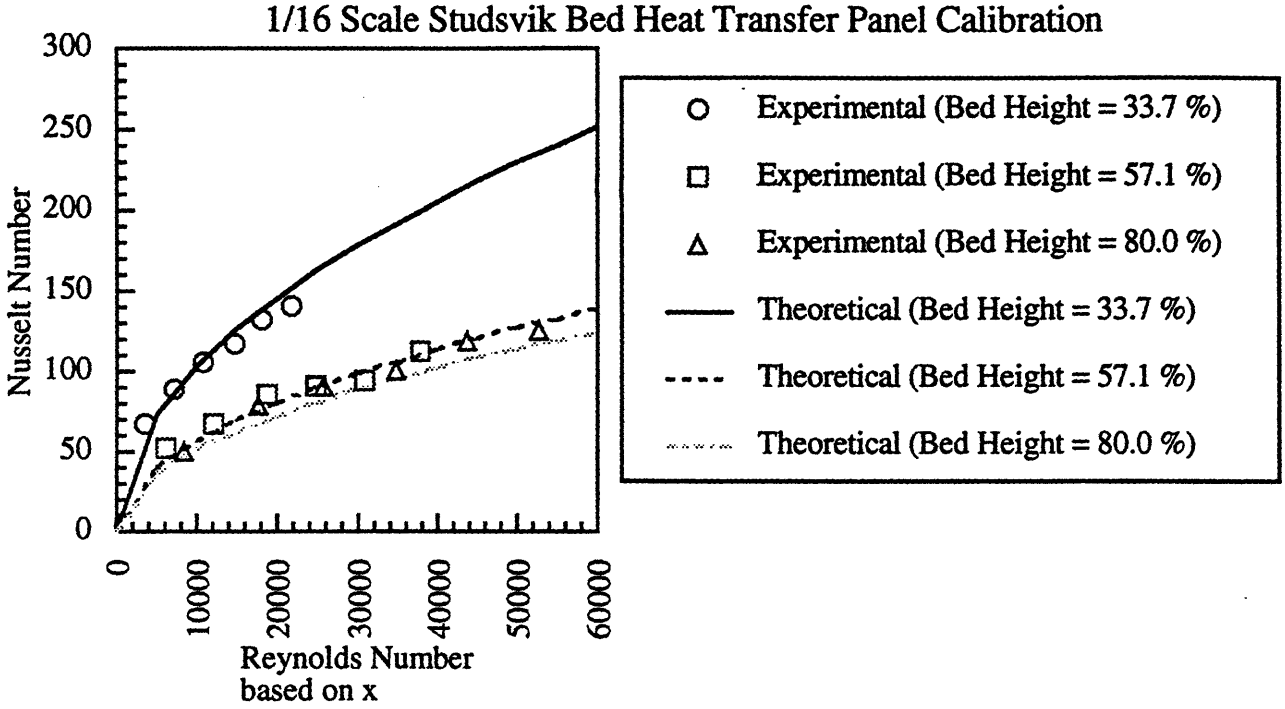

2.5 Uncertainty Analysis

2.5.1 Air Flow

The air flows were measured with 2-10 cfm rotameters fitted with exit pressure gauges. Calibration of the rotameters involved about 70 data points for each rotameter. The standard deviation from the linear calibration curves was about 0.05 cfm for each rotameter. The low end of the measurement range used in the experiments was about 3 scfm. The standard deviation represents about 2 percent of this lowest measurement.

The minimum fluidization test bed air flows for the glass were measured with 20-scfh and 100-scfh nominal rotameters. Fifteen test points were used in calibrating the 20-scfh rotameter. The standard deviation from the linear calibration curve for this rotameter was 0.093 scfh, or about 0.5 percent of full scale. Thirty-nine points were used in calibrating the 100-scfh rotameter. Standard deviation from the calculated linear calibration curve was 0.59, or about 0.6 percent of full scale.

2.5.2 Solid Circulation Rate

Confidence in the accuracy of the solid circulation rate measurements was based on the repeatability of solid loose-packed density measurements and the repeatability of solid fraction profile results when measurements indicate that flow conditions are the same. In addition, previous study has indicated that the various methods used provide similar agreement (Westphalen, 1990). The study performed by Westphalen also addresses the expected errors as a result of different rates of solid entrainment at the top of the bed, uncertainty about the solid bulk density as solid accumulates during measurement, and the variation in accumulation rates for successive measurements. It was determined that both the visual tracking and valve methods provide an adequate degree of accuracy for the solid circulation rate.

In an attempt to estimate the standard deviation of successive measurements in solid circulation using the valve and visual descent techniques, ten measurements were made at three different solids fluxes for both the valve and visual techniques. Table 2.2 presents the results of these tests. The standard deviation for the valve measurement techniques ranged from 2 to 5 percent of the average value.

Figure 2.10 shows solid fraction profiles for three tests of the same operating conditions in the bed used. The tests used the valve measurement technique. The similarity of the profiles indicate that either method produces a repeatable measurement, and that variation in successive measurements is not a problem.

Table 2.2

Valve and Visual Techniques for Solids Flux Measurement

	Valve Technique (Time to Fill 2 inches)			Visual Technique (Time to Descend 2 inches)		
Run	1	2	3	1	2	3
1	3.24	4.12	5.07	3.03	4.07	5.01
2	3.16	4.37	5.21	3.22	4.17	4.77
3	3.55	4.27	5.17	3.15	4.20	4.92
4	3.11	4.11	5.03	2.95	4.11	4.88
5	3.22	3.95	4.99	2.87	4.10	5.10
6	3.45	3.87	5.18	3.11	4.01	4.89
7	3.14	4.05	5.12	3.15	4.31	4.81
8	3.13	4.14	5.02	2.85	4.27	5.12
9	3.07	4.05	4.95	3.30	3.94	5.08
10	3.32	4.01	5.19	3.05	3.87	5.13
Avg.	3.24	4.09	5.09	3.07	4.11	4.97
Std. Dev.	0.157	0.146	0.0932	0.147	0.140	0.134

Figure 2.10

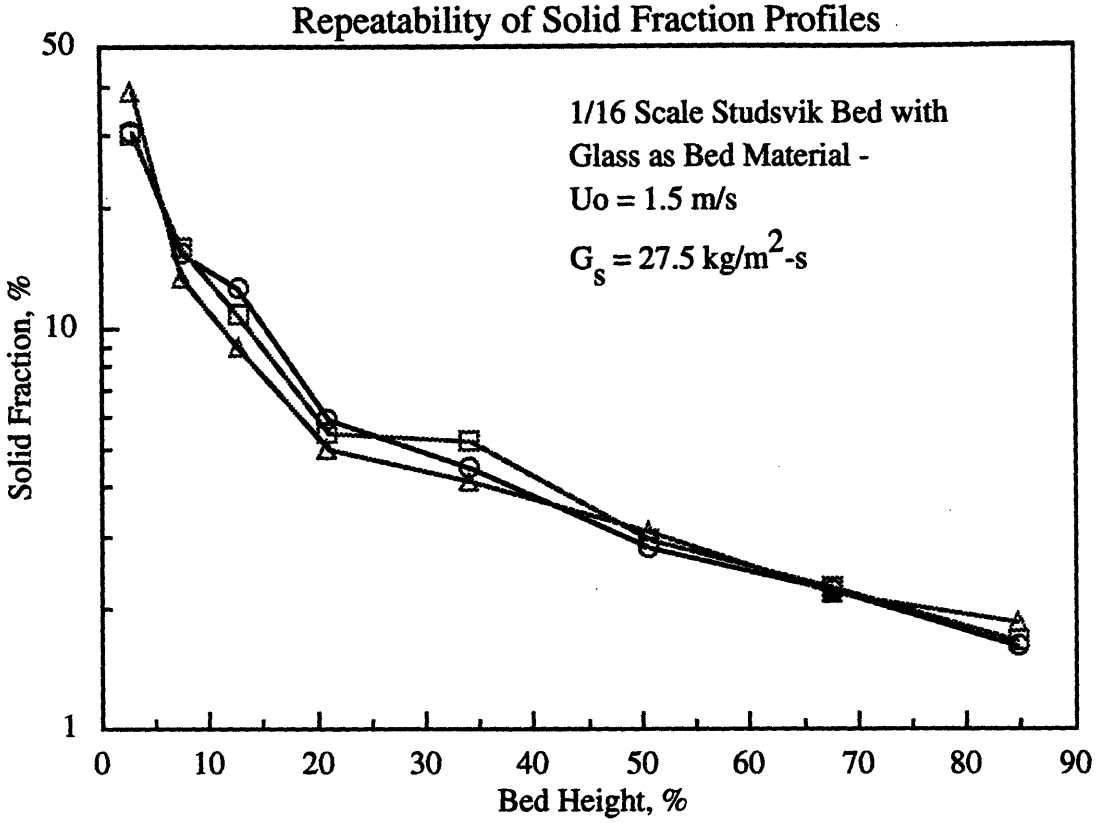

2.5.3 Pressure Measurements

All bed pressures were measured using pressure transducers whose output voltages were recoreded by a computer-based data acquisition system. Calibration of the transducers was accomplished by comparison with an oil filled inclined manometer. Linear calibration curves were used for reduction of data to convert the transducer output voltages to differential pressures. Table 2.3 presents typical values for the standard deviation of pressure transducers in the various beds.

Table 2.3 Standard Deviation of Transducers Used in Study

	Ratio of Standard Deviation to Average Voltage Output	
Bed	Worst Case	Typical
1/16 Scale Studsvik Bed (Bottom Four Transducers)	20%	5%
1/16 Scale Studsvik Bed (Top Four Transducers)	< 1%	<1%

The data acquisition board is rated for 12 bit resolution; this represents 0.024 percent of full scale. Typical full scale range used for the pressure transducers was +/- 50 mv, allowing 24.4 mv resolution. The worst case voltage resolution represented about 4 percent of the smallest measured mean pressure difference of about 0.13 cm wc when running at very lean conditions.

In order to determine the possibility that pressure signals may be attenuated in the pressure tap lines between the pressure tap opening and pressure transducer, a rough analysis was conducted which indicated that the break (maximum transmission) frequency based on for the cold bed setups would be about 3500 Hz. The maximum frequency of the data acquisition board A/D conversion may be as low as 500 Hz when all eight pressure taps are being sampled which suggests that this is not a limiting condition. In addition, it has been shown that the fluctuations of interest in the bed would have frequencies less than 100 Hz (Westphalen, 1990).

Pressures time traces were taken for 10 seconds at a frequency of 100 Hz. For each trace, the average and standard deviation was calculated. These standard deviations, along with the standard deviation in solids flux measurement, were used in constructing error bars for the cold bed solid fraction profiles. Error bars represent one standard deviation (i.e., 67 percent of the data fell into the interval based on a normal distribution).

2.5.4 Temperature Measurements

All temperatures were measure with an Omega DP462 digital thermometer with multi-channel input. This thermometer has 0.1 °F resolution up to 1000 °F, an accuracy of 0.9 °F (0.5 °C), and a reading rate of 1 per second. Since all temperature measurements were taken at steady state, it is not anticipated that the thermometer added any significant error.

The thermocouples which measured the wall temperature were imbedded in the copper plate covers. A thin layer of thermally conductive silicone paste was used to hold the copper cover plate to the heater. This paste was also used to surround the thermocouples to thermally connect the thermocouple bead to the copper cover plate. This paste has a thermal conductivity of 16 Btu-in/hr-ft^2-F (0.0055 cal-cm/s-cm^2-C) and a temperature range of use from -40 - 392 ^{o}F (-40 - 200 ^{o}C). Rough calculations indicate the maximum temperature drop from the thermocouple to the wall surface did not exceed 1 ^{o}C.

One possible source of error in the measurement of heat transfer coefficients is the loss of heat through the back of the beds. In order to minimize this effect, the back and half the sides of the bed were covered with 1/2-inch (1.3 cm) foam insulation.

Lateral heat transfer losses from the heat transfer panels in the bed were minimized by a 1/4-inch (0.64 cm) of acrylic, the bed walls (3/8-inch acrylic), and another 1/2-inch (1.3 cm) of foam insulation.

Vertical heat transfer between heaters was reduced by keeping the heaters as close in temperature to each other as possible. In addition, the heaters were separated by 0.33 -inches (0.84 cm) of acrylic. Estimates of heat transfer losses from the panel are shown in Table 2.4.

Table 2.4: Maximum Heat Losses from Heat Transfer Panel

Area of Loss	1/16 Scale Studsvik Bed
Through Back	3.4%
Through Sides	0.9%
Between Heaters	0.1%

As was discussed earlier, the heat transfer panels were calibrated by measuring the heat transfer coefficient with only air flowing over it while keeping the temperature of the heated section of the panel constant. Results of the heat transfer panel calibration are given in Figure 2.8.

Because the heaters did not heat completely evenly, thermocouple readings were taken at the top and bottom of each copper cover. The temperatures were then averaged for use in the

calculation of the heat transfer coefficient at the midpoint of the heater. The temperatures at the ends of the heaters never differed by more than 4.5 °F (2.5 °C). Typical differences were normally 1-1.5 °C.

2.6 Data Reduction

The following Section discusses the manner in which the data was reduced to develop average solid fraction profiles, histograms, power spectral densities, and Nusselt numbers.

2.6.1 Average Solid Fraction Profiles

Solid fraction profiles discussed in the following Sections are based on pressure drop measurements. In converting pressure drop to solid fraction, it has been assumed that pressure differentials are due entirely to solid hold up

$$SF = \frac{\Delta P}{\rho_s g \Delta L}$$

This relation neglects acceleration effects and wall shear stresses, which may comprise a portion of the total pressure drop. Therefore, measured solid fractions are more correctly defined as dimensionless pressure differences, which are equal to the true solid fraction in the limit of negligible acceleration and wall shear.

Solid fractions are plotted versus the average of the heights of the associated pressure taps.

2.6.2 Heat Transfer Coefficients

Steady state heat transfer coefficients were calculated by measuring the bed temperature and the wall temperature at steady state. Total power inputs were then computed by measuring the voltage input to the heaters, and the heater resistances. A corrected power input to the bed to account for heat losses through the back and sides of the bed was calculated by using the calibration curve described earlier. For each run in which heat transfer data was taken, temperatures at the top and bottom of each heater (total of six temperatures) along with the bed temperature were recorded three times at steady state during a period of about five minutes. The average of these temperature differences was then used in the heat transfer coefficient calculations.

While recording the temperature data, differential pressure data was taken utilizing the computer based data acquisition system to allow correlation between Nusselt numbers and average bed solid fraction. Immediately after bed and wall temperatures were recorded, total voltage inputs and heater resistance's were recorded to allow determination of total power input.

3.0 EXPERIMENTAL RESULTS

This Section presents the results of the heat transfer experiments. For each heat transfer surface configuration, measurements were taken at two solid circulation rates. The superficial velocity for all tests was 1.5 m/s. No secondary air was used during the tests. The variation in average solid fractions in the plots are due to the variation in the axial height of the heaters. Heat transfer measurements were taken at heights of 41%, 64%, and 88% up the bed riser.

3.1 Flat Wall Tests

The heat transfer results are plotted as a function of the average solid fraction, α_{avg}, at a given height. The average bed solid fraction at a given height was obtained from the vertical pressure gradient assuming acceleration and wall fraction effects can be neglected. Figures 3.1 through 3.3 depicts the results of the flat wall heat transfer tests. Figure 3.1 shows the heat transfer results for the lower solids circulation rate while Figure 3.2 shows the results for the higher solids circulation rate. The parameter 'a' shown in the legend is the coefficient to the least squares curve fit to the square root function

$$h = a\sqrt{\alpha_{avg}} \qquad (1)$$

Representative error bars are shown on each plot. The error bars for the solid fraction represent the standard deviation determined from the time varying pressure trace. The error bars for the heat transfer coefficients represent the combined error from:

1. Error in bed and wall temperature measurements
2. Error due to change in resistivity of heaters with temperature
3. Error in voltage measurements
4. Error due to heat loss from the heat transfer panel

Figure 3.3 is a combined plot for all flat wall heat transfer tests plotted as a function of the average bed solid fraction.

Figure 3.1

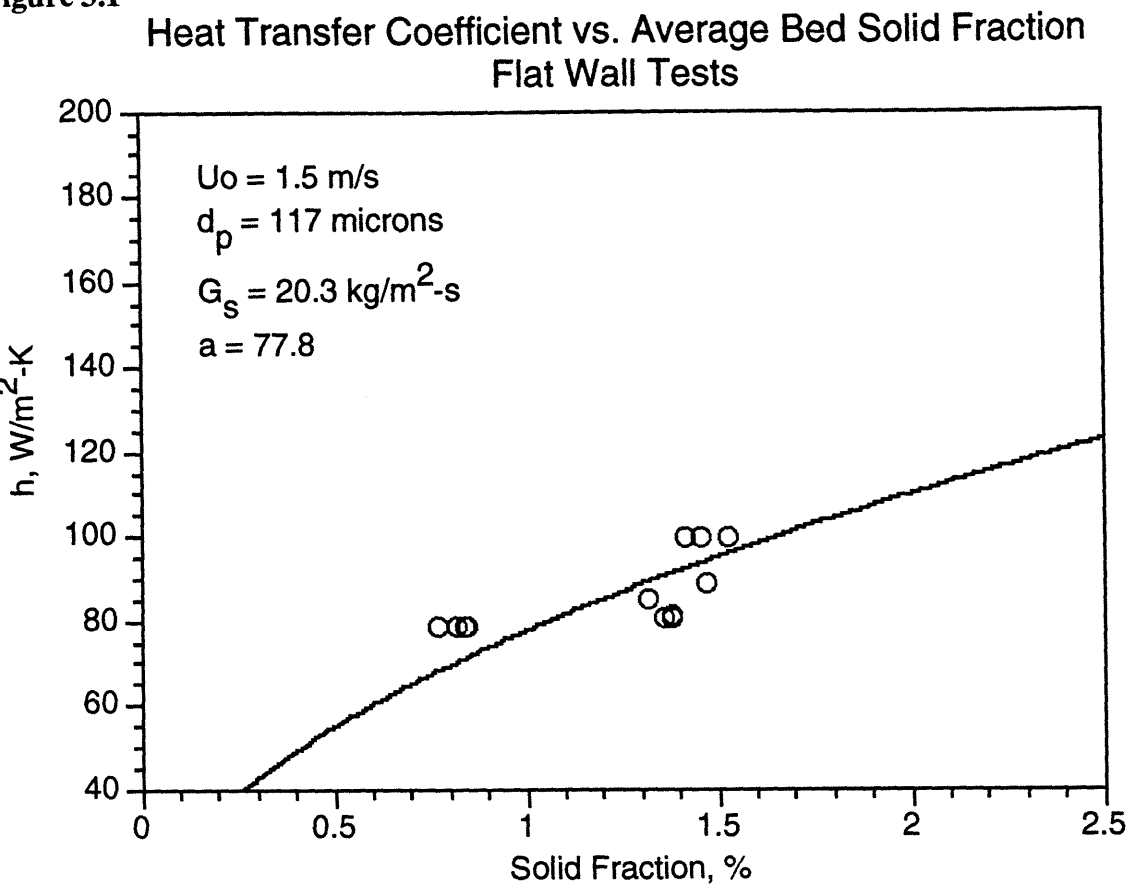
Heat Transfer Coefficient vs. Average Bed Solid Fraction
Flat Wall Tests
Uo = 1.5 m/s
d_p = 117 microns
G_s = 20.3 kg/m^2-s
a = 77.8
h, W/m^2-K
200
180
160
140
120
100
80
60
40
0
0.5
1
1.5
2
2.5
Solid Fraction, %

Figure 3.2

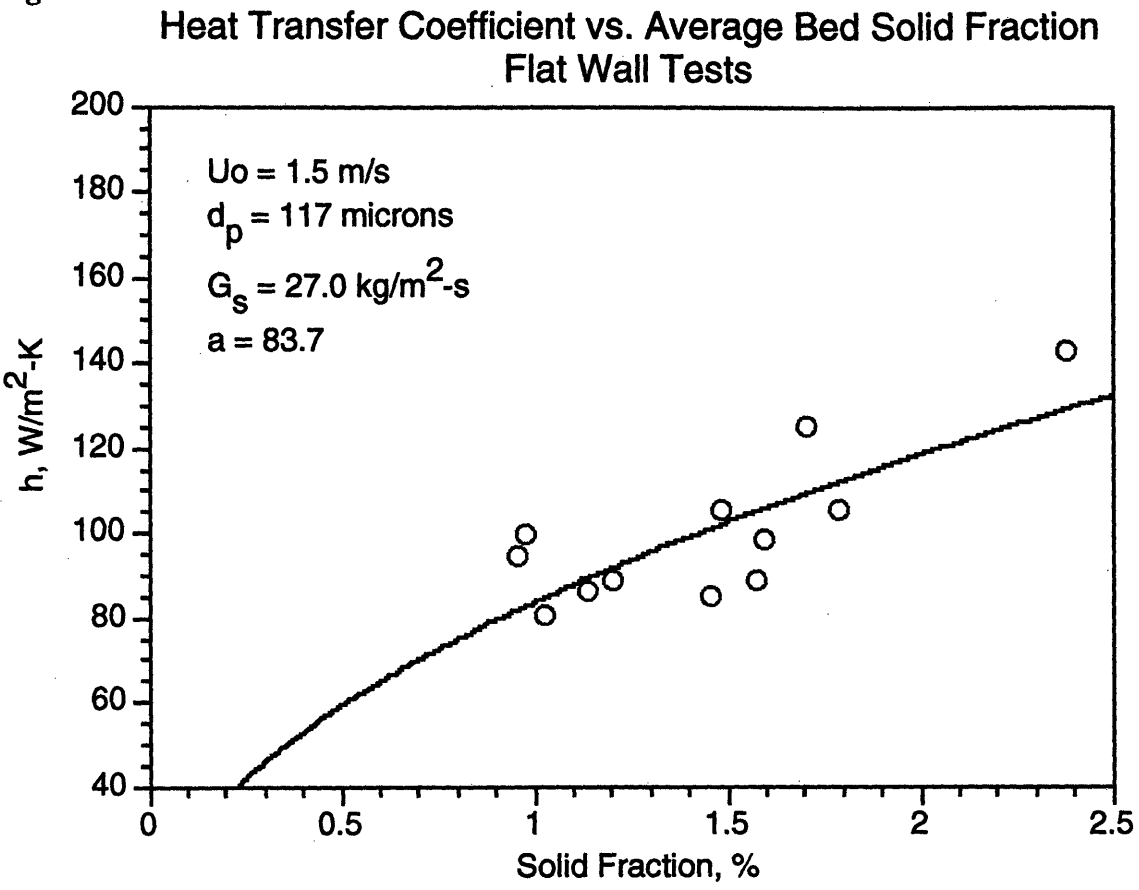
Heat Transfer Coefficient vs. Average Bed Solid Fraction
Flat Wall Tests
Uo = 1.5 m/s
d_p = 117 microns
G_s = 27.0 kg/m^2-s
a = 83.7
h, W/m^2-K
200
180
160
140
120
100
80
60
40
0
0.5
1
1.5
2
2.5
Solid Fraction, %

Figure 3.3

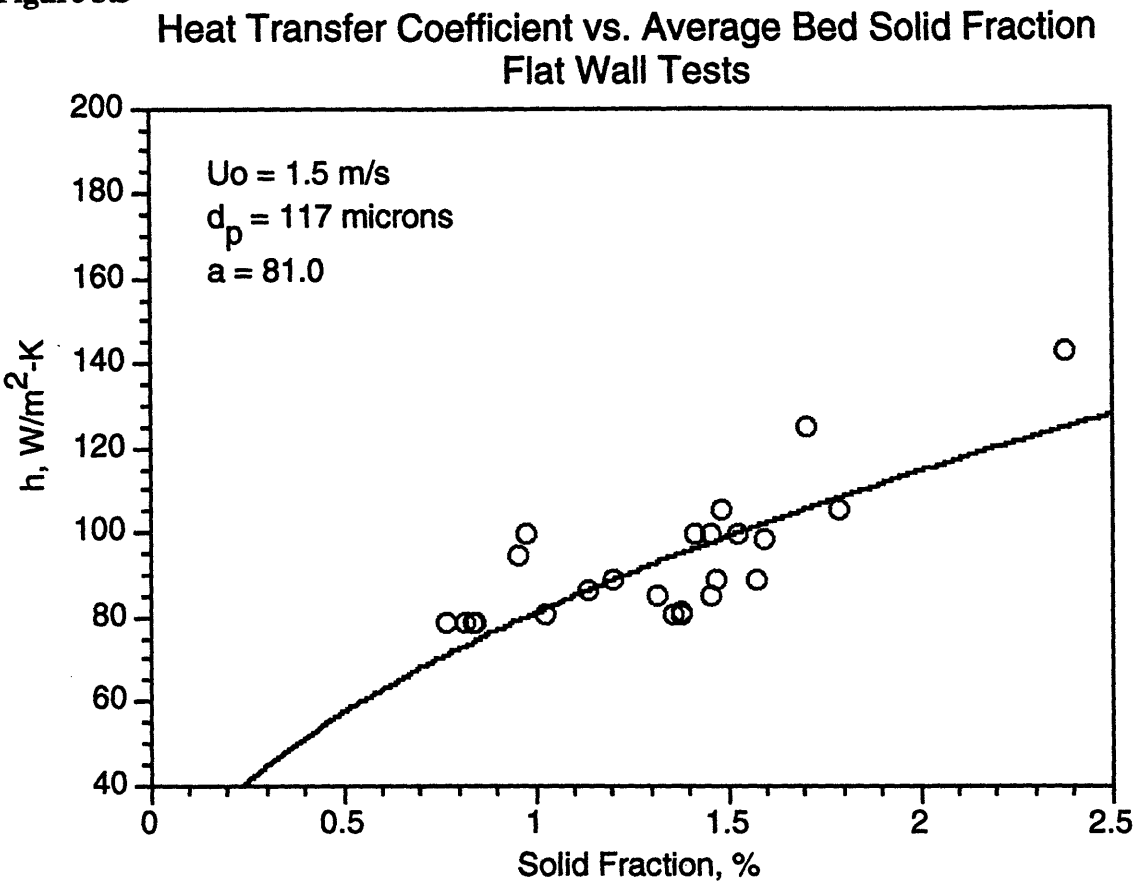

3.2 Ridge Spacing = 20 mm

Figures 3.4 through 3.6 depicts the results of the 20mm ridge spacing heat transfer tests. Figure 3.4 shows the heat transfer results for the lower solids circulation rate while Figure 3.5 shows the results for the higher solids circulation rate. The parameter 'a' shown in the legend is the coefficient to the least squares curve fit to the square root function

Figure 3.6 is a combined plot for all 20mm ridge spacing heat transfer tests plotted as a function of the average bed solid fraction.

Figure 3.4

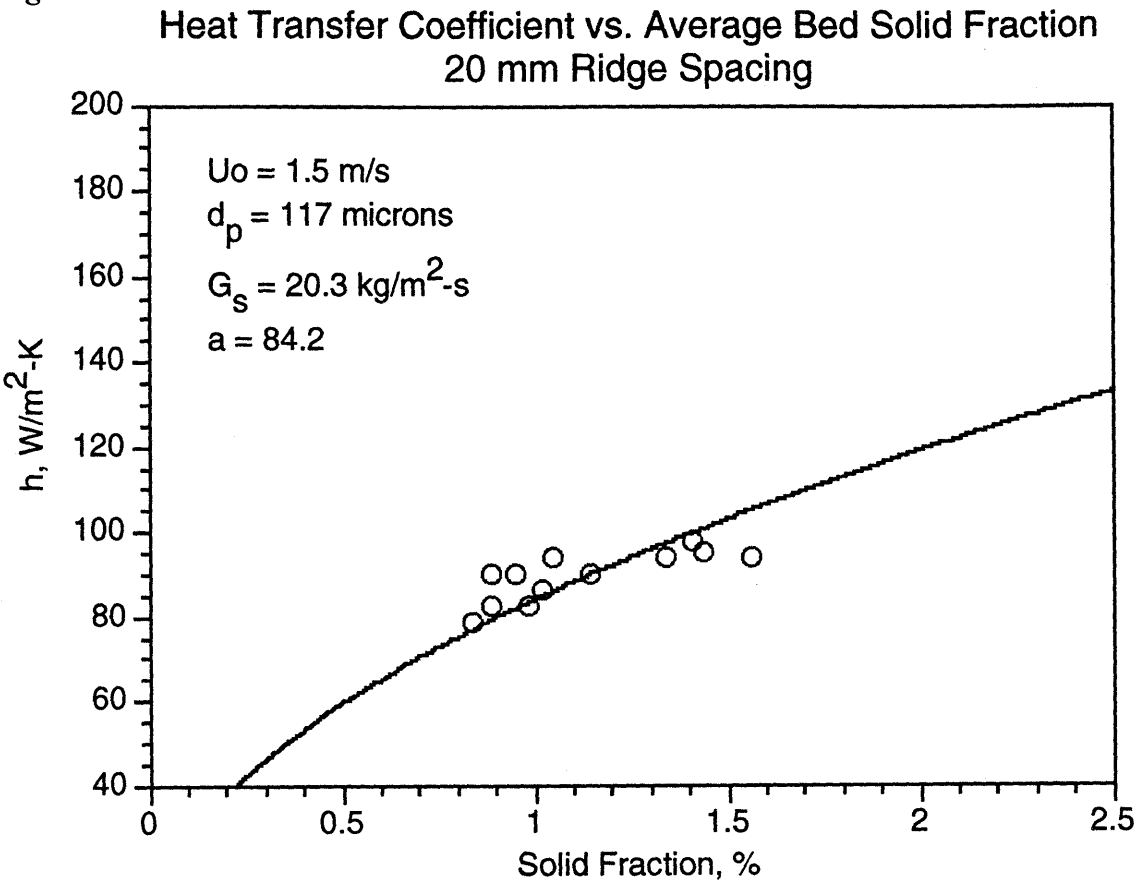
Heat Transfer Coefficient vs. Average Bed Solid Fraction
20 mm Ridge Spacing
Uo = 1.5 m/s
d_p = 117 microns
G_s = 20.3 kg/m^2-s
a = 84.2
h, W/m^2-K
200
180
160
140
120
100
80
60
40
0
0.5
1
1.5
2
2.5
Solid Fraction, %

Figure 3.5

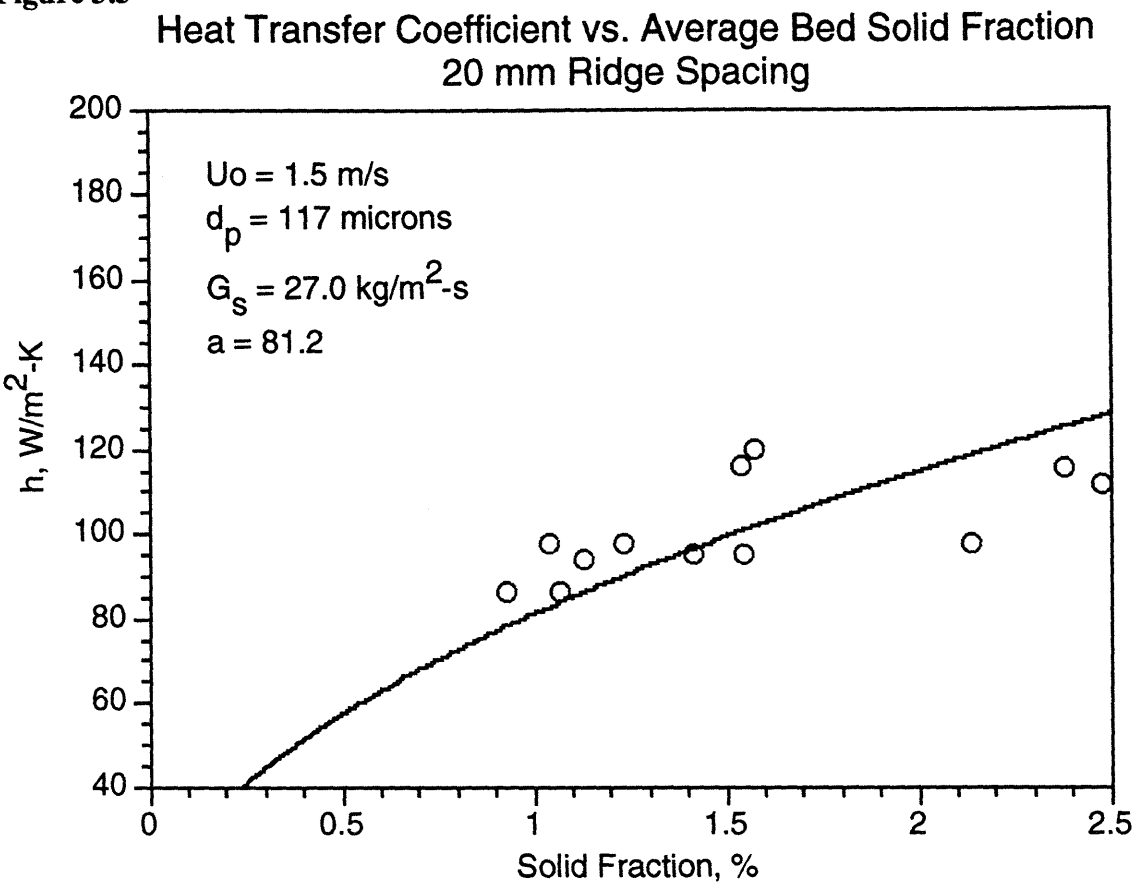
Heat Transfer Coefficient vs. Average Bed Solid Fraction
20 mm Ridge Spacing
Uo = 1.5 m/s
d_p = 117 microns
G_s = 27.0 kg/m^2-s
a = 81.2
h, W/m^2-K
200
180
160
140
120
100
80
60
40
0
0.5
1
1.5
2
2.5
Solid Fraction, %

Figure 3.6

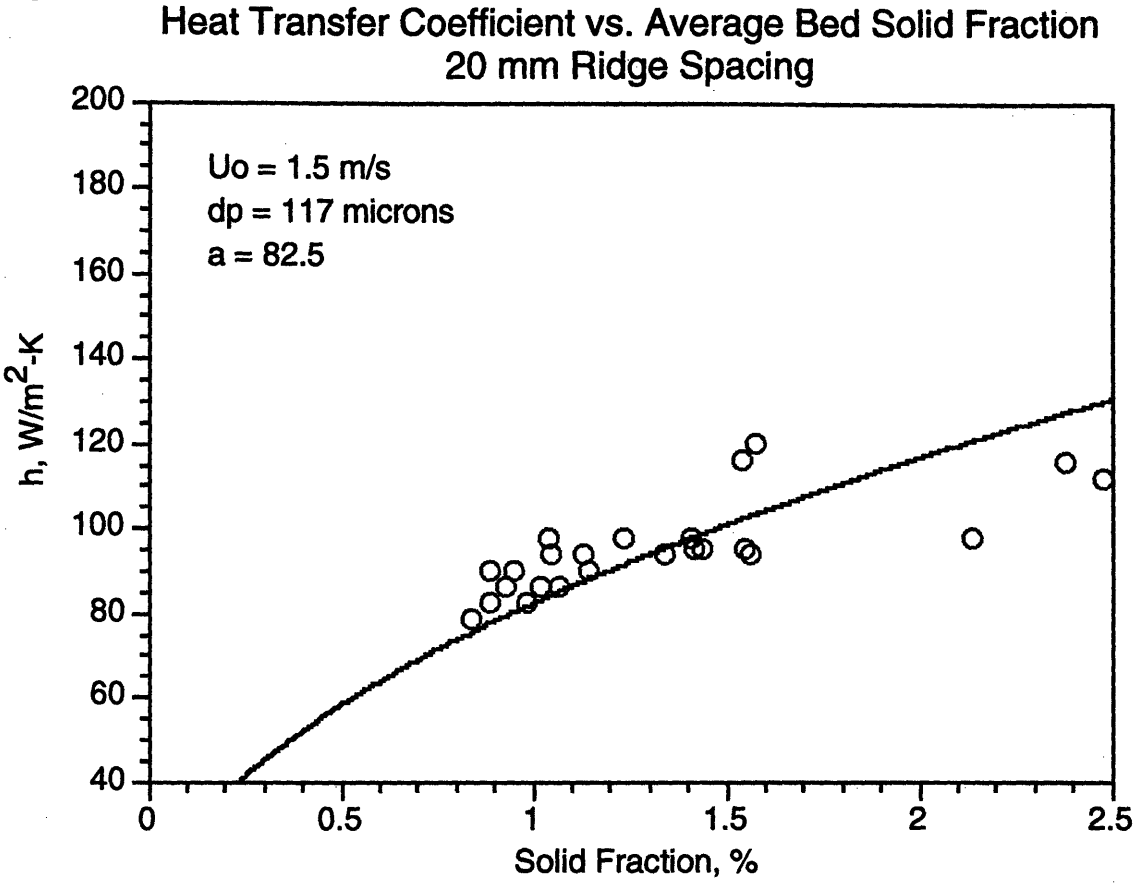

3.3 Ridge Spacing = 10 mm

Figures 3.7 through 3.9 depicts the results of the 10mm ridge spacing heat transfer tests. Figure 3.7 shows the heat transfer results for the lower solids circulation rate while Figure 3.8 shows the results for the higher solids circulation rate. The parameter 'a' shown in the legend is the coefficient to the least squares curve fit to the square root function

Figure 3.9 is a combined plot for all 10mm ridge spacing heat transfer tests plotted as a function of the average bed solid fraction.

Figure 3.7

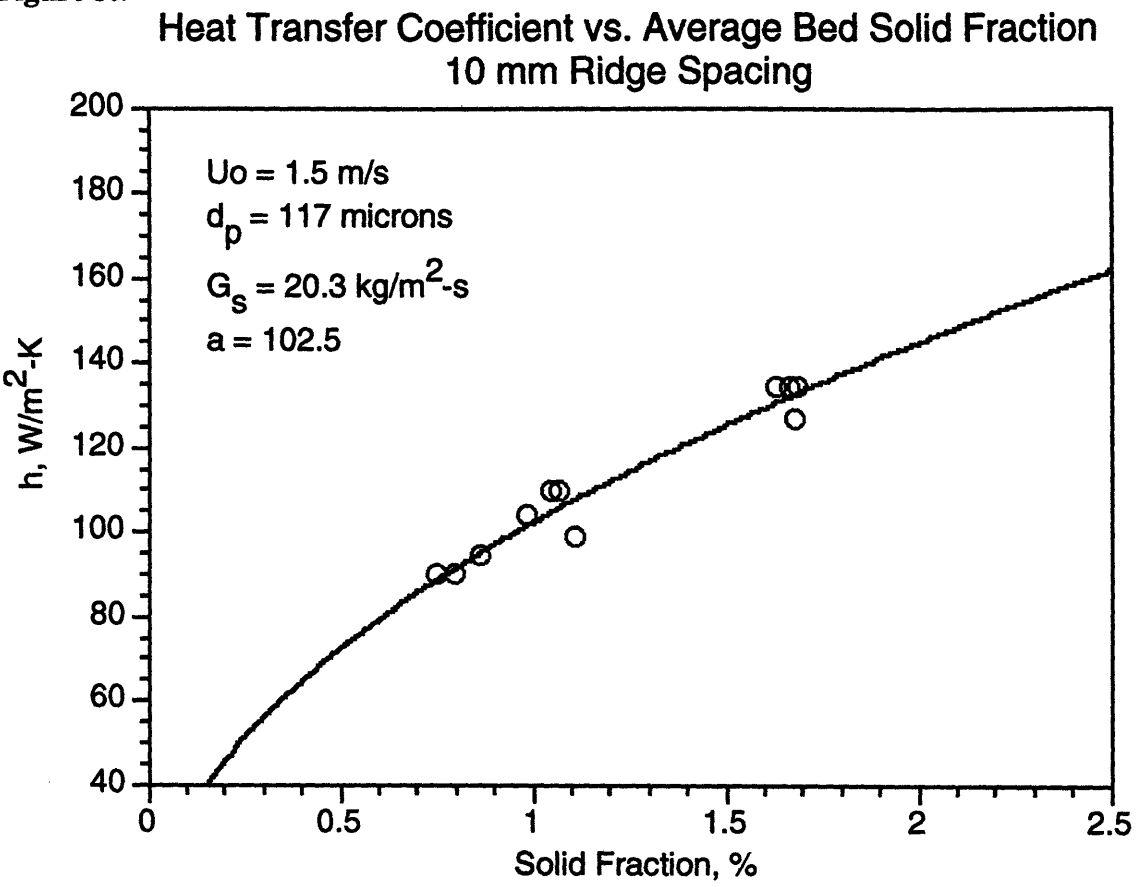
Heat Transfer Coefficient vs. Average Bed Solid Fraction
10 mm Ridge Spacing
Uo = 1.5 m/s
d_p = 117 microns
G_s = 20.3 kg/m^2-s
a = 102.5
h, W/m^2-K
200
180
160
140
120
100
80
60
40
0
0.5
1
1.5
2
2.5
Solid Fraction, %

Figure 3.8

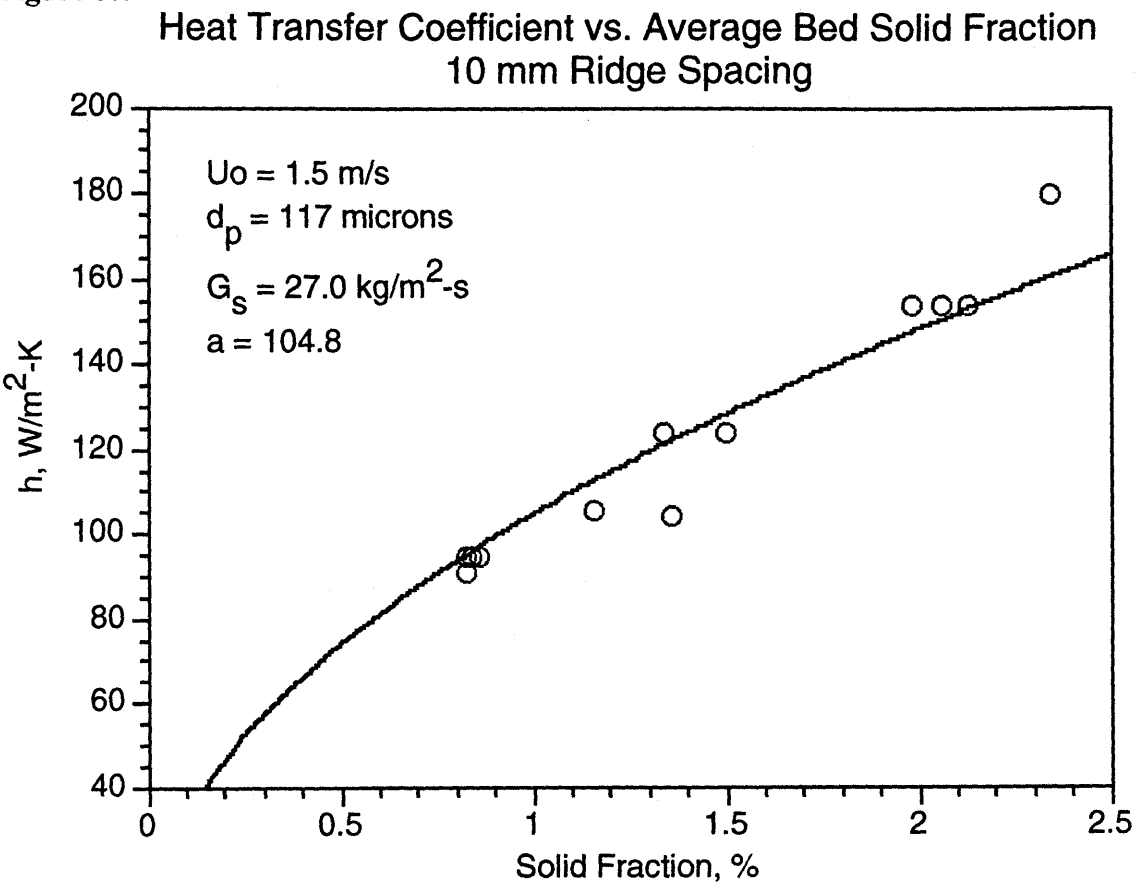
Heat Transfer Coefficient vs. Average Bed Solid Fraction
10 mm Ridge Spacing
Uo = 1.5 m/s
d_p = 117 microns
G_s = 27.0 kg/m^2-s
a = 104.8
h, W/m^2-K
200
180
160
140
120
100
80
60
40
0
0.5
1
1.5
2
2.5
Solid Fraction, %

Figure 3.9

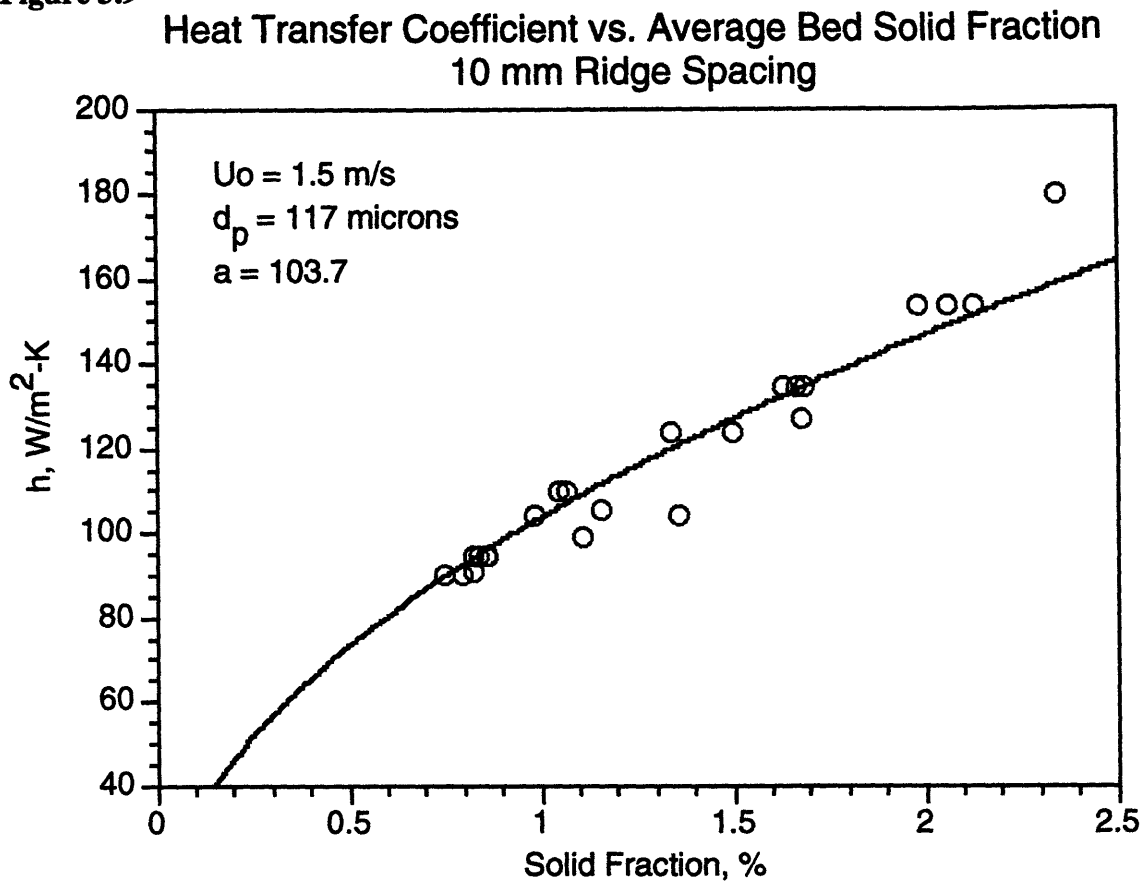

3.4 Ridge Spacing = 5 mm

Figures 3.10 through 3.12 depicts the results of the 5mm ridge spacing heat transfer tests. Figure 3.10 shows the heat transfer results for the lower solids circulation rate while Figure 3.11 shows the results for the higher solids circulation rate. The parameter 'a' shown in the legend is the coefficient to the least squares curve fit to the square root function

Figure 3.12 is a combined plot for all 5mm ridge spacing heat transfer tests plotted as a function of the average bed solid fraction.

Figure 3.10

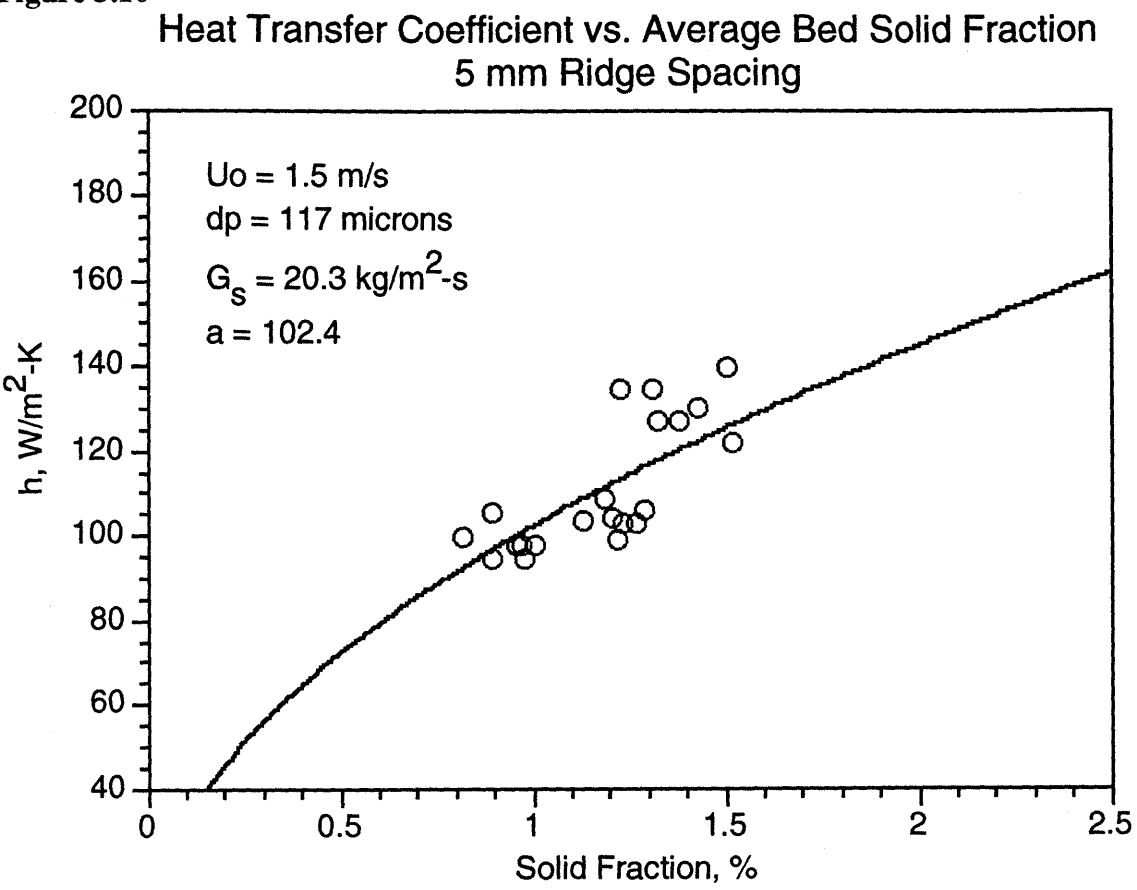
Heat Transfer Coefficient vs. Average Bed Solid Fraction
5 mm Ridge Spacing
Uo = 1.5 m/s
dp = 117 microns
G_s = 20.3 kg/m^2-s
a = 102.4
h, W/m^2-K
200
180
160
140
120
100
80
60
40
0
0.5
1
1.5
2
2.5
Solid Fraction, %

Figure 3.11

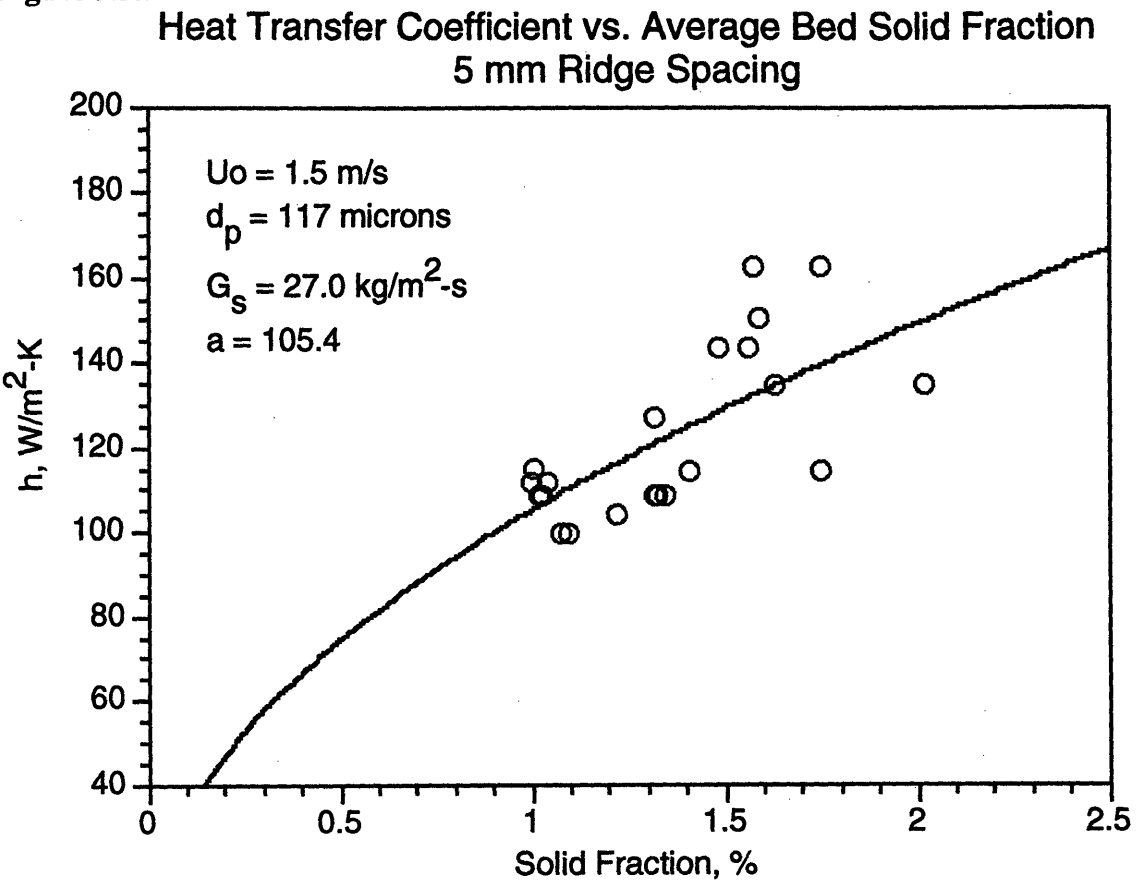
Heat Transfer Coefficient vs. Average Bed Solid Fraction
5 mm Ridge Spacing
Uo = 1.5 m/s
d_p = 117 microns
G_s = 27.0 kg/m^2-s
a = 105.4
h, W/m^2-K
200
180
160
140
120
100
80
60
40
0
0.5
1
1.5
2
2.5
Solid Fraction, %

Figure 3.12

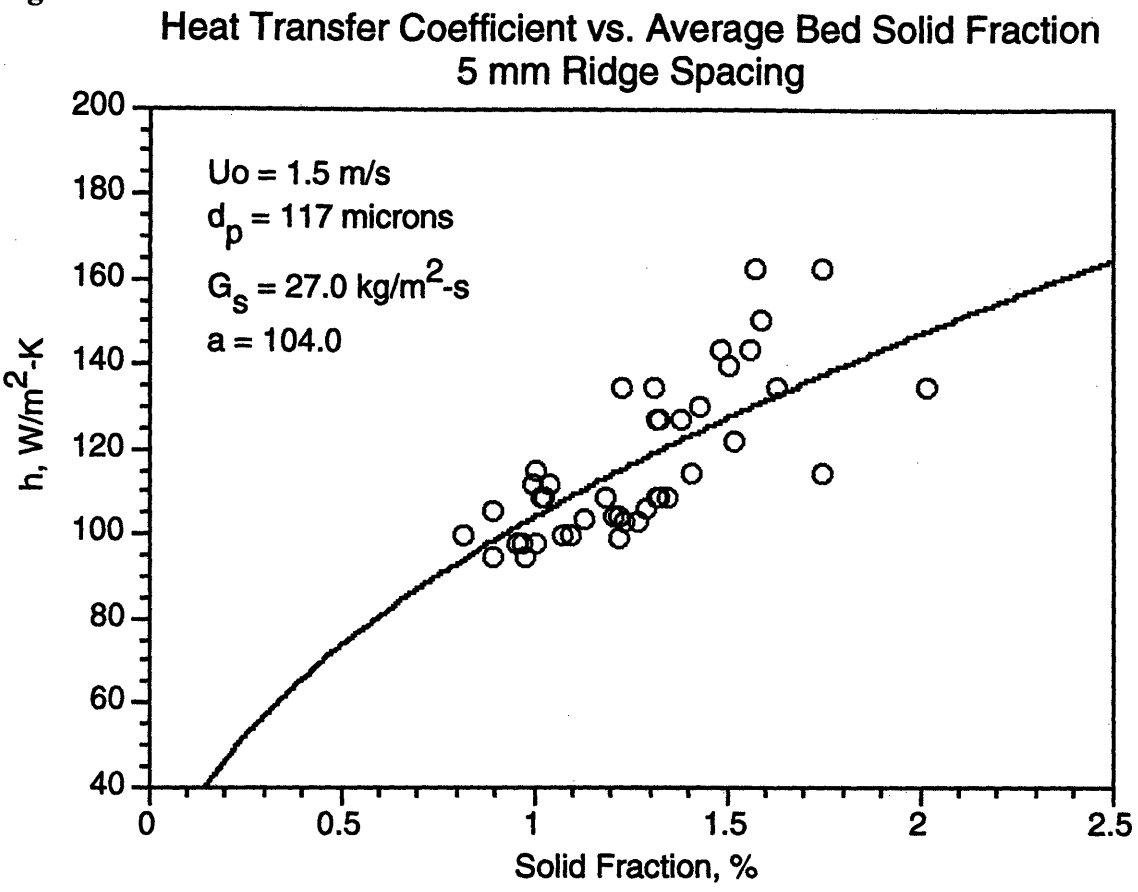

3.5 Discussion of Results

3.5.1 Effect of Solids Circulation Rate

In all cases the increase in solids circulation rate resulted in higher average bed solids fraction. It also resulted in higher heat transfer coefficients. Nevertheless, the heat transfer coefficient dependence with solids fraction remained the same at the two solids circulation rates. In other words, the coefficient of the square root curve fit did not vary significantly from the lower to higher solids circulation rate. Table 3.1 shows the variation in the coefficient. Figures 3.13 through 3.16 present comparisons of data taken at the two different solids circulation rates.

Table 3.1: Variation in Curve Fit Coefficient

Test Case	Coefficient for Low Flux Case	Coefficient for High Flux Case	Percent Deviation
Flat Wall	77.8	83.7	7.6
20mm Case	84.2	81.2	3.6
10mm Case	102.5	104.8	2.2
5mm Case	102.4	105.4	2.9

Figure 3.13

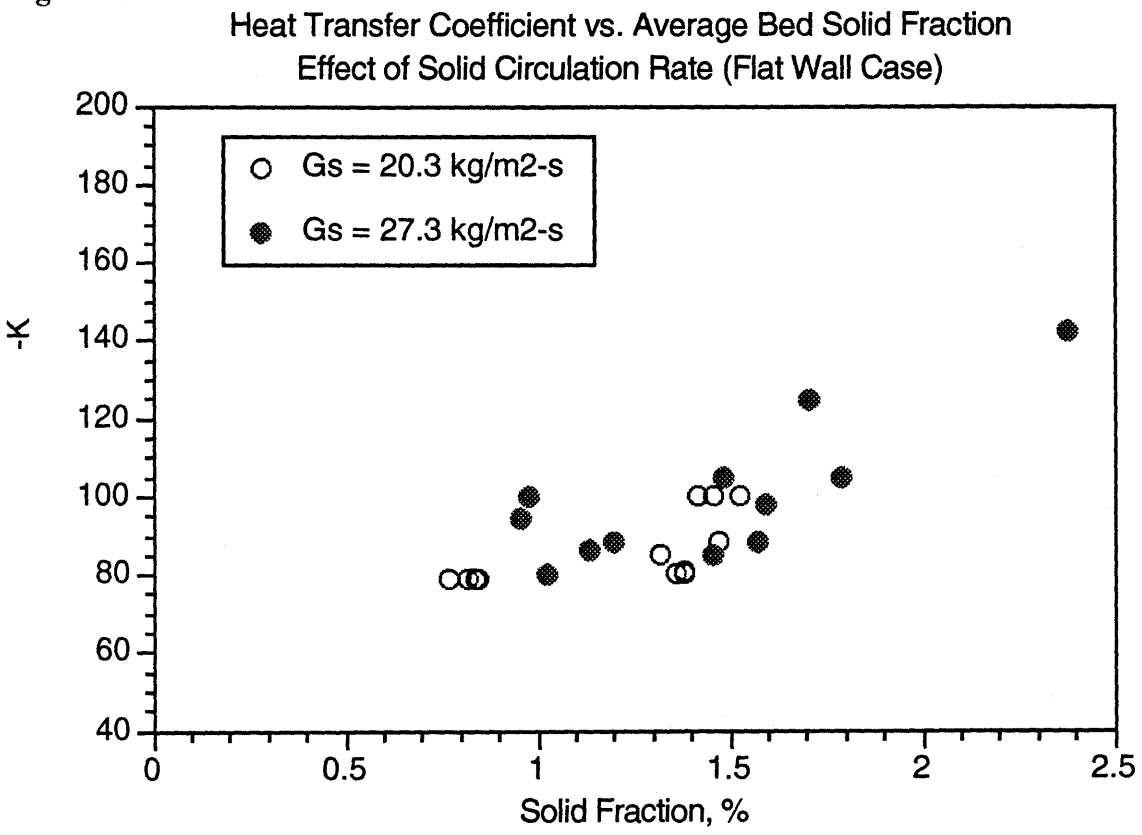

Figure 3.14

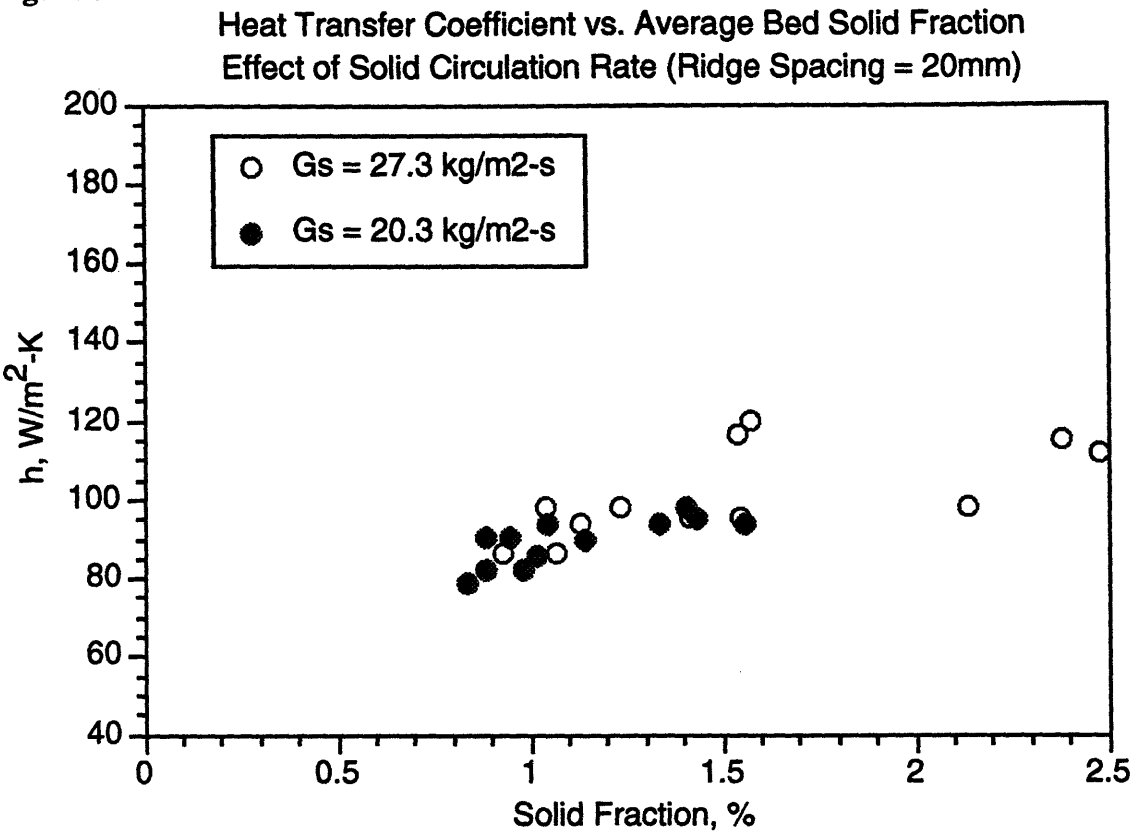

Figure 3.15

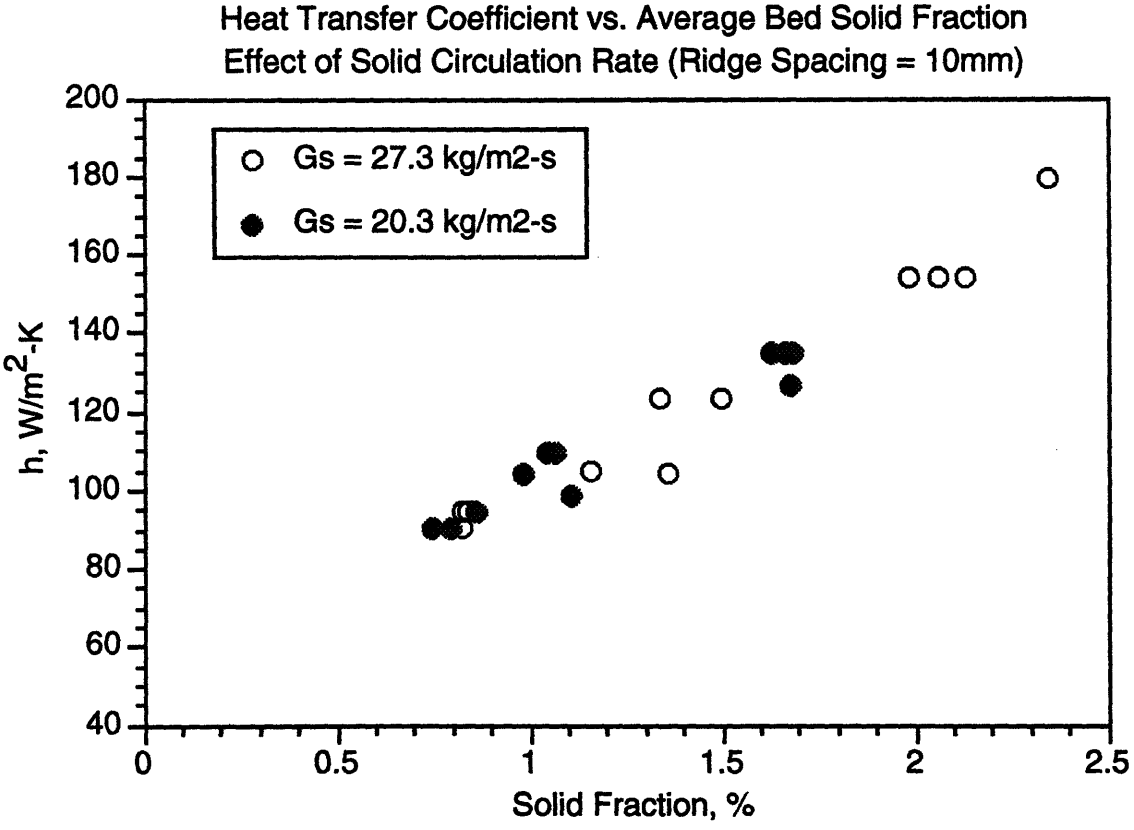

Figure 3.16

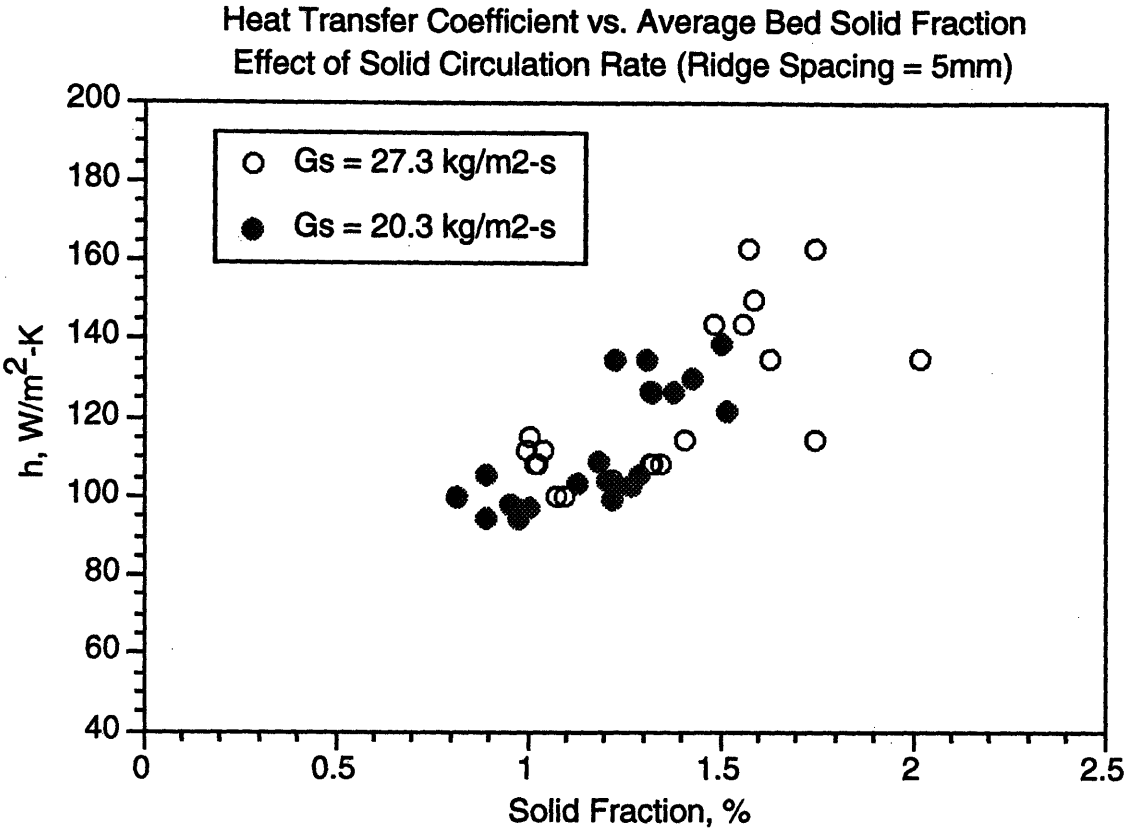

3.5.2 Effect of Bed Height

No influence of bed height on the heat transfer coefficient was evident in the data.

3.6 Effect of Ridge Spacing

The effect of ridge spacing is depicted in Figure 3.17. Values for the square root curve fit coefficient are given in Table 3.2. Curves for the 5mm and 10mm ridge spacing cases are nearly indistinguishable.

Figure 3.17

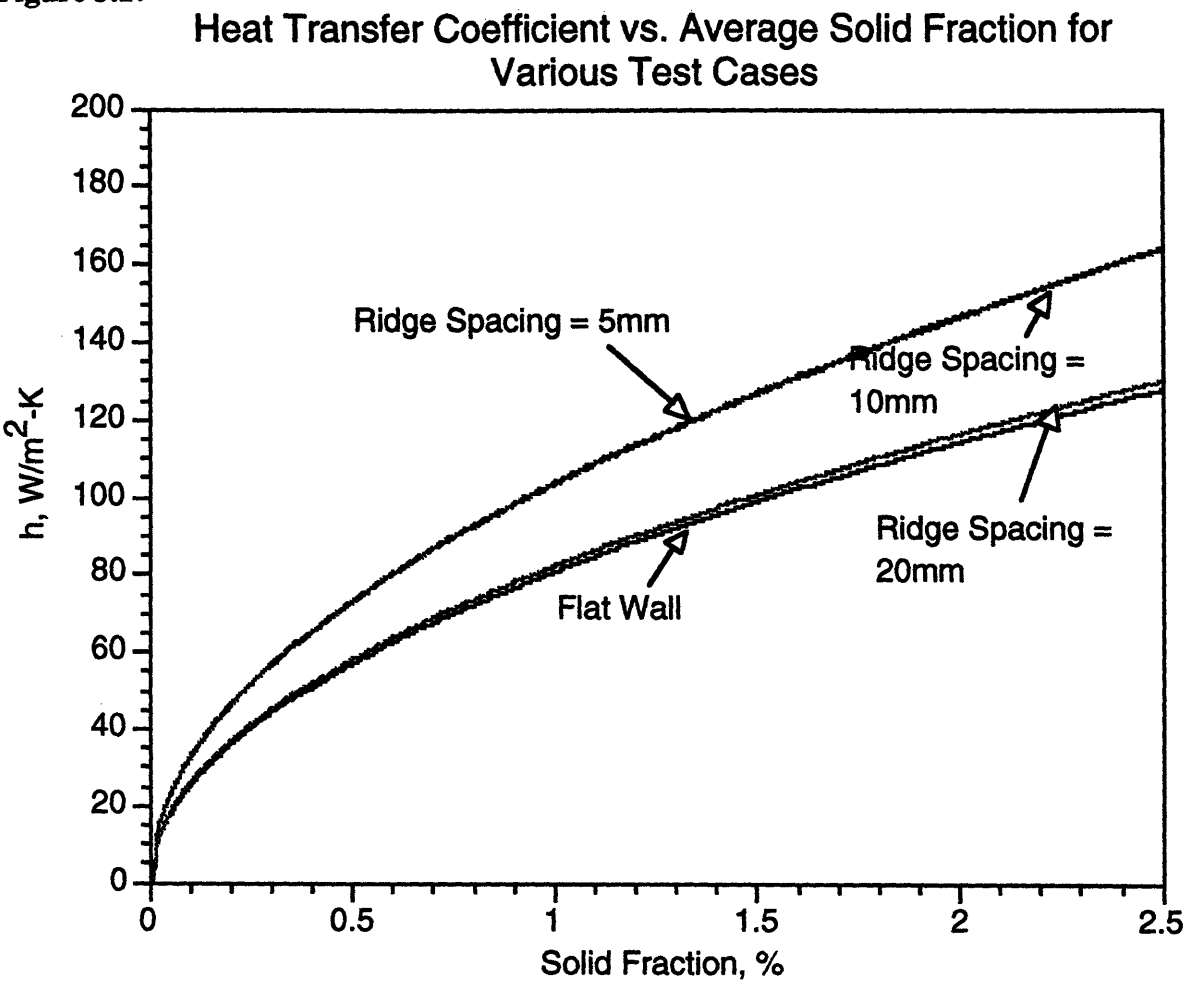

Table 3.2

Test Case	Square Root Curve Coefficient	Percent Increase from Flat Wall Case
Flat Wall	81.0	---
Ridge Spacing = 20mm	82.5	1.85
Ridge Spacing = 10mm	103.7	28.0
Ridge Spacing = 5mm	104.0	28.4

There was an increase in the square root curve fit coefficient for all cases, with a trend of increasing coefficients as the ridge spacing decreased. The increase between the flat wall case and the 20mm spacing case was very small indicating very little heat transfer enhancement. There was a large jump in the coefficient between the 20mm spacing case and the 10mm spacing case. This may indicate that the clusters which flow down the wall stay at the wall for distances which are greater than 10mm but less than 20mm. The

increase in heat transfer coefficient between the 10mm and 5mm case was small. This may be due to a tradeoff between the decreasing time the clusters are at the wall and the decreasing fractional wall coverage. The former effect increases wall to cluster heat transfer, while the latter results in a decrease in heat transfer. If the clusters are separated from the wall at each ridge, the mean residence time is reduced but the wall becomes bare and must be recovered by fresh clusters from the core. This tradeoff will be discussed in more detail in Sections 4 and 5. Note that the two closer ridge spacings gave a 20 percent increase in the heat transfer coefficient over the smooth surface at a solid fraction between one and two percent.

3.7 Effect of Ridges on Bed Hydrodynamics

Figures 3.18 and 3.19 show average solid fraction profiles for the four cases at the low and high solids loading. Representative error bars are included on the flat wall case. The profiles are in good agreement for all cases indicating that the ridges did not have a significant impact on the overall bed hydrodynamics. Note that the ridges are only on one of the four walls. If all sides had ridges, a larger impact may have been observed.

Figure 3.18

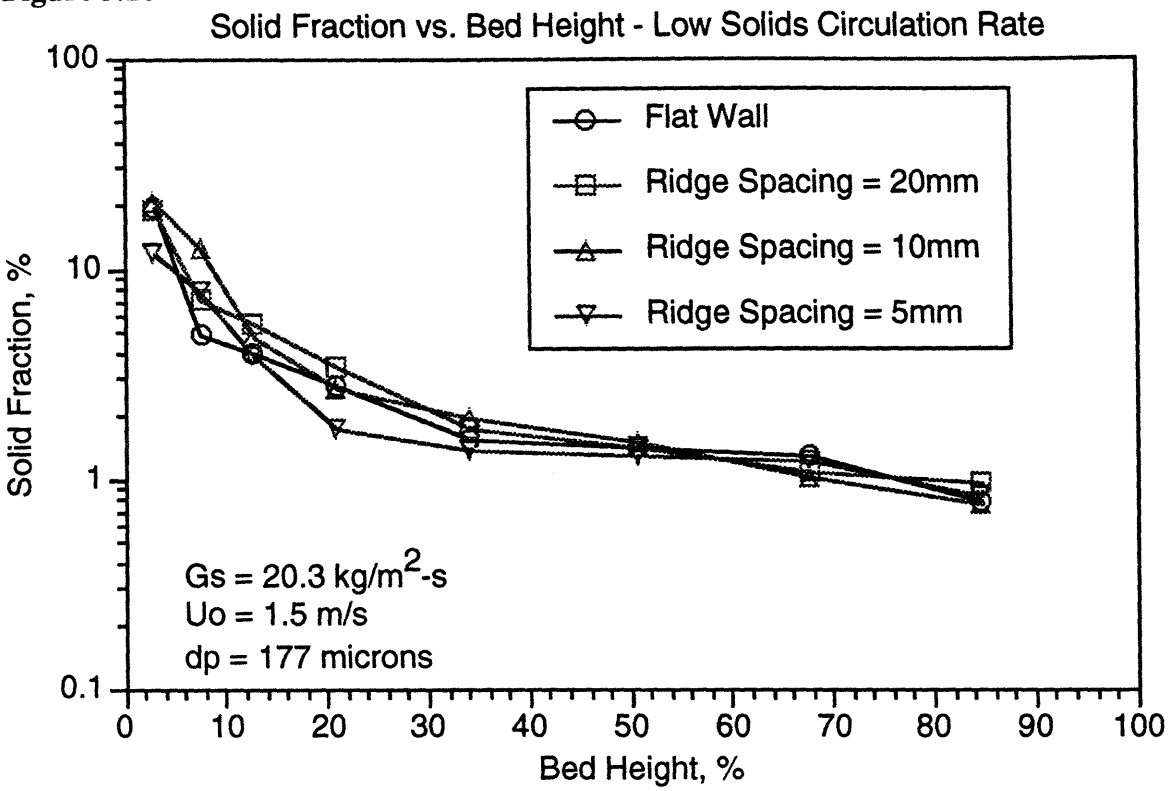

Figure 3.19

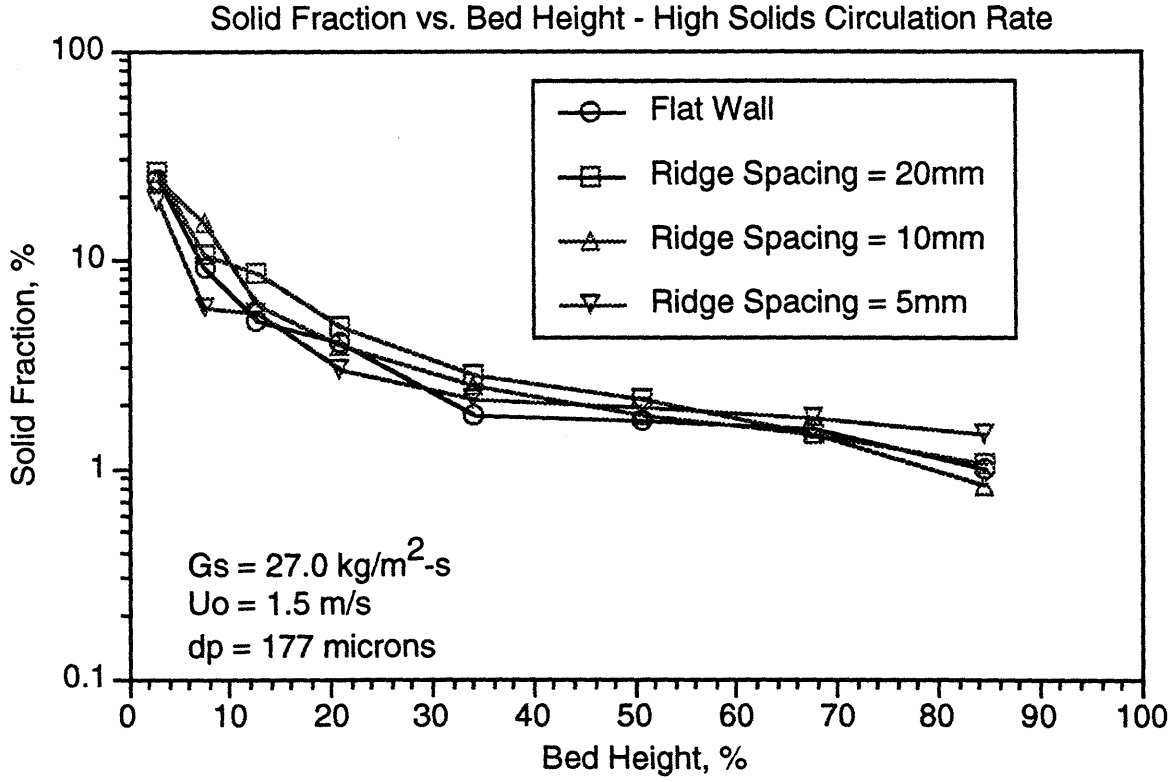

4.0 HEAT TRANSFER MODEL

4.1 Convective Heat Transfer

The flow of the gas-particle suspension in the riser of fast fluidized beds is characterized by dilute rapidly rising core and a dense annular region near the walls where the solid particles congregate and fall as dense structures similar to waves of strands or streamers. Such observations have been reported by many investigators [see for example, Weinstein *et al.* (1986), Herb *et al.* (1989), Brereton (1987), Horio *et al.* (1988), Hartge *et al.* (1988), Bader *et al.* (1988), and Rhodes *et al.* (1992)]. In the design of CFB combustors, the heat transfer mechanism from the gas-solid suspension to the wall is strongly influenced by the dense down flowing wall layer.

This study concentrates on the heat transfer from particles very close to or in contact with the wall, which is the dominant mechanism at moderate temperatures. In the wall region, at low bed densities, the wall is alternately covered by high density clusters and a dilute phase. Within the annular dense phase of a CFB, particles are observed to flow down the wall grouped into clusters or streamers. The heat transfer may be treated as between a layer of particles which are initially at the bulk temperature of the bed, T_b, and the wall at T_w. The thickness of the cluster layer has been reported to be from about 1-2 mm for 60 micron FCC particles in a 15 cm bed [Bolton and Davidson, (1988)] to as much as 10 mm for a the same particles in a 5 cm bed [Horio *et al.*, (1988)]. Thus, it may be considered to be at least several particle diameters thick. For very short residence times, the heat transfer from the particles to the wall will be controlled by the interfacial or wall heat transfer resistance. If the particles touch the wall, the wall resistance should be the same as that found for an emulsion layer in a bubbling bed [Decker and Glicksman, (1983)],

$$\frac{h_w d_p}{k_g} = 12 + 0.5\,RePr \qquad (1)$$

where the second term on the right hand side of Equation (1), which is due to gas convection augmentation, should only be important for large particles and for beds at elevated pressures. If, however, the particles are separated from the wall by a thin gas layer, then the added thermal conduction resistance of the gas layer will reduce the value of h_w. The magnitude of the effect of the gas layer on the wall resistance will depend upon the thickness of the layer.

When the cluster is first in contact with the walls, the heat flux on surface area dA is

$$dq = h_w \left(T_B - T_W\right) dA \tag{2}$$

If the particle remains at an active heat transfer surface, the particle temperature will approach the temperature of the wall, and the heat transfer rate will fall drastically. The influence of this on the heat transfer rate is a function of the thermal properties of the particle layer at the wall and the contact time for the particles at the wall. The former can be dealt with using conventional heat transfer models once the contact time can be established.

For short intervals, only particles adjacent to the surface will change in temperature. The time constant for a single particle can be found from an energy balance for that particle

$$\frac{\rho_s c_{p_s} \pi d_p^3}{6} \frac{dT}{dt} = \frac{24\, k_f}{d_p} \frac{\pi d_p^2}{4} \left(T_w - T_b\right) \tag{3}$$

where the average conduction heat transfer through the gas between the particle and the wall is $24k_f/d_p$ times the projected area of the particle. The particle time constant becomes

$$\tau_p = \frac{\rho_s c_{p_s} d_p^2}{36\, k_g} \tag{4}$$

For typical fluidized bed particles with a mean diameter of 250 microns, the time constant will be of order 0.1 seconds.

If the contact time is much less than the thermal time constant of the particle, Equation (1) applies for the entire contact time. For time periods of order one third to one tenth the thermal time constant, the particle temperature variation as given by Equation (3) must be included in the heat transfer analysis. For contact times greater than one third the thermal time constant, particles one or more rows removed from the wall become influenced by the heat transfer.

If radiation is neglected, heat transfer to the bed wall can be stated as an average of the heat transfer from clusters and dilute phases (Subbarao and Basu, 1986):

$$h = f h_c + (1\text{-}f) h_d \tag{5}$$

where h_c and h_d are the time-averaged heat transfer coefficients for the dense (cluster) phase and the dilute phase, respectively, and f is the fraction of the wall covered by clusters (dense phase). As the clusters move down the wall, they cool until they are shed and replaced by fresh material at the bed temperature. Mickley and Fairbanks (1955) suggested that a cluster of particles at the wall could be modeled as a homogeneous semi-infinite medium with an effective conductivity, density and specific heat. For transient heat transfer between "packets" of particles which remain at the wall for time t and then are displaced from the heat transfer surface:

$$q = \Delta T \sqrt{\frac{k_c c_{p_{cl}} \rho_{cl}}{\pi t}} \tag{6}$$

This expression for heat flux can be used to define a heat transfer coefficient for transient conduction within the dense phase (or emulsion phase):

$$h_e = \sqrt{\frac{k_c c_{p_{cl}} \rho_s \left(1 - \varepsilon_{cl}\right)}{\pi t}} \tag{7}$$

To account for the nonuniformity of particle packing near the heat transfer surface and the contact resistance between the particles and the wall, Baskakov (1964) introduced an additional "contact" thermal resistance between the wall and the packet:

$$R_w = \frac{1}{h_w} = \frac{\delta d_p}{k_f} \tag{8}$$

where δ ranges from 1/6 to 1/12 for bubbling beds. The exact expression for transient conduction from a semi-infinite body to a constant temperature surface with a series resistance is complicated. However, experimental measurements (Gloski, Glicksman and Decker, 1984) have shown that a close approximation to the actual heat transfer coefficient from a cluster, even at short times, is given by assuming that these two mechanisms, the contact resistance and the transient conduction to a homogeneous cluster of particles, act independently and in series with each other:

$$h_c = \left[\frac{1}{h_w} + \frac{1}{h_e}\right]^{-1} = \left[\frac{\delta d_p}{k_f} + \sqrt{\frac{\pi t}{k_{cl} c_{p_s} \rho_s \left(1 - \varepsilon_{cl}\right)}}\right]^{-1} \tag{9}$$

where the thermal conductivity of the cluster of particles can be calculated from the expression developed by Gelperin and Einstein (1971):

$$k_{cl} = k_f \left[1 + \frac{\left(1 - \varepsilon_{cl}\right)\left(1 - \frac{k_f}{k_s}\right)}{\frac{k_f}{k_s} + 0.28\varepsilon_{cl}^{0.63\left(\frac{k_s}{k_f}\right)^{0.18}}} \right] \tag{10}$$

Substituting Equation (9) into Equation (5) gives

$$h = f\left[\frac{\delta d_p}{k_g} + \sqrt{\frac{\pi t}{k_{cl} c_{p_s} \rho_s \left(1 - \varepsilon_{cl}\right)}} \right]^{-1} + \left(1 - f\right) h_d \tag{11}$$

4.2 Radiation

Heat transfer between the suspension and the wall as well as the core and wall takes place by radiation as well as convection at fluidized bed combustor operating temperatures. Kobro and Brereton (1986) measured heat transfer coefficients in a 2.5 MW_{th} pilot CFB combustor at room temperature (25 ^{o}C) and at a typical operating temperature (850 ^{o}C). Their data show that radiation varied from about 50 percent of the total heat transfer at a low bed density (10 kg/m^3) to 25 percent or less at a higher bed density (80 kg/m^3). Basu and Konuche's (1988) results are in general agreement with those of Kobro and Brereton.

Radiation will act in parallel to the other forms of heat transfer. If the simplified model of a contact resistance at the cluster-wall interface along with a transient heat transfer to a homogeneous cluster of particles is used, there will be radiation as well as conduction from a cluster to the wall. Thus h_w is supplemented by a radiative wall-to-cluster component h_r acting in parallel,

$$h_r = \frac{\sigma\left(T_w^4 - T_s^4\right)}{\left(\frac{1}{\varepsilon_w} + \frac{1}{\varepsilon_s}\right)\left(T_w - T_s\right)} \tag{12}$$

where T_s is the effective temperature of the cluster surface at any instant and ε_s is the effective emissivity of the cluster surface. As the cluster remains at the wall it will be cooled by both conduction and radiation. Wall radiation will be more sensitive than wall conduction to any temperature change since it varies as the cluster surface temperature to the fourth power. For example, when the cluster surface adjacent to a water cooled wall is reduced from 800 °C to 600 °C conduction heat transfer is reduced by 30 percent while radiation is reduced by 55 percent. For transient heat transfer through the cluster interior, radiation must also be considered. For heat transfer effects which extend many particle diameters into the cluster, the radiation contribution can be considered as an effective radiative conductivity k_r which is add to k_c given above in Equation (10) [Glicksman and Decker (1982)]. k_r can be approximated as

$$k_r = \frac{8}{9} d_p \sigma T^3 \tag{13}$$

Radiation from the cluster covered wall area must be considered separately from radiation from the bed to the portions of the wall covered by the dilute phase. In the latter case, the wall can exchange radiation directly with hot particles at the core of the bed or with particles in the intermediate temperature gradient zone found by Leckner (1991). h_d in Equation (5) must be replaced by the sum of dilute phase convection plus radiation. While the radiation from the clusters to the wall decreases rapidly with cluster residence time, the dilute portion of the wall continues to receive a high radiative flux from the core. Thus the total radiation heat transfer to the wall will be a strong function of the fraction of the wall covered by clusters as well as the mean time the clusters remain at the wall.

4.3 Overall Heat Transfer Model

Equation (11) can be rewritten to include the radiative terms

$$h = f\left[\frac{1}{h_w + h_r} + \sqrt{\frac{\pi t}{\left(k_{cl} + k_r\right) c_{p_s} \rho_s \left(1 - \varepsilon_{cl}\right)}}\right]^{-1} + \left(1 - f\right)\left(h_d + h_r\left(T_b\right)\right) \tag{14}$$

Where $h_r(T_b)$ is evaluated from Equation (12) with T_s replaced by T_b, the bulk temperature in the bed cross section. With k_c fixed by ε_c according to Equation (10), and the surface emissivity

fixed by ε_c and material properties, Equation (14) has six parameters related to the bed hydrodynamics which must be determined:

- f: fraction of wall covered by clusters
- δ: dimensionless effective gas layer thickness between wall and cluster
- t: time of contact between cluster and wall
- ε_c: void fraction of cluster
- h_d: dilute phase heat transfer coefficient
- ε_s: effective emissivity of the cluster surface

4.4 Evaluation of the Heat Transfer Parameters

Since the heat transfer tests conducted in conjunction with this study were performed in a cold scale model, only the first five parameters were evaluated. Radiation effects were considered to be negligible. Lints (1992) has conducted an extensive study to determine reasonable values for these parameters. In what follows, a brief summary of the parameters will be given along with suggested values which are, for the most part, improved approximations based on more recent experimental data and more a more thorough investigation of the hydrodynamics which control each parameter.

4.4.1 Cluster Void Fraction

An extensive examination of the cluster void fraction has been conducted by Lints (1992). Along with the examination of data in the literature, Lints used an impact probe to determine the structure of particle clusters at the wall. The frequency of particle strikes on the impact probe was used to determine the cluster solid fraction. In his analysis the cluster was assumed to be homogeneous, and a least-squares fit to the data gave the cluster strike frequency per unit depth of the probe. The cluster solid concentration was estimated by scaling those values using the results obtained with a calibrated channel flow. Figure 4.1 shows the data and model (solid line) of Lints plotted along with the data of Wu (1989), Dou (1990), and Louge (1990). All the data were taken in beds with nearly the same diameter [Wu (D=0.152m), Dou (D=0.152m), Louge (D=0.192m), Lints (D=0.20m)]. Also shown is the correlation proposed by Tung *et al.* (1988) (dashed line).

$$\varepsilon(r) = \varepsilon_{avg}^{\left[3.62\left(\frac{r}{R}\right)^{6.47} + 0.191\right]} \tag{15}$$

$$1 \geq \frac{r}{R} > 0.75$$

At r/R = 1, $\varepsilon_{cl} = \varepsilon_{avg}^{3.811}$. This correlation was used by Lu *et al.* (1990) to determine the void fraction in the cluster phase.

The cluster solid fraction appears to increase with average bed solid fraction. The functional relationship developed by Lints (1992) which gives better agreement to the data than the correlation of Lu *et al.*, will also be used in this study:

$$\alpha_{cl} = \alpha_{avg}^{0.5} \tag{16}$$

Figure 4.1
Cluster Solid Fraction as a Function of Average Cross Section Solid Fraction

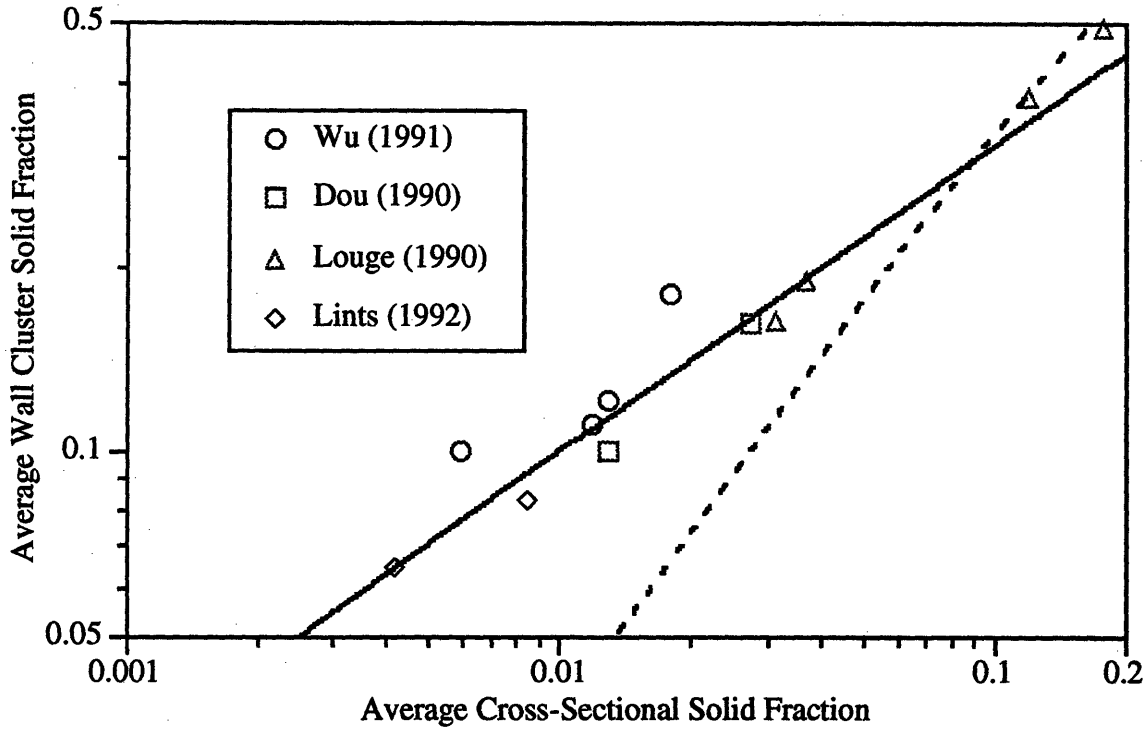

4.4.2 Time of Contact Between Wall and Cluster

The renewal model for the clusters at the wall requires the mean time or renewal time of the clusters at the wall to predict the heat transfer coefficient The discrepancy between the heat transfer coefficient measured for very short and long active heat transfer surfaces is primarily

due to the different contact time between the clusters and the active surface. In an actual circulating bed combustor, the water cooled walls will, in all likelihood, be much longer than the mean contact distance of a falling cluster at the wall. For long contact distances and times the renewal or emulsion resistances will be larger than the surface resistance. It is important to be able to predict the contact time in order to determine both radiative and convective heat transfer between the walls and clusters.

There have been very few measurements reported in the literature of the mean time or distance of a falling cluster at the wall. Bader, Findlay, and Knowlton (1988) measured a residence time of salt tracer particles in a CFB which exceeded 15 seconds. One possible explanation of this long residence time is the existence of one or more long periods of contact in the wall region between periods of material recycle to the bed core. Rhodes, Mineo, and Hirama (1992) made high speed video observations of the high density swarms along with a dilute phase. They found that the downward velocity of the swarms was independent of the superficial gas velocity as well as bed density. This is consistent with measurements made by Lints (1992). They determined the length of swarms from the measured duration and velocity as observed under magnification. However, given the limited field of view it is difficult to relate the swarm length to the mean distance the swarms move before they were displaced from the surface; the measured value of the swarm length reported appears to be smaller than the reported mean distances discussed below.

Most of the reported values for the mean distance a cluster moves while it remains at the wall are derived from the observed heat transfer behavior for different heat transfer lengths. When the heat transfer coefficient decreased with vertical distance down the surface, it indicates that the mean length is of the order of, or longer, than the heat transfer surface height. There is a disagreement between the values derived from Wu *et al.* (1987), measured on a vertical membrane wall which indicated vertical lengths greater than a meter, and Dou's (1990) results for a smooth surface which derived mean values of the mean vertical length between 2.5 and 12.5 cm, varying linearly with the particle diameter. In a later study Wu *et al.* (1991) derived the mean length by taking a cross correlation between two vertically separated heat transfer probes with short time constants. The derived mean vertical length for a smooth surface ranged from about 7 to 18 cm, with the length increasing with suspension density

$$L = 0.0178\, \rho_{susp}^{0.596} \qquad (17)$$

Rewriting in terms of the average solid fraction gives

$$L = 1.95\left(1 - \varepsilon\right)_{susp}^{0.596} \qquad (18)$$

The authors caution that since the degree of cross correlation was low some of the data was omitted especially at longer separation distances. They also made high speed video studies which indicated that clusters on vertical membrane walls had much longer mean lengths than those on smooth surfaces. They conclude that the mean length appears to be a strong function of the particular surface geometry, which they recommended should be studied in more detail.

A study by Rhodes *et al.* (1992) tends to confirm that the cluster fall length increases with increasing suspension density. Figure 4.2 shows the measured fall distances taken from the Rhodes study compared with curve fit of Wu (Equation 18).

Figure 4.2

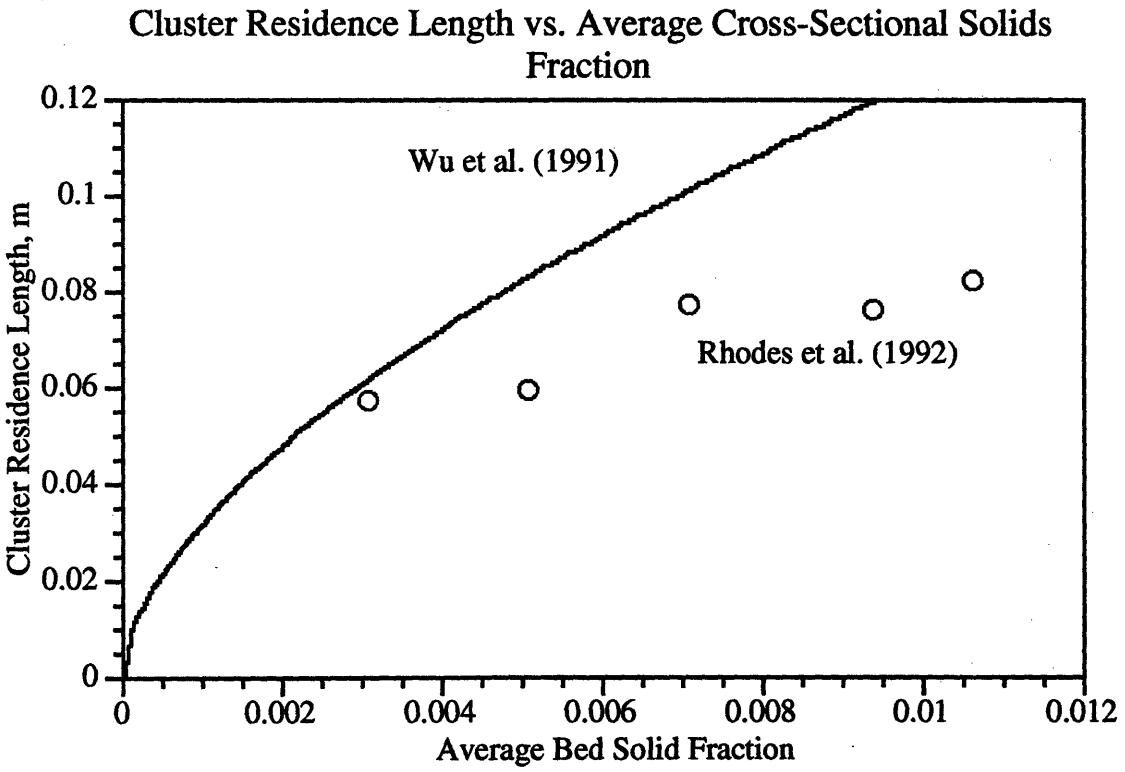

The influence of surface geometry is borne out by the results of work previously done [Glicksman, (1988)]. Visual studies indicated that the falling layer of clusters was disrupted and displaced from the wall by very small steps in the bed wall, with step widths of the order of one particle diameter. This may be important in resolving discrepancies such as those between Dou

and Wu *et al.*; very minor roughness elements or misalignments in wall sections can substantially alter the mean residence length. By the same token, if properly understood, controlled wall roughness elements have the potential for enhancing the wall heat transfer. Enhancement requires an adequate radial solids flux from the core to recover the wall with clusters a short distance below the disruption. The wall geometry must also be designed to avoid producing excessive erosion.

For the purposes of this study, the Wu correlation will be used with a modification based on the results of Dou mentioned above that the fall distance is linearly dependent on particle diameter. One would also expect that the fall distance would not be simply a function of the average bed density since when constructing cold scale models such a correlation would predict the same cluster fall length in each bed. For small scale models, this would indicate that a cluster could fall the entire length of the bed without leaving the wall. Visual observations of scale mode fluidized beds have indicated that this is not realistic. The correlation used was:

$$L = 1.95 \frac{d_p}{(d_p)_{Wu}} \left(1 - \varepsilon_{avg}\right)^{0.596} \qquad (18a)$$

where the particle diamter of Wu was 171 microns. The line on Figure 4.2a shows the Wu correlation as modified by Equation (18a) for the Rhodes data. While the chi-squared goodness of fit curve improved by a factor of 3 (300 percent), the amount of data available is sparse and more studies need to be undertaken to better quantify this parameter.

Figure 4.2a

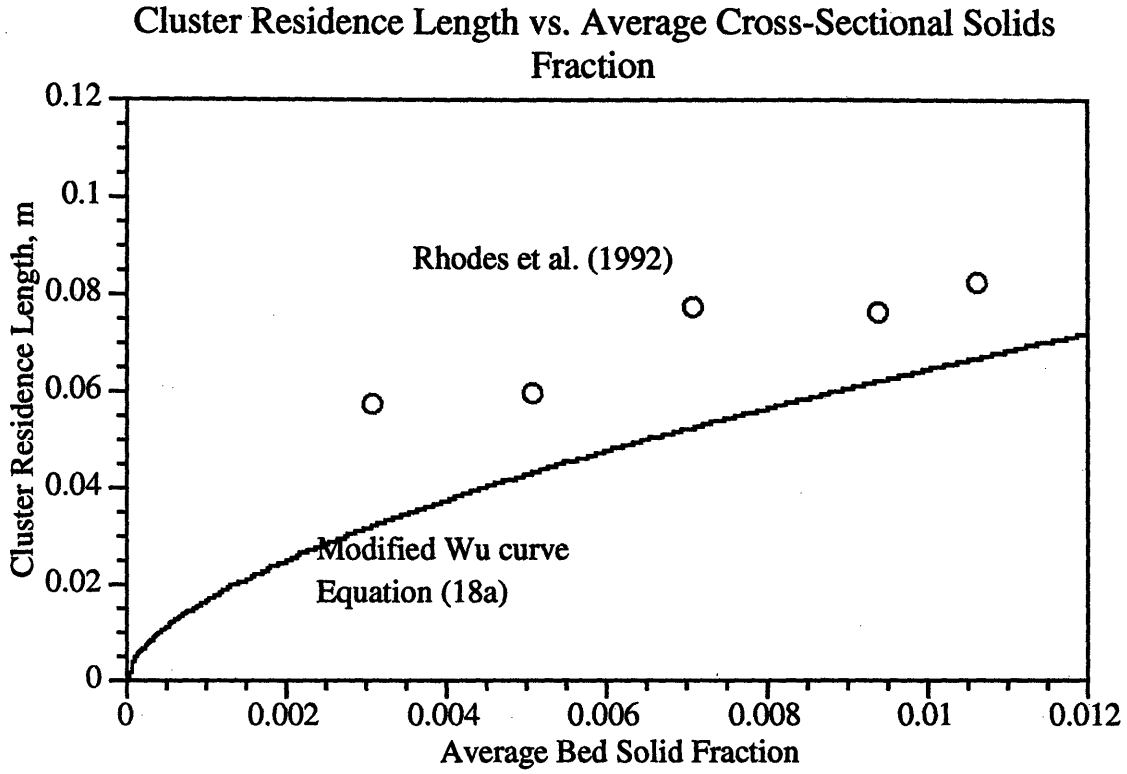

The time the clusters are at the wall can be defined as

$$t = \frac{L}{V_c} \tag{19}$$

assuming that the cluster velocity remains approximately constant.

The equation governing the motion of a cluster, considered as a horizontally aligned cylindrical body of unit length and diameter d_c neglecting any special interaction between the wall and the cluster is

$$\frac{1}{4}\pi d_c^2 \rho_c \frac{dV_c}{dt} = -C_{D_c} d_c \left(\frac{1}{2}\rho_f V_c^2\right) + \frac{1}{4}\rho d_c^2 (\rho_c - \rho_f) g \tag{20}$$

If the cluster is considered to be a sphere the equation of motion is

$$\frac{1}{6} p\, d_c^3 \rho_c \frac{dV_c}{dt} = -C_{D_c} d_c^2 \left(\frac{\pi}{8}\rho_f V_c^2\right) + \frac{1}{6}\pi d_c^3 (\rho_c - \rho_f) g \tag{21}$$

Scaling the time derivatives as $\frac{V_c^2}{d_c}$, the nondimensional form of Equations (20) and (21) read:

$$1 = -\frac{2}{\pi} C_{D_c} \frac{\rho_f}{\rho_c} + \frac{d_c g}{V_c^2} \frac{\left(\rho_c - \rho_f\right)}{\rho_c} \tag{22}$$

and

$$1 = -\frac{3}{4} C_{D_c} \frac{\rho_f}{\rho_c} + \frac{d_c g}{V_c^2} \frac{\left(\rho_c - \rho_f\right)}{\rho_c} \tag{23}$$

respectively.

Assuming that the cluster drag coefficient is a function of the Reynolds number based on cluster diameter, and that the cluster density is much larger than the gas density, the following nondimensional groups appear as controlling parameters.

$$\left[\frac{\rho_c}{\rho_f}; \frac{g d_c}{V_c^2}; \frac{V_c d_c \rho_f}{\mu}\right] \tag{24}$$

Defining the cluster density as

$$\rho_c = \rho_s \left(1 - \varepsilon_c\right) \tag{25}$$

the controlling nondimensional groups are

$$\left[\frac{\rho_s}{\rho_f}; \frac{g d_c}{V_c^2}; \frac{V_c d_c \rho_f}{\mu}; \varepsilon_c\right] \tag{26}$$

If the structure of the cluster is cylindrical and approaches the wall with negligible velocity in the axial direction, a first order approximation of the cluster velocity can be found as:

$$V_c \cong \frac{-\frac{\frac{\pi}{4} d_c^2 \rho_c}{t} + \sqrt{\left(\frac{\frac{\pi}{4} d_c^2 \rho_c}{t}\right)^2 + \frac{\frac{\pi}{2} C_{D_c} d_c^3 \rho_c g}{\rho_f}}}{C_{D_c} d_c \rho_f} \tag{27}$$

The video recordings of Marzocchella *et al.* (1991) show that shape deformations and surface perturbations of clusters of solid particles were similar to deformations and perturbations which precede shattering of drops. Following their development and assuming that the cluster behaves as an impermeable continuum, shape deformations are related to the non-uniform aerodynamic pressure profiles set-up in the surrounding gas (Lane, 1951). A front wave perturbation can be due to Taylor interface instability (Taylor, 1950). Aerodynamic forces which govern the shape deformation of the cluster are proportional to $\rho_g V^2$ (Hinze, 1955), and gravity forces determining front surface perturbations are a function of $g(\rho_c - \rho_g)d_c$ (Clift, 1975).

Internal flows initiated by the deformation of the cluster set up viscous stresses, τ. If Hinze's analysis is applied to the case of a cluster, internal flow velocities are of the order of

$$\left(\frac{\tau}{\rho_c}\right)^{\frac{1}{2}} \tag{28}$$

and the viscous stresses counteracting τ are of order

$$\frac{\mu_c}{d_c}\sqrt{\frac{\tau}{\rho_c}} \tag{29}$$

where τ is the acting stress. The ratio of acting to counteracting forces is then

$$\frac{\tau}{\frac{\mu_c}{d_c}\sqrt{\frac{\tau}{\rho_c}}} \tag{30}$$

Depending on the forces controlling the break-up mechanism, the group yields two dimensionless numbers:

1. $$\frac{\rho_g V_{c_{sl}}^2}{\frac{\mu_c}{d_c}\sqrt{\frac{\rho_g V_{c_{sl}}^2}{\rho_c}}} = \frac{d_c V_{c_{sl}}}{\mu_c}\sqrt{\rho_c \rho_g} \tag{31}$$

Here, the aerodynamic forces control cluster breakup.

2. $$\frac{g\left(\rho_c - \rho_g\right) d_c}{\frac{\mu_c}{d_c}\sqrt{\frac{g\left(\rho_c - \rho_g\right) d_c}{\rho_c}}} = \frac{d_c}{\mu_c}\sqrt{g\left(\rho_c - \rho_g\right)\rho_c d_c} \tag{32}$$

Here, surface perturbations control cluster breakup.

From (31),

$$d_c \sim \frac{\mu_c}{V_{c_{sl}}\sqrt{\rho_c \rho_g}} \tag{33}$$

assuming that aerodynamic forces control cluster stability. Substituting Kynch's (1956) model for viscosity of dilute systems with first-order interaction effects gives:

$$d_c \sim \frac{\mu_f\left(1 + 2.5\alpha_c + 7.5\alpha_c^2 + O\left(\alpha_c^3\right)\right)}{V_{c_{sl}}\sqrt{\rho_s\left(\alpha_c\right)\rho_g}} \tag{34}$$

Equation (34) indicates that the cluster diameter depends on the cluster voidage, the fluid viscosity, the cluster/fluid slip velocity, and the solid and gas density. It should be noted that for higher solids fraction within the cluster, the equation for the apparent cluster viscosity merely becomes a more complex function of the cluster voidage [Happel and Brenner (1963)], and does not change the parameters which govern the cluster diameter as predicted by Equation (34).

If gravity forces control cluster deformations, Equation (32) gives

$$d_c \sim \left(\frac{\mu_c}{\sqrt{g\rho_c \rho_g}}\right)^{\frac{2}{3}} \tag{35}$$

Again utilizing Kynch's apparent viscosity equation:

$$d_c \sim \left[\frac{\mu_f \left(1 + 2.5\alpha_c + 7.5\alpha_c^2 + O\left(\alpha_c^3\right) \right)}{\rho_c \sqrt{g}} \right]^{2/3} \tag{36}$$

or

$$d_c \sim \left[\frac{\mu_f \left(1 + 2.5\alpha_c + 7.5\alpha_c^2 + O\left(\alpha_c^3\right) \right)}{\rho_s \alpha_c \sqrt{g}} \right]^{2/3} \tag{37}$$

Equations (34) and (37) may prove useful in determining critical values for the dimensionless parameter governing cluster breakup.

Table 4.1 shows typical wall cluster and bed parameters. The cluster data was taken from Rhodes (1992). Equation (27) does remarkably well in predicting the cluster fall velocity utilizing the experimentally determined cluster diameter. If cluster breakup in Rhodes' bed was governed by surface instabilities, the critical value for the dimensionless interface instability [Equation (32)] is 92000. If the cluster breakup is governed by aerodynamic forces (expansion of the cluster), the critical value for the dimensionless aerodynamic forces [Equation (31)] is 7725.

Table 4.1

Parameter	Equation or Source	Value
Particle Density	Rhodes *et al.* (1992)	2456 kg/m^3
Average Bed Solid Fraction in Upper Region	Various Researchers	0.01
Cluster Solid Fraction	$\varepsilon_c = \varepsilon_{avg}^{1/2}$ Lints (1992)	0.10
Cluster Apparent Viscosity	$\frac{\mu_c}{\mu_o} = \left(1 + 2.5\alpha_c + 7.5\alpha_c^2 + O\left(\alpha_c^3\right)\right)$ Kynch (1956)	2.44E-5 kg/m-s
Cluster Diameter	Rhodes (1992) Horio and Kuroki (1994)	~ 2 cm
Cluster Duration Time at Wall	Rhodes (1992)	0.08 s
Cluster Drag Coefficient	$C_{D_c} = 1 + 10Re_{d_c}^{-2/3}$ White (1975)	1.12
Cluster Velocity	Equation (27) [Measured by Rhodes (1992)]	0.54 m/s [0.3 - 0.4 m/s]
Critical Value of Dimensionless Parameter for Surface Perturbation Controlled Cluster Breakup	$\frac{d_c}{\mu_c}\sqrt{g\left(\rho_c - \rho_g\right)\rho_c d_c}$	92000
Critical Value of Dimensionless Parameter for Aerodynamically Controlled Cluster Breakup	$\frac{d_c V_{c_{sl}}}{\mu_c}\sqrt{\rho_c \rho_g}$	7725

From the visual study of Rhodes (1992) and from visual observation made during the course of this study, it appears that the clusters at the wall of a CFB are broken up by surface instabilities as opposed to aerodynamic forces which effect the cluster expansion ratio. If this is the case, estimations for the wall cluster size can be made utilizing Equation (32) with a critical value of 92000.

Horio (1992) has observed that clusters in the dilute *core* region of a CFB tend to get smaller with an increase in superficial velocity, all other parameters remaining constant. Assuming that an increase in superficial velocity corresponds to an increase in cluster slip velocity, this suggests that cluster size in the *core* region of a CFB is determined from a balance of aerodynamic and internal viscous stresses as given in Equation (31). Consistent with Equation (31) as the cluster slip velocity increases, the cluster diameter should decrease if all other parameters remain constant.

During the tests to determine the relationship between cluster diameter and superficial velocity, Horio *et al.* noticed that the cluster voidage seemed to increase with increasing superficial velocity - although the trend was not consistent for all cases. If the voidage did increase, the only other parameter in the surface perturbation equation [Equation (32)] which could compensate to keep this dimensionless group constant is the cluster apparent viscosity. The cluster diameter appears to a be a strong function of superficial velocity [Horio (1992)]. In their experiments, when the superficial velocity increased by a factor of two, the cluster diameter decreased by about a factor of four, and the cluster voidage increased by 20 percent. For the dimensionless parameter in Equation (32) to remain constant, the cluster viscosity would need to decrease by a factor of ten. The Kynch (1956) equation only predicts a decrease by a factor of 1.7. This indicates that this parameter does not adequately describe the force balance for a cluster in the core of a CFB.

If the same analysis is applied utilizing Equation (31), for a factor of two increase in gas superficial velocity [assuming the cluster slip velocity changes by about the same factor; a supposition supported by the data of Arena *et al.* (1992) and Horio and Kuroki (1994)], the change in apparent viscosity need only change by a factor of two. The Kynch equation predicts a change by a factor of 1.7. Considering the uncertainty in the cluster diameter measurements and error inherent in the viscosity calculation, Equation (31) appears to do a satisfactory job in describing the force balance on clusters in the core of CFB.

Table 4.2 presents data of Horio *et al.* (1992) which was used to calculate the critical value of the dimensionless parameter which governs cluster size in the core of a CFB [Equation (31)]. From the limited data available, a value on the order of 1500 can be used to determine cluster velocities in the core of a CFB.

Table 4.2

Parameter	Equation or Source	Value
Particle Density	Horio and Kuroki (1994)	1780 kg/m^3
Average Bed Solid Fraction in Upper Region	Horio *et al.* (1992)	~ 0.01 - 0.03
Cluster Solid Fraction	$\varepsilon_c = \varepsilon_{avg}^{1/2}$ Lints (1992) Measured (Horio *et al.* 1992)	0.10 - 0.17 0.09 - 0.25
Cluster Apparent Viscosity	$\frac{\mu_c}{\mu_o} = \left(1 + 2.5\alpha_c + 7.5\alpha_c^2 + O\left(\alpha_c^3\right)\right)$ Kynch (1956)	2.1E-5 - 3.8E-5 kg/m-s
Cluster Diameter	Horio and Kuroki (1994)	0.05 - 2.5 cm
Cluster Drag Coefficient	$C_{D_c} = 1 + 10Re_{d_c}^{-2/3}$ White (1975)	~ 1.1
Cluster Slip Velocity	Horio and Kuroki (1994) Equation (25)	0.0 - 0.6 m/s
Critical Value of Dimensionless Parameter for Aerodynamically Controlled Cluster Breakup	$\frac{d_c V_c}{\mu_c}\sqrt{\rho_c \rho_g}$	~ 1500

Returning to the discussion of the cluster fall velocity at the wall of a CFB, if the cluster is assumed to have a diameter typical of that in a circulating bed (about 2 cm, Rhodes (1992)), and is assumed to behave as an impermeable cylinder or sphere, the drag coefficient is nearly constant over typical CFB conditions (see Figure 4.3). Both drag correlations were taken from White (1974).

Figure 4.3

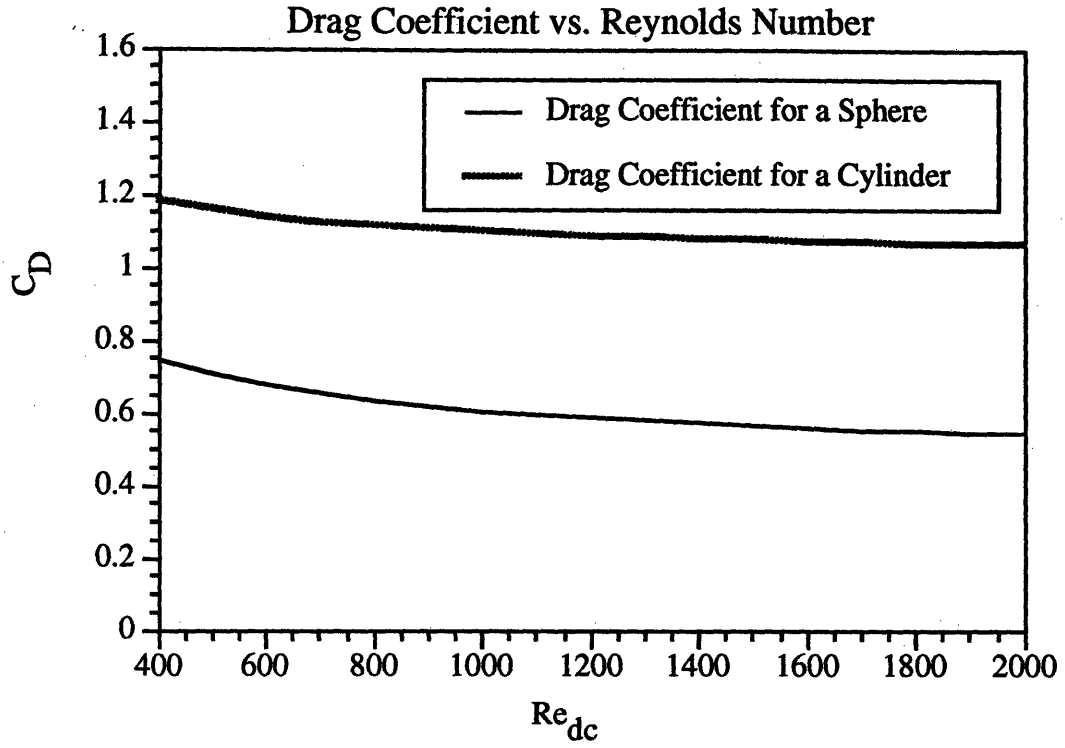

This suggests that the cluster velocity is only a function of the cluster voidage, the solid density, and the gas properties [see Equation (26)]. Assuming that measurements are taken in cold beds where the gas properties are air at ambient conditions, the cluster velocity will only vary with the cluster voidage and the solid density since the gas properties are constant. Additionally, in Section 4.4.1 it was shown that the cluster voidage scaled as the square root of the average bed voidage; this allows one to write the cluster velocity as a function of the solid density and the average bed voidage.

The next series of plots are included to provide an indication that the dimensionless groups identified in Equation (26) as the controlling parameters for cluster motion at the wall of a CFB are, in fact, correct. From (26) or (27),

$$V_{c_{sl}} = f\left(d_c, \rho_s, \rho_f, \varepsilon_c, C_D, t\right) \tag{38}$$

Figure 4.4 shows the cluster velocity measurements made by several researchers as a function of bed diameter. As expected, no clear trend is evident.

Figure 4.4

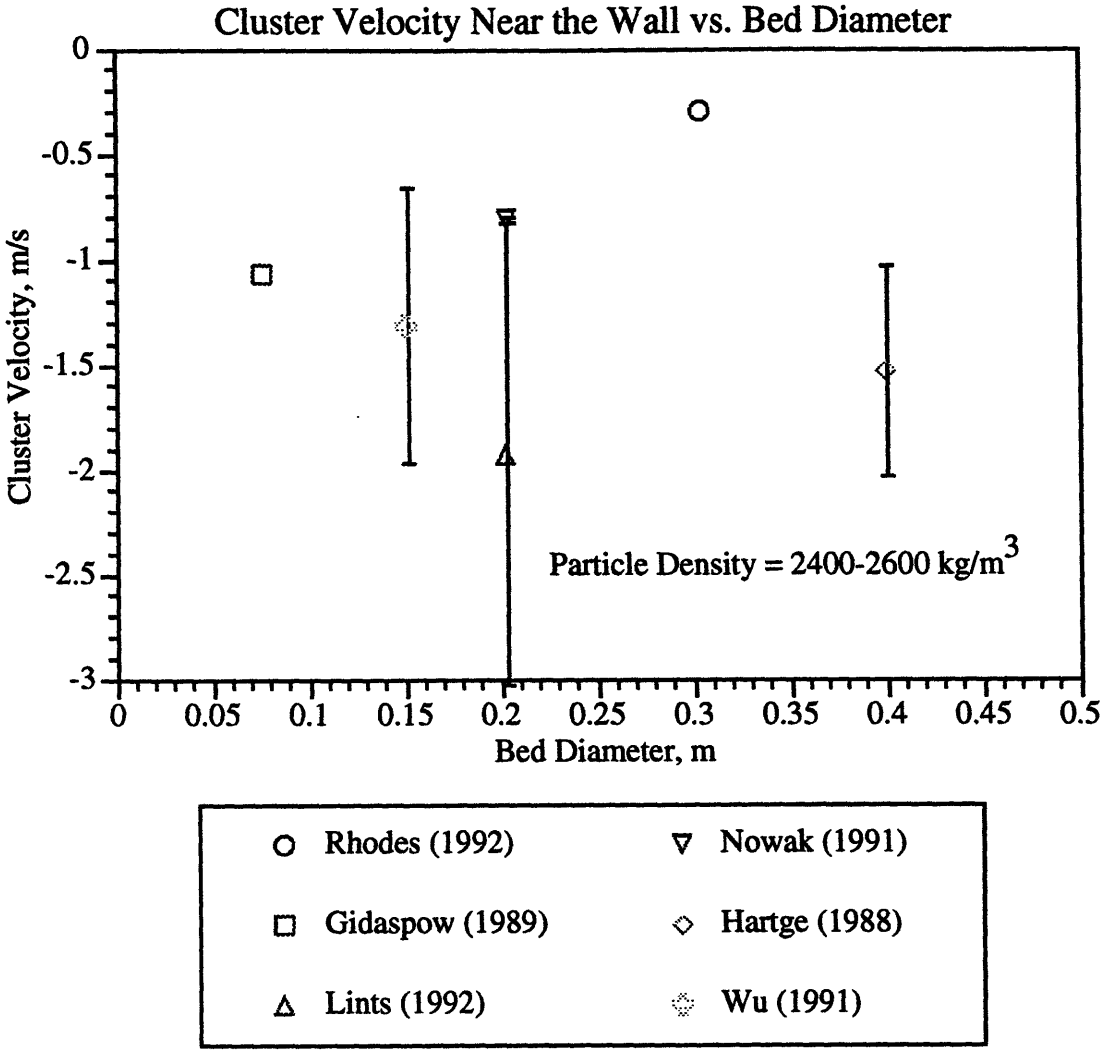

Figure 4.5 shows the cluster velocity as function of superficial velocity. No trend is apparent. This is consistent with other researchers (Lints, 1992, Wu, 1991). This provides another indication that Equation (33) is not the correct functional relation for the cluster diameter since as the superficial velocity increases, the cluster slip velocity increases if the downward cluster velocity remains nearly constant. However, if Equation (33) is substituted into Equation (27), one would predict that the cluster velocity is a function of the cluster slip velocity, which is not supported by Figure 4.5.

Figure 4.5

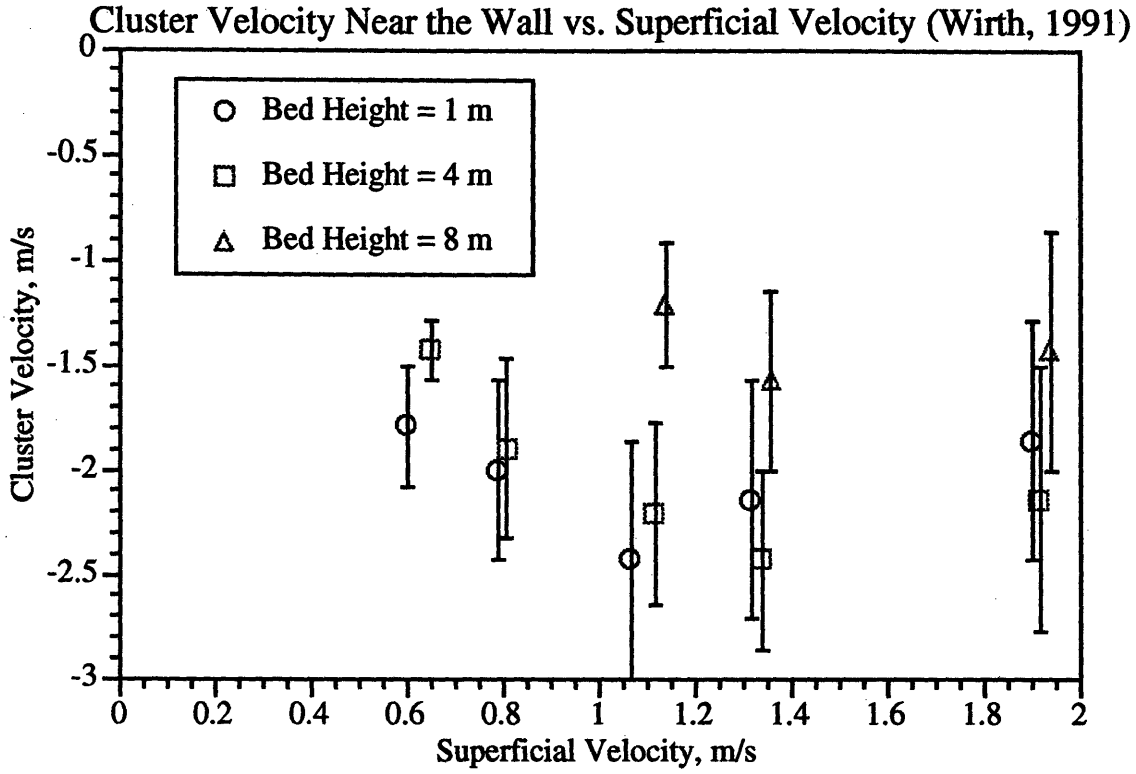

Figure 4.6 shows the cluster velocity as function of average solid fraction. The only clear trend in the cluster velocity as a function of average bed solid fraction occurs with the data by Wirth *et al.* (1991). There are not enough points to discern a trend from the other two sets of data. It is clear from Figure 4.6 that solid density does have an impact on cluster fall velocity. The magnitude of the cluster velocity tends to decrease with decreasing solid density at a given average bed solid fraction.

Equation (27) does predict that the cluster velocity is a function of average bed solid fraction since the cluster solid fraction was found to be a function of the average bed solid fraction. The solid line in Figure 4.6 is the predicted trend in cluster velocity as a function of average bed solid fraction determined from Equation (27) assuming a cluster diameter of 2 cm, time at the wall of 0.08 seconds [from Rhodes (1992)], and a particle density of 2500 kg/m^3. It is evident from Figure 4.6 that the predicted effect of the average bed cross section solid fraction is very weak.

Figure 4.6

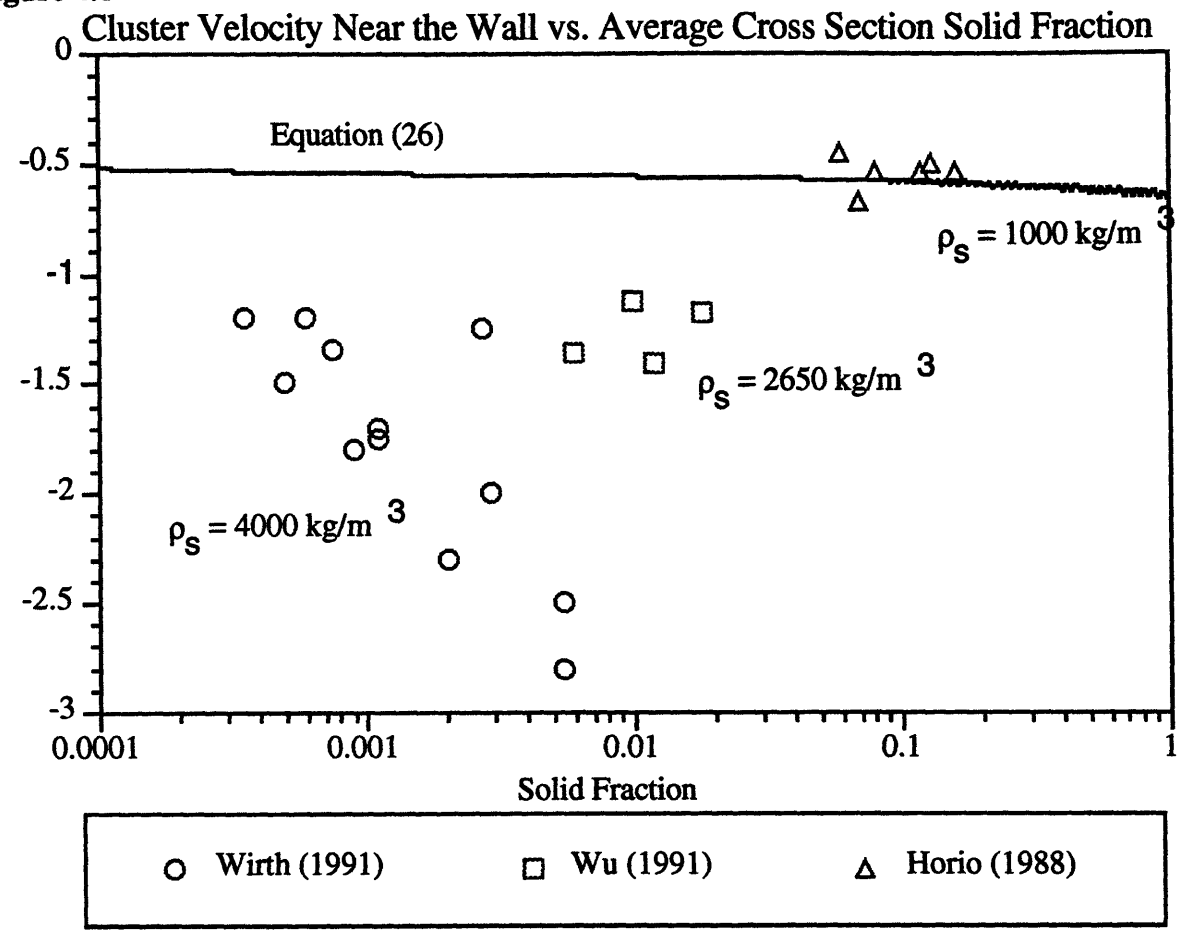

Figure 4.7 shows the cluster velocity as a function of particle diameter for particle densities which were in the range of 2350-2600 kg/m^3. It does not appear that the particle diameter has a significant impact on cluster velocity. Marzocchella *et al.* (1991) also found this to be the case when determining fall velocities of cylindrical clusters of known initial diameter and length. The characteristic fall velocities were on the order of that for a solid horizontal cylinder with a density equal to the particle density times the cluster solid fraction and a diameter equal to initial cluster release diameter (3.2 cm). The magnitude of the cluster fall velocity depended on particle diameter only insofar as the interparticle forces changed when there was an extreme change in particle diameter. This affected the cluster breakup mechanism and, therefore, the maximum velocity the cluster achieved before breakup. If the particles were in the same Geldart particle classification group, they predicted there would be no change in cluster fall velocity.

Figure 4.7

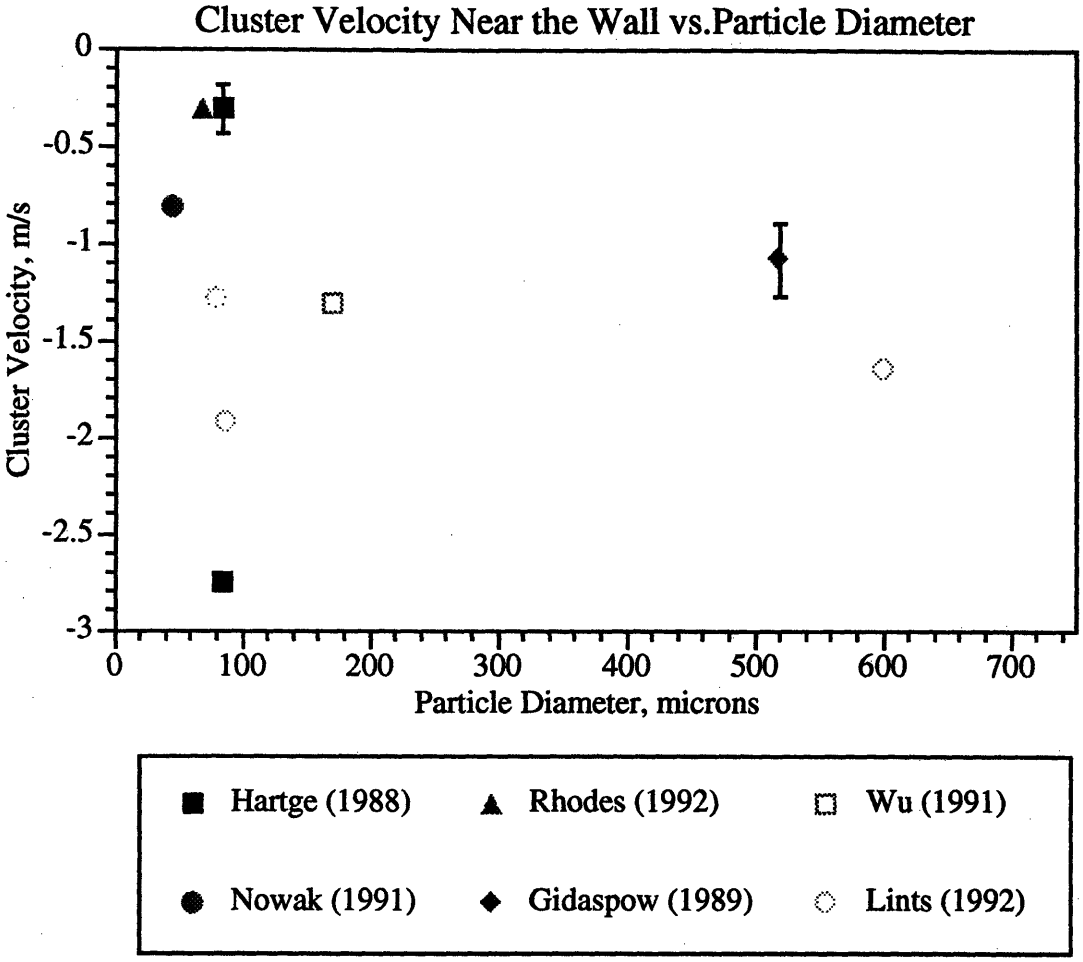

Figure 4.8 shows the cluster velocity as a function of solid density along with a linear least squares fit of the data. While not strong, there does seem to be a trend towards a higher magnitude of cluster velocity with increasing solid density.

Figure 4.8

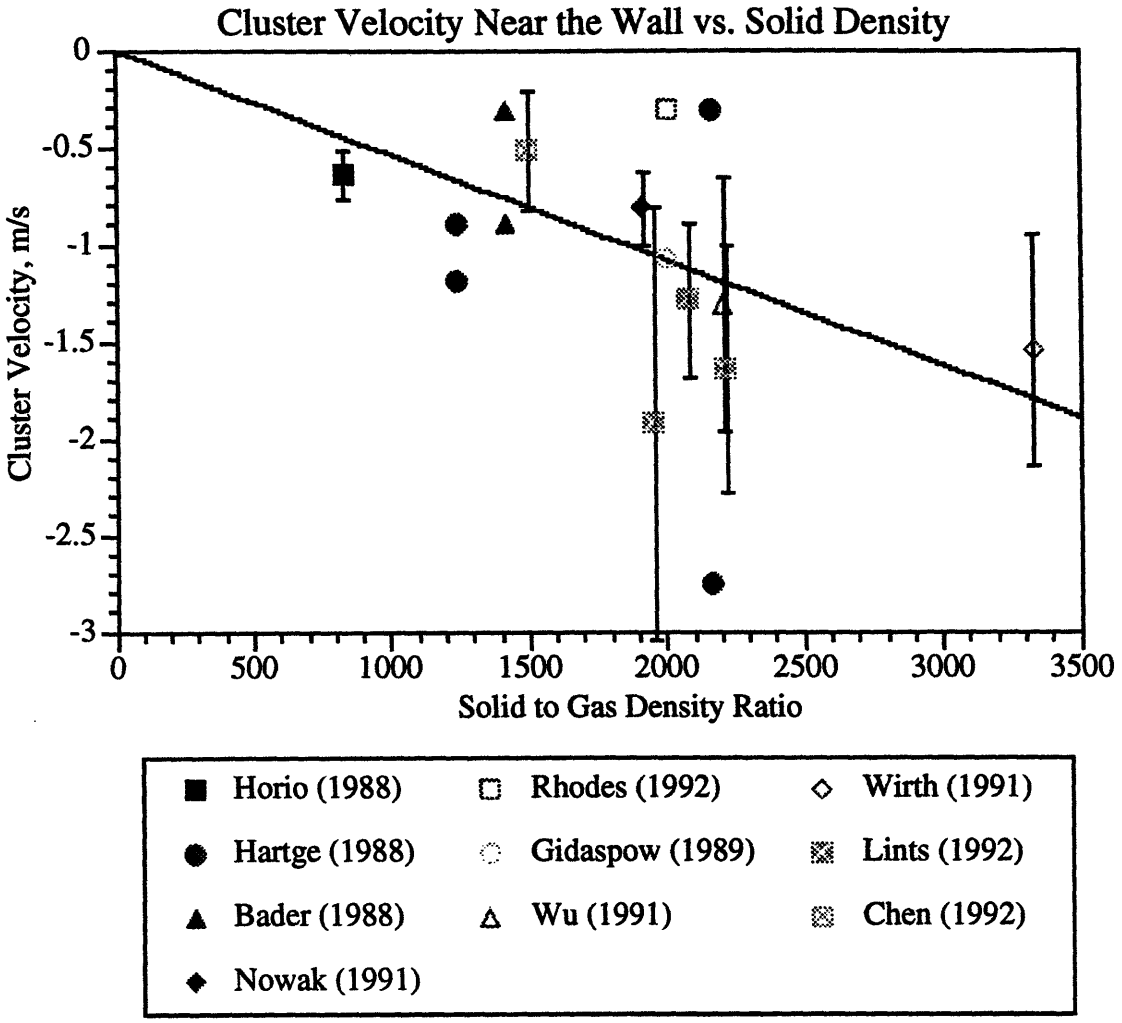

For the purposes of this model, since the functional relationship between the cluster velocity and average bed solid fraction is not clear or strong, the cluster velocity will only be correlated with the solid density. The correlation should be used with caution since one would predict that the average bed solid fraction should have an impact on the cluster velocity based on Equation (26). Figure 4.9 presents the results of a linear least squares fit which resulted in the following correlation:

$$V_c\left(\frac{\rho_f}{g\mu_c}\right)^{1/3} \cong 0.01\left(\frac{\rho_f}{\rho_s}\right) \tag{39}$$

Figure 4.9

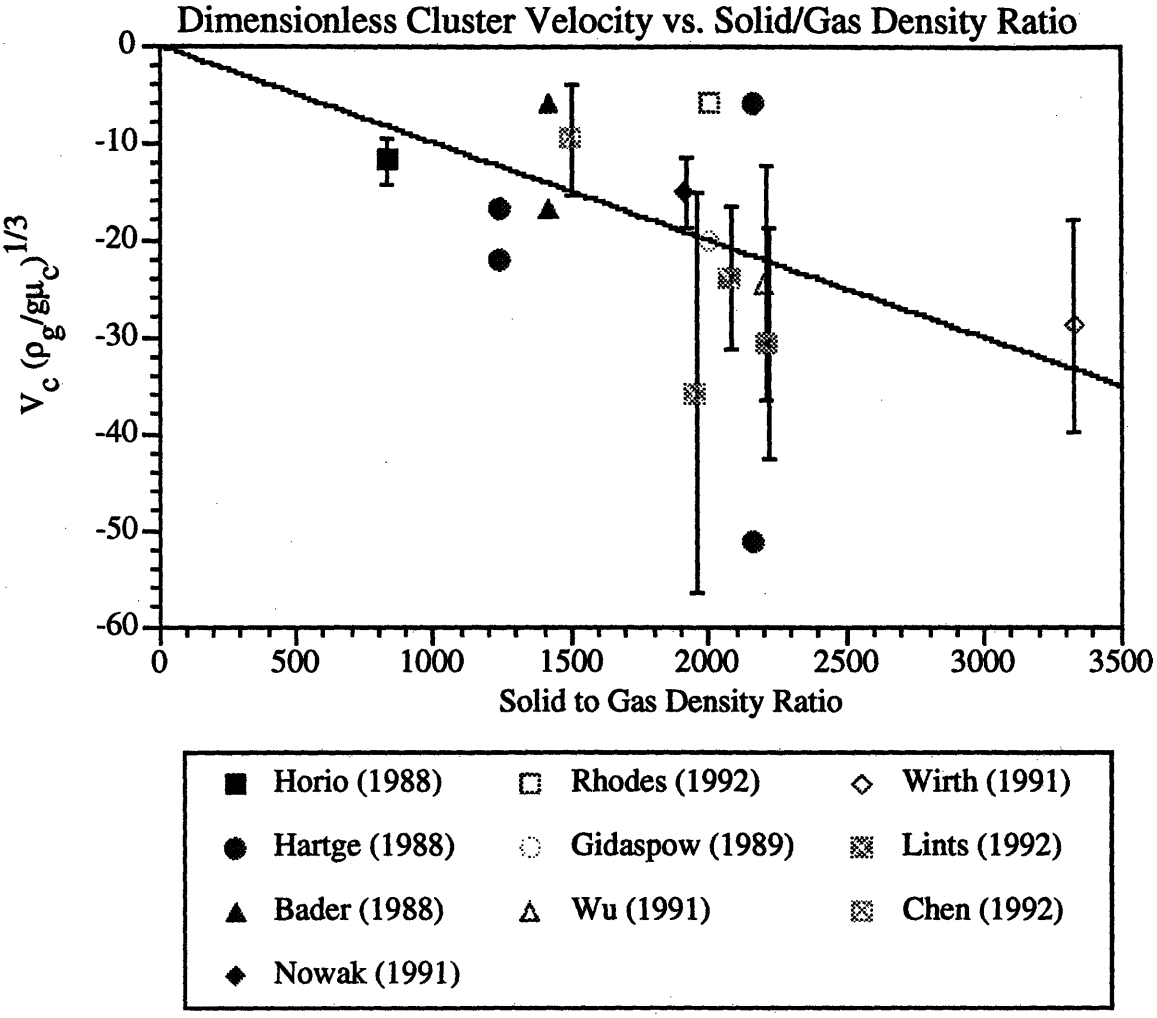

If Equation (32) at its critical value is substituted into Equation (27), the equation for the velocity of a wall cluster is:

$$V_c \cong \frac{-\frac{\frac{\pi}{4}\rho_s\alpha_c}{t}\left(\frac{92000\mu_c\sqrt{g}}{\rho_s\alpha_c}\right)^{4/3}}{C_{D_c}\left(\frac{92000\mu_c\sqrt{g}}{\rho_s\alpha_c}\right)^{2/3}\rho_f} + \frac{\sqrt{\left(\frac{\frac{\pi}{4}\left(\frac{92000\mu_c\sqrt{g}}{\rho_s\alpha_c}\right)^{4/3}\rho_s\alpha_c}{t}\right)^2 + \frac{\frac{\pi}{2}C_{D_c}\left(\frac{92000\mu_c\sqrt{g}}{\rho_s\alpha_c}\right)^2\rho_s\alpha_c g}{\rho_f}}}{C_{D_c}\left(\frac{92000\mu_c\sqrt{g}}{\rho_s\alpha_c}\right)^{2/3}\rho_f} \quad (40)$$

Figure 4.10 shows the same data if the relation between the cluster velocity and the solid density ratio is assumed predicted by Equation (40). The average cross-sectional solid fraction was assumed to be 0.01, and the time of contact at the wall was taken from the study of Rhodes (1992) (0.08 seconds).

Figure 4.10 shows that the Equation (40) predicts that the cluster velocity is a very weak function of the solid density. This is consistent with the findings of Lints (1992). Equation (40) also predicts that the magnitude of the cluster velocity has a constant value of about 1 m/s. This is of the same order as nearly all experimental data. Both curve fits [linear least squares and Equation (40)] have nearly the same value of the chi-squared goodness of fit parameter. While neither of the curve fits have a particular advantage, Equation (40) has more physical significance. Therefore, Equation (27), with the cluster diameter determined from Equation (32) (with a critical value of 92000) will be used as the basis for the determination of the cluster velocity. The residence time of the cluster will be determined using Equation (19).

Figure 4.10

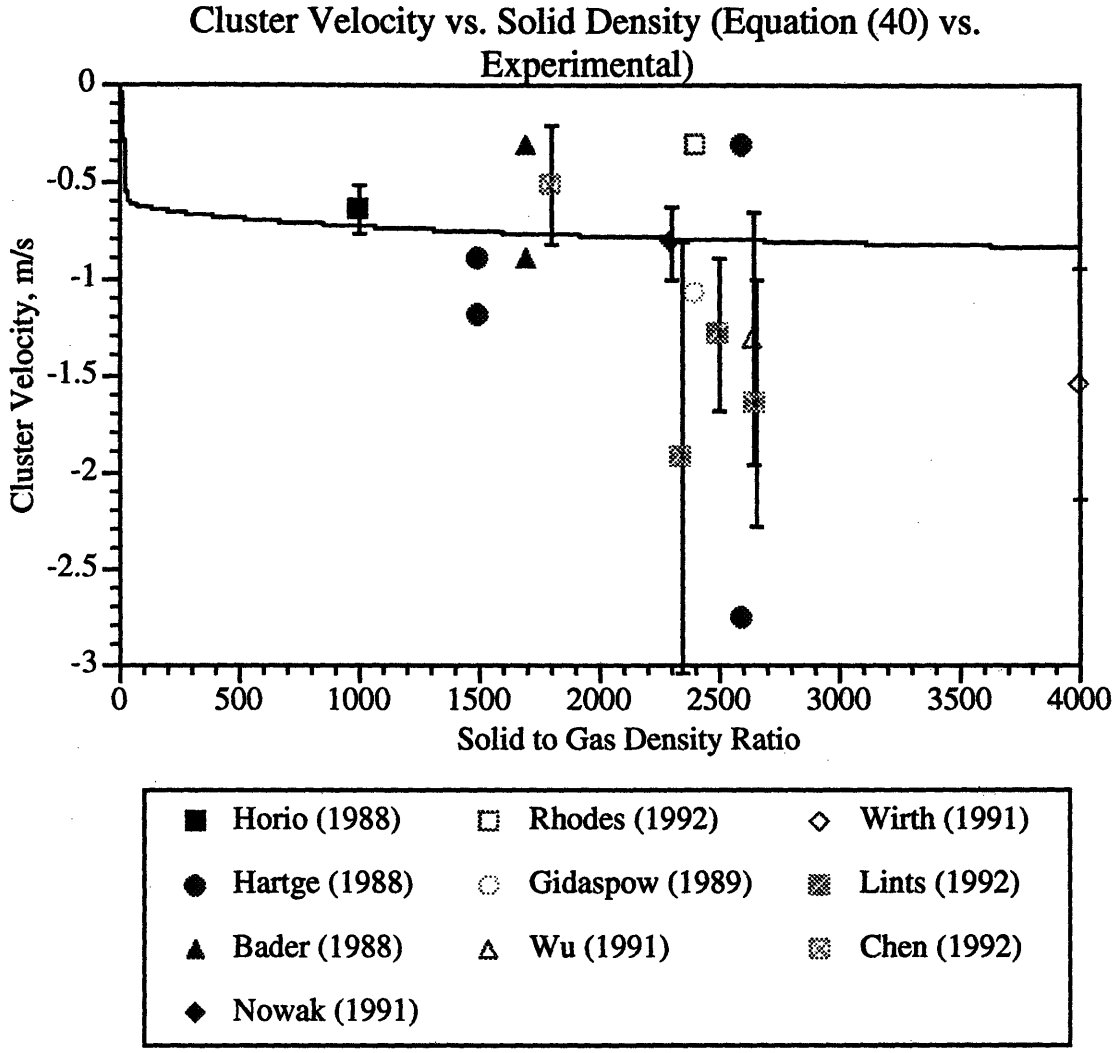

Finally, Figure 4.11 shows the variation in cluster velocity with the time at the wall. There is a significant deviation in the cluster velocity over the range of time used in the plot. In the range most often cited by authors (0.05 to 0.15 seconds), the predicted cluster velocity range is -0.33 to -1.0 m/s; values typically measured in CFB's.

Figure 4.11

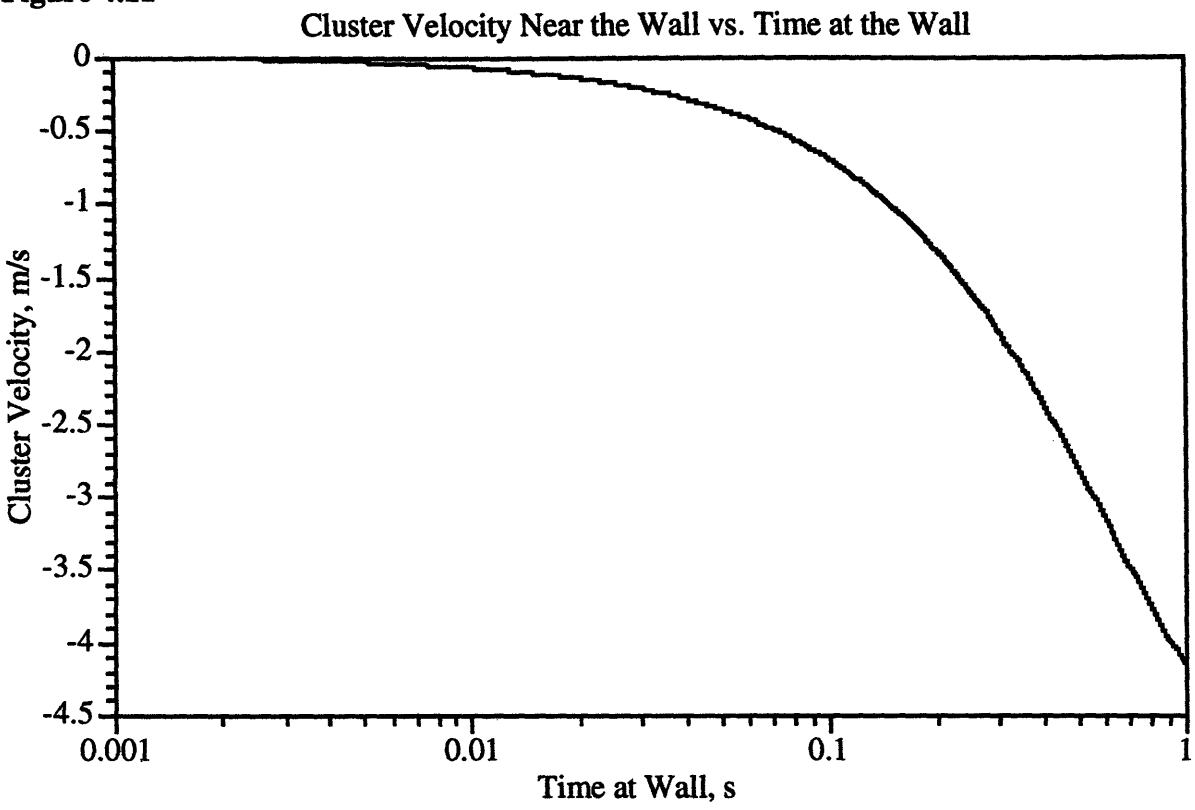

Glicksman (1988) has proposed a model for the cluster velocity in which the cluster is taken as a sheet N particle diameters thick. The sheet is accelerated by gravity down the wall and retarded by shear at the wall and at the interface with the up-flowing core. Assuming the sheet moves as a rigid body, the equation of motion for a sheet of unit depth is

$$M\frac{d^2x}{dt^2} = Mg - \tau_w - \tau_c \tag{41}$$

with the mass per unit of wall perimeter given as

$$M = \rho_s\left(1 - \varepsilon_c\right)Nd_p dx \tag{42}$$

When the particle layer is less than the viscous sublayer, the wall shear will be the controlling flow resistance.

The maximum velocity of the falling particles occurs when the weight of the sheet equals the shear stress at the wall. Taking the shear stress as laminar then it is proportional to the relative velocity

$$\tau_w = cv = c\frac{dx}{dt} \tag{43}$$

the maximum fall velocity is then

$$V_{c_{max}} = \frac{Mg}{c} \tag{44}$$

Equation (41) can then be written as

$$M\frac{d^2x}{dt^2} = Mg - \frac{Mg}{V_{c_{max}}}\frac{dx}{dt} \tag{45}$$

The solution of Equation (45) with an initial condition of zero velocity at time zero is

$$V_c = V_{c_{max}}\left[1 - e^{-gt/V_{c_{max}}}\right] \tag{46}$$

where the maximum fall velocity can be found if the wall shear and the average thickness of the sheet of particles is known.

Glicksman (1988) measured a maximum fall velocity of between 1.2 to 2 m/s. Equation (46) was shown to give reasonable estimates of cluster fall velocities by Lints (1988). If a value of 1.5 m/s is used for V_{max}, Figure 4.12 shows the predicted velocity time curve using Equation (46) and also that predicted by Equation (40). The two equations are in remarkable agreement in the area of interest (between 0.05 and 0.15 seconds). This indicates that either equation can be used in order to estimate the cluster fall velocity. Equation (40) has the advantage that the maximum fall velocity is not required.

Figure 4.12

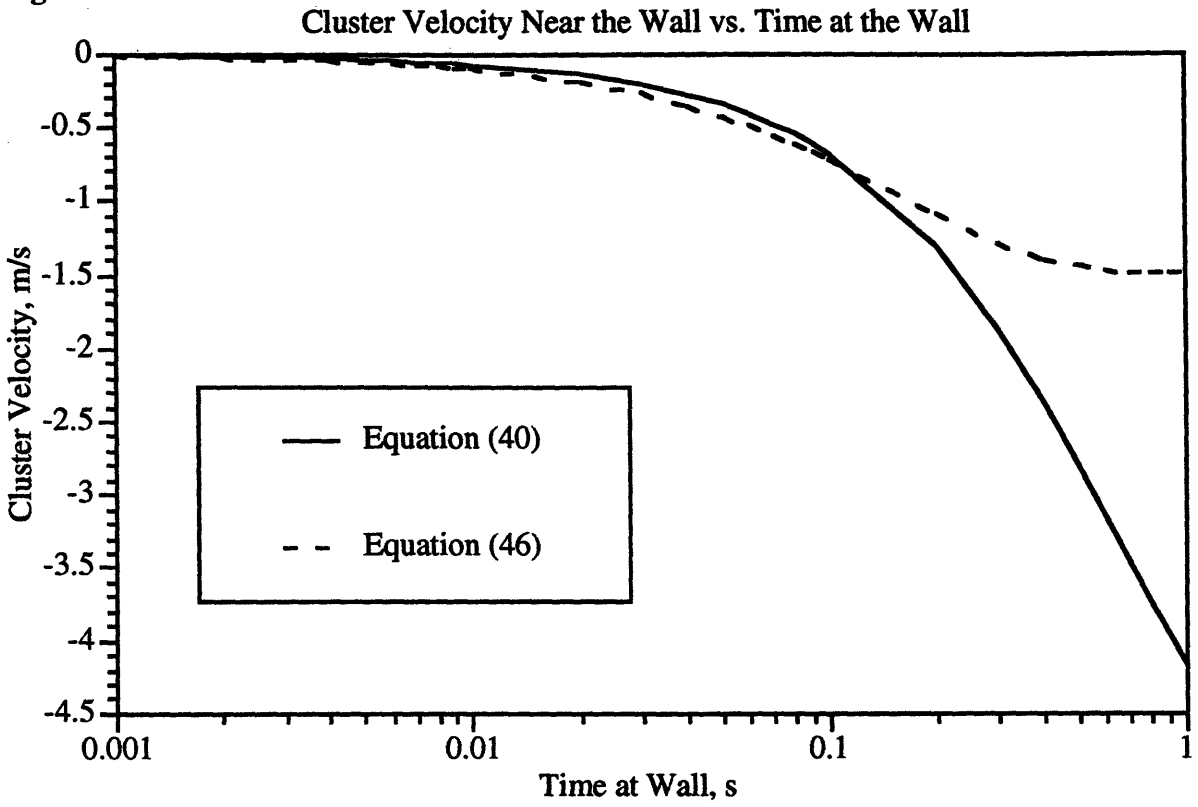

It is evident that because of the significant impact of the time the cluster is at the wall on the cluster fall velocity, this parameter needs to be investigated further in order to provide better input into the cluster velocity model.

4.4.3 Effective Gas Layer Thickness Between Wall and Cluster

The gas layer thickness between the wall and the cluster was investigated in detail by Lints (1992). Lints used an impact probe to determine the standoff distance to the first layer of clusters. He found that the gas layer is actually a dilute gas/solid suspension which has nearly the same thermal conductivity as the gas alone. Figure 4.13 shows a plot of the gas layer thickness nondimensionalized by the particle diameter for a variety of operating conditions. The least-square power curve fit to the experimental data gave the expression:

$$\delta = 0.0282\ \alpha_{avg}^{-0.59} \qquad (46)$$

where δ is the gas layer thickness nondimensionalized by the particle diameter. Lints found that δ ranged from about 0.2 to 1, and tended to increase with increasing superficial gas velocity and decrease with increasing average bed density. For an extensive discussion of the measurements of the gas layer thickness, the reader is referred to Lints (1992).

Figure 4.13

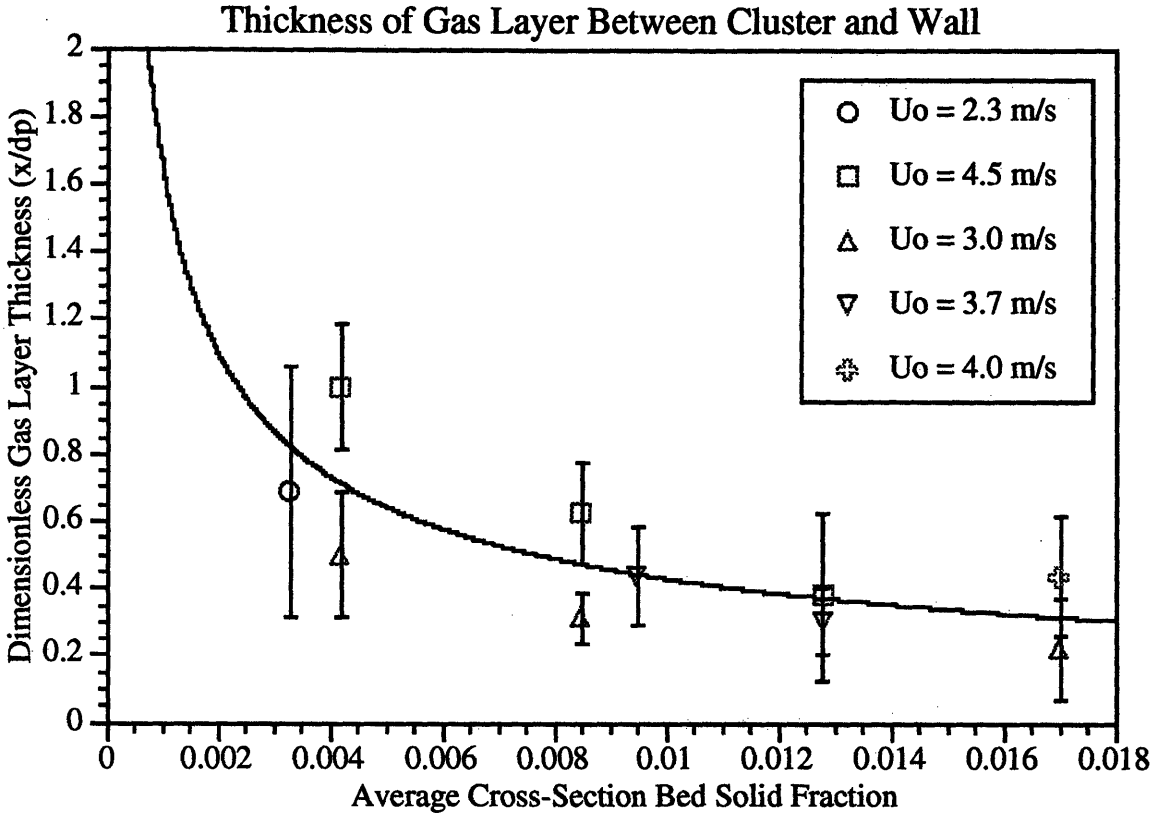

One possible cause for the gas layer thickness is lift forces which arise from the movement of particles in a shear flow. The equations of motion for a dense particle moving in a shear flow when the main flow is directed vertically upwards are:

In the streamwise direction

$$\frac{4\pi}{3} d_p^3 \rho_p \frac{du_s}{dt} = -6\pi\mu d_p \left(u_s - u_f\right) - \frac{4\pi}{3} d_p^3 \left(\rho_s - \rho_f\right) g \qquad (48)$$

In the transverse direction

$$\frac{4\pi}{3} d_p^3 \rho_p \frac{dv_s}{dt} = -6\pi\mu d_p \left(v_s\right) - 6.46\,\mu \frac{d_p^2}{\nu^{\frac{1}{2}}} \left(u_s - u_f\right) \left(\frac{du_f}{dy}\right)^{\frac{1}{2}} \qquad (49)$$

Equation (48) is a force balance on the particle in the direction of flow (x-direction) where x is positive upward. Equation (49) is the force balance in the y-direction, y being taken as zero at the wall, increasing positively toward the center line of the channel. The subscripts s and f refer to the particle and fluid respectively. The first terms in on the right hand side of both equations are Stokes friction force terms. The second term in Equation (48) is the gravitational term, negative for upward flow which was assumed here. The second term in Equation (49) is Saffman's (1965,1968) shear-flow lift term, which is negative (toward the wall) when the particle velocity in the positive x-direction (upwards) (u_s) is greater than the local stream velocity (u_f).

In viscous motion through a stagnant fluid in the absence of external forces, the Stokes drag is the only force acting on the particle. However, the viscous sublayer is not stagnant. It is characterized by very steep velocity gradients. A sphere in a viscous shear flow experiences lift force in the direction of higher slip velocity. This has been demonstrated by many investigators in various types of flows such as liquid/solid (Segre and Silberberg, 1962), gas/solid (Lee and Durst, 1982), and gas/liquid (Charles and Okinowo, 1974). The Saffman lift force has proved to be successful in aiding in the prediction of particle deposition rates to the walls of dilute pneumatic lines.

Most researchers who considered the possibility of the shear-flow lift force causing radial migration were reluctant to accept it on the ground that the magnitude of the lift force was too small to produce such an effect. If the expression derived by Saffman (1965) for the lift force experienced by a small sphere moving in an *unbounded* viscous shear flow is used

$$F_L = \frac{6.46\mu(u_s - u_f)d_p^2}{\nu^{0.5}}\left(\frac{du_f}{dy}\right)^{0.5} \tag{50}$$

the ratio of the shear lift flow force to the Stokes drag force is

$$\frac{|F_L|}{|F_s|} = \frac{6.46(u_s - u_f)d_p}{6\pi\nu^{0.5}(v_s)}\left(\frac{du_f}{dy}\right)^{0.5} \tag{51}$$

Looking at Equation (51), in a viscous sublayer, even if the axial particle/gas slip velocity is not large in that region, the ratio of the axial particle/gas slip velocity to the particle transverse

velocity may be significant yielding a significant ratio of F_L to F_S and having a measurable effect on particle motion.

Saffman (1965) and McLaughlin (1991) considered the lift force acting on a small sphere in an unbounded linear shear flow. Cox and Hsu (1977) used the theory developed by Cox and Brenner (1968) to obtain analytical expressions for the migration velocity of a particle sedimenting parallel to a vertical wall. Their results are valid provided that the Reynolds number based on the distance to the particle from the wall and a characteristic flow velocity is small compared to unity. This assumption implies that the wall lies within the 'inner' region of the particle disturbance flow. Vasseur and Cox (1976) used the Cox-Brenner theory to obtain numerical results for the inertial migration velocity of a sphere sedimenting between two vertical walls.

Relatively little information is available about the situation in which the wall lies in the outer region of the disturbance flow. Vasseur and Cox (1977) removed the restriction $Re_l << 1$, where l is the distance between the particle and wall, for the case of a particle translating through a stagnant fluid next to a single planar wall or between two parallel walls. The only restriction in their analysis is that the Reynolds number based on the sphere diameter and the sedimentation velocity of the sphere should be small compared to unity.

Drew (1988) extended Saffman's analysis by including the effects of a distant wall. Drew assumed that, to zeroth order in inertial effects, the sphere moves parallel to a rigid flat wall. He further assumed that $a << l$, where a is the sphere radius and l is the distance between the center of the sphere and the wall, so that the sphere may be treated as a point source acting on the fluid. Finally, he assumed that the sphere was sufficiently far from the wall that inertial effects were of the same order as viscous effects when the distance of the sphere was of order l. With these assumptions, he argued that the wall effects could be obtained by solving a fourth-order ordinary differential equation for the Fourier transform of the disturbance to the normal component of velocity due to the presence of the wall. Drew solved the ordinary differential equation by numerical means.

Assume that a rigid sphere is located at the origin of a Cartesian coordinate system and that, in the absence of the sphere, the velocity profile is $\mathbf{v}_f = Gx\mathbf{e}_3$, were $\mathbf{e}_3$ is a unit vector in the z-direction and G is the shear rate of the undisturbed flow. A planar, rigid wall is located at x=-l and it is assumed that the sphere moves parallel to the wall at velocity $-u_{rel}\mathbf{e}_3$ (u_{rel} is the velocityof the sphere relative to the undisturbed fluid). In this frame of reference, the wall moves

at velocity $-Gle_3$. It is required to derive an expression for the x-component of the force acting on the particle. It is convenient to pose the problem in a frame of reference moving with the particle so that the fluid velocity field is time-independent. There are two different ways of justifying the assumption of time-independent flow. One may assume that a force equal and opposite to the lift force acts on the sphere and prevents it from migrating. An alternative is to assume that the migration velocity is very small in comparison with the sedimentation velocity so that one can treat the problem as quasi-steady. This assumption can be verified in a self-consistent manner.

The fluid surrounding the sphere is incompressible and Newtonian. When written in terms of the disturbance velocity created by the sphere, $\mathbf{v}$, and the disturbance velocity in the x-direction, the Navier-Stokes equation takes the form [see Saffman (1965) or McLaughlin (1993)]

$$\mathbf{v}_f \cdot \nabla \mathbf{v} + \left(u_{rel} + Gx\right)\frac{\partial \mathbf{v}}{\partial z} + Gv_1\mathbf{e}_3 = -\nabla\frac{p}{\rho_f} + \nu\nabla^2\mathbf{v}$$

The boundary conditions on $\mathbf{v}$ are that it must vanish at infinite distance from the sphere and it must be consistent with rigid no-slip boundary conditions on the surface of the sphere.

Even though Re_G and Re_s are small compared to unity, at sufficiently large distances from the sphere, inertial effects are comparable in magnitude to viscous effects. In this outer region, the Navier-Stokes equation may be approximated by

$$\left(u_{rel} + Gx\right)\frac{\partial \mathbf{v}}{\partial z} + Gv_1\mathbf{e}_3 = -\nabla\frac{p}{\rho_f} + \nu\nabla^2\mathbf{v} - \frac{\mathbf{F}}{\rho_f}\delta(\mathbf{r}) \tag{52}$$

where $\mathbf{r}$ denotes the position vector of a point in the fluid and $\mathbf{F}$ denotes the force exerted by the fluid on the particle to zeroth order in inertial effects, $\mathbf{F} = 6\pi\mu a u_{rel}\mathbf{e}_3$, were a is the sphere radius.

The disturbance flow velocity field is assumed to be incompressible:

$$\nabla \cdot \mathbf{v} = 0 \tag{53}$$

McLaughlin (1991) considered the case of sphere translating through an unbounded fluid. In this case, one assumes that the disturbance flow vanishes at large distances from the particle

$$\mathbf{v} = 0, \mathbf{r} = \infty \tag{54}$$

McLaughlin (1991) showed that the migration velocity in the x-direction, u_m, may be expressed as follows:

$$u_m = \left(\frac{3}{2\pi^2}\right) a u_{rel} \left(\frac{G}{\nu}\right)^{\frac{1}{2}} J \tag{55}$$

where

$$J = \int_0^{2\pi} \int_0^1 \int_0^{\infty} \left[\zeta \left\{ s^2 - 2s^2(1-s^2)\cos^2\phi - \zeta s^3 (1-s^2)^{\frac{1}{2}} \cos\phi \right\} \left(\frac{\pi^{\frac{1}{2}}}{4A^3}\right) \left(\frac{1-B^2}{2A^2}\right) - \left(\frac{\pi^{\frac{1}{2}} B}{4\varepsilon A^3}\right) s^2 (1-s^2)^{\frac{1}{2}} \cos\phi \right] e^{\frac{B^2}{4A^2}} d\zeta \, ds \, d\phi \tag{56}$$

$$A^2 = \frac{1}{3} s^2 \zeta^3 + s(1-s^2)^{\frac{1}{2}} \cos(\phi) \zeta^2 + \zeta$$

$$B = \frac{\zeta s}{\varepsilon}$$

$$\varepsilon = \frac{Re_G^{\frac{1}{2}}}{Re_s}$$

$$Re_G = \frac{G d_p^2}{\nu}$$

$$Re_s = \frac{u_{rel} d_p}{\nu}$$

In the above equations, $s = \cos\theta$ and ϕ and θ denote the angular coordinates of a spherical system in Fourier space.

For large ε, with an error of order $1/\varepsilon^4$, J may be approximated by

$$J = 2.255 - \frac{0.6463}{\varepsilon^2} \tag{57}$$

For $\varepsilon = 1$, the error involved in using the asymptotic formula to compute J is 3.4 percent and the error involved in using the asymptotic formula to compute the difference between J and Saffman's value for J (2.255) is 7.7 percent.

The lowest-order corrections are of order ε^5. At intermediate values of ε, J must be evaluated by numerical integration, and the results are tabulated by McLaughlin (1991).

The lift force is related by the migration velocity, u_m, by

$$F_L = 6\pi\mu a u_m \tag{58}$$

Some insight into the origin of the inertial lift force may be obtained by considering the characteristic scales of the problem and the relative importance of the convective and viscous terms. Two lengths of interest are the Stokes length, $L_s = \nu/u_{rel}$, and the Saffman length, $L_G = \left(\frac{\nu}{G}\right)^{\frac{1}{2}}$. For $\varepsilon >> 1$, $L_s >> L_G$ and, for $\varepsilon << 1$, $L_s << L_G$. For small values of Re_G and Re_s, the viscous term in (51) is small compared to the convective terms provided that the distance from the center of the sphere, r, is small compared to both L_G and L_s.

If $\varepsilon >> 1$, the case considered by Saffman, inertia will become significant when $r \sim L_G$. For distances of this order, the terms $\mathbf{v} \cdot \nabla \mathbf{v}$ and $u_{rel}\frac{\partial \mathbf{v}}{\partial Z}$ may be neglected in comparison with the terms involving G. In fact, the terms involving G remain dominant at distances that are large compared with L_G. As shown by Saffman, the lift force is caused by a transverse component of the disturbance flow that originates at distances of order L_G. The form of the lift force can be guessed on the basis of dimensional analysis guided by this intuitive notion. It is plausible that the inertial migration velocity should be proportional to u_{rel} and that it should involve L_G. Thus one might guess that the inertial migration velocity should be proportional to $\frac{u_{rel}a}{L_G} = u_{rel}a\left(\frac{G}{\nu}\right)^{\frac{1}{2}}$. To obtain the lift force one uses (58).

When $\varepsilon << 1$, the Stokes length is small compared to the Saffman length. For distances from the sphere, r, satisfying $r \sim L_s$, the term involving u_{rel} in (51) is comparable to the viscous term. In addition, the term involving u_{rel} is larger than the other convective terms. Thus, for distances satisfying $r << LG/\varepsilon$, the disturbance flow should be well approximated by axisymmetric Oseen flow. Since there is no lift in an axisymmetric flow, it is plausible that the lift force should be very small compared to the Saffman lift force, which ignores the convective term involving u_{rel}.

The terms involving G in (51) become large compared to the terms involving u_{rel} for $r >> L_G/\varepsilon$. However, the disturbance flow has decayed to very small values at such large distances. The above estimates do not apply in the Oseen wake. Within the Oseen wake, the terms involving G in (51) are comparable in magnitude to the terms involving u_{rel} at points satisfying $r \sim \varepsilon^3 L_G$. However, inertial effects will only become important for $r \sim L_G$ within the wake.

McLaughlin (1993) determined the influence of the wall on the inertial migration velocity on a sphere by deriving a solution for the partial Fourier transform the disturbance flow

$$u_m = u_m^u + u_m^w \tag{59}$$

In (59) v_m^u denotes the inertial migration velocity of the sphere in an unbounded fluid. For large values of l^*, $\frac{l}{L_G}$, one may obtain an analytical expression for the wall contribution to the migration velocity

$$u_m^w = \frac{-0.2855 a u_{rel}\left(\frac{G}{\nu}\right)^{\frac{1}{2}}}{l_*^{\frac{5}{3}}} \tag{60}$$

The sign of u_m^w indicates that the wall exerts an attractive force on the sphere when the product $v_{rel}G$ is positive and repulsive force when $v_{rel}G < 0$. This appears to be inconsistent with Drew's (1988) numerical results for $\varepsilon = \infty$. Drew states that, when $v_{rel}G$ is positive (so that the particle experiences a lift force that points away from the wall), the wall disturbances tends to increase the magnitude of the lift force for $l* >> 1$. However, McLaughlin's analysis indicates that the reverse is true.

In the weak shear limit, $\varepsilon << 1$, the disturbance flow is well approximated by the Oseen differential equation for distances r satisfying $a << r << \frac{L_G}{\varepsilon}$. Vasseur and Cox (1977) have shown that , in this case, the sign of u_m^w is always positive. The physical mechanism is that, as the sphere translates parallel to the wall, it displaces fluid laterally and the wall creates a counterflow that pushes the sphere away from the wall. For $\varepsilon << 1$, the asymptotic result applies only for $l_* = O\left(\frac{1}{\varepsilon^3}\right)$. For values of $l*$ that are order unity, one must evaluate the wall induced contribution to the lift force numerically.

In order to facilitate comparisons with the results for the migration velocity in an unbounded fluid and the disturbance flow in an unbounded fluid, the non-dimensional quantity J will be used:

$$J = \frac{2\pi^2}{3}\left(\frac{\nu}{G}\right)^{\frac{1}{2}}\frac{u_m}{au_{rel}} \tag{61}$$

and

$$J = J^u + J^w \tag{62}$$

where the superscripts u and w denote the values in an unbounded fluid and the wall contributions, respectively.

Figure 4.14 shows the values of J versus $l*$ for $\varepsilon = \infty$, as predicted by McLaughlin's results. The predictions of the Cox-Hsu theory for small values of $l*$ are also plotted.

Figure 4.14

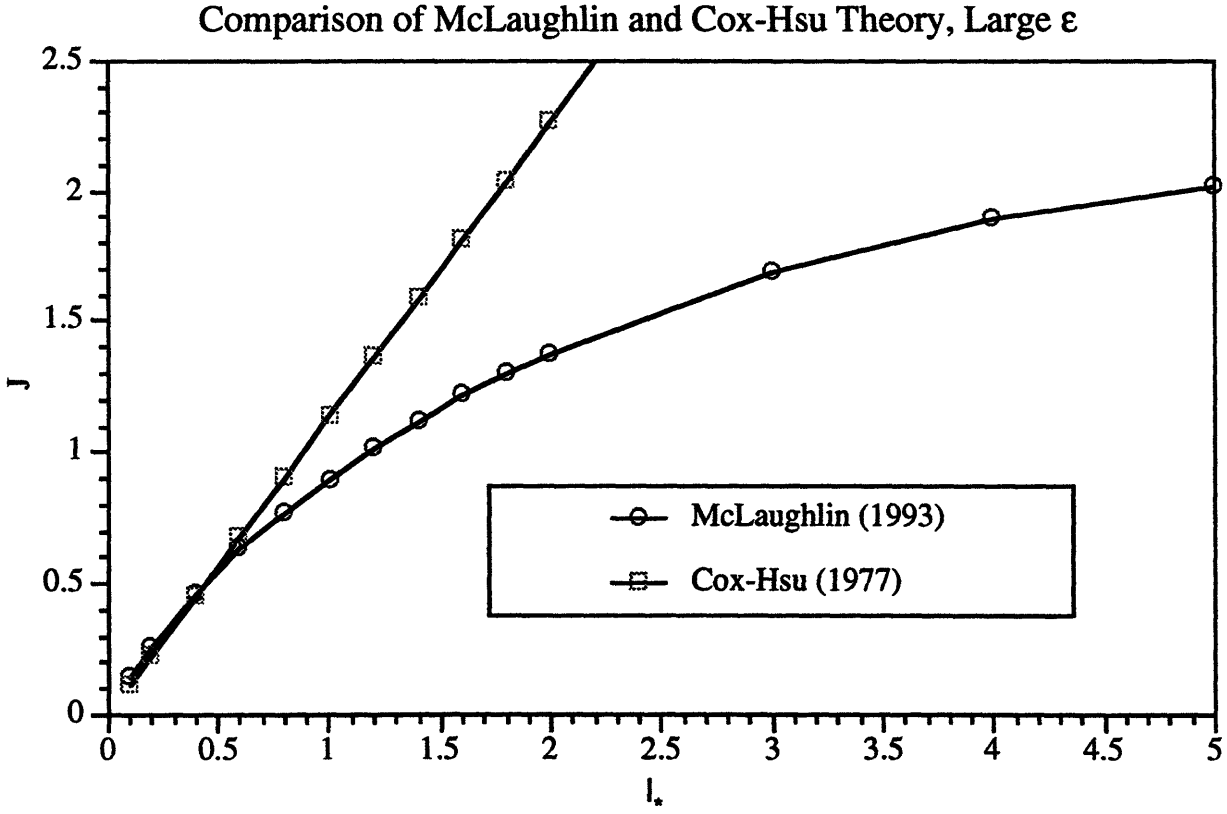

Cox and Hsu (1977) considered the problem of a small sphere sedimenting in a vertical parabolic flow next to a vertical rigid wall. They considered three cases: a non-neutrally buoyant sphere in a strong shear flow; a non-neutrally buoyant sphere in a weak shear flow; and a neutrally buoyant sphere. The first two cases are relevant for the comparison with the case of particle settling near the wall of a CFB. The Cox-Hsu theory provides the following expression for the inertial migration of a non-neutrally buoyant sphere in a vertical linear shear flow:

$$u_m = \frac{3}{32}\frac{a u_{rel}^2}{\nu} + \frac{11}{64}\frac{G a u_{rel} l}{\nu} \tag{63}$$

This result is valid provided that $a << l << \min\left(L_G, L_s\right)$. In other words, the wall is assumed to lie within an 'inner' region where inertial effects are a small perturbation of the Stokes equation.

If (63) is written in terms of the 'outer' coordinate l_*, one obtains

$$J = \frac{\pi^2}{16}\left(\frac{1}{\varepsilon} + \frac{11}{6} l_*\right) \tag{64}$$

In the strong shear limit ($\varepsilon >> 1$) the second term dominates.

McLaughlin's results should reduce to the Cox-Hsu result for sufficiently small values of l_*. The Cox-Hsu theory treats the particle as a point force acting on the fluid (for non-neutrally buoyant particles). Furthermore, the nonlinear term in the Navier-Stokes equation may be approximated by (52) to leading order for $r >> a$, where r is the distance from the center of the particle. The primary difference is that, within its domain of validity, the Cox-Hsu theory treats the nonlinear term as small compared to the viscous term so that ordinary perturbation methods may be used to obtain the leading-order result. Cox and Hsu divide the flow field into inner and outer regions on the basis of whether the distance from the sphere is comparable to the sphere's radius (the inner region) or whether the distance from the sphere is comparable to the distance of the sphere from the wall. In both regions, the inertial terms are small compared to the viscous terms. In the outer region, the sphere is treated as a point force to leading order. Cox and Hsu show that the leading contribution of the lift force comes from the outer region. All terms in (51) are treated in their analysis. However, the term $\mathbf{v} \cdot \nabla \mathbf{v}$ contributes at a higher order in the ratio a/l than the other terms. Thus, to leading order, the nonlinear term may be treated as in (52) and McLaughlin's results must reduce to the Cox-Hsu theory for sufficiently small values of l.

In figure 4.14, for $\varepsilon = \infty$, J converges to the Cox-Hsu for small values of $l*$. In figure 4.15, the ratio of the computed value of J_W to the power-law value (eqn. 60) is plotted versus $l*$ for $\varepsilon = \infty$. For values of $\varepsilon > 1$, the power-law formula gives estimates for J_W that are accurate to within 25 percent for $l* > 10$.

Figure 4.15

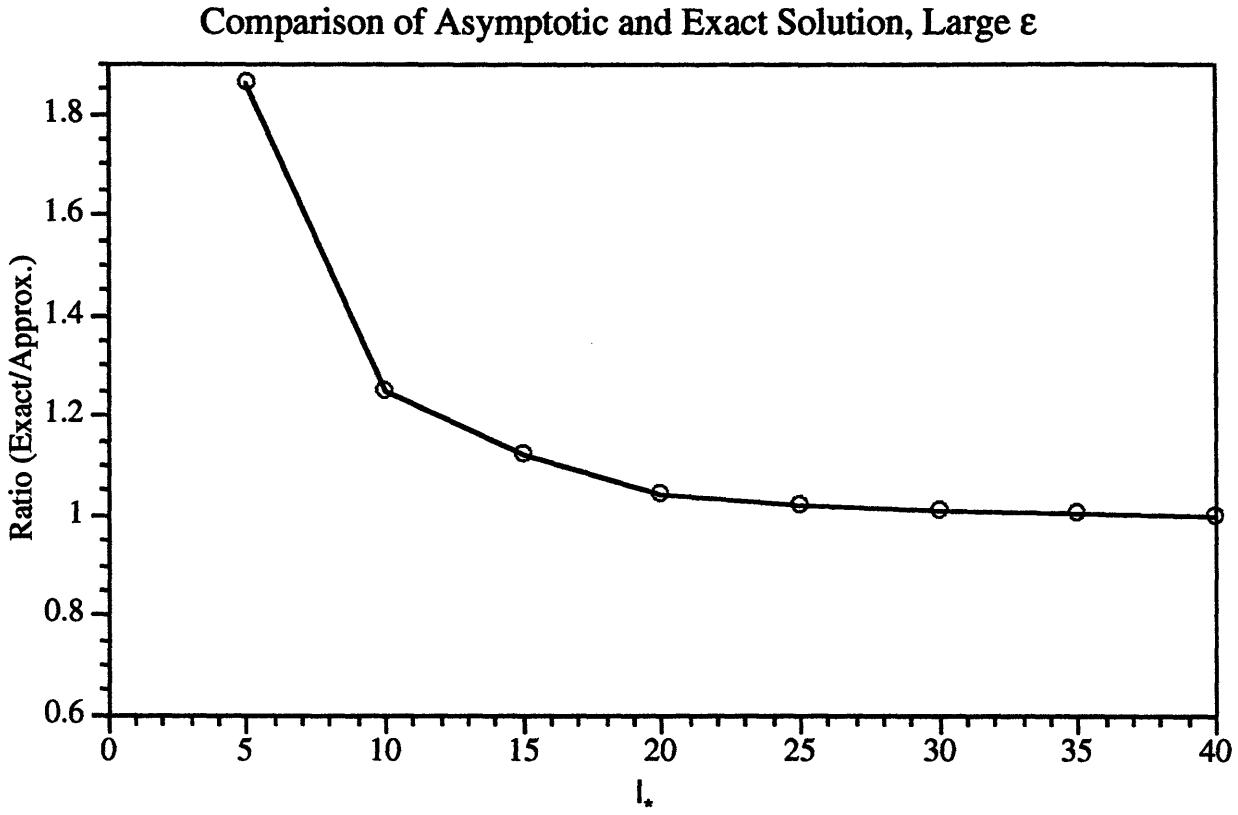

In figure 4.16, the values of J determined from McLaughlin's theory are plotted versus $l*$ for $\varepsilon =$ 1. The computed results agree well with the Cox-Hsu theory for small values of $l*$.

Figure 4.16

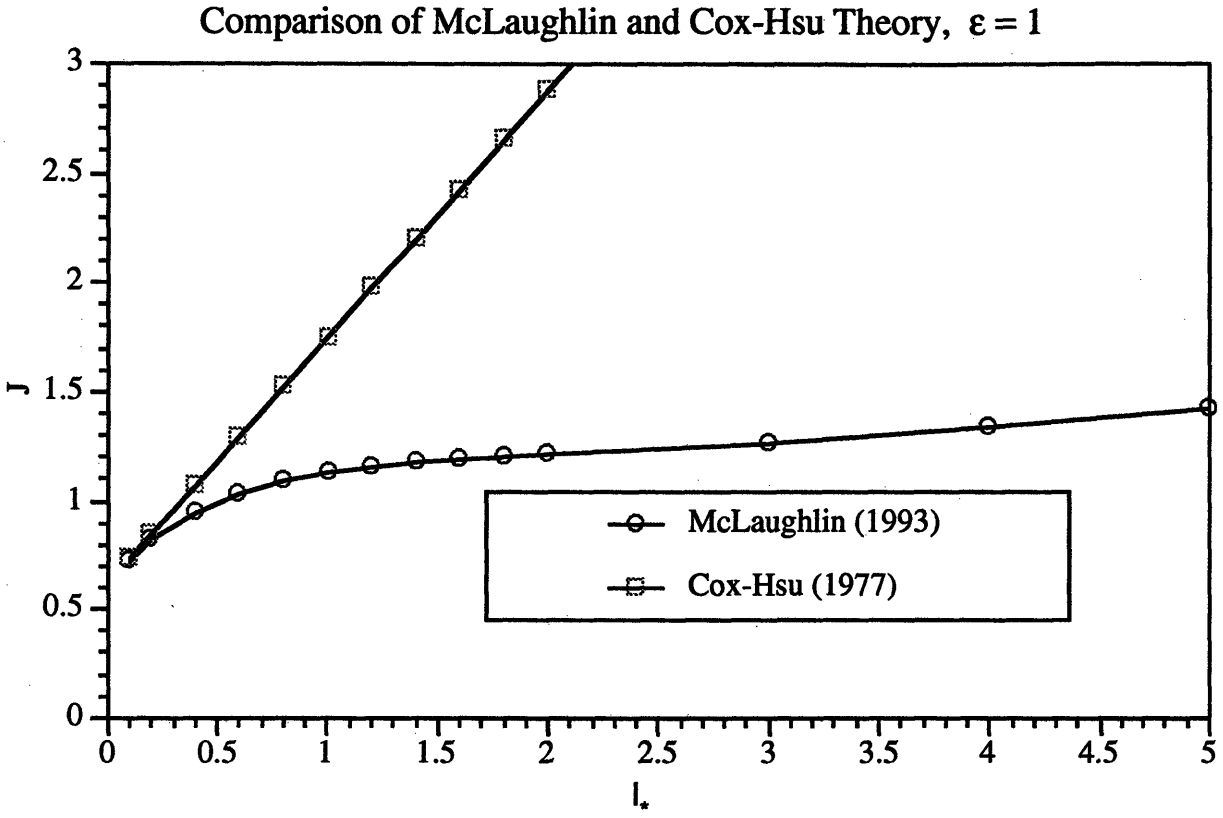

For small values of ε, the Cox-Hsu theory is valid only for $l* << \varepsilon$. Within its small region of validity, the Cox-Hsu theory predicts that the shear contribution to the lift is unimportant. For $Re_G^{\frac{1}{2}} << l_* << \frac{1}{\varepsilon}$, the Vasseur-Cox (1977) theory should provide a good approximation to the inertial migration velocity. Figure 4.17 compares the computed results of McLaughlin to the results predicted by the Vasseur-Cox theory for ε = 0.2.

Figure 4.17

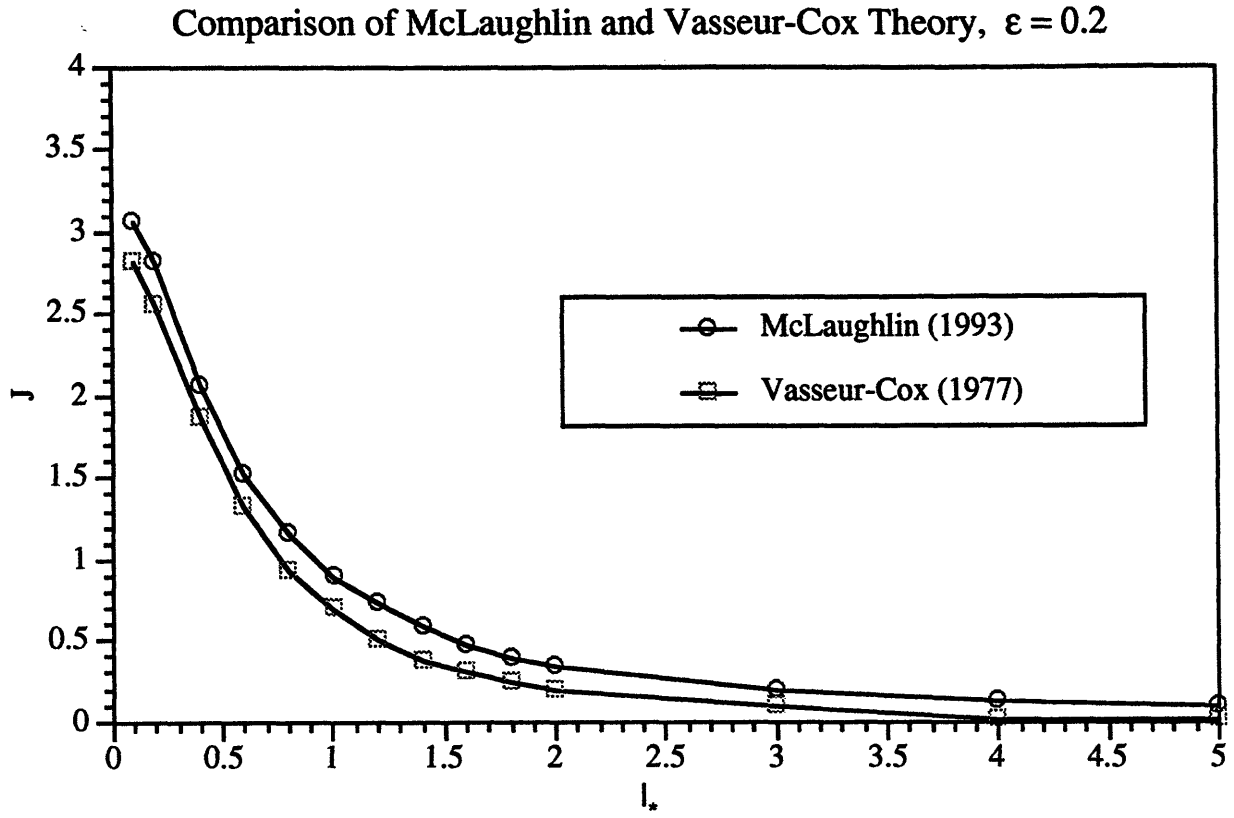

Values of J are given in tables 1 and 2 of McLaughlin (1993) for several values of ε. For values outside the range given in the tables, the asymptotic results of Saffman, Cox and Hsu, Vasseur and Cox, and McLaughlin give good approximations. For values of l_* larger than 5, the large-distance form of (60) may be used to estimate J_W for $\varepsilon > 1$. For small values of ε, wall effects are small enough to be negligible for most purposes when $l_* > 5$.

By combining the results of McLaughlin with various asymptotic limits, approximate fits to the lift force on a particle moving near a solid boundary for conditions found in a CFB can be constructed. Equations (48) and (49) were solved numerically for conditions for typical CFB conditions assuming the particles at the edge of a downward flowing cluster behave as individual particles and using the combinded McLaughlin/Cox-Hsu/Vasseur-Cox/Saffman method outlined above. (48) and (49) were also solved assuming $\varepsilon >> 1$ (Saffman's case). Figure 4.18 shows that modifications due to the presence of a wall have significant effects on the trajectory of the particle.

In summary, to solve for the particle trajectory as it enters the viscous sublayer near the wall, equations (48) and (49) are solved simultaneously. The expression for the shear lift force, represented by the second term on the r.h.s. of (49) is determined as follows:

$$F_{lift} = \frac{9}{4\pi}\mu d_p^2 (u_p - u_f)\left(\frac{G}{\nu}\right)^{0.5} J$$

where J is found from:

Region	Investigator	J_u	J_w	$J = J_u + J_w$
$l_* > 5$	McLaughlin (1991)	Equation (56)	$\frac{-1.8785}{l_*^{5/3}}$	Equation (56) + $\frac{-1.8785}{l_*^{5/3}}$
$l_* < 0.1$	Cox and Hsu (1977)			$\frac{\pi^2}{16}\left(\frac{1}{\varepsilon} + \frac{11}{6} l_*\right)$
$0.1 < l_* < 5$ $0.2 < \varepsilon < 2$	McLaughlin (1993)			Table Lookups from Reported Values
$\varepsilon < 0.2$	Vassuer and Cox (1977)			$\frac{\pi^2}{4\sqrt{\nu G}}\lvert u_f - u_p \rvert \times \left(\left(\frac{\nu}{d_p \lvert u_f - u_p \rvert}\right)^2 + 2.22\left(\frac{\nu}{d_p \lvert u_f - u_p \rvert}\right)^{5/2}\right)$
$\varepsilon > 2$	Saffman (1965,68)			2.26

where $\varepsilon = \frac{Re_G^{0.5}}{Re_s}$, $Re_G = \frac{Gd_p^2}{\nu}$, $Re_s = \frac{\lvert u_f - u_p \rvert d_p}{\nu}$, $l_* = l\left(\frac{G}{\nu}\right)^{0.5}$, G is the shear rate of the undisturbed flow, and l is the distance from the sphere centerline to the wall.

Figure 4.18

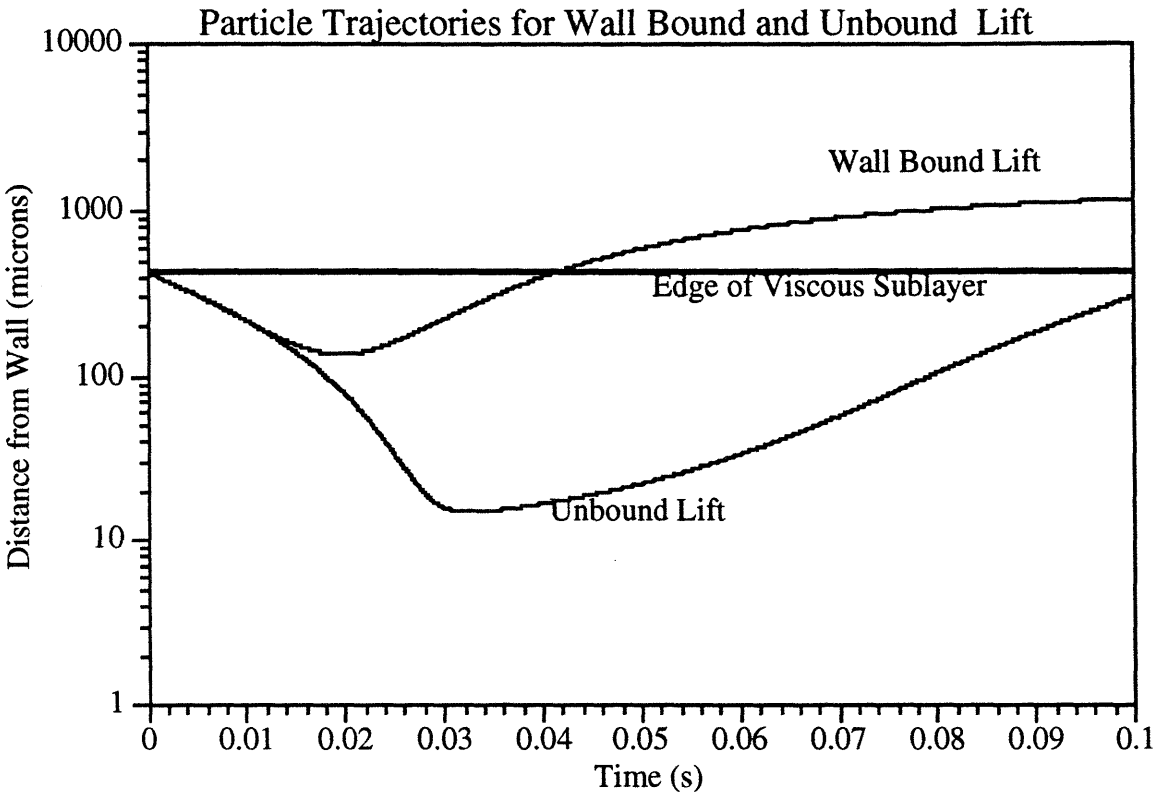

Because the particle velocity will always lag the fluid velocity in a CFB ($\rho_s > \rho_f$), the lift force is always oriented radially inward. This is consistent with the development of particle free zone near the wall. Several simulations were conducted in order to approximate the trajectory of individual particles near the wall of CFB. Table 4.3 lists the parameters used in the numerical simulation to determine standoff distances for two sets of CFB data for which standoff distances have been determined experimentally.

Table 4.3: Numerical Model Input Parameter Values

Parameter	Equation and/or Reference	Values for Configuration of Wirth (1991)	Values for Lint's (1992) Configuration
Superficial Velocity	Wirth (1991) Lints (1992)	2.0 m/s	3.0 m/s
Particle Density	Wirth (1991) Lints (1992)	2350 kg/m3	2350 kg/m3
Particle Terminal Velocity	$\frac{Ar}{18} = Re_t + 0.15Re_t^{1.687}$ Wen and Yu (1966)	0.45 m/s	1.1 m/s
Particle Diameter	Wirth (1991) Lints (1992)	80 microns	182 microns
Bed Diameter	Wirth (1991) Lints (1992)	0.168 m	0.203 m
Re_D	$Re_D = \frac{u_o D}{\nu}$	2.2E+4	4.0E+4
Friction Factor	$f = 0.3164Re_D^{-0.25}$ Blasius, 1908	2.6E-2	2.2E-3
Friction Velocity	$u_\tau = u_o\sqrt{\frac{f}{8}}$ Hinze, 1975	0.11 m/s	0.16 m/s
Sublayer Fluid Velocity Gradient	$\frac{du_f}{dy} = \frac{u_o^2}{\nu}\frac{f}{8}$ (Rouhiainen, 1970)	830 (1/s)	1606 (1/s)
Sublayer Thickness	$y^+ = \frac{\delta_{vsl}u_\tau}{\nu} = 5$	d_{vsl} = 700 microns	d_{vsl} = 500 microns
Eddy Length Scale for Gas Turbulence	$l_e = \frac{7}{8}\frac{u_\tau}{u_o}D$ Hinze (1975)	8.1E-3 m	9.5E-3 m
Fluid y-dir Fluctuating Velocity	$u'_{rms} = 2*0.04u_o$ [Hinze, (1975) modified by Westphalen (1993)]	0.16 m/s	0.24 m/s
Particle y-dir Fluctuating Velocity	$\frac{u'_{p_{rms}(x,y)}}{u'_{f_{rms}(x,y)}} = \left(1 + \frac{1}{\phi}\frac{\left(u'_{f_{rms}(x,y)}\right)^2}{gl_e}\frac{u_t}{u'_{f_{rms}(x,y)}}\sqrt{1+\left(\frac{u_t}{u'_{f_{rms}(x,y)}}\right)^2}\right)^{-1/2}$ [Friedlander (1957) and Csanady (1963)]	0.083 m/s	0.067 m/s

Figure 4.18 shows the trajectory of a particle as it enters the viscous limit utilizing the bed configuration of Wirth *et al.* (1991). The transverse velocity of the particle was assumed to be equal to the root mean squared transverse fluctuating velocity of the particle as the particle entered the laminar sublayer. The experimentally determined standoff distance was 0.7mm. The predicted particle free zone is about 0.64mm.

Figure 4.18

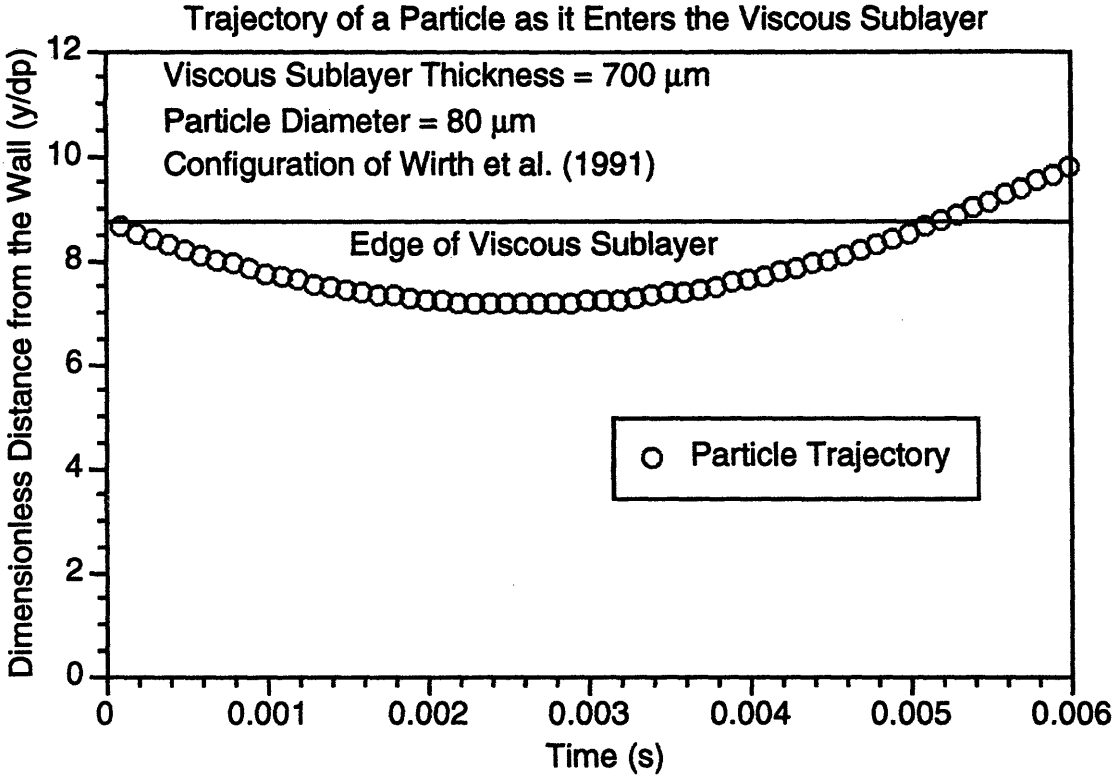

Figure 4.19 shows the predicted trajectory of a particle as it enters the viscous sublayer with a velocity equal to the root mean square of the y-direction fluctuating velocity for the configuration of Lints (1992). This plots predicts that a particle free zone would occur for a distance of about one half the particle diameter from the wall for the given conditions. This is in good agreement with the data of Lints (1992) where he measured standoff distances between 1/3 and 1 particle diameters.

Figure 4.19

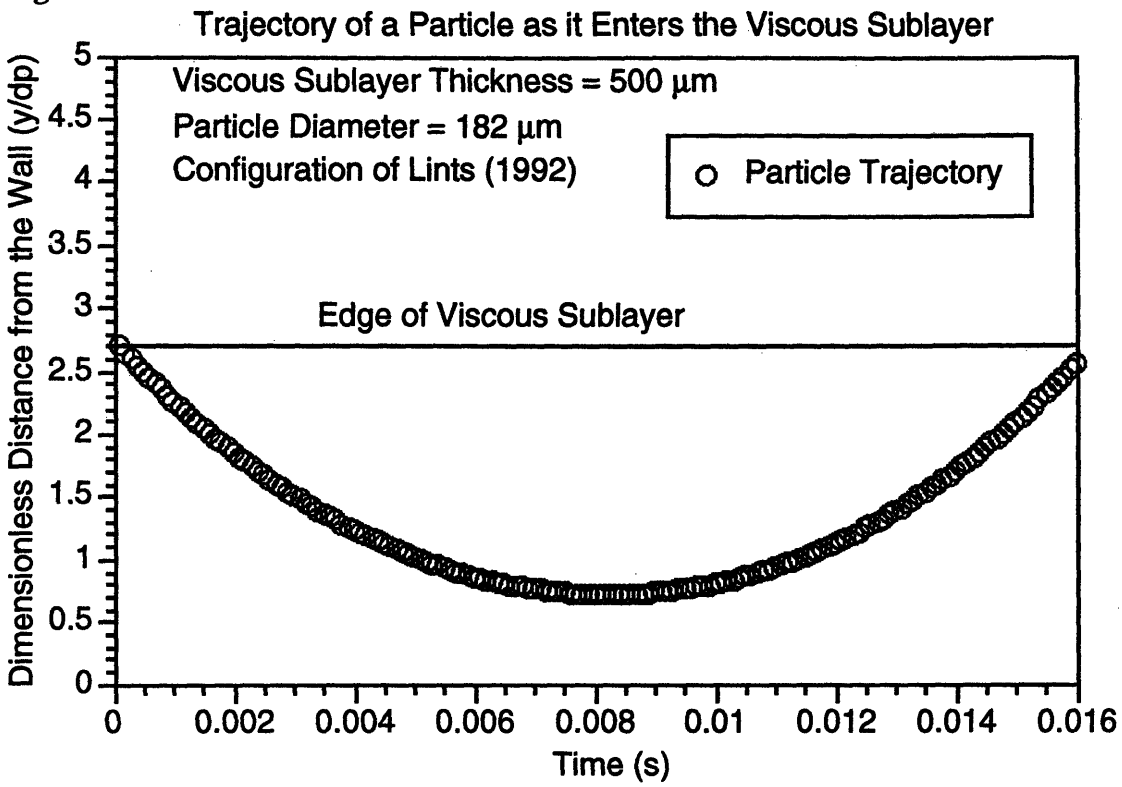

For regions outside the viscous sublayer where the fluid velocity gradient is much smaller, the force on a particle is very small. For example, for a distance of about 1 cm away from the wall, the lift force is only about 1 percent of the value in the viscous sublayer.

Initial evaluations have indicated the particle standoff distance is on the order of or smaller than the laminar sublayer thickness. If the above discussion is an accurate representation of the physics behind the standoff distance, then the gas gap should vary with the viscous sublayer thickness. In this study, it was assumed that the wire ridges eliminated the viscous sublayer and that the regrowth of this sublayer proceeded proportional to [Hinze, (1975)]

$$\delta_{vsl} \sim \sqrt{\nu\tau} \tag{65}$$

The relationship between the laminar sublayer thickness and the gas gap was found to be quadratic such that it also grew as νt after the ridges, i.e.

$$\delta \sim \frac{\delta_{vsl}^2}{d_p} \sim \frac{\nu t}{d_p} \tag{65a}$$

Figure 4.20 presents the numerical data which depicts the dependence of the dimensionless standoff distance as a function of $\frac{\delta_{vsl}}{\delta}$ for an 8-inch (20 cm) diameter CFB operating at 1100 K and 14 bar, along with the best quadratic curve fit $\left[\frac{\delta}{d_p} = 0.032\left(\frac{\delta_{vsl}}{d_p}\right)^2\right]$.

Figure 4.20

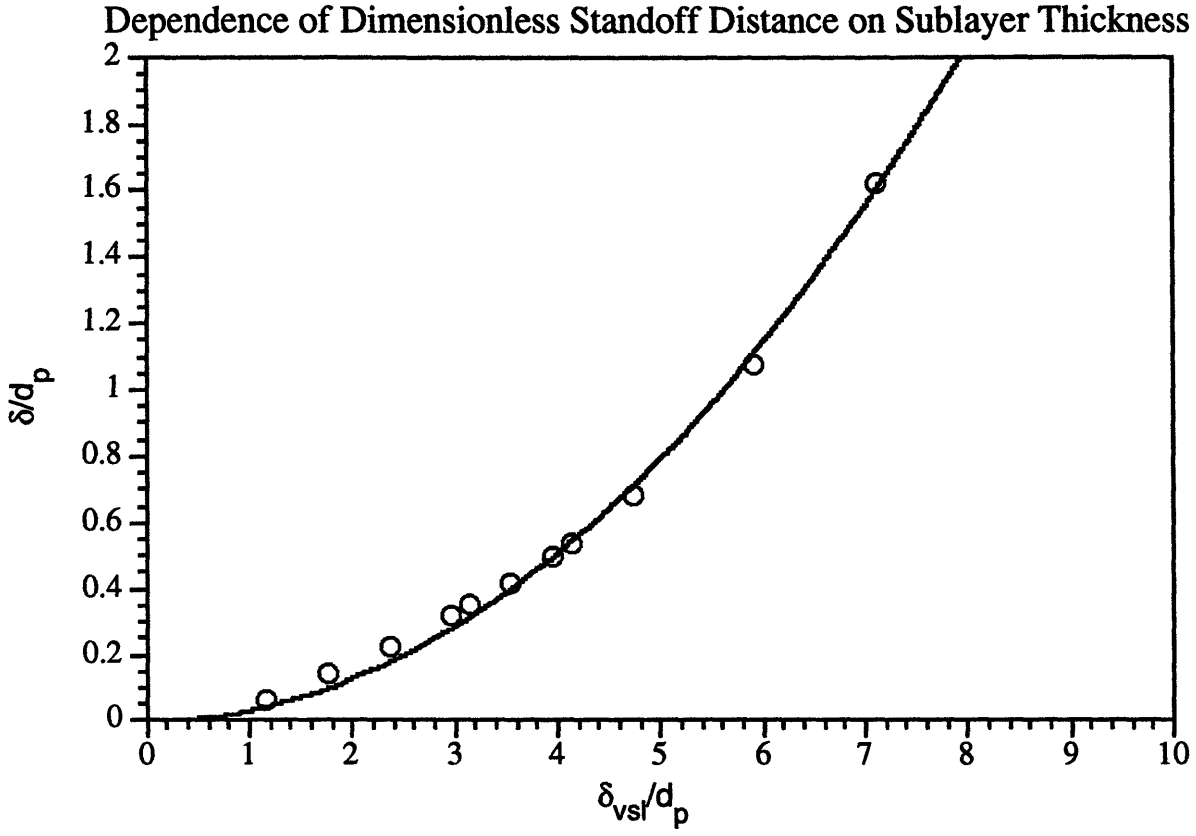

It is acknowledged that the above discussion makes some rather bold assumptions, and that experimental verification of the theory is required. However, it will be used in this study in an attempt to correct for the cluster standoff distance in situations where the viscous sublayer thickness is a function of time.

4.4.4 Fractional Wall Coverage

Measurements at the wall of a circulating bed has revealed that the wall does not contain a continuous layer, [Glicksman and Lints, (1993), Louge, (1987), Wu *et al.* (1991), Rhodes et al. (1992)]. Rather, the wall is partially covered by a series of clusters which move down along the

surface. The appearance of clusters or large wall density fluctuations correspond to enhanced instantaneous heat transfer coefficients as observed by Wu and Dou. At higher bed densities, the wall becomes fully covered by these streamers or clusters; however, the densities and the heat transfer coefficients reported for commercial circulating bed combustors suggest that the upper portions of the bed will not be fully covered with clusters. For example, Leckner and Andersson (1992) measured temperature fluctuations in the boundary layer of a 1.7 m square combustor which indicate the periodic appearance of hot particle clusters. Thus, the average heat transfer from the bed to the wall will be a function of the wall coverage. It is important to relate the fraction of wall coverage to the hydrodynamic conditions of the bed.

The wall coverage is determined from a balance between the deposition of clusters from the core to the wall and the shedding or break off of clusters from the wall. Rhodes *et al.* (1992) studied videos of the wall region and concluded that swarms, or clusters, were formed as particles were ejected from the core and thrown against the wall. The wall concentration would be determined by a balance of clusters or particles transported to the wall region from the core less the clusters shed from the wall which rejoin the core.

The wall coverage is a function of the distribution of clusters at the wall. If the deposition is a random process then some of the clusters will combine and overlap existing clusters rather than filling dilute zones at the wall. Two extremes are random spatial distribution of clusters deposited at the wall and uniform distribution of clusters at the wall.

If the coverage is random, i.e., location of incoming clusters which strike the wall region are independent of locations of clusters already at the wall, then the coverage can be described by a Poisson distribution; the probability of finding a layer of the wall n particles thick is equivalent to having a two dimensional surface with n particle centers within a diameter of d_p. The probability of a layer n diameters thick is

$$P_n = e^{-\bar{n}}\left(\frac{\bar{n}^n}{n!}\right) \tag{66}$$

where $\bar{n}$ is the mean wall layer thickness. The probability of coverage at least one particle layer thick is

$$P_{1+} = 1 - e^{-\bar{n}}\left(\frac{\bar{n}^0}{0!}\right) = 1 - e^{-\bar{n}} \tag{67}$$

Figure 4.21 shows P_{1+} versus $\bar{n}$. Note that in the random case, the coverage varies approximately with the square root of the average total thickness of material at the wall. Rewriting $\bar{n}$ as $f\,\delta_w$,

$$f \sim \left(f\,\delta_w\right)^{\frac{1}{2}} \tag{68}$$

Figure 4.21

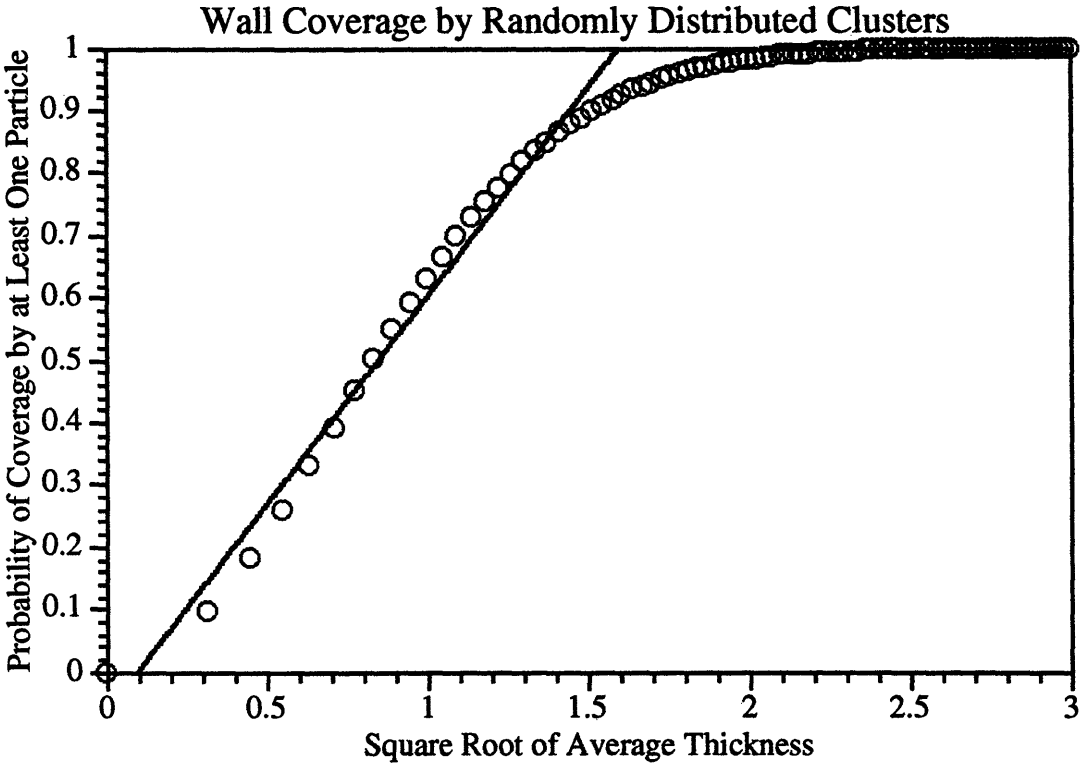

If the mean time for shedding is t_w (mean time a layer stays at the wall) and the shedding process is random in time, then the fraction of surface coverage lost due to shedding in time dt is

$$df = -\frac{f\,dt}{t_w} \tag{69}$$

For an element of the wall with a radial volumetric flux of particles from the core per unit area, J_r, the conservation of mass for the wall layer becomes,

$$\frac{d\left[\delta\left(1-\varepsilon_c\right)f\right]}{dt} = J_r - \frac{f}{t_w}\delta_w\left(1-\varepsilon_c\right) \tag{70}$$

where δ_w is the mean layer thickness upon shedding. At steady state with a uniform coverage along the wall, the left hand side is zero and Equation (70) can be solved if δ_w and t_w are known.

When the left hand side of (70) is zero,

$$J_r \sim \frac{f}{t_w}\delta_w \sim \frac{f^2}{t_w} \tag{71}$$

If J_r varies linearly with the cross section concentration (which will be shown below), then from Equation (71), f varies with the square root of the cross sectional concentration. This may help to explain why the measured heat transfer varies with the square root of the cross section concentration.

Assuming the build up and shedding do not interact,

$$\frac{df}{dt} = C_1\sqrt{J_r} - \frac{f}{t_w} \tag{72}$$

where C_1 is inversely proportional to the thickness of the new layer added.

The first term on the right hand side of Equation (72) was determined as follows:

From Equations (71) and (68)

$$J_r \sim \frac{f^{1/2}\left(\delta_w\right)^{3/2}}{t_w} \tag{73}$$

Also from Equation (71)

$$f^{1/2} \sim \left(\frac{J_r t_w}{\delta_w}\right)^{\frac{1}{2}} \tag{74}$$

Combining (73) and (74) gives

$$J_r \sim \left(\sqrt{\frac{J_r}{t_w}}\right)\delta_w \tag{75}$$

Assuming that

$$\delta \approx \delta_w \tag{76}$$

and

$$\delta \frac{df}{dt} >> f \frac{d\delta}{dt} \tag{77}$$

the first term on the right hand side of Equation (72) can be written as

$$\left(t_w\left(1 - \varepsilon_c\right)\right)^{-\frac{1}{2}}\sqrt{J_r} \quad \left[C_1 \sim \left(t_w\left(1 - \varepsilon_c\right)\right)^{-\frac{1}{2}}\right] \tag{78}$$

Rewriting Equation (72),

$$\frac{df}{dt} + \frac{f}{t_w} = C_1\sqrt{J_r} \tag{79}$$

Assuming shedding and regrowth occurs in a region with constant J_r

$$f(t) = C_2\, e^{-\frac{t}{t_w}} + C_1\, t_w\sqrt{J_r} \tag{80}$$

and at steady state,

$$f_{ss} = C_1\, t_w\sqrt{J_r} \tag{81}$$

such that $\frac{df}{dt}=0$ for the local value of J_r.

If J_r is a function of time, as a first approximation assume that

$$J_r(t) = J_{r0} \cdot t \tag{82}$$

Note that if the cluster velocity is constant this is the same as $J_r = J_{r0}h$, where h is measured vertically down.

Substituting (82) into (79) gives,

$$\frac{df}{dt} + \frac{f}{t_w} = C_1\sqrt{J_{r0}t} \tag{83}$$

Integrating with the initial condition that at $t = 0$, $f = f_0$,

$$f(t) = e^{-t/t_w} C_1 \sqrt{J_{r0}} \int_0^t \sqrt{t}\, e^{t/t_w}\, dt + f_0\, e^{t/t_w} \tag{84}$$

Expanding the exponential term inside the integral into a series and integrating gives,

$$f(t) = 2\, e^{-t/t_w} C_1 \sqrt{t_w^3 J_{r0}} \sum_{n=0}^{\infty} \frac{1}{n!} \left(\frac{1}{(2n+3)}\right)\left(\frac{t}{t_w}\right)^{\left(\frac{2n+3}{2}\right)} + f_0\, e^{-t/t_w} \tag{85}$$

or

$$f(t) = 2\, f_{ss}\, e^{-t/t_w} \sqrt{\frac{t_w}{t}} \sum_{n=0}^{\infty} \frac{1}{n!} \left(\frac{1}{(2n+3)}\right)\left(\frac{t}{t_w}\right)^{\left(\frac{2n+3}{2}\right)} + f_0\, e^{-t/t_w} \tag{86}$$

If instead of a linear variation of J_r with time, J_r is assumed to vary linearly with ε_{avg}, and the model of Kunii and Levenspiel (1991) is used to determine ε_{avg} as a function of bed height (and thus time),

$$\frac{\alpha_s - \alpha_s^*}{\alpha_{sd} - \alpha_s^*} = e^{-a(h - z_f)} \tag{87}$$

where

α_s = volume fraction of solids

α_s^* = saturated carrying capacity

α_{sd} = volume fraction of solids in lower dense bed

z_f = height from top of the bed to the lower dense bed

Then the expression for J_r is

$$J_r = C_3\left[\alpha_{sd}e^{a(z-h)} + \alpha_s^*\right] \tag{88}$$

where z~t assuming the cluster velocity is constant and h is the bed height assuming the lower dense bed is much smaller than the dilute section of the riser. Equation (88) differs somewhat from Equation (87) since it was assumed that z was being measured from the top of the bed so that as z increases as the clusters slide down the wall. In addition it was assumed that $\alpha_{sd} + \alpha_s^* \equiv \alpha_{sd}$.

Substituting Equation (88) into Equation (78) gives

$$f\,e^{t/t_w} = \int_0^t C_1\sqrt{C_3\left[\alpha_{sd}e^{a(t-t_i)} + \alpha_s^*\right]}\; e^{t/t_w}dt + C_4 \tag{89}$$

where t_i is the bed length divided by the cluster velocity.

Rearranging and collecting terms results in

$$\frac{f(t)}{f_{ss}} = \frac{\displaystyle\int_0^{t/t_w} \sqrt{\left[\alpha_{sd}e^{a(t-t_i)} + \alpha_s^*\right]}\; e^{t/t_w}d\left(\frac{t}{t_w}\right)}{\sqrt{\left[\alpha_{sd}\,e^{a(t-t_i)} + \alpha_s^*\right]}\; e^{t/t_w}} + \frac{f_0\,e^{-t/t_w}}{f_{ss}} \tag{90}$$

In later sections of this report a discussion of the differences which result in utilizing Equation (90) versus using Equation (86) will be given.

In both Equations (86) and (90) the steady state value of the fractional wall coverage is required. Lints (1992) has brought together the data available in the literature in an effort to develop a

correlation for the steady state fractional wall coverage. Figure 4.22 depicts the results of that study. In addition to the results of the Lints study, the correlations proposed by Lu *et al.* (1990):

$$f_c = \frac{\left(1-\varepsilon\right)}{\left(1-\varepsilon_{cl}\right)} \tag{91}$$

and Basu (1990)

$$f_c = \frac{1}{2}\frac{\left(1-\varepsilon^{3.811}-Y\right)}{\left(1-\varepsilon_{cl}\right)} \tag{92}$$

are plotted. Y is the volume fraction of solid in the dispersed phase (in Figure 4.21 $1-\varepsilon_{cl} = \sqrt{1-\varepsilon}$). Both the Lu and Basu correlation underestimate the fractional wall coverage significantly.

In an effort to develop a more accurate correlation (notice Lints' correlation is not valid over average bed solid fractions above about 0.02), a study was conducted to determine which dimensionless groups govern the radial flux from the core (assuming that the fractional wall coverage goes as the square root of the radial flux, as discussed above). The first method of determining the governing dimensionless parameters was a general approach which made use of the two-phase governing equations of motion in an Eulerian frame of reference which were developed in Chapter 2. The second approach was based on a more mechanistic model which was developed, to a large extent, by Friedlander (1957) and Csanady (1963).

Figure 4.22

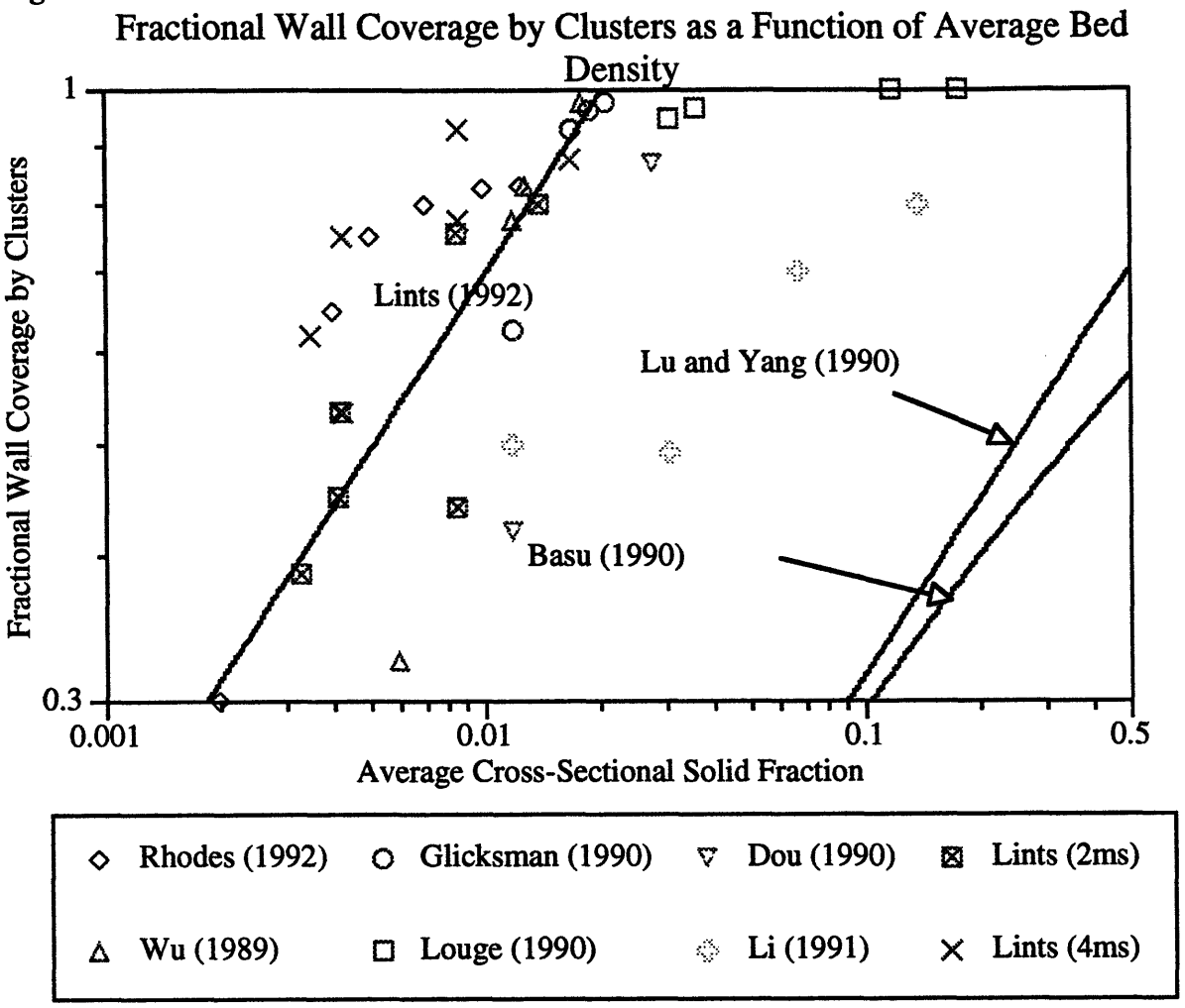

In the first analysis, the following assumptions were made:

1. The particle phase does not significantly effect the fluid phase turbulence

2. The mass flux due to Brownian motions can be neglected

3. Since the solid density is much larger than the fluid density, the solid pressure term, virtual mass term, and the Basset history term can be neglected.

4. The electrostatic force term due to mirror charging can be neglected

5. The shear induced lift force on the particles can be neglected in the core of the CFB since the fluid velocity gradients in this region are not sufficiently large to make this term significant

The resulting non-dimensional governing equations are [see Johansen (1988)]:

$$J^{+}\frac{\partial \overline{U_p^{+}}}{\partial y^{+}} = -\frac{\partial}{\partial y^{+}}\left(-\bar{\alpha}^{+}\nu_p{}^{+}\frac{\partial \bar{U}_p{}^{+}}{\partial y^{+}}\right) + \frac{\bar{\alpha}^{+}}{t_p{}^{+}}\left(\bar{U}_f{}^{+} - \bar{U}_p{}^{+}\right)\left(\frac{C_D Re_p}{24}\right) - \bar{\alpha}^{+}\left(\frac{gv}{u_\tau^3}\right) \tag{93}$$

$$\left(J^{+} - \nu_p{}^{+}\frac{\partial \bar{\alpha}^{+}}{\partial y^{+}}\right)\frac{\partial \bar{V}_p{}^{+}}{\partial y^{+}} = -\frac{\partial \bar{\alpha}^{+}\left\langle v_p'^{2+}\right\rangle}{\partial y^{+}} - \bar{V}_p{}^{+}\frac{\partial}{\partial y^{+}}\left(n_p{}^{+}\frac{\partial \bar{a}^{+}}{\partial y^{+}}\right) - \frac{\bar{\alpha}^{+}}{t_p{}^{+}}\left(\bar{V}_p{}^{+}\right)\left(\frac{C_D Re_p}{24}\right) \tag{94}$$

The dimensionless parameters are defined as

$$\left\langle v_p'^{2}\right\rangle^{+} = \frac{\left\langle v_p'^{2}\right\rangle}{u_\tau^2} \tag{95}$$

$$t_p^{+} = \frac{t_p u_\tau^2}{\nu} \tag{96}$$

$$y^{+} = \frac{y u_t}{\nu} \tag{97}$$

$$d_p^{+} = \frac{d_p u_\tau}{\nu} \tag{98}$$

$$R^{+} = \frac{D u_\tau}{2\nu} \tag{99}$$

$$\nu_t{}^{+} = \frac{\nu_t}{\nu} \tag{100}$$

$$\nu_p{}^+ = \frac{\nu_t^p}{\nu} \tag{101}$$

$$J^+ = \frac{J}{u_\tau \alpha_{avg}} \tag{102}$$

$$\overline{V}_p^+ = \frac{\overline{V}_p}{u_\tau};\ \overline{U}_p^+ = \frac{\overline{U}_p}{u_\tau};\ \overline{V}_f^+ = \frac{\overline{V}_f}{u_\tau};\ \overline{U}_f^+ = \frac{\overline{U}_f}{u_\tau};\ \bar{\varepsilon}^+ = \frac{\bar{\varepsilon}}{\varepsilon_{avg}} \tag{103}$$

and the friction velocity is calculated as for single phase pipe flow.

In addition, representations of the turbulent kinematic viscosity, the Lagrangian time scale, the fluid r.m.s. velocity and the mean fluid velocity throughout the riser are required.

The relations for $\nu_t^+ = g\left(y^+\right)$ and $\left\langle v_f'^2 \right\rangle^+ = f\left(\frac{y^+}{R^+}\right)$ proposed by Kim *et al.* (1987) and Kutateladze *et al.* (1979) were used to close the problem (here $R^+ = \frac{Ru_\tau}{\nu}$).

Hence, the dimensionless quantities which control the deposition flux are:

$$\frac{\rho_s}{\rho_f};\ t_p^+;\ \frac{g\nu}{u_\tau^3};\ \alpha_{avg};\ \text{and}\ R^+ \tag{104}$$

which can also be written as:

$$\frac{\rho_s}{\rho_f};\ d_p^+;\ \frac{gd_p}{u_\tau^2};\ \alpha_{avg};\ \text{and}\ R^+ \tag{105}$$

The bulk particle volume fraction also enters since this parameter was used to nondimensionalize the average and fluctuating components of the volumetric solid fraction.

Several other approaches models have been analyzed to determine the dimensionless groups which govern particle radial flux. Another which will be described in this study is based on the particle turbulence model of Friedlander (1957) with correlations developed by Csanady (1963).

The equation for particle spread in a reference frame moving with the particles assuming axial diffusion and radial convection are neglected is:

$$\frac{\partial\left(1-\bar{\varepsilon}_p\right)}{\partial t} = \varepsilon_{rp}\frac{1}{r}\frac{\partial}{\partial r}\left(r\frac{\partial\left(1-\bar{\varepsilon}_p\right)}{\partial r}\right) \tag{106}$$

The derivation for the average radial flux is given in Chapter 5. The result is

$$\bar{j} = \sqrt{\frac{2}{\pi}}\, v'_{p_{rms}}\, \alpha_{avg} \tag{109}$$

Indicating

$$\frac{\bar{j}}{v_{f_{rms}}} = fnc\left(\alpha, \frac{v_{p_{rms}}}{v_{f_{rms}}}\right) \tag{110}$$

The Friedlander approach assumes that

1. Validity of a linear drag expression: the added mass of gas is negligible; the Basset history integral is negligible; the gas phase pressure gradient at a distance from the particle is negligible; either the particle is small enough that drag forces are entirely viscous or the particle terminal velocity is large compared to the particle's vertical fluctuating velocity.

2. The particle is smaller that the gas phase turbulence microscale

Friedlander's model, with the appropriate corrections suggested by Csanady for the crossing trajectory effect gives:

$$\frac{v_{p_{rms(x,y)}}}{v_{f_{rms(x,y)}}} = \left(1 + \frac{1}{\phi}\frac{\left(v_{f_{rms(x,y)}}\right)^2}{gl_e}\frac{u_t}{v_{f_{rms(x,y)}}}\sqrt{1+\left(\frac{u_t}{v_{f_{rms(x,y)}}}\right)^2}\right)^{-1/2} \tag{111}$$

where l_e is the eddy lengthscale and the value of ϕ is one for lateral fluctuations and two for axial fluctuations.

A first estimate of gas turbulence can be based on single-phase pipe flow measurements. In the core region of a pipe, the quantities of interest are as listed below (Hinze, 1975). The eddy length scale l_e is calculated as shown. Turbulence in the pipe core is assumed relatively homogeneous and isotropic

$$v_{f_{rms(y)}} = 0.04u_o \tag{112}$$

$$l_e = \frac{7}{8}\frac{u_\tau}{u_o}D \tag{113}$$

$$u_\tau = u_o\sqrt{\frac{f}{8}} \tag{114}$$

$$f = 0.3164Re_D^{-0.25} \tag{115}$$

Using these relations, the following dimensionless correlations can be found:

$$\frac{v_{f_{rms(y)}}}{u_\tau} = 0.2Re_D^{1/8} \tag{116}$$

$$\frac{l_e u_\tau}{\nu} = 0.35R^+Re_D^{-1/8} \tag{117}$$

In order to determine a functional relationship between the Archimedes number and the Reynolds number based on terminal velocity and particle diameter, if the particles are assumed to be small

$$Re_t \cong \frac{Ar}{18} \tag{118}$$

and

$$u_t \cong \frac{\rho_s d_p^2 g}{18\mu} \tag{119}$$

$$\frac{u_t}{v_{f_{rms(y)}}} \cong \frac{0.28Ar}{d_p^+ Re_D^{1/8}} \tag{120}$$

or

$$\frac{u_t}{v_{f_{rms(y)}}} \cong \frac{0.28 d_p^+ \left(\frac{\rho_s}{\rho_f}\right)\left(\frac{d_p g}{u_\tau^2}\right)}{Re_D^{1/8}} \tag{121}$$

Substituting these relations back into the equation for the lateral particle fluctuating velocity gives:

$$\frac{v_{p_{rms(y)}}}{u_\tau} = 0.2 Re_D^{1/8} \left(1 + 0.064 Re_D^{1/4} \frac{d_p}{D} \frac{\rho_s}{\rho_f} d_p^+ \sqrt{1 + \left(0.28 Re_D^{-1/8} \frac{d_p g}{u_\tau^2} \frac{\rho_s}{\rho_f} d_p^+ \right)} \right)^{-1/2} \tag{122}$$

or

$$\frac{v_{p_{rms(y)}}}{u_\tau} = 0.2 Re_D^{1/8} \left(1 + 5.8 Re_D^{1/4} \frac{t_p^+}{R^+} \sqrt{1 + \left(5\, Re_D^{-1/8} \frac{d_p g}{u_\tau^2} \frac{t_p^+}{d_p^+} \right)} \right)^{-1/2} \tag{123}$$

Since the Reynolds number based on bed diameter and shear velocity is a function only of the Reynolds number based on bed diameter and superficial velocity, the independent governing parameters for the lateral fluctuating particle velocity are:

$$d_p^+; t_p^+; \frac{g d_p}{u_\tau^2}; \text{and } R^+ \tag{124}$$

or

$$\frac{\rho_s}{\rho_f}; t_p^+; \frac{g\nu}{u_\tau^3}; \text{and } R^+ \tag{125}$$

Utilizing Equation (110), the parameters which govern the deposition flux are

$$\frac{\rho_s}{\rho_f}; t_p^+; \frac{gn}{u_\tau^3}; \alpha_{avg}; \text{and } R^+ \tag{126}$$

These parameters are identical to those which resulted in the evaluation of the two-phase governing equations.

Several other models of particle deposition were examined [the model of Kallio and Reeks (1989) and the deposition coefficient model of Bolton and Davidson (1988)]. Nondimensionalization of these models resulted in either identical results or parameters which were a subset of those given above.

When the parameters in (105) or (126) are used to correlate the fractional wall coverage (assuming the fractional wall coverage goes as the square root of the deposition flux), the best least squares curve fit of a single parameter model based on multiples of these parameters results in a chi-squared goodness of fit nearly an order of magnitude better than the square root curve fit proposed by Lints (1992) [see Figure 4.23 for the proposed correlation, see Figure 4.22 for the correlation proposed by Lints (1992)].

Figure 4.23

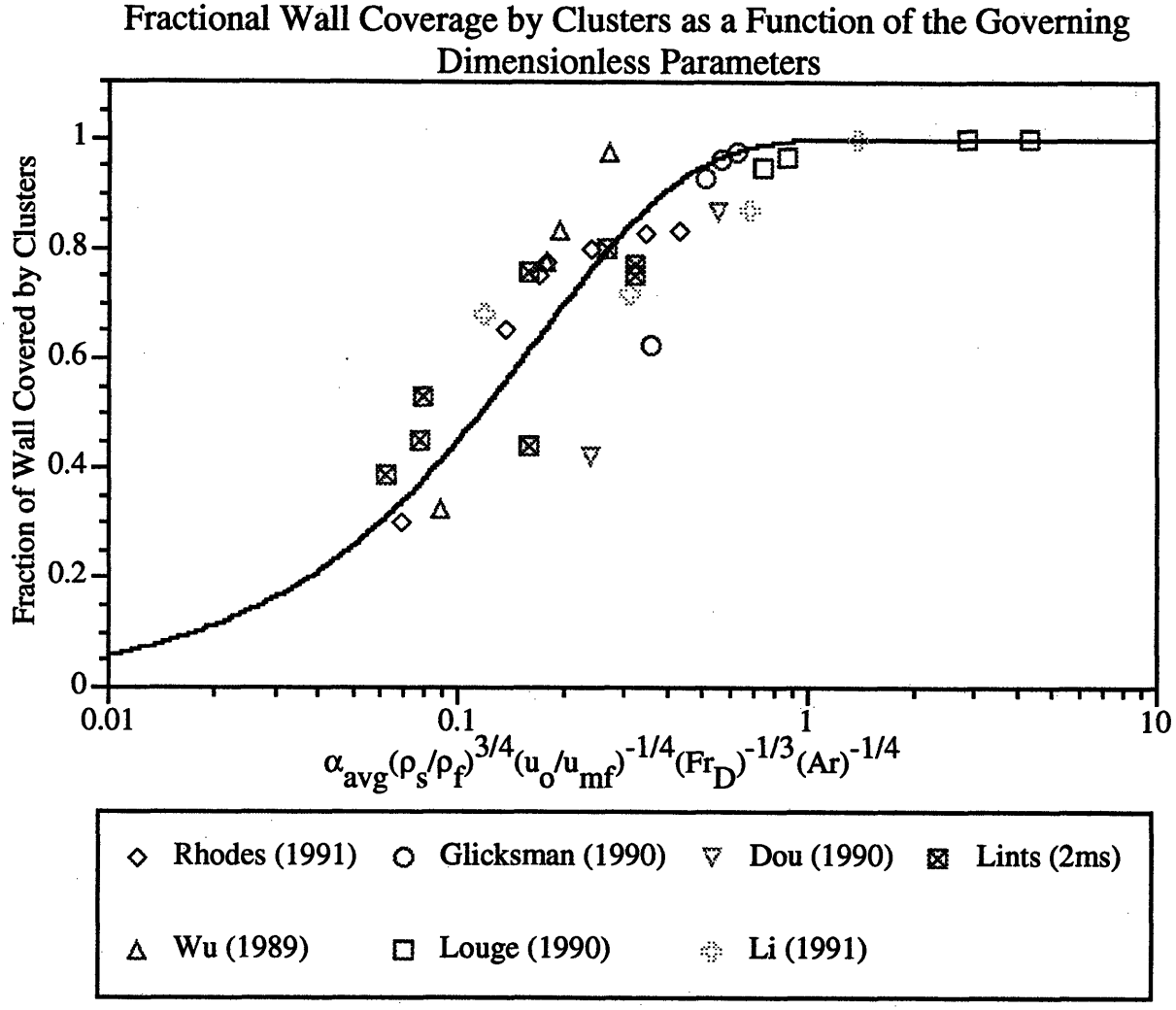

The functional relationship which will be used to determine the steady state value of the fractional wall coverage is

$$f_{ss} = 1 - \mathrm{Exp}\left[- 6.0 \left(\frac{u_o}{u_{mf}}\right)^{-1/4} \left(\frac{\rho_s}{\rho_f}\right)^{3/4} \left(Fr_{D,u_o}\right)^{-1/3} \left(Ar\right)^{-1/4} \left(\alpha_{avg}\right) \right] \qquad (127)$$

If the simplified scaling parameters identified in Chapter 2 are used to correlate the fractional wall coverage in the same form as Equation (127), some error will be introduced due to the exclusion of the Archimedes number. Figure 4.24 shows the error in the fractional wall coverage which would result in using the simplified set of scaling parameters.

Figure 4.24

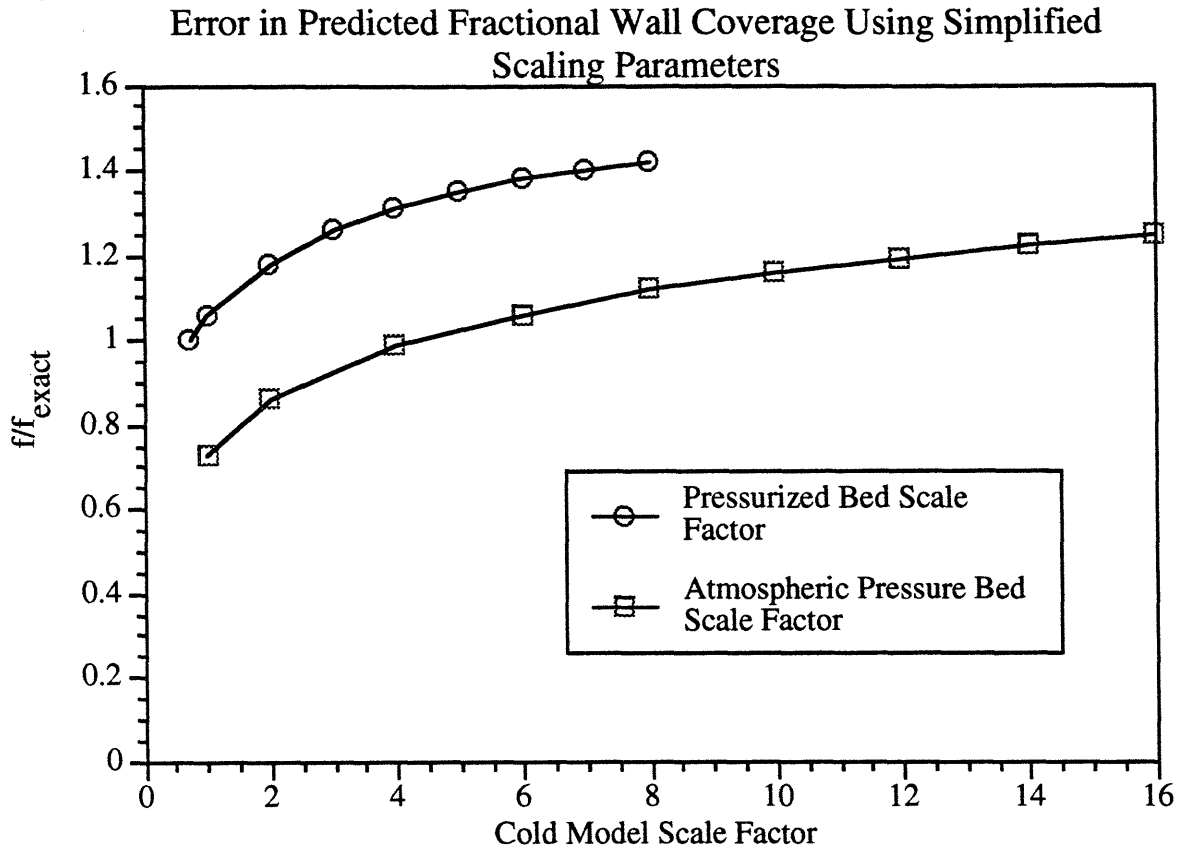

Pressurized Bed Scale Factor	f/fexact - 14 bar CFB	Atmospheric Pressure Bed Scale Factor	f/fexact - Atmospheric Pressure CFB
0.74	1	1	0.73
1	1.06	2	0.86
2	1.18	4	0.99
3	1.26	6	1.06
4	1.31	8	1.12
5	1.35	10	1.16
6	1.38	12	1.19
7	1.4	14	1.22
8	1.42	16	1.25

For pressurized beds, errors in fractional wall coverage can reach 20 percent even for a scale factor as small as 2. For atmospheric beds, the error does not exceed 25 percent even for scale factors as large as 16. This indicates that it may not be possible to use large scale factors to accurately scale heat transfer in pressurized fluidized beds due to the resulting error in the fraction of the wall covered by clusters.

Figure 4.25 shows the fractional wall coverage correlation when the dependence on Archimedes number is eliminated.

Figure 4.25

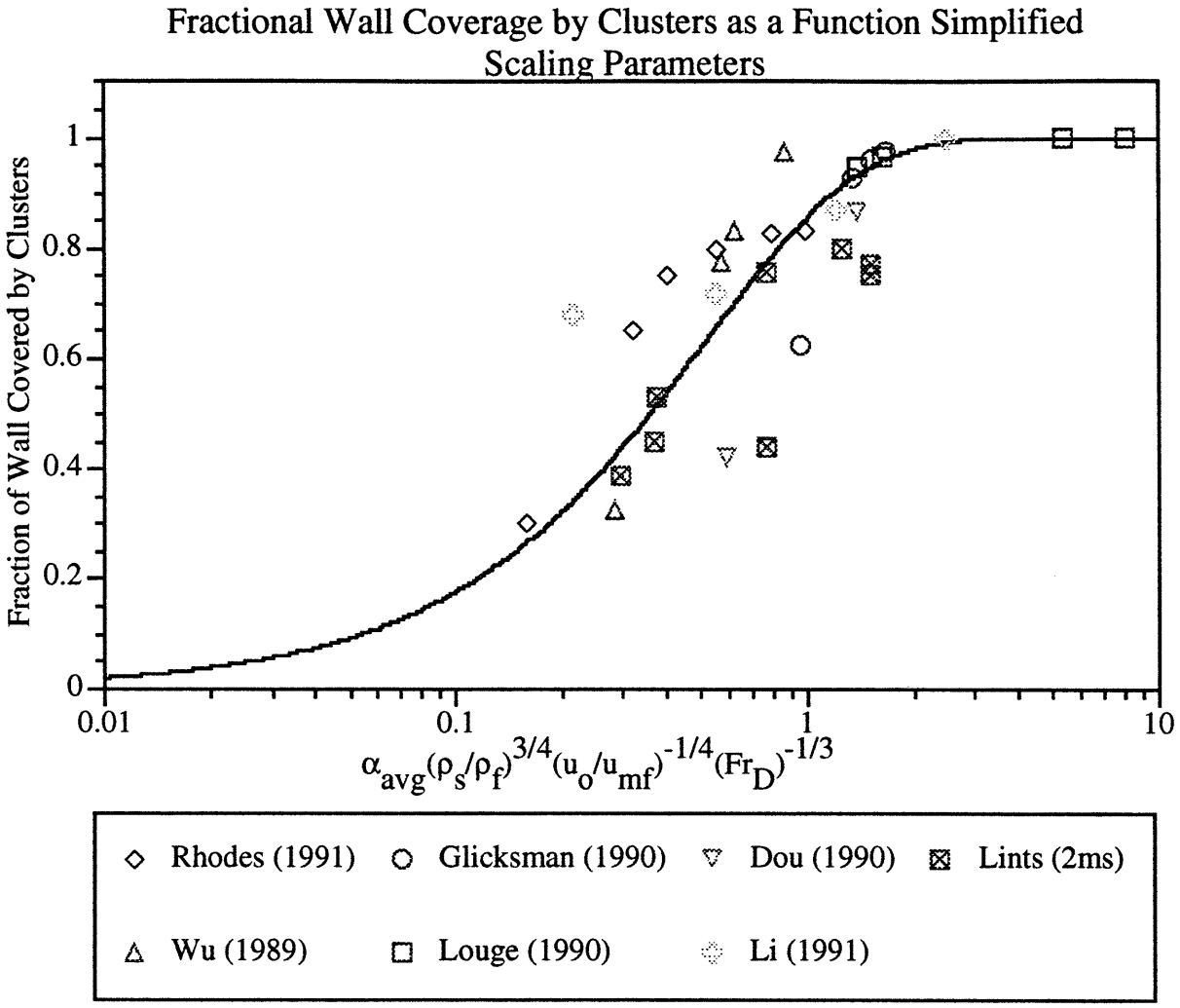

The use of the simplified scaling parameters offers a large advantage over the correlation offered by Lints (Figure 4.22). However, the full set of scaling parameters offers an improvement in the chi squared goodness of fit parameter of about 36 percent over the correlation utilizing the simplified scaling parameters.

4.4.5 Dilute Phase Heat Transfer Coefficient

Lints (1992) investigated the applicability of using single phase gas heat transfer coefficients for the dilute phase heat transfer. The data of several investigators was plotted against the well known correlations of Petukhov (1970) for turbulent tube flow:

$$Nu = \frac{\left(\frac{f}{8}\right) RePr}{1.07 + 12.7\sqrt{\frac{f}{8}}\left(Pr^{2/3} - 1\right)} \tag{128}$$

$$f = \left[1.82\log_{10}(Re) - 1.64\right]^{-2} \tag{129}$$

and the analytical expression for the Nusselt number in laminar flat plate flows

$$Nu = 0.664Re^{1/2}Pr^{1/3} \tag{130}$$

It was determined that these types of correlations could be used if it was assumed that:

1. The length of flow along the heat transfer surface was not greater than the cluster fall length at the wall.

2. The conductivity of the dilute phase was $k_d = 1.1k_g$.

In this study the analytical expression flat plate heat exchange was used with the proper modifications as suggested by items (1) and (2) above.

4.4.6: Effective Emissivity of the Cluster Surface

Because all the measurements were performed in a cold bed, this parameter was not investigated.

5.0 COMPARISON OF EXPERIMENTAL RESULTS WITH THE MODEL

This Section presents the results of the heat transfer model developed in Section 4 and compares it with the experimental results presented in Section 3. A series of plots which evaluates the sensitivity of the heat transfer model to the required input parameters discussed in Section 4 is given.

The initial solid fraction at the wall after the wire ridges was assumed to be 10 percent of the final value. This assumption was based on visual observations of a ridge placed on one of the acrylic sides. The sensitivity of the model to this value is discussed later in this Section.

Table 5.1 presents a summary of the equations used in the model which were developed in Section 4.

Table 5.1

Parameter	Equation
Fractional wall coverage (Linear Model)	$f(t) = 2 f_{ss} e^{-t/t_w} \sqrt{\frac{t_w}{t}} \sum_{n=0}^{\infty} \frac{1}{n!} \left(\frac{1}{(2n+3)}\right) \left(\frac{t}{t_w}\right)^{\left(\frac{2n+3}{2}\right)} + f_0 e^{-t/t_w}$
Fractional wall coverage (Exponential Model)	$\frac{f(t)}{f_{ss}} = \frac{\int_0^{t/t_w} \sqrt{\left[\alpha_{sd} e^{a(t-t_i)} + \alpha_s^*\right]} e^{t/t_w} d\left(\frac{t}{t_w}\right)}{\sqrt{\left[\alpha_{sd} e^{a(t-t_i)} + \alpha_s^*\right]} e^{t/t_w}} + \frac{f_0 e^{-t/t_w}}{f_{ss}}$
Exponential Model constants [Kunii and Levenspiel (1990)]	$\alpha_{sd} = 0.25$ $\alpha_s^* = 0.01$ $a = 1$
Ratio of initial to final fractional wall coverage	$f_0/f_{SS} = 0.10$
Steady state fractional wall coverage	$f_{ss} = 1 - Exp\left[-6.0 \left(\frac{u_o}{u_{mf}}\right)^{-1/4} \left(\frac{\rho_s}{\rho_f}\right)^{3/4} (Fr_{D,u_o})^{-1/3} (Ar)^{-1/4} (\alpha_{avg})\right]$
Cluster standoff distance	$\frac{\delta}{\delta_{ss}} = \left[\frac{\nu t}{\nu t_{ss}}\right]$
Steady state cluster standoff distance	$\delta_{ss} = 0.0282\, \varepsilon_{avg}^{-0.59}$
Cluster residence time	$t = \frac{L}{V_c}$
Cluster velocity	$V_c \cong \frac{-\frac{\pi}{4} d_c^2 \rho_c}{t} + \sqrt{\left(\frac{\frac{\pi}{4} d_c^2 \rho_c}{t}\right)^2 + \frac{\frac{\pi}{2} C_{D_c} d_c^3 \rho_c g}{\rho_f}}}{C_{D_c} d_c \rho_f}$
Cluster diameter	$d_c \sim \left(\frac{92000 \mu_c}{\sqrt{g \rho_c \rho_g}}\right)^{\frac{2}{3}}$
Cluster voidage	$\varepsilon_{cl} = \varepsilon_{avg}^{0.5}$
Dilute phase heat transfer coefficient	$Nu = 0.664 Re^{1/2} Pr^{1/3}$ $k_d = 1.1 k_g$
Cluster fall distance	$L = 1.95 \frac{d_p}{(d_p)_{Wu}} (1 - \varepsilon_{avg})^{0.596}$

5.1 Flat Wall Tests

Figure 5.1 depicts the results of the heat transfer model and experimental tests as a function of the average bed solid fraction. For this case, the fractional wall coverage was equal to the steady state fractional wall coverage.

Figure 5.1

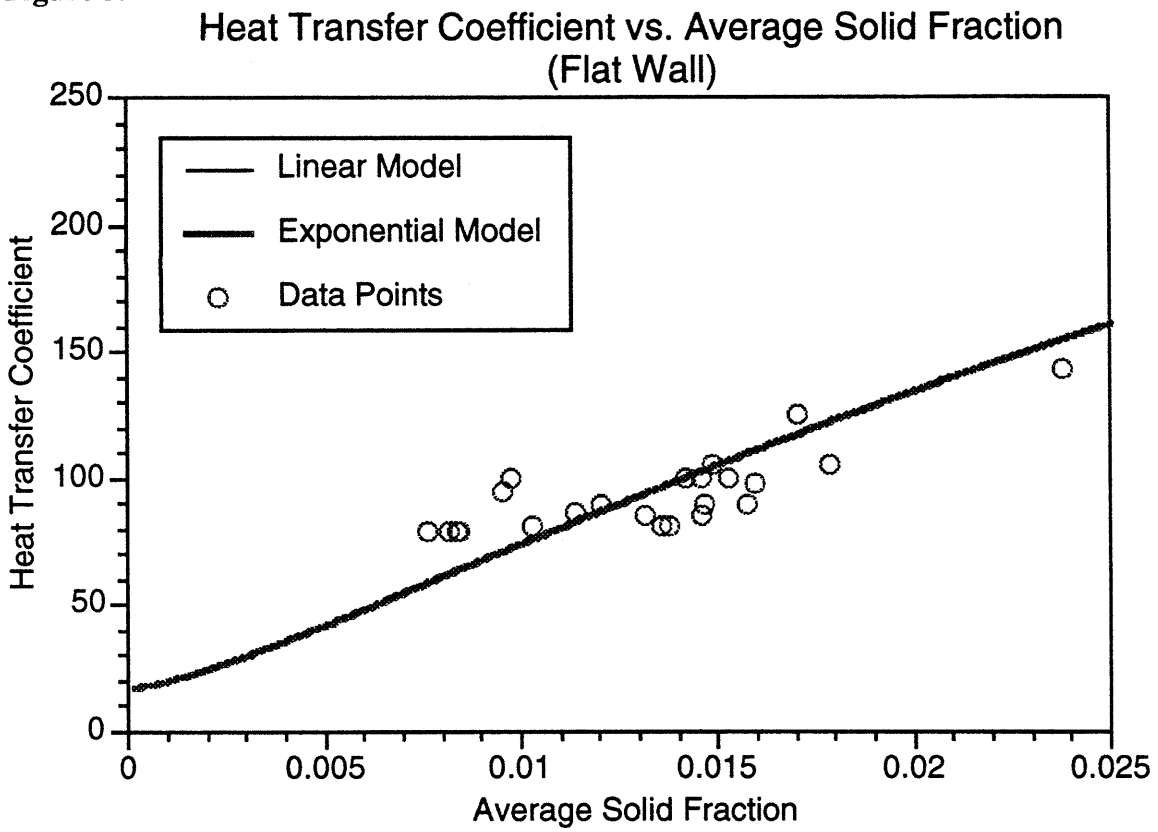

The model does a good job in predicting the bed to wall heat transfer coefficient for a wide range of average cross-sectional solid fractions. Both the slope and the magnitude of the predicted curve is in agreement with the experimental data. Since the Exponential model and Linear model were evaluated at steady state, the results were identical.

5.2 Ridge Spacing = 20 mm

Figure 5.2 depicts predicted versus experimental results for the 20mm ridge spacing case. The model slope is larger than that of the experimental data for which it is difficult to notice any slope at all. The fact that the experimental heat transfer coefficients did not increase with increasing average cross-sectional solid fraction indicates that the data points taken at the higher solids concentrations may not be accurate. The model does predict the magnitude of the heat transfer coefficients quite well. The Exponential model seems to

provide a better prediction of the experimental data. However, because the difference in the two models is not terribly large, it is not possible to recommend one model over the other.

Figure 5.2

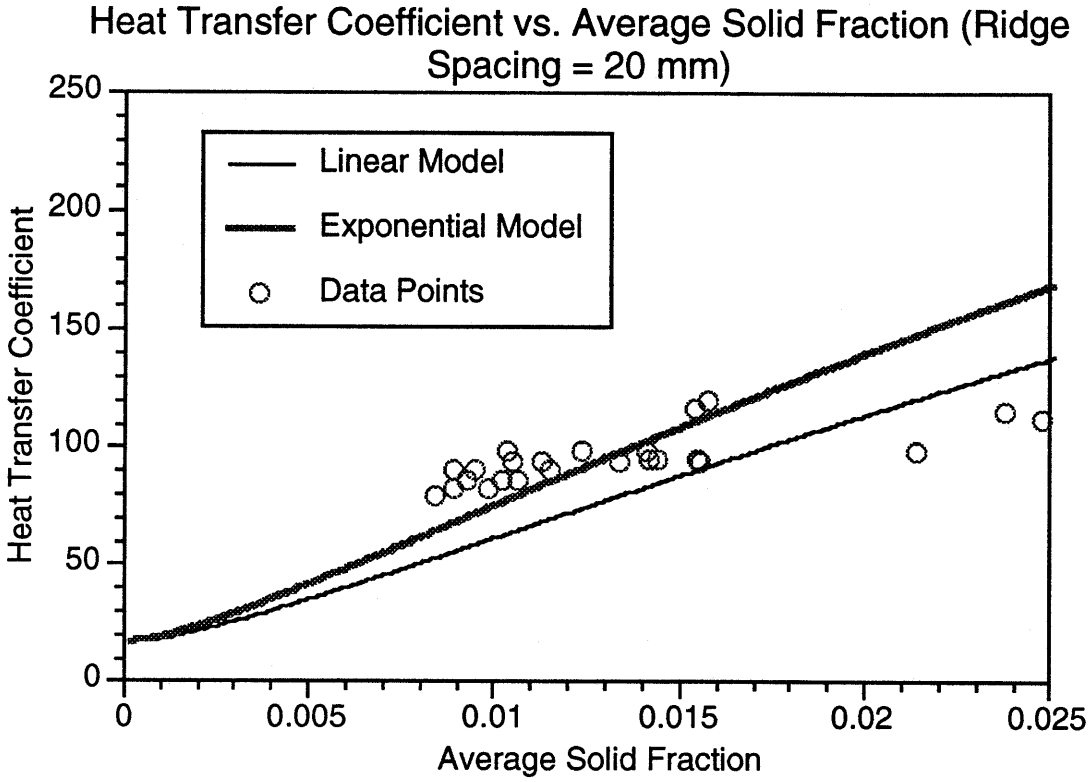

5.3 Ridge Spacing = 10mm

Figure 5.3 depicts the results of the model and experiments when the ridge spacing was 10mm. Both the magnitude and the slope of the data were predicted quite well by the model - especially at higher solids concentrations. Both the Linear and Exponential models predict the data equally well.

Figure 5.3

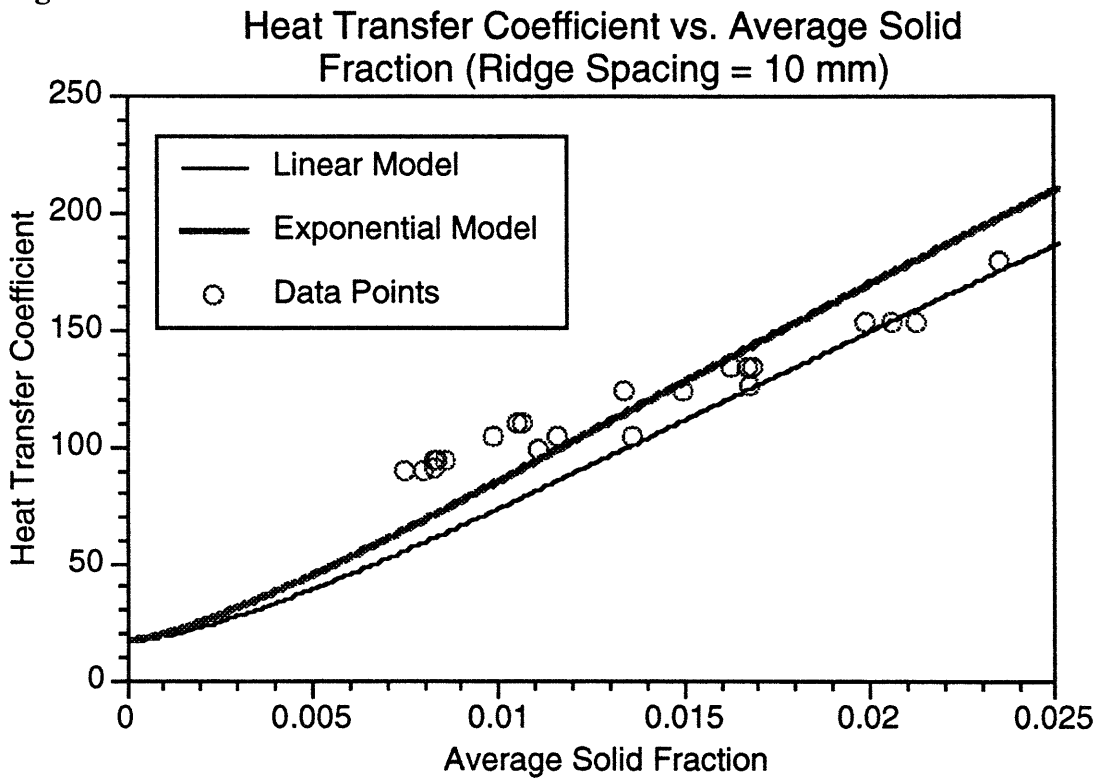

5.4 Ridge Spacing = 5mm

Figure 5.4 presents the results of the 5mm ridge spacing comparison. Again, the model does a good job in predicting the magnitude of the heat transfer coefficients in the range of cross-sectional solids fraction of interest. The difference between the Linear and Exponential model is again small indicating that both models are equally valid. It appears that the model predicts a greater slope than the data indicates. This is consistent with the 20mm and 10mm cases.

Figure 5.4

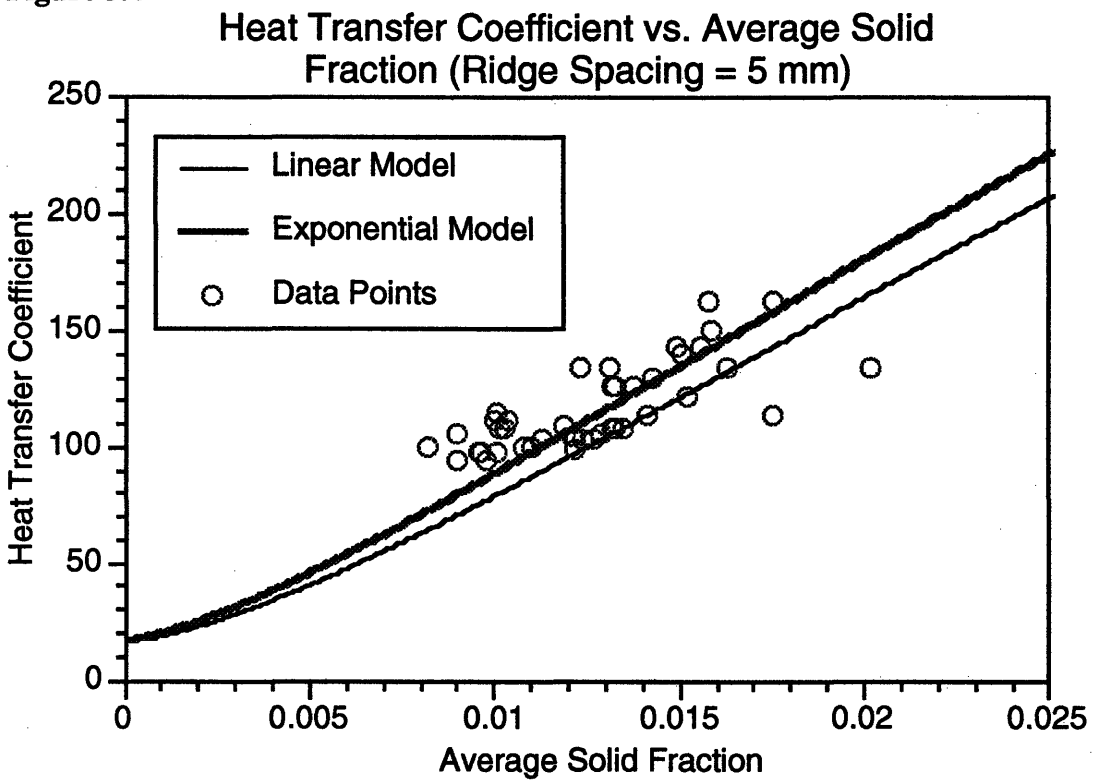

5.5 Summary

Both the Exponential and Linear flux models did a good job in predicting the magnitude of the bed to wall heat transfer coefficients. In general, the model tended to over predict the slope of the heat transfer coefficient versus average cross-sectional solid fraction curve which brings into question the validity of using this model outside the dilute region of a circulating fluidized bed.

5.6 Comparison of Heat Transfer Model Results for Various Ridge Spacings

Figures 5.5 and 5.6 present the results of the Linear and Exponential flux models for the various ridge spacings.

Figure 5.5

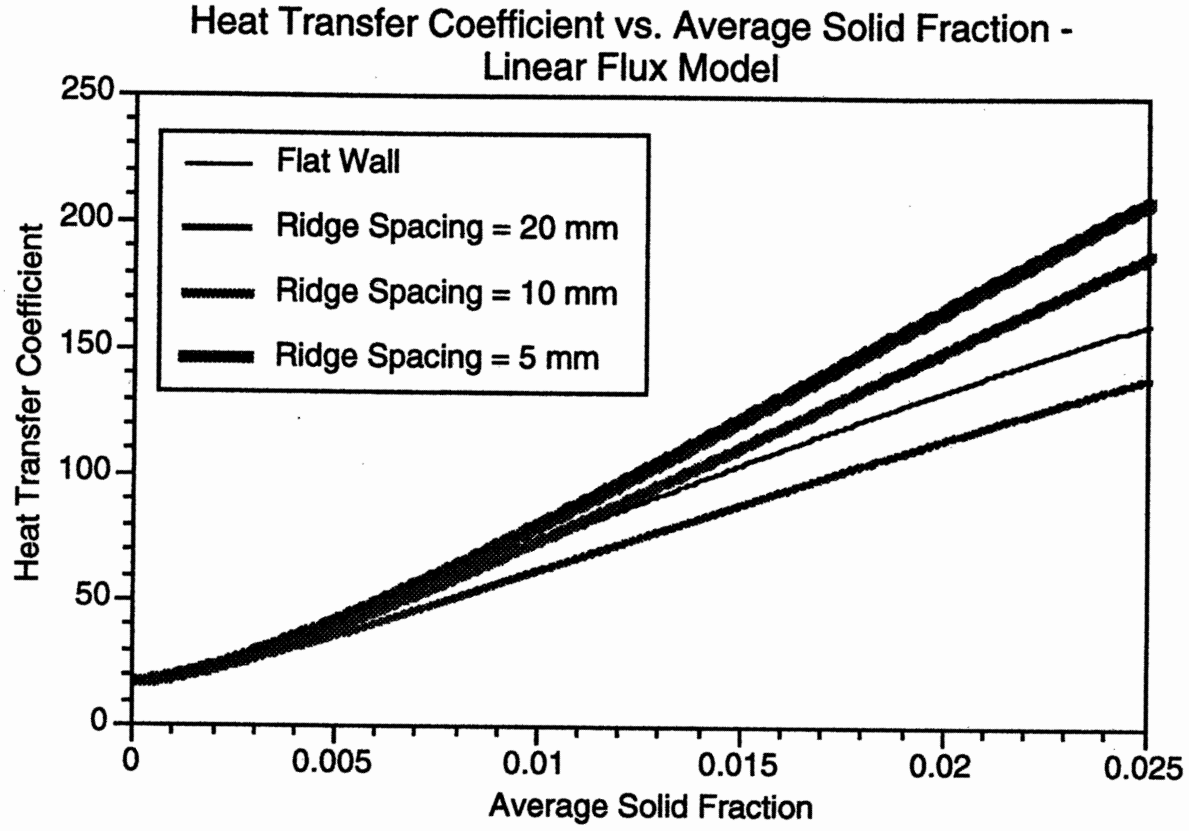

Figure 5.6

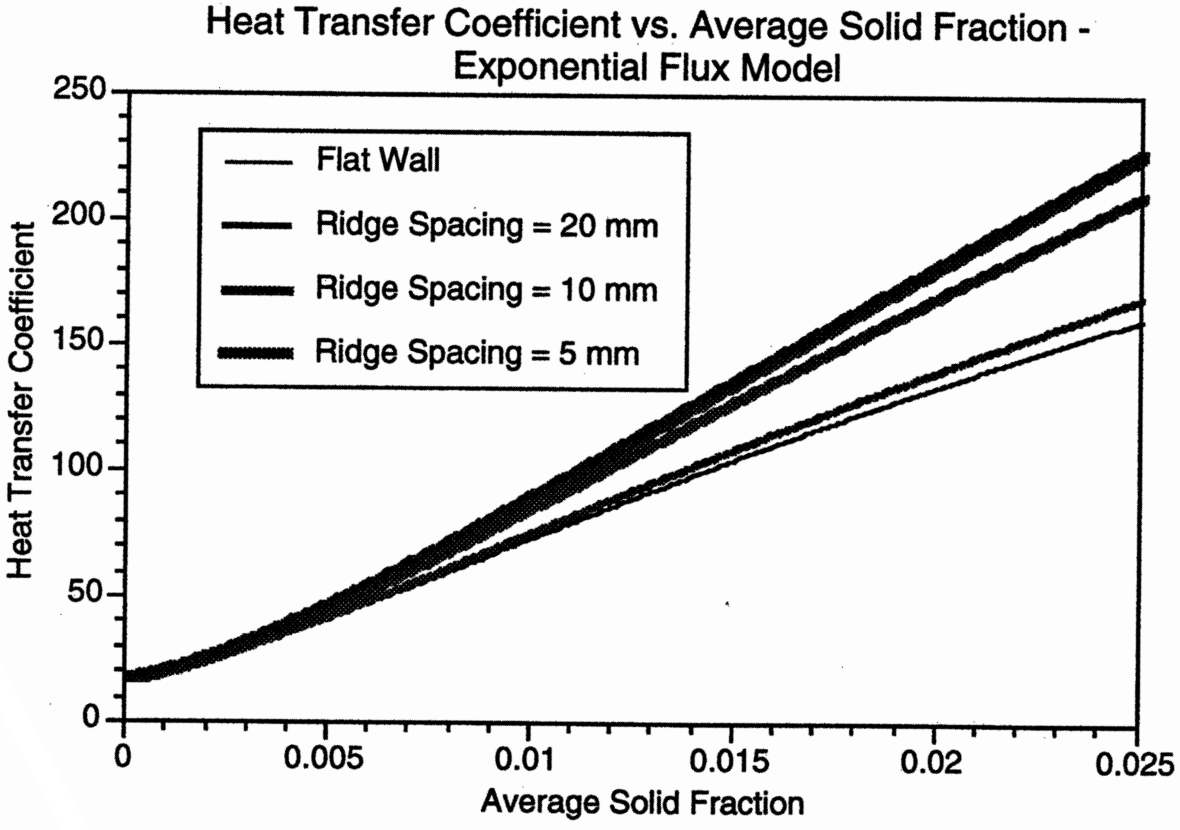

The Linear model predicts a decrease in heat transfer coefficient for the 20mm ridge spacing case over the flat wall case while the Exponential model predicts a slight increase. Both models predict increases in heat transfer coefficients for the 10mm and 5mm ridge spacing cases. The Exponential model follows the trend of the data better (i.e. small increase in heat transfer coefficient for the 20mm spacing case over the flat wall case followed by a large jump to the 10mm spacing case and a smaller increase from the 10mm case to the 5mm case).

If the heat transfer data is fit to the curve $h \sim a\sqrt{\alpha_{avg}}$, the 10mm ridge spacing shows a 28 percent increase in the coefficient 'a' over the flat wall case. For close rib spacing, the clusters are renewed frequently and the viscous sublayer remains thin leading to large values of h_e and h_w, respectively. At the same time, for moderate solid fraction, the wall coverage by clusters is low. As the ridge spacing is increased the viscous sublayer thickness (Figure 5.7), and the mean contact time increases. Thus, the resistance due to the wall ($1/h_w$) and the emulsion ($1/h_e$) increased with ridge spacing as seen on Figure 5.8. At the same time the fraction of surface covered by clusters increases (Figure 5.7). The increase of heat transfer resistance for each cluster and the increase of f with ridge spacing give conflicting trends. When these are combined to give the average heat transfer for the entire surface covered by clusters along with the dilute phase heat transfer the results, shown on Figure 5.9, exhibit a maximum at a 7mm rib spacing. Although the predicted values of h are roughly the same at the 5mm and 10mm spacings, the individual heat transfer parameters differ. For the 10mm predicted results, the combined emulsion and wall resistance was 67 percent lower than the smooth wall while the fractional wall coverage was 59 percent lower. For the 5mm spacing, the emulsion and wall resistance decreased another 25 and 22 percent over the 10mm case while the fractional wall coverage was 22 percent lower than the 10mm case. At 20mm spacing, the reduction in the combined cluster heat transfer resistance is approximately matched by the reduction in the average wall coverage by clusters. The predicted trends are borne out by the heat transfer results for the different rib spacings as shown in Figure 5.10 (using Linear flux model) where the 5 and 10mm spacings show roughly the same increase in heat transfer and the 20mm spacing shows performance worse than that of the smooth surface.

Figure 5.7

Predicted Variation of Fractional Wall Coverage and Dimensionless Standoff Distance with Wire Spacing

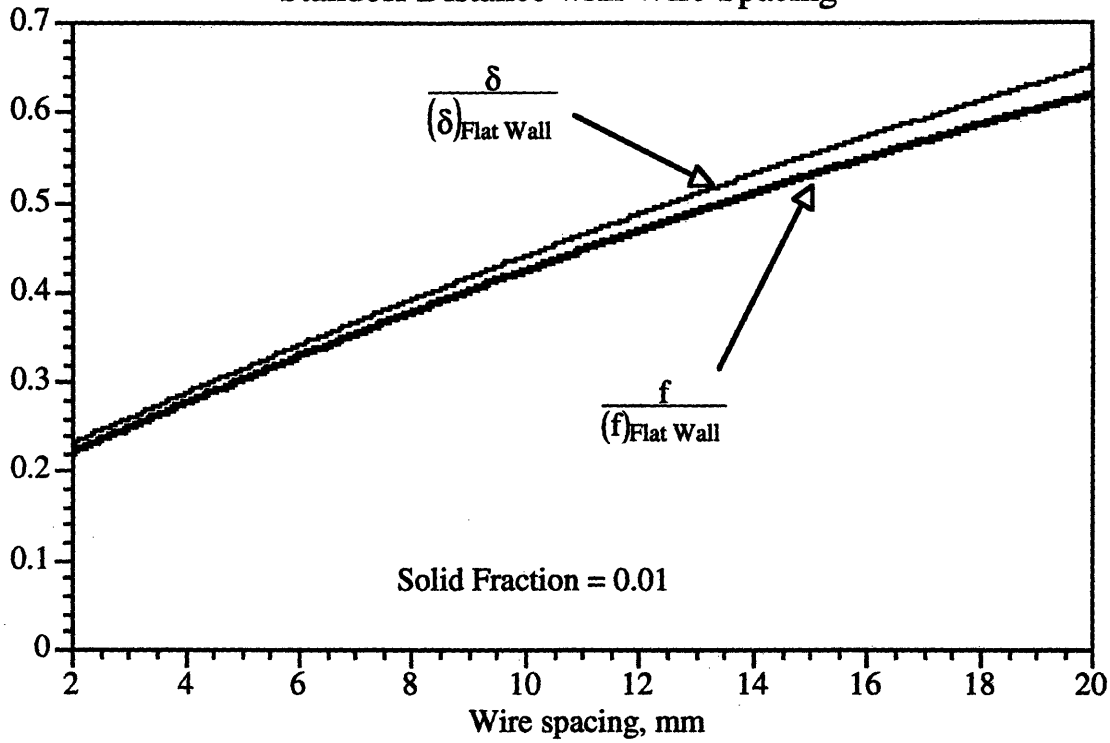

Figure 5.8

Predicted Variation of Emulsion and Wall Resistances with Wire Spacing

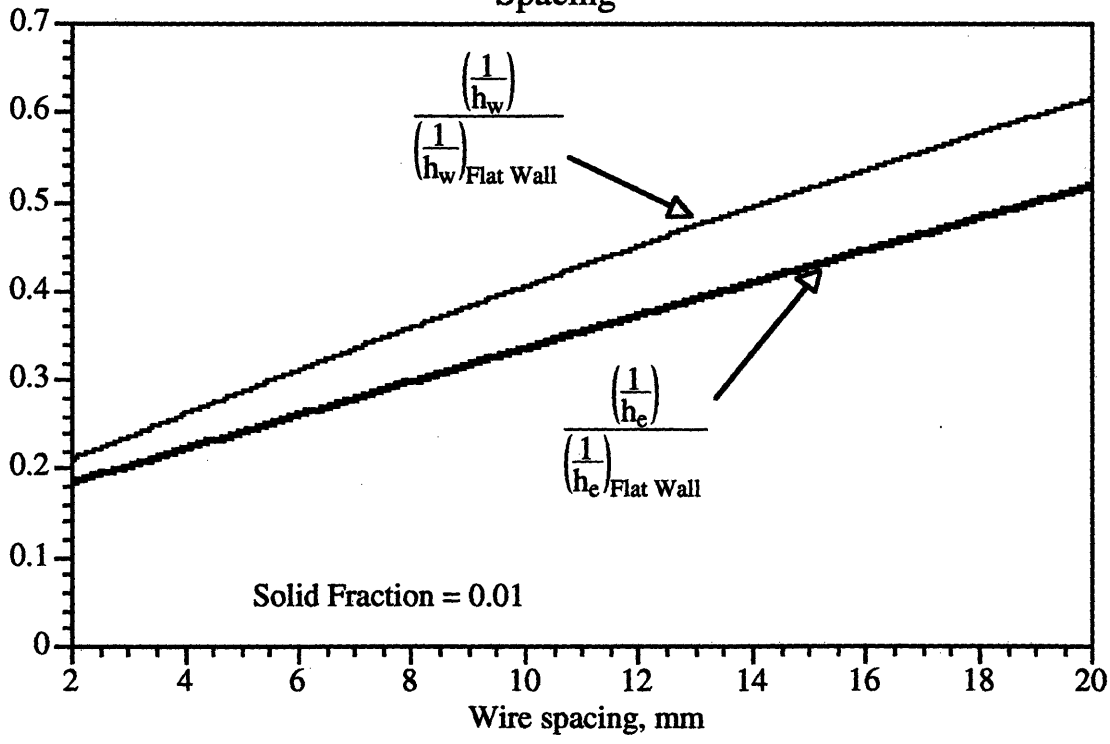

Figure 5.9

Predicted Variation of Heat Transfer Coefficient with Wire Spacing

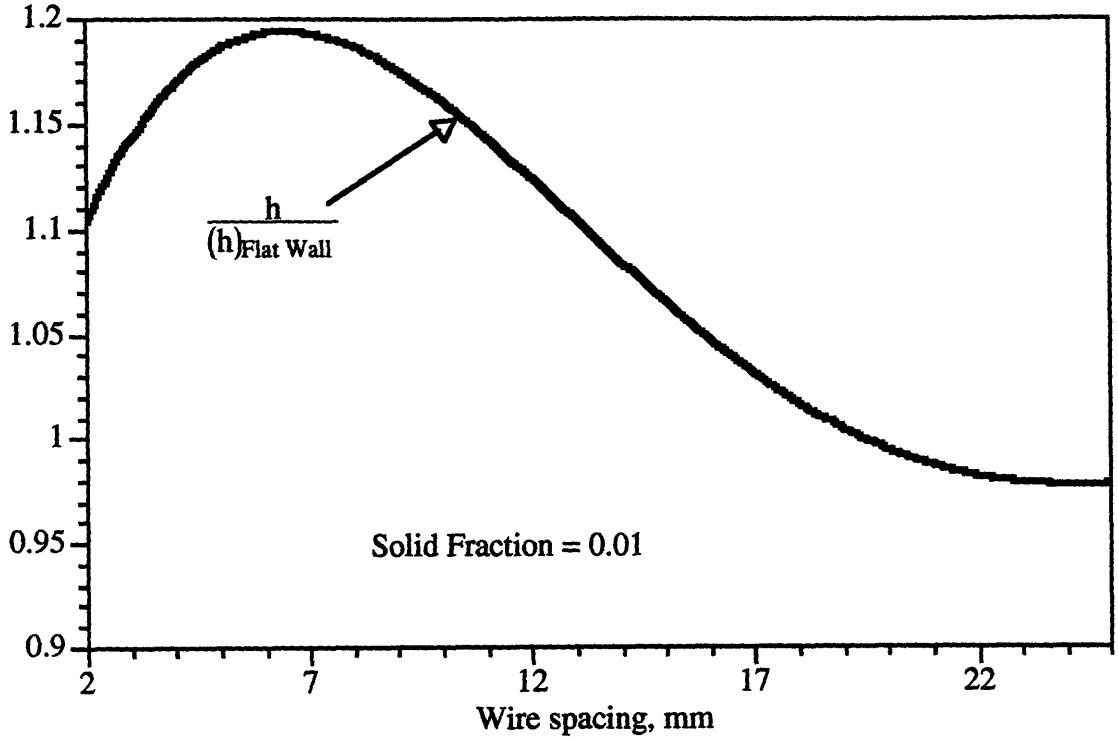

Figure 5.10

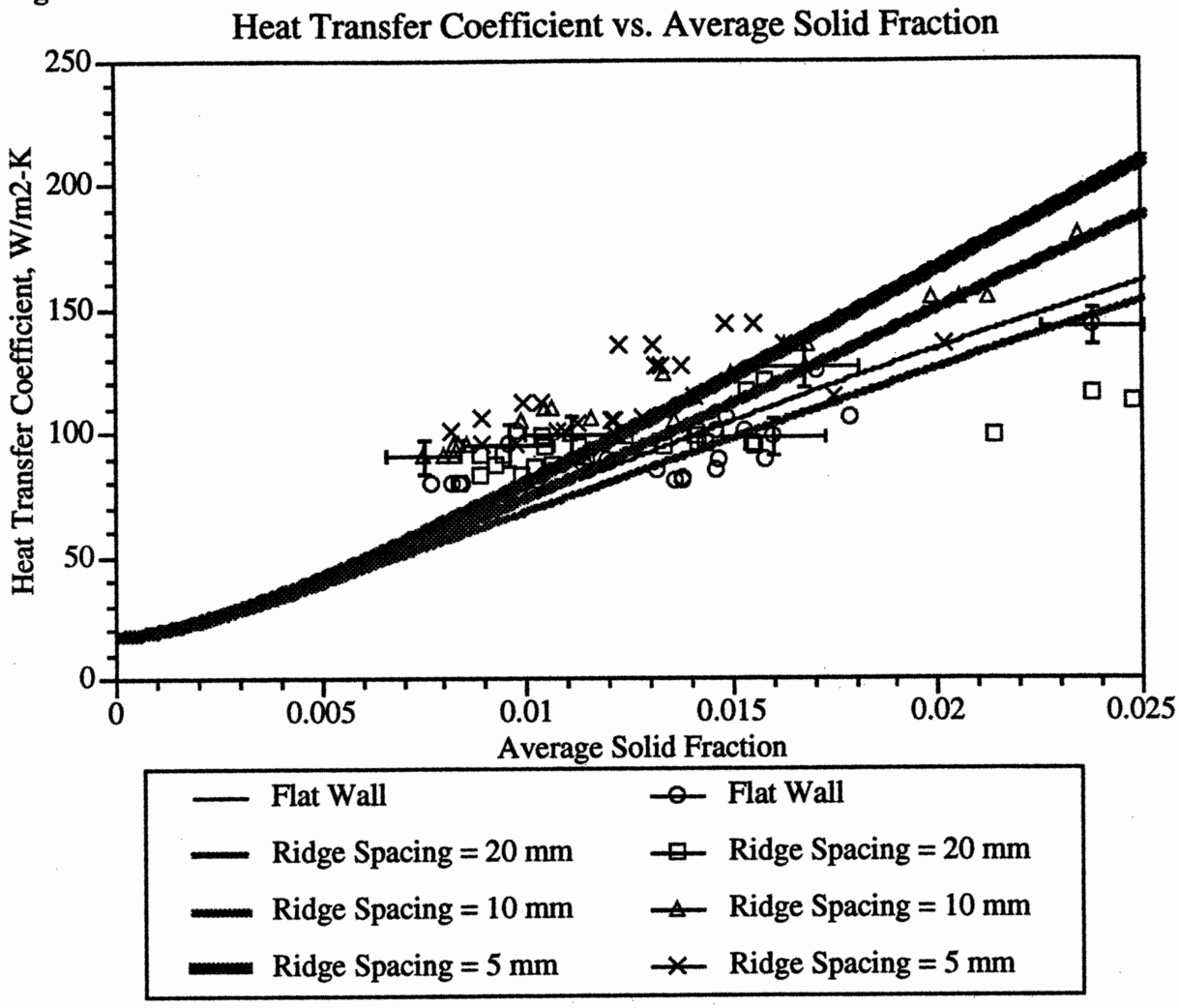

The difference in the Linear and Exponential models is the approximation used to model the solid fraction of the core as a function of bed height. Figure 5.11 compares the two models to a typical solid fraction profile. It is obvious that the Exponential model does a better job at predicted the solid fraction profile (and therefore the solids flux) over the entire bed. In the region of interest, however, both models do a reasonable job of estimating. Due to the uncertainty associated with the experimental data, it would be premature to assert that the Exponential model better represents the physics of the problem. More data would be needed to evaluate which flux model better predicts CFB heat transfer.

Figure 5.11

Kunii and Levenspiel Model (Exponential Model) Comparison to Actual Bed Data and a Linear Approximation

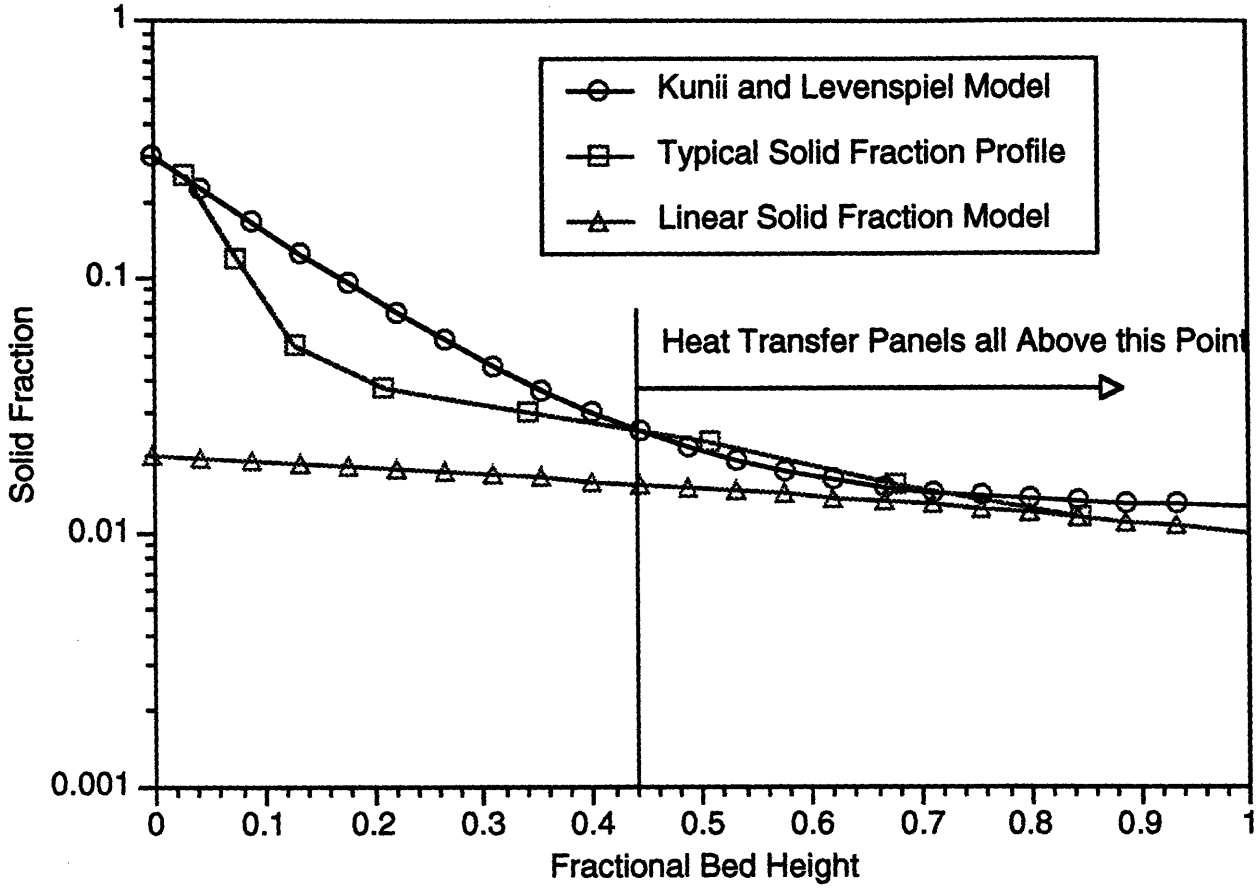

5.7 Sensitivity to Cluster Voidage

Figures 5.12 through 5.15 show the sensitivity of the model to the cluster voidage for the various ridge spacing cases.

Figure 5.12

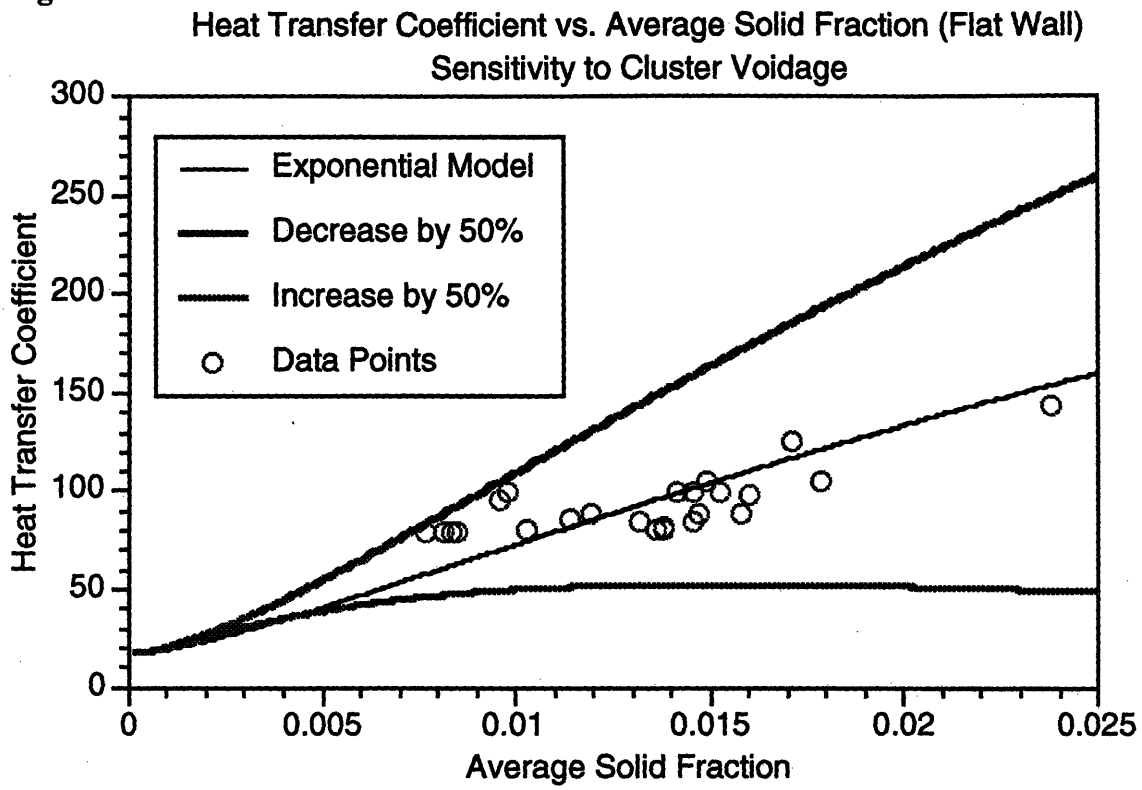

Figure 5.13

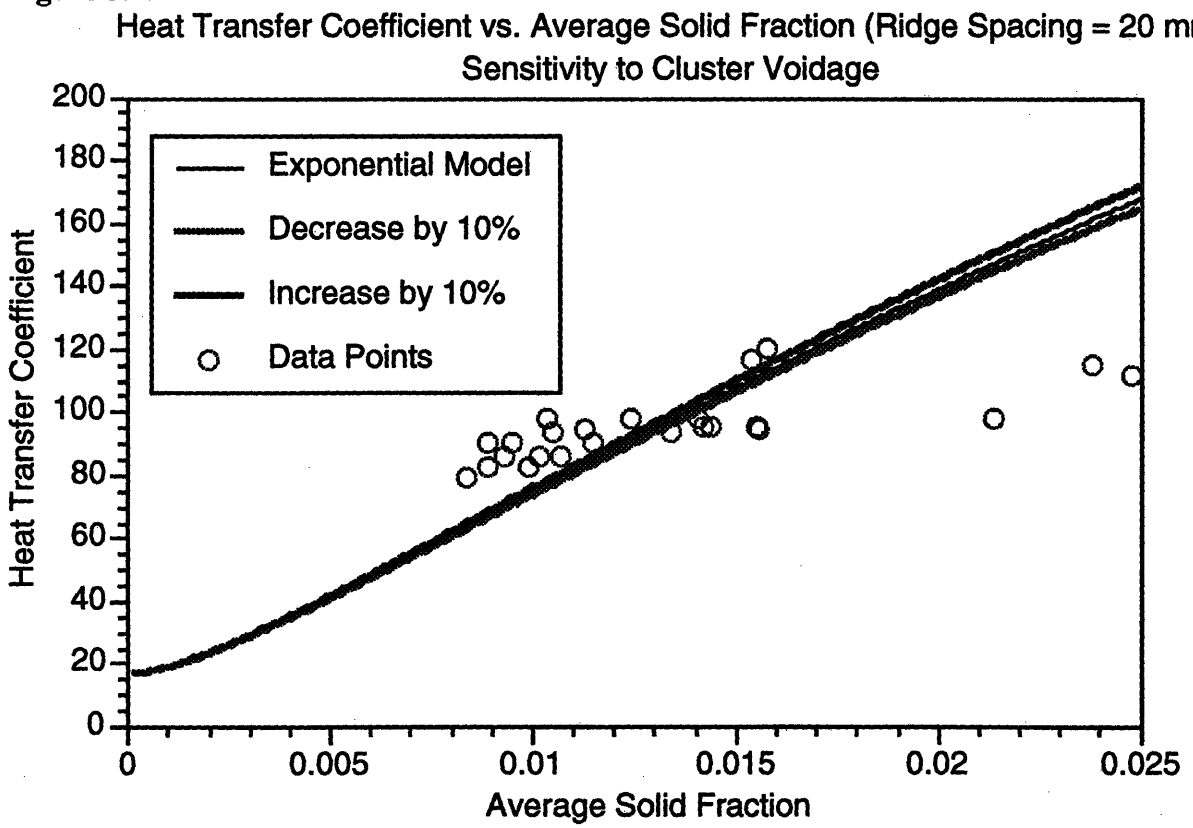

Figure 5.14

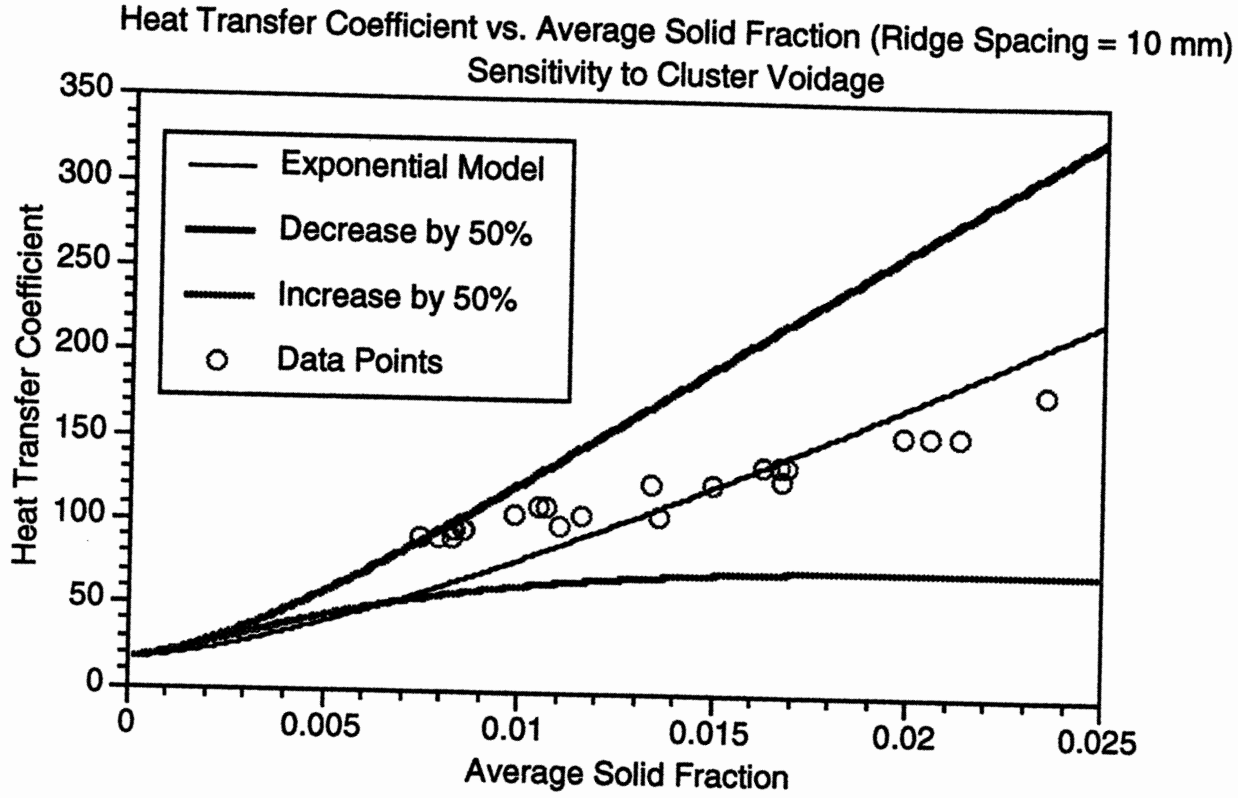

Figure 5.15

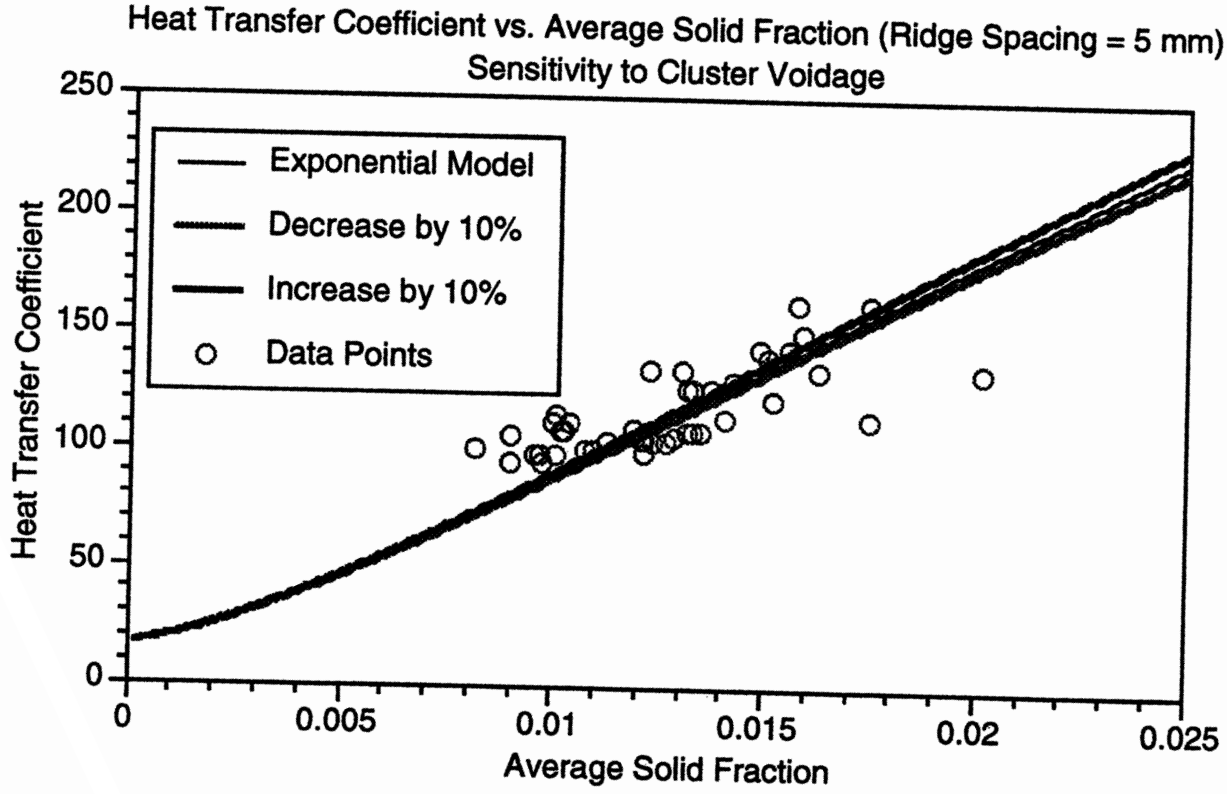

The model is not very sensitive to the cluster voidage for small deviations, but is very sensitive at large deviations. The sensitivity does not change significantly between the various ridge spacing cases.

5.8 Sensitivity to the Cluster Standoff Distance

Another parameter which is difficult to evaluate is the cluster standoff distance. Figures 5.16 through 5.19 show the sensitivity of the model to a 10 percent increase and decrease in the standoff distance.

Figure 5.16

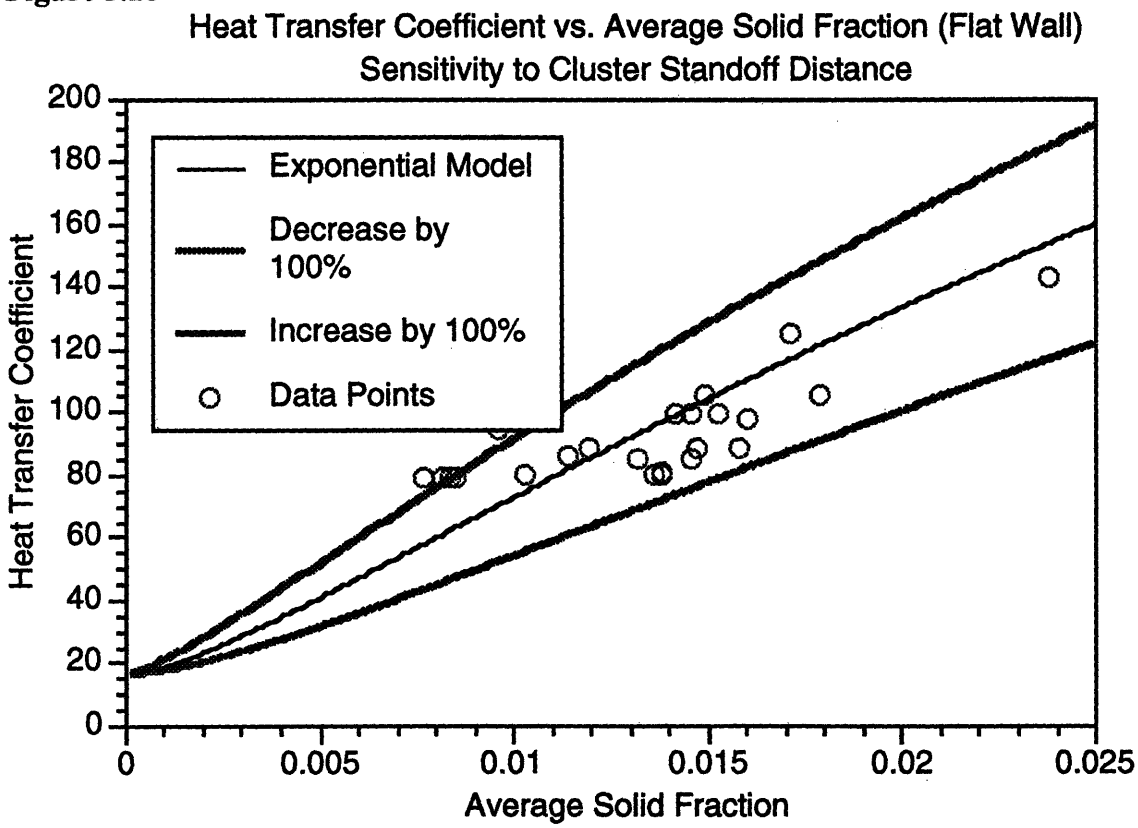

Figure 5.17

Heat Transfer Coefficient vs. Average Solid Fraction (Ridge Spacing = 20 mm)
Sensitivity to Cluster Standoff Distance

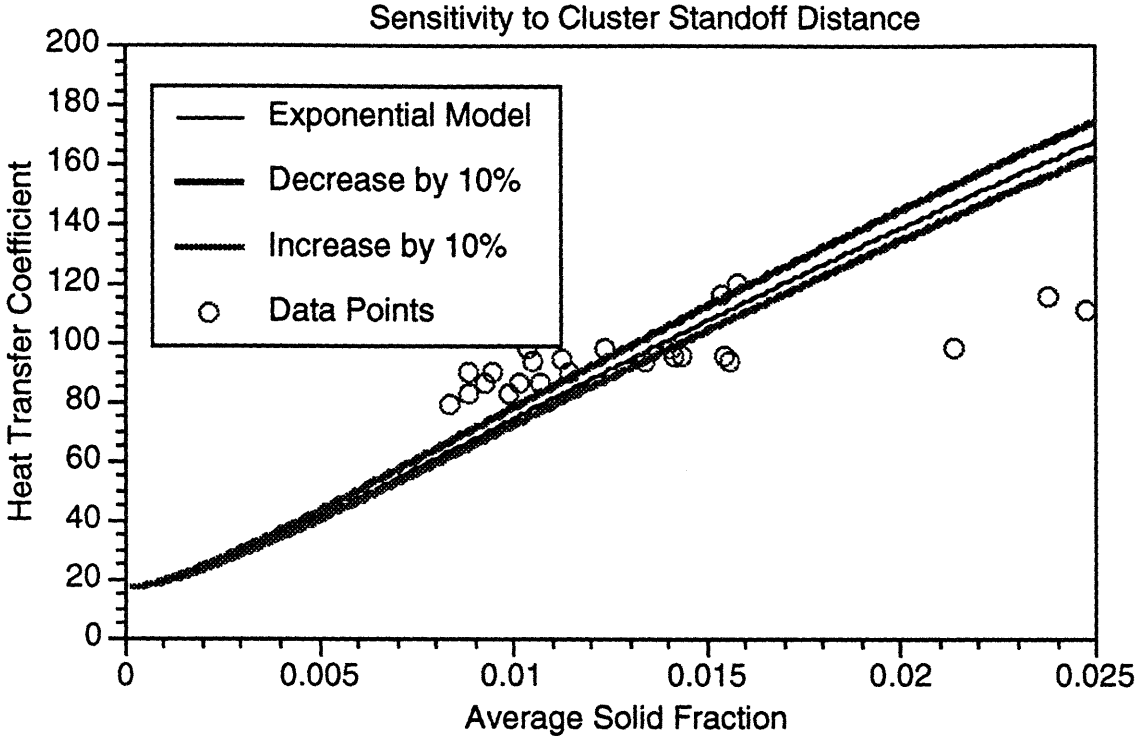

Figure 5.18

Heat Transfer Coefficient vs. Average Solid Fraction (Ridge Spacing = 10 mm)
Sensitivity to Cluster Standoff Distance

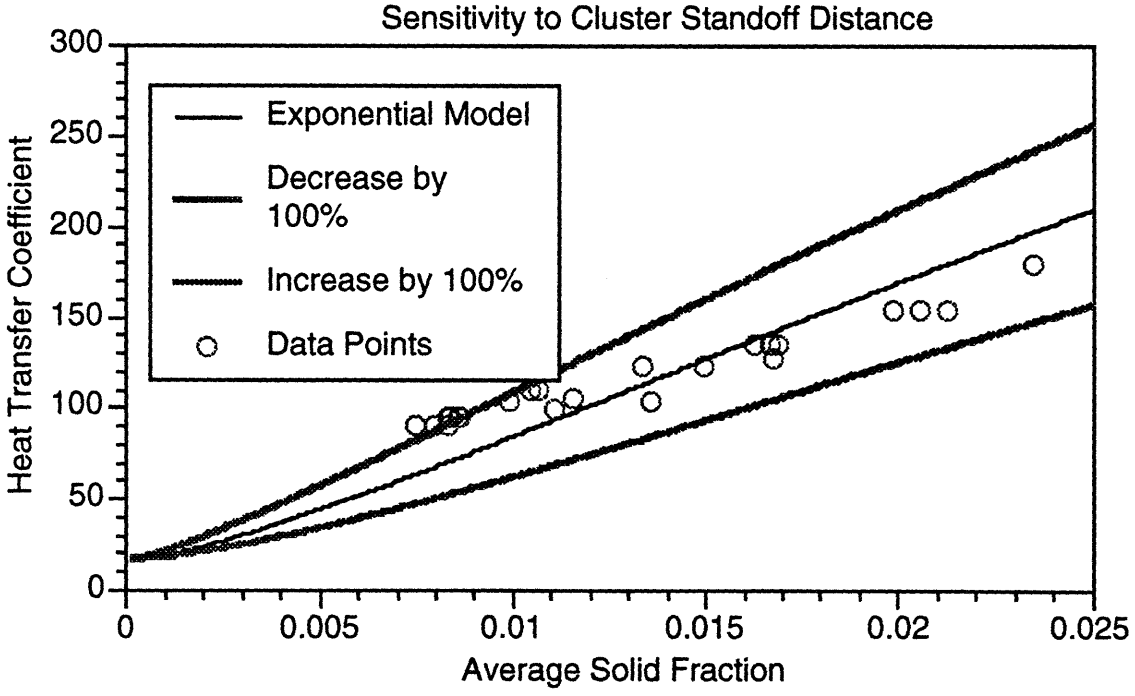

Figure 5.19

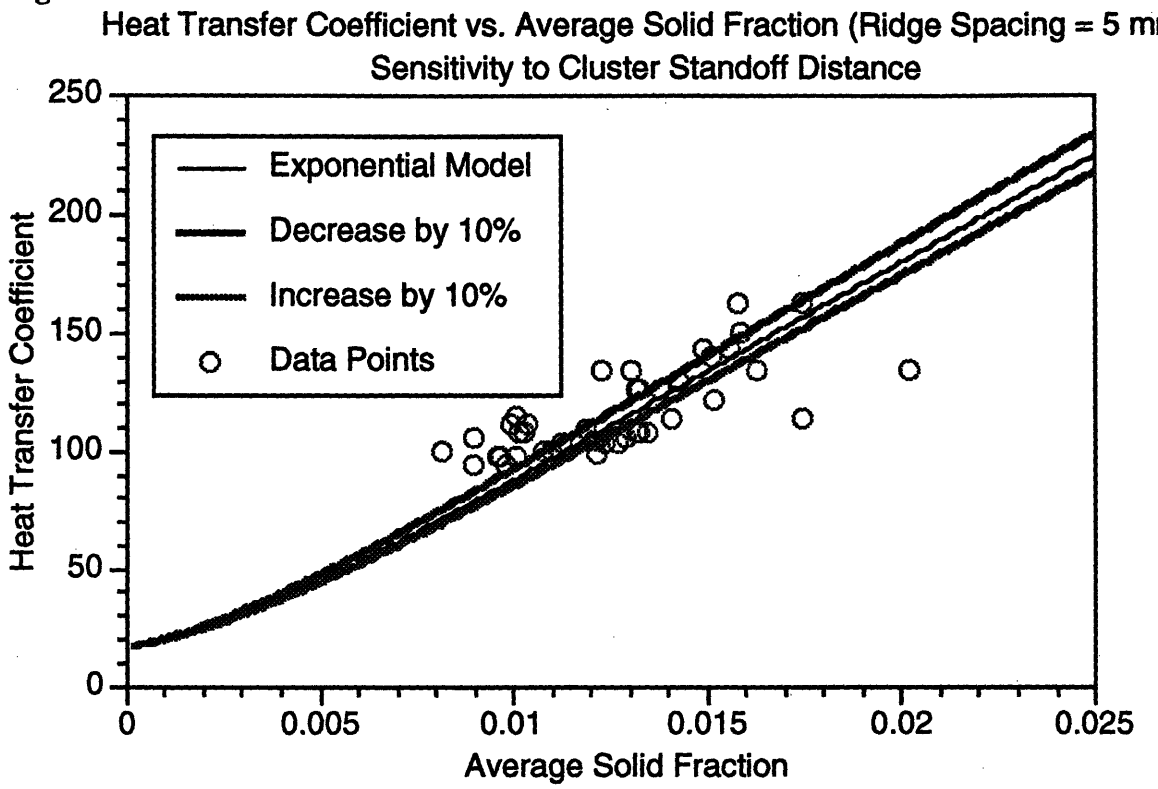

The model is slightly more sensitive to the cluster standoff distance than it was to the cluster voidage at lower deviations. However, it is less sensitive at large deviations.

It should be mentioned that the underlying physics to the cause of the standoff distance is still being studied. If the mechanism which was proposed in Section 4 does not adequately model the change in standoff distance when wall ridges are present, the deviation in the standoff distance may be much larger than 10 percent. Further investigations to characterize the standoff distance are currently underway.

5.9 Sensitivity to the Fraction of Wall Covered by Clusters

Figures 5.20 through 5.23 show the sensitivity of the model to the fraction of the wall covered by clusters. For all cases the Exponential flux model was used.

Figure 5.20

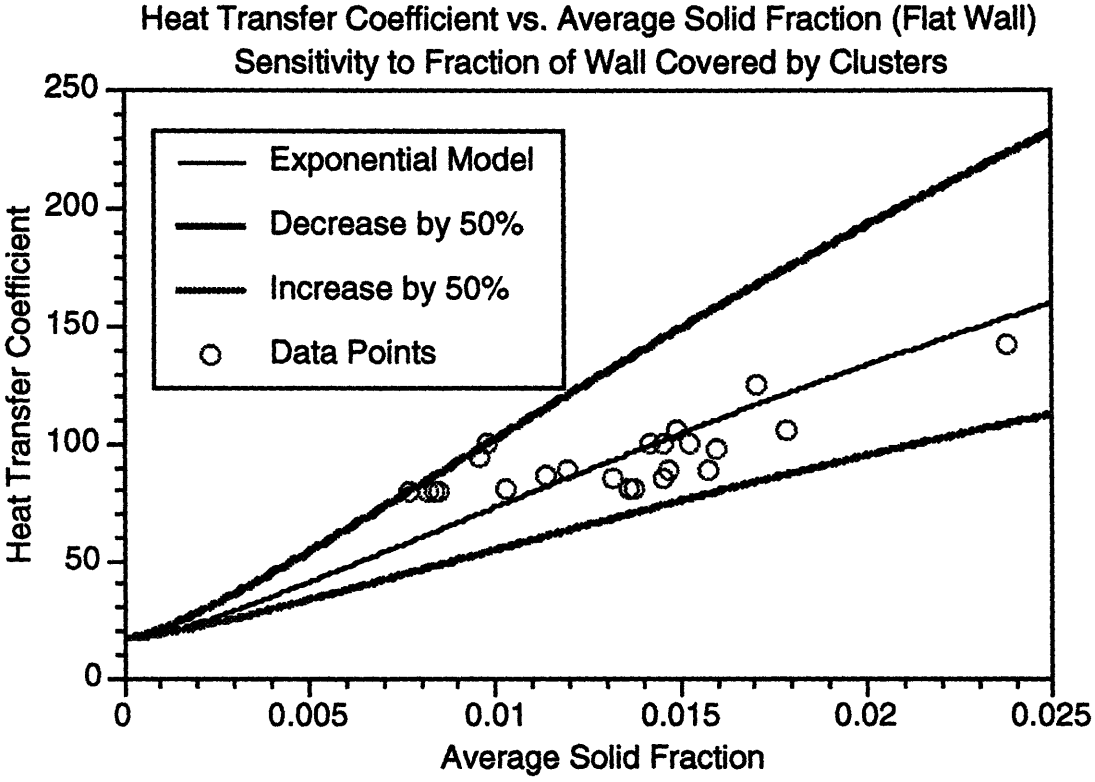

Figure 5.21

Heat Transfer Coefficient vs. Average Solid Fraction (Ridge Spacing = 20 mm)
Sensitivity to Fraction of Wall Covered by Clusters

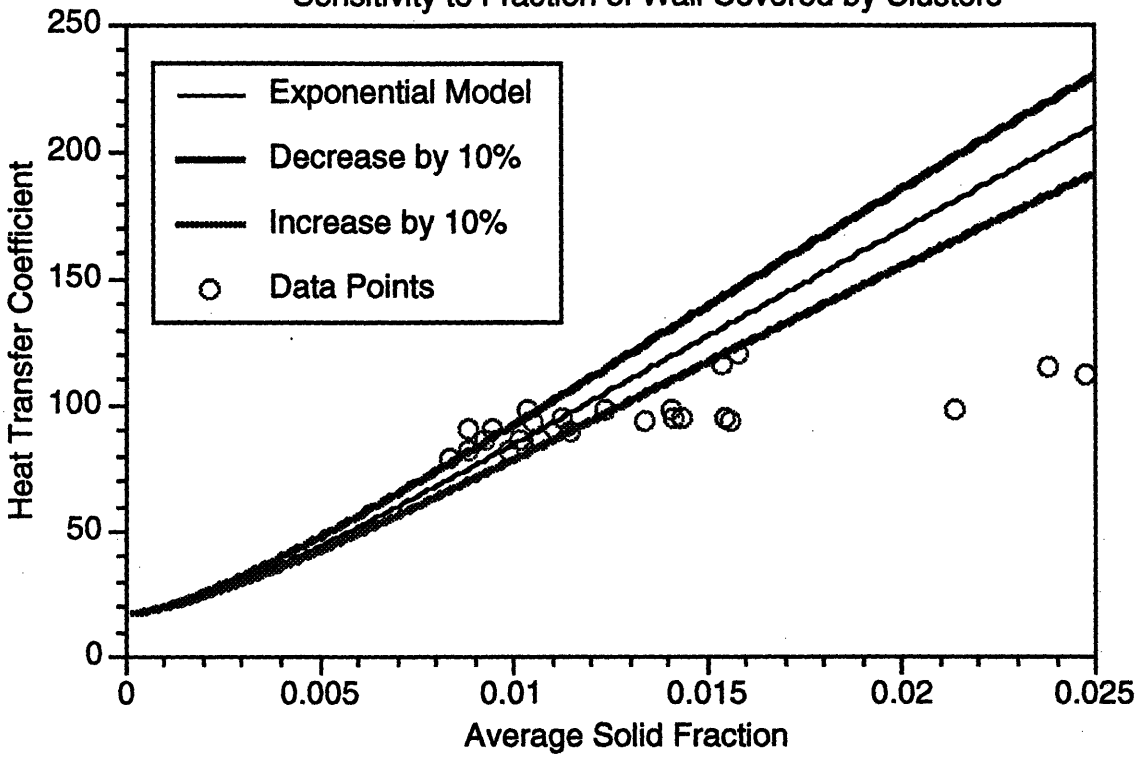

Figure 5.22

Heat Transfer Coefficient vs. Average Solid Fraction (Ridge Spacing = 10 mm)
Sensitivity to Fraction of Wall Covered by Clusters

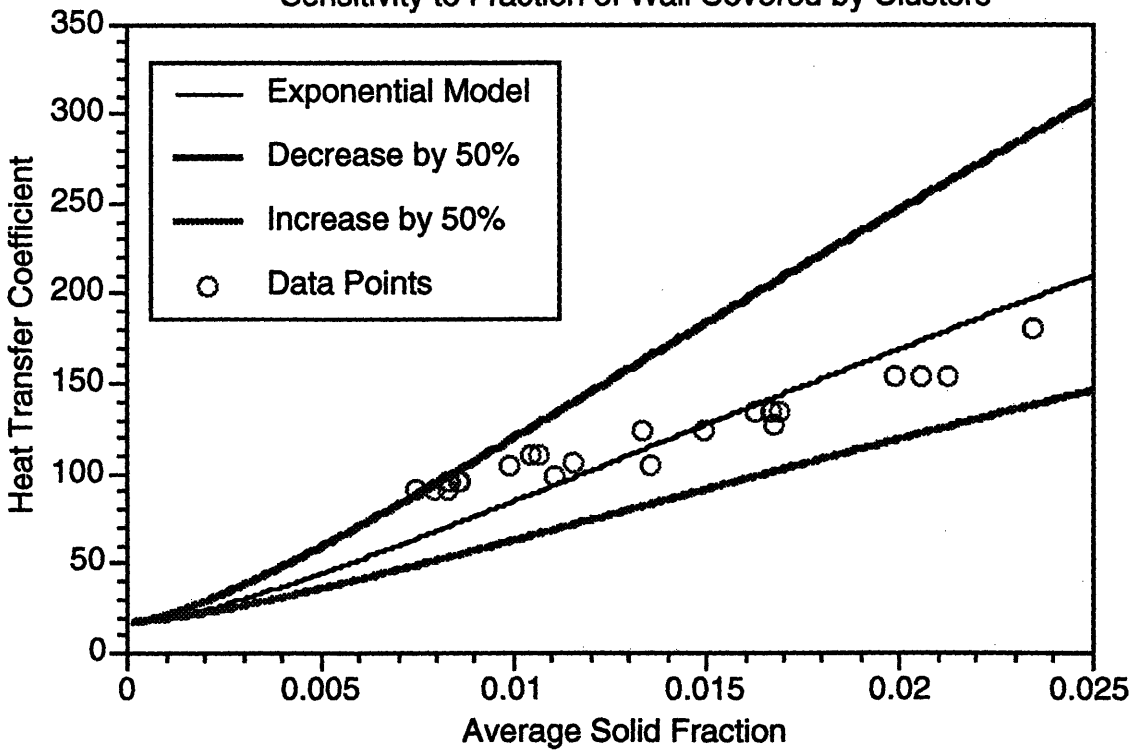

Figure 5.23

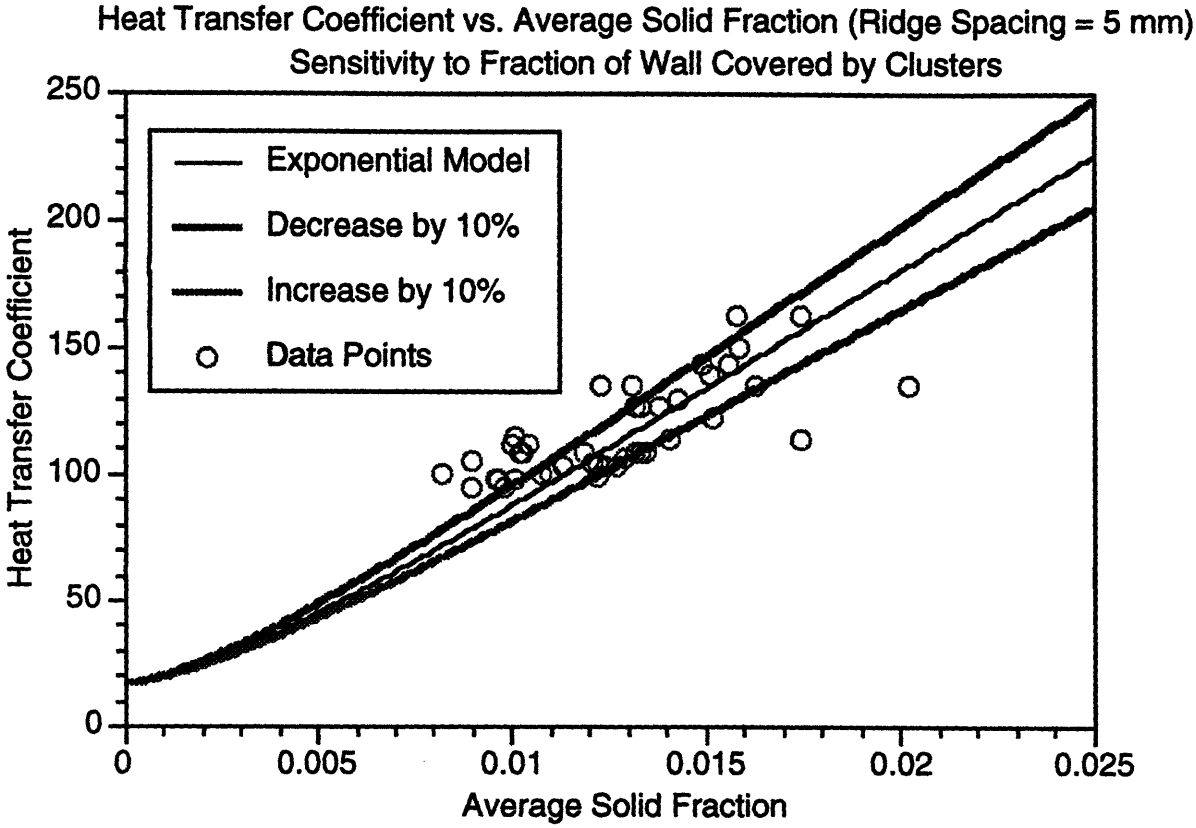

The model appears to be very sensitive to the fractional wall coverage for both large and small deviations. Section 4 presents a lengthy discussion of the models used in the determination of the fraction of the wall covered by clusters. Figures 5.20 through 5.23 indicated that this parameter merits further investigation in order to reduce model uncertainties. It is worth mentioning that the model is equally sensitive to the deviations in the Linear flux model and the Exponential flux model. This is not surprising since both models predict the same magnitude in fractional wall coverages and the model has a linear dependence on the wall coverage.

5.10 Sensitivity to Cluster Residence Time

Figures 5.24 through 5.27 show the sensitivity of the model to deviations in the cluster residence time.

Figure 5.24

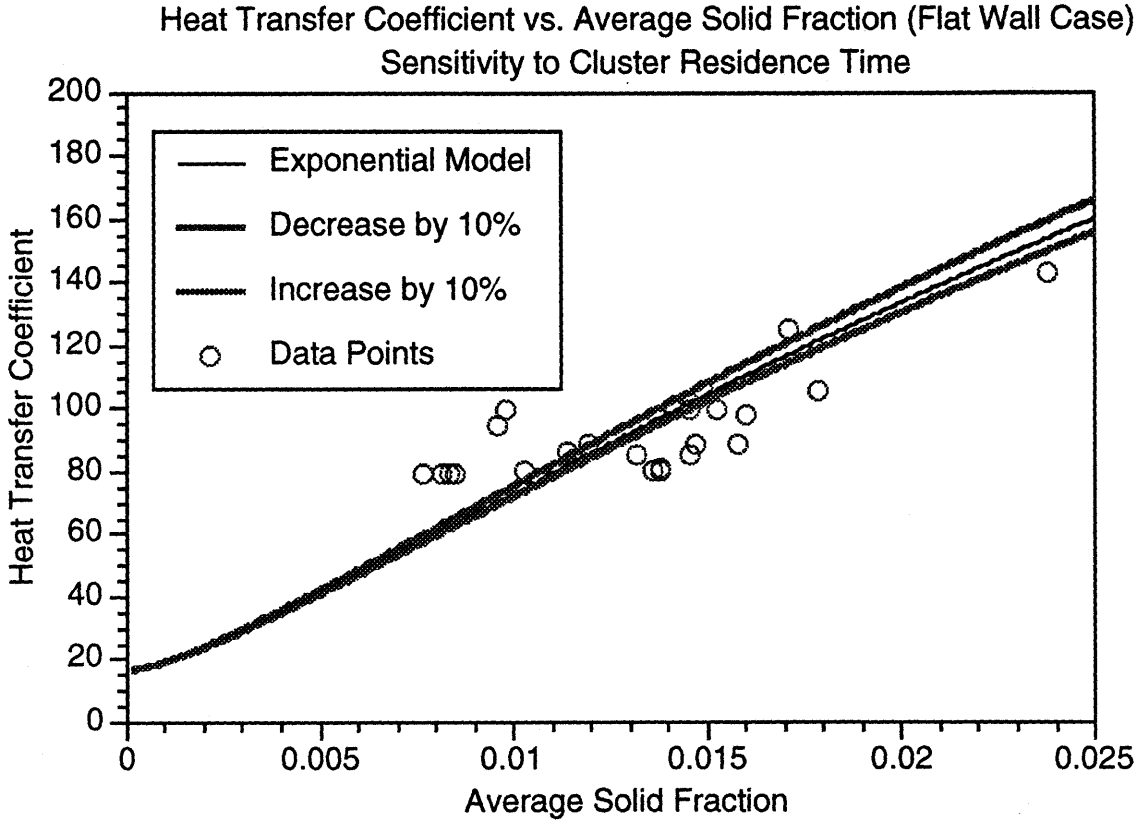

Figure 5.25

Heat Transfer Coefficient vs. Average Solid Fraction (Ridge Spacing = 20mm)
Sensitivity to Cluster Residence Time

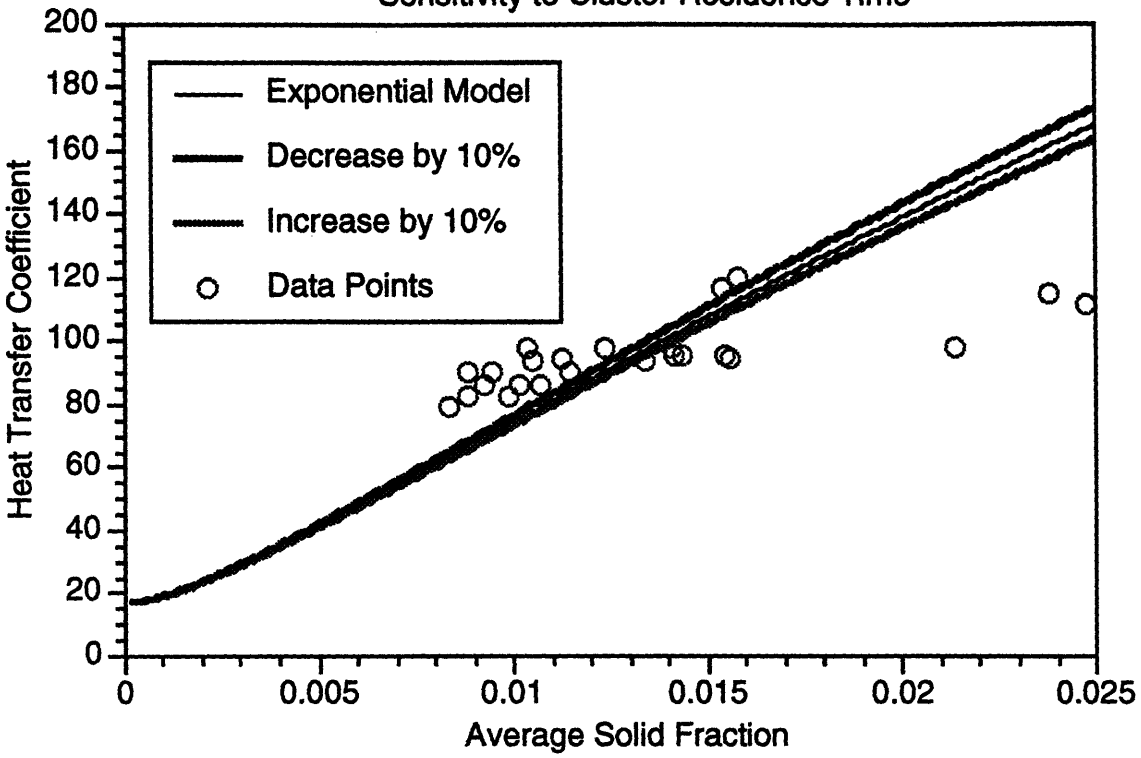

Figure 5.26

Heat Transfer Coefficient vs. Average Solid Fraction (Ridge Spacing = 10 mm)
Sensitivity to Initial Fractional Wall Coverage

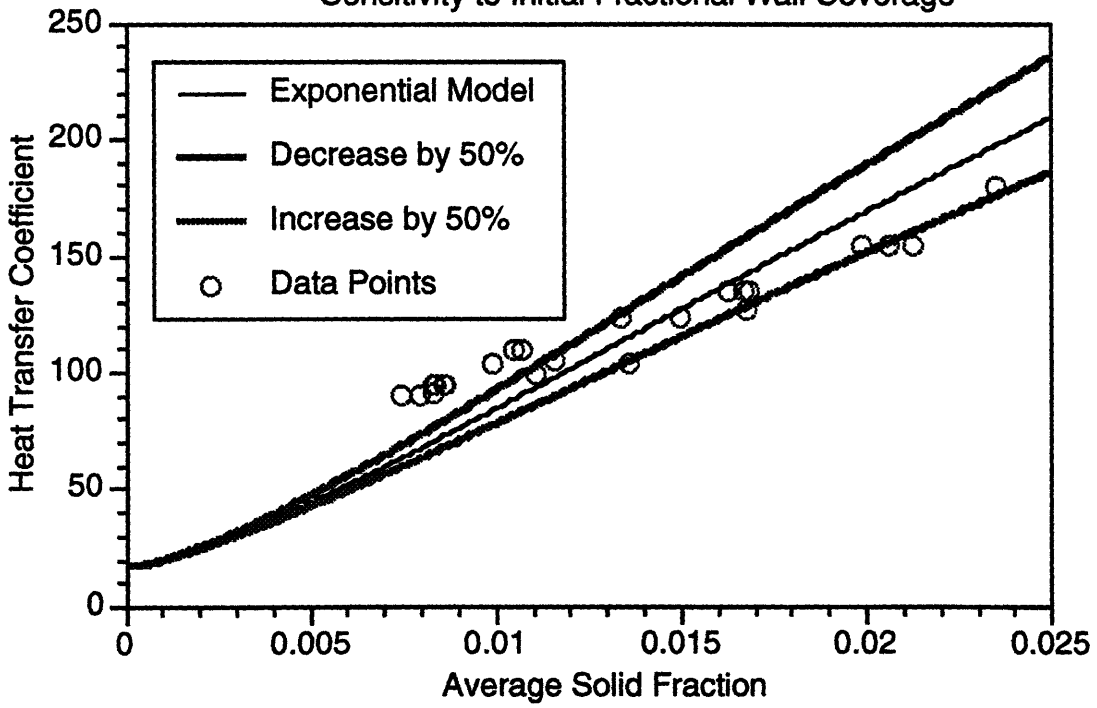

Figure 5.27

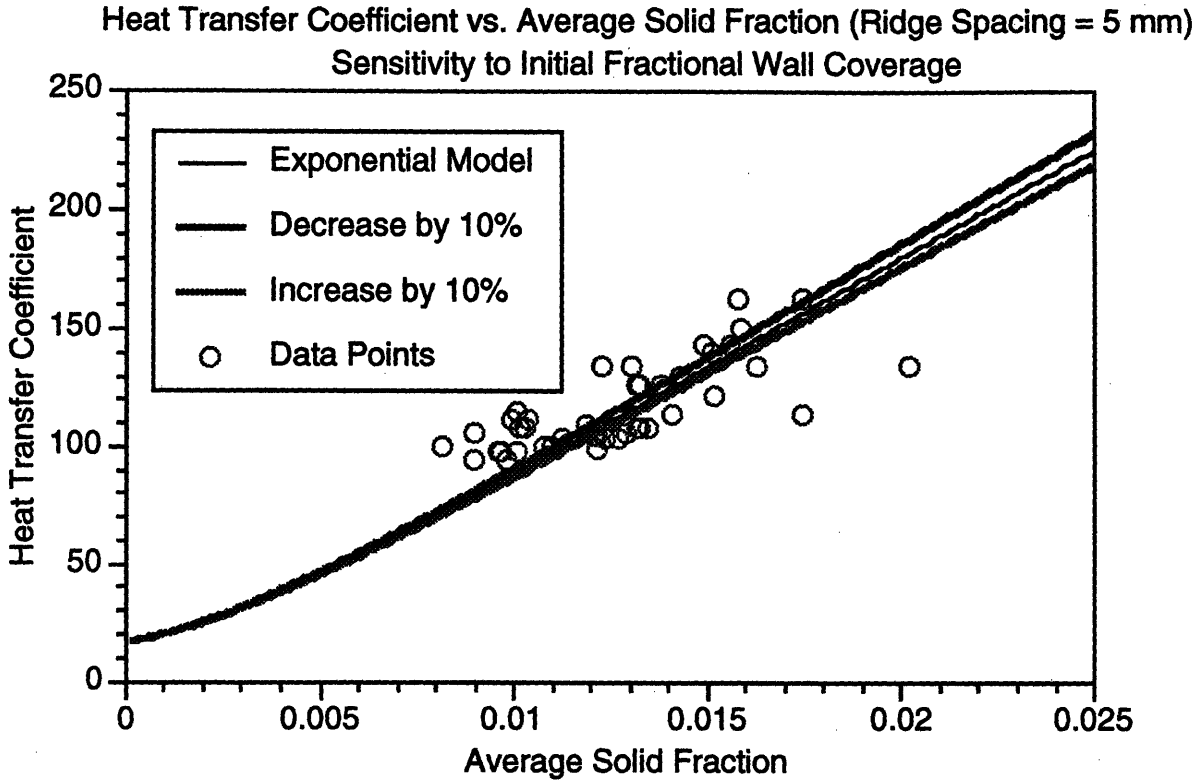

Figures 5.24 through 5.27 indicate that the model is only mildly sensitive to the cluster residence time for both large and small deviations. This is encouraging since this parameter contains the most uncertainty.

For short residence times, only the particles adjacent to the surface will change in temperature. Glicksman (1988) has shown that the thermal time constant of a particle is

$$\tau_p = \frac{c_{p_s} d_p^2}{36 k_g}$$

For the particles used in this study, the thermal time constant is about 0.02 seconds. Even for the smallest ridge spacing, the contact time may exceed 0.01 seconds.

For contact times greater than about one third of the thermal time constant, particles one or more layers away from the wall are influenced by heat transfer. Using the Mickley and Fairbanks (1955) model described in Section 4, assuming the average cross-sectional solid fraction is 0.01, and the cluster fall velocity is 0.5 m/s, Figure 5.28 shows the heat transfer coefficient as a function of cluster fall distance down the wall.

Figure 5.28

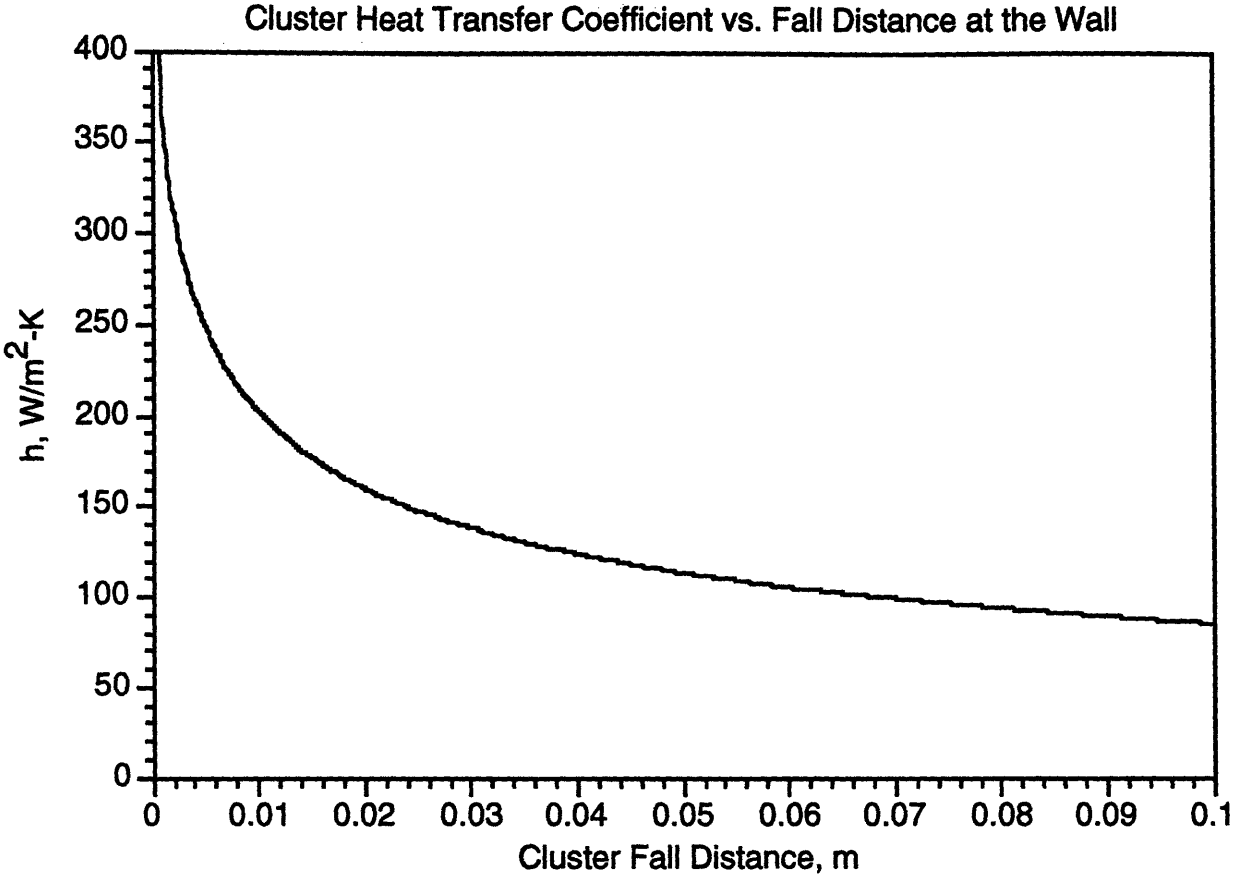

The cluster residence time is evaluated from the cluster fall distance at the wall and the cluster fall velocity. No accurate cluster fall length model exists, and experimental studies have produced only order of magnitude data. Section 4 shows that the cluster fall velocity is nearly constant at about 0.5 m/s. Further investigation into both of these parameters is warranted.

5.11 Sensitivity to the Initial Fractional Wall Coverage

Figures 5.29 through 5.31 depict model sensitivity to the fraction of the wall covered by clusters after a ridge. This parameter was approximated by visual observations of the solids on one of the side walls on which a single ridge was placed.

Figure 5.29

Heat Transfer Coefficient vs. Average Solid Fraction (Ridge Spacing = 20mm)
Sensitivity to Initial Fractional Wall Coverage

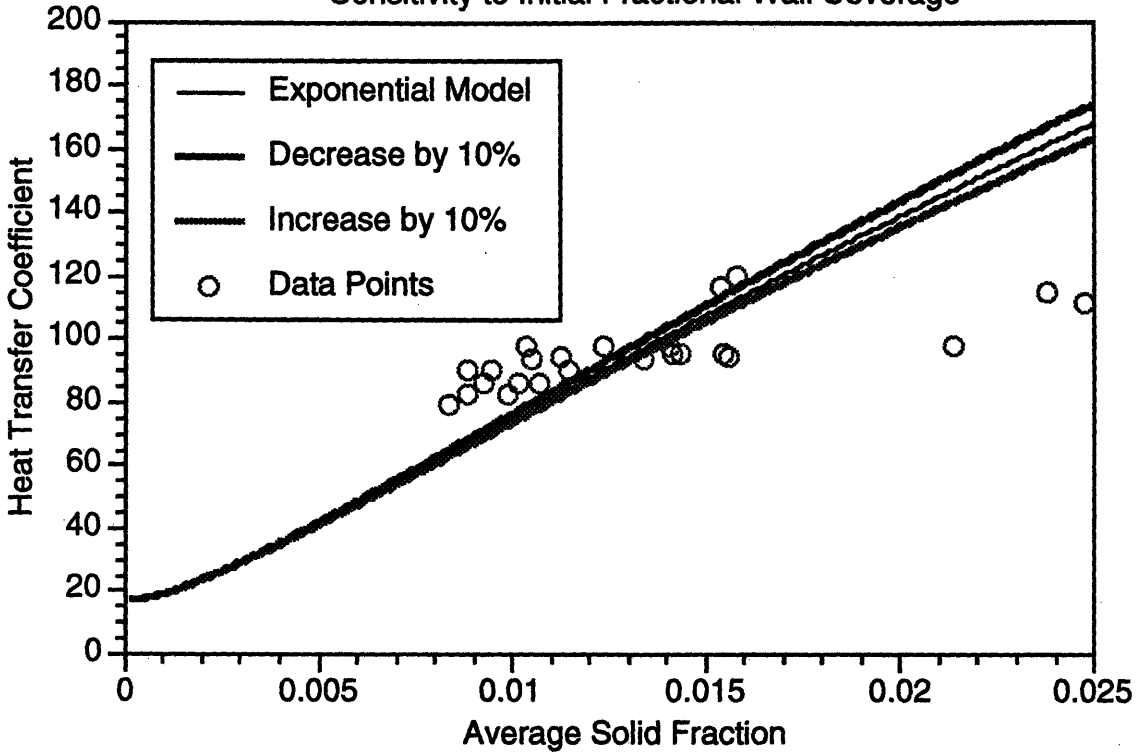

Figure 5.30

Heat Transfer Coefficient vs. Average Solid Fraction (Ridge Spacing = 10 mm)
Sensitivity to Initial Fractional Wall Coverage

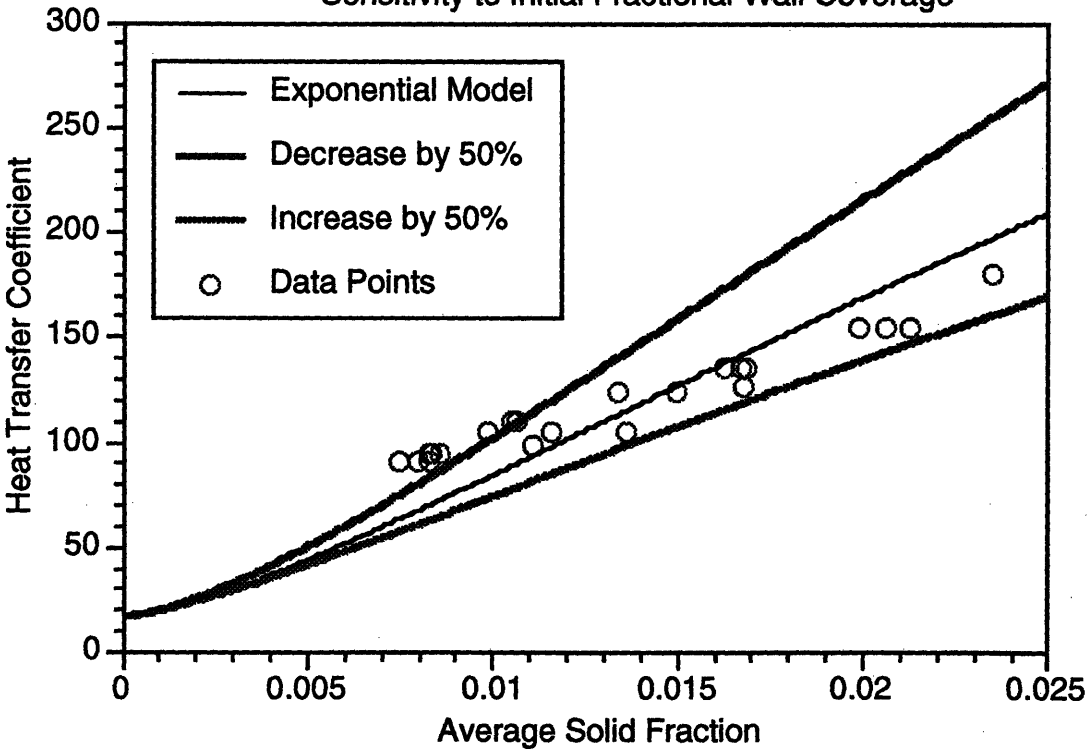

Figure 5.31

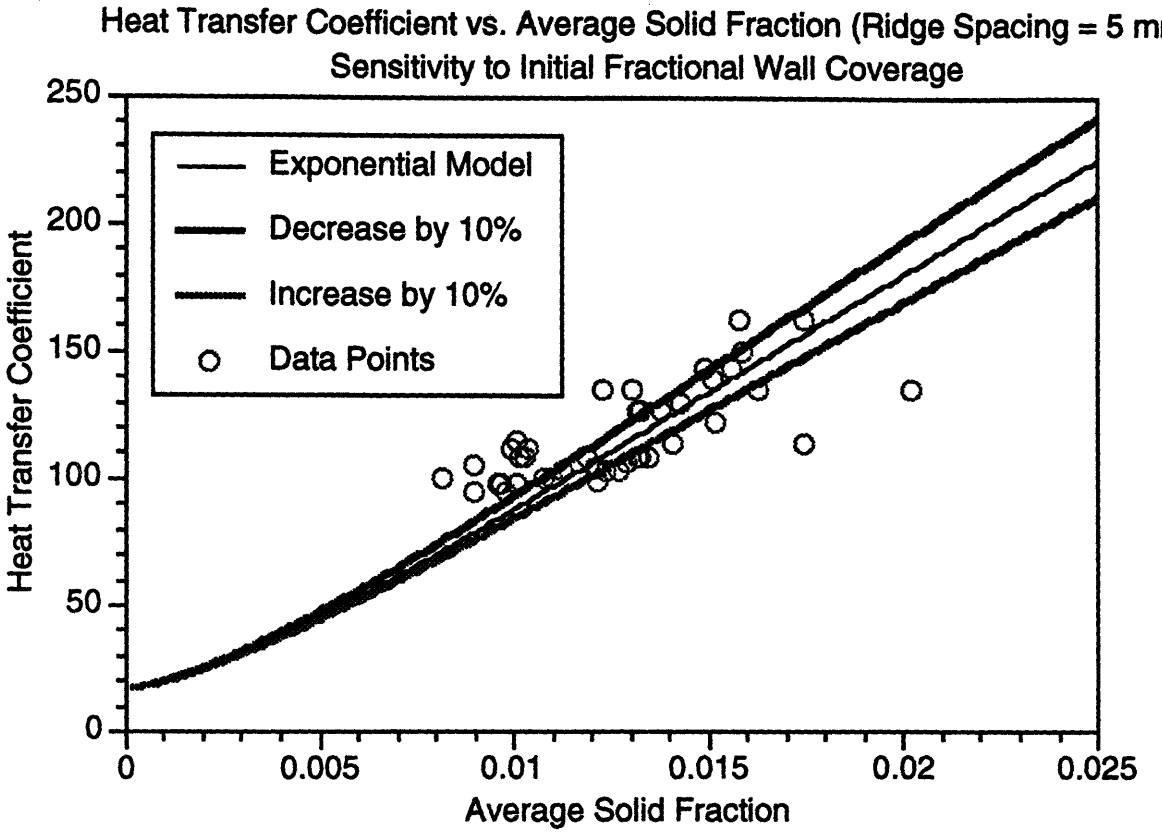

Figures 5.29 through 5.31 show that the model is fairly sensitive to the initial fractional wall coverage. The sensitivity increases with decreasing ridge spacing. This is due to the fact that at larger ridge spacing the fractional wall coverage approaches the steady state value while for the closer ridge spacing cases the fractional wall coverage is much more dependent on the initial value.

Figure 5.32 shows fractional wall coverage as a function of time for an average solid fraction of 0.01 and an initial coverage equal to 10 percent of the steady state fractional wall coverage. Figure 5.32 indicates that the Exponential model predicts a faster increase in wall coverage than does the Linear Model.

Figure 5.32

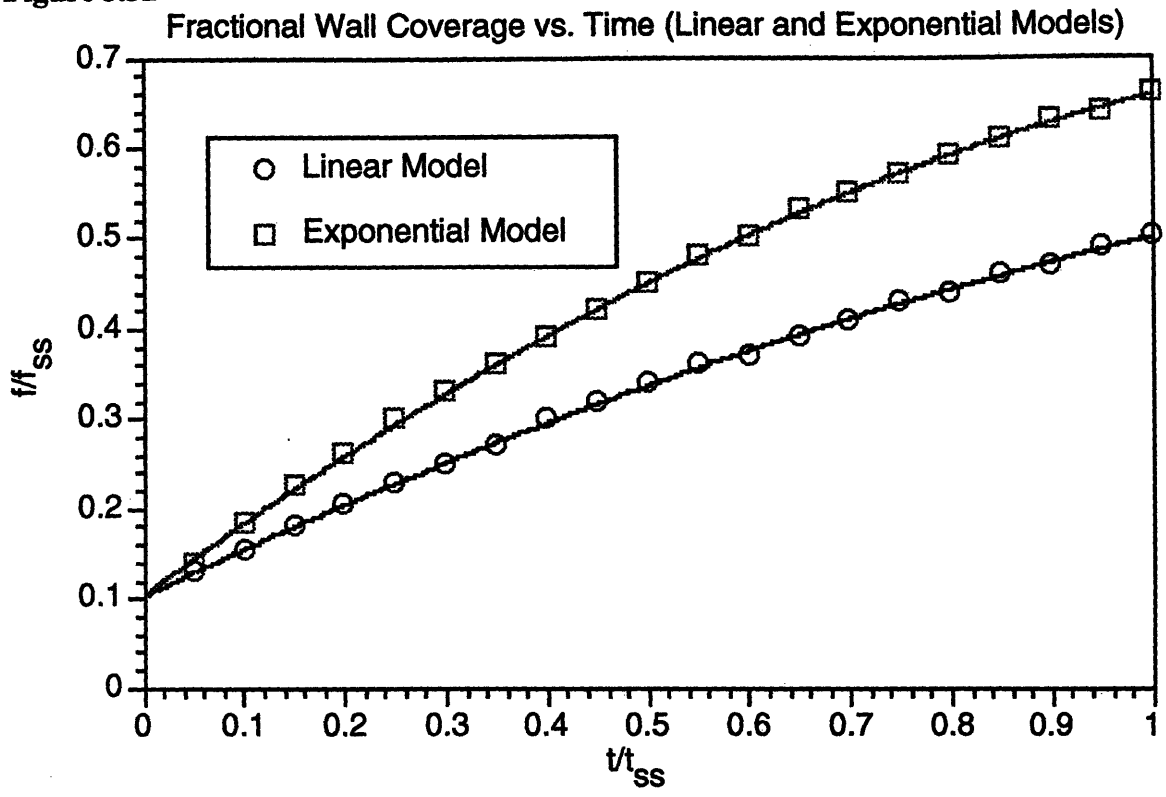

5.12 Sensitivity to the Dilute Phase Heat Transfer Coefficient

Figure 5.33 shows the sensitivity of the model to deviations in the dilute phase heat transfer coefficient for the flat wall case. The model is not sensitive to variations in this parameter. While the sensitivity increases slightly as the ridge spacing decreases since less of the wall is covered by clusters, the magnitude of the model deviations are insignificant because at most 10 percent of the total heat flux is through the dilute phase.

Figure 5.33

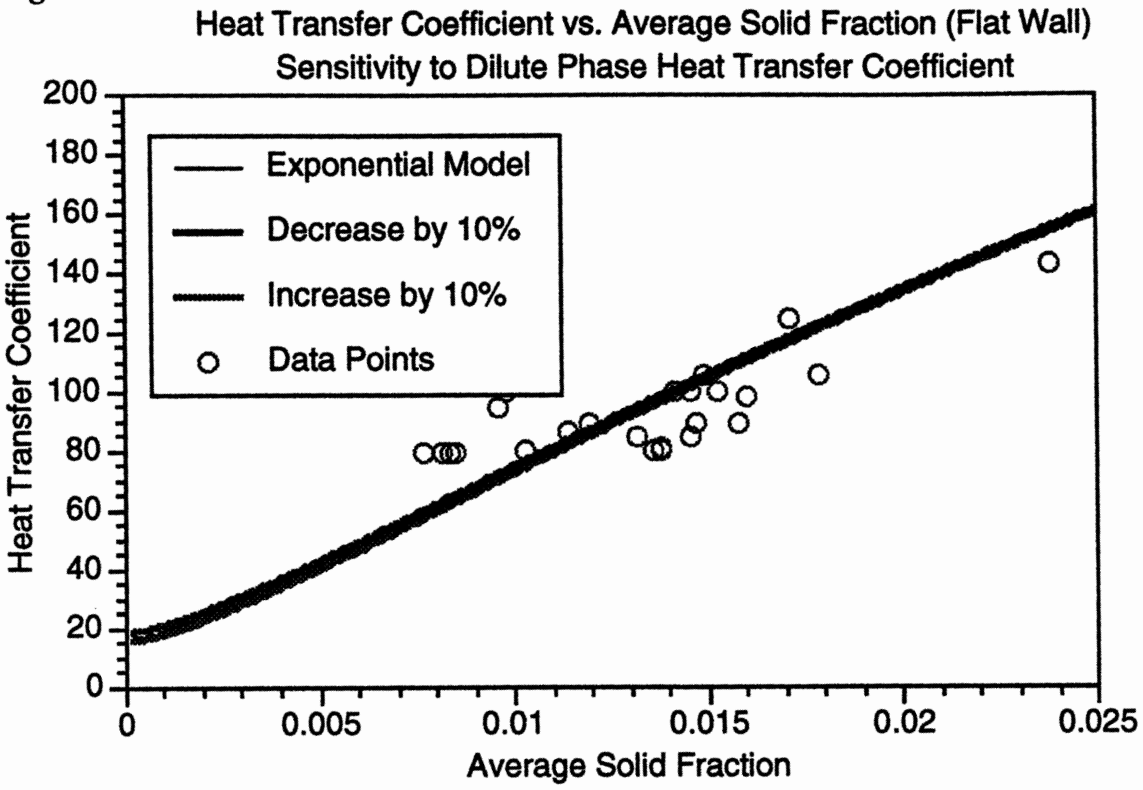
Heat Transfer Coefficient vs. Average Solid Fraction (Flat Wall)
Sensitivity to Dilute Phase Heat Transfer Coefficient
Exponential Model
Decrease by 10%
Increase by 10%
Data Points
Heat Transfer Coefficient
Average Solid Fraction
0
20
40
60
80
100
120
140
160
180
200
0
0.005
0.01
0.015
0.02
0.025

6.0 CONCLUSIONS AND RECOMMENDATIONS

Convective heat transfer measurements were taken at three separate axial locations in a 1/16 scale cold model of the Studsvik 2.5 MWth circulating fluidized bed combustor. The bed wall geometry was altered to include small horizontal ridges placed at systematic intervals along a heat transfer panel. In addition to the heat transfer measurements, time resolved pressure measurements were recorded to determine the effects of the various wall configurations on overall bed hydrodynamics. For each heat transfer surface configuration, measurements were taken at two solids circulation rates.

The use of the altered heat transfer geometries was found to increase the bed to wall heat transfer by up to 28 percent over the flat wall case. Very small amplitude roughness elements (on the order of a single particle diameter) were effective in disrupting wall cluster flow. The altered heat transfer surfaces did not have a significant effect on overall bed hydrodynamics. The spacing of roughness elements was found to be important. Widely spaced elements, 20 mm between elements, did not give improvements over a smooth wall. Roughness elements which were very closely spaced (5 mm) did not give significant improvements over the 10 mm roughness spacing surface. This is because while the mean cluster residence time is decreased, the radial flux of clusters to the wall is insufficient to provide enough wall coverage to increase the overall heat transfer coefficient.

Other surface geometries need to be investigated. Specifically, performing similar tests on surfaces which more closely approximate commercial beds would provide a better indication of possibilities of using carefully designed waterwall surfaces to improve convective heat transfer. Additionally, tests need to be conducted to determine the impact of such surfaces on wall erosion. The roughness elements had a height of approximately one particle diameter. Smaller heights should also be investigated.

The heat transfer model for circulating fluidized beds has been expanded to include transient effects. This model was shown to give reasonable predictions for surfaces constructed to enhance bed to wall heat transfer by controlling the time a cluster remains at the wall. There is an optimum spacing of horizontal ribs which gives the maximum heat transfer enhancement.

7.0 REFERENCES

Arena, U., A. Marzocchella, L. Massimilla, and A. Malandrino, "Hydrodynamics of Circulating Fluidized Beds with Risers of Different Shape and Size," *Powder Technol.*, **70**, p. 237, 1992.

Bader, R., J. Findlay, and T.M. Knowlton, "Gas/Solid Flow Patterns in a 30.5 -cm-Diameter Circulating Fluidized Bed," *Circulating Fluidized Bed Technology II*, P. Basu and J.F. Large, eds., Pergamon Press, 1988.

Baskakov, A.P., "The Mechanism of Heat Transfer Between a Fluidized Bed and a Surface," *Int. Chem. Eng.*, **4**, p. 320, 1964.

Basu, P., and F. Konuche, "Radiative Heat Transfer from a Fast Fluidized Bed," *Circulating Fluidized Bed Technology II*, P. Basu and J.F. Large, eds., Pergamon Press, 1988.

Basu, P., "Heat Transfer in High Temperature Fast Fluidized Beds," *Chem. Eng. Sci.*, **45**, p. 3123, 1990.

Blasius, H., "The Boundary Layers in Fluids with Little Friction," (in German), *Zeitschrift fur Nathematik und Physik*, **56**, p. 1, 1908. English translation available as NACA TM 1256, Feb, 1950.

Bolton, L.W., and J.F. Davidson, "Recirculation of Particles in Fast Fluidized Risers," *Circulating Fluidized Bed Technology II*, P. Basu and J.F. Large, eds., Pergamon Press, p. 139, 1988.

Brereton, C., *Fluid Mechanics of High Velocity Fluidised Beds*, Doctoral Thesis, University of British Columbia, 1987.

Chen, C.C., and C.L. Chen, "Experimental Study of Bed-to-Wall Heat Transfer in a Circulating Fluidized Bed," *Chem. Eng. Sci.*, **47**, p. 1017, 1992

Clift, R., J.R. Grace, and M.E. Weber, "Stability of Bubbles in Fluidized Beds," *Ind. Eng. Chem., Fundam.*, **13**, p. 45, 1975.

Cox, R. G., and H. Brenner, "The Lateral Migration of Solid Particles in Poiseuille Flow -I Theory," 1968, *Chem. Eng. Sci.*, **23**, pp. 147-173.

Cox, R.G., and S.K. Hsu, "The Lateral Migration of Solid Particles in a Laminar Flow Near a Plane," *Intl. J. Multiphase Flow*, **3**, p. 201, 1977.

Csanady, G.T., "Turbulent Diffusion of Heavy Particles in the Atmosphere," *J. Atmos. Sci.*, **2**, p.201, 1963.

Decker, N., and L.R. Glicksman, "Heat Transfer in Large Particle Fluidized Beds," *Int. J. Heat Mass Transfer*, **26**, p. 1307, 1983.

Dou, S., *Experimental Study of Heat Transfer in Circulating Fluidized Beds*, Doctoral Thesis, Lehigh University, 1990.

Drew, D.A., "The Lift Force on a Small Sphere in teh Pressence of a Wall," *Chem. Engng. Sci.*, **43**, p. 769, 1988.

Friedlander, S.K., "Behavior of Suspended Particles in a Turbulent Fluid," *A.I.Ch.E. J.*, **3**, p. 381, 1957.

Gelperin, N.I., and V.G. Einstein, "Heat Transfer in Fluidized Beds," *Fluidization*, J.F. Davidson and D. Harrison, eds., Academic Press, 1971.

Gidaspow, D., Y.P. Tsuo, and K.M. Luo, "Computed and Experimental Cluster Formation and Velocity Profiles in Circulating Fluidized Beds," *Fluidization VI*, J.R. Grace, L.W. Shemilt and M.A. Bergougnou, eds., Engineering Foundation, 1989.

Glicksman, L.R., and N.A. Decker, "Heat Transfer From an Immersed Surface to Adjacent Particles in Fluidized Beds," *Proc. 7th Int. Conf. on Fluidized Beds*, Philadelphia, p. 45, 1982.

Glicksman, L.R., "Circulating Fluidized Bed Heat Transfer," *Circulating Fluidized Bed Technology II*, P. Basu and J.F. Large, eds., Pergamon Press, 1988.

Gloski, D., L. Glicksman, and N. Decker, "Thermal Resistance at a Surface in Contact with Fluidized Bed Particles," *Int. J. Heat Mass Transfer*, **27**, p. 599, 1984.

Gore, R., and C.T. Crowe, "Effects of Particle Size on Modulating Turbulent Intensity," *Int. J. Multiphase Flow*, **15**, p. 279, 1989a.

Happel, J, and H. Brenner, *Low Reynolds Number Hydrodynamics*, Kluwer Academic Publishers, Boston, 1963.

Hartge, E.-U., D. Rensner, and J. Werther, "Solids Concentration and Velocity Patterns in Circulating Fluidized Beds," *Circulating Fluidized Bed Technology II*, P. Basu and J.F. Large, eds., Pergamon Press, 1988.

Herb, B., S. Dou, K, Tuzla, and J.C. Chen, "Solid Mass Fluxes in Circulating Fluidized Beds," *Powder Technol.*, **70**, p. 197, 1992.

Hinze, J.O. *Turbulence*, 2nd edn., McGraw-Hill, New York, 1975.

Hinze, J.O., "Fundamentals of the Hydrodynamic Mechanism of Splitting in Dispersion Processes," *AIChE J.*, **1**, p. 289, 1955.

Horio, M., and H. Kuroki, "Three-Dimensional Flow Visualization of Dilutely Dispersed Solids in Bubbling and Circulating Fluidized Beds," *Chem. Eng. Sci.*, **49**, p. 2413, 1994.

Horio, M., H. Ishii, and M. Nishimuro, "On the Nature of Turbulent and Fast Fluidized Beds," *Powder Technol.*, **70**, p. 229, 1992.

Horio, M., K. Morishita, O. Tachibana, and N. Murata, "Solid Distribution and Movement in Circulating Fluidized Beds," *Circulating Fluidized Bed Technology II*, P. Basu and J.F. Large, eds., Pergamon Press, 1988.

Hyre, M.R. and L.R. Glicksman, "Experimental Investigation of Heat Transfer Enhancement in Cirulating Fluidized Beds," *4th ASME/JSME Thermal Engineering Conf.*, Maui, Hawaii, March, 1993.

Hyre, M.R. and L.R. Glicksman, "Heat Transfer Enhancment in Circulating Fluidized Beds," *Fluidization VIII*, Tours, France, May, 1995.

Johansen, S.T., "The Deposition of Particles on Vertical Walls," *Int. J. Multiphase Flow*, **17**, p. 355, 1991.

Kallio, G.A., and M.W. Reeks, "A Numerical Simulation of Particle Deposition in Turbulent Boundary Layers," *Int. J. ultiphase Flow*, **15**, p. 433, 1989.

Kim, J., P. Moin, and R. Moser, "Turbulence Statistics in a Fully Developed Channel Flow at Low Reynolds Number," *J. Fluid Mech.*, **177**, p. 133, 1987.

Kobro H., and C. Brereton, "Control and Fuel Flexibility of Circulating Fluidized Beds," *Circulating Fluidized Bed Technology*, P. Basu, ed., Pergamon Press, 1986.

Kunii, D., and O. Levenspiel, "A General Equation for the Heat-Transfer Coefficient at Wall Surfaces of Gas/Solid Contactors," *Ind. Eng. Chem. Res.*, **30**, p. 136, 1991.

Kutadeladze, S.S., W.M. Khabakhpasheva, V.V. Orlov, P.V. Perepelitsa, and E.S. Michailova, *In Turbulent Shear Flows I*, pp. 91-103, Springer-Verlag, Berlin, 1979.

Kynch, G.J., "The Effective Viscosity of Suspensions of Spherical Particles," *Proc. Roy. Soc. A* (London), **237**, p. 90, 1956.

Lane, W.R., "Shatter of Drops in Streams of Air," *Ind. Eng. Chem.*, **43**, p. 1312, 1951.

Leckner, B., and B.-A. Andersson, "Characteristic Features of Heat Transfer in Circulating Fluidized Bed Boilers," *Powder Technol.*, **70**, p. 303, 1992.

Leckner, B., "Heat Transfer in Circulating Fluidized Beds," *Circulating Fluidized Bed Technology III*, P. Basu, M. Horio and M. Hasatani, eds., Pergamon Press, 1991.

Lee, M.M., T.J. Hanratty, and R.J. Adrian, "The Interpretation of Droplet Deposition Measurements with a Diffusion Model," *Int. J. Multiphase Flow*, **15**, p. 459, 1989.

Lee, S.L., and F. Durst, "On the Motion of Particles in Turbulent Duct Flows," *Int. J. Multiphase Flow*, **8**, p. 125, 1982.

Li, J., Y. Xia, Y. Tung, and M. Kwauk, "Micro-Visualization of Two-Phase Structure in a Fast Fluidized Bed," *Circulating Fluidized Bed Technology III*, P. Basu, M. Horio and M. Hasatani, eds., Pergamon Press, 1991.

Lints, M.C., and L.R. Glicksman, "The Structure of Particle Clusters Near the Wall of a Circulating Fluidized Bed," *AIChE Sump. Series*, **89**, p. 35, 1993.

Lints, M.C., *Particle-to-Wall Heat Transfer in Circulating Fluidized Beds*, Ph.D. Thesis, Massachusetts Institute of Technology, 1992.

Lints, M.C., *The Behavior of Falling Particle Clusters Under the Approximate Conditions of a Circulating Fluidized Bed*, Massachusetts Institute of Technology Internal Report, 1987.

Louge, M., J. Lischer, and H. Chang, "Measurements of Voidage Near the Wall of a Circulating Fluidized Bed Riser," *Powder Technol.*, **62**, p. 269, 1990.

Lu, H.L., and L.D. Yang, "A Model for Heat Transfer and Experimental Research in Circulating Fluidized Beds," *Proc. Third Conference of Universities on Thermodynamics*, p. 293, Xian, China, 1990.

Lu, H.L., L.D. Yang, Y.L. Bao, and L.Z. Cheng, "Heat Transfer of Vertical Tube at Radial Positions in a Circulating Fluidized Bed," *Proc. Fifth National Symp. on Eng. Thermophysics (China)*, **2**, VII-145, 1991.

Marzocchella, A., U. Arena, A. Cammarota, and L. Massimilla, "Break-up of Cylindrical Clusters of Solid Particles Under Gravity Flow in a Two-Dimensional Column," *Powder Technol.*, **65**, p. 453, 1991.

McLaughlin, J.B., "Inertial Migration of a Small Sphere in Linear Shear Flows," *J. Fluid Mech.*, **224**, p. 261, 1991.

McLaughlin, J.B., "The Lift on a Small Sphere in Wall-Bounded Linear Shear Flows," *J. Fluid Mech.*, **246**, p. 249, 1993.

Mickley, H.S., and D.F. Fairbanks, "Mechanisms of Heat Transfer to Fluidized Beds," *AIChE Journal*, **1**, p. 374, 1955.

Nowak, W., H. Mineo, R. Yamazaki, and K. Yoshida, "Behavior of Particles in a Circulating Fluidized Bed of a Mixture of Two Different Sized Particles," *Circulating Fluidized Bed Technology III*, P. Basu, M. Horio and M. Hasatani, eds., Pergamon Press, 1991.

Oshinowo, Toks, and M. E. Charles, "Vertical Two-Phase Flow - Part I. Flow Pattern Correlations," 1974, *Canadian J. of Chem Eng.*, **52**, pp. 25-35.

Pewtukhov, B.S., "Heat Transfer and Friction in Turbulent Pipe Flow with Variable Physical Properties," *Advances n Heat Transfer*, T.F. Irvine, Jr. and J.P. Hartnett, eds., Academic Press, 1970.

Rhodes, M., H. Mineo, and T. Hirama, "Particle Motion at the Wall of a Circulating Fluidized Bed," *Powder Technol.*, **70**, p. 207, 1992.

Rogers, C. B., and J.K. Eaton, "The Behavior of Solid Particles in a Vertical Turbulent Boundary Layer in Air," *Int. J. Multiphase Flow*, **16**, p. 819, 1990.

Rouhiainen, P.O., and J.W. Stachiewicz, "On the Deposition of Small Particles From Turbulent Streams," *J. Heat Transfer, Transactions of the ASME*, **92**, p. 169, 1970.

Saffman, P.G., "Corrigendum to the Life on a Small Sphere in a Slow Shear Flow," *J. Fluid Mech.*, **31**, p. 624, 1968.

Saffman, P.G., "The Life on a Small Sphere in a Slow Shear Flow," *J. Fluid Mech.*, **22**, p. 385, 1965.

Segre', G., and A. Silberberg, "Behavior of Macroscopic Rigid Spheres in Poiseuille Flow," 1962, *J. Fluid Mech.*, **14**, pp. 115-157.

Subbarao, D., and P. Basu, "A Model for Heat Transfer in Circulating Fluidized Beds," *Int. J. Heat Mass Transfer*, **29**, p. 487, 1986.

Taylor, G.I., "The Instability of Liquid Surfaces when Accelerated in a Direction Perpendicular to their Planes. I.," *Proc. R. Soc. London, Serr.*, **A 201**, p. 192, 1950.

Tung, Y., J. Li, and M. Kwauk, "Radial Voidage Profile in a Fast Fluidized Bed," *Fluidization* (Edited by M. Kwauk and D. Kunii), p. 139, Science Press, Beijing, 1988.

Vasseur, P., and R.G. Cox, "The Lateral Migration of Spherical Particles Sedimenting in a Stagnant Bounded Fluid," *J. Fluid Mech.*, **80**, p. 561, 1977.

Weinstein, H., M. Shao, and M. Schnitzlein, "Radial Variation in Solid Density in High Velocity Fluidization," *Circulating Fluidized Bed Technology*, P. Basu, ed., Pergamon Press, p. 201,1986.

Wen, C.Y., and Y.H. Yu, "Mechanics of Fluidization," *Chem. Eng. Progress Symp. Series*, **62**, p. 200, 1966.

Westphalen, D., *Scaling and Lateral Solid Mixing in Circulating Fluidized Beds*, Ph.D. Dissertation, Massachusetts Institute of Technology, 1993.

Wirth, K.E., M. Seiter, and O. Molerus, "Concentration and Velocities of Solids in Areas Close to the Walls in Circulating Fluidized Bed Systems," *VGB Kraftwerkstechnik*, **10**, p. 824, 1991.

Wu, R.L., C.J. Lim, and J.R. Grace, "The Measurement of Instantaneous Local Heat Transfer Coefficients in a Circulating Fluidized Bed," *Can. J. Chem. Eng.*, **67**, p. 301, 1989a.

Wu, R.L., C.J. Lim, J. Chaouki, and J.R. Grace, "Heat Transfer from a Circulating Fluidized Bed to Membrane Waterwall Surfaces," *AIChE Journal*, **33**, p. 1888, 1987.

Wu, R.L., C.J. Lim, J.R. Grace, and C.M.H. Brereton, "Instantaneous Local Heat Transfer and Hydrodynamics in a Circulating Fluidized Bed," *Int. J. Heat Mass Transfer*, **34**, p. 2019, 1991.

Wu, R.L., *Heat Transfer in Circulating Fluidized Beds*, Doctoral Thesis, University of British Columbia, 1989.

Wu, R.L., J.R. Grace, C.J. Lim and C.M.H. Brereton, "Suspension-to-Surface Heat Transfer ina Circulating-Fluidized-Bed Combustor," *AIChE Journal*, **35**, p. 1685, 1989b.

APPENDIX A: HEAT TRANSFER DATA

The following 8 Charts and Tables contain the heat transfer data used in this study.

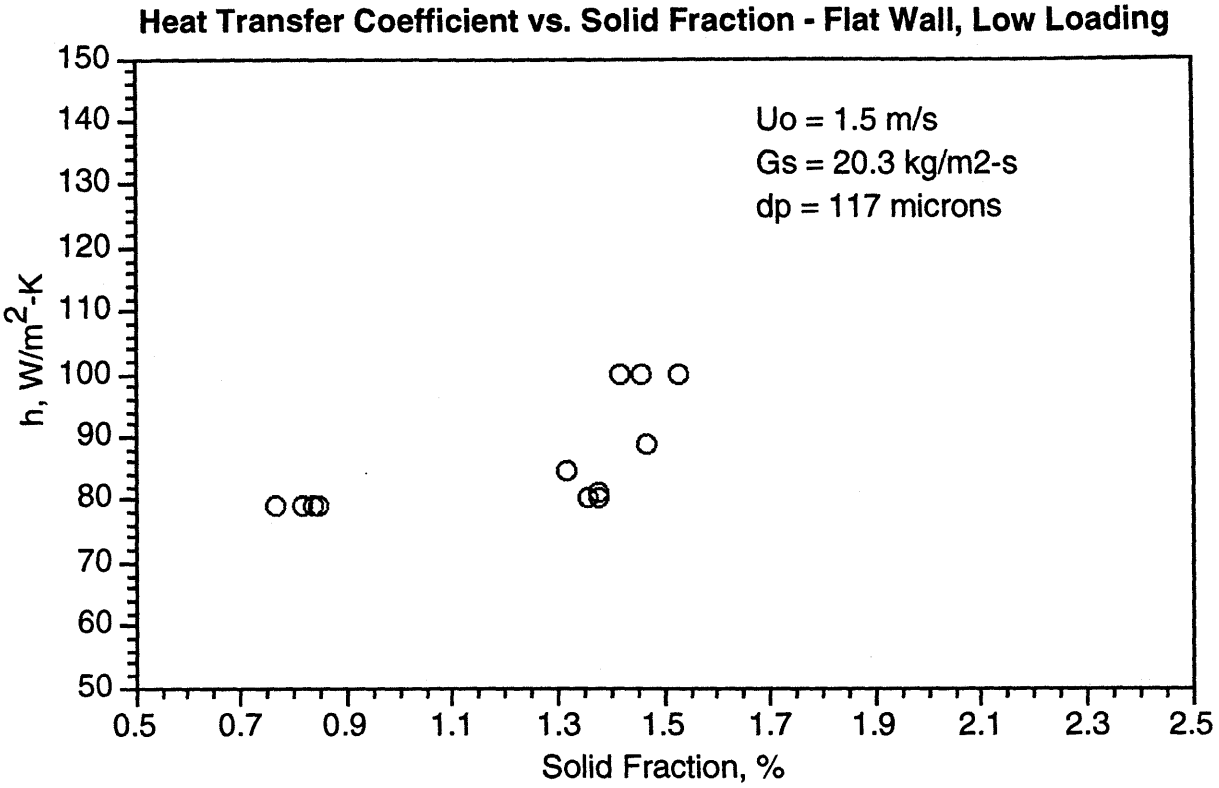

	SF. %	h. W/m^2-K	Htr. No.
	1.53	99.7	1
	1.38	80.9	2
	0.85	78.8	3
	1.42	99.7	1
	1.32	84.6	2
	0.77	78.8	3
	0.84	78.8	3
	1.38	80.2	2
	1.46	99.7	1
	0.82	78.8	3
	1.36	80.2	2
	1.47	88.6	1

Heater Locations (% up riser):

1. 41.4
2. 64.4
3. 85.7

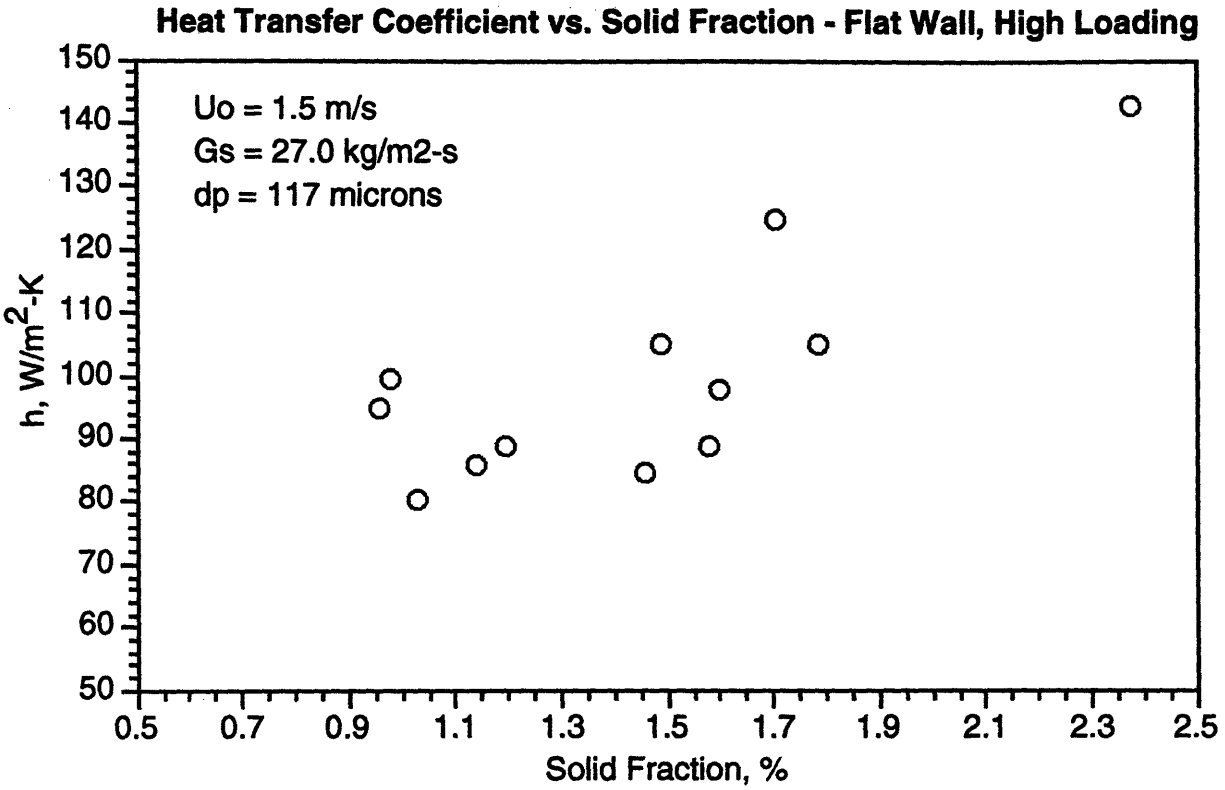

SF. %	h. W/m^2-K	Htr. No.
0.96	94.5	3
1.6	97.9	2
2.38	142.5	1
0.98	99.6	3
1.58	88.6	2
1.71	124.7	1
1.14	85.9	3
1.2	88.6	2
1.49	105	1
1.03	80.2	3
1.46	84.6	2
1.79	105	1

Heater Locations (% up riser):

1. 41.4
2. 64.4
3. 85.7

Heat Transfer Coefficient vs. Solid Fraction - Ridge Spacing = 20mm, Low Loading

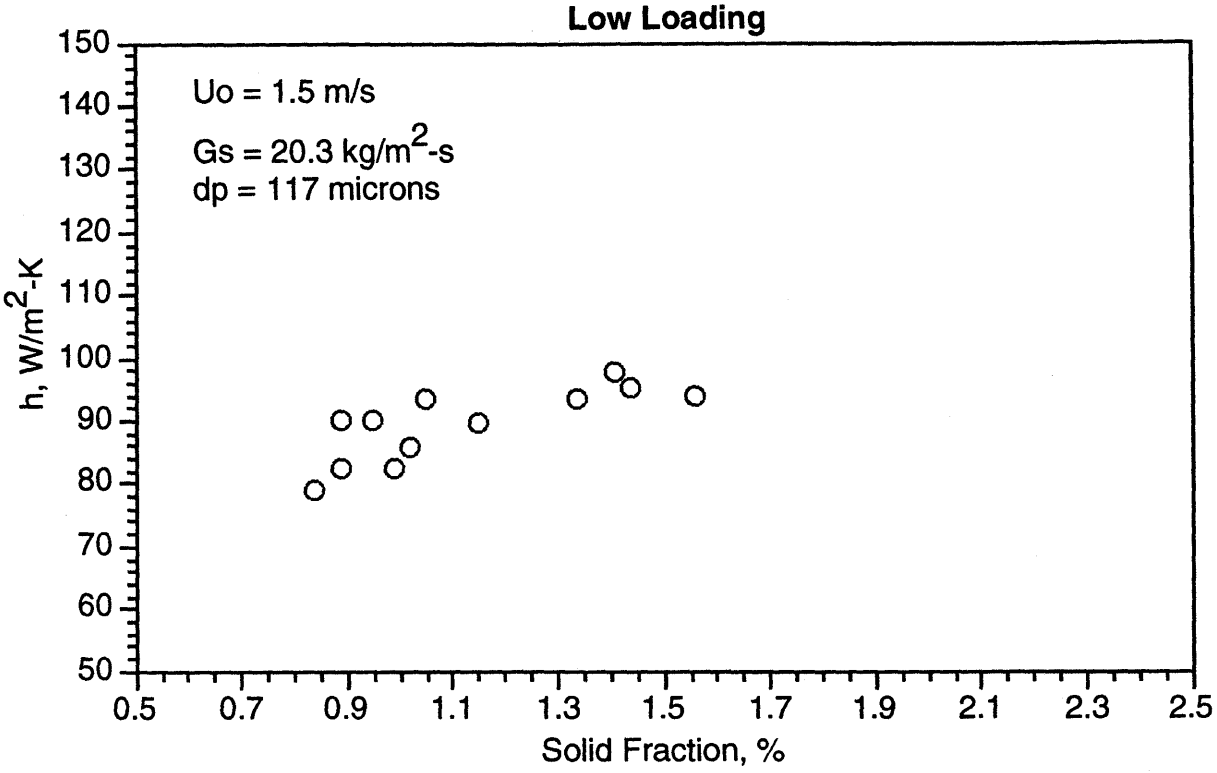

	SF. %	h. W/m^2-K	Htr. No.
	1.56	93.9	1
	1.15	89.7	2
	0.95	90.1	3
	1.41	97.8	1
	1.02	85.8	2
	0.89	90.1	3
	0.84	78.8	3
	0.99	82.3	2
	1.34	93.6	1
	0.89	82.3	3
	1.05	93.6	2
	1.44	95	1

Heater Locations (% up riser):

1. 41.4
2. 64.4
3. 85.7

Heat Transfer Coefficient vs. Solid Fraction - Ridge Spacing = 20mm, High Loading

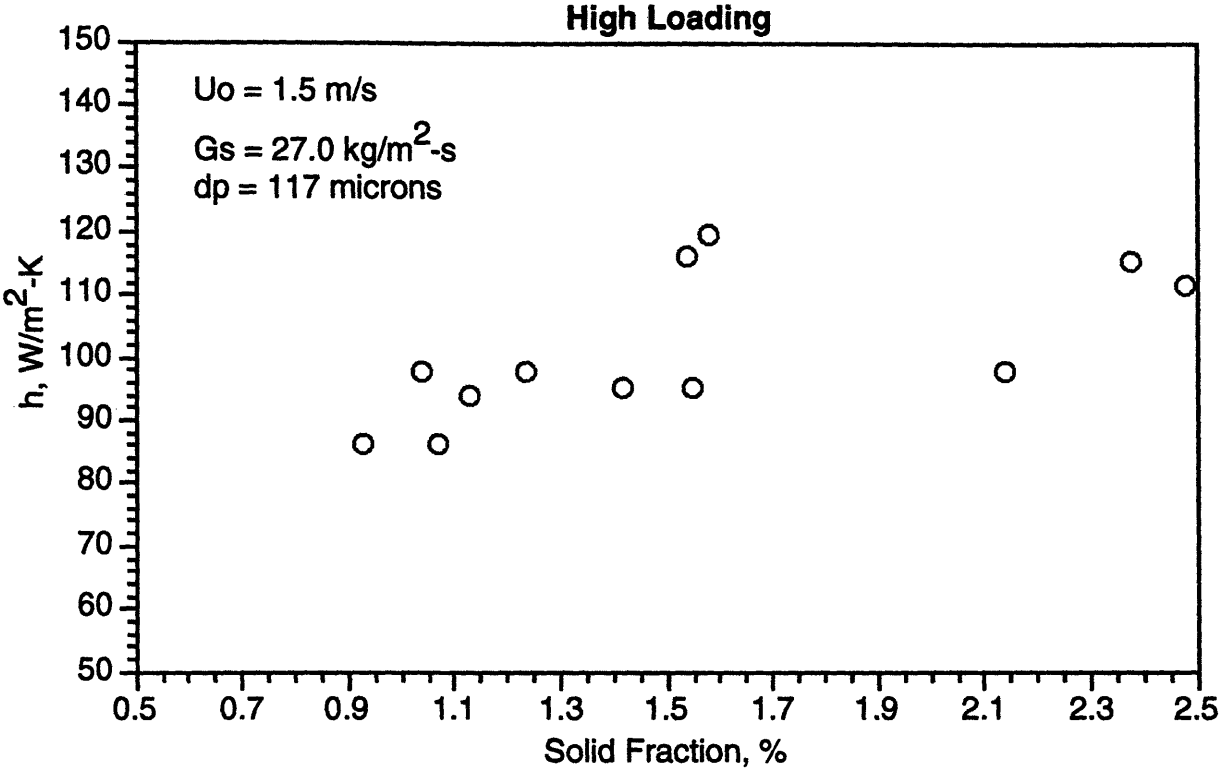

SF. %	h. W/m^2-K	Htr. No.
2.38	115.1	1
1.58	119.7	2
1.04	97.8	3
2.48	111.3	1
1.54	116.1	2
1.24	97.8	3
0.93	86	3
1.13	94	2
1.55	95	1
1.07	86	3
1.42	95	2
2.14	97.8	1

Heater Locations (% up riser):

1. 41.4 *697*
2. 64.4
3. 85.7

Heat Transfer Coefficient vs. Solid Fraction - Ridge Spacing = 10mm, Low Loading

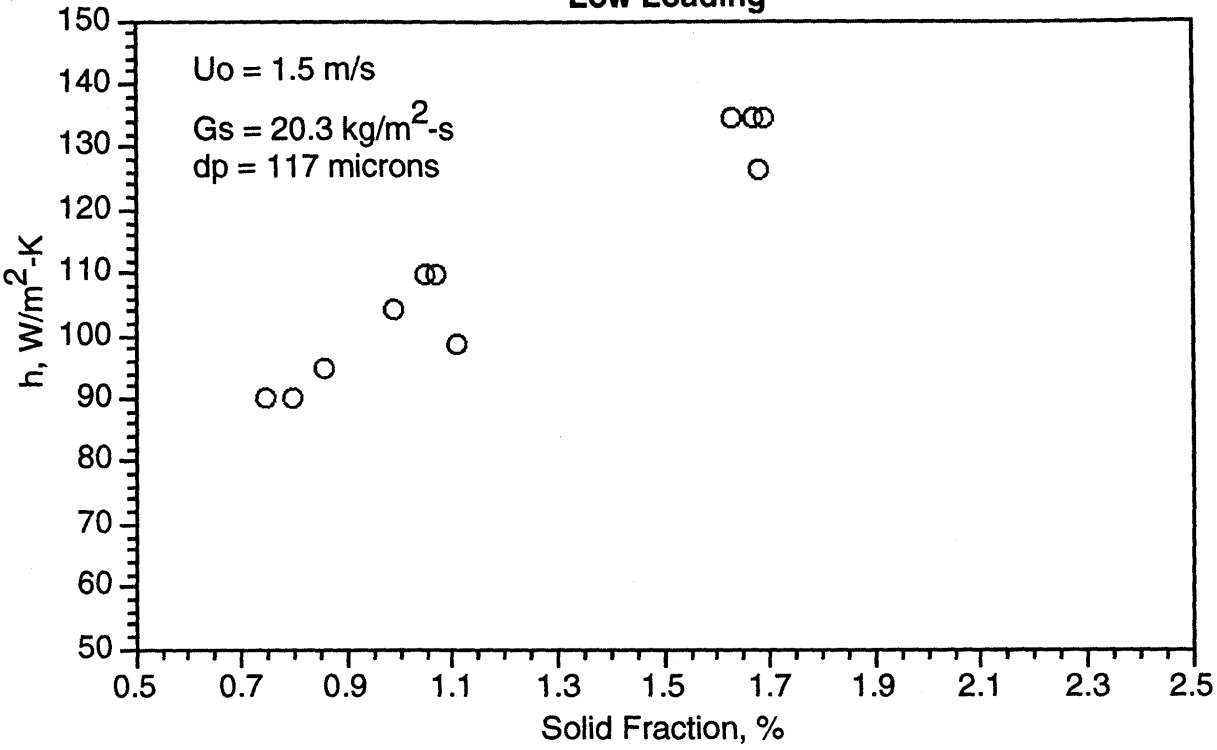

	SF. %	h. W/m^2-K	Htr. No.
	1.68	126.5	1
	1.11	98.77	2
	0.75	90.1	3
	1.69	134.5	1
	0.99	103.9	2
	0.8	90.1	3
	0.86	94.6	3
	1.07	109.7	2
	1.63	134.5	1
	0.8	90.1	3
	1.05	109.7	2
	1.67	134.5	1

Heater Locations (% up riser):

1. 41.4 *698*
2. 64.4
3. 85.7

Heat Transfer Coefficient vs. Solid Fraction - Ridge Spacing = 10mm, High Loading

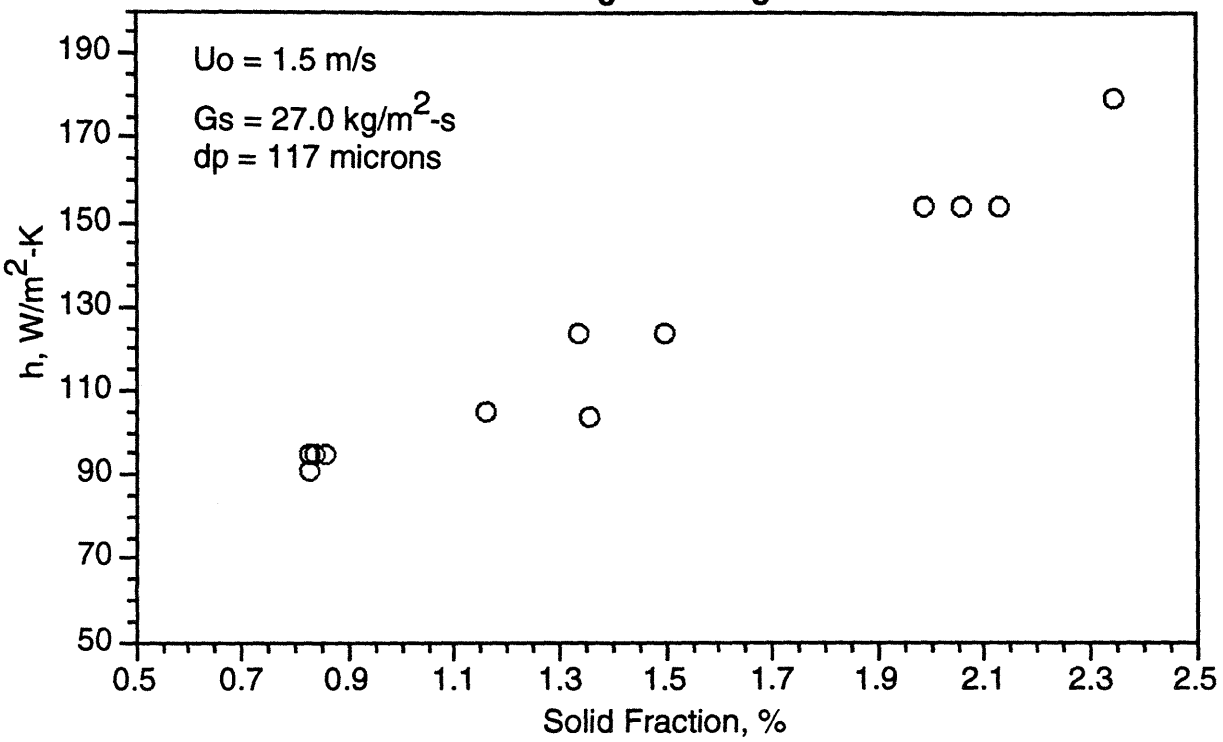

SF. %	h. W/m^2-K	Htr. No.
2.06	153.7	1
1.5	123.4	2
0.83	90.5	3
2.35	179.3	1
1.36	103.9	2
0.86	94.6	3
0.83	94.6	3
1.16	104.9	2
1.99	153.7	1
0.84	94.6	3
1.34	123.4	2
2.13	153.7	1

Heater Locations (% up riser):

1. 41.4
2. 64.4
3. 85.7

699

Heat Transfer Coefficient vs. Solid Fraction - Ridge Spacing = 5mm, Low Loading

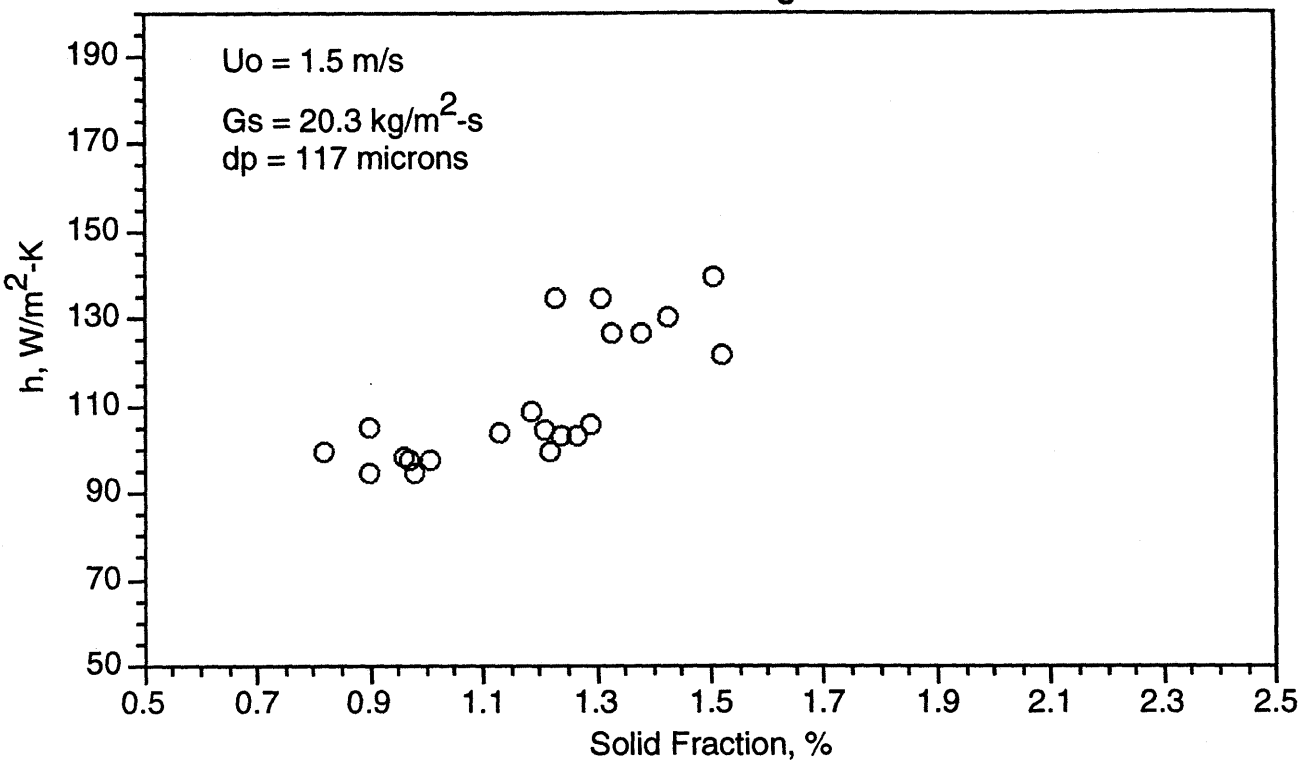

SF. %	h. W/m^2-K	Htr. No.
1.33	126.6	1
1.22	99.04	2
0.82	99.6	3
1.38	126.5	1
1.29	105.7	2
0.9	105.1	3
0.98	94.5	3
1.13	103.4	2
1.23	134.5	1
0.9	94.5	3
1.21	104	2
1.31	134.5	1

1.51	139.2	1
1.27	102.8	2
1.01	97.5	3
1.43	130	1
1.19	108.6	2
0.96	97.8	3
1.52	121.8	1
1.24	102.8	2
0.97	97.5	3

Heater Locations (% up riser):

1. 41.4
2. 64.4
3. 85.7

Heat Transfer Coefficient vs. Solid Fraction - Ridge Spacing = 5mm, High Loading

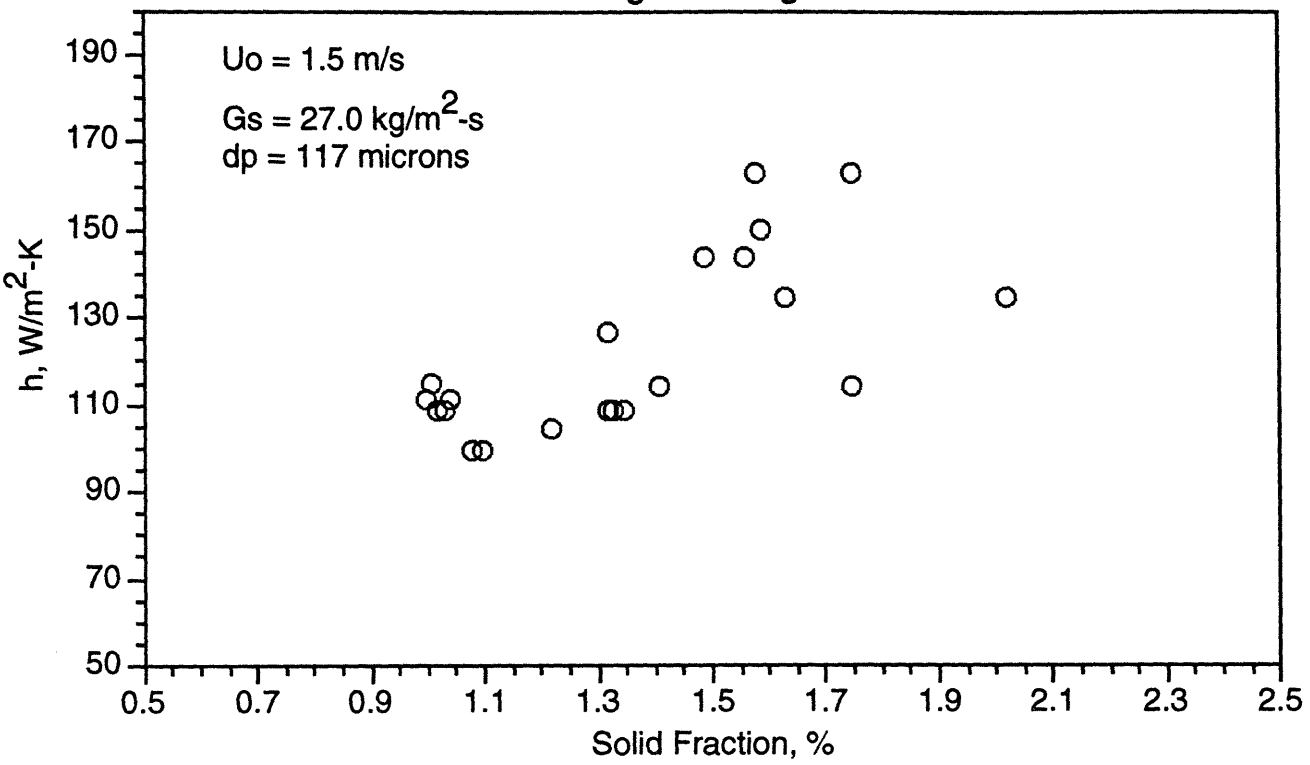

SF. %	h. W/m^2-K	Htr. No.
1.63	134.5	1
1.41	114	2
1.04	111.3	3
2.02	134.5	1
1.75	114	2
1	111.3	3
1.1	99.6	3
1.22	104	2
1.49	143.4	1
1.08	99.6	3
1.32	126.6	2
1.56	143.4	1

1.01	114.7	3
1.35	108.3	2
1.58	162.5	1
1.02	108.3	3
1.33	108.3	2
1.75	162.5	1
1.03	108.3	3
1.32	108.3	2
1.59	150	1

Heater Locations (% up riser):

1. 41.4
2. 64.4
3. 85.7

APPENDIX B: PRESSURE TRANSDUCER CALIBRATIONS

B.1 1/16 Scale Studsvik Bed

Pressure transducers A through D used to measure bed differential pressures near the bottom of the bed, were all calibrated for pressures spanning their expected range of +/- 14 in. wc (+/- 3.5 kPa). Pressure transducers E through H, also used to measure the differential pressures, were calibrated for its range of 0-1 psi (0-6.9 kPa). These transducers were used to measure differential pressures near the top of the bed. During calibration and subsequent use of the pressure transducers, power supply voltage was 12.2 volts. All transducers were calibrated with a manometer inclined at 17.5 degrees from the horizontal. Calibration data and linear curve fit constants are tabulated below. The constants are defined based on the following equation for measure pressure:

$$\text{Pressure} = G^*(\text{Voltage}) + P_r$$

Table B.1: Pressure Transducer Calibrations for 1/16 Scale Studsvik Bed			
Transducer	G (cm wc/V)	P_r (cm wc)	σ (cm wc)
A	949	-0.137	0.65
B	941	0.209	0.49
C	936	-0.308	0.93
D	971	-0.143	0.27
E	0.642	-1.802	0.00941
F	0.628	-1.764	0.00695
G	0.635	-1.533	0.00546
H	0.632	-1.793	0.00745

APPENDIX C: ROTAMETER CALIBRATION

C.1 1/16 Scale Studsvik Bed Air Flow Setup

In the 1/16 scale Studsvik bed (no boot, secondary air or simulated refractory), air enters the bed through the distributor box and at the bottom of the pneumatic return line. The two air flows are measured separately with rotameters fitted with exit pressure gauges. The rotameters measure in the range from 2 to 10 cfm, and the pressure gauges are 15 psig full scale. Calibration of the rotameters and gauge combinations was accomplished with a square-edged orifice plate fitted with flange taps. The tests covered flow ranges at expected pressure ranges with the data being fit to the equation:

$$Q_a = (AR+B)\sqrt{\left(1+\frac{P_g}{P_a}\right)}$$

C.2 Calibration of the Primary Air Rotameter

Calibration data for the rotameter used to measure primary air flow are presented below. The rotameter used to measure the primary flow had a nominal range from 2 to 10 cfm. The exit pressure gauge had a 1-15 psig range. The rotameter was calibrated with a square edge orifice plate fitted with flange taps. The orifice plate pipe size was two-inches, and the diameter ratio b was 0.15. Calibration covered rotameter indications ranging from 1.6 to 8 cfm at exit pressure ranging from about 1 to 10 psig. A valve at the exit of the rotameters allowed variation of exit pressure as well as flow rate. Orifice plate pressure drop was measured in a water-filled manometer.

The calibration data was fit to modified linear curve fits of the form

$$Q_a = (AR+B)\sqrt{\left(1+\frac{P_g}{P_a}\right)}$$

Were Q_a is the volumetric flow rate at atmospheric pressure, R is the rotameter reading, P_g is the rotameter exit gauge pressure, P_a is atmospheric pressure, and A and B are the calibration constants. Least squares solutions for A and B were determined.

Air flow with the orifice plate was calculated based on the ASME standard for square edge orifice plates (Bean, 1971). The calculation procedure was automated in a FORTRAN program.

The calculated calibration constants for the rotameter are as tabulated below. Standard deviation for the calibration data, also provided below, represents deviation of actual flow divided by the pressure correction function from the linear curve fit AR + B.

Table C.1: Rotameter Calibration Constants

Rotameter	Bed Used	A	B	σ
Primary Air (2-10 cfm)	1/16 Scale Studsvik	1.0347	0.0239	0.0422

C.3 References

Bean, H. S., ed., "Fluid Meters - Their Theory and Application, ed., 6", ASME, 1971.

Westphalen, Detlef, "Experimental Verification of Scaling Relationships for Circulating Fluidized Beds," M.S. Thesis, Massachusetts Institute of Technology, 1990.

Researcher	D, m	L, m	d_p microns	ρ_s, kg/m^3	u_0, m/s	Bed Material	Heat Transfer Length (cm)
Bader (1988)	0.305	12.2	76	1714	3.7 - 6.1	FCC	
Basu (1987)	0.102	5.5	87	2650	3.7 - 5.0	Sand	2.5
Basu (1987)	0.102	5.5	227	2650	3.0 - 5.0	Sand	2.5
Basu (1990)	0.101	5.5	87, 130, 227, 250	2650	3.0 -5.0 ?	Sand	10.1
Basu (1991)	0.102	5.5	130, 280	2650	3.5 - 5.0	Sand	30
Basu (1991)	0.100	5.15	310	~2600	5.6 - 11.4	Sand	30
Chen (1992)	0.094	6.0	71	1800	2.5 - 3.6	FCC	12
Dou (1990)	0.152	10.8	87	~1800	2.4 - 3.5	FCC	3.2
Dou (1990)	0.152	10.8	125	~2650	4.25 - 7.5	Sand	3.2
Dou (1990)	0.152	10.8	268	~2650	5.1 - 7.1	Sand	3.2

Feugier (1987)			95		10	Sand	95
Feugier (1987)			625		10	Sand	95
Feugier (1987)			215		10	Sand	95
Furchi (1988)	0.072	6.0	109	2500	5.8 - 12.8	Glass	100
Furchi (1988)	0.072	6.0	196	2500	5.8 - 12.8	Glass	100
Furchi (1988)	0.072	6.0	269	2500	5.8 - 12.8	Glass	100
Gidaspow (1989)	0.0762	6.5	520	2620	5	Glass	
Glicksman (1990)	0.203	7.5	88	2540	1.25 - 2.5	Glass	
Hartge (1988)	0.400	8.4	85	1500	1.2 - 5.4	FCC	
Hartge (1988)	0.400	8.4	120	2600	3.8 - 5.4	CFBC Ash	
Horio (1988)	0.050	2.79	60	1000	1.2 - 1.3	FCC	
Kobro (1986)			170		8.0 - 10.0	Sand	10

Kobro (1986)			250		8.0 - 10.0	Sand	10
Li (1991)	0.09	10.0	54	929.5	1.3 - 3.5	FCC	
Lints (1992)	0.203	7.5	182	2350	3.0 - 5.0	Quartz Glass	
Louge (1990)	0.197	7.0	61	~1800	2.0 - 5.0	FCC	
Nowak (1991)	0.205	6.65	46	2300	4.0	FCC	
Rhodes (1992)	0.305	6.6	70	2430	2.0 5.0	Alumina	
Sekthira (1988)	0.088		300		5.0 - 12.0	Sand	70
Sekthira (1988)	0.088		500		5.0 - 12.0	Sand	70
Subbarao (1986)	0.10	4.5	130	~2600	> 1.7	Sand	2.5
Subbarao (1986)	0.10	4.5	260	~2600	> 2.4	Sand	2.5
Wirth (1991)	0.168	11.0	50	4000	0.5 - 2.5	ZnS	
Wirth (1991)	0.168	11.0	200	2500	0.5 - 2.5	Glass	

Wirth (1991)	0.168	11.0	80	2500	0.5 - 2.5	Glass	
Wu (1987)	0.152	7.3	188	2637	4.0 - 7.0	Sand	153
Wu (1987)	0.152	7.3	356	2642	4.0 - 7.0	Sand	153
Wu (1989)	0.152	9.3	171	2650	7.0	Sand	1
Wu (1989)	0.152	7.3	241	3066	6.5 - 9.5	Sand	159
Wu (1991)	0.152	9.3	171	2650	7.0	Sand	1

CHAPTER 5

THE HYDRODYNAMIC MODELING OF CIRCULATING FLUIDIZED BEDS

1.0 INTRODUCTION

The dynamics of CFB solids dispersion has been a subject of intensive study over the past decade as the importance and use of fluidization techniques have increased. An essential element in that process is the way in which particles are dispersed throughout the bulk of the fluid under the action of turbulent forces which are random in both space and time. Although such motion for large particles is stochastically equivalent to Brownian motion and is well understood, no transport equation has yet been formulated to describe the collective motion of particles over the entire range of time scales of the particle fluid interaction. For the most part gradient transport models based on Fick's law have been used in analogy with both Brownian motion and the transport of a passive scalar by a turbulent field. In the case of the latter, the experimental and theoretical evidence as to the validity of such models is restricted to very simple types of turbulence [Batchelor (1952); Corrsin (1974)]. Although motion of a passive scalar is a special case of 'real' particle motion it illustrates some of the inherent problems in obtaining a collective description of their motion. For the most part transport of a passive scalar has been formulated in an Eulerian framework, where the problem reduces to one of closure of the statistical moment equations central to the transport mechanism. Studies by Roberts (1961), who used direct interaction, and Saffman (1969) and Phythian (1972), who used approximations based on functional expansions in Gaussian random field variables, are examples of this type of treatment. In each method, within the limit of the implied closure approximation gradient, transport equations are derived for isotropic, homogeneous and stationary turbulence for times greater than the time scale of the turbulence.

None of these techniques, however, give an adequate description of 'real' particles with finite size and finite inertia since they fail to take account of the lack of coincidence between the particle and fluid-point trajectories.

1.1 Eulerian Models

In Eulerian models, a first- or second-order closure scheme is employed to solve the time-averaged conservation equations for both phases. Often, a Boussinesq approximation is chosen to relate the turbulent particle flux to the average particle concentration gradient in the particulate phase equations. Therefore, particle dispersion is modeled as a Fickian diffusion process, requiring the use of an "effective" particle diffusivity. Choosing this

constant is similar to choosing the time and length scales in the trajectory (Lagrangian) model, for which little reliable analytical experimental information is available.

To address the problem of the lack of coincidence between the particle and fluid, most researchers have assumed the validity of Fick's law and have calculated the particle diffusion coefficient from the basic expression given by Taylor (1921) in his theory of diffusion by continuous movements, namely that for a stationary homogeneous field the time-varying particle diffusion coefficient, $\varepsilon_{p_{ij}}(\tau)$ is given by

$$\varepsilon_{p_{ij}}(\tau) = \int_0^\tau \left\langle \Delta v_{p_i}(0) \Delta v_{p_j}(t) \right\rangle dt \qquad (1)$$

where $\Delta v_{p_j}(t)$ is the velocity of the particle in the j direction at time t relative to its mean and the angle brackets indicate an ensemble average over all realizations of the particle motion. In this respect we refer specifically to the work of Tchen (1947), Friedlander (1957), Peskin (1962), Csanady (1963) and Hutchinson et al., (1971). Although Taylor's theory circumvents closure, as is well known, the relevant statistical correlations are those obtained along a particle trajectory for all realizations of the particle motion (Lagrangian) and the essential problem of nonlinearity is made manifest in finding a relationship between Lagrangian variables and those of the field at a stationary point (Eulerian). Tchen's analysis used an equation of motion which was consistent with a particle accelerating through a viscous time-varying fluid field in which the particle Reynolds number was small compared with unity (Hinze, 1959). The significant feature of this analysis was that in the long-time limit, equation (1) is equal to

$$\varepsilon_{p_{ij}}(\infty) = \int_0^\infty \left\langle \Delta v_{f_i}(0) \Delta v_{f_j}(t) \right\rangle dt \qquad (2)$$

where $\Delta v_{f_j}(t)$ is the equivalent fluctuation in the fluid velocity relative to its mean at a point instantaneously occupied by the particle at a time t for a particular realization of the particle's motion. Tchen, however, identified $\left\langle \Delta v_{f_i}(0) \Delta v_{f_j}(t) \right\rangle$ with the Lagrangian velocity correlation of the fluid itself and concluded that the particle and fluid diffusion coefficients were equal in the limit when both became time independent. This correlation function is clearly dependent upon particle motion, reflecting a dependence on particle inertia made manifest in an inability to follow the fluid oscillations, and also upon the effect of any external force acting upon the particle. The effect of a constant external force was first recognized by

Yudine (1959) and later used by Csanady (1963) in his analysis of the turbulent diffusion of heavy particles in the atmosphere. Here the particle inertia was considered sufficiently small for a particle to follow the fluid oscillations but the particle was considered sufficiently heavy for its gravitational drift significantly to affect its velocity correlation compared with that of the fluid. If $R_{fij}(\mathbf{x}, t)$ is the fluid Eulerian space-time velocity autocorrelation in a frame of reference moving with the fluid mean velocity, then the effect of a constant drift velocity, $\mathbf{v}_{p_\infty}$ on particle diffusion is seen by replacing $\left\langle \Delta v_{f_i}(0)\Delta v_{f_j}(t)\right\rangle$ by $R_{fij}(\mathbf{v}_{p_\infty}t, 0)$. Yudine has referred to this phenomenon as the 'effect of crossing trajectories.' It is clear that such an effect will entirely dominate particle diffusion at large $\mathbf{v}_{p_\infty}$ when the time scale associated with $R_{fij}(\mathbf{v}_{p_\infty}t, 0)$ can be made arbitrarily small compared with the eddy decay time. For zero $\mathbf{v}_{p_\infty}$, $\left\langle \Delta v_{f_i}(0)\Delta v_{f_j}(t)\right\rangle$ becomes the Lagrangian fluid-point correlation in Csanady's system. On this basis, Csanady describes the behavior of $\left\langle \Delta v_{f_1}(0)\Delta v_{f_1}(t)\right\rangle$ in the vertical direction due to eddy decay and crossing trajectories by the two numbers $\frac{v'_{f_{rms}}t}{l_a}$ and $\frac{v_{p_\infty}t}{l_a}$ respectively, where $v'_{f_{rms}}$ is the intensity of the turbulence and l_a is the vertical integral length scale. By choosing a functional form for $\left\langle \Delta v_{f_1}(0)\Delta v_{f_1}(t)\right\rangle$ consistent with similar shapes for Eulerian spatial and Lagrangian fluid-point correlations, Csanady obtained a formula for $\varepsilon_{p_{11}}(\infty)$ (axial direction) of the form

$$\varepsilon_{p_{11}}(\infty) = \varepsilon_{p_a}(\infty) = \varepsilon_f(\infty)\left\{\left(\frac{v'_{f_{rms}}}{v_{p_\infty}}\right)^2 + \frac{l_a}{\tau_L v'_{f_{rms}}}\right\}^{-1/2} \tag{3}$$

where τ_L is the Lagrangian integral time scale. Using similar arguments Csanady also obtained a formula for the particle diffusion coefficient in the horizontal direction. Here, because of the continuity of flow, the Eulerian length scale is different from the equivalent vertical scale. The relationship of scales existing in isotropic stationary turbulence is assumed and the form for $\varepsilon_{p_{22}}(\infty)$ (radial direction) suggested by Csanady is

$$\varepsilon_{p_{22}}(\infty) = \varepsilon_{p_r}(\infty) = \varepsilon_f(\infty)\left\{4\left(\frac{v'_{f_{rms}}}{v_{p_\infty}}\right)^2 + \frac{l_a}{\tau_L v'_{f_{rms}}}\right\}^{-1/2} \tag{4}$$

Clearly the effect of increasing v_{p_∞} is to reduce the particle diffusion coefficient both in the direction parallel and in the direction normal to v_{p_∞}. In the limit $\left(\frac{v'_{f_{rms}}}{v_{p_\infty}}\right) \to \infty$, the diffusion coefficient normal to v_{p_∞} is half that parallel to v_{p_∞}, both coefficients being inversely proportional to v_{p_∞}, a result first obtained by Yudine (1959). It is worth pointing out that equation (1) was used as the basis of Csanady's analysis, and because of neglect of inertial effects $\left\langle \Delta v_{p_i}(0)\Delta v_{p_j}(t)\right\rangle$ was equivalent to $\left\langle \Delta v_{f_i}(0)\Delta v_{f_j}(t)\right\rangle$. However, because of the validity of (2) for linear drag, in the limit of large v_{p_∞} the same results would apply for particles for which inertia effects were significant (Lumley, 1976). However, in the absence of a constant drift these formulae are not longer valid except in the limit of zero inertia. It is reasonable to suppose that the effect of inertia in this instance is such that as the particle inertia is increased from zero $\left\langle \Delta v_{f_i}(0)\Delta v_{f_j}(t)\right\rangle$ changes smoothly from the fluid Lagrangian autocorrelation to the single-point Eulerian velocity-time correlation. Whether the long-time particle diffusion coefficient is greater or less than that of the fluid depends upon whether for the fluid the Eulerian integral time scale is greater or less than the Lagrangian integral time scale. The most notable theoretical work on this subject began with Corrsin's (1959) independence approximation, known as Corrsin's hypothesis, and later with the work of Kraichnan (1964). Kraichnan (1964) described Eulerian and Lagrangian velocity fields for which one would expect Lagrangian time scales to be less than the equivalent Eulerian times scales. This conclusion is corroborated by his computer simulations of fluid-point dispersion in a Gaussian random velocity field [Kraichnan, (1970)]. It was also significant that good agreement was found between these 'exact' results and those obtained from the direct-interaction approximation. This Eulerian Lagrangian time-scale relationship is also an implication of Phythian's (1975) formulation. Phythian's method uses a 'second approximation' to the solution of the equation of motion of the fluid point moving through a random isotropic homogeneous and stationary Gaussian velocity field. Considering the crudity of the approximation compared with the fully iterated solution, it will appear surprising that, as far as the finally calculated fluid Lagrangian velocity autocorrelation is concerned, the results are in remarkably good agreement with Kraichnan's computer simulations for random velocity fields of characteristic of real turbulence. Reeks (1977) showed that as a basis for calculating random particle motion with finite inertia, this approximation is strictly a perturbation about the motion of particles of large inertia. The greatest discrepancy between real and approximate motion occurs in calculating fluid-point motion, for which the method was originally used. Reeks (1977) presented a solution to the dispersion of small particles suspended in a turbulent fluid is presented, based on the

approximation proposed by Phythian for the dispersion of fluid points in an incompressible random fluid. He showed that, in the absence of gravity, the long-time particle diffusion coefficient is in general greater than that of the fluid, approaching with increasing particle relaxation time a value consistent with the particle being in an Eulerian framer of reference. The effect of gravity is consistent with Yudine's crossing trajectories, reducing unequally the particle diffusion in directions normal to and parallel to the direction of the gravitational field. To characterize the effect of flow and gravity on particle diffusion it has been found useful to use a Froude number based on the turbulent intensity rather than the mean velocity. Depending upon the value of this number it found that the particle integral time scale may initially decrease with increasing particle relaxation time though it eventually rises and approaches the particle relaxation time.

Nir and Pisman (1979) examined the effect of a steady deterministic drift on the dispersion of particles suspended in a stationary homogeneous turbulent field by neglecting the off-diagonal terms in the spatial Fourier components of the fluid velocity correlation function which is equivalent to the use of Corrsin's hypothesis. In addition, they assumed a Gaussian property of the functional distribution of particle velocities. Their formulation is nearly identical to that of Reeks (1977). The existence of negative particle velocity correlations was demonstrated. The dependence of the particle diffusivity and kinetic energy on the inertial and drift factors was evaluated for model turbulence spectrum.

1.2 Lagrangian Models

A Lagrangian model usually accounts for dispersion effects by tracking particles through a continuous succession of turbulent eddies superimposed upon the mean gas flow. Ideally, this approach requires knowledge of the full time history of the turbulent flow, obtained by solving the instantaneous (unaveraged) Navier-Stokes equations. Since this is not realistic, the turbulence is typically simulated as a stochastic process, where mean values are determined from the time-average, Navier-Stokes solutions. Each eddy is then characterized by a mean time and length scale, and the velocity fluctuations are randomly-generated in a Gaussian manner as a particle enters an eddy. This approach results in a Monte-Carlo procedure where many particle trajectories (realizations) must be computed to obtain averaged properties. The difficulty in this approach is choosing the appropriate Lagrangian time and length scales of the turbulence. Number simulations of dispersion of an ensemble of particles, in which the trajectory of each particle is calculated as a series of interactions with discrete pseudo-random turbulent eddies are relatively easy to implement, but are costly

and time consuming because a large number of particles must be modeled. Examples of its use include the studies of Brown and Hutchinson (1979), Boysan *et al.* (1982), James *et al.* (1980), Weber *et al.* (1984), and Gouesbet *et al.* (1987).

In this Chapter, the Lagrangian simulation model has been used to study particle dispersion and deposition in a CFB. The simulation includes the effects of particle inertia, 'crossing-trajectories, particle sphericity, bed voidage, and particle-particle interactions. Calculated dispersion coefficients are then used to predict the average axial solid fraction profile in the dilute core of a CFB. Overall mass and momentum equations for the core-annular structure of a CFB are solved to determine the annular layer thickness, solid fraction, and average fall velocity. A procedure for approximating the radial distribution of solids concentration, and particle velocities is also presented.

An approximate method based on Eulerian techniques and the relations derived for the Lagrangian numerical model is given to provide a quick estimate of dispersion coefficients and axial average solid fraction in the dilute region of CFB's.

Finally, model results are compared with experimental data for CFB's, FCC reactors, and dilute pneumatic transport multiphase flows.

2.0 DETERMINATION OF DISPERSION COEFFICIENT

2.1 Structure of Gas Turbulence

Townsend (1956) has proposed a relationship for the persistence length or characteristic size of the large eddies which is related, but not equal to, the macroscale

$$l_e = 1.6\frac{(q^2)^{3/2}}{3\sqrt{3\varepsilon}}$$

$$q^2 = \overline{(u_x')^2} + \overline{(u_y')^2} + \overline{(u_z')^2}$$

$$\varepsilon = \nu\left[\frac{\partial u_i'}{\partial x_j}\right] \quad i,j = 1,2,3$$

l_e is the eddy length scale, q^2 is 1/2 of the turbulent kinetic energy, and e is the turbulent energy dissipation.

Laufer (1954) provides data for flow in pipes at Reynolds number of 5E+4 and 5E+5. Hutchinson *et al.* (1971) used this data to calculate the ratio of l_e/R from the equations. The ratio was found to be remarkably constant both with respect to a ten fold change in Reynolds number and with radial position. A ratio of $l_e/R = 0.22$ was found to fit the range of data very well.

Assume the particle suspension is dilute enough such that one-way coupling is valid - the presence of the particles does not significantly modify the gas flow field. If the turbulence is isotropic and profile effects are not important, the simple gas turbulence model of Hutchinson et al. (1971) described above can be used:

$$l_e = 0.11D \tag{1}$$

$$u_e = u_\tau = u_o\sqrt{\frac{f}{2}} \tag{2}$$

where u_τ is the friction velocity, u_e is the eddy velocity, and f is the single phase friction factor.

Eddies are characterized by a mean decay time, τ_e, and the contact time between a particle and eddy cannot exceed this decay time. Townsend (1956) estimated this time from Laufer's data and gives its variation with radial position. Again, a reasonably position free constant can be assume for all radial locations,

$$\frac{\tau_e}{R/u_\tau} = 0.35 \tag{3}$$

From this it follows that

$$\tau_e = 1.6\frac{l_e}{u_e} \tag{4}$$

In (4), the factor 1.6 is the ratio of Lagrangian and Eulerian time scales of turbulence; there is considerable uncertainty over the actual value, reported values showing a wide range (Laufer, 1954). However, for fluidized beds, the particles are sufficiently large that their motion is essentially Eulerian and, with the exception of developing particle motion, the time scale of eddy-particle interaction is determined mainly by the particle-eddy crossing time in the vertical direction. This is consistent with the findings of previous works [e.g. Reeks (1977); Lee (1989); Wells (1983)] that the crossing-trajectory effect, due to gravity, is dominant if the particle terminal velocity is greater that u_e.

Assume the turbulent flow field can be described by a sequence of eddies which have characteristic speed u_e and length l_e, and a decay time of τ_e, but whose direction is random, characterized by a sign S, which can be either positive or negative with equal probability. In terms of its mean,

$$\langle u_e(t) \rangle = 0 \tag{5}$$

The Lagrangian and Eulerian auto-correlations are (for the fluid):

$$\begin{aligned} R_L(\tau) &= u_e^2\left(1 - \frac{|\tau|}{\tau_e}\right), \quad |\tau| \le t \\ &= 0 \qquad\qquad \text{otherwise} \end{aligned} \tag{6}$$

$$R_E(\tau) = u_e^2\left(1 - \frac{|\tau|}{\left(\frac{l_e}{u_e}\right)}\right), \quad |\tau| \le \left(\frac{l_e}{u_e}\right)$$
$$= 0 \qquad \text{otherwise} \tag{7}$$

< > brackets denote an ensemble average. The auto-correlation function $R(\tau) = \langle u(t)u(t+\tau)\rangle$.

For the Lagrangian case, $R_L(\tau)$ averages are taken for fluid points and for the Eulerian case, $R_E(\tau)$, at a point in fixed space.

2.2 Determination of Particle Mean Square Displacement

Consider the force balance on a single sphere far from the flow boundaries:

$$\frac{1}{6}\pi d_p^3 \rho_s \frac{d\mathbf{v}_p}{dt} = \frac{1}{6}\pi d_p^3(\rho_s - \rho_f)\mathbf{g} - \frac{\rho_f \pi C_D d_p^2}{8}\left(\mathbf{v}_p - \mathbf{v}_{fp} - \frac{1}{24}d_p^2\nabla^2\mathbf{v}_{fp}\right)\left|\mathbf{v}_p - \mathbf{v}_{fp}\right|$$
$$- \frac{\pi\mu d_p^2 C_H}{4}\int_{t_0}^{t}\frac{d}{d\tau}\left[\mathbf{v}_p - \mathbf{v}_{fp} - \frac{1}{24}d_p^2\nabla^2\mathbf{v}_{fp}\right]\frac{d\tau}{\left(\pi\nu(t-\tau)\right)^{1/2}} \tag{8}$$
$$- \frac{1}{6}\pi d_p^3 \rho_f C_A \frac{d}{dt}\left[\mathbf{v}_p - \mathbf{v}_f - \frac{1}{40}d_p^2\nabla^2\mathbf{v}_{fp}\right] + \frac{1}{6}\pi d_p^3 \rho_f \frac{D\mathbf{v}_{fp}}{dt}$$

The Eulerian fluid velocity at $\mathbf{x}$ is denoted by $\mathbf{v}_f(\mathbf{x},t)$ and the Lagrangian position and velocity of the particle are denoted by $\mathbf{r}(t)$ and $\mathbf{v}_p(t)$ respectively. The fluid velocity seen by the particle is $\mathbf{v}_{fp} = \mathbf{v}_f(\mathbf{r}(t),t)$. It assumed to have zero mean, or the coordinate system is assumed to be moving with a mean fluid velocity that is uniform in space.

Terms on the r.h.s. of (8) are the gravitational force (minus the buoyancy force), the Stokes drag, the Boussinesq-Basset history force, the force due to added mass and the force resulting from the stress gradients of the fluid flow in the absence of a particle. The added mass term is expressed in terms of the time derivative seen by the particle as it moves through trajectory d/dt. The term defining the influence of fluid stress-gradients on the particle is expressed in terms of the change in fluid velocity along its own trajectory.

If it is assumed that the ratio of solid to fluid density is large, the virtual mass, Boussinesq-Basset history, Faxen, and fluid stress gradient terms can all be neglected. Additionally if it is assumed that the macroscopic fluid velocity gradients are small, shear lift forces can be ignored. Then, in the direction normal to the gravitational field:

$$\frac{1}{6}\pi d_p^3 \rho_s \frac{dv_{p_r}}{dt} = -\frac{\rho_f \pi C_D d_p^2}{8}\left(v_{p_r} - v_{fp}\right)\left|\mathbf{v}_p - \mathbf{v}_{fp}\right| \tag{9}$$

2.2.1 Result for Vanishing Particle Reynolds Number

For small particles

$$C_D = \frac{24}{Re_{u_{rel},\, d_p}} \tag{10}$$

which is Stokes law. The equation of the motion (9) reduces to

$$\frac{dv_{p_r}}{dt} + \beta v_{s_r} = \beta u_e \tag{11}$$

where $\beta = \frac{18\mu_f}{d_p^2 \rho_s}$.

Assume equations (5) and (6) characterize the fluid velocity encountered by the particles. Strictly speaking, this is only valid for vanishingly small particles with zero inertia, as will be discussed later.

The solution of a linear stochastic equation of the form (11) is well known. With boundary conditions

$$v_{s_r}(0) = 0 \tag{12}$$

it is possible to show that

$$\left\langle v_{s_r}^2(t)\right\rangle = \beta u_e^2\left(\frac{1}{\beta}\frac{1}{\tau_e\beta^2}\left(1-e^{-\beta\tau_e}\right)\right) + \beta u_e^2 e^{-2\beta t}\left(\frac{1}{\beta}\frac{1}{\tau_e\beta^2}\left(1-e^{\beta\tau_e}\right)\right) \qquad (13)$$

$$t > \tau_e$$

Similarly for the particle displacement given that

$$x_p(0) = 0 \qquad (14)$$

one can show

$$\left\langle x_{s_r}^2(t)\right\rangle = u_e^2\tau_e t + u_e^2\left(\frac{4-\left(1+\tau_e\beta\right)^3}{3\tau_e\beta^3} - \frac{e^{-\beta\tau_e}}{\tau_e\beta^2}\right)$$

$$+ \beta u_e^2 e^{-\beta t}\left(\frac{\tau_e^2\beta^2-2-2\tau_e\beta}{\tau_e\beta^3} - \frac{2e^{\beta\tau_e}}{\tau_e\beta^3}\right) + u_e^2 e^{-2\beta t}\left(\frac{\left(1+\beta\right)}{\tau_e\beta^3} - \frac{e^{\beta\tau_e}}{\tau_e\beta^3}\right) \qquad (15)$$

$$t > \tau_e$$

2.2.2 Solution for Non-Vanishing Particle Reynolds Numbers

For a circulating fluidized bed operating with 200 micron dolomite at 12 atmospheres and 1150 K, the particle based Reynolds number is bout 11.5, assuming the particle-fluid relative velocity is equal to the particle terminal velocity. For a room temperature model using the same particles, the Reynolds number is about 20. In general no explicit solution exists for equation (9) with the proposed fluid turbulence model when the fluid-particle drag cannot be expressed in the form of Stokes drag.

It is necessary to assume the particle motion is described as a stochastic process the parameters of which are determined from the drag interaction between gas and particle with the dominant interaction controlled by the large scale structure of the turbulence. The particles are not assumed to move with the eddies, the history of their displacement and velocity being determined form the dynamics of the gas-particle interaction. It is also assumed that the particles move with an upward velocity u_o - u_t, and that the particles execute a random walk in the plane normal to the gas flow.

To solve for $\left\langle x_{p_r}^2 \right\rangle$ and $\left\langle v_{p_r}^2 \right\rangle$, a random sequence of random signs, S_i, can be generated. The equation of motion for each particle-eddy interaction can then be solved and the effects summed for many interactions.

For large particles in a vertical gas flow, the settling velocity, u_t, is usually greater than the gas turbulence velocity u_e, so that in equation (9),

$$\left| v_p - v_{fp} \right| \simeq u_t \tag{16}$$

For particles which have reached long-time behavior, equation (9) is then

$$\frac{1}{6}\pi d_p^3 \rho_s \frac{dv_{p_r}}{dt} = -\frac{\rho_f \pi C_D d_p^2}{8}\left(v_{p_r} - v_{fp}\right)u_t \tag{17}$$

where

$$C_D = f\left(Re_{u_{rel},\, d_p}\right) \tag{18}$$

and

$$Re_{u_{rel},\, d_p} \simeq \frac{\rho_f d_p u_t}{\mu_f} \tag{19}$$

For eddy-particle interactions,

$$v_{fp} = \pm u_e \tag{20}$$

Equation (17) can be integrated to give

$$\frac{v_{p_r}}{u_e} = \pm 1 - \left(\pm 1 - \frac{v_{p_{r_o}}}{u_e}\right)\exp\left(-\beta t\right) \tag{21}$$

where the inverse relaxation time is given by

$$\beta = \frac{3}{4} C_D \frac{\rho_f}{\rho_s} \frac{u_t}{d_p} \tag{22}$$

In the random walk process, u_e is assumed constant during each interaction between eddy and particle. For large particles, the interaction time is always the crossing time due to gravity

$$t_i = \frac{l_e}{u_t} \tag{23}$$

Table 1 presents a comparison of various time scales in a CFB. In the Table, t_v is the interaction time due to crossing trajectories, t_e is the eddy time scale, $t_e = \frac{l_e}{u_e}$, and τ_e is the eddy decay time. In a 0.5 meter CFB operating at 1150 K and 12 atm with 200 microns dolomite, the eddy decay time falls below the vertical crossing time only at velocities above 8.0 m/s - well above the normal operating conditions of these beds.

Table 1: Comparison of Various Time scales in a Pressurized CFB

u_o (m/s)	u_e (m/s)	u_t (m/s)	l_e (m)	t_v (s)	t_e (s)	τ_e (s)	$1/\beta$ (s)
3.0	0.28	0.70	0.055	0.079	0.31	.20	0.071
4.0	0.36	0.70	0.055	0.079	0.24	0.15	0.071
5.0	0.44	0.70	0.055	0.079	0.20	0.12	0.071
6.0	0.52	0.70	0.055	0.079	0.17	0.11	0.071
7.0	0.60	0.70	0.055	0.079	0.15	0.092	0.071
8.0	0.68	0.70	0.055	0.079	0.13	0.081	0.071
9.0	0.75	0.70	0.055	0.079	0.12	0.073	0.071
10.0	0.83	0.70	0.055	0.079	0.11	0.067	0.071

The interaction time is therefore limited, at least up to 9 m/s, by the time due to particle eddy crossing in the vertical direction $\left(t_v < t_e, \tau_e\right)$. Most likely it will be limited well beyond this value since the particle will never move with the eddy unless it is very small or the interaction time scales become very large ($l_e >> 1$).

Integrating the equation of motion again gives the particle position

$$x_{p_r} = x_{p_{r_o}} \pm u_e t_i + \frac{\left(v_{p_r} \pm u_e\right)\left(1 - \exp\left(-\beta t\right)\right)}{\beta} \tag{24}$$

where the interaction time, t_i

$$t_i = \min\left(t_v, t_e, t_p = \frac{l_e}{V_{p_r}}\right) \tag{25}$$

Govan (1986) showed that for small values of $A = \beta t_i$ (for CFB's, $A \sim O(0.01)$)

$$\left\langle \left(\frac{V_{p_r}}{u_t}\right)_n \left(\frac{V_{p_r}}{u_t}\right)_{n-r} \right\rangle = \frac{A}{2}\exp\left(-rA\right) \tag{26}$$

$$= \left\langle \left(\frac{V_{p_r}}{u_t}\right)^2 \right\rangle \exp\left(-rA\right) \tag{27}$$

$$\left\langle x_{p_{rn}} x_{p_{rn-r}} \right\rangle = \left(\frac{u_e l_e}{u_t}\right)^2 \frac{A}{2}\exp\left(-rA\right) \tag{28}$$

$$\left\langle x_{p_{rn}} x_{p_{rn-r}} \right\rangle = \left\langle x_i^2 \right\rangle \exp\left(-rA\right) \tag{29}$$

where x_n is the particle displacement during the nth interaction.

Setting

$$\theta = rt_i = r\,\frac{l_e}{u_t} \tag{30}$$

gives the auto-correlation

$$R_p(\theta) = \exp\left(-\beta\theta\right) \tag{31}$$

which is consistent with the idea that the large particles are in an essentially Eulerian frame of reference.

The particle mean square displacement is

$$\left\langle x_{p_r}^2 \right\rangle = \left\langle \left(\sum_i x_i\right)^2 \right\rangle \tag{32}$$

$$\left\langle x_{p_r}^2 \right\rangle = 2\left\langle \left(\sum_{i} \sum_{j>i} x_i x_j \right) \right\rangle \tag{33}$$

$$\left\langle x_{p_r}^2 \right\rangle = 2\left\langle \left(\sum_{i}^{N} \sum_{r=0}^{N-i} x_i x_{i-r} \right) \right\rangle \tag{34}$$

$$\left\langle x_{p_r}^2 \right\rangle = 2N \sum_{r=0}^{N} \left\langle x_i x_{i-r} \right\rangle \tag{35}$$

For a large number of interactions and constant $\left\langle x_i^2 \right\rangle$,

$$\left\langle x_{p_r}^2 \right\rangle = 2N \sum_{r=0}^{N} \left\langle x_i{}^2 \right\rangle \exp\left(-rA\right) \tag{36}$$

$$\left\langle x_{p_r}^2 \right\rangle = 2N \left\langle x_i{}^2 \right\rangle \int_0^N \exp\left(-rA\right) dr \tag{37}$$

$$\left\langle x_{p_r}^2 \right\rangle = 2\left(\frac{u_t}{l_e}\right)\left\langle x_i{}^2 \right\rangle \left(\frac{t}{\beta t_i}\right)\left(1 - \exp(\beta t)\right) \tag{38}$$

where the definition of the total number of interactions has been used,

$$N = t\left(\frac{u_t}{l_e}\right) \tag{39}$$

If Govan's approximation holds (equation 29),

$$\left\langle x_{p_r}^2 \right\rangle = 2\left(\frac{u_t}{l_e}\right)\left(\frac{A}{2}\right)\left(\frac{u_e l_e}{u_t}\right)^2 \left(\frac{t}{A}\right)\left(1 - \exp(\beta t)\right) \tag{40}$$

since

$$\left\langle x_i^2 \right\rangle = \left(\frac{A}{2}\right)\left(\frac{u_e l_e}{u_t}\right)^2 \tag{41}$$

From (40),

$$\left\langle x_{p_r}^2 \right\rangle = \left(\frac{u_e^2 l_e}{u_t}\right) t\left(1 - \exp(\beta t)\right) \tag{42}$$

At long times,

$$\left\langle x_{p_r}^2 \right\rangle = \left(\frac{u_e^2 l_e}{u_t}\right) t \tag{43}$$

For large particles, two expressions have been derived for the mean square displacement in the radial direction; and exact expression equations (38) and an approximate expression, (43).

2.3 Evaluation of Particle Dispersion Coefficient

To calculate the particle diffusion coefficient, the analysis is similar to that of Taylor (1921) for a stationary process in homogeneous turbulence

$$\left\langle x_{p_r}^2 \right\rangle = 2\left\langle v_{p_r}^2 \right\rangle \int_0^t \left(\int_o^{t'} R_p(\theta) d\theta \right) dt \tag{44}$$

where $R_p(\theta)$ is the Lagrangian correlation coefficient of the velocity of the particle at two different times

$$R_p(\theta)\left\langle v_p^2 \right\rangle = \left\langle v_p(t') v_p(t' + \theta) \right\rangle \tag{45}$$

for small times,

$$R_p(\theta) \simeq 1 \tag{46}$$

and

$$\left\langle x_p^2 \right\rangle = \left\langle v_p^2 \right\rangle t^2 \tag{47}$$

For large times, (44) gives

$$\frac{1}{2}\left(\frac{d\langle x_p^2\rangle}{dt}\right) = \langle v_p^2\rangle \tau_p^2 = \varepsilon_p \tag{48}$$

where

$$\tau_p = \int_0^\infty R(\theta)d\theta \tag{49}$$

The long time diffusion (dispersion) coefficient can be found from

$$\frac{1}{2}\left(\frac{d\langle x_p^2\rangle}{dt}\right) = \varepsilon_p \tag{50}$$

$$\frac{1}{2}\left(\frac{\langle x_p^2\rangle}{t_i}\right) = \varepsilon_p \tag{51}$$

This is the same result arrived at by Chandrasekhar (1945) for the diffusion coefficient of a particle undergoing a large number of displacements in a two-dimensional random walk, i.e.,

$$\left(\frac{n\langle x_p^2\rangle}{2}\right)\nabla^2 W(r,t) = \frac{\partial}{\partial t}W(r,t) + S(r,t) \tag{52}$$

n is the frequency of interaction

$$n = \frac{1}{t_i} \tag{53}$$

and W(r,t) is a probability density function for particles with source S(r,t).

2.4 Determination of Average Bed Axial Solid Concentration Profile

2.4.1 Derivation of Dispersion Equation

Consider the mass conservation equation over a volume element in the core of a CFB

$$\int_{\forall}\left(\frac{\partial}{\partial z}\left(\bar{u}\,C(r,z)\right)-S(r,z)+\frac{\partial}{\partial t}\left(C(r,z)\right)\right)d\forall-\int_{\Sigma}\varepsilon_{p_r}\nabla_r C(r,z)\cdot\hat{n}\,d\Sigma=0 \tag{54}$$

where S(r,z) is a source term, C(r,z) is the local mean concentration, Σ is the surface area of the elemental volume, $d\forall$ is the volume element, $\bar{u}$ is the local particle axial velocity, and

$$\nabla_r=\hat{r}\frac{\partial}{\partial r} \tag{55}$$

$$\nabla_r^2=\frac{\partial^2}{\partial r^2}+\frac{1}{\hat{r}}\frac{\partial}{\partial r} \tag{56}$$

The first term in (54) gives the effect of dilation arising from a varying axial velocity, and the final term accounts for the loss of particles by diffusion in direction perpendicular to the direction of gas flow.

Using Green's theorem

$$\int_{\Sigma}\left(U\nabla V-V\nabla U\right)d\Sigma=\int_{\forall}\left(U\nabla^2V-V\nabla^2U\right)d\forall \tag{57}$$

the volume integral can be eliminated resulting in

$$\left(\frac{\partial}{\partial z}\left(\bar{u}(z)\,C(r,z)\right)-S(r,z)+\frac{\partial}{\partial t}\left(C(r,z)\right)\right)-\varepsilon_{p_r}\nabla_r^2C(r,z)=0 \tag{58}$$

Diffusive motion in the axial direction has been neglected. If it is assumed that at any point along the bed axis, the bed mean properties of the flow are time independent, i.e. startup effects are neglected, then

$$\frac{\partial}{\partial t}\left(C(r,z)\right)=0 \tag{59}$$

and equation (58) can be written as

$$\left(\frac{\partial}{\partial z}\left(\bar{u}(z)\,C(r,z)\right)\right)-S(r,z)-\varepsilon_{p_r}\nabla_r^2C(r,z)=0 \tag{60}$$

or

$$\left(\bar{u}(z)\frac{\partial}{\partial z}\left(\bar{u}(z)\,C(r,z)\right)-\bar{u}(z)\,S(r,z)\right)-\varepsilon_{p_r}\nabla_r^2\left(\bar{u}(z)\,C(r,z)\right)=0 \tag{61}$$

Assume that the particles move with a velocity near that of the gas, hence $\bar{u}(z)$ may be identified as the axial gas velocity. Transformation to a system of coordinates moving with the axial velocity of the gas implies that

$$z=z_o+\int_{t_o}^{t}u(t')dt' \tag{62}$$

$$\frac{\partial}{\partial z}=\frac{1}{\bar{u}(t)}\frac{\partial}{\partial t} \tag{63}$$

$$\bar{u}(t)=\frac{\partial z}{\partial t} \tag{64}$$

Combination of (64) with (61) gives the equation of the variation of particle concentration in a coordinate system moving with the gas

$$\left(\frac{\partial}{\partial t}\left(\bar{u}(t)\,C(r,z)\right)-\bar{u}(t)\,S(r,z)\right)-\varepsilon_{p_r}\nabla_r^2\left(\bar{u}(t)\,C(r,z)\right)=0 \tag{65}$$

Equation (65) has the form of a two dimensional diffusion equation for the axial mass flux of the particles.

2.4.2 Source Term

In a circulating fluidized bed, sources of particles to the core come from two regions:

1. Particles fed in the bottom of the bed from the downcomer
2. Particles entrained from the downward flowing annular layer at the wall

Therefore, the source term is assumed to be a plug source of radius r_p originating at the bottom of the bed, and a continuous source arising from the re-entrainment of particles from the wall cluster layer

$$S(r,t) = \frac{D}{2r_e}E(t)\delta(r - r_e) + \frac{D^2}{4r_p^2}\bar{C}_p u(r_p - r)\delta(t) \tag{66}$$

where r_e is the instantaneous radial position of the cluster wave height for entrainment, $\delta(r)$ is the Dirac delta function, E(t) is the instantaneous rate per unit time area of bed wall, $\bar{C}_p$ is the mean concentration over the tube of a plug source of radius r_p present at the bed entrance (t = 0). In (66), the delta function term represents the continuous time varying source arising from re-entrainment of particles from the cluster layer, and the factor $\frac{D}{2r_e}$ appear as E(t) is given per unit area of bed wall surface. The step function term is used to represent the presence of particles in the core from solids feed at the bottom of the bed, and the factor $\frac{D^2}{4r_p^2}$ arises as $\bar{C}_p$ is taken as an average over the entire tube cross section. In the calculation, r_p is taken to be $r_e(0)$.

2.4.3 Boundary Conditions

For the boundary conditions, it is assumed that all particles which reach the downward flowing wall layer are absorbed and no longer act as individual particles or have a radial velocity. There has been some discussion about whether one can simply specify the concentration at the wall to be zero. In a molecular diffusion scenario, for example diffusion of water vapor with condensation at the wall, a concentration is specified at the wall. Westphalen (1993) postulated that in the case of particle diffusion, the particle motion length scale is not negligible when compared to the pipe diameter. Therefore, it was concluded that, as with Knudsen flows where the no-slip boundary condition does not apply when the system size approaches the mean free path of molecules, the concentration cannot be simply specified. In such a case a radiation boundary condition must be specified at the wall

$$-\varepsilon_p \frac{\partial C}{\partial r}\Big]_{r=R} = VC(R) \tag{67}$$

where V is the velocity with which the particles are carried to the wall. If ε_p is represented as the product of V and the characteristic length L than (67) can be rewritten as

$$-VL\frac{\partial C}{\partial r}\Big]_{r=R} \simeq VC(R) \tag{68}$$

If L is very small (as is the case for molecular diffusion) and $\left.\frac{\partial C}{\partial r}\right]_{r=R}$ is finite, then $C(R) = 0$. However, if L is of the order of the length scale characterizing $\frac{\partial C}{\partial r}$, then C(R) is a finite number.

The question of interest here which was not addressed by Westphalen is whether the scale of the CFB is large compared to the scale characterizing the motion of the particles. It is difficult to answer this question because it could depend on the method by which the particles enter the field. However, some criteria can be suggested for the simple system considered in this analysis. A Lagrangian scale of particle motion can be defined as

$$\frac{L_p}{R} = \frac{\varepsilon_{p_r}}{\left(\overline{\left(v'_{p_r}\right)^2}\right)^{1/2}} \tag{69}$$

The requirement of a haphazard motion of the particles in the neighborhood of the wall necessitates that $\frac{L_p}{R}$ is small.

Lee *et al.* (1989) have developed approximations for the turbulence measurements near the wall of pipe flow for a review article by Vames and Hanratty (1988):

$$\frac{\varepsilon_{f_r}}{u_\tau 2R} = 0.037 \tag{70}$$

$$\left(\overline{\left(v'_{f_r}\right)^2}\right)^{1/2} \simeq 0.9u_\tau \tag{71}$$

$$\frac{\tau_{L_f} u_\tau}{2R} \simeq 0.046 \tag{72}$$

Using these relations, (69) can be written as

$$\frac{L_p}{R} = 0.082 \frac{\varepsilon_{p_r}\left(\overline{\left(v'_{f_r}\right)^2}\right)^{1/2}}{\varepsilon_{f_r}\left(\overline{\left(v'_{p_r}\right)^2}\right)^{1/2}} << 1 \tag{73}$$

Using the data taken by Westphalen (1993) in the core of a CFB, the order of magnitude for these terms are

$$\frac{\left(\overline{\left(v'_{f_r}\right)^2}\right)^{1/2}}{\left(\overline{\left(v'_{p_r}\right)^2}\right)^{1/2}} \sim 1 \tag{74}$$

$$\frac{\varepsilon_{p_r}}{\varepsilon_{f_r}} \sim 0.5 \tag{75}$$

Thus the ratio of the Lagrangian scale of particle motion to the bed radius is of the order

$$\frac{L_p}{R} \sim O\left(10^{-2}\right) \tag{76}$$

Clearly the particle Lagrangian length scale is small compared with the bed length scale. It also indicates that the net diffusion of particles from the lean core to the dense annulus cannot be explained by the mean free path of the particles being of the same order as the bed radius. Thus (68) reduces to

$$C(R) = 0 \tag{77}$$

at the wall. No radiation boundary condition is required.

The above analysis indicates that, in fact, the boundary condition can be simply specified as

$$C\left(\frac{D}{2}, t\right) = 0 \tag{78}$$

assuming that the cluster thickness at the wall is much smaller than the bed diameter. This assumption is valid over most regions of the bed.

2.5 Solution of the Two Dimensional Dispersion Equation

The two-dimensional dispersion equation along with the source term and the boundary conditions can be solved using Greens function. Solutions of this type for similar problems can be found in Carslaw and Jeager (1959) and Crank (1972).

If

$$W(r,t) = \bar{u}(t)C(r,t) \tag{79}$$

then

$$\frac{\partial W(r,t)}{\partial t} = \lambda\left(\frac{\partial^2 W(r,t)}{\partial r^2} + \frac{1}{r}\frac{\partial W(r,t)}{\partial t}\right) + \bar{u}(t)S(r,t) \tag{80}$$

Say that

$$X = \exp\left(-\varepsilon_{p_r}\gamma^2 t\right)V \qquad \text{where } V = V(r) \text{ only} \tag{81}$$

then

$$\frac{d^2V}{dr^2} + \frac{1}{r}\frac{dV}{dr} = 0 \tag{82}$$

which is Bessel's equation of order zero. The solution of the second kind is infinite at r = 0, which allows one to write

$$W(r,t) = AJ_o(\gamma r)\exp\left(-\varepsilon_{p_r}\alpha^2 t\right) \tag{83}$$

where $J_o(x)$ is the Bessel function of order zero of the first kind. To satisfy the boundary condition, γ must be a root of

$$J_o(a\gamma_n) = 0 \qquad (W = 0 \text{ when } r = R) \tag{84}$$

Equation (84) has an infinite number of roots. For the other boundary conditions

$$\begin{aligned} W(r,0) &\geq 0 \\ &= f(r) \end{aligned} \tag{85}$$

Assume that f(r) can be expanded in a Bessel series

$$f(r) = A_1 J_o(\gamma_1 r) + A_2 J_o(\gamma_2 r) + \ldots \tag{86}$$

where $\gamma_1 .. \gamma_n$ are roots of (84).

The boundary conditions are satisfied when

$$W(r,t) = \sum_{n=1}^{\infty} A_1 J_o(\gamma_n r) \exp\left(-\varepsilon_{p_r} \gamma_n^2 t\right) \tag{87}$$

Now, multiply (86) through by $J_o(\gamma_n r) r$ and integrate from 0 to R and solve for A_n:

$$A_n = \frac{2}{R^2 J_1^2(a\gamma_n)} \int_0^R r\, f(r) J_0(r\gamma_n) \tag{88}$$

Then from (87)

$$W(r,t) = \frac{2}{R^2} \sum_{n=1}^{\infty} \frac{J_0(r\gamma_n)}{J_1^2(R\gamma_n)} \exp\left(-\varepsilon_{p_r} \gamma_n^2 t\right) \int_0^R r\, f(r) J_o(\gamma_n r) \tag{89}$$

Using the dimensionless variable

$$\beta_n = a\gamma_n \tag{90}$$

$$W(r,t) = \frac{2}{R^2} \sum_{n=1}^{\infty} \frac{J_0\left(\frac{r}{R}\beta_n\right)}{J_1^2(\beta_n)} \exp\left(-\frac{\varepsilon_{p_r} \beta_n^2 t}{R^2}\right) \int_0^R r\, f(r) J_o\left(\beta_n \frac{r}{R}\right) \tag{91}$$

where β_n are the roots to

$$J_0(\beta_n) = 0 \tag{92}$$

Table 2 gives the first 20 values of β_n.

Table 2: Values for β_n

$\beta_1 = 2.4048$	$\beta_5 = 14.9309$	$\beta_9 = 27.4935$	$\beta_{13} = 40.0584$	$\beta_{17} = 52.6241$
$\beta_2 = 5.5201$	$\beta_6 = 18.0711$	$\beta_{10} = 30.6346$	$\beta_{14} = 43.1998$	$\beta_{18} = 55.7656$
$\beta_3 = 8.6537$	$\beta_7 = 21.2116$	$\beta_{11} = 33.7758$	$\beta_{15} = 46.3412$	$\beta_{19} = 58.9070$
$\beta_4 = 11.7915$	$\beta_8 = 24.3524$	$\beta_{12} = 36.9171$	$\beta_{16} = 49.4826$	$\beta_{20} = 62.0485$

2.5.1 Integration of the Source Term

The source term (equation 66) must be substituted in equation (91) for f(r) and integrated. From (66), f(r) is defined as

$$f(r) = \int_0^t \frac{D}{2r_e} E(t)\delta(r - r_e)dt + \frac{D^2}{4r_p^2}\bar{C}_p u(r_p - r)\delta(t) \tag{93}$$

Considering only the integration of the source term:

$$\int_0^a r\, f(r) J_o\left(\beta_n \frac{r}{R}\right)dr = \int_0^{r_p}\int_0^t \frac{Dr}{2r_e} J_o\left(\beta_n \frac{r}{R}\right)E(t)\delta(r - r_e)dtdr + \int_0^{r_e} \frac{D^2 r}{4r_p^2}\bar{C}_p \bar{u}(r_p - r) J_o\left(\beta_n \frac{r}{R}\right)\delta(t)dr$$

(94)

The first term on the r.h.s of (94) can be integrated using Duhamel's theorem

$$\int_0^{r_p}\int_0^t \frac{Dr}{2r_e} J_o\left(\beta_n \frac{r}{R}\right)E(t)\delta(r - r_e)dtdr = R\left(\frac{r_e}{r_e}\right) J_o\left(\beta_n \frac{r_e}{R}\right)\int_0^t \bar{u}(t')E(t')\exp\left(\frac{-\varepsilon_{p_r}\beta_n^2 t'}{R^2}\right)dt' \tag{95}$$

The second term on the r.h.s. of (94) can be integrated using the identity

$$\int_0^r r^{n+1} J_n(\alpha r)dr = \frac{1}{\alpha} r^{n+1} J_{n+1}(\alpha r) \tag{96}$$

and the relations

$$\begin{aligned} u(r_p - r) &= 1 \quad \text{if} \quad r \le r_p \\ u(r_p - r) &= 0 \quad \text{if} \quad r > r_p \end{aligned} \tag{97}$$

Then

$$\int_0^{r_e} \frac{D^2 r}{4r_p^2}\bar{C}_p\bar{u}(r_p - r)J_o\left(\beta_n\frac{r}{R}\right)\delta(t)dr = \frac{D^2}{4r_p^2}\bar{C}_p\left[\frac{Rr}{\beta_n}\bar{u}(r_p - r)J_1\left(\beta_n\frac{r}{R}\right)\right]\Bigg|_0^{r_p} \tag{98}$$

$$\int_0^{r_e} \frac{D^2 r}{4r_p^2}\bar{C}_p u(r_p - r)J_o\left(\beta_n\frac{r}{R}\right)\delta(t)dr = \frac{D^2}{4r_p^2}\bar{C}_p\left[\frac{Rr_p}{\beta_n}J_1\left(\beta_n\frac{r}{R}\right)\right]\bar{u}(0) \tag{99}$$

$$\int_0^{r_e} \frac{D^2 r}{4r_p^2}\bar{C}_p u(r_p - r)J_o\left(\beta_n\frac{r}{R}\right)\delta(t)dr = \frac{R^3}{r_p}\bar{C}_p\left[\frac{J_1\left(\beta_n\frac{r}{R}\right)}{\beta_n}\right]\bar{u}(0) \tag{100}$$

Substituting (95) and (99) back into (91) gives

$$W(r,t) = \sum_{n=1}^{\infty}\left\{\begin{array}{l}\dfrac{J_0\left(\dfrac{r}{R}\beta_n\right)}{J_1^2(\beta_n)}\dfrac{2}{R^2}\exp\left(-\dfrac{\varepsilon_{p,r}\beta_n^2 t}{R^2}\right)\cdot \\ \left[a\left(\dfrac{r_e}{r_e}\right)J_o\left(\beta_n\dfrac{r_e}{R}\right)\displaystyle\int_0^t \bar{u}(t')E(t')\exp\left(\frac{\varepsilon_{p,r}\beta_n^2 t'}{R^2}\right)dt' + \frac{R^3}{r_p}\bar{C}_p\left[\frac{J_1\left(\beta_n\dfrac{r}{R}\right)}{\beta_n}\right]\bar{u}(0)\right]\end{array}\right\} \tag{101}$$

Since

$$C(r,t) = \frac{W(r,t)}{\bar{u}(t)} \tag{102}$$

The concentration profile can be written as

$$C(r,t) =$$

$$\frac{2}{R\bar{u}(t)}\sum_{n=1}^{\infty}\left\{\frac{J_0\left(\frac{r}{R}\beta_n\right)J_0\left(\beta_n\frac{r_e}{R}\right)}{J_1^2(\beta_n)}\int_0^t \bar{u}(t')E(t')\exp\left(\frac{-\varepsilon_{p_r}\beta_n^2(t-t')}{R^2}\right)dt'\right\}$$

$$+\frac{2R\overline{C}_p\bar{u}(0)}{r_p\bar{u}(t)}\sum_{n=1}^{\infty}\left\{\frac{J_0\left(\frac{r}{R}\beta_n\right)J_1\left(\beta_n\frac{r_p}{R}\right)}{\beta_n J_1^2(\beta_n)}\exp\left(\frac{-\varepsilon_{p_r}\beta_n^2 t'}{R^2}\right)\right\} \tag{103}$$

The deposition rate is given by

$$j_{p_r}\rho_s = -\varepsilon_{p_r}\frac{\partial C(r,t)}{\partial r} \tag{104}$$

and the upward mass flux is given by

$$j_{p_a}\rho_s = \overline{C}(t)\bar{u}(t) \tag{105}$$

where $\overline{C}(t)$ is the mean particle density over the bed cross-section, i.e.

$$\overline{C}(t) = \frac{2}{R^2}\int_0^R r\,C(r,t)dr \tag{106}$$

Integration of the first term on the r.h.s. of (103) gives

$$\frac{2}{R^2}\int_0^R const_1 \cdot r\,J_0\left(\frac{r}{R}\beta_n\right)dr = \frac{R}{\beta_n}r\,J_1\left(\frac{r}{R}\beta_n\right)\Big]_0^R const \cdot \frac{2}{R^2} \tag{107}$$

$$= const_1 \cdot \frac{2}{\beta_n}J_1(\beta_n) \tag{108}$$

where

$$const_1 = \frac{2}{R\bar{u}(t)}\sum_{n=1}^{\infty}\left\{\frac{J_0\left(\beta_n\frac{r_e}{R}\right)}{J_1^2(\beta_n)}\int_0^t \bar{u}(t')E(t')\exp\left(\frac{-\varepsilon_{p_r}\beta_n^2(t-t')}{R^2}\right)dt'\right\} \tag{109}$$

Integration of the second term on the r.h.s of (103) gives

$$\frac{2}{R^2}\int_0^R const_2 \cdot r\,J_0\left(\frac{r}{R}\beta_n\right)dr = \frac{R}{\beta_n} r\,J_1\left(\frac{r}{R}\beta_n\right)\Big]_0^R const \cdot \frac{2}{R^2} \tag{110}$$

$$= const_2 \cdot \frac{2}{\beta_n} J_1(\beta_n) \tag{111}$$

where

$$const_2 = + \frac{2R\bar{C}_p\bar{u}(0)}{r_p\bar{u}(t)}\sum_{n=1}^{\infty}\left\{\frac{J_1\left(\beta_n\frac{r_p}{R}\right)}{\beta_n J_1^2(\beta_n)}\exp\left(\frac{-\varepsilon_{p_r}\beta_n^2 t'}{R^2}\right)\right\} \tag{112}$$

Thus the expression for the mean particle density over the bed is

$$C(t) = \frac{4}{R\bar{u}(t)}\sum_{n=1}^{\infty}\left\{\frac{J_0\left(\beta_n\frac{r_e}{R}\right)}{\beta_n J_1(\beta_n)}\int_0^t \bar{u}(t')E(t')\exp\left(\frac{-\varepsilon_{p_r}\beta_n^2(t-t')}{R^2}\right)dt'\right\} + \frac{4R\bar{C}_p\bar{u}(0)}{r_p\bar{u}(t)}\sum_{n=1}^{\infty}\left\{\frac{J_1\left(\beta_n\frac{r_p}{R}\right)}{\beta_n^2 J_1(\beta_n)}\exp\left(\frac{-\varepsilon_{p_r}\beta_n^2 t'}{R^2}\right)\right\} \tag{113}$$

For long times and large numbers of interactions, it has been shown above that

$$\varepsilon_{p_r} = \frac{1}{2}\frac{d}{dt}\left\langle x_{p_r}^2\right\rangle \tag{114}$$

or

$$\varepsilon_{p_r} = \frac{1}{2}\nu\left\langle x_{p_r}^2 \right\rangle \tag{115}$$

where ν is the interaction frequency. If the interaction time scale is controlled by the vertical particle eddy crossing trajectories

$$\nu = \frac{u_t}{l_e} \tag{116}$$

and the mean particle density can be written as

$$C(t) = \frac{4}{R\bar{u}(t)}\sum_{n=1}^{\infty}\left\{\frac{J_0\left(\beta_n\frac{r_e}{R}\right)}{\beta_n J_1(\beta_n)}\int_0^t \bar{u}(t')E(t')\exp\left(\frac{-u_t l_e\beta_n^2\left\langle\frac{x_{p_r}^2}{l_e^2}\right\rangle(t-t')}{2R^2}\right)dt'\right\}$$
$$+\frac{4R\overline{C}_p\bar{u}(0)}{r_p\bar{u}(t)}\sum_{n=1}^{\infty}\left\{\frac{J_1\left(\beta_n\frac{r_p}{R}\right)}{\beta_n^2 J_1(\beta_n)}\exp\left(\frac{-\left\langle\frac{x_{p_r}^2}{l_e^2}\right\rangle l_e u_t\beta_n^2 z}{\bar{u}(t)DR}\right)\right\} \tag{117}$$

The particles do not actually travel at the same velocity as the particle, and their position is more accurately given as

$$z = \int_0^t (u_o - u_t)dt \tag{118}$$

so that time can be defined as

$$t \simeq \frac{z}{(u_o - u_t)} \tag{119}$$

where z is the axial position up the bed.

Finally, the expression for the axial concentration profile in the bed is

$$C(z) =$$

$$\frac{4}{R\bar{u}(t)}\sum_{n=1}^{\infty}\left\{\frac{J_0\left(\beta_n\frac{r_e}{R}\right)}{\beta_n J_1(\beta_n)}\int_0^{\frac{z}{(u_o-u_t)}}\bar{u}(t')E(t')\exp\left(\frac{-u_t l_e\beta_n^2\left\langle\frac{x_{p_r}^2}{l_e^2}\right\rangle\left(\frac{z}{(u_o-u_t)}-t'\right)}{2R^2}\right)dt'\right\}$$

$$+\frac{4R\overline{C}_p\bar{u}(0)}{r_p\bar{u}(t)}\sum_{n=1}^{\infty}\left\{\frac{J_1\left(\beta_n\frac{r_p}{R}\right)}{\beta_n^2 J_1(\beta_n)}\exp\left(\frac{-\left\langle\frac{x_{p_r}^2}{l_e^2}\right\rangle l_e u_t\beta_n^2\frac{z}{(u_o-u_t)}}{\bar{u}(t)DR}\right)\right\} \tag{120}$$

2.6 Case of Constant Concentration at the Wall

For the case where the walls are not perfects absorbers with C(R) = 0, but rather have a specified concentration, the boundary conditions are no longer homogeneous. If the concentration of the disperse phase is constant at the wall, the boundary conditions become

$$C(R,t) = const = C_w \tag{121}$$

$$C(0,t) = \text{finite} \tag{122}$$

Begin by treating the case of initial concentration f(r) and zero concentration at the bed wall

$$f(r) = A_1 J_0(\alpha_1 r) + A_2 J_0(\alpha_2 r) + \ldots \tag{123}$$

where α_1, α_2, ... are roots to

$$J_0(\alpha r) = 0 \tag{124}$$

Multiply both sides of (123) by $r\,J_0(\alpha_n r) = 0$, integrating from 0 to R, and using the relationships

$$\int_0^R r\,J_0(\alpha_m r)\,J_0(\alpha_n r)dr = 0\,,\quad m \neq n \tag{125}$$

$$\int_0^R r\left[J_0(\alpha_m r)\right]^2 dr = \frac{1}{2}R^2\left[J_0'(\alpha_n R)\right]^2 = \frac{1}{2}R^2\left[J_1(\alpha_n R)\right]^2 \tag{126}$$

then

$$A_n = \frac{2}{R^2\left[J_1(\alpha_n R)\right]^2}\int_0^R r\,f(r)\,J_0(\alpha_n r)dr \tag{127}$$

Therefore,

$$C(r,t) = \frac{2}{R^2}\sum_{n=1}^{\infty}\exp\left(-\varepsilon_{p_r}\alpha_n^2 t\right)\frac{J_0(\alpha_n r)}{\left[J_1(\alpha_n R)\right]^2}\int_0^R r\,f(r)\,J_0(\alpha_n r)dr \tag{128}$$

For a constant initial concentration, $f(r) = C_i$, the integral in (128) can be evaluated from the identity

$$\int_0^r r^{n+1}\,J_n(\alpha r)dr = \frac{1}{\alpha}r^{n+1}\,J_{n+1}(\alpha r) \tag{129}$$

to give

$$C(r,t) = \frac{2C_i}{R}\sum_{n=1}^{\infty}\exp\left(-\varepsilon_{p_r}\alpha_n^2 t\right)\frac{J_0(\alpha_n r)}{\alpha_n\left[J_1(\alpha_n R)\right]} \tag{130}$$

This result can be used to find

1. The case when the bed has zero initial concentration and the wall has a constant dilute phase concentration

2. By superposition, the case where there is a source term at the wall and at the bottom of the bed, with a constant dilute phase concentration at the wall

For the first case, the solution is simply obtained by subtracting (130) from the specified wall concentration

$$C(r,t) = C_w\left(1 - \frac{2}{R}\sum_{n=1}^{\infty} \exp\left(-\varepsilon_{p_r}\alpha_n^2 t\right)\frac{J_0(\alpha_n r)}{\alpha_n\left[J_1(\alpha_n R)\right]}\right) \tag{131}$$

For the second case, (120) can be added to (130) to give the overall result

$$\frac{2}{R\bar{u}(t)}\sum_{n=1}^{\infty}\left\{\frac{J_0\left(\frac{r}{R}\beta_n\right)J_0\left(\beta_n\frac{r_c}{R}\right)}{J_1^2(\beta_n)}\int_0^t \bar{u}(t')E(t')\exp\left(\frac{-\varepsilon_{p_r}\beta_n^2(t-t')}{R^2}\right)dt'\right\}$$

$$C(r,t) = + \frac{2R\overline{C}_p\bar{u}(0)}{r_p\bar{u}(t)}\sum_{n=1}^{\infty}\left\{\frac{J_0\left(\frac{r}{R}\beta_n\right)J_1\left(\beta_n\frac{r_p}{R}\right)}{\beta_n J_1^2(\beta_n)}\exp\left(\frac{-\varepsilon_{p_r}\beta_n^2 t'}{R^2}\right)\right\} +$$

$$C_w\left(1 - \frac{2}{R}\sum_{n=1}^{\infty}\exp\left(-\varepsilon_{p_r}\alpha_n^2 t\right)\frac{J_0(\alpha_n r)}{\alpha_n\left[J_1(\alpha_n R)\right]}\right) \tag{132}$$

For the average solid concentration profile, the first two terms in (132) reduce to r.h.s. of (120). The third term on the r.h.s. of (132) is averaged as

$$\int_0^R \frac{2rC_w}{R^2}\left(1 - \frac{2}{R}\sum_{n=1}^{\infty}\exp\left(-\varepsilon_{p_r}\alpha_n^2 t\right)\frac{J_0(\alpha_n r)}{\alpha_n\left[J_1(\alpha_n R)\right]}\right)dr \tag{133}$$

$$= C_w\left(1 - 4\sum_{n=1}^{\infty}\frac{1}{\beta_n^2}\exp\left(-\frac{\varepsilon_{p_r}\beta_n^2 z}{(u_o - u_t)}\right)\right) \tag{134}$$

where equations (119) and (90) have been used.

So that the expression for the average solid fraction profiles is

$$C(z) =$$

$$\frac{4}{R\bar{u}(t)}\sum_{n=1}^{\infty}\left\{\frac{J_0\left(\beta_n\frac{r_e}{R}\right)}{\beta_n J_1(\beta_n)}\int_0^{\frac{z}{(u_o-u_t)}}\bar{u}(t')E(t')\exp\left(\frac{-u_t l_e\beta_n^2\left\langle\frac{X_{p_r}^2}{l_e^2}\right\rangle\left(\frac{z}{(u_o-u_t)}-t'\right)}{2R^2}\right)dt'\right\}$$

$$+\frac{4R\overline{C}_p\bar{u}(0)}{r_p\bar{u}(t)}\sum_{n=1}^{\infty}\left\{\frac{J_1\left(\beta_n\frac{r_p}{R}\right)}{\beta_n^2 J_1(\beta_n)}\exp\left(\frac{-\left\langle\frac{X_{p_r}^2}{l_e^2}\right\rangle l_e u_t\beta_n^2\frac{z}{(u_o-u_t)}}{\bar{u}(t)DR}\right)\right\}$$

$$+C_w\left(1-4\sum_{n=1}^{\infty}\frac{1}{\beta_n^2}\exp\left(-\frac{\left\langle\frac{X_{p_r}^2}{l_e^2}\right\rangle l_e u_t\beta_n^2 z}{2R^2(u_o-u_t)}\right)\right) \tag{135}$$

For the model proposed in the study, the concentration profile in the core will be determined through the use of equation (120) unless it is specifically noted that equation (135) was used.

2.7 Entrainment Model

Equations (120) and (135) requires a model for the entrainment rate. A good approximation is that the entrainment rate from a given axial point on the wall depends on the average cross-sectional solid fraction at a distance equal to the fall distance of a cluster above that point on the wall. The fall distance of a cluster can be approximated from the result obtained in Chapter 4:

$$L = 1.95\left(\frac{d_p}{171 \times 10^{-6}}\right)\phi_{c_{avg}}^{0.596}(z) \tag{136}$$

The equation for the entrainment rate at any given axial location z, is then given by

$$E = (Const)\phi_{c_{avg}}(z)\left[z + 1.95\left(\frac{d_p}{171 \times 10^{-6}}\right)\phi_{c_{avg}}^{0.596}(z')\right] \tag{137}$$

where

$$z' = 1.95\left(\frac{d_p}{171 \times 10^{-6}}\right)\phi_{c_{avg}}^{0.596}(z') + z \tag{138}$$

and the constant in front of (137) is determined from a mass balance over the CFB riser (total mass entrained must equal total mass deposited over the reactor height).

The solution for the entrainment rate is an interative process. For the first interation, the entrainment rate is caculated using simple linear model, with increasing entrainment as the axial location decreases:

$$E = Const(H - z) \tag{139}$$

H is the riser height. This allows for the initial calculation of the cross-sectionally averaged core solid concentration, $\phi_c(z)$.

Subsequent evaulations are made by assuming a value for z', finding the average cross-sectional solid fraction at this point from the previous iteration result of $\phi_c(z)$, substituing this result into equation (138) and comparing the assumed values of z' to the calculated value. The next guess for the value for z' is then adjusted accordingly.

For locations in the riser where z'>H, the simple relation

$$E = Const\ \phi_{c_{avg}}(z) \tag{140}$$

is used.

2.8 Determination of $\overline{C_p}$

Equations (120) and (135) also require the concentration of solids at the bottom of the riser, $\overline{C_p}$. $\overline{C_p}$ is determined by specifying the concentration at the riser exit. Once the value at the riser exit is determined, $\overline{C_p}$ can be found interatively. The method by which the average core concetration at the riser exit is determined is discussed in Section 4.0.

3.0 MODEL ENHANCEMENTS

3.1 Particle-Particle Collisions

In his stability analysis of fluidized beds, Jackson (1963) included particle inertia, and assumed that the drag force is of the form $\mathbf{D} = \beta(n)(\mathbf{v}_f - \mathbf{v}_p)$. Here, $\beta(n)$ is a function of the number density, $\mathbf{v}_f$ is the mean fluid velocity, and $\mathbf{v}_p$ is the mean velocity of the particle phase. This theory led to the conclusion that the homogeneous state of the fluidized bed is always unstable. More recent continuum theories [Didwania and Homsy (1982), Batchelor (1988)] incorporate the particle interactions in the form of a 'particle pressure' and a particle diffusivity and thereby obtain criteria for the stability of the homogeneous bed. In the kinetic theory of gases, the pressure is proportional to the mean square of the fluctuating velocity of the molecules. By analogy, in particle gas suspensions the particle pressure has been related to the mean square of the fluctuating velocities of the particles [Koch (1990), Jenkins and Richman (1985)].

Kumaran and Koch (1993) have studied the velocity distributions of dilute bidisperse suspensions of particles settling in a gas in the low Reynolds number, high Stokes number limit. The volume fraction of the particles, ϕ, is assumed to be small compared to 1. The Stokes number is defined as

$$St = \frac{m_p(\mathbf{v}_f - \mathbf{v}_p)}{6\pi\mu a^2} \tag{1}$$

In the low Reynolds limit, the viscous forces are large compared to the inertial forces in the gas phase. Particles with a density of 2500 kg/m3 having a diameter between 20 and 200 microns settling in air can be analyzed using the low Reynolds number, high Stokes number approximation, since their Reynolds number varies between 0.027 and 13.2, and the Stokes number varies between 17 and 8400. Moreover, the calculation of the velocity distribution can be simplified by the following assumptions

1. The particle drag can be approximated by the Stokes law
2. The inertia of the gas can be neglected
3. The particles interact only by solid-body collisions

The conservation equation for the particle velocity distribution function is similar to the Boltzmann equation used in the kinetic theory of gases, except that the drag depends on its velocity. The conservation equation is a non-linear, integro-differential equation and is, in general, hard to solve. For the special case of gas at equilibrium, the Maxwell-Boltzmann distribution of the molecular velocities can be obtained as the analytical solution of the Boltzmann equation. This distribution is derived using the principle of detailed balancing which states that for every collision which changes a particles velocity from $\mathbf{v}_p \rightarrow \mathbf{v}_p'$, there is an inverse collision which changes another particle from $\mathbf{v}_p' \rightarrow \mathbf{v}_p$. So the collision process does not change the density of particles in velocity space. This method was used by Senior *et al.* to model particle collisions in a CFB. Kumaran and Koch (1993) showed that this principle is not valid for the velocity distribution at steady-state since the viscous drag force is not divergence free in velocity space.

Another difference in particle suspensions and gas suspensions at equilibrium is that while the total energy of the molecular fluctuations is conserved, in a particle suspension there is a force on the particles due to the differences in mean velocities and terminal velocities of the particles. The work done by this force acts as a source of fluctuating energy. The source is balanced by the energy dissipation due to the viscous drag on the particles. The energy source is driven by the difference in terminal velocities in the vertical direction, and due to the directional nature of this source, the steady-state velocity distribution can be anisotropic; the Maxwell-Boltzmann distribution is not correct.

Particle collisions have been incorporated into the theories for the rapid shearing of granular materials (Jenkins, 1987). Here, the shearing of the material drives collisions between particles and acts as a source of fluctuating energy. The energy is dissipated due to inelastic collisions between particles. Generally, the suspension is analyzed in the limit where the coefficient of restitution of the particles is close to 1. In this limit, the dynamics of the particles resemble that of molecules in a gas whose equilibrium distribution is the Maxwell Boltzmann distribution. The particle distribution is assumed to be an anisotropic Gaussian functions, which is a small perturbation to the Maxwell distribution. The momentum and energy balance equations are derived using this distribution, by averaging methods similar to those used in the kinetic theory of gases.

3.1.1 Limit 1: Viscous Relaxation Time < Time Between Particle Collisions

In the limit where the viscous relaxation time is much smaller than the time between successive collisions, particles relax to near their terminal velocities between collisions. Assume the suspension is bidisperse and contains particles of radius a_1 and a_2 which are perfectly elastic. The viscous relaxation time for the particles is

$$\tau_{v_i} = \frac{m_i}{6\pi\mu a_i} \tag{2}$$

If

$$\mathbf{u}_i = \mathbf{v}_{p_i} - u_{t_i}\mathbf{i}_z \tag{3}$$

the particle acceleration can be written as

$$\frac{d\bar{\mathbf{u}}_i}{d\bar{t}} = \bar{\mathbf{u}}_i\left(\frac{\tau_{v_1}}{\tau_{v_i}}\right) \tag{4}$$

where the velocities have been scale by $\left(u_{t_1} - u_{t_2}\right)$ and time variables are scaled by τ_{v_1}.

The time scale for collision can be defined as

$$\tau_{c_{ij}} = \frac{1}{n_j \pi d_{ij}^2 \left(u_{t_1} - u_{t_2}\right)} \tag{5}$$

where

$$d_{ij} = a_i + a_j \tag{6}$$

and n_j is the number density of particles

This time scale is much different than that defined by Westphalen (1993), whose result was

$$\tau_c = \frac{d_p}{v'_{p_r}\phi} \tag{7}$$

The reason the time scales are different is that equation (5) assumes the collision frequency is determined mainly by the difference in terminal velocities of the particles in the suspension, whereas equation (7) assumes all particles are the same size and the collision frequency is determined by the horizontal motion of the particles. Equation (7) will significantly overestimate the time between successive collisions when the particle suspension is not made up of uniform spheres.

In the dilute limit,

$$\varepsilon = \frac{\tau_{v_i}}{\tau_{c_{ij}}} << 1 \tag{8}$$

The conservation equation for the distribution function is (Chapman and Cowling, 1970)

$$\frac{\partial f_i}{\partial t} = -\nabla \bar{u}_i \cdot \left(\frac{\partial \bar{u}_i}{\partial t} f_i \right) + \frac{\partial_c f_i}{\partial t} \tag{9}$$

The first and second terms on the r.h.s. represent the change in distribution function due to viscous forces and collisional interactions respectively.

The balance equations for the moments of $\bar{u}_i$ are obtained by multiplying (9) by the velocity and the square of the velocity and integrating over the domain of $\bar{u}_i$. The steady state balance equations for the velocity are (Chapman and Cowling, 1970):

$$-\left(\frac{\tau_{v_1}}{\tau_{v_i}}\right)\langle u_{i_z}\rangle + \frac{\partial_c \langle u_{i_z}\rangle}{\partial t} = 0 \tag{10}$$

$$-2\left(\frac{\tau_{v_1}}{\tau_{v_i}}\right)\langle u_i^2\rangle + \frac{\partial_c \langle u_i^2\rangle}{\partial t} = 0 \tag{11}$$

$$-2\left(\frac{\tau_{v_1}}{\tau_{v_i}}\right)\langle u_{i_r}^2\rangle + \frac{\partial_c \langle u_{i_r}^2\rangle}{\partial t} = 0 \tag{12}$$

where $\frac{\partial_c \langle \beta \rangle}{\partial t}$ is the change in the moment $\langle \beta \rangle$ due to collisions, and the factor $\left(\frac{\tau_{v_1}}{\tau_{v_i}}\right)$ appears because the time variable is scaled by τ_{v_1}. The suspension momentum and energy equations at steady state are:

$$\frac{n_1 m_1 \langle u_{1_z} \rangle}{\tau_{v_1}} + \frac{n_2 m_2 \langle u_{2_z} \rangle}{\tau_{v_2}} = 0 \tag{13}$$

$$\frac{n_1 m_1 \left(\langle u_{1_z} \rangle u_{t_1} + \langle u_1^2 \rangle \right)}{\tau_{v_1}} + \frac{n_2 m_2 \left(\langle u_{2_z} \rangle u_{t_2} + \langle u_2^2 \rangle \right)}{\tau_{v_2}} = 0 \tag{14}$$

In the limit where the viscous relaxation time is much smaller than the time between successive collisions, the particles relax close to their terminal velocities between collisions, and the fraction of particles that have velocities significantly different from the terminal velocities is small at any point in time. To obtain the leading-order collisional change in the mean and mean-square velocities, Kumaran and Koch (1993) assumed that the velocities of colliding particles can be approximated as equal to their terminal velocities. The change in the mean and mean-square velocities of the particles for elastic and inelastic collisions can be easily found by writing the velocities of the particles in terms of the velocity of the center of mass and the velocity difference. The rate of change of a function of the velocity, $\beta_i(\mathbf{u}_i)$ can then be calculated by integrating the product of the collision frequency, and the change in the property during a collision over the velocity space. The mean and mean-square velocities are then found by substituting the collisional changes into the balance equations (10-12). The result is:

$$\langle u_{i_z} \rangle = (-1)^i \varepsilon \left(\frac{\tau_{v_i}}{\tau_{v_1}} \right) \left(\frac{\tau_{c_{12}}}{\tau_{v_{ik}}} \right) \left(\frac{m_k}{m_i + m_k} \right) \left(\frac{e+1}{2} \right) \tag{15}$$

$$\langle u_i^2 \rangle = \varepsilon \left(\frac{\tau_{v_i}}{\tau_{v_1}} \right) \left(\frac{\tau_{c_{12}}}{\tau_{v_{ik}}} \right) \left(\frac{m_k}{m_i + m_k} \right)^2 \left(\frac{e(e+1)}{2} \right) \tag{16}$$

$$\langle u_{i_z}^2 \rangle = \frac{\varepsilon}{3} \left(\frac{\tau_{v_i}}{\tau_{v_1}} \right) \left(\frac{\tau_{c_{12}}}{\tau_{v_{ik}}} \right) \left(\frac{m_k}{m_i + m_k} \right)^2 \frac{(e+1)^2}{12} \tag{17}$$

where e is the coefficient restitution.

Equations (15) through (17) indicate that in the dilute limit, the velocity distribution is highly anisotropic, since the mean-square of the vertical fluctuating velocity is twice the fluctuating velocity in the horizontal plane. Note that in an isotropic distribution, the mean-

square of the vertical fluctuating velocity is half that of the fluctuating velocity in the horizontal plane.

To determine the range of validity for this result, consider a CFB operating at 12 atmospheres and 1150 K, with a suspension that can be reasonably divided into a 50-50 percent by mass of 180 and 220 micron particles. Table 1 shows the values of the mean and mean-square velocities of the particles for such a suspension.

Table 1: Calculation of Various Mean and Mean-Square Velocities

ϕ	ε	$\langle u_{1_z} \rangle$	$\langle u_1^2 \rangle$	$\langle u_{1_r}^2 \rangle$	$\langle u_{2_z} \rangle$	$\langle u_2^2 \rangle$	$\langle u_{2_r}^2 \rangle$
0.0005	0.33	0.12	0.04	0.014	0.079	0.05	0.017
0.001	0.65	0.23	0.08	0.027	0.15	0.09	0.034
0.002	1.30	0.46	0.16	0.054	0.31	0.19	0.069
0.003	1.96	0.69	0.24	0.082	0.46	0.30	0.10
0.004	2.62	0.93	0.33	0.11	0.62	0.40	0.14
0.005	3.27	1.16	0.41	0.14	0.77	0.50	0.17
0.006	3.92	1.39	0.49	0.16	0.93	0.60	0.21
0.007	4.58	1.62	0.57	0.19	1.08	0.70	0.24
0.008	5.23	1.85	0.65	0.22	1.23	0.80	0.28
0.009	5.89	2.08	0.74	0.25	1.39	0.90	0.31
0.01	6.54	2.31	0.82	0.27	1.54	1.00	0.35

From the gas turbulence induced dispersion model described in Section 2, if the bed is operating at a superficial gas velocity of about 4 m/s, and the bed diameter is 20 cm, the radial mean-square velocity is $\left\langle \left(v'_{p_r} \right)^2 \right\rangle$ = 0.067 m^2/s^2. Figure 1 shows the percent of the radial mean-square velocity due to particle collisions as a function of average solid concentration.

Figure 1

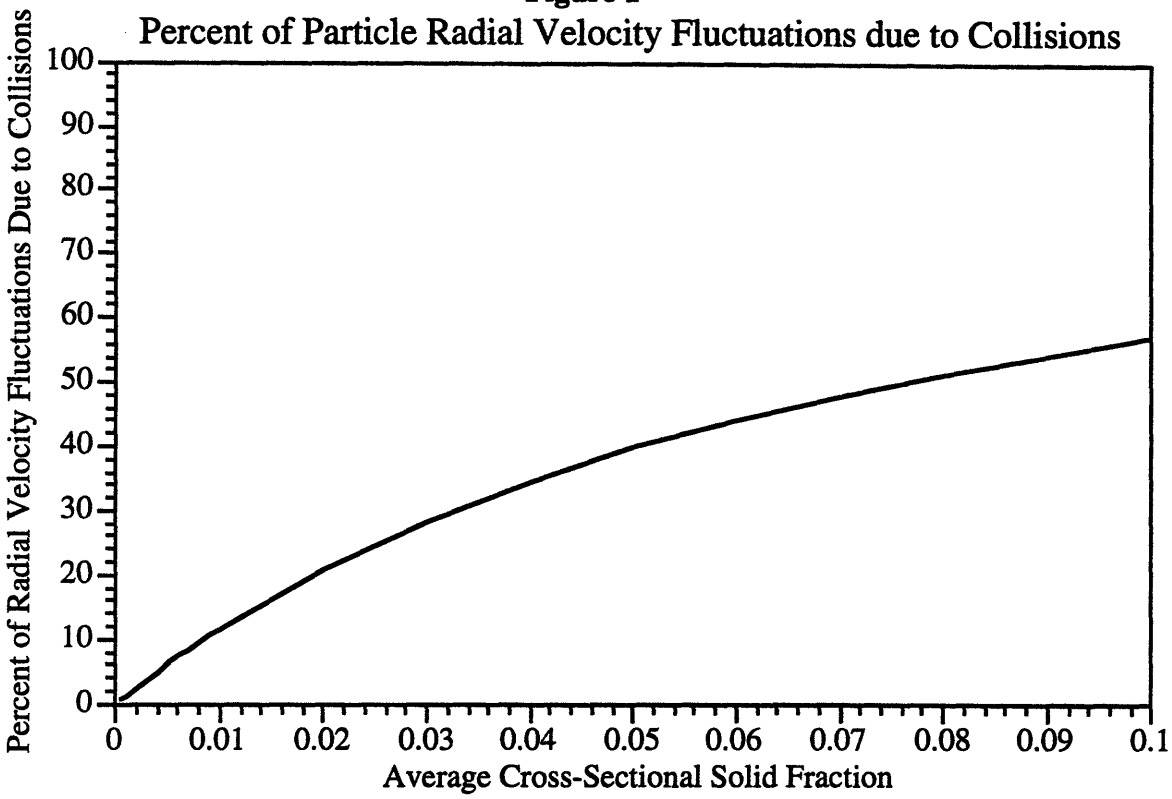

Figure 1 indicates that the collisions become significant at an average solid fraction of about 0.007. Note that if equation (7) were used, the limit at which collisions become important would be

$$\phi < \frac{\left(v'_{p_r}\right)d_p}{\varepsilon_{p_r}} = \frac{\left(0.128\ \frac{m^2}{s^2}\right)\left(200E\text{–}6\ m\right)}{\left(0.001\ \frac{m^2}{s}\right)} = 0.026 \qquad (18)$$

As expected, this criterion significantly overestimates the solid fraction limit at which particle collisions become important.

Strictly speaking, the derivation used above is not valid for large values of ε (the limit where the collision time scale becomes much smaller than the viscous relaxation time). However, Kumaran *et al.* have shown that the results are a good approximation for values of ε out to about 5.

3.1.2 Limit 2: Time Between Particle Collisions < Viscous Relaxation Time

In the limit where the time between particle collisions is much smaller than the viscous relaxation time, particles do not experience significant viscous deceleration between successive collisions. To the leading order, deceleration can be neglected and the distribution functions for the species are the Maxwell-Boltzmann distribution with equal mean velocities.

In this case, the collision time scale is

$$\tau_{c_{ij}} = \frac{1}{n_j \pi d_{ij}^2 \left(v'_{p_r} \right)} \tag{19}$$

In the limit of dense suspensions,

$$\nu = \frac{\tau_{c_{ij}}}{\tau_{v_i}} << 1 \tag{20}$$

and the leading-order distribution functions of the two species are Gaussian distributions. Kumaran and Koch also calculated expressions which can be used for the calculation of the mean and mean-square velocities in this limit. The fluctuating velocities of the particles were found to be $O\left(\varepsilon_1^{-1/3}\right)$ smaller than the mean velocity, where

$$\varepsilon_1 = \frac{n_1 4\pi a_1^2 u_{t_1} m_1}{6\pi\mu a_1} \tag{21}$$

is the ratio of the collisional and viscous relaxation time for particles of species 1. Additionally, one can see that ε_1 is proportional to $St\phi$. The velocity variances were calculated correct to $O\left(\varepsilon_1^{-2/3}\right)$ from the balance equations for the velocity moments. The $O\left(\varepsilon_1^{-2/3}\right)$ corrections to the velocity variances are small for ε_1 of $O\left(10^3\right)$, but they are of the same order of magnitude as the leading-order terms for ε_1 of $O\left(10^2\right)$, indicating that the asymptotic analysis is only accurate for very large values of ε_1. For a CFB, the voidage will rarely exceed a value of about 0.20 for the solid fraction. At this solid fraction, the magnitude of ε_1 is about 300. This suggests that this limit is only applicable in the most dense regions of a CFB, an even then the results are suspect.

In order to calculate estimates for the mean-square fluctuating velocities in the intermediate range one must resort to numerical solutions of the Boltzmann equation, or an approximate analysis based on an assumed form of the distribution function since exact solutions to the Boltzmann equation do not exist.

Distribution functions that are small perturbations about a Gaussian distribution have been used in the kinetic theory of dense gases, and in theories for granular flows. In the Chapman-Enskog theory for gas mixtures, the first perturbation to the distribution function is proportional to the gradients in the temperature and the mean velocities of the components (Chapman and Cowling, 1970). The coefficients of the gradient terms are expanded in a Sonine polynomial series, since the orthogonality of these polynomial simplifies the evaluation of the collision integral. The thermal conductivity and viscosity of the gas are determined from the first correction to the distribution function. However, this procedure is not appropriate for the case of particulate flows. The analysis in kinetic theory uses a perturbation about the isotropic Maxwell-Boltzmann distribution, whereas in a bidisperse suspension one would expect the leading-order distribution function to be anisotropic and skewed in the intermediate regime. The forces on the particles are dependent on velocity, therefore the kinetic theory analysis gives an erroneous expression for the work done due to gravitational and viscous forces. Also, since the force is not divergence free in velocity space, the principle of detailed balancing is not applicable for suspensions, as discussed in Kumaran and Koch (1993a).

In granular flows there is a source of energy due to the shearing motion of the suspension, and the dissipation of energy due to viscous drag is assumed to be small compared to that due to inelastic collisions between particles (Jenkins, 1987). If the coefficient of restitution is close to 1, this system is similar to a dense gas of hard spheres in equilibrium, which has a Maxwell-Boltzmann distribution of velocities. The shearing of the suspension causes a perturbation to the leading-order distribution, and this is usually assumed to be an expansion in Hermite polynomials. Since the Hermite polynomials constitute an orthogonal function space, in which the inner product is defined with a Gaussian weighting function, the moments of the distribution are relatively easy to calculate. However, this distribution function has the disadvantage that the highest power of the polynomial in the expansion is odd, the distribution function becomes negative at large velocities. For small perturbations, the fraction of particles have a negative distribution function is small, but for larger deviations from the Maxwell distribution this expansion assigns a negative distribution function to a significant fraction of the particles.

To form the expressions for the mean and mean-square velocities, consider a uniform suspensions of particles of species 1 and 2 having masses m_1 and m_2, and radii a_1 and a_2 settling in a gas. The conservation equation for f_i, the distribution function of species i is

$$\frac{\partial f_i}{\partial t} = -\nabla \bar{u}_i \cdot \left(\frac{\partial \bar{u}_i}{\partial t} f_i \right) + \frac{\partial_c f_i}{\partial t} \tag{22}$$

The first term on the r.h.s. of (22) is the accumulation of particles due to gravitational and drag forces. The acceleration of the particle due to these forces is given by

$$\frac{d\bar{u}_i}{dt} = \bar{u}_i \left(\frac{\tau_{v_j}}{\tau_{v_i}} \right) \tag{23}$$

The second term on the r.h.s. of (22) is the collision integral or the rate of change of the distribution function due to collisions. For convenience the collision integral is normally divided into two components:

$$\frac{\partial_c f_i}{\partial t} = N_i^{in}(\mathbf{u}_i) - N_i^{out}(\mathbf{u}_i) \tag{24}$$

Here the collisional accumulation, $N_i^{in}(\mathbf{u}_i)$, is the number of particles scattered into the differential volume $d\mathbf{u}_i$ per unit time due to collisions between particles outside this volume, and the collisional depletion, $N_i^{out}(\mathbf{u}_i)$, is the number of particles scattered out of $d\mathbf{u}_i$ per unit time due to collisions involving a particle in this volume. The conservation equation is the same as the Boltzmann equation used in kinetic theory of gases, except for the important difference that the particle's acceleration is dependent on its velocity.

The collisional depletion of particles due to collisions is calculated by carrying out an ensemble average over the velocities of the second particle in the collisions and the orientations of the impact vector. Here the impact vector is a vector joining the centers of the particles at the point of collision. The procedure for calculating the collisional depletion was described in Chapman and Cowling (1970), and the final expression for $N_i^{out}(\mathbf{u}_i)$ is

$$N_i^{out}(\mathbf{u}_i) = \sum_{j=1}^{2} \frac{1}{\tau_{c_{ij}}} \int_{u_j} \int_{\eta=0}^{2\pi} \int_{?} f_i(\mathbf{u}_i) f_j(\mathbf{u}_j) w \cos(\psi) \sin(\psi) \, d\psi \, d\eta \, d\mathbf{u}_j \tag{25}$$

where w is $\left|\mathbf{u}_i - \mathbf{u}_j\right|$, the magnitude of the relative velocity between the particles before collision and ψ and η are the azimuthal and meridional angles of the impact vector relative to the direction of the relative velocity. $\tau_{c_{ij}}$ is the time between successive collisions of a particle of species i with particles of species j.

The collisional accumulation is calculated by carrying out an ensemble average over all collisions that transport particles into this volume. The relations between the particle velocities before and after collision are given in Kumaran and Koch (1993a), and the final expression is

$$N_i^{in}(\mathbf{u}_i) = \sum_{j=1}^{2} \frac{1}{\tau_{c_{ij}}} \int_{\mathbf{u}_j^*} \int_{\eta=0}^{2\pi} \int_{|\mathbf{u}_i - \mathbf{u}_j|}^{?} f_i(\mathbf{u}_i^*) f_j(\mathbf{u}_j^*) w^* \cos(\psi) \sin(\psi)\, d\psi\, d\eta\, d\mathbf{u}_j^* \qquad (26)$$

where $\mathbf{u}_i^*$ and $\mathbf{u}_j^*$ are the velocities of the particle species i and j before collision, w^* is the magnitude of the relative velocity between the particles before collision and the angles ψ and η are as defined above.

At this point, it is necessary to assume an approximate form for the distribution function. The form used in this study is that developed by Kumaran *et al.*, (1993)

$$f_i(\mathbf{u}_i) = \frac{2}{\pi^{3/2}\xi_{ir}\left[\sqrt{\xi_{iz+}} + \sqrt{\xi_{iz-}}\right]} \exp\left[-\left(\frac{u_{ir}^2}{\xi_{ir}} + \frac{(u_{iz} - u_{is})^2}{\xi_{iz}}\right)\right] \qquad (27)$$

where $\xi_{iz+} = \xi_{iz}$ for $v_{iz} > v_{is}$ and $\xi_{iz-} = \xi_{iz}$ for $v_{iz} < v_{is}$. This distribution function is shown in Figure 2 for $v_{is} = 0$, $\xi_{iz+} = 1$, and $\xi_{iz-} = 0.5$. The distribution function is two Gaussian distributions patched together at their maximum and is continuous and differentiable about the plane $v_{iz} = v_{is}$. The distribution has a non-zero skewness in the vertical direction, and is always positive. The moments of this distribution function are given by Kumaran *et al.* (1993),

Figure 2

Distribution of Vertical Velocities for Kumaran *et al.* Composite Gaussian

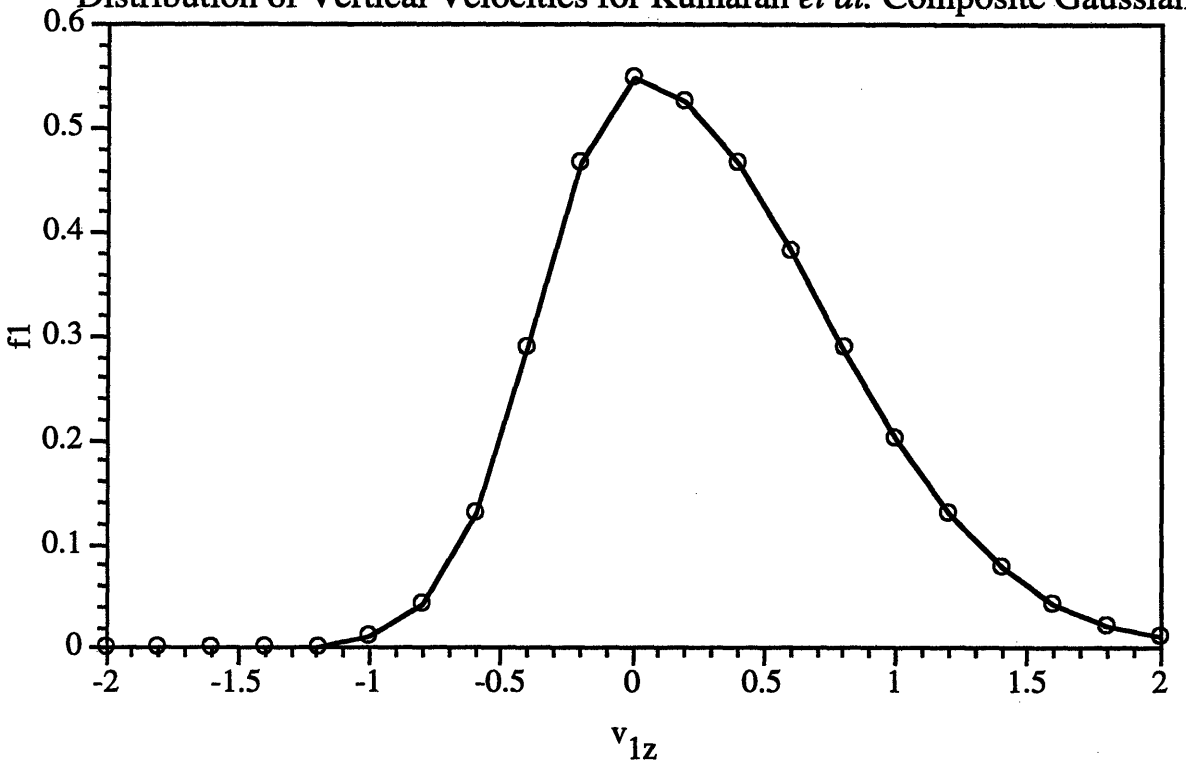

$$\left\langle u_{i_z} \right\rangle = u_{i_s} + \frac{\xi_{i_{z+}} - \xi_{i_{z-}}}{\sqrt{\pi}\left(\sqrt{\xi_{i_{z+}}} + \sqrt{\xi_{i_{z-}}}\right)} \tag{28}$$

$$\left\langle u_{i_z}^2 \right\rangle = u_{i_s}^2 + \frac{\xi_{i_{z+}} - \xi_{i_{z-}} - \sqrt{\xi_{i_{z+}}\xi_{i_{z-}}}}{2} + \frac{2u_{i_s}\left(\xi_{i_{z+}} - \xi_{i_{z-}}\right)}{\sqrt{\pi}\left(\sqrt{\xi_{i_{z+}}} + \sqrt{\xi_{i_{z-}}}\right)} \tag{29}$$

$$\left\langle u_{i_r}^2 \right\rangle = \xi_{i_r} \tag{30}$$

$$\left\langle u_{i_z}^3 \right\rangle = u_{i_s}^3 + \frac{3u_{i_s}\left(\xi_{i_{z+}} - \xi_{i_{z-}} - \sqrt{\xi_{i_{z+}}\xi_{i_{z-}}}\right)}{2} + \frac{3u_{i_s}^2\left(\xi_{i_{z+}} - \xi_{i_{z-}}\right)}{\sqrt{\pi}\left(\sqrt{\xi_{i_{z+}}} + \sqrt{\xi_{i_{z-}}}\right)} + \frac{\xi_{i_{z+}}^2 - \xi_{i_{z-}}^2}{\sqrt{\pi}\left(\sqrt{\xi_{i_{z+}}} + \sqrt{\xi_{i_{z-}}}\right)} \tag{31}$$

The parameters u_{i_s}, ξ_{i_r}, $\xi_{i_{z+}}$, and $\xi_{i_{z-}}$ are calculated from the balance equations for the above moments:

$$\frac{\partial\left\langle\beta_i(\mathbf{u}_i)\right\rangle}{\partial t} = -\left\langle\left(\frac{\partial \mathbf{u}_i}{\partial t}\cdot\nabla\beta_i(\mathbf{u}_i)\right)\right\rangle + \frac{\partial_c\left\langle\beta_i(\mathbf{u}_i)\right\rangle}{\partial t} \tag{32}$$

The collisional rate of change of the velocity moments are calculated using the ensemble-averaging procedure described in Kumaran and Koch (1993a). The steady state values of the parameters u_{i_s}, ξ_{i_r}, $\xi_{i_{z+}}$, and $\xi_{i_{z-}}$ are calculated by starting with an initial guess and integrating the unsteady-state balance equations in time until they converge to their final steady-state value. The cylindrical coordinate system is employed over a finite domain in the velocity space of species i in the same manner as Kumaran *et al.*. This domain extends from 0 to $3.6\sqrt{\xi_{i_r}}$ in the u_{i_r} direction, and $-3.6\sqrt{\xi_{i_z}}$ to $3.6\sqrt{\xi_{i_z}}$ in the u_{i_z} direction. Here, ξ_{i_z} is the greater of $\xi_{i_{z+}}$ and $\xi_{i_{z-}}$. The distribution function is specified at 325 nodes. Each of these nodes is at the center of a control volume. The viscous fluxes at each control surface are calculated using a 4-point interpolation scheme. The error due to the interpolation scheme is less than one percent of the flux through the surface.

The collisional accumulation and depletion are five dimensional integrals over the coordinates u_{j_r}, u_{j_z}, ϕ, ψ, and η, where ϕ is the polar angle between the horizontal velocities of species i and j. These integrals are evaluated using a 12-point Gauss-Legendre quadrature for the ϕ, ψ, and η coordinates, and a 12-point Gauss-Hermite quadrature for the u_{j_r} and u_{j_z} coordinates (this is the same method employed by Kumaran *et al.*). The accuracy of this method was verified for a Gaussian velocity distribution which can be evaluated analytically. Error in the integration scheme was less than 5 percent.

Kumaran *et al.* have shown that this result provides adequate agreement with results obtained from direct-simulation Monte Carlo numerical solution of the non-linear Boltzmann equation (Bird, 1970).

3.1.3 Modifications to the Radial Dispersion Coefficient Due to Particle Collisions

Including collisions in the analysis introduces the possibility that the particle-eddy interaction time is no longer controlled by either the horizontal or vertical particle-eddy crossing trajectories, or by the eddy decay time. Rather particles within an eddy may collide with one another due to both the distribution in fluctuating velocities and the different axial slip velocities of different fractions. During the time the particles are in the eddy, they gain

a component of velocity due to the drag force in the direction of the eddy gas velocity and also due to collisions with other particles as described above:

$$\left\langle u_{p_r}^2 \right\rangle_{\text{total}} = \left\langle u_{p_r}^2 \right\rangle_{\text{gas induced}} + \left\langle u_{p_r}^2 \right\rangle_{\text{collision induced}} \tag{33}$$

If the time between successive collisions is less than the viscous relaxation time, the particle mean square displacement is

$$\left\langle x_{p_r}^2 \right\rangle = \left\langle \left(\sum_i x_i \right)^2 \right\rangle \tag{34}$$

$$\left\langle x_{p_r}^2 \right\rangle = 2\left\langle \left(\sum_i \sum_{j>i} x_i x_j \right) \right\rangle \tag{35}$$

$$\left\langle x_{p_r}^2 \right\rangle = 2\left\langle \left(\sum_i^N \sum_{r=0}^{N-i} x_i x_{i-r} \right) \right\rangle \tag{36}$$

$$\left\langle x_{p_r}^2 \right\rangle = 2N \sum_{r=0}^{N} \left\langle x_i x_{i-r} \right\rangle \tag{37}$$

For a large number of interactions and constant $\left\langle x_i^2 \right\rangle$,

$$\left\langle x_{p_r}^2 \right\rangle = 2N \sum_{r=0}^{N} \left\langle x_i{}^2 \right\rangle \exp\left(-rA\right) \tag{38}$$

$$\left\langle x_{p_r}^2 \right\rangle = 2N \left\langle x_i{}^2 \right\rangle \int_0^N \exp\left(-rA\right) dr \tag{39}$$

$$\left\langle x_{p_r}^2 \right\rangle = 2\left(\frac{t}{\tau_c}\right)\left(\frac{\left\langle x_i{}^2 \right\rangle}{\beta\tau_c}\right)\left(1 - \exp(\beta t)\right) \tag{39a}$$

where the definition of the total number of interactions is now,

$$N = \left(\frac{t}{\tau_c}\right) \tag{39b}$$

If Govan's approximation holds (equation 29, Section 2),

$$\left\langle x_{p_{rn}} x_{p_{rn-r}} \right\rangle = \left(u_e \tau_c\right)^2 \frac{A}{2} \exp\left(-rA\right) \tag{40}$$

$$\left\langle x_{p_{rn}} x_{p_{rn-r}} \right\rangle = \left\langle x_i^2 \right\rangle \exp\left(-rA\right) \tag{41}$$

and using the methodology described in Section 2,

$$\left\langle x_{p_r}^2 \right\rangle = 2\left(\frac{t}{\tau_c}\right)\left(\frac{\beta\tau_c}{2}\right)\left(u_e\tau_c\right)^2\left(\frac{1}{\beta\tau_c}\right)\left(1 - \exp(\beta t)\right) \tag{42}$$

so that

$$\left\langle x_{p_r}^2 \right\rangle = t\left(u_e^2\tau_c\right)\left(1 - \exp(\beta t)\right) \tag{43}$$

In general, it is not known which mechanism (vertical crossing trajectory, horizontal crossing trajectory, eddy decay time, or collisional effects) will control the interaction time. The general form of (43) can be written as

$$\left\langle x_{p_r}^2 \right\rangle = 2\left(\frac{t}{t_i}\right)\left\langle x_{i_r}^2 \right\rangle\left(\frac{1}{\beta t_i}\right)\left(1 - \exp(\beta t)\right) \tag{44}$$

or

$$\left\langle x_{p_r}^2 \right\rangle = t t_i u_e^2\left(1 - \exp(\beta t)\right) \tag{45}$$

where t_i is given by the minimum of the particle-eddy vertical crossing time, particle-eddy horizontal crossing time, eddy decay time, or time between successive collisions. Table 2 gives the expression for these characteristic times.

Table 2: Expressions for Various Time Scales

Time Scale	Equation	Region where Time Scale Will be Controlling
Particle-Eddy Vertical Crossing Time	$\frac{l_e}{u_t}$	Large particles, relatively dilute suspensions
Particle-Eddy Horizontal Crossing Time	$\frac{l_e}{u_e}\left(\frac{\exp\left(\frac{3}{8}C_D\frac{l_e}{R}\frac{D}{d_p}\frac{\rho_f}{\rho_s}\right)-1}{\frac{3}{8}C_D\frac{l_e}{R}\frac{D}{d_p}\frac{\rho_f}{\rho_s}\left(1\pm\frac{v_{p_{r0}}}{u_e}\right)}\right)$	Small particles, relatively dilute suspensions
Eddy Decay Time	$1.6\left(\frac{l_e}{u_e}\right)$	Very large diameter beds, or very small particles, dilute suspensions
Time Between Collisions Relatively Dilute Suspensions	$\tau_{c_{ij}}=\frac{1}{n_j\pi d_{ij}^2\left(u_{t_1}-u_{t_2}\right)}$	Relatively dilute suspensions, large particle size distributions
Time Between Collisions Dense Suspensions	$\tau_{c_{ij}}=\frac{1}{n_j\pi d_{ij}^2\left(v'_{p_r}\right)}$	Very dense suspensions

The particle radial dispersion coefficient can then be calculated using (45) with the appropriate expression for ti, and the expression

$$\frac{1}{2}\left(\frac{\langle x_p^2\rangle}{t_i}\right)=\varepsilon_p \tag{46}$$

3.1.4 Modifications to the Average Axial Concentration Profile Due to Particle Collisions

Modifications to the axial average solid fraction can be made based on (46) and Table 2. The expression for the axial concentration profile was derived in Section 2:

$$C(t) =$$

$$\frac{4}{R\bar{u}(t)}\sum_{n=1}^{\infty}\left\{\frac{J_0\left(\beta_n\frac{r_e}{R}\right)}{\beta_n J_1(\beta_n)}\int_0^t \bar{u}(t')E(t')\exp\left(\frac{-\varepsilon_{p_r}\beta_n^2(t-t')}{R^2}\right)dt'\right\}$$

$$+\frac{4R\overline{C_p}\bar{u}(0)}{r_p\bar{u}(t)}\sum_{n=1}^{\infty}\left\{\frac{J_1\left(\beta_n\frac{r_p}{R}\right)}{\beta_n^2 J_1(\beta_n)}\exp\left(\frac{-\varepsilon_{p_r}\beta_n^2 t'}{R^2}\right)\right\} \qquad (47)$$

where for long times and large numbers of interactions, the particle radial dispersion coefficient was defined as

$$\varepsilon_{p_r} = \frac{1}{2}\frac{d}{dt}\left\langle x_{p_r}^2\right\rangle \qquad (48)$$

or

$$\varepsilon_{p_r} = \frac{1}{2}\nu\left\langle x_{p_r}^2\right\rangle \qquad (49)$$

where ν is the interaction frequency. If the interaction time scale is controlled by the vertical particle eddy crossing trajectories

$$\nu = \frac{u_t}{l_e} \qquad (50)$$

In general, however

$$\nu = \frac{1}{t_i} \qquad (51)$$

Equation (48), (51), and the appropriate expression in Table 2 along with the calculated value for $\left\langle x_{p_r}^2\right\rangle$ can be used to evaluate ε_{p_r} to take into consideration suspensions where the particle-eddy interaction time is not controlled by the vertical crossing trajectories.

3.2 Gas Turbulence Modification

The analysis described in Section 2 was based on the assumption that the gas phase turbulence was not affected by the presence of particles. This assumption is only valid in the limit of very dilute suspensions. For solid fractions typically found in CFB's, the intensity of gas phase fluctuations will deviate significantly from the single phase limit.

The particle-turbulence interaction is of great importance in understanding the mechanism of turbulence generation and transfer in two-phase flows. This problem is also important for developing calculational methods for devices which use multiphase mixtures, such as fluidized beds. During the last decade this problem has been the motivation for a number of investigations covering various aspects of this phenomenon [Hetsroni (1989), Gore and Crowe (1989), Rashidi *et al.* (1990, 1991)]. Table 3 lists some of the particle-turbulence flow configurations which have been studied in the past.

Table 3

Flow Configuration	Investigators
Particle-Laden Jets	Hetsroni and Sokolov, 1971 Laats and Frishman, 1973 Parthasarathy and Faeth, 1987 Shuen *et al.*, 1985
Two-Phase Pipe Flow	Tsuji and Morikawa, 1982 Tsuji *et al.*, 1984 Zisselmar and Molerus, 1979 Maeda *et al.*, 1980 Alajbegovic *et al.*, 1994
Two-Phase Boundary Layers	Rashidi *et al.*, 1990, 1991
Two-Phase Homogeneous Turbulence	Parthasarathy and Faeth, 1987, 1990

In the early investigations on particle-laden turbulent jets, it was discovered that the presence of solid particles can lead to either a modulation or enhancement of the turbulence of the carrier fluid. Gore and Crow (1989a,b) compiled most of the available experimental data and presented the effect of the particle sizes on the reduction or enhancement of turbulence. They concluded that small particles reduced the turbulence intensity of the flow, while larger particles increased it.

The early investigations on particle-laden turbulent jets concluded that the presence of solid particles leads to the modulation of the turbulence of the carrier fluid [Hetsroni and Sokolov (1971); Laats and Frishman (1973)]. This effect manifests itself both in the modulation of the turbulence intensity and in a change in the energy spectra (a decrease in the spectral components at high-frequency and a corresponding change in the distribution of the fluctuations energy). The subsequent measurements [Shuen *et al.*, (1985); Parthasarathy and Faeth, (1987); Tsuji *et al.*, (1988)] made for wide variations in particle sizes, phase-density ratio, total mass content and other variables corroborated these results. Subsequently, a number of new effects reflecting specific features of the particles-turbulence interaction have been discovered. It was shown [Tsuji and Morikawa, (1982); Tsuji *et al.*, (1984); Lee and Durst, (1982)] that carrier fluid turbulence in particle-laden flows with coarse particles does not always decrease; the turbulence intensity may also increase. This phenomenon has a common character and may be observed in various types of particle-laden flows: jets, pipe flows, flows in the boundary layer and in homogeneous turbulence. The turbulence intensity of the carrier fluid in a two-phase mixture may be several times that of a single-phase flow.

A number of investigations have dealt with a theoretical description of the particles-turbulence interaction [Abramovich, (1970); Elghobashi and Abou-Arab, (1983); Shuen *et al.*, (1985); Abou-Arab and Roco, (1988);, Shraiber *et al.*, (1990)]. They approached the problem by extending the single phase models of turbulence (mixing length theory, the k-ε model etc.) to calculate the particles-turbulence interaction. One of the first attempts was that of Abramovich (1970), who used Prandtl's (1925) mixing length theory and derived a simple expression determining the dependence of the velocity fluctuations intensity on the carrier fluid and the particles' physical properties as well as the flow regime parameters. This theory does not result in turbulence modification and may be used only for estimation of the fluctuations in two-phase flows with fine particles. In this case, fairly good agreement between the theoretical and experimental data was achieved. Later this approach was used in a number of investigations to study the effects of flow non-equilibrium, gravity, and other variables on the turbulence intensity [Abramovich, (1984)].

A number of theoretical methods have been developed to describe turbulent flows laden with coarse particles. The turbulence modulation has been investigated by Al-Taweel and Landau (1977), Parthasarathy and Faeth (1990), and Yuan and Michaelides (1991). In the latter work a simple estimation was proposed by using a turbulent kinetic energy balance.

Gore and Crowe (1989) attempted to generalize the experimental data on the particles-turbulence interaction and suggested the use of the ratio of particle size to a characteristic length scale of flow. The analysis of the data for various types of particle-laden flows has shown that there exists a fairly distinct particle dimensionless size below which particles suppress turbulence and above which they enhance it. This boundary corresponds to the ratio

$$\frac{d_p}{l_e} \simeq 0.1 \tag{51}$$

Hetsroni (1989) used the data of Gore and Crowe (1989) and suggested that larger particles, with a Reynolds number greater than 110 cause vortex shedding behind them. These vortices actually cause enhancement of the turbulence (the particles cause energy to be transferred from the average velocity to higher frequencies).

Previous numerical studies of multiphase flows used turbulence models, such as the k-ε models, and extrapolated the coefficients from single-phase flows [Danon, et al., (1974)]. These computations may serve useful purposes, but do little to enhance the physical understanding of multiphase flows.

In general, it is known that the following six mechanisms, which are not independent of each other, contribute to the turbulence modification in dispersed two-phase flows:

1. Dissipation of turbulent kinetic energy by the particles
2. Increase of the apparent viscosity due to the presence of particles
3. Shedding of vortices or the presence of wakes behind the particles
4. Fluid moving with the particle as added fluid mass to the particles
5. Enhancement of the velocity gradients between two rigid spheres
6. Deformation of the dispersed phase

Of these mechanisms, number (6) is not applicable to particulate flows, and numbers (5) and (2) are negligible for relatively dilute suspensions.

The mechanism of turbulence modification which is developed in this Thesis is consistent with the proposed mechanism for particle dispersion. Two predominant mechanisms for the enhancement and production of turbulence are assumed:

1. The dissipation of power from an eddy for the acceleration of a particle - resulting in turbulence reduction
2. The flow velocity disturbance due to the wake of the particle or the vortices shed - resulting in turbulence enhancement

The effects of these two phenomena combine to yield the overall turbulence modification.

3.2.1 Particle-Eddy Interactions

As was discussed in Section 2, the turbulent fluid is characterized by eddies moving with a velocity u_e which can be approximated as:

$$u_e = u_\tau = u_o\sqrt{\frac{f}{2}} \tag{52}$$

where u_τ is the friction velocity, u_e is the eddy velocity, and f is the single phase friction factor. A particle moving with a velocity v_p enters the eddy and interacts with it for an amount of time determined by the minimum of the eddy decay time, vertical particle-eddy crossing time, horizontal particle-eddy crossing time, or the time between successive collisions, as discussed above. In general, the equation describing the particle motion is:

$$\begin{aligned}
&\frac{1}{6}\pi d_p^3\rho_s\frac{dv_p}{dt} = \frac{1}{6}\pi d_p^3(\rho_s-\rho_f)g - \frac{\rho_f\pi C_D d_p^2}{8}\left(v_p - v_{fp} - \frac{1}{24}d_p^2\nabla^2 v_{fp}\right)\left|v_p - v_{fp}\right| \\
&-\frac{\pi\mu d_p^2 C_H}{4}\int_{t_0}^{t}\frac{d}{d\tau}\left[v_p - v_{fp} - \frac{1}{24}d_p^2\nabla^2 v_{fp}\right]\frac{d\tau}{\left(\pi\nu(t-\tau)\right)^{1/2}} \\
&-\frac{1}{6}\pi d_p^3\rho_f C_A\frac{d}{dt}\left[v_p - v_f - \frac{1}{40}d_p^2\nabla^2 v_{fp}\right] + \frac{1}{6}\pi d_p^3\rho_f\frac{Dv_{fp}}{dt}
\end{aligned} \tag{53}$$

In CFB's, the particle-gas density ratio is normally on the order of 1000 or higher. This allows one to neglect the history and added mass terms, along with the Faxen force, and the terms representing the fluid stresses in the absence of a particle. Therefore, the steady state drag force, F_{drag}, is the dominant force on the particle. The rate of work done by the fluid is

equal to $F_{drag}u_e$ and the change of the kinetic energy of the particle is $F_{drag}v_p$. The rate of energy dissipation is then

$$= \frac{\pi C_D d_p^2 \rho_f \left(u_e - v_p\right)^2 \left|u_e - v_p\right|}{8} \tag{54}$$

During the time of particle-eddy interaction, t_i, when the particle finds itself in the eddy, its velocity changes because of the action of the drag force. From the equation of motion of the particle, the approximate expression for the velocity of the particle during the time interval t_i is

$$v_p = v_{p_0} + \left(u_e - v_{p_0}\right)\left[1 - \exp\left(-\frac{Ct}{\tau_p}\right)\right];\ t \le t_i \tag{55}$$

where C is the correction to the Stokes drag, i.e.

$$C = \left(1 + 0.15 Re_{u_{rel}, d_p}^{0.687}\right) \tag{56}$$

and τ_p is the characteristic time of the particle

$$\tau_p = \frac{\rho_s d_p^2}{18\mu} \tag{57}$$

Strictly speaking, Re_{u_{rel}, d_p} is not constant over the interaction period, however, this assumption introduces errors less than 12 percent in particle velocity [Michaelides, (1988)], and allows the resulting equations to be simplified greatly.

The total work done during the time of interaction between the particle and the eddy is simply the integral of the rate of energy dissipation with respect to time

$$W = \frac{\pi d_p^3 \rho_s}{12}\left(u_e - v_{p_0}\right)^2\left[1 - \exp\left(-\frac{2Ct_i}{\tau_p}\right)\right];\ t \le t_i \tag{58}$$

The work performed by the eddy on the particle is equal to the energy dissipation in the eddy. This dissipation results in a turbulence intensity reduction of the same amount. The term $\left(u_e - v_{p_0}\right)$ can be approximated as the local relative velocity of the fluid with respect to

the particle since the calculation of the time-average reduction in turbulence intensity requires an ensemble of particles, i.e.:

$$\left(u_e - v_{p_0}\right) \simeq u_{rel} \simeq u_t \tag{59}$$

Clift *et al.*, (1978) have shown that when $Re_{u_{rel}, d_p} > 20$, there is an evident wake behind the particle. At $Re_{u_{rel}, d_p} > 400$, vortices are shed behind the particles at a frequency which is a function of Re_{u_{rel}, d_p}. Both the wake behind the particle and the vortex shedding contribute to the velocity disturbance by the particle and are considered here as the sources of turbulence production. The change in the kinetic energy per unit volume associated with the produced turbulence is proportional to the difference of the squares of the two velocities and to the volume where the velocity disturbance occurs:

$$\Delta E = d_p^2 \rho_f \left(u_e^2 - v_p^2\right) f\left(l_w\right) \tag{60}$$

where $f\left(l_w\right)$ is a function which represents a measure of the region behind the particle where the fluid velocity is close to that of the particle. A reasonable estimate for this length is the effective length of the wake, or the length behind the particle where the shed vortices remain. Michaelides (1992) assumed that the wake is half of a complete ellipsoid, with a base diameter d_p and height l_w; where l_w is obtained from Clift *et al.* (1978). The resulting equation for the change in kinetic energy due to wake shedding is then

$$\Delta E = \frac{\pi d_p^2 \rho_f u_t}{12}\left(2u_e - u_t\right) f\left(l_w\right) \tag{61}$$

the term $\pi/12$ results from the multiplication of the volume of the ellipsoidal wake by 1/2, which multiplies the kinetic energy expression.

The total change in turbulent kinetic is the combination of equations (58) and (61)

$$\Delta E = \frac{-\pi d_p^3 \rho_s}{12} u_t^2 \left[1 - \exp\left(-\frac{2Ct_i}{\tau_p}\right)\right] + \frac{\pi d_p^2 \rho_f u_t}{12}\left(2u_e - u_t\right) f\left(l_w\right) \tag{62}$$

For the case of small particles where the interaction time is much larger than the particle time scale, the change in turbulent kinetic energy is

$$\Delta E = \frac{-\pi d_p^3 \rho_s}{12} u_t^2 \tag{63}$$

For conditions typical of a CFB, the eddy-particle interaction time will not be much greater than the particle relaxation time. However, most will operate with particle Reynolds numbers less than the cutoff of 20 suggested by Clift *et al.* (1978). Therefore, the change in turbulent kinetic energy can be approximated as

$$\Delta E = \frac{-\pi d_p^3 \rho_s}{12} u_t^2 \left[1 - \exp\left(-\frac{2Ct_i}{\tau_p} \right) \right] \tag{65}$$

Equation (65) represents the change in turbulent kinetic energy due to one particle interacting with an eddy. To develop an expression which is valid for a suspension of many particles, assume that a fluid element acquires momentum at time t = 0 under the influence of a hydrodynamic field disturbance (pressure fluctuation). Further it moves by inertia and interacts with the particles inside. Then the carrier fluid is described by the following equation of conservation of momentum:

$$d\left[v_f' + \sum_{i=1}^{n} \gamma_i v_{p_i}' \right] = 0 \tag{66}$$

where γ represents the ratio of particle to fluid mass flux. The summation is included to represent particles of n different diameters.

The initial condition for (66) is

$$v_f' = v_{f_0}' \quad \text{at } t = 0 \tag{67}$$

where v_{f_0}' represents the fluid mean-square velocity fluctuations without particles.

Integration of (66) gives

$$v_f' + \sum_{i=1}^{n} \gamma_i v_{p_i}' = v_{f_0}' \tag{68}$$

(68) can also be written as

$$v_f' + \sum_{i=1}^{n} \left[\gamma_i \left(v_{p_i}' - v_f' \right) + \gamma_i v_f' \right] = v_{f_0}' \tag{69}$$

or

$$v_f' = \frac{1}{\left(1 + \gamma_i\right)} \left[v_{f_0}' + \sum_{i=1}^{n} \gamma_i \left(v_{p_i}' - v_f' \right) \right] \tag{70}$$

The second term on the r.h.s. of (70) represents the turbulent dissipation due to the viscous interaction between the particles and the carrier fluid. Using the analysis developed above and correcting for the possibility of more than one particle per eddy, (70) can be rewritten to give

$$v_f' = \frac{1}{\left(1 + \gamma_i\right)} \left[v_{f_0}' + \sum_{i=1}^{n} \gamma_i \left(\frac{u_{rel}}{2} \right) \left[1 - \exp\left(- \frac{2Ct_i}{\tau_p} \right) \right] \right] \tag{71}$$

The kinetic energy of the fluid per unit volume without particles is (Hinze, 1975)

$$E_0 = \frac{\pi \rho_f l_e^3 u_e^2}{6} \tag{72}$$

The fluid mean-square velocity fluctuation with particles can then be written as

$$v_f' = \frac{1}{\left(1 + \gamma_i\right)} \left[u_e + \sum_{i=1}^{n} \gamma_i \left(\frac{u_{rel}}{2} \right) \left[1 - \exp\left(- \frac{2Ct_i}{\tau_p} \right) \right] \right] \tag{73}$$

If the relative eddy-particle velocity can be approximated as being equal to the terminal velocity for an ensemble average of particles

$$v_f' = \frac{1}{\left(1 + \gamma_i\right)} \left[u_e + \sum_{i=1}^{n} \gamma_i \left(\frac{u_t}{2} \right) \left[1 - \exp\left(- \frac{2Ct_i}{\tau_p} \right) \right] \right] \tag{74}$$

In the case where the ratio of the particle to eddy length scale is much less than unity, the analysis indicates

$$v_f' = \frac{1}{(1+\gamma_i)}[u_e] \tag{75}$$

In this case the turbulence modulation by wake shedding mechanism does not take place and the process of the particles-turbulence interaction is determined only by the total mass content. This result reflects the leading role of particle inertia in particle-laden flows with fine particles. Figure 4 presents experimental data for the enhancement of the carrier fluid fluctuations at the axis of an axisymmetric jet which was taken by Laats and Frishman (1973). In this plot and the plots that follow, the enhancement coefficient is defined as

$$\Psi = \frac{v_f' - v_{f_0}'}{v_{f_0}'} \times 100 \tag{76}$$

where v_{f_0}' is the mean-square fluctuating velocity of the fluid without particles.

Figure 4

Dependence of Enhancement Coefficient on Mass Flux Ratio: Data of Laats and Frishman (1972)

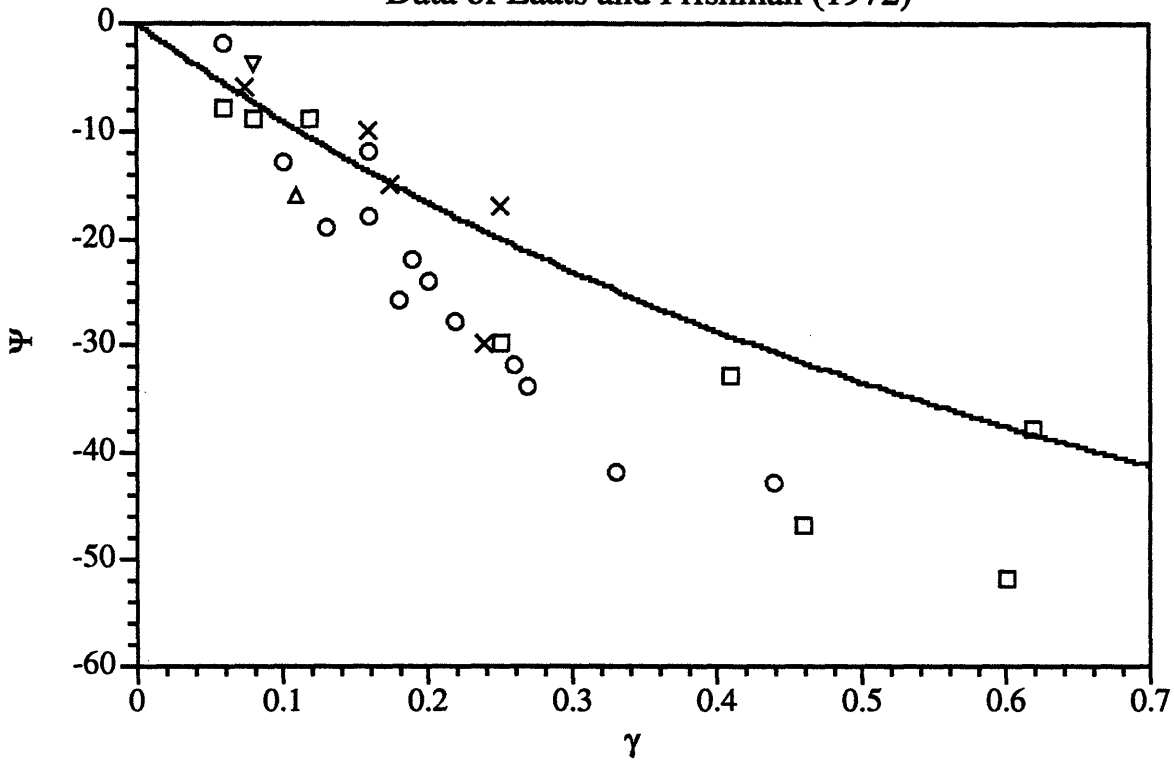

○ dp = 7 microns	▽ dp = 80 microns
□ dp =17 microns	× dp = 120 microns
△ dp = 32 microns	

The particle sizes in these experiments changed between 7 and 120 microns and the total mass content from 0 to 0.6. The plot also includes the asymptotic limit of equation (74) as given in equation (75). From (76) and (75), where $u_e = v'_{f_0}$ for flow in jets, the enhancement coefficient in the limit of very small particles is

$$\frac{\Psi}{100} = \frac{v'_f - v'_{f_0}}{v'_{f_0}} = -\frac{\gamma}{1+\gamma} \tag{77}$$

The effect of the mass content on the enhancement coefficient for various radial locations across a pipe is shown in Figure 5. Also shown is equation (74) (solid line). The match is not exact, although the general trend is captured. One reason that the prediction may not be as good for this set of data is the flow setup was horizontal liquid-solid pipe flow. The

density ratio in this flow was of the order 1, indicating that virtual mass and history forces may be significant. These forces were neglected in the derivation of (74). It is important to note that at each radial location, an increase in the mass flux ratio increased the reduction in fluid phase turbulence velocity. This supports the result that for a wide variety of flows where the wakes behind the particles can be neglected, the turbulence modulation is only a function of the mass flux ratio.

Figure 5

Dependence of Enhancement Coefficient on Mass Flux Ratio

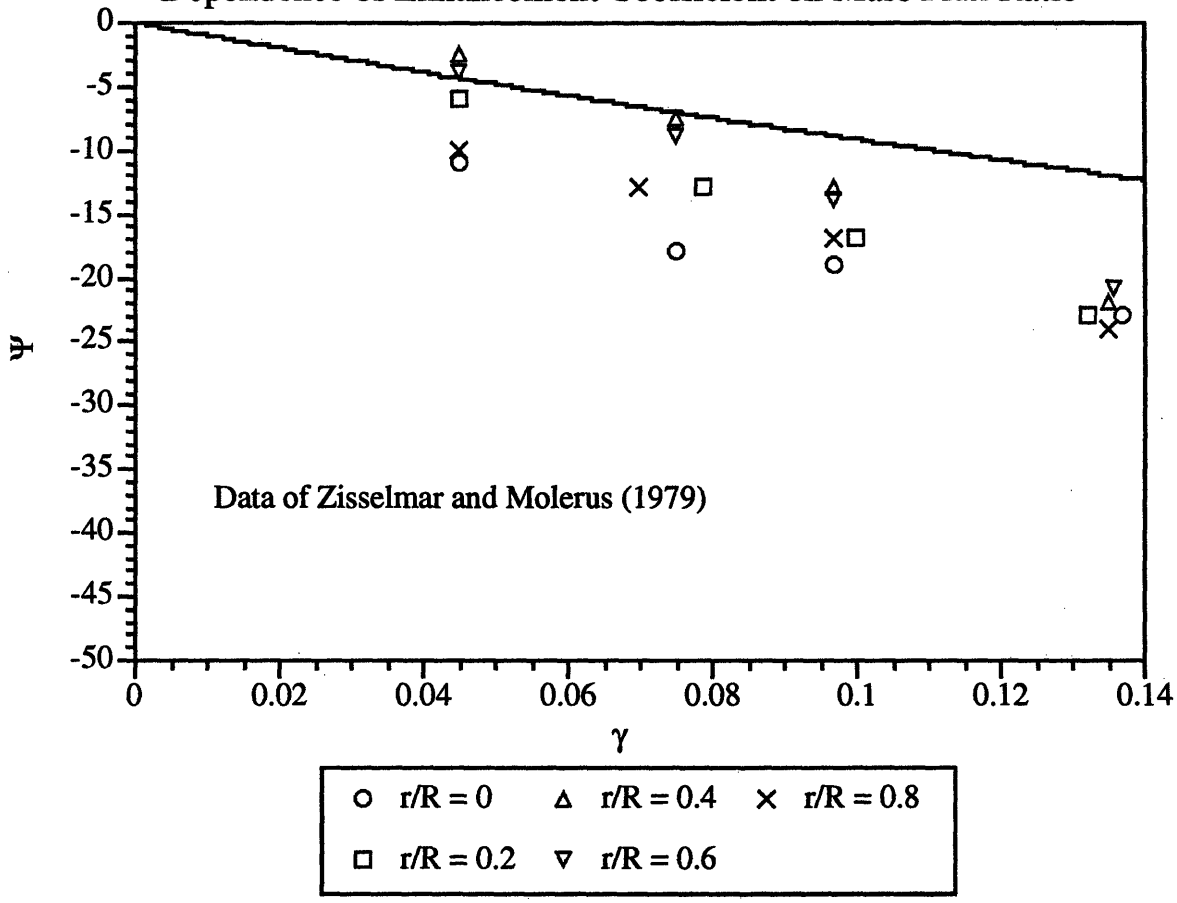

In Figure 6, the enhancement coefficient is plotted versus the mass flux ratio for the experimental data of pipe flows as taken by Tsuji and Morikawa (1982), Tsuji et al. (1984), Zisselmar and Molerus (1979), and Maeda et al. (1980). In these experiment, the mass loading and the particle diameters were larger than those in the study by Laats and Frishman such that the assumption of the limit of small particles which move at the same velocity as the gas does not hold. Even though the simple formulation resulting in (77) does not hold, equation (74) (the solid line given in the plot) provides an adequate prediction of the

turbulence modulation. In all cases, an increase in the total mass content of the particles leads to a decrease in the level of fluctuations.

Figure 6
Dependence of Enhancement Coefficient on Mass Flux Ratio

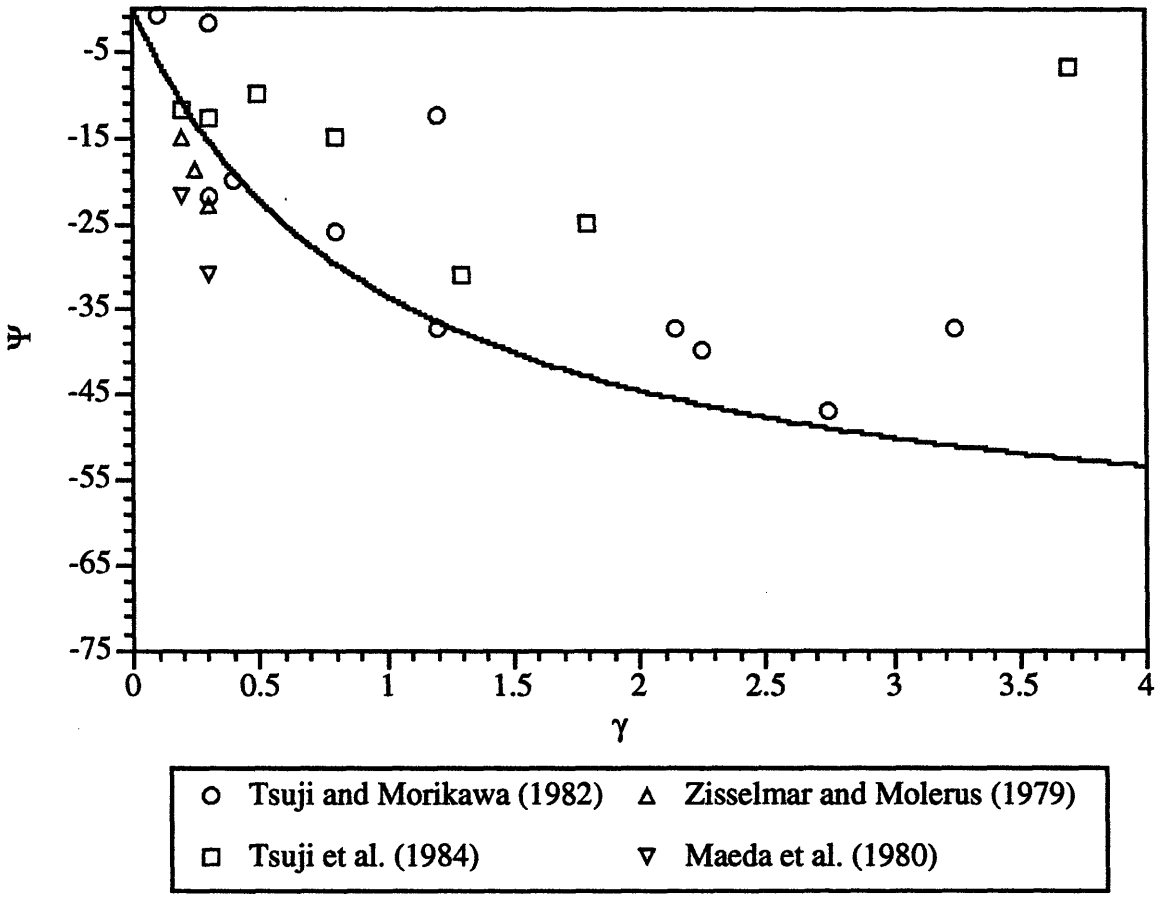

In CFB's, the mass flux ratio can be much larger than the range given in Figure 6 (up to about 10). While it is not certain that (74) will hold much beyond the range where experimental data is available, for the purposes of this Thesis, it will be used to predict the effect of the particles on gas phase turbulence.

3.3 Drag Coefficient

The relative velocity between a mulitparticle cloud and the continuous fluid medium is a function of the size, volumetric concentration, and particle sphericity, taking into account the physical parameters of the system. The quantitative relationship linking these factors is needed in many fields of engineering: fluidized and moving beds, liquid-liquid mixing and

settling, drops-gas contacting, fixed-bed reactors, and solid fluid separations. Despite the numerous experimental and theoretical studies devoted to this problem, relatively few reliable design methods are available. Various empirical correlations proposed so far are limited to certain ranges of variables.

The present discussion deals with systems of particles, of common specific gravity, with a relatively narrow size distribution which can be reduced to an average characteristic size. Additionally, it will be assumed that there are no interactions between the particles, except hydrodynamic effects through the fluid. Additionally, the effect of the fluid bed walls is neglected. In reality, both drag in the normal and tangential direction are affected when the ratio of particle diameter to wall distance from the particle center of mass is of the order 1. This is discussed in greater detail in Chapter 2 of this Thesis.

3.3.1 Determination of Drag as a Function of Solid Fraction

The terminal velocity of a single (spherical) solid particle surrounded by an infinite fluid has been given much attention. Generally, the effects of the fluid viscosity and density, the particle density and diameter, the gravitational acceleration, and the relative velocity are determined by grouping these variables according to the theory of similarity, into two dimensionless groups: the particle Reynolds number

$$Re = \frac{u_{rel} d_p \rho_f}{\mu_f} \tag{78}$$

and the empirical drag coefficient (the ratio of the drag forces and inertial forces)

$$C_D = \frac{F_D}{\frac{1}{2}\rho_f S u_{rel}^2} = \frac{\left(\frac{\pi}{6}\right) g d_p^3 (\rho_s - \rho_f)}{\frac{1}{2}\rho_f S u_{rel}^2} \tag{79}$$

where S is the largest cross sectional area of the particle and is equal to $\frac{\pi d_p^2}{4}$ for a sphere.

These parameters are then plotted against each other, as in Figure 7. If the physical parameters are known, data plots, or empirical equations (one of which was used to plot Figure 7) can be used to link the parameters.

Figure 7
Drag Coefficient vs Particle Reynolds

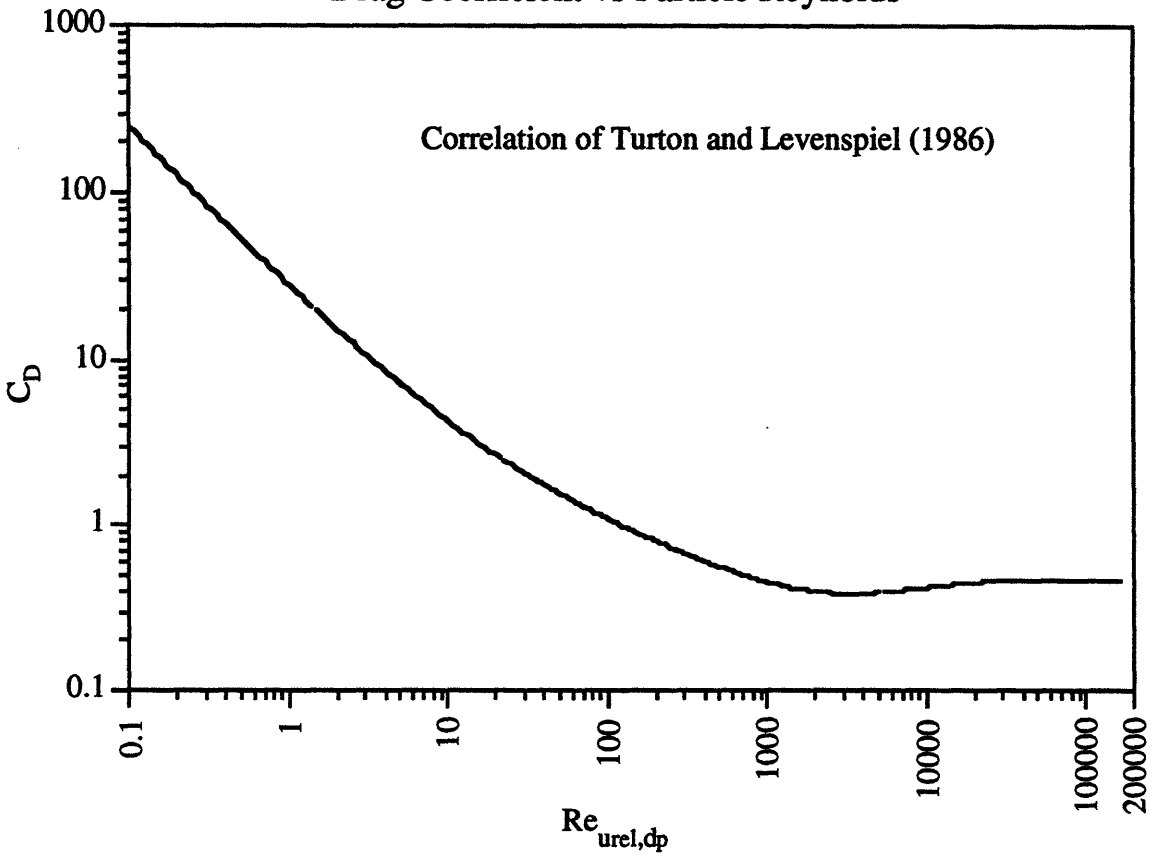

Empirical curves can be divided into several zones. The first zone is the Stoke's region. In this region, the drag forces can be obtained analytically by solving the Navier-Stokes equations, neglecting the inertial term and assuming, as boundary conditions zero velocity on the particle surface and a constant velocity u_{rel} in the vertical direction at an infinite distance.

$$F_D = 3\pi\mu_f d_p u_{rel} \tag{80}$$

and

$$C_D = \frac{24\mu_f}{d_p u_{rel}\rho_f} = \frac{24}{Re_{u_{rel},\,d_p}} \tag{81}$$

$$u_{rel} = \frac{d_p^2(\rho_s - \rho_f)g}{18\mu_f} \tag{82}$$

In the region of the constant drag coefficient

$$C_D = 0.44 \pm 0.04 \tag{83}$$

between Reynolds numbers of 700 and 200,000 where viscous forces are negligible (Newton's law).

Various empirical formulae have been proposed for the entire Reynolds number range. The equation of Turton and Levenspiel (1986) provides good agreement from the Stokes region through Reynolds numbers of the order 10^6:

$$C_D = \frac{24}{Re_{u_{rel}, d_p}}\left[1 + 0.173Re_{u_{rel}, d_p}^{0.657}\right] + \frac{0.413}{1 + 16300Re_{u_{rel}, d_p}^{-1.09}} \tag{84}$$

In multiparticle systems the following fundamental complications are present:

1. A third variable is introduced: the volumetric fraction ϕ occupied by the particles
2. The unique particle diameter becomes a size distribution characteristic (mean, median, variance).

The general problem is to relate u_ϕ, the relative average velocity between the solid particles and the fluid phase (equal to the vectorial difference between the superficial velocity of the particles and the superficial velocity of the gas), to d_p and ϕ. Since u_ϕ is always less than u_t, the superficial gas velocity, many authors have proposed that u_ϕ/u_t should be related to ϕ.

The hindrance effects in a multiparticle system can be broken down into three effects. The first is the pseudo-hydrostatic effect. The average effective hydrostatic pressure gradient of the suspension is greater than that of the fluid alone, and consequently the effective buoyancy force is greater. This force is the integration of the vertical component of the hydrostatic pressure normal to the particle surface. Therefore, in the expression of the driving force, the effective density ρ_ϕ of the suspension should be used instead of the fluid density:

$$\rho_\phi = \rho_s\phi + \rho_f(1 - \phi) \tag{85}$$

However, the dynamic fluid pressure, relevant to the inertial forces, should still be related to the fluid density, since the particles are moving all together relative to the fluid and not relative to the suspension. Therefore, ρ_ϕ should be used in the expressions of the Reynolds number and the drag force.

The second effect is the momentum transfer. The presence of the other particles affects the mechanism of the transfer of momentum between each particle and the fluid medium. This effect is related, although not strictly equivalent, to the increase of the apparent bulk viscosity of the suspension, which becomes evident when the bulk suspension is sheared. This effect calls for a correction factor as a function of ϕ.

The final effect is the wall hindrance effect. Significant wall effects are detectable even when a single particle is settling in a vessel whose diameter is larger than the particle size by one or two orders of magnitude. This is caused by the dissipation of energy by friction between the moving fluid and the walls and by the limitation of the flow field around the particle. Analogously, a settling cloud of particles causes an opposite motion of the fluid, which develops drag forces on all the particles present and limits the flow field around the individual particles. This effect calls for another correction factor linked to ϕ.

Pure theoretical attempts to relate u_ϕ and u_t are based on analytical solutions of the differential Navier-Stokes equations, with particular sets of assumptions on limiting conditions but without any empirical constant. Almost all of these attempts are based on the simplifying assumption of the creeping flow region. The most common mathematical models used are the method of reflections, the point force technique, the cell models, and the multipole representation technique. Only the cell model allows for calculation beyond the range of creeping flow.

A general correlation should account for the role of ϕ in the three effects mentioned above. The development of a correlation which takes these into account was developed by Barnea and Mizrahi (1973). They successfully correlated the ratio u_ϕ/u_t in the creeping flow region by deriving correction factors for each effect. For the momentum hindrance, the expression for the apparent viscosity of the form

$$\frac{\mu_\phi}{\mu} = \exp\left(\frac{K_1\phi}{1-K_2\phi}\right) \tag{86}$$

This is the same form as Vand's (1948) theoretical result, and Mooney's (1951) semi-theoretical correlation. It should be noted that the apparent viscosity of the suspension, when sheared as a bulk by the motion of a solid wall, is not necessarily the same as the suspension viscosity encountered by a particle moving with respect to the fluid while keeping a constant average position with regard to the other particles.

The wall effect was derived in the form of $\left(1 + K_3\phi^{1/3}\right)$, which is a common result for analytical solutions in the creeping flow region. The constant K_3 pertains to truly random spatial positions of the particles, a case which has not been analytically resolved. Thus K_3 must be found from the correlation of experimental data.

$$F_D = 3\pi d_p \mu_f u_\phi \left(1 + K_3\phi^{1/3}\right) \exp\left(\frac{K_1\phi}{\left(1 - K_2\phi\right)}\right) \tag{87}$$

The driving force takes into account the hydrostatic effect by using the suspension density

$$F_D = \frac{1}{6}\pi d_p^3 \left(\rho_s - \rho_f\right) g\left(1 - \phi\right) \tag{88}$$

From (87) and (88), the relative terminal velocity is

$$u_\phi = \frac{d_p^2 \left(\rho_s - \rho_f\right) g\left(1 - \phi\right)}{18\mu_f \left(1 + K_3\phi^{1/3}\right) \exp\left(\frac{K_1\phi}{\left(1 - K_2\phi\right)}\right)} \tag{89}$$

In the creeping flow region, it was determined that $K_1 = 1.66$, and both K_2 and K_3 were 1.0.

Barnea and Mizrahi then extended their analysis to cover a wide range of Reynolds numbers. The Reynolds number, which characterizes the flow regime, is a measure of the relative contribution of the inertial forces and frictional forces to the total drag forces. The former are not affected by the presence of other particles (being related to the suspension density provided that the characteristic velocity is taken as u_ϕ), but the frictional forces are increased by the presence of other particles, as indicated by the increase in suspension viscosity. The relevant form of the Reynolds number is

$$Re_{u_\phi, d_p} = \frac{d_p \rho_f u_\phi}{\mu_\phi} = Re_{u_t, d_p} \left[\frac{\left(\frac{u_\phi}{u_t}\right)}{\exp\left\{\frac{5\phi}{3(1-\phi)}\right\}} \right] \tag{90}$$

The drag coefficient is the ratio of the drag forces to the dynamic pressure on the particle cross sectional area. It should take into account both the wall effect and the hydrostatic effect

$$C_{D_\phi} = \frac{F_D}{\frac{1}{2}\rho_f S u_\phi^2 \left(1+\phi^{1/3}\right)} = \frac{C_D}{\left(1+\phi^{1/3}\right)} \tag{91}$$

$$C_{D_\phi} = \left[\frac{4 d_p (\rho_s - \rho_f) g}{3 \mu u_t^2}\right]\left[\frac{(1-\phi)}{\left(1+\phi^{1/3}\right)}\right] \tag{92}$$

$$C_{D_\phi} = C_D \left(\frac{u_\phi^2}{u_t^2}\right)\left(\frac{(1-\phi)}{\left(1+\phi^{1/3}\right)}\right) \tag{93}$$

The main hypothesis by Barnea and Mizrahi was that the relationship between C_{D_ϕ} and Re_{u_ϕ, d_p} in multiparticle systems is identical to the relationship between C_D and Re_{u_{rel}, d_p} for a single particle. They plotted experimental data from eight different sources beyond the creeping flow region along with extensive data representing the creeping flow range and used the relationship of Lappel and Shepherd (1940) to link C_D and Re_{u_{rel}, d_p}. The exceptional agreement between the model and all experimental data suggests that this methodology provides a universal correlation.

The following steps summarize how one would compute the drag coefficient C_{D_ϕ} :

1. Assume a value for u_ϕ/u_t
2. Calculate Re_{u_ϕ, d_p} from equation (90)
3. Calculate C_{D_ϕ} from equation (93)
4. Calculate C_{D_ϕ} from the single particle drag expression

$$C_{D_\phi} = \frac{24}{Re_{u_\phi, d_p}}\left[1 + 0.173 Re_{u_\phi, d_p}^{0.657}\right] + \frac{0.413}{1 + 16300 Re_{u_\phi, d_p}^{-1.09}}$$

or any other suitable expression

5. Compare the values of C_{D_ϕ} from step 3 with that from step 4. Adjust the guess for u_ϕ/u_t as necessary until convergence

A comparison of the calculated drag curve using this methodology and the standard single particle drag curve is given below after a discussion of the effects of particle sphereicity.

3.3.2 Effect of Particle Sphericity on Drag

Analytical results for predicting the drag on isolated spherical and nonspherical particles exist only in the Stokes regime. Drag prediction for nonspherical particles over the entire range of Reynolds numbers is an extremely difficult theoretical problem because of the large number of shape descriptors needed to classify irregular shapes.

The work of Haider and Levenspiel (1989) is the first attempt to solve this problem through empirical correlation. They collected data on the drag coefficient as a function of particle Reynolds number for particles of different shapes, and proposed a functional dependence which works well for the shapes analyzed in their study. This correlation contains adjustable parameters whose values are determined by the sphericity, defined as the ratio of the surface area of a sphere with equivalent volume to the actual surface area of the particle. The resulting formula for the drag closely resembles earlier studies conducted by Levenspiel [Turton and Levenspiel, (1986)]. The Turton and Levenspiel expression for the drag coefficient for a spherical particle is

$$C_D = \frac{24}{Re_{u_{rel}, d_p}}\left[1 + 0.173Re_{u_{rel}, d_p}^{0.657}\right] + \frac{0.413}{1 + 16300Re_{u_{rel}, d_p}^{-1.09}} \tag{94}$$

After studying the literature, Haider and Levenspiel concluded that the following function is the most suitable form for drag prediction

$$C_D = \frac{24}{Re_{u_{rel}, d_p}}\left[1 + ARe_{u_{rel}, d_p}^{B}\right] + \frac{C}{1 + \frac{D}{Re_{u_{rel}, d_p}}} \tag{95}$$

The values of A, B, C, and D were determined by minimizing the sum of squares error Q, which for n data points is

$$Q = \sum_{i=1}^{n} \left(\log_{10} C_{D_{exp}} - \log_{10} C_D \right)^2 \tag{96}$$

Goodness of fit was measured by the root mean square deviation defined as

$$RMS = \left(\frac{Q}{n} \right)^{1/2} \tag{97}$$

Data for four isometric nonspherical shapes were gathered by Haider and Levenspiel from Pettyjohn and Christiansen (1948), and for thin disks from Schmiedel (1928), Squires and Squires (1937), and Wilmarth et al. (1964). They quantitatively measured the sphericity of eight shapes in order to interpolate C_D for a new shape. The resulting relationships were approximated with polynomials yielding:

$$A = \exp\left(2.3288 - 6.4581\phi_s + 2.4486\phi_s^2 \right) \tag{98}$$

$$B = \exp\left(0.0964 + 0.5565\phi_s \right) \tag{99}$$

$$C = \exp\left(4.905 - 13.8944\phi_s + 18.4222\phi_w^2 - 10.2599\phi_w^3 \right) \tag{100}$$

$$D = \exp\left(1.4681 + 12.2584\phi_s - 20.7322\phi_s^2 + 15.8855\phi_s^3 \right) \tag{101}$$

This allows one to calculate the drag coefficient as a function of the particle Reynolds number and particle sphericity. The RMS deviation of this correlation with the data was less than 0.15 over the entire range of particle Reynolds numbers and sphericities. Haider and Levenspiel also provided simplified expressions for (98) through (101)

$$A = 8.1716\exp\left(-4.0655\phi_s \right) \tag{102}$$

$$B = 0.0964 + 0.5565\phi_s \tag{103}$$

$$C = 73.69\exp\left(-5.074\phi_s \right) \tag{104}$$

$$D = 5.378\exp\left(6.2122\phi_s \right) \tag{105}$$

When (102) through (105) are used, the RMS deviation was less than 0.2 over the entire range of particle Reynolds numbers and sphericities investigated. The recommended range of the particle Reynolds number for the Haider and Levenspiel correlation varies from $Re_{u_{rel}, d_p} < 2.5 \times 10^4$ for isometric particles to $Re_{u_{rel}, d_p} < 500$ for discs.

Thompson and Clark (1991) investigated a method of quantitatively distinguishing shapes as they pertain to particle drag that can be measured for all particles. They introduced the scruple (K_2), also called, the Newton shape factor, defined as the ratio of the drag coefficient of particles of the same shape to the drag coefficient of a sphere, both at a Reynolds number of 10,000. Using Newton's shape factor instead of sphericity as the shape descriptor, Thompson and Clark (1991) determine the drag as a function of Reynolds number and K_2.

Leith (1987) evaluated the drag on nonspherical particles in the Stokes' regime. He introduced the Stokes' shape factor, K_1. Like Newton's shape factor, K_1 was evaluated empirically from the data on drag. Leith concluded that in addition to sphericity, other shape factors such as a shape factor measuring projected area of the particle in the direction of flow, are needed to determine K_1. Leith's own formula depends on four shape descriptors.

Ganser (1993) developed an expression through dimensional analysis which predicts that C_D/K_2 is a function of $Re_{u_{rel}, d_p} K_1 K_2$ only. A plot of $\log(C_D/K_2)$ versus $\log(Re_{u_{rel}, d_p} K_1 K_2)$ for all 731 data points gathered from the studies of Pettyjohn and Christiansen (1948), Schmiedel (1928), Squires and Squires (1937), and Wilmarth et al. (1964) showed that C_D/K_2 can be considered a function of the generalized Reynolds number $Re_{u_{rel}, d_p} K_1 K_2$. The form for this dependence was assumed to be given by the general form of Haider and Levenspiel [equation (95)] with Re_{u_{rel}, d_p} replaced by $Re_{u_{rel}, d_p} K_1 K_2$, and C_D replaced by C_D/K_2, and A, B, C, and D are universal constants. The values for A, B, C, and D for spheres were assumed to be those found by Haider and Levenspiel, since their data was based on all available data. The parameter values for other shapes were calculated directly from the data of Pettyjohn and Christiansen. This includes all the data used by Haider and Levenspiel for isometric shapes plus the small Reynolds number data they ignored.

Equation (106) gives the result of Ganser.

$$\frac{C_D}{K_2} = \frac{24}{Re_{u_{rel},d_p} K_1 K_2}\left[1 + 0.1118\left(Re_{u_{rel},d_p} K_1 K_2\right)^{0.6567}\right] + \frac{0.4305}{1 + \frac{3305}{Re_{u_{rel},d_p} K_1 K_2}} \quad (106)$$

Equation (106) results in a decrease in the RMS deviation for isometric particles from 0.041 to 0.034, for disks from 0.114 to 0.067, and for all data from 0.057 to 0.040. Values recommended for the Stokes' shape factor K_1 and the Newton's shape factor K_2 as given by Ganser are:

For isometric particles:

$$K_1 = \left(\frac{1}{3} + \frac{2}{3}\phi_s^{-1/2}\right)^{-1} - 2.25\frac{d_v}{D} \quad (107)$$

$$K_2 = 10^{\left(1.8148\left[\log(\phi_s)\right]^{0.5743}\right)} \quad (108)$$

and for non isometric particles:

$$K_1 = \left(\frac{1}{3}\frac{d_n}{d_v} + \frac{2}{3}\phi_s^{-1/2}\right)^{-1} - 2.25\frac{d_v}{D} \quad (109)$$

$$K_2 = 10^{\left(1.8148\left[\log(\phi_s)\right]^{0.5743}\right)} \quad (110)$$

where d_v is the diameter of a sphere with equivalent volume, D is the bed diameter, ϕ_s is the particle sphericity, and d_n is the diameter of a sphere with equivalent projected area. For fluid beds with isometric particles, equation (107) can bed simplified to

$$K_1 = \left(\frac{1}{3} + \frac{2}{3}\phi_s^{-1/2}\right)^{-1} \quad (111)$$

since the ratio of particle diameter to bed diameter is very small.

Equation (106) developed by Ganser provides a simple and accurate formula for predicting drag for spherical and nonspherical particles and will be used in this Thesis for the prediction of drag on non-spherical particles. For suspensions of nonspherical particles, the following methodology is used:

1. Assume a value for u_ϕ/u_t
2. Calculate Re_{u_ϕ, d_p} from equation (90)
3. Calculate C_{D_ϕ} from equation (93)
4. Calculate C_{D_ϕ} from

$$\frac{C_{D_\phi}}{K_2} = \frac{24}{Re_{u_\phi, d_p} K_1 K_2}\left[1 + 0.1118\left(Re_{u_\phi, d_p} K_1 K_2\right)^{0.6567}\right] + \frac{0.4305}{1 + \frac{3305}{Re_{u_\phi, d_p} K_1 K_2}}$$

$$K_1 = \left(\frac{1}{3} + \frac{2}{3}\phi_s^{-1/2}\right)^{-1}$$

$$K_2 = 10^{\left(1.8148\left[\log(\phi_s)\right]^{0.5743}\right)}$$

5. Compare the values of C_{D_ϕ} from step 3 with that from step 4. Adjust the guess for u_ϕ/u_t as necessary until convergence

Figure 9 shows a comparison of the single particle drag expression for particles with a sphericity of 1.0 and 0.8 where the voidage is 1.0. Figure 10 shows a comparison of the drag coefficient for a particle with a sphericity of 0.8 for voidages of 1, 5 and 10 percent. Figures 9 and 10 indicate that at the lower Reynolds number, it is the voidage effect which causes the deviation from the standard single particle drag, while at higher Reynolds numbers, it is the sphericity effect which dominates. For Reynolds number typical in CFB's (on the order of 10 -20), both effects contribute to the deviation, although at lower voidages, the sphericity effect is larger.

Figure 9
Drag Coefficient vs Particle Reynolds Number for Different Sphericities

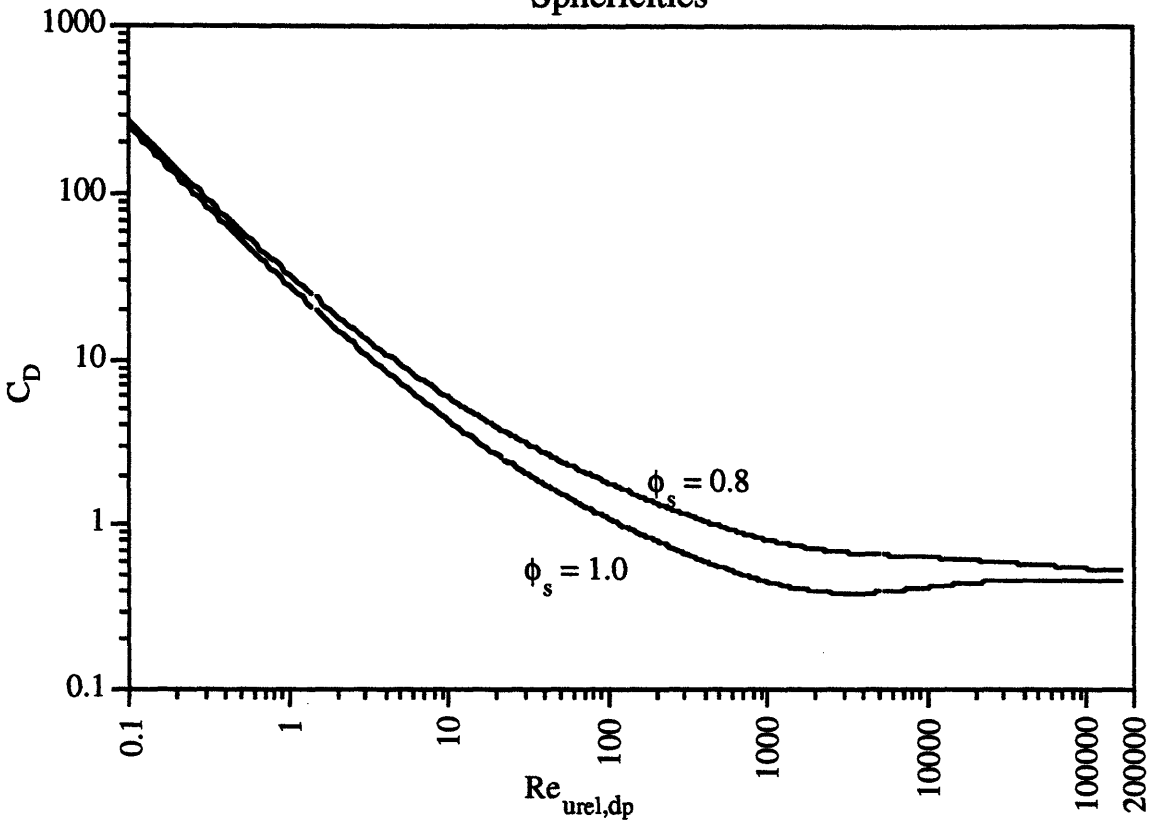

Figure 10
Drag Coefficient vs Particle Reynolds Number for Different Voidages

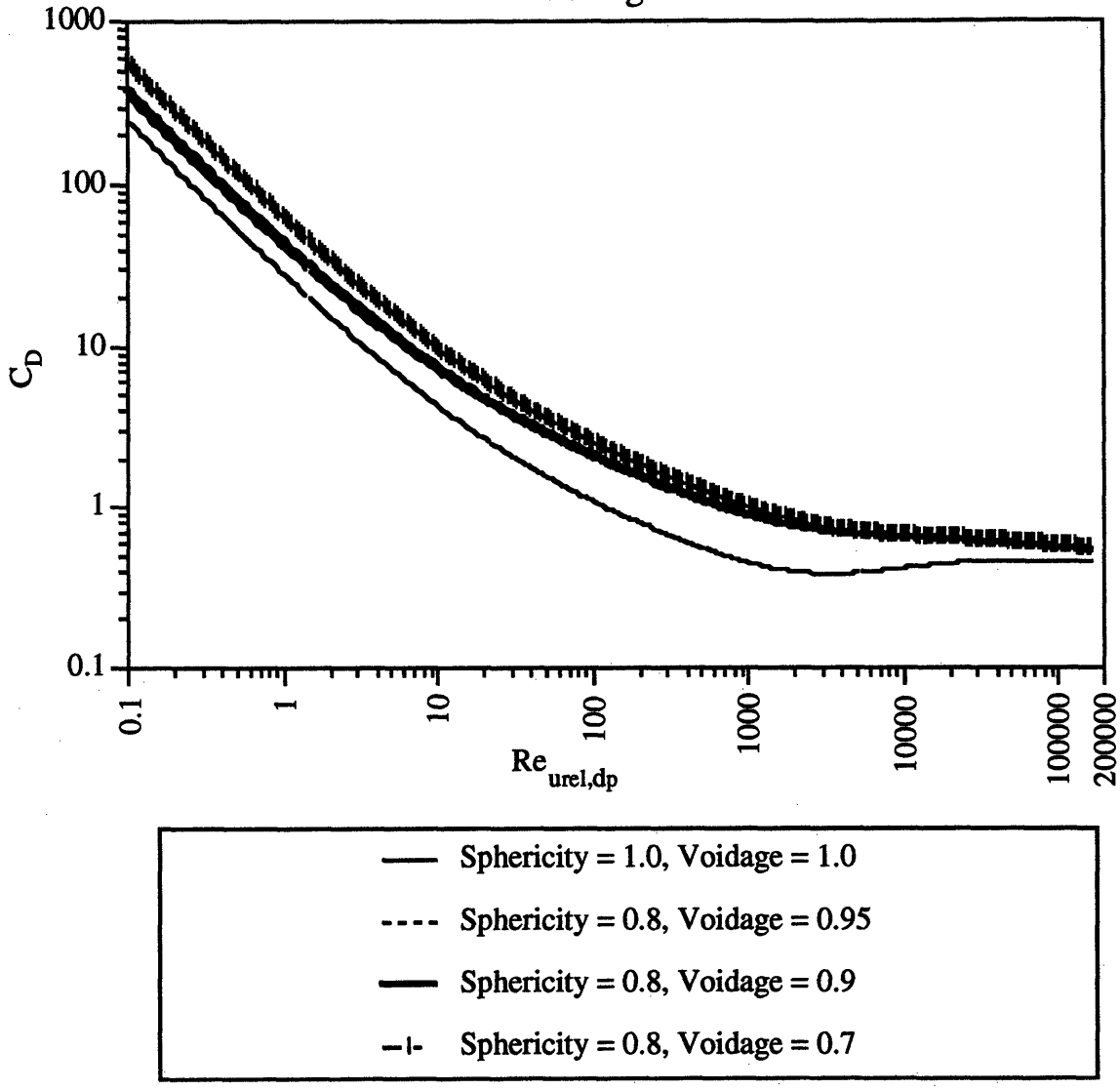

Corrections to the drag coeffcient due to voidage and sphericity may seem to be insignificant in view of the overall model. However, it must be kept in mind that thousands of particle are tracked through hundreds of thousands of interactions. Small errors in the expression for the particle equation of motion tend to amplify themselves. On the other hand, errors in such items as the end conditions and entrainment rate models are not amplified from the cumulative effect of millions of interations between particles and eddys since they are not used in the dispersion calculation - rather they are used once in the overall balance equations. Therefore, while corrections to the drag are small, they can have a

significant effect on the calculated dispersion coefficient - and hence the average solid fraction profile.

4.0 OVERALL CFB HYDRODYNAMIC MODEL

The model described above allows for the prediction of the axial distribution of the disperse phase in the core of a CFB. To complete the hydrodynamic model, equations will be written for the core/annulus structure observed in the fast fluidization regime. According to this model, flow is upward in the core and downward in the annulus. The net solid flow is equal to the upward flow in the core minus the downward flow in the annulus. The core flow is described as dilute pneumatic transport flow and is given as the solution of the radially averaged 2-D dispersion equation as solved above. The characteristics of the annulus flow are determined through the solution of the equations of mass and momentum for the particles and the gas for the annular and core regions.

4.1 Development of the Mass and Momentum Equations for the Core and Annulus

Before writing the equations of mass and momentum, the assumptions upon which they are based are given:

1. The flow riser is divided into two regions, a dilute upward flowing core, and a dense downward flowing annulus

2. The core region consists of a dilute up-flowing suspension of dispersed phase particles traveling upward at a velocity of u_{c_s} and solids volume fraction ε_{c_s}

3. The annulus region consists of a downward flowing suspension with a velocity u_{a_s}, and solids volume fraction ε_{a_s}

4. All the gas flows upward in the core at a velocity u_{c_f} - the gas flow in the annulus can be neglected

5. There is a negligible radial variation in the velocity across the core and the annulus

6. The solids volume fraction in the core is small, such that the slip velocity between the gas and solids phase is equal to the particle terminal velocity.

Where the terminal velocity is corrected for the particle sphericity and core solids fraction.

7. The gas velocity in the core is much greater than the particle terminal velocity such that the slip velocity between the particles and gas is small

8. Inlet effects are small. The pressure drop due to the initial acceleration of the particles is negligible compared to the overall pressure drop.

9. Gas/wall frictional effects are small

10. Gas momentum flux is small compared to the particle momentum flux

11. The pressure is uniform across the riser cross-section.

Of the above assumptions, numbers (2), (3), (5) and (7) are the most questionable. Regarding (2), (3), and (5), it is well known that there is a radial variation in gas and particle velocity, and average solid fraction in a CFB. However, most studies indicate that the radial variations *within* the downward flow wall layer (annulus layer) and the upward core region are small compared with the change between the two regions.

With regard to assumption (7), in a CFB operating at 12 atmospheres and 1100K with 200 micron particles, the particle terminal velocity is about 0.50 m/s. The gas velocity is typically of the order of 4.0 m/s. Thus, the terminal velocity is generally less than 20 percent of the superficial velocity for typical conditions in a pressurized CFB. In an atmospheric CFB, the terminal velocity would be about 0.8 m/s. In this case, the terminal velocity is still less than 20 percent of the superficial velocity. It seems reasonable, therefore, that for modest particle sizes and superficial velocities normally seen in commercial CFB's, assumption (7) holds.

With these assumptions, the mass conservation equations for the core and annular regions can be written starting with the equations developed by Hinze (1962) who considered the effects of suspended discrete particles as external forces acting on the continuous phase. Hinze developed mechanical energy and momentum balance equations for a flowing suspension. The corresponding equations for turbulent flow were obtained by applying Reynolds' procedure. The general equations were then applied to the case of vertical

upward flow through a tube of uniform, circular cross-section. In the case of a core-annular structure, the equations for mass and momentum are:

Particles in the core

$$\rho_s \frac{d\left(u_{c_s}\phi_{c_s}\frac{D_c^2}{D^2}\right)}{dz} = -\frac{1}{A}\left(\frac{d\dot{m}_{c\to a}}{dz} - \frac{d\dot{m}_{a\to c}}{dz}\right) \tag{1}$$

Particles in the annulus

$$\rho_s \frac{d\left(u_{a_s}\phi_{a_s}\left(1-\frac{D_c^2}{D^2}\right)\right)}{dz} = \frac{1}{A}\left(\frac{d\dot{m}_{c\to a}}{dz} - \frac{d\dot{m}_{a\to c}}{dz}\right) \tag{2}$$

Gas in the core

$$\rho_f \frac{d\left(u_{c_f}\left(1-\phi_{c_s}\right)\frac{D_c^2}{D^2}\right)}{dz} = 0 \tag{3}$$

In the above equations, $\frac{d\dot{m}_{c\to a}}{dz}$ represents the mass transfer rate from the core to the annulus, and $\frac{d\dot{m}_{a\to c}}{dz}$ represents the mass transfer rate from the annulus to the core. D_c is the diameter of the core region, D is the CFB riser diameter, A_c is the core area, A is the riser area, and ϕ represents volumetric solids fraction.

Similarly, the momentum equations can be written as

Particles in the core

$$\rho_s \frac{d\left(u_{c_s}^2 \phi_{a_s}\left(\frac{D_c^2}{D^2}\right)\right)}{dz} + \rho_s\left(\frac{D_c^2}{D^2}\right)\phi_{c_s} g + \frac{4\tau_{c \leftrightarrow a}}{\sqrt{\frac{D_c^2}{D^2}}\, D} + \left(\frac{D_c^2}{D^2}\right)\frac{dP}{dz} + \frac{1}{A}\left(u_{c_s}\frac{d\dot{m}_{c \to a}}{dz} - u_{a_s}\frac{d\dot{m}_{a \to c}}{dz}\right) = 0 \tag{4}$$

Particles in the annulus

$$\rho_s \frac{d\left(u_{a_s}^2 \phi_{a_s}\left(1 - \frac{D_c^2}{D^2}\right)\right)}{dz} + \rho_s\left(1 - \frac{D_c^2}{D^2}\right)\phi_{a_s} g - \frac{4\tau_{c \leftrightarrow a}}{\sqrt{\frac{D_c^2}{D^2}}\, D} - \frac{4\tau_{a \leftrightarrow w}}{D} + \left(1 - \frac{D_c^2}{D^2}\right)\frac{dP}{dz} - \frac{1}{A}\left(u_{c_s}\frac{d\dot{m}_{c \to a}}{dz} - u_{a_s}\frac{d\dot{m}_{a \to c}}{dz}\right) = 0 \tag{5}$$

In the momentum equations, $\tau_{c \leftrightarrow a}$ represents the core-annulus interfacial shear, and $\tau_{a \leftrightarrow w}$ represents the annulus-wall shear.

Defining

$$K_1 = \frac{1}{A\rho_s}\left(\frac{d\dot{m}_{c \to a}}{dz} - \frac{d\dot{m}_{a \to c}}{dz}\right) \tag{6}$$

and using of the chain rule, the core mass balance equations become

$$\frac{d\phi_{c_s}}{dz}\left(u_{c_s}\frac{D_c^2}{D^2}\right) + \frac{d\left(\frac{D_c^2}{D^2}\right)}{dz}\left(u_{c_s}\phi_{c_s}\right) + \frac{du_{c_s}}{dz}\left(\frac{D_c^2}{D^2}\phi_{c_s}\right) = K_1 \tag{7}$$

and

$$\frac{d\left(\phi_{c_s}\right)}{dz}\left(u_{c_s}\frac{D_c^2}{D^2}\right) + \frac{d\left(\frac{D_c^2}{D^2}\right)}{dz}\left(u_{c_s}\left(1 - \phi_{c_s}\right)\right) + \frac{du_{c_s}}{dz}\left(\frac{D_c^2}{D^2}\left(1 - \phi_{c_s}\right)\right) = 0 \tag{8}$$

The annulus mass balance equation is

$$\frac{d\phi_{a_s}}{dz}\left(u_{a_s}\left[1-\frac{D_c^2}{D^2}\right]\right)-\frac{d\left(\frac{D_c^2}{D^2}\right)}{dz}\left(u_{a_s}\phi_{a_s}\right)+\frac{du_{a_s}}{dz}\left(\left[1-\frac{D_c^2}{D^2}\right]\phi_{a_s}\right)=-K_1 \tag{9}$$

Similarly, expanding the momentum equations using the chain rule gives:

Particle core momentum

$$\begin{aligned}&\rho_s\frac{d\left[\frac{D_c^2}{D^2}\right]}{dz}\left(u_{c_s}^2\phi_{c_s}\right)+2\rho_s\frac{du_{c_s}}{dz}\left(u_{c_s}\phi_{c_s}\left[\frac{D_c^2}{D^2}\right]\right)+\rho_s\frac{d\phi_{c_s}}{dz}\left(\left[\frac{D_c^2}{D^2}\right]u_{c_s}^2\right)\\&+\left[\frac{D_c^2}{D^2}\right]\phi_{c_s}\rho_s g+\frac{4\tau_{c\leftrightarrow a}}{\sqrt{\left[\frac{D_c^2}{D^2}\right]}D}+\left[\frac{D_c^2}{D^2}\right]\frac{dP}{dz}\\&+\frac{1}{A}\left[u_{c_s}\frac{d\dot{m}_{c\to a}}{dz}-u_{a_s}\frac{d\dot{m}_{a\to c}}{dz}\right]=0\end{aligned} \tag{10}$$

Particle annulus momentum

$$\begin{aligned}&-\rho_s\frac{d\left[\frac{D_c^2}{D^2}\right]}{dz}\left(u_{a_s}^2\phi_{a_s}\right)+2\rho_s\frac{du_{a_s}}{dz}\left(u_{a_s}\phi_{a_s}\left[\frac{D_c^2}{D^2}\right]\right)+\rho_s\frac{d\phi_{a_s}}{dz}\left(\left[\frac{D_c^2}{D^2}\right]u_{a_s}^2\right)\\&+\left[1-\frac{D_c^2}{D^2}\right]\phi_{a_s}\rho_s g-\frac{4\tau_{c\leftrightarrow a}}{\sqrt{\left[\frac{D_c^2}{D^2}\right]}D}-\frac{4\tau_{a\leftrightarrow w}}{D}+\left[1-\frac{D_c^2}{D^2}\right]\frac{dP}{dz}\\&-\frac{1}{A}\left[u_{c_s}\frac{d\dot{m}_{c\to a}}{dz}-u_{a_s}\frac{d\dot{m}_{a\to c}}{dz}\right]=0\end{aligned} \tag{11}$$

(7) through (11) represent the governing equations of the core-annulus model. The unknowns are $\frac{D_c^2}{D^2}$, u_{a_s}, u_{c_s}, ϕ_{a_s}, ϕ_{c_s}, and $\frac{dP}{dz}$. The solutions of the two-dimensional

dispersion equation gives the results for ϕ_{c_s}. Thus the problem reduces to the solution of five differential equations for the variables $\frac{D_c^2}{D^2}$, u_{a_s}, u_{c_s}, ϕ_{a_s}, and $\frac{dP}{dz}$.

After considerable algebraic manipulation and defining the variable

$$\gamma = \left[u_{c_s} \frac{d\dot{m}_{c \to a}}{dz} - u_{a_s} \frac{d\dot{m}_{a \to c}}{dz} \right] \tag{12}$$

the equations for the differentials of the five variables can be written as

$$\begin{aligned} \frac{dP}{dz} &= -\rho_s u_{c_s} \phi_{c_s} \frac{du_{c_s}}{dz} - \frac{\rho_s u_{c_s}^2}{\left(1-\phi_{c_s}\right)} \frac{d\phi_{c_s}}{dz} - \phi_{c_s} \rho_s g \\ &- \frac{4\tau_{c \leftrightarrow a}}{\sqrt{\frac{D_c^2}{D^2}} \frac{D_c^2}{D}} - \frac{\gamma}{A \frac{D_c^2}{D^2}} \end{aligned} \tag{13}$$

$$\begin{aligned} \frac{du_{a_s}}{dz} &= \frac{d\phi_{c_s}}{dz} \left[\frac{u_{a_s}}{\left(1-\phi_{c_s}\right)} \left(1 - \frac{\frac{D_c^2}{D^2}}{\left(1-\frac{D_c^2}{D^2}\right)} \right) \right] + \frac{u_{c_s}^2}{u_{a_s}\left(1-\phi_{c_s}\right)} \frac{\left(1-\frac{D_c^2}{D^2}\right)}{\phi_{a_s}} \\ &+ \frac{du_{c_s}}{dz} \left[\frac{u_{a_s}}{u_{c_s}} \left(-1 + \frac{\frac{D_c^2}{D^2}}{\left(1-\frac{D_c^2}{D^2}\right)} \right) + \frac{u_{c_s} \phi_{c_s}}{u_{a_s} \phi_{a_s}} \frac{\left(1-\frac{D_c^2}{D^2}\right)}{\frac{D_c^2}{D^2}} \right] \\ &+ \frac{K_1}{\left(1-\frac{D_c^2}{D^2}\right)\phi_{a_s}} + \frac{\left(1-\frac{D_c^2}{D^2}\right)}{\frac{D_c^2}{D^2}} \frac{g}{u_{a_s}} \left[\frac{\phi_{c_s}}{\phi_{a_s}} - 1 \right] \\ &- \frac{4\tau_{c \leftrightarrow a}}{\sqrt{\frac{D_c^2}{D^2}} D \rho_s u_{a_s} \left(\frac{D_c^2}{D^2}\right)^2 \phi_{a_s}} + \frac{4\tau_{a \leftrightarrow w}}{D \rho_s u_{a_s} \left(\frac{D_c^2}{D^2}\right) \phi_{a_s}} \\ &+ \frac{\gamma}{A \left(\frac{D_c^2}{D^2}\right)^2 \rho_s u_{a_s} \phi_{a_s}} \end{aligned} \tag{14}$$

$$\frac{d\phi_{a_s}}{dz} =$$

$$\frac{d\phi_{c_s}}{dz}\left[\frac{\dfrac{D_c^2}{D^2}}{\left(1-\dfrac{D_c^2}{D^2}\right)}\frac{\phi_{a_s}}{\left(1-\phi_{c_s}\right)} - \frac{\phi_{a_s}}{\left(1-\phi_{c_s}\right)}\left(1-\frac{\dfrac{D_c^2}{D^2}}{\left(1-\dfrac{D_c^2}{D^2}\right)}\right)\right] - \frac{u_{c_s}^2}{u_{a_s}\left(1-\phi_{c_s}\right)}\left(1-\frac{D_c^2}{D^2}\right)$$

$$+\frac{du_{c_s}}{dz}\left[\frac{\dfrac{D_c^2}{D^2}}{\left(1-\dfrac{D_c^2}{D^2}\right)}\frac{\phi_{a_s}}{u_{c_s}} + \frac{\phi_{a_s}}{u_{c_s}}\left(-1+\frac{\dfrac{D_c^2}{D^2}}{\left(1-\dfrac{D_c^2}{D^2}\right)}\right) + \frac{u_{c_s}}{u_{a_s}^2}\phi_{c_s}\frac{\left(1-\dfrac{D_c^2}{D^2}\right)}{\dfrac{D_c^2}{D^2}}\right]$$

$$-\frac{2K_1}{\left(1-\dfrac{D_c^2}{D^2}\right)u_{a_s}} - \frac{\left(1-\dfrac{D_c^2}{D^2}\right)}{\dfrac{D_c^2}{D^2}}\frac{g\phi_{a_s}}{u_{a_s}}\left[\frac{\phi_{c_s}}{\phi_{a_s}}-1\right]$$

$$-\frac{4\tau_{c\leftrightarrow a}}{\sqrt{\dfrac{D_c^2}{D^2}}\,D\rho_s u_{a_s}^2\left(\dfrac{D_c^2}{D^2}\right)^2} - \frac{4\tau_{a\leftrightarrow w}}{D\rho_s u_{a_s}^2\left(\dfrac{D_c^2}{D^2}\right)} \qquad (15)$$

$$+\frac{\gamma}{A\left(\dfrac{D_c^2}{D^2}\right)^2\rho_s u_{a_s}^2 u_{a_s}}$$

$$\frac{d\left(\dfrac{D_c^2}{D^2}\right)}{dz} = \frac{d\phi_{c_s}}{dz}\frac{\left(\dfrac{D_c^2}{D^2}\right)}{\left(1-\phi_{c_s}\right)} - \frac{du_{c_s}}{dz}\frac{\left(\dfrac{D_c^2}{D^2}\right)}{u_{c_s}} \qquad (16)$$

and

$$\frac{du_{c_s}}{dz} = \frac{K_1\left(1-u_{c_s}\right)\left(\dfrac{d\phi_{c_s}}{dz}\right)}{\left(\dfrac{D_c^2}{D^2}\right)\left(\dfrac{d\phi_{c_s}}{dz}\right) - \left(1-\phi_{c_s}\right)K_1} \qquad (17)$$

4.2 Initial Conditions

Equations (13) through (17) are integrated from the top of the bed to the bottom. The values of $\frac{D_c^2}{D^2}$, u_{a_s}, u_{c_s}, ϕ_{a_s}, and $\frac{dP}{dz}$ at the bed exit must be specified.

To estimate the core diameter at the exit of the bed, assume that any particles not swept from the riser form the annulus, similar to the assumption made by Harris and Davidson (1993).

The core diameter and solid fraction at the riser is then estimated as follows. The solids circulation rate is

$$G_s = \rho_s u_{c_{s_{exit}}} \left(\left(\frac{D_c^2}{D^2} \right)_{exit} \phi_{c_{s_{exit}}} - \left(1 - \left(\frac{D_c^2}{D^2} \right)_{exit} \right) \phi_{a_{s_{exit}}} \right) \tag{18}$$

The solids velocity at the exit can be written as

$$u_{c_{s_{exit}}} = \frac{u_o}{\left[\left(\frac{D_c^2}{D^2} \right)_{exit} \left(1 - \phi_{c_{s_{exit}}} \right) \right]} \tag{19}$$

This allows the solids circulation rate to be rewritten

$$G_s = \frac{\rho_s u_o}{\left[\left(\frac{D_c^2}{D^2} \right)_{exit} \left(1 - \phi_{c_{s_{exit}}} \right) \right]} \left(\left(\frac{D_c^2}{D^2} \right)_{exit} \phi_{c_{s_{exit}}} - \left(1 - \left(\frac{D_c^2}{D^2} \right)_{exit} \right) \phi_{a_{s_{exit}}} \right) \tag{20}$$

G_S is also equal to

$$G_s = \rho_s \eta' u_{c_{s_{exit}}} \phi_{c_{s_{exit}}} \left(\frac{D_c^2}{D^2} \right)_{exit} \tag{21}$$

where η' is defined as:

$$\eta' = \left(\frac{D_{exit}^2}{D_c^2}\right)_{exit} \simeq \frac{\left(D_c(1-\eta) + \eta D_{exit}\right)^2}{D_c^2} \tag{22}$$

and η is the collection efficiency of the riser exit.

From (21), the core solid fraction at the riser exit is

$$\phi_{a_{s_{exit}}} = \frac{G_s\left(\frac{D_{exit}^2}{D_c^2}\right)_{exit}}{\eta'' \rho_s u_o + G_s\left(\frac{D_{exit}^2}{D_c^2}\right)_{exit}} \tag{23}$$

where

$$\eta'' = \simeq \frac{\left(D_c(1-\eta) + \eta D_{exit}\right)^2}{D^2} \tag{24}$$

$$\frac{\eta'}{\eta''} = \frac{D^2}{D_{\hat{e}_{exit}}^2} \tag{24a}$$

Eliminating $u_{c_{s exit}}^2$ from (21) and (19), and using (22), (23), and (24a) gives

$$G_s\left(\frac{D_{exit}^2}{D_{\hat{e}}^2}\right)_{exit} - \frac{G_s^2\left(\frac{D_{exit}^2}{D_c^2}\right)_{exit}^2}{\rho_s \eta'' u_o + G_s\left(\frac{D_{exit}^2}{D_c^2}\right)_{exit}} = \frac{G_s \rho_s u_o \left(\frac{D_{exit}^2}{D_c^2}\right)_{exit}^2}{\rho_s \eta'' u_o + G_s\left(\frac{D_{exit}^2}{D_c^2}\right)_{exit}}$$
$$- \rho_s u_o \phi_{a_{s_{exit}}} + \rho_s u_o \phi_{a_{s_{exit}}} \left(\frac{D_{exit}^2}{D_c^2}\right)_{exit} \tag{25}$$

$$G_s\left(\frac{D_{exit}^2}{D_c^2}\right)_{exit} \eta'' \rho_s u_o + G_s\left(\frac{D_{exit}^2}{D_c^2}\right)_{exit}^2 - G_s\left(\frac{D_{exit}^2}{D_c^2}\right)_{exit}^2 =$$
$$\rho_s u_o G_s\left(\frac{D_{exit}^2}{D_c^2}\right)_{exit}^2 - \eta'' \rho_s^2 u_o^2 \phi_{a_{s_{exit}}} - \rho_s u_o \phi_{a_{s_{exit}}} G_s\left(\frac{D_{exit}^2}{D_c^2}\right)_{exit} \tag{26}$$
$$\eta'' \rho_s^2 u_o^2 \phi_{a_{s_{exit}}} \left(\frac{D_{exit}^2}{D_{\hat{e}}^2}\right)_{exit} + \rho_s u_o G_s \left(\frac{D_{exit}^2}{D_{\hat{e}}^2}\right)_{exit}^2 \phi_{a_{s_{exit}}}$$

Dividing by $G_s\eta^*\rho_s u_o$ and rearranging results in a second order equation for $\left(\frac{D_{exit}^2}{D_c^2}\right)_{exit}$

$$\left(\frac{D_{exit}^2}{D_c^2}\right)^2_{exit}\left[\frac{G_s\left(\phi_{a_{s_{exit}}}+1\right)}{\eta^*}\right]+\left(\frac{D_{exit}^2}{D_c^2}\right)_{exit}\left[\phi_{a_{s_{exit}}}\rho_s u_o - G_s - \frac{G_s\phi_{a_{s_{exit}}}}{\eta^*}\right] - \phi_{a_{s_{exit}}}u_o\rho_s = 0 \tag{27}$$

where it can be shown that

$$\eta^* \equiv \frac{\left[D_c\left(1-\eta\right)+\eta D_{outlet}\right]^2}{D^2} \tag{28}$$

The voidage at the exit in the core is given from (23), i.e.

$$\phi_{c_{s_{exit}}} = \left[\frac{G_s\left(\frac{D_{exit}^2}{D_c^2}\right)_{exit}}{\eta^* u_o\rho_s + G_s\left(\frac{D_{exit}^2}{D_c^2}\right)_{exit}}\right] \tag{29}$$

The voidage in the annulus can be estimated from the correlations given in Chapter 3 (heat transfer enhancement section) of this thesis

$$\phi_{f_{s_{exit}}} = \sqrt{\phi_{c_{s_{exit}}}} \times\left\{1-\exp\left[-0.01\left(\frac{u_o}{u_{mf}}\right)^{-1/4}\left(\frac{\rho_s}{\rho_f}\right)^{3/4}Fr_D^{-1/3}Ar^{-1/4}\phi_{c_{s_{exit}}}\right]\right\} \tag{30}$$

where

$$u_{mf} \simeq \left(\frac{600 g\rho_s d_p^2}{\mu}\right) \tag{31}$$

If one assumes elastic collisions at the riser exit

$$u_{a_{s_{exit}}} \simeq -u_{c_{s_{exit}}} \tag{32}$$

where

$$u_{c_{s_{exit}}} \cong \frac{u_o}{\left(\frac{D_c^2}{D^2}\right)\left(1-\phi_{c_{s_{exit}}}\right)} \tag{33}$$

Equations (27), (29), (30), (32), and (33) are the initial conditions for $\frac{D_c^2}{D^2}$, $\phi_{c_{s_{exit}}}$, $\phi_{a_{s_{exit}}}$, $u_{a_{s_{exit}}}$, and $u_{c_{s_{exit}}}$ respectively.

4.3 Collection Efficiency of Exit

The riser exit is modeled using the impact separator theory method described Harris et al., (1994). The geometry of the bed exit is approximated as a flat end plate with a central circular orifice. The collection efficiency is defined for two dimensional motion as the ratio of the dimension within which particles will be retained in the riser (x_1) to the dimension of the exposed end flange (x_2). The dependence of η on particle density, diameter, and fluid velocity is given in Perry *et al.* (1984) as a function of the separation number

$$N_s = \frac{\rho_s d_p u_{c_s}}{18\mu x_2} \tag{34}$$

Perry *et al.* (1984) give plots of the collection efficiency as a function of the separation number using impact separator theory. Once the collection efficiency of the exit is specified, the core solid fraction profile can be calculated. The core solid fraction at the bottom of the riser is selected to give a solid fraction at the riser exit equal to that calculated from (27).

4.4 Determination of $\frac{d\dot{m}_{c\to a}}{dz} - \frac{d\dot{m}_{a\to c}}{dz}$

The core to annulus deposition rate is determined from the two-dimensional dispersion equation described in Section 2. The solution of the 2-D dispersion equation given in Section 2, provides an expression for the cross-sectionally averaged dilute core

concentration as a function of bed height, C(z). Using this concentration profile, a mass balance can be written

$$\frac{dC(z)}{dz} = \frac{4k_D}{Du_{c_s}}C(z) \tag{35}$$

where k_D is the well known deposition velocity.

Rearranging (35) to solve for k_D gives

$$k_D = \frac{Du_{c_s}\dfrac{dC(z)}{dz}}{4C(z)} \tag{36}$$

This allows $\frac{d\dot{m}_{c\to a}}{dz} - \frac{d\dot{m}_{a\to c}}{dz}$ to be written as

$$\frac{d\dot{m}_{c\to a}}{dz} - \frac{d\dot{m}_{a\to c}}{dz} = \left[D\left(\frac{D_c^2}{D^2}\right)^2 \rho_s \phi_{c_s} k_D\right] \tag{37}$$

$$\frac{d\dot{m}_{c\to a}}{dz} - \frac{d\dot{m}_{a\to c}}{dz} = \left[\frac{\pi D^2\left(\dfrac{D_c^2}{D^2}\right)^2 \rho_s \phi_{c_s} u_{c_s}\dfrac{dC(z)}{dz}}{4C(z)}\right] \tag{38}$$

where $\frac{dC(z)}{dz}$ is determined from the dispersion model given in Section 2.

4.5 Determination of $\tau_{a\leftrightarrow w}$

The shear stress between the wall and the annular layer is approximated from the expression developed by Stemerding (1962) for shear stresses in suspensions:

$$\tau_{a\leftrightarrow w} = \frac{f_p \phi_{a_s} \rho_s u_{a_s}^2}{2} \tag{39}$$

where

$$f_p = a\left|u_{a_s}\right|^b \tag{40}$$

For dense suspensions

$$a = 0.003 \tag{41}$$

and

$$b = 0.0 \tag{42}$$

so that

$$\tau_{a\leftrightarrow w} = \frac{0.003\phi_{a_s}\rho_s u_{a_s}^2}{2} \tag{43}$$

This correlation was developed for FCC reactors under condtions similar to that found in CFB combustors (cross-sectionally averaged solid fractions ranged from 1 to 10 percent, superficial gas velocities ranged from 5 to 10 m/s, and the particles were FCC catalyst with a mean particle diameter of 65 microns).

4.6 Determination of $\tau_{c\leftrightarrow a}$

To approximate the interfacial shear stress between the annulus and the core, the results from gas/liquid two-phase flow modified for gas/solid flows is used. From Hewitt and Hall-Taylor (1970),

$$\tau_{c\leftrightarrow a} = C_{c\leftrightarrow a}\phi_{c_s}\rho_s\left(u_{c_s} - u_{a_s}\right)^2 \tag{44}$$

where

$$C_{c\leftrightarrow a} = 0.079\mathrm{Re}_c^{-1/4}\left(1 + 180\left(1 - \sqrt{\frac{D_c^2}{D^2}}\right)\right) \tag{45}$$

and

$$Re_c = \frac{\left[\phi_{c_s}\rho_s + \left(1-\phi_{c_s}\right)\rho_f\right] u_{c_s} D \sqrt{\left(\frac{D_c^2}{D^2}\right)}}{\mu} \tag{46}$$

The simulations were found to be insensitive to the cofficient used for the equation for the gas/wall shear stress. This supports the results of Ishii *et al.* (1989) who found that the wall-gas shear stress can be neglected.

5.0 RADIAL PARTICLE DISTRIBUTION IN DILUTE REGIONS OF CIRCULATING FLUIDIZED BEDS

If the flow in the upper regions of CFB's is dilute, one should be able to estimate the radial distribution of particles through a solution of the hydrodynamic relationships underlying low Reynolds number phenomena involving particles suspended in a fluid. The gas equation of motion can be employed in conjunction with spherical shaped particles in a tube to form an idealized system for mathematical analysis. In the following treatment the simplest possible approximation is explored as a means of relating the phenomena of fluidization and pneumatic conveying. It will be expected to apply only in dilute systems, but it is in these regimes that the necessary boundary surface which laterally confines any actual bed is of greatest importance.

Attention is confined to the purely hydrodynamic aspects of the behavior of the particulate systems involved. Approximations are presented for the effect of the various parameters involved on the particle velocities and spatial distribution of particles as well as the pressure drop experienced by passage of fluid. For any given system these parameters include the physical dimensions of spheres and cylinder, the specific gravity of the spheres, the viscosity and specific gravity of the fluid, fluid velocity, and geometrical distribution of particles entering the system. Only hydrodynamic forces are considered though in some cases inter particle friction and electrostatic effects may assume great importance. The treatment here should furnish a framework for further studies on systems possibly included heat, mass transfer, and chemical reaction effects

5.1 Model Formulation

The procedure adopted here is to develop the behavior of a single sphere in a cylinder and then to extend the treatment to more complicated cases involving more than one sphere. In order to furnish a suitable basis the case must be treated for a sphere which is free to occupy any position in a tube. Previously [Happel and Brenner (1963)] the behavior of a single sphere suspended at the axis of a cylindrical tube was treated. The sphere moves with an arbitrary constant velocity v_p relative to the cylinder wall in the direction parallel to the cylinder wall (Z direction), while the fluid flow is turbulent with a velocity V_{max} (with respect to the cylinder wall) at the axis of the cylinder at a sufficiently great distance from the sphere. The sphere radius is 'a', the cylinder radius is 'R'.

The equations of motion to be satisfied are, in vector notation

$$(\mathbf{v}_f \cdot \nabla)\mathbf{v}_f + \nu\nabla^2\mathbf{v}_f = \frac{1}{\rho_f}\nabla p \tag{1}$$

together with the continuity equation for incompressible fluids

$$\nabla \cdot \mathbf{v}_f = 0 \tag{2}$$

where $\mathbf{v}_f$ is the fluid velocity with respect to an origin which moves with the sphere. The boundary conditions which define the filed $\mathbf{v}_f$ are

$$\begin{aligned} &\mathbf{v}_f = 0 \quad \text{on the particle surface} \\ &\mathbf{v}_f = -\mathbf{i}_z V_{max} \quad \text{at} \quad r = R \end{aligned} \tag{3}$$

The fluid velocity distribution can be approximated by the data of Yang *et al.* (1993). Yang found that in the dilute regions of a CFB

$$\mathbf{v}_f = -\mathbf{i}_z\left[V_{max}\left(1-\left(\frac{r}{R}\right)^n\right)\right] - \mathbf{v}_p \tag{4}$$

The solution of this type of problem is considered by Happel and Brenner (1963) where the method of reflections is used, the solution consisting of the sum of a series of velocity fields all of which satisfy equations (1) and (2) and each partially satisfies the boundary conditions. For the present treatment, only the first reflection is considered for the velocity field and the first two reflections are considered for pressure drop. In this approximation the effect of (a/R) is not evaluated. The zeroth approximation for the drag is then

$$W = C_D\frac{\pi d_p^2}{8}\rho_f\left[V_{max}\left[1-\left(\frac{r}{R}\right)^n\right] - v_p\right]^2 \tag{5}$$

The gravity force in the direction of flow experience by a particle is

$$F_g = \frac{4\pi d_p^3}{24}(\rho_s - \rho_f)g \tag{6}$$

Assuming a form for the drag coefficient, (6) is equal to

$$C_D \frac{\pi d_p^2}{8} \rho_f u_t^2 = F_g \tag{7}$$

where u_t is the terminal velocity of the particle.

When no net force acts on the particle it will move with a constant velocity v_p, which is obtained by equating the drag and gravitational forces.

$$C_D \frac{\pi d_p^2}{8} \rho_f u_t^2 = C_D \frac{\pi d_p^2}{8} \rho_f \left[V_{max} \left[1 - \left(\frac{r}{R} \right)^n \right] - v_p \right]^2 \tag{8}$$

$$u_t^2 = \left[V_{max} \left[1 - \left(\frac{r}{R} \right)^n \right] - v_p \right]^2 \tag{9}$$

$$v_p = \left[V_{max} \left[1 - \left(\frac{r}{R} \right)^n \right] - u_t \right] \tag{10}$$

Equation (10) gives the equilibrium velocity of a particle situated at a distance r from the bed axis.

Equation (10) implies that there is a radius S [$r > S > 0$] where $v_p = 0$. Where gravitational and frictional forces exactly balance one another. Setting $v_p = 0$ and $r = S$,

$$u_t = V_{max} \left[1 - \left(\frac{S}{R} \right)^n \right] \tag{11}$$

$$\left(\frac{S}{R} \right) = \left[1 - \left(\frac{u_t}{V_{max}} \right) \right]^{\frac{1}{n}} \tag{12}$$

The region $R \geq r > S$, is the annular region where particles have a downward motion. Similarly in the inner cylindrical space where $S > r \geq 0$, the particle velocity is positive (upward). In the former case net gravitational forces exceed those due to friction, as a result of lower fluid velocity in the neighborhood of the wall accounting for the downward particle motion. The reverse effect predominates in the inner cylindrical space.

5.2 Particle Velocity Distributions

Any radial distribution of particles is possible depending on conditions prevailing at the bed entrance and exit. Now consider a case where particles at the entrance and exit conditions move independently of the fluid motion. This assumption is reasonable since the movement of particles at the top of the bed is determined, to a large extent, by the exit geometry of the bed. Moreover, movement of particles in the lower regions of the bed is more likely to be determined by interparticle collisions and gas turbulent fluctuations, than by the mean gas motion. In addition to the assertion that particles move indepently of the gas at the bed entrance and exit, assume that a particle has an equal probability of entering the outer annular space, down which particles are moving, at any point. The same reasoning applies to a particle leaving the annular space and enter the bed core. The equal distribution of particles results in a constant flux over the annular and core cross-sectional area. This assumption is supported by the solid flux data of Gidaspow et al. (1989), Hartge et al. (1988, 1986), Miller and Gidaspow (1992) and Horio (1988), who measured the vertical solids flux as a function of bed radius. These researchers report solids flux profiles which are flat in the annulus and core in the upper region of the bed. It should be noted however, that all researchers do not report a vertical flux which is independent of radial poition. Herb et al. (1992), and Bader et al. (1988) present flux profiles which are much more parabolic.

When a particle leaves the bed core and enters the wall layer, the probability that it enters area dA_a if the particles are mixed is

$$\frac{dA_a}{A_a} = \frac{r dr d\phi}{\pi\left(R^2 - S^2\right)} \tag{13}$$

The relative distribution of particles to any differential area will be given by this fraction. If v_p is the particle velocity at any point, then the average particle velocity will be obtained by summing local velocities over the total area and dividing by the total area through which they flow. For a continuous distribution

$$\bar{v}_p = \frac{\int_A v_p dA}{A} \tag{14}$$

The average velocity of fall of a particle in the annular space will be

$$\bar{V}_{a_p} = \frac{\int_0^{2\pi}\int_{r=S}^{r=R} v_p r\,dr\,d\phi}{\pi\left(R^2 - S^2\right)} \tag{15}$$

$$\bar{V}_{a_p} = \frac{-2\int_{r=S}^{r=R}\left[V_{max}\left[1-\left(\frac{r}{R}\right)^n\right]-u_t\right]r\,dr}{\left(R^2-S^2\right)} \tag{16}$$

$$\bar{V}_{a_p} = \frac{-2\left[\left(V_{max}-u_t\right)\left(\frac{R^2-S^2}{2}\right)-\frac{V_{max}}{n+2}\left(R^2-\frac{S^{n+2}}{R^n}\right)\right]}{\left(R^2-S^2\right)} \tag{17}$$

Using the equation (12)

$$\bar{V}_{a_p} = -\left(V_{max}-u_t\right)+\frac{2V_{max}}{n+2}\left[\frac{1-\left(1-\frac{u_t}{V_{max}}\right)^{\frac{(n+2)}{n}}}{1-\left(1-\frac{u_t}{V_{max}}\right)^{\frac{2}{n}}}\right] \tag{18}$$

Similarly for the core

$$\bar{V}_{c_p} = \frac{\int_0^{2\pi}\int_{r=0}^{r=S} v_p r\,dr\,d\phi}{\pi S^2} \tag{19}$$

$$\bar{V}_{c_p} = \frac{2\int_{r=0}^{r=S}\left[V_{max}\left[1-\left(\frac{r}{R}\right)^n\right]-u_t\right]r\,dr}{S^2} \tag{20}$$

$$\bar{V}_{c_p} = \left(V_{max}-u_t\right)-\frac{2V_{max}S^n}{R^n\left(n+2\right)} \tag{21}$$

$$\bar{v}_{c_p} = \left(V_{max} - u_t\right)\left(1 - \frac{1}{n+2}\right) \tag{22}$$

Equations (12), (18) and (22) predict that for a given gas velocity profile, as the terminal velocity of the particles increase, the velocity of particles in the core and the core radius decrease, while the velocity of particles in the annluar layer increase. This makes perfect sense, since if one assumes that the particle velocity is approximately the gas velocity less the particle terminal velocity, as the particle terminal velocity increases the particle velocity decreases. On the other hand, since the annular particle velocity is measured positive downward, it would increase as the particle terminal velocity is increased. Moreover, when the particle terminal velocity increases, the point at which the drag forces and the gravity forces exactly balance one another ($v_p = 0$) moves toward a higher gas velocity region, i.e. the core radius decreases. Figure 5.1 presents the variation in the core diamter along with the core and annulus velocities as a function of the ratio of terminal velocity to V_{max} for conditions typical of pressurized CFB's (n is calculated from the correlation of Yang *et al.* (1994) described below). The curves support the trends discussed above.

Figure 5.1

Particle Velocity in Core and Annulus and Core Radius vs. u_t/V_{max}

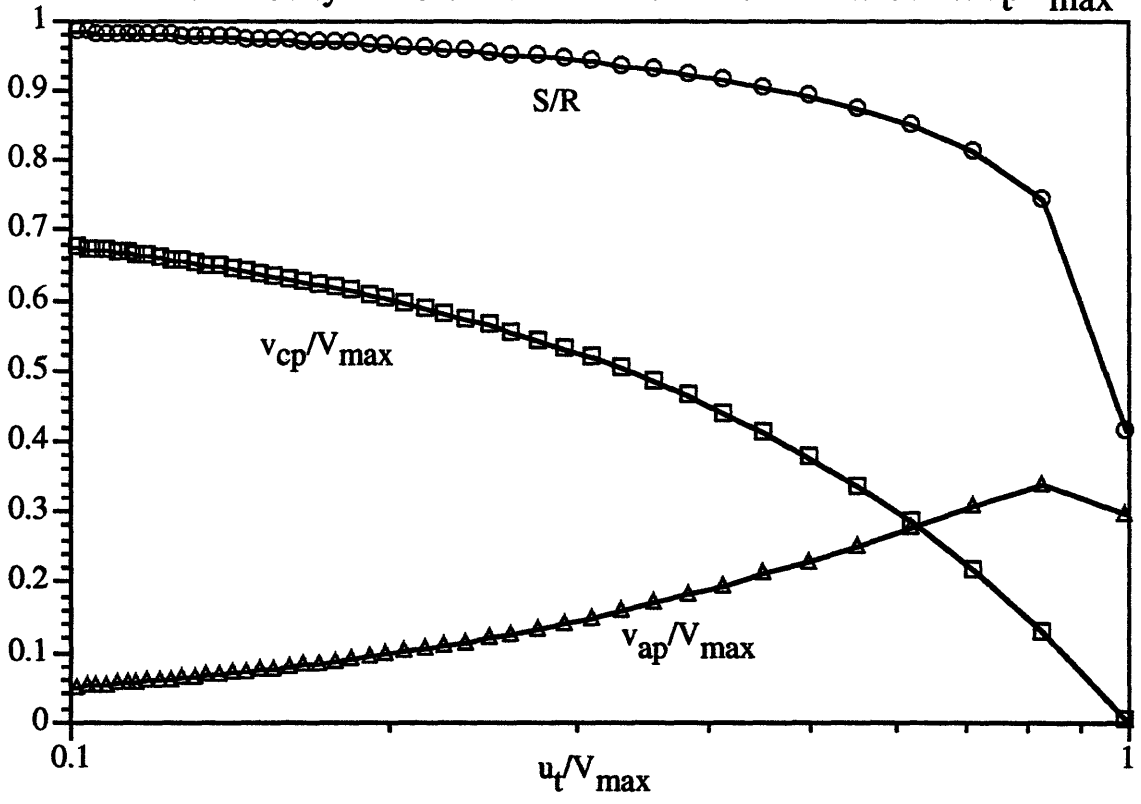

5.3 Radial Concentration Distribution

Assuming the number of particles which pass up through the core is constant and equal to ψ_c and the number of particles passing down in the annulus is ψ_a. The number of particles passing a given area per unit time divided by their average velocity will give the number of particles contained in the unit length of path. The sum of these concentrations for upward and downward flowing particles must equal the average particle content of a unit length of bed

$$\frac{\psi_a}{\bar{v}_{a_p}} + \frac{\psi_c}{\bar{v}_{c_p}} = N_m \pi R^2 \tag{23}$$

The net particle transport across the tube is

$$\psi_a + \psi_c = \psi \tag{24}$$

For a specified ψ

$$\psi_c = N_m \pi R^2 \bar{v}_{c_p} - \psi_a \frac{\bar{v}_{c_p}}{\bar{v}_{a_p}} \tag{25}$$

The inner core area may be expressed as

$$A_c = \pi S^2 = \pi R^2 \left(1 - \frac{u_t}{V_{max}}\right)^{2/n} \tag{26}$$

Therefore, the flux or number of particles per unit area per unit time passing through the core is

$$\frac{\psi_c}{A_c} = \frac{N_m \pi R^2 \bar{v}_{c_p} - \psi_a \left(\frac{\bar{v}_{c_p}}{\bar{v}_{a_p}}\right)}{\pi R^2 \left(1 - \frac{u_t}{V_{max}}\right)} = \text{const.} \tag{27}$$

Similarly, the area of the annular space is

$$A_c = \pi\left(R^2 - S^2\right) = \pi R^2\left(1 - \left(1 - \frac{u_t}{V_{max}}\right)^{2/n}\right) \tag{28}$$

and the flux through the annular region is

$$\frac{\psi_a}{A_a} = \frac{N_m \pi R^2 \bar{v}_{a_p} - \psi_c\left(\frac{\bar{v}_{a_p}}{\bar{v}_{c_p}}\right)}{\pi R^2\left(1 - \left(1 - \frac{u_t}{V_{max}}\right)^{2/n}\right)} = \text{const.} \tag{29}$$

$\frac{\psi_c}{A_c}$ and $\frac{\psi_a}{A_a}$ are constant since the equal distribution of particles implies a constant flux in both the core and annulus.

The spatial distribution of particles may now be determined by noting that the flux at a given radial location is obtained by multiplying the local particle velocity by local concentration. For the annulus this gives

$$\frac{N_m \pi R^2 \bar{v}_{a_p} - \psi_c\left(\frac{\bar{v}_{a_p}}{\bar{v}_{c_p}}\right)}{\pi R^2\left(1 - \left(1 - \frac{u_t}{V_{max}}\right)^{2/n}\right)} = n_a\left(u_t - V_{max}\left(1 - \left(\frac{r}{R}\right)^n\right)\right) \tag{30}$$

$$n_a = \frac{N_m \pi R^2 \bar{v}_{a_p} - \psi_c\left(\frac{\bar{v}_{a_p}}{\bar{v}_{c_p}}\right)}{\pi R^2\left(u_t - V_{max}\left(1 - \left(\frac{r}{R}\right)^n\right)\right)\left(1 - \left(1 - \frac{u_t}{V_{max}}\right)^{2/n}\right)} \tag{31}$$

$$R \geq r \geq S$$

and for the core gives

$$\frac{N_m \pi R^2 \bar{v}_{c_p} - \psi_a \left(\frac{\bar{v}_{c_p}}{\bar{v}_{a_p}} \right)}{\pi R^2 \left(1 - \left(1 - \frac{u_t}{V_{max}} \right)^{2/n} \right)} = n_c \left(V_{max} \left(1 - \left(\frac{r}{R} \right)^n \right) - u_t \right) \tag{32}$$

$$n_c = \frac{N_m \pi R^2 \bar{v}_{c_p} - \psi_c \left(\frac{\bar{v}_{c_p}}{\bar{v}_{a_p}} \right)}{\pi R^2 \left(V_{max} \left(1 - \left(\frac{r}{R} \right)^n \right) - u_t \right) \left(1 - \left(1 - \frac{u_t}{V_{max}} \right)^{2/n} \right)} \tag{33}$$

$$S \geq r \geq 0$$

Figure 5.2 presents the ratio of the core and annluar concentrations to the mean concentration, N_m, as a function of the dimensionless radius r/R for conditions typical of pressurized fluidized beds (n is calculated from the correlation of Yang *et al.* (1994) described below). Equations (31) and (33) predict that the radial structure consists of a dilute core region which has a fairly uniform concentration and a dense annular region. A large buildup of particles occurs at r = S (in the case of Figure 5.2, r = 0.935). This type of radial structure is consistent with what many investigators have observed in CFB's and FCC reactors [see for example, Weinstein et *al.* (1986), Horio *et al.* (1988), Hartge *et al.* (1988), Bader *et al.* (1988), and Rhodes *et al.* (1992)].

Figure 5.2

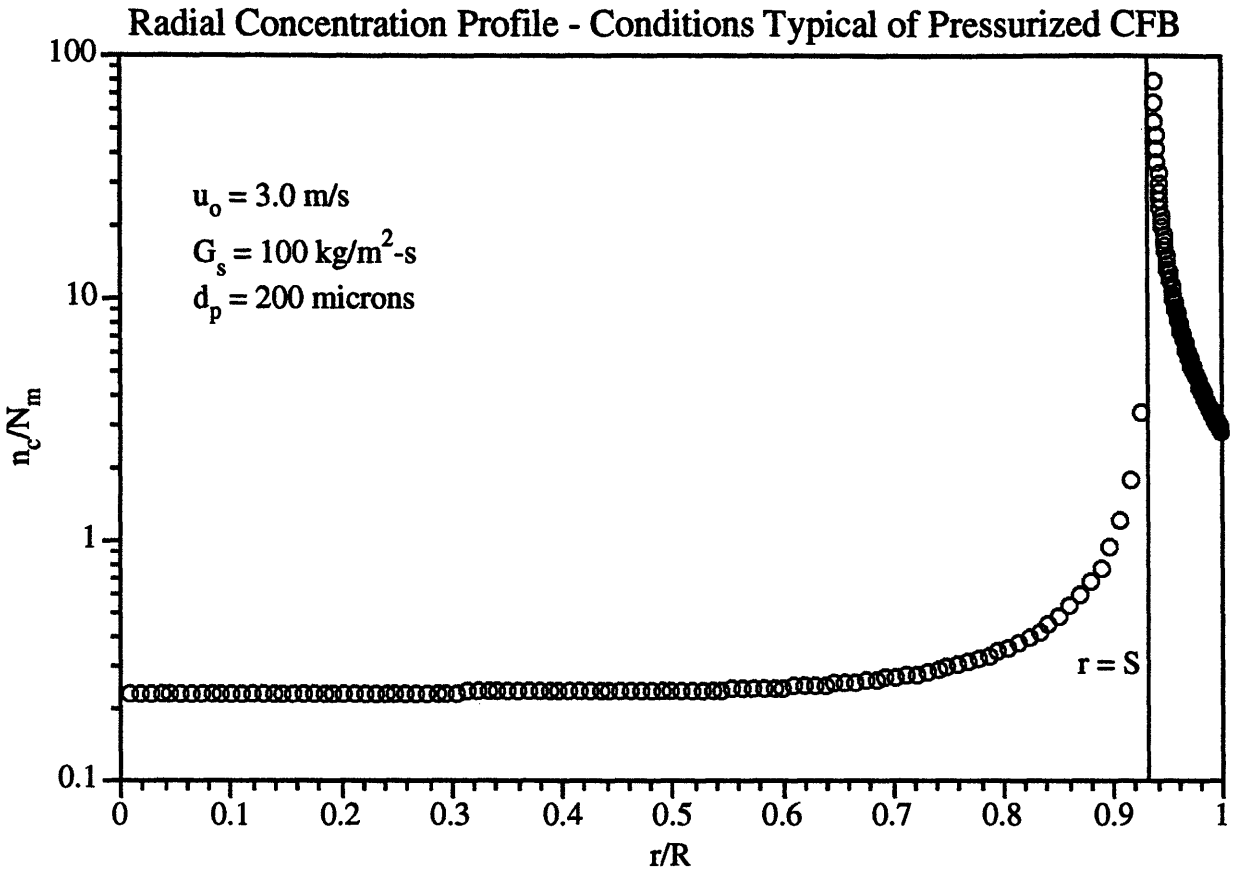

Particle distribution in the ideal system described above depends on the particle terminal velocity and the fluid centerline velocity. To establish a condition of no net transport, the mean fluid velocity would need to be less than n/(n+2) times the value of the particle terminal velocity. When the mean fluid velocity is greater than n/(n+2) times the particle terminal velocity, particles will begin to collect near the wall. This type of buildup of downward-moving particles at the walls is a common observation in FCC reactors and CFB's.

5.4 Pressure Drop

The pressure drop through an assemblage for each sphere at a distance r from the axis is [Brenner, (1956)]

$$\Delta P = 2\left(1-\left(\frac{r}{R}\right)^n\right)C_D\frac{\left(\frac{d_p^2}{8}\right)}{R^2}\rho_f\left[V_{max}\left[1-\left(\frac{r}{R}\right)^n\right]-v_p\right]^2 \tag{34}$$

$$\Delta P = \left(1-\left(\frac{r}{R}\right)^n\right)C_D\frac{\left(\frac{d_p^2}{4}\right)}{R^2}\rho_f\left[u_t\right]^2 \tag{35}$$

The pressure drop in the differential element of volume dV is

$$d(\Delta P) = \left(1-\left(\frac{r}{R}\right)^n\right)C_D\frac{\pi H\left(\frac{d_p^2}{2}\right)}{R^2}\rho_f\left[u_t\right]^2 n r dr \tag{36}$$

where H is the length of the particle assemblage.

If ψ is the net number of particles transported per unit time in the axial direction

$$\int_0^R n\bar{v}_p 2\pi r dr = \psi \tag{37}$$

$$2\pi\int_0^R\left[V_{max}\left[1-\left(\frac{r}{R}\right)^n\right]-u_t\right]n r dr = \psi \tag{38}$$

$$\int_0^R\left[\left[1-\left(\frac{r}{R}\right)^n\right]\right]n r dr = \frac{\psi}{2\pi V_{max}} + \int_0^R\frac{2\pi u_t}{2\pi V_{max}}n r dr \tag{39}$$

If N_m is the mean number of particles per unit volume averaged over the assemblage,

$$N_m\pi R^2 = \int_0^R 2\pi n r dr \tag{40}$$

and

$$\Delta P = \pi H C_D \frac{\left(\frac{d_p^2}{2}\right)}{R^2} \rho_f [u_t]^2 \left[\frac{\psi}{2\pi V_{max}} + \frac{u_t N_m R^2}{2 V_{max}} \right] \quad (41)$$

It is interesting to note that with the mechanism described here an increase in fluid velocity will result in a reduction in pressure drop for a given total bed weight supported, once the terminal velocity exceeds the mean fluid velocity. This phenomenon was observed in experiments conducted by Lewis and Bowerman (1952) in which cracking catalysts were fluidized at low velocities with liquid hydrocarbons. Pressure drops relative to bed weight of solids decreased 20 percent while the average fluid velocity increased by 300 percent from the point of incipient fluidization. Further velocity increases by another tenfold factor resulted in a gradual approach of pressure drop to that required for the support of the weight of the particles. Circulation can thus explain how particles without touching each other can cause pressure drops less that the weight of bed supported. In most commercial operations, where velocities are much higher than corresponds to incipient fluidization, the pressure drop is maintained approximately equal to the weight of suspended solids. Reduction in pressure drop with increase in velocity according to the mechanism described here is an unstable phenomenon resulting from a corresponding increase in particle segregation. Eventually a readjustment would occur owing to movement of particles back toward the middle of the tube, perhaps in an intermittent fashion as discussed by Miller and Logwinuk (1951) with a consequent increase in pressure drop.

5.5 Estimation of the Exponent 'n'

Few measurements of gas velocity profiles in CFB risers have been reported in the literature. Yang et al. (1994) present a set of time averaged local gas velocity distribution data covering a range of solids circulation rates, superficial velocities, and solids properties. A custom built Pitot-static tube was used for measuring differential pressures, which were then converted to local gas velocities. Their experiments were carried out in a 20 cm diameter, 5.5 meter high CFB utilizing 116 and 247 micron particles with densities of 2305 kg/m^3 and 2245 kg/m^3, respectively. The experimental results showed that the local gas velocity varied with radial position, elevation, solids circulation rate, superficial velocity and particle size. An emprical relationship for the gas velocity distribution in a CFB riser was obtained based on these variables:

$$\frac{1}{n} = \frac{1}{n_o} + 0.8231\left(\frac{G_s}{G_{s_{sat}}}\right)^{1.413}\left(\frac{h}{D}\right)^{-1.879} Re_{u_o,D}^{-0.262} \tag{42}$$

where n_0 is the exponent for single phase flow (7 for turbulent flows), h is the probe elevation above the distributor, G_s is the solids circulation rate, and $G_{s_{sat}}$ is the saturation carrying capacity of the gas which can be found from the expression of Yang (1983)

$$G_{s_{sat}} = \rho_s\left(1 - \varepsilon_{choke}\right)\left(u_o - u_t\right) \tag{43}$$

In equation (43), ε_{choke} is the voidage at choking which can be approximated from [Yang (1983)]:

$$\frac{2gD\left(\varepsilon_{choke}^{-4.7} - 1\right)}{\left(u_o - u_t\right)^2} = 6.81 \times 10^5\left(\frac{\rho_f}{\rho_s}\right)^{2.2} \tag{44}$$

Figure 5.3 shows the value of the exponent as a function of the ratio of solids circulation rate to the saturation carrying capacity of the gas - the parameter n is most sensitive to - for the typical operating condtions of the Foster Wheeler pressurized CFB described in Chapter 2. In general, Foster Wheeler CFB's operate with $\frac{G_s}{G_{s_{sat}}}$ less than 0.1. Thus, the n would vary somewhere between 5 and 7.

Figure 5.3
n vs. G_s/G_{sat}

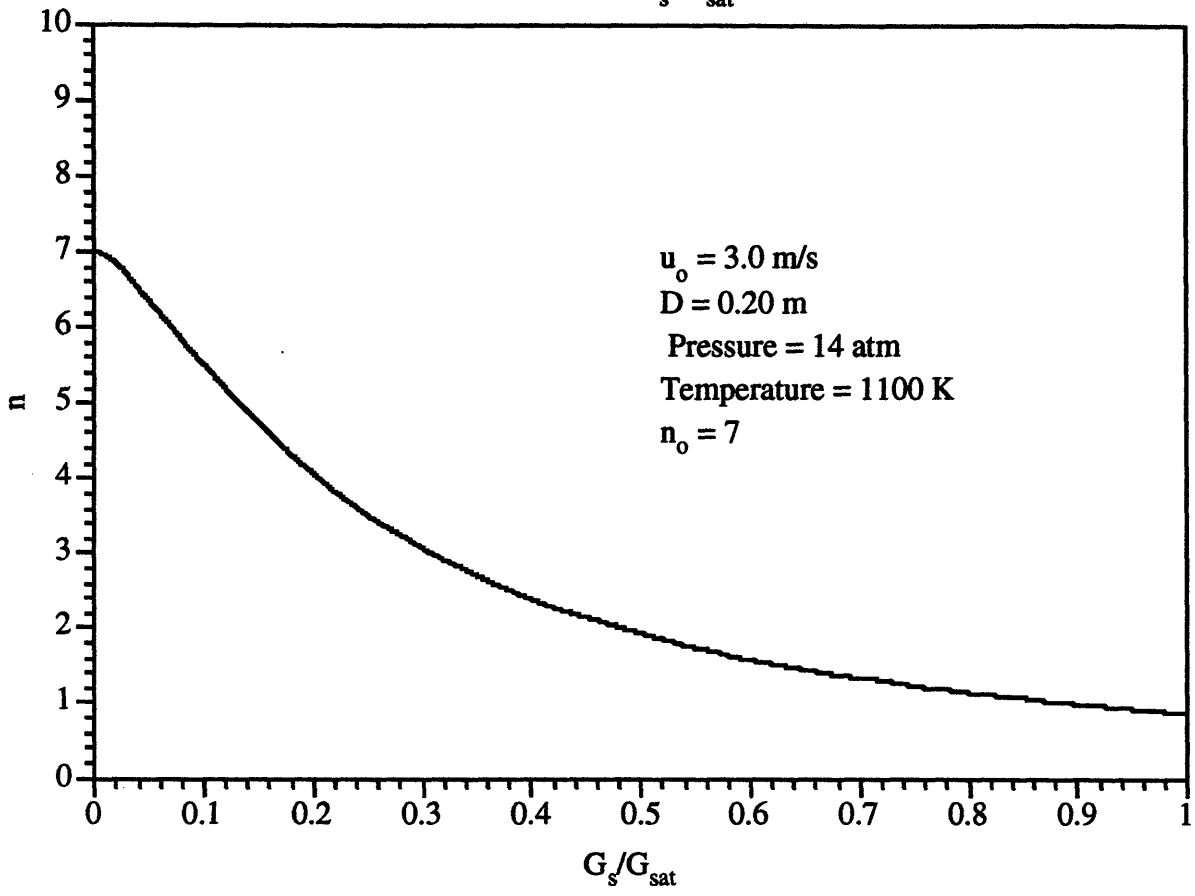

It should be noted that equation (42) is a rather rough approximation based on the data of one investigator. However, the expected variation in the expononent is relatively small (5 - 7). Figure 5.4 shows the difference in the radial concentration profiles for 'n' of 5 and 7. The small variation in both S/R and the radial concentration profile indicates that while (42) is not exact, it is adequate for the approximate theory proposed.

Figure 5.4

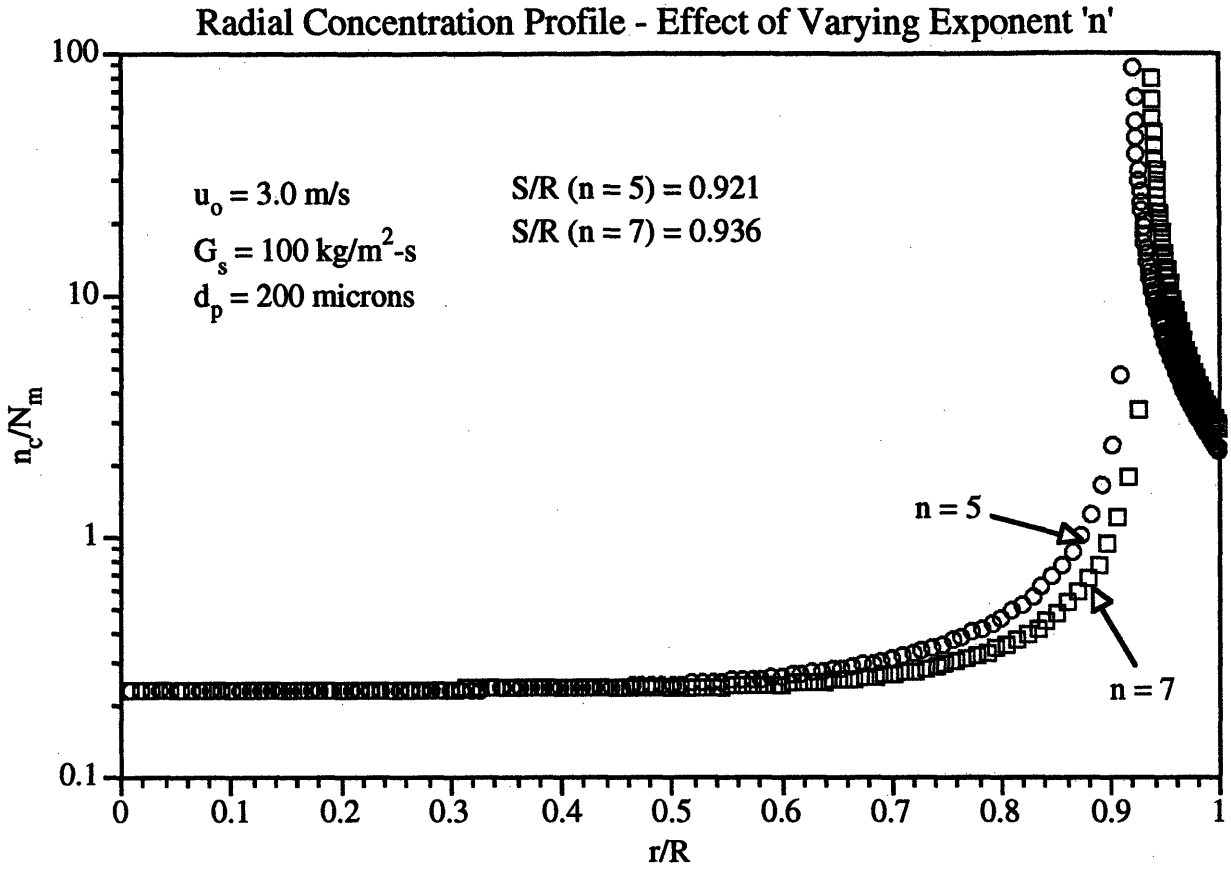

5.6 Summary

The theory presented in this Section only addresses the ideal case of steady flow in a vertical cylindrical tube of infinite length. In effect, the system is assumed to be sufficiently dilute so that a wide range of particle concentrations might exist. It is realized that some means must be provided at the ends of the tube to effect the particle distributions assumed for the cases of moving particles. Nothing in the theory developed explains how and where the top and bottom interfaces are produced in the case of a bed of finite length.

For dilute beds where the entrance and exit effects are not important, the present theory can be employed to predict other characteristics of interest in the application of CFB's. Given an appropriate bed corresponding to a definite concentration of particles, one may estimate such items as fraction of particles present in annular space and time of contact of fluid with particles in the bed.

The simple hydrodynamic theory above based on the motion of a dilute system of spherical particles in a cylinder through which fluid is passing may shed some light on phenomena observed in practical applications involving behavior of particles suspended in fluids. Recirculation effects and distribution of particles can be examined in a qualitative fashion. Recirculation of a uniformly dispersed suspension results in a lower pressure drop. If redistribution as well as recirculation occurs, still lower pressure drops are attainable.

6.0 ROLE OF CLUSTERS

A major concern associated with the application of any dispersion model based on individual particle movement as the primary mechanism of lateral solids movement is that it neglects the clusters which form in the core of a CFB. It has long been noted from visual observations that particle aggregates or "clusters" exist in the core of a CFB [see, for example, Horio (1988, 1994), Hartge *et al.*, (1988), and Gidaspow *et al.*, (1989)]. Although there are numerous references throughout the literature of clusters, there is little quantitative knowledge of the nature of clusters. Recent attempts to characterize clusters include the work of Horio (1988) who used optical probes to detect clusters in a CFB riser of 5 cm diameter and 2.8 m height, operating with 60 micron FCC particles. Hartge *et al.* (1988) also used optical probes to detect variations in local solid concentrations, seeking indications of structure elements. A valuable contribution to the field was made by Brereton and Grace (1993) who defined an intermittency index, which would be zero for perfect core-annulus flow and one for perfect cluster flow, to characterize the flow. They showed that the behavior is always between these two limits but tends toward the former with increasing height up the column. More recent studies have shown that in the core of CFB, clusters are present at any given radial location up to 15 percent of the time [Soong, *et al.*, (1994)].

In light of the body of data which supports their existence, it is imperative to develop an understanding of how important clusters are in the transport of solid material, if a lateral dispersion model valid for CFB's is to formulated. Consider a 10 mm cluster of 2600 kg/m^3 particles with a concentration of 10 percent in the upper region of a pressurized CFB where the cross-sectionally averaged solid fraction is 0.01. The effective cluster density is then 260 kg/m^3. For such an aggregate, the terminal velocity in a 14 atm combustor is about 5 m/s. The terminal velocity of 200 micron particle in the bed is about 0.6 m/s. If the bed has a diameter of 1 meter and has a superficial velocity of 3 m/s, the size and velocity of the most energetic eddy will be of the order of 0.1 m and 0.26 m/s for single phase flow [see Laufer (1956)], respectively. Therefore, during one interaction with an eddy, the eddy would impart a velocity of about 2.3E-3 m/s on the cluster , while the eddy would impart a velocity of about 0.20 m/s on the single particle. Hence the radial flux due to cluster movement ($\rho_{cl}*v_{cl}$) is about 10 times less than that due to individual particle movement ($\rho_s*v_p*\phi$). Clearly, the amount of lateral solids movement due to the gas turbulence induced dispersion of clusters is negligible. This is consistent with the conclusions of Westphalen and Glicksman (1995).

However, if the cluster movement is modeled as a ballistic trajectory either from the bottom of the bed, or from the wall region, the amount of radial flux due to clusters may be important if they travel for relatively long distances before breaking up. For example, say the radial component of the cluster velocity is 1/10 the axial velocity which is approximated as the absolute value of the gas velocity less the effective cluster terminal velocity. Thus, the radial component of the cluster velocity in the bed described above is about 0.2 m/s. In this case, the radial solids flux due to lateral cluster movement is 10 times that due to individual particle movement. To determine the importance of lateral solids movement in clusters, it is important to know how quickly the ejected clusters break up. If the clusters rapidly break up, such that the distance they travel in cluster form is small relative to the distance the particles in the cluster travel in the dispersed phase, then the contribution the clusters make to the radial flux may be insignificant.

The time scale representing the time which the particles remain in an aggregate or cluster state is:

$$t_{cl_r} \sim \frac{r_{cl}^2}{\varepsilon_{cl_r}} \tag{1}$$

where r_{cl} is the cluster radius and ε_{cl_r} is the cluster dispersion coefficient which describes the rate at which clusters expand radially outward. While the time scale representing the time it takes for a particle to disperse laterally to the wall through interactions with gas turbulence is:

$$t_{p_r} \sim \frac{R^2}{\varepsilon_{p_r}} \tag{2}$$

The ratio of the two time scales introduces a new dimensionless parameter which represents the ratio of the time it takes a cluster to breakup to the time it takes a particle to disperse laterally to the wall:

$$Di_r \sim \left(\frac{r_{cl}}{R}\right)^2 \left(\frac{\varepsilon_{p_r}}{\varepsilon_{cl_r}}\right) \tag{3}$$

When Di_r is small, the lateral movement of solids is dominated by the dispersion of individual particles, while if Di_r is of order 1 or higher, the lateral cluster movement will represent a significant fraction of the transport mechanisms of solids to the wall of a CFB.

6.1 Axial Cluster/Particle Movement

It should be noted that a similar dimensionless group can be defined for the axial movement of particles and clusters. The distance a cluster travels in time t is approximated as:

$$x \sim \left| u_{t_{cl}} t \right| \tag{4}$$

The time scale for cluster breakup is still defined by equation (1), so that the distance a cluster travels vertically before breakup scales as

$$x \sim \left| u_{t_{cl}} \frac{r_{cl}^2}{\varepsilon_{cl_r}} \right| \tag{5}$$

The length scale representing vertical transport is the bed height. So that in the vertical direction

$$Di_a \sim \frac{\left| u_{t_p} \frac{r_{cl}^2}{\varepsilon_{cl_r}} \right|}{H} \tag{6}$$

Here Di_a represents the ratio of the distance traveled by a cluster before breakup to the total bed height. In this case, when Di_a is much less than one, the clusters represent a small fraction of the axial particle movement - clusters travel only a small fraction of the bed total bed height before breaking up. Note that this parameter is *not* a measure of the ratio of time it takes a cluster to break up to the time it takes the individual particles to disperse axially to the top of the bed. The reason such a parameter is not appropriate is that the axial solids flux due to dispersion by gas turbulence is much less than the flux due to particle convection. This will be shown below.

6.2 Determination of the Relative Importance of Particle Axial Convection and Particle Axial Dispersion

6.2.1 Experimental Measurements of Axial Particle Dispersion in CFB's

Rhodes *et al.* (1991)

Measurement of CFB axial solid dispersion have been made by Rhodes (1991) in two risers with diameters of 0.152 m and 0.305 m. The larger riser was 6.6 m tall, the smaller was 6.2 m tall. A salt tracer technique was used. The bed solid had a mean diameter of 71 microns and a density of 2460 kg/m3. The tracer, sodium chloride (NaCl), had a density of 2160 kg/m3, was prepared with a size distribution similar to that of the bed solid. The tracer was injected at the bottom of the bed; three sampling locations were used during each test. Bed samples were tested by measuring the conductivity of a water solution in which the tracer was dissolved.

The resulting concentration measurements were compared to a one-dimensional axial diffusion model in order to determine a best-fit axial diffusion coefficient from the data. The diffusion model was expressed as

$$\phi_{tr} = \phi_0 \sqrt{\frac{t_0}{t}} \exp\left(-\frac{\left(\Delta H - v_{p_z} t\right)^2}{4\varepsilon_{p_a} t}\right) \tag{7}$$

where ϕ_{tr} is the tracer volume fraction, ϕ_0 and t_0 are constants, v_{p_z} is the velocity of the center of mass from which the solids spread, ε_{p_a} is the axial diffusion coefficient, and ΔH is the distance between the probe and the tracer injector. Note that the tracer solid fraction is expressed as tracer volume per entire bed volume; this is in contrast to the usual definition of concentration where it is equal to tracer volume per total solid volume. Rhode's model assumes that the concentration profile was a delta function at the injection location. The estimated axial diffusion coefficients, were correlated with flow conditions and bed diameter D as

$$Pe_{p_z} = \frac{u_o \Delta H}{\varepsilon_{p_a}} = 9.2\left(G_s D\right)^{0.33} \tag{8}$$

The evaluated Peclet numbers were in the range of 1 to 8. This represents a range of D_{p_z} from about 2 to 20 m^2/s. These are extremely high diffusion coefficients which probably are not representative of dispersion in the core region above the dense zone of the bed bottom.

Westphalen (1995) proposes an alternate model for the data of Rhodes et al. (1991). This model assumes complete mixing in the bed bottom section and no mixing above this region. For the alternate model, the solid velocity above the bed bottom is assumed to be equal to the superficial gas velocity. The initial concentration of tracer in the bed bottom region is equal to the ratio of injected tracer to the bed solid volume in the region. The concentration of tracer leaving the bed bottom is equal to the concentration in the region because of the complete mixing assumption. The concentration decays exponentially with a time constant equal to the ratio of the solid volume and the sum of internal and external solid circulation. The delay time for the signal to reach the sampling location is equal to the transit distance divided by the solid velocity. The resulting model is:

$$\frac{\text{mass NaCl}}{\text{mass bed solid}} = \begin{bmatrix} 0 & t < t_d \\ c_o \exp\left[-\dfrac{(t-t_d)}{\tau_b}\right] & t > t_d \end{bmatrix} \tag{9}$$

$$t_d = \frac{\Delta H - H_b}{v_{p_z}} \tag{10}$$

$$\tau_b = \frac{\rho_s H_b (1-\varepsilon_b)}{(\gamma+1) G_s} \tag{11}$$

$$c_o = \frac{4M_i}{\rho_s H_b \pi D^2 (1-\varepsilon_b)(\gamma+1)} \tag{12}$$

where M_i is the mass of injected tracer, ε_b and H_b are the bed bottom voidage and length, γ is the ratio of internal to external solid circulation rates. Such a model with, reasonable assumptions for the height of the bed bottom section and ratio of internal to external circulation rates, results in predictions as good as the dispersion model of Rhodes. Westphalen's analysis makes the point that the actual upper bed axial solid dispersion is probably much less than the average overall dispersion suggested by the fit of equation (7).

Martin *et al.* (1992)

Martin *et al.* measured solid axial dispersion in a 0.94 cm diameter, 26 m meter high CFB using FCC with a mean volumetric diameter of 62 microns and a particle density of 1560 kg/m^3. In these experiments the lanthanum contained in the cracking catalyst was activated by a neutron flux, and a small sample was injected into the feed stock injection level. Its passage was recorded by external detectors. This enabled the average velocity to be determined between the detectors and the average concentration calculated by the formula:

$$c_s = \frac{G_s}{v_s} \tag{13}$$

where G_s is the solid mass flux, and v_s is the actual solid velocity. The axial dispersion was computed by normalizing the bottom outputs and using the classic dispersed axial plug flow dispersion model to yield calculated outputs. A flat gas and solid velocity profile was used to obtain the overall reactor performance, because a more complicated model would have required knowledge of this profile and of the radial dispersion. The best fit with the top experimental data was found by optimization of the actual particle velocity and the axial dispersion to minimize the surface difference between the calculated and target output. The results of Martin *et al.* are summarized in Table 1.

Table 1: Results of Axial Solid Dispersion of Martin *et al.*

Catalyst Flux (kg/m^2-s)	Height of Detectors (m)	Catalyst Actual Velocity (m/s)	Axial Catalyst Dispersion (m^2/s)	Peclet Number	Outputs Surface Difference (%)
298	8 - 14	8.7	10.4	5.0	-
298	8 - 14	9.8	12.2	4.8	-
325	4 - 18	10.7	17.8	8	5
325	4 - 18	11.5	10.1	16	4

Note that, as was the case with the experiments of Rhodes *et al.* (1991), the tracer was injected at the bottom of the reactor. As a result, the dispersion coefficients are very high. It is probable that the axial dispersion in the core region alone is much lower.

Viitanen (1993)

Viitanen (1993) recorded axial solids dispersion data in a 1.0 m diameter, 39 meter high fluidized catalyst cracking plant, operating at 2.6 bar and 529 °C. The catalyst was FCC with a mean particle diameter of about 70 microns and a bulk density of 2400 kg/m^3. In a manner similar to Martin et al. (1993), Viitanen irradiated the catalyst with thermal neutrons to activate the lanthanum. The tracer pulses were fed into the bottom of the riser with a purge stream used to clean up the output of the oil inlet nozzles. Since the flow rate of the purge stream is quite low, the initial momentum of the tracer after the injection was almost completely due to drag by the vertical main flow inside the reactor. The propagation of tracer pulses was detected using 15 thallium-activated sodium iodide scintillation detectors. The detectors were located at seven different heights along the riser. The detectors were checked with a standard radiation source to give equal signals within a range of about 5 percent.

The axial velocity profile of the solids was estimated from the mean velocity between successive measuring points. This velocity was set to correspond to the velocity in the middle of the two measuring points. The Peclet numbers and respective axial dispersion coefficients obtained by Viitanen are presented in Table 2. The values of Peclet numbers were found to of the same order of magnitude as those reported by Bernard *et al.* (1989). These were also obtained for a commercial FCC riser and varied from 4 to 25 for the gas phase and 1 to 10 for the catalyst.

Table 2: Results of Axial Solid Dispersion of Viitanen

Height (m)	Peclet Number	Dispersion Coefficient (m^2/s)
1.3	5	0.3
3.3	6	0.8
7.4	7	3.3
9.9	8	5.0
22.1	13	10.0
31.9	13	15.5

Again, the dispersion coefficients reported by Viitanen (1993) represent overall effective dispersion coefficients, rather than axial dispersion in the core.

van Zoonen (1962)

The earliest study of the diffusional phenomenal in reactors operating in the fast fluidization regime is that of van Zoonen (1962). van Zoonen measured axial solids dispersion in a two-stage catalytic cracker with a vertical riser of 5.1 cm diameter by 10 meters high, operating at ambient pressure and temperature. The catalyst was FCC with a mean particle diameter of 65 microns and a density of 1600 kg /m^3.

To measure axial particle diffusion, a certain amount of catalyst tagged with ammonium chloride was injected into the riser above the solids feed point. The injection time was a few tenths of a second. Near the top of the riser twenty samples of catalyst were taken in small vessels on a turn-table. The samples were then weighed and then mixed with a known amount of water to dissolve the ammonium chloride. By measuring the relative electric conductivity of these solutions , the relative concentration of ammonium chloride was determined.

The relative concentration of tracer material at a given point at a (dimensionless time) τ, after injection of a pulse of tracer was characterized by (van de Laan, E. Th., 1957):

$$\frac{c}{c_{mix}} = \frac{1}{2\sqrt{\pi\tau\frac{\varepsilon_{p_a}}{u_o L}}} \exp\left[-\frac{(1-\tau)^2}{4\tau\frac{\varepsilon_{p_a}}{u_o L}}\right] \qquad (14)$$

The experimentally determined curves were compared with the theoretical equation to find the best value of $\frac{\varepsilon_{p_a}}{u_o L}$.

These experiments are nearly identical to those conducted by Rhodes et al. (1991). Table 3 presents the result of van Zoonen for axial particle diffusion.

Table 3: Results of Axial Solid Dispersion of van Zoonen

u_0 (m/s)	G_s (kg/m^2-s)	Peclet Number
1.5	56	0.15
1.5	835	0.06
2.5	110	0.19
2.5	150	0.13
2.5	153	0.27
4	195	0.11
5.5	280	0.14
5.5	334	0.07
12	360	0.08
12	1000	0.23

The riser described by van Zoonen was a FCC reactor with an extremely large L/D. Although the bed solid fraction was less than 5 percent over 90 percent of the riser, the tracer was injected immediately above the solids feed port where the bed average cross-section solid fraction was generally about 20 percent. Therefore, these axial dispersion tests suffer from the same pitfalls as the experiments of Rhodes *et al.* (1991), Viitanen (1993), and Martin *et al.* (1992) where the tracer material was injected into the bottom dense zones. The dispersion coefficients provide a measure of the effective axial dispersion over the entire bed, rather than in the dilute core.

Kojima *et al.* (1989)

Measurements of axial solid dispersion using an optical fiber technique were made by Kojima *et al.* (1989) in a 3.6 m higher riser with a 5 cm diameter. The solids were FCC with a mean diameter of 60 microns and a density of 1000 kg/m^3. The tracer particles were FCC particles treated with fluorescent dye. The optical fiber technique was described in detail by Kuramoto *et al.* (1986). Ultraviolet light was used to illuminate the treated tracer particles; the intensity of visible light emitted from the particles was measured. The experiments were all conducted above the bottom region of the bed in the dilute core of the bed, eliminating any effect of bed bottom mixing.

The diffusion model used in the data interpretation is expressed as

$$\frac{\partial \phi_{tr}}{\partial t} + v_{p_z}\frac{\partial \phi_{tr}}{\partial z} = \frac{\varepsilon_{p_z}}{(1-\varepsilon)}\frac{\partial^2 \phi_{tr}}{\partial z^2} \tag{15}$$

Westphalen (1993) has correctly pointed out that the term $(1-\varepsilon)$ should not appear. The solid velocities for the tests were determined by calculated the difference in average times of the pulses at the two probes. These average times were called first absolute moments by Kojima et al. and were defined:

$$\mu_1 = \frac{\int_0^\infty \phi_{tr} t\, dt}{\int_0^\infty \phi_{tr}\, dt} \tag{16}$$

Tracer volume fraction was assumed to be proportional to the signal strength measured with the probe. The spread in tracer was calculated based on the differences at the two probes of the second relative moments defined as:

$$\mu_2 = \frac{\int_0^\infty \phi_{tr}(t-\mu_1)^2\, dt}{\int_0^\infty \phi_{tr}\, dt} \tag{17}$$

The diffusion coefficients were calculated from

$$\varepsilon_{p_a} = \frac{(1-\varepsilon)v_{p_a}^3 \Delta\mu_2}{2\Delta z} \tag{18}$$

where the term $(1-\varepsilon)$ is erroneously present. Westphalen has shown that this method of determining ε_{p_a} is good, especially for values of the Peclet number which are high.

Axial diffusion coefficients ranging from 1 to 900 cm^2/s were calculated by Kojima *et al.* for a range of superficial gas velocities. The median value was about 35 cm^2/s. The Peclet number, defined as $Pe_a = \frac{u_o \Delta H}{\varepsilon_{p_a}}$, calculated for the median diffusion coefficient is about 80 ($\Delta H = 0.15$ m, and $u_o = 1.85$ m/s). The Rhodes *et al.* (1991) correlation and Martin data indicate Peclet numbers on the order of 1. The difference is partially explained by the incorrect inclusion of $(1-\varepsilon)$ in the diffusion coefficient calculation of Kojima et al. If a

value of about 0.1 is assumed for this term, the Peclet number are still an order of magnitude higher than that for the Rhodes, Viitanen, and Martin data. This indicates that bed bottom mixing may, in fact, have played a large role in the axial mixing experiments of Rhodes, Viitanen, and Martin.

Avidan (1990)

Axial diffusion data has also been reported by Avidan (1990) for measurements in a 15 cm diameter, 8.5 meter high CFB. The bed particles had a mean particle diameter of 49 microns and a density of 1450 kg/m^3. Ferromagnetic tracer particles were injected horizontally into the riser with a pneumatic injector. Inductor based sensors were then used to measure tracer concentrations. The measured axial dispersion coefficients ranged from 0.1 to 1 m^2/s.

Because the tracer particles were "shot" laterally across the bed, the axial diffusion of particles in the Avidan experiments may have been aided by the down flowing particle layer at the wall. For example, if it is assumed that the particles in the core travel upward at a velocity of 2 m/s and the particles in the wall layer flow downward with a velocity of about 1 m/s, the ratio of time it would take for the particles to spread across a distance δ due to the velocity difference to the time it would take the particles to spread across δ only by axial diffusion is

$$= \frac{2\varepsilon_{p_a}}{\Delta v \delta} \tag{19}$$

Using the values of ε_{p_a} reported by Kojima et al., this ratio is as small as 0.01 for distances of the order of 1 meter (the distance between probes in the Avidan experiments). This indicates that a large amount of the axial dispersion measured by Avidan may have been due to the down flowing wall layer, rather than strictly a turbulent diffusional effect. This may explain much of the discrepancy between the Kojima and Avidan data.

Wei *et al.* (1994)

The final set of experiments which will be discussed is that of Wei *et al.* (1994) who evaluated the radial and axial dispersion of solids in a cocurrent down flow CFB (CDCFB). In a CDCFB, particles and gas move in the direction of gravity. Such a reactor has been

found to have advantages over CFB's for gas-solid contacting in the chemical industry. The bed used in evaluating the axial dispersion had a 14 cm diameter and was 7.6 meters long. The particles were FCC catalyst with a mean diameter of 54 microns and a particle density of 1710 kg/m^3.

Wei *et al.* used a phosphor tracer technique to determine solids mixing. An electric flash tube was fixed in the axis of the CDCFB, 2.0 meters below the recirculating solids inlet. After the bed reached steady state, a strong light impulse was suddenly produced by the flash tube to excite the phosphor particles surrounding the flash tube. The excited phosphor particles gave out emissive light immediately. At the moment the one-million -lumen flash tube flashed, the intensity of the emissive light was saturated, and was not proportional to the light impulse. The strength of the emitted light was proportional to the tracer concentration, allowing the tracer concentration to be determined. When the tracer passed by a detector, the emissive light signals were detected by a photomultiplier and collected by a computer data acquisition system as a function of time. Four locations were chosen to measure the RTD at different axial positions. Five radial positions were chosen to measure the local RTD curves of the solids.

A plug-flow model for Fickian diffusion was adopted to model the solids dispersion in the CDCFB. This model was though to be especially applicable to CDCFB's because of the uniform velocity profiles, bulk flow only in the downward axial direction, and dispersion coefficients which are independent of position. Provided the tracers are injected as a delta function at the origin and measured tracer RTD profiles are evaluated using the dispersed plug-flow model, diffusion and convection under conditions of uniform flow can be described by:

$$\varepsilon_{p_a}\frac{\partial^2 c}{\partial z^2}+\frac{\varepsilon_{p_r}}{r}\frac{\partial}{\partial r}\left(r\frac{\partial c}{\partial r}\right)-v_p\frac{\partial c}{\partial z}=\frac{\partial c}{\partial t} \tag{20}$$

with boundary conditions

$$\begin{aligned} &r=R,\ \frac{\partial c}{\partial r}=0;\ \ r=0,\ \frac{\partial c}{\partial r}=0 \\ &z=-\infty, c=0;\ \ r=0,\ c(r,t)=C_o\delta(t) \end{aligned} \tag{21}$$

The distance L between the point of tracer injection and the measuring plane is positive in the direction of flow. The analytical solution is:

$$\frac{c}{C_o} = \frac{\exp(\xi\varphi)}{2\pi\sqrt{\pi\theta}} \sum_{n=0}^{\infty} \frac{J_0(\beta_n \rho)}{J_0^2(\beta_n)} \left[-\frac{\xi^2}{4\theta} - (\varphi^2 + \beta_n^2)\theta \right] \tag{22}$$

$$\rho = \frac{r}{R};\ \xi = \frac{z}{R}\sqrt{\frac{\varepsilon_{p_r}}{\varepsilon_{p_a}}};\ \varphi = \frac{v_p R}{2\sqrt{\varepsilon_{p_r}\varepsilon_{p_a}}};\ \theta = \frac{\varepsilon_{p_r} t}{R^2} \tag{23}$$

The mixing parameters ε_{p_r} and ε_{p_a} were determined by a two-dimensional regression method. The results were then correlated with the bed Reynolds number and the bed voidage resulting in the following relations:

$$\begin{aligned} Pe_a &= \frac{8.93 \times 10^{-7}\, Re}{(1-\varepsilon)} + 101 \\ Pe_r &= 140 Re^{0.61}(1-\varepsilon)^{1.23} \end{aligned} \tag{24}$$

Because these tests were conducted in a test section which operates at cross-sectionally averaged solid fractions and velocities close to that in the core of a CFB, they should provide a good approximation to the axial and radial dispersion in the core region of a CFB. Additionally, the experiments are not hindered by the effects of a enhanced mixing in a lower dense zone, since none exists in a CDCFB.

6.2.2 Summary of Experimental Axial Solids Dispersion Data

Table 4 presents a summary of the axial dispersion data taken by the investigators listed above. The data of Kojima et al. (1989) and Wei et al. (1994) most accurately reflect the actual axial solids dispersion coefficient in the dilute core of a CFB. The data of Yerushalmi and Avidan (1985) measures the effective dispersion when the solids are dispersed across the entire cross section, including the down flowing annular layer. The other studies, for which there is good agreement between the measured Peclet numbers, provide measures of effective dispersion across the entire riser - including the dense bottom zone. For the purposes of evaluating the importance of the contribution of clusters to the axial particle flux, the data of Kojima *et al.* (1989) and Wei *et al.* (1994) will be used since they most accurately represent the dispersion coefficient in the upward flowing dilute core of a CFB.

Table 4: Axial Solid Dispersion Coefficient Measurements in CFB's

Researcher	D (cm)	L (m)	d_p (μm)	ρ_s (kg/m^3)	u_o (m/s)	ε_{p_a} (m^2/s)	Pe_a
Rhodes *et al.* (1991)	15.2 20.5	6.2 6.6	71	2456	2 - 5	2 - 20	2 - 20
Martin *et al.* (1992)	94	26	62	1560	10 - 15	10 - 20	5 - 16
Viitanen (1993)	100	39	70	2400	6 - 15	0.3 - 15	5 - 13
van Zoonen (1962)	5	10	65	1600	1.5 - 12	0.8 - 24.5	3 - 16
Kojima *et al.* (1989)	5	3.6	60	1000	1.5 - 2.2	10^{-4} - 10^{-1}	10 - 200
Yerushalmi and Avidan (1985)	15.2	8.5	49	1450	1 - 5	0.1 - 1	0.1 - 1
Wei *et al.* (1994)	14	7.6	54	1710	2.3 - 9	0.03 - 0.06	100 - 180

6.3 Evaluation of Axial Particle Flux Due to Dispersion and Convection

Equation (6) is only valid if the axial flux due to particle dispersion is much less than that due to particle convection. The axial flux due to particle convection can be approximated as:

$$G_{s_{axial-conv.}} = \rho_s(u_o - u_t)\phi \tag{25}$$

The axial flux due to particle dispersion is approximated as

$$G_{s_{axial-disp.}} = \rho_s \frac{\varepsilon_{p_a}}{\delta}\phi \tag{26}$$

where δ is the distance between measurment locations. The ratio of the flux due to dispersion to that due to convection can then be approximated by a Peclet number describing the ratio of axial particle convection to axial particle dispersion:

$$\frac{G_{s_{axial-conv.}}}{G_{s_{axial-disp.}}} = \frac{\delta(u_o - u_t)}{\varepsilon_{p_a}} \tag{27}$$

Using the data of Wei *et al.* or Kojima *et al.*, the Peclet numbers will be larger than 10. This indicates that the convective flux is much greater than the diffusive flux. This supports the argument made above that the axial flux is mostly due to particle convection.

6.4 Evaluation Di_r and Di_{cl}

To determine if clusters represent a significant mode of lateral and axial solids movement, the particle lateral dispersion coefficient, and the cluster dispersion coefficient must be determined.

6.4.1 Experimental Determination of ε_{p_r}

There is little experimental information on the lateral dispersion of particles in turbulent gases above volumetric solid fractions of about 0.001, and almost no data on lateral particle dispersion in CFB's. The following is a brief summary of the lateral solids dispersion data in CFB's currently available in the literature.

Westphalen and Glicksman (1995)

The most comprehensive attempt to measure lateral solids dispersion coefficients in CFB's was conducted by Westphalen (1993). Westphalen developed a thermal technique for measurement of solid mixing in the dilute core of a CFB (the same technique was subsequently used to gain a qualitative measure of the lateral dispersion in the bottom of a CFB). The mixing measurements were made in a 7 meter tall CFB riser with a diameter of 20 cm. Quartz sand with a mean diameter of 180 microns and a density of 2350 kg/m^3 was used as the bed solid material.

The thermal tracer technique is very similar to that of Valenzuela and Glicksman (1984). The technique involved injection of heated particles and detection with thermistors. About 10 ml bulk volume of bed particles were placed in a vertical heating section a pneumatic injector. The injection air accelerated the particles upward so that they left the injector at a vertical velocity close to the core region velocity of the bed particles. An array of thermistor probes was located at heights from 0 cm to 90 cm above the injection location. The probes were mounted so that they could be moved radially.

Analysis of the data involved the use of models for the tracer spread and energy conservation in the measurement zone and a model for thermistor response. Values for all model parameters (gas diffusivity, vertical solid velocity, initial tracer concentration, average bed solid fraction) except the radial particle dispersion are estimated. The value of ε_{p_r} was adjusted to give a best fit with the data.

The gas diffusivity was determined based on a calculation of eddy viscosity in the core region for a single phase gas flow, trends of radial gas diffusivity in CFB's, and measurements of the velocity fluctuations in the test bed when no solids were present. The vertical solid velocity is determined by examination of the temperature traces of the centerline thermistors. The initial response times of these thermistors gave an indication of the velocity of the front of the tracer plume.

The initial tracer concentration was determined by application of a mass balance to the injection tube assuming that the solids are fully accelerated before reaching the top of the tube and the particle/gas relative velocity is equal to the particle terminal velocity.

The average bed solid fraction in the core was determined from pressure drop measurements neglecting the frictional and accelerational pressure drop.

The flow model assumed steady state flow of tracer particles upward out of the injector. The flow was divided into three components: tracer solid, bed solid, and gas. The mean velocity of each component was assumed to be vertically upward with no velocity gradients in the axial, radial or tangential directions. A cylindrical coordinate system moving with the bed solids was chosen to eliminate all but one axial derivative from the equations. Heat transfer between the solid components and the gas , but not directly between the solid components was included in the model. The spread of tracer particles was described by a diffusion equation. The gas is assumed to take up the remaining space; it is assumed to be incompressible. The resulting equations were:

Mass

$$\frac{\partial \alpha_{tr}}{\partial t} = \varepsilon_{p_r} \frac{1}{r} \frac{\partial}{\partial r}\left(r \frac{\partial \alpha_{tr}}{\partial r} \right)$$

$$\alpha_{bed} = \text{const.} \qquad (28)$$

$$\alpha_{tr} + \alpha_{bed} + \alpha_{gas} = 1$$

Energy

$$\alpha_i\left[\frac{\partial T_i}{\partial t}+u_{rel_i}\frac{\partial T_i}{\partial z}\right]=\frac{H_i}{\rho_i c_{p_i}}+\varepsilon_{r_i}\left[\alpha_i\frac{\partial^2 T_i}{\partial r^2}+2\frac{\partial \alpha_i}{\partial r}\frac{\partial T_i}{\partial r}+\frac{\alpha_i}{r}\frac{\partial T_i}{\partial r}\right] \tag{29}$$

where H_i represents heat transferred from each of the solid components to the gas. The boundary conditions involved zero radial gradients at the walls and on centerline for concentration and temperature. The initial conditions were:

$$\begin{aligned} T_{bed}(0,r) &= T_{amb.} \\ \alpha_{bed} &= \phi \end{aligned} \tag{30}$$

for $0 \le r \le R_{injector}$

$$\begin{aligned} T_{tr.}(0,r) &= T_{gas}(0,r) = T_{tr.\,init.} \\ \alpha_{tr.}(0,r) &= \phi_{inj.\,exit} \end{aligned} \tag{31}$$

for $R_{injector} \le r \le R$

$$\begin{aligned} T_{tr.}(0,r) &= T_{gas}(0,r) = T_{amb.} \\ \alpha_{tr.}(0,r) &= 0 \end{aligned} \tag{32}$$

The radial particle diffusivities were then calculated by using a least squares approach for determination of the best fit to equations (28) and (29). Table 5 presents the best fit solid diffusivities of Westphalen.

Table 5: Best Fit Solid Lateral Solid Diffusivities Measured by Westphalen (1993)

u_o (m/s)	ϕ_{bed}	G_s (kg/m^2-s)	ε_{p_r} (cm^2/s)	Pe_r
3.5	0	0	7.1	490
3.5	0.0034	8	8.0	437
3.5	0.0064	15	8.5	412
4.0	0.0068	23	3.7	1050
4.0	0.011	31	8.6	465
4.0	0.0034	16	2.0	2000
4.0	0	0	0.4	10000
3.0	0.0064	13	1.7	1500
4.9	0.0098	23	1.0	4500
3.5	0.010	24	7.4	473
4.0	0.011	26	1.6	2500

van Zoonen (1962)

In addition to the axial particle dispersion data taken (see above discussion), van Zoonen also measured particle lateral dispersion. To do this, a central injection tube was inserted into the riser to give a point of injection at various heights. Cracking catalyst tagged with about 5 percent wt of ammonium chloride was used as the tracer. Adjustable sampling tubes, which could be moved across the diameter of the riser, were located downstream of the injection tube. The samples obtained were each weighed and then mixed with a known amount of water to dissolve the ammonium chloride into the water. By measuring the electric conductivity of these solutions, the relative concentration of ammonium chloride was be determined.

To interpret the data, the relation between the dimensionless concentration of the tracer particles and the coordinates z and r in the riser given by Schlinger and Sage (1953) was used:

$$\frac{c}{C_o} = \frac{2}{R^2}\sum_{n=0}^{\infty} \frac{bJ_0\left(\beta_n \frac{r}{R}\right)J_1\left(\beta_n \frac{b}{R}\right)}{\beta_n\left[J_0^2(\beta_n)\right]^2} \exp\left[-\beta_n z \frac{\varepsilon_{p_r}}{u_o R^2}\right] \tag{32}$$

About 30 experiments were performed, in which the gas velocity was varied from 2.5 to 12 m/s and particle recycle rates from 100 to 700 kg/m2-s. The results of these tests is summarized in Table 6.

Table 6: Best Fit Solid Lateral Solid Diffusivities Measured by van Zoonen (1962)

z (m)	u_o (m/s)	G_s (kg/m^2-s)	ε_{p_r} (cm^2/s)	Pe_r
0.51	2.5	500	1.2	526
0.52	5.5	305	5.5	250
0.52	12.0	264	6.6	455
0.52	12.0	514	12.0	250
1.0	2.5	380	0.94	667
1.0	5.5	370	2.9	476
1.0	5.5	570	3.3	417
1.0	12.0	510	6.0	500
1.96	5.5	320	1.6	833
1.96	12.0	300	5.1	588

Viitanen (1993)

Viitanen (1993) recorded radial solids dispersion data in addition to the axial dispersion data in a 1.0 m diameter, 39 meter high fluidized catalyst cracking plant, operating at 2.6 bar and 529 °C. The catalyst was FCC with a mean particle diameter of about 70 microns and a bulk density of 2400 kg/m^3. Viitanen irradiated the catalyst with thermal neutrons to activate the lanthanum. The tracer pulses were fed into the bottom of the riser with a purge stream used to clean up the output of the oil inlet nozzles. Since the flow rate of the purge stream is quite low, the initial momentum of the tracer after the injection was almost completely due to drag by the vertical main flow inside the reactor. The propagation of tracer pulses was detected using 15 thallium-activated sodium iodide scintillation detectors. The detectors were located at seven different heights along the riser. At four levels, three detectors were collimated side by side in such a way that information about the radial distribution of the different phases could be obtained. The detectors were checked with a standard radiation source to give equal signals within a range of about 5 percent.

Experimental determination of the radial dispersion coefficient was then made by measuring the amount of spreading of the δ-input of tracer. Different constructions for the measuring

system are possible depending on the geometry of the studied vessel. The principle of the method was to measure the radiation intensity by at least two detectors. The maximum count rates measured were fitted to the solution of the dispersion equation without convection. This solution has the form of the standard normal distribution:

$$c = \frac{1}{(4\pi Dt)^{1/2}} \sum_{n=0}^{\infty} \exp\left[-\frac{r^2}{4\varepsilon_{p_r} t}\right] \tag{33}$$

The radial dispersion coefficients were determined at the bottom of the bed and at a height 3.3 meters above the bed bottom. At the bottom of the bed, the radial solids dispersion coefficient was found to range between 0.03 and 0.06 m^2/s. At the 3.3 meter height, the dispersion coefficient was about 0.02 m^2/s. The Peclet numbers and respective radial dispersion coefficients obtained by Viitanen are presented in Table 7.

Table 7: Best Fit Solid Lateral Solid Diffusivities Measured by Viitanen (1993)

z (m)	u_0 (m/s)	G_s (kg/m^2-s)	ε_{p_r} (cm^2/s)	Pe_r
0.0	6 - 15	480	300 - 600	100 - 175
3.3	6 - 15	480	200	250

Wei *et al.* (1994)

Wei *et al.* (1994) evaluated the radial and axial dispersion of solids in a cocurrent down flow CFB (CDCFB). The experimental apparatus and methodology is discussed under the axial dispersion Section given. The result for the lateral dispersion of solids was found to be:

$$Pe_a = \frac{8.93 \times 10^{-7}\,Re}{(1-\varepsilon)} + 101$$
$$Pe_r = 140 Re^{0.61}(1-\varepsilon)^{1.23} \tag{34}$$

Because these tests were conducted in a test section which operates at cross-sectionally averaged solid fractions and velocities close to that in the core of a CFB, they should provide a good approximation to the axial and radial dispersion in the core region of a CFB.

Koenigsdorff and Werther (1995)

Koenigsdorff and Werther presented a model for the flow structure and mixing processes in the upper dilute zone of a CFB. As part of their modeling, they determined radial dispersion and interphase transfer coefficients. These were determined from radial temperature profiles generated by local electrical heat sources. The electrical heat source and Pt 100 resistance thermometers used to measure the radial solid dispersion were located in the dilute core region of a 20 cm diameter, 3.25 meter high CFB operating with 60 micron silicon carbide particles with a particle density of 3217 kg/m^3. The temperature sensors located in the upper dilute zone of the CFB were assumed to indicate a time-averaged temperature which was between the temperature of the lean and the dense phases. This measured time-averaged temperature was assumed to be the weighted sum of the local temperature of the two phases:

$$T_m(r, \varphi, z) = \frac{f_l T_l + w f_d T_d}{f_l + w f_d} \tag{35}$$

where the subscripts l and d refer to the lean and dense phases respectively, and f is the volume fraction.

Energy balances to calculate temperature distributions in the two phases were written.

$$\begin{aligned} & f_l\left[\psi_l \rho_f v_{f_l} c_{p_f} + c_{v,l} \rho_s v_{s_l} c_{p_s}\right]\frac{dT}{dz} = \frac{1}{r}\frac{\partial}{\partial r}\left(f_l \lambda_{eff} r \frac{\partial T}{\partial r}\right) \\ & + S_l + f_d\left[\beta_s \rho_s v_{f_l} c_{v_d} c_{p_s} + \beta_f \rho_f \psi_d v_{f_l} c_{p_f}\right](T_d - T_l) \end{aligned} \tag{36}$$

$$\begin{aligned} & f_d\left[\psi_d \rho_f v_{f_d} c_{p_f} + c_{v,d} \rho_s v_{s_d} c_{p_s}\right]\frac{dT_d}{dz} = \\ & + S_l + f_d\left[\beta_s \rho_s v_{f_l} c_{v_d} c_{p_s} + \beta_f \rho_f \psi_d c_{p_f}\right](T_l - T_d) \end{aligned} \tag{37}$$

where ψ is the time averaged gas volume fraction, β is the coefficient of interphase transfer based on unit dense-phase volume, S is the local heat source per unit riser volume, and λ_{eff} is the effective thermal conductivity in the radial direction given by:

$$\lambda_{eff_r} = \psi_l\left(\lambda_f + \varepsilon_{f,r} \rho_f c_{p_f}\right) + \left(c_{v_l} \varepsilon_{p,r} \rho_s c_{p_s}\right) \tag{38}$$

The boundary conditions were:

$$
\begin{aligned}
&T_1\left(z = Z_o\right) = T_b \\
&\left.\frac{\partial T_1}{\partial r}\right]_{r=0} = 0 \\
&\left. - f_1 \lambda_{eff_r} \frac{\partial T_1}{\partial r}\right]_{r=0} = k_a\left(T_1 = T_a\right) \\
&T_d\left(z = Z\right) = T_o
\end{aligned}
\tag{39}
$$

where Z_o and T_b are the height and temperature at the bottom of the riser, T_o is the temperature at the riser exit, T_a is the ambient temperature, and k_a is the coefficient of heat loss to ambient air.

Because the flow was heated isotropically in the circumferential direction, only net heat transport in the axial and radial directions had to be accounted for. To evaluate the radial particle dispersion coefficients, only the core region of the riser was considered. It was assumed that the radius of this core region was 90 percent of the total riser radius, and that the dense phase could be neglected in the core region. With these assumptions, the temperature profile caused by the axial wire heater was calculated from the interphase energy equations. Gas dispersion was evaluated assuming the Peclet number based on radial gas dispersion was equal to 321. The radial solid dispersion coefficient was then determined from a least squares fit to the energy equations. The resulting regression curve was:

$$Pe_r = 150 + \left(5.0 \times 10^6\right)\phi \tag{40}$$

6.4.2 Summary of Experimental Radial Solids Dispersion Data

Table 8 presents a summary of the axial dispersion data taken by the investigators listed above. The data of Westphalen and Glicksman (1995), van Zoonen (1962), Wei *et al.* (1994) and Koenigsdorff and Werther (1995) most accurately reflect the actual axial solids dispersion coefficient in the dilute core of a CFB. The data of Viitanen (1993) measures the dispersion very low in the bed, which results in values of Peclet number which are lower than what would be expected high in the dilute core. Taking into account the uncertainty in

all the measurements, the agreement is fairly good for all the data, with the bulk of the Peclet numbers falling between 100 and 500.

Table 8: Lateral Solid Dispersion Coefficient Measurements in CFB's

Researcher	D (cm)	L (m)	d_p (μm)	ρ_s (kg/m^3)	u_o (m/s)	ε_{p_r} (cm^2/s)	Pe_r
Westphalen and Glicksman (1995)	20.5	7.0	180	2350	2.5 - 5.5	0.4 - 8.6	412 - 10000
van Zoonen (1962)	5	10	65	1600	2.5 - 12	0.94 - 12.0	250 - 833
Viitanen (1993)	100	39	70	2400	6 - 15	200 - 600	100 - 250
Wei *et al.* (1994)	14	7.6	54	1710	2.3 - 9	12 - 50	70 - 300
Koenisgsorff and Werther (1995)	20	3.5	60	3217	3 - 4	18 - 47	150 - 400

6.5 Determination of Cluster Dispersion Coefficient

As mentioned above, little quantitative information exists on the behavior of clusters in the core of a CFB. Horio and Kuroki have used a three dimensional laser sheet technique to examine the structure of solids above the freeboard of a CFB in a bed with a 20 cm diameter and a height of 1.6 meters. The particles used were FCC with a mean diameter of 61.3 microns and a density of 1780 kg/m^3. Cluster size was estimated to be about 1/10 to 1/20 the size of the bed diameter, and its shape was found to be paraboloid heading downward and having a long skirt upward. However, the data taken by Horio was obtained for a bed operating with very low gas superficial velocities (0.6 - 1.3 m/s) and very low solids recycle rates (0.2 - 16.5 kg/m^2-s). These conditions are not representative of those found in commercial units (gas superficial velocities on the order of 5.0 m/s and solids recycle rates on the order of 50 kg/m^2-s).

Arena *et al.* (1989) and Reh (1971) took images in two-dimensional CFB's, and concluded that clusters have a long string shape and form a network structure in the bed. In contrast, Li *et al.* (1991) observed small clusters (on the order of 3 mm) which were irregular but spherical near the wall region and strand-like in the core. Marzochella *et al.*, dropped

artificial circular clusters into a vertical gas up-flow in a two-dimensional plastic bed and presented observations on its shape and acceleration.

No data currently exists on the dispersion of these clusters in the core of a CFB. In order to investigate the rate of cluster breakup, a series of simple experiments was conducted in a scale model of a Foster Wheeler pressurized fluidized bed combustor. The Foster Wheeler combustor is 11.6 meters high, with a diameter of 33 cm, and operates at 14 atm and 1100 K. The particles used are dolomite, with a mean diameter of 165 microns and a particle density of 2650 kg/m^3. The scale model was constructed using the simplified scaling parameters described in Chapter 2. The scale factor was 6.5, resulting in a bed which had a height of 1.8 meters and a diameter of 5 cm. The particles in the scale model were polyethylene plastic with a mean particle diameter of about 120 microns, and a density of 710 kg/m^3. A detailed description of this bed is given in Chapter 2.

The device used to create clusters was a 1 cm diameter cylindrical thimble. This thimble was suspended in the bed on a thin Kevlar fishing line with a small conical sinker underneath in and a small washer above it. The Kevlar line above the thimble was connected to a spring which was in turn connected to the top of the bed. The other end of the Kevlar line was extended down through the distributor, through a small brass fitting in the inlet piping and out to a fishing reel which was attached to the side of the bed. In addition to the Kevlar line, a thin steel wire was strung from the top of then bed vertically down, through the distributor and the brass fitting, and attached to the floor. This wire served as a vertical guide. The equilibrium position of the thimble was 0.6 meters above the distributor. A schematic of this apparatus is given in Figure 6.1.

Figure 6.1: Cluster Dispersion Measurement Apparatus

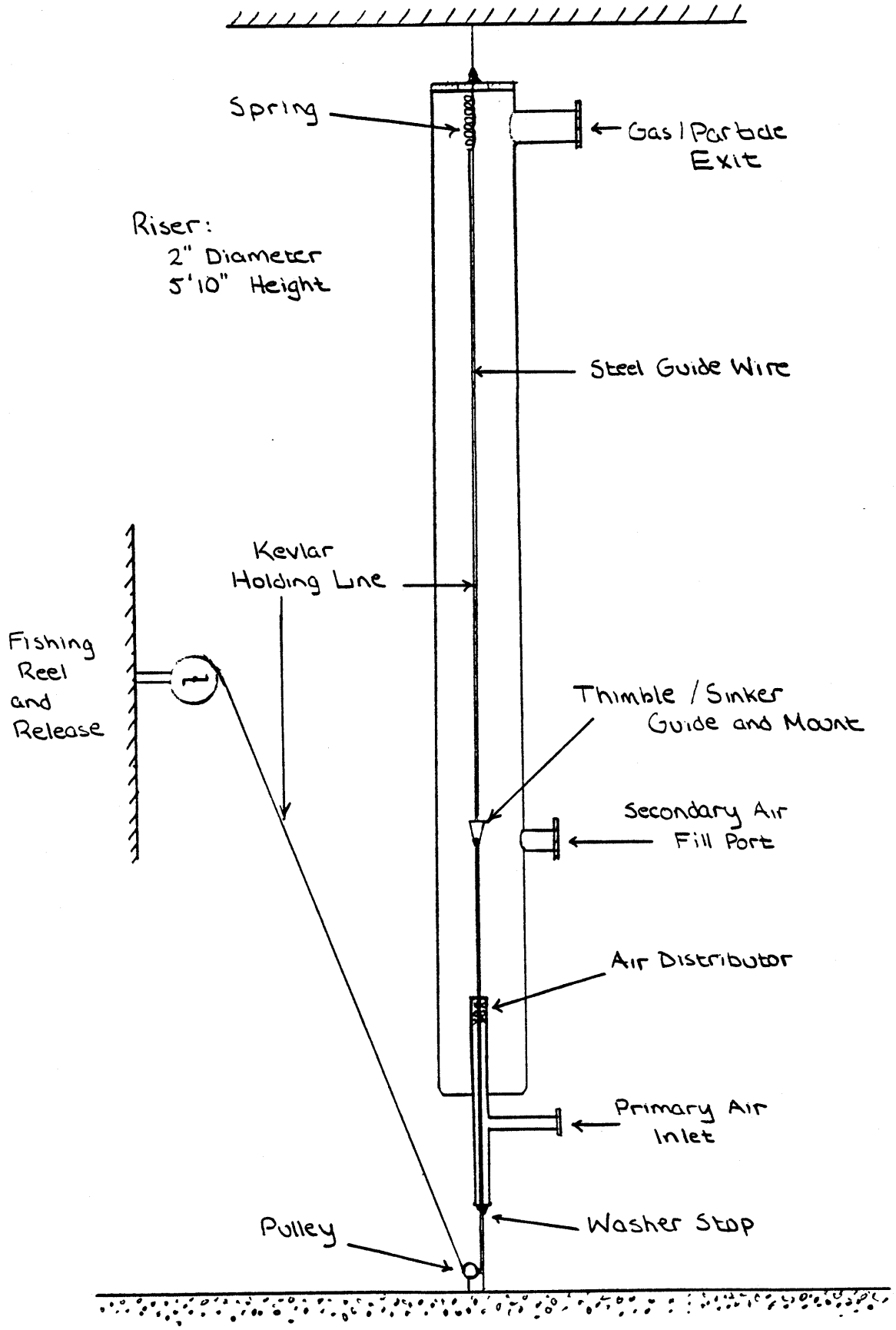

To operate the "cluster tosser", the fishing reel was wound back a specified distance, stretching the spring and lowering the thimble. The thimble was then filled with particles through the secondary air ports (which were not being used for these tests). The tension button on the reel was released, sending the thimble upward until the stop washer on the Kevlar line between the brass fitting and the fishing reel, hits the brass fitting stopping the thimble. The guide wire ensures the thimble path is vertical. The particles continue upward in the form of a cluster which is entrained and dispersed by the up-flowing gas. Videos were then taken with a high speed image analysis system as the cluster travels upward dispersing radially outward.

6.5.1 Determination of Initial Cluster Velocity

The thimble was filled so that particles were 1 cm high in the thimble (approximating a cylindrical cylinder 1 cm in diameter, and 1 cm high). This gives a ratio of cluster to bed diameter of 1/5. The "cluster tosser" was calibrated by correlating the distance the spring is stretched to the velocity of the thimble at the point where the stop washer hits the brass fitting. The velocity was determined by tracking the leading edge of the particles leaving the thimble with the high speed video system over a short distance (5 cm) when there was no gas flowing. The equation of motion for a sphere neglecting all forces except gravity and drag is:

$$z = \left(v_f - \frac{g}{F}\right)t + \frac{\left(v_{cl} - v_f + \frac{g}{F}\right)\left[1 - \exp\left(-Ft\right)\right]}{F}$$
$$F = \frac{3}{4}\frac{C_D}{d_{cl}}\frac{\rho_f}{\rho_{cl}}\left|v_{cl} - v_f\right| \qquad (41)$$

For short distance, the distance-time plot is nearly linear such that the velocity can be approximated as the distance traveled divided by the elapsed time, as determined from the video images. Figure 6.3 present the calibration curve of the distance the spring is stretched from equilibrium versus the velocity when the spring returns to equilibrium. Using this curve allowed the cluster to be launched at a velocity equal to the gas superficial velocity.

Figure 6.3
Calibration Curve for Initial Cluster Velocity

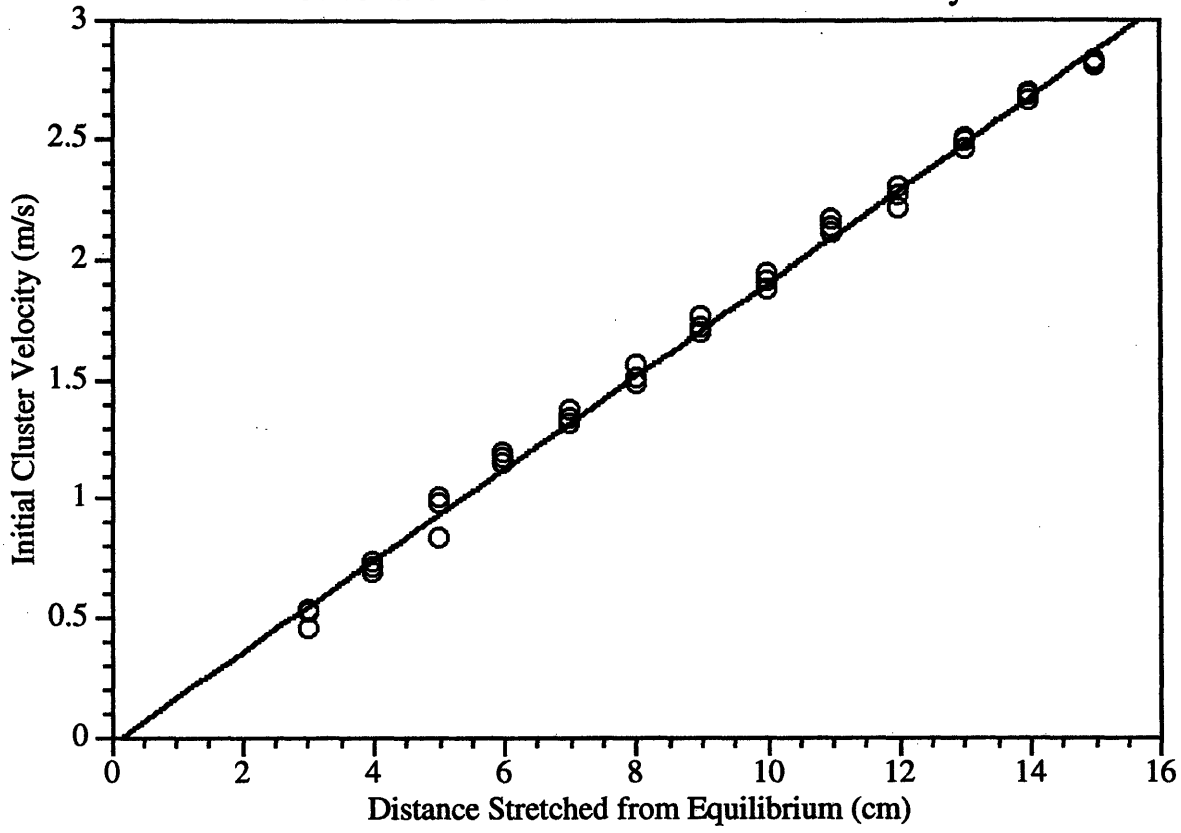

6.5.2 Recording Data

The high speed video images were used to approximate the cluster radius as a function of time, $r_{cl}(t)$. The average cluster concentration as a function of time was determined by assuming the cluster could be approximated as a sphere, and dividing the initial cluster mass by the mass of a solid sphere with a radius equal to the cluster radius, $r_{cl}(t)$, determined from the videos. This procedure resulted in sets of data consisting of both cluster radius and average concentration as a function of time.

6.5.3 Data Interpretation

For an instantanteous point source on an infinite plan surface, the diffusion equation is

$$\frac{\partial^2 C}{\partial x^2} + \frac{\partial^2 C}{\partial y^2} = \frac{1}{\varepsilon_r}\frac{\partial C}{\partial t} \tag{42}$$

Where ε_r is the diffusion coefficient.

The solution of (36) is

$$C = \frac{A}{t}\exp\left(-\frac{\left(x^2 + y^2\right)}{4\varepsilon_r t}\right) \tag{43}$$

The constant A is defined in terms of M, the total amount of material diffusing:

$$M = \int_{-\infty}^{\infty}\int_{-\infty}^{\infty} C\,dxdy = 4\pi\varepsilon_r A \tag{44}$$

C is the amount of diffusing substance per unit area. The concentration at a distance r from a point source is then

$$C = \frac{M}{4\pi Dt}\exp\left(-\frac{r^2}{4\varepsilon_r t}\right) \tag{45}$$

The solution of an instantaneous point source in an infinite volume is

$$C = \frac{M}{8\left(\pi Dt\right)^{3/2}}\exp\left(-\frac{r^2}{4\varepsilon_r t}\right) \tag{46}$$

Equation (40) can be used to find the solution of a line of source of strength M per unit length (kg/m-s) in an infinite volume:

$$C = \frac{M}{8\left(\pi\varepsilon_r t\right)^{3/2}}\int_{-\infty}^{\infty}\exp\left[\frac{-\left(\left(x-x'\right)^2 + \left(y-y'\right)^2 + \left(z-z'\right)^2\right)}{4\varepsilon_r t}\right]dz' \tag{47}$$

$$C = \frac{M}{4\pi\varepsilon_r t}\exp\left[\frac{-r^2}{4\varepsilon_r t}\right] \tag{48}$$

For a cylindrical surface of radius a,

$$C = \frac{Mr'}{4\pi\varepsilon_r t}\int_0^{2\pi} \exp\left[\frac{-r^2}{4\varepsilon_r t}\right]d\theta' \tag{49}$$

$$C = \frac{Mr'}{4\pi\varepsilon_r t}\int_0^{2\pi} \exp\left[\frac{-\left(r^2 + r'^2 - 2rr'\cos\left(\theta'\right)\right)}{4\varepsilon_r t}\right]d\theta' \tag{50}$$

$$C = \frac{Mr'}{4\pi\varepsilon_r t}\exp\left[\frac{-\left(r^2 + r'^2\right)}{4\varepsilon_r t}\right]\int_0^{2\pi} \exp\left[\frac{-\left(rr'\cos\left(\theta'\right)\right)}{2\varepsilon_r t}\right]d\theta' \tag{51}$$

where the equation

$$r^2 = r^2 + r'^2 - 2rr'\cos\left(\theta - \theta'\right) \tag{52}$$

was used.

From the well known identity

$$I_\nu(z) = \frac{\left(\frac{z}{2}\right)^\nu}{\Gamma\left(\nu + \frac{1}{2}\right)\Gamma\left(\frac{1}{2}\right)}\int_0^\pi \exp\left[\pm\cos\left(\theta\right)\right]\sin^{2\nu}\left(\theta\right)d\theta \tag{53}$$

(41) becomes

$$C = \frac{Mr'}{2\varepsilon_r t}\exp\left[\frac{-\left(r^2 + r'^2\right)}{4\varepsilon_r t}\right]I_0\left(\frac{rr'}{2\varepsilon_r t}\right) \tag{54}$$

For a solid cylindrical source,

$$C = \frac{M}{2\varepsilon_r t}\exp\left[\frac{-(r^2)}{4\varepsilon_r t}\right]\int_0^a \exp\left[\frac{-(r'^2)}{4\varepsilon_r t}\right] I_0\left(\frac{rr'}{2\varepsilon_r t}\right) r'dr' \tag{55}$$

Here M is the amount of substance per unit cross sectional area, per unit length - the initial concentration, i.e.,

$$C = \frac{C_o}{2\varepsilon_r t}\exp\left[\frac{-(r^2)}{4\varepsilon_r t}\right]\int_0^a \exp\left[\frac{-(r'^2)}{4\varepsilon_r t}\right] I_0\left(\frac{rr'}{2\varepsilon_r t}\right) r'dr' \tag{56}$$

At the axis, where r = 0,

$$C_o\left(1 - \exp\left[\frac{-(a^2)}{4\varepsilon_r t}\right]\right) \tag{57}$$

The average cluster concentration can be found from

$$\bar{C}(t) = \frac{2}{r_c^2}\int_0^{r_c} rC(r, t)dr \tag{58}$$

$$\bar{C}(t) = \frac{2}{r_c^2}\int_0^{r_c}\left[\frac{C_o}{2\varepsilon_{cl} t}\exp\left[\frac{-(r^2)}{4\varepsilon_{cl} t}\right]\int_0^a \exp\left[\frac{-(r'^2)}{4\varepsilon_{cl} t}\right] I_0\left(\frac{rr'}{2\varepsilon_{cl} t}\right) r'dr'\right]dr \tag{59}$$

The mixing parameter, D_{cl}, is the dispersion rate of the cluster. This parameter is determined by a least squares technique using the high speed video data, as discussed above. Figure 6.4 shows equation (53) plotted against the data for the cluster dispersion resulting from the minimization of the total variance between (53) and the data.

Figure 6.4
Average Cluster Solid Fraction vs. Time

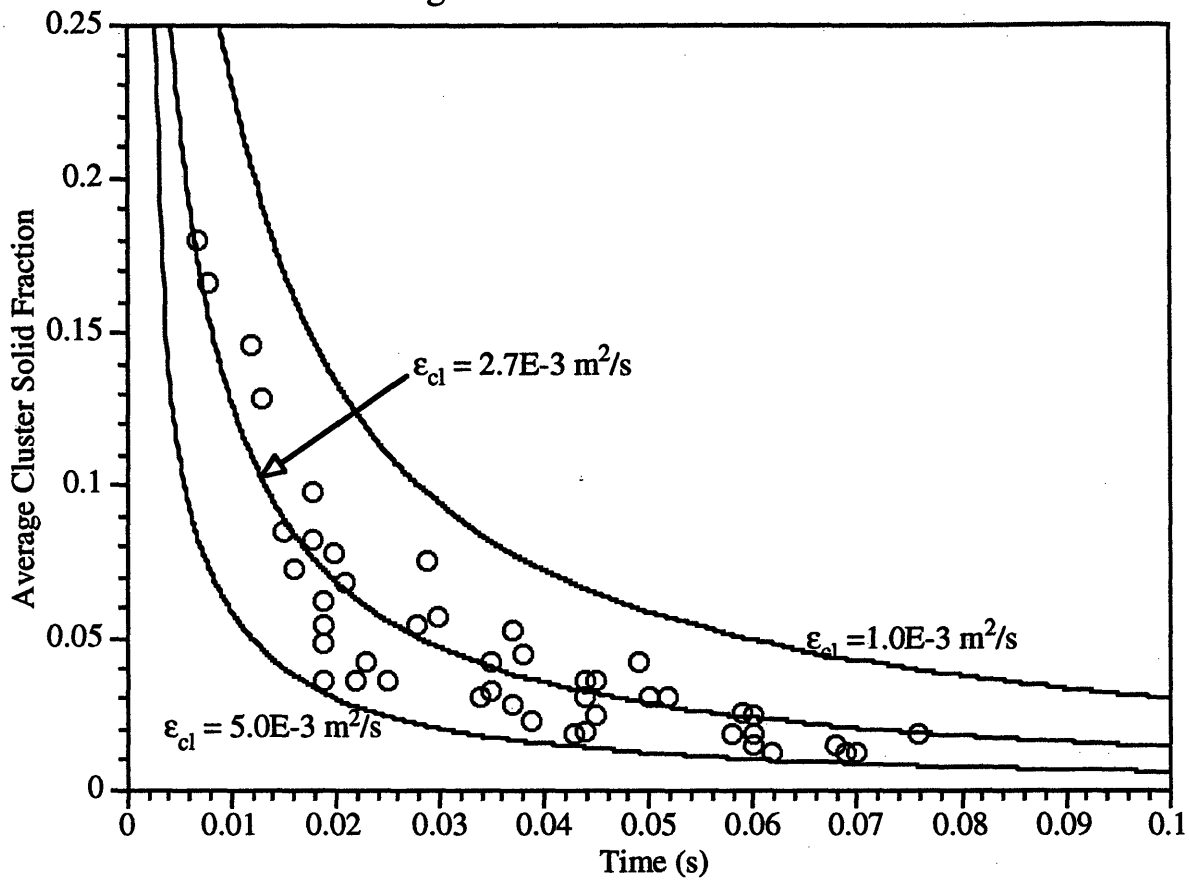

The best value of the cluster dispersion based on a least squares curve fit of equation (53) was 2.7E-3 m^2/s. All of the data falls between values of between 1.0E-3 m^2/s and 5.0E-3 m^2/s. The data follows the trend of equation (53) quite well, indicating that the cluster spreads in a manner described by diffusion from an instantanesous solid cyclindrical source.

6.6 Evaluation of Di_a and Di_r

Using the experimental data of previous investigators discussed in Sections 6.3 amd 6.4, and the estimated cluster dispersion coefficient of 2.7 m2/s, evaluated in a 5 cm CFB, the values of Di_a and Di_r can be determined from equations (3) and (6).

6.6.1 Evaluation of Di_r

For the radial Peclet number, a value of 300 will be used. This value falls within the range of data taken by most of the investigators listed in Table 8, and is within an order of magnitude of all the data. From this value, the lateral dispersed phase solids dispersion coefficient in the 5 cm bed, which had a superficial gas velocity of 1.5 m/s, is 2.5E-4 m^2/s. The rate of cluster dispersion was 2.7E-3 m^2/s. This gives a value for Di_r of about 1.0E-3. This indicates that the lateral movement of solids is dominatd by the dispersion of individual particles because the clusters break up very quickly and subsequently disperse as individual particles to the walls. In other words, the ratio of the time it takes a cluster to break up to the time it takes individual particles to disperse to the walls of a CFB is very small. This supports using a single particle diffusion model of the type developed in the previous Sections for lateral solids dispersion in CFB's.

6.6.2 Evaluation of Di_a

To determine Di_a, equation (6) is used. For a 0.5 cm cluster with an effective density of 7.2 kg/m^3 (one tenth the particle density), the terminal velocity is approximately 6 m/s. The rate of cluster dispersion was 2.7E-3 m^2/s resulting in a value for Di_a of about 3.0E-2. This indicates that the axial movement of solids is dominatd by the convection of individual particles rather than clusters because the clusters break up very quickly. The ratio of the distance a particle travels in a cluster is insignificant compared to the overall bed height. This supports using a single particle convective model of the type developed in this Chapter for describing the axial movment of particles in the core of a CFB. This assumption was used in developing the overall mass and momentum equations for the core/annulus structure, and also used in developing the model for the prediction of radial solids concentration.

7.0 EFFECT OF THE BOUSSINESQ-BASSET HISTORY TERM

7.1 Introduction

Most of the attention in determining dispersion coefficients has been focused on the evaluation of the long time particle diffusion in stationary homogeneous turbulence. Solution of the exact form of the equation of motion of particles has the drawback of only applying to very low Reynolds number flows. Additionally, the full equation of motion as developed by Maxey and Riley contains terms which are time-consuming when calculated repetitively. To address the first problem, investigators have resorted to using empirical coefficients for several of the terms in the equation of motion [Hjelmfelt and Mockros, (1966); Odar and Hamilton (1964); Clift *et al.* (1978)]. These coefficients multiply the Stokes drag , the added mass, and the Boussinesq-Basset history term. The use of these empirical coefficients has enabled accurate calculations of particle trajectories in flow fields at high Reynolds numbers. These calculations have resulted in predictions of particle characteristics and behavior, such as dispersion in a turbulent field.

The second problem has not been addressed by most investigators. The majority of Lagrangian computations, such as the ones conducted in this study, have been made for cases were the history term was assumed to be small. By using dimensional arguments this term is almost always neglected, a very convenient assumption which not only reduces the order of the differential equation of motion of the particle and makes it explicit in velocity, but also diminishes the memory requirements of the computations by not retaining information of the history of the acceleration of the particle. Neglecting the history term does not change appreciably the calculations for particles of large size. However, it was observed that for small particles the history term accounts for approximately 20 percent of the total force [Li and Michaelides (1992)]. Neglecting the history term, therefore, may result in a substantial error in particle velocities and positions. In this Section calculations are performed to determine the effect of the history term on the trajectories of particles under various flow conditions.

7.2 Particle Equation of Motion

The equation of motion of a single particle in a an unsteady flow can be written in terms of the dimensionless relative velocity, $w_i = \frac{V_{p_i} - V_{f_i}}{u_o}$, in the ith direction:

$$\frac{dw_i}{dt} + \lambda C_D w_i + \lambda(1-\beta)\frac{dv_{fi}}{dt} + \lambda\Delta_H\sqrt{\frac{9\beta}{2\pi}}\left\{\int_0^t \frac{\frac{dw_i}{d\tau}}{\sqrt{(t-\tau)}}d\tau + \frac{w_i(0)}{\sqrt{t}}\right\}$$

$$-\lambda(1-\beta)G_i = 0 \qquad (1)$$

where β is the ratio of the fluid and particle densities, and λ is a parameter which includes the added mass term:

$$\lambda = \frac{1}{1+\frac{\Delta_A\beta}{2}} \qquad (2)$$

Since Δ_A is function of the acceleration number [Odar and Hamilton, (1964)], λ is not a constant. In equation (1), time is made dimensionless by using the characteristic time of the particle:

$$\tau_p = \frac{\rho_s d_p^2}{18\mu} \qquad (3)$$

The first term on the l.h.s. of (1) is the particle acceleration. The second term is the drag term. The third term represents the local acceleration of the fluid phase. The fourth term is the history of the particle as it moves in the unsteady flow field. The history term includes the effect of a finite initial velocity of the particle. This part is often absent in commonly used expressions where the assumption of zero initial velocity is made. The final term is the gravity/buoyancy effect, where

$$G_i = \frac{g_i\tau_p}{u_o} \qquad (4)$$

The Lagrangian derivative d/dt is with respect to the moving particle. The drag, added mass, and history term coefficients C_D, Δ_A, and Δ_H are empirical expressions, which account for the finite Reynolds number effect. In the limit of very small particle Reynolds number, they reduce to 1.

The initial condition for this equation is

$$w_i(0) = w_{i0} \tag{5}$$

and the initial acceleration is given by

$$\begin{aligned} &\frac{dw_i}{dt}(0) - \lambda C_D w_{i0} + \lambda(1-\beta)\frac{dv_{fi}}{dt}(0) + \lambda\Delta_H\sqrt{\frac{9\beta}{2\pi}}\, w_i(0)\delta(t) \\ &-\lambda(1-\beta)G_i = 0 \end{aligned} \tag{6}$$

where $\delta(t)$ is the Dirac delta function. The fourth term in (6) accounts for the impulse on particles which are introduced with finite velocity into the fluid.

It must be pointed out that recent results by Lawrence and Weinbaum (1988) and Yang and Leal (1991) indicate that the kernel of the history integral is a special case applied only to rigid spheres. They have observed that when the sphere diverges from sphericity or perfect rigidity, the kernel of the history integral attains a more complicated form. Also, Mei *et al.* (1991) and Lovalenti and Brady (1993) allude to a different decay of the history integral (initially the decay is of the order $\sqrt{t}$ and later of the order t^2) when the inertial terms in the momentum equation of the fluid are considered. However, even with the different kernel or the faster decay in the latter stages of motion, the history integral is always present.

Realistic Lagrangian calculations with the equation of motion at finite Reynolds numbers are always done with coefficients similar to those used in (4). Clift *et al.* (1978) report such calculations for the acceleration of a particle from rest, where they show that the history term may account for as much as 20 percent of the acceleration at the early stages of the particle motion.

Equation (4) is not explicit in terms of the relative velocity. Solving it numerically involves time consuming iterations. If the history term is neglected, the equation becomes explicit in the relative velocity and one may obtain particle velocities and trajectories much faster. However, when the size of the particles is small and the fluid velocity varies at high frequency, the history term is not insignificant.

7.3 Solution of the Equation of Motion

The equation of motion was solved using a Monte-Carlo simulation scheme as outlined in Press *et al.* (1990). Throughout the calculations, the following empirical equations were used for the three coefficients, C_D, Δ_A , and Δ_H

$$C_D = \frac{24}{Re_{u_{rel}, d_p}}\left[1 + 0.173Re_{u_{rel}, d_p}^{0.657}\right] + \frac{0.413}{1 + 16300Re_{u_{rel}, d_p}^{-1.09}} \tag{7}$$

$$\Delta_A = 2.1 - \frac{0.132Ac^2}{\left(1 + 0.12Ac^2\right)} \tag{8}$$

$$\Delta_H = 0.48 - \frac{0.5Ac^3}{\left(1 + Ac\right)^3} \tag{9}$$

In terms of the dimensionless velocity and acceleration and the other quantities defined above, the particle Reynolds number and Acceleration number, Ac, are

$$Re_{u_{rel}, d_p} = \frac{d_p \left| w_i u_o \right| \rho_f}{\mu} \tag{10}$$

$$Ac = \frac{18}{\beta Re_{u_{rel}, d_p}} \left| \frac{dw_i}{dt} \right| \tag{11}$$

The drag coefficient is the one given by Turton and Levenspiel (1986), and the other expressions were derived by Odar and Hamilton (1964). These expressions are frequently used and have been verified by Tsuji *et al.* (1991) for particle flows at non-zero Reynolds numbers.

The particle trajectory was calculated for the type of fluid field described in Section 2. The turbulent flow field was described by a sequence of eddies which have characteristic speed u_e and length l_e, and a decay time of τ_e, but whose direction is random, characterized by a sign S, which can be either positive or negative with equal probability. The eddy length, eddy speed, and eddy decay time were determined from the model of Hutchinson *et al.* (1971):

$$l_e = 0.11D \tag{12}$$

$$u_e = u_\tau = u_o\sqrt{\frac{f}{2}} \tag{13}$$

$$\tau_e = 1.6\frac{l_e}{u_e} \tag{14}$$

where u_τ is the friction velocity, u_e is the eddy velocity, f is the single phase friction factor, and τ_e is the eddy decay time.

The particle/fluid interaction time is determined from the minimum of the particle eddy vertical crossing time, the particle eddy horizontal crossing time, and the eddy decay time, as given in Table 1.

Table 1: Expressions for Various Time Scales

Time Scale	Equation	Region where Time Scale Will be Controlling
Particle-Eddy Vertical Crossing Time	$\frac{l_e}{u_t}$	Large particles, relatively dilute suspensions
Particle-Eddy Horizontal Crossing Time	$\frac{l_e}{u_e}\left(\frac{\exp\left(\frac{3}{8}C_D\frac{l_e}{R}\frac{D}{d_p}\frac{\rho_f}{\rho_s}\right)-1}{\frac{3}{8}C_D\frac{l_e}{R}\frac{D}{d_p}\frac{\rho_f}{\rho_s}\left(1\pm\frac{v_{pr0}}{u_e}\right)}\right)$	Small particles, relatively dilute suspensions
Eddy Decay Time	$1.6\left(\frac{l_e}{u_e}\right)$	Very large diameter beds, or very small particles, dilute suspensions

7.4 Results

Simulations were performed for several flow conditions. Figures 1 and 2 present results for a case where the solid to fluid density ratio was assumed to be 710 and 2 respectively. In these runs, the gas superficial velocity was 5.0 m/s, the bed diameter was assumed to be 20 cm, and the particle diameter was 50 microns. The initial relative velocity was assumed to be equal to the calculated eddy velocity as given in equation (13). The change in velocity is due to the particle entering or leaving and eddy.

The simulation where the density ratio is 710 represents typical operating conditions of a pressurized fluidized bed. It is clear from the plot that the exclusion of the history term does not cause significant deviations from the predictions of the complete equation of motion.

However, significant deviations occurred between simulations run with and without the history term for the case where the solid to gas density ratio was lowered to 2. This trend is not surprising, since the history force scales as the inverse of the solid to gas density ratio. For large density ratios, this force is negligible, while for density ratios lower than about 10, significant effects were detected.

Figure 1

Comparison of Particle Velocity Response with and Without History Term

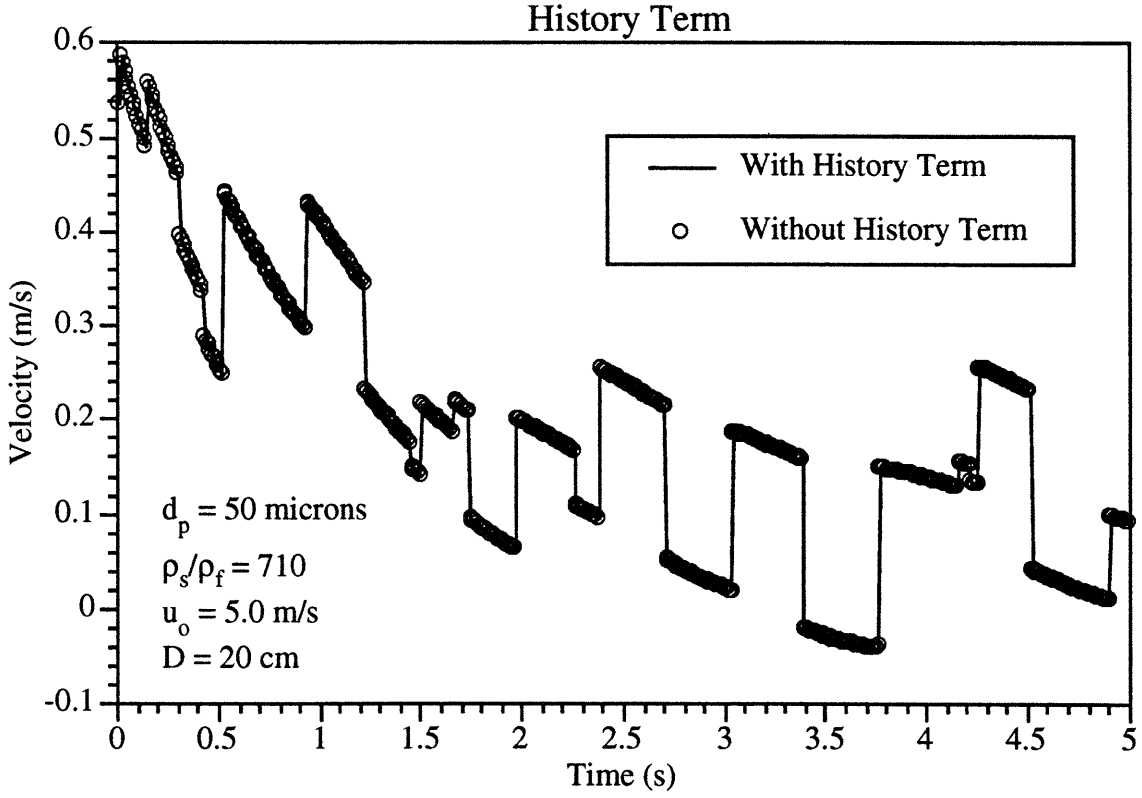

Figure 2
Comparison of Particle Velocity Response with and Without History Term

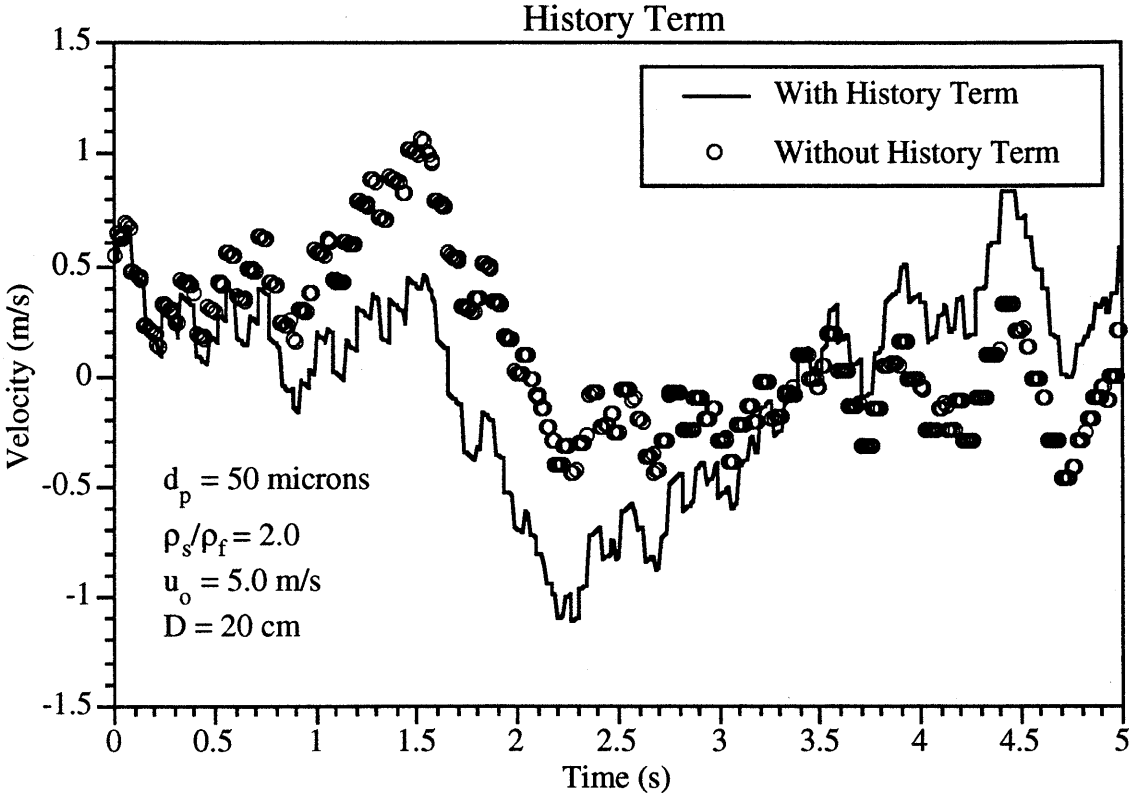

The simulations run indicate that for conditions typical of both hot and cold CFB's, the history term can be neglected. Noticeable deviations between the full equation of motion, and the equation of motion without the history term did not occur until the solid to gas density ratio fell below 500, with significant deviations occurring for density ratio's below 100 (see Figure 3). This corresponds to a pressure limit of about 16 atmospheres for a CFB operating at 1100 K with dolomite having a significant mass fraction of particles below 100 microns. Even the small deviations indicated in Figure 3 can become important in the Lagrangian simulations since the cumulative effect of these small deviations over many interactions can become large. While for the purposes of this study this force can be neglected, it should be remembered that as PCFB's go to higher pressures, this term may become significant in any Lagrangian simulation of particle movement in the dilute core.

Figure 3

Comparison of Particle Velocity Response with and Without History Term

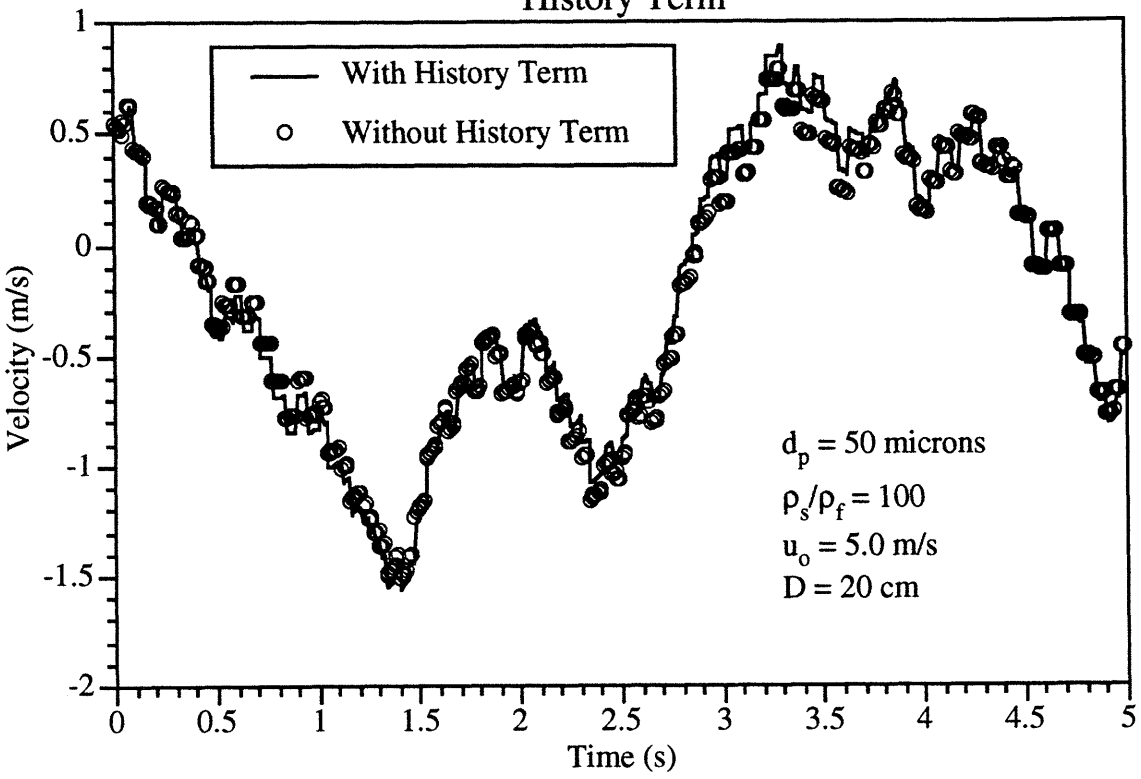

8.0 SUMMARY OF CFB HYDRODYNAMIC MODELING

The following Section provides a brief summary of the equations used to calculate the axial and radial solid fraction profiles in a CFB, along with how the lateral solids dispersion coefficient is determined. For a rigorous derivation of the equations, the reader is referred to Sections 1 through 7.

8.1 Determination of Lateral Solids Dispersion Coefficient

The turbulence is assumed isotropic and profile effects are not important. The simple gas turbulence model of Hutchinson *et al.* (1971) described above is used:

$$l_e = 0.11D \tag{1}$$

$$u_e = u_\tau = u_o\sqrt{\frac{f}{2}} \tag{2}$$

where u_τ is the friction velocity, u_e is the eddy velocity, and f is the single phase friction factor.

Eddies are characterized by a mean decay time, τ_e, and the contact time between a particle and eddy cannot exceed this decay time. A reasonably position free constant can be assume for all radial locations,

$$\frac{\tau_e}{R/u_\tau} = 0.35 \tag{3}$$

For this it follows that

$$\tau_e = 1.6\frac{l_e}{u_e} \tag{4}$$

In (4), the factor 1.6 is the ratio of Lagrangian and Eulerian time scales of turbulence; there is considerable uncertainty over the actual value, reported values showing a wide range (Laufer, 1954). However, for fluidized beds, the particles are sufficiently large that their motion is essentially Eulerian and, with the exception of developing particle motion, the time scale of eddy-particle interaction is determined mainly by the particle-eddy crossing time in the vertical direction.

The turbulent flow field is described by a sequence of eddies which have characteristic speed u_e and length l_e, and a decay time of τ_e, but whose direction is random, characterized by a sign S, which can be either positive or negative with equal probability.

Integrating the equation of motion, neglecting the history and virtual mass terms gives the particle position

$$x_{p_r} = x_{p_{r_o}} \pm u_e t_i + \frac{\left(v_{p_r} \pm u_e\right)\left(1 - \exp\left(-\beta t\right)\right)}{\beta} \tag{5}$$

Ensemble averaging (5) over many interactions and simplifying for small values of βt_i gives the mean square displacement of the particle:

$$\left\langle x_{p_r}^2 \right\rangle = 2\left(\frac{u_t}{l_e}\right)\left\langle x_{p_i}{}^2 \right\rangle\left(\frac{t}{\beta t_i}\right)\left(1 - \exp(\beta t)\right) \tag{6}$$

where t_i is given by the minimum of the particle-eddy vertical crossing time, particle-eddy horizontal crossing time, eddy decay time, or time between successive collisions. In general, it is not known which mechanism (vertical crossing trajectory, horizontal crossing trajectory, eddy decay time, or collisional effects) will control the interaction time. Table 1 gives the expression for these characteristic times.

Table 1: Expressions for Various Time Scales

Time Scale	Equation	Region where Time Scale Will be Controlling
Particle-Eddy Vertical Crossing Time	$\frac{l_e}{u_t}$	Large particles, relatively dilute suspensions
Particle-Eddy Horizontal Crossing Time	$\frac{l_e}{u_e}\left(\frac{\exp\left(\frac{3}{8}C_D\frac{l_e}{R}\frac{D}{d_p}\frac{\rho_f}{\rho_s}\right)-1}{\frac{3}{8}C_D\frac{l_e}{R}\frac{D}{d_p}\frac{\rho_f}{\rho_s}\left(1\pm\frac{v_{p_{r0}}}{u_e}\right)}\right)$	Small particles, relatively dilute suspensions
Eddy Decay Time	$1.6\left(\frac{l_e}{u_e}\right)$	Very large diameter beds, or very small particles, dilute suspensions
Time Between Collisions Relatively Dilute Suspensions	$\tau_{c_{ij}}=\frac{1}{n_j\pi d_{ij}^2\left(u_{t_1}-u_{t_2}\right)}$	Relatively dense suspensions, large particle size distributions
Time Between Collisions Dense Suspensions	$\tau_{c_{ij}}=\frac{1}{n_j\pi d_{ij}^2\left(v'_{p_r}\right)}$	Very dense suspensions

The particle radial dispersion coefficient can be calculated by simulating many particle-eddy interactions using equation (5), and then using (6) to determine the particle mean square displacement. The lateral dispersion coefficient is then determined in the usual way

$$\frac{1}{2}\left(\frac{\left\langle X_{p_r}^2\right\rangle}{t_{i_{avg}}}\right)=\varepsilon_p \tag{7}$$

using the appropriate expression for the average interaction time $t_{i\,avg}$.

8.2 Axial Concentration Profile

The axial concentration profile in the dilute core is calculated starting with the mass conservation equation over a volume element in the core of a CFB

$$\int_{\forall}\left(\frac{\partial}{\partial z}\left(\bar{u}\,C(r,z)\right)-S(r,z)+\frac{\partial}{\partial t}\left(C(r,z)\right)\right)d\forall-\int_{\Sigma}\varepsilon_{p_r}\nabla_r C(r,z)\cdot\hat{n}\,d\Sigma=0 \tag{8}$$

where S(r,z) is a source term, C(r,z) is the local mean concentration, Σ is the surface area of the elemental volume, $d\forall$ is the volume element, $\bar{u}$ is the local particle axial velocity, and

$$\nabla_r=\hat{r}\frac{\partial}{\partial r} \tag{9}$$

$$\nabla_r^2=\frac{\partial^2}{\partial r^2}+\frac{1}{\hat{r}}\frac{\partial}{\partial r} \tag{10}$$

The first term in (8) gives the effect of dilation arising from varying axial velocity, and the final term accounts for the loss of particles by diffusion in direction perpendicular to the direction of gas flow.

The source term is assumed to be a plug source of radius r_p originating at the bottom of the bed, and a continuous source arising from the re-entrainment of particles from the wall cluster layer

$$S(r,t)=\frac{D}{2r_e}E(t)\delta(r-r_e)+\frac{D^2}{4r_p^2}\bar{C}_p u(r_p-r)\delta(t) \tag{11}$$

where r_e is the instantaneous radial position of the cluster wave height for entrainment, $\delta(r)$ is the Dirac delta function, E(t) is the instantaneous rate per unit time area of bed wall, $\bar{C}_p$ is the mean concentration over the tube of a plug source of radius r_p present at the bed entrance (t = 0). In (11), the delta function term represents the continuous time varying source arising from re-entrainment of particles from the cluster layer, and the factor $\frac{D}{2r_e}$ appears since E(t) is given per unit area of bed wall surface.

Entrainment from the wall layer is obtained by assuming that E(t) at a given axial point on the wall depends on the average cross-sectional solid fraction at a distance equal to the fall distance of a cluster above that point on the wall. The fall distance of a cluster can be approximated from the result obtained in Chapter 4:

The boundary conditions are:

$$C\left(\frac{D}{2}, t\right) = 0 \tag{12}$$

$$C(r, t) \geq 0 \text{ everywhere else} \tag{13}$$

The solution of equation (8) with the above source terms and boundary conditions is:

$$C(t) = \frac{4}{R\bar{u}(t)} \sum_{n=1}^{\infty} \left\{ \frac{J_0\left(\beta_n \frac{r_e}{R}\right)}{\beta_n J_1(\beta_n)} \int_0^t \bar{u}(t') E(t') \exp\left(\frac{-\varepsilon_{p_r} \beta_n^2 (t - t')}{R^2}\right) dt' \right\} + \frac{4R\overline{C_p}\bar{u}(0)}{r_p \bar{u}(t)} \sum_{n=1}^{\infty} \left\{ \frac{J_1\left(\beta_n \frac{r_p}{R}\right)}{\beta_n^2 J_1(\beta_n)} \exp\left(\frac{-\varepsilon_{p_r} \beta_n^2 t'}{R^2}\right) \right\} \tag{14}$$

where

$$t \simeq \frac{z}{(u_o - u_t)} \tag{15}$$

8.3 Particle Collisions

In the limit where the viscous relaxation time is much smaller than the time between successive collisions, particles relax to near their terminal velocities between collisions. The mean and mean-square velocities due only to collisions in this limit are found by substituting the changes in the particle velocity due to collisions into kinetic energy balance equations. The result is:

$$\langle u_{i_z} \rangle = (-1)^i \varepsilon \left(\frac{\tau_{v_i}}{\tau_{v_1}}\right)\left(\frac{\tau_{c_{12}}}{\tau_{v_{ik}}}\right)\left(\frac{m_k}{m_i + m_k}\right)\left(\frac{e+1}{2}\right) \tag{16}$$

$$\langle u_i^2 \rangle = \varepsilon \left(\frac{\tau_{v_i}}{\tau_{v_1}}\right)\left(\frac{\tau_{c_{12}}}{\tau_{v_{ik}}}\right)\left(\frac{m_k}{m_i + m_k}\right)^2 \left(\frac{e(e+1)}{2}\right) \tag{17}$$

$$\left\langle u_{i_r}^2 \right\rangle = \frac{\varepsilon}{3}\left(\frac{\tau_{v_i}}{\tau_{v_1}}\right)\left(\frac{\tau_{c_{12}}}{\tau_{v_{ik}}}\right)\left(\frac{m_k}{m_i + m_k}\right)^2 \frac{(e+1)^2}{12} \tag{18}$$

where e is the coefficient of restitution.

For regions where the time between successive collisions is of the order or less than the viscous relaxation time of the particles, the approximate solution of Kumaran and Koch is used. This solution calculates the properties of the suspension by approximating the distribution function as a composite Gaussian distribution. This distribution reduces to a Gaussian distribution when the collisional time scale is much small than the particle relaxation time. In the intermediate region, the composite Gaussian has a non-zero skewness. The dilute limit equations are used up to a ratio of viscous to collisional time scales of 5. Beyond that the Kumaran and Koch distribution function is used to determine the collisional contribution to the fluctuating velocity of the particles.

8.4 Gas Turbulence Modification

A simple theory was developed for the modification of turbulence intensity due to the presence of particles in dilute solid-gas flows. The mechanism for turbulence reduction was assumed be the energy dissipation due to the acceleration of a particle. The expression for the reduction in kinetic energy due to a particle eddy interaction is

$$\Delta E = \frac{-\pi d_p^3 \rho_s}{12} u_t^2 \left[1 - \exp\left(-\frac{2Ct_i}{\tau_p}\right)\right] \tag{19}$$

To develop an expression which is valid for a suspension of many particles, assume that a fluid element acquires momentum at time t = 0 under the influence of a hydrodynamic field disturbance (pressure fluctuation). Further, it moves by inertia and interacts with the particles inside. Then the carrier fluid is described by the following equation of conservation of momentum:

$$d\left[v_f' + \sum_{i=1}^{n} \gamma_i v_{p_i}'\right] = 0 \tag{20}$$

where γ represents the ratio of particle to fluid mass flux. The summation is included to represent particles of n different diameters.

Integration of (20) and using (19) gives (after some manipulation)

$$v_f' = \frac{1}{\left(1+\gamma_i\right)}\left[u_e + \sum_{i=1}^{n}\gamma_i\left(\frac{u_t}{2}\right)\left[1-\exp\left(-\frac{2Ct_i}{\tau_p}\right)\right]\right] \tag{21}$$

This expression, along with the simple gas turbulence based on Laufer's data discussed above, is used to determine the gas root mean square fluctuating velocity.

8.5 Expression for Particle Drag

A survey of methods used to correct the standard single particle drag curve was conducted. For suspensions of non spherical particles, the following methodology resulted:

1. Assume a value for u_ϕ/u_t (u_ϕ is the terminal velocity of the particle with other particles present)
2. Calculate Re_{u_ϕ, d_p} from $Re_{u_\phi, d_p} = \frac{d_p \rho_f u_\phi}{\mu_\phi} = Re_{u_t, d_p}\left[\frac{\left(\frac{u_\phi}{u_t}\right)}{\exp\left\{\frac{5\phi}{3\left(1-\phi\right)}\right\}}\right]$
3. Calculate C_{D_ϕ} from $C_{D_\phi} = C_D\left(\frac{u_\phi^2}{u_t^2}\right)\left(\frac{\left(1-\phi\right)}{\left(1+\phi^{1/3}\right)}\right)$
4. Calculate C_{D_ϕ} from

$$\frac{C_{D_\phi}}{K_2} = \frac{24}{Re_{u_\phi, d_p} K_1 K_2}\left[1 + 0.1118\left(Re_{u_\phi, d_p} K_1 K_2\right)^{0.6567}\right] + \frac{0.4305}{1+\frac{3305}{Re_{u_\phi, d_p} K_1 K_2}}$$

$$K_1 = \left(\frac{1}{3} + \frac{2}{3}\phi_s^{-1/2}\right)^{-1}$$

$$K_2 = 10^{\left(1.8148\left[\log(\phi)\right]^{0.5743}\right)}$$

5. Compare the values of C_{D_ϕ} from step 3 with that from step 4. Adjust the guess for u_ϕ/u_t as necessary until convergence

8.6 Overall CFB Hydrodynamic Model

The model described above allows for the prediction of the axial distribution of the disperse phase in the core of a CFB. To complete the hydrodynamic model, equations were written for the core/annulus structure observed in the fast fluidization regime. According to this model, flow is upward in the core and downward in the annulus. The net solid flow is equal to the upward flow in the core minus the downward flow in the annulus. The core flow is described as dilute pneumatic transport flow and is given as the solution of the radially averaged 2-D dispersion equation solved above. The characteristics of the annulus flow are determined through the solution of the equations of mass and momentum for the particles and the gas for the annular and core regions.

The assumptions upon which the governing equations are based can be summarized as:

1. The flow riser is divided into two regions, a dilute upward flowing core, and a dense downward flowing annulus

2. The core region consists of a dilute up-flowing suspension of dispersed phase particles traveling upward at a velocity of u_{c_s} and solids volume fraction ε_{c_s}

3. The annulus region consists of a downward flowing suspension with a velocity u_{a_s}, and solids volume fraction ε_{a_s}

4. All the gas flows upward in the core at a velocity u_{c_f} - the gas flow in the annulus can be neglected

5. There is a negligible radial variation in the velocity across the core and the annulus

6. The solids volume fraction in the core is small, such that the slip velocity between the gas and solids phase is equal to the particle terminal velocity. The terminal velocity is corrected for the particle sphericity and core solids fraction.

7. The gas velocity in the core is much greater than the particle terminal velocity such that the slip velocity between the particles and gas is small

8. Inlet effects are small. The pressure drop due to the initial acceleration of the particles is negligible compared to the overall pressure drop.

9. Gas/wall frictional effects are small

10. Gas momentum flux is small compared to the particle momentum flux

11. The pressure is uniform across the riser cross-section.

With these assumptions, the mass conservation equations for the core and annular regions can be written as follows:

Particles in the core

$$\rho_s \frac{d\left(u_{c_s}\phi_{c_s}\frac{D_c^2}{D^2}\right)}{dz} = -\frac{1}{A}\left(\frac{d\dot{m}_{c\to a}}{dz} - \frac{d\dot{m}_{a\to c}}{dz}\right) \tag{22}$$

Particles in the annulus

$$\rho_s \frac{d\left(u_{a_s}\phi_{a_s}\left(1-\frac{D_c^2}{D^2}\right)\right)}{dz} = \frac{1}{A}\left(\frac{d\dot{m}_{c\to a}}{dz} - \frac{d\dot{m}_{a\to c}}{dz}\right) \tag{23}$$

Gas in the core

$$\rho_f \frac{d\left(u_{c_s}\left(1-\phi_{c_s}\right)\frac{D_c^2}{D^2}\right)}{dz} = 0 \tag{24}$$

In the above equations, $\frac{d\dot{m}_{c\to a}}{dz}$ represents the mass transfer rate from the core to the annulus, and $\frac{d\dot{m}_{a\to c}}{dz}$ represents the mass transfer rate from the annulus to the core. D_c is

the diameter of the core region, D is the CFB riser diameter, A_c is the core area, A is the riser area, and ϕ represents volumetric solids fraction.

Similarly, the momentum equations can be written as

Particles in the core

$$\rho_s \frac{d\left(u_{c_s}^2 \phi_{a_s}\left(\frac{D_c^2}{D^2}\right)\right)}{dz} + \rho_s\left(\frac{D_c^2}{D^2}\right)\phi_{c_s} g + \frac{4\tau_{c \leftrightarrow a}}{\sqrt{\frac{D_c^2}{D^2}}\, D} + \left(\frac{D_c^2}{D^2}\right)\frac{dP}{dz} + \frac{1}{A}\left(u_{c_s}\frac{d\dot{m}_{c \to a}}{dz} - u_{a_s}\frac{d\dot{m}_{a \to c}}{dz}\right) = 0 \tag{25}$$

Particles in the annulus

$$\rho_s \frac{d\left(u_{a_s}^2 \phi_{a_s}\left(1 - \frac{D_c^2}{D^2}\right)\right)}{dz} + \rho_s\left(1 - \frac{D_c^2}{D^2}\right)\phi_{a_s} g - \frac{4\tau_{c \leftrightarrow a}}{\sqrt{\frac{D_c^2}{D^2}}\, D} - \frac{4\tau_{a \leftrightarrow w}}{D} + \left(1 - \frac{D_c^2}{D^2}\right)\frac{dP}{dz} - \frac{1}{A}\left(u_{c_s}\frac{d\dot{m}_{c \to a}}{dz} - u_{a_s}\frac{d\dot{m}_{a \to c}}{dz}\right) = 0 \tag{26}$$

In the momentum equations, $\tau_{c \leftrightarrow a}$ represents the core-annulus interfacial shear, and $\tau_{a \leftrightarrow w}$ represents the annulus-wall shear.

8.6.1 Initial Conditions - Conditions at the Riser Exit

It was assumed that all material not exiting the riser form the annular layer at the exit. This assumption leads to the following equation which sets the core diameter at the riser exit,

$$\left(\frac{D_{exit}^2}{D_c^2}\right)_{exit}^2 \left[\frac{G_s\left(\phi_{a_{s_{exit}}} + 1\right)}{\eta''}\right] + \left(\frac{D_{exit}^2}{D_c^2}\right)_{exit}\left[\phi_{a_{s_{exit}}}\rho_s u_o - G_s - \frac{G_s \phi_{a_{s_{exit}}}}{\eta''}\right] - \phi_{a_{s_{exit}}} u_o \rho_s = 0 \tag{27}$$

where

$$\eta'' \equiv \frac{\left[D_c(1-\eta)+\eta D_{outlet}\right]^2}{D^2} \tag{28}$$

and η is the riser exit collection efficiency. To determine the collection efficiency, η, The riser exit is modeled using the impact separator theory method described Harris *et al.*, (1994). The geometry of the bed exit is approximated as a flat end plate with a central circular orifice. The collection efficiency is defined for two dimensional motion as the ratio of the dimension within which particles will be retained in the riser (x_1) to the dimension of the exposed end flange (x_2).

The voidage at the exit in the core is

$$\phi_{c_{s_{exit}}} = \left[\frac{G_s\left(\frac{D_{exit}^2}{D_c^2}\right)_{exit}}{\eta'' u_o \rho_s + G_s\left(\frac{D_{exit}^2}{D_c^2}\right)_{exit}}\right] \tag{29}$$

The voidage in the annulus can be estimated from the correlations given in Chapter 3 of this Thesis

$$\phi_{f_{s_{exit}}} = \sqrt{\phi_{c_{s_{exit}}}} \times \left\{1-\exp\left[-0.01\left(\frac{u_o}{u_{mf}}\right)^{-1/4}\left(\frac{\rho_s}{\rho_f}\right)^{3/4} Fr_D^{-1/3} Ar^{-1/4}\phi_{c_{s_{exit}}}\right]\right\} \tag{30}$$

where

$$u_{mf} \simeq \left(\frac{600 g \rho_s d_p^2}{\mu}\right) \tag{31}$$

If one assumes elastic collisions at the riser exit

$$u_{a_{s_{exit}}} \simeq -u_{c_{s_{exit}}} \tag{32}$$

where

$$u_{c_{s_{exit}}} \equiv \frac{u_o}{\left(\frac{D_c^2}{D^2}\right)\left(1-\phi_{c_{s_{exit}}}\right)} \tag{33}$$

Equations (22) through (26) can be solved using equations (27), (29), (30), (32), and (33) as the initial conditions for $\frac{D_c^2}{D^2}$, $\phi_{c_{s_{exit}}}$, $\phi_{a_{s_{exit}}}$, $u_{a_{s_{exit}}}$, and $u_{c_{s_{exit}}}$ respectively.

8.6.2 Determination of $\frac{d\dot{m}_{c\to a}}{dz} - \frac{d\dot{m}_{a\to c}}{dz}$

The core to annulus deposition rate is determined from the two-dimensional dispersion equation described in Section 2. Using this concentration profile, a mass balance can be written

$$\frac{dC(z)}{dz} = \frac{4k_D}{Du_{c_s}}C(z) \tag{34}$$

Manipulation of (34) allows one to write an expression for $\frac{d\dot{m}_{c\to a}}{dz} - \frac{d\dot{m}_{a\to c}}{dz}$

$$\frac{d\dot{m}_{c\to a}}{dz} - \frac{d\dot{m}_{a\to c}}{dz} = \left[\frac{\pi D^2\left(\frac{D_c^2}{D^2}\right)^2 \rho_s \phi_{c_s} u_{c_s} \frac{dC(z)}{dz}}{4C(z)}\right]$$

8.6.3 Determination of $\tau_{a\leftrightarrow w}$

The shear stress between the wall and the annular layer is approximated from the expression developed by Stemerding (1962) for shear stresses in suspensions:

$$\tau_{a\leftrightarrow w} = \frac{0.003\phi_{a_s}\rho_s u_{a_s}^2}{2} \tag{35}$$

8.6.4 Determination of $\tau_{c \leftrightarrow a}$

To approximate the interfacial shear stress between the annulus and the core, the results from gas/liquid two-phase flow modified for gas/solid flows is used. From Hewitt and Hall-Taylor (1970),

$$\tau_{c \leftrightarrow a} = C_{c \leftrightarrow a} \phi_{c_s} \rho_s \left(u_{c_s} - u_{a_s} \right)^2 \tag{36}$$

where

$$C_{c \leftrightarrow a} = 0.079 Re_c^{-1/4} \left(1 + 180 \left(1 - \sqrt{\frac{D_c^2}{D^2}} \right) \right) \tag{37}$$

and

$$Re_c = \frac{\left[\phi_{c_s} \rho_s + \left(1 - \phi_{c_s} \right) \rho_f \right] u_{c_s} D \sqrt{\left(\frac{D_c^2}{D^2} \right)}}{\mu} \tag{38}$$

8.7 Radial Distribution of Solids in Dilute Region of CFB

To determine the radial solid fraction profiles in the dilute region of a CFB, an approximate theory for the behavior of multiparticle systems suspended in a fluid was developed based on a treatment of the case of a single sphere occupying any position in a cylindrical tube. This model is completely independent of the model described above.

The result for the annular region is:

$$n_a = \frac{N_m \pi R^2 \bar{v}_{a_p} - \psi_c \left(\frac{\bar{v}_{a_p}}{\bar{v}_{c_p}} \right)}{\pi R^2 \left(u_t - V_{max} \left(1 - \left(\frac{r}{R} \right)^n \right) \right) \left(1 - \left(1 - \frac{u_t}{V_{max}} \right)^{2/n} \right)} \tag{39}$$

$$R \geq r \geq S$$

and for the core is:

$$n_c = \frac{N_m \pi R^2 \bar{v}_{c_p} - \psi_c \left(\frac{\bar{v}_{c_p}}{\bar{v}_{a_p}} \right)}{\pi R^2 \left(V_{max} \left(1 - \left(\frac{r}{R} \right)^n \right) - u_t \right) \left(1 - \left(1 - \frac{u_t}{V_{max}} \right)^{2/n} \right)} \qquad S \geq r \geq 0 \tag{40}$$

n_a and n_c are the particle number densities in the annulus and core, respectively. The boundary between the core and annular region was determined as

$$\left(\frac{S}{R} \right) = \left[1 - \left(\frac{u_t}{V_{max}} \right) \right]^{\frac{1}{n}} \tag{41}$$

and

$$\frac{1}{n} = \frac{1}{n_o} + 0.8231 \left(\frac{G_s}{G_{s_{sat}}} \right)^{1.413} \left(\frac{h}{D} \right)^{-1.879} Re_{u_o, D}^{-0.262} \quad \text{[Yang } et\ al.\text{, 1994]} \tag{42}$$

9.0 NUMERICAL SOLUTION STRUCTURE

The following Section summarizes the actual numerical implementation of the model described in the previous Sections.

9.1 Required Input

The following variables are required input to the model.

1. Bed Diameter
2. Bed Height
3. Mean Particle Diameter
4. Standard Deviation of Particle Size Distribution (assumed to be equal to the mean particle diameter if not input)
5. Particle Sphericity (assumed to be 0.8 if not input)
6. Particle Density
7. Bed Temperature
8. Bed Pressure
9. Gas Superficial Velocity
10. Solids Recycle Rate
11. Particle/Particle Coefficient of Restitution (assumed to be 1 if not input)
12. Exit Collection Efficiency (assumed to be 0.8 if not input)
13. Number of Particles to Simulate
14. Number of Interactions per Particle to Simulate

9.2 Determination of Lateral Solids Dispersion Coefficient

Step 1:

The simulation to determine the lateral solids dispersion coefficient is initialized by selecting a particle diameter. The particle diameter is taken from a Gaussian distribution with a mean equal to the input mean particle diameter and a standard deviation based on the input particle size distribution standard deviation. The mean eddy length and eddy speed are then calculated from the model based on the data of Hutchinson *et al.* (1971) modified for the presence of particles, as described above.

Step 2:

At this point, the particle-eddy interactions begin for the particle determined in Task 1. For each interaction, an eddy length is selected from a Gaussian distribution with a mean equal to the length determined from the model of Hutchinson *et al.* (1971) and a standard deviation equal to one half the mean. An eddy speed is also determined from a Gaussian distribution with a mean equal to zero and a r.m.s value equal to the eddy speed calculated from the Hutchinson model as modified for the presence of particles. The eddy velocity (direction of speed) is determined by randomly multiplying the speed by either 1 or -1. Finally, the component of particle velocity due to collisions is determined. The mean collisional component of the radial particle fluctuating velocity is determined using the particle collision model described in Section 3 with a solid fraction equal to the least squares value evaluated in Step 10, and a particle diameter ratio equal to the ratio of the current particle diameter to the previous particle diameter. The direction of the collisional component of the particle fluctuating velocity is determined by randomly multiplying the r.m.s. value by either 1 or -1. For the initial dispersion coefficient calculation, the collisional component is obviously zero.

Step 3:

For each interaction, the interaction time is determined from the minimum of the vertical particle-eddy crossing time, horizontal particle-eddy crossing time, eddy decay time, and the time between successive collisions. The time between successive collisions is determined from the solid fraction profile developed from the previous value of lateral dispersion. For the initial calculation, the time between successive collisions is assumed to be infinite. After the interaction time is determined, the particle equation of motion is solved using the final velocity of the previous interaction as the starting velocity. For the initial interaction, the particle velocity at the beginning of the interaction was assumed to be zero (the particle velocity at the beginning of the initial interaction has no influence on the final results if more than 100 interactions are used).

Step 4:

After the particle has proceeded through the user specified number of interactions, another particle is selected based on the Gaussian distribution, and steps 2 and 3 are repeated. This

process continues until the total number of particles specified by the user has been tracked through the interaction process.

Step 5:

After all the particles have been tracked through the particle-eddy interaction process, the average mean square displacements, velocities, and interaction times, along with all other pertinent data are evaluated. The dispersion coefficient is then calculated using the equations described in detail in Section 2, and outlined in Section 8.

9.3 Determination of Axial Disperse Phase Concentration Profile

Step 6:

The dispersion coefficient determined from the first part of the model is used as an input to the core (dilute phase) axial concentration profile equation. At this point, a value for the entrainment constant is assumed, along with a value for the concentration at the bottom of the bed.

Step 7:

The equation for the core axial concentration distribution is solved using the values of the entrainment constant and bed bottom concentration assumed in Step 6.

Step 8:

The resulting concentration at the top of the bed is then compared to that which was calculated from the collection efficiency. The bed bottom concentration is then adjusted accordingly, and Step 7 is repeated until the calculated concentration at the top of the riser equals that determined from the solids recycle rate, and the exit collection efficiency, as discussed in previous Sections.

Step 9:

Once Step 8 has converged, the total amount of solids deposited to the walls is determined. Additionally, the total amount of solids entrained from the wall is calculated. These two

numbers are compared, and the entrainment constant is adjusted accordingly. The simulation then returns to step 7 until the total amount of solids deposited to the walls equals the total amount of solids entrained.

Step 10:

After the solution for the core axial solids concentration has converged, an effective overall dilute region solid fraction is determined.

Step 11:

The lateral dispersion coefficient determined in most recent iteration is compared to the previous value. If these values are within 5 percent, the model was assumed to have converged. If the values differed by more than 5 percent, the simulation returns to Step 1.

9.4 Overall CFB Hydrodynamic Model

Step 12:

Once the CFB core axial solids concentration profile is determined, the overall CFB model described in Section 4 can be solved using the core axial profile as input. The solution of the overall CFB mass and momentum balance is relatively straightforward - involving the numerical integration of five coupled first order differential equations.

9.5 Radial Solids Distribution

Step 13:

The average core axial solids concentration profile is also used as input to the radial concentration profile estimations described in Section 5. The axial concentration profile is used to determine the mean number of particles per unit volume in the core.

Step 14:

The particle flux in the core is then determined by using the estimated gas velocity profile in the core in the manner described in Section 5. The particle flux in the annulus is determined from the difference between the recycle rate and the core particle flux.

Step 15:

The radial distribution of solids is then estimated from the algebraic equations given in Section 5.

10.0 MODEL RESULTS

The following Section presents the results of the model described in the previous nine Sections. The model is compared to experimental data taken in both hot and cold beds. In order to present the results, lateral dispersion coefficients, average axial solid fraction profiles, and radial solid fraction profiles will be compared between the numerical model and available experimental data.

10.1 Comparison of Experimentally Determined Lateral Dispersion Coefficients in CFB's with the Numerical Model

Section 6 discusses the experimental data currently available on the lateral dispersion coefficients in the dilute region of CFB's or FCC reactors. Table 10.1 summarizes this data:

Table 10.1: Lateral Solid Dispersion Coefficient Measurements in CFB's

Researcher	D (cm)	L (m)	d_p (μm)	ρ_s (kg/m^3)	u_0 (m/s)	ε_{p_r} (cm^2/s)	Pe_r
Westphalen and Glicksman (1995)	20.5	7.0	180	2350	3 - 5.5	0.4 - 8.6	412 - 10000
van Zoonen (1962)	5	10	65	1600	2.5 - 12	0.94 - 12.0	250 - 833
Viitanen (1993)	100	39	70	2400	6 - 15	200 - 600	100 - 250
Wei *et al.* (1994)	14	7.6	54	1710	2.3 - 9	12 - 50	70 - 300
Koenisgdorff and Werther (1995)	20	3.5	60	3217	3 - 4	18 - 47	150 - 400

Figures 10.1 through 10.6 present comparisons between the predicted and experimentally determined lateral solids dispersion coefficients. In all cases, the present model is in good agreement with the experimental data. Figures 10.1 through 10.6 indicate that the dispersion model is able to predict effect lateral solids dispersion coefficients over a wide range of conditions: from the standard cold CFB models [Westphalen and Glicksman, (1995); Koenigsdorff and Werther (1995)], to large scale FCC reactors [Viitanen (1993) and van Zoonen (1962)].

The validity of the numerical model is not limited to long time particle dispersion measurements. This is not the case with most diffusivity type models. For diffusivity models, when the particles have been in the gas flow for times smaller than $\frac{1}{\tau_f \beta^2}$ (where τ_f is the time scale of the gas turbulence), models which predict long time diffusivity coefficients are not valid [Vames and Hanratty, (1988)]. In a circulating fluidized bed, $\frac{1}{\tau_f \beta^2}$ is usually 0.4 seconds. The trend for diffusion coefficients smaller than $\frac{1}{\tau_f \beta^2}$ can be determined by an examination of the single particle drag equation. Results of such an analysis have been presented by Vames and Hanratty (1988). It was found that for small times, the particle diffusivity was less than the long time value. Westphalen has indicated that the average diffusivity for the time range of measurements was roughly 0.4 times the long time diffusivity. Although this reduction in diffusivity does not explain the the lowest diffusivities estimated from Westphalen's experimental data, it does help explain why the measured diffusivities are lower than his model predictions which is based on the assumption that the dispersion coefficient has reached steady state. This correction in diffusivity required by Eulerian models where the diffusivity is assumed to be the long time diffusivity is not required in the Lagrangian model developed in Section 2 because the particle displacement is tracked as a function of time.

The agreement with the data of Koenigsdorff and Werther (1995) is very good. It is worth pointing out that Koenigsdorff and Werther measured particle dispersion coefficients greater than single phase gas dispersion coefficients at volumetric solids fraction greater than 0.3 percent. They concluded that this was due to a strong influence of particle-particle collisions on particle dispersion, since "in the case of solely gas-induced particle mixing, the particle dispersion coefficients would be less than the gas dispersion coefficients." Two aspects of this statement are suspect. First, their experiments indicated a decrease in lateral solids dispersion with increasing solids concentration, even at very low values of ϕ. Their curve suggests that the highest lateral particle dispersion should occur with no particles present (recall their correlation $Pe_r = 150 + 5.6 \times 10^4 \left(\text{solids volumetric concentration}\right)$). It is not clear, why they would explain an increase in particle dispersion over the gas dispersion by the presence of particle collisions.

The second issue is that there is no reason why the particle dispersion coefficient must be less than the gas dispersion coefficient. In general, the particle spectral tensor will always be smaller than that of the gas, and the Lagrangian temporal correlation tensor for particle velocities are conversely (as a whole) greater than the fluid Lagrangian temporal correlation. In other words,

the particles tend to keep their previous motions longer than the fluid particles. Furthermore, both Lagrangian correlation tensors exhibit negative loops, meaning that the ratio between the time dependent particle dispersion coefficient and the long time fluid dispersion coefficient can become greater than one at some times.

Additionally, the ratio of the time dependent particle dispersion coefficient and the time dependent fluid dispersion coefficient can also become greater than 1. This ratio can be written as

$$\frac{\overline{\varepsilon_{p_r}(t)}}{\overline{\varepsilon_{p_r}(t)}} = \frac{\left(\overline{v'^2_{p_{rms}}}\right)}{\left(\overline{v'^2_{p_{rms}}}\right)} \frac{\int_0^t R_{pL}(\tau)d\tau}{\int_0^t R_{fL}(\tau)d\tau} \qquad (1)$$

The first term $\frac{\left(\overline{v'^2_{p_{rms}}}\right)}{\left(\overline{v'^2_{p_{rms}}}\right)}$ is smaller than one, but the second term, which is the ratio of the particle and fluid cumulated memories, will overcome that handicap when t is large enough. So the ratio of the time dependent and the long time particle dispersion and fluid dispersion can be greater than one even for dense particles. This has been confirmed in a very rigorous manner by Gouesbet *et al.* (1984).

Figure 10.1

Comparison of Model with Dispersion Data of Westphalen and Glicksman (1995)

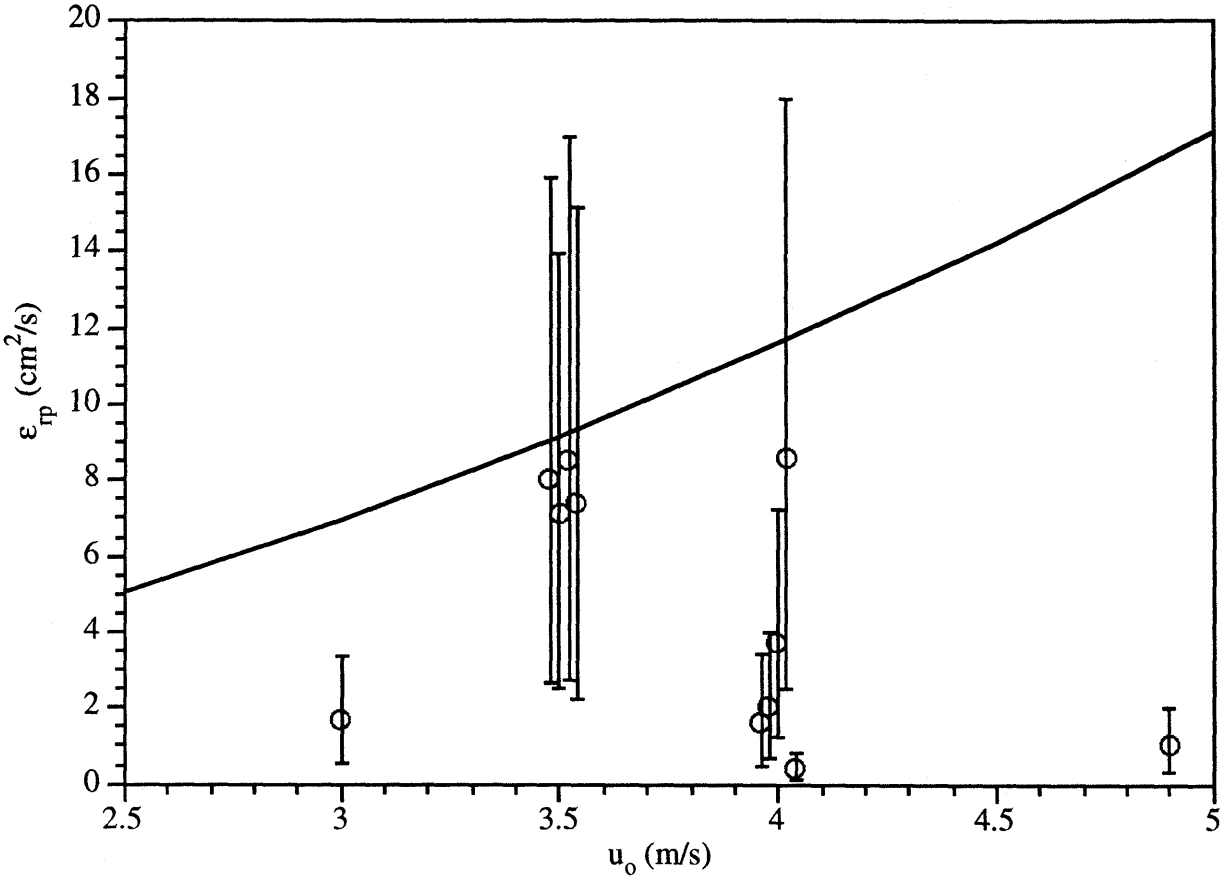

Figure 10.2
Comparison of Model with Dispersion Data of van Zoonen (1962)

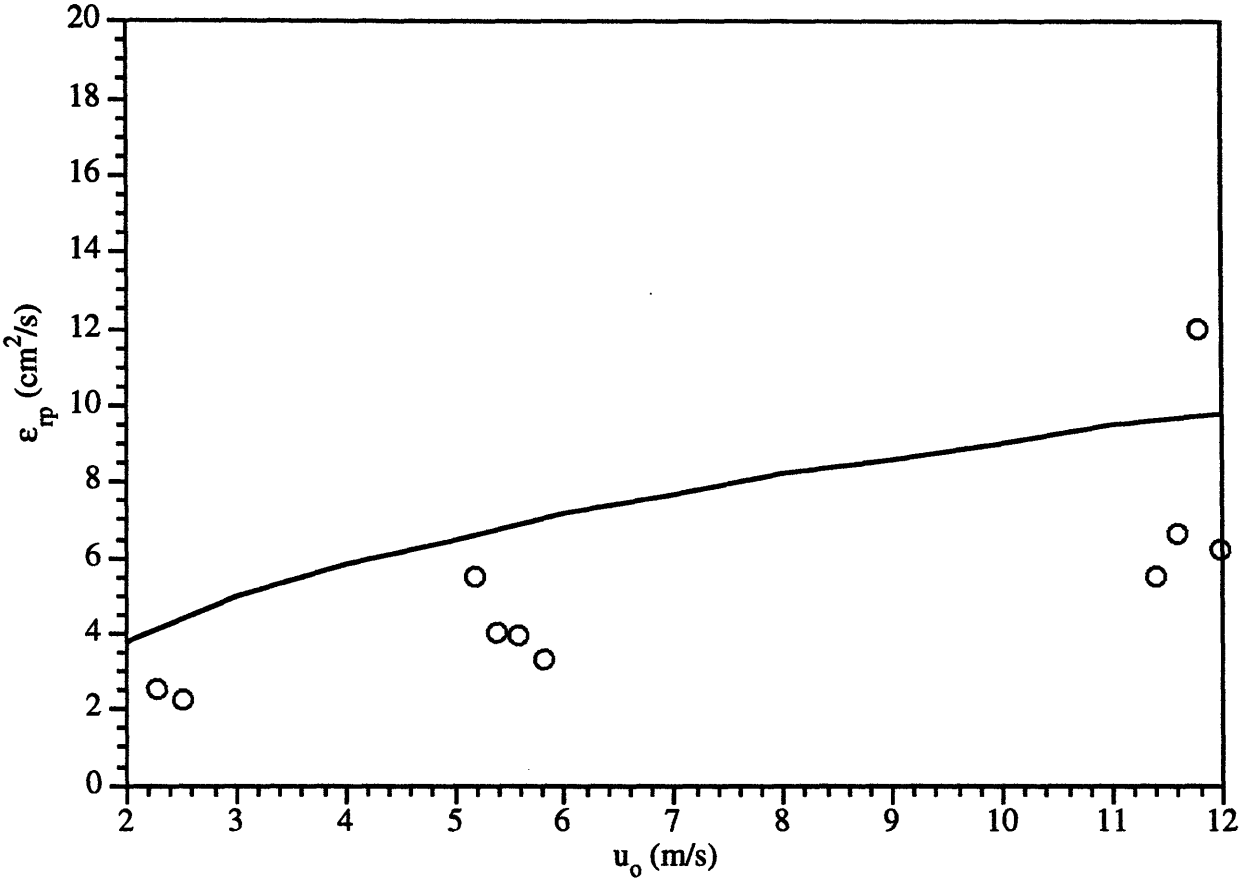

Figure 10.3

Comparison of Model with Dispersion Data of Wei et al. (1994)

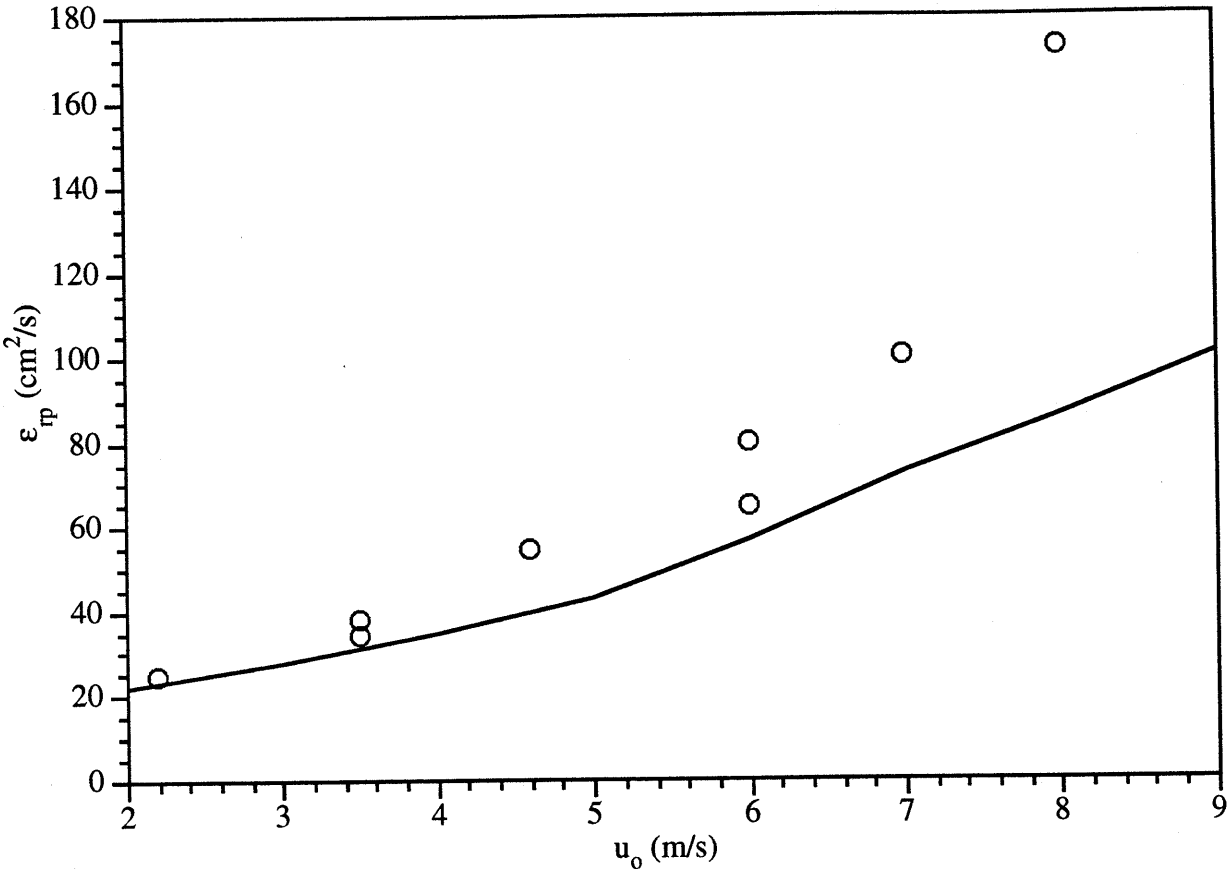

Figure 10.4

Comparison of Model with Dispersion Data of Wei et al. (1994)

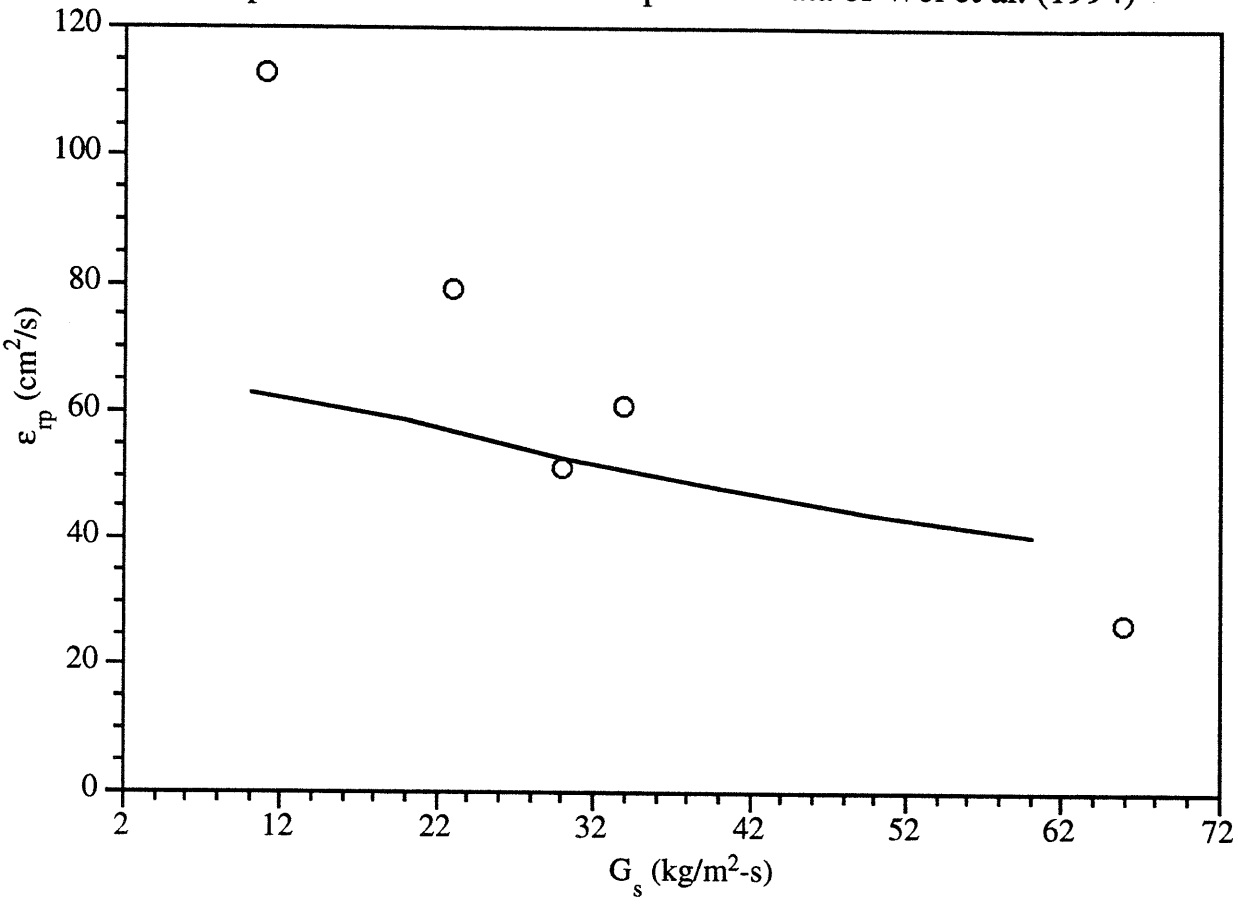

Figure 10.5

Comparison of Model with Dispersion Data of Koenigsdorff and Werther (1995)

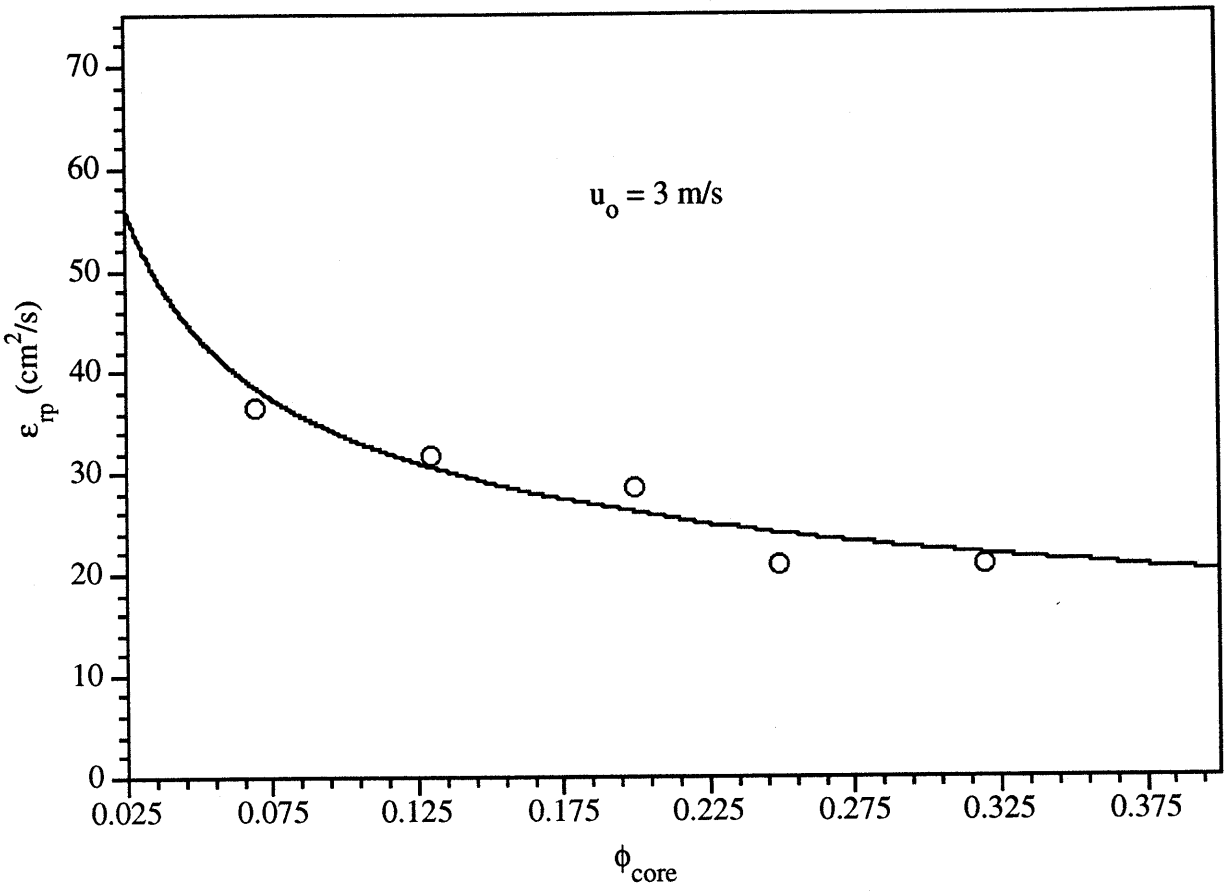

Figure 10.6
Comparison of Model with Dispersion Data of Koenigsdorff and Werther (1995)

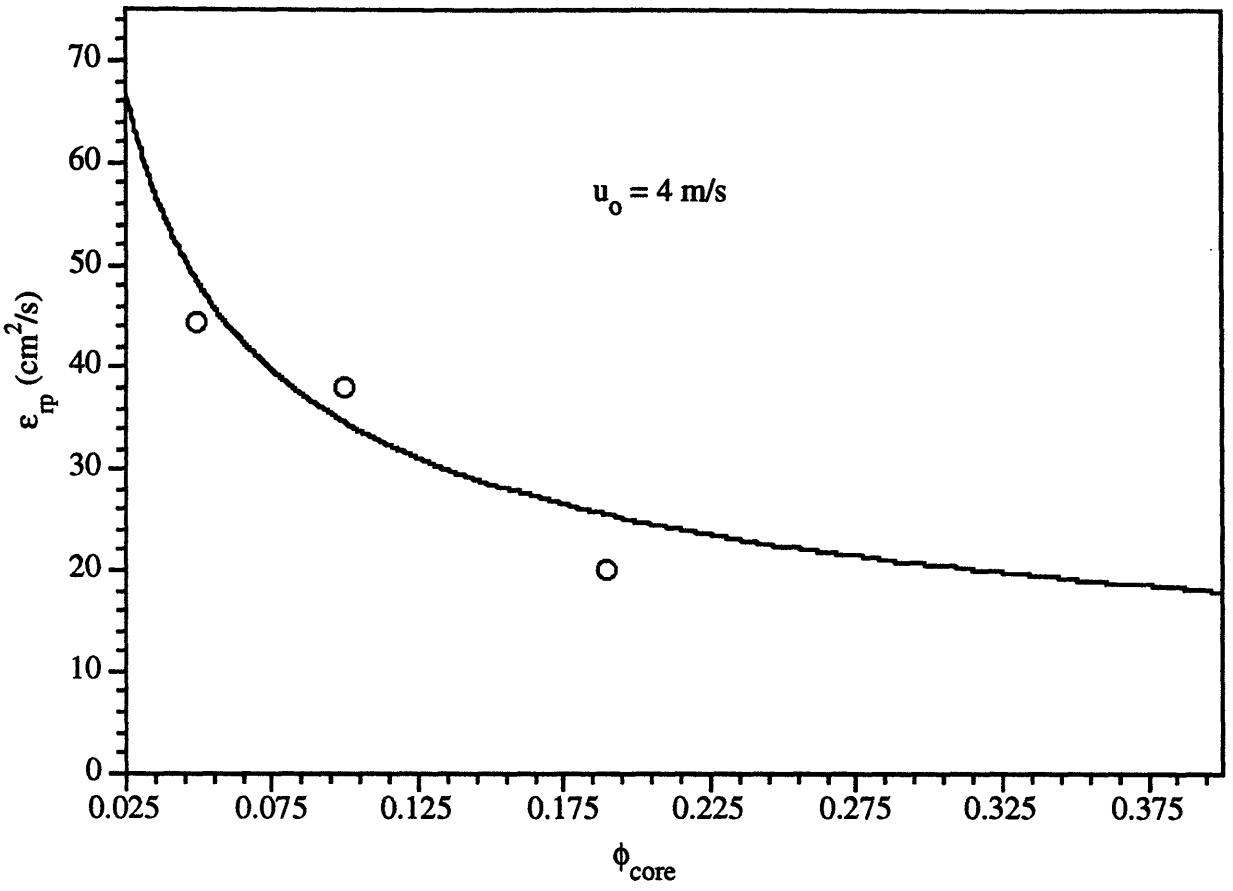

10.2 Estimated Mixing Times in CFB's

Once the lateral dispersion coefficient is known, the lateral mixing times in CFB's can be easily determined. The time required to laterally mix particles over a region of radius r from a source is

$$\tau_{r_p} \sim \frac{r^2}{2\varepsilon_{r_p}} \qquad (2)$$

For a 1 meter diameter PCFB operating at 14 bar and 1100 K with 165 micron dolomite, the numerically determined dispersion coefficient is on the order of 10 cm^2/s. The mixing time for the spread of solids from centerline to the walls for typical combustor is on the order of 125 seconds. The high value of the mixing time emphasizes the importance of achieving good solids

mixing in the bottom of the CFB through strategically locating the fuel and sorbent feed ports, since solids mixing is likely to be much better here (Westphalen , 1993).

10.3 Comparison of Experimentally Determined Hydrodynamic Data in Cold Model CFB's with the Numerical Model

A summary of the cold beds to which were simulated by the model is given in Table 10.2.

Table 10.2: Summary of Simulated Experimental Conditions

Researcher	D (cm)	η (exit collection efficiency)	u_o (m/s)	d_p (microns)	ρ_s (kg/m^3)	G_s (kg/m^2-s)	H (m)
Hartge *et al.* (1986)	40	0.25	4.0	58	1500	90	7.8
Hartge *et al.* (1988)	40	0.25	2.9	85	1500	49	7.8
Rhodes and Laussman (1992)	15.2	0.25	2.8	75	2456	30	5.8
Brereton and Grace (1993)	15.2	0.45	6.5	148	2650	42	9.3
Horio *et al.* (1988)	5	0.3	1.3	60	1000	11.75	2.79
Gidaspow et al. (1989)	7.62	0.5	5.0	520	2540	25	3.4
Bader *et al.* (1988)	30.5	estimated 0.25	9.1	76	1714	147	5.5
Herb *et al.* (1992)	15	0.3	2.5	87	~1500	20	10.8
Miller and Gidaspow (1992)	7.5	0.4	3.0	75	~1500	12	6.58

10.3.1 Axial Solid Fraction Profiles

Figures 10.1 through 10.11 compare experimentally determined solid fraction profiles for those researcher who reported this data with a numerical simulation of the cold model. The solid fraction is based on the dimensionless pressure gradient:

$$\text{Solid Fraction} = \frac{\frac{dP}{dz}}{\rho_s g} \tag{3}$$

where $\frac{dP}{dz}$ is determined from the core-annulus model.

Figure 10.7
Numerical Model vs. Experimental Data: Bader *et al.* (1988)

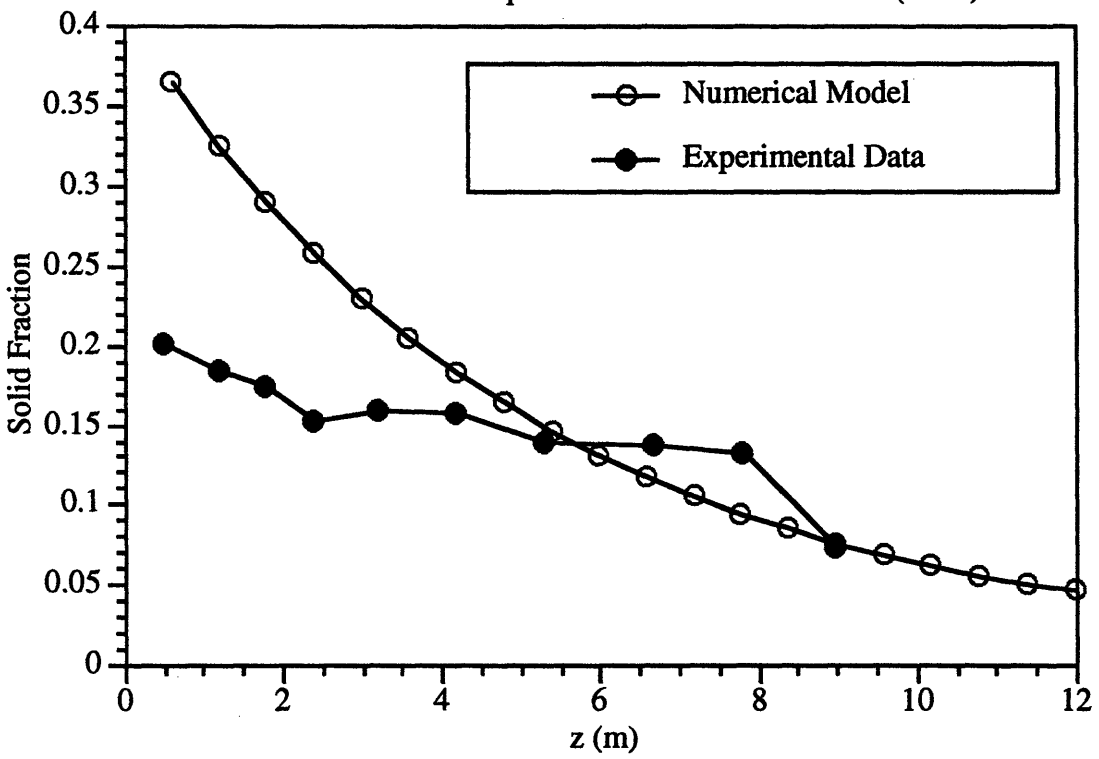

Figure 10.8
Numerical Model vs. Experimental Data: Brereton and Grace (1993)

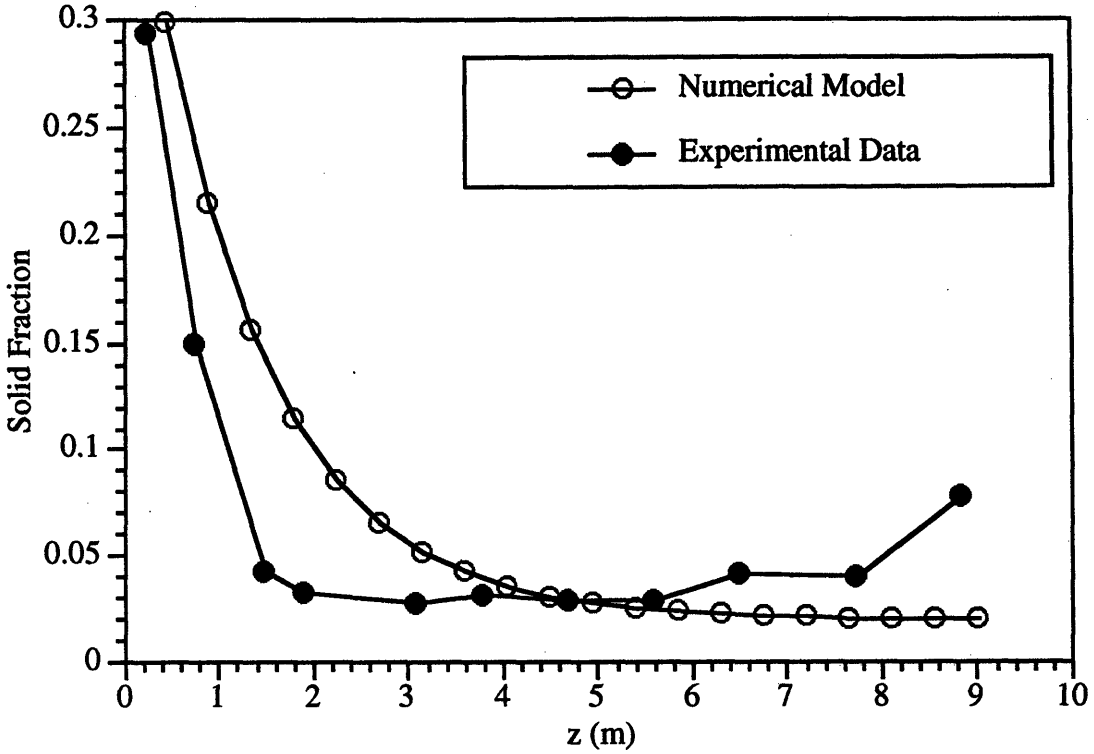

Figure 10.9
Numerical Model vs. Experimental Data: Hartge *et al.* (1986)

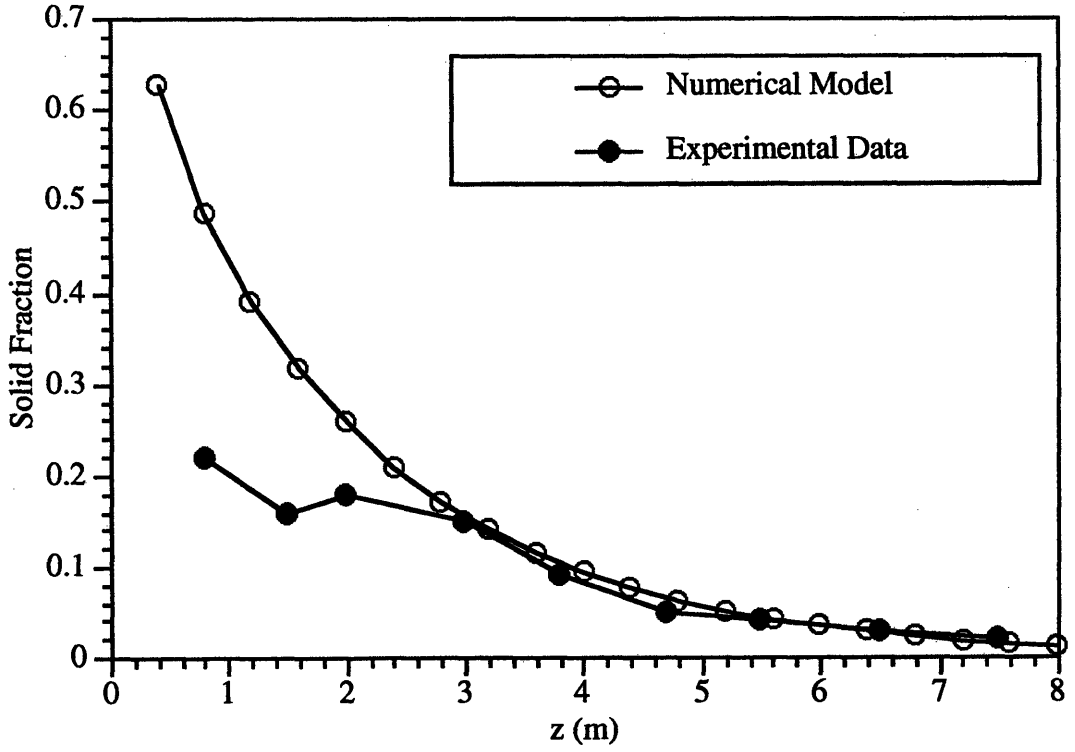

Figure 10.10
Numerical Model vs. Experimental Data: Herb *et al.* (1992)

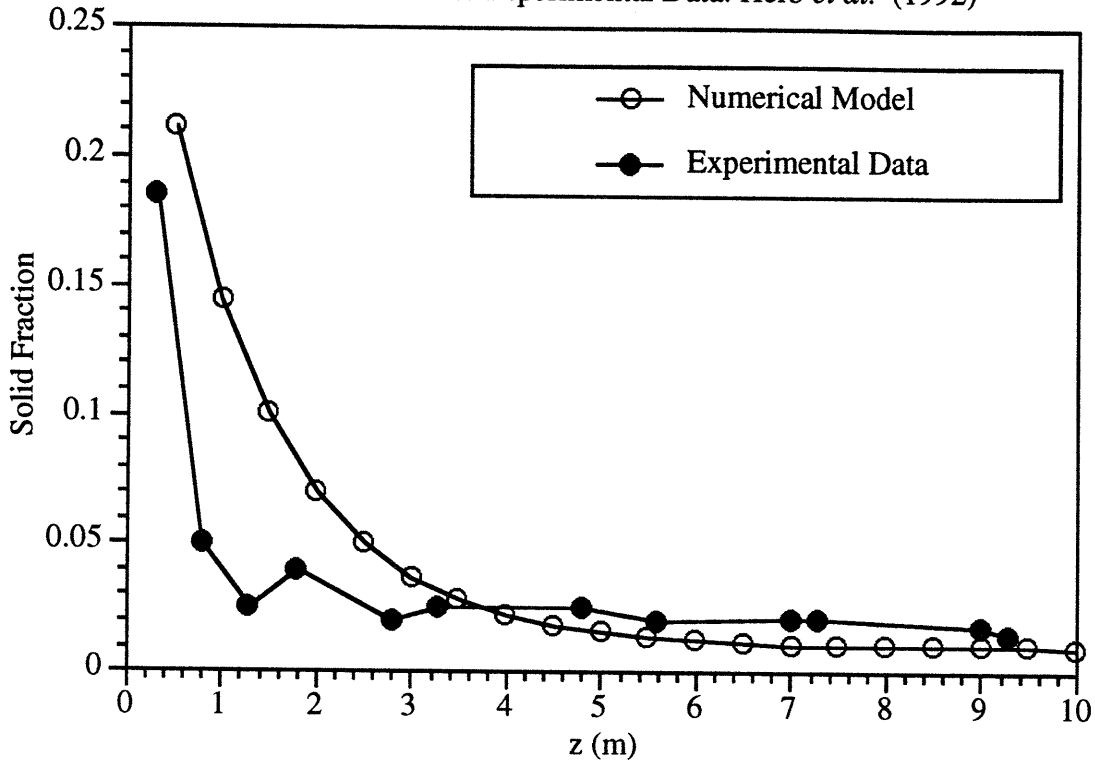

Figure 10.11
Numerical Model vs. Experimental Data: Horio *et al.* (1988)

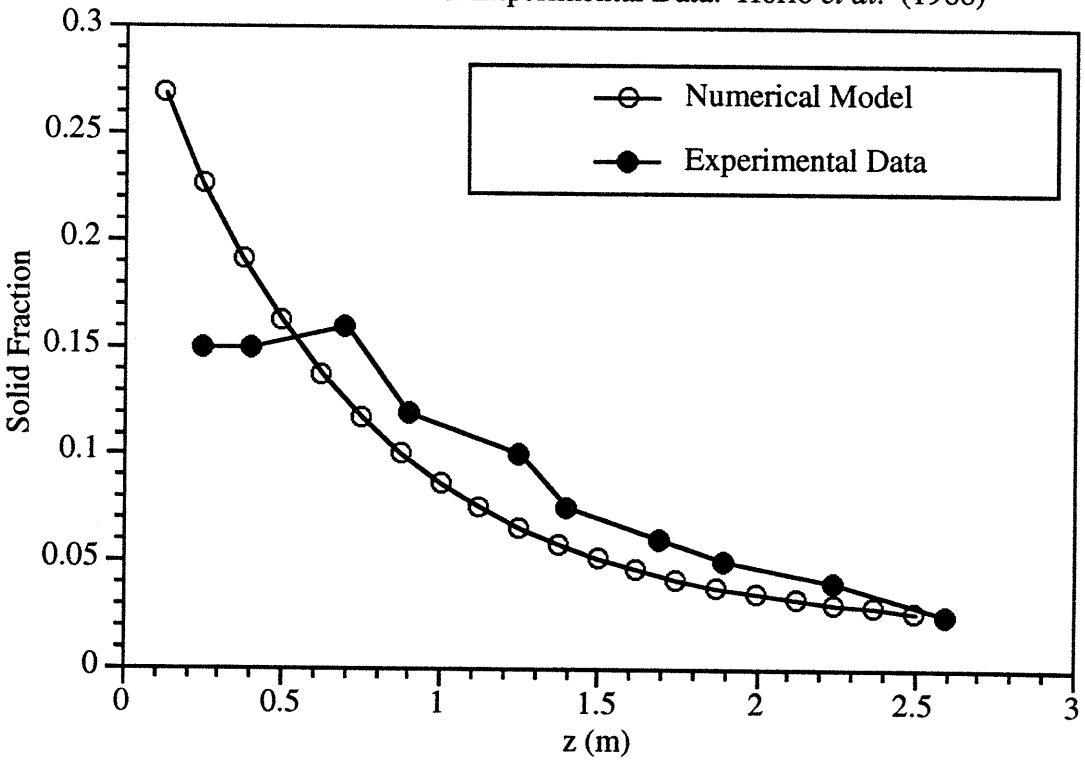

Agreement between the model and the data is good, especially near the top of the bed where one would expect the model to be more applicable. In the lower regions of a CFB, the suspension becomes dense enough such that the particle-eddy interaction mechanism and the gas turbulence modification mechanism postulated in the modeling of the lateral solids dispersion coefficient are not valid. Additionally, in these regions, the assumption that the bed can be broken down into a dilute rising core and a dense falling annulus breaks down. The suspension looks like a slugging or bubbling bed. Except for the data of Bader *et al.* (1988), the model does a good job in predicting the trend of the solid fraction profile. The profile of Bader is extremely flat. The model predicts a much greater drop off in solid fraction over the bed height. The probable reason for the disagreement is the unique exit geometry of the cold bed. The exit of cold model consisted of a 135-degree bend (rather than the typical 90 degree), thus the effective collection efficiency of the exit is much higher than that predicted by the simple impact separation efficiency used by the model. If a high collection efficiency is input into the model (say, on the order of 70 percent returned to the riser), the agreement is much better (see Figure 10.12). It should be pointed out that for the other beds which used standard types of exits, the model does a good job in predicting the solid fraction near the top of the bed - indicating the impact separator model is adequate as an initial assumption of how to model the exit geometry. Prediction of exit geometry effects is the weakest part of the model. Further work needs to be done to better model the effects of different types of exit structures.

Figure 10.12
Numerical Model vs. Experimental Data: Bader *et al.* (1988)

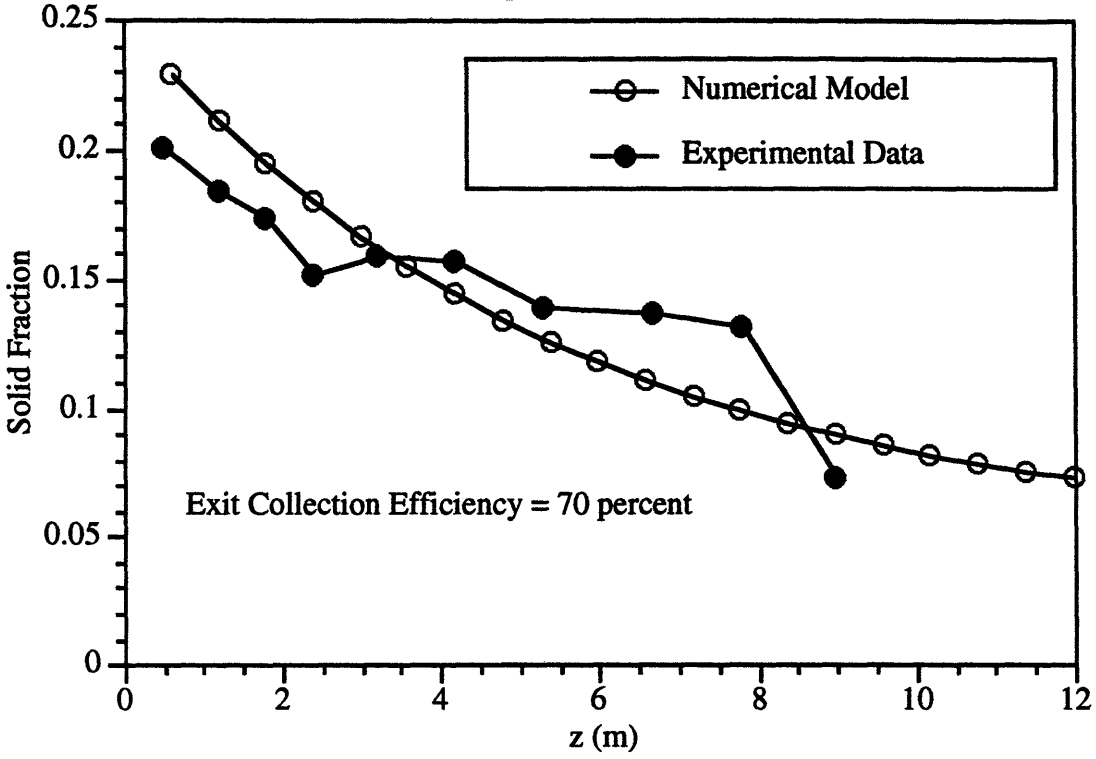

10.3.2 Radial Solid Fraction Profiles

Figures 10.13 through 10.21 present comparisons of the predicted radial solid fraction profiles with the experimentally determined values. Predictions are based on the model presented in Section 5.

Figure 10.13
Numerical Model vs. Experimental Data: Bader et al. (1988)

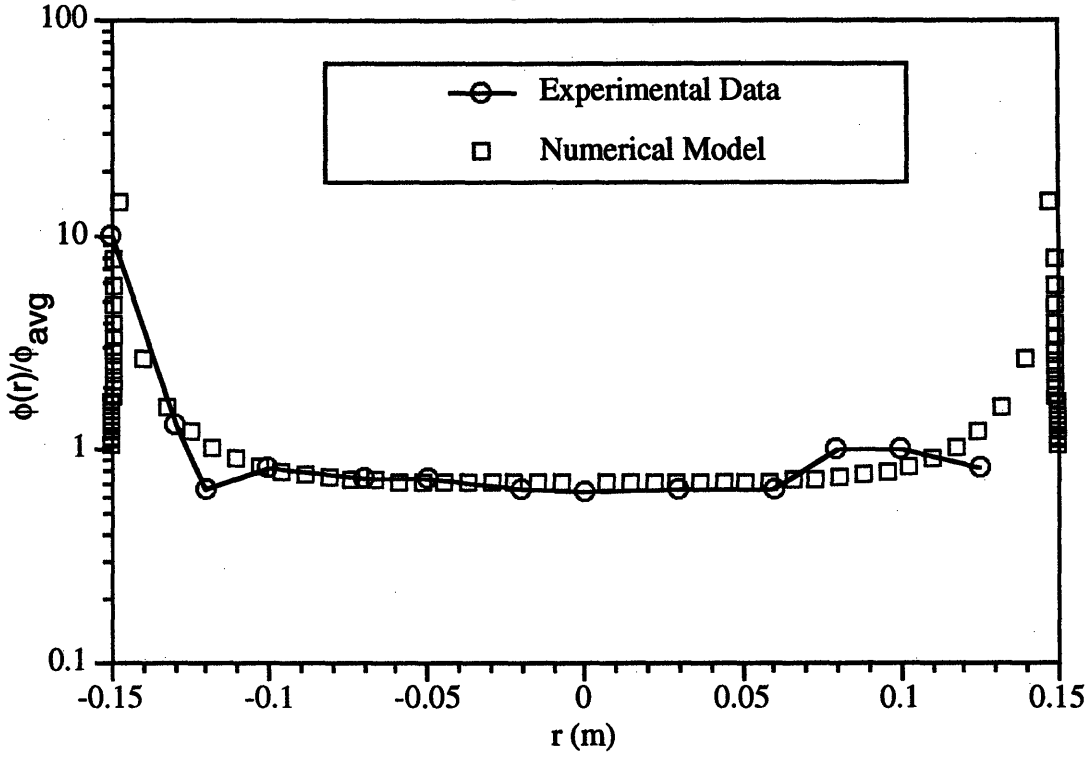

Figure 10.14
Numerical Model vs. Experimental Data: Brereton and Grace (1993)

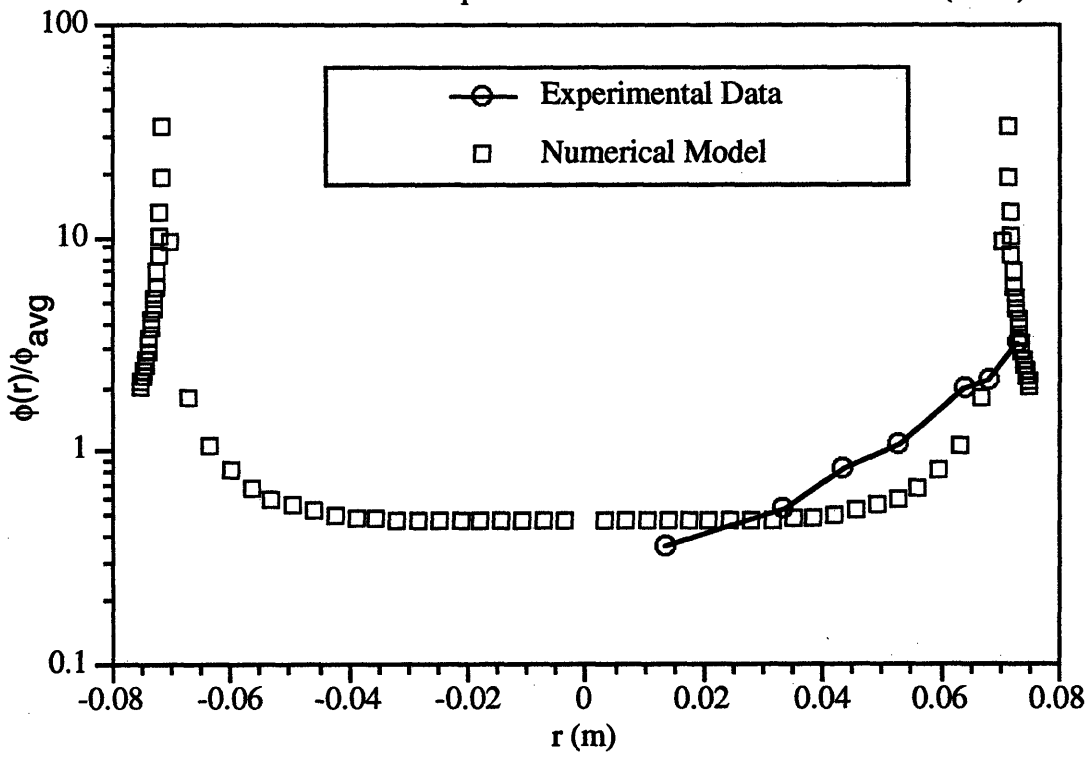

Figure 10.15
Numerical Model vs. Experimental Data: Gidaspow et al. (1989)

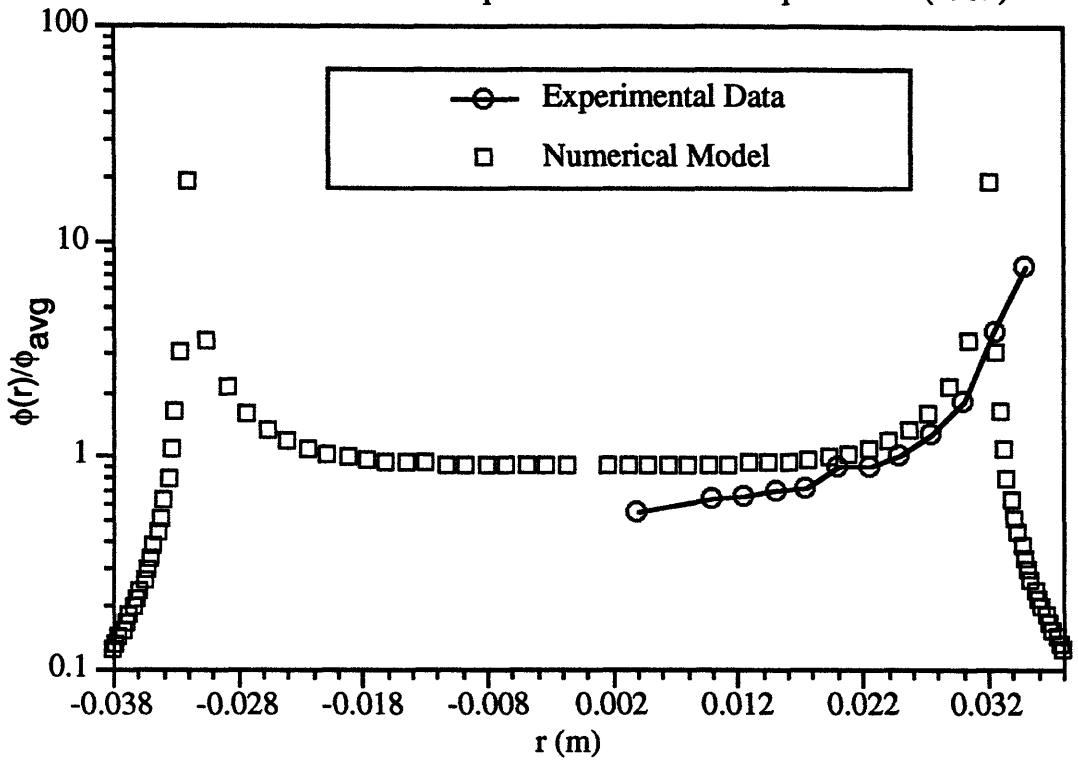

Figure 10.16
Numerical Model vs. Experimental Data: Hartge *et al.* (1986)

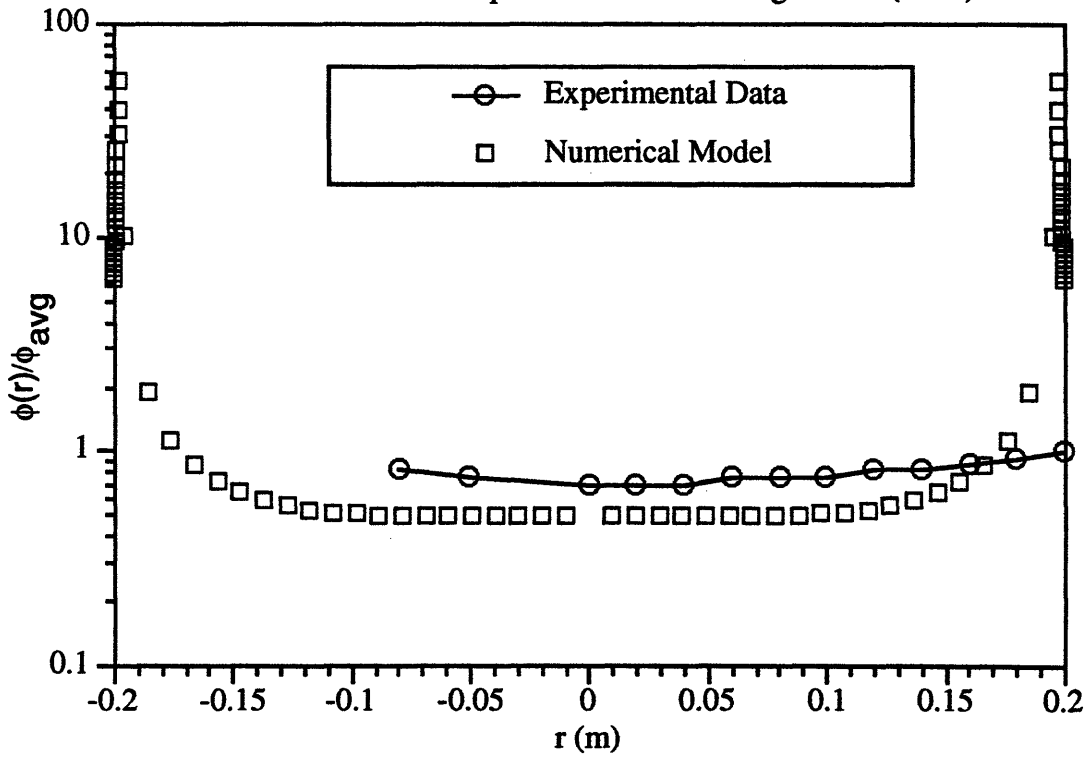

Figure 10.17
Numerical Model vs. Experimental Data: Hartge *et al.* (1988)

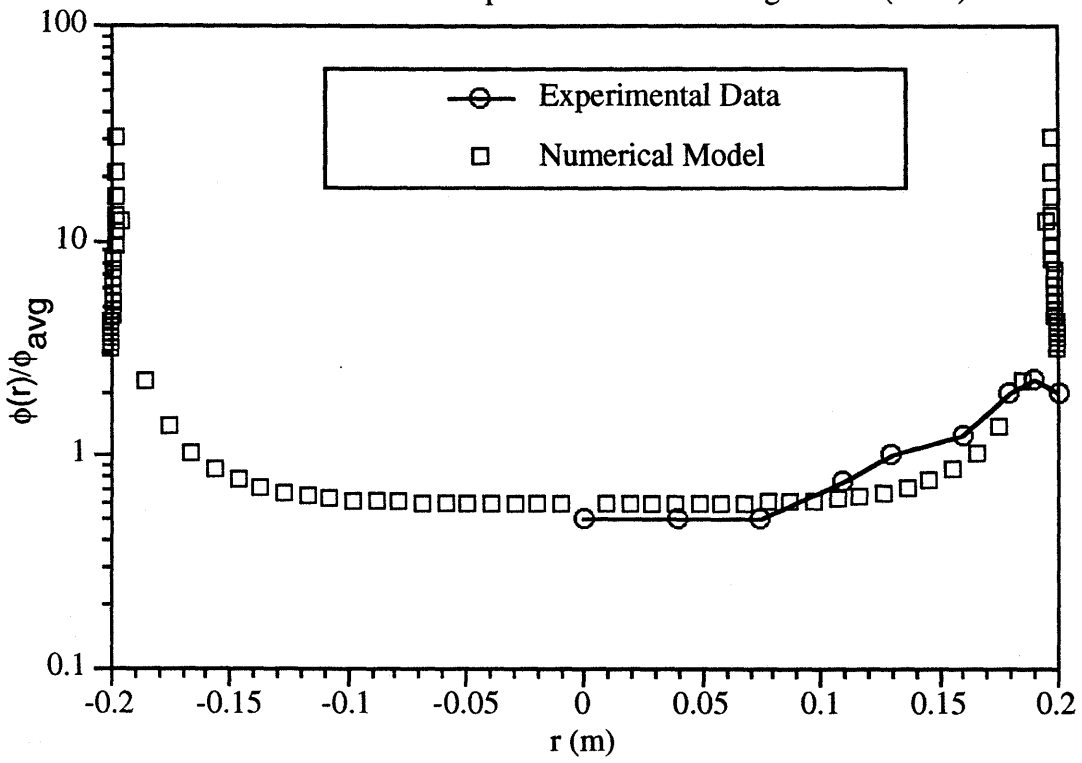

Figure 10.18
Numerical Model vs. Experimental Data:Herb et al. (1992)

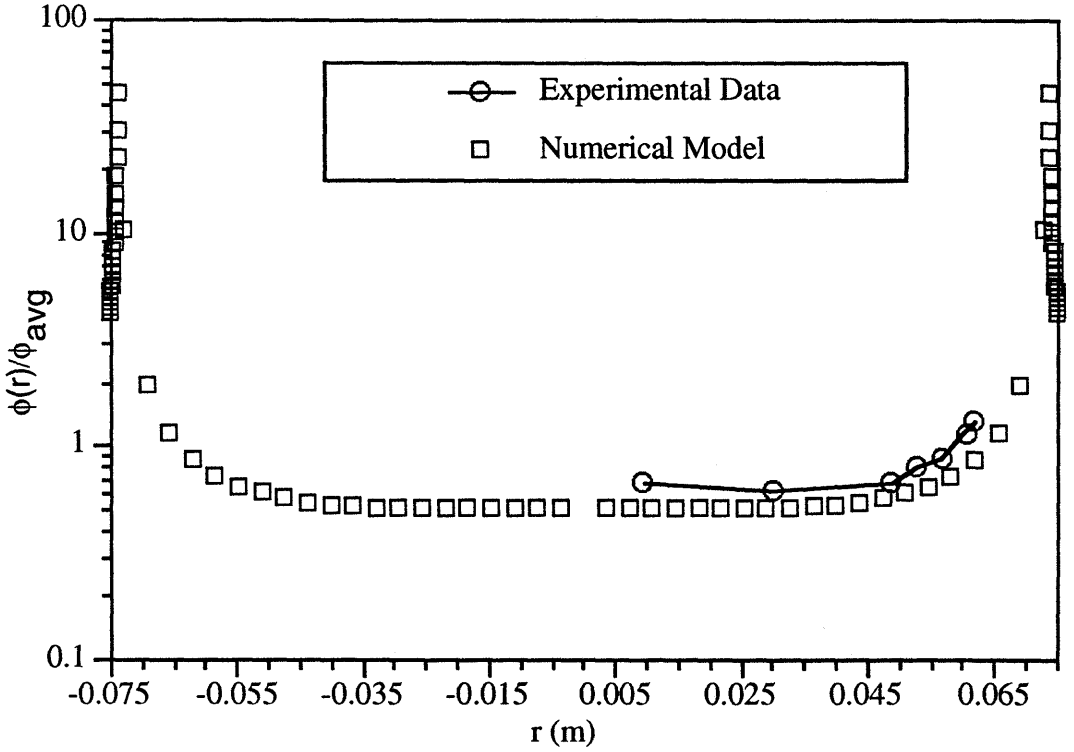

Figure 10.19
Numerical Model vs. Experimental Data: Horio et al. (1988)

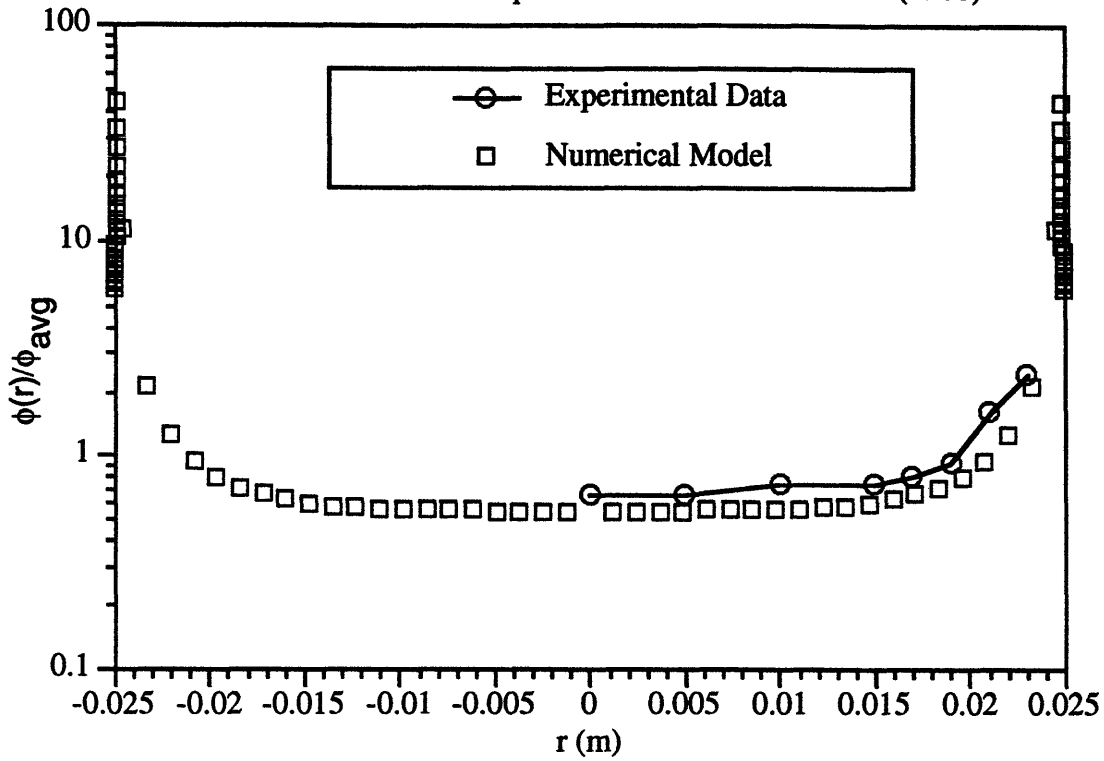

Figure 10.20
Numerical Model vs. Experimental Data:Miller and Gidaspow (1992)

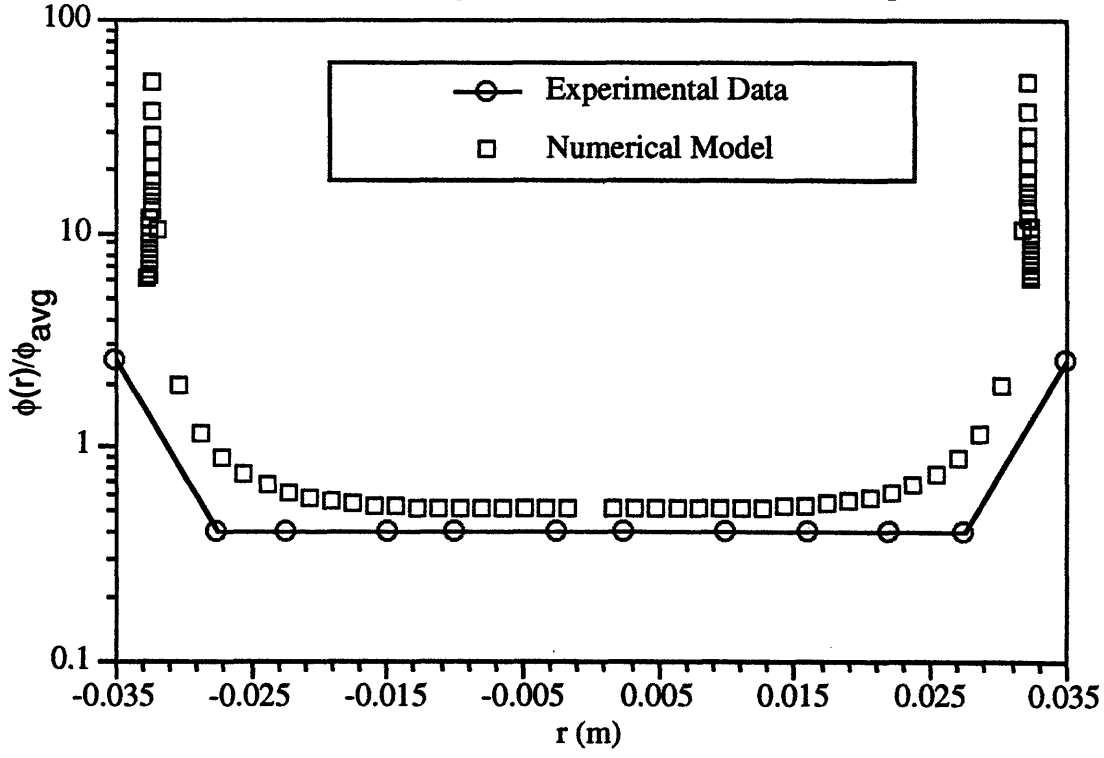

Figure 10.21
Numerical Model vs. Experimental Data: Rhodes and Laussmann (1992)

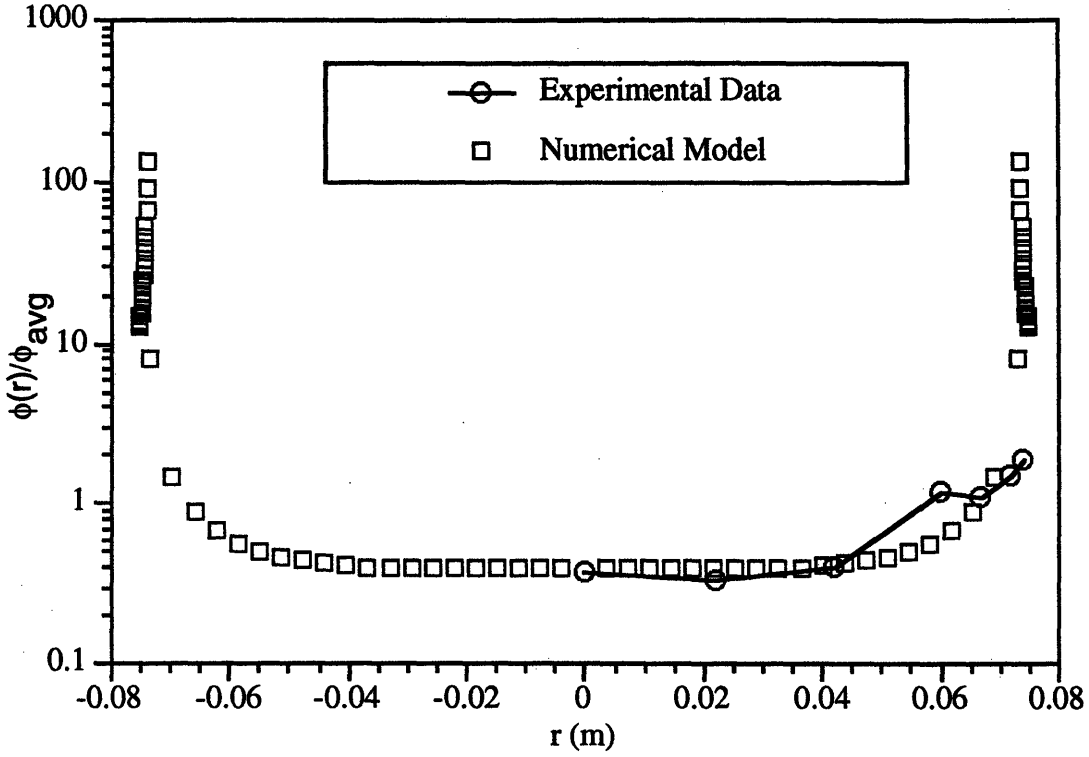

In all cases, the model predicts the general shape of the radial profile, and in most cases does a good job in predicting the magnitude of the radial concentration normalized by the cross-sectional averaged value. Note that these are normalized values; offsets due to differences in the predicted versus the experimental values in the cross-sectionally averaged solids fraction are not directly shown.

It is interesting to see that in all cases the model predicts the buildup of solids at the wall of the beds, and the rapid dropoff in solids concentration as one moves radially inward. The results indicate that the proposed method for determining radial solids concentration profiles is a good first approximation.

10.3.3 Radial Velocity Profiles

No model was proposed which predicted the radial variation in solids velocity in the bed. To compare the data with that of the investigators, the top-hat profile assumed by the core-annulus model with the numerically determined values in the core and annulus regions will be compared to the experimental data. Figures 10.22 through 10.28 present comparisons of the results.

Figure 10.22
Numerical Model vs. Experimental Data: Bader et al. (1988)

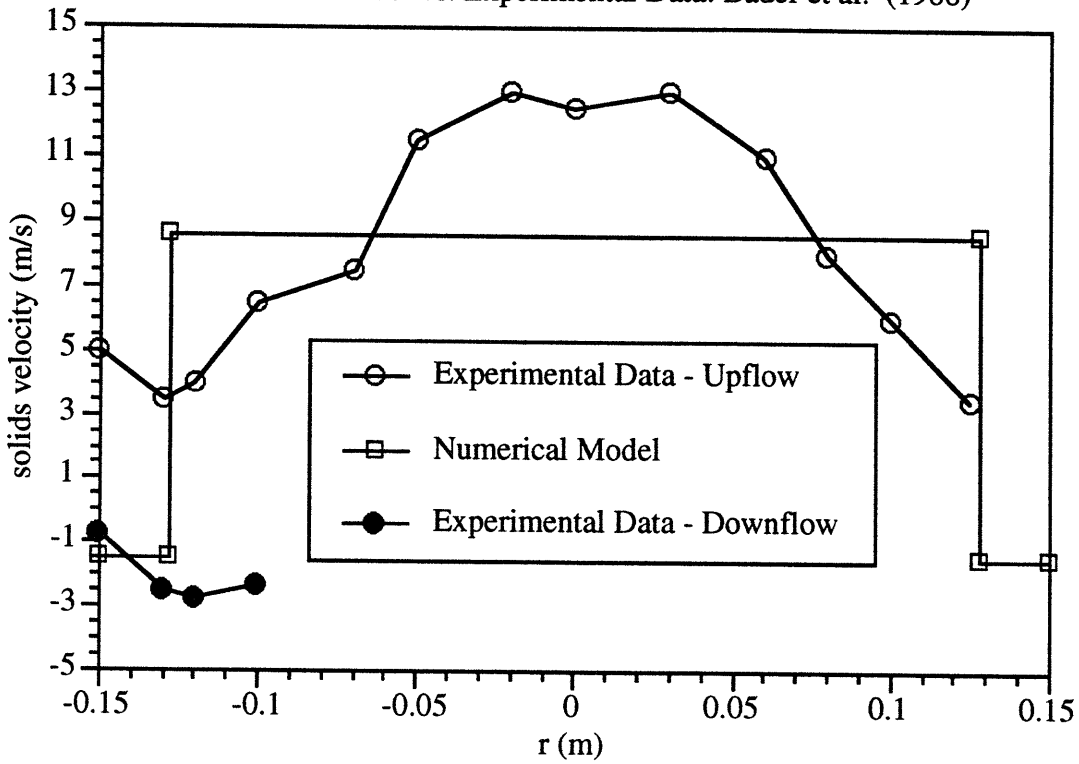

Figure 10.23
Numerical Model vs. Experimental Data: Gidaspow et al. (1989)

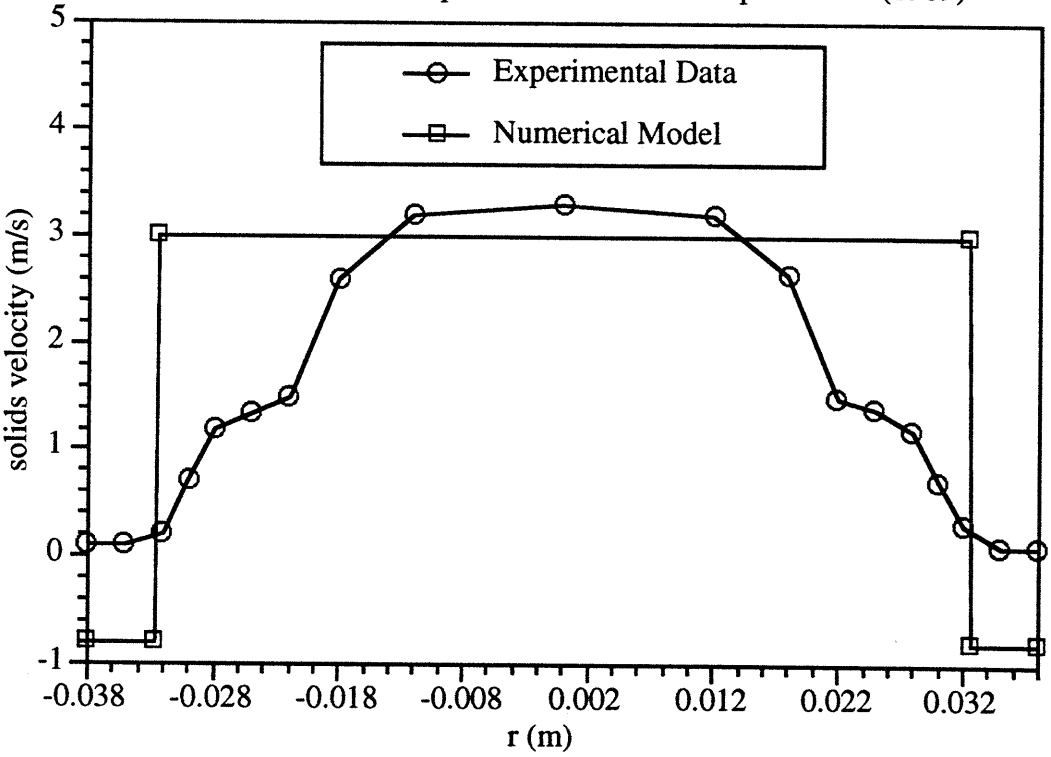

Figure 10.24
Numerical Model vs. Experimental Data: Hartge *et al.* (1988)

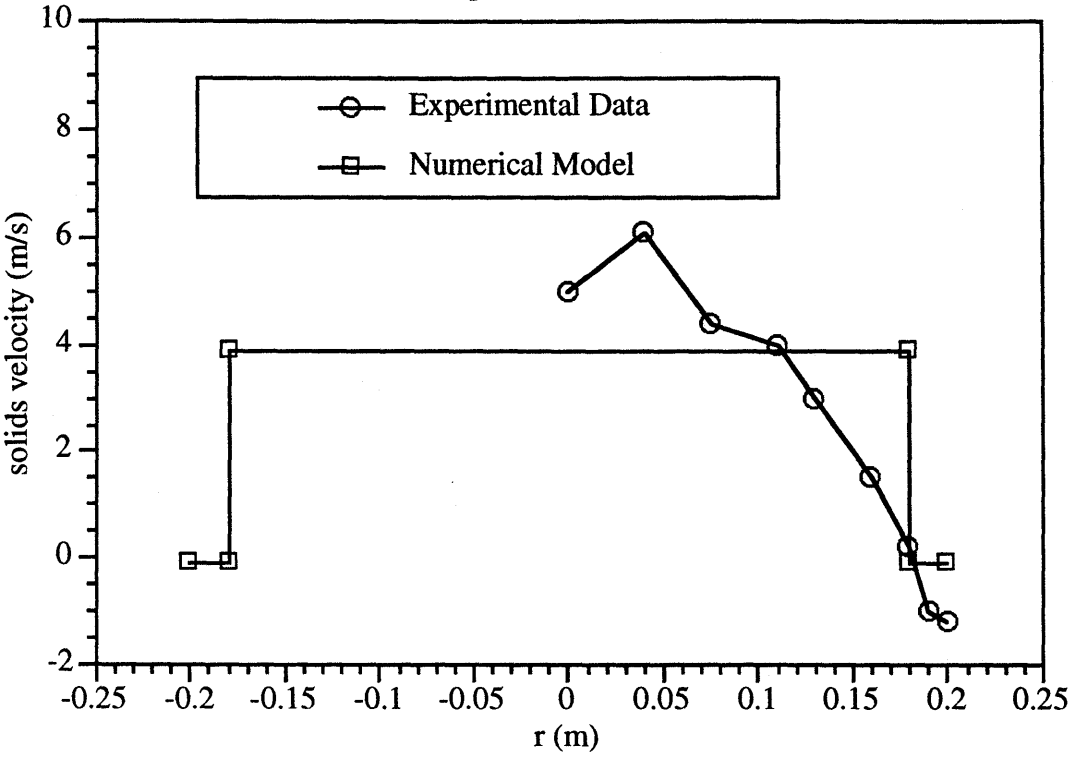

Figure 10.25
Numerical Model vs. Experimental Data:Herb et al. (1992)

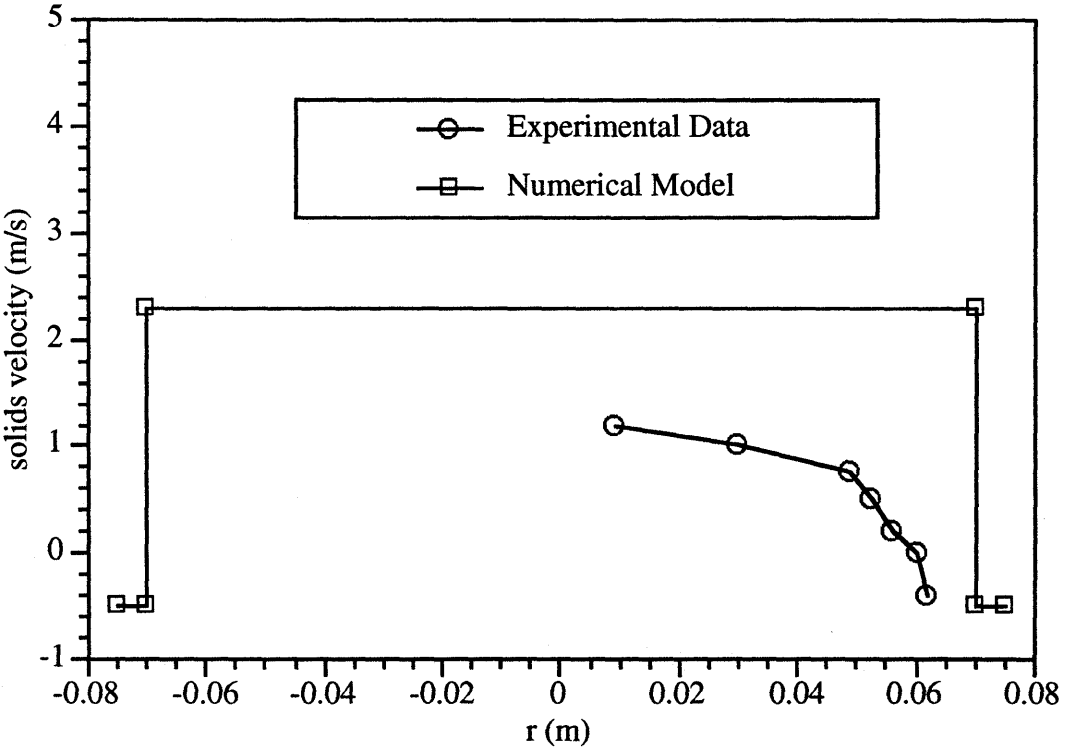

Figure 10.26
Numerical Model vs. Experimental Data: Horio et al. (1988)

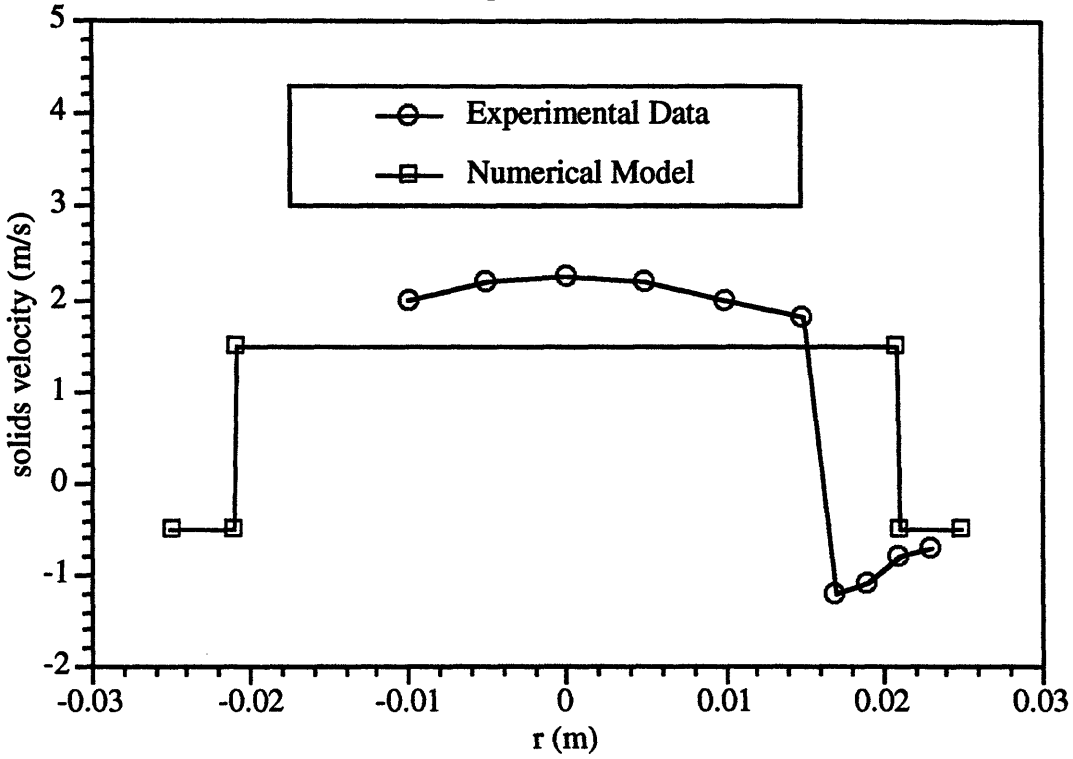

Figure 10.27
Numerical Model vs. Experimental Data:Miller and Gidaspow (1992)

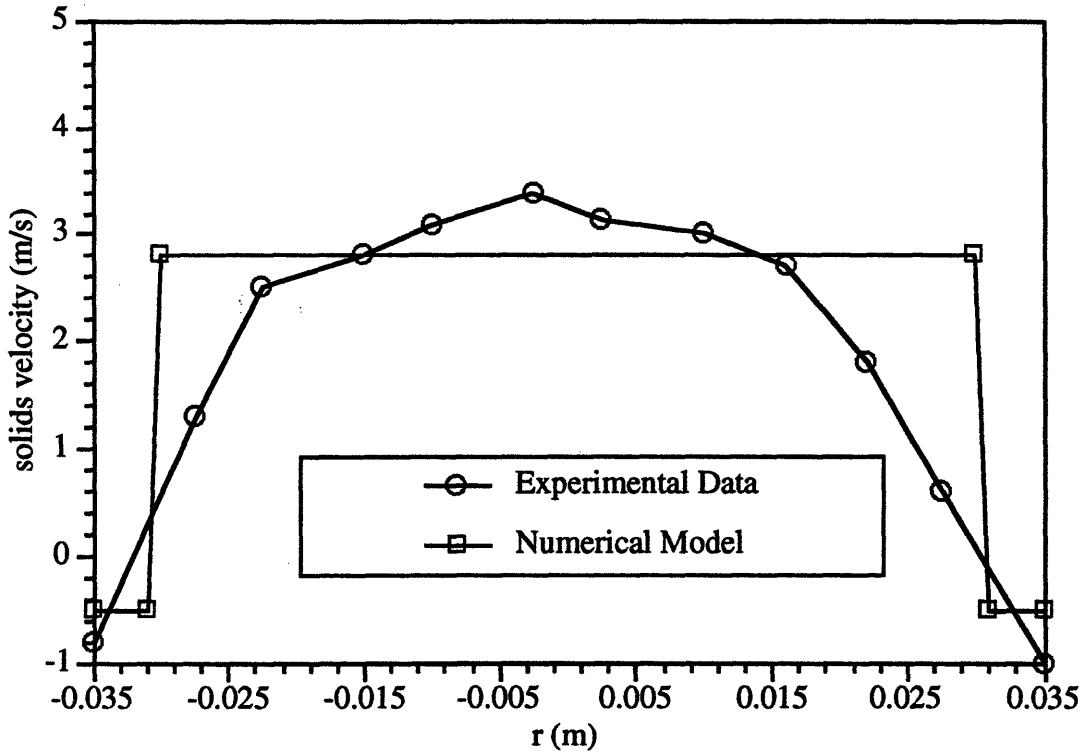

Figure 10.28
Numerical Model vs. Experimental Data: Rhodes and Laussmann (1992)

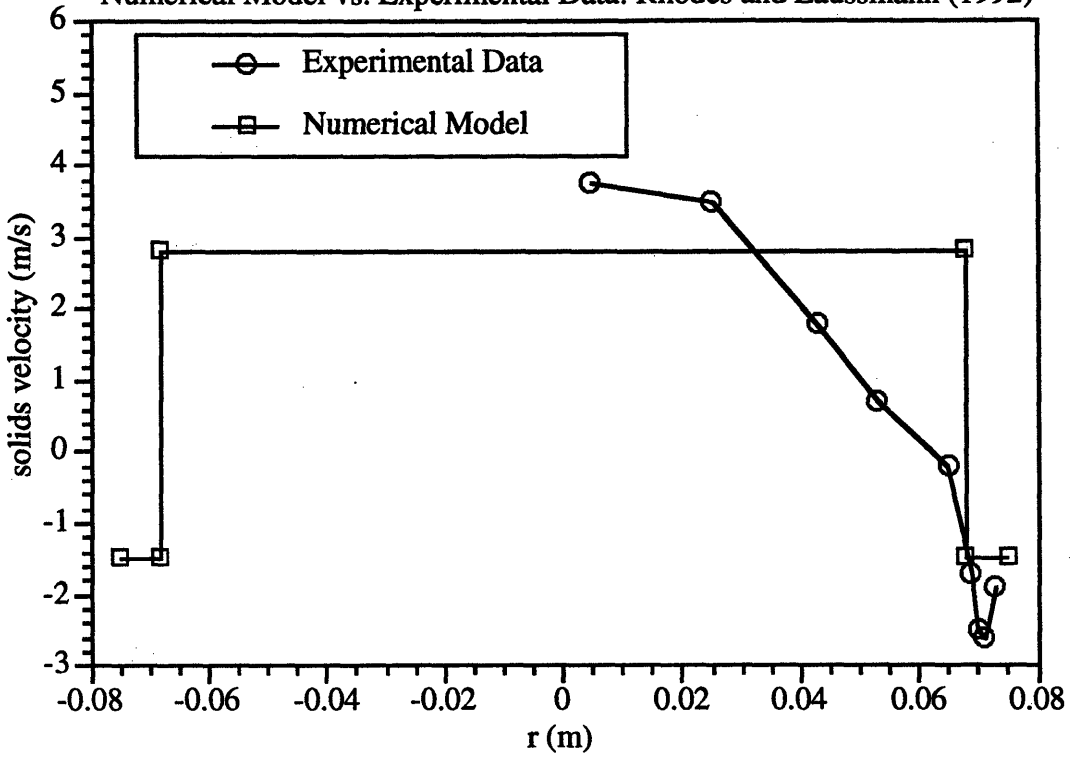

Except for the data of Herb *et al.* (1992), the model does a fairly good job at predicting the magnitude of the solids velocity in the core and annulus. For all cases, the solids velocity at the wall was between -0.5 m/s and -2.0 m/s. This is in good agreement with the experimentally determined values in the above plots, and is also in agreement with the data compiled in Chapter 4. In Chapter 4, it was shown that almost all available experimental data for the solids velocity at the wall of a CFB lies between 0 and -3.0 m/s.

The shape of the radial velocity profiles of the solids given above suggest that the solids move in a profile similar to the gas profile in a tube. This further supports the hypothesis that individual particles are the primary means of vertical transport of solids, rather than clusters. If the particles can be described as non-interacting individual particles moving in tube flow, the equation for the particle profile is simply

$$v_{p_a} = V_{max}\left[1 - \left(\frac{r}{R}\right)^n\right] - u_t \qquad (4)$$

as discussed in Section 5.0. Figures 10.29 through 10.34 present comparisons with the experimental data using equation (4).

Figure 10.29
Equation (4) vs. Experimental Data: Bader et al. (1988)

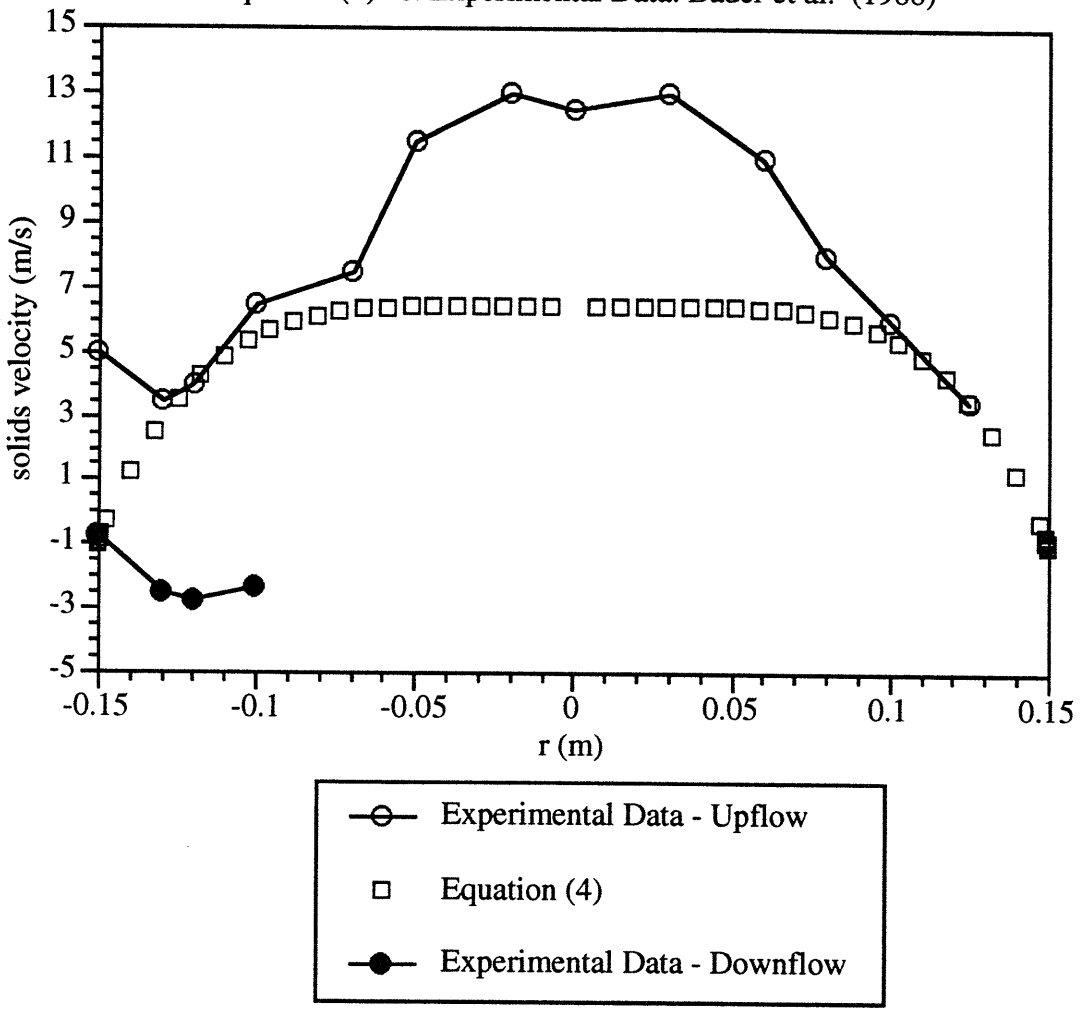

Figure 10.30
Equation (4) vs. Experimental Data: Gidaspow et al. (1989)

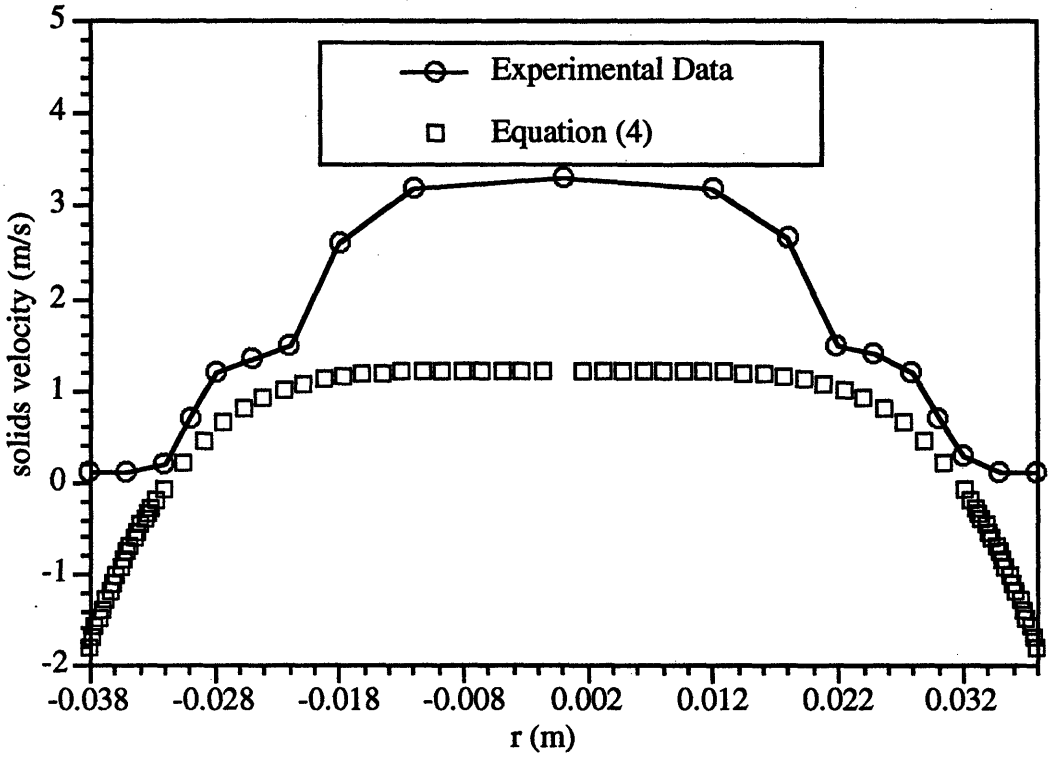

Figure 10.31
Equation (4) vs. Experimental Data: Hartge *et al.* (1988)

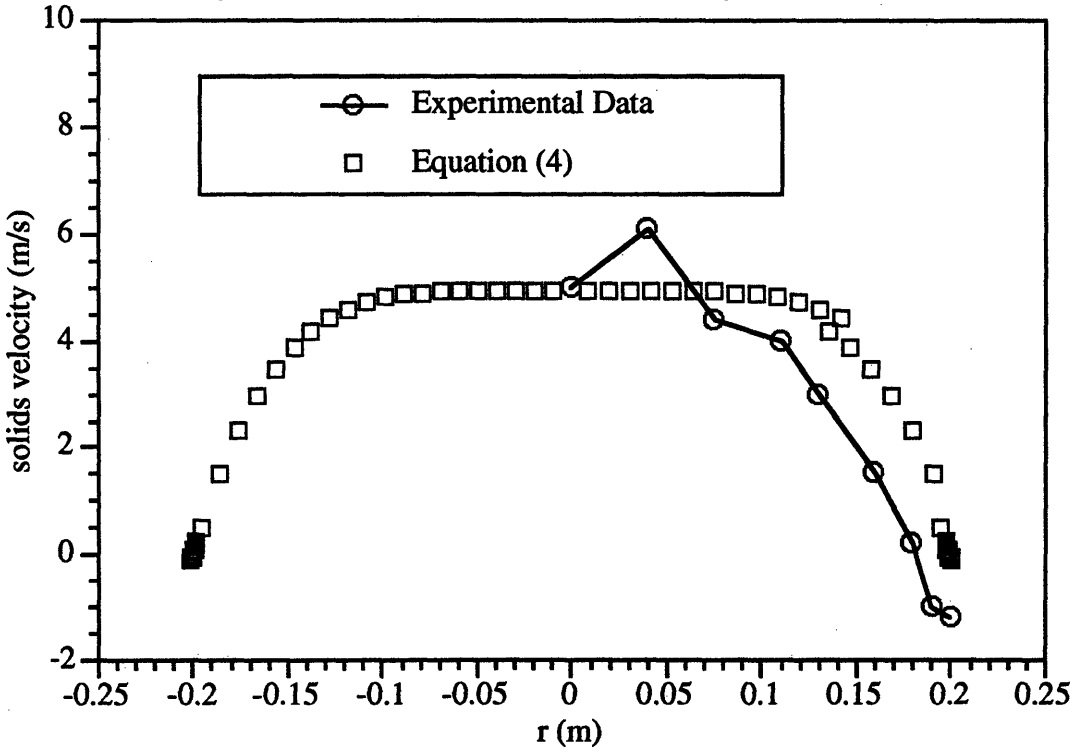

Figure 10.32

Equation (4) vs. Experimental Data:Herb et al. (1992)

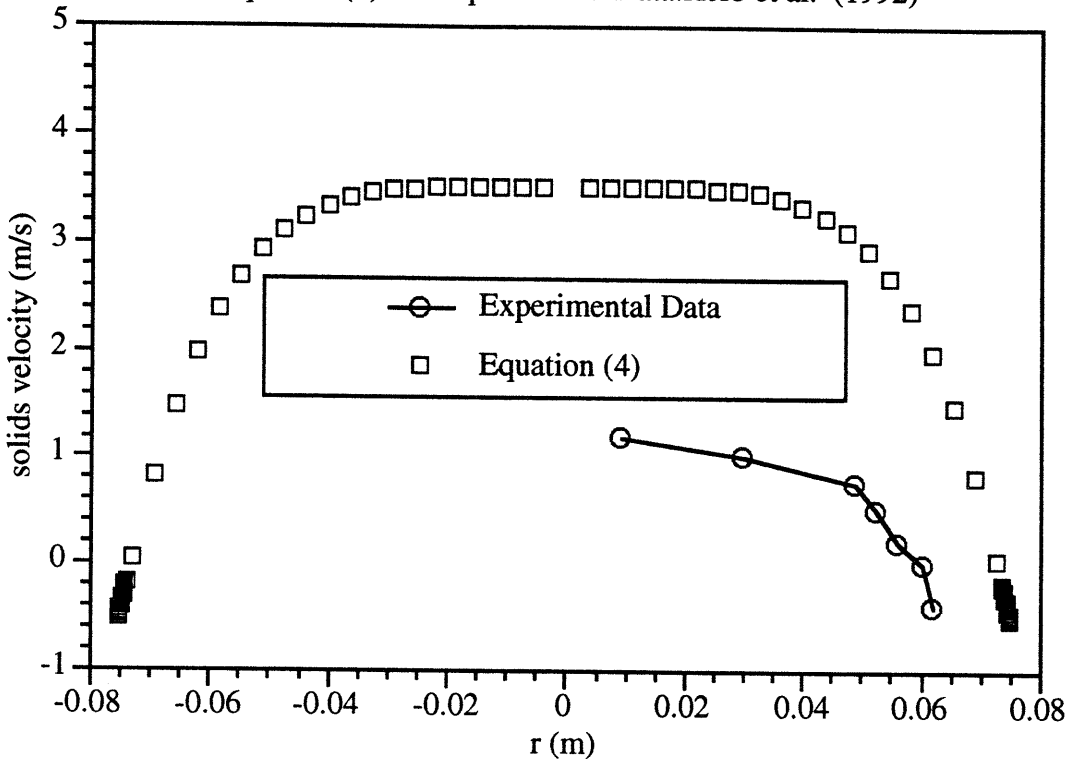

Equation (4) vs. Experimental Data: Horio et al. (1988)

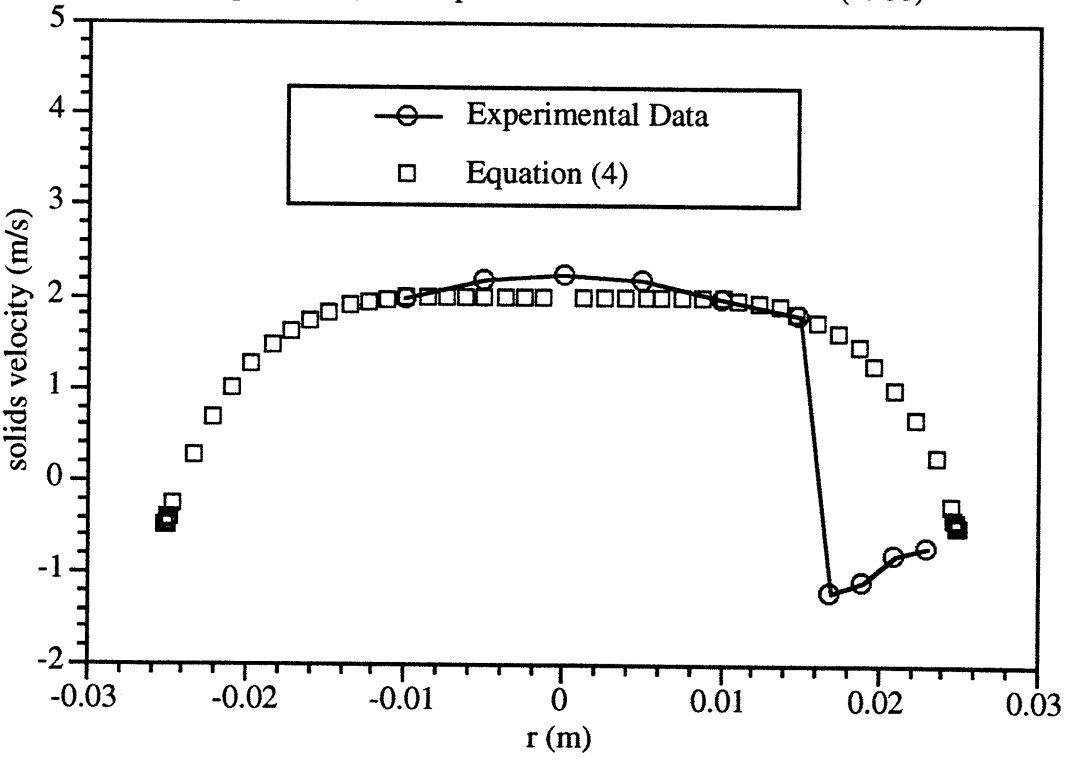

Figure 10.33

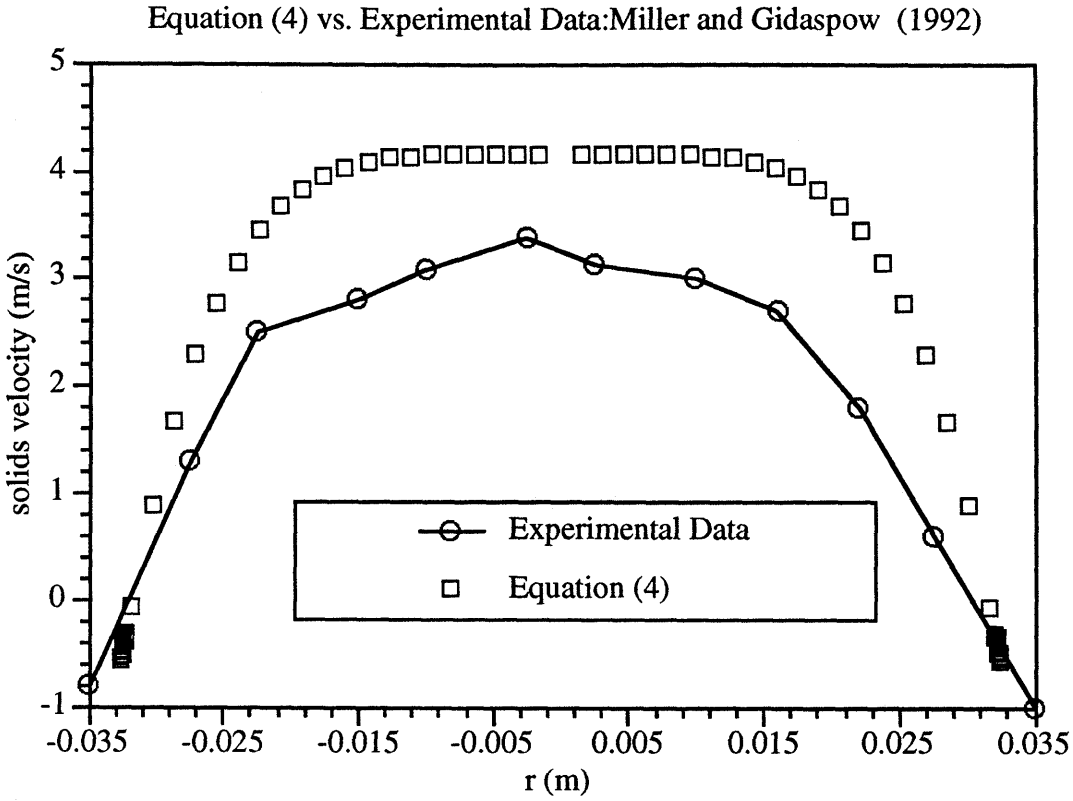
Equation (4) vs. Experimental Data:Miller and Gidaspow (1992)
solids velocity (m/s)
r (m)
Experimental Data
Equation (4)
5
4
3
2
1
0
-1
-0.035
-0.025
-0.015
-0.005
0.005
0.015
0.025
0.035

Figure 10.34

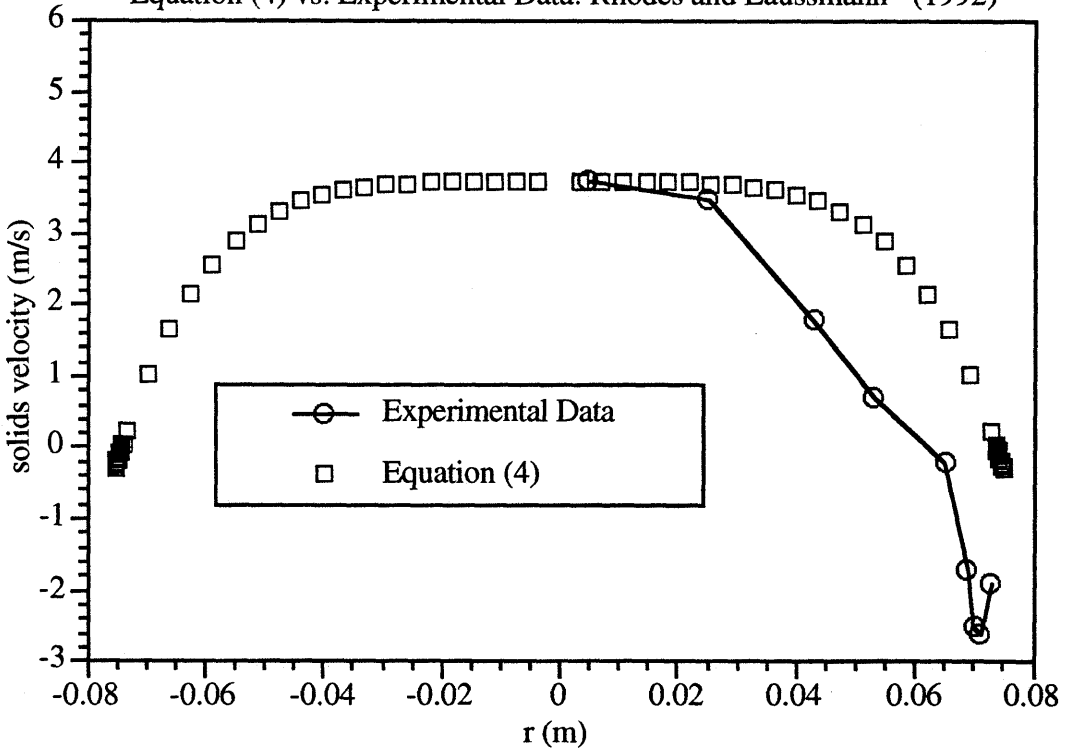
Equation (4) vs. Experimental Data: Rhodes and Laussmann (1992)
solids velocity (m/s)
r (m)
Experimental Data
Equation (4)
6
5
4
3
2
1
0
-1
-2
-3
-0.08
-0.06
-0.04
-0.02
0
0.02
0.04
0.06
0.08

In general, equation (4) does not offer any significant advantages in terms of accuracy, over the top hat profile. It does better capture the shape of the solids velocity profile, but is at best an approximation of the magnitude.

10.4 Comparison of Experimentally Determined Hydrodynamic Data in CFB Combustors with the Numerical Model

The true test of any numerical CFB model is how well it can predict the hydrodynamics of an actual hot combustor. The average solid fraction profile data taken in the 2.5 MWth Studsvik atmospheric CFB combustor and the Foster Wheeler pilot scale pressurized CFB combustor can serve as a baseline for the model. Radial variations in solid fraction and velocity are not available for these combustors, so that the only comparisons which can be made are between the cross-sectionally average axial solid fraction profiles (dimensionless pressure gradients).

Figures 10.35 through 10.40 present comparisons between the Studsvik combustor and the model. Table 3 provides a summary of the Studsvik combustor operating conditions.

Table 3: Studsvik 2.5 MWth Combustor Operating Conditions

Test	Condition 1	Condition 2	Condition 3	Condition 4	Condition 5	Condition 6
Bed	Hot	Hot	Hot	Hot	Hot	Hot
u_o (m/s)	6/07	7.92	7.65	6.05	6.16	7.94
System Pressure (bar)	1	1	1	1	1	1
G_s (kg/m^{2}s)	10.2	16.6	30.7	13.8	9.0	37.6
% Primary Air	49	69	52	71	69	70
ρ_s/ρ_f	8413	8413	8413	8413	8413	8413
u_o/u_{mf}	106	138	133	105	107	138
Fr_L	0.51	0.87	0.82	0.51	0.53	0.88
$G_s/\rho_s u_o$	6.22E-4	7.91E-4	1.51E-3	8.61E-4	5.51E-4	1.79E-3
Re_{dp}	10.3	13.6	13.2	10.4	10.6	13.7

Figure 10.35

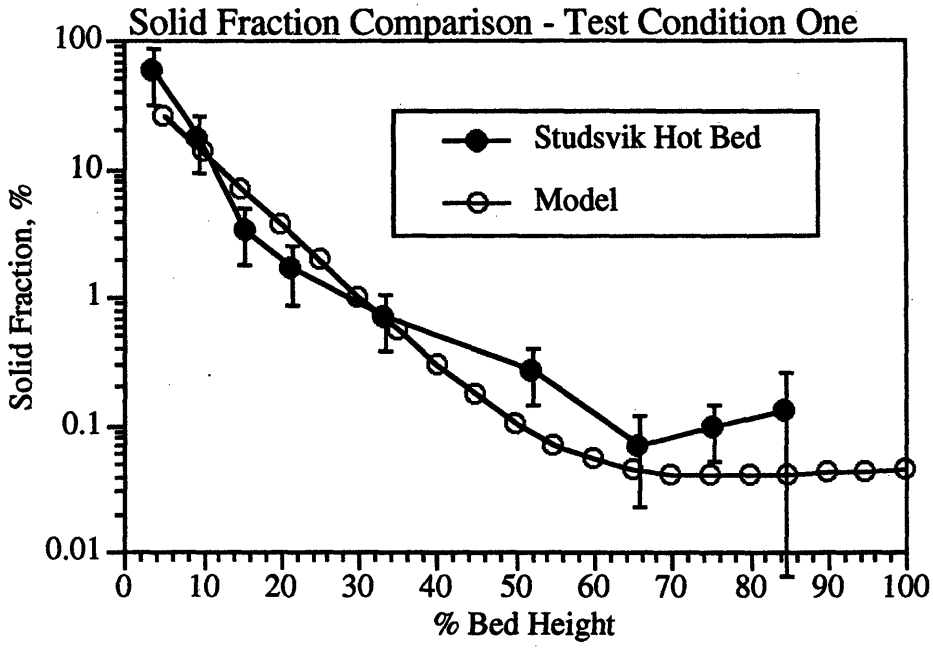

Figure 10.36

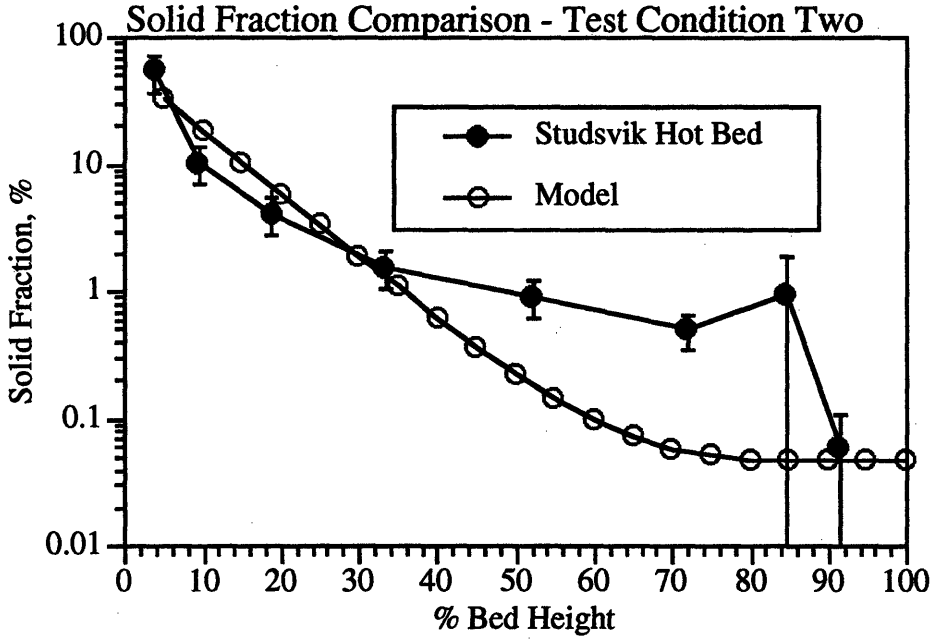

Figure 10.37

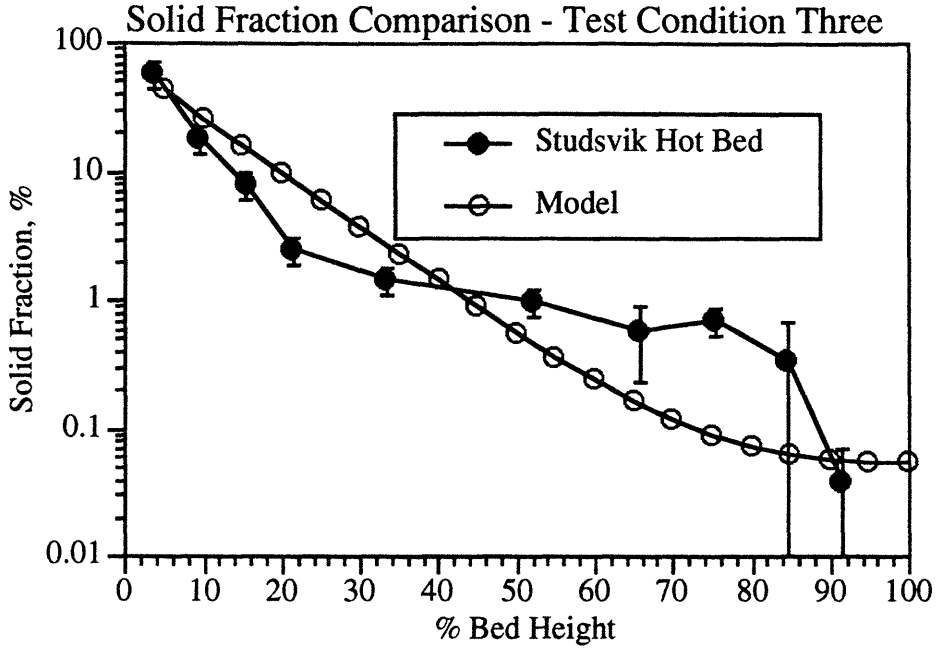

Figure 10.38

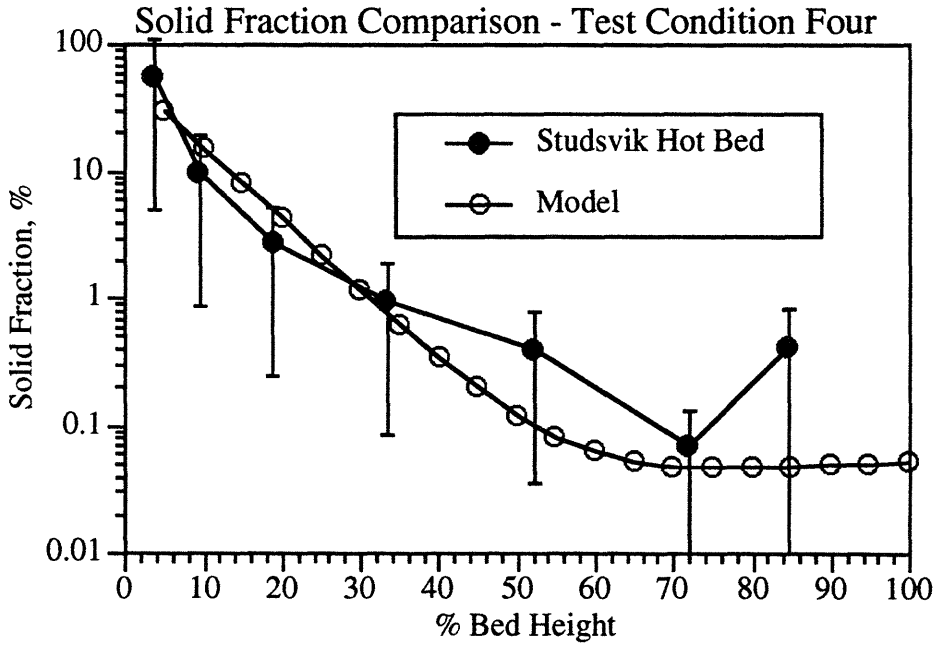

Figure 10.39

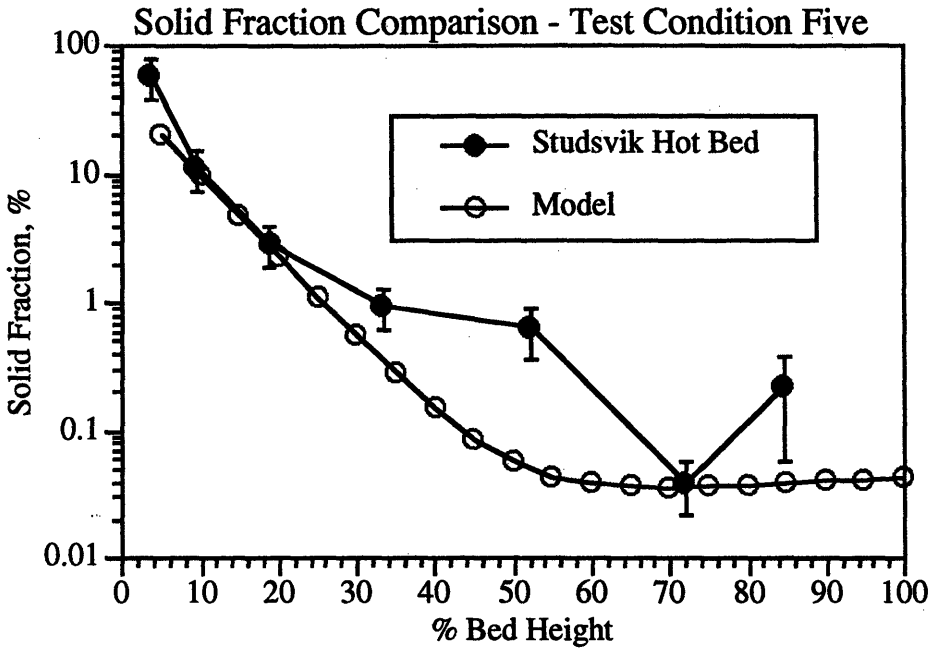

Figure 10.40

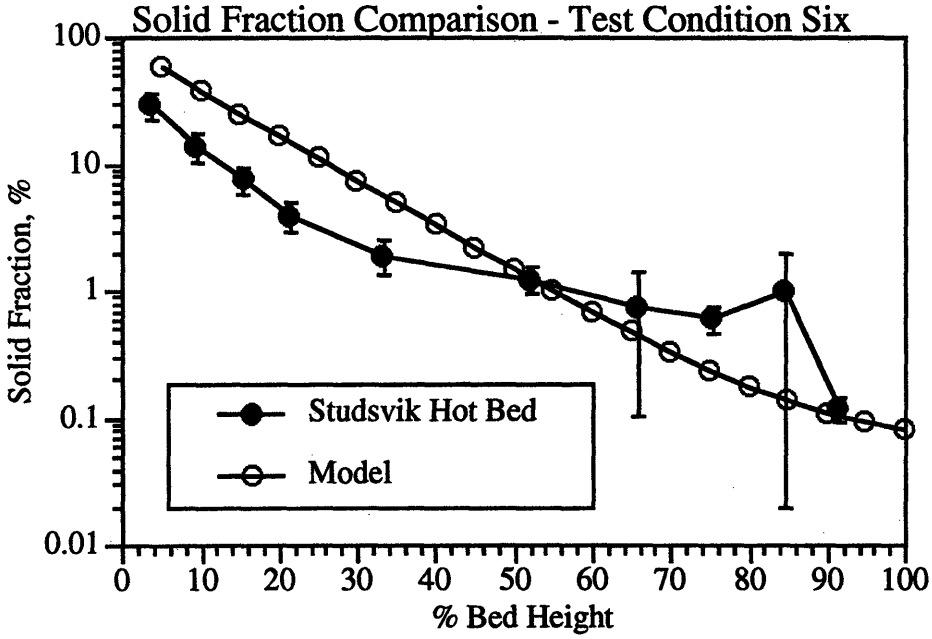

For most of the conditions, the model does a good job of predicting the solid fraction profile. Similar to the scaling results, several of the model results fall outside error bars. It is interesting to note that the worst matched cases (conditions 2, 5, and 6) are also the worst matched cases in

the hydrodynamic scaling tests described in Chapter 2. This suggests that some of the error may be in hot bed measurements rather than scale or numerical model results.

Surprisingly, agreement is fairly good at the bottom of the bed. This is probably a result of the fact that bottom conditions are determined by setting them such that the exit boundary conditions are met. Therefore, if the general shape of the solid fraction profile resembles that of the hot bed combustor, it will match at the bottom of the bed even though many of the assumptions made in the determination of the model (particle drag formulation, core-annulus structure, gas turbulence modeling) are no longer valid. There is no reason to believe that the model accurately models the physics of the dense region of the bed.

Figures 10.41 through 10.44 present comparisons between the Foster Wheeler pressurized combustor and the model. Table 4 provides a summary of the Foster Wheeler combustor operating conditions.

Table 4: Foster Wheeler Pressurized CFB Combustor Operating Conditions

Test	Condition 1	Condition 2	Condition 3	Condition 4
Bed	Hot	Hot	Hot	Hot
u_o - primary zone (m/s)	1.49	1.71	1.31	1.19
u_o - secondary zone (m/s)	2.74	2.96	2.83	2.77
System Pressure (bar)	11.7	13.0	12.4	13.0
G_s (kg/m^{2}s)	115	124	111	25.8
% Primary Air	54.0	58.0	46.2	42.0
ρ_s/ρ_f	758	681	718	688
u_o/u_{mf}	113	124	118	116
Fr_D	3.66	4.40	4.02	3.85
$G_s/\rho_s u_o$	0.016	0.016	0.015	0.0035
Re_{dp}	35.3	43.2	39.2	40.0

Figure 10.41

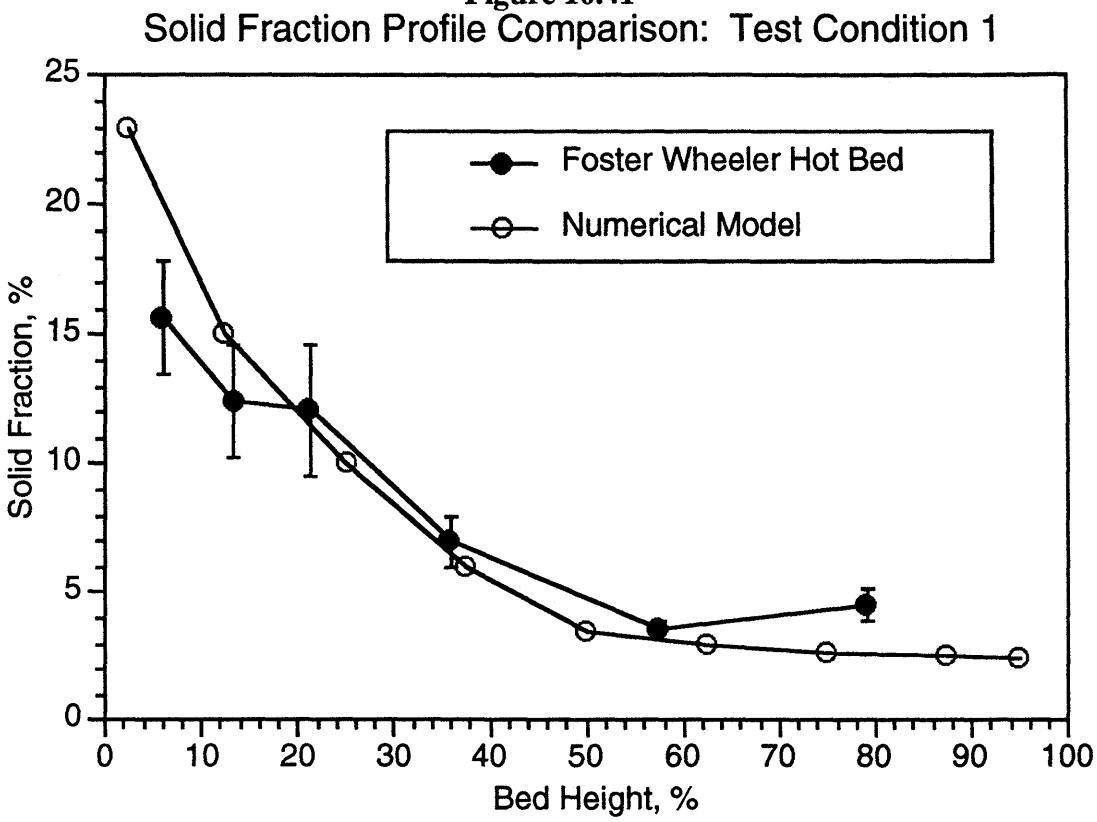

Figure 10.42

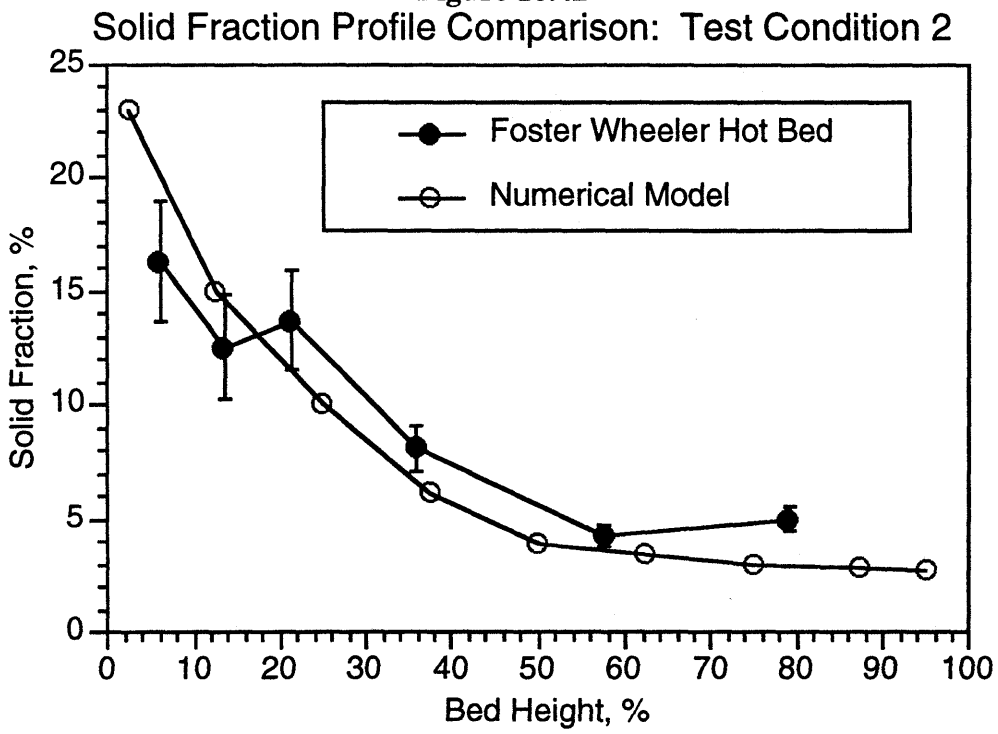

Figure 10.43

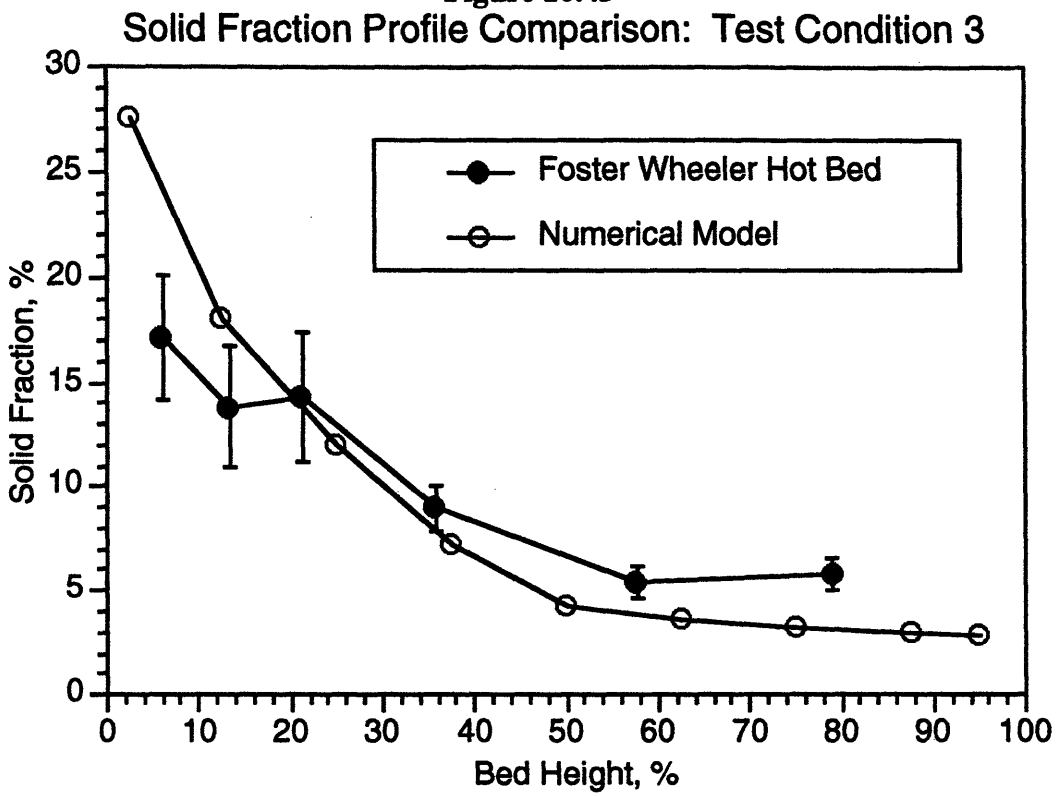

Figure 10.44

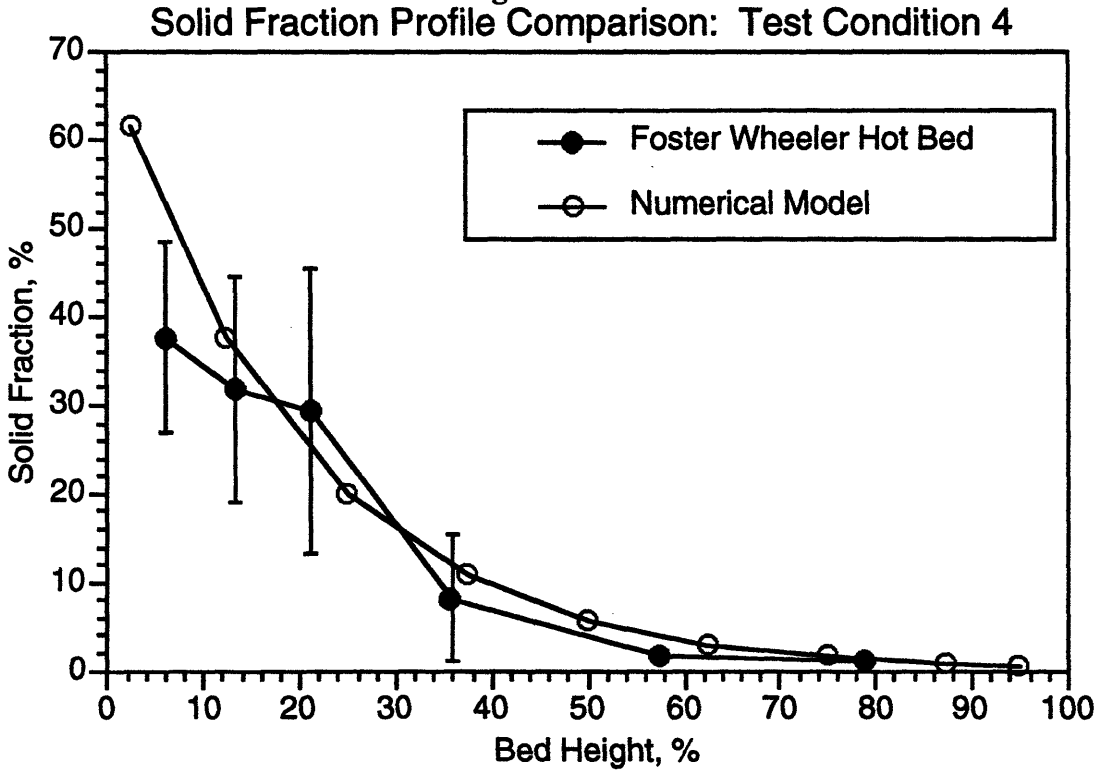

Again, the model does a good job in predicting the average solid fraction profiles of the combustor. Note the model profile does not have the characteristic "hitch" the combustor exhibits at about 20 percent bed height. This is because the secondary air ports are not modeled. Were all air to be introduced at the bottom of the Foster Wheeler combustor, one would expect a smoother profile, closer to that of the model.

The good agreement between the Studsvik and Foster Wheeler combustor solid fraction profiles with the model provides strong evidence that the model proposed can be used as a method to approximate the hydrodynamics in CFB combustors. Comparisons of the radial predictions with cold bed data further supports the proposition that the model characterizes the physics in the dilute regions fairly well. The most glaring deficiency in the model is the specification of the exit solid fraction. The model deviation from the axial solid fraction profile data of Bader *et al.* (see Section 10.3.1) suggests that reasonably good approximations of the exit conditions are necessary to assure model agreement. It must be remembered, however, that this deficiency effects the lateral solids dispersion results indirectly (a change in the predicted solid fraction changes the gas turbulence modulation and particle collisional fluctuations). Therefore, while it may significantly change the shape of the average solid fraction profile, the lateral dispersion coefficient may remain fairly constant (for instance, the lateral dispersion coefficient changed by less than 20 percent between the two runs made for Bader *et al.* - one with an exit collection efficiency of 0.8, and one with a collection efficiency of 0.6).

10.5 Effects of Operating Conditions

Sensitivity studies were conducted to determine the effects of several of the input parameters on the resultant axial solid fraction profile. All runs were made starting from a baseline pressurized CFB operating at 14 bar and 1100 K with 200 micron particles, an 20 cm bed diameter, and a superficial velocity of 4.0 m/s. These conditions are similar to those of the Foster Wheeler pilot CFB.

10.5.1 Bed Diameter

Figure 10.45 shows the effect of a change in bed diameter. As one goes to larger bed diameters, the predicted solid fraction tends to flatten out. Higher bed diameters mean larger eddy lengths which would result in larger dispersion coefficients and a solid fraction profile with a steeper solid fraction profile. However, if collisions control the time a particle remains in an eddy, then the effect of the larger eddy size is, to a larger extent, negated. The mean eddy speed in the

larger bed is lower than that in the smaller bed due to the larger bed Reynolds number. This effect becomes important now that the time a particle remains in an eddy is of the same order in the two beds (time between successive collisions is about the same). The higher eddy speed in the smaller bed results in a steeper solid fraction profile, which is depicted in the plots. This trend is confirmed in the experimental results of Bai *et al.* (1992) and Arena *et al.* (1992).

Figure 10.45

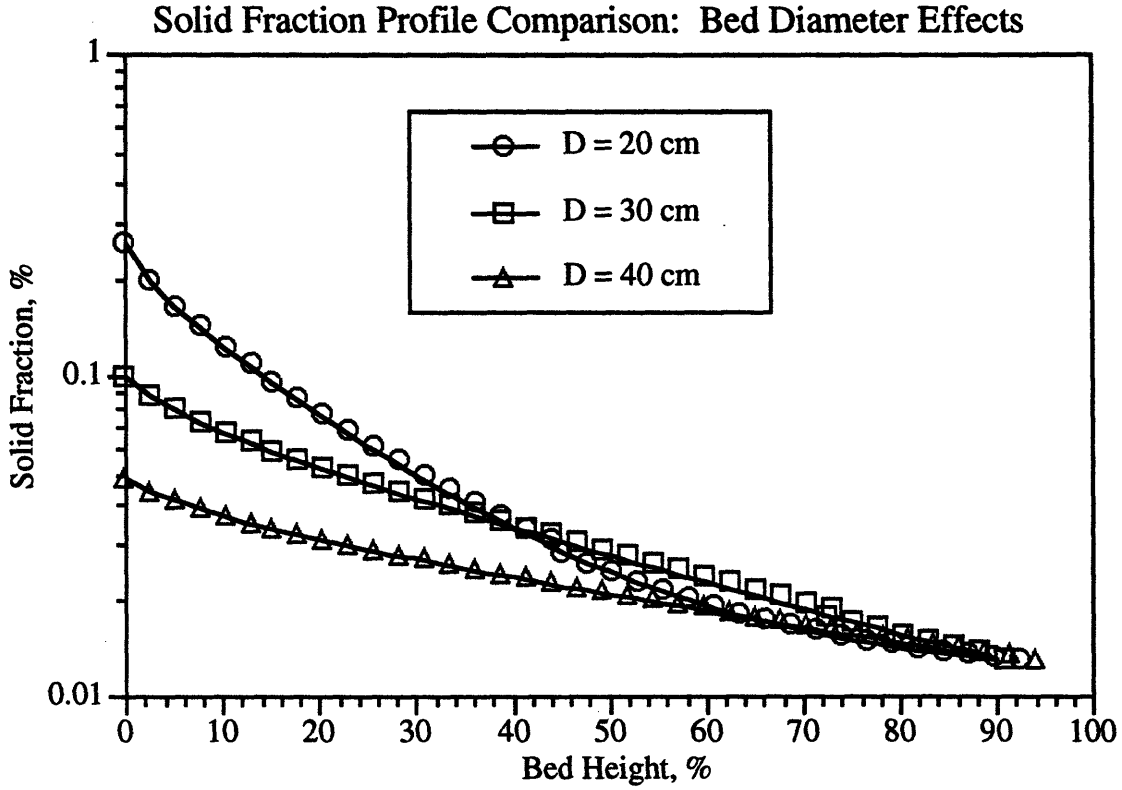

10.5.2 Particle Diameter

The effects of particle diameter are given in Figure 10.46. As one goes to larger particle diameter, the solids fraction profile tends to get steeper, indicating a larger lateral solids dispersion coefficient (for a given solids fraction at the bottom of the bed, larger dispersion coefficients result in a faster dropoff of core solids concentration since solids are moving more quickly to the wall - see equation (91) in Section 2). This again is counterintuitive to a model based strictly on a gas turbulence induced particle dispersion model. In such a model, the lateral solids dispersion coefficient for the smaller particles would be larger due to the longer particle-eddy interaction time (equal to the ratio of the eddy length and the particle terminal velocity).

However, if one considers the effects of particle collisions and gas turbulence modulation, it becomes evident that this is not that case.

For relatively dense beds (greater than about 1 percent in the upper regions) particle collisions will have a significant effect on the eddy-particle contact time. Although the time of interaction between the particle and eddy is nearly the same due as that due to collisions between particles, this in itself does not explain the larger dispersion coefficients for the larger particles. Even if the interaction times were the same, a model based on gas turbulence induced dispersion would still predict a higher dispersion coefficient for the smaller particles since they are able to respond to the gas turbulence much more readily because of the smaller inertia. However, because in many regions of the bed collisions are the primary mechanism for the particle lateral r.m.s. velocity, the larger sized particle lateral dispersion is greater because they are affected least by gas turbulence modulation due to the presence of particle. Additionally, the gas, which in the denser regions tends to damp the particle velocity fluctuations due to collisions, affects the smaller particles to a greater extent than the larger particles. The trend predicted by the model has been confirmed experimentally in the work of Adanez *et al.* (1994) and Bai *et al.* (1992).

The trends predicted in 10.46 show the proposed numerical model offers significant advantages over simple gas turbulence induced dispersion models. The trends predicted by those types of models are incorrect.

Figure 10.46

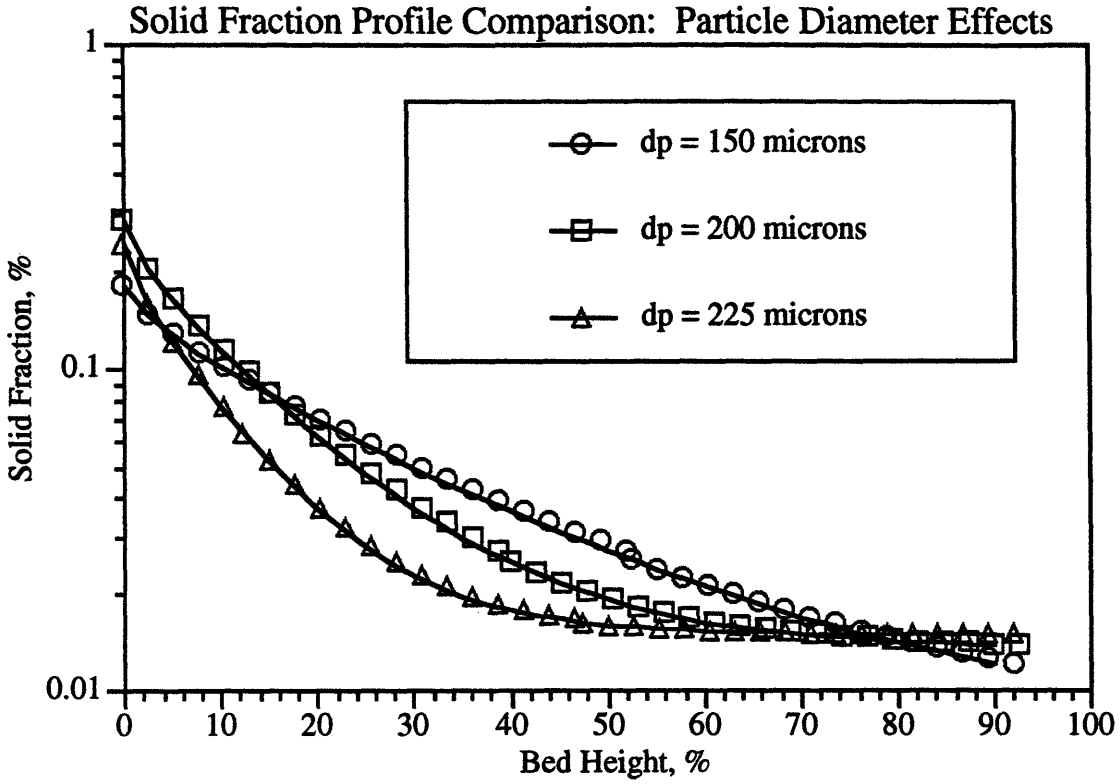

10.5.3 Bed Pressure

Effects of bed pressure are given in Figure 10.47. At lower pressures, the effect tended to be relatively small, but increased significantly once about 10 bar was reached. Bed pressure effects the gas properties; at higher bed pressure the eddy speed decreases (higher bed Reynolds number), but the particle-eddy interaction time increases (lower particle terminal velocity). Additionally, the particle responds more readily to the gas turbulence due to the larger gas inertia. The smaller eddy-particle relative velocity lowers the gas turbulence modulation. This suggests that the lateral dispersion would be greater at small pressures, although the reasoning is not straightforward. Little experimental results exist on pressurized units, and no results exist which compare the effects of pressure on the solid fraction profile. Looking at the results from the scaling of the Studsvik combustor described in Chapter 4 can provide some insight. Throughout the scaling experiments, the cold models were operated at a slightly lower solid to gas density ratio, which is equivalent to increasing the gas pressure. In almost every case, the cold model results resulted in curves which were flatter than the hot bed curves, indicating a smaller dispersion coefficient. Additionally, one can compare the results of the Foster Wheeler cases 1 and 2 where the pressure changed from 11.7 to 13.0 bar (see Figure 10.48). The axial

solid fraction profile for the higher pressure case is slightly less steep than for the lower pressure case. This is consistent with the trend predicted by the model.

Finally, Tsukada *et al.* (1993) have studied the effect of pressure on the hydrodynamics of fluidized beds. Their results indicate that as the pressure is raised, the solid fraction profile becomes flatter, and less dense at the bottom of the riser. These results are consistent with the model predictions.

Figure 10.47
Solid Fraction Profile Comparison: Pressure Effects

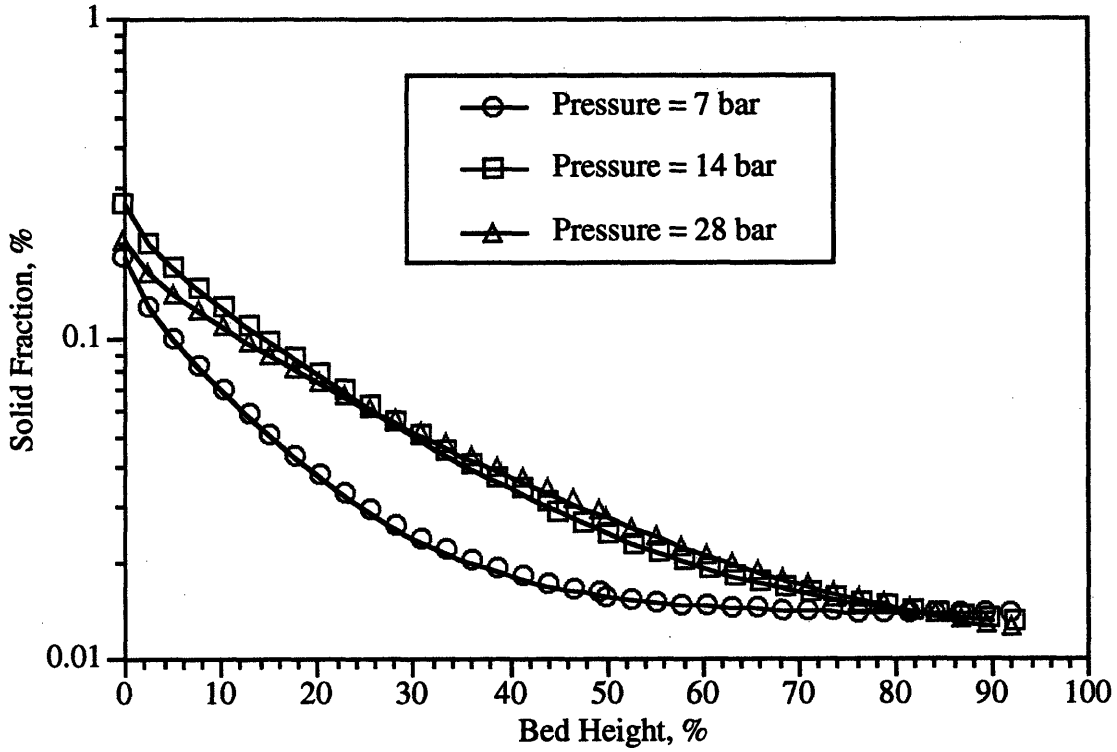

Figure 10.48
Comparison of Average Solid Fraction Profiles for Various Pressures

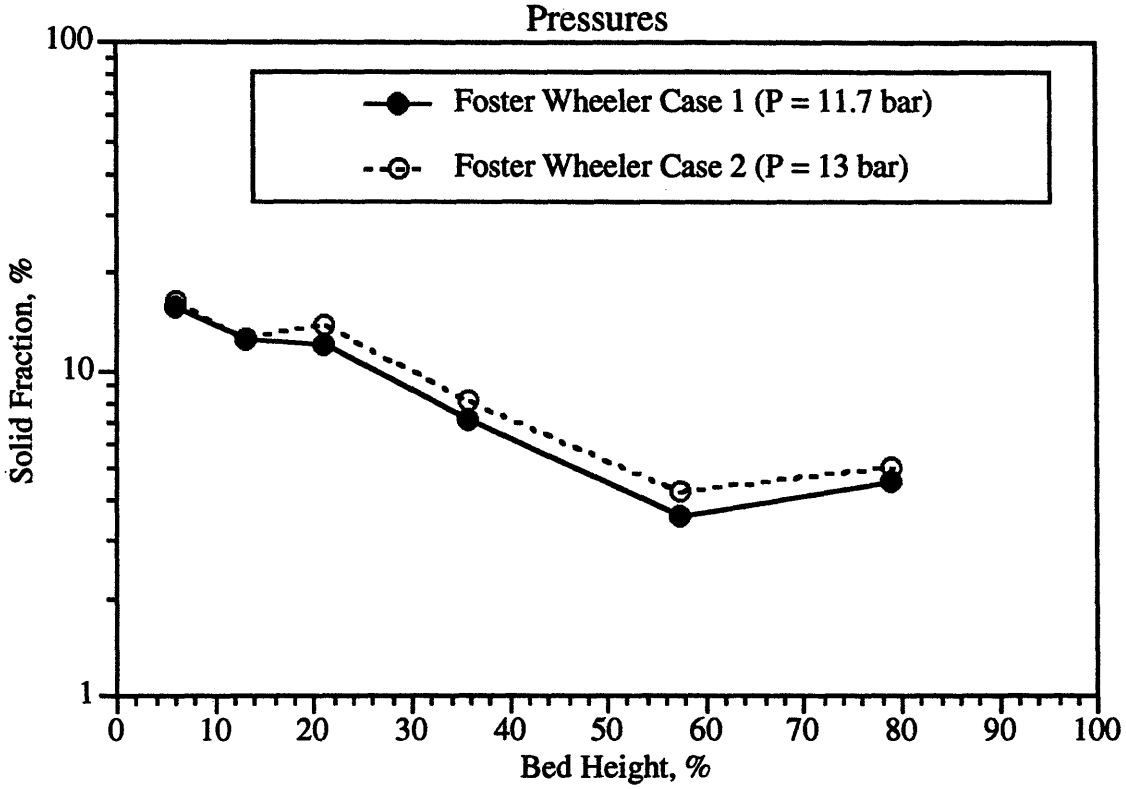

10.5.4 Particle Collisions

Figure 10.49 shows the effects of the model for a run with and without particle collisions. The effects are significant. In general, a model which does not include collisions predicts an exponential falloff of solid fraction with height. The trend with collisions is more steep. This is due to the increase in effective lateral particle fluctuating velocity. The path to the trend is somewhat complex: including particle collisions tends to decrease particle-eddy interaction times in the denser regions, but may increase or decrease the effective lateral particle fluctuating velocity depending on the magnitude of the particle fluctuating velocity caused by particle collisions. For the rather dense conditions of the Foster Wheeler pilot PCFBC, the particle collisions increase the lateral dispersion coefficient causing a steeper dropoff in the axial solid fraction profile.

Figure 10.49 indicates that particle collisions cannot be disregarded. As discussed in Section 3, for solids fractions above 1 percent in the bed, particle collisions have a significant effects. Above solids fractions of about 10 percent, they dominate the bed hydrodynamics.

Figure 10.49
Solid Fraction Profile Comparison: Collisional Effects

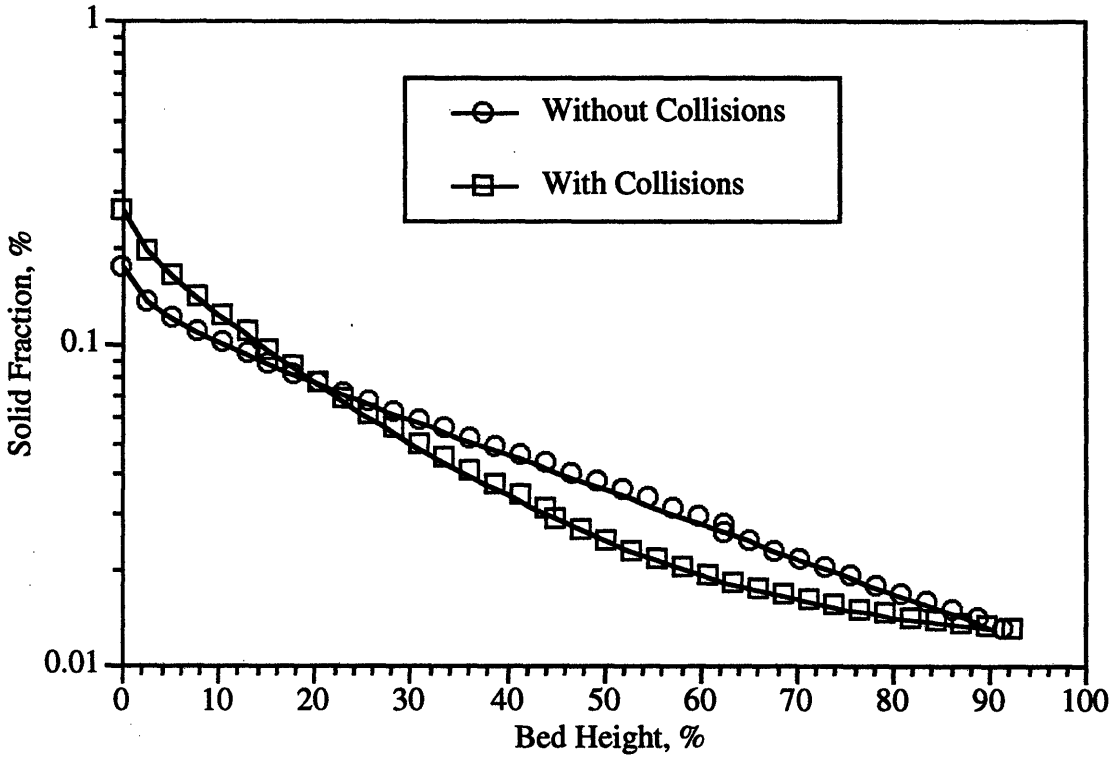

10.5.5 Coefficient of Restitution

Figure 10.50 shows the effects of the particle coefficient of restitution on the average solid fraction profile. The effects are insignificant for the range of coefficients of restitution typical of the materials in CFB's (dolomite and limestone). This result is consistent with the experimental results of Glicksman *et al.* (1991), Litka and Glicksman (1985) and Change and Louge (1992), who found the coefficient of restitution had little effect on the overall hydrodynamics of bubbling and circulating fluidized beds. The small influence of the coefficient of restitution was also indicated in the scaling results in Chapter 2. In these tests, a combustor using dolomite sorbent was successfully scaled utilizing polyethylene plastic - materials with significantly different coefficients of restitution.

Table 10.50

Solid Fraction Profile Comparison: Coefficient of Restitution Effects

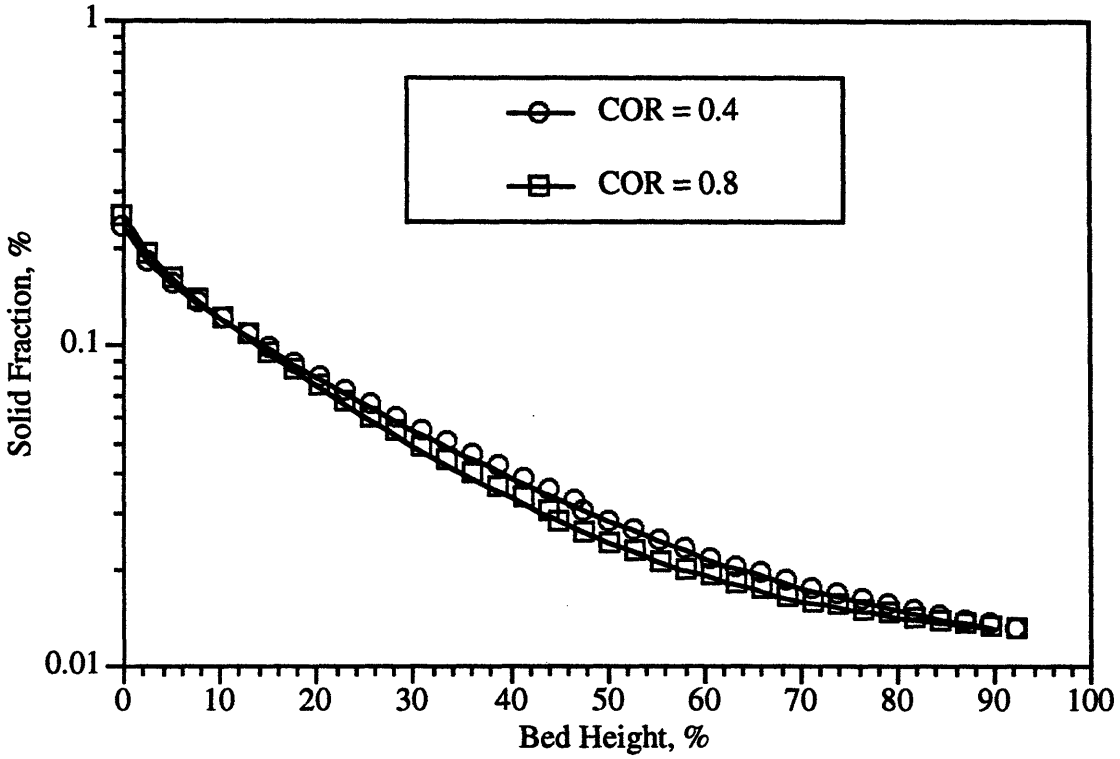

10.5.6 Gas Turbulence Modulation

Figure 10.51 shows the effects of the numerical model run with and without the gas turbulence modulation effects as outlined in Section 3. The effects of gas turbulence modulation are significant. As expected, when the gas turbulence modulation effects are included, the particle dispersion coefficient is smaller (eddy velocity is smaller resulting in smaller lateral particle velocities). For the same exit solid fraction, the bed bottom solid fraction is then smaller when turbulence modulation effects are included. The model used to predict the effects of particles on gas turbulence is somewhat crude. The fact that the model is somewhat sensitive to this effect indicates that futher work needs to be conducted to quantify this phenomenon more accurately.

Figure 10.51
Solid Fraction Profile Comparison: Gas Turbulence Modulation Effects

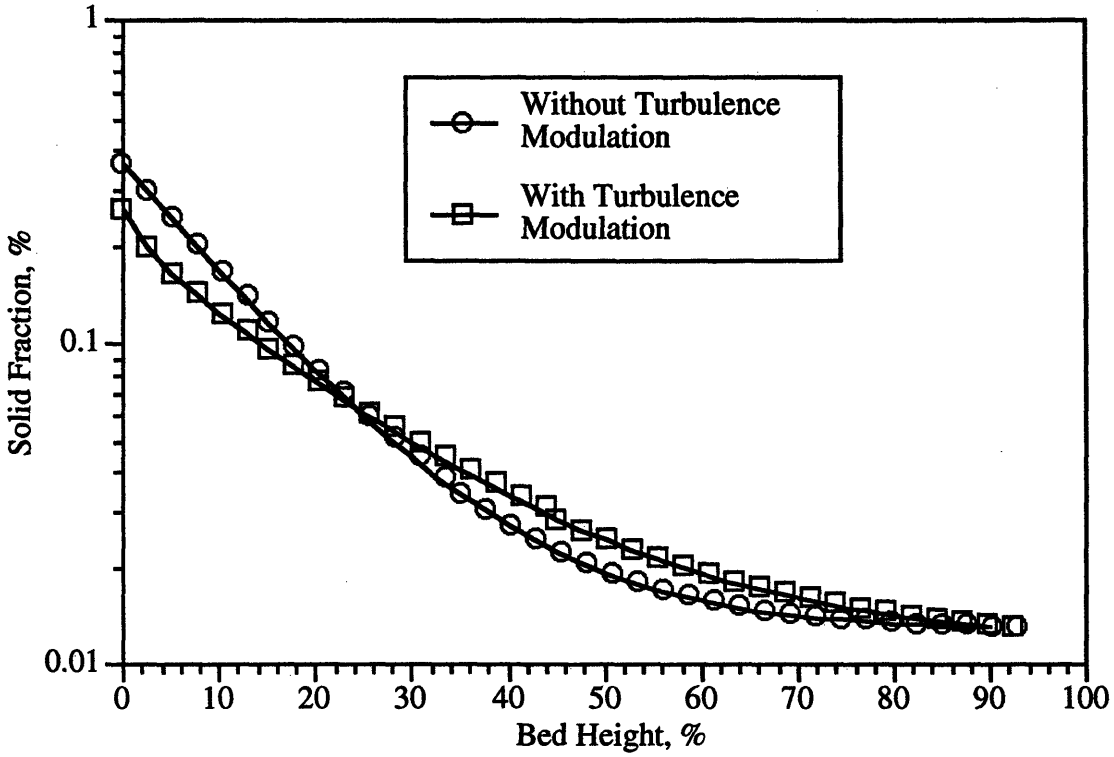

11.0 RADIAL FLUX MODEL

11.1 Introduction

When calculating the deposition velocity, it is usual to assume that the particle concentration at the wall is zero (Chandrasekar, 1943, Hutchinson *et al.* 1971). This assumption was shown to be valid for conditions typical of CFB's earlier in this Chapter. Dirichlet boundary conditions of this type, however, are not convenient for walls of arbitrary "stickiness." Therefore, to calculate a deposition velocity, a formulation common to neutron theory is used. Through any given surface dS situated at $\mathbf{r}_o$ within a space continuum in which diffusion is taking place, the neutron currents j^+ and j^- in the positive and negative directions in relation to the outward pointing normal $\hat{\mathbf{x}}_i$ through dS are given by (Lamarsh, 1979):

$$j^+ = \frac{\phi(\mathbf{r}_o)}{4} - \frac{D_n}{2}\frac{\partial\phi(\mathbf{r}_o)}{\partial x_i} \tag{1}$$

$$j^- = \frac{\phi(\mathbf{r}_o)}{4} + \frac{D_n}{2}\frac{\partial\phi(\mathbf{r}_o)}{\partial x_i} \tag{2}$$

where $\phi(\mathbf{r}_o)$ is the neutron flux at $\mathbf{r}_o$and D_n is the isotropic neutron diffusion coefficient.

For particle transport in turbulent streams, motion is caused by a continuous driving force, originating in the interaction of particles with turbulent eddies, which can only be specified stochastically. Under these conditions, Reeks and Skyrme (1976) have shown that a corresponding relationship exists for particle fluxes through an arbitrary surface dS in the direction of the outward pointing normal at dS, $\hat{\mathbf{x}}_i$, which also defines one of the co-ordinate axes i, j, k. The result is:

$$j^+ = w(\mathbf{r}_o)\int_0^\infty\int_{-\infty}^\infty\int_{-\infty}^\infty v_{p_i}P\left(v_{p_i},v_{p_j},v_{p_k}\right)dv_{p_i}dv_{p_j}dv_{p_k} - \frac{D_{n_{ii}}}{2}\frac{\partial w(\mathbf{r}_o)}{\partial x_i} \tag{3}$$

$$j^+ = w(\mathbf{r}_o)\int_0^\infty\int_{-\infty}^\infty\int_{-\infty}^\infty v_{p_i}P\left(-v_{p_i},v_{p_j},v_{p_k}\right)dv_{p_i}dv_{p_j}dv_{p_k} + \frac{D_{n_{ii}}}{2}\frac{\partial w(\mathbf{r}_o)}{\partial x_i} \tag{4}$$

where $v_{p_i}, v_{p_j}, v_{p_k}$ refer to the particle velocities in the i, j, and k directions, $w(\mathbf{r}_o)$ the concentration of particles at $\mathbf{r}_o$, $D_{n_{ii}}$ the particle diffusion coefficient relevant to the i-direction and P(v) the probability density that a particle has a velocity in the range v to v + dv.

The integrals developed by Reeks and Skyrme can be evaluated by applying the Central Limit Theorem which requires turbulence phenomena at a single point to be jointly normal in v_{pi} [Monin and Yaglom, (1971)]. Thus for the probability density function P(v):

$$P(\mathbf{v}) = (2\pi)^{-3/2} \left|\overline{\overline{M}}\right|^{-1/2} \exp\left(-\frac{1}{2}\mathbf{v}'\overline{\overline{M}}^{-1}\mathbf{v}\right) \tag{5}$$

where v and v' are the row and column vectors of v_{pi}, $\overline{\overline{M}}^{-1}$ is the matrix inverse of $\overline{\overline{M}}$. $\overline{\overline{M}}$ begin the square matrix composed of the second moments of v_{pi}.

$$\overline{\overline{M}} = \begin{vmatrix} \mu_{11} & \mu_{12} & \mu_{13} \\ \mu_{21} & \mu_{22} & \mu_{23} \\ \mu_{31} & \mu_{32} & \mu_{33} \end{vmatrix} \tag{6}$$

where $\mu_{ij} = \left\langle \left(v_{p_i} - \bar{v}_{p_i}\right)\left(v_{p_j} - \bar{v}_{p_j}\right) \right\rangle = \left\langle \Delta v_{p_i} \Delta v_{p_j} \right\rangle$, $\bar{v}_{p_i}$ and $\bar{v}_{p_j}$ being means of v_{pi} and v_{pj} respectively.

Using the normal probability density function and assuming the mean lateral velocity of the particle (neutrons) is zero,

$$j_i^+ = \frac{\sigma_i}{\sqrt{2\pi}} w(\mathbf{r}_o) - \frac{D_{n_{ii}}}{2} \frac{\partial w(\mathbf{r}_o)}{\partial x_i} \tag{7}$$

$$j_i^- = \frac{\sigma_i}{\sqrt{2\pi}} w(\mathbf{r}_o) + \frac{D_{n_{ii}}}{2} \frac{\partial w(\mathbf{r}_o)}{\partial x_i} \tag{8}$$

where the relation between the second moments of v_{pi} and the particle rms velocity, $\sigma_i^2 = \left(v_{p_i}'\right)^2$, was used. σ_i is determined by the Lagrangian particle dispersion simulations discussed in Section 2.

Assume that as the particles enter the cluster layer at the wall, they are absorbed into the dense down flowing annulus and are no longer laterally transported by turbulent eddies. In this case, j- is zero, and j+ can be written as

$$j_i^+ = \sqrt{\frac{2}{\pi}}\,\sigma_i w(r_o) \tag{9}$$

In reality, there is some diffusion back into the turbulent core from the cluster layer at the wall. However, for the simple approach taken, the assumption of zero negative diffusional flux is adequate.

It is interesting to note that this result is identical to that of Lee *et al.* (1989) and Westphalen (1993) except that it differs by a factor of 2. This is a direct result of the assumption of a perfectly absorbing cluster layer at the wall. If the cluster layer was assumed to be perfectly reflecting, the result of Lee and Westphalen is obtained. A discussion as to the applicability of the perfectly absorbing cluster layer vs. the perfectly reflecting cluster layer given earlier in this Chapter showed that the former is the appropriate boundary approximation in CFB flows.

The result given above is also in agreement with that of Reeks and Skyrme who considered the deposition of small particles to a tube wall. Their model assumed that the deposition was controlled by:

(a) Diffusion of particulate in the bulk flow to a region near the wall where the flow is heavily damped,

(b) penetration of this wall region, either by Brownian motion, inertial coasting, or the action of 'down sweeps' [Cleaver and Yates (1975)].

They also took into account the lack of coincidence between particle and fluid motions so that both (a) and (b) were regarded as being dependent on particle inertia. Their resulting equation for lateral particle flux was

$$j_i^+ = \sqrt{\frac{2}{\pi}}\,\sigma_i w(r_o)\,\mathrm{erfc}\left(\frac{\alpha \Delta r}{\sqrt{2}\sigma_i}\right) \tag{10}$$

where Δr is the boundary layer thickness and $\alpha = \frac{36\mu}{(2\rho_s + \rho_s)d_p^2}$. For flows typical of CFB's, the term inside the brackets is of the order 10^{-2} and (10) reduces to (9).

11.2 Verification of Radial Flux Model

To check the validity of the radial flux model, its predictions are compared to data available in the CFB literature.

11.2.1 Bolton and Davidson Deposition Coefficients

Bolton and Davidson (1988) reported measurements of the downward solid flux in the wall layer of a 0.15 meter 5.5 meter high CFB. The variation in wall flux with height was explained with a deposition model where the deposition of solid on the wall was assumed proportional to the bed concentration. The assumption results in an exponential decrease of downward wall flux with bed height. The deposition constant was defined as

$$j_{p_r}(R, z) = k_d\left[\overline{\phi_{avg}}(z) - \overline{\phi_{avg}}(z = \infty)\right] \tag{11}$$

Here $\overline{\phi_{avg}}(z = \infty)$ is the limiting concentration at finite heights. This concentration is small compared to concentrations in other regions of the bed. From the previous derivation of the radial solids flux,

$$k_d = \sqrt{\frac{2}{\pi}}\sqrt{\left(v'_{p_r}\right)^2} \tag{12}$$

Through a mass balance, Bolton and Davidson devised a decay coefficient for the decrease in wall flux with height :

$$K = \frac{4k_d}{Dv_{p_a}} \tag{13}$$

Deposition constants were reported for six bed conditions. A summary of this data is given in Table 11.1. The results of Westphalen (1993) are also included along with the results of the proposed radial flux model. Westphalen used the model of Friedlander (1957) as modified by Csanady (1963) for the effect of gas-eddy crossing trajectories to determine

the relation between the gas and particle lateral fluctuating velocity. The resultant equation was:

$$\frac{\sqrt{\left(v_{ip}^{'}\right)^2}}{\sqrt{\left(v_{if}^{'}\right)^2}} = \sqrt{\frac{\beta_i}{\alpha_i + \beta_i}} = \left(1 + \frac{\sqrt{\left(v_{if}^{'}\right)^2}}{1_e \beta_i} \sqrt{1 + \frac{u_t}{\left(v_{if}^{'}\right)^2}}\right)^{-1/2} \tag{14}$$

The model assumed that the flow was very dilute such that particle collisions were insignificant. All gas turbulence properties were determined from single phase gas pipe flow. Additionally, the fluid-particle drag relation was assumed to be linear, and the particles were assumed to be perfectly spherical.

Table 11.1: Prediction of CFB Deposition Coefficients

d_p (microns)	ρ_p (kg/m^3)	u_t (m/s)	u_o (m/s)	measured k_d (m/s)	predicted k_d (m/s) Bolton and Davidson	predicted k_d (m/s) Westphalen	predicted k_d (m/s) Proposed Model
60	1000	0.10	1.27	0.043	6.7E-3	0.019	0.089
60	1000	0.10	1.79	0.031	9.6E-3	0.026	0.100
200	384	0.325	1.79	0.047	9.6E-3	0.018	0.056
200	384	0.325	2.19	0.044	0.017	0.022	0.081
200	384	0.325	2.51	0.042	0.013	0.026	0.091
200	384	0.325	2.81	0.088	0.015	0.029	0.100

The model proposed by Bolton and Davidson is

$$k_d = \frac{0.1\sqrt{\pi\left(v_{f_r}^{'}\right)^2}}{\left(1 + \frac{Sh}{12}\right)} \tag{14}$$

where Sh is the Sherwood number which was assumed equal to 4. This model results in poor predictions of the deposition constant if gas fluctuating velocities based on single phase pipe flow are used (k_d ranges from 0.007 to 0.015 m/s). Table 11.1 indicates that the proposed deposition model predicts the 200 micron data better than the model of

Westphalen and is about as accurate for the 60 micron particles. It does a better job than the Bolton and Davidson model of predicting the deposition constants for both particles.

As pointed out by Westphalen (1993), use of the classic deposition correlation given by McCoy and Hanratty (1977), results in good predictions for the 200 micron particles (k_d ~ 0.051), but gives a poor prediction of the 60 micron results (k_d.~ 0.0005 m/s).

11.2.2 Decay Coefficients of Kunii and Levenspiel

Decay coefficients for the vertical particle concentration were estimated by Kunii and Levenspiel (1990) for a large body of CFB literature data. Some of this data is compared herein with estimates of deposition constants as suggested by the radial flux model. A summary of the operating parameters appears in Table 11.2. References to the data are included below. Calculation of these coefficients is based on the decay with bed height of cross-sectional average solid fraction rather than wall layer flux. The coefficients are equivalent.

Table 11.2: Summary of Operating Parameters for Decay Constants Determined by Kunii and Levenspiel (1990)

Investigators	D (cm)	L (m)	ρ_s (kg/m^3)	d_p (μm)	u_o (m/s)
Hartge *et al.* (1986a, 1986b, 1988)	40	8.4	2500	58	1.2-4.2
Hartge *et al.* (1986a, 1986b, 1988)	5	3.3	2500	58	3.4
Weinstein *et al.* (1983, 1984a,b, 1986)	15.2	8.5	1460	49	2.9-3.4
Takeuchi *et al.* (1986)	10	5.5	1080	61	1.3-3.0
Schnitzlein (1987)	15.2	8.5	1500	59	0.7-5.0
Li and Kwauk (1980, 1986, 1988)	9	8.0	7500	105	4.1-5.7
Yang *et al.* (1983, 1985)	11.5	8.0	1500	220	5.3
Arena *et al.* (1986, 1988)	4.1	6.4	2500	88	3.0-7.0
Furchi *et al.* (1988)	7.2	6.0	2500	196	7.2
Furchi *et al.* (1988)	7.2	6.0	2500	269	8.3

Hartge, E.U., Y. Li, and J. Werther, *Circulating Fluidized Bed Technology*, P. Basu (ed.), Pergamon Press, p. 153, 1986a.

Hartge, E.U., Y. Li, and J. Werther, *Fluidization V*, K. Ostergaard, and A. Sorensen (eds.) Engineering Foundation, New York, 1986b.

Hartge, E.U., D. Resner, and J. Werther, *Circulating Fluidized Bed Technology II*, P. Basu (ed.),Compiegne, Poster Paper No. 7, 1988.

Weinstein, H., R.A. Graf, M. Meller, M.J. Shao, *Fluidization IV*, D. Kunii and R. Toei (eds.), Engineering Foundation, New York, p. 299, 1983.

Weinstein, H., R.A. Graf, M. Meller, M.J. Shao, *AIChE Symp. Ser.*, **80**, p. 52, 1984a.

Weinstein, H., R.A. Graf, M. Meller, M.J. Shao, *AIChE Symp. Ser.*, **80**, p. 117, 1984b.

Weinstein, H., R.A. Graf, M. Meller, M.J. Shao, *Fluidization V*, K. Ostergaard and A. Sorenson (eds.), Engineering Foundation, p. 329, 1986.

Takeuchi, H., T. Kirama, T. Chiba, L.S. Leung, in *Proc. Third World Congress Chem. Eng.*, Tokyo, Vol. 3, p. 477, 1986.

Schnitzlein, M.G., Ph.D. Dissertation, City University of New York, 1987.

Li, Y., and M. Kwauk, *Fluidization III*, J.R. Grace adn J. Matsen (eds.), Plenum, New York, p. 537, 1980.

Kwauk, M., N. Wang, Y. Li, B. Chen, Z. Shen, *Circulating Fluidized Bed Technology*, P. Basu (ed.), Pergamon Press, p. 33, 1986.

Li, Y., Y. Tung, M. Kwauk, *Circulating Fluidized Bed Technology II*, P. Basu (ed.), Compiegne, Poster Paper No. 5, 1988.

Yang, G., Z. Huang, L. Zhao, *Fluidization IV*, D. Kunii and R. Toei (eds.), Engineering Foundation, New York, p. 145, 1983.

Zhang, R., D. Chen, G. Yang, *Fluidization '85, Science and Technology*, M. Kwauk, D. Kunii, J. Zheng, H. Hasatani (eds.), Science Press, Beijing, p. 148, 1985.

Arena, U., A. Cammarota, L. Pistone, *Circulating Fluidized Bed Technology*, P. Basu (ed.), Pergamon Press, p. 119, 1986.

Arena, U., A. Cammarota, L. Massimilla, D. Pirozzi, *Circulating Fluidized Bed Technology II*, P. Basu (ed.), Compiegne, p. 16, 1988.

Furchi, J.C.L., L. Goldstein Jr., M. Mohseni, G. Lombardi, *Circulating Fluidized Bed Technologyy II*, P. Basu (ed.), Compiegne, p. 69, 1988.

Deposition constants are calculated from the decay coefficients using equation (13); the average axial solid velocity is assumed equal to the superficial velocity minus the particle terminal velocity. The measurements are plotted versus the predictions as calculated by the model of Westphalen in Figure 11.1. The Bolton and Davidson data from above are also shown. The predicted deposition coefficients are consistently low. The measured values are up to an order of magnitude higher than the predicted values. In Figure 11.2 the same comparison is made with the proposed radial flux model. The predictions are significantly better. This suggests that a model which assumes particle velocity fluctuations are only due to gas turbulence which can be modeled from single phase gas flow turbulence is not adequate to describe CFB particle dynamics.

Figure 11.1

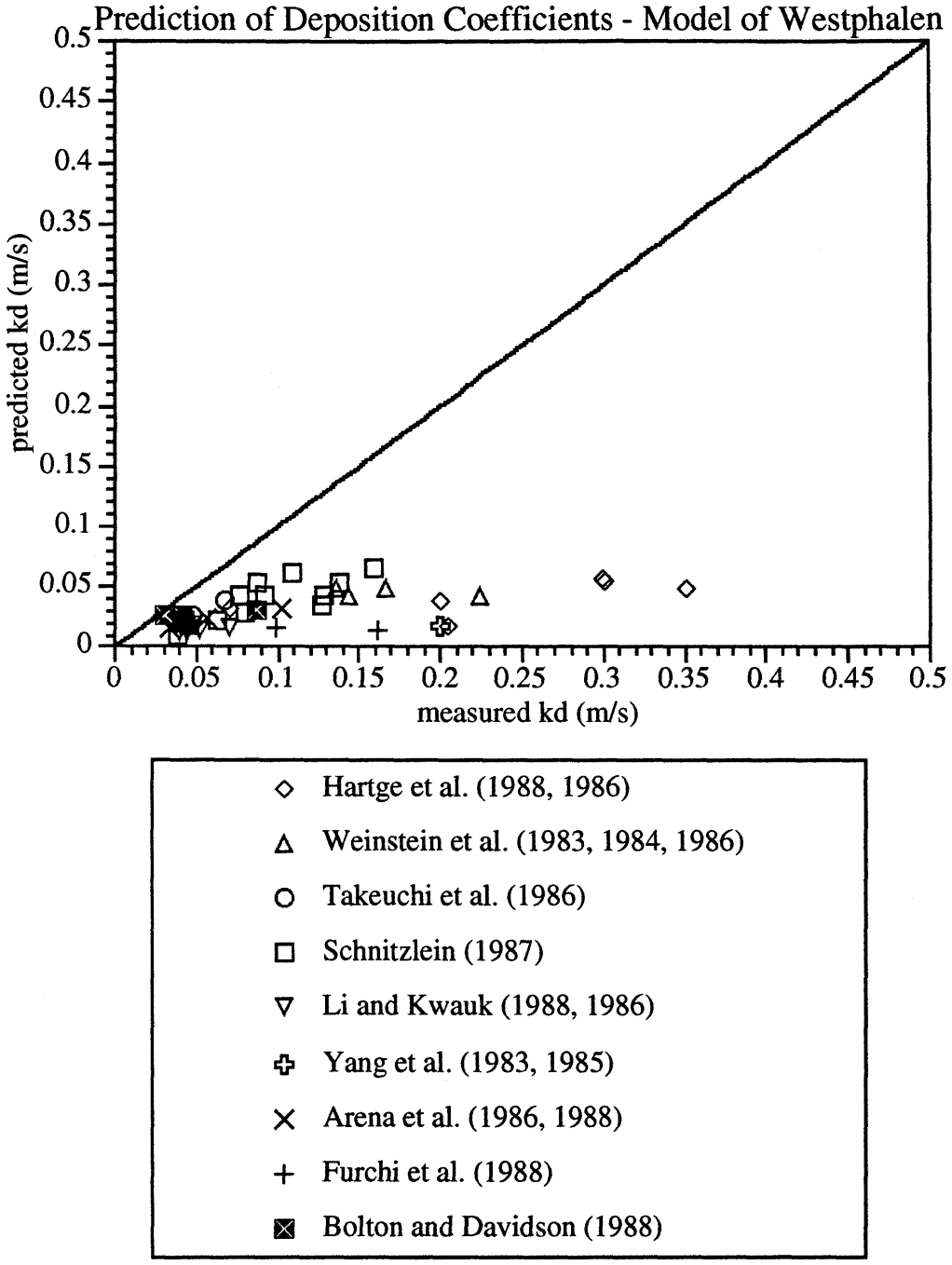
Prediction of Deposition Coefficients - Model of Westphalen
predicted kd (m/s)
measured kd (m/s)
0
0.05
0.1
0.15
0.2
0.25
0.3
0.35
0.4
0.45
0.5
Hartge et al. (1988, 1986)
Weinstein et al. (1983, 1984, 1986)
Takeuchi et al. (1986)
Schnitzlein (1987)
Li and Kwauk (1988, 1986)
Yang et al. (1983, 1985)
Arena et al. (1986, 1988)
Furchi et al. (1988)
Bolton and Davidson (1988)

Figure 11.2

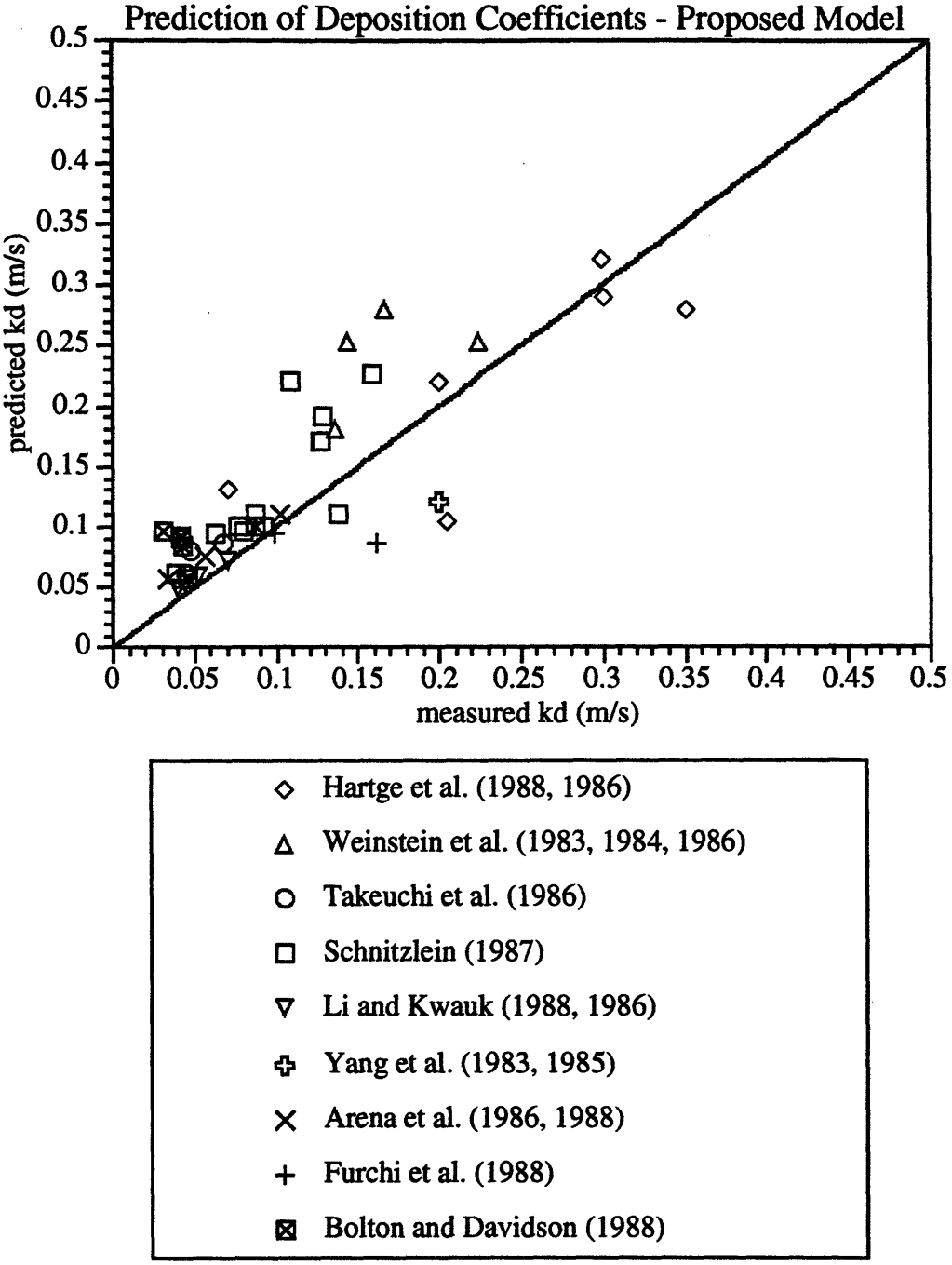

Westphalen felt that the inability of his model to adequately predict the deposition constants was a direct result of the rough gas turbulence model used (gas turbulence was assumed to be equal to unmodified single phase pipe flow turbulence). It was suggested that gas fluctuation velocity of 2.5 times the pipe flow prediction is a reasonable assumption to correct for the presence of particles and the fact that the turbulence may not be homogeneous. Unfortunately, the presence of particles would tend to decrease, not increase,

the fluid turbulence levels for the particle sizes examined in his study. Additionally, even after the larger value for gas turbulence was used the predictions for the data sets involving large particles or a large bed diameter diverged significantly from the measurements, suggesting that application of the model to large combustors, where particle diameters are roughly 200 μm, is not be valid. It is worth pointing out that the equation for radial flux derived above differs by a factor of 2 from the equation of Westphalen. This suggests that the correction factor of 2.5 he used in obtaining a better fit to the data may have more to do with how he specified the boundary conditions than with turbulence enhancement. Had the perfectly absorbing boundary condtions been used, his results would have increased by a factor of 2 - close the the suggested ad hoc increase of 2.5.

The good agreement between the proposed model and the measured deposition coefficients suggest that clusters do not play a significant role in the lateral deposition of particles to the walls of a CFB. This is contrary to the suggestion of Westphalen who felt that the lateral movement of clusters may help explain the discrepancy between his predictions and the experimental results.

11.3 CFB Radial Solid Flux Measurements

Radial solid flux measurements have been made by Qi and Farag (1992), Roth (1990) and recently by Zhou *et al.* (1995). The equipment and flow conditions used in these studies is summarized in Table 11.3.

Table 11.3: Comparison of Experimental and Measured Radial Fluxes

Researcher	D (cm)	H (m)	d_p (microns)	ρ_s (kg/m^3)	G_s (kg/m^2-s)	u_o (m/s)	Range of Measured Fluxes (kg/m^2-s)	Predicted Fluxes (kg/m^2-s)
Qi and Farag (1992)	14	3.4	200	2500	21.3	3.9	2 - 33	1.35
Roth (1990)	20	7	40	2500	10.3	3.1	0.6 - 1.4	1.45
Zhou *et al.* (1995)	15 (square)	9.1	213	2640	40 and 60	5.5 and 7.0	0.05 - 1	0.87 - 1.73

The normalized measurements of Qi and Farag are from two to eight times those of Roth and Zhou *et al.* Capacitance probe measurements made by Qi and Farag for the same bed conditions show that solid concentration and radial solid flux measurements are nearly proportional.

Qi and Farag interpreted the flux measurements as an average radial solid flux and calculated an average radial solid velocity of 0.26 m/s. A more reasonable interpretation is that the measurement represents the positive-direction component of the fluctuating solid flux. If interpreted as average flux, the measurements indicate that internal solid circulation is extremely high. Westphalen estimated the degree of internal circulation by application of a mass balance on a control volume in the core of radius r:

$$\frac{\partial j_{p_r}}{\partial z} = -\frac{2}{r} j_{p_r} \tag{15}$$

He assumed that the core diameter is three quarters of the riser diameter, that there is no downward flux at the top of the riser, and that the core-to-wall radial flux throughout the riser is about equal to the net axial flux, as indicated by the measurements. At the bottom of the riser, the calculated core axial flux is about 130 times the net axial flux. The same estimate of this flux ratio for the Roth data is 30. Centerline axial flux measurements reported in the literature (Rhodes *et al.*, 1988; Herb *et al.*, 1992; Monceaux *et al.*, 1986) range from 1.5 to 3.5 times the net axial solid flux. Comparison of these numbers suggests that most of the radial solid flux measurement represents the positive component of the fluctuating flux.

Prediction of the fluctuating radial flux is based on equation (9) and is presented in the Table 11.3. The average cross sectional solid concentrations are used as an order of magnitude for $w(r_o)$.

The prediction of radial flux is on the order of the range of the measured fluxes for the Roth and Zhou *et al.* data. For the Qi and Farag data, the measured fluxes are much higher. This may be because gas phase turbulence in the experiment was much higher than for the pipe flow estimates, or because air leakage from the receiver or connecting tubing could have caused much higher efflux of particles into their sampling system, accounting for the substantial measured fluxes. Westphalen also compared his model to the data of Roth and Qi and Farag with similar results (good agreement with the Roth data, substantially lower

predictions than the Qi and Farag data). However, the equation formulated by Westphalen to represent average radial flux at the wall is not equal to the positive component of the fluctuating flux as stated. At the wall, a radiation boundary conditions was used as opposed to the boundary of perfect absorption into the cluster layer. Therefore, the positive radial flux is not equal to the average radial flux, as assumed.

12.0 REFERENCES

Abou-Arab, T.W., and M.C. Roco, "Solid Phase Contribution in the Two-Phase Turbulence Kinetic Energy Equation," *Proc. 3rd Int. Symp. on Liquid-Solid Flows*, p. 13, 1988.

Abramovich, G.N., T.A. Girshovich, S. Yu Krasheninnikov, A.N. Sekundov, and I.P. Smirnova, "Theory of Turbulent Jets," *Science*, Moscow (in Russian), 1984.

Abramovich, G.N., "The Effect of Admixture of Solid Particles or Droplets on the Structure of a Turbulent Gas Jet," *Soviet Phys. Dokl*, **190**, p. 1052, 1970.

Adanez, J., P. Gayan, F. Garcia-Labiano, and L.F. de Diego, "Axial Voidage profiles in Fast Fluidized Beds," *Powder Tech.*, **81**, p. 259, 1994.

Al-Taweel, A.M., and J. Landau, "Turbulence Modulcation in Two-Phase Jet," *Int. J. Multiphase Flow*, **3**, p. 341, 1977.

Alajbegovic, A., A. Assad, F. Bonetto, and R.T. Lahey, jr., "Phase Distribution and Turbulence Structure for Solid/Fluid Upflow in a Pipe," *Int. J. Multiphase Flow*, **20**, p. 453, 1994.

Arena, U., A. Marzocchella, L. Massimilla, and A. Malandrino, "Hydrodynamics of Circulating Fluidized Beds with Risers of Different Shape and Size," *Powder Tech.*, **70**, p. 237, 1992.

Avidan, A.A., *Bed Expansion and Solid Mixing in High Velocity Fluidized Beds*, Ph.D. Dissertation, City University of New York, 1980.

Bader, R., J. Findlay, and T.M. Knowlton, "Gas/Solid Flow Patterns in a 30.5 -cm-Diameter Circulating Fluidized Bed," *Circulating Fluidized Bed Technology II*, P. Basu and J.F. Large, eds., Pergamon Press, 1988.

Bai, D.-R., Y. Jin, Z.-Q. Yu, and J.-X Zhu, The Axial Distribution of the Cross-Sectionally Averaged Voidage in Fast Fluidized Beds," *Powder Tech.*, **71**, p. 51, 1992.

Barnea, E., and J. Mizrahi, "A Generalized Approach to the Fluid Dynamics of Particulate Systems. Part 1. General Correlation for Fluidization and Sedimentation in Solid Multiparticle Systems," *Chem. Eng. Jl.*, **5**, p. 171, 1973.

Batchelor, G.K., "A New Theory of the Instability of a Fluidized Bed," *J. Fluid Mech.*, **193**, p. 75, 1988.

Batchelor, G.K., "Diffusion in a Field of Homogeneous Turbulence. II. The Relative Motion of Particles," *Proc. Camb. Phil. Soc.*, **48**, p 345, 1952.

Bernard, J.R., H. Santos-Cottin, and R. Margrita, "Use of Radioactive Tracers for Studies on Fluidized Cracking Catalytic Plants," *Isotopenpraxis*, **25** (4), p. 161, 1989.

Boysan, F., W.H. Ayers, and J. Swithenbank, "A Fundamental Mathematical Modelling Approach to Cyclone Design," *Trans IChemE*, **60**, p. 222, 1982.

Brereton, C.M.H., and J.R. Grace, "Microstructural Aspects of the Behaviour of Circulating Fluidized Beds," *Chem. Eng. Sci.*, **14**, p. 2565, 1993.

Brown, D.J., and P. Hutchinson, "The Interaction of Solid or Liquid Particles and Turbulent Fluid Flow Fields - A Numerical Simulation," *J. of Fluids Engng.*, **101**, p. 265, 1979.

Carslaw, H.S., and J.C. Jaeger, *Conduction of Heat in Solids*, Clarendon Press: Oxford, 1959.

Chandrasekhar, S., "Stochastic Problems in Physics and Astronomy," *Rev. Mod. Phys.*, **15**, p. 1, 1943.

Change, H., and M. Louge, "Fluid Dynamic Similarity of Circulating Fluidized Beds," *Powder Technol.*, **70**, p. 259, 1992.

Chapman, S., and T.G. Cowling, *The Mathematical Theory of Non-Uniform Gases*, Cambridge University Press, 1970.

Cleaver, J.W., and D. Yates, "A Sub Layer Model for the Deposition of Particles from a Turbulent Flow," *Chem. Engng Sci.*, **30**, p. 983, 1975.

Clift, R., J.R. Grace, and M.E. Weber, *Bubbles, Drops and Particles*, Academic Press, New York, 1978.

Corrsin, S., "Limitations of Gradient Transport Models in Random Walks and in Turbulence," *Adv. in Geophys.*, **A 18**, p. 25, 1974.

Corrsin, S., "Progress Report on Some Turbulent Diffusion Research," *Proc. Oxford Symp. Atmos. Diff. Air Poll., Adv. Geophys.*, **6**, p. 161, 1959.

Crank, J., *The Mathematics of Diffusion*, Clarendon Press: Oxford, 1979.

Csanady, G.T., "Turbulent Diffusion of Heavy Particles in the Atmosphere," *J. Atmos. Sci.*, **2**, p.201, 1963.

Danon, H., M. Wolfshtein, and G. Hetsroni, "Numerical Calculations of Two-Phase Turbulent Jets," *Int. J. Multiphase Flow*, **3**, p. 223, 1974.

Didwania, A.K., and G.M. Homsy, "Resonant Sideband Instabilities in Wave Propogation in Fluidized Beds," *J. Fluid Mech.*, **122**, p. 433, 1982.

Elghobashi, S.E., and T.W. Abou-Arab, "A Two-Equation Turbulent Closure for Two-Phase Flows," *Phys. Fluids*, **26**, p. 931, 1983.

Friedlander, S.K., "Behavior of Suspended Particles in a Turbulent Fluid," *A.I.Ch.E. J.*, **3**, p. 381, 1957.

Gidaspow, D., Y.P. Tsuo, and K.M. Luo, "Computed and Experimental Cluster Formation and Velocity Profiles in Circulating Fluidized Beds," *Fluidization VI*, J.R. Grace, L.W. Shemilt and M.A. Bergougnou, eds., Engineering Foundation, 1989.

Glicksman, L.R., D. Westphalen, C. Brereton, and J. Grace, "Verfication of the Scaling Laws for Circulating Fluidized Beds," in *Circulating Fluidized Bed Technology III*, P. Basu, M. Horio, and M. Hasatani, eds., Pergamon Press, Oxford, 1991.

Gore, R., and C.T. Crowe, "Effect of Particle Size on Modulating Turbulence Intensity," *Turbulence Modification in Dispersed Phase Flows*, ASME FED Vol. 80, p. 31, 1989b.

Gore, R., and C.T. Crowe, "Effects of Particle Size on Modulating Turbulent Intensity," *Int. J. Multiphase Flow*, **15**, p. 279, 1989a.

Gouesbet, G., A. Berlemont, and A. Picart, "Dispersion of Discrete Particles by Continuous Turbulent Motions. Extensive Discussion of the Tchen's Theory, using a Two-Parameter Family of Lagrangian Correlation Functions," *Phys. Fluids*, **27**, p. 827, 1984.

Govan, A.H., *A Diffusion Model for Large Particles in a Turbulent Gas Flow*, Harwell Report AERE-R12353, 1986.

Haider, A., and O. Levenspiel, "Drag Coefficient and Terminal Velocity of Spherical and Nonshperical Particles," *Powder Technol.*, **58**, p. 63, 1989.

Happel, J, and H. Brenner, *Low Reynolds Number Hydrodynamics,* Kluwer Academic Publishers, Boston, 1963.

Harris, B.J., and J.F. Davidson, "Modelling Options for Circulating Fluidized Beds: A Core/Annulus Depositoin Model," *4th Int. Conf. on Circulating Fluidized Beds*, p. 35, Somerset, PA, August 1-5, 1993.

Harris, B.J., J.F. Davidson, and Y. Xue "Axial and Radial Variation of Flow in Circulating Fluidized Bed Risers" *4th Int. Conf. on Circulating Fluidized Beds*, p. 137, Somerset, PA, August 1-5, 1993.

Hartge, E.-U., D. Rensner, and J. Werther, "Solids Concentration and Velocity Patterns in Circulating Fluidized Beds," *Circulating Fluidized Bed Technology II*, P. Basu and J.F. Large, eds., Pergamon Press, 1988.

Hartge, E.-U., Y. Li, and J. Werther, "Flow Structures in Fast Fluidized Beds," *Fluidization V*, K. Ostergaard and A. Sorensen, eds., Engineering Foundation, New York, p. 345, 1986.

Herb, B., S. Dou, K. Tuzla, and J.C. Chen, "Solid Mass Fluxes in Circulating Fluidized Beds," *Powder Technol.*, **70**, p. 197, 1992.

Hetsroni, G., and M. Sokolov, "Distribution of Mass, Velocity and Intensity of Turbulence in a Two-Phase Turbulent Jet," *Trans. ASME Jl Appl. Mech.*, **38**, p. 315, 1971.

Hetsroni, G., "Particles-Turbulence Interaction," *Int. J. Multiphase Flow*, **15**, p. 735, 1989.

Hewitt, G.F., and N.S. Hall-Taylor, *Annular Two-Phase Flow*, Pergamon Press, Osford, 1970.

Hinze, J.O. *Turbulence*, 2nd edn., McGraw-Hill, New York, 1975.

Hinze, J.O., "Momentum and Mechanical-Energy Balance Equations for a Flowing Homogeneous Suspension with Slip Between the Two Phases," *Appl. Sci. Res.*, **11**, p. 33, 1962.

Hjelmfelt, A.T., and L.F. Mockros, "Motion of Discrete Particles in a Turbulent Fluid," *Appl. Scient. Res.*, **16**, p. 149, 1966.

Horio, M., and H. Kuroki, "Three-Dimensional Flow Visualization of Dilutely Dispersed Solids in Bubbling and Circulating Fluidized Beds," *Chem. Eng. Sci.*, **49**, p. 2413, 1994.

Horio, M., "Hydrodynamics of Circulating Fluidization - Present Status and Research Needs," *Circulating Fluidized Bed Technology III*, P. Basu, M. Horio and M. Hasatani, eds., Pergamon Press, 1991.

Horio, M., K. Morishita, O. Tachibana, and N. Murata, "Solid Distribution and Movement in Circulating Fluidized Beds," *Circulating Fluidized Bed Technology II*, P. Basu and J.F. Large, eds., Pergamon Press, 1988.

Hutchinson, P., F.G. Hewitt, and A.E. Dukler, "Deposition of Liquid or Solid Dispersions from Turbulent Gas Streams: A Stochastic Model," *Chem. Engng. Sci.*, **26**, p. 419, 1971.

Jackson, R., "The Mechanics of Fluidised Beds. Parts 1 and 2," *Trans. Inst. Chem. Engrs.*, **41**, p. 13, 1963.

James, P.W., G.F. Hewitt, and P.B. Whalley, *Droplet Motion in Two-Phase Flow*, UKAEA, Report AERE-R9711, 1980.

Jenkins, J.T., and M.W. Richman, "Kinetic Theory for Plane Flows of a Dense Gas of Identical, Rough, Inelastic Circular Disks," *Phys. Fluids*, **A 28**, p. 3485, 1985.

Jenkins, J.T., "Balance Laws and Constitutive Relations for Rapid Flows of Granular Materials," *Constitutive Models of Deformation* (ed. J. Chandra and R. Srivastava), SIAM, 1987.

Koch, D.L., "Kinetic Theory for Monodisperse Gas-Solid Suspension," *Phys. Fluids*, **A2**, p. 1711, 1990.

Koenigsdorff, R., and J. Werther, "Gas-Solids Mixing and Flow Structure Modeling of the Upper Dilute Zone of a Circulating Fluidized Bed," *Powder Technol.*, **82**, p. 317, 1995.

Kojima, T., K.I.Ishihara, Y. Guilin, and T. Furusawa, "Measurement of Solids Behaviour in a Fast Fluidized Bed," *Journal of Chemical Engineering of Japan*, **22**, p. 341, 1989.

Kraichnan, R.H., "Diffusion by a Random Velocity Field," *Phys. Fluids*, **13**, p. 22, 1970.

Kraichnan, R.H., "Relation Between Lagrangian and Eulerian Correlation Times of a Turbulent Velocity Field," *Phys. Fluids*, **7**, p. 142, 1964.

Kumaran, V., and D.L. Koch, "Properties of a Bidisperse Particle-Gas Suspension Part 1. Collision Time Small Compared with Viscous Relaxation Time," *J. Fluid Mech.*, **247**, p. 623, 1993a.

Kumaran, V., and D.L. Koch, "Properties of a Bidisperse Particle-Gas Suspension, Part 2. Viscous Relaxation Time Small Compared to Collision Time," *J. Fluid Mech.*, **247**, p. 643, 1993b.

Kumaran, V., and D.L. Koch, "Velocity Distribution Functions for a Bidisperse, Sedimenting Particle-Gas Suspension," *Intl J. Multiphase Flow*, **19**, p. 665, 1993c.

Kuramoto, M., D. Kunii, and T. Furusawa, "Flow of Dense Fluidized Particles Through an Opening in a Circulation System," *Powder Technol.*, **47**, p. 141, 1986.

Laats, M.K., and F.M. Frishman, "The Development of the Methodics and Investigation of Turbulence Intensity at the Axis of Two-Phase Turbulent Jet," *Fluid Dynam.*, **8**, p. 153, 1973.

Lamarsh, J.R., *Introduction to Nuclear Reactor Theory*, Addison Wesley: Reading, MA, 1972.

Lapple, C.E., and C.B. Shepherd, "Calculation of Particle Trajectories," *Ind. Eng. Chem.*, **32**, p. 605, 1940.

Laufer, J., *The Structure of Turbulence in Fully Developed Pipe Flow*, NACA Rep., Report 1174, 1954.

Lawrence, C.J., and S. Weinbaum, "The Unsteady Force on a Body at Low Reynolds Number; the Axisymmetric Motion of a Spheroid," *J. Fluid Mech.*, **189**, p. 463, 1988.

Lee, M.M., T.J. Hanratty, and R.J. Adrian, "An Axial Viewing Photographic Technique to Study Turbulence Characteristics of Particles," *Int. J. Multiphase Flow*, **15**, p. 787, 1989.

Lee, M.M., T.J. Hanratty, and R.J. Adrian, "The Interpretaion of Droplet Deposition Measurements with a Diffusion Model," *Int. J. Multiphase Flow*, **15**, p. 459, 1989.

Lee, S.L., and F. Durst, "On the Motion of Particles in Turbulent Duct Flow," *Int. J. Multiphase Flow*, **8**, p. 125, 1982.

Leith, D., "Drag on Nonspherical Objects," *Aerosol Sci. Technol.*, **6**, p. 153, 1987.

Lewis, W.K., and E.W. Bowerman, "Fluidization of Solid Particles in Liquids," *Chem. Eng. Progr.*, **48**, p. 603, 1952.

Li, L., and E.E. Michaelides, "The Magnitude of Basset Forces in Unsteady Multiphase Flow Computations," *J. Fluids Engng*, **114**, p. 352, 1992.

Litka, A. and L.R. Glicksman, "The Influence of Particle Mechanical Properties on Bubble Characterisitics and Solid Mixing in Fluidized Beds," *Powder Technol.*, **42**, p. 231, 1985.

Lovalenti, P.M., and J.F. Brady, "The Hydrodynamic Force on a Rigid Particle Undergoing Arbitrary Time-Dependent Motion at Small Reynolds Numbers," *J. Fluid Mech.*, **256**, p. 342, 1993.

Lumley, J.L., Topics in Applied Physics, Vol. 12, *Turbulence*, Edited by Bradshaw, P., Springer-Verlag, Berlin, Heidelberg and New York, p. 289, 1976.

Maeda, M., K. Hishida, and T. Furutani, "Optical Measurements of Local Gas and Particle Velocity in an Upward Flowing Dilute Gas-Solid Suspension," *Polyphase Flow and Transport Technology*, p, 211, 1980.

Martin, M.P., P. Turlier, J.R. Bernard, and G. Wild, "Gas and Solid Behavior in Cracking Circulating Fluidized Beds," *Powder Technol.*, **70**, p. 249, 1992.

Mei, R., C.J. Lawrence, and R.J. Adrian, "Unsteady Drag on a Sphere at Finite Reynolds Number with Small Fluctuations in the Free-Stream Velocity," *J. Fluid Mech.*, **233**, p. 613, 1991.

Michaelides, E.E., L. Li, and A. Lasek, "The Effect of Turbulence on the Phase Change of Droplets and Particles Under Nonequilibrium Conditions," *Int. J. Heat Mass Transfer*, **35**, p. 2069, 1992.

Miller, A., and D. Gidaspow, "Dense, Vertical Gas-Solid Flow in a Pipe," *AIChE Journal*, **38**, p. 1801, 1992.

Miller, C.O., and A.K. Logwinuk, "Fluidization Studies of Solid Particles," *Ind. Eng. Chem.*, **43**, p. 1220, 1951.

Monin, A.S., and A.M. Yaglom, *Statistical Fluid Mechanics*, MIT Press, Cambridge, MA, 1971.

Mooney, M., "The Viscosity of a Concentrated Suspension of Spherical Particles," *J. Colloid Sci.*, **6**, p. 162, 1951.

Nir, A., and L.M. Pismen, "The Effect of a Steady Drift on the Dispersion of a Particle in Turbulent Fluid," *J. Fluid Mech.*, **94**, p. 369, 1979.

Odar, F., and W.S. Hamilton, "Forces on a Sphere Accelerating in a Viscous Fluid," *J. Fluid Mech.*, **18**, p. 302, 1964.

Parthasarathy, R.N., and G.M. Faeth, "Structure of a Turbulent Particle-Laden Water Jet in Still Water," *Int. J. Multiphase Flow*, 13, p. 699, 1987.

Parthasarathy, R.N., and G.M. Faeth, "Turbulence Modulation in Homogeneous Dilute Particle-Laden Flows," *J. Fluid Mech.*, 220, p. 485, 1990.

Perry, R.H., D.W. Green, and J.O'Maloney (eds.), *Perry's Chemical Engineering Handbook*, 6th edn., McGraw-Hill, New York, 1984.

Peskin, R.L., "The Diffusivity of Small Suspended Particles in Turbulent Fluids," Presented at *Nat. Meeting A.I.Ch.E.*, Baltimore, 1962.

Pettyjohn, ES., and E.B. Christiansen, "Effect of Particle Shape on Free Settling Rates of Isometric Particles," *Chem. Eng. Prog.*, **44**, p. 157, 1948.

Phythian, R., "Dispersion by Random Velocity Fields," *J. Fluid Mech.*, **67**, p. 145, 1975.

Phythian, R., "Some Variational Methods in the Theory of Turbulent Diffusion," *J. Fluid Mech.*, **53**, p. 469, 1972.

Prandtl, L., "Uber Die Ausgebildete Turbulenz," *Z. Angew. Math. Mech.*, **5**, p. 136, 1925.

Press, W.H., B.P. Flannery, S.A. Teukolsky, and W.T. Vetterling, *Numerical Recipes*, Cambridge University Press, 1990.

Qi, C., and I.H. Farag, "Lateral Particle Motion and Its Effect on Particle Concentration Distribution in the Riser of CFB," *AIChE Symp. Series*, **89**, p. 73, 1993.

Rashidi, M. G. Hetsroni, and S. Banerjee, "Mechanisms of Heat and Mass Transport at a Gas-Liquid Interface," *Int. J. Heat Mass Transfer*, **34**, p. 1799, 1991.

Rashidi, M., G. Hetsroni, and S. Banerjee, "Particle-Turbulence Interaction in a Boundary Layer," *Int. J. Multiphase Flow*, **16**, p. 935, 1990.

Reeks, M.W., and G. Skyrme, "The Dependence of Particle Deposition Velocity on Particle Inertia in Turbulent Pipe Flow," *J. Aerosol Sci.*, **7**, p. 485, 1976,

Reeks, M.W., "On the Dispersion of Small Particles Suspended in an Isotropic Turbulent Fluid," *J. Fluid Mech.*, **83**, part 3, p. 529, 1977.

Rhodes, M., H. Mineo, and T. Hirama, "Particle Motion at the Wall of a Circulating Fluidized Bed," *Powder Technol.*, **70**, p. 207, 1992.

Rhodes, M.J., and P. Laussmann, "Characterising Non-Uniformities in Gas-Particle Flow in the Riser of a Circulating Fluidized Bed," *Powder Technol.*, **72**, p. 277, 1992.

Rhodes, M.J., H. Mineo, and T. Hirama, "Particle Motion at the Wall of the 305 mm Diameter Riser of a Cold Model Circulating Fluidized Bed," *Circulating Fluidized Bed Technology III*, P. Basu, M. Horio and M. Hasatani, eds., Pergamon Press, 1991.

Rhodes, M.J., S. Zhou, T. Hirama, and H. Cheng, "Effects of Operating Conditions on Longitudinal Solids Mixing in a Circulating Fluidized Bed Riser," *AIChE Jl.*, **37**, p. 1450, 1991.

Roberts, P.H., "Analytical Theory of Turbulent Diffusion," *J. Fluid Mech.*, **11**, p. 257, 1961.

Saffman, P.G., "Application of the Weiner-Hermite Expansion to the Diffusion of a Passive Scalar in a Homogeneous Turbulent Flow," *Phys. Fluids*, **12**, p. 1786, 1969.

Schlinger, W.G., and B.H. Sage, "Material Transfer in Turbulent Gas Streams," *Industr. Engng, Chem.*, **45**, 657, 1953.

Schmiedel, V.J., "Expermentelle Untersuchungen Uber die Fallbewegung von Kugeln und Scheiben in Reibenden Flussigkeiten," *Phys. Z.*, **29**, p. 593, 1928.

Shraiber, A.A., L.B. Galvin, V.A. Naumov, and V.P. Yatsenko, "Turbulent Flows in Gas Suspension," Hemisphere, New York, 1990.

Shuen, J.S., A.S. Solomon, Q.F. Zhang, and G.M. Faeth, "Structure of Particle-Laden Jet: Measurements and Predictions," *AIAA Jl*, **23**, p. 396, 1985.

Soong, C.H., K. Tuzla, and J.C. Chen, "Identification of Particle Clusters in Circulating Fluidized Bed," *4th Int. Conf. on Circulating Fluidized Beds*, p. 137, Somerset, PA, August 1-5, 1993.

Squires, L. and W. Squires, Jr., "The Sedimentation of Thin Discs," *Trans. Am. Inst. Chem. Eng.*, **33**, p. 1, 1937.

Stemerding, S., "The Pneumatic Transport of Cracking Catalyst in Vertical Risers," *Chem. Eng. Sci.*, **17**, p. 599, 1962.

Taylor, G.I., "Diffusion by Continuous Movements," *Proc. Lond. Math. Soc.*, **20**, p. 196, 1921.

Tchen, C.M., *Mean Value and Correlation Problems Connected with the Motion of Small Particles Suspended in a Turbulent Fluid.* The Hague: Martinus Nishoff, 1947.

Thompson, T.L., and N.N. Clark, "A Holistic Approach to Particle Drag Prediction," *Powder Technol.*, **67**, p. 57, 1991.

Townsend, A.A., *The Structure of Turbulent Shear Flow*, Cambridge Press, 1956.

Tsuji, Y., and Y. Morikawa, "LDV-Measurements of an Air-Solid Two-Phase Flow in Horizontal Pipe," *J. Fluid Mech.*, **120**, p. 358, 1982.

Tsuji, Y., N. Kato, and T. Tanaka, "Experiments on the Unsteady Drag and Wake of a Sphere at High Reynolds Numbers," *Int. J. Multiphase Flow*, **17**, p. 343, 1991.

Tsuji, Y., Y. Morikawa, and H. Shiomi, "LDV-Measurements of Air-Solid Two-Phase Flow in Horizontal Pipe," *J. Fluid Mech.*, **139**, p. 417, 1984.

Tsuji, Y., Y. Morikawa, T. Tanaka, K. Kazimine, and S. Nishida, "Measurements of an Axisymmetric Jet Laden with Coarse Particles," *Int. J. Multiphase Flow*, **14**, p. 565, 1988.

Tsukada, M., D. Nakanishi, and M. Horio, "The Effect of Pressure on the Phase Transition from Bubbling to Turbulent Fluidization," *Int. J. Multiphase Flow*, **19**, p. 27, 1993.

Turton, R., and O. Levenspiel, "A Sort Note on the Drag Correlation for Spheres," *Powder Technol.*, **47**, p. 83, 1986.

Valenzuela, J.A., and L.R. Glicksman, "An Experimental Study of Solids Mixing in a Freely Bubbling Two-Dimensional Fluidized Bed," *Powder Technol.*, **38**, p. 63, 1984.

Vames, J.S., and T.J. Hanratty, "Turbulent Dispersion of Droplets for Air Flow in a Pipe," *Expts Fluids*, **6**, P. 94, 1988.

Van Zoonen, D., "Measurements of Diffusional Phenomina and Velocity Profiles in a Vertical Riser," *Proceedings of Symposium on Interaction between Fluids and Particles, London, Inst. Chemical Engineers*, London, p. 64, 1962.

van der Laan, E. Th., "Notes on the Diffustion-Type Model for Longitudinal Mixing in Flow," *Chem. Eng. Sci.*, **7**, p. 187, 1957.

Vand, V., "Viscosity of Solutions and Suspensions. I. Theory," J. Phys. Colloid Chem., 52, p. 277, 1948.

Viitanen, P.I., "Tracer Studies on a Riser Reactor of a Fluidized Catalyst Cracking Plant," *Ind. Eng. Chem. Res.*, **32**, p. 577, 1993.

Weber, R., F. Boysan, W.H. Ayers, and J. Swithenbank, "Simulation of Dispersion of Heavy Particles in Confined Turbulent Flows," *AIChE J.*, **30**, p. 490, 1984.

Wei, F., Z. Wang, Y. Jin, Z. Yu, and W. Chen, "Dispersion of Lateral and Axial Solids in a Concurrent Downflow Circulating Fluidized Bed," *Powder Technol.*, **81**, p. 25, 1994.

Weinstein, H., M. Shao, and M. Schnitzlein, "Radial Variation in Solid Density in High Velocity Fluidization," *Circulating Fluidized Bed Technology*, P. Basu, ed., Pergamon Press, p. 201,1986.

Wells, M.R., and D.E. Stock, "The Effects of Crossing Trajectories on the Dispersion of Particles in a Turbulent Flow," *J. Fluid Mech.*, **136**, p. 31, 1983.

Westphalen, D., and L.R. Glicksman, "Lateral Solid Mixing Measurements in Circulating Fluidized Beds," *Powder Technol.*, **82**, p. 153, 1995.

Westphalen, D., *Scaling and Lateral Solid Mixing in Circulating Fluidized Beds*, Ph.D. Dissertation, Massachusetts Institute of Technology, 1993.

Willmarth, W.W., N.E. Hawk, and R.L. Harvey, "Steady and Unsteady Motions and Wakes of Freely Falling Disks," *Phys. Fluids*, **7**, p. 197, 1964.

Yang, H., M. Gautam, and J.S. Mei, "Gas Velocity Distribution in a Circular Circulating Fluidized Bed Riser," *Powder Technol.*, **78**, p. 221, 1994.

Yang, S.M., and L.G. Leal, "A Note on Memory-Integral Contributions to the Force of an Accelerating Spherical Drop at Low Reynolds Number," *Phys. Fluids*, **A 3**, p. 1822, 1991.

Yang, W.C., "Criteria for Choking in Vertical Pneumatic Conveying Lines," *Powder Technol.*, **35**, p. 143, 1983.

Yerushalmi, J., and A. Avidan, "High-Velocity Fluidization," *Fluidization*, 2nd ed., J.F. Davidson, R. Clift, D. Harrison, eds., Academic Press, London, p. 225, 1985.

Yuan, Z., and E.E. Michaelides, "Turbulence Modulation in Particulate Flows-a Theoretical Approach," *Int. J. Multiphase Flow*, **18**, p. 779, 1992.

Yudine, M.I., "Physical Considerations in Heavy Particle Diffusion," *Advances in Geophysics*, **6**, p. 185, 1959.

Zhang, W., Y. Tung, and F. Johnsson, "Radial Voidage Profiles in Fast Fluidized Beds of Different Diameters," *Chem. Eng. Sci.*, **12**, p. 3045, 1991.

Zhou, J., J.R. Grace, C.J. Lim, and C.M.H. Brereton, ,"Particle Velocity Profiles in a Circulating Fluidized Bed of Square Cross-Section," *Chem. Engrg Sci.*, **50**, p. 237, 1995.

Zhou, J., J.R. Grace, C.J. Lim, C.M.H. Brereton, S. Qin, and K.S. Lim, "Particle Cross-Flow, Lateral Momentum Flux and Lateral Velocity in a Circulating Fluidized Bed," Accepted for publication, *Can. J. of Chem. Eng.*, 1995.

Zhou, J., J.R. Grace, S. Qin, C.M.H. Brereton, C.J. Lim, and J. Zhu, "Voidage Profiles in a Circulating Fluidized Bed of Square Cross-Section," *Chem. Engrg Sci.*, **49**, p. 3217, 1994.

Zisselmar, R., and O. Molerus, "Investigation of Solid-Liquid Jet Pipe-Flow with Regard to Turbulence Modulation," *Chem. Engng J.*, **18**, p. 233, 1979.

CHAPTER 6

THE INFLUENCE OF BED DIAMETER ON HYDRODYNAMICS AND HEAT TRANSFER IN CIRCULATING FLUIDIZED BEDS

1.0 INTRODUCTION

On issue facing designers of CFB combustors is the applicability of heat transfer data from laboratory-size scaled beds or pilot plants to full-sized commercial beds. In some early work on circulating beds, there was the implicit assumption that bed-to-wall heat transfer could be correlated with respect to flow parameters in the small bed, e.g. the local cross-sectional averaged solids concentration. Recent results from larger CFB's have shown an important dependence of heat transfer on bed diameter as well as average solid concentration [Glicksman, L.R., Heat Transfer in Circulating Fluidized Beds, in Circulating Fluidized Beds, A. Avidan, J. Grace, and T. Knowlton, eds., to be published, 1995. This is expected since a larger-diameter bed has a lower ratio of perimeter to cross-sectional area and will accumulate more particles on the circumference for the same flow of solids per unit area in the core. Therefore, the influence of bed diameter on heat transfer is a basic phenomenon which must be understood if laboratory units are to be relevant to largescale combustors.

2.0 HEAT TRANSFER MODEL

The flow of the gas-particle suspension in the riser of fast fluidized beds is characterized by dilute rapidly rising core and a dense annular region near the walls where the solid particles congregate and fall as dense structures similar to waves of strands or streamers. The CFB heat transfer model considers clusters coming to the wall from the core at the bed temperature and remaining there for a short period of time. If radiation is neglected, heat transfer to the bed wall can be stated as an average of the heat transfer from clusters and dilute phases (Subbarao and Basu, 1986):

$$h = fh_c + (1\text{-}f)h_d \tag{1}$$

where h_c and h_d are the time-averaged heat transfer coefficients for the dense (cluster) phase and the dilute phase, respectively, and f is the fraction of the wall covered by clusters (dense phase). As the clusters move down the wall, they cool until they are shed and replaced by fresh material at the bed temperature. Mickley and Fairbanks (1955) suggested that a cluster of particles at the wall could be modeled as a homogeneous semi-infinite medium with an effective conductivity, density and specific heat. For transient heat transfer between "packets" of particles which remain at the wall for time t and then are displaced from the heat transfer surface:

$$q = \Delta T \sqrt{\frac{k_c c_{p_{cl}} \rho_{cl}}{\pi t}} \tag{2}$$

This expression for heat flux can be used to define a heat transfer coefficient for transient conduction within the dense phase (or emulsion phase):

$$h_e = \sqrt{\frac{k_c c_{p_{cl}} \rho_s \left(1 - \varepsilon_{cl}\right)}{\pi t}} \tag{3}$$

To account for the nonuniformity of particle packing near the heat transfer surface and the contact resistance between the particles and the wall, Baskakov (1964) introduced an additional "contact" thermal resistance between the wall and the packet:

$$R_w = \frac{1}{h_w} = \frac{\delta d_p}{k_f} \tag{4}$$

where d ranges from 1/6 to 1/12 for bubbling beds. The exact expression for transient conduction from a semi-infinite body to a constant temperature surface with a series resistance is complicated. However, experimental measurements (Gloski, Glicksman and Decker, 1984) have shown that a close approximation to the actual heat transfer coefficient from a cluster, even at short times, is given by assuming that these two mechanisms, the contact resistance and the transient conduction to a homogeneous cluster of particles, act independently and in series with each other:

$$h_c = \left[\frac{1}{h_w} + \frac{1}{h_e}\right]^{-1} = \left[\frac{\delta d_p}{k_f} + \sqrt{\frac{\pi t}{k_{cl} c_{p_s} \rho_s \left(1 - \varepsilon_{cl}\right)}}\right]^{-1} \tag{5}$$

where the thermal conductivity of the cluster of particles can be calculated from the expression developed by Gelperin and Einstein (1971):

$$k_{cl} = k_f \left[1 + \frac{\left(1 - \varepsilon_{cl}\right)\left(1 - \frac{k_f}{k_s}\right)}{\frac{k_f}{k_s} + 0.28\varepsilon_{cl}^{0.63\left(\frac{k_s}{k_f}\right)^{0.18}}}\right] \tag{6}$$

Substituting Equation (5) into Equation (1) gives

$$h = f\left[\frac{\delta d_p}{k_g} + \sqrt{\frac{\pi t}{k_{cl} c_{p_s} \rho_s \left(1 - \varepsilon_{cl}\right)}}\right]^{-1} + \left(1 - f\right) h_d \tag{7}$$

3.0 EXPERIMENTAL ARRANGEMENT

Two CFB's designed to run at room temperature were constructed and operated identically, with the exception that the diameters differed by 50 percent (5.1 cm vs. 7.6 cm). The risers were made of clear PVC, allowing for direct visual measurement of the flow at the wall. The beds used solids and were operated at test points which simulated a 13" (33 cm) ID x 42' (12.8 m) high pressurized CFB. These parameters were determined using the simplified scaling parameters discussed in Chapter 2.

In what follows, three topics will be discussed in the following order:

1. Bed geometry
2. Particle characteristics
3. Measurement equipment and associated uncertainty

3.1 Dimensions and Construction of the Cold CFB's

The first bed utilized was a 1/6.5 scale model of the Foster Wheeler Phase III pressurized circulating bed operated by Foster Wheeler Development Corp. The bed consists of five main sections:

1. Main bed test section
2. J-valve section
3. Lower secondary air port section
4. Upper secondary air port section
5. Exhaust section

The 1/6.5 scale model riser is round and consists of a 2" (5 cm) ID x 8" (20 cm) high primary zone and a 2" (5 cm) ID x 5.35' (1.6 m) high secondary zone both made of clear PVC plastic. Four nozzles, to 8" (20 cm) and two 1.7' (53 cm) above the distributor.permit the injection of varying amounts of secondary air into the riser. Each set of ports is equipped with its own valving to allow for varying combinations of secondary air flows. Primary air is introduced radially into the riser through a 1/2" (1.3 cm) pipe. Both the primary and secondary air flows are measured using rotameters with a 1 scfm to 10 scfm span. The larger diameter bed was identical, except that the riser diameter was 3" (7.6 cm).

The J-valve connects to the riser thorugh a 1.5" (3.8 cm) clear PVC pipe which enters at a 45° angle 3" (7 cm) above the distributor pipe. A 1.5" (7 cm) ball valve controlled the flow solids through the J-valve, allowing for good control of the solids recycle rate.

The primary separator consists of a Plexiglas cyclone. The cyclone, constructed primarily of 1/4-inch (0.635 cm) Plexiglas, has a total length of 3 feet (0.91 m) with the top 18 inches (45.7 cm) having an inside diameter of 9-7/16" (24.0 cm). The bottom 18 inches (45.7 cm) tapers down to a flanged 2.0" (5.1 cm) solids exit. Air exits to a secondary cyclone through a 4.0" (10.2 cm) outlet in the top of the cyclone. Below the primary cyclone, a flexible hose was connected to help relieve stresses. To determine the solids circulation rate, the rate of descent of solids below the cyclone was timed and converted to an overall solids recycle rate. Final filtration was achieved by means of a fabric bag attached to the air exhaust line. The short vertical section below the cyclone connects to the the 45° 1.5" (3.8 cm) pipe which contains the ball valve and J-valve, and eventually penetrates the base of the riser.

Six pressure taps used to measure axial pressure drop are located on one of the side walls of the bed. These taps are angled down in order to prevent solids from accumulating in the lines. Pressure tap locations are located at similar fractional bed heights as that of the hot bed. Hot bed pressure transducer locations which were included on the cold model are given in Table 3.1 (see Figure 3.1).

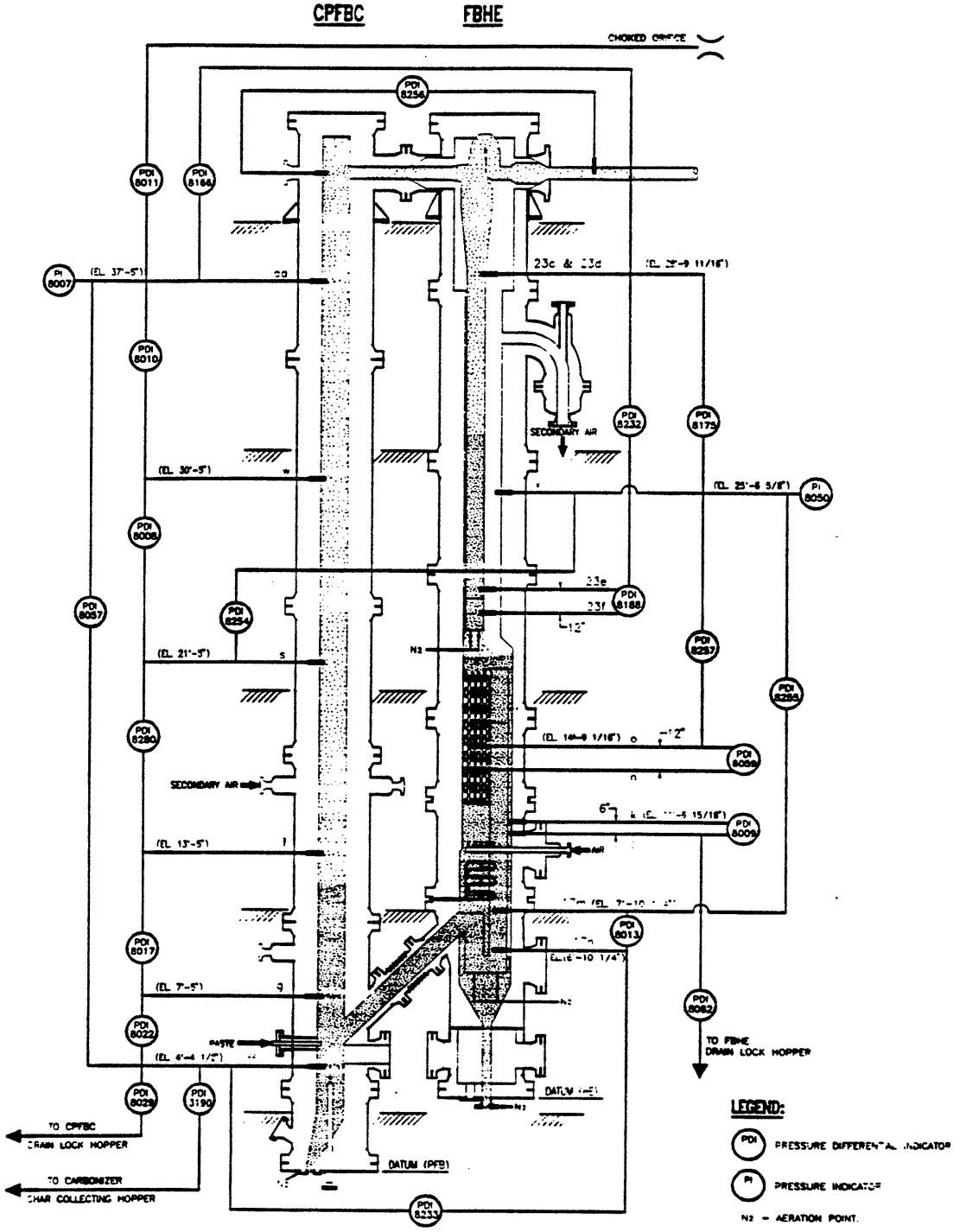

PHASE III CPFBC PRESSURE MEASUREMENTS

Table 3.1

Cold Bed Pressure Transducers (see Figure 3.1)

Transducer	Location
1	PDI-8022
2	PDI-8017
3	PDI-8280
4	PDI-8008
5	PDI-8010
6	PI-8007

3.2 Bed Solid Materials

In order that the beds simulate the hydrodynamics of the Foster Wheeler PCFB, polyethylene particles were utilized in this study. The same particles were used in both the 2" and 3" diameter beds. The mean particle diameter was determined using laboratory sieves. Minimum fluidization velocity for the plastic particles was determined in a small 4-inch (10.2 cm) bubbling bed operating at room temperature and atmospheric pressure. A summary of polyethylene particle properties is given in Table 3.2. The particle size distribution is given in Figure 3.2.

Table 3.2 Polyethylene Plastic Properties

	Glass Properties
Density	0.91 g/cc
Mean Diameter	120 microns
Loose Pack Voidage	49%
Sphericity	0.85
u_{mf}	0.97 cm/s

Figure 3.2

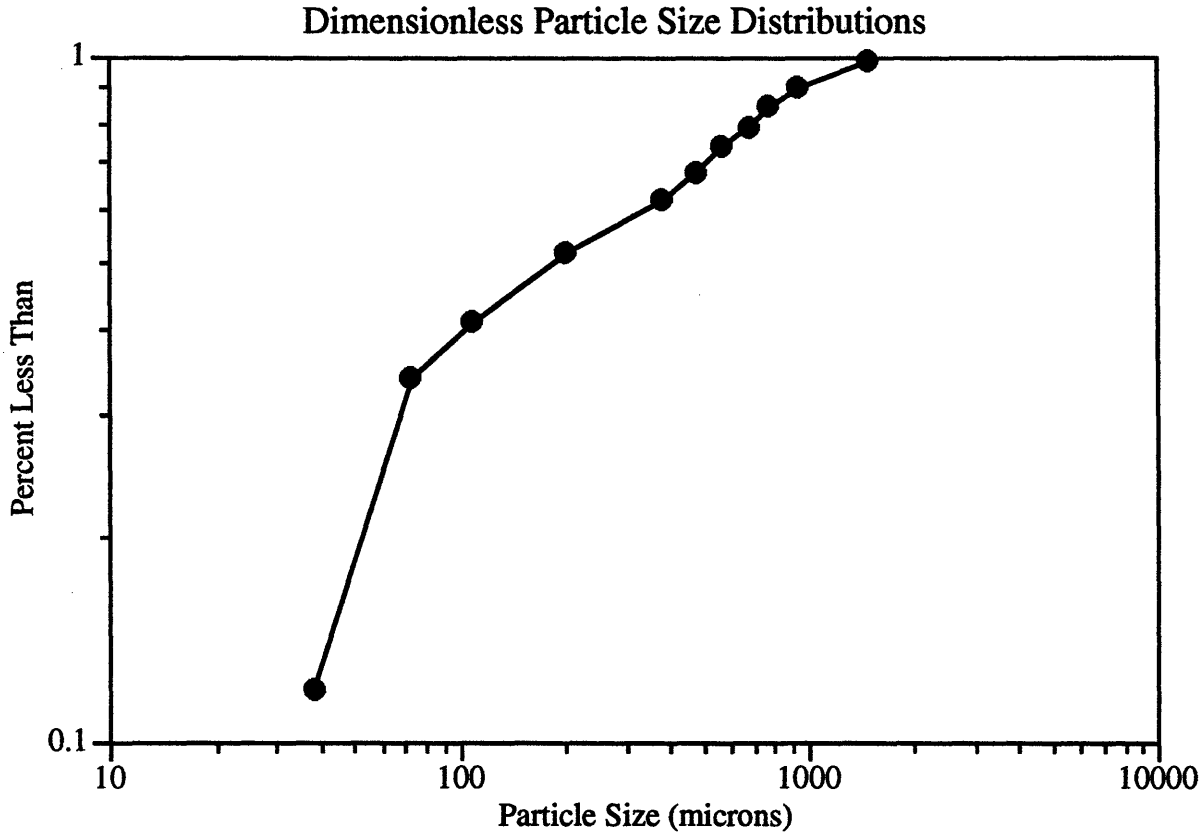

3.2.1 Preparation of Plastic Particles

In addition to the separation and recombination process in order to achieve satisfactory size distributions, the plastic particles were treated with anti-static compounds in an attempt to reduce the level of static electricity generated in the bed. The first compound was Larostat 519, a fine powder which was mixed in with the plastic powder. Since the mass fraction of Larostat in the mixtures was very small, it was not anticipated that this would have any

significant effect on the hydrodynamics of the beds other than through the reduction of static electricity.

While the Larostat worked quite well in the reduction of static, as more was added during operation, it began to severely inhibit the flow characteristics of the glass and plastic mixtures in the L-Valves and other constricted areas, limiting the amount of Larostat allowable in the beds. In order to further reduce bed static levels, the plastic particles in the Foster Wheeler cold scale model along with the entire cold scale model was coated with electrically conductive floor wax.[1] Re-sieving the particles indicated that the wax coating did not significantly affect the mean diameter or size distribution of the plastic powder. The conductive floor wax was found to be superior in eliminating static electricity effects in the Foster Wheeler scale model.

3.2.2 Elimination of Static Electricity Effects

In addition to the use of Larostat and wax as described above, several other precautions were taken to reduce problems caused by static electricity. The first measure taken was to wrap copper gauze around areas of the beds which accumulated large amounts of static electricity (this included the cyclones, pneumatic return lines, and sections of the downcomers). Copper ribbon was then used to ground the gauze as well as the supporting structure and other metallic components .

3.3 Variable Measurement

Bed measurement techniques are described in the following sections.

3.3.1 Air Flow

Air entered the beds through the primary distributor pipe and at the secondary air ports. The two air flows were measured separately with rotameters fitted with exit pressure gauges. The rotameters measured in the range from 2 to 10 cfm, and the pressure gauges were 15 psig full scale. Calibration of the rotameters and gauge combinations was done with a square-edged orifice plate fitted with flange taps. The tests covered flow ranges at expected pressure ranges with the data being fit to the equation:

---

[1]Statguard electrically conducting floor wax - available from Charleswater Products.

$$Q_a = (AR+B)\sqrt{\left(1+\frac{P_g}{P_a}\right)}$$

Table 3.3 gives the results of the rotameter calibrations.

Table 3.3: Rotameter Calibrations

Rotameter	A	B	σ
Primary Air (2 - 10 scfm)	1.0347	0.0239	0.0422
Secondary Air (2 - 10 scfm)	1.0141	0.0003	0.0449

3.3.2 Solid Circulation

Measurement of solid circulation in the beds was done by timing the descent of the solids in the vertical pipe section below the cyclone.

3.3.3 Pressure Measurement

The pressure measurement technique for the bed utilized in this study is described below. Measurement and recording of the pressure transducer voltage output was done with a Dell 386 PC comptuer alogn with a Metrabyte 16 channel data acquisition board and EasyLX, a high speed data acquisition program. The pressure transducer calibration curves were entered into the data acquistion program allowing for direct conversion of voltages to pressures.

There were six pressure taps in the main bed section of the beds which were used to measure axial pressure differences. The pressure taps and lines were 1/8" (0.32 cm) in diameter. All pressure lines were less than 0.5 m in length. Pressure measurements were obtained using a set of pressure transducers.

The pressure transducers were located near their associated pressure taps. The transducers measured differential pressures between adjacent pressure taps. The transducers were

series 600 transducers supplied and calibrated by Auto Tran, Inc. They had output on the order of 1-4 volts, and utilized a 12 volt DC power supply. A summary of the transducers and their locations is given in Figure 3.1 and Table 3.4. The Figure depicts the Foster Wheeler Phase III PCFBC. The distances between taps are therefore 1/6.5 times the distances shown on the plot.

The pressure taps were angled down 40° into the bed. Since the particle motion is downward at the wall, this proved successful in preventing particles from entering the lines.

Table 3.4: Transducer Summary

Transducer	Corresponding Transducer on FW PCFB	Pressure Range (inches H2O)	ΔH Between Taps (cm)
1	PDI-8022	0 - 10"	14
2	PDI-8017	0 - 5"	28
3	PDI-8280	0 - 5"	37.5
4	PDI-8008	0 - 5"	42
5	PDI-8010	0 - 2"	33
6	PI-8007	0 - 10"	---

3.4 Uncertainty Analysis

3.4.1 Air Flow

The air flows were measured with 2-10 cfm rotameters fitted with exit pressure gauges. Calibration of the rotameters involved about 70 data points for each rotameter. The standard deviation from the linear calibration curves was about 0.05 cfm for each rotameter. The low end of the measurement range used in the experiments was about 3 scfm. The standard deviation represents about 2 percent of this lowest measurement.

The minimum fluidization test bed air flows for the glass were measured with 20-scfh and 100-scfh nominal rotameters. Fifteen test points were used in calibrating the 20-scfh rotameter. The standard deviation from the linear calibration curve for this rotameter was 0.093 scfh, or about 0.5 percent of full scale. Thirty-nine points were used in calibrating the

100-scfh rotameter. Standard deviation from the calculated linear calibration curve was 0.59, or about 0.6 percent of full scale.

3.4.2 Solid Circulation Rate

Confidence in the accuracy of the solid circulation rate measurements was based on the repeatability of solid loose-packed density measurements and the repeatability of solid fraction profile results when measurements indicate that flow conditions are the same. In addition, previous study has indicated that the various methods used provide similar agreement (Westphalen, 1990). The study performed by Westphalen also addresses the expected errors as a result of different rates of solid entrainment at the top of the bed, uncertainty about the solid bulk density as solid accumulates during measurement, and the variation in accumulation rates for successive measurements. It was determined that the visual tracking provided an adequate degree of accuracy for the solid circulation rate. See Chapter 2 for a complete discussion of the errors expected from the visual solid circulation measurement technique.

3.4.3 Pressure Measurements

All bed pressures were measured using pressure transducers whose output voltages were recoreded by a computer-based data acquisition system. Calibration of the transducers was accomplished by comparison with an oil filled inclined manometer. Linear calibration curves were used for reduction of data to convert the transducer output voltages to differential pressures. Table 3.5 presents typical values for the standard deviation of pressure transducers in the beds.

Table 3.5 Standard Deviation of Transducers Used in Study

	Ratio of Standard Deviation to Average Voltage Output	
Bed	Worst Case	Typical
1/6.5 Scale FWDC Bed (3" and 2") diameters	< 1%	< 1%

The data acquisition board is rated for 12 bit resolution; this represents 0.024 percent of full scale. Typical full scale range used for the pressure transducers was -1 to +5 volts,

allowing 144 mv resolution. The worst case voltage resolution represented about 7 percent of the smallest measured mean pressure difference when running at very lean conditions.

In order to determine the possibility that pressure signals may be attenuated in the pressure tap lines between the pressure tap opening and pressure transducer, a rough analysis was conducted which indicated that the break (maximum transmission) frequency based on for the cold bed setups would be about 3500 Hz. The maximum frequency of the data acquisition board A/D conversion may be as low as 500 Hz when all six pressure taps are being sampled which suggests that this is not a limiting condition. In addition, it has been shown that the fluctuations of interest in the bed would have frequencies less than 100 Hz (Westphalen, 1990).

Pressures time traces were taken for 10 seconds at a frequency of 100 Hz. For each trace, the average and standard deviation was calculated. These standard deviations, along with the standard deviation in solids flux measurement, were used in constructing error bars for the cold bed solid fraction profiles. Error bars represent one standard deviation (i.e., 67 percent of the data fell into the interval based on a normal distribution).

3.5 Hydrodynamic Data Reduction

The following Section discusses the manner in which the data was reduced to develop average solid fraction profiles.

Solid fraction profiles discussed in the following Sections are based on pressure drop measurements. In converting pressure drop to solid fraction, it has been assumed that pressure differentials are due entirely to solid hold up

$$SF = \frac{\Delta P}{\rho_s g \Delta L}$$

This relation neglects acceleration effects and wall shear stresses, which may comprise a portion of the total pressure drop. Therefore, measured solid fractions are more correctly defined as dimensionless pressure differences, which are equal to the true solid fraction in the limit of negligible acceleration and wall shear.

Solid fractions are plotted versus the average of the heights of the associated pressure taps.

4.0 EXPERIMENTS AND RESULTS

4.1 Visual Experiments

Observations were made approximately 55% of the way up the bed (approximately 1.2 m above the air distributor), in a wall region 33 mm by 33 mm in the smaller (2" diameter) and 50 mm by 50 mm in the larger (3" diameter) bed. The flow of particles at the wall was recorded with a digital high-speed video system operating at an exposure rate of 250 Hz. Lighting was provided by a synchronized strobe lamp, and a thin (0.25 mm), black-colored plate was inserted concentrically roughly 5-10 mm from the wall in order to provide the contrast needed to identify particles in the wall region. The regions defined by the plate were roughly 11 cm^2 in the smaller bed and 25 cm^2 in the larger bed. Post-processing of the digital video images with an image-analysis software package allowed for measurements of cluster size and determination of the fraction of the wall covered by clusters. Some level of judgment was required to enable the software package to define clusters. Differential pressure measurements were also made in order to determine the average cross-sectional concentration of particles, an important indicator for both heat transfer and hydrodynamic behavior.

4.2 Results

Six wall coverage experiments were run; two in the larger bed and four in the smaller bed. Two experiments were first run in the larger bed to observe the behavior at the wall with both dense and lean average cross-sectional solid concentrations. Four experiments were then run in the smaller bed to duplicate the dense and lean conditions by matching either the solids flux rate or by matching the average cross-sectional solid concentration at the viewing location. Both matching methods were chosen in order to better understand how the wall coverage relates to the average cross-sectional solids fraction and the riser solids circulation rate. Table 4.1 summarized the various conditions for each run. Because of the difference in bed diameter, matching the operating conditions did not guarantee that two beds would operate in a hydrodynamically similar manner (see Chapter 2).

Table 4.1: CFB Conditions

Run	Bed Size	Solid Flux (kg/m^2-s)	Solid Concentration at 55% Bed Height
1	large (3")	30	1.8%
2	large (3")	18	1.3%
3	small (2")	not matched	1.2% (matched)
4	small (2")	not matched	1.8% (matched)
5	small (2")	30 (matched)	1.6% (not matched)
6	small (2")	18 (matched)	1.1% (not matched)

Because of the difference in bed diameter, matching the operating conditions did not guarantee that the hydrodynamic conditions at a given cross-sectional location would be the same. In fact, the smaller-diameter bed runs at a higher value of Froude number based on superficial velocity and bed diameter and will tend toward lower cross-sectional solid concentrations for a given solids flux rate. This behavior is depicted in Figures 4.1 and 4.2 which present the solid fraction profiles for the dense and lean cases, respectively. This behavior has also been reported in previous research (Arena, *et al.*, 1992).

Figure 4.1: Solid Fraction Profile Comparison, Runs 1,4, and 5

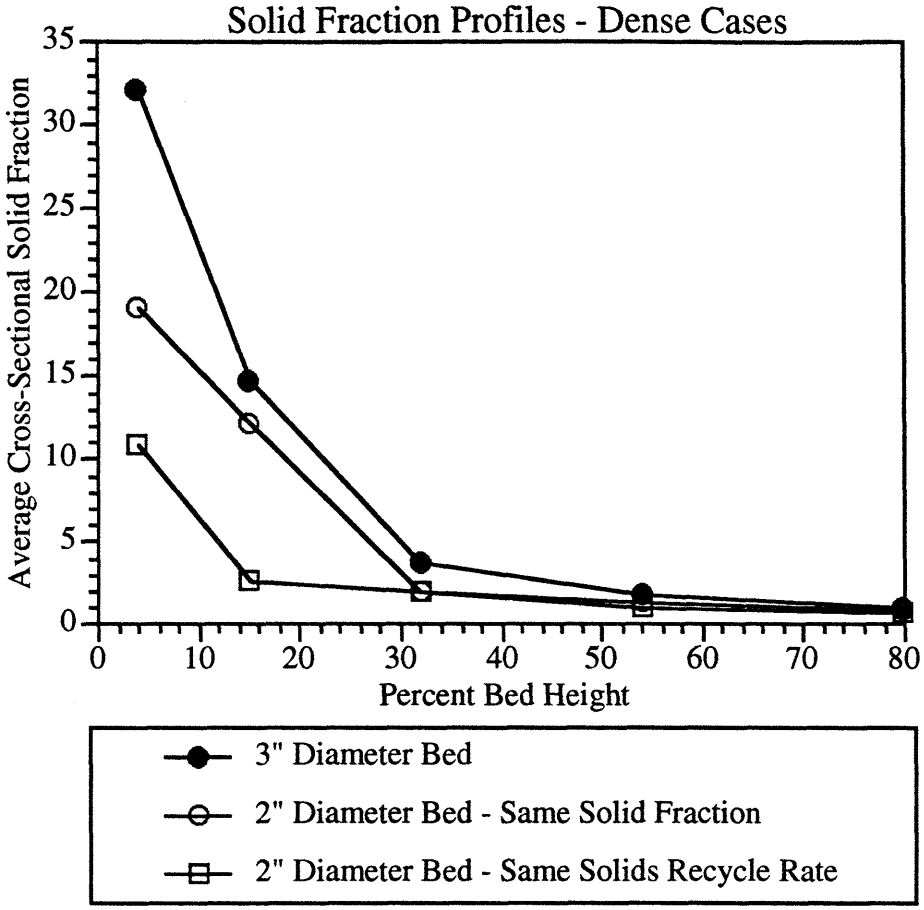

Figure 4.2: Solid Fraction Profile Comparison, Runs 2,3, and 6

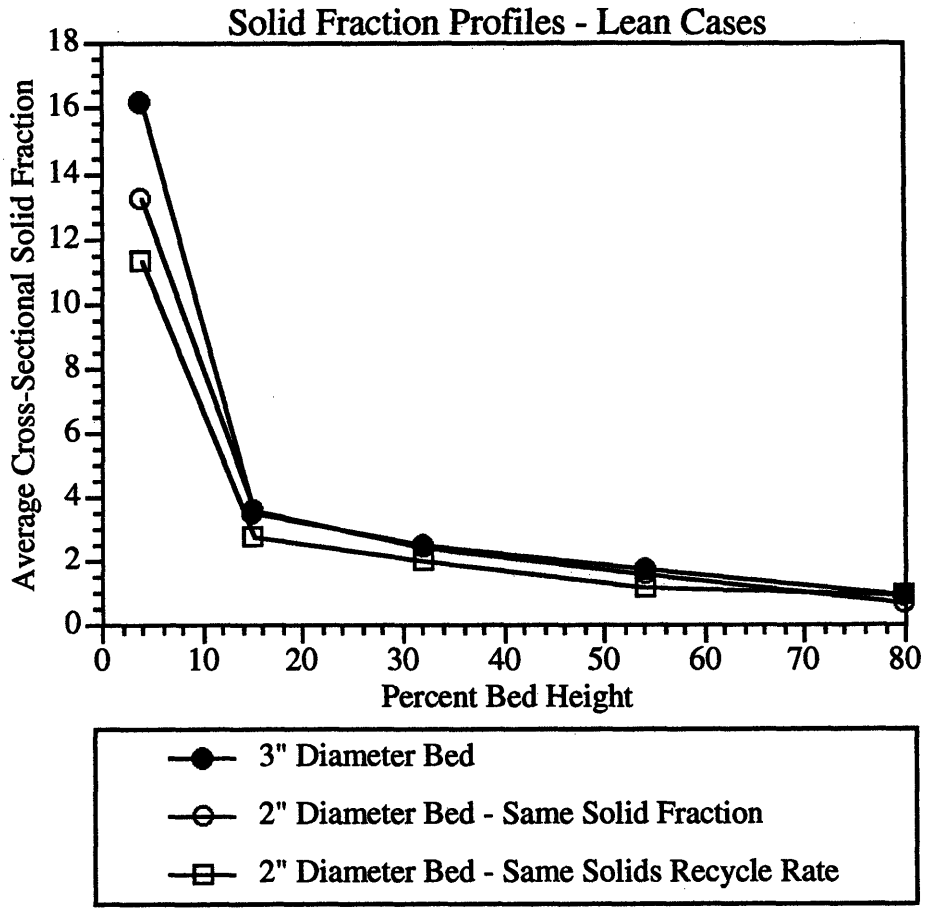

In Figure 4.1, the large bed (run 1) has a higher average cross-sectional solid concentration than the small bed for the same solids flux rate (run 5). The same can be said for the lean cases, shown in Figure 4.2, when comparing run 2 to run 6. There is little difference between the solid-fraction profiles in the small bed when running at either the same operating hydrodynamic conditions.

The results from these runs show that the bed with the larger diameter has a higher fraction of the wall covered by clusters. Also, as expected, the cases with the higher average cross-sectional solid concentrations show greater wall coverage. Figures 4.3 through 4.8 present the time-dependent values and time-averaged values of the fractional wall coverage for each of the six runs. The time-averaged results are also summarized in Table 4.2.

Table 4.2: Visual Experiment Results

Run	Bed Size	Matched Variable	Average Cross-Sectional Solid Fraction (%)
Dense Cases			
1	Large (3")	---	69
4	Small (2")	Solid Fraction	39
5	Small (2")	Solids Recycle Rate	24
Lean Cases			
2	Large (3")	---	9.1
3	Small (2")	Solid Fraction	8.4
6	Small (2")	Solids Recycle Rate	6.6

Figures 4.9 through 4.14 compare the distribution of instantaneous measurements in each case with a representative Poisson distribution. The open circles represent measurements and the solid circles represent theoretical distributions. This implies the arrival of clusters at a given area of the wall is a Poisson process wherein the wall coverage can be described and characterized by a steady arrival of clusters in which each arrival event and the number of clusters arriving in each event is independent of the other events. In this analysis, the steady arrival rate, represented by lambda, should be the same as the fractional wall coverage. As shown in Table 4.3, the value of lambda that best fits the data for each case is close in value to the measured fractional wall coverage.

Figure 4.3: Fractional Wall Coverage vs. Time - Run 1

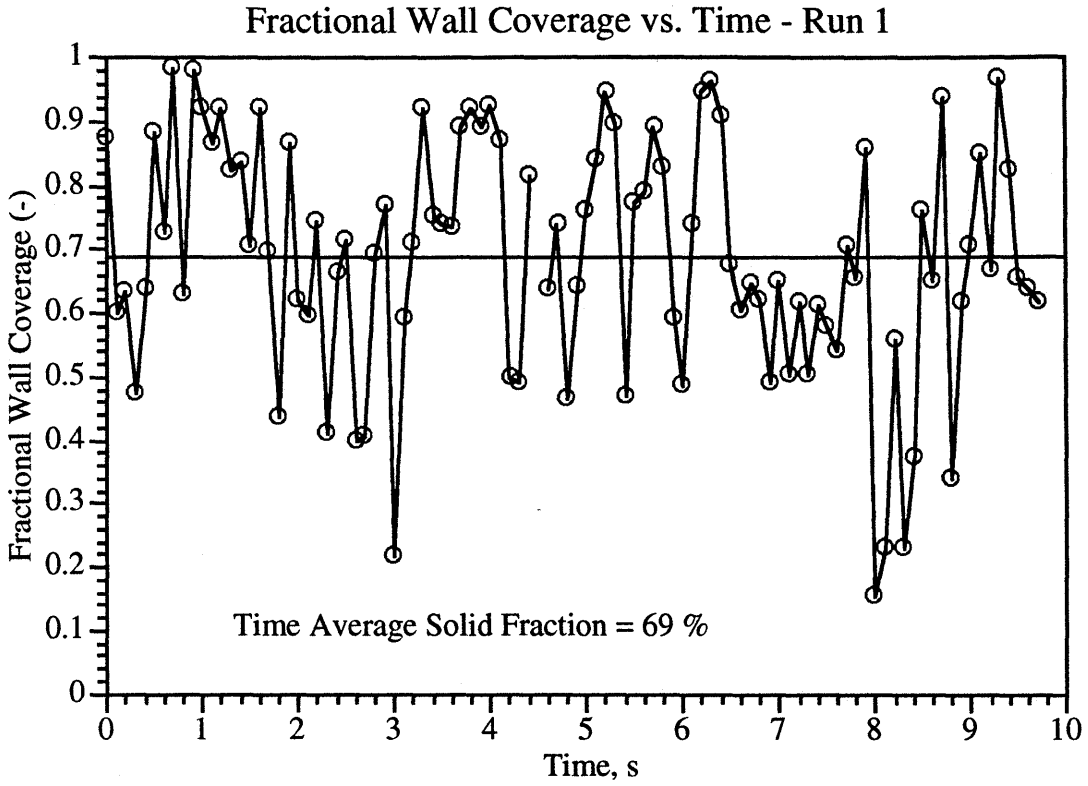

Figure 4.4: Fractional Wall Coverage vs. Time - Run 2

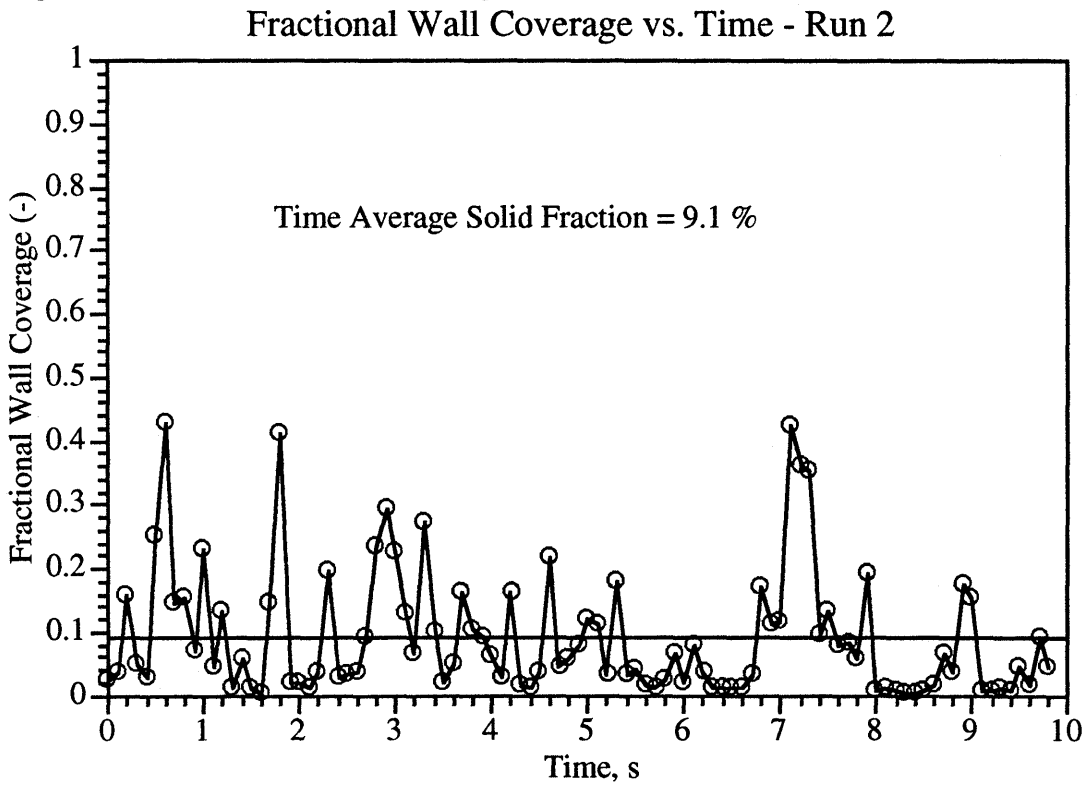

Figure 4.5: Fractional Wall Coverage vs. Time - Run 3

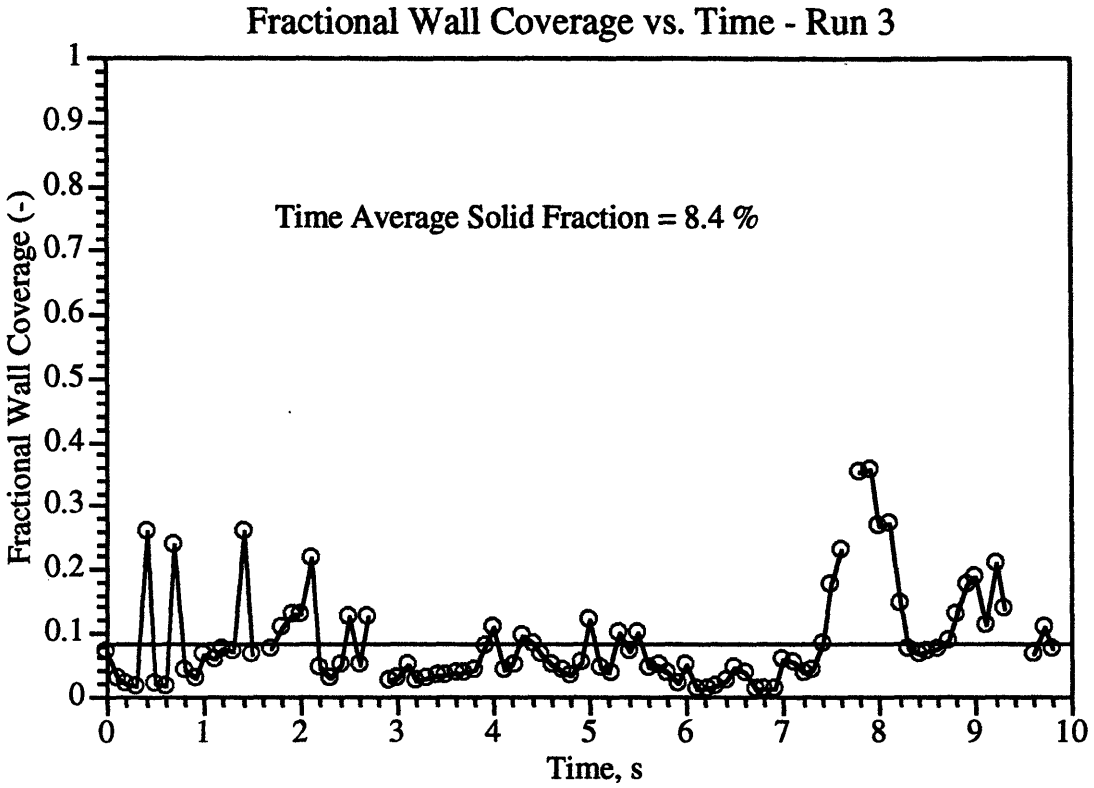

Figure 4.6: Fractional Wall Coverage vs. Time - Run 4

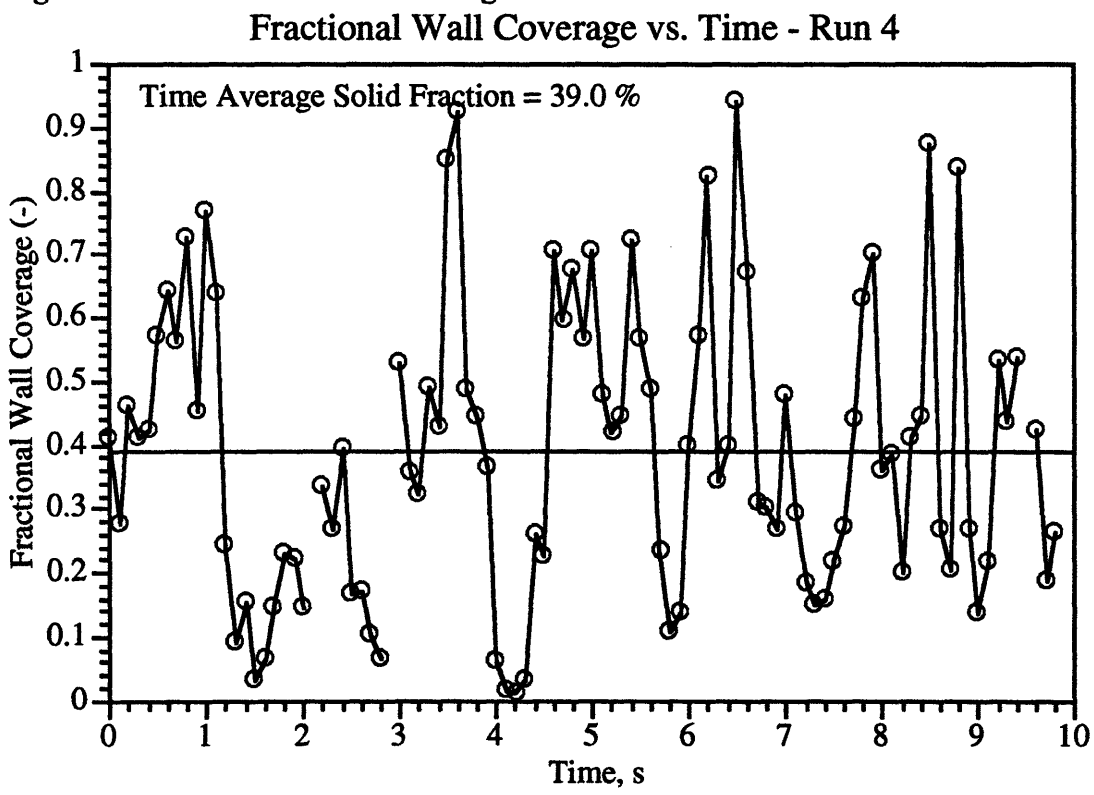

Figure 4.7: Fractional Wall Coverage vs. Time - Run 5

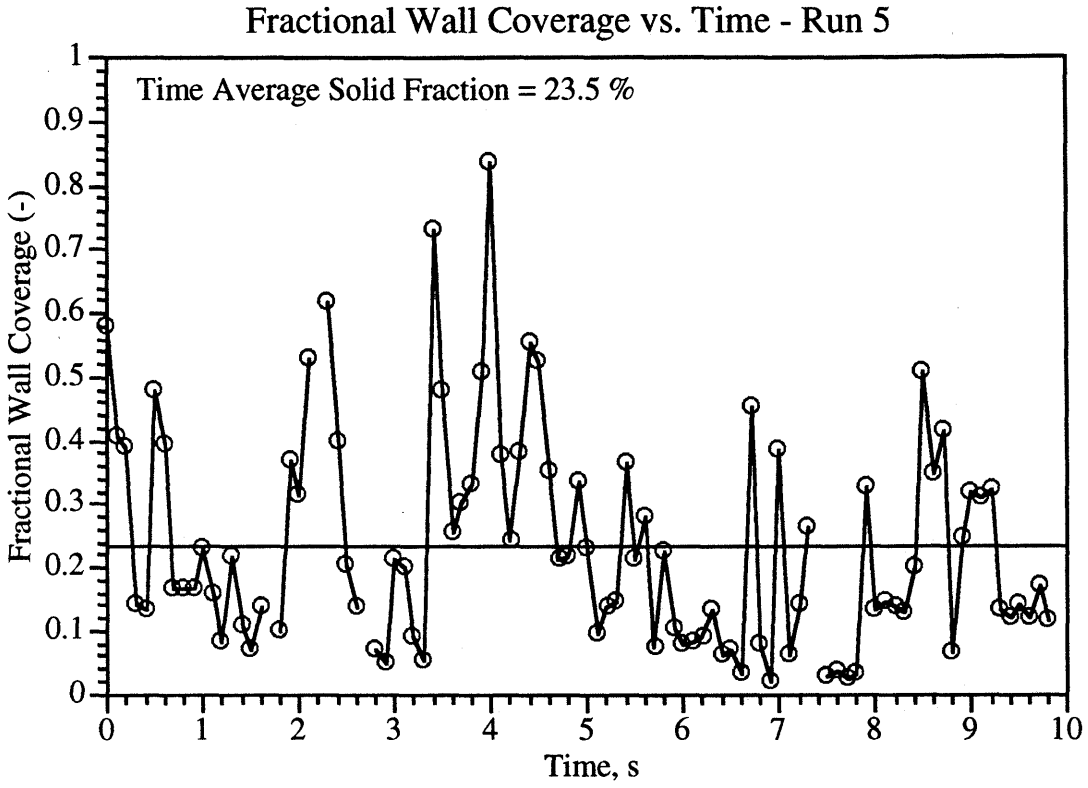

Figure 4.8: Fractional Wall Coverage vs. Time - Run 6

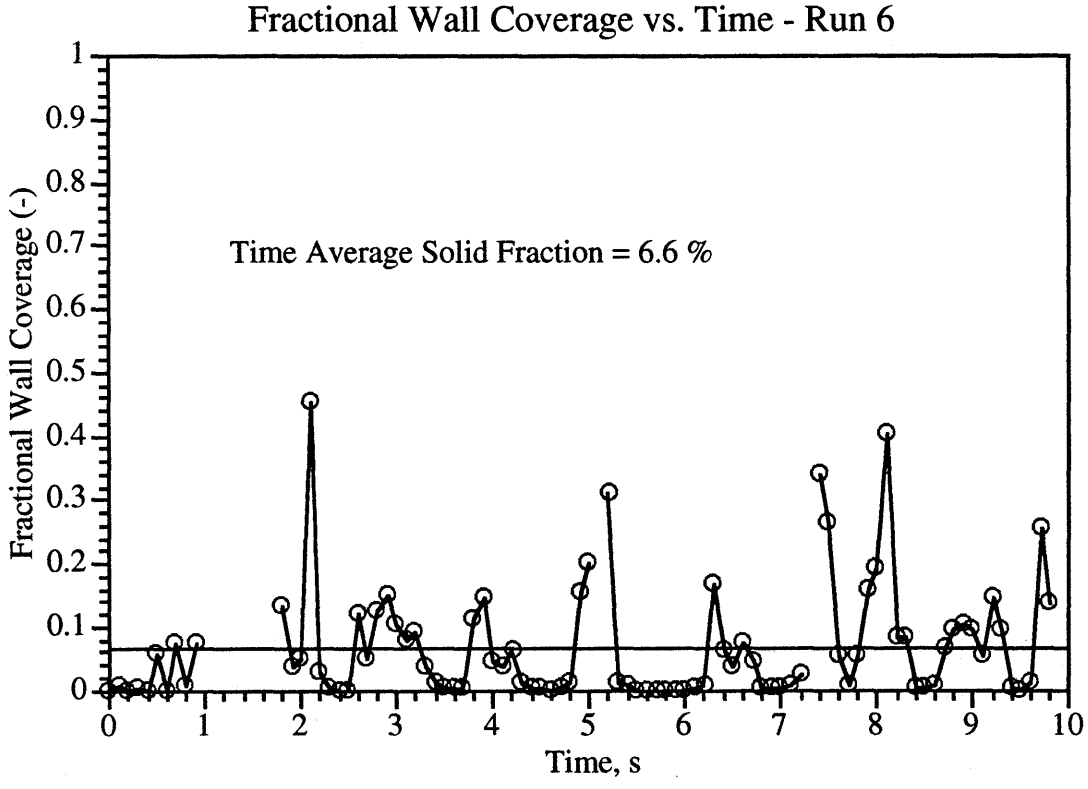

Figure 4.9: Fractional Wall Coverage Probability Density Function-Run 1

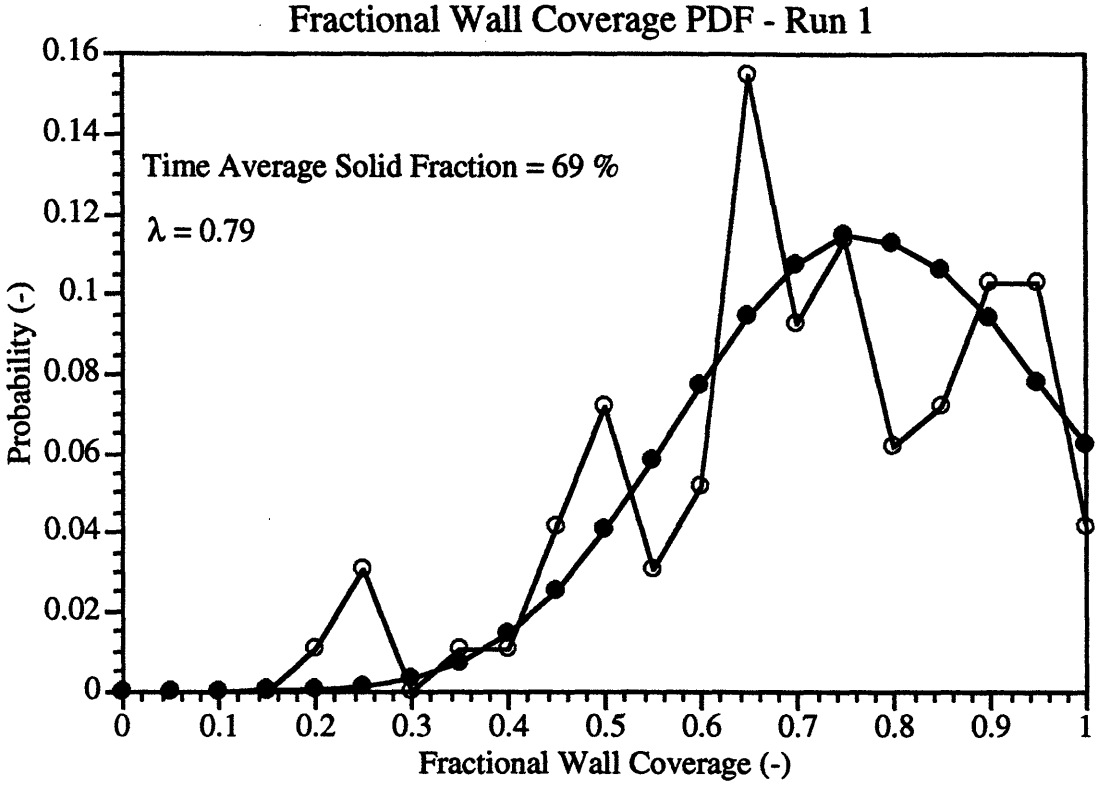

Figure 4.10: Fractional Wall Coverage Probability Density Function-Run 2

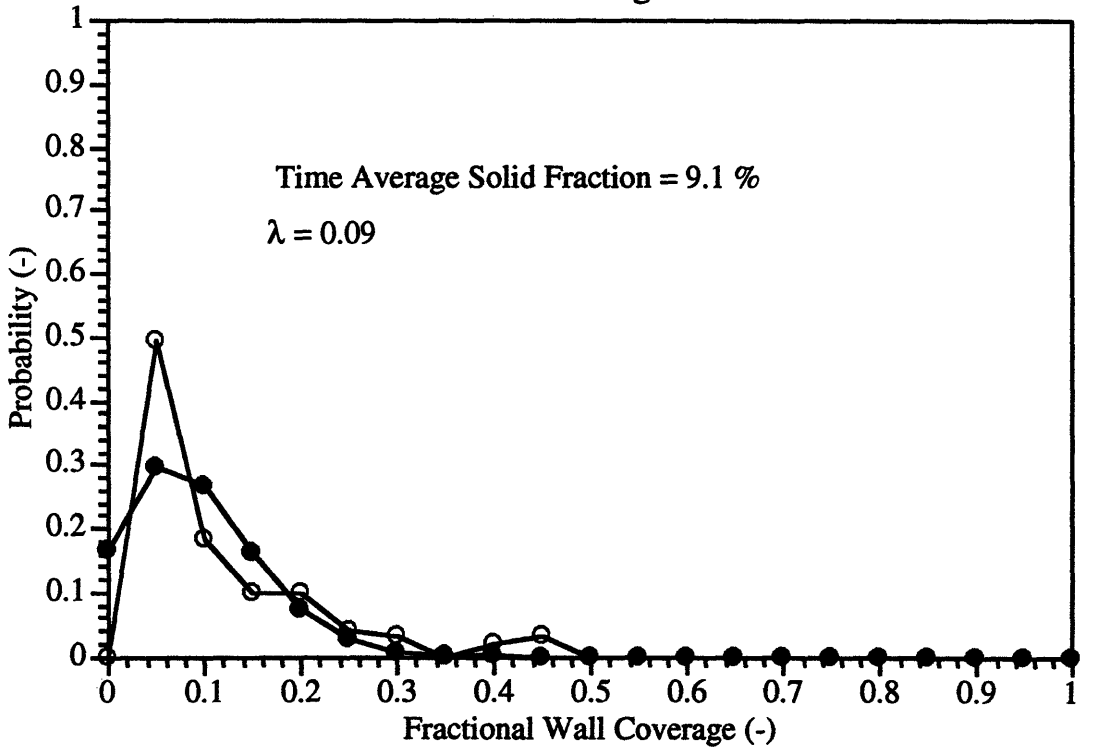

Figure 4.11: Fractional Wall Coverage Probability Density Function-Run 3

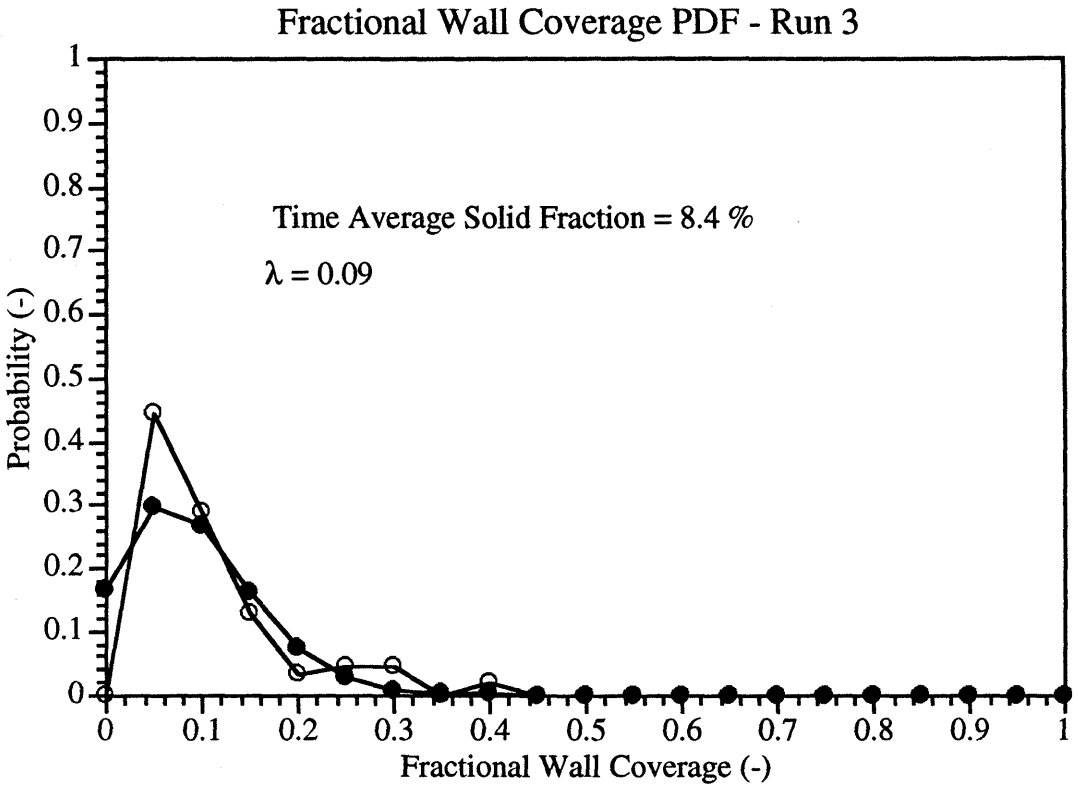

Figure 4.12: Fractional Wall Coverage Probability Density Function-Run 4

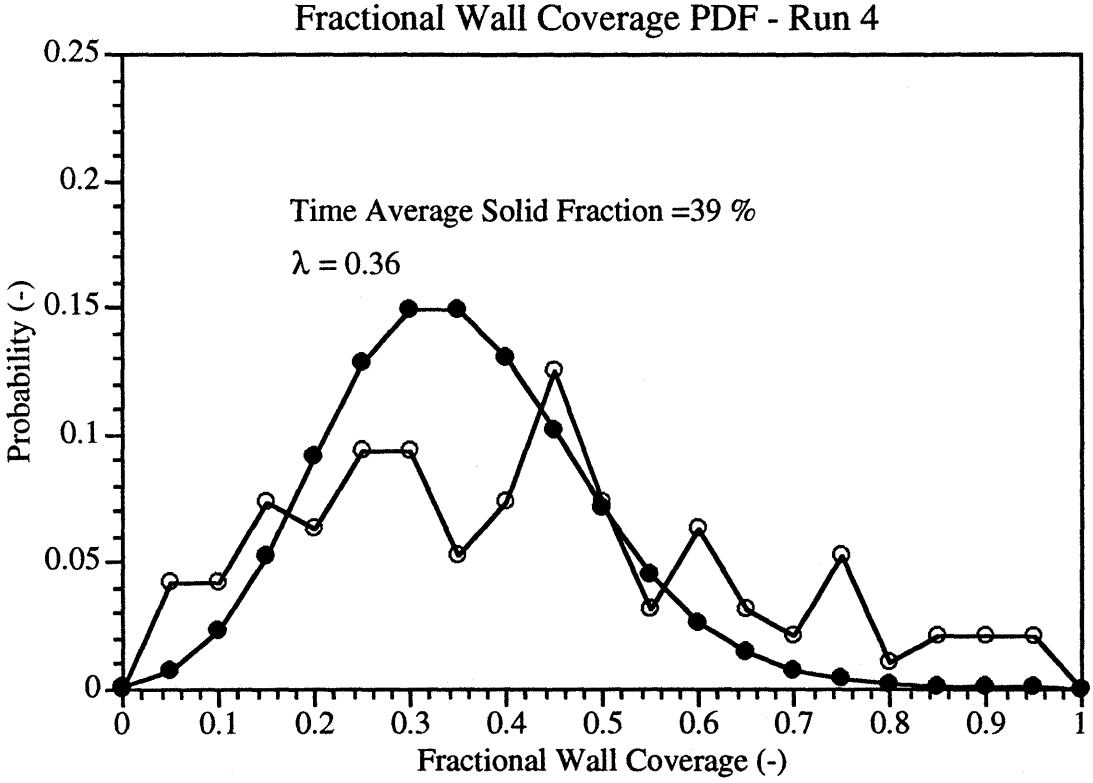

Figure 4.13: Fractional Wall Coverage Probability Density Function-Run 5

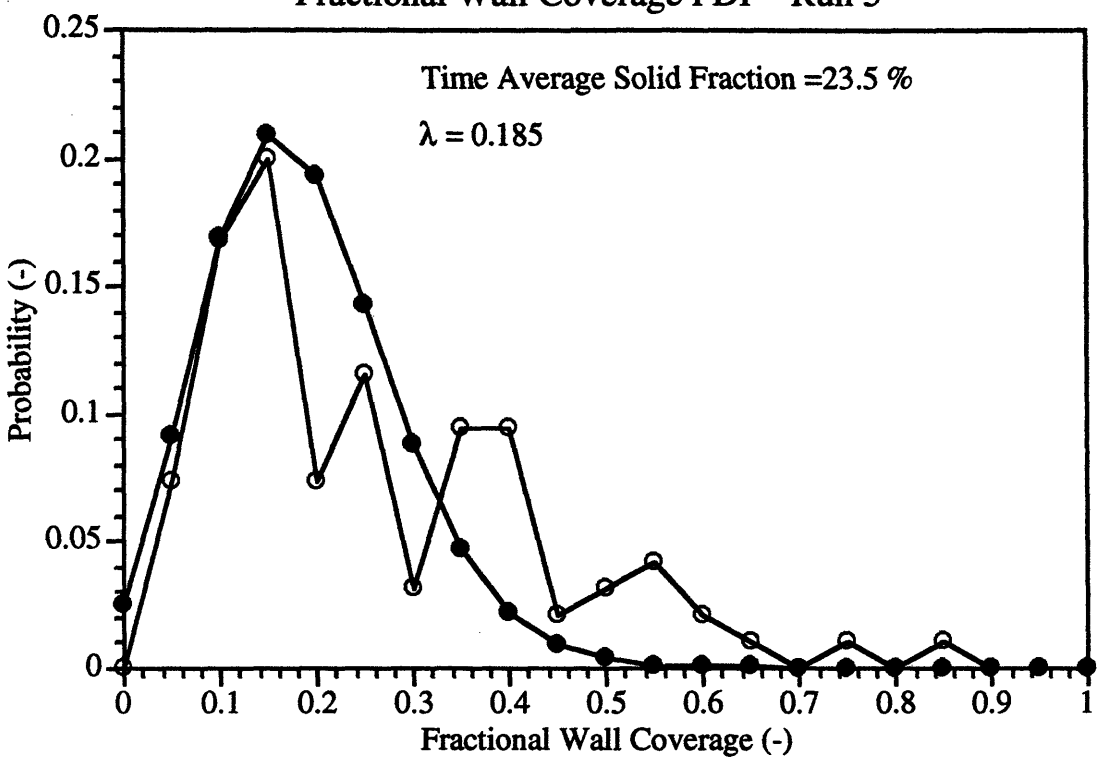

Figure 4.14: Fractional Wall Coverage Probability Density Function-Run 6

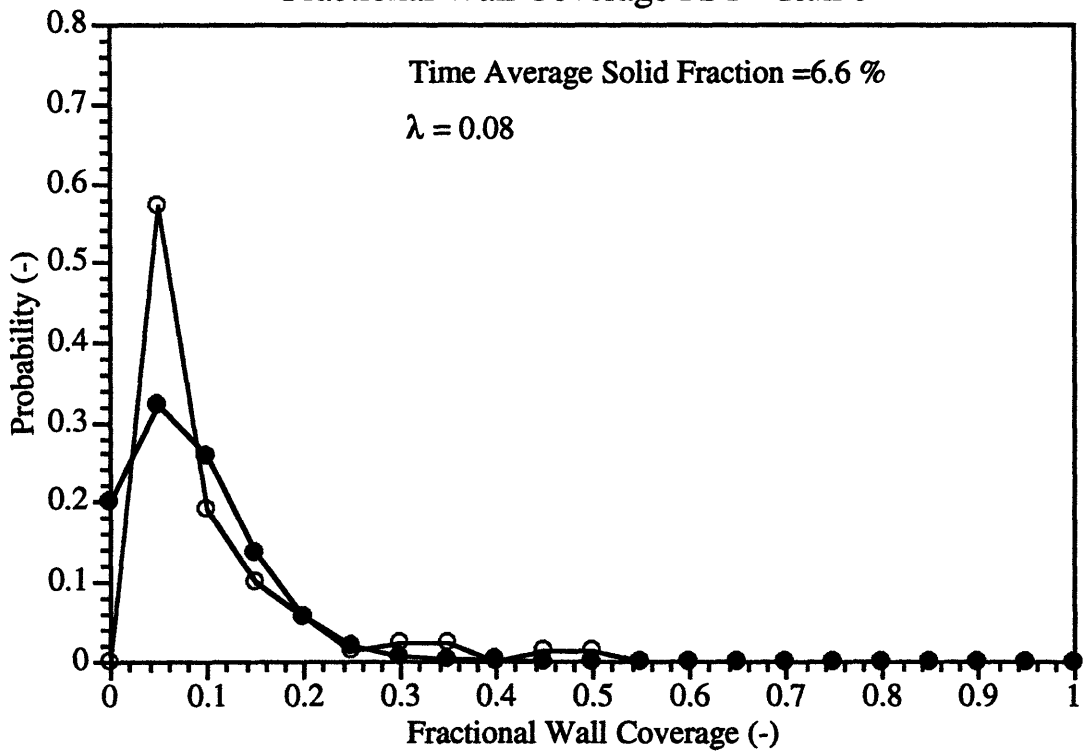

Table 4.3: Visual Experiment Results

Run	Bed Size	Matched Variable	Best Fit λ	Average Cross-Sectional Solid Fraction (%)
Dense Cases				
1	Large (3")	---	79	69
4	Small (2")	Solid Fraction	36	39
5	Small (2")	Solids Recycle Rate	18.5	24
Lean Cases				
2	Large (3")	---	9	9.1
3	Small (2")	Solid Fraction	9	8.4
6	Small (2")	Solids Recycle Rate	8	6.6

The major uncertainty in the interpretation of the visual data is in defining a cluster within the image analysis software. With white particles on a black background, a density threshold can be set for a particular grey-scale value in regions on the image (with 256 grey-scale levels, values range from 0 for black to 255 for white). Above this density threshold, particles are assumed close enough together to be defined as a cluster, below the density threshold, the space is either empty or the particle concentration is dilute enough to not contribute significantly to the particle-convective heat transfer. Setting the proper density threshold requires sampling some of the images to see what threshold best defines the transition between the dense phase and the dilute phase. A density threshold of 30 was used to identify clusters; this values was used for all cases since all were run with the same materials under the same lighting conditions. Although this method adds uncertainty to the data, analysis of each of the cases indicates that the trends observed in the data do not change with the selected density threshold. Figure 4.15 and 4.16 show that even as the density threshold varies, the various cases compare similarly. In other words, regardless of the uncertainty in this part of the analysis, the average fractional wall coverage is always higher in the larger bed for a given set of operating conditions.

Figure 4.15: Sensitivity to Cluster Definition - Dense Cases

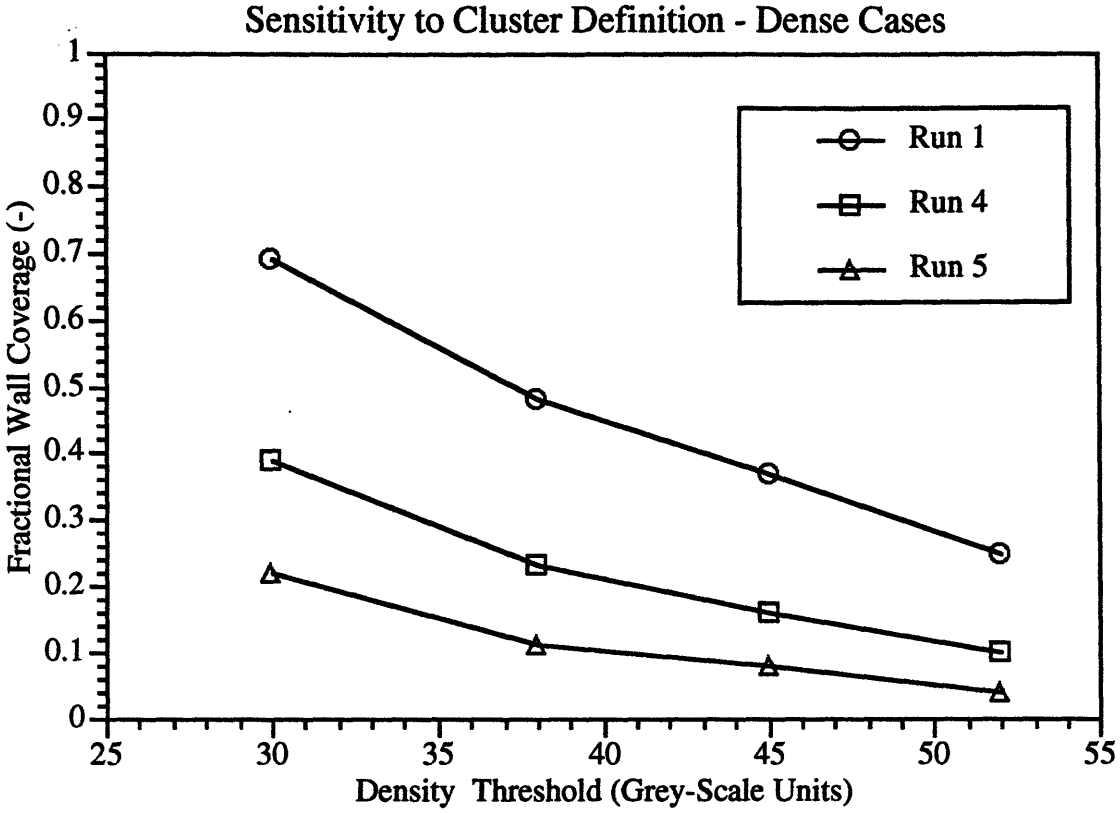

Figure 4.16: Sensitivity to Cluster Definition - Lean Cases

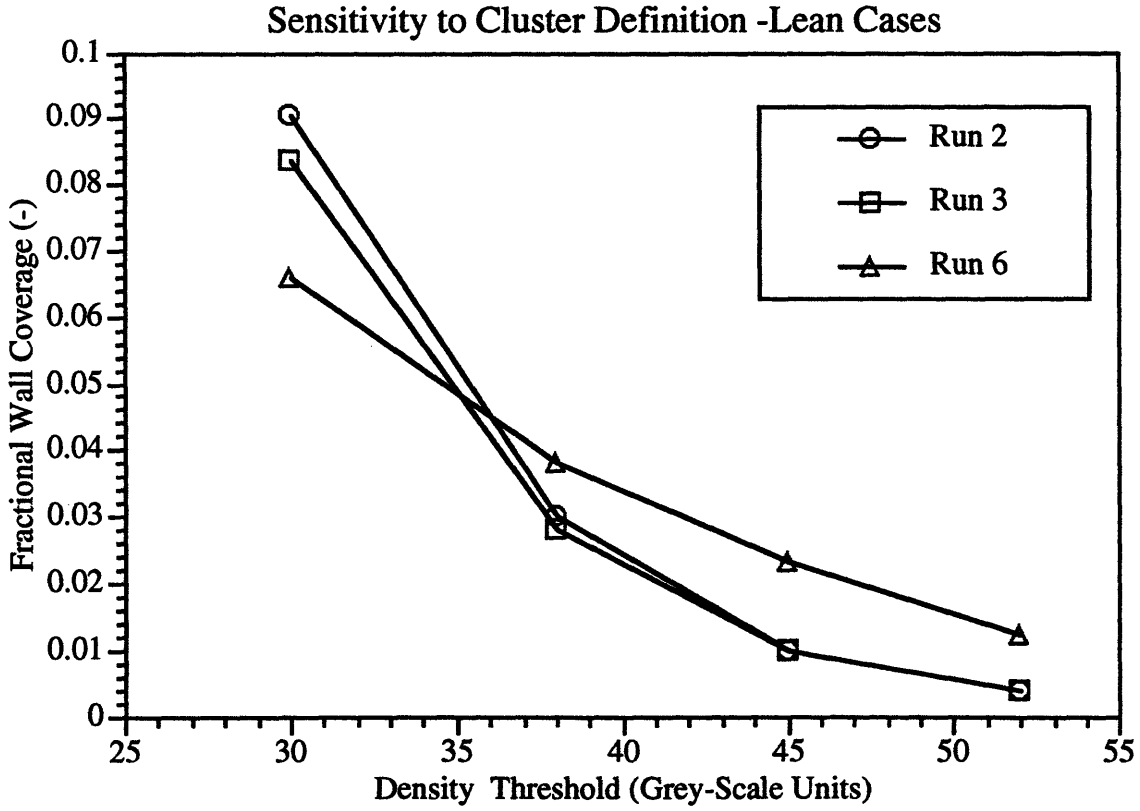

5.0 CONCLUSIONS

There is clearly a relationship between bed diameter, average solids concentration, and fractional wall coverage by clusters of particles. Between two beds which only differed in diameter, there was a consistent trend of wall coverage increasing with bed diameter. The trend was more pronounced at higher levels of particle concentration. Using the heat transfer model described in Chapter 4, the convective heat transfer coefficient (neglecting radiation) increased from 30 to 60 percent for a 50 percent increase in bed diameter at the same local cross-sectionally averaged solids concentration.

It is interesting to note that in the cases for which the particle concentration was leaner (Runs 2, 3, and 6), the trend of increasing f with D is not as pronounced; in fact, based on the subsequent statistical analysis, there appears to be a dependence only on average cross-sectional solid concentration. Runs 2 and 3 are the ones for which the hydrodynamic conditions were matched and they have roughly the same fractional wall coverage, while Run 6, which has slightly lower average cross-sectional solid concentration (but the same solids flux rate as Run 2), has a slightly lower value for f or λ. The apparently different trend in f vs. D for the leaner cases may be indicative of a different mechanism governing the wall coverage under lean conditions, however, more research would be required before such a statement could be made confidently.

6.0 REFERENCES

Arena, U., A. Marzocchella, L. Massimilla, and A. Malandrino, "Hydrodynamics of Circulating Fluidized Beds with Different Shape and Size," *Powder Technol.*, **70**, p.237, 1992.

Baskakov, A.P., "The Mechanism of Heat Transfer Between a Fluidized Bed and a Surface," *Int. Chem. Eng.*, **4**, p. 320, 1964.

Gelperin, N.I., and V.G. Einstein, "Heat Transfer in Fluidized Beds," *Fluidization*, J.F. Davidson and D. Harrison, eds., Academic Press, 1971.

Gloski, D., L. Glicksman, and N. Decker, "Thermal Resistance at a Surface in Contact with Fluidized Bed Particles," *Int. J. Heat Mass Transfer*, **27**, p. 599, 1984.

Mickley, H.S., and D.F. Fairbanks, "Mechanisms of Heat Transfer to Fluidized Beds," *AIChE Journal*, **1**, p. 374, 1955.

Subbarao, D., and P. Basu, "A Model for Heat Transfer in Circulating Fluidized Beds," *Int. J. Heat Mass Transfer*, **29**, p. 487, 1986.